

FUNDAMENTALS OF ENHANCED OIL RECOVERY

**Larry W. Lake, Russell T. Johns,
William R. Rossen, and Gary A. Pope**

Fundamentals of Enhanced Oil Recovery

Fundamentals of Enhanced Oil Recovery

Larry Lake
University of Texas at Austin

Russell T. Johns
The Pennsylvania State University

William R. Rossen
Delft University of Technology

Gary A. Pope
University of Texas at Austin

Society of Petroleum Engineers

© Copyright 2014 Society of Petroleum Engineers

All rights reserved. No portion of this book may be reproduced in any form or by any means, including electronic storage and retrieval systems, except by explicit, prior written permission of the publisher except for brief passages excerpted for review and critical purposes.

Printed in the United States of America

Disclaimer

This book was prepared by members of the Society of Petroleum Engineers and their well-qualified colleagues from material published in the recognized technical literature and from their own individual experience and expertise. While the material presented is believed to be based on sound technical knowledge, neither the Society of Petroleum Engineers nor any of the authors or editors herein provide a warranty either expressed or implied in its application. Correspondingly, the discussion of materials, methods, or techniques that may be covered by letters patents implies no freedom to use such materials, methods, or techniques without permission through appropriate licensing. Nothing described within this book should be construed to lessen the need to apply sound engineering judgment nor to carefully apply accepted engineering practices in the design, implementation, or application of the techniques described herein.

ISBN 978-1-61399-448-1
ISBN 978-1-61399-328-6 (print)

Society of Petroleum Engineers
222 Palisades Creek Drive
Richardson, TX 75080-2040 USA

<http://www.spe.org/store>

service@spe.org

1.972.952.9393

Contents

Foreword

1 Defining Enhanced Oil Recovery

- 1.1 Introduction to EOR
- 1.2 The Need for EOR
- 1.3 Incremental Oil
- 1.4 Category Comparisons
- 1.5 Summary
- 1.6 Units and Notation

2 Basic Equations for Fluid Flow in Permeable Media

- 2.1 Mass Conservation
- 2.2 Definitions and Constitutive Equations for Isothermal Flow
- 2.3 Energy-Balance Equations
- 2.4 Entropy-Balance Equations
- 2.5 Special Cases of the Strong Form
- 2.6 Overall Balances
- 2.7 Summary

3 Petrophysics and Petrochemistry

- 3.1 Porosity and Permeability
- 3.2 Capillary Pressure
- 3.3 Relative Permeability
- 3.4 Residual Phase Saturations
- 3.5 Three-Phase Effects
- 3.6 Permeable-Media Chemistry
- 3.7 Summary

4 Phase Behavior and Fluid Properties

- 4.1 Fundamentals of Phase-Equilibrium Thermodynamics
- 4.2 Phase Behavior of Pure Components
- 4.3 Phase Behavior of Mixtures
- 4.4 Ternary Diagrams
- 4.5 Quantitative Representation of Two-Phase Equilibria
- 4.6 Concluding Remarks

5 Displacement Efficiency

- 5.1 Definitions
- 5.2 Immiscible Displacement
- 5.3 Dissipation in Immiscible Displacements

- [5.4 Ideal Miscible Displacements](#)
- [5.5 Dissipation in Miscible Displacements](#)
- [5.6 Generalization of Fractional-Flow Theory](#)
- [5.7 Application to Three-Phase Flow](#)
- [5.8 Modeling EOR Processes With Two-Phase Fractional-Flow Theory](#)
- [5.9 Concluding Remarks](#)

6 Volumetric Sweep Efficiency

- [6.1 Definitions](#)
- [6.2 Areal Sweep Efficiency](#)
- [6.3 Measures of Heterogeneity](#)
- [6.4 Displacements With No Vertical Communication](#)
- [6.5 Vertical Equilibrium](#)
- [6.6 Special Cases of Vertical Equilibrium](#)
- [6.7 VE Summary](#)
- [6.8 Instability Phenomena](#)
- [6.9 Gravity Segregation in Gas EOR](#)
- [6.10 Summary](#)

7 Solvent Methods

- [7.1 General Discussion of Solvent Flooding](#)
- [7.2 Solvent Properties](#)
- [7.3 Solvent and Crude-Oil Properties](#)
- [7.4 Solvent-Water Properties](#)
- [7.5 Solvent Phase-Behavior Experiments](#)
- [7.6 Dispersion and Slug Processes](#)
- [7.7 Two-Phase Flow in Solvent Floods](#)
- [7.8 Solvent Floods With Viscous Fingering](#)
- [7.9 Solvent Flooding and Residual Oil Saturation](#)
- [7.10 Estimating Field Recovery](#)
- [7.11 Concluding Remarks](#)

8 Polymer Methods

- [8.1 The Polymers](#)
- [8.2 Polymer Properties](#)
- [8.3 Profile Control](#)
- [8.4 Polymer Degradation](#)
- [8.5 Fractional Flow in Polymer Floods](#)
- [8.6 Elements of Polymer-Flood Design](#)
- [8.7 Field Results](#)
- [8.8 Concluding Remarks](#)

9 Surfactant Methods

- [9.1 The Processes](#)
- [9.2 The Surfactants and Surfactant Selection](#)

- [9.3 Surfactant/Oil/Brine Phase Behavior](#)
- [9.4 Nonideal Effects](#)
- [9.5 Phase Behavior and IFT](#)
- [9.6 Other Phase Properties](#)
- [9.7 High-Capillary-Number Relative Permeabilities](#)
- [9.8 Alkaline/Surfactant Flooding](#)
- [9.9 Surfactant Formation](#)
- [9.10 Displacement Mechanisms](#)
- [9.11 Rock-Fluid Interactions](#)
- [9.12 Fractional-Flow Theory in SP and ASP Floods](#)
- [9.13 Typical Production Responses](#)
- [9.14 Designing SP/ASP Floods](#)
- [9.15 Concluding Remarks](#)

10 Foam-Enhanced Oil Recovery

- [10.1 Introduction](#)
- [10.2 Nature of Foam in Permeable Media](#)
- [10.3 Mobility of Gas and Water in Foam](#)
- [10.4 Strong Foams in Two Regimes](#)
- [10.5 Foam Propagation](#)
- [10.6 Effect of Oil and Wettability on Foam](#)
- [10.7 Modeling Foam Flow: Mechanistic Foam Models](#)
- [10.8 Modeling Foam Flow: Local Steady-State Models](#)
- [10.9 Summary](#)

11 Thermal Methods

- [11.1 Process Variations](#)
- [11.2 Physical Properties](#)
- [11.3 Fractional Flow in Thermal Displacements](#)
- [11.4 Heat Losses From Equipment and Wellbores](#)
- [11.5 Heat Losses to Overburden and Underburden](#)
- [11.6 Steamdrives](#)
- [11.7 Steam Soak](#)
- [11.8 In-Situ Combustion](#)
- [11.9 SAGD](#)
- [11.10 Concluding Remarks](#)

[Nomenclature](#)

[References](#)

[Author Index](#)

[Subject Index](#)

Foreword

This book is the second edition of the 1989 book by the name *Enhanced Oil Recovery*. As such, it reflects the substantial changes that have taken place in enhanced oil production technology since that time: from a collection of minor technologies in the early 1980s to a significant and growing portion of the worldwide oil production today.

While it is true that a textbook is out of date the day it is published, there are a couple of ways to head off obsolescence:

First, broaden the topical material. Although the current book is on enhanced oil recovery (EOR), and EOR is *not* waterflooding, there is substantial coverage on waterflooding, as there is on basic equations, petrophysics, and phase behavior. Indeed, the 1989 book has served as a text for courses (or portions thereof) in numerical simulation, waterflooding, thermodynamics, and petrophysics.

Second, stick to the fundamentals. The fundamentals change slowly if at all, and the current text continues to focus on the basics of material and energy balances, phase behavior, and fractional flow theory.

The target audience remains the same as for the 1989 text: It is a graduate-level textbook whose material is intended to be taught over two long semesters.

So what are the differences with the 1989 text? We have done the following:

- Added example calculations to several of the chapters
- Included explanations of combined condensing and vaporizing displacements in gas floods and their impact on the developed miscible process
- Expanded coverage of foam EOR to an entire chapter

- Added discussion of EOR types, such as steam-assisted gravity drainage and alkaline-surfactant polymer flooding, that were not prominent in 1989
- Deleted coverage of material that did not readily lend itself to classroom instruction (based on many years of classroom experience)
- Added new material on dispersion, decline curves, and the use of so-called Walsh diagrams
- Added material on new technological advances, most notably in the coverage of chemical EOR

The biggest change is that the current text now has four co-authors whose classroom and research expertise in their respective technologies has made the text much stronger than before. It also helps to have four sets of eyes to spot inconsistencies, unclarities, errors, and all around goofs, especially in the equations.

Even with the new version, we are aware of several omissions:

- Low or adjusted salinity water flooding
- Gravity stable surfactant floods
- Hybrid methods such as heated surfactant floods and polymer floods
- Technologies involving in-situ modification of polymers
- Electromagnetic oil recovery
- Seismic oil recovery

These could become glaring omissions depending on future practice. However, we continue to think that reliance on fundamentals—conservation laws, phase behavior, and fractional flow theory—will at least make extension to new methods easier.

Acknowledgments are owed all around:

Larry W. Lake would like to thank Joanna Castillo for substantial and consistent help with the figures, and Mary Pettengill for tirelessly looking up and correcting the references.

Russell T. Johns would like to acknowledge Hung Lai who did the unenviable task of scanning in the first edition of the book and

formatting it in preparation for the second edition.

William R. Rossen would like to thank Joeri Brackenhoff for helping with revising figures and references.

Gary A. Pope would like to acknowledge the many talented graduate students who contributed to the numerous advances in chemical EOR over the past 25 years.

And finally, we dedicate this text to the help and instruction provided by decades of university and short course students. We learn more from you than you from us.

Chapter 1

Defining Enhanced Oil Recovery

Enhanced oil recovery (EOR) is oil recovery by the injection of materials not normally present in petroleum reservoirs. This definition covers all modes of oil-recovery processes (drive, push-pull, and well treatments) and most oil-recovery agents. EOR technologies are also being used for in-situ extraction of organic pollutants from permeable media. In these applications, the extraction is referred to as *cleanup* or *remediation* and the pollutant as *product*. Aspects of these technologies also apply to carbon dioxide (CO_2) storage.

The definition does not restrict EOR to a particular phase (primary, secondary, or tertiary) in the producing life of a reservoir. Primary recovery is oil recovery by natural drive mechanisms: solution gas, water influx, gas-cap drive, or gravity drainage, as illustrated in [Fig. 1.1](#). Secondary recovery refers to techniques, such as gas or water injection, that have the main purpose of boosting or maintaining reservoir pressure. Tertiary recovery is any technique applied after secondary recovery. Nearly all EOR processes have been at least field tested as secondary displacements. Many thermal methods are commercial in both primary and secondary modes. Much interest has been focused on tertiary EOR, but our definition does not impose any such restriction.

A related definition is *improved* oil recovery, which is EOR plus several technologies that are also intended to increase ultimate oil recovery. Examples of these are hydraulic fracturing, horizontal and multilateral wells, infill drilling, well stimulation, and optimizing the production or injection rates of individual wells.

Definitions of EOR can be important in areas where regulatory agencies give tax or price credits to promote use of EOR. The definition given above is the one used throughout this text.

The definition does exclude waterflooding and is intended to exclude all pressure-maintenance processes. The distinction between pressure maintenance and displacement is fuzzy because displacement occurs in many pressure-maintenance processes. Moreover, agents such as methane in a high-pressure gas drive, or carbon dioxide in a reservoir with substantial native CO₂, do not satisfy the definition, yet both are clearly EOR processes. The same can be said of CO₂ storage. Usually, the EOR cases that fall outside the definition can be clearly classified by the intent of the process.

[Fig. 1.1](#) also shows the major categories of EOR. This text is largely organized around the solvent ([Chapter 7](#)), chemical ([Chapters 8–10](#)), and thermal ([Chapter 11](#)) categories. Although EOR does not include waterflooding, this technology is the mother of all displacement techniques, and some (in fact extensive) coverage is provided in [Chapters 3–6](#). Note that so-called unconventional recovery, or oil and gas recovery from very low-permeability media through fracturing, is part of primary recovery.

Another perspective on the recovery phases is provided in [Fig. 1.2](#). This figure shows oil rate (top in std volumes/time) on the upper plot, pressure (well pressure P_{wf} , average reservoir pressure \bar{P} , and injection well pressure P_{Inj}) on the middle plot, and average oil saturation on the bottom plot, all on a common time axis. The figure is a schematic that treats injection and production as occurring through a single well (in reality, most fields have many wells). The time axis is divided into primary, secondary, and tertiary recovery phases as indicated.

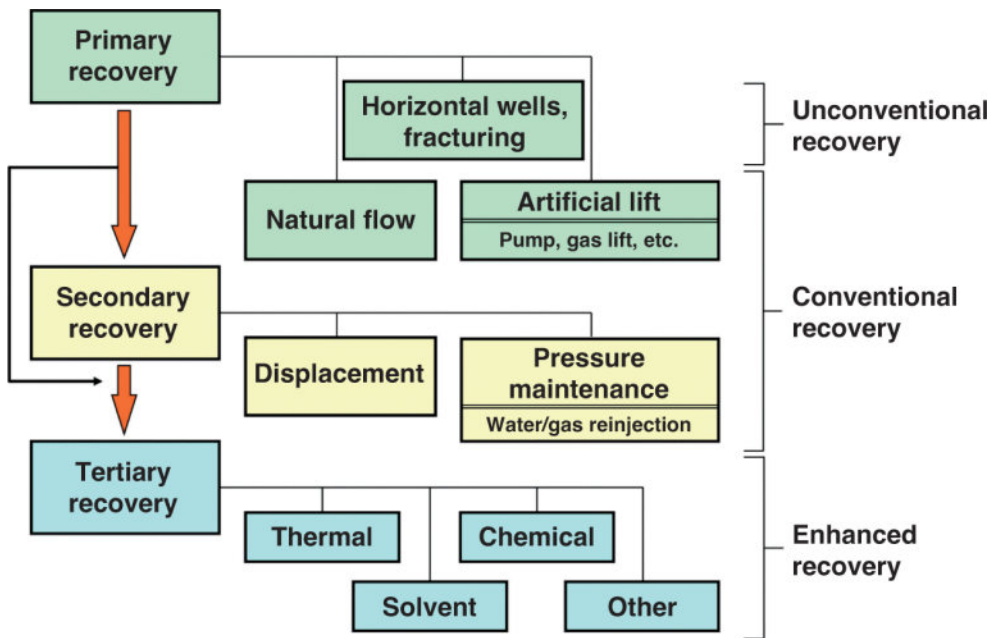


Fig. 1.1—Oil-recovery classifications (adapted from *Oil & Gas Journal*).

Much depends on the economically limiting rate (labeled EL) and the limiting pressure (P_{Lim}) on the upper and middle plots respectively. EL is the rate at which the revenue from production equals the operating costs of the field. P_{Lim} is the well pressure below which fluids cannot flow to the surface without external support. Of the two, EL is the most important because it is the portal between the engineering and economic worlds.

Primary production is typically production by fluid expansion and pore-volume contraction caused by pressure decline. In this period, there is no injection and average oil saturation stays roughly constant (there are exceptions). The rate is characterized by a rapid increase, limited mainly by the rate at which wells are drilled, followed by a plateau period and then a decline. The plateau period ends when the well pressure falls to P_{Lim} . The average pressure falls throughout, and primary recovery ends when the drawdown pressure ($\bar{P} - P_{Lim}$) is insufficient to maintain the oil rate above the EL. There is usually little or no water production during primary production. The absence of water production and the prevalence of natural (unassisted) flow usually make this the most profitable phase of the field life.

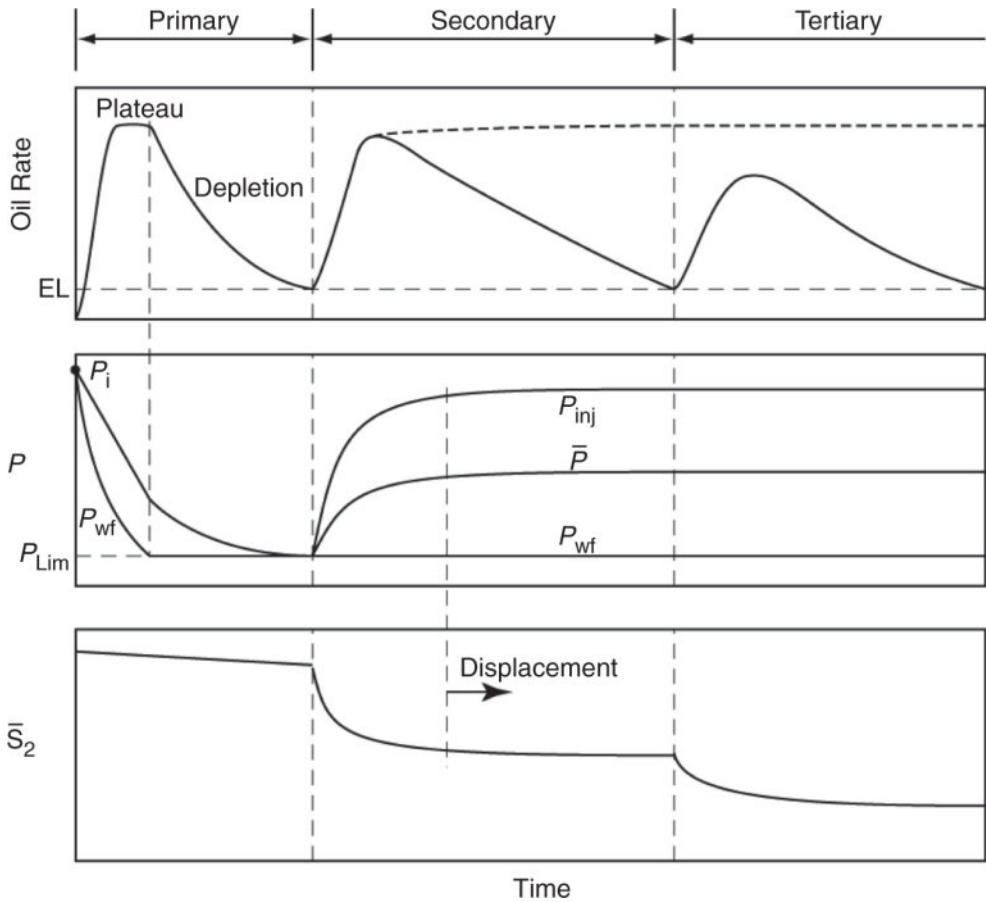


Fig. 1.2—Schematic of production phases.

Secondary production is production by injection of a second fluid, occasionally natural gas, but most commonly water. In this period and throughout the remainder of the field life, the producing well pressure is at P_{Lim} (wells are said to be pumped off), and the average pressure rises. There is a new pressure P_{Inj} for the injection well. Of course we must have $P_{Inj} > \bar{P} > P_{wf} = P_{Lim}$ to maintain flow. When \bar{P} becomes constant, the pressure is said to be “maintained,” and, of course, production rises because of the increased drawdown.

The increased drawdown, however, causes the injected fluid to be produced, as indicated by the dotted line in the upper plot. An increase in \bar{P} would cause fluids to contract; therefore, production would proceed from this point mainly by displacement. The displacement causes the average oil saturation to decline. Secondary production ends when the rate again approaches the EL, at which point water production can be many times the oil production.

Tertiary production commences when waterflooding becomes uneconomical or when the rate falls below the EL. At this time, chemical agents (surfactants or solvents) or heat are injected that cause physical or chemical changes in the oil. The entire nature of the recovery is based on displacement now, and the pressures change little with time. All the production occurs because of declining average oil saturation.

Several points deserve to be summarized from [Fig. 1.2](#).

1. Production can be increased by lowering P_{Lim} throughout the life of the field. Much oilfield technology is directed to exactly this goal.
2. In the same fashion, production can be increased by increasing the proportionality constant between drawdown and rate, the so-called productivity index (PI) of a producer. Much oilfield technology, including some forms of EOR, is devoted to this.
3. As conditions change, EL need not be constant. Indeed, it is probable that EL will increase during tertiary recovery when agent costs become a principal factor in production. EL is exceptionally sensitive to oil price.
4. The lengths of the periods in the figure are highly variable; usually, primary production occurs over a shorter time than secondary production. The lengths for primary and tertiary production are approximately the same. The total field life can exceed 100 years.
5. Typical ultimate recoveries for primary, secondary, and tertiary recovery are 10%, 25%, and 10% of the original oil in place (OOIP), but with much variation. This gives a typical ultimate recovery of 35% with conventional production. In most cases,

the peak waterflood oil rate is less than the primary plateau. The ultimate recoveries are the areas under the rate plot in [Fig. 1.2](#).

6. Remember that the plot in [Fig. 1.2](#) is a schematic. There are many varieties of primary production (Walsh and Lake 2003). For example, sometimes there is no primary plateau. In others, economic conditions do not justify EOR regardless of other favorable factors. Moreover, of course, wells can be added and removed (which is roughly equivalent to changing the PI) throughout the life of the field. For steeply dipping reservoirs, flow potentials should replace pressures in [Fig. 1.2](#).
7. In practice, operations in a reservoir are normally converted or switched before the rate reaches the EL. The switching occurs in anticipation of the time that the rate attains the EL.
8. Although the sequence shown in [Fig. 1.2](#) is typical, sometimes entire phases are missing. As discussed previously, many thermal projects have not undergone primary or even secondary recovery. Furthermore, the times of switching from one phase to another may be different from those shown. Parra-Sanchez (2010) has shown that earlier switching times (i.e., switching from primary to secondary production before reaching the economic limit) can be more profitable.

This text is about the displacement part of the figure, which includes waterflooding and, of course, EOR. Because the pressures are constant during these phases, the fluids behave as though they were incompressible, a fact that justifies the widespread use of this assumption throughout this text. Incompressibility also moves the drawdown pressure and pressure changes to the background in most of our discussion, although it must be remembered that if there is no drawdown, there can be no production.

1.1 Introduction to EOR

1.1.1 The EOR Target. Interest in EOR centers on the amount of oil to which it can be applied. This EOR target oil is the amount that is unrecoverable by conventional means ([Fig. 1.1](#)). A large body of

statistics shows that conventional ultimate oil recovery (the percentage of the OOIP at the time that further conventional recovery becomes uneconomical) is approximately 35%. This means, for example, that a field that originally contained 1 billion barrels will have 650,000,000 barrels left in it at the end of its conventional life. Considering the OOIP in all the reservoirs in the United States, this value is much larger than targets from exploration or increased drilling.

The ultimate recovery efficiency expected after primary and secondary recovery is shown in [Fig. 1.3](#). This figure also shows that there is enormous variability in ultimate recovery within a single geographic region, which is why we cannot target reservoirs with EOR by region. [Fig. 1.3](#) shows also that the median ultimate recovery is the same for most regions, a fact no doubt bolstered by the large variability within each region. The median ultimate recovery of approximately 35% shows that 65% remains, a significant target for EOR.

1.2 The Need for EOR

Enhanced oil recovery is one of the technologies needed to maintain reserves. What follows is only a brief discussion of reserves because this is a complex and extensive subject. See Cronquist (2001) for more details.

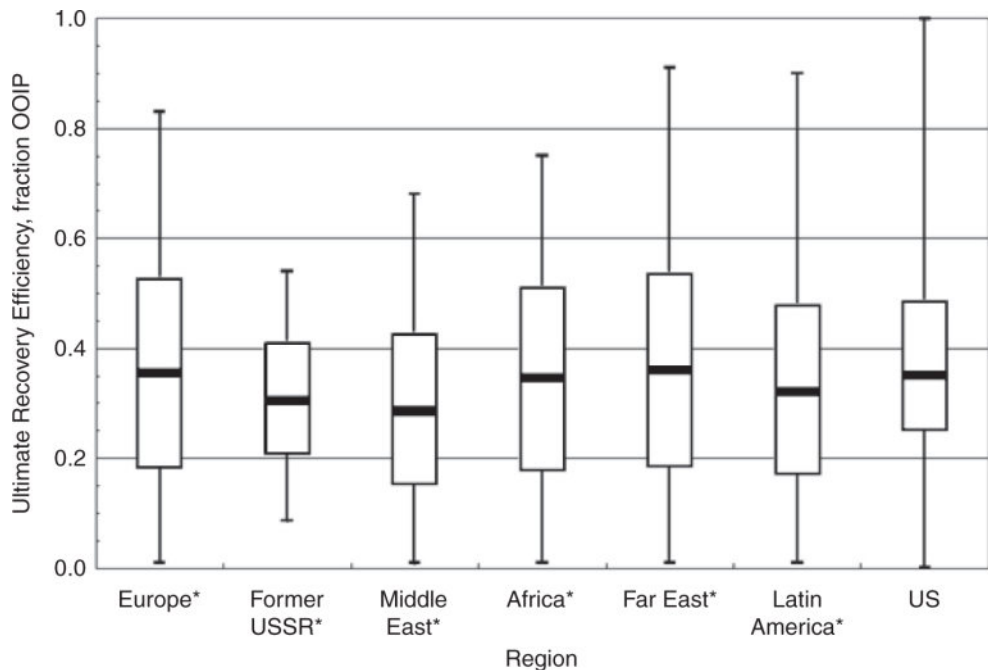


Fig. 1.3—Box plots of ultimate oil recovery efficiency. 75% of the ultimate recoveries in a region fall within the vertical boxes; the median recovery is the horizontal line in the box; the vertical lines give the range. Ultimate recovery is highly variable, but the median is approximately the same everywhere [data from Laherrere (2001); US data from TORIS].

1.2.1 Reserves. One definition of reserves is that they are petroleum (crude and condensate) recoverable from known reservoirs under prevailing economics and technology. They are given by the following material-balance equation:

$$\begin{pmatrix} \text{Present} \\ \text{reserves} \end{pmatrix} = \begin{pmatrix} \text{Past} \\ \text{reserves} \end{pmatrix} + \begin{pmatrix} \text{Additions} \\ \text{to reserves} \end{pmatrix} - \begin{pmatrix} \text{Production} \\ \text{from} \\ \text{reserves} \end{pmatrix}.$$

There are actually several categories of reservoirs (proven, probable, etc.); the distinctions between these are very important to economic evaluation (Rose 2001; Cronquist 2001). Reserves can change with time because the last two terms on the right can change with time. It is in the best interests of producers to maintain reserves constant with time, or even for them to increase.

1.2.2 Adding to Reserves. The four categories of reserve additions are

1. Discovering new fields
2. Discovering new reservoirs
3. Finding more oil in known fields
4. Redefining reserves because of changes in the economics of extraction technology

We discuss Category 4 in the remainder of this text.

EOR is in competition with conventional oil recovery because most producers have assets or access to assets in all the categories in [Fig. 1.1](#). The competition is based largely on economics in addition to reserve replacement. Currently, many EOR technologies are competitive with drilling-based reserve additions. The key to economic competitiveness is how much oil can be recovered with EOR. The estimation of this is the next topic to be discussed.

1.3 Incremental Oil

1.3.1 Definition. A universal technical measure of the success of an EOR process is the amount of incremental oil recovered, or IOR. (We note the possible confusion between IOR as improved oil recovery and IOR as incremental oil recovery. What is meant should be clear from the context of the text. IOR as improved oil recovery is not used further here.) [Fig. 1.4](#) defines the concept of incremental oil. Imagine a field, reservoir, or well in which the oil rate is declining, for example, from A to B . At B , an EOR project is initiated, and, if this is successful, the rate should show a deviation from the projected decline at some time after B . Incremental oil is the difference between what was actually recovered, B to D , and what would have been recovered had the process not been initiated, B to C . Because areas under rate vs. time curves are amounts, this is the shaded region in [Fig. 1.4](#).

As simple as the concept in [Fig. 1.4](#) is, IOR is difficult to determine in practice. There are several reasons for this.

1. Combined (commingled) production from EOR and non-EOR wells. Such production makes it difficult to allocate the EOR-produced oil to the EOR project. Commingling occurs when, as is usually the case, the EOR project is phased into a field undergoing other types of recovery.
2. Oil from other sources. Usually the EOR project has experienced substantial well cleanup or other improvements before startup. The oil produced as a result of such treatment is not easily differentiated from EOR oil.
3. Inaccurate estimate of the hypothetical decline. The curve from *B* to *C* in [Fig. 1.4](#) must be estimated accurately. However, because the decline did not occur, there is no way of assessing this accuracy.

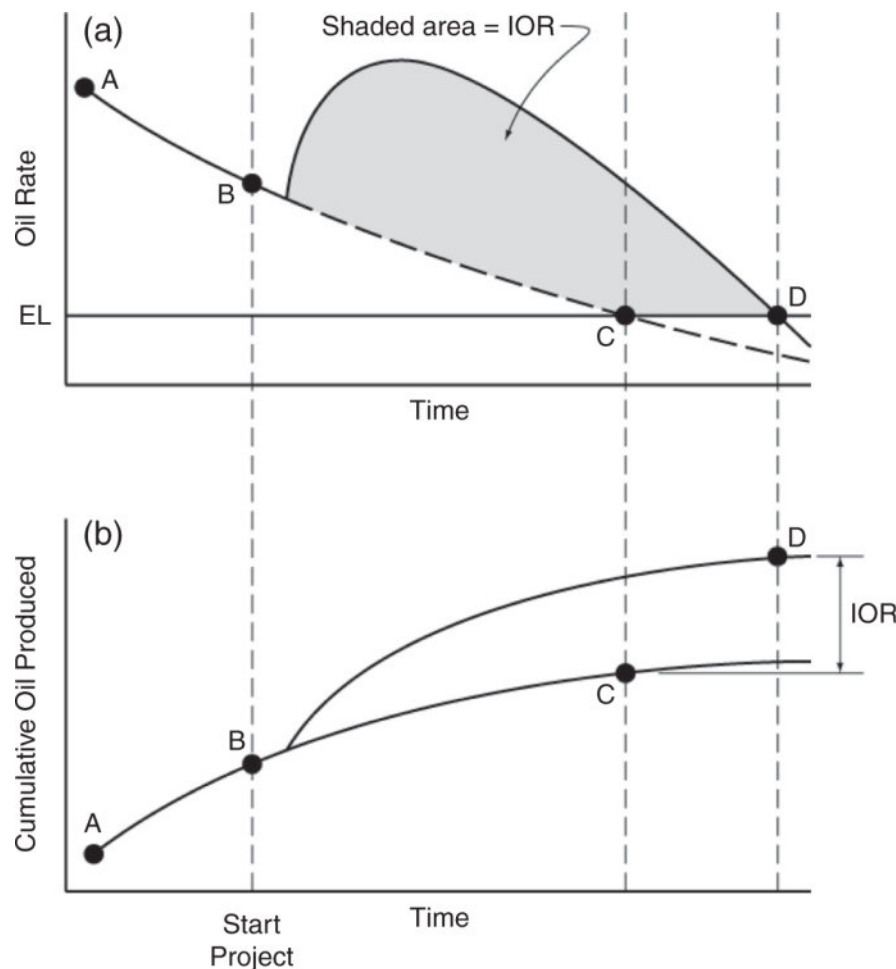


Fig. 1.4—Schematic of IOR from typical EOR response: (a) rate vs. time and (b) cumulative vs. time.

Ways to infer IOR from production data range from highly sophisticated numerical models to graphical procedures. One of the latter, based on decline-curve analysis, is covered in the next section.

1.3.2 Estimating IOR Through Decline Curves. Decline-curve analysis can be applied to almost any hydrocarbon-production operation. The following is an abstraction of the practice as it applies to EOR. See Walsh and Lake (2003) for a more in-depth discussion. The basic idea was outlined in the classic paper by Arps (1956); see also Fetkovich (1980). The objective is to derive relations between oil rate and time, and then between cumulative production and rate.

The oil rate q changes with time t in a manner that defines a decline rate D according to

The rate has units of (or [=]) amount or standard volume per time and D [=]1/time. Time is in units of days, months, or even years consistently with q . D itself can be a function of rate, but here it is assumed to be constant (representing an exponential decline). Integrating Eq. 1.1 gives

where qi is the initial rate or q evaluated at $t = 0$, the start of the decline-curve period. Eq. 1.2 suggests a semilogarithmic relationship between rate and time, as illustrated in [Fig. 1.5a](#). Exponential decline is the most common type of analysis used.

[Fig. 1.5](#) illustrates schematically a set of data points that begin an exponential decline at the ninth point, where by definition $t = 0$. The solid line represents the fit of the decline-curve model to the data points. q_i is the rate given by the model at $t = 0$, not necessarily the measured rate at this point. The slope of the model is the negative of the decline rate divided by 2.303 because the semilog scale plots base-10 rather than natural logarithms.

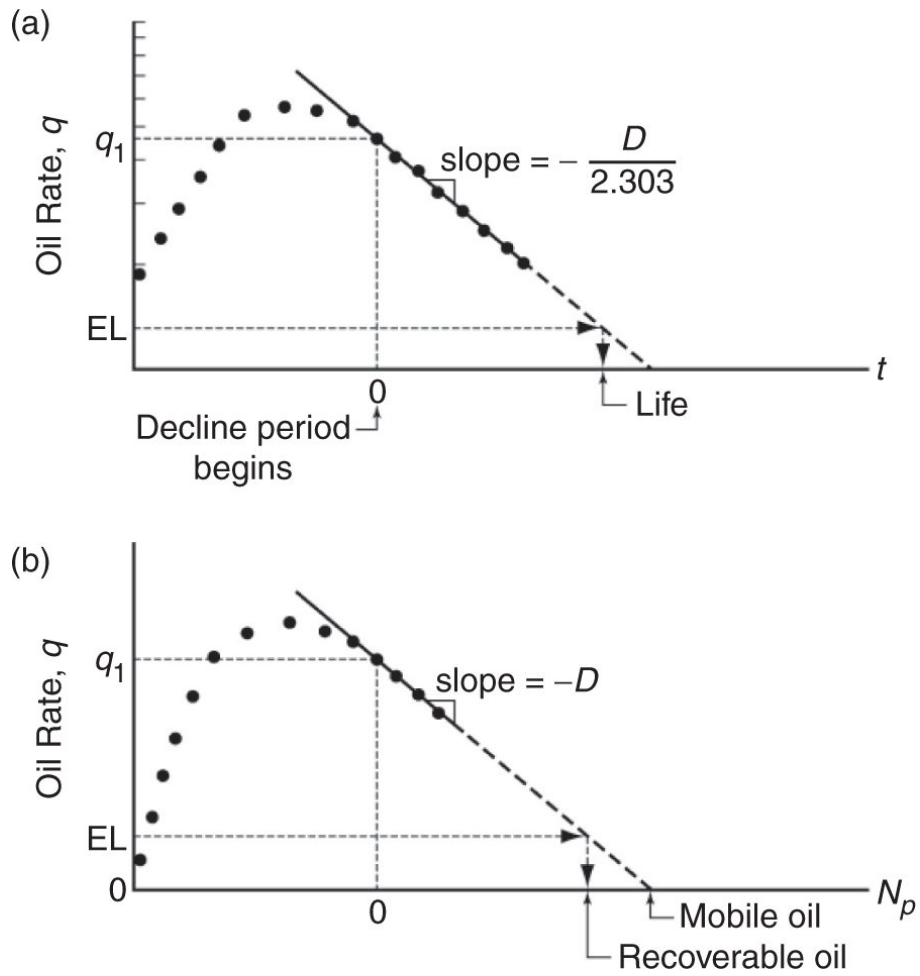


Fig. 1.5—Schematic of exponential decline on (a) rate vs. time and (b) rate vs. cumulative plots.

Because the model plot is a straight line, it can be extrapolated (solid line in Fig. 1.5) to some future rate. If q_{EL} designates the EL (the *economic limit* discussed previously) of the project under consideration, then the point at which the model extrapolation reaches q_{EL} is an estimate of the project's (or well's) economic life. The economic limit is a nominal measure of the rate at which the revenues become equal to operating expenses plus overhead. q_{EL} can vary from a fraction to a few hundred barrels per day depending on operating conditions. It is also a function of the prevailing economics: as the oil price increases, q_{EL} decreases, which is an important factor in reserve calculations.

The rate vs. time analysis is useful, but the rate vs. cumulative curve is more helpful for estimating IOR. The cumulative oil produced is given by

The definition in this equation is general and will be used throughout the text, but especially in [Chapter 2](#). To derive a rate vs. cumulative expression, insert Eq. 1.1, integrate, and identify the resulting terms with (again) Eq. 1.1. This gives

Eq. 1.4 says that a plot of oil rate vs. cumulative production should be a straight line on linear coordinates, as illustrated in Fig. 1.5b.

Note that the cumulative oil points plotted on the horizontal axis of this figure come from the oil-rate data, not from the decline curve. If this were not so, the rate vs. cumulative plot would provide no additional information. Calculating N_p normally requires numerical integration of the rate data.

Using the model Eqs. 1.3 and 1.4 to interpret data, as illustrated in Fig. 1.5, is the essence of reservoir engineering practice, which can be described as follows:

1. Develop a model as we have done to arrive at Eqs. 1.3 and 1.4. Often the model equations are far more complex than these, but the method is the same regardless of the complexity.
 2. Fit the model to the data. Remember that the points in [Fig. 1.5](#) are data. The lines are the model.
 3. With the model as fitted to the data (the model is now calibrated), extrapolate the model to make predictions.

At the onset of the decline period, the data again start to follow a straight line through which one can fit a linear model. In effect, what has occurred on this plot is that we have replaced time in [Fig. 1.3](#) with cumulative oil produced in [Fig. 1.5b](#), but there is one very important

distinction: both axes in [Fig. 1.5b](#) are now linear. This linearity has three important consequences:

1. The slope of the model is now $-D$ because no correction for log scales is required.
2. The origin of the model can be shifted in either direction by simple additions.
3. The rate can now be extrapolated to zero.

Point 2 means that we can plot the cumulative oil produced for all periods before the decline-curve period (or for previous decline-curve periods) on the same rate vs. cumulative plot. Point 3 means that we can extrapolate the model to find the total mobile oil (when the rate is zero) rather than just the recoverable oil (when the rate is at the economic limit).

Rate vs. cumulative plots are simple yet informative tools for interpreting EOR processes because they allow estimates of IOR by distinguishing between recoverable and mobile oil. We illustrate how this comes about through some idealized cases.

[Fig. 1.6](#) shows rate vs. cumulative plots for cases that feature an exponential decline just before and immediately after the initiation of an EOR process. We are showing the model lines (not the points) only for ease of presentation. Placing both periods on the same horizontal axis is permissible because of the scaling arguments mentioned previously.

In the case shown in [Fig. 1.6a](#), the EOR process did not accelerate production because the decline rates in both periods are the same; however, the process did increase the amount of mobile oil, which in turn caused some incremental oil production. In this case, incremental recovery and mobile oil are the same. Such idealized behavior would be characteristic of thermal, surfactant/polymer (SP), and solvent processes.

[Fig. 1.6b](#) shows another extreme case in which production is only accelerated, the pre- and post-EOR decline rates being different. Now the curves extrapolate to a common value of mobile oil, but still with a positive IOR. We expect correctly that processes that behave

this way will produce less oil than those that increase mobile oil, but they can still be profitable, particularly if the agent used to bring about this result is inexpensive. Processes that ideally behave in this manner are polymer floods and polymer gel processes, which do not affect residual oil saturation, but displace previously bypassed oil and cause it to be produced. Acceleration processes are especially sensitive to the economic limit; large economic limits imply large IOR.

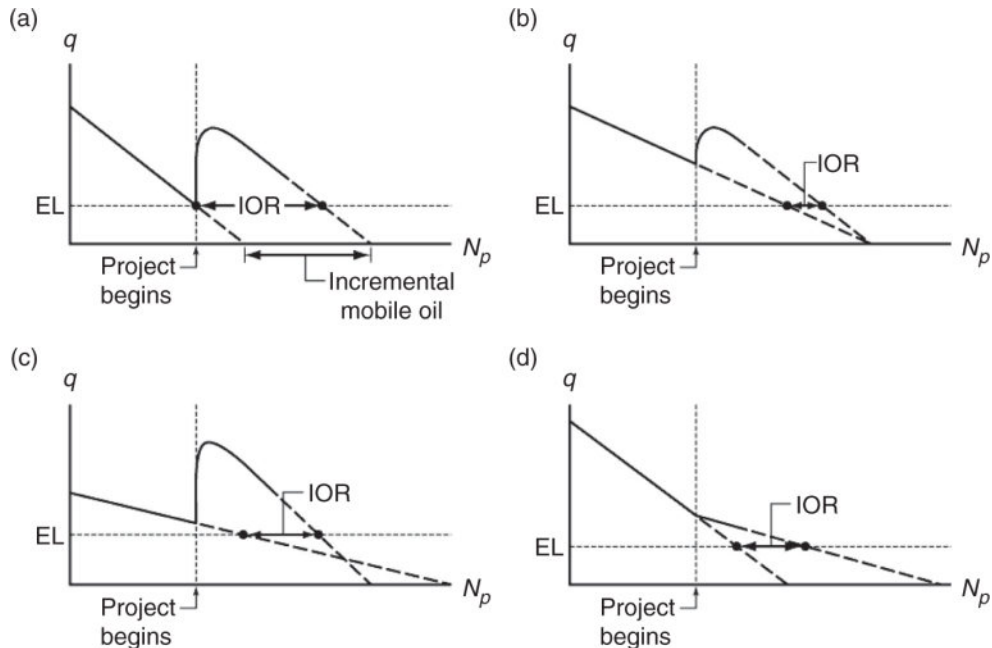


Fig. 1.6—Schematic of rate vs. cumulative plots for various EOR responses. All projects show a positive IOR: (a) the mobile oil increases; (b) the mobile oil is unchanged; (c) the mobile oil decreases; and (d) the mobile oil increases, but there is no peak in the oil rate.

[Fig. 1.6c](#) shows an unfavorable case in which the process actually reduced mobile oil. We would never deliberately try to reduce mobile oil in practice, but the project could still be profitable if, as in the case shown, the accelerated production offsets the loss of mobile oil enough so that the IOR is still nonzero. Behavior like this probably indicates a target for a future EOR application.

[Fig. 1.6d](#) illustrates another common case. Here, the EOR process increases mobile oil, but also reduces the decline rate. Processes like these are common in solvent floods.

1.4 Category Comparisons

1.4.1 Comparative Performances. Most of this text covers the details of EOR processes. At this point, we compare the performance of the three basic EOR processes and introduce some issues to be discussed later in the form of screening guides. The performance is represented as typical oil recoveries (IOR expressed as a percent of OOIP) and by various utilization factors. Both are based on actual experience. Utilization factors represent the amount of an EOR agent required to produce a barrel of incremental oil. They are a rough measure of process profitability.

[**Table 1.1**](#) shows these summaries for chemical EOR processes. Sensitivity to high brine salinities is common to all chemical-flooding EOR. Total dissolved solids should be less than 100,000 g/m³, and hardness should be less than 2,000 g/m³. See [Chapters 8](#) and [9](#) for more details. Chemical agents are also susceptible to loss through rock-fluid interactions. Maintaining adequate injection rates is a persistent issue with chemical methods.

Historical oil recoveries have ranged from small for polymer floods (5%) to moderately large (15%) for other methods. Chemical utilization factors have meaning only when compared with the costs of the individual agents; polymer, for example, is usually three to four times as expensive (per unit mass) as surfactants. The average for polymer floods is based on data that include both mobility-control floods and profile-control treatments. The latter generally recovers less oil. Mobility-control floods, particularly those performed recently, have averaged approximately 10% recovery. The alkaline-flooding process is generally not used today, having been supplanted by alkaline/surfactant/polymer (ASP) flooding. The latter technology is too new to report summary statistics, but initial results indicate that it performs as well or better than SP floods.

TABLE 1.1—CHEMICAL EOR PROCESSES				
Process	Recovery Mechanism	Issues	Typical Recovery (%)	Typical Agent Utilization*
Polymer	Increases volumetric sweep by mobility reduction	Injectivity Stability High salinity	5	1 lb polymer per incremental bbl
Surfactant/polymer	Same as polymer, plus reduces capillary forces	Same as polymer, plus chemical availability, retention, and high salinity	15	15–25 lb surfactant per incremental bbl
Alkaline/polymer	Same as SP, plus oil solubilization and wettability alteration	Same as SP, plus oil composition	5	35–45 lb chemical per incremental bbl
Alkaline/surfactant/polymer	Same as SP	Same as SP with lower salinity requirements, mineral precipitation	—	—

*1 lb/bbl \equiv 2.86 kg/m³.

TABLE 1.2—THERMAL EOR PROCESSES				
Process	Recovery Mechanism	Issues	Typical Recovery (%)	Typical Agent Utilization*
Steam (drive and stimulation)	Reduces oil viscosity; vaporization of light ends	Depth Heat losses Override Pollution	50–65	0.5 bbl oil consumed per incremental bbl
In-situ combustion	Same as steam, plus cracking	Same as steam, plus control of combustion	10–15	10 Mcf air per bbl oil produced*
SAGD	Same as steam	Vertical permeability; surface handling of heavy crudes	Same as steamdrive	Same as steamdrive
EM heating	Same as steam, plus some cracking and distillation	Propagation of heat	—	—

*1 Mcf/STB \equiv 178 std m³ gas/std m³ oil.

[**Table 1.2**](#) shows a similar comparison for thermal processes. These methods are usually directed toward recovery of heavy to extra-heavy crudes. Recoveries are larger for these processes than for chemical methods. Again, the issues are similar within a given category, centering on heat losses, override, and air pollution. Steam is usually generated by burning a portion of the resident oil or an equivalent amount of other fuel. In many locations, natural gas is used as the fuel rather than crude. If this burning occurs on the

surface, the emission products contribute to air pollution; if the burning is in situ, production wells can be a source of pollutants. A recent variation of in-situ combustion is high-pressure air injection (HPAI).

Two recent entries in this category are steam-assisted gravity drainage (SAGD) and electromagnetic (EM) heating. SAGD is similar to a steam drive except that injection and production are done through paired horizontal wells. The principal mechanism for oil recovery is gravity drainage, not viscous forces. SAGD is also too new for a good statistical base to exist, although there are many ongoing projects. As of the time of writing, it appears to be comparable to steam drives.

EM heating is also a new technology that is intended for so-called stranded oil. Its field recoveries have not been compiled, but its thermal efficiency appears to be equivalent to the other thermal methods.

[Table 1.3](#) compares the solvent-flooding processes. Only two groups of processes are in this category, corresponding to whether or not the solvent develops miscibility with the oil. Oil recoveries are generally lower than in SP and thermal recoveries. The solvent utilization factors as well as the relatively low cost of the solvents have brought these processes, particularly CO₂ flooding in the United States, to commercial application. The distinction between a miscible and an immiscible process is one of degree: an immiscible flood can achieve good oil recovery if the process is close to miscibility and poor recovery if the reservoir pressure is substantially below the minimum pressure for miscibility.

TABLE 1.3—SOLVENT EOR METHODS				
Process	Recovery Mechanism	Issues	Typical Recovery (%)	Typical Agent Utilization*
Immiscible	Reduces oil viscosity	Stability Override	5–15	10 Mcf solvent per incremental bbl
	Oil swelling	Supply		
	Solution gas			
Miscible	Same as immiscible, plus development of miscible displacement	Same as immiscible	5–10	10 Mcf solvent per incremental bbl

*1 Mcf/STB \cong 178 SCM solvent/SCM oil.

1.4.2 Screening Guides. Many of the issues in Tables 1.1 through 1.3 can be better illustrated by giving quantitative limits. These binary screening guides can also serve as a first approximation of when a process would apply to a given reservoir.

[**Table 1.4**](#) gives screening guides for EOR processes in terms of oil and reservoir properties. These should be regarded as rough guidelines, not as hard limits, because other considerations (e.g., economics and gas supply) and reservoir properties (e.g., vertical permeability, fractures, and thief zones) can extend or prohibit the applications.

The limits have a physical basis, as we will see. For example, the restriction of thermal processes to relatively shallow reservoirs exists because of potential heat losses through lengthy wellbores. The restriction on many of the processes to light crudes comes about because of sweep-efficiency considerations; displacing viscous oil is difficult because of the propensity of a displacing agent to channel through the fluid being recovered. Some of the categorizations in [**Table 1.4**](#) are fairly coarse. Steam methods, in particular, contain additional divisions into steam-soak, steamdrive, and gravity-drainage methods. There are likewise several variations of combustion and chemical methods. Furthermore, the property boundaries are somewhat diffuse and continually subject to revision. The viscosity limits on polymer flooding, for example, are likely a little too low. Finally, the information in [**Table 1.4**](#) represents a road map for the material to be covered in later chapters. The information in the table

is only a first step toward screening, which itself requires much more information and effort (Dickson and Leahy-Dios 2010).

TABLE 1.4—SUMMARY OF SCREENING CRITERIA FOR EOR METHODS [ADAPTED FROM TABER ET AL. (1997)]								
EOR Method	Oil Properties				Reservoir Characteristics			
	Gravity (°API)	Reservoir Viscosity (mPa·s)	Composition	Initial Oil Saturation (% PV)	Formation Type	Net Thickness (m)	Average Permeability (md)	Depth (m)
Solvent Methods								
Nitrogen and flue gas	>35	<0.4	Large percent of C ₁ to C ₇	>40	NC*	NC	NC	>1800
Hydrocarbon	>23	<3	Large percent of C ₂ to C ₇	>30	NC	NC	NC	>1250
CO ₂	>22	<10	Large percent of C ₅ to C ₁₂	>20	NC	NC	NC	>750
Immiscible gases	>12	<600	NC	>35	NC	NC	NC	>640
Chemical Methods								
Micellar/polymer, ASP, and alkaline flooding	>20	<35	Light, intermediate, some organic acids for alkaline floods	>35	Sandstone preferred	NC	>10	<2700
Polymer flooding	>15	10–150	NC	>50	Sandstone preferred	NC	>10	<2700
Thermal Methods								
Combustion	>10	<5,000	Some asphaltic components	>50	—	>3	>50	<3450
Steam	13.5	<200,000	NC	>40	—	>6	>200	<1350

*NC = Not critical.

1.4.3 Cash Flow. Many of the screening guides are implicit assessments of the ability of an EOR process to make money (sometimes called the economics). Performing such calculations is an important part of the decision to implement EOR. See Flaaten (2012) for a discussion of oilfield economics and of how to calculate cumulative discounted cash flow. The key variables in this calculation are the oil rate (the subject of this text and of [Fig. 1.7b](#)), the price of oil, and the discount rate.

Each EOR process has its unique economic profile, but there are common features for all, as illustrated in [Fig. 1.7](#). [Fig. 1.7a](#) shows the cumulative discounted cash flow (CDCF) as a function of time. The time axis in the figure is aligned with the figure below it. As the name

implies, the CDCF is the accumulation (or integration) of the discounted cash flow or DCF. The CDCF is the net amount of money returned by a project over time.

[Fig. 1.7b](#) shows a rate vs. time history of an EOR project that is approaching its economic limit. The economic limit occurs when the slope of the CDCF curve vs. time is zero. Remember that the DCF is the derivative of the CDCF curve.

All EOR processes require some capital investment, labeled as CAPEX in [Fig. 1.7b](#). The figure shows this decline as taking place at the onset of the project, but often it is spread out over several years.

EOR agents are generally expensive, especially compared to injecting water. For this reason, the CDCF decreases even further beyond the CAPEX. However, once revenue from oil production starts, the curve begins to increase at the time labeled “positive cash flow.” For many EOR processes, positive cash flow begins within a year of initiation. Payout occurs when the CDCF reaches a positive value. (Recall that all costs and revenue are being discounted with time).

The CDCF now begins to level off as a consequence of the declining oil rate. The project life is reached when the CDCF is at maximum or when the cash flow becomes negative. The value of the CDCF at its maximum is the net present value or NPV.

The NPV is the primary decision variable determining whether to go forward with an EOR project. It should be compared with (a) what the CDCF was before the process began (a project with NPV less than this amount should not be performed); (b) alternatives within the portfolio of the producer (there may be other non-EOR projects that will result in a larger NPV); and, (c) when divided by some measure of expenditure (this quotient is called the rate of return), targets set by the producer.

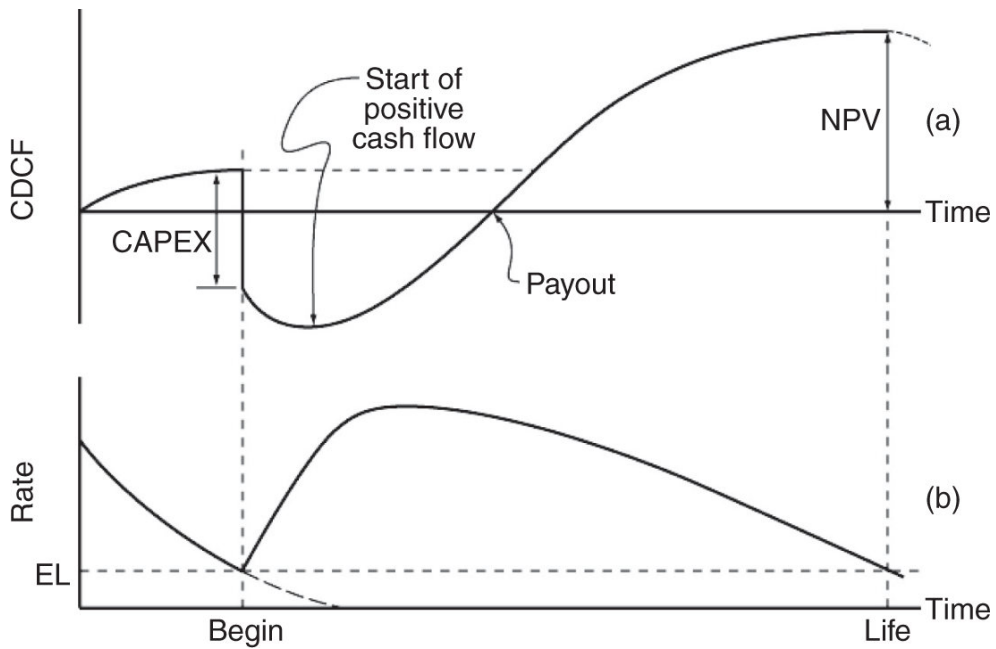


Fig. 1.7—Schematic of the behavior of the CDCF for an EOR project.

We end by noting that Fig. 1.7 contains several aspects that are not part of this text: oil price, discount rate, and CAPEX to name a few. Projects that produce incremental hydrocarbon, but fall short of an NPV limit, are *technical successes*. There are several of these projects in the history of EOR. Other factors always play a role in the EOR decision. Some of these are access to alternate projects, competition for capital, or both. However, the basic idea, with much more complexity to be sure, is always of the form shown in Fig. 1.7.

1.5 Summary

No summary can do justice to what is a large, diverse, continuously changing, and complex technology. An excellent example of such changes is the current emphasis on so-called unconventional oil recovery (Fig. 1.1). This technology is now producing more crude than EOR, and the oil production rate is likely to go up. On the other hand, there is no reason to suspect that the ultimate oil recovery for these processes will be any greater than that for waterflooding. Hence, unconventional production will leave a target for EOR.

The *Oil & Gas Journal* has provided an excellent service in documenting the progress of EOR, and you should consult those

surveys for up-to-date information. The fundamentals of the processes change more slowly than the applications, and it is to these fundamentals that the remainder of the text is devoted.

1.6 Units and Notation

1.6.1 SI Units. The basic set of units in the text is the Système International (SI). We cannot use SI units exclusively because a great body of figures and tables has been developed in more traditional units. It is impractical to convert these; therefore, we give a list of the more important conversions in [Table 1.5](#) and provide some helpful pointers in this section.

TABLE 1.5—AN ABRIDGED SI UNITS GUIDE [ADAPTED FROM CAMPBELL ET AL. (1977)]

SI Base Quantities and Units			
Base Quantity or Dimension	SI Unit	SI Unit Symbol (Use Roman Type)	SPE Dimensions Symbol (Use Roman Type)
Length	Meter	M	L
Mass	Kilogram	kg	m
Time	Second	s	t
Thermodynamic temperature	Kelvin	K	T
Amount of substance	Mole*	mol	—
Some Common SI Derived Units			
Quantity	Unit	SI Unit Symbol (Use Roman Type)	Formula (Use Roman Type)
Acceleration	Meters per second squared	—	m/s^2
Area	Square meters	—	m^2
Density	Kilograms per cubic meter	—	kg/m^3
Energy, work	Joules	J	$\text{N}\cdot\text{m}$
Force	Newtons	N	$\text{kg}\cdot\text{m/s}^2$
Pressure	Pascals	Pa	N/m^2
Velocity	Meters per second	—	m/s
Viscosity, dynamic	Pascal-seconds	—	$\text{Pa}\cdot\text{s}$

Viscosity, kinematic Volume	Square meters per second Cubic meters	— —	m ² /s m ³
Selected Conversion Factors			
<u>To Convert From</u>	<u>To</u>	<u>Multiply By</u>	
Acre (US survey)	Meter ² (m ²)	4.046 872 E+03	
Acres	Feet ² (ft ²)	4.356 000 E+04	
Atmosphere (standard)	Pascal (Pa)	1.013 250 E+05	
Bar	Pascal (Pa)	1.000 000 E+05	
Barrel (for petroleum, 42 gal)	Meter ³ (m ³)	1.589 873 E-01	
Barrel	Feet ³ (ft ³)	5.615 E+00	
British thermal unit (International Table)	Joule (J)	1.055 056 E+03	
Darcy	Meter ² (m ²)	9.869 232 E-13	
Day (mean solar)	Second (s)	8.640 000 E+04	
Dyne	Newton (N)	1.000 000 E-05	
Gallon (US liquid)	Meter ³ (m ³)	3.785 412 E-03	
Gram	Kilogram (kg)	1.000 000 E-03	
Hectare	Meter ² (m ²)	1.000 000 E+04	
Mile (US survey)	Meter (m)	1.609 347 E+03	
Pound (lbm)	Kilogram (kg)	4.535 924 E-01	
Ton (short, 2,000 lbm)	Kilogram (kg)	9.071 847 E+02	

Selected SI Unit Prefixes				
Factor	SI Prefix	SI Prefix Symbol (Use Roman Type)	Meaning (US)	Meaning in Other Countries
10^{12}	tera	T	One trillion times	Billion
10^9	giga	G	One billion times	Milliard
10^6	mega	M	One million times	—
10^3	kilo	K	One thousand times	—
10^2	hecto	H	One hundred times	—
10	deka	Da	Ten times	—
10^{-1}	deci	D	One tenth of	—
10^{-2}	centi	C	One hundredth of	—
10^{-3}	milli	M	One thousandth of	—
10^{-6}	micro	μ	One millionth of	—
10^{-9}	nano	N	One billionth of	Milliardth

*When the mole is used (by convention, the *gram-mole*), the elementary entities must be specified; they may be atoms, molecules, ions, electrons, other particles, or specified groups of such particles in petroleum work. The terms *kilogram mole*, *pound mole*, and so on are often erroneously shortened to mole.

- There are several cognates, quantities having the exact or approximate numerical value, between SI and practical units. The most useful for EOR are

$$\begin{aligned}
 1 \text{ cp} &= 1 \text{ mPa.s} \\
 1 \text{ dyne/cm} &= 1 \text{ mN/m} \\
 1 \text{ Btu} &\approx 1 \text{ kJ} \\
 1 \text{ Darcy} &\approx 1 \text{ } \mu\text{m}^2 \\
 1 \text{ ppm} &\approx 1 \text{ g/m}^3 \\
 1 \text{ atm} &\approx 0.1 \text{ MPa}
 \end{aligned}$$

- Use of the unit prefixes (lower part of [Table 1.5](#)) requires care. When a prefixed unit is raised to an exponent, the exponent applies to the prefix as well as the unit. Thus, $1 \text{ km}^2 = 1(\text{km})^2 =$

$1(10^3 \text{ m})^2 = 1 \times 10^6 \text{ m}^2$. An example is $1 \mu\text{m}^2 = 10^{-12} \text{ m}^2 \cong 1$ darcy.

3. Two troublesome conversions are between pressure (147 psia $\cong 1 \text{ MPa}$) and temperature ($1 \text{ K} = 1.8 \text{ R}$). Because neither the Fahrenheit scale nor the Celsius scale is absolute, an additional translation is required:

$${}^\circ\text{C} = \text{K} - 273$$

and

$${}^\circ\text{F} = \text{R} - 460.$$

The superscript “ $^\circ$ ” is not used on absolute temperature scales.

4. The volume conversions are complicated by the interchangeable use of mass and standard volumes. Therefore, we have

$$0.159 \text{ m}^3 = 1 \text{ reservoir barrel, or bbl}$$

and

$$0.159 \text{ std. m}^3 = 1 \text{ standard barrel, or STB.}$$

The standard cubic meter, std m^3 , is not standard SI; it represents the amount of mass contained in one cubic meter evaluated at standard temperature and pressure.

1.6.2 Consistency. Maintaining unit consistency is important in all exercises. Both units and numerical values should be carried in all calculations. This ensures that the unit conversions are calculated correctly and indicates whether the calculation procedure itself is appropriate. In maintaining consistency, three steps are required.

1. Clear all unit prefixes.
2. Reduce all units to the most primitive level necessary. For many cases, this will mean reverting to the fundamental units given in [Table 1.5](#).
3. After calculations are complete, reincorporate the unit prefixes so that the numerical value of the result is as close to unity as

possible. Many adopt the convention of using only the prefixes representing multiples of 1,000.

The physical laws are valid regardless of the system of units used. This text eschews the now-standard petroleum-engineering practice of writing equations in a specific set of units (i.e., with conversion factors embedded).

1.6.3 Naming Conventions. The diversity of EOR makes it impossible to assign symbols to components without some duplication or undue complication. In the hope of minimizing the latter by adding a little of the former, [Table 1.6](#) gives the naming conventions of phases and components used throughout this text. The nomenclature section defines other symbols.

TABLE 1.6—NAMING CONVENTIONS FOR PHASES AND COMPONENTS

<u>Phases</u>		
<u>Index <i>j</i></u>	<u>Identity</u>	<u>Text Locations</u>
1	Water-rich or aqueous	Throughout
2	Oil-rich or oleic	Throughout
3	Gas-rich, gaseous, or light hydrocarbon	Section 5.4; and Chapters 7 and 10
	Microemulsion	Chapter 9
<i>s</i>	Solid	Chapters 2, 3, and 8–10
<i>w</i>	Wetting	Throughout
<i>nw</i>	Nonwetting	Throughout
<u>Components</u>		
<u>Index <i>i</i></u>	<u>Identity</u>	<u>Text locations</u>
1	Water	Throughout
2	Oil or intermediate hydrocarbon	Throughout
3	Gas	Section 5.4
	Light hydrocarbon	Chapter 7
	Surfactant	Chapter 9 (not Chapter 10)
4	Polymer, foaming surfactant	Chapters 8, 9, and 10
5	Anions	Sections 3.6 and 9.5
6	Divalents	Sections 3.4 and 9.3
7	Divalent-surfactant component	Section 9.6
8	Monovalents	Section 3.6 and Chapter 9

Phase always carries the subscript *j*, which occupies the second position in a doubly subscripted quantity. *j* = 1 is always a water-rich, or aqueous, phase, thus freeing up the symbol *w* for wetting (and *nw*)

for nonwetting). The subscript s designates the solid, nonflowing phase. Singly subscripted quantities are phase properties.

A subscript i occurring in the first position indicates the component. In general, $i = 1$ is always water; $i = 2$ is oil or hydrocarbon; and $i = 3$ refers to a displacing component, whether surfactant or light hydrocarbon. Component indices greater than three are used exclusively in [Chapters 8–10](#), the chemical-flooding portion of the text.

Exercises

1.1 Determining Incremental Oil Production. The easiest way to estimate IOR is through decline-curve analysis, which is the subject of this exercise. The oil rate and cumulative oil produced vs. time data for the Sage Spring Creek Unit A field are shown below (Mack and Warren 1984).

Date	Oil Rate, std m ³ /d
1/76	274.0
7/76	258.1
1/77	231.0
7/77	213.5
1/78	191.2
7/78	175.2 (Start Polymer)
1/79	159.3
7/79	175.2
1/80	167.3
7/80	159.3
1/81	159.3
7/81	157.7
1/82	151.3
7/82	148.2
1/83	141.8
7/83	132.2

1/84	111.5
7/84	106.7
1/85	95.6
7/85	87.6
1/86	81.2
7/86	74.9
1/87	70.1
7/87	65.3

In July 1978, the ongoing waterflood was replaced with a polymer flood. (A polymer-gel treatment was conducted in 1984, but we neglect it here.) The economic limit is 50 std m³/d in this field.

- a. Plot the oil rate vs. cumulative oil produced on linear axes. The oil-rate axis should extend to $q = 0$.
- b. Extrapolate the straight-line portion of the data to determine the ultimate economic oil to be recovered from the field and the total mobile oil, both in Mstd m³, for both the water and the polymer flood. Determine the IOR and the incremental mobile oil caused by the polymer flood.
- c. Determine the decline rates appropriate for the waterflood and the polymer flood.
- d. Use the decline rates determined in Step c to determine the economic life of the polymer flood (when the oil rate reaches the EL). Also determine what the economic life would have been if there had been no polymer flood.

Chapter 2

Basic Equations for Fluid Flow in Permeable Media

Successful enhanced oil recovery (EOR) requires knowledge of equal parts of chemistry, physics, geology, and engineering. Each of these enters our understanding through elements of the equations that describe flow through permeable media. Each EOR process involves at least one flowing phase that may contain several components. Moreover, because of varying temperature, pressure, and composition, these components may mix completely in some regions of the flow domain, causing the disappearance of a phase in those regions. Atmospheric pollution, groundwater flow, and chemical and nuclear waste storage lead to similar problems.

This chapter gives the equations that describe multiphase, multicomponent fluid flow through permeable media on the basis of conservation laws for mass, energy, entropy, and linear constitutive theory. Initially, we strive for the most generality possible by considering the transport of each component in each phase. Then, we obtain special cases from the general equations by making additional assumptions. The approach in arriving at the special equations is as important as the equations themselves because it will help to understand the specific assumptions—and the limitations—that are being imposed for a particular application.

The formulation for conservation of mass initially contains two fundamentally different forms for the general equations: overall compositional balances and phase-conservation equations. The overall compositional balances are useful for modeling the way in which components in local thermodynamic equilibrium are transported through permeable media. The phase-conservation

equations are useful for modeling finite mass transfer among phases.

Our formulation differs from other sources in its generality for multiphase, multicomponent flows. For example, it contains as special cases the multicomponent, single-phase flow equations (Bear 1972) and the three-phase, multicomponent equations (Crichlow 1977; Peaceman 1977; Coats et al. 1980; Skjaveland 1991). In addition, others (Todd and Chase 1979; Fleming et al. 1981; Larson 1982) have presented multicomponent, multiphase formulations for flow in permeable media, but with assumptions such as ideal mixing or incompressible fluids. Many of these assumptions must be made before the equations are solved, but we try to keep the formulation as general as possible for as long as possible.

2.1 Mass Conservation

This section describes the conceptual nature of multiphase, multicomponent flows through permeable media and the mathematical formulation of the conservation equations.

The four most important mechanisms causing transport of chemical components in naturally occurring permeable media are viscous forces, gravity forces, dispersion (diffusion), and capillary forces. The driving forces for the first three are pressure, density, and concentration gradients, respectively. Capillary or surface forces are caused by high-curvature boundaries between the various homogeneous phases. This curvature is the result of such phases being constrained by the pore walls of the permeable medium. Capillary forces cause differing pressures in each homogeneous fluid phase, so that the driving force for capillary pressure, as for viscous forces, is pressure differences.

The ratios of these forces are often described as dimensionless groups and given particular names. For example, the ratio of gravity to capillary forces is the Bond number. When capillary forces are small compared to gravity forces, the Bond number is large, and the process (or displacement) is said to be gravity dominated. The ratio of viscous to capillary forces is the capillary number, a quantity that

will figure prominently throughout this text. The ratio of gravity to viscous forces is the gravity or buoyancy number. The magnitude of these and other dimensionless groups help in comparing or scaling one process to another.

2.1.1 The Continuum Assumption. Transport of chemical components in multiple homogeneous phases occurs because of the aforementioned forces, with the flow restricted to the highly irregular flow channels within the permeable medium. The form of the conservation equations that we will use the most applies at each point in the medium, including the solid phase. In principle, given constitutive relations, reaction rates, and boundary conditions, it is possible to formulate a complete mathematical statement for all flow channels in the medium. However, the phase boundaries in these channels are extremely tortuous, and their locations are unknown; hence, we cannot solve component conservation equations in individual channels except for the very simplest microscopic permeable-media geometries.

The practical method of avoiding this difficulty is to apply a continuum definition to the flow so that a point within a permeable medium is associated with a representative elementary volume (REV), a volume that is large with respect to the pore dimensions of the solid phase, but small compared to the dimensions of the permeable medium. In particular, we assume that the REV is so small compared to the porous medium that we can treat it as a differential volume element in applying calculus to the properties of the medium. The REV is defined as a volume less than that in which local fluctuations in some primary property of the permeable medium, usually the porosity, become large (Bear 1972). A volume-averaged form of the component-conservation equations applies for each REV within the now continuous domain of the macroscopic permeable medium. Volume averaging is a formal process; see Bear (1972), Gray (1975), Quintard and Whitaker (1988), and Faghri and Zhang (2006). The volume-averaged component-conservation equations are identical to the conservation equations outside a permeable medium except for altered definitions for the

accumulation, flux, and source terms. These definitions now include permeable-media porosity, permeability, tortuosity, and dispersivity, all made locally smooth because of the definition of the REV. Approximating the locally discontinuous permeable medium with a locally smooth medium is called the *continuum assumption*.

A good way to understand the REV scale is to consider a microscopic view of pores and grains within a medium. [Fig. 2.1](#) illustrates a cube of small volume placed within a permeable medium. The porosity in the cube is defined as the pore volume within the cube divided by the bulk volume of the cube. If the cube volume is infinitesimally small, the porosity will be either 1.0 or 0.0 depending on whether it is initially located inside a grain or a pore. We now let the cube increase from its original size. As the cube volume increases, the porosity changes in an erratic fashion as more and more grains and pores pass inside the cube (see [Fig. 2.2](#)).

As the cube volume increases sufficiently, the porosity approaches a constant value that is representative of the porous medium. This is the porosity at the REV scale, which defines the onset of the permeable-medium domain. Above the REV size, the cube porosity remains constant within the domain of the permeable medium. As the cube volume increases further, however, the cube porosity is affected by layering and other heterogeneities. The formation is homogeneous if the porosity remains fixed as the REV-sized cube is moved to any location within the permeable medium. A heterogeneous formation is one in which the porosity (or any other petrophysical property) varies from one spatial location to another when measured at the REV scale.

Rather than beginning with the nonpermeable-media flow equations and then volume-averaging over the REV, we invoke the continuum assumption at the outset and derive the mass conservation equations on this basis. This approach skips over many of the physical insights obtained from volume averaging, but it is far more direct.

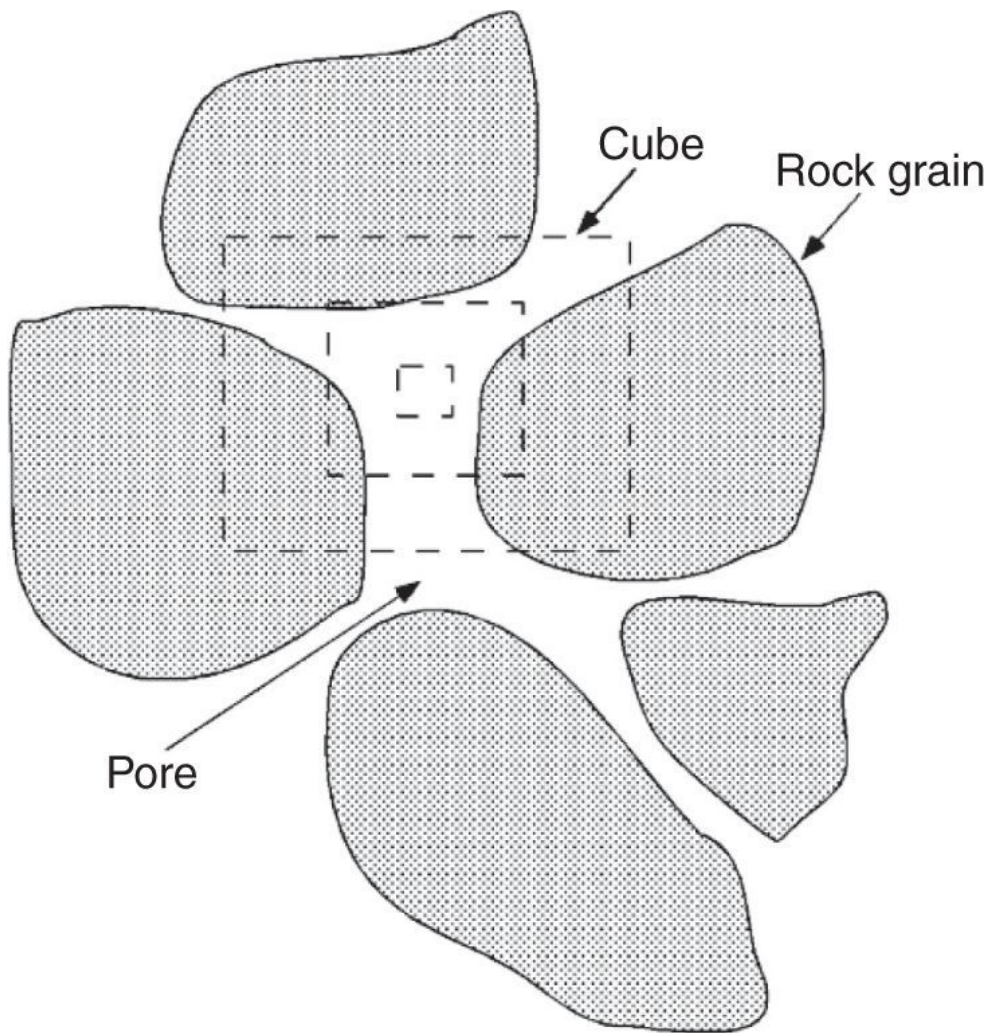


Fig. 2.1—Illustration of microscopic cubes placed within a permeable medium. The dashed cube is initially within a pore, so that the porosity is 1.0. As the cube volume increases (successively larger cubes), it takes in more grains (shaded), so that its porosity decreases.

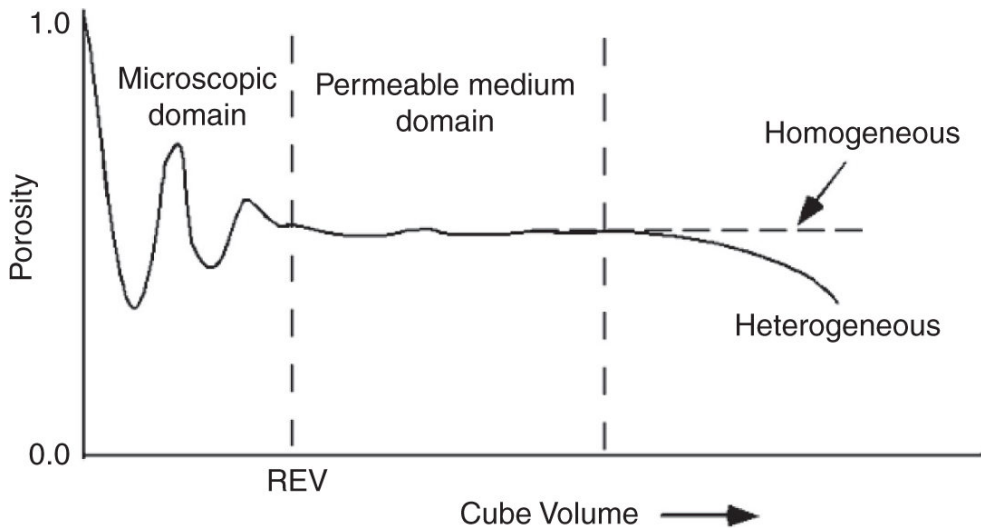
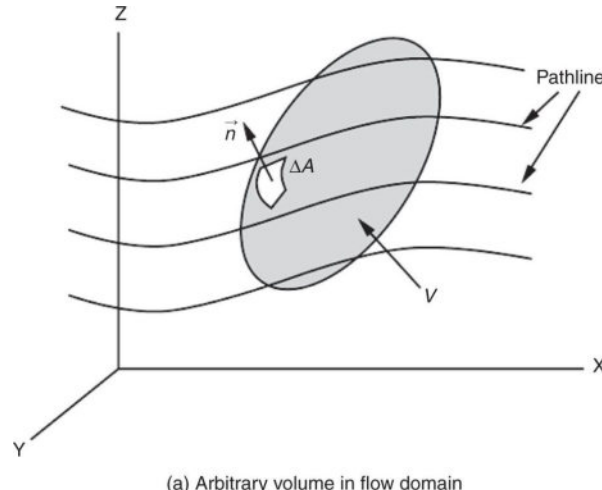


Fig. 2.2—Idealization of the microscopic and continuous permeable-medium domains. The REV size separates these two domains [adapted from Bear (1972)].

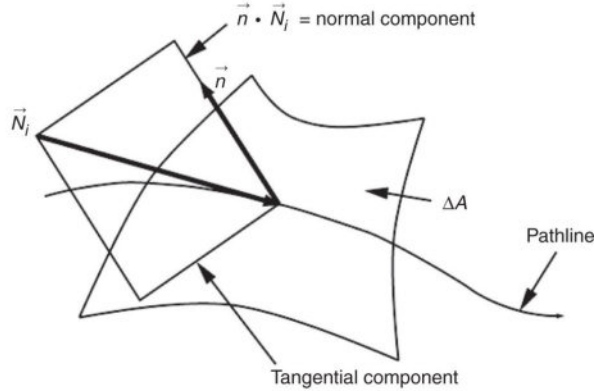
Mass-Conservation Equations. Consider an arbitrary, fixed volume V embedded within a permeable medium through which are flowing N_C chemical components and N_P phases. You must constantly be aware of the distinction between components and phases in this discussion. (This can be a source of confusion because under some circumstances, phases and components are the same.) A *component* is any identifiable chemical entity. Components can be pure substances, such as methane, a cation, or even combinations of elements. See Lake et al. (2002) for a more in-depth discussion. A *phase* is a physically distinct part of a region in space that is bounded by interfaces with macroscopic physical properties such as density and viscosity. A phase can consist of many components. There are up to $i = 1, \dots, N_C$ components, and up to $j = 1, \dots, N_P$ phases. The “up to” expresses the fact that both components and phases can vanish in certain regions of the flow domain.

The conservation laws are written over a control volume V , which is greater than or equal to the REV, but less than or equal to the permeable-medium dimensions. Except for some restrictions on the connectivity of the surface, V can be quite general. As [Fig. 2.3a](#) shows, the surface area A of V is made up of elemental surface

areas ΔA , from the center of each of which is pointing a unit outward normal vector \vec{n} . The sum of all the surface elements ΔA is the total surface area A of V . This sum of all the ΔA becomes the total surface area A as the largest ΔA approaches zero.



(a) Arbitrary volume in flow domain



(b) Surface element detail

Fig. 2.3—Geometries for conservation-law derivations.

The conservation equation for a component in volume V is

A total of N_C equations are represented by Eq. 2.1. This equation is the *rate* form of the conservation equation; an equivalent form based

on cumulative flow follows from integrating Eq. 2.1 with respect to time (see Section 2.6). From left to right in Eq. 2.1, the terms are the accumulation, flux, and source terms. A component can be transported by convection or hydrodynamic dispersion within a phase. The generation of a component can be the result of chemical or biological reactions or of injection or production of a component into or from wells. These physical processes are discussed in more detail in Section 2.2.

The first term on the right side of Eq. 2.1 can be written as

We give mathematical form to each term in the following paragraphs.

The accumulation term for component i is

$$\left\{ \begin{array}{l} \text{Rate of} \\ \text{accumulation} \\ \text{of } i \text{ in } V \end{array} \right\} = \frac{d}{dt} \left\{ \begin{array}{l} \text{Total mass of} \\ i \text{ in } V \end{array} \right\} = \frac{d}{dt} \left\{ \int_V W_i dV \right\}, \dots \quad (2.3)$$

where W_i is the component concentration in units of mass of i per unit bulk volume. The units of Eq. 2.3 are mass per unit time. The volume integral represents the sum of infinitesimal volume elements in V weighted by the concentration.

Because V is fixed over time,

This entire development may be repeated with a time-varying V with the same result (Slattery 1972).

The net flux term follows from considering the rate of transport across a single surface element into V , as shown in Fig. 2.3b. Let \vec{N}_i be the flux vector of component i evaluated at the center of ΔA in units of mass of i per surface area per time. \vec{N}_i consists of

components normal and tangential to \vec{n} . However, only the normal component $\vec{n} \cdot \vec{N}$ is crossing ΔA , and the rate of transport across ΔA is

The minus sign occurs because \vec{n} and \vec{N} are in opposing directions for transport across ΔA into V ($\vec{n} \cdot \vec{N} < 0$), and this term must be positive from Eq. 2.1. The summation of infinitesimal surface elements yields

Because the surface integral is over the entire surface of V , both flows into and from V are included in Eq. 2.6.

The net rate of generation of i inside V is

where R_i is the rate of mass generation in units of mass of i per bulk volume per time. This term can account for both generation ($R_i > 0$) and disappearance ($R_i < 0$) of i , either through one or more chemical or biological reactions or through physical sources (wells) in V .

Substitution of Eqs. 2.3, 2.4, 2.6, and 2.7 into Eq. 2.1 gives the following scalar equation for the conservation of i :

Eq. 2.8 is an overall balance, or a “weak” form of the conservation equation. Versions of this equation will be used in solving for solutions that have discontinuities, such as those that involve shocks

or fronts. The weak form, which is called an overall balance in the last section of this chapter, is also useful in numerical simulation primarily because it is not tied to a particular coordinate control volume (CV).

The surface integral in Eq. 2.8 can be converted to a volume integral through the divergence theorem:

where B can be any scalar, vector, or tensor function of position in V (with appropriate changes in the operator definitions). The symbol $\vec{\nabla}$ is the divergence operator, a kind of generalized derivative, with a specific form depending on the coordinates used. [Table 2.1](#) gives forms of $\vec{\nabla}$ in rectangular, cylindrical, and spherical coordinates. The function B must be single valued in V , a requirement that is met by most physical properties as long as the continuum assumption applies. Finally, implicit in the representation of the surface integral of Eqs. 2.8 and 2.9 is the requirement that the integrand be evaluated on the surface A of V .

Application of the divergence theorem to Eq. 2.8 gives

Using Eq. 2.10 restricts the formulation somewhat. V must now be simply connected (a point on the exterior surface of V is always exterior), and the spatial derivatives implied by the divergence exist because of the continuum assumption discussed above. However, because V is arbitrary in location and size, the integrand must be zero:

TABLE 2.1—SUMMARY OF DIFFERENTIAL OPERATORS IN RECTANGULAR, CYLINDRICAL, AND SPHERICAL COORDINATES

Rectangular coordinates (x, y, z)	Cylindrical (or radial) coordinates (r, θ, z)	Spherical coordinates (r, θ, ϕ)
$\vec{\nabla} \cdot \vec{B} = \frac{\partial B_x}{\partial x} + \frac{\partial B_y}{\partial y} + \frac{\partial B_z}{\partial z}$	$\vec{\nabla} \cdot \vec{B} = \frac{1}{r} \frac{\partial(rB_r)}{\partial r} + \frac{1}{r} \frac{\partial B_\theta}{\partial \theta} + \frac{\partial B_z}{\partial z}$	$\vec{\nabla} \cdot \vec{B} = \frac{1}{r^2} \frac{\partial(r^2 B_r)}{\partial r} + \frac{1}{r \sin \theta} \frac{\partial}{\partial \theta}(B_\theta \sin \theta) + \frac{1}{r \sin \theta} \frac{\partial B_\phi}{\partial \phi}$
$[\vec{\nabla} S]_x = \frac{\partial S}{\partial x}$	$[\vec{\nabla} S]_r = \frac{\partial S}{\partial r}$	$[\vec{\nabla} S]_r = \frac{\partial S}{\partial r}$
$[\vec{\nabla} S]_y = \frac{\partial S}{\partial y}$	$[\vec{\nabla} S]_\theta = \frac{1}{r} \frac{\partial S}{\partial \theta}$	$[\vec{\nabla} S]_\theta = \frac{1}{r} \frac{\partial S}{\partial \theta}$
$[\vec{\nabla} S]_z = \frac{\partial S}{\partial z}$	$[\vec{\nabla} S]_z = \frac{\partial S}{\partial z}$	$[\vec{\nabla} S]_\phi = \frac{1}{r \sin \theta} \frac{\partial S}{\partial \phi}$
$\vec{\nabla}^2 S = \frac{\partial^2 S}{\partial x^2} + \frac{\partial^2 S}{\partial y^2} + \frac{\partial^2 S}{\partial z^2}$	$\vec{\nabla}^2 S = \frac{1}{r} \frac{\partial}{\partial r} \left(r \frac{\partial S}{\partial r} \right) + \frac{1}{r^2} \frac{\partial^2 S}{\partial \theta^2} + \frac{\partial^2 S}{\partial z^2}$	$\vec{\nabla}^2 S = \frac{1}{r^2} \frac{\partial}{\partial r} \left(r^2 \frac{\partial S}{\partial r} \right) + \frac{1}{r^2 \sin \theta} \frac{\partial}{\partial \theta} \left(\sin \theta \frac{\partial S}{\partial \theta} \right) + \frac{1}{r^2 \sin^2 \theta} \frac{\partial^2 S}{\partial \phi^2}$

Note: B = vector function, and S = scalar function.

The time derivative in Eq. 2.11 is now a partial derivative, with the introduction of other independent variables—the spatial coordinates—making this necessary. From left to right in Eq. 2.11, the terms are now the *accumulation*, *transport*, and *source* terms, the last consisting of two types.

The strong form, Eq. 2.11, is useful in developing analytic solutions, which are a mainstay of this text. Eq. 2.11 and its analogous conservation equations are called the strong form because they express conservation at a point (an REV) within a medium. The word “strong” means that if Eq. 2.11 is satisfied at all points within V , Eq. 2.8, the weak form, is also satisfied. The converse is not necessarily true. The exact form of the equations depends on the coordinates being used, as shown in [Table 2.1](#). The next section gives specific definitions of the component concentration W_i , the flux \vec{N}_i , and the source terms R_i .

2.2 Definitions and Constitutive Equations for Isothermal Flow

Each term in Eq. 2.11 represents an important physical process or mechanism. This section examines each of these processes in further detail and defines some key formation and fluid parameters. The units of Eq. 2.11 are amount per bulk volume per unit time. *Amount* means either mass or moles; we will continue to use mass generically to mean either mass or moles. When a distinction between the two is important, we will be explicit.

Consider first a bulk volume V_b at the REV scale in which N_p phases exist. [Fig. 2.4](#) illustrates such a volume that contains three phases: a solid phase consisting of rock grains or soil, an aqueous phase, and an oleic phase. The porosity ϕ is defined as the fraction of the bulk permeable medium that is pore space; that is, the pore volume divided by the bulk volume V_b . The phase saturation S_j is defined as the fraction of the pore volume occupied by phase j .

The volume fraction of phase j , ε_j , is the volume of phase j divided by the bulk volume V_b . For fluid phases such as liquids and vapors, $\varepsilon_j = \phi S_j$, where ϕS_j is also called the fluid *content*. For the solid phase, $\varepsilon_s = 1 - \phi$, which is the grain volume divided by the bulk volume. By definition, $\sum_{j=1}^{N_p} \varepsilon_j = 1$. The parameter ϕ_j is useful in writing general equations for any phase, including the solid phase, as is done next. In summary, the fraction of the bulk volume that is occupied by phase j is

Accumulation Term. The accumulation term in Eq. 2.11 contains the concentration of component i for a given phase j (W_{ij}), which we write now in terms of the volume fraction ε_j . For solid or fluid phases, the mass of phase j in the bulk volume V_b is given by $\varepsilon_j \rho_j V_b$. As before, the inherent assumption here is that the density of each

phase is uniform in V_b , which is strictly valid only as V_b approaches the REV scale.

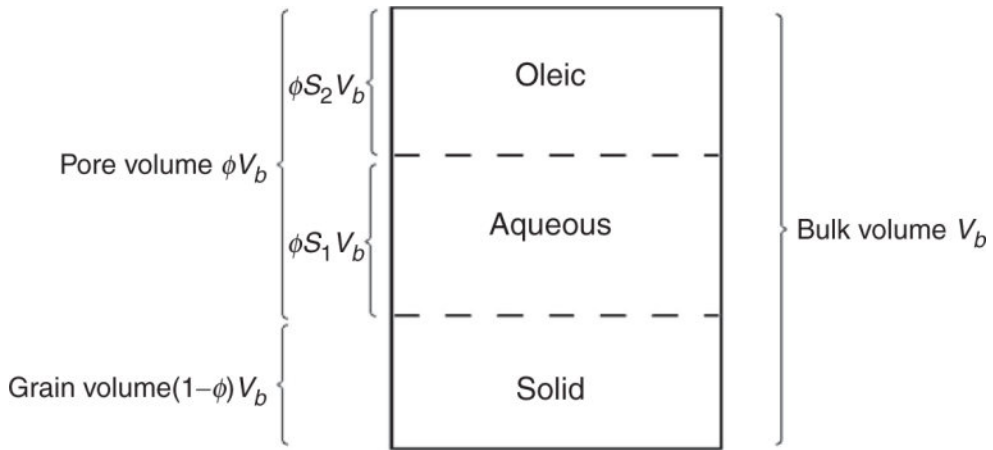


Fig. 2.4—Representative bulk volume occupied by two fluid phases and one stationary phase. The volume of each of the fluid phases in the bulk volume is equal to $\phi S_j V_b$. The volume of the solid phase is $(1-\phi)V_b$.

We now define the mass fraction of component i in V_b to be ω_{ij} , where ω_{ij} is the mass of component i in phase j divided by the total mass of all components in that same phase. Hence, $\sum_{i=1}^{N_c} \omega_{ij} = 1$. With this definition, the total mass of component i in phase j in V_b is $W_{ij}V_b$, where $W_{ij} = \varepsilon_j \rho_j \omega_{ij}$.

Fluxes. For advective transport of component i , we assume that phase j moves with its volume-averaged (superficial or Darcy) velocity \vec{u}_j . The component of the net (in-out) volumetric flow rate of phase j that enters the elemental surface ΔA is $-\vec{n} \cdot \vec{u}_j \Delta A$. The mass flow rate of component i in phase j that enters V through the elemental surface ΔA is, therefore, $-\vec{n} \cdot \rho_j \omega_{ij} \vec{u}_j \Delta A$. The component i flux in phase j attributable to advective transport alone is therefore equal to $\vec{j}_{Cij} = \rho_j \omega_{ij} \vec{u}_j$. The interstitial velocity for phase j is given by $\vec{v}_j = \vec{u}_j / \varepsilon_j$.

As is customary, hydrodynamic dispersion is assumed to have a Fickian form (see below and [Chapter 5](#)) that is empirically modified to account for the volume fraction ε_j of each phase. The flux of

component i in phase j with respect to the volume-averaged velocity (the Darcy velocity), which is attributable to hydrodynamic dispersion alone, is taken to be $\vec{j}_{Dij} = -\varepsilon_j \vec{K}_{ij} \cdot \vec{\nabla}(\rho_j \omega_{ij})$, where the product $\rho_j \omega_{ij}$ is the mass concentration of component i in phase j . Alternatively, the flux with respect to mass-averaged velocity is sometimes taken as $\vec{j}_{Dij} = -\varepsilon_j \rho_j \vec{K}_{ij} \cdot \vec{\nabla} \omega_{ij}$. The negative sign in both expressions indicates that positive flux occurs in the direction of decreasing mass fraction (or concentration). $\vec{\nabla} \omega_{ij}$ has units of inverse length, whereas \vec{K}_{ij} has units of squared length per unit time.

The total mass flux is the sum of both advective and dispersive transport. Therefore, the component flux for phase j attributable to both advective and hydrodynamic dispersive transport is

$$\rho_j \omega_{ij} \vec{u}_{ij} = \vec{j}_{Cij} + \vec{j}_{Dij} = \rho_j \omega_{ij} \vec{u}_j - \varepsilon_j \vec{K}_{ij} \cdot \vec{\nabla}(\rho_j \omega_{ij}),$$

where \vec{u}_{ij} is the statistical average apparent velocity of a component in phase j attributable to both convection and dispersion. The velocity \vec{u}_{ij} is, therefore, the sum of the molecular velocities divided by the total number of molecules (Bird et al. 2002). The convective and dispersive flux for a component in the solid phase is negligible for most permeable media. The total mass flux of a component is simply the sum of $\rho_j \omega_{ij} \vec{u}_j - \varepsilon_j \vec{K}_{ij} \cdot \vec{\nabla}(\rho_j \omega_{ij})$ over all phases.

Volume- or mass-averaged velocities are used interchangeably, even though the form of the dispersion term depends on the choice of velocity. The volume-averaged velocity \vec{u}_j for multicomponent flow is

$$\vec{u}_j = \sum_{i=1}^{N_c} \rho_j \omega_{ij} \vec{u}_{ij} \hat{V}_{ij},$$

where \hat{V}_{ij} is the partial mass volume of a component in phase j , and from thermodynamics, $\sum_{i=1}^{N_c} \rho_j \omega_{ij} V_{ij} = 1$ (Sandler 2006). The partial mass

volume depends on the mass fractions ω_{ij} , pressure, and temperature. The mass-averaged velocity is

$$\vec{u}_j = \sum_{i=1}^{N_c} \rho_j \omega_{ij} \vec{u}_{ij} / \sum_{i=1}^{N_c} \rho_j \omega_{ij} = \sum_{i=1}^{N_c} \omega_{ij} \vec{u}_{ij}.$$

The volume-averaged velocity is equal to the mass-averaged velocity for an incompressible fluid. Applications tend to use volume-averaged velocities because volumetric rates are measured directly at the inlets and outlets of a medium. Phase velocities, however, are rarely measured directly *in situ* and are estimated from empirical flux laws such as Darcy's law. Therefore, the choice of volume- or mass-averaged velocities is not likely to result in significant errors for real mixtures because uncertainties in other formation properties tend to be much greater; see Exercise 2.4.

Hydrodynamic dispersion includes both molecular diffusion and mechanical dispersion. Molecular diffusion is independent of the direction or magnitude of flow, whereas mechanical dispersion in permeable media flows is anisotropic and depends on the magnitude of flow. Dispersion has the same form as does diffusion in nonpermeable-media flows and, in fact, collapses to molecular diffusion in the limit of small \vec{u}_j (see [Chapter 5](#)). At large \vec{u}_j the components of $\vec{\vec{K}}_{ij}$, a second-order tensor, can be many times larger than molecular diffusion because they now contain contributions from fluctuations of the velocity \vec{u}_j and the mass fraction ω_{ij} about their average values in the REV (Gray 1975). Two components of $\vec{\vec{K}}_{ij}$ for a homogeneous, isotropic permeable medium (Bear 1972) are

$$(K_{xx})_{ij} = \frac{D_{ij}}{\tau} + \frac{\alpha_{ij} u_{xj}^2 + \alpha_{ij} (u_{yj}^2 + u_{zj}^2)}{\phi S_j |\vec{u}_j|} \dots \quad (2.13)$$

and

$$(K_{xy})_{ij} = \frac{(\alpha_{ij} - \alpha_{ij}) u_{xj} u_{yj}}{\phi S_j |\vec{u}_j|}, \dots \quad (2.14)$$

where the subscript l refers to the spatial coordinate in the direction parallel, or *longitudinal*, to bulk flow, and subscript t is any direction perpendicular, or *transverse*, to l . D_{ij} is the effective binary diffusion coefficient of component i in phase j (Bird et al. 2002), α_{lj} and α_{tj} are the longitudinal and transverse dispersivities, and τ is the permeable-medium tortuosity. $(K_t)_{ij}$ is positive because $(\alpha_{lj} - \alpha_{tj})$ is positive.

Sources. The source term R_i in Eq. 2.11 accounts for the rate of appearance or generation of component i because of chemical or biological reactions (Levenspiel 1999). In weak forms of the conservation laws, it is also convenient to use R_i to represent physical sources (wells) for which the values are either specified or related to phase pressures and saturations.

There is no general function for R_i , although the volume fractions of each phase are handled through $\varepsilon_j r_{ij}$, where r_{ij} is the reaction rate of component i in phase j . Both R_i and r_{ij} have units of mass per volume per time, but r_{ij} is per phase volume, not the bulk volume. Each r_{ij} could represent the sum of several reactions within phase j if component i participates in simultaneous reactions. In a given phase, mass is conserved, so that $\sum_{i=1}^{N_c} r_{ij} = 0$ when r_{ij} is in mass units. This statement is not correct if mole units are used to express the reaction rates because moles are not conserved in a chemical reaction. An example of a first-order reaction rate for radioactive decay or biodegradation is $r_{ij} = -k_i \rho_j \omega_{ij}$, where k_i is the decay constant or reaction-rate coefficient in units of inverse time.

The total mass-generation rate of component i per bulk volume of permeable medium is $R_i = \sum_{i=1}^{N_p} \varepsilon_j r_{ij}$. For the strong forms, injection and production of component i by wells are not explicitly included in this term; for our purposes, these are better treated as boundary conditions or point sources.

Overall Compositional Balances. Overall balances are written over all phases for each component. When we insert Eqs. 2.2-1 through 2.2-3 from [Table 2.2](#) into Eq. 2.11, we arrive at a general

form of the overall conservation equations in which N_P now refers only to fluid phases:

$$\begin{aligned} \frac{\partial}{\partial t} \left[\phi \sum_{j=1}^{N_p} \rho_j S_j \omega_{ij} + (1-\phi) \rho_s \omega_{is} \right] + \vec{\nabla} \cdot \left\{ \sum_{j=1}^{N_p} \left[\rho_j \omega_{ij} \vec{u}_j - \phi S_j \vec{\bar{K}}_{ij} \cdot \vec{\nabla} (\rho_j \omega_{ij}) \right] \right\} \\ = \phi \sum_{j=1}^{N_p} S_j r_{ij} + (1-\phi) r_{is}, \quad i = 1, \dots, N_c. \end{aligned} \quad (2.15)$$

The compositional equations are useful for modeling the overall flow of component concentrations, especially when mass transfer between fluid phases occurs. Of course, some detail is omitted because of the disappearance of the interphase transport terms. The detail can be partially restored by invoking the local equilibrium assumption (Lake et al. 2002), which provides algebraic relations between concentrations in the phases. This assumption forms the justification for the material in [Chapter 4](#), which covers equilibrium thermodynamics. The local equilibrium assumption, used in the majority of the cases dealt with in this text and in the remainder of this chapter, is discussed further below.

[Table 2.2](#) summarizes the overall balance equations needed for a complete description of isothermal, multicomponent, multiphase flow in permeable media. Column 1 in [Table 2.2](#) gives the strong form of the equation named in Column 2. Column 3 gives the number of scalar equations represented by the equation in Column 1. Columns 4 and 5 give the identity and the number of independent variables added to the formulation by the equation in Column 1. N_D is the number of spatial dimensions ($N_D \leq 3$). The solid phase is a single homogeneous phase, although more than one solid can exist.

TABLE 2.2—DEFINITIONS AND CONSTITUTIVE RELATIONS FOR OVERALL COMPOSITIONAL STRONG-FORM EQUATIONS, EQ. 2.11, FOR ISOTHERMAL FLUID FLOW IN PERMEABLE MEDIA

Equation	Name	Number of Independent Scalar Equations*	Dependent Variables**	
			Identity	Number
$W_i = \phi \sum_{j=1}^{N_c} \rho_j S_j \omega_j + (1-\phi) \rho_s \omega_n \dots \quad (2.2-1)$	Overall concentration	$N_c - 1$	$\rho_j, S_j, \omega_j, \omega_n$	$2N_p + N_c + N_n$
$\dot{N}_i = \sum_{j=1}^{N_c} [\rho_j \omega_j \bar{u}_j - \phi S_j \bar{K}_j \cdot \vec{\nabla}(\rho_j \omega_j)] \dots \quad (2.2-2)$	Component i total flux	$N_c N_o$	\bar{u}_j	$N_o N_c$
$R_i = \phi \sum_{j=1}^{N_c} S_j r_j + (1-\phi) r_n \dots \quad (2.2-3)$	Component i total source	$N_c - 1$	r_{ij}, r_{in}	$N_p N_c + N_n$
$\sum_{i=1}^{N_c} R_i = 0 \dots \quad (2.2-4)$	Total-reaction definition	1		
$\bar{u}_j = -\lambda_g \bar{K} \cdot (\vec{\nabla} P_j - P_g \vec{x}) \dots \quad (2.2-5)$	Darcy's law	$N_p N_o$	λ_g, P_j	$2N_p$
$\lambda_g = \lambda_g(S, \omega, \bar{u}_j, \vec{x}) \dots \quad (2.2-6)$	Relative mobility	N_p	—	—
$P_j - P_n = P_{gp}(S, \omega, \vec{x}) \dots \quad (2.2-7)$	Capillary-pressure definition	$N_p - 1$	—	—
$\sum_{i=1}^{N_c} \omega_i = 1 \dots \quad (2.2-8)$	Mass-fraction definition	N_p	—	—
$\sum_{i=1}^{N_c} \omega_n = 1 \dots \quad (2.2-9)$	Solid-phase mass-fraction definition	1	—	—
$\sum_{j=1}^{N_c} S_j = 1 \dots \quad (2.2-10)$	Saturation definition	1	—	—
$r_j = r_j(\omega_j, P_j) \dots \quad (2.2-11)$	Homogeneous kinetic reaction rates	$(N_c - 1) N_o$	—	—
$r_n = r_n(\omega_n) \dots \quad (2.2-12)$	Solid-phase reaction rates	$N_c - 1$	—	—
$\sum_{i=1}^{N_c} r_i = 0 \dots \quad (2.2-13)$	Total phase-reaction definition	N_o	—	—
$\sum_{i=1}^{N_c} r_{ij} = 0 \dots \quad (2.2-14)$	Solid-phase total reaction rates	1	—	—
$\omega_j = \omega_j(\omega_n)_{\text{eq}_j} \dots \quad (2.2-15)$	Equilibrium relations (or phase balances)	$N_c(N_p - 1)$	—	—
$\omega_n = \omega_n(\omega_i) \dots \quad (2.2-16)$	Solid-phase equilibrium relations (or phase balances)	N_c	—	—
$\rho_j = \rho_j(T, P_j) \dots \quad (2.2-17)$	Equations of state	N_p	—	—

* Total independent equations (including N_c strong-form equations from equations) = $N_o(N_o + N_c) + 2N_o N_c + 4N_p + 4N_n$.

** Total dependent variables (including $2N_o + N_c N_o$ variables from equations) = $N_o(N_o + N_c) + 2N_o N_c + 4N_p + 4N_n$.

In the list of dependent variables, the primary media properties, such as the porosity ϕ and the permeability tensor \vec{k} , are given functions of position \vec{x} within the permeable medium. These quantities are, strictly speaking, functions of the fluid pressure within the medium (Dake 1978), but for pressures nondestructive (no fracturing occurs) to the permeable medium, this effect is generally weak. We also assume that the solid-phase density ρ_s is given, as is the dispersion tensor \vec{K}_{ij} , even though the latter is a function of phase velocities and molecular diffusivities. The remaining terms in Table 2.2 are defined in the nomenclature and in the following subsections.

The first four equations in Table 2.2 are the component conservation Eq. 2.11 and the definitions of the accumulation, flux, and source terms in this equation. We take the N_c conservation

equations to be an independent set of equations; the conservation of overall mass or continuity equation, which follows from summing Eq. 2.11 from 1 to N_C , is not listed as an independent equation (see Section 2.4). In solving specific problems, it may be more convenient to take the problem statement as the continuity equation and $N_C - 1$ mass conservation equations, with the major component (for example, water in flow of dissolved salts in an aqueous solution) being the one omitted.

Definition of Terms in the Overall Compositional Equations. The accumulation term W_i , the overall concentration of component i , is the sum of the component i in the N_P flowing phases plus the solid phase, as shown in Eq. 2.2-1 from [Table 2.2](#). There are only $N_C - 1$ independent W_i because summing on i by use of the mass-fraction definitions in Eqs. 2.2-8 and 2.2-9 from [Table 2.2](#) gives

$$\sum_{i=1}^{N_C} W_i = \phi \sum_{i=1}^{N_P} \rho_j S_j + (1-\phi) \rho_s \equiv \rho(\omega_i, P), \quad (2.16)$$

where ρ is the overall density of the permeable medium (total mass flowing plus solid phase divided by the bulk volume). We can regard the overall density as a complex function of some local pressure P and the set of overall mass fractions, which can be defined as

$$\omega_i = \frac{W_i}{\sum_{i=1}^{N_C} W_i}, \quad (2.17)$$

where ω_i is the mass of component i in all phases divided by the total mass of the permeable medium. The combination of Eqs. 2.16 and 2.17 yields a constraint on the W_i :

$$\rho(W_1, \dots, W_{N_C}, P) = \sum_{i=1}^{N_C} W_i, \quad (2.18)$$

which means that they are $N_C - 1$ independent W_i , not N_C . The notation on the left side of Eq. 2.18 indicates that ρ is a function of

two variables: the set of overall concentrations and the pressure. Eqs. 2.16 through 2.18 can be construed as a constraint on the mass fractions ω_{ij} , phase pressures P_j , and saturations S_j .

Auxiliary Relations. Eq. 2.2-5 from [Table 2.2](#) is a multiphase version of Darcy's law for flow in permeable media (Collins 1976). The single-phase version of Darcy's law is actually a volume-averaged form of the momentum equation (Slattery 1972; Hubbert 1956). The form given in Eq. 2.2-5 ([Table 2.2](#)) assumes creeping flow in the permeable medium with no fluid slip at the solid-phase boundaries. Corrections to account for non-Darcy effects appear in standard references (Collins 1976; Bear 1972). The potential function for the phase superficial velocity \vec{u}_j is the vector sum $\vec{\nabla}P_j - \rho_j\vec{g}$, where P_j is the pressure within the continuous phase j . \vec{g} is the gravitational vector, which is assumed constant and directed toward the Earth's center. Hereafter in this text, we assume that the coordinate direction parallel to \vec{g} is positive upward, away from the Earth's center. The gravitational vector can be written as

$$\vec{g} = g\vec{\nabla}D_z, \dots \quad (2.19)$$

where g is the magnitude of the gravitational vector and D_z is a positive distance below some horizontal reference plane, typically depth. For Cartesian coordinates with a constant inclination with the reference plane, $\vec{\nabla}D_z$ becomes a vector consisting of the cosines of the inclination angles between the respective axis and the vertical.

The tensor form of the permeability \vec{k} implies an anisotropic permeable medium with coordinate axes unaligned with the principal axis of \vec{k} . With the inclusion of \vec{k} we have now included all the primary permeable-media properties, ϕ , \vec{k} , a_{ij} , a_{tj} , and τ , into the formulation. These properties and their spatial distributions are geologic in nature and are characterized by the details of the individual flow paths.

The other quantity in Eq. 2.2-5 ([Table 2.2](#)) is the relative mobility λ_{rj} of phase j , which can be defined as the quotient of the relative permeability k_{rj} and the viscosity μ_j :

$$\lambda_{rj} = \frac{k_{rj}(S, \omega, \vec{x})}{\mu_j(\omega, \vec{u}_j)}. \dots \quad (2.20)$$

Eq. 2.20 decomposes λ_{rj} into a rock-fluid property k_{rj} and a fluid property μ_j . k_{rj} is a function of the tendency of phase j to wet the permeable medium, of pore size distribution, and of the entire set of phase saturations (see [Chapter 3](#)). μ_j is a function of the phase composition and, if phase j is non-Newtonian, the magnitude of the superficial velocity \vec{u}_j (see [Chapter 8](#)). The relative permeabilities and viscosities k_{rj} and μ_j are usually determined experimentally to give λ_{rj} . It is slightly more general to write the $\lambda_{rj} \vec{k}$ product in Eq. 2.2-5 ([Table 2.2](#)) as

$$\lambda_{rj} \vec{k} = \frac{\vec{k}_j}{\mu_j}, \dots \quad (2.21)$$

where \vec{k}_j is the phase permeability tensor. This form allows for anisotropic relative permeabilities, but little is known about the anisotropic nature of these relative permeabilities, and, therefore, it remains a scalar function here (i.e., $\vec{k}_j = k_{rj} \vec{k}$). Relative permeabilities and viscosities are chemical properties.

The difference between the phase pressures of any two phases flowing in the REV is the capillary pressure, which is defined in Eq. 2.2-7 ([Table 2.2](#)). The capillary pressure between phases j and n is a function of most of the same variables as the relative permeability (Fatt and Dykstra, 1951). That there are $N_P - 1$ independent relations follows from considering the set of all capillary pressures with j fixed, $P_{c1j}, P_{c2j}, \dots, P_{cN_{Pj}}$. Ignoring the trivial case of P_{cjj} (=0), there

are clearly $N_P - 1$ capillary pressures. The capillary pressure P_{ckn} between any two other phases k and n may be expressed as a linear combination of members from the original set:

$$P_{ckn} = P_k - P_n = (P_k - P_j) + (P_j - P_n) = P_{ckj} + P_{cjn}. \dots \quad (2.22)$$

Hence, there are only $N_P - 1$ independent capillary pressure relations, which are usually determined experimentally under static conditions. We discuss capillary pressure in more detail in [Chapter 3](#).

The pressures P_j are the continuous-phase pressures, not the pressures that would exist in disconnected “globules” of phase j . In the latter case, the phase-pressure differences still exist, but because they are a reflection of the local permeable-medium pore configuration, they are not uniquely determined by the functions given in Eq. 2.2-7 ([Table 2.2](#)).

Eqs. 2.2-8 through 2.2-10 ([Table 2.2](#)) follow from the definitions of mass fraction and phase saturation. Eqs. 2.2-11 through 2.2-14 ([Table 2.2](#)) are definitions of the reaction rate of component i in phase j or in the solid phase. As was true for R_i , there can be no net accumulation of mass in a phase because of chemical reactions. For this reason, the reaction-rate terms r_{ij} and r_{is} sum to zero, as indicated by Eqs. 2.2-13 and 2.2-14 ([Table 2.2](#)), if the equation is written in mass units.

Local Equilibrium. Eqs. 2.2-15 and 2.2-16 from [Table 2.2](#) are relations among the mass fractions of the N_P flowing phases and the solid phase present in the REV. These relations arise from solving the conservation equation for each component in each phase (Eq. 2.2-15 from [Table 2.2](#)):

$$\frac{\partial W_{ij}}{\partial t} + \vec{\nabla} \cdot \vec{N}_{ij} = R_{ij} + r_{mij},$$

where the second subscript on W_i , \vec{N}_i , and R_i refers to a single term in the sums over all phases in their original definition. The term r_{mij}

expresses the rate of mass transfer of species i from or into phase j . To maintain consistency with Eq. 2.11, we must have $\sum_{i=1}^{N_P} r_{mij} = 0$, a relation following from the inability to accumulate mass at an interface. Because the sum of the conservation equations over all flowing phases for component i is Eq. 2.11, there are $N_C(N_P - 1)$ independent phase balances. Because there are also N_C phase balances for the solid phase, the total number of independent relations is $N_C N_P$. There are a similar number of additional unknowns, the r_{mij} , which must be independently specified.

The phase balance is formally correct, but requires considerable additional work to be useful. A much more practical approach is to assume local thermodynamic equilibrium; that is, the mass fractions of component i are related through thermodynamic equilibrium relations (Pope and Nelson 1978). For flow through naturally occurring permeable media, the assumption of local equilibria among phases is usually adequate (Raimondi and Torcaso 1965). Exceptions are flows at very high rates or leachant flows such as might occur in alkaline floods. The local equilibrium approximation (LEA) is discussed further in Lake et al. (2002).

If local equilibrium applies, the number $N_C N_P$ of independent scalar equations may be derived from the Gibbs phase rule (see [Chapter 4](#)). The equilibrium relations themselves are very strong functions of the particular EOR process, and much of the behavior and many of the important features of a given process can be understood from these considerations. [Chapter 4](#) discusses phase behavior generally; we reserve more specifics for the relevant sections on solvent, chemical, and thermal flooding.

The final equation in [Table 2.2](#) is the equation of state, Eq. 2.2-17, which relates each phase density to its composition, temperature, and pressure. For flow following the LEA, the equilibrium relations for the flowing phases (Eqs. 2.2-15 and 2.2-16 from [Table 2.2](#)) can be derived from the equation of state as discussed in [Chapter 4](#). This practice enforces internal consistency between the equilibrium

relations and the equation of state. In this text, however, we will often invoke simpler equilibrium relations for pedagogical purposes.

Phase-Conservation Equations. Another important set of equations are the phase-conservation equations, which are derived from performing a mass balance on a given phase. The result gives

where we used Eqs. 2.2-13 and 2.2-14 (from [Table 2.2](#)) and $\sum_{i=1}^{N_c} \vec{\nabla} \cdot \vec{j}_{Dij} = \vec{\nabla} \cdot \sum_{i=1}^{N_c} \vec{j}_{Dij} = 0$ (net dispersive flux in a phase is zero). The dispersive flux term vanishes strictly only for the case when the flux is written with respect to mass-averaged velocity (see Exercise 2.4). Nevertheless, we assume that this is also approximately correct when the dispersive flux is written with respect to volume-averaged velocity. The phase-conservation equations are useful for modeling fluid flow of several phases. In general, this is the case when fluids are immiscible so that the phase compositions are fixed.

Under the assumption of no mass transfer and no sorption, $r_{mij} = 0$, and Eq. 2.23 reduces to the immiscible phase-conservation equations,

where $\varepsilon_j = \phi S_j$ from Eq. 2.12 and N_P represents only flowing phases. The solid-phase equation is omitted because its solution is trivial when it is nondeformable; that is, when $(1 - \phi)\rho_s$ is temporally constant.

Continuity Equation. We sum Eq. 2.15 over the N_C components to obtain the equation of *continuity*, or conservation of total mass. We could have also obtained the equation of continuity by summing the phase-conservation equations, Eq. 2.23, over N_P phases, including the solid phase. The equation of continuity is

Eq. 2.25 can be written totally in terms of pressure and saturation derivatives by use of Eqs. 2.2-5 (from [Table 2.2](#)) and 2.16; this equation is a form of the “pressure” equation.

2.3 Energy-Balance Equations

For steam, hot-water injection, and in-situ combustion—some of the most important EOR and remediation processes—temperature changes over both space and time. The equations in [Table 2.2](#) apply equally well to nonisothermal flow, but with an additional dependent variable, temperature, added to the formulation. The additional equation required to make the problem statement deterministic is the conservation of energy, or the first law of thermodynamics. The first law is based on our everyday observation that for any change of thermodynamic properties, total energy (which includes internal, potential, kinetic, heat, and work) is conserved.

A statement of the energy balance or first law of thermodynamics suitable for our purposes is

$$\left\{ \begin{array}{l} \text{Rate of} \\ \text{accumulation} \\ \text{of energy in } V \end{array} \right\} = \left\{ \begin{array}{l} \text{Net rate} \\ \text{of energy} \\ \text{transported into } V \end{array} \right\} + \left\{ \begin{array}{l} \text{Net rate of} \\ \text{generation of energy} \\ \text{inside } V \end{array} \right\}, \dots \quad (2.26)$$

where V is an arbitrary volume as in Fig. 2.3. From left to right in Eq. 2.26 are the accumulation, flux, and source terms. We use the parallel between the component conservation Eq. 2.1 and Eq. 2.26 to shorten the following development. By analogy to the procedure in Section 2.2, the accumulation term in Eq. 2.26 for stationary V can be written as

$$\left\{ \begin{array}{l} \text{Rate of} \\ \text{accumulation} \\ \text{of energy in } V \end{array} \right\} = \frac{d}{dt} \left\{ \begin{array}{l} \text{Total energy} \\ \text{in } V \end{array} \right\}$$

$$= \frac{d}{dt} \left\{ \int_V \sum_{j=1}^{N_p} \left[\varepsilon_j \rho_j \left(\hat{U}_j + \frac{1}{2} |\vec{v}_j|^2 - gD_z \right) \right] dV \right\}, \dots \quad (2.27)$$

where the total energy includes internal, kinetic, and potential energy. Eq. 2.27 can also be written as

$$\left\{ \begin{array}{l} \text{Rate of} \\ \text{accumulation} \\ \text{of energy in } V \end{array} \right\} = \frac{d}{dt} \int_V \left(\rho \hat{U} + \frac{1}{2} \rho |\vec{v}|^2 - \rho g D_z \right) dV, \dots \quad (2.28)$$

where \hat{U} is an overall specific internal energy (total energy/total mass) and ρ is the overall density given by Eq. 2.16. In Eq. 2.28, the term $\frac{1}{2}(\rho|\vec{v}|^2)$ represents total kinetic energy per unit bulk volume and $-\rho g D_z$ total potential energy per unit bulk volume with reference to the vertical distance below some horizontal plane.

The remaining terms in Eq. 2.26 are represented by

$$\frac{d}{dt} \int_V \left(\rho \hat{U} + \frac{1}{2} \rho |\vec{v}|^2 - \rho g D_z \right) dV = - \int_V \vec{\nabla} \cdot \vec{E} dV + \dot{W}, \dots \quad (2.29)$$

where the terms \vec{E} and \dot{W} represent energy flux and energy source, respectively, to which we give specific form below. The negative sign in front of the first term on the right is required to make the energy flux positive when it flows into volume V . See [Chapter 4](#) for a more in-depth treatment of the first law of thermodynamics with application to phase behavior.

The source term requires more elaboration than do the other terms in Eq. 2.29. The form of the first law of thermodynamics for open CVs expressed by Eq. 2.29 requires the \dot{W} term to be composed of work components only in the absence of external heating sources. External heating sources can often be handled through boundary conditions. Heats of reaction, vaporization, and solution are, of course, important in several processes, but these are

implicitly present in the equation in the concentration and flux terms. Here we consider only the rate of work done against a pressure field \dot{w}_{pv} , although other types of work could be included (see Exercise 2.15). In this derivation, there is no compression or expansion work done on volume V because it is assumed to be fixed.

Returning to Fig. 2.3b, consider an element in the multiphase, multicomponent flow field crossing ΔA . Because work is the product of force times distance, the rate of work is force times velocity. The element crossing ΔA is, therefore, doing work $\Delta \dot{W}_{PV}$, where

The term $P_j \Delta A \vec{n}$ is the force exerted on ΔA by the pressure in phase j . The scalar product in Eq. 2.30 expresses a general definition of work rate when using vector forces and velocities. The negative sign in Eq. 2.30 is to satisfy the usual thermodynamic sign convention for work because $\Delta \dot{W}_{pv}$ must be positive for work done on a fluid element flowing into V ($\vec{n} \cdot \vec{u}_j < 0$). The total pressure/volume work is the sum of Eq. 2.30 over all surface elements, which, in the limit of the largest ΔA approaching zero, becomes a surface integral. Using the divergence theorem, Eq. 2.9, on this integral gives the final form for \dot{W}_{pv} :

The expression for work fits well into Eq. 2.29. After collecting all terms under the same volume integral and making the integrand zero because V is again arbitrary, we have the strong form of the energy balance:

$$\frac{\partial}{\partial t} \left(\rho \hat{U} + \frac{1}{2} \rho |\vec{v}|^2 - \rho g D_z \right) + \vec{\nabla} \cdot \vec{E} + \sum_{j=1}^{N_p} \vec{\nabla} \cdot (P_j \vec{u}_j) = 0. \quad \dots \quad (2.32)$$

The energy-flux term is made up of convective contributions from the flowing phases (internal, kinetic, and potential energy),

conduction, and radiation, all other forms being neglected:

For brevity, we neglect radiation in the following discussion, although this transport mechanism can be an important source of heat loss from wells and in certain forms of EOR and remediation that involve electromagnetic sources. For multiphase flow, the conductive heat flux is derived from Fourier's law,

where k_{Tt} is the scalar total thermal conductivity. k_{Tt} is a complex function of the phase saturations and the phase (k_{Tj}) and solid (k_{Ts}) thermal conductivities, which we assume to be known (see [Chapter 11](#)). The parallel between Eq. 2.34 and the dispersive flux term in Eq. 2.2-2 (from [Table 2.2](#)) is obvious. We have also invoked the requirement of local thermal equilibrium in this definition by taking the temperature T to be the same in all phases within the REV.

Inserting the definitions of Eqs. 2.33 and 2.34 into Eq. 2.32 yields

$$\frac{\partial}{\partial t} \left(\rho \hat{U} + \frac{1}{2} \rho |\vec{v}|^2 - \rho g D_z \right) + \vec{\nabla} \cdot \left[\sum_{j=1}^{N_p} \rho_j \vec{u}_j \left(\hat{U}_j + \frac{1}{2} |\vec{v}_j|^2 - g D_z \right) \right] - \vec{\nabla} \cdot (k_{Ti} \vec{\nabla} T) + \sum_{j=1}^{N_p} \vec{\nabla} \cdot (P_j \vec{u}_j) = 0 \dots (2.35)$$

The first sum in the energy flux term and that in the pressure-volume work expression may be combined to give

$$\frac{\partial}{\partial t} \left(\rho \hat{U} + \frac{1}{2} \rho |\vec{v}|^2 - \rho g D_z \right) + \vec{\nabla} \cdot \left[\sum_{j=1}^{N_p} \rho_j \vec{u}_j \left(\hat{H}_j + \frac{1}{2} |\vec{v}_j|^2 - g D_z \right) \right] - \vec{\nabla} \cdot (k_{Ti} \vec{\nabla} T) = 0, \dots \quad (2.36)$$

where $\hat{H}_j = \hat{U}_j + P / \rho_j$ is the phase-specific enthalpy, defined as the enthalpy of phase j per unit mass of j .

The conservation equations discussed in this section and in [Table 2.3](#) are “overall” in the sense that the balances are written over a REV that contains all the phases. We could have written balances on each phase or each component just as was done in the previous

section for mass conservation. These balances would have in them terms describing the rate of energy transport between phases and would not necessarily assume equality of temperature in all phases within a REV.

TABLE 2.3—DEFINITIONS AND CONSTITUTIVE RELATIONS FOR ENERGY STRONG-FORM
(EQ. 2.36) FOR NONISOTHERMAL FLUID FLOW IN PERMEABLE MEDIA

Equations	Name	Number of Independent Scalar* Equations	Dependent Variables**	
			Identity	Number
$\rho \hat{U} = \phi \sum_{j=1}^{N_p} \rho_j S_j \hat{U}_j + (1-\phi) \rho_s \hat{U}_s$(2.3-1)	Total internal energy	1	\hat{U}_j, \hat{U}_s	$N_p + 1$
$U_j = \sum_{i=1}^{N_c} \omega_{ij} \hat{U}_{ij}$ $U_s = \sum_{i=1}^{N_c} \omega_{is} \hat{U}_{is}$(2.3-2)	Phase internal energy	N_p	\hat{U}_{ij}	$N_p N_c$
$H_j = \sum_{i=1}^{N_c} \omega_{ij} \hat{H}_{ij}$(2.3-3)	Phase enthalpy	N_p	\hat{H}_{ij}	$N_p N_c$
$\hat{U}_{ij} = \hat{U}_{ij}(T, P_j, \omega)$ $\hat{U}_{is} = \hat{U}_{is}(T, P_j, \omega)$(2.3-4)	Partial mass internal energy	$N_p N_c$		
$\hat{H}_{ij} = \hat{H}_{ij}(T, P_j, \omega)$(2.3-5)	Partial mass enthalpy	$N_p N_c$		

* Total independent equations including 1 strong-form equation from Eq. 2.36 = $2(N_p N_c) + 2N_p + N_c + 3$.

** Total dependent variables including $N_p + 2$ variables from Eq. 2.36 = $2(N_p N_c) + 2N_p + N_c + 3$.

Eq. 2.36 can also be obtained if the volume V is no longer stationary and both pressure/volume and compression/expansion work are present (see Exercise 2.16). For example, consider a control volume across the surface of which only energy is flowing (thermodynamics texts call this a *closed system*) in which the volume V expands or contracts at the same rate as the fluid-flow velocity. In that case, compression-expansion work is done on the boundary of

V as it deforms, and pressure-volume work is zero because there is no mass flow into V . This type of work is given by $\Delta\dot{W}_{CE} = \vec{F}_{ext} \cdot \vec{u}$, is the component of external force acting along the velocity vector \vec{u}

. Work is always related to an external pressure or force. If the external pressure were zero, there would be no work done by the CV because the surroundings offer no resistance. The rate of work done on a surface element of V is therefore

$$\Delta\dot{W}_{CE} = -\sum_{j=1}^{N_p} P_j \Delta A \vec{n} \cdot \vec{u}_j, \dots \quad (2.37)$$

which is identical to Eq. 2.30. The development then proceeds as before, but with the accumulation term for a time-varying V deforming at a Darcy rate \vec{u}_j written as (Slattery 1972)

$$\begin{aligned} \frac{d}{dt} \int_V \sum_{j=1}^{N_p} \left[\varepsilon_j \rho_j \left(\hat{U}_j + \frac{1}{2} |\vec{v}_j|^2 - gD_z \right) \right] dV &= \int_{V(t)} \frac{\partial}{\partial t} \sum_{j=1}^{N_p} \left[\varepsilon_j \rho_j \left(\hat{U}_j + \frac{1}{2} |\vec{v}_j|^2 - gD_z \right) \right] dV \\ &\quad + \int_{A(t)} \nabla \cdot \sum_{j=1}^{N_p} \left[\rho_j \vec{u}_j \left(\hat{U}_j + \frac{1}{2} |\vec{v}_j|^2 - gD_z \right) \right] dA \end{aligned}$$

by use of Leibnitz's rule.

Eq. 2.37 can be rewritten in a more familiar form by combining the surface-element areas with the component of the velocity vector perpendicular to that surface element, ($\Delta q_{j\perp} = \vec{n} \cdot \Delta A \vec{u}_j = \vec{n} \cdot \Delta \vec{q}_j$), summing over all surface elements, and taking the limit as the largest ΔA approaches zero. The result is

$$\dot{W}_{CE} = -\sum_{j=1}^{N_p} \int_{q_{j\perp} \in A(t)} P_j dq_{j\perp}. \dots \quad (2.38)$$

Furthermore, when the phase pressures are uniform along the boundary of V , the phase pressures can pass through the integral, so that

$$\dot{W}_{CE} = -\sum_{j=1}^{N_p} P_j \frac{dV_j}{dt}. \dots \quad (2.39)$$

V_j in Eq. 2.39 is now the total volume of phase j within V . Eq. 2.39 is valid regardless of the shape or size of volume V as long as the pressure is uniform at its boundary.

2.3.1 Auxiliary Relations. [Table 2.3](#) summarizes the equations that, together with those of [Table 2.2](#), completely specify nonisothermal fluid-flow problems. The first three equations have already been discussed.

The energy concentration per unit bulk volume must include internal energy contributions from all flowing phases and the solid phase,

$$\rho \hat{U} = \phi \sum_{j=1}^{N_p} \rho_j S_j \hat{U}_j + (1 - \phi) \rho_s \hat{U}_s \quad (\text{Eq. 2.3-1 from Table 2.3}),$$

where \hat{U}_j is the internal energy per unit mass of phase j . The total kinetic-energy term includes kinetic-energy contributions from all flowing phases,

$$\frac{1}{2} \rho |\vec{v}|^2 = \phi \sum_{j=1}^{N_p} \left(\frac{1}{2} \rho_j S_j |\vec{v}_j|^2 \right), \dots \quad (2.40)$$

where the solid-phase velocity is negligible.

The phase-specific internal energies \hat{U}_j and \hat{U}_s and the specific enthalpies \hat{H}_j are functions of temperature T , phase pressure P_j , and composition ω_{ij} . One form this dependency can take is Eq. 2.3-2 ([Table 2.3](#)), where the doubly subscripted internal energies (and enthalpies) are partial mass quantities. Partial mass quantities, as in Eq. 2.3-4 ([Table 2.3](#)), are analogous to partial molar quantities in solution thermodynamics (Sandler 2006). For example, the partial mass internal energy of component i in phase j is the change in \hat{U}_j as ω_{ij} is changed, all other variables being held constant,

$$\hat{U}_{ij} = \left(\frac{\partial \hat{U}_j}{\partial \omega_{ij}} \right)_{P_j, T, \omega_{kj, k \neq i}}, \dots \quad (2.41)$$

and similarly for \hat{U}_{is} and \hat{H}_{ij} . The partial mass properties themselves may be calculated from equations of state, Eq. 2.2-17 (from [Table 2.2](#)), or empirical correlations as functions of temperature, pressure, and composition.

Eqs. 2.3-2 and 2.3-3 (from [Table 2.3](#)) readily revert to simple forms. For example, if phase j is an ideal solution, the partial mass quantities become pure component quantities, which are functions of temperature and pressure only. Furthermore, if j is an ideal gas, the partial mass quantities \hat{U}_j and \hat{H}_j are functions only of temperature.

The equations presented in Tables 2.2 and 2.3 are complete, but they can only be solved with the specification of a similarly complete set of initial and boundary conditions.

2.4 Entropy-Balance Equations

The equations for conservation of total mass and energy are not enough to solve many thermodynamic problems. For example, experience has shown that a pond on a hot summer day will not freeze, but instead will approach the temperature of its surroundings. The first law of thermodynamics, however, is satisfied whether the pond freezes (loses energy to surroundings) or heats up (gains energy from surroundings). In other words, the direction of energy transfer is irrelevant to the first law of thermodynamics; there must be more information that describes which changes are permissible.

As long as there are no outside influences (this makes the control volume an isolated CV or one that has no energy or mass transfer), changes in concentration, temperature, and pressure eventually vanish, and these properties reach a time-invariant state. This state is called the *equilibrium* state. The need to study this equilibrium state, primarily in [Chapter 4](#), is why we discuss entropy here.

The second law of thermodynamics provides a mathematical statement that describes the unidirectional change to equilibrium

through a thermodynamic property, called *entropy*. Entropy is also used to describe the equilibrium state itself. Although we are less familiar with entropy, it is a property just like internal energy and enthalpy. Just as for internal energy and enthalpy, we must infer entropy from sensible thermodynamic properties such as temperature, pressure, and volume.

A good definition of the second law is that the entropy of an isolated system will always increase from a state of high probability (well-ordered, small entropy) to a state of lower probability (more disordered, large entropy) until it reaches a maximum entropy at equilibrium. This increase (or generation) of entropy is always related to initial gradients in the CV, and over time the rate of generation of entropy decreases as fluids mix or heat is exchanged. If a system is initially at equilibrium and remains so, no entropy is generated.

An entropy balance is used to represent mathematically the tendency of processes to approach equilibrium. The steps to write the entropy balance are similar to those for the first law of thermodynamics, except that entropy is *always* created as fluids mix or heat is exchanged. Entropy for a CV that is not isolated can increase or decrease depending on the direction and magnitude of mass transport and heat exchange with its surroundings. A statement of the entropy balance is

$$\left\{ \begin{array}{l} \text{Rate of} \\ \text{accumulation} \\ \text{of entropy in } V \end{array} \right\} = \left\{ \begin{array}{l} \text{Net rate} \\ \text{of entropy} \\ \text{transported into } V \end{array} \right\} + \left\{ \begin{array}{l} \text{Rate of} \\ \text{generation of entropy} \\ \text{inside } V \end{array} \right\}, \dots \quad (2.42)$$

where V is an arbitrary volume as shown in Fig. 2.3. By analogy to the procedure for the first law of thermodynamics in Section 2.3, the accumulation term in Eq. 2.42 for a stationary V can be written as

$$\left\{ \begin{array}{l} \text{Rate of} \\ \text{accumulation} \\ \text{of entropy in } V \end{array} \right\} = \frac{d}{dt} \left\{ \begin{array}{l} \text{Total entropy} \\ \text{in } V \end{array} \right\} = \frac{d}{dt} \left[\int_V \sum_{j=1}^{N_p} (\varepsilon_j \rho_j \hat{S}_j) dV \right], \dots \quad (2.43)$$

where the total entropy includes contributions from all phases and \hat{S}_j is the specific entropy of phase j defined as the entropy of phase j per mass of phase j . Eq. 2.42 can now be expressed as

$$\frac{d}{dt} \left[\int_V \sum_{j=1}^{N_p} (\varepsilon_j \rho_j \hat{S}_j) dV \right] = - \int_A (\bar{n} \cdot \vec{S}) dV + \int_V \dot{\sigma}_G dV. \dots \quad (2.44)$$

The first term on the right side is the entropy flux term. The second term is the rate of entropy generation per unit bulk volume.

The net rate of entropy transport into volume V is the result of heat and mass transfer into V from its surroundings. Entropy transport arising from advection is handled similarly to energy. Therefore, the total entropy transport attributable to mass convection and heat exchange is

$$\vec{S} = \sum_{j=1}^{N_p} \rho_j \vec{u}_j \hat{S}_j + \frac{\vec{q}_c}{T}. \dots \quad (2.45)$$

Similarly to the energy balance, we assume the temperature T to be the same in all phases within the REV. Substitution of Eq. 2.45 into Eq. 2.44 gives,

$$\frac{d}{dt} \left[\int_V \sum_{j=1}^{N_p} (\varepsilon_j \rho_j \hat{S}_j) dV \right] = - \int_A \bar{n} \cdot \left(\sum_{j=1}^{N_p} \rho_j \vec{u}_j \hat{S}_j \right) dV - \int_A \left(\bar{n} \cdot \frac{\vec{q}_c}{T} \right) dV + \int_V \dot{\sigma}_G dV. \dots \quad (2.46)$$

Eq. 2.46 is the weak form of the entropy balance.

To obtain the strong form, move the time derivative inside the volume integral (V is fixed), apply the divergence theorem, collect all terms under the same volume integral, and set the integrand to zero because V is again arbitrary:

$$\frac{\partial}{\partial t} \left(\sum_{j=1}^{N_p} \varepsilon_j \rho_j \hat{S}_j \right) = - \vec{\nabla} \cdot \left(\sum_{j=1}^{N_p} \rho_j \vec{u}_j \hat{S}_j \right) - \vec{\nabla} \cdot \frac{\vec{q}_c}{T} + \dot{\sigma}_G. \dots \quad (2.47)$$

Analogously to the procedure in Section 2.3, Eq. 2.47 could also be obtained for time-varying V .

2.4.1 Second Law of Thermodynamics. The inequality $\dot{\sigma}_G \geq 0$ is the second law of thermodynamics, the equality holding at equilibrium. This simple condition provides the restriction on bidirectional transport of energy. You can show that Eq. 2.47 is consistent with the preceding discussion about entropy increasing in an isolated control volume by setting the two terms on the right equal to zero.

As we are about to show, the creation of entropy is related to gradients within the CV. When gradients are kept negligible within a CV, entropy generation within that CV is also negligible.

The relationship between entropy generation and gradients within a CV is most easily seen by assuming single-phase flow and neglecting changes in kinetic or potential energies. The mass, energy, and entropy balances become, respectively,

$$\frac{\partial}{\partial t}(\phi\rho) = -\vec{\nabla} \cdot (\rho\vec{u}),$$

$$\frac{\partial}{\partial t}(\phi\rho\hat{U}) = -\vec{\nabla} \cdot (\rho\vec{u}\hat{U}) - \vec{\nabla} \cdot (P\vec{u}) - \vec{\nabla} \cdot \vec{q}_c,$$

and,

$$\frac{\partial}{\partial t}(\phi\rho\hat{S}) = -\vec{\nabla} \cdot (\rho\vec{u}\hat{S}) - \frac{1}{T} \vec{\nabla} \cdot \vec{q}_c + \frac{\vec{q}_c}{T^2} \cdot \vec{\nabla} T + \dot{\sigma}_G,$$

where the conduction term in the entropy equation has been expanded and the definition of enthalpy $\hat{H} = \hat{U} + P/\rho$ is used. Elimination of the $\vec{\nabla} \cdot \vec{q}_c$ term between the last two equations and rearranging with the total derivative ($D/Dt = \partial/\partial t + \vec{v} \cdot \vec{\nabla}$) gives,

$$\phi\rho \left(\frac{D\hat{S}}{Dt} - \frac{1}{T} \frac{D\hat{U}}{Dt} - \frac{P}{T} \frac{D\hat{V}}{Dt} \right) = \frac{1}{T} \vec{u} \cdot \vec{\nabla} P + \frac{\vec{q}_c}{T^2} \cdot \vec{\nabla} T + \dot{\sigma}_G, \dots \quad (2.48)$$

where $\hat{V} = 1/\rho$ and under the assumption of constant porosity, $\vec{\nabla} \cdot \vec{u} = \phi \rho (D\hat{V}/Dt)$.

The left side of Eq. 2.48 describes the temporal changes in thermodynamic properties; it is zero from the definition of entropy. The right side of Eq. 2.48 involves terms that depend on gradients of pressure and temperature. Therefore, because entropy generation is the result of spatial gradients, we must have

Substitution of Darcy's law for horizontal single-phase flow, $\vec{u} = -(\vec{k} / \mu) \cdot \vec{\nabla} P$, and Fourier's law of heat conduction, $\vec{q}_c = -k_{Tt} \nabla T$, into Eq. 2.49 gives the desired result,

$$\dot{\sigma}_G = \frac{1}{T} \left[\left(\frac{\vec{k}}{\mu} \cdot \vec{\nabla} P \right) \cdot \vec{\nabla} P + \left(\frac{k_{Tl}}{T} \vec{\nabla} T \right) \cdot \vec{\nabla} T \right] \dots \dots \dots \quad (2.50)$$

Eq. 2.50 shows that entropy creation is proportional to the square of the pressure and temperature gradients. Therefore, entropy creation is minimized when gradients are small, as they are when equilibrium is approached or when gradients are kept small in a succession of quasi-equilibrium steps (i.e., under reversible conditions). The rate of entropy generation is, therefore, a measure of the degree of irreversibility of a process.

Eq. 2.50 also shows that $\dot{\sigma}_G \geq 0$ because the properties in Eq. 2.50 are positive and the square of the gradients is always positive. The expression for entropy creation can be extended to account for multiple components, diffusive flux, electrical current flow, and other processes.

2.5 Special Cases of the Strong Form

We now turn to several important special cases of the phase-conservation equations, Eq. 2.23, the overall compositional equations Eq. 2.15, and Tables 2.2 and 2.3. Each special case is used to describe various EOR processes occurring in fluid flow

through permeable media. These special cases can be accurately approximated by much simpler forms of the general equations described previously with fewer and simpler associated auxiliary equations and boundary conditions. We will work only with the strong form of the conservation equations; you should be able to develop weak forms from the discussion. All flows discussed here are in local thermodynamic equilibrium.

Example 2.1—1D Immiscible Flow. Phases are said to be *immiscible* if their compositions do not change. The flow of oil and water is an excellent example of immiscibility because the group of components defined as “oil” does not change when contacted with water. This immiscible flow occurs whenever $r_{mij} = r_{is} = 0$ for Eq. 2.23 or $C_{ij} = \rho_j w_{ij}$ is constant for Eqs. 2.2-1 and 2.2-2 (from [Table 2.2](#)). Holding the phase compositions fixed eliminates the dispersion term from Eq. 2.2-2 (from [Table 2.2](#)). Therefore, we can apply the above assumptions to the phase-conservation equations, Eq. 2.23. For this case, the energy-conservation equation and the solid-phase equation are trivial, and Eq. 2.23 reduces to Eq. 2.24:

$$\frac{\partial}{\partial t} \left(\phi S_j \rho_j \right) + \vec{\nabla} \cdot \left(\rho_j \vec{u}_j \right) = 0 \quad j = 1, \dots, N_p.$$

Next, we specialize the equation for one-dimensional linear flow in a medium dipping at a constant angle α and constant rock and fluid properties (ϕ held constant temporally and ρ_j held constant temporally and spatially). Because the porosity and the phase densities are constant, these properties can be removed from the respective derivatives and the phase densities cancelled. Eq. 2.24 further simplifies to

To eliminate the need to solve for pressure, Eq. 2.51 is usually written in terms of a fractional-flow function, which can be defined as

where $u = \sum_{j=1}^{N_p} u_j$. As we will see in [Chapter 5](#) or in Exercise 2.10, u is a function of time only, and f_j is a function of saturation only, which enables us to write Eq. 2.51 in a final form:

To solve Eq. 2.53 for the phase saturations $S_j(x, t)$, the total volumetric fluid flux u injected at the inflow boundary and the experimentally measured fractional-flow dependences of $N_P - 1$ phases (note $\sum_{j=1}^{N_P} f_j = 1$) are needed. Eq. 2.53 is called the *fractional-flow equation*.

Buckley and Leverett (1941) first solved this equation for two-phase flow, and the resulting estimation of waterflood oil recovery is called the Buckley-Leverett theory (see [Chapter 5](#)). Other similar cases, including three-phase flow and compositional effects, such as interphase mass transfer and adsorption, have been solved in closed form (e.g., Pope 1980; Johns et al. 1993, Guzmán Ayala 1995; LaForce and Johns 2005).

Example 2.2—1D Miscible Flow. The preceding fractional-flow equation (Eq. 2.53) applies to the simultaneous flow of immiscible fluids. We now treat the analogous but opposite case of many components flowing simultaneously in a single fluid phase in isothermal flow. This means that only one phase is flowing, regardless of its composition, but both convection and dispersion of its components must be included. Components (or groups of components) that mix in all proportions without forming an interface (that is, only one phase exists) are said to be miscible.

Miscible processes of interest include (1) true (first-contact) miscible displacement of oil by a solvent from a reservoir; (2) chromatographic processes of various sorts, such as analytical

chromatography, separation chromatography, ion-exchange processes, and adsorption of chemicals as they percolate through soils and other naturally occurring permeable media; (3) leaching processes, such as the in-situ mining of uranium; and (4) chemical reaction processes of many types in fixed-bed reactors.

Eq. 2.15 for single-phase flow is

This equation arises because the saturations for all phases but one are zero and the saturation of that remaining phase is one. The second subscript j is now superfluous and has been dropped. The auxiliary Eqs. 2.2-5, 2.2-6, 2.2-8, 2.2-9, and 2.2-11 through 2.2-17 (from [Table 2.2](#)) are still needed, but the others are no longer pertinent. The principal one of these, Eq. 2.2-5 or Darcy's law, has a considerably simpler form as well:

$$\vec{u} = -\frac{\vec{k}}{\mu} \cdot (\vec{\nabla} P - \rho \vec{g}).$$

Because the relative permeability is now constant (typically unity), it is lumped with \vec{k} .

For miscible solvents (see [Chapter 7](#)), the sorption term, the second term in Eq. 2.54, is negligible. That assumption, coupled with that of no chemical reactions ($R_i = 0$), gives

$$\frac{\partial(\phi\rho\omega_i)}{\partial t} + \vec{\nabla} \cdot [\rho\omega_i\vec{u} - \phi\vec{K}_i \cdot \vec{\nabla}(\rho\omega_i)] = 0, \quad i = 1, \dots, N_c. \quad (2.55)$$

A special 1D linear case of Eq. 2.55 is obtained when both porosity and \vec{K}_i are constant. Letting $C_i = \rho\omega_i$ be the mass concentration of component i , it follows that

where $K_{||j}$, the longitudinal dispersion coefficient, is now a scalar,

as a special case of the more general definition given by Eq. 2.13. D_i is usually considered to be a constant, yielding the linear convection-diffusion (CD) equation, which is alternatively called the advection-dispersion equation. Several closed-form solutions for simple initial and boundary conditions are available for the CD equation (see [Chapters 5](#) and [7](#)).

Example 2.3—1D Chromatographic Equations. Chromatography refers to the separation of components through interactions with the solid phase. The “chroma” in chromatography refers to the fact that components were identified by their characteristic colors.

Chromatographic processes are special cases of Eq. 2.56. We must restore the C_{is} term ($C_{is} = \rho\omega_{is}$) that describes the accumulation of component i through sorption reactions, for this is the essence of a chromatographic process. These sorption reactions may be adsorption, the exchange of one ion for another on the solid substrate, or precipitation-dissolution reactions (see [Chapters 8 to 10](#) and Lake et al. 2002). All these processes lead to selective separation of the components as they percolate through the permeable medium. Dispersion does not alter the separation in chromatographic columns (Lake et al. 2002), and therefore we neglect the second-order term, a step that results in a set of strongly coupled (through the sorption term) first-order partial differential equations:

For linear sorption, Eq. 2.58 can be rewritten in terms of a retardation factor by first collecting like terms:

The retardation factor for each component is defined as

where $K_{di} = \frac{\omega_{is}}{C_i}$ is the partition coefficient for component i , which relates the mass fraction of the component adsorbed onto the solid to the concentration of the component in the single-phase mixture. Substitution of the definition of the retardation coefficient into Eq. 2.59 gives

When the retardation factor and porosity are temporally held constant,

Eqs. 2.62 and 2.56, with dispersion neglected, are nearly identical. The only difference is that the flow rate is divided by $1 + D_i$, resulting in an effective flow rate of $u_{ei} = u(1/D_i)$ for each component. The retardation factor is aptly named because its presence causes an apparent reduction in the velocity at which a component moves through a medium. With no sorption, the retardation factor is zero, and the component moves at the average flow rate of the fluid. Because of the slowing of the velocity, the retardation factor is sometimes called a delay factor (Lake et al. 2002).

Example 2.4—Semimiscible Flow. In several EOR applications, a description of flow in permeable media on the basis of strictly miscible or immiscible flow is insufficient. For these situations, the equations in [Table 2.2](#) reduce to a simpler form consistent with the

known complexities of flow behavior. As an example of this, consider the isothermal flow of N_C components up to N_P phases in the absence of chemical reaction. Such flows are characteristic of solvent (see [Chapter 7](#)) and surfactant/polymer flooding (see [Chapter 5](#)) EOR applications.

We first assume that the change in pressure over the displacement length has no effect on fluid properties. Eq. 2.15 can then be divided by the respective pure component density ρ_i^o to give

$$\frac{\partial}{\partial t} \left[\phi \sum_{j=1}^{N_p} C_{ij} S_j + (1-\phi) C_{is} \right] + \vec{\nabla} \cdot \left(\sum_{j=1}^{N_p} C_{ij} \vec{u}_j - \phi S_j \vec{\tilde{K}}_{ij} \cdot \vec{\nabla} C_{ij} \right) = 0 \quad i = 1, \dots, N_c, \dots \dots \dots \quad (2.63)$$

where, under the additional assumption of ideal mixing, $C_{ij} = \rho_j \omega_{ij} / \rho_i^o$ is the volume fraction of component i in phase j . Ideal mixing states that the volume of a mixture is equal to the sum of the pure component volumes weighted by the component mass fractions ([Chapter 4](#)). We show in Exercise 2.12 that this assumption may be relaxed.

We can derive a simpler form by summing Eq. 2.63 over the N_C components as for the development of Eq. 2.18; that is,

$$\frac{\partial}{\partial t} \left[\phi \sum_{i=1}^{N_p} \left(S_j \sum_{j=1}^{N_C} C_{ij} \right) + (1-\phi) \sum_{i=1}^{N_C} C_{is} \right] + \vec{\nabla} \cdot \left[\sum_{j=1}^{N_p} \vec{u}_j \left(\sum_{j=1}^{N_C} C_{ij} \right) \right] = 0, \quad i = 1, \dots, N_C, \dots \dots \dots \quad (2.64)$$

where the sum of the dispersive fluxes vanishes. Therefore,

where we have used Eq. 2.2-10 (from [Table 2.2](#)), $\sum_{i=1}^{N_C} C_{ij} = 1$, and $\sum_{i=1}^{N_C} C_{is} = 1$. For 1D flow, Eq. 2.65 implies that the total flow rate is only a function of time (see Exercise 2.10). Therefore, Eq. 2.65 can be used along with the definition of fractional flow (Eq. 2.52) to write Eq. 2.65 in 1D form:

$$\frac{\partial}{\partial t} \left[\phi \sum_{j=1}^{N_p} C_{ij} S_j + (1-\phi) C_{is} \right] + u \frac{\partial}{\partial x} \left(\sum_{j=1}^{N_p} C_{ij} f_j \right) - \frac{\partial}{\partial x} \left(\sum_{j=1}^{N_p} \phi S_j K_{lij} \frac{\partial C_{ij}}{\partial x} \right) = 0, \quad i = 1, \dots, N_c \dots \quad (2.66)$$

Even with the preceding assumptions, Eq. 2.66 is still fairly general and must be solved simultaneously with Darcy's law and with the definitions of relative mobility, capillary pressure, mass fractions, saturations, equations of state, and equilibrium relations (Eqs. 2.2-5, 2.2-10, and 2.2-15 through 2.2-17 from [Table 2.2](#)). This form is particularly convenient because many cases of binary- and ternary-phase equilibria are represented conventionally as volume fractions rather than mass fractions (see [Chapter 4](#)).

We often define the overall component volume fraction as $C_i = \sum_{j=1}^{N_p} C_{ij} S_j$ and the component fractional flux as $F_i = \sum_{j=1}^{N_p} C_{ij} f_j$. With these definitions, constant porosity, and the assumption of dispersion-free flow with no sorption, Eq. 2.66 becomes

This equation, the *fractional-flux equation*, is used in [Chapter 7](#) to develop analytical solutions and basic insights for miscible flooding theory.

Example 2.5—Richards (1931) Equation for Unsaturated Flow in Aquifers. The general equations developed here also apply to groundwater flow. Aquifers are divided into two regions, an unsaturated region near the Earth's surface in which both water and air are present, and a saturated region near and below the unsaturated region, where only the aqueous phase is present. The surface separating the two zones is near the water table. The water table is also known as the phreatic surface because water flows freely to this level in wells drilled through the aquifer (Charbeneau 2000). The Richards equation applies to flow in the unsaturated zone.

We begin the development of the unsaturated-flow equation by assuming no mass transfer ($r_{mij} = 0$) in the phase-conservation equation (Eq. 2.23):

$$\frac{\partial}{\partial t} \left(\phi S_j \rho_j \right) + \vec{\nabla} \cdot \left(\rho_j \vec{u}_j \right) = 0 \quad j = 1, \dots, N_p,$$

where there are only two phases, an aqueous phase and a gaseous (air) phase. The two phases are assumed immiscible; hence, phases and components are synonymous in this example. Because air near the Earth's surface is at low pressure, its density and viscosity are near zero, and it provides little resistance to water flow (except where there is a physical restriction in the pore volume available for water flow). This is equivalent to assuming that the air is at atmospheric pressure everywhere it is present in the aquifer. Therefore, because only the aqueous phase flows, the solution to the air-phase equation is trivial and can be dropped along with the subscripts for the aqueous phase. The aqueous-phase equation becomes

The aqueous-phase density is also assumed constant, a good assumption because the water pressure remains near atmospheric even under flowing conditions. Eq. 2.68 becomes

$$\frac{\partial}{\partial t}(\phi S) + \vec{\nabla} \cdot \vec{u} = 0. \quad \dots \dots \dots \quad (2.69)$$

The Richards equation is often formally written in terms of the moisture content ($\theta = \phi S$), hydraulic head, and hydraulic conductivity. The hydraulic head, which is often defined with reference to atmospheric pressure and surface elevation, is

The hydraulic conductivity tensor is defined as $\vec{K} = \bar{k} \rho_g / \mu$. With those definitions and the use of Eq. 2.2-5 (from [Table 2.2](#)), Eq. 2.69 gives the Richards equation,

$$\frac{\partial \theta}{\partial t} - \vec{\nabla} \cdot (k_r \vec{K} \cdot \vec{\nabla} h) = 0, \dots \quad (2.71)$$

where $\vec{\nabla} h = \vec{\nabla} P / \rho_g$ and k_r is the relative permeability of the aqueous phase, which is a function of the water saturation (moisture content). Although we dropped the air-phase equation, the air phase does impact the flow of the aqueous phase through relative permeability.

Phillips (1957) wrote the Richards equation in a form commonly used by soil scientists. He split the hydraulic head into two parts: the suction head ($-\vec{\nabla} \psi$) and the elevation head, where $\vec{\nabla} h = -\vec{\nabla} \psi + \vec{\nabla} z$ and $\psi = P_c / \rho_g = -P / \rho_g$. The capillary pressure is equal to the negative of the water pressure because the air pressure is assumed constant at atmospheric pressure, which is often taken to be zero. The suction head is always positive because water is in tension above the phreatic surface (i.e., the aqueous-phase pressure is less than atmospheric above the water table). The unsaturated flow equation used by Phillips as derived from Eq. 2.71 is then

$$\frac{\partial \theta}{\partial t} + \vec{\nabla} \cdot (k_r \vec{K} \cdot \vec{\nabla} \psi) = \vec{\nabla} \cdot (k_r \vec{K} \cdot \vec{\nabla} z). \dots \quad (2.72)$$

For Cartesian coordinates aligned in the principal flow directions, the term on the right side of Eq. 2.72 can be simplified to give

$$\frac{\partial \theta}{\partial t} + \vec{\nabla} \cdot (k_r \vec{K} \cdot \vec{\nabla} \psi) = \frac{\partial}{\partial z} (k_r K_{zz}), \dots \quad (2.73)$$

where K_{zz} is the component of the hydraulic conductivity in the z -direction. Finally, we can rewrite Eq. 2.73 in terms of the capillary diffusivity $\vec{D} = -\vec{K} \psi'$, where ψ' is the derivative of the suction head with respect to the moisture content:

$$\frac{\partial \theta}{\partial t} = \vec{\nabla} \cdot (k_r \vec{D} \cdot \vec{\nabla} \theta) + \frac{\partial}{\partial z} (k_r K_{zz}). \dots \quad (2.74)$$

The capillary diffusivity is positive and has units of length squared per time (hence its name). Phillips (1957) used Eq. 2.74 to develop semi-analytical solutions for rainfall infiltration.

Example 2.6—Standard Black-Oil Equations. A common representation (Peaceman 1977) of the flow of fluids in oil and gas reservoirs is the “black-oil” equations, in which up to three phases, aqueous ($j = 1$), oleic ($j = 2$), and gaseous ($j = 3$), flow simultaneously. The aqueous and gaseous phases each consist of a single pseudocomponent, water ($i = 1$) and gas ($i = 3$), respectively. The oleic phase consists of two pseudocomponents, oil ($i = 2$) and a dissolved-gas component. The components are *pseudocomponents* because each is really a group of true components with a constant composition.

The use of pseudocomponents is quite common in EOR descriptions because this simplification often results in greater understanding of the processes and can significantly reduce the computational effort involved in numerical simulation with little loss of accuracy. Because of these advantages, the black-oil equations are often used to model many EOR processes, including those in which the black-oil assumptions may not strictly apply. Black-oil equations, for example, may not accurately model miscible EOR processes or other processes that deviate significantly from the black-oil assumption of pseudocomponents with constant composition. In these cases, more rigorous fully compositional simulators are used.

[Fig. 2.5](#) illustrates the black-oil assumptions. The model relates downhole reservoir volumes to standard temperature and pressure (STP) conditions. Definitions for STP vary slightly, but typical values are 14.7 psia and 60°F. Formation volume factors B_i are defined that express the ratio between volumes at STP conditions and reservoir conditions as indicated by the dashed lines in [Fig. 2.5](#). For gas and water, the B_i represent the expansion in volume resulting from the decrease in pressure from reservoir conditions; for oil, they also include the (usually greater) decrease in volume resulting from loss

of gaseous components. The solution gas/oil ratio R_s is the volume of gas that evolves from a known volume of oil at STP conditions.

The black-oil equations are compositional equations in that they are developed from the overall compositional equations, Eq. 2.15. We invoke the following additional assumptions: no reaction ($R_i = 0$), no dispersion ($\vec{\bar{K}}_{ij} = 0$), and no adsorption ($\omega_{is} = 0$). The black-oil assumption itself becomes the following: the aqueous phase contains only water ($\omega_{11} = 1$, $\omega_{21} = 0$, $\omega_{31} = 0$), the oleic phase contains only oil and gas ($\omega_{12} = 0$, $\omega_{22} = 0$, $\omega_{32} = 0$), and the gas phase contains only the gas component ($\omega_{13} = 0$, $\omega_{23} = 0$, $\omega_{33} = 1$). For Component 1 (the water component), Eq. 2.15 becomes

For Component 2 (the oil component), Eq. 2.15 gives

$$\frac{\partial}{\partial t}(\phi\rho_2S_2\omega_{22}) + \vec{\nabla} \cdot (\rho_2\omega_{22}\vec{u}_2) = 0. \dots \quad (2.76)$$

For Component 3 (the gas component), Eq. 2.15 gives

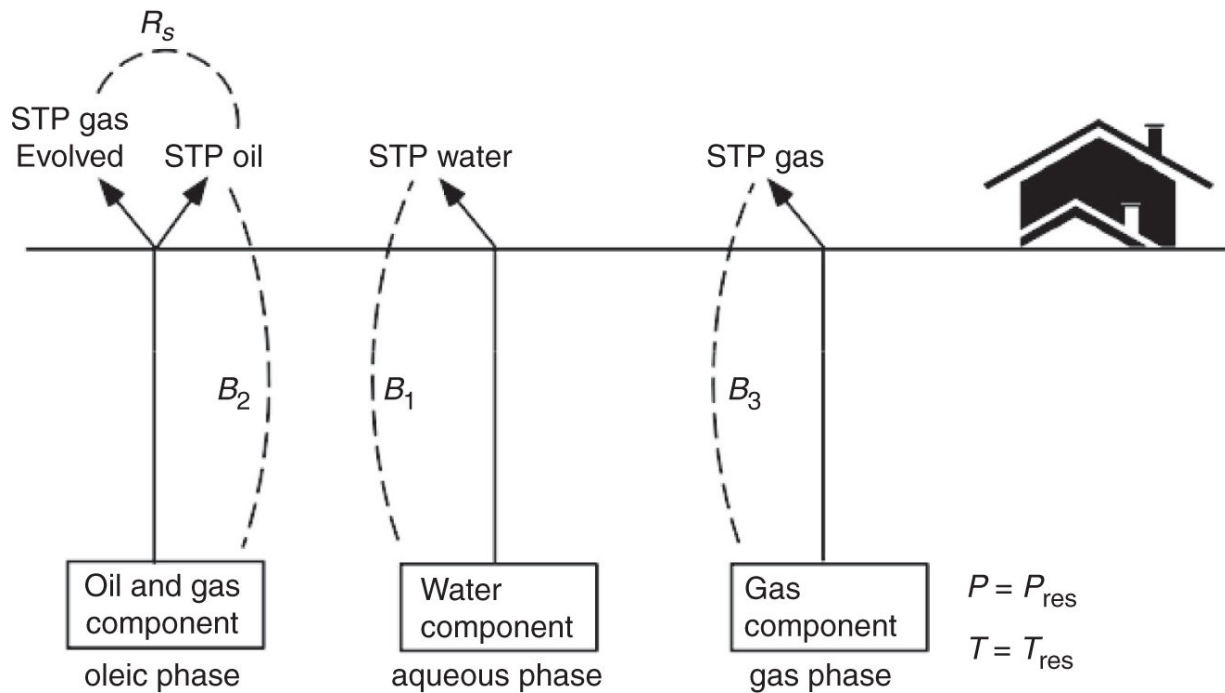


Fig. 2.5—Illustration of standard black-oil assumptions. STP means standard temperature and pressure.

We now want to eliminate the mass fractions and rewrite Eqs. 2.75 through 2.77 in favor of formation-volume factors and the solution gas/oil ratio. B_1 is the water formation-volume factor (volume of a given mass of water at the prevailing temperature and pressure divided by the volume of the same mass of water at standard temperature and pressure):

$$B_1 = \frac{\rho_1^s}{\rho_1}$$

B_2 is the oil formation-volume factor (volume of a given mass of oil at prevailing temperature and pressure divided by the volume of the same mass of oil at standard conditions):

$$B_2 = \frac{\rho_2^s}{\omega_{22} \rho_2}$$

B_3 is the gas formation-volume factor (volume of a given mass of gas at prevailing temperature and pressure divided by the volume of

the same mass at standard temperature and pressure):

$$B_3 = \frac{\rho_3^s}{\rho_3}.$$

R_s is the solution gas/oil ratio (volume of dissolved gas divided by volume of oil phase, with both volumes evaluated at standard temperature and pressure):

$$R_s = \frac{\omega_{32}\rho_2^s}{\omega_{22}\rho_3^s}.$$

The preceding definitions may be introduced into the mass balances of [Table 2.2](#) by dividing each by their respective standard densities ρ_j^s and recognizing that each ρ_j^s is independent of time and space. Eqs. 2.75 through 2.77 become

$$\frac{\partial}{\partial t} \left(\frac{\phi S_j}{B_j} \right) + \vec{\nabla} \cdot \left(\frac{\vec{u}_j}{B_j} \right) = 0, \quad j = 1, 2,$$

and for gas,

$$\frac{\partial}{\partial t} \left[\phi \left(\frac{S_3}{B_3} + \frac{S_2 R_s}{B_2} \right) \right] + \vec{\nabla} \cdot \left(\frac{R_s}{B_2} \vec{u}_2 + \frac{\vec{u}_3}{B_3} \right) = 0.$$

Modified black-oil models, where carbon dioxide (CO_2) is added as a fourth component, are sometimes used to account for oil displacement by CO_2 or other miscible gases (Todd and Longstaff 1972).

Example 2.7—Steamflooding Equations (Condensable Phases). As a special case of nonisothermal flow, we derive the “steam” equations given by Stegemeier et al. (1980) and Hong (1994). These equations are combinations of mass and energy balances.

We assume that, at most, $N_P = 3$ phases—an aqueous phase $j = 1$, a hydrocarbon phase $j = 2$, and a gas phase $j = 3$ —are present. Furthermore, at most, two unreactive, nonsorbing pseudocomponents—water and oil—are present. The hydrocarbon phase contains only oil, and the aqueous and gaseous phases contain only water, assumptions that eliminate volatile hydrocarbons from the equations. With these assumptions, the mass-conservation equation (Eq. 2.15) becomes, for the water component,

and for oil,

$$\frac{\partial}{\partial t}(\phi\rho_2S_2) + \vec{\nabla} \cdot (\rho_2\vec{u}_2) = 0. \quad \dots \quad (2.79)$$

The dispersion terms are absent from these equations because the phase compositions are constant. The conservation of energy Eq. 2.36 becomes

where kinetic and potential energy terms have been neglected. We further neglect pressure/volume work by setting the enthalpies equal to the internal energies (a good assumption for liquids and solids) and by assuming porosity to be constant. The derivatives in Eq. 2.80 may then be expanded to give

$$\begin{aligned} & \left(1-\phi\right) \frac{\partial(\rho_s \hat{H}_s)}{\partial t} + \phi \rho_1 S_1 \frac{\partial \hat{H}_1}{\partial t} + \phi \rho_2 S_2 \frac{\partial \hat{H}_2}{\partial t} + \phi \rho_3 S_3 \frac{\partial \hat{H}_3}{\partial t} + \phi (\hat{H}_3 - \hat{H}_1) \frac{\partial(\rho_3 S_3)}{\partial t} \\ & + \rho_1 \vec{u}_1 \cdot \vec{\nabla} \hat{H}_1 + \rho_2 \vec{u}_2 \cdot \vec{\nabla} \hat{H}_2 + (\hat{H}_3 - \hat{H}_1) \vec{\nabla} \cdot (\rho_3 \vec{u}_3) + \rho_3 \vec{u}_3 \cdot \vec{\nabla} \hat{H}_3 - \vec{\nabla} \cdot (k_n \vec{\nabla} T) = 0, \dots \quad (2.81) \end{aligned}$$

where Eqs. 2.78 and 2.79 have been used to eliminate several terms. The term $(\hat{H}_3 - \hat{H}_1)$ equals L_V , the latent heat of vaporization of water, and we assume that enthalpies are independent of pressure,

$d\hat{H}_j = C_{pj}dT$, where C_{pj} is the specific heat of phase j . If the C_{pj} are constant, Eq. 2.81 becomes

$$M_{Tt} \frac{\partial T}{\partial t} + (\rho_1 C_{p1} \vec{u}_1 + \rho_2 C_{p2} \vec{u}_2) \cdot \vec{\nabla} T - \vec{\nabla} \cdot (k_{Tt} \vec{\nabla} T) = -L_v \left[\phi \frac{\partial(\rho_3 S_3)}{\partial t} + \vec{\nabla} \cdot (\rho_3 S_3 \vec{u}_3) \right], \dots \quad (2.82)$$

where M_{Tt} is the overall volumetric heat capacity

$$M_{Tt} = \phi (\rho_1 C_{p1} S_1 + \rho_2 C_{p2} S_2) + (1-\phi) \rho_s C_{ps}. \dots \quad (2.83)$$

In this definition (Eq. 2.83) and in Eq. 2.82, the terms multiplying the gaseous-phase density ρ_3 have been neglected because gas densities are usually much lower than liquid densities. The term on the right side of Eq. 2.82 represents the production or destruction of the steam phase times the latent heat; it serves as a source term for the energy equation. If steam disappears (condenses), the source term is positive, which causes the temperature to rise. This rise results in a decrease in oil viscosity, the primary recovery mechanism in thermal flooding (see [Chapter 11](#)). The latent heat, phase pressures, and temperature are related through the vapor vs. pressure curve for water and through capillary-pressure relations.

2.6 Overall Balances

The weak forms of the conservation equations are often useful in their own right. Following Bird et al. (2002), we call them *macroscopic* or *overall* balances.

Rather than balances on each point within a permeable medium, overall balances apply to finite volumes within a reservoir, such as a cell in numerical simulation, or even, as is the case here, the entire reservoir. Because the spatial component is absent from the equations, overall balances are much simpler and far easier to integrate (indeed, they are themselves partially integrated) than differential balances. This simplification is achieved at the expense of losing spatial detail for the concentration variables; therefore, to

be useful, overall balances must be supplemented with independently derived or analytical correlations.

2.6.1 Material Balance. To derive the overall mass balance for component i , we begin with the weak form written on volume V in the compositional form (Eq. 2.8):

$$\int_V \frac{\partial W_i}{\partial t} dV + \int_A \vec{n} \cdot \vec{N}_i dA = \int_V R_i dV, \quad i = 1, \dots, N_C.$$

We then identify the control volume V with the total bulk volume V_b exclusive of the small volumes associated with a finite number of sources and sinks embedded within it. The boundary of V_b may also be a fluid source or sink term, as would be the case for an oil column abutting an aquifer or a free gas cap. If we assume that the fluxes across the boundaries of V are normal to the cross-sectional area, Eq. 2.8 becomes

where the superscript bar denotes volume-averaged quantities. The terms \dot{N}_{P_i} and \dot{N}_{J_i} are the mass production and injection rates of component i for all the source and sink terms in V_b . These are functions of time because they are evaluated at fixed positions on V_b . \bar{R}_i is the volume-averaged reaction rate term of component i and is also a function of time. We integrate Eq. 2.84 with respect to time to arrive at a cumulative form of material balance:

In writing Eq. 2.85, we have assumed that the cumulative injection and production of component i at $t = 0$ is zero. In what follows, we ignore the cumulative reaction-rate term.

The most common application of Eq. 2.85 is to calculate N_{pi} with W_i , \bar{W}_{il} and N_{Ji} specified. In particular, $\bar{w}_i(t)$ is difficult to evaluate without actually integrating the differential balances. This difficulty is circumvented by defining E_{Ri} , the recovery efficiency of component i , as

E_{Ri} is the net amount of component i produced expressed as a fraction of the amount of component initially present. For a component injected into the reservoir, E_{Ri} is negative, but for a component to be recovered, such as oil or gas (to which it is almost exclusively applied), E_{Ri} is positive and lies between 0 and 1. From Eq. 2.85, $\bar{W}_i(t)$ is

for a nonreacting system.

For either Eqs. 2.86 or 2.87 to be useful, E_{Ri} must be expressed independently as a function of time. This is commonly done by decomposing E_{Ri} into the displacement efficiency E_{Di} and the volumetric sweep efficiency E_{Vi} of component i ,

where

$$E_{D_i} = \frac{\text{Amount of } i \text{ displaced}}{\text{Amount of } i \text{ contacted}}, \dots \quad (2.89)$$

and

$$E_{Vi} = \frac{\text{Amount of } i \text{ contacted}}{\text{Amount of } i \text{ in place}} \dots \quad (2.90)$$

These quantities in turn must be specified independently: E_{Di} as a function of time and fluid viscosities, relative permeabilities, and

capillary pressures (see [Chapter 5](#)) and E_V as a function of time, viscosities, well arrangements, heterogeneity, gravity, and capillary forces (see [Chapter 6](#)). Eqs. 2.87 through 2.90 assume for simplicity that all material displaced from the swept zone is produced from the reservoir. In reality, some displaced material may become stranded on its way to a production well. The volumetric sweep efficiency in Eq. 2.88 can also be split into an areal and vertical sweep efficiency so that $E_V = E_A E_I$.

2.6.2 Energy Balance. A similar procedure applied to the energy conservation equation (Eq. 2.36) yields

$$V_b \frac{d}{dt} (\overline{\rho U}) + \dot{H}_P - \dot{H}_J = - \int_A \bar{q}_c \cdot \bar{n} dA = -\dot{Q}, \dots \quad (2.91)$$

where kinetic- and potential-energy terms have been neglected, and \dot{H}_P and \dot{H}_J represent the rates of enthalpy production and injection, respectively, into and from V . \dot{Q} is positive when heat is lost from the reservoir. This equation (Eq. 2.91), of course, is a version of the first law of thermodynamics that, depending on the selection of V , will be useful in calculating heat losses to wellbores and the overburden and underburden of a reservoir (see [Chapter 11](#)).

The time-integrated or cumulative form of Eq. 2.91 is

$$V_b \left[(\overline{\rho U}) - (\overline{\rho U})_I \right] = H_J - H_P - Q, \dots \quad (2.92)$$

from which we may define a thermal efficiency \bar{E}_{hs} as the ratio of thermal energy remaining in volume V to the net thermal energy injected:

$$\bar{E}_{hs} = \frac{V_b \left[(\overline{\rho U}) - (\overline{\rho U})_I \right]}{H_J - H_P} = 1 - \frac{Q}{H_J - H_P} \dots \quad (2.93)$$

Eq. 2.93 is used to calculate Q independently.

Another familiar form of the overall energy balance pertains to phase-equilibrium thermodynamics (see [Chapter 4](#)). We again

neglect potential and kinetic energies, but allow for both pressure/volume and compression/expansion work (see Exercise 2.16). The mass that enters the control volume V flows at a relative flow rate of \vec{u}_{fj} , which is the difference between the actual flow rate and the rate of deformation of V . Furthermore, we rewrite the accumulation term to account for a deformed V by use of the weak form. The result is

$$\frac{d}{dt} \left[\int_V (\rho U) dV \right] = - \int_A \vec{n} \cdot \sum_{j=1}^{N_p} \rho_j \vec{u}_{fj} \hat{H}_j dA - \int_A \vec{n} \cdot \vec{q}_c dA - \sum_{j=1}^{N_p} P_j \frac{dV_j}{dt}. \dots \quad (2.94)$$

From left to right, the terms represent accumulation, energy flux as a result of mass inflow, energy flux as a result of conduction, and compression/expansion work. The first three terms in Eq. 2.94 must now be evaluated. The accumulation term is

$$\frac{d}{dt} \int_V (\rho \hat{U}) dV = \frac{\partial U}{\partial t},$$

where U is the total energy within volume V . The energy-flux term is evaluated under the assumption that the enthalpy of the flowing mass for any phase is constant over the entrance or exit for mass flow. The result is

$$- \int_A \vec{n} \cdot \sum_{j=1}^{N_p} \rho_j \vec{u}_{fj} \hat{H}_j dA = - \sum_{j=1}^{N_p} \hat{H}_j \int_A \vec{n} \cdot (\rho_j \vec{u}_{fj}) dA = \sum_{j=1}^{N_p} \hat{H}_j \dot{m}_j,$$

where \dot{m}_j is the total net mass inflow of phase j into the CV. The sign is positive to accommodate the convention that mass flow rate is positive *into* the CV. Finally, the conduction term is,

$$- \int_A \vec{n} \cdot \vec{q}_c dA = \dot{Q}.$$

With these additional assumptions and identifications, Eq. 2.94 reduces to

$$\frac{dU}{dt} = \sum_{j=1}^{N_p} \hat{H}_j \dot{m}_j + \dot{Q} - \sum_{j=1}^{N_p} P_j \frac{dV_j}{dt} \dots \quad (2.95)$$

When only one phase exists, Eq. 2.95 reduces to a familiar form of the first law of thermodynamics,

$$\frac{dU}{dt} = \hat{H}\dot{m} + \dot{Q} - P \frac{dV}{dt} \dots \quad (2.96)$$

The pressure at the boundary of the CV in Eq. 2.96 is assumed equal to the pressure in the CV for the case in which pressure gradients are negligible (corresponding, as shown in Eq. 2.49, to zero entropy generation). Along with the entropy balance discussed next, [Chapter 4](#) will use Eq. 2.96 to determine the equilibrium conditions for phase-behavior calculations.

2.6.3 Entropy Balance. To derive the overall entropy balance, we start by rewriting Eq. 2.46 as

$$\frac{d}{dt} \left[\int_V \sum_{j=1}^{N_p} (\varepsilon_j \rho_j \hat{S}_j) dV \right] = - \int_A \vec{n} \cdot \sum_{j=1}^{N_p} \rho_j \vec{u}_j \hat{S}_j dA - \int_A \vec{n} \cdot \frac{\vec{q}_c}{T} dA + \int_V \dot{\sigma}_G dV \dots \quad (2.97)$$

Following the same procedure as for the overall energy balance,

$$\frac{dS}{dt} = \sum_{j=1}^{N_p} \hat{S}_j \dot{m}_j + \frac{\dot{Q}}{T} + \dot{S}_G, \dots \quad (2.98)$$

where we have assumed that both temperature and phase entropies along the CV boundary are independent of position. The term \dot{S}_G is now the total entropy generated within the CV, that is, $\dot{S}_G = \int_V \dot{\sigma}_G dV$.

When only one phase exists, Eq. 2.98 reduces to

$$\frac{dS}{dt} = S\dot{m} + \frac{\dot{Q}}{T} + \dot{S}_G \dots \quad (2.99)$$

This equation will be used in [Chapter 4](#) to determine the equilibrium conditions for phase-behavior calculations. As before, the second law of thermodynamics is $\dot{S}_G \geq 0$, the equality applying at equilibrium

or approximately so for quasi-equilibrium processes in which gradients are small (reversible conditions).

2.7 Summary

We will use the equations introduced and developed in this chapter in the remainder of the text. Introducing all the equations here eliminates repetition in later chapters. The compilation also emphasizes one of the main points of this text: the behavior of all EOR and aquifer-remediation processes is described by specializations of the same underlying conservation laws. Solving these specializations and deducing physical observations from the solutions will occupy much of the remainder of this text. You should keep in mind that all the relationships discussed in the preceding sections and henceforth are ways of quantifying the chemical, physical, and geologic bases of EOR.

Exercises

2.1 Oil Balance. Derive a material balance equation for the oil phase using the procedure given in Section 2.1. Assume immiscible flow of constant-composition oil. Your derivation should begin with a statement of the oil mass balance in words. Then you should write each term with symbols and use the divergence theorem. Your result should be identical to the phase-flow equations for oil. See Eq. 2.24.

2.2 Volatile-Oil Equations. Example 2.6 derived the black-oil equations in which the oleic and gaseous phases are immiscible and of constant composition except for the solubility of a hydrocarbon gas in the oleic phase. The next step up in complexity is the “volatile-oil” equations, which accommodate vaporization of oil into the gaseous phase (Walsh and Lake 2003).

Derive the volatile-oil equations in terms of the oil-vaporization ratio R_V , where

$$R_v = \frac{\text{Standard volumes of oil in gaseous phase}}{\text{Standard volumes of gas}}.$$

State all assumptions and show all work.

2.3 Hydrostatics. Show that for static ($\vec{u}_j = 0$) conditions, Eq. 2.2-5 from [Table 2.2](#) reduces to

$$\frac{dP_c}{dD_z} = (\rho_1 - \rho_2)g$$

for two-phase flow, where P_c is the oil/water capillary pressure curve.

2.4 Net Dispersion in a Phase. Show that in a given phase, $\sum_{i=1}^{N_c} \nabla \cdot \vec{j}_{Dij} = 0$ when dispersive flux is defined with respect to the mass-averaged velocity ($\vec{u}_j = \sum_{i=1}^{N_c} \omega_{ij} \vec{u}_{ij}$). Start by writing $\vec{j}_{Dij} = \vec{N}_{ij} - \vec{j}_{Cij} = \rho_j \omega_{ij} \vec{u}_{ij} - \rho_j \omega_{ij} \vec{u}_j$.

2.5 Single-Phase Flow. Show that for the flow of a single phase ($j = 2$) in the presence of an immiscible, immobile phase ($j = 1$), the isothermal strong form of the mass-balance equations in 1D radial coordinates reduces to the *diffusivity* equation

$$\frac{\phi c_t}{k \lambda_{r2}} \frac{\partial P}{\partial t} = \frac{1}{r} \frac{\partial}{\partial r} \left(r \frac{\partial P}{\partial r} \right),$$

where

$$c_t = S_1 c_1 + S_2 c_2 + c_f$$

$$c_j = \frac{1}{\rho_j} \left(\frac{\partial \rho_j}{\partial P} \right)_T$$

$$c_f = \frac{1}{\phi} \left(\frac{\partial \phi}{\partial P} \right)_T.$$

The first equation above has been derived assuming that terms of the form $c_2(\partial P/\partial r)^2$ are negligible and that the reservoir is homogeneous with uniform thickness. The diffusivity equation forms the starting point for many well-test techniques (Earlougher 1977).

2.6 Confined Flow of Water in an Aquifer. Show that the final result for problem 2.5 can be rewritten for soil fully saturated with water as

$$\frac{1}{r} \frac{\partial}{\partial r} \left(r \frac{\partial h}{\partial r} \right) = \frac{1}{\eta} \frac{\partial h}{\partial t},$$

where

$$c_t = c_1 + c_f,$$

$$\eta = \frac{K}{S_s} = \frac{T}{S},$$

$$K = \frac{k \rho g}{\mu},$$

$$S_s = \phi c_t \rho g.$$

The parameter S_s is the specific storage coefficient for the aquifer in units of inverse length. The dimensionless storage coefficient of the aquifer is equal to $S = S_s b$, where b is the thickness of the confined aquifer. A confined aquifer is an aquifer fully saturated with water that cannot escape at the top and bottom. The storage coefficient is defined as the volume of water stored (or released) per unit area of aquifer per unit increase (or decrease) in the hydraulic head h . The aquifer transmissivity is $T = Kb$. Finally, the parameter η is known as the diffusivity constant.

2.7 Unconfined Flow in an Aquifer. An unconfined aquifer is an unsaturated aquifer that contains both air and water. The water table (phreatic surface at which capillary pressure is zero) can rise and fall as water is pumped from the aquifer. A common assumption when modeling changes in the water table is to assume that the hydraulic head is constant vertically and is a

function only of the horizontal coordinates (this is a vertical equilibrium assumption, as discussed in [Chapter 6](#)). Show that under this assumption, the equation for flow in a 2D unconfined homogeneous aquifer is

$$\frac{\partial}{\partial x} \left(h \frac{\partial h}{\partial x} \right) = \frac{S_y}{K} \frac{\partial h}{\partial t},$$

where

$$K = \frac{k \rho g}{\mu}$$

$$S_y = \phi(1 - S_{1r}).$$

The dimensionless parameter S_y is the specific yield of the aquifer, defined as the volume of water added (or lost) because of a unit increase (or decrease) in the water table height per unit horizontal area of aquifer. The residual water saturation S_{1r} is assumed constant whether the water table is rising or falling. The water saturation above the water table is assumed constant at S_{1r} .

To derive the unconfined flow equation, start with the equation for a confined aquifer given in Exercise 2.6, but expressed in x - and z -coordinates, and integrate it vertically from the base of the aquifer to the water table. Use Liebnitz's rule to evaluate the integral expressions that result. Finally, let the water-table surface be given by $F(x, z, t) = z - a(x, t) = 0$ where $a(x, t)$ is the elevation of the water table as measured from the assumed horizontal base of the aquifer. The unit total derivative of $F(x, z, t)$ must be zero, which makes it possible to relate the movement of the water table in the horizontal and vertical directions to the time rate of change of the water table. State all assumptions clearly.

2.8 Convection-Dispersion Equation With Retardation. Show that when dispersion is constant, the 1D convection-dispersion equation with adsorption becomes

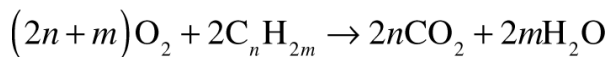
$$\phi \frac{\partial C_i}{\partial t} + \frac{u}{1+D_i} \frac{\partial C_i}{\partial x} - \frac{\phi K_{li}}{1+D_i} \frac{\partial^2 C_i}{\partial x^2} = 0, \quad i = 1, \dots, N_c,$$

where the delay factor $D_i = (1-\phi)C_{is}/\phi C_i$ is independent of time and K_{li} is the longitudinal dispersion coefficient for component i . State all assumptions required to obtain this equation. How does adsorption affect the transport of a component?

2.9 Simplified Combustion Model. On the basis of two-phase ($j = 2$ = liquid, $j = 3$ = gas), four-component [$i = 1$ = water, $i = 2$ = oil (C_nH_{2m}), $i = 3$ = CO_2 , $i = 4$ = O_2] 1D flow, show that the energy-conservation equations in [Table 2.3](#) reduce to

$$M_n \frac{\partial T}{\partial t} + (\rho_2 C_{p2} u_2 + \rho_3 C_{p3} u_3) \frac{\partial T}{\partial x} - \frac{\partial T}{\partial x} \left(k_n \frac{\partial T}{\partial x} \right) = \phi S_3 \Delta H_{RXN},$$

where ΔH_{RXN} is the heat of reaction for the gaseous-phase reaction



$$\Delta H_{RXN} = - \sum_{i=1}^4 H_{io} r_{i3}.$$

Further assumptions for the above equation are that there is only oil present in the liquid phase; there is no sorption or dispersion; ideal solution behavior (specific heat of gaseous phase is the mass fraction-weighted sum of the component specific heats); no heat of vaporization of oil ($H_{22} = H_{23}$); enthalpies and internal energies are equal; kinetic and potential energies are negligible; and solid-phase density and porosity are constant.

2.10 Total Velocity. Show that for immiscible and incompressible flow,

$$\vec{\nabla} \cdot \vec{u} = 0,$$

and that for 1D flow, the total velocity is a function only of time.

2.11 Continuity Equation. Derive Eq. 2.25 from the phase-conservation equations, Eq. 2.23.

2.12 Volume Change on Mixing. The development of the semimiscible equations in Example 2.4 assumed no volume change on mixing to obtain volume fractions. When volume changes upon mixing, the total velocity can change with both position and time, and volume fractions are not needed. Relax the no-volume-change assumption and re-derive the equations in a form similar to Eq. 2.67. Neglect hydrodynamic dispersion in the derivation.

2.13 Formation-Volume Factor. Show that in a black-oil model equation, the oil formation-volume factor can also be written as

$$B_2 = \frac{\rho_2^s + R_s \rho_3^2}{\rho_2}.$$

2.14 Oil Recovery by NH₃ Injection. An inventor believes that he has discovered a new EOR technique that you are to evaluate. The process injects anhydrous (water-free) ammonia (NH₃), which is to dissolve in and vaporize some of the connate water, into a medium containing oil and water. This mass transfer is highly nonideal in that there is a substantial heat of mixing. The heat released by this mixing will raise the temperature of the

crude and cause it to flow more readily than when it is cold, just as in a thermal process.

There might also be some benefit from a pH increase, but the main objective is to increase temperature. To this end, the inventor has commissioned a commercial laboratory to do some displacements in a laboratory core. The initial condition of the core is a uniform temperature T_o and 100% water saturation. The injected ammonia is pure and at the same temperature T_o .

Beginning with the general equations, develop a set of strong-form working equations that will describe the experiment. There will be several equations, but these should be as simple as possible without omitting the important features discussed in this problem. You should state all assumptions you made and ensure that the numbers of equations and unknowns are equal.

2.15 Work Done by Gravity. The derivation of Eq. 2.36 included potential energy directly. Re-derive this equation for the case in which gravity on a fluid element in V is included in the source term by the work sum $\dot{W} = \dot{W}_{PV} + \dot{W}_G$. To account for the gravity work, use a scalar product of a velocity and the gravity vector \vec{g} ,

$$\Delta\dot{W}_G = \sum_{j=1}^{N_p} \rho_j \vec{u}_j \cdot \vec{g} \Delta V.$$

The positive sign arises in this equation because a fluid phase flowing against gravity ($\vec{u}_j \cdot \vec{g} < 0$) is having work performed on it. Note the distinction between the elemental forms in Eqs. 2.30 and the equation above. Eq. 2.30 is appropriate for work performed against forces on the surface of V , whereas the above equation is appropriate for work performed against body forces.

Show that the potential energy terms in Eq. 2.36 can be derived by inclusion as a work term, where the total work done by gravity in the volume V is

$$\dot{W}_G = \int_V \sum_{j=1}^{N_p} \rho_j \vec{u}_j \cdot \vec{g} dV.$$

Hint: You must use Eq. 2.25 and the identity
 $\sum_{j=1}^{N_p} \rho_j \vec{u}_j \cdot \vec{g} = -g \sum_{j=1}^{N_p} \vec{\nabla} \cdot (\rho_j \vec{u}_j D_z) + g \sum_{j=1}^{N_p} D_z \vec{\nabla} \cdot (\rho_j \vec{u}_j).$

2.16 First Law of Thermodynamics. Derive Eq. 2.94 for the first law of thermodynamics, which includes both compression/expansion and pressure/volume work. Show that the equation reduces to Eq. 2.36 when the CV is stationary. In addition, derive the energy equation when the CV deforms at the same rate as the phase velocities. Neglect kinetic and potential energies in your derivations.

2.17 Thermal-Diffusivity Equation. From Eq. 2.82, state the assumptions required to obtain the thermal-diffusivity equation,

$$\vec{\nabla}^2 T = \frac{M_{Tt}}{k_{Tt}} \frac{\partial T}{\partial t},$$

where

$$M_{Tt} = \phi \rho_1 C_{p1} S_1 + (1-\phi) \rho_s C_{ps}.$$

2.18 Second Law of Thermodynamics. Consider an isolated CV (fixed total volume, internal energy, and temperature) that contains two compartments, A and B, separated by a movable internal frictionless piston. If $P_A > P_B$, the internal piston should move so that Compartment A expands and Compartment B contracts until $P_A = P_B$. Show that the total entropy change of the isolated CV (entropy generation) is positive when

Compartment A expands as expected and is zero once equilibrium is reached. The total entropy change is the sum of the entropy changes of the two compartments.

Chapter 3

Petrophysics and Petrochemistry

In [Chapter 2](#), we saw that a complete specification of the fluid flow equations in permeable media required functions for capillary pressure, relative permeabilities, and phase behavior. [Chapter 4](#) discusses enhanced-oil-recovery (EOR) phase behavior and some of the equations for its quantitative representation. Here, we discuss petrophysical relations in a similar fashion. We begin with the properties of immiscible phases (oil and water) and then proceed to EOR-related quantities, most importantly the capillary desaturation curve (CDC).

These topics are by no means an exhaustive study of petrophysics. The study of petrophysics, which is literally the physics of rock, is itself enormous; entire texts have been devoted to aspects of it. For a very readable and complete exposition of the topic, see Peters (2012).

Development of each petrophysical property follows the same basic procedure. First, we describe the property mathematically in terms of simplified physical laws, usually based on incompressible, steady-state flow in even simpler geometries. The simple geometry is intended to represent the smallest element of the permeable medium—the connected pore or the microscopic scale. Second, we modify the petrophysical properties of the connected pore to account for the local geometry of the actual permeable medium—variable pore cross sections, lengths, nonlinear dimensions (tortuosity), and multiple connections of one pore with another. This step translates the relation from the actual locally discontinuous permeable-medium flow domain to that of the locally continuous representative elementary volume (REV) first discussed in [Chapter 2](#). The translation, which is so important that it is the subject of the cover art for the Bird et al. (2002)

text, constitutes a large enough part of the topic that we are restricted to fairly simple idealizations of the local pore geometry. These idealizations are mainly pedagogical; enormous strides have been made in modeling flow in complex geometries in recent years (Balhoff and Thompson 2004).

3.1 Porosity and Permeability

Porosity is the ratio of void or *pore volume* to total or *bulk volume*; the rock- or solid-phase volume is the bulk volume less the pore volume. For most naturally occurring media, the porosity is between 0.10 and 0.40, although on occasion, values outside this range occur. Porosity is often reported as a percentage, but in calculations, it should always be used as a fraction. For any typical value, the rock-phase volume is clearly the largest in any medium.

The porosity of a permeable medium is a function of the variance of the local pore- or grain-size distribution and a weak function of the average pore size itself. For both sandstone and carbonate media, the porosity is strongly determined by the geochemical processes that deposited solids (minerals or cements) into the medium after it was laid down. For limestone formations of commercial interest, the porosity is almost exclusively the result of such changes.

The pore space as well as the porosity can be divided into an interconnected or *effective* porosity that is available to fluid flow and a disconnected porosity that is unavailable to fluid flow. The latter porosity is of no concern to the EOR processes discussed here; hence, in the rest of this text, the word *porosity* means effective porosity only (Collins 1976). Certain EOR processes exhibit behavior that results in shielding some of the effective porosity from the displacing agent. Such is the case for the “dead-end” pore volume to solvents (see [Chapter 7](#)) and the “inaccessible” pore volume to polymer solutions (see [Chapter 8](#)).

For some media, the pore space includes a portion that is extremely susceptible to fluid flow. Such *fracture* porosity usually makes up only 1 to 2% of the total porosity, but can have a disproportionate effect on flow if the fractures are conductive (open)

and connected. In such cases, it is the fracture permeability that is important, rather than the porosity.

Permeability is also a basic permeable-medium property that is as important to EOR as porosity. As discussed in Section 2.2, permeability is a tensorial property that is in general a function of direction, position, and pressure. Usually, the variation with position can be quite pronounced. In fact, permeability varies spatially by three or more orders of magnitude in a typical formation, whereas porosity varies by only a few percent. This variation is a form of reservoir heterogeneity that seriously influences the outcome of nearly all EOR displacements (see [Chapter 6](#)).

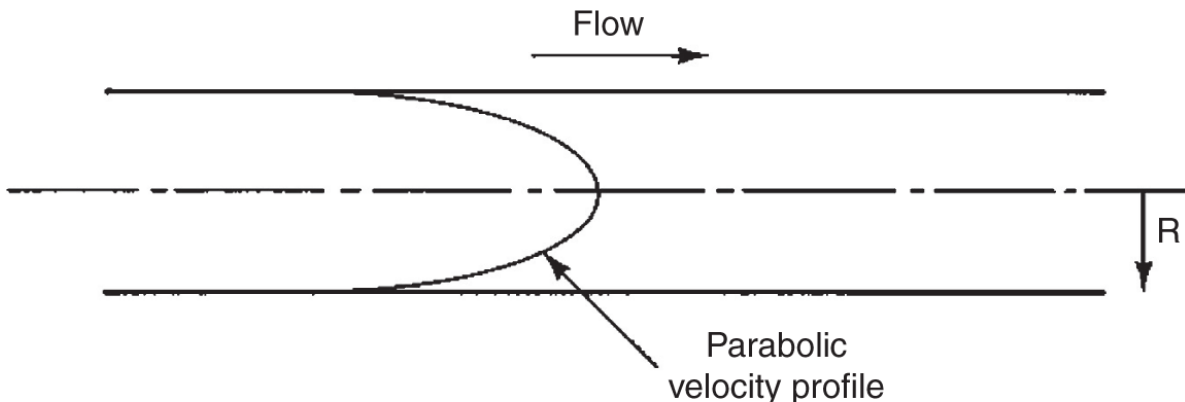
The permeability of a medium is a strong function of the local pore size and a weak function of the grain-size distribution. The fact that both porosity (strong) and permeability (weak) are functions of the grain-size distribution is manifest in correlations between the two quantities.

To demonstrate the dependence of permeability on pore size and to illustrate the procedure for transforming a local property to the REV scale, we derive the Carmen-Kozeny (CK) equation. The local pore model in this case is the capillary tube, which is probably the most common such model used in permeable-media studies.

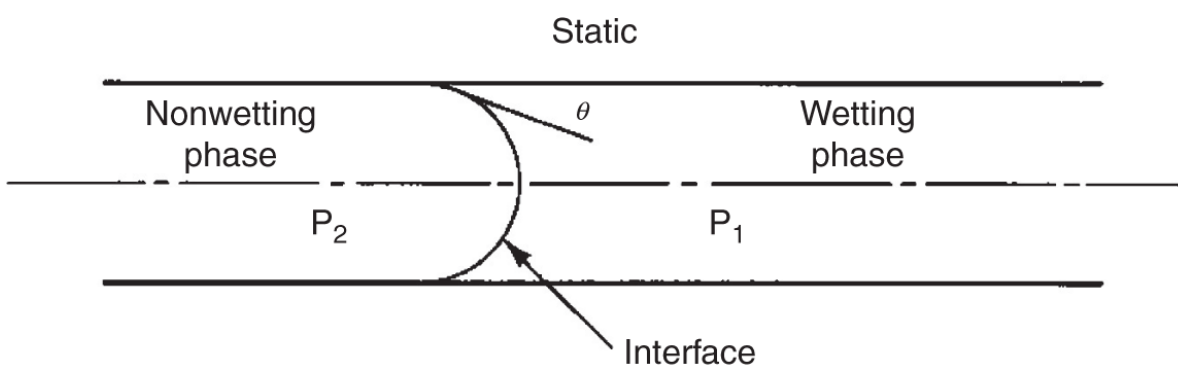
Consider the single-phase, steady-state, laminar flow of a constant-viscosity Newtonian fluid through a horizontal capillary of radius R and length L_t , as shown in [Fig. 3.1a](#). A force balance on an annular element of fluid yields an ordinary differential equation for the fluid velocity that can be solved, subject to radial symmetry and a no-slip condition at the tube wall, to give the volumetric flow rate q (Bird et al. 2002):

Eq. 3.1 is the Hagen-Poiseuille equation for laminar flow in a tube. For this equation to apply, the tube must be smooth and long enough so that the flow is free of entrance or exit effects. These conditions never occur in a permeable-medium pore, but the simplicity of the

equation and its similarity to Darcy's law suggest that we continue this development. The average velocity in the tube is



(a) Steady laminar flow



(b) Configuration of an interface between two phases

Fig. 3.1—Tube flow analogues to REV conditions.

This equation is the starting point in the transformation to the REV scale. As the equations suggest, we will assume the velocities and permeabilities to be scalar quantities in this development.

We wish to make the travel time of a fluid element in the capillary tube equal to that in an REV, or

This equation introduces the interstitial fluid velocity v on the right side, where $v = u/\phi$ from the Dupuit-Forchheimer assumption relating the interstitial v and the superficial velocities u (Bear 1972).

V and u are the two most important scalar velocity definitions for permeable-media work. The superficial, or “Darcy,” velocity u is the volumetric flow rate divided by the macroscopic cross-sectional area normal to flow. The interstitial or “front” velocity is the true velocity of a fluid element as it crosses the medium macroscopic dimension. This text uses the symbols u and v to differentiate between these velocities.

When a discrete, single-phase flow form of Darcy’s law is used to eliminate v from the right side of Eq. 3.3, we can solve for the single-phase, scalar permeability component k to obtain

$$k = \frac{R^2 \phi}{8\tau}, \dots \dots \dots \quad (3.4)$$

where $\tau = (L_t / L)^2$ (the squared ratio of the capillary tube length to the REV length) is the tortuosity, another basic permeable-medium property. Tortuosity is always greater than one and can be greater than ten, but is usually between two and five for the media of interest here. The experimental best-fit tortuosity for an assemblage of regularly packed spheres is a 25/12 ratio. Values of tortuosity for electrical conductivity are estimated, but electrical and hydrodynamic tortuosity are not the same.

The value of R in an REV is difficult to visualize. To make it easier, we invoke the concept of a hydraulic radius (Bird et al. 2002):

$$R_h = \frac{\text{Cross-sectional area open to flow}}{\text{Wetted perimeter}}, \dots \dots \dots \quad (3.5a)$$

where R_h is $R/2$ for the tube geometry. The reason for replacing R with R_h is that the latter may be defined for virtually any particle type or pore geometry with the following modification to the basic definition (Eq. 3.5a):

$$R_h = \frac{\text{Volume open to flow}}{\text{Wetted surface area}} \dots \dots \dots \quad (3.5b)$$

Using the definition for porosity, this becomes

where a_V is the specific internal surface of the medium (surface area to volume), an intrinsic permeable-media property. Substituting this into Eq. 3.4 gives

For a medium consisting of uniform spheres, a_V is

where D_p is the sphere or particle diameter (size). Combining Eqs. 3.4 through 3.8 gives the CK equation,

Eq. 3.9 illustrates many important features of permeability. Permeability is a strong function of the pore or particle size D_p and of packing through porosity. This accounts for the low permeabilities in media that have large clay contents and where particle sizes are small. Although Eq. 3.9 applies, strictly speaking, to assemblages of spheres, the effect of nonspherical particles does not become large until the eccentricity of the spheroids becomes large (see Exercise 3.1). Nonspherical particles tend to pack more closely than spherical particles, and therefore, there is an indirect effect on permeability through porosity. Experimentally, permeability is well correlated with the square of the particle diameter ([Fig. 3.2](#)) for permeable media consisting of beads.

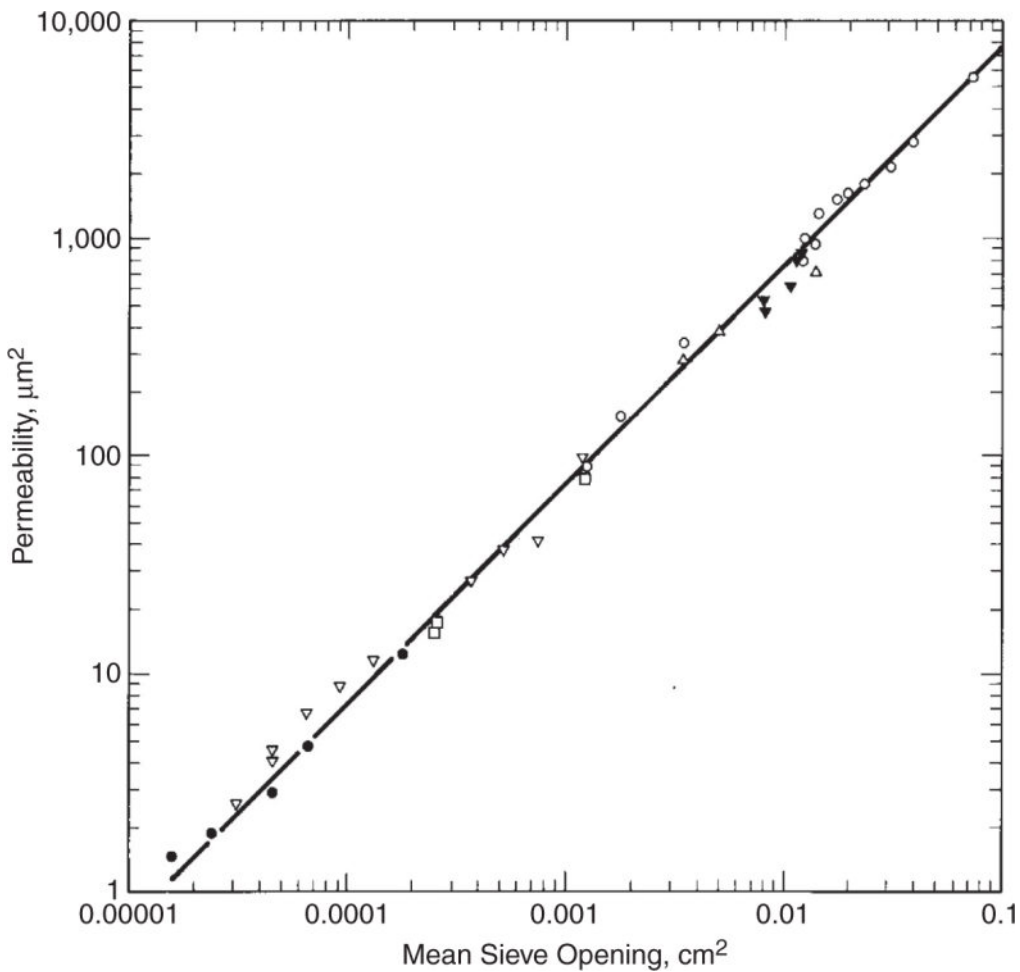


Fig. 3.2—Experimental permeabilities as a function of bead size [adapted from Stegemeier (1976)].

In the primitive form of the CK equation (Eq. 3.7), the specific surface-area term depends on the parameters of the grain size (Panda and Lake 1994) and on the extent and type of mineral content (Panda and Lake 1995) to interpret the effects of these quantities on permeability. Because of the immense variety of naturally occurring media, general statements are difficult to make; however, permeability seems to depend most strongly on porosity, followed by cementing (depending on cement type), and then grain size. Tortuosity and sorting (except as these determine porosity) seem to be less important.

The CK equation enables order-of-magnitude estimates of permeability and estimation of pore size from knowledge of permeability. The pore size is particularly relevant to EOR because it

can be used to develop theoretical expressions relating to the mobility of polymer solutions. To do this, we estimate the local shear rate from an expression for the wall shear rate in a capillary tube:

Eq. 3.10a defines an equivalent permeable-media shear rate,

by use of Eq. 3.3 and the definition of tortuosity. Eliminating R by means of Eq. 3.4 gives

The shear rate given by Eq. 3.11 is useful in correlating and predicting the rheological properties of non-Newtonian fluids in permeable-media flow (see [Chapter 8](#)).

Considering its simplicity, Eq. 3.9 does remarkably well in describing permeability. However, the capillary-tube model of a permeable medium is limited because of its uniform cross section and because it does not provide alternative pathways for fluid flow within each REV. [For more complex local permeable-medium models, see Dullien (1979).] Indeed, one school of thought asserts that permeability is best predicted by considering the resistance to flow to be only in the pore necks or throats (Bryant et al. 1993). This is likely to be true, especially in low-porosity media; however, most local properties are correlated, and therefore, qualitative, if not quantitative, trends are captured by either point of view.

The consequence of these deficiencies is that models without pore throats cannot be made to predict relative permeabilities or trapped-phase saturations without modification. We discuss the latter effects, which play major roles in EOR, separately in the following sections. First, however, we will discuss two-phase flow and its attendant phenomenon, capillary pressure.

3.2 Capillary Pressure

Interfacial forces, as manifested in capillary pressures, are easily the strongest forces within the REV in multiphase flow at typical reservoir flow velocities; hence, capillary pressure is the most basic rock-fluid characteristic of multiphase flows, just as porosity and permeability are the most basic properties of single-phase flow. To discuss capillary pressure, we begin with the capillary-tube concept and then proceed, through qualitative arguments, to the capillary phenomena actually observed in multiphase flow.

Returning to Fig. 3.1b, consider a capillary tube with the same dimensions as in Fig. 3.1a, except that the tube now contains two phases, a nonwetting phase on the left and a wetting phase on the right. Phase 1 wets the tube surface because the contact angle θ , measured through this phase, is less than 90° . By convention, contact angles are measured through the densest phase. The boundary between the two phases is a phase boundary or interface across which one or more of the intensive fluid properties change discontinuously. This boundary is not the same as the concentration boundaries between miscible fluids, across which intensive properties, if they change at all, change continuously.

Although there are superficial similarities, Figs. 3.1a and 3.1b are quite different. The fluid in Fig. 3.1a is flowing, and that in Fig. 3.1b is static. We try to reconcile these points of view below. If the phases and the interface in the tube are not flowing, a higher pressure is required in the nonwetting phase than in the wetting phase to keep the interface from moving. A static force balance across the interface in the direction parallel to the tube axis gives an expression for the nonwetting/wetting phase pressure difference:

Eq. 3.12 defines capillary pressure. The definition is pressure in the least dense phase minus pressure in the densest phase to be consistent with the convention for measuring contact angles. The interface shape in Fig. 3.1b should not be confused with the velocity

profile in [Fig. 3.1a](#). The latter is a static condition, whereas the former is a plot of dynamic velocity.

Eq. 3.12, a simple form of Laplace's equation, relates the capillary pressure across an interface to the radius of curvature of the interface R , the interfacial tension (IFT) σ , and the contact angle θ . If either the interfacial tension is zero or the interface is perpendicular to the tube wall, the capillary pressure will be zero. The first condition is satisfied when the absence of interfacial tension (and hence the interface) renders the two adjoining phases miscible. The second condition holds only for the simple uniform tube geometry. The contact angle can take on all values between 0° and 180° ; if it is greater than 90° , the wetting pattern of the two fluids is reversed, and the capillary pressure, as defined by Eq. 3.12, becomes negative.

In more complex geometries, the form of the $1/R$ term in Eq. 3.12 is replaced by the mean curvature, which is a more general expression. There are several such expressions. For example, Embid-Droz (1997) used minimization of the Helmholtz free-energy function to arrive at

$$P_c = \sigma \left(\frac{dA_{12}}{dV_2} + \cos \theta \frac{dA_{2s}}{dV_2} \right), \dots \quad (3.13)$$

where V_2 is the volume of Phase 2 and A_{12} and A_{2s} are the areas between Phases 1 and 2 and between Phase 2 and the solid, respectively. The term in parentheses in Eq. 3.13 is the mean curvature. Eq. 3.13 separates the capillary-pressure contribution of the fluid-fluid surface energy (first term in the curvature) from that of the fluid-solid surface energy (second term). You can see that many of the items discussed in the previous paragraph pertain here: P_c is non-zero if $\theta = 90^\circ$ (in which case, capillary pressure is entirely caused by the fluid-fluid surface, and P_c may be negative). The equation also provides a link to the surfaces required to estimate relative permeabilities, as will be discussed in Example 3.1 below.

Example 3.1—Special Cases of Eq. 3.13. Eq. 3.13 reverts to simpler forms for special geometries. In solving this example, note how the curvature depends parametrically on the local geometry.

- a. ***Isolated Spherical Drop.*** In this case, $A_{2s} = 0$, and

$$dA_{12} = d(4\pi R^2) = 8\pi R dR, \quad dV_2 = d\left(\frac{4}{3}\pi R^3\right) = 4\pi R^2 dR,$$

where R is the radius of the drop. Inserting this into Eq. 3.13 gives

$$P_c = \sigma \left(\frac{dA_{12}}{dV_2} \right) = \sigma \left(\frac{8\pi R}{4\pi R^2} \right) = \frac{2\sigma}{R}.$$

- b. ***Interface in a Smooth, Uniform Tube.*** If the tube is uniform, the fluid-fluid surface area does not change with interface position; hence, $\frac{dA_{12}}{dV_2} = 0$. The areas and volumes are given in terms of an interface position L as

$$dA_{2s} = d(2\pi RL) = 2\pi R dL, \quad dV_2 = d(\pi R^2 L) = \pi R^2 dL.$$

Substituting these into Eq. 3.13 gives Eq. 3.12 as a special case. Of course, many other special cases are possible; see Exercise 3.2.

In the following discussion, remember that capillary pressure is inversely proportional to mean interfacial curvature ($1/R$); the more curved the interface (the smaller the radius of curvature), the higher will be the capillary pressure. We will now consider a series of entries and exits of a nonwetting phase into a simple medium originally filled by a wetting phase. You should remember three things in reading this material:

1. The discussion is entirely restricted to phases that are strongly wetting (nonwetting) to the solid surface,
2. We identify capillary pressure with pressure in the nonwetting phase, which causes a given degree of penetration of the interface, and,
3. The fluids being static, capillary pressure is the difference in pressures between the inlet and outlet of the cell. The cell is horizontal to eliminate gravity effects; see Exercise 3.8.

Eq. 3.13 is fairly general, but is difficult to apply to complex geometries. Three aspects of the geometry must be accounted for:

1. Variable pore sizes
2. Nonuniform pores
3. Connectivity

All express heterogeneity at the REV scale, the non-uniform pores being at the smallest scale. Aspect 2 is the most important for our discussion because the existence of different radii in pore throats and bodies is unavoidable in any permeable medium, no matter how carefully or artificially constructed. This means that no permeable medium can be locally homogeneous. We can incorporate the first two effects into capillary pressure fairly easily, as the following discussion indicates, but the issue of multiple connections requires more sophisticated treatment.

3.2.1 Uniform Walls, Pore-Size Distribution. We illustrate the effects of variable pore size through the schematic in [Fig. 3.3](#).

The tapering cell is uniform; it does not have pore throats and bodies. The varying radii are a surrogate to represent a pore-size distribution. See Example 3.2 for a quantitative calculation of this behavior. Pressures that are measured at the cell outlet and inlet are pressures on either side of the interface because there is no flow. One of the great strengths of capillary pressures is that large-scale measurements directly relate to small-scale phenomena. This will be true in all the cells we are to consider.

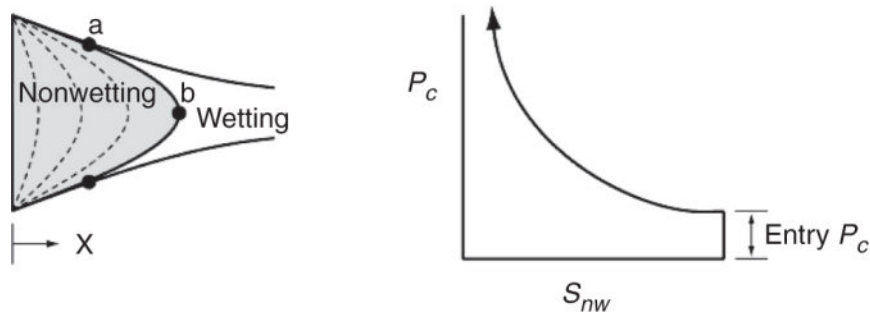


Fig. 3.3—Schematic of a tapering cell, a surrogate for variable pore-size distribution. The dotted lines on the left figure indicate successive interface positions at increasing capillary pressure.

Let us introduce the nonwetting phase from the left in Fig. 3.3 and hold the interface at a given position with a fixed value of P_{nw} , or the pressure in the nonwetting phase. Forcing the interface to enter the cell will require some threshold pressure; this pressure is the *entry* or *displacement pressure*. Sometimes it is called the *bubbling* pressure. Larger and larger values of P_{nw} are required to force the interface into the narrow portions of the cell. We can translate each interface position into a nonwetting-phase saturation S_{nw} to construct the capillary-pressure curve shown on the right from Eq. 3.12. An entry pressure is observed in most actual drainage P_c measurements; it is a measure of the largest pore size in the sample, as discussed in the following example. Furthermore, the rate of increase of the P_c curve reflects the rate of taper of the cell; hence, the shape of the curve is a measure of the pore-size distribution.

Example 3.2—Capillary Pressure in a Tapered Channel. Consider a slit of unit width that does not contain a permeable medium. The half-width of the slit varies with position x between 0 and x_1 according to

$$W(x) = R_0 + (R_1 - R_0) \left(\frac{x}{x_1} \right)^m,$$

where m is a positive constant (see Fig. 3.4). The channel is originally filled with a wetting phase, and a nonwetting phase is

introduced at $x = 0$ while the wetting fluid remains in contact with R_1 and exits at $x = x_1$. The slit described by the preceding equation is a surrogate for a pore-size distribution in a permeable medium. R_0 is the largest pore and R_1 is the smallest. The parameter m describes the shape of the pore-size distribution it is represented for $R_0 / R_1 = 10$ and three values of m in Fig.3.4. The quantity x_1 has no analogous meaning in permeable media.

A dimensionless capillary-pressure function P_{cD} is

$$P_{cD} = \frac{P_c R_0}{\sigma \cos \theta}$$

for $\cos \theta \neq 0$.

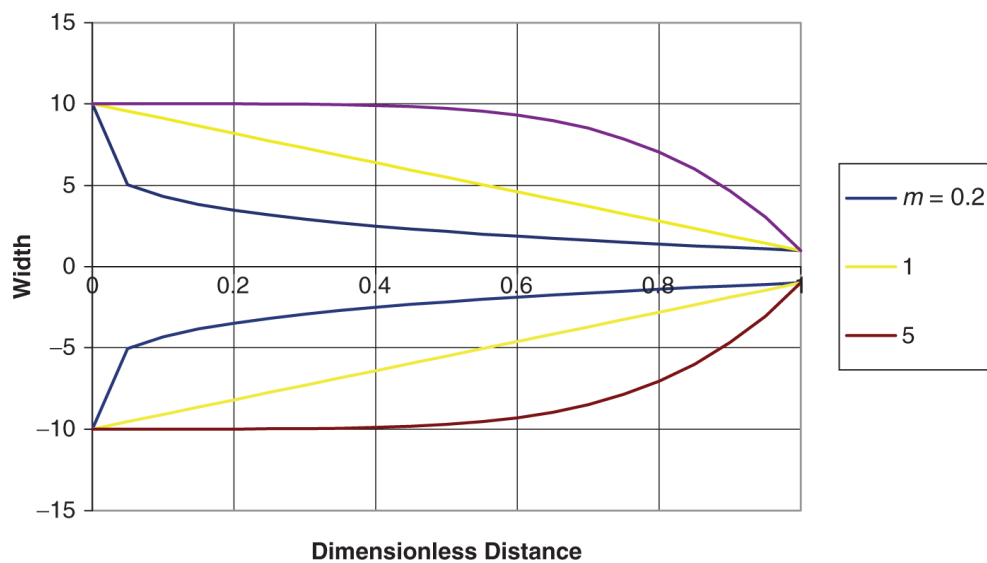


Fig. 3.4—Geometries of various types of tapered cells.

- Derive a set of equations that relates P_{cD} to the wetting-phase saturation S_w . These equations should show that P_{cD} is a function of S_w , wettability (through θ), pore-size distribution (through m), and the ratios (R_1/R_0) and (R_0/x_1). Neglect the contribution of the fluid-fluid surface area in this calculation. That is, neglect the region abc at the left of [Fig. 3.3](#).

With the fluid-fluid area neglected, the capillary pressure becomes

$$P_c = \sigma \cos \theta \frac{dA_{2s}}{dV_2}.$$

Because the definitions involve differentials, they are easy to evaluate as

$$dA_{2s} = \left[1 + \left(\frac{dW}{dx} \right)^2 \right]^{1/2} dx \text{ and } dV_2 = W dx,$$

so that

$$P_c = \sigma \cos \theta \left[1 + \left(\frac{dW}{dx} \right)^2 \right]^{1/2},$$

which yields, after substituting the channel-width equation,

$$P_c = \sigma \cos \theta \frac{\left\{ 1 + \left[m \frac{(R_i - R_0)}{x_i} \left(\frac{x}{x_i} \right)^{m-1} \right]^2 \right\}^{1/2}}{R_0 + (R_i - R_0) \left(\frac{x}{x_i} \right)^m}.$$

Using the definition of the dimensionless capillary pressure, this gives

$$P_{cd} = \frac{P_c R_0}{\sigma \cos \theta} = \frac{\left\{ 1 + \left[m \left(\frac{R_1 - R_0}{x_1} \right) \left(\frac{x}{x_1} \right)^{m-1} \right]^2 \right\}^{1/2}}{1 + \left(\frac{R_1 - R_0}{R_0} \right) \left(\frac{x}{x_1} \right)^m}. \quad \dots \dots \dots \quad (A)$$

The x in these equations is the position of the interface.

The saturation is determined by first giving an expression for the volume of the slit. The volume of the slit out to a distance x is

$$V(x) = \int_{\xi=0}^{\xi=x} W(\xi) d\xi = \int_{\xi=0}^{\xi=x} R_0 + (R_1 - R_0) \left(\frac{x}{x_1} \right)^m d\xi = R_0 x + \frac{(R_1 - R_0)x_1}{m+1} \left(\frac{x}{x_1} \right)^{m+1}.$$

The pore volume of the slit is therefore

$$V(x_1) = R_0 x_1 + \frac{(R_1 - R_0)x_1}{m+1},$$

so that the saturation of the entering nonwetting phase is

$$S_{nw}(x) = \frac{R_0 x + \frac{(R_1 - R_0)x_1}{m+1} \left(\frac{x}{x_1}\right)^{m+1}}{R_0 x_1 + \frac{(R_1 - R_0)x_1}{m+1}} = \frac{\frac{x}{x_1} + \frac{(R_1 - R_0)}{(m+1)R_0} \left(\frac{x}{x_1}\right)^{m+1}}{1 + \frac{(R_1 - R_0)}{(m+1)R_0}}.$$

From this, it follows that

$$S_w(x) = 1 - S_{nw}(x) = \frac{1 - \frac{x}{x_1} + \frac{(R_1 - R_0)}{(m+1)R_0} \left[1 - \left(\frac{x}{x_1}\right)^{m+1}\right]}{1 + \frac{(R_1 - R_0)}{(m+1)R_0}} \dots \dots \dots \quad (B)$$

Eq. B for x cannot be solved generally, and therefore, the relationship sought is parametric in these quantities.

- b. Assume the following as base-case values: $m = 3/4$, $R_1/R_0 = 10$, and $R_0/x_1 = 1$. Illustrate the sensitivity to the items in part (a) by plotting four curves of P_{cD} vs. S_w . Curve 1 will be for the base-case values, and Curves 2 through 5 will be for each of the above parameters at double their base-case values. The results are shown in [Fig. 3.5](#).
- c. From the results of part (b), comment on how realistic the curves are and state which quantities have the most effect on the dimensionless capillary-pressure function.

All the curves are realistic in that they have a nonzero entry pressure. Three of the four curves are realistic in that they are monotonically increasing with decreasing wetting-phase saturation. The sensitivity of the quantities depends on the saturation range. Evidently the small pore sizes R_1 are sensitive only at very low wetting-phase saturation. The “length” of the cell x_1 is most sensitive at higher wetting saturations. The non-monotonic behavior of the $m =$

1.5 curve is not possible. This behavior is likely attributable to neglect of the fluid-fluid interfacial area.

The dimensional capillary pressure is most sensitive to the normalizing factors in Eq. A, to which it is directly proportional.

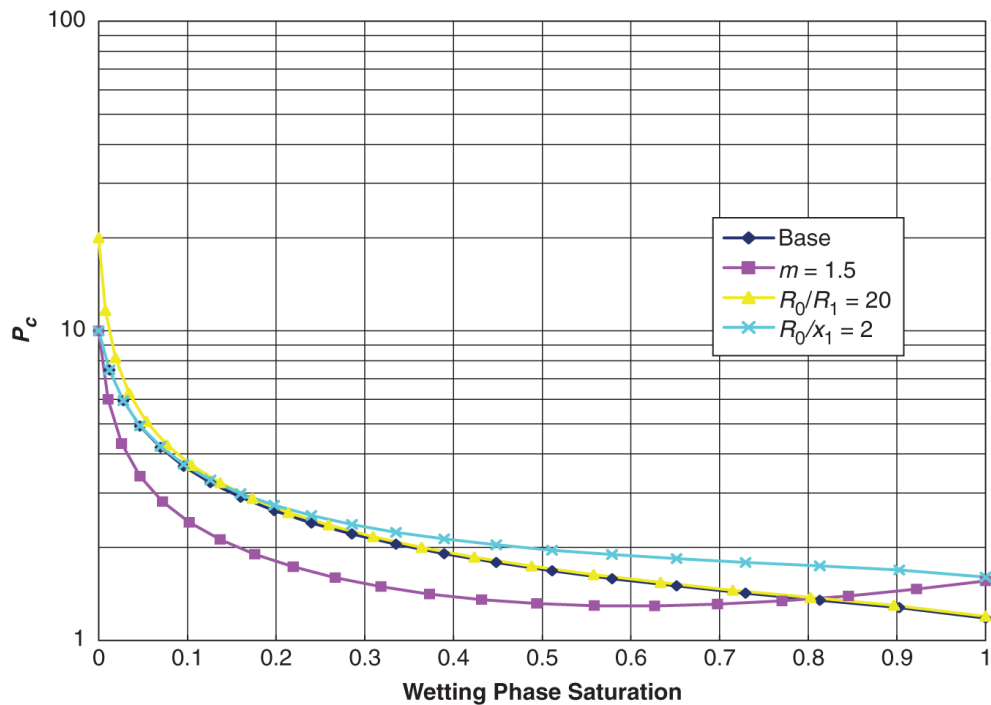


Fig. 3.5—Calculated capillary pressure curves.

3.2.2 Nonuniform Walls. The P_c curves in the uniform cell are reversible. In other words, the same capillary pressure would occur at a given saturation, regardless of how that saturation was arrived at. What follows is a potentially confusing phenomenon that is important for EOR, so we divert the narrative to consider it.

Regardless of whether the interface arrives at the position at the left of Fig. 3.3—from the left, as we have been discussing, or from the right as a consequence of nonwetting fluid withdrawal—the P_c at this point will be the same. Obtaining the same value for injection and for withdrawal of a nonwetting phase is definitely *not* what is observed in practice. This effect, known as *hysteresis* or the dependency of a property on its history, is a major feature of *all* petrophysical properties. The process we are describing is a *drainage* process in

which the nonwetting-phase saturation is increasing. The opposite process, *imbibition*, involves increasing the wetting-phase saturation. The fact that the drainage and imbibition P_c curves are different indicates a form of hysteresis.

The simple cell in [Fig. 3.2](#) does a fair job of reproducing (first) drainage capillary-pressure curves, certainly a much better job than the uniform tube in [Fig. 3.1](#). However, it still has two deficiencies when compared with behavior in actual media. When the interface reaches the narrowest portion of the cell, the wetting-phase saturations may be very close to zero, but it is impossible to remove the wetting phase entirely from the medium by displacement alone because of the tendency of the wetting phase to form continuous layers. In fact, the presence of these films complicates the definition of contact angle at low nonwetting-phase saturations. Experiments have shown that surface roughness leads to low wetting-phase saturation because there are more flow paths for fluid to escape.

As discussed above, a more serious deficiency of the nonuniform cell is that it suggests that the imbibition and drainage processes are entirely reversible. We must complicate the model further before we see the reasons for this lack of reversibility.

For geometries in which the uniform grains are the same size, but there is now a difference between throats and bodies, consider the entry of a nonwetting phase into a single pore in [Fig. 3.6](#). The pore has a toroidal geometry and is bounded by the sphere assemblage shown. The capillary pressures corresponding to the various entry positions of the interface are shown in [Fig. 3.6b](#). We continue to associate the pressure difference between the inlet and outlet of the cell with capillary pressure.

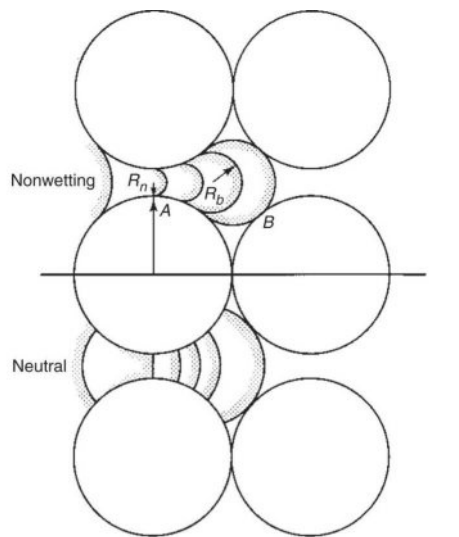
To force the interface into the pore, it must be compressed through the pore neck or throat radius R_n , causing a decrease in the interface curvature and an increase in P_c to point A. (We could alternatively regard the pressure difference as the cause of the penetration.) Once inside the pore body, which has a larger dimension R_b than the throat, the interface curvature increases, and the capillary pressure decreases. The decrease would, in principle, continue until the

interface became constrained by the walls on the opposite side of the pore at point *B*. However, this capillary-pressure decrease does not actually occur. Instead, the interface at pore-throat point *A* jumps across the pore body to an exit pore throat where P_c is the same as at the entry. This jump, a *Haynes* jump or *recon*, is a consequence of the fact that the capillary pressure cannot decrease (Embid-Droz 1997). The practical consequence of the jump phenomenon is that the capillary pressure is really interrogating the pore-throat radius rather than the pore-body radius.

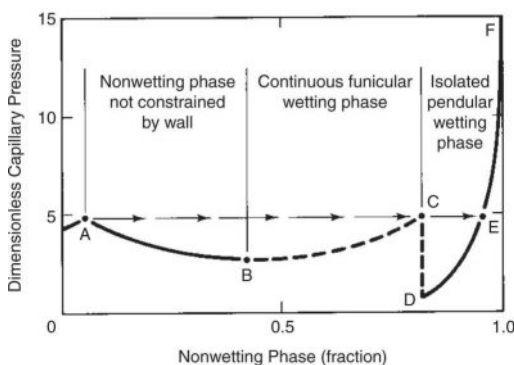
If the nonwetting-phase saturation is again increased after the jump, the nonwetting phase is now forced farther into the rock-rock contacts, which manifests itself in very large P_c increases. The wetting phase at this point retreats to saturations approximated by monolayer coverage of the rock surfaces. Although this would seem to result in very low wetting-phase saturation, Melrose (1982) has shown that wetting-phase saturations greater than 10% are possible at this limit, but that saturation values substantially lower than this can be obtained if the rock surface is not smooth.

The same process occurs even if the displacing fluid has neutral wettability with respect to the solid curve in [Fig. 3.6a](#). Hence, for an irregular pore geometry, $\cos \theta = 0$ does not imply zero capillary pressure.

A natural permeable medium has many assemblages, such as the toroids in [Fig. 3.6a](#), that differ in size, shape, and internal geometry. If these differences are distributed continuously in the medium, the discontinuous capillary-pressure curve in [Fig. 3.6b](#) becomes continuous, as shown in [Fig. 3.7b](#). Many of the same features are still present—the existence of an entry pressure at low nonwetting saturations (mercury in this case) and the sharp increase at high saturations. However, the decreases in P_c with increasing nonwetting saturation are absent. Capillary-pressure experiments conducted at a pre-specified rate tend to show the discontinuities in [Fig. 3.6b](#). See Yuan and Swanson (1989) for examples. These experiments are not routine.



(a) Entry of nonwetting and neutral fluids in toroidal pore model



(b) Resulting capillary pressure for nonwetting fluid entry

Fig. 3.6—Schematic of interface entrance into a toroidal pore [adapted from Stegemeier (1976)].

The most complex geometry considered in this text is illustrated in [Fig. 3.7a](#). These six cells contain both pore throats and bodies and a distribution of pore sizes. The connectivity issue is still not present, but we can illustrate nearly all the important features of capillary-pressure curves nevertheless. As simple as it is, this figure illustrates some important features of residual nonwetting-phase saturation.

The entry of a nonwetting phase into a single pore has many of the features discussed in the preceding paragraphs in connection with the toroid; however, now a continuous increase in nonwetting-phase saturation will give the capillary-pressure curve from Points 1 to 6 shown in [Fig. 3.7b](#).

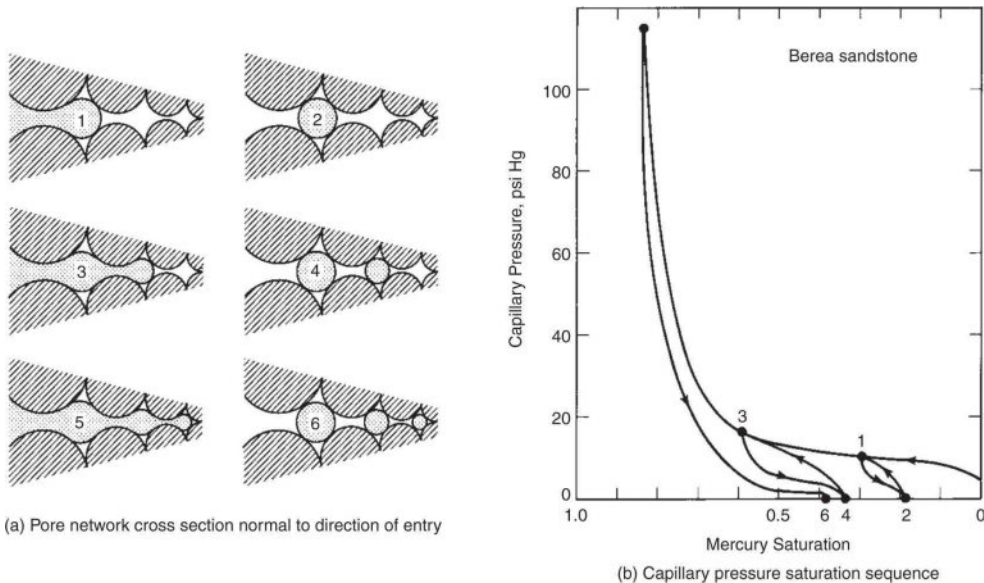


Fig. 3.7—Distribution of a nonwetting phase at various saturations [adapted from Stegemeier (1976)].

The curve from Points 1 to 6 is much like the curve in [Fig. 3.2](#), where there were no throats and bodies; the interface entry follows a sequence of continually decreasing pore throats as the nonwetting saturation increases. Hysteresis occurs when the nonwetting saturation decreases from any point on the drainage curve. In the following discussion, remember that the pores must have an exit for the wetting fluid somewhere on the right.

Beginning at $S_{nw} = 0$, we inject up to the saturation shown at Point 1. As always, the pressure difference between the exit and entrance of the cell is the capillary pressure at that saturation. Now, release the pressure in the nonwetting phase. This will cause the wetting phase to flow spontaneously into the pore from the right. The spontaneous flow will occur along the surface of the solid, which will cause an accumulation of the wetting phase at the throat at the original entrance of the nonwetting phase. If conditions are right, the nonwetting phase disconnects, leaving a *glob* of nonwetting phase in the largest pore (Condition 2).

The capillary-pressure curve from Points 2 to 1 is an imbibition curve; its principal difference from the drainage curve (from Points 1 to 2) is that it terminates ($P_c = 0$) at a different saturation. At static-

condition 2, the entrance/exit pressure difference is zero because both pressures are being measured in the same wetting phase. The nonwetting phase at Condition 2 is considered to be trapped because it is discontinuous.

Going from Condition 2 to 3 is a *second* drainage process, involving reconnection of the disconnected glob and further penetration, which results in a nonwetting saturation greater than at Point 2, a larger P_c , and greater trapped nonwetting-phase saturation (Condition 4) after imbibition. At the highest capillary pressure (Condition 5), all pores contain some of the nonwetting phase, and the post-imbibition trapped saturation is at a maximum. The capillary-pressure curve that runs from the largest nonwetting-phase saturation to the largest nonwetting-phase trapped saturation is the imbibition curve (Curve 6). Curve 1 is the drainage curve; all others are designated as second drainage, second imbibition, and so forth. The entire set of curves is known as a scanning or hysteresis loop.

The forming of such discontinuous blobs by a wetting phase that moves around a nonwetting phase is known as *snap-off*. The consequences of snap-off are described in more depth below, but it arises largely because of the difference in size between the pore throat and pore body. The larger the disparity, the more trapping will occur. In fact, the hysteresis loop itself, particularly the imbibition cycles, is a measure of the size of the pore bodies. This is an admittedly biased measure because of the complexities caused by the connectivity issues mentioned above. Furthermore, snap-off itself is governed by the specific pore geometry (Toledo et al. 1994). See Mohanty (1981) for an alternative view of snap-off in foam flow. Snap-off has been captured in the thermodynamics-based modeling of Prodanovic et al. (2010).

The representations in [Figs. 3.3](#) to [3.7](#) explain many features of actual capillary-pressure curves. Imbibition curves are generally different from drainage curves, but the difference shrinks at high nonwetting-phase saturations as more of the originally disconnected globs are reconnected.

The above mechanisms have meaning from the flow standpoint once we associate the disconnected nonwetting glob with residual nonwetting saturation. Residual nonwetting saturation, therefore, increases as the disparity between pore throats and pore body sizes increases. Because capillary pressures are static measurements, the residual saturations should be somewhat higher than they would be under flow. The effect of velocity is discussed in more detail below. The saturation at $P_c = 0$ does not correspond to zero local capillary pressure because, after all, the disconnected blobs still have interfacial tension and curvature. The local capillary pressure is what hinders nonwetting movement and limits ultimate recovery of the nonwetting phase. This phenomenon is discussed further later in this chapter.

The saturation at the other extreme of the capillary-pressure curve, the *irreducible* or residual wetting-phase saturation, is probably flowing at very low saturations. However, there is a practical residual saturation corresponding to the asymptote of the curve, where the wetting-phase flow is so small as to be considered essentially immobile.

The hysteresis discussed above is called *trapping* hysteresis. Drag hysteresis is caused by differences in the advancing and receding contact angles, which is in turn caused by sorption of polar substances on a solid surface (Morrow and Chatzis 1976), as discussed below. Drag hysteresis would occur in the smooth wall cells shown in [Fig. 3.3](#). It is not possible to determine which form of hysteresis dominates in a given case. What we can say is that trapping hysteresis is always present because pore throats are always smaller than pore bodies.

The nonwetting-phase residual saturation depends on the largest nonwetting-phase saturation. A plot of these two quantities is the initial-residual (IR) curve. The IR curve manifests many of the same permeable-media properties as the capillary-pressure curves. [Fig. 3.8](#) shows a set of typical IR curves.

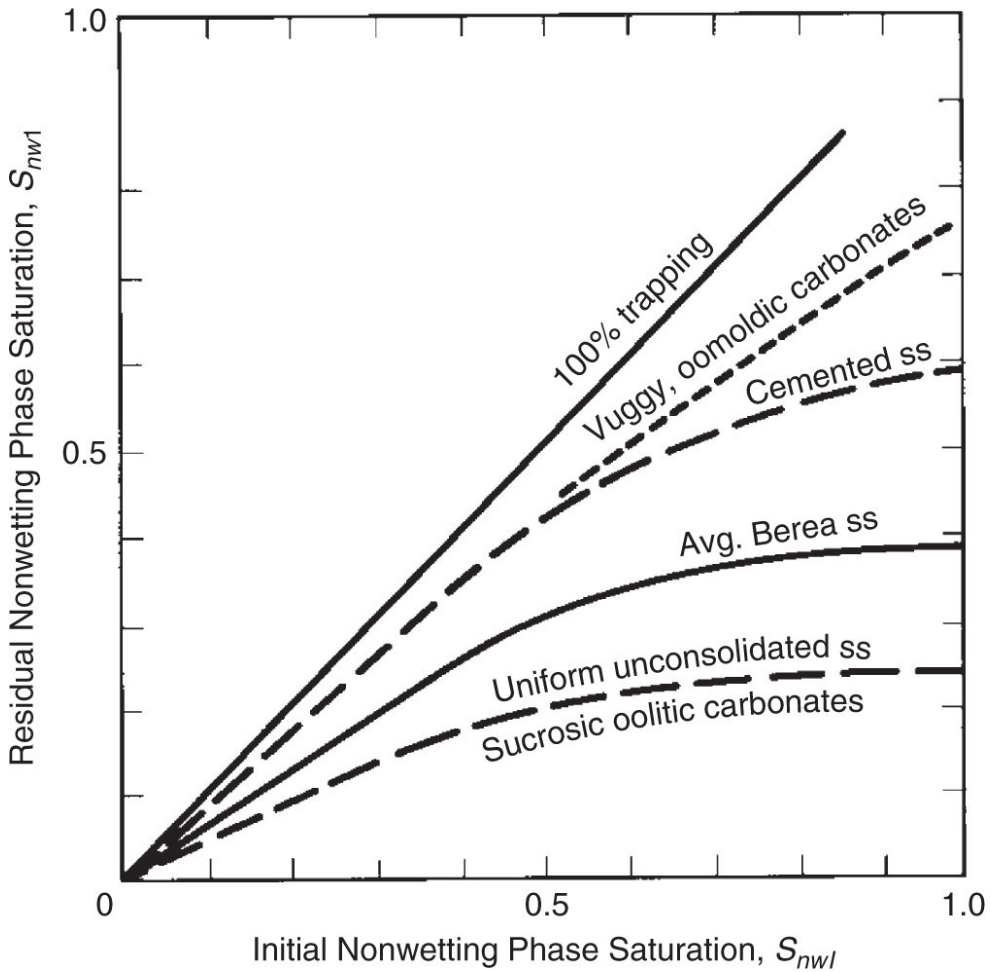


Fig. 3.8—Typical initial residual-nonwetting-phase saturations curves (ss = sandstone) (Stegemeier 1976).

Remember that the quantity being plotted on the y -axis of capillary-pressure curves is the pressure difference between continuous nonwetting and wetting phases. When either phase exists in a disconnected form, such as Conditions 2, 4, and 6 in Fig. 3.7a, a local capillary pressure exists, but it is not unique because of the variable glob sizes. We use these concepts and the IR curve to estimate the CDC in Section 3.4, but first, let us see how the IR curve can be estimated from the hysteresis in the capillary-pressure curves.

The capillary pressure at a given saturation is a measure of the smallest pore being entered by the nonwetting phase at that point, which suggests that the curvature of the capillary-pressure curve is a function of the pore-size distribution. The height of the curve is determined by the mean pore size. In an effort to separate the effects

of pore size and pore-size distribution, Leverett (1941) proposed a nondimensional form of the drainage capillary-pressure curve that should be independent of pore size. We first replace the capillary-tube radius R in Laplace's Eq. 3.12 with a function $R/j(S_{nw})$, where j is a dimensionless function of the nonwetting-phase saturation S_{nw} . By eliminating the hydraulic radius between the new Eq. 3.12 and Eq. 3.4, we arrive at the Leverett j -function,

$$j(S_{nw}) = \frac{P_c \sqrt{\frac{k}{\phi}}}{\sigma \cos \theta} \dots \dots \dots \quad (3.14)$$

The numerical constants and the tortuosity have been absorbed into j in Eq. 3.14. As shown in the original work (Leverett 1941), the j -function is independent of the pore size, as was intended, but is also independent of the interfacial tension between the pair of fluids used to measure P_c . j as a function of S_{nw} is presented in several standard works (Collins 1976; Bear 1972). The process used in deriving Eq. 3.14 is a form of pore size-to-REV scaling (see Peters 2012). For alternative capillary-pressure correlations, see Thomeer (1960), Morrow and Chatzis (1976), and Skjaeveland et al. (2000).

By a similar procedure, the first drainage capillary-pressure curve can be used to calculate pore-size distributions. At each capillary-pressure value, Eq. 3.12 may be used, with $\sigma \cos \theta$ known, to calculate the radius R of the largest pore being entered at that nonwetting saturation. The nonwetting saturation itself is the volume fraction occupied by pores of this size or larger. This information can be converted into a pore-size percentile plot, which can then be converted into a frequency of occurrence of pores at a given R . [Fig. 3.9](#) illustrates the wide variety of pore sizes exhibited by natural media as obtained by this procedure.

The scaling ideas in the above development are useful in estimating the capillary pressures in a rock sample of arbitrary k and ϕ from a single capillary-pressure curve on a rock sample of known k and ϕ . Of course, this scaling assumes that all samples have the same pore-size distribution and tortuosity. The scaling can also be

used to estimate the capillary pressure for a fluid pair different from that used to measure the capillary-pressure curve. Unfortunately, the j -function was derived for a drainage capillary-pressure curve, so it cannot by itself be used to estimate imbibition capillary-pressure curves. Moreover, the effect of permeable-media wettability is insufficiently represented by the contact angle (see [Fig. 3.3](#)). Even if it were, wettability is difficult to estimate.

3.2.3 Wettability. Wettability is a generic term that describes the degree to which a phase contacts (or “wets”) the internal surface in a permeable medium. It is at the same time one of the most complex, important, and controversial subjects to be covered in this text.

At least three tests are commonly used to measure permeable-media wettability (Anderson 1986).

1. In the Amott test (Amott 1959), wettability is determined by the amount of oil or water spontaneously imbibed by a core sample compared to the same values when the sample is flooded. Amott wettability values range from +1 for complete water wetting to -1 for complete oil wetting. This measure is the most widely cited wettability index in the literature.
2. In the US Bureau of Mines test (Donaldson et al. 1969), the wettability index W is the logarithm of the ratio of the areas under centrifuge-measured capillary-pressure curves in both wetting-phase saturation increasing and decreasing directions. W can range from $-\infty$ (oil-wet) to $+\infty$ (water-wet), but is characteristically between -1.5 and +1.0.

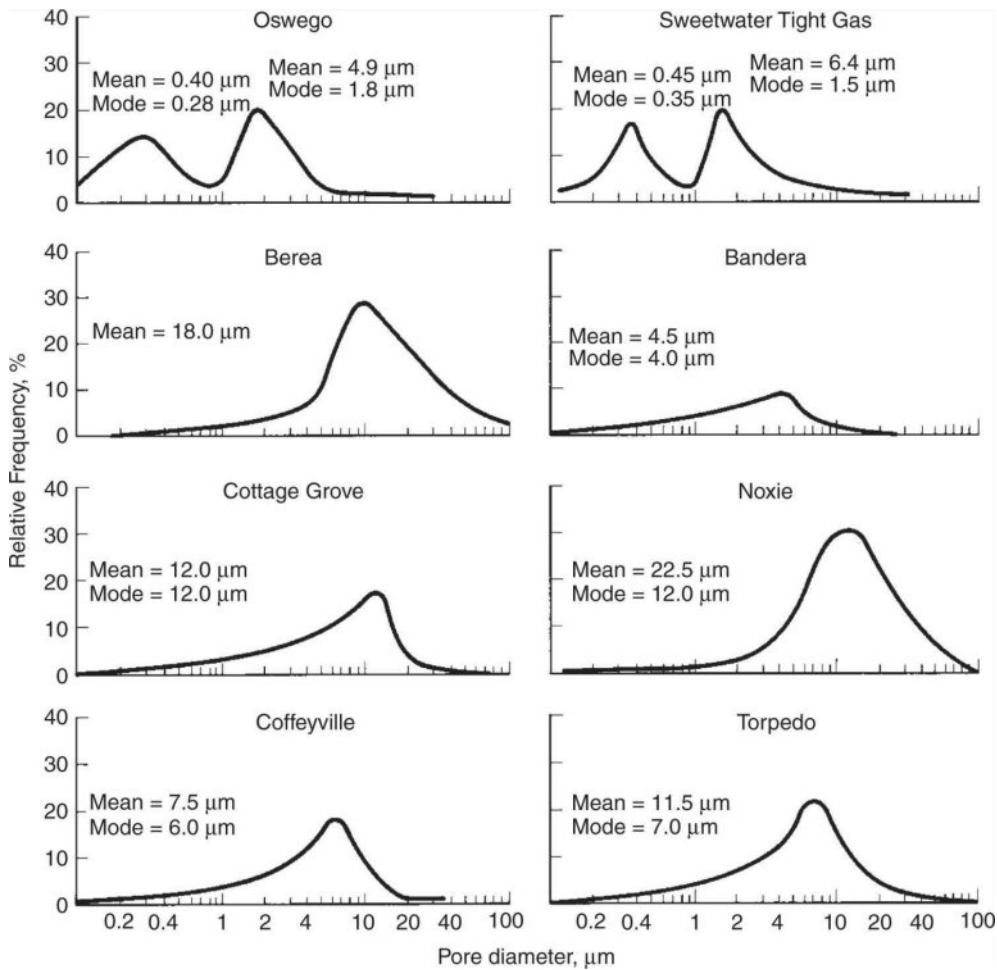


Fig. 3.9—Pore-throat size distributions of sedimentary rocks (Crocker et al. 1983).

3. In a third test, contact angles can be measured directly on polished silica or calcite surfaces (Wagner and Leach 1959). These are the most direct measurement of wettability. The contact angle is measured through the densest phase, which means that it can be near zero for strongly water-wet media and near 180° for strongly oil-wet media.

As a means of estimating wettability in permeable media, none of these tests is entirely satisfactory. The Amott index and the W index can be measured in actual permeable media, but their correspondence to capillary pressure is indirect. Furthermore, both these tests are measures of aggregate rather than local wettability. The contact-angle measurement is of course direct, but a polished synthetic surface may not represent the internal surface of the

permeable media. Implicit in the use of contact-angle measurements is the assumption that, in determining wettability, oil-brine properties are more important than solid-surface properties. Contact-angle measurements do exhibit hysteresis ([Fig. 3.10](#)). Moreover, all wettability measures are not used routinely.

The contact angle has been used to survey the wettability of 55 oil reservoirs, with the results shown in [Table 3.1](#). Neither the total number of reservoirs nor the two major reservoir lithology classes (sandstone and carbonate) are exclusively of one wetting state. Most sandstone reservoirs tend to be water-wet or intermediate-wet, whereas most carbonate reservoirs tend to be intermediate-wet or oil-wet. The contact angle has also been used to correlate relative-permeability measurements (Owens and Archer 1971), but in actual practice, these measurements are so rare that, as we show, they are usually used to infer wettability.

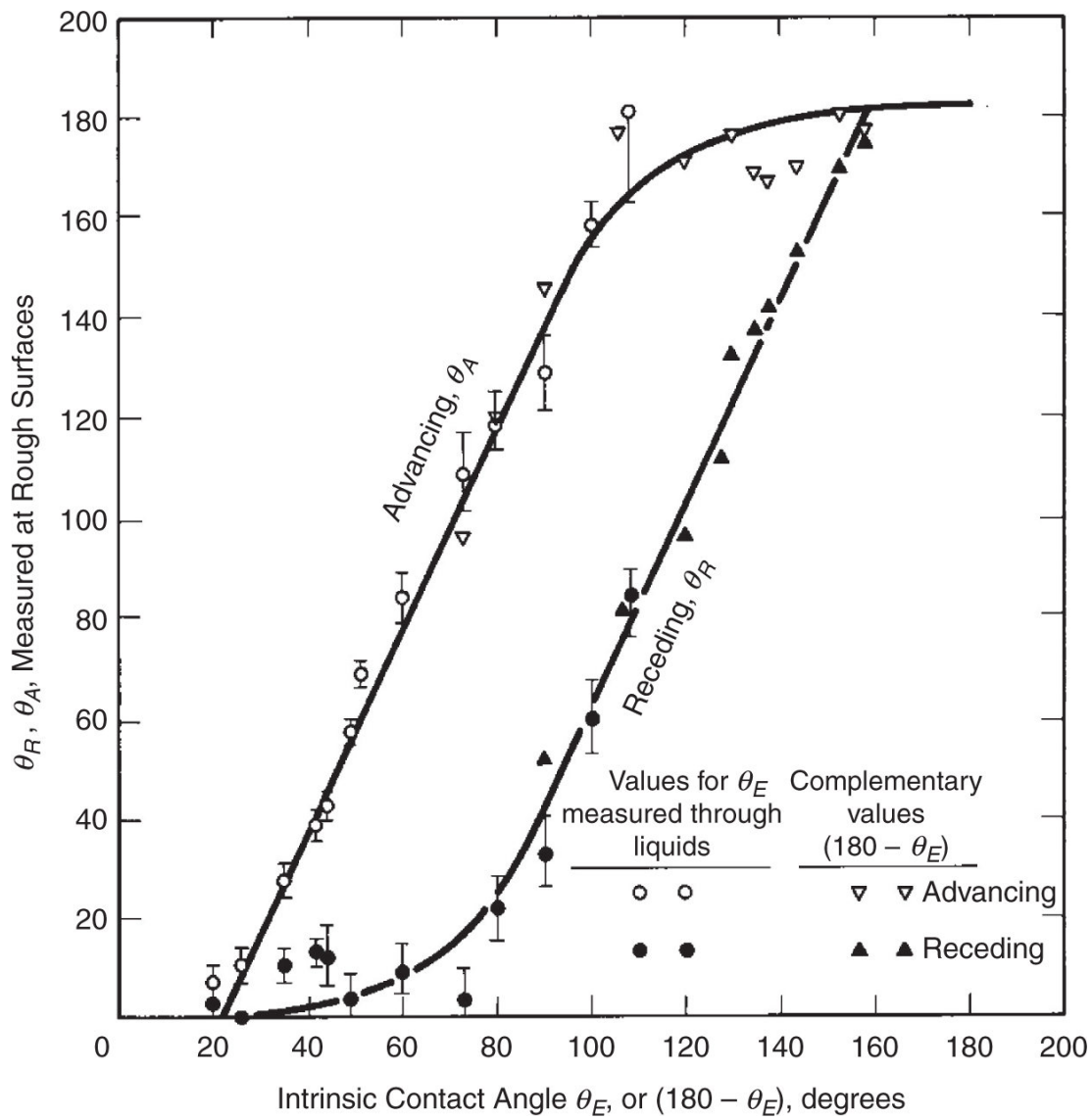


Fig. 3.10—Advancing (θ_A) and receding (θ_R) contact angles observed at rough surfaces vs. intrinsic contact angle (θ_E) (Morrow 1976).

TABLE 3.1—DISTRIBUTION OF WATER-WET, INTERMEDIATE-WET, AND OIL-WET RESERVOIRS ON THE BASIS OF ADVANCING CONTACT-ANGLE MEASUREMENTS ON SMOOTH MINERAL SURFACES FOR FLUIDS FROM 55 RESERVOIRS [AFTER MORROW (1976); BASED ON TREIBER ET AL. (1972)]

Wettability Class	Water-Wet	Intermediate-Wet	Oil-Wet
Defining contact-angle range used by Triebel et al. (θ_A at smooth mineral surface)	0°–75°	75°–105°	105°–180°
No. of sandstone reservoirs	13 (43%)	2 (7%)	15 (50%)
No. of carbonate reservoirs	2 (8%)	2 (8%)	21 (84%)
Total	15 (27%)	4 (7%)	36 (66%)
Defining contact-angle range from classification used in Morrow (1976)	$\theta_A < 62^\circ$	$\theta_A > 62^\circ$ $\theta_R > 133^\circ$ ($\theta_R = \theta_A$)	$\theta_A > 133^\circ$
No. of sandstone reservoirs	12 (40%)	10 (33%)	8 (27%)
No. of carbonate reservoirs	2 (8%)	16 (64%)	7 (28%)
Total	14 (26%)	26 (47%)	15 (27%)

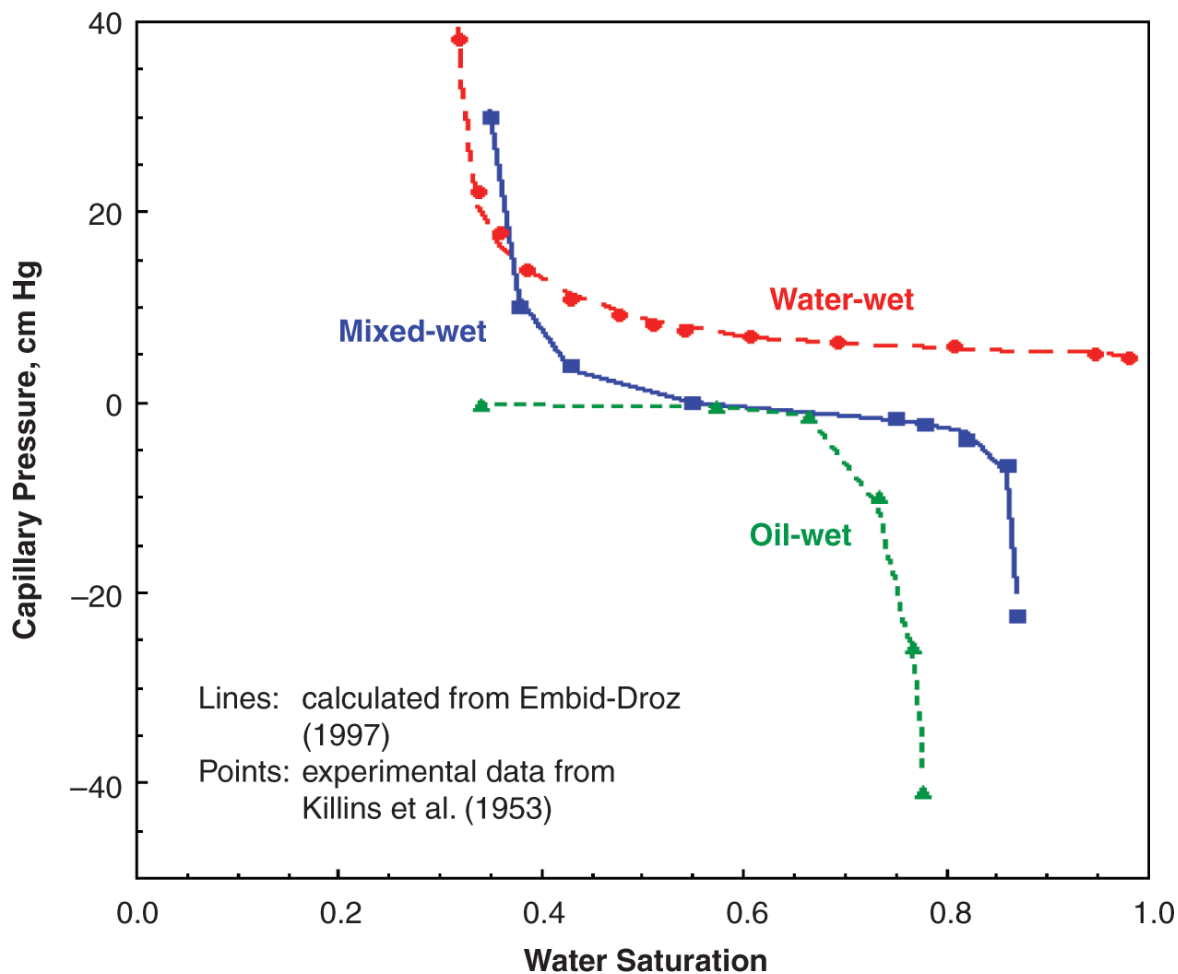


Fig. 3.11—Measured capillary-pressure curves for various wetting states.

The capillary pressure discussed so far applies to strongly wet media, those in which one phase is clearly wetting and the other nonwetting. Despite 40 years of evidence that most naturally occurring media are not strongly wet, the subject of the behavior of fluids in weakly or neutrally wet media has been explored only superficially.

In weakly wet media, it is ambiguous to refer to a phase as wetting or nonwetting. Phases must be referred to as what they actually are: oil, water, gas, etc. Considering the definition of capillary pressure given in Eq. 3.12, it is now entirely possible for capillary pressure to be negative when the contact angle is greater than 90 degrees. [Fig. 3.11](#) illustrates this effect on capillary-pressure curves. Now the curves progress from entirely positive for water-wet behavior to entirely negative for oil-wet behavior.

Much remains to be learned about this type of behavior; it is clear that some of the topics discussed earlier no longer apply. For example, it is no longer true that the saturation at which $P_c = 0$ defines residual saturation. Evidently, the residual saturations are more closely aligned with both asymptotes in the most general case, as discussed further in the following paragraphs.

Interfacial forces, as represented by capillary pressure, will turn out to be very important in multiphase flow through permeable media. We therefore pause here to reconcile, after a fashion, capillary pressure and flow. You will recall that the entire earlier discussion represented behavior under equilibrium conditions in the absence of flow.

Let us start with single-phase laminar flow in a single tube of uniform cross section, with the transport behavior given by Eq. 3.1, and imagine that this applies to the regions of Fluid 1 and Fluid 2, as shown in the tube in the upper part of [Fig. 3.12](#).

The flow is to the right (the flow direction will change later), and the fluids are allowed to have different viscosities and the contact angle to take on the range of values from $\cos\theta = 1$ (Fluid 1 wetting) to $\cos\theta = -1$ (Fluid 2 wetting). The key assumption here is that the interface shape and the corresponding capillary pressure across it are unaffected by flow. This cannot be rigorously true in as much as the

existence of a fixed interface is clearly at odds with the no-slip condition at the tube wall, as illustrated in Fig. 3.1. Despite this inconsistency, the final results will prove both insightful and ultimately useful.

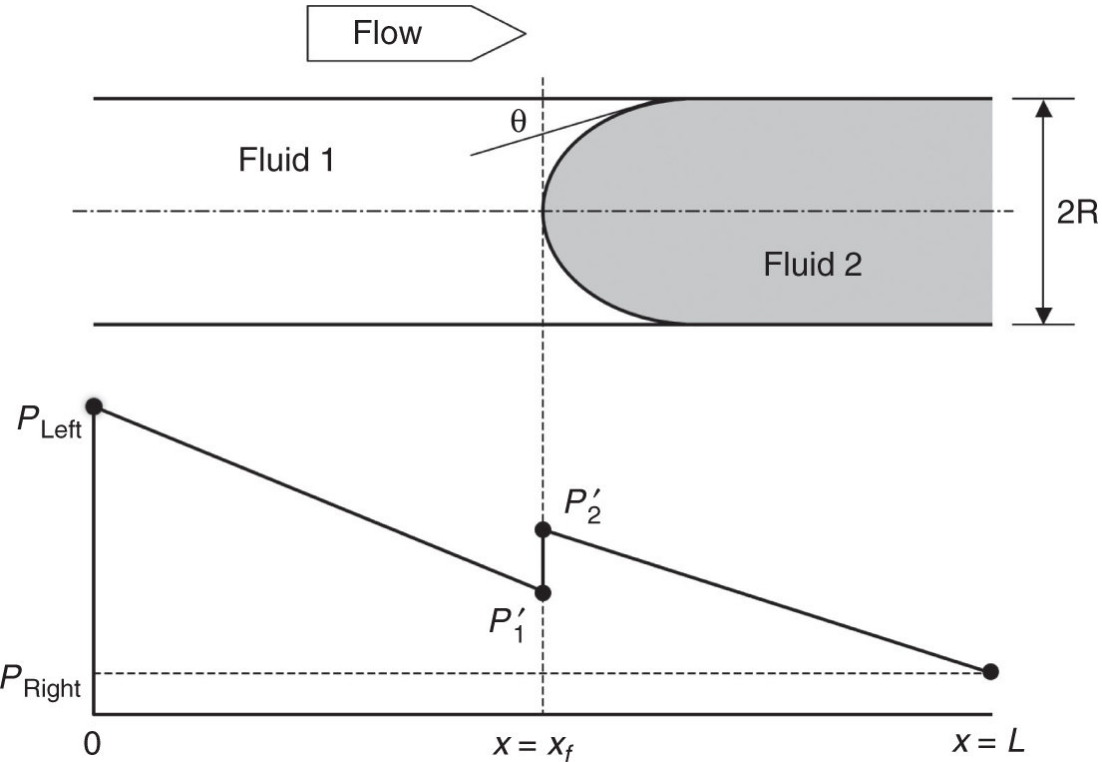


Fig. 3.12—Schematic of flow with capillary pressure in a single tube.

If flow is incompressible, the flow rate is the same on both sides of the interface, or

$$q = \frac{\pi R^4}{8\mu_1} \left(\frac{P_{\text{Left}} - P'_1}{x_f} \right) = \frac{\pi R^4}{8\mu_2} \left(\frac{P'_2 - P_{\text{Right}}}{L - x_f} \right). \quad (3.15)$$

The objective is to manipulate this equation into an expression that relates the flow rate q to the total pressure drop,

$$\frac{P_{\text{Left}} - P'_1}{\mu_1 x_f} = \frac{P'_1 + P_c - P_{\text{Right}}}{\mu_2 (L - x_f)}.$$

Although versions of this derivation appear in several places in this text, we will go through it carefully here. Let us start by introducing the capillary-pressure definition into the second equation on the right of Eq. 3.15:

$$\frac{P_{\text{Left}} - P'_1}{\mu_1 x_f} = \frac{P'_1 + P_c - P_{\text{Right}}}{\mu_2 (L - x_f)}.$$

Solve this for the interface pressure in Phase 1 as

$$P'_1 = \frac{P_{\text{Left}} \mu_2(L - x_f) - (P_c - P_{\text{Right}}) \mu_1 x_f}{\mu_1 x_f + \mu_2(L - x_f)}.$$

Finally, we insert this into the left equation in Eq. 3.15 to give

The flow rate is independent of front position if the viscosities are equal. The quantity $(\Delta P + P_c)$ is now the new driving force for this flow. The new driving force can be either greater than or less than the capillary-pressure free force, depending on the sign of P_c .

[**Fig. 3.13**](#) shows the behavior of Eq. 3.17 graphically for matched-viscosity flow. The vertical axis is a normalized flow rate, and the horizontal axis is ΔP , the external pressure difference. On this plot, Eq. 3.17 plots as lines with unit slope and an x-intercept; that is,

where $q = 0$, of $-P_c$. The unit slope lines divide the plots into regions of Phase 1 wetting ($P_c > 0$) above the line through the origin, and Phase 2 wetting ($P_c < 0$) below the line. The sign of the capillary pressure is consistent with the small figures labeled I through IV.

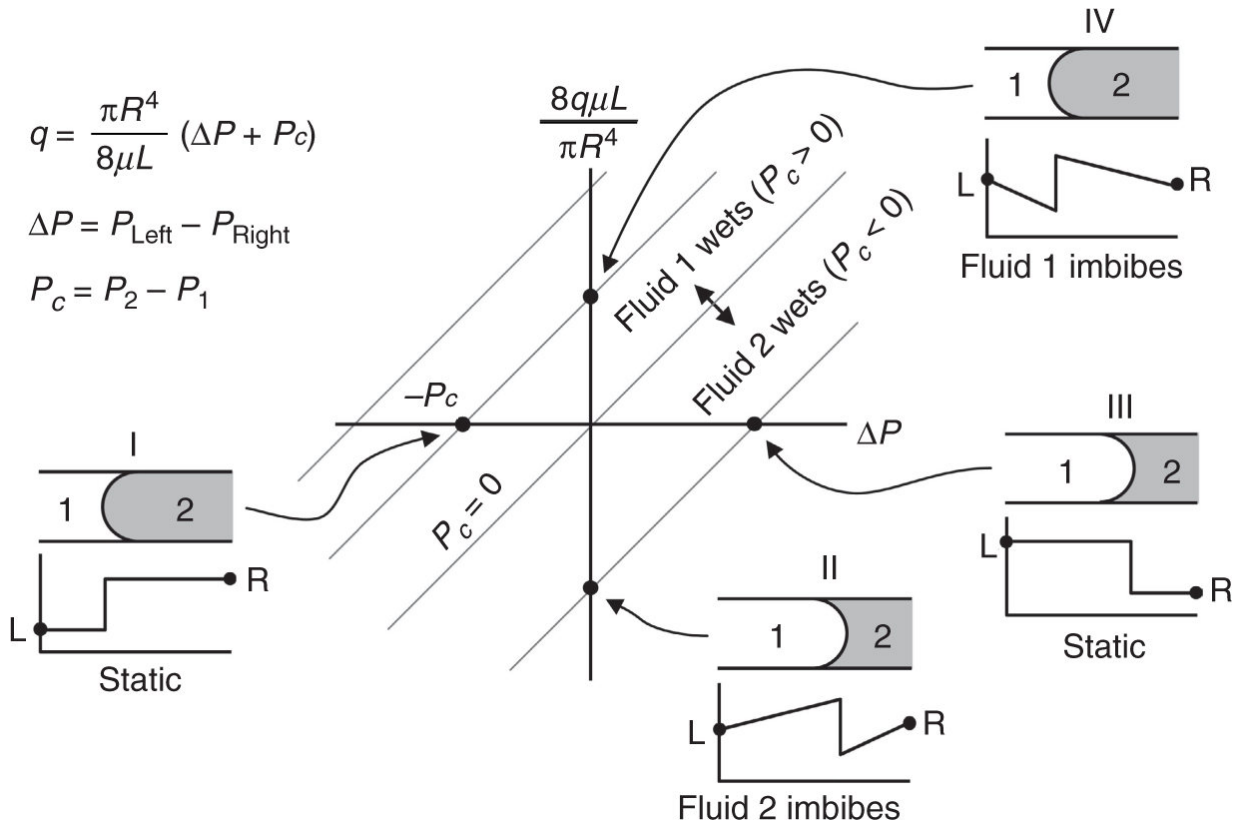


Fig. 3.13—Schematic of capillary pressure and flow for matched viscosity flows.

Case I is the same as that shown in Fig. 3.1-1b, but now with the nonwetting phase penetrating from the right. It includes the existence of an external pressure difference ($\Delta P < 0$) in the absence of flow ($q = 0$). This situation, with more complex geometries, was discussed in the previous section. In Case II, there is no external pressure difference ($\Delta P = 0$), but there is flow because of the pressure gradients within the phases. Case III is the reverse of Case I: Phase 1 wetting, a nonzero pressure gradient $\Delta P > 0$, and again no flow. In Case IV, Phase 2 is wetting, but again there is flow in the absence of an external pressure gradient.

Although highly simplified, the cases shown in [Fig. 3.13](#) promote two broad observations:

1. If there is capillary pressure (or alternatively if two or more phases are present), an external pressure difference is needed to hold the phases in the medium, as in Cases I and II. This is the basis for most experimental measurements of capillary pressure in which P_c is identical to the external pressure difference, a fact that we used in earlier explanations.
2. Flow can occur in the absence of an external pressure difference. Such flows are called natural or *spontaneous* imbibition, a type of flow that is becoming important in EOR and has been important for years in recovery from fractured reservoirs. Imbibition always involves a wetting phase displacing a nonwetting phase, as in Cases II and IV. Capillary pressure by itself does not cause flow; it is pressure gradients within the phase that do this. However, capillary pressure can set up pressure gradients that will cause flow.

These observations hold even for more complex flows involving viscosity differences, density differences, and non-uniform channels. Capillary pressure plays a significant role in relative-permeability descriptions, as discussed in the following section.

3.3 Relative Permeability

Relative-permeability curves and their associated parameters are easily the most relevant petrophysical relations for EOR. In fact, a broad interpretation of all EOR technologies is that they are a means to alter relative-permeability relationships, specifically to increase the oil relative permeability (or to increase the oil mobility).

Consider the flow of several incompressible, single-pseudocomponent phases in a 1D linear permeable medium. If the flow is steady-state—that is, if the saturation of all phases does not vary with time and position—Darcy's law can be integrated over a finite distance Δx to give

$$u_j = -\lambda_j \frac{\Delta\Phi_j}{\Delta x}, \dots \quad (3.18)$$

where λ_j is the mobility of phase j . The mobility is the “constant” of proportionality between the flux of phase u_j and the potential difference $\Delta\Phi_j = \Delta(P_j - \rho_j g D_z)$. λ_j can be decomposed into a rock property, the absolute permeability k ; a fluid property, the phase j viscosity μ_j ; and a rock-fluid property, the relative permeability k_{rj} :

$$\lambda_j = k \left(\frac{k_{rj}}{\mu_j} \right). \dots \quad (3.19)$$

The relative permeability is a strong function of the saturation of phase S_j . Being a rock-fluid property, the relationship between k_{rj} and S_j is also a function of rock properties (pore-size distribution, for example) and wettability. It is not, in general, a strong function of fluid properties, although when certain properties (e.g., interfacial tension) change dramatically, relative permeability can be affected.

Other definitions involving the mobility and relative permeability are the relative mobility λ_{rj} , described as

$$\lambda_{rj} = \frac{k_{rj}}{\mu_j}, \dots \quad (3.20a)$$

and the phase permeability k_j :

$$k_j = k k_{rj}. \dots \quad (3.20b)$$

k_j is a tensorial property in three dimensions. It is important to keep the four definitions (mobility, relative mobility, phase permeability, and relative permeability) separate and clear.

Although there have been attempts to calculate relative permeabilities on theoretical grounds, by far the most common source of k_r curves has been experimental measurements. [Experimental procedures can be found in Jones and Roszelle (1978).]

[**Fig. 3.14**](#) gives schematic oil/water relative-permeability curves. The relative permeability to a phase decreases as the saturation of that phase decreases; however, the relative permeability to a phase vanishes at some point well before the phase saturation becomes zero. If the relative permeability of a phase is zero, the phase can no longer flow, and the saturation at this point, the trapped or residual saturation, cannot be lowered any further with continuing displacement. Reducing the “trapped” oil saturation is one of the most important objectives of EOR (see Section 3.4). The residual oil saturation is designated by the symbol S_{2r} . In later chapters, we illustrate that certain EOR fluids can lower residual-oil-saturation values.

Residual oil saturation is not the same as the remaining oil saturation S_{2R} . The residual oil saturation is the oil remaining behind in a thoroughly water-swept region of the permeable medium; the remaining oil saturation is the oil left after a waterflood, well swept or not. Therefore, $S_{2R} \geq S_{2r}$. The trapped water saturation S_{1r} is the *irreducible* water saturation. It is not the connate water saturation, which is the water saturation in a reservoir before any water is injected and is equal to many times S_{1r} .

Two other important landmarks on the relative-permeability curves are the endpoint relative permeabilities. These are the constant relative permeability of a phase at the other phase’s residual saturation. In this text, we designate the endpoint relative permeability by a superscript o. The word *relative* in the name of the k_r functions indicates that the phase permeability has been normalized by some quantity. As the definition in Eq. 3.20b implies, the normalizing permeability is assumed to be the absolute permeability to some reference fluid (usually 100% air or water), although this is not always the case in the literature. This choice of normalizing factor means that the endpoint permeabilities will usually be less than one, although they can be greater than one as well.

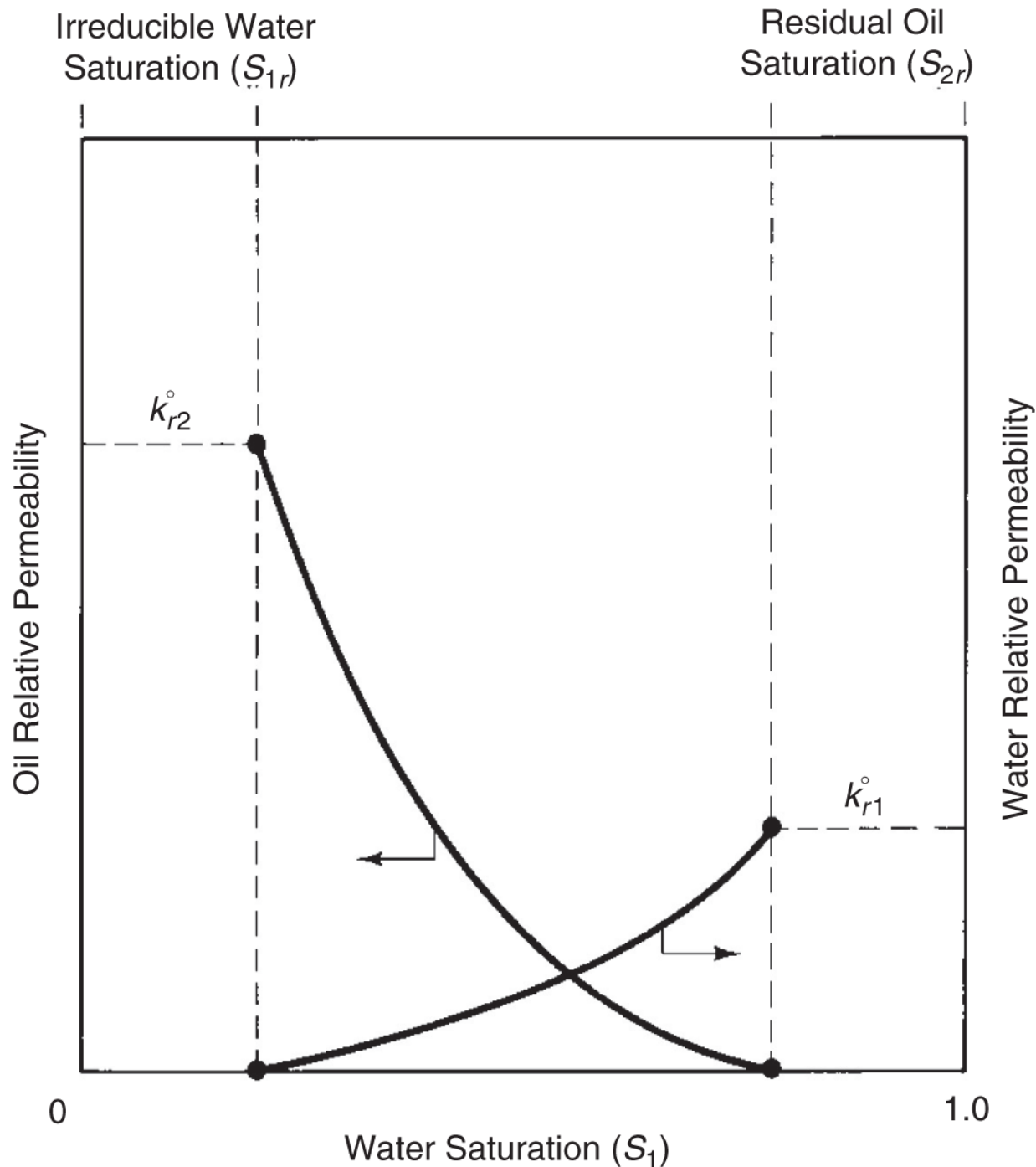


Fig. 3.14—Typical water/oil relative permeabilities.

The endpoint values are measures of wettability. The nonwetting phase occurs in isolated globules several pore diameters in length that occupy the centers of the pores. Trapped wetting phase, on the other hand, occupies the crevices between rock grains and coats the

rock surfaces. Therefore, we would expect the trapped nonwetting phase to be a greater obstacle to the wetting phase than the trapped wetting phase is to the nonwetting phase. The wetting-phase endpoint relative permeability will, therefore, be smaller than that of the nonwetting-phase endpoint. The ratio of wetting to nonwetting endpoints proves to be a good qualitative measure of the wettability of the medium. The permeable medium in Fig. 3.13 is water-wet because k_{r1}^o is less than k_{r2}^o . For extreme cases of preferential wetting, the endpoint relative permeability to the wetting phase can be 0.05 or less.

Others view the crossover saturation (where $k_{r2} = k_{r1}$) of the relative permeabilities as a more appropriate indicator of wettability, perhaps because it is less sensitive to the value of the residual phase saturations. [Fig. 3.15](#) illustrates both the shift in the crossover point and the movement of the water-endpoint relative permeability as a function of wettability. [Fig. 3.14](#) also illustrates that relative permeability can change by several orders of magnitude over a normal saturation range; hence, experimental curves are often presented on semi-log plots as shown.

Although no general theoretical expression exists for the relative-permeability function, several empirical functions for the oil/water curves are available (see, for example, Honarpour et al. 1982). When analytical expressions are needed, we use the following exponential forms for oil/water flow:

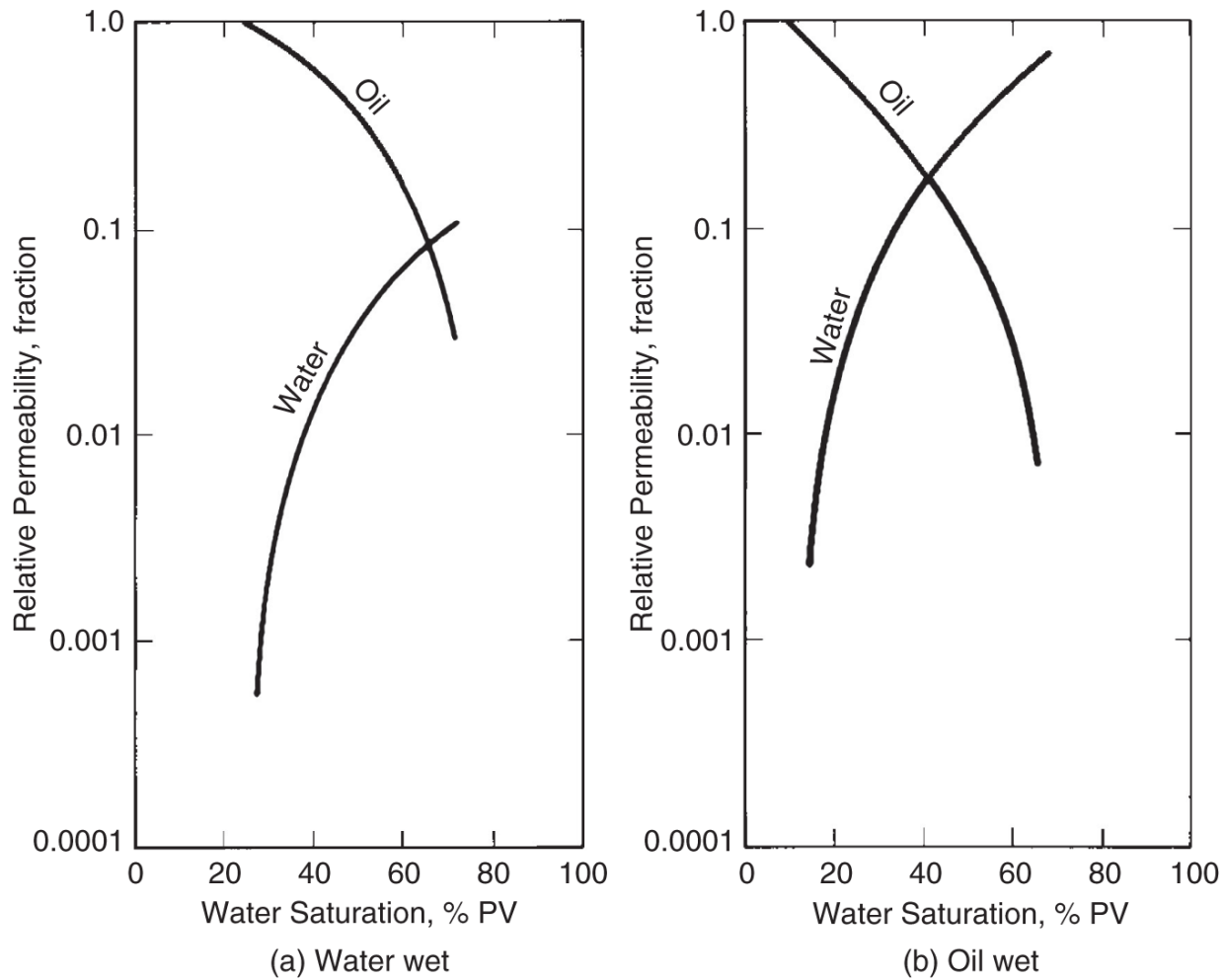


Fig. 3.15—Effect of wettability on relative permeability (Craig 1971).

and

$$k_{r2} = k_{r2}^o \left(\frac{1 - S_1 - S_{2r}}{1 - S_{1r} - S_{2r}} \right)^{n_2} \dots \dots \dots \quad (3.21b)$$

These equations fit most experimental data and separate explicitly the relative-permeability curvatures (through the exponents n_1 and n_2) and the endpoints. [Fig. 3.16](#) gives typical values of the parameters in Eq. 3.21.

There are, of course, several other models, some of which are more commonly used by hydrologists (Lenhard and Parker 1987, for example). A particularly popular model for aquifers is that of van

Genuchten (1980). Several quantities of immediate use come directly from the relative permeabilities.

If capillary pressure is negligible, we may add all the phase fluxes to obtain an expression relating the total flux to the pressure gradient dP/dx in horizontal flow $u = -k\lambda_{rt}(dP/dx)$, where

is the total relative mobility, a measure of the resistance of the medium to multiphase flow. Plots of λ_{rt} vs. saturation frequently show a minimum ([Fig. 9.28](#)), meaning that it is more difficult to make multiple phases flow through a medium than any one of the phases alone. Even in the presence of trapped saturations, λ_{rt} is reduced because the phases mutually interfere during flow.

By neglecting capillary pressures, we can also solve for the pressure gradient in the total flux expression and use it to eliminate the pressure gradient in the differential form of Eq. 3.18 to give, after some rearranging, the fractional flow of phase j in Eq. 2.52. If capillary pressure is negligible, f_j is a generally nonlinear function of saturation(s) only. This functionality forms the basis of the fractional-flow analyses in [Chapter 5](#) and the remaining chapters. Fractional-flow curves are functions of phase viscosities and densities as well as of relative permeabilities.

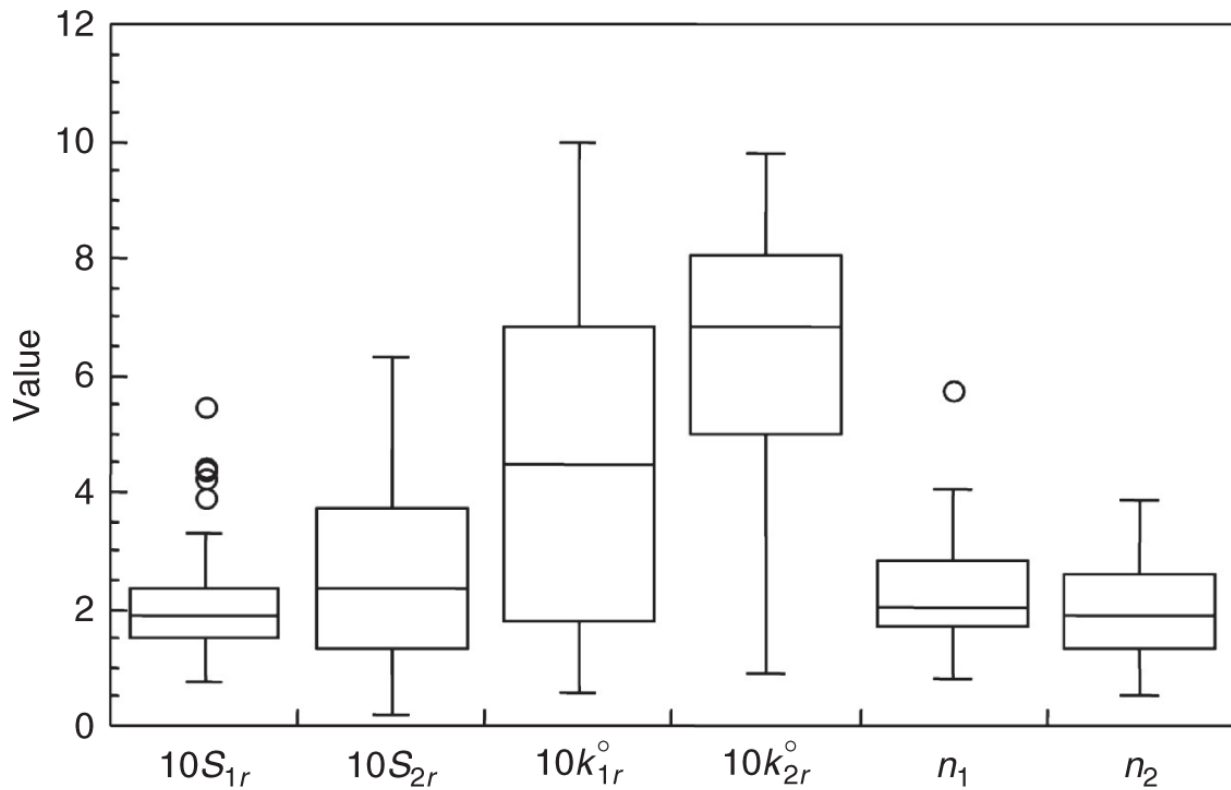


Fig. 3.16—Typical values for the parameters in Eq. 3.21. The figure is a box plot. The vertical boxes give the range over which 75% of the measured values fall. The extended vertical lines give the 95% range. The midpoint of the box is the median value, and the points are outliers (Alpak et al. 1999).

3.4 Residual Phase Saturations

This section discusses the two-phase flow behavior of residual wetting (S_{wr}) or nonwetting (S_{nwr}) saturations. These can be identified with residual oil or water saturations according to [Table 3.1](#). The discussion below is largely based on one phase being strongly wetting.

The notion of a wetting-phase residual saturation is consistent with our discussion of capillary pressure. As in [Fig. 3.17a](#), increasing pressure gradients force ever more of the nonwetting phase into pore bodies, causing the wetting phase to retreat into the contacts between the rock grains and other crevices in the pore body. At very high pressures, the wetting phase approaches monolayer coverage and a low residual saturation. Because of film instability, S_{wr} is theoretically zero when P_c is infinite, as shown in [Fig. 3.6a](#).

The residual nonwetting-phase saturation, on the other hand, is a paradox because the nonwetting phase, being repelled by the solid surfaces, would be expelled from the medium given enough contact time. Repeated experimental evidence has shown this not to be the case, and, in fact, under most conditions, S_{nwr} is as large as S_{wr} . The residual nonwetting phase is trapped in the larger pores in globules several pore diameters in length ([Fig. 3.17b](#)). [Fig. 3.18](#) shows several pore casts of these globules after waterfloods in consolidated and unconsolidated sands. The globules give the appearance of disconnected blobs.

The mechanism for residual phase saturation can be illustrated using two simplified REV-scale models. [Fig. 3.19](#) shows the double-pore, or pore-doublet, model, which involves a bifurcating path in the permeable medium, and [Fig. 3.20](#) shows three versions of the pore snap-off model, which involves a single flow path with variable cross-sectional area. Each model contains a degree of local heterogeneity: the pore-doublet model contains flow paths of different radii, and the pore snap-off model contains different cross-sectional areas along a flow path. Some form of “local” heterogeneity is needed for there to be residual nonwetting-phase saturation. The simple capillary-tube model discussed in Section 3.1 does not have heterogeneity and, therefore, will not exhibit a nonzero S_{nwr} .

3.4.1 The Pore-Doublet Model (Moore and Slobod 1956). This model assumes that well-developed Poiseuille flow occurs in each path of the doublet and that the presence of the interface does not affect flow. Both assumptions would be accurate if the length of the doublet were much larger than the largest path radius and the flow were very slow. The latter condition also permits the use of the static capillary-pressure function (Eq. 3.12) in this flowing field. The wetting and nonwetting phases have equal viscosity in this treatment, although this assumption can be relaxed (see Exercise 3.5). Most importantly, we assume that when the wetting-nonwetting interface reaches the outflow end of the doublet in either path, it traps the resident fluid, as shown in [Fig. 3.19b](#).

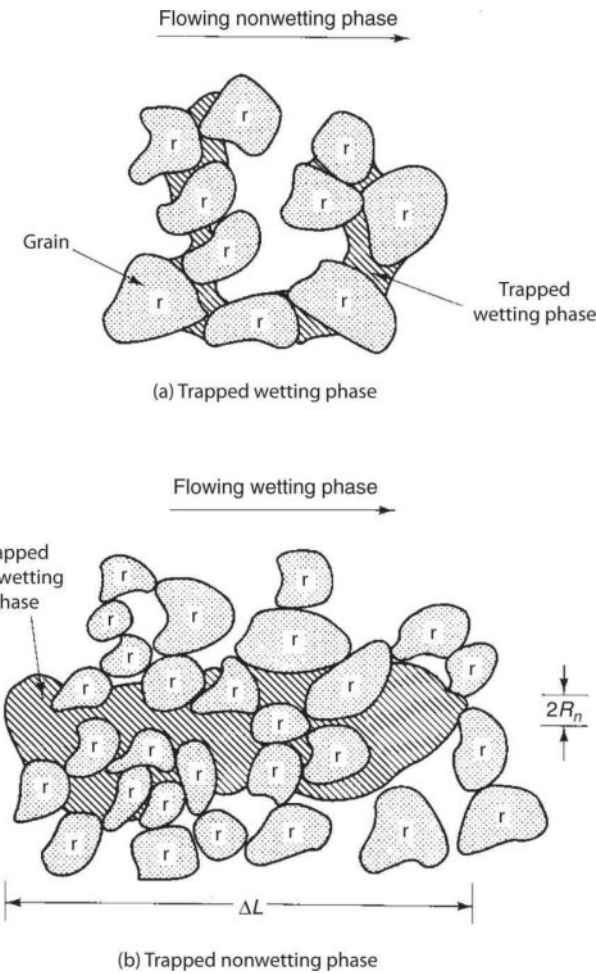


Fig. 3.17—Schematic of trapped wetting and nonwetting phases.

On the basis of these assumptions, the volumetric flow rate in either path is given by Eq. 3.12, which was derived by use of the assumptions just discussed. The total volumetric flow rate through the doublet is, therefore,

$$q = q_1 + q_2 = \frac{\pi R_1^4}{8\mu L_t} (\Delta P_1 + P_{c1}) + \frac{\pi R_2^4}{8\mu L_t} (\Delta P_2 + P_{c2}), \dots \quad (3.23)$$

and, because the paths are parallel, the driving force across each path must be equal:

In Eq. 3.24, the capillary pressures are positive for the imbibition (wetting phase displacing nonwetting phase) shown in Fig. 3.19; for a

drainage process, the capillary pressures would be negative. Using these equations, we can write the volumetric flow rate in either path in terms of the total volumetric flow rate, the doublet geometry, and the interfacial tension-contact angle product from Eq. 3.23:

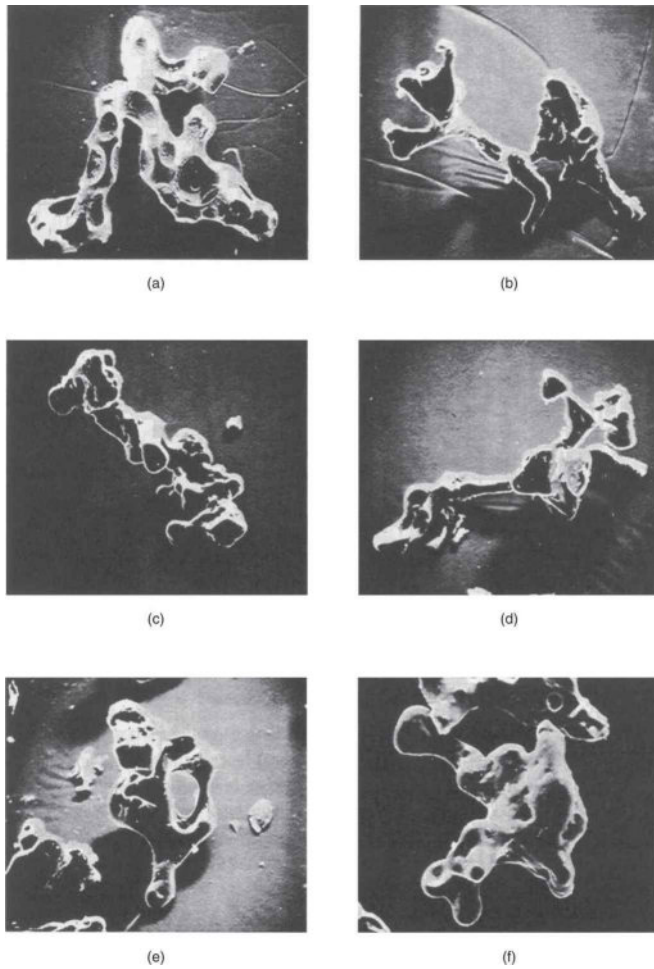
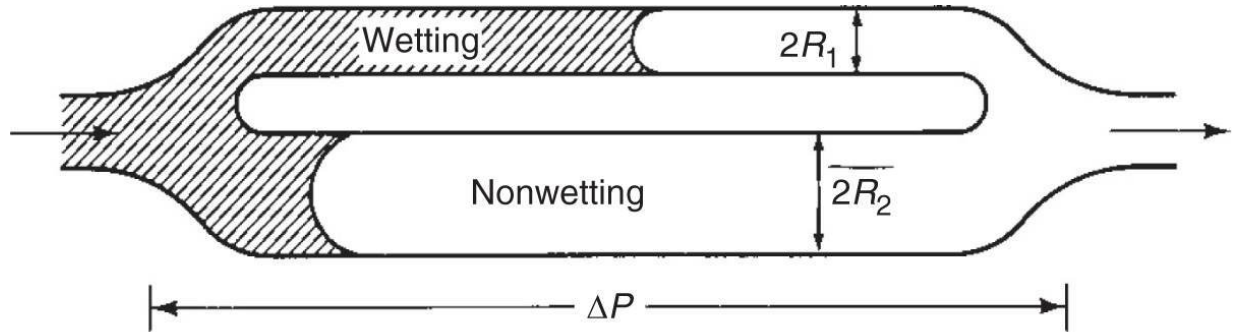
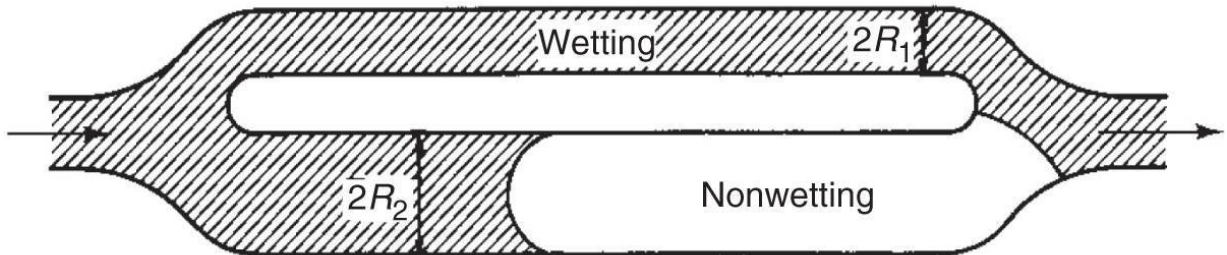


Fig. 3.18—Typical large oil blobs in (a) bead packs and (b) to (f) Berea sandstone (Chatzis et al. 1983).

$$q_1 = \frac{q - \frac{\pi R_2^4 \sigma \cos \theta}{4\mu L_t} \left(\frac{1}{R_2} - \frac{1}{R_1} \right)}{1 + (R_2 / R_1)^4} \quad \dots \dots \dots \quad (3.25a)$$



(a) Before trapping



(b) After trapping

Fig. 3.19—Schematic of pore-doublet model.

$$q_2 = \frac{q \left(\frac{R_2}{R_1} \right)^4 + \frac{\pi R_2^4 \sigma \cos \theta}{4 \mu L_t} \left(\frac{1}{R_2} - \frac{1}{R_1} \right)}{1 + \left(\frac{R_2}{R_1} \right)^4} \quad \dots \quad (3.25b)$$

To investigate the trapping behavior of the doublet, form the ratio of the average velocities in the paths:

$$\frac{v_2}{v_1} = \frac{\frac{4N_{vc}}{R_1} + \left(\frac{1}{\beta} - 1 \right)}{\frac{4N_{vc}}{\beta^2} - \beta^2 \left(\frac{1}{\beta} - 1 \right)}, \quad \dots \quad (3.26)$$

where $\beta = R_2/R_1$ is a heterogeneity factor, and

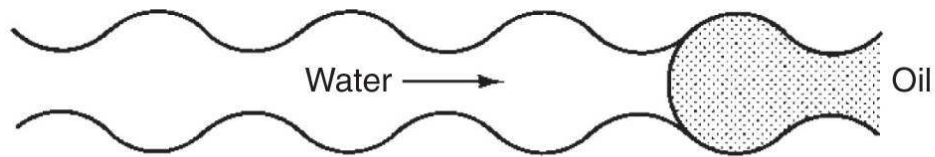
$$N_{vc} = \left(\frac{\mu L_t q}{\pi R_1^3 \sigma \cos \theta} \right) \quad \dots \quad (3.27)$$

is a dimensionless ratio of viscous to capillary forces, which we henceforth call the local *capillary number*.

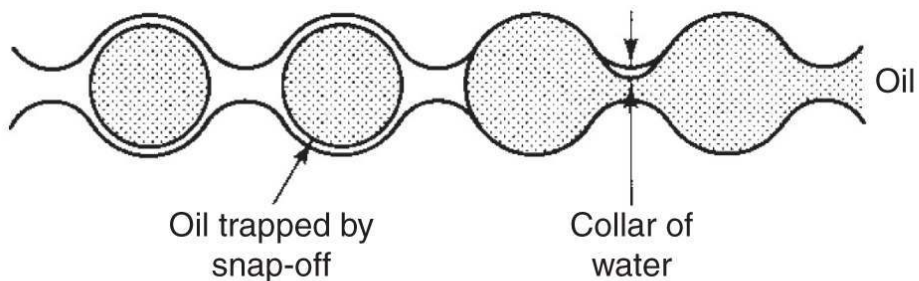
The trapping behavior of the pore doublet follows from Eq. 3.26 and the definition of the capillary number. In the limit of negligible capillary forces (large N_{vc}), the velocity in each path of the doublet is proportional to its squared radius. Hence, the interface in the large-radius path will reach the outflow end before the interface in the small-radius path, and the nonwetting phase will be trapped in the small-radius path.

However, if viscous forces are negligible, the small-radius path will imbibe fluid at a faster rate than the fluid is supplied at the doublet inlet. From Eqs. 3.24 and 3.25, the interface velocity in the large-radius path will be negative in the fluid-starved doublet, whereas the velocity in the small-radius path will be higher than that at the doublet inlet. This situation is in disagreement with the premises of the derivation: if the interface seals off the small-radius path at the doublet inlet, the flow in the small-radius tube will be zero.

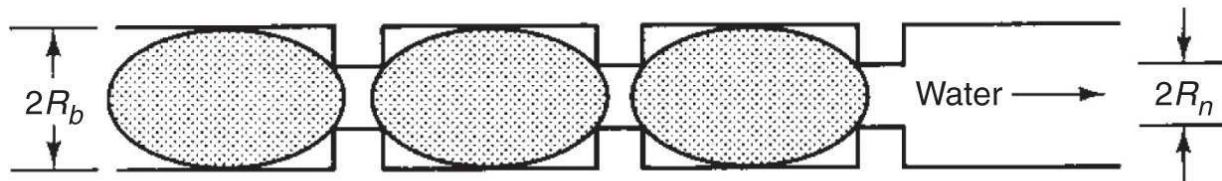
Although the extreme of negligible viscous forces is difficult to visualize, it is easy to imagine an intermediate case in which viscous forces are small, but not negligible, compared to capillary forces. Now the doublet is no longer starved for fluid, but the interface in the small-radius path is still faster than that in the large-radius path. The nonwetting phase becomes trapped in the large-radius path, as shown in [Fig. 3.19](#). For typical values of pore radii ([Fig. 3.9](#)) in Eq. 3.26, most flows in permeable media will be approximated by this intermediate case.



(a) Low aspect ratio



(b) High aspect ratio



(c) Idealized geometry

Fig. 3.20—Various geometries of the pore snap-off model [Figs. a and b from Chatzis et al. (1983)].

Besides explaining how a nonwetting phase can become trapped at all, the simplified behavior of the pore doublet illustrates several qualitative observations about phase trapping.

1. The nonwetting phase is trapped in large pores; the wetting phase is trapped in small cracks and crevices.
2. Reducing capillary forces will cause a decrease in trapping. This decrease follows from simple volumetric calculations because fluids trapped in small pores will occupy a smaller volume fraction of the doublet than those in large pores.

3. There must be some local heterogeneity to cause trapping. In this case, the heterogeneity factor β must be greater than one. Simple calculations with the pore doublet show that increasing the degree of heterogeneity increases the capillary-number range over which the residual phase saturation changes.

However, as a quantitative tool for estimating trapping, the pore doublet greatly overestimates the amount of residual nonwetting phase at low capillary number. At high capillary number, little evidence supports nonwetting-phase trapping in small pores. Most importantly, the capillary number defined by Eq. 3.27 is difficult to define in actual media; hence, the pore-doublet model is rarely used to translate to the REV scale.

3.4.2 The Snap-Off Model. The snap-off model can readily translate to the REV scale. The exact geometry of the model ([Fig. 3.20](#)) is usually dictated by the ease with which the resulting mathematics can be solved. The sinusoidal geometry in [Fig. 3.20a](#) has been used by Oh and Slattery (1976) for theoretical investigation and by Chatzis et al. (1983) for experimental work. The pore snap-off model was earlier discussed by Melrose and Brandner (1974), who included the effects of contact-angle hysteresis in their calculations. Later in this section, we use the idealized geometry in [Fig. 3.20c](#) to translate to the REV scale.

The snap-off model assumes a single flow path of variable cross-sectional area through which a nonwetting phase is flowing. The sides of the flow path are coated with a wetting phase so that a uniquely defined local capillary pressure exists everywhere. However, this capillary pressure varies with position in the flow path; it is high where the path is narrow and low where the path is wide. For certain values of the potential gradient and pore geometry, the potential gradient in the wetting phase across the path segment can be smaller than the capillary-pressure gradient across the same segment. The external force is now insufficient to compel the nonwetting phase to enter the next pore constriction. The nonwetting phase then snaps off into globules that are localized in the pore bodies of the flow path. By

this hypothesis, then, the condition for reinitializing the flow of any trapped globule is

$$\Delta\Phi_w + \Delta\rho g \Delta L \sin\alpha \geq \Delta P_c, \dots \quad (3.28)$$

where $\Delta\Phi_w$ and ΔP_c are the wetting-phase potential and capillary-pressure changes across the globule. ΔL is the globule size $\Delta\rho = \rho_w - \rho_{nw}$, and α is the angle between the globule's major axis and the horizontal axis. Eq. 3.28 suggests a competition between external forces (viscous and gravity) and capillary forces that was also present in the pore-doublet model. Although the two models appear to be quite different, the basic idea of competition between viscous/gravity forces and capillarity remains.

In any real permeable medium, local conditions approximating both the pore-doublet and the snap-off model will occur. Using detailed experimental observations in consolidated cores, Chatzis et al. (1983) have determined that approximately 80% of the trapped nonwetting phase occurs in snap-off geometries, with the remaining 20% in pore doublets or in geometries that are combinations of both categories. These authors used a more elaborate classification scheme in which the snap-off model is combined with the pore-doublet model in several ways. These combinations remove many of the *ad hoc* assumptions about the nature of trapping in the pore-doublet model when the wetting/nonwetting interface reaches the outflow end. The theoretical treatment of the snap-off model again illustrates the basic requirements for nonwetting-phase trapping: nonwetting-phase trapping in large pores, the need for local heterogeneity, and strong capillary forces.

3.4.3 Trapping in Actual Media. Much of EOR technology is directed toward reducing residual or trapped oil saturation in previously swept zones of a reservoir. Reducing such oil saturation is one of the principle goals of EOR.

We can now discuss experimental observations of trapping in actual permeable media. The most common experimental observation is a relationship between residual nonwetting- or wetting-

phase saturations and a local capillary number. We call this relationship the CDC. [Fig. 3.21](#) shows a schematic CDC.

Typically, CDCs plot percent residual (nonflowing) saturation for the nonwetting (S_{nwr}) or wetting (S_{wr}) phases on the y-axis vs. a capillary number on a logarithmic x-axis. The capillary number N_{vc} is a dimensionless ratio of viscous to local capillary forces. The capillary number can be variously defined. The simplest definition,

is the one most commonly used. The more general definition used in UTChem includes multiphase flow as well as buoyancy effects (UTChem 2013; Delshad et al. 1996)

At small N_{vc} , both S_{nwr} and S_{wr} are roughly constant at plateau values, [Fig. 3.21](#). At some N_{vc} , designated as the critical capillary number $(N_{vc})_c$, a knee in the curves occurs, and the residual saturations begin to decrease. Complete desaturation—zero residual-phase saturation—occurs at the total desaturation capillary number $(N_{vc})_t$ shown in [Fig. 3.20](#). Most waterfloods are well onto the plateau region of the CDC, where, as a rule, the plateau S_{wr} is less than S_{nwr} . Frequently, the two CDCs are normalized by their respective plateau values.

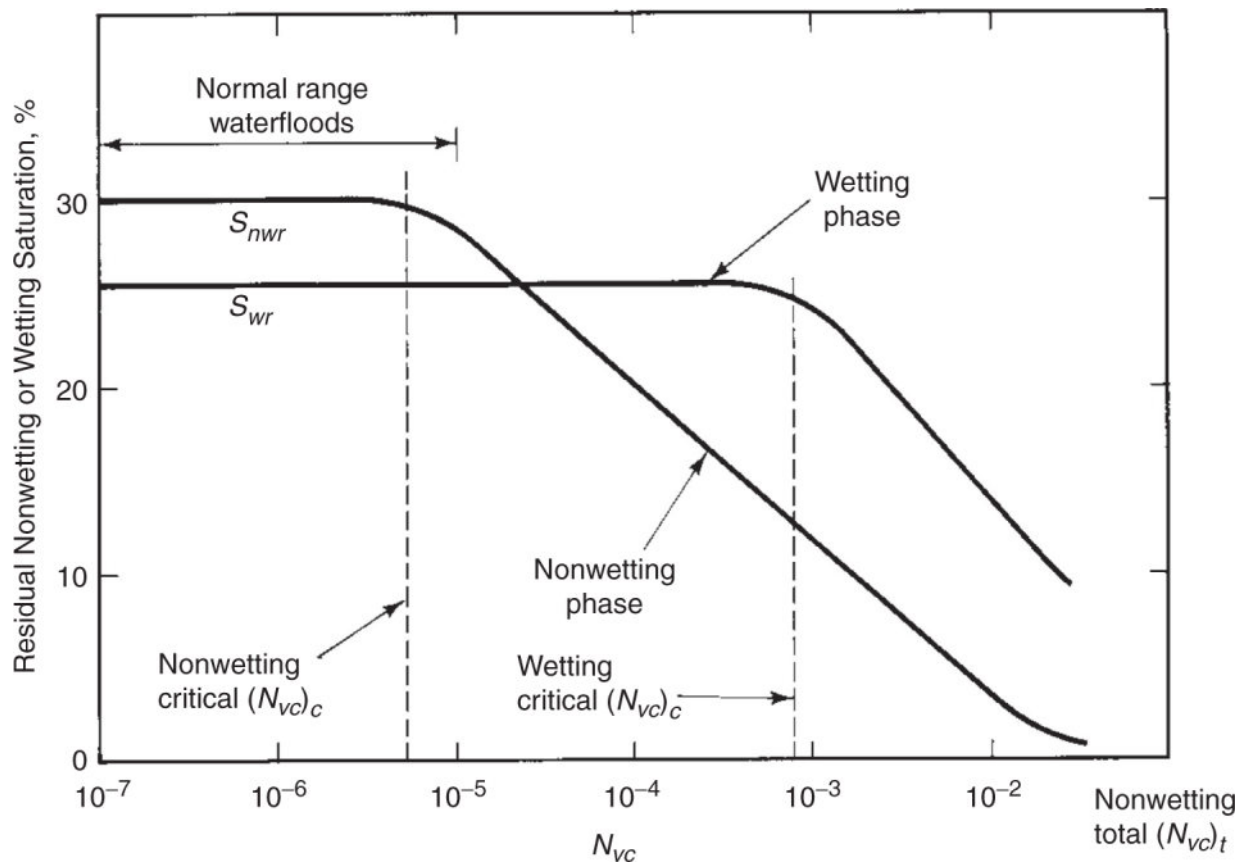


Fig. 3.21—Schematic capillary desaturation curve.

When the CDC knee is absent altogether, this indicates an extreme manifestation of the effect of a wide pore-size distribution. See [Fig. 3.22](#). The range between $(N_{vc})_c$ and $(N_{vc})_t$ is considerably greater for the nonwetting phase (10^{-7} to 10^{-1}) than for the wetting phase (10^{-4} to 10^0). [Fig. 3.23](#) shows a compilation of experimental CDC data, each using a common definition of N_{vc} , in a Berea core.

Example 3.3—Using Capillary Numbers. The ideas embodied within the capillary number constitute one of the fundamental principles of EOR. This example is to make these ideas specific. This example uses the definition of capillary number in Eq. 3.29.

1. Estimate the capillary number for a waterflood at an interstitial velocity of 1 ft/D. The water viscosity is 0.8 mPa and IFT is 30 mN·m. The porosity is 0.2.

This is mainly a units conversion problem. The definition of capillary number is

$$N_{vc} = \frac{u\mu}{\sigma}$$

Because N_{vc} is a ratio of forces, the definition uses a superficial velocity, this being in Darcy's law a measure of viscous forces:

$$N_{vc} = \frac{(1 \text{ ft/D})(0.2)(0.8 \text{ mPa-s})}{(30 \text{ mN}\cdot\text{m})} \left[\frac{1 \text{ day}}{(24)(3600) \text{ s}} \right] \left(\frac{1 \text{ mN}\cdot\text{m}^2}{1 \text{ mPa}} \right) \left(\frac{0.305 \text{ m}}{1 \text{ ft}} \right) = 2.8 \times 10^{-8}$$

An interstitial velocity of 1 ft/D is typical for waterflooding. The capillary number says that capillary forces are 100 million times larger than viscous forces. Waterfloods typically fall on the plateau of Fig. 3.21, where normal fluctuations in velocity do not change residual oil saturation. Furthermore, the water viscosity cannot be increased enough to reduce residual oil saturation. It is for this reason that polymer floods are not considered to lower residual oil saturation. (Remember that Fig. 3.21 shows only viscous effects. Evidently, viscoelastic effects will reduce residual oil saturation.)

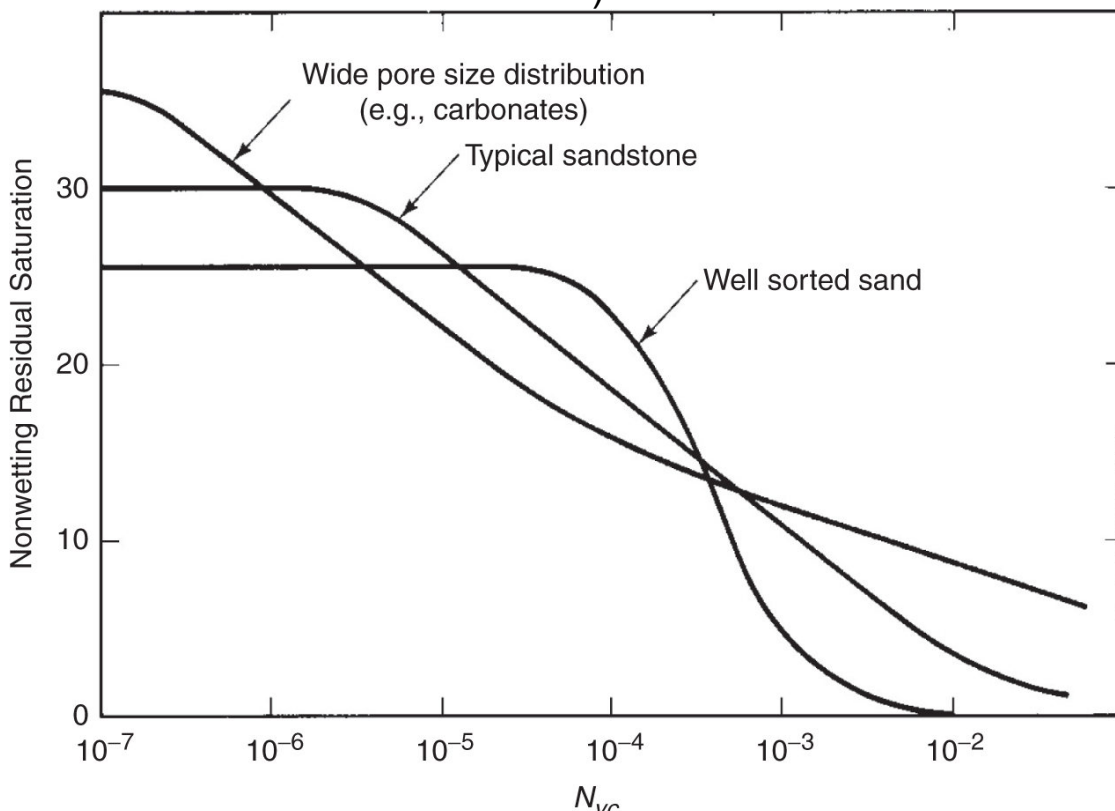


Fig. 3.22—Schematic of the effect of pore-size distribution on the CDC.

2. What would N_{vc} be if the IFT were reduced to $\sigma = 10^{-3} \text{ mN}\cdot\text{m}$?

Again,

$$N_{vc} = \frac{(1 \text{ ft}/D)(0.2)(0.8 \text{ mPa}\cdot\text{s})}{(10^{-3} \text{ mN}\cdot\text{m})} \left[\frac{1 \text{ day}}{(24)(3600) \text{ s}} \right] \left(\frac{1 \text{ mN}\cdot\text{m}^2}{1 \text{ mPa}} \right) \left(\frac{0.305 \text{ m}}{1 \text{ ft}} \right) = 8.5 \times 10^{-4}.$$

Although still small, this value is well past the knee on the CDC and will result in a substantial reduction in S_{2r} . $\sigma = 10^{-3} \text{ mN}\cdot\text{m}$ is the nominal target for substantial residual-oil saturation reduction in surfactant polymer flooding. Sometimes the simplest calculation can yield the most profound insights.

Most of the data on CDCs have been obtained from synthetic or outcrop media using synthetic (refined) oil and brine. The displacements were conducted at room conditions for the most part. How well these conditions mimic reservoir conditions is conjecture because experimentally determining CDCs under reservoir conditions is difficult.

A deviation from this practice is the work of Kamath et al. (2001), which measured CDCs on four carbonate-reservoir rock samples.

[Fig. 3.24](#) summarizes this work. The fact that only four rock samples were measured testifies to the difficulties of generating this information. It also lessens the generality of the conclusions drawn. Nevertheless, this was a very broad investigation involving pore-size distribution ([Fig. 3.24a](#)), geologic characterization ([Fig. 3.24b](#)), relative permeabilities, and scanning experiments. Some observations are

1. The capillary number and its range are smaller than in [Fig. 3.22](#). This difference probably exists because of differences in the definitions of N_{vc} used.
2. Samples K2 and K4 show residual saturations that are consistent with [Fig. 3.22](#). Both samples are relatively homogeneous, and both have larger average pore-throat sizes.

3. No samples show the well-defined knee suggested in [Fig. 3.22](#) over the range of N_{vc} shown.
4. Samples K4 and K5 show very large residual oil saturations. This is possibly a cause of the absence of the knee, as mentioned above, and of the very small N_{vc} numbers.

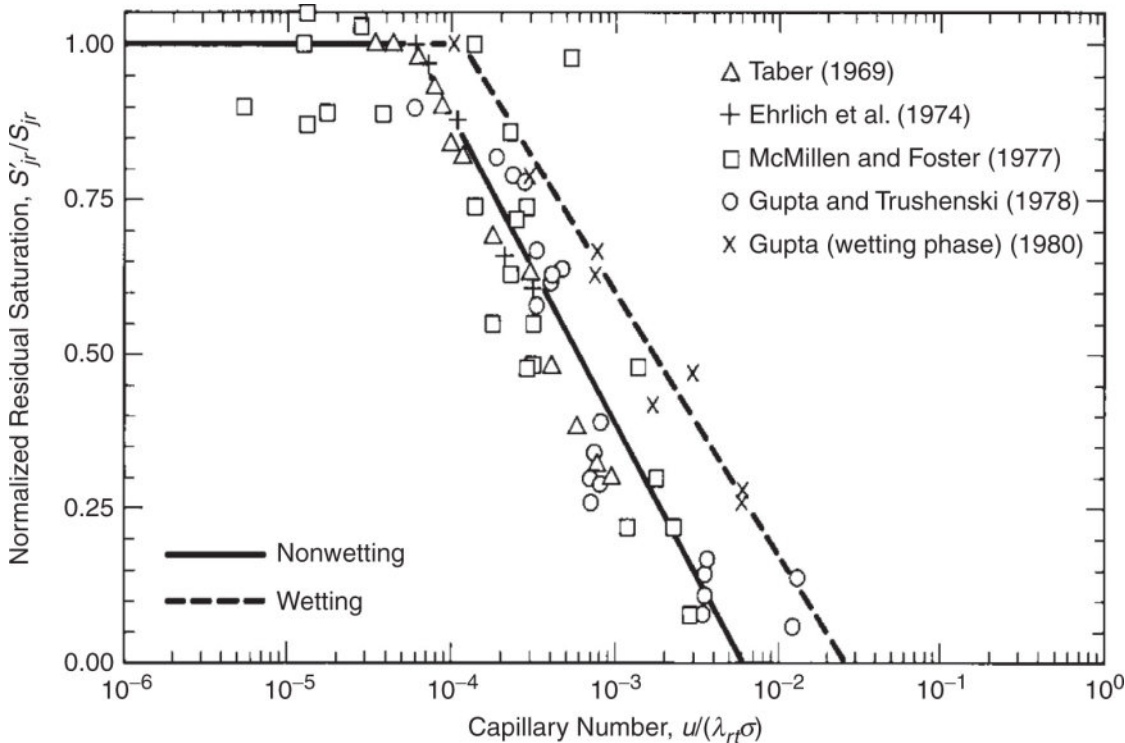


Fig. 3.23—Capillary desaturation curve by use of a common definition for capillary number (Camilleri 1983). The curves are normalized by their plateau values.

5. The behavior of the CDC for Sample K4 is largely the result of the very small pore throats shown in [Fig. 3.24a](#) and of a large pore body-to-throat ratio ([Fig. 3.24b](#)).

We have made several references in the above discussion to the effect of the wetting state. Let us conclude this section by addressing this topic directly. [Fig. 3.25](#) shows a summary of literature values in which residual oil saturation is correlated with the Amott index (see Section 3.2.3).

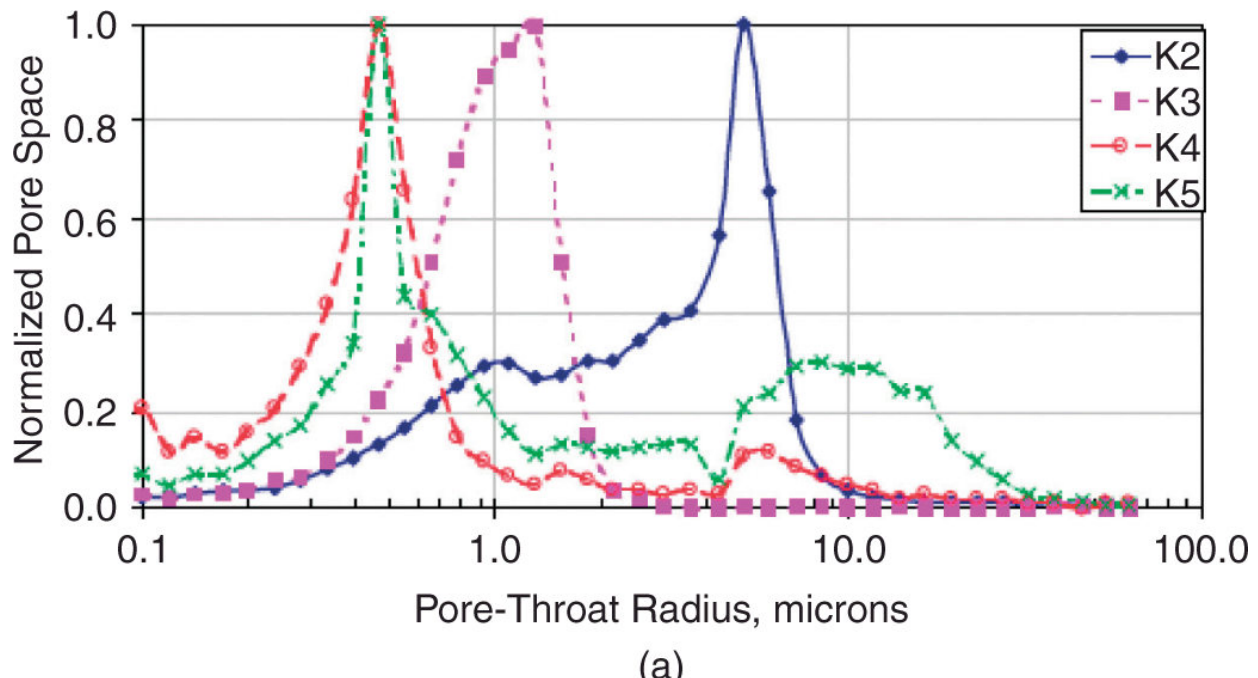
As in all petrophysical correlations, there is considerable scatter. Nevertheless, [Fig. 3.25](#) shows a trend of decreasing residual saturation from either extreme water- or oil-wetting to minima at neutral or slightly water-wet media. The change can involve a

decrease of up to a factor of three, which suggests that EOR processes that alter wetting state can reduce residual oil saturation almost to the same extent as does increasing N_{vc} . The effect of N_{vc} has been eliminated from [Fig. 3.25](#) as much as possible by keeping N_{vc} small.

Four other general observations can be made on the basis of the CDC curve and the models.

1. It will be more difficult to reduce residual saturation for media with small average pore sizes than for media with larger pores.
2. Pore-size distribution is also important. The critical-to-total N_{vc} range should increase with increasing pore-size distribution for both wetting and nonwetting phases.
3. The ratio of pore-body to throat size will play a significant role in the CDC. Media with large ratios of body-to-throat size will require large N_{vc} values for a given degree of desaturation.
4. Wettability is important. Small N_{vc} residual saturations should be smaller than values measured at the extremes.

Regardless of the capillary-number definition used, note that an $(N_{vc})_c = 10^{-6}$ means that capillary forces are one million times greater than viscous forces under normal waterflooding conditions. Without some means of increasing N_{vc} , such as those discussed throughout this text, capillary forces tenaciously hold the phases in the rock.



(a)

Sample	k (md)	Φ (%)	Rock Type	Thin Section
K2	49	26	Limestone micrite consists of 1–10 micrometer-size crystals of calcite with significant porosity between crystals. Pore body-throat ratio is probably close to unity. Homogeneous rock.	
K3	12	20	Heterogeneous compound limestone with peloid-skeletal packstone to wackestone and skeletal-intraclast-oid packstone to grainstone textures with moldic, microcrystalline, and chalky intraparticle porosity.	
K4	6	17	Oolitic limestone with grainstone texture and abundant calcite cement. Cement is heterogeneously distributed. Pore body-throat ratio is quite large with pore bodies 200–400 micrometers across and pore throats a few micrometers across	
K5	85	24	Heterogeneous, compound limestone with grainstone texture and abundant calcite cement. The interparticle porosity is occluded with later, pore-filling cement. Pore body-throat ratio is probably large, but not as large as in K4.	

(b)

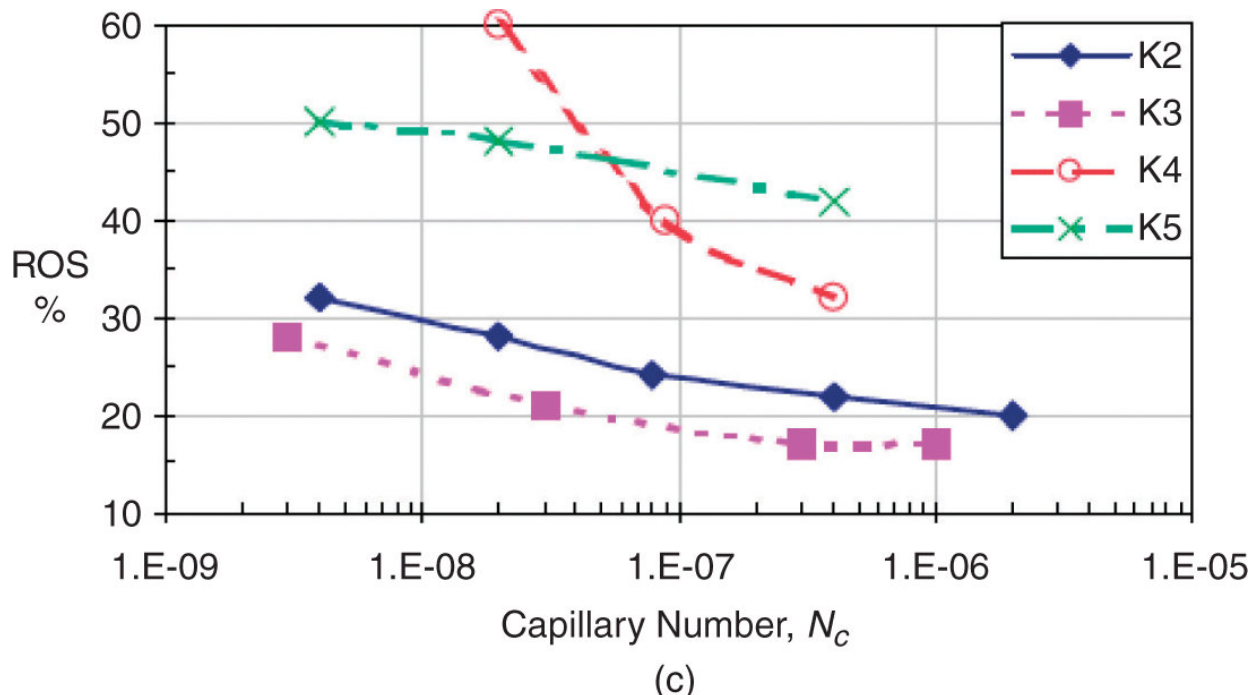


Fig. 3.24—(a) Pore-throat size distribution, (b) geologic description for capillary desaturation curves (c) for four carbonate rock samples from Kamath et al. (2001).

3.4.4 CDC Estimation. Given the difficulty in constructing a CDC experimentally—each point on a curve constitutes a separate experiment—and given the importance of the CDC to recovering residual oil saturation, a nonexperimental method for calculating the CDC would be valuable.

All theoretical attempts to calculate the CDC must have some means to translate microscopic physics—force balances and blob mechanics—to the REV scale. In probabilistic models, this translation is completed through statistics (Larson 1977; Mohanty and Salter 1982). In deterministic models, the microscopic-to-REV translation follows by giving microscopic meaning to some macroscopic measurements, such as capillary-pressure curves or permeability (Melrose and Brandner 1974; Oh and Slattery 1976; Payatakes et al. 1978).

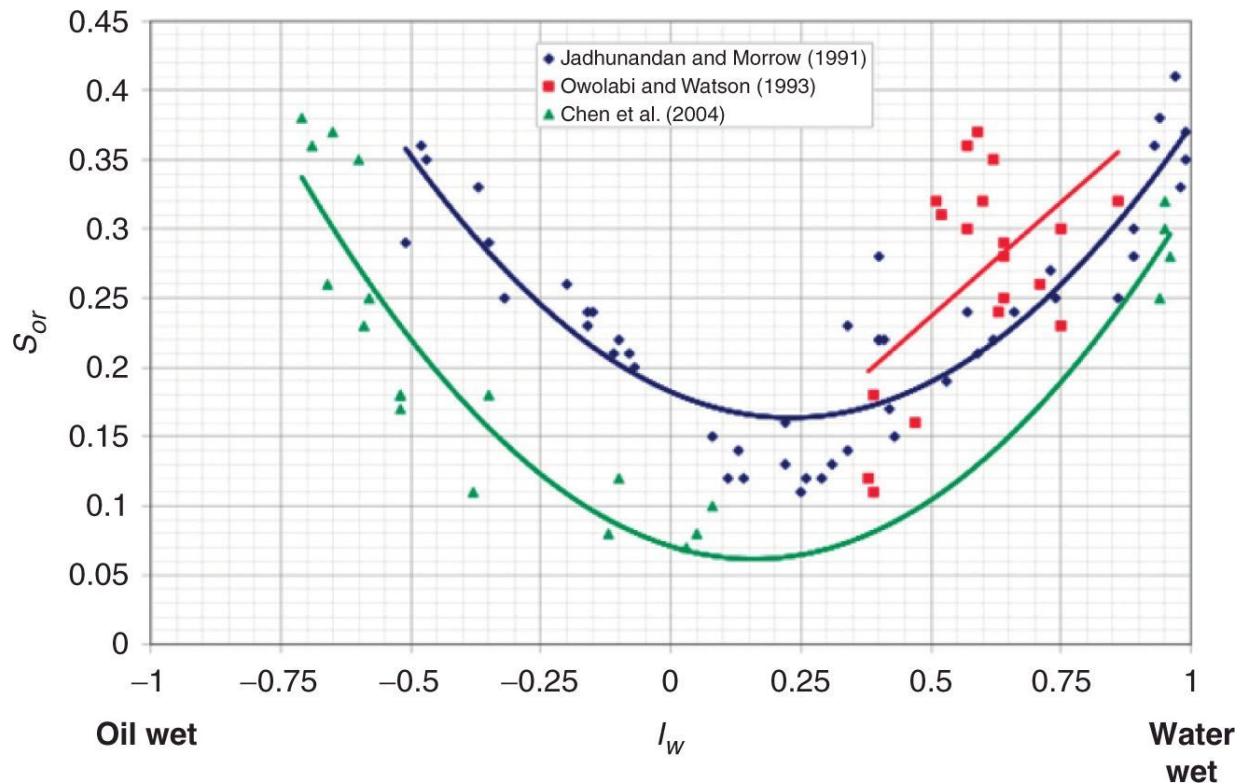


Fig. 3.25—Variation of small N_{VC} residual oil saturations with wetting state (Anderson 2006). The lines are used to highlight trends within the groups.

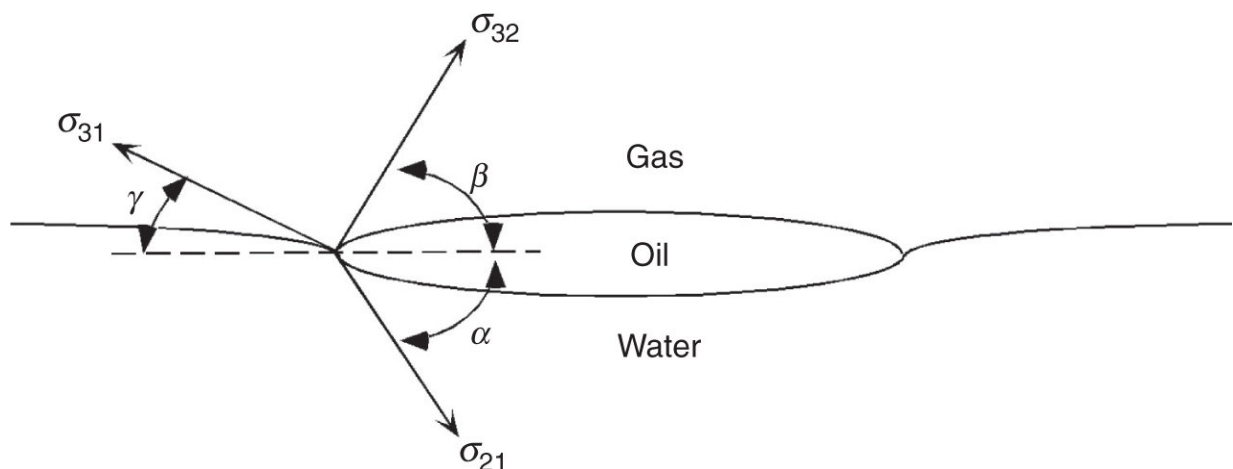


Fig. 3.26—Interfacial tensions and contact angles between three bulk phases.

Statistical models have been successful in predicting CDC curves, but at the same time have required calibration using experimental curves (Larson 1977). These approaches hold the best promise for

nonwetting-phase trapping in which the disconnected nature of the trapped phase invites statistical treatment.

The deterministic models use conventional permeable-media measurements, appear to allow greater rock specificity, and are easier to calculate. Examples of this approach can be found in the work of Stegemeier (1974, 1976) and Melrose and Brandner (1974). However, they tend to require a significant amount of associated data; in statistical models, these data would serve the function of calibration.

3.5 Three-Phase Effects

Three or more phases present in a medium interact in more complex ways than when only two phases are present. The phases are arranged in the pores depending on their preference for the solid phase and the interfacial tension between each phase. Gas is nearly always nonwetting compared to liquid phases, but the liquid phases can exhibit varying degrees of wettability.

Even without the solid phase, the phases can exhibit a preference for each other. [Fig. 3.26](#) shows three phases that meet at a contact line (or point in this 2D diagram) where oil has spread between the gas and water. The degree of spreading of the oil depends on interfacial tensions. If the spreading coefficient, defined as $S = \sigma_{31} - (\sigma_{32} + \sigma_{21})$, is positive, the oil spreads spontaneously to a very thin film. Benjamin Franklin observed this spreading phenomenon in an experiment he performed on Clapham Pond in England (Franklin et al. 1774). In that experiment, Franklin placed a small drop of mineral oil near the center of the pond and noticed that the small drop spread out over a great area until the oil was one molecule thick. If the spreading coefficient is negative or becomes negative over time, spreading will cease.

Experiments confirm that the spreading of oil to thin films can also occur in porous media under gravity drainage. Blunt et al. (1994) showed that residual oil saturation can be reduced significantly by film drainage when gas is introduced into a vertical core filled with residual oil and mobile water. The reduction in oil saturation under

gravity forces can be very slow, but residual oil saturations as low as 1.0% have been reported.

Although varying degrees of wettability exist in oil reservoirs, the oil on balance must be intermediate-wetting for spreading to occur. The oil is intermediate-wetting in [Fig. 3.27](#) because it separates the gas from the water. If the water completely wets the solid surface (the spreading coefficient is positive), the oil separates the gas from the water everywhere (Leverett 1941). This scenario is known as the Leverett assumptions. The oil saturation becomes greater near the center of the pores and thinner in the tighter pore regions.

The implication of this wetting arrangement in [Fig. 3.27](#) is that the gas does not touch the water phase, and, therefore, that the gas saturation is affected only by the total liquid saturation and the interfacial tension between gas and oil. In other words, the water and oil phases can be lumped into a total liquid saturation ($S_l = S_1 + S_2$) and identified as the wetting phase as far as the gas phase is concerned. The water takes up space within the porous media only so that the saturations sum to unity: $S_l + S_g = 1.0$.

The presence of the liquid wetting phase and the lack of contact between gas and water imply that the gas/oil capillary pressure should be a function of the total liquid saturation using measured or modeled two-phase gas/oil capillary pressures. Experimental measurements of the gas/oil capillary-pressure curve are typically made in the presence of irreducible water so that all pores are occupied for a water-wet rock.

Moreover, the water does not contact the gas phase, so that the oil/water capillary pressure is a function solely of the water saturation. The oil/water capillary pressure can then be obtained from a two-phase oil/water capillary measurement or model in which the oil is the nonwetting phase. When gas is present in the reservoir, the nonwetting phase is the sum of the oil and gas saturations. In other words, the gas simply takes up space within the porous media, but does not contact the water.

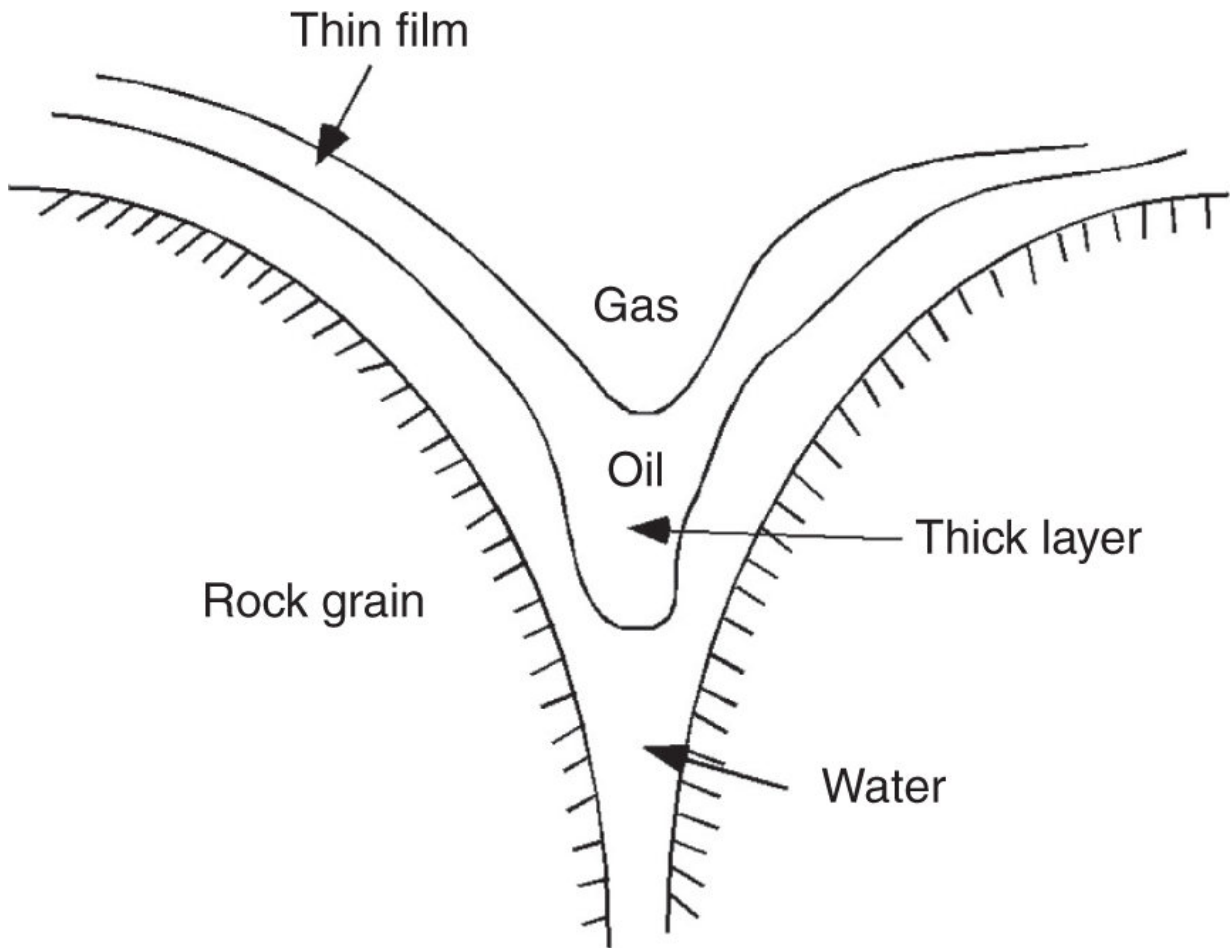


Fig. 3.27—Idealization of gas/oil/water arrangement in a pore. The gas is nonwetting while the oil is intermediate-wetting, and the water is wetting.

For these wetting and spreading assumptions, three-phase capillary pressures can be estimated from measured (or modeled) oil/water and gas/oil (with irreducible water) capillary pressures. If needed, the gas/water capillary pressure can be determined from $P_c^{31} = P_c^{32} + P_c^{21}$.

Example 3.4—Brooks-Corey (BC) Three-Phase Capillary-Pressure Curves. The two-phase BC model for two-phase capillary pressure under drainage is given by $P_c = P_d S^{-1/\lambda}$, where P_d is the capillary entry pressure of the nonwetting phase, S is the normalized wetting-phase saturation equal to $(S_1 - S_{1r}) / (1 - S_{1r})$, and λ is the pore-size distribution coefficient that controls the shape of the

capillary-pressure curve. Using the Leverett assumptions, this same equation for two phases can represent three-phase capillary pressures.

We begin at a very low pressure at which the water saturation is equal to 1.0 and is therefore not sufficient for the nonwetting phase (the lumped gas and oil phases) to enter. Therefore, at pressures less than the entry pressure of the measured oil/water system:

$$S_1 = 1 \text{ for } P_c^{21} < P_d^{21}.$$

Just above the oil/water entry pressure, the water saturation is less than one. From the BC model:

$$S_1 = S_{1r} + (1 - S_{1r}) \left(\frac{P_c^{21}}{P_d^{21}} \right)^{-\lambda} \text{ for } P_c^{21} > P_d^{21}.$$

Below the gas/oil entry pressure, gas does not exist, so that

$$S_l = S_1 + S_2 = 1 \text{ for } P_c^{32} < P_d^{32}.$$

Above the gas/oil entry pressure, gas enters the largest pores, so that three phases are now present. Here, the liquid saturation is the wetting phase for the gas, and the gas/oil capillary pressure is given by

$$S_l = S_2 + S_1 = S_{lr} + (1 - S_{lr}) \left(\frac{P_c^{32}}{P_d^{32}} \right)^{-\lambda} \text{ for } P_c^{32} > P_d^{32},$$

where $S_{lr} = S_{1r} + S_{2r}$. The water/oil capillary pressure in the three-phase region is still given by the two equations for S_1 given at the start of this Example.

Three-phase capillary-pressure hysteresis can also be modeled in the same way, assuming that the Leverett assumptions apply.

3.5.1 Leverett j -Function Scaling. The Leverett j -function can be used to represent the three-phase capillary-pressure curves from one single capillary-pressure curve. The use of the j -function assumes that the pore structure remains the same and that the capillary pressure can be scaled from one j -function to account for changing fluids within the pores. With the assumption of complete wetting so that $\cos\theta = 1$, the three-phase capillary pressures are scaled by the j -function Eq. 3.14, which is repeated here as

and

The Leverett j -function (or any capillary-pressure curve) always decreases with increasing wetting-phase saturation. Therefore,

Substitution of Eqs. 3.30 and 3.31 into Eq. 3.32 gives a unique relationship for three-phase capillary pressures:

3.5.2 Three-Phase Relative Permeability. To develop three-phase relative-permeability relationships, we make the same Leverett assumptions used to develop the three-phase capillary-pressure functions: the water is wetting, the gas nonwetting, and the oil is in the intermediate-wetting spreading phase. These assumptions enable the three-phase relative-permeability curves to be derived from the gas/oil and oil/water relative-permeability curves.

The relative permeability of the water phase is now a function of the water saturation only because the water is the wetting phase and the oil separates the water from the gas [i.e., $k_w = k_w(S_1)$]. The

measured two-phase relative-permeability curves for water and oil, in the absence of gas, are used to represent the relative permeability of water.

In a similar way, the relative permeability of gas is also assumed to be a function of its own phase saturation [i.e., $k_{r3} = k_{r3}(S_3)$]. The measured two-phase relative-permeability curves for gas and oil, usually in the presence of irreducible water saturation, are used to represent the gas relative permeability.

The oil relative permeability is more complex than those for gas and water because it is the intermediate wetting phase. The oil will occupy the intermediate-sized pores, whereas water occupies the smallest pores and gas the largest. Nearly all three-phase relative-permeability models that have been proposed change the functional form of the oil relative permeability, but most have the same water and gas relative permeabilities. In the first developments by Stone (Aziz and Settari 1979), the oil relative permeability is assumed to be proportional to the product of the water and gas relative permeabilities (i.e., $k_{r2} \propto k_{r1}k_{r3}$).

3.6 Permeable-Media Chemistry

The performance of several EOR processes, particularly those affected by the electrolytes in the aqueous phase, depend on the chemical makeup of the medium. We conclude this chapter by introducing a few general observations that serve as a base for subsequent chemical insights.

3.6.1 Component Abundance. The composition of naturally occurring permeable media is rich in the number of elements and compounds. [Table 3.2](#) shows a comparative elemental analysis for seven sandstones and one carbonate media. The numbers in this table are percentages of the total mass reported by at least one of three methods: the value came from point counting on an image from a scanning electron micrograph (SEM), analysis based on an energy dispersive X-ray spectrometer (EDS), and analysis from an inductively coupled plasma (ICP) emission spectrophotometer [for

more details about this, see Crocker et al. (1983)]. SEM and EDS sample the surfaces of the rock pores; ICP is a measure of bulk chemistry. Any systematic differences between SEM/EDS and ICP, such as the persistently lower silica amounts obtained from SEM/EDS, are the result of surface localizations of the object mineral.

[Table 3.2](#) indicates that sandstones are approximately 64 to 90% silica, with the remainder distributed fairly evenly among lesser species and clays (last three columns). Silica is important in EOR because it dissolves in aqueous solutions, particularly at high temperature or high pH. The first reaction occurs readily in thermal floods, where the reaction products induce injectivity loss on precipitation. Silica minerals also have a minor anion-exchange capacity at neutral or elevated pH.

TABLE 3.2—COMPARATIVE ELEMENTAL ANALYSIS (WEIGHT PERCENTAGE) OF ROCKS AND CLAYS (CROCKER ET AL. 1983)																
Rocks		SiO ₂	Al ₂ O ₃	Fe ₂ O ₃	MgO	CaO	TiO ₂	SrO	K ₂ O	Na ₂ O	Mn ₂ O ₃	SO ₃	Loss on Ignition	Kaolinite	Chlorite	Illite/Mica
Bandera sandstone	ICP	71.4	8.7	3.1	1.7	3.1	0.4	0.01	1.1	1.7			6.2			
	EDS	64.4	17.4	9.5		4.2			4.1					6.0	5.0	8.0
	X-ray	65.0	8.0	8.0												
Berea sandstone	ICP	84.6	4.5	1.4	0.5	0.8	0.2	0.03	2.1	2.2	0.06		2.6			
	EDS	78.0	10.3	3.1		2.8	2.1		4.4					7.0	0.0	4.0
	X-ray	75.1	3.5	5.5	0.8	0.8			3.4							
Coffeyville sandstone	ICP	81.5	7.7	3.5	0.7	0.5	1.1	0.00	1.7	3.1			2.6			
	EDS	65.1	15.4	10.5		2.7	3.8		2.4					4.0	4.0	6.0
	X-ray	70.1	10.0			6.0										
Cottage Grove sandstone	ICP	84.6	4.7	1.2	0.08	0.08	0.1	0.01	0.4	2.9	0.07		1.7			
	EDS	70.4	15.9	11.2		0.6	1.1		2.8		0.4			6.0	1.0	6.0
	X-ray	75.4	5.8						5.7							
Noxie sandstone	ICP	87.6	4.9	1.6	0.2	0.2	0.6	0.02	0.8	1.8	0.07		1.3			
	EDS	64.4	9.5	22.5		0.7	0.6		1.5		3.1			5.0	1.0	7.0
	X-ray	77.8	4.7						4.6							
Oswego limestone	ICP	0.7	0.2	0.09	0.5	50.0		0.2	0.5	0.8		0.4	42.5			
	EDS	2.0	1.0			53.0					1.3			4.0	0.0	0.0
	X-ray	5.0				51.0										
Sweetwater sandstone (tight gas sand)	ICP	88.7	4.2	0.4	0.2	0.05	0.1	0.02	0.8	1.9	0.02		1.2			
	EDS	72.4	13.3	8.1		2.9			3.3					0.0	2.0	8.0
	X-ray	90.0														
Torpedo sandstone	ICP	90.5		1.9	0.2	0.2	0.5	0.8	0.8	0.2	0.2		1.6			
	EDS	72.3		11.0		0.7	1.9		2.3		2.6			6.0		7.0
	X-ray	77.0	5.1						5.0							

The carbonate sample in [Table 3.2](#) is only 50 to 53% calcium. This relatively low value may be explained by a high loss on ignition in the ICP method. Calcium minerals in both sandstones and carbonates are important because they are a source of multivalent cations in solution. These cations affect the properties of polymer and

surfactant solutions considerably and can provide a source of pH loss in alkaline and ASP floods through metal hydroxide precipitation.

3.6.2 Clays. Clays are hydrous aluminum silicates with a molecular lattice that can also contain (in decreasing prevalence) magnesium, potassium, sodium, and iron. [Table 3.3](#) shows a summary of the most common clays. The suffix *ite* designates a clay.

Clay minerals constitute 40% of the minerals in sediments and sedimentary rocks (Weaver and Pollard 1973). Their prevalence in commercial hydrocarbon-bearing permeable media is much less than this (see the last three columns in [Table 3.2](#)), but their importance to oil recovery far exceeds their relative abundance. This importance derives from the following properties of clays: they are generally located on the pore-grain surfaces, they have a large specific surface area, and they are chemically reactive. Clays affect EOR processes by influencing the medium permeability or by changing the ionic state of the resident fluids. The following paragraphs provide a brief exposition of clay-mineral properties (for more details, see Grim 1968; Weaver and Pollard 1973; or Rieke et al. 1983).

Clays are classified by their chemical formula, crystal structure, particle size, morphology, water sensitivity, and chemical properties (see [Table 3.3](#)). The principal building block of a clay mineral is the element silicon surrounded by three oxygens in a tetrahedral structure. These tetrahedra are merged with octahedra with the Al species in the center and OH or oxygen groups at the corners. With the bond lengths of the octahedra and tetrahedra being almost identical, these geometrically regular shapes arrange themselves into planar or sheet-like structures. Hence, a major classification of clays in [Table 3.3](#) is the number of sheets in a crystal. Kaolinite is the simplest example of this structure. Such a regular structure lends itself very well to analysis by X-ray diffraction. The proportion of foreign atoms (Mg, K, Fe, and Na) increases with the number of sheets.

TABLE 3.3—CLASSIFICATION OF PRINCIPAL CLAY MINERALS IN SEDIMENTS [ADAPTED FROM DEGENS (1965)]

Layers	Population of Octahedral Sheet	Expansion	Group	Species	Crystalllochemical Formula
Two sheet (1:1)	Dioctahedral	Nonswelling	Kaolinite	Kaolinite	$\text{Al}_4(\text{OH})_8[\text{Si}_4\text{O}_{10}]$
				Dickite Nacrite	
Three sheet (2:1)	Trioctahedral	Nonswelling and swelling	Halloysite	Halloysite	$\text{Al}_4(\text{OH})_8[\text{Si}_4\text{O}_{10}] \cdot (\text{H}_2\text{O})_4$
		Nonswelling	7 \AA -chlorite (septechlorite)	Metahalloysite Berthierine (kaolin-chamosite)	$\text{Al}_4(\text{OH})_8[\text{Si}_4\text{O}_{10}]$ $(\text{Fe}^{2+}, \text{Fe}^{3+}, \text{Al}, \text{Mg})_6(\text{OH})_8$ $[(\text{Al}, \text{Si})_4\text{O}_{10}]$
Three sheet and one sheet (2:2)	Dioctahedral	Swelling	Montmorillonite* (smectite)	Montmorillonite	$\{(\text{Al}_{2-x}\text{Mg}_x\text{XOH})_2[\text{Si}_4\text{O}_{10}]\}^{-x}$
		Nonswelling	Illite (hydromica)*	Beidellite Nontronite	$\text{Na}_x \cdot n\text{H}_2\text{O}$ $\{(\text{Al}_2(\text{OH})_2)_2[(\text{Al}, \text{Si})_4\text{O}_{10}]\}^{-x}$ $\text{Na}_x \cdot n\text{H}_2\text{O}$ $\{(\text{Fe}^{3+}_{2-x}\text{Mg}_x\text{XOH})_2[\text{Si}_4\text{O}_{10}]\}^{-x}$ $\text{Na}_x \cdot n\text{H}_2\text{O}$
Three sheet and one sheet (2:2)	Trioctahedral	Swelling	Vermiculite**	Vermiculite	$(\text{Mg}, \text{Fe})_3(\text{OH})_2[\text{Al Si}_3\text{O}_{10}]$ $\text{Mg} \cdot (\text{H}_2\text{O})_4$
		Nonswelling [†]	14 \AA -chlorite** (normal chlorite)	Chlorite varieties	$(\text{Al}, \text{Mg}, \text{Fe})_3(\text{OH})_2[(\text{Al}, \text{Si})_4\text{O}_{10}]$ $\text{Mg}_3(\text{OH})_6$

* Also trioctahedral varieties.

** Also dioctahedral varieties.

[†] Swelling chlorites are rare and are intermediate forms between vermiculite and chlorite.

Despite the regularity of their crystal structure, clays in permeable media are usually the smallest particles. The inference that a clay is usually any particle less than approximately 50 nm is imprecise: in fact, many permeable-media constituents can have particle sizes this small. However, larger clay particles are not common. Because of their small size, clay particles can frequently exist as colloidal suspensions in aqueous solution.

The small particle size means that clays are generally much less permeable to flow than are sandstones. Low permeability impacts EOR in two ways. Segregated clays or *shales* are regions of very high clay content that generally are not considered part of the reservoir. Because they lack permeability, shales are barriers to fluid flow, particularly vertical flow, and will hinder gravity segregation. Dispersed clays, on the other hand, occur distributed among the pores of permeable media. These are of more concern to EOR than segregated clays because they are more chemically reactive.

Dispersed clays, though, also cause a reduction of the medium permeability; in fact, the clay content is a good indicator of the receptiveness of the formation to fluid injection (**Fig 3.28**).

Dispersed clays have a separate morphological classification (Neasham 1977). [Fig. 3.29](#) illustrates this schematically, along with representative SEM micrographs of each type.

Clays can occur as discrete platelets randomly arranged within the pores ([Fig. 3.29a](#)), as pore-lining clays coating the pore walls in thin films ([Fig. 3.29b](#)), and as pore-bridging clays exhibiting filaments that extend across the pores ([Fig. 3.29c](#)). Permeable media with pore-bridging clays will have a lower permeability than what would be expected on the basis of the sand-grain size. Pore-lining clays have little effect on permeability, but clay platelets can be induced to cause permeability loss when the electrolyte balance of the fluid in the pore space is changed. These observations are translated into quantitative expressions in Panda and Lake (1995b).

Permeability loss or clay sensitivity of media containing clay platelets is a well-documented problem in waterflooding. Many of these clays are readily swelled by very fresh water or by high concentrations of sodium cations. When swelled, they detach from the pore surface, become entrained in the flowing fluid, and then collect and bridge pore entrances farther downstream (Khilar and Fogler 1981). The damage caused is only temporarily reversible because platelets can bridge in reverse flow. The sensitivity to fresh water is a concern in steamdrives and soaks in which the condensed water is quite fresh. This sensitivity to fresh water and sodium cations affects polymer and micellar-polymer floods, during which efforts to remove divalent cations by preflush are common. Only swelling clays (see [Table 3.3](#)) show this effect, most prominently when the clay is in the platelet morphology.

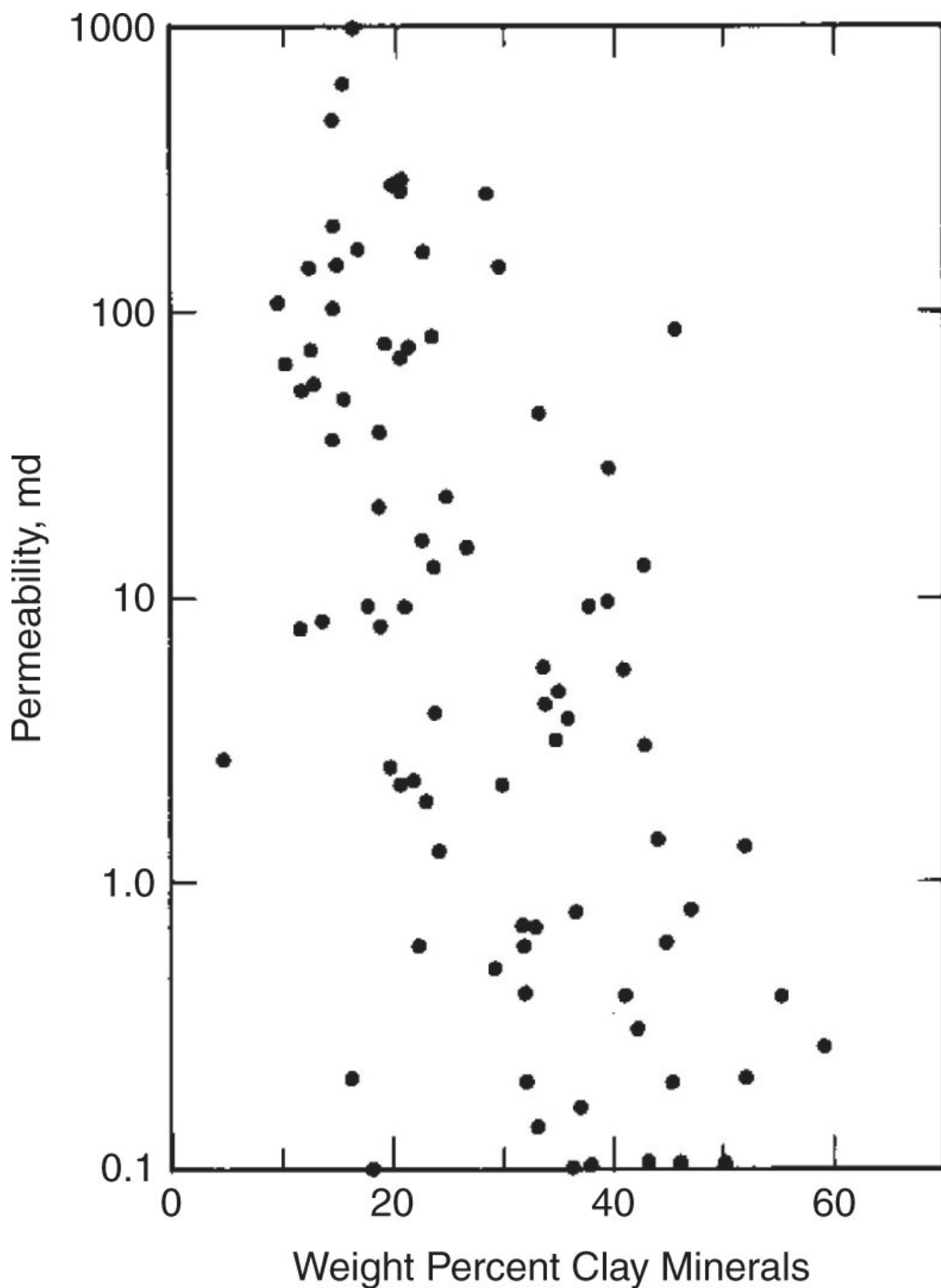


Fig. 3.28—Permeability vs. weight percentage of clay minerals (Simlote et al. 1983).

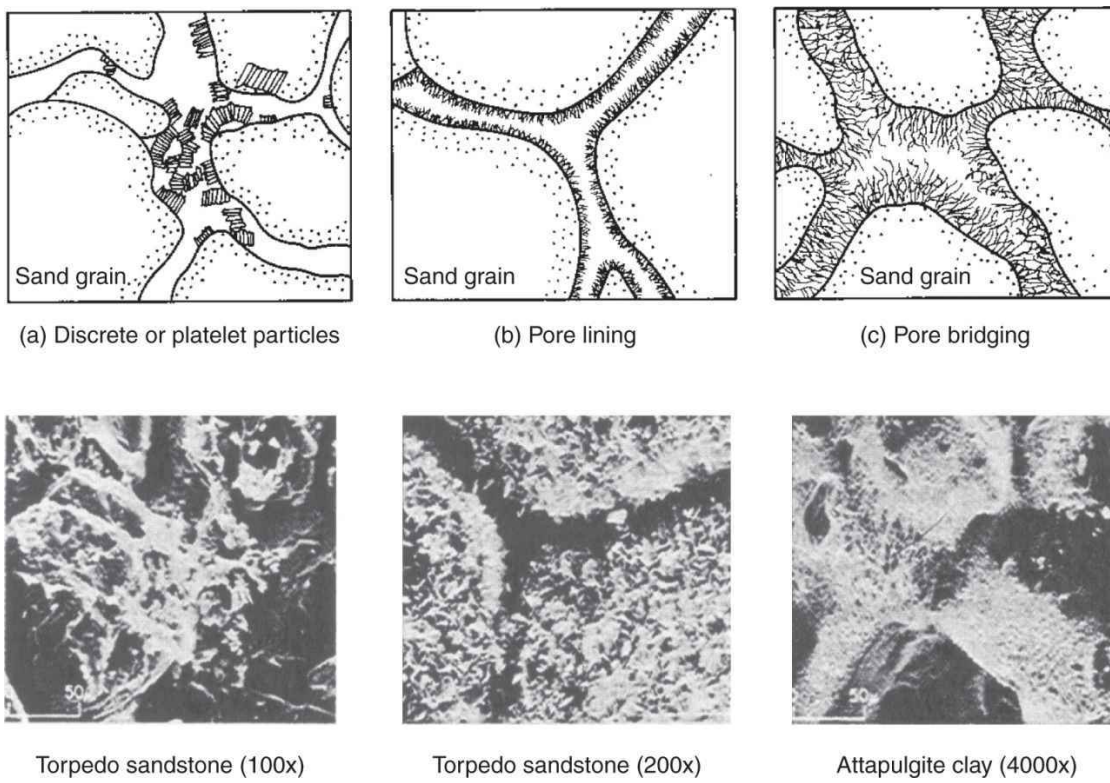


Fig. 3.29—Examples of natural clays [upper panels from Nesham (1977); lower from Crocker et al. (1983)].

3.6.3 Cation Exchange. Among the most interesting of clay characteristics, and that with the most relevance to EOR, is the ability of clays to swap or exchange cations with cations from fluids in the pore space. With diagenesis, the aluminum atoms in the simple clay structure become replaced with lower-valence cations like Mg^{2+} or K^+ (see [Table 3.3](#)). This substitution imparts a deficiency of positive charge to the clay, which must be countered by cations from the fluid if the clay is to remain electrically neutral. This exchange of stationary cations affects the concentrations in the aqueous phase and thereby the performance of chemical EOR methods.

The cation exchange capacity Q_V is a measure of the concentration of these excess negative charges. The units of Q_V are milliequivalents (meq) per unit mass of substrate. The equivalent weight of a species is the molecular weight divided by the absolute value of its charge, or basically the amount of mass per unit charge.

Q_V is expressed in this fashion to enable the concentration of any bound cation to be expressed in consistent units. The units of solution concentrations may also be expressed in milliequivalents per mass of substrate, but it is usually more convenient to work on a unit pore-volume basis. The cation exchange capacity expressed per unit pore volume is Z_V , where

and ρ_s is the substrate density.

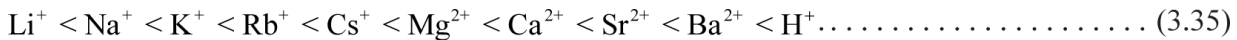
The cation exchange capacity increases with degree of substitution. Because the substituted sites are in the interior of the lattice, Q_V is also a function of clay morphology. Platelet clays have more edges and therefore more exposed sites. Following Grim (1968), typical Q_V for montmorillonites, illites, and kaolinites are 700–1300, 200–400, and 30–150 meq/kg of clay. These numbers should be compared to Q_V for typical reservoir rocks (see [Table 3.4](#)), which are expressed in milliequivalents per kilograms of rock. Clays with large Q_V are usually swelling clays.

TABLE 3.4—PHYSICAL CHARACTERISTICS OF TYPICAL PERMEABLE MEDIA
 [ADAPTED FROM CROCKER ET AL. (1983)]

	Porosity (fraction)	Permeability (μm^2)	Density (g/cm^3)	Surface Area (m^2/g)	Clay Dispersion Classification	Cation Exchange Capacity (meq/ $\text{kg}\cdot\text{rock}$)
Bandera sandstone	0.174	0.012	2.18	5.50	Pore lining	11.99
Berea sandstone	0.192	0.302	2.09	0.93	Grain cementing	5.28
Coffeyville sandstone	0.228	0.062	2.09	2.85	Pore bridging	23.92
Cottage Grove sandstone	0.261	0.284	1.93	2.30	Pore bridging	17.96
Noxie sandstone	0.270	0.421	1.85	1.43	Pore lining	10.01
Oswego limestone	0.052	0.0006	2.40	0.25	Mixed in the carbon matrix	—
Sweetwater sandstone	0.052	0.0002	2.36	1.78	Discrete particles	—
Torpedo sandstone	0.245	0.094	1.98	2.97	Pore bridging	29.27

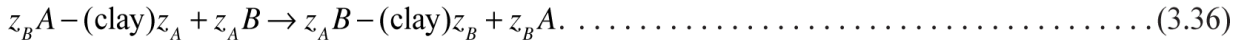
The bonds between the exchange sites and the cations are chemical, but they are readily reversible. The relative ease of the

replacement of one cation by another is



Species that have large charge densities (multivalents or those with small ionic radii) are more tightly held by the anionic sites. This observation suggests a possible explanation for the permeability-reducing behavior of Na^+ . The large Na cations disrupt the clay particles when they intrude into the structure. However, only a small amount of another cation is sufficient to prevent this because most other naturally occurring cations are more tightly bound than Na^+ .

3.6.4 Equilibrium Relations. The sequence in inequality (Eq. 3.35) is qualitative. The actual replacement sequence depends weakly on clay type and strongly on the total composition of the fluid contacting the clays. More quantitative representations follow from chemical equilibria. For example, the exchange reaction between a cation A of charge z_A and another B of charge z_B is given by



The reaction in Eq. 3.36 suggests an equilibrium isotherm,

$$K_N = \frac{\left(\frac{C_{Bs}}{Z_v}\right)^{1/z_B} (C_A)^{1/z_A}}{\left(\frac{C_{As}}{Z_v}\right)^{1/z_A} (C_B)^{1/z_B}}, \dots \quad (3.37a)$$

where K_N is the *selectivity* or *selectivity coefficient* of species A on the clay with respect to species B . In Eq. 3.37a, (C_A) and (C_B) are species concentrations in molal units, and C_{As} and C_{Bs} are in equivalents per unit pore volume (meq/cm^3 is convenient). The subscript s indicates a clay-bound species, and the equation assumes ideal behavior. For calculations, it is more direct to write Eq. 3.37a as

$$K_{BA} = \left(\frac{Z_v}{\rho_1} \right)^{(z_A - z_B)} (K_N)^{z_A z_B} \left(\frac{z_A}{z_B} \right)^{z_A} = \frac{C_{B_s}^{z_A} C_A^{z_B}}{C_{A_s}^{z_B} C_B^{z_A}}, \dots \quad (3.37b)$$

TABLE 3.5—TYPICAL SELECTIVES [ADAPTED FROM BRUGGENWERT AND KAMPHORST (1979)]

Equation A – Clay + B →	Material	Selective Coefficient (K_N)
Na – mont.* + H ⁺	Various	0.37–2.5
Na – mont. + NH ₄ ⁺	C. berteau maroc	4.5–6.3
Na – mont. + K ⁺	Bentonite	2.7–6.2
Na – kaol. + K ⁺	George kaolinite	2.7–7.8
2Na – mont. + Ca ⁺²	Clay spur	1.9–3.5
2Na – clay + Ca ⁺²	Berea	0.3–10.5
2Na – clay + Mg ⁺²	Berea	0.2–10.0
3Na – mont. + Al ⁺³	Wyoming bentonite	2.7

*mont. = montmorillonite; kaol. = kaolinite.

where K_{BA} is another form of the selectivity coefficient, and C_A and C_B are now in units of equivalents per unit pore volume.

In general, K_N varies with the exchanging pair and the identity of the clay. For cations of interest in EOR and clays commonly encountered in permeable media, this dependency is not great. [Table 3.5](#) shows typical selectivities for Na⁺ exchange. The selectivity for any other pair on this table may be obtained by eliminating the Na⁺ between the two isotherms.

The cation preference expressed in inequality (Eq. 3.35) is determined by the valences appearing in the isotherm. If we let A = monovalent and B = divalent be the only exchanging cations, electroneutrality of the clay requires that

$$C_{8s} + C_{6s} = Z_v, \dots \quad (3.38a)$$

where $C_{iD} = C_{is}/Z_V$. Furthermore, Eq. 3.37b becomes

where $r = C_8^2 / C_6$. The isotherm Eq. 3.39 is now expressed entirely in units of equivalents per unit volume. Using Eq. 3.38a to eliminate C_{8D} and solving for the positive root gives

$$C_{6D} = 1 + \frac{r}{2K_{68}Z_v} \left[1 - \left(\frac{4K_{68}Z_v}{r} + 1 \right)^{1/2} \right]. \dots \dots \dots \quad (3.40)$$

This equation is plotted in **Fig 3.30** (6 is Ca^{2+}), with the anion concentration C_5 as a parameter. C_5 appears in the equation because the solution must be electrically neutral:

The preference of the clay for divalent ions is apparent because all curves are above the 45° line. This preference increases as the water salinity (anion concentration) decreases. Isotherm representations like Eq. 3.40 are used in Lake et al. (2002) to calculate the changes in flowing water compositions.

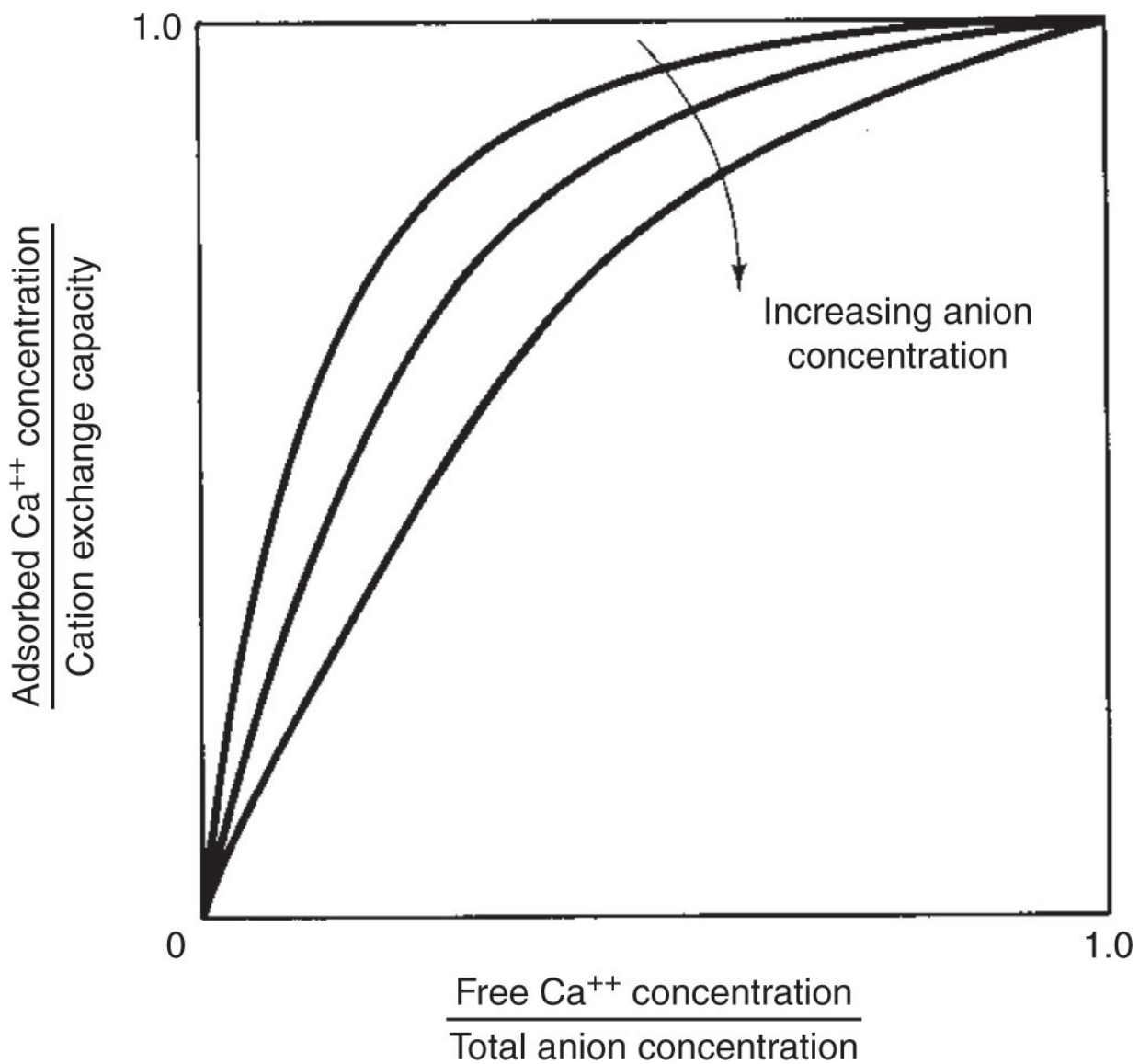
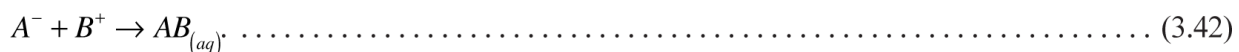


Fig. 3.30—Typical isotherm for sodium-calcium exchange.

3.6.5 Dissolution and Precipitation. Other rock-fluid interactions that affect EOR are intra-aqueous reactions and dissolution-precipitation reactions. An example of the former is the combination of an anion A and cation B to form aqueous component AB :



The chemical equilibrium for this reaction is

$$K_r = \frac{(C_{AB_{(aq)}})}{(C_A) \cdot (C_B)}, \dots \quad (3.43)$$

where K_r is the equilibrium constant for this ideal reaction at the temperature and pressure of interest. If the concentration of A or B exceeds a certain value, $AB_{(aq)}$ can precipitate to form $AB_{(s)}$, a solid:



The reverse of this is the dissolution of $AB_{(s)}$. The equilibrium relation for Eq. 3.44 is

$$K_r^{sp} \geq (C_A) \cdot (C_B), \dots \quad (3.45)$$

where K_r^{sp} is the solubility product of the reaction. Generally, the Cs in Eqs. 3.43 and 3.45 should be the activity of the designated component. For ideal solutions—the only kind we deal with here—the activities are equal to the molal concentrations.

Eq. 3.45 has a most interesting contrast with Eq. 3.43. The product concentration for the precipitation-dissolution reaction does not appear in the equilibrium expression. The state of the system must be obtained from a material balance of the individual elements, rather than the species, to be consistent with the phase rule (see [Chapter 4](#)) when each solid precipitate is considered as a separate phase.

[**Table 3.6**](#) gives $\log K_r$ and $\log K_r^{sp}$ for the more important reactions in permeable media. The standard enthalpies of formation in this table are to be used to correct the $T_1 = 298$ K equilibrium constants and solubility products approximately to another temperature according to

TABLE 3.6—SELECTED SOLUBILITY DATA AT 298 K FOR AQUEOUS AND SOLID SPECIES IN NATURALLY OCCURRING PERMEABLE MEDIA [ADAPTED FROM DRIA ET AL. (1988)]

Aqueous Species or Complexes		Log K_r	ΔH^0 J/kg-mole
OH^-	$= \text{H}_2\text{O} - \text{H}^+$	14.00	-133.5
CaOH^+	$= \text{Ca}^{2+} + \text{H}_2\text{O} - \text{H}^+$	12.70	-173.2
Ca(OH)_2	$= \text{Ca}^{2+} + 2\text{H}_2\text{O} - 2\text{H}^+$	27.92	-267.2
CaCO_3	$= \text{Ca}^{2+} + \text{CO}_3^{2-}$	-3.23	44.1
CaHCO_3^+	$= \text{Ca}^{2+} + \text{CO}_3^{2-} + \text{H}^+$	-11.23	45.0
$\text{Ca(HCO}_3)_2$	$= \text{Ca}^{2+} + 2\text{CO}_3^{2-} + 2\text{H}^+$	-20.73	66.8
HCO_3^-	$= \text{CO}_3^{2-} + \text{H}^+$	-8.84	35.5
$\text{CO}_2(\text{dissolved})$	$= \text{CO}_3^{2-} - \text{H}_2\text{O} + 2\text{H}^+$	-16.68	53.8
FeOH^+	$= \text{Fe}^{2+} + \text{H}_2\text{O} - \text{H}^+$	6.79	-120.1
Fe(OH)_2	$= \text{Fe}^{2+} + 2\text{H}_2\text{O} - 2\text{H}^+$	17.60	-240.2
FeOOH^-	$= \text{Fe}^{2+} + 2\text{H}_2\text{O} - 3\text{H}^+$	30.52	-416.3
Fe(OH)_3^-	$= \text{Fe}^{2+} + 3\text{H}_2\text{O} - 3\text{H}^+$	23.03	-314.1
H_3SiO_4^-	$= \text{H}_4\text{SiO}_4 + \text{OH}^- - \text{H}_2\text{O}$	-4.0	-
$\text{H}_3\text{SiO}_4^{2-}$	$= \text{H}_3\text{SiO}_4^- + \text{OH}^- - \text{H}_2\text{O}$	-5.0	-
Solids and Bases		Log K_r^{sp}	ΔK_r^0 J/kg-mole
Ca(OH)_2	$= \text{Ca}^{+2} + 2\text{H}_2\text{O} - 2\text{H}^+$	22.61	194.0
CaCO_3	$= \text{Ca}^{+2} + \text{CO}_3^{2-}$	-8.80	-28.0
Fe(OH)_2	$= \text{Fe}^{+2} + 2\text{H}_2\text{O} - 2\text{H}^+$	12.10	-219.3
FeCO_3	$= \text{Fe}^{+2} + \text{CO}_3^{2-}$	-10.90	-66.4
$\text{CO}_2(\text{gas})$	$= \text{CO}_2^{2-} - \text{H}_2\text{O} + 2\text{H}^+$	-17.67	5.3
$\text{SiO}_2(\text{quartz})$	$= \text{H}_4\text{SiO}_4 - 2\text{H}_2\text{O}$	-3.98	14.0

Note: Elements = H^+ , Na^+ , Ca^{2+} , Fe^{2+} , CO_3^{2-} , Cl^- , Si^{4-}

$$\log K_r|_{T_2} = \frac{\Delta H_r^0}{2.303R_g} \left(\frac{1}{T_1} - \frac{1}{T_2} \right) + \log K_r|_{T_1}, \dots \quad (3.46)$$

where T_2 is the temperature of interest. The K 's in Eq. 3.46 may be either equilibrium constants or solubility products.

3.7 Summary

The scope of this chapter—from permeability to mineral chemistry—partly justifies the brevity of treatment. Indeed, entire books have been written on petrophysical properties (Dullien 1979) and on aquatic chemistry (Garrels and Christ 1965). The coverage is by no means uniform; each item was selected because it recurs in at least one later chapter. We do not cover the basics of these topics there because the EOR application is usually more advanced and many of the phenomena are important for more than one process. Most important, the introduction here and in the next chapter emphasizes that the chemistry and physics of flow in permeable media are a

common base for *all* EOR processes, so that proficiency in one area of a particular process inevitably supplies insights into other processes.

No theme in this text is more important than the mechanisms of lowering residual oil saturation. We have attempted to explain that this is done (mainly) by increasing the capillary number, and to some extent by changing wetting states. Other phenomena are important, but increasing capillary number touches on so many aspects of EOR that it deserves to be called a fundamental principle of EOR.

Exercises

3.1 CK Equation for Spheroids.

- Re-derive the CK equation (Eq. 3.4) for a permeable medium made of oblate spheroids (ellipses rotated about their minor axes). For these shapes, the surface area A of the spheroid is

$$A = 2\pi a^2 + \pi \frac{b^2}{\varepsilon} \ln\left(\frac{1+\varepsilon}{1-\varepsilon}\right)$$

and the volume V is

$$V = \frac{4}{3} \pi a^2 b.$$

In these equations, a and b are the distances from the particle center to the major and minor vertices respectively ($a > b$), and ε is the eccentricity ($\varepsilon \leq 1$), defined as

$$\varepsilon = \frac{(a^2 - b^2)^{1/2}}{a}.$$

- b. Show that the permeability of the medium is a weak function of particle shape for $\varepsilon < 0.5$ by plotting $k/(k)_{\varepsilon=0}$ vs. ε ($\varepsilon = 0$ is a sphere). A valid comparison is possible only if the spheres and oblate spheroids have equal volume.

3.2 Calculating a Capillary Transition Zone. Using the capillary-pressure data in [Fig. 3.31](#),

- a. Calculate and plot water saturation vs. depth profiles in a water-wet reservoir knowing that the water/oil contact ($S_1 = 1$) is 152 m deep. The water and oil densities are 0.9 and 0.7 g/cm³, respectively.
- b. Construct an IR oil-saturation plot for the capillary-pressure data given.
- c. Using the IR curve of Part b, plot on the graph of Part a the residual-oil-saturation profile vs. depth.
- d. If the net pay interval of the reservoir is 31 m, estimate the maximum waterflood recovery for these conditions. Compare this to the case with both the residual and initial oil saturations constant and equal to their values at the formation top.

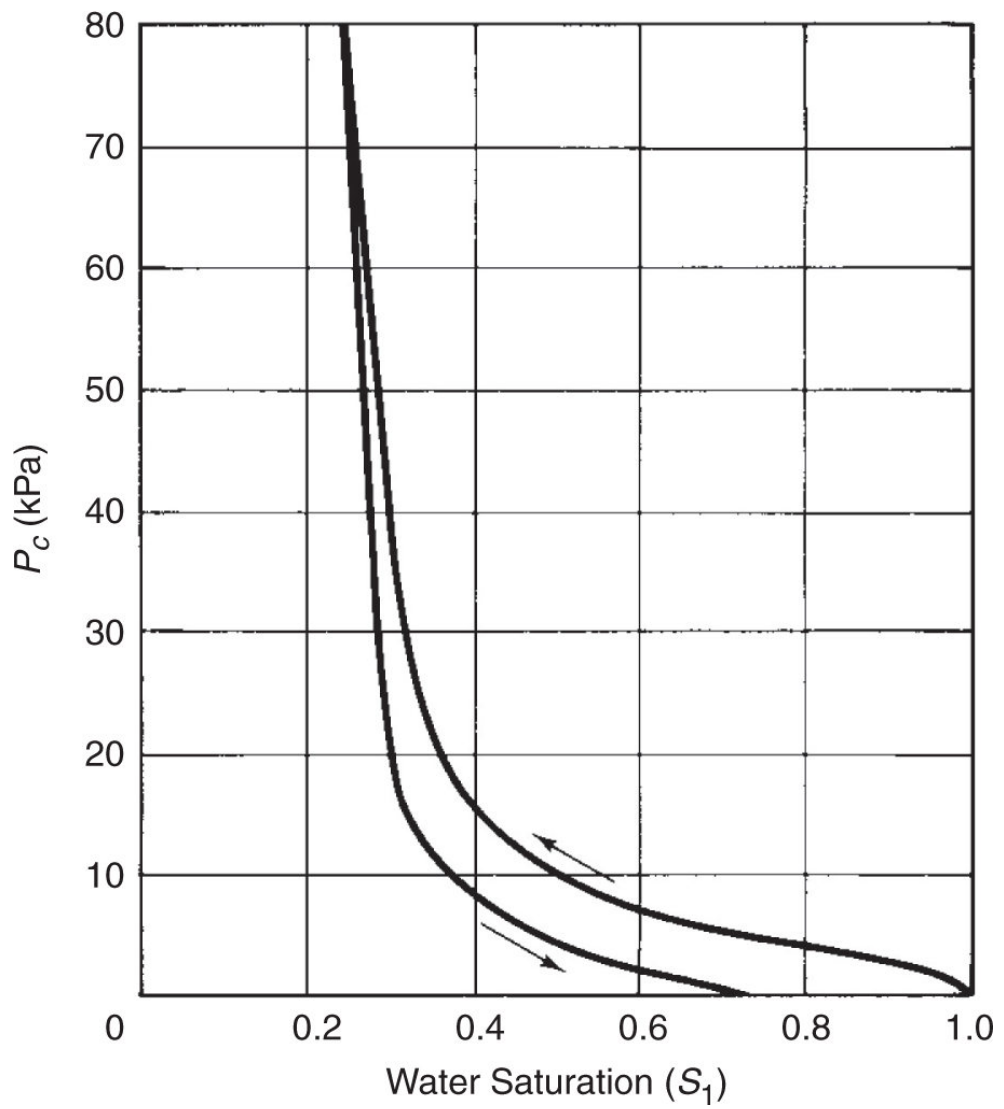


Fig. 3.31—Water/oil capillary pressure curves.

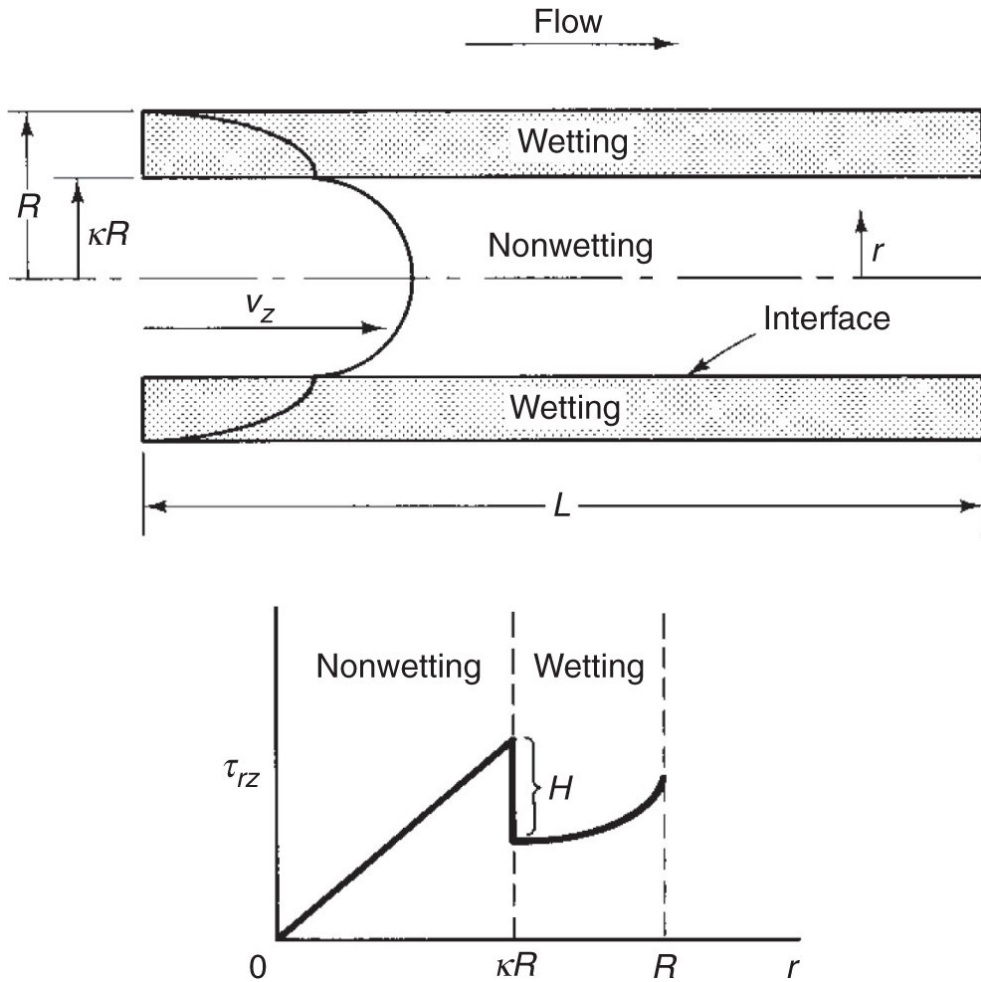


Fig. 3.32—Simultaneous two-phase laminar flow in a tube with shear-stress discontinuity at the interface.

3.3 Discontinuities in Shear Stress at the Interface. Non-equilibrium mass transfer of surfactants from bulk phases to interfaces can cause interfacial tension gradients, which in turn can cause discontinuities in the shear stress at the interface.

Consider the steady-state, simultaneous laminar flow of two equal-viscosity, immiscible fluids in a tube, as in [Fig. 3.32](#), where $0 \leq \kappa \leq 1$. The wetting phase is adjacent to the tube wall, and the nonwetting phase flows in the tube core. At the interface between the two phases, there is a discontinuity H in the shear stress ($H > 0$).

- a. By performing a force balance on cylindrical fluid elements, derive an expression for the shear stress τ_{rz} , including the discontinuity.

- b. If both phases are Newtonian fluids for which

$$\tau_{rz} = -\mu \frac{dv_z}{dr},$$

derive the local velocities and volumetric flow rates for each phase in terms of the phase viscosities, the overall pressure drop, and the tube length.

- c. Using the results of Part b in analogy to Darcy's law, derive expressions for the wetting- and nonwetting-phase relative permeabilities as functions of phase saturations. Express the relations in terms of a capillary number of the form

$$N_{vc} = \frac{R\Delta P}{HL}.$$

Plot the relative-permeability curves for each phase vs. the wetting-phase saturation with capillary number as a parameter.

- d. Set the relative permeability for the wetting phase equal to zero to derive an expression between the residual wetting phase and the capillary number. Plot your results in the form of a CDC (S_{1r} vs. N_{vc}).
- e. On the basis of the discussion in the text, state whether you think the CDC in Part d is qualitatively reasonable for the wetting phase. List the aspects of the above model that are physically unrealistic.

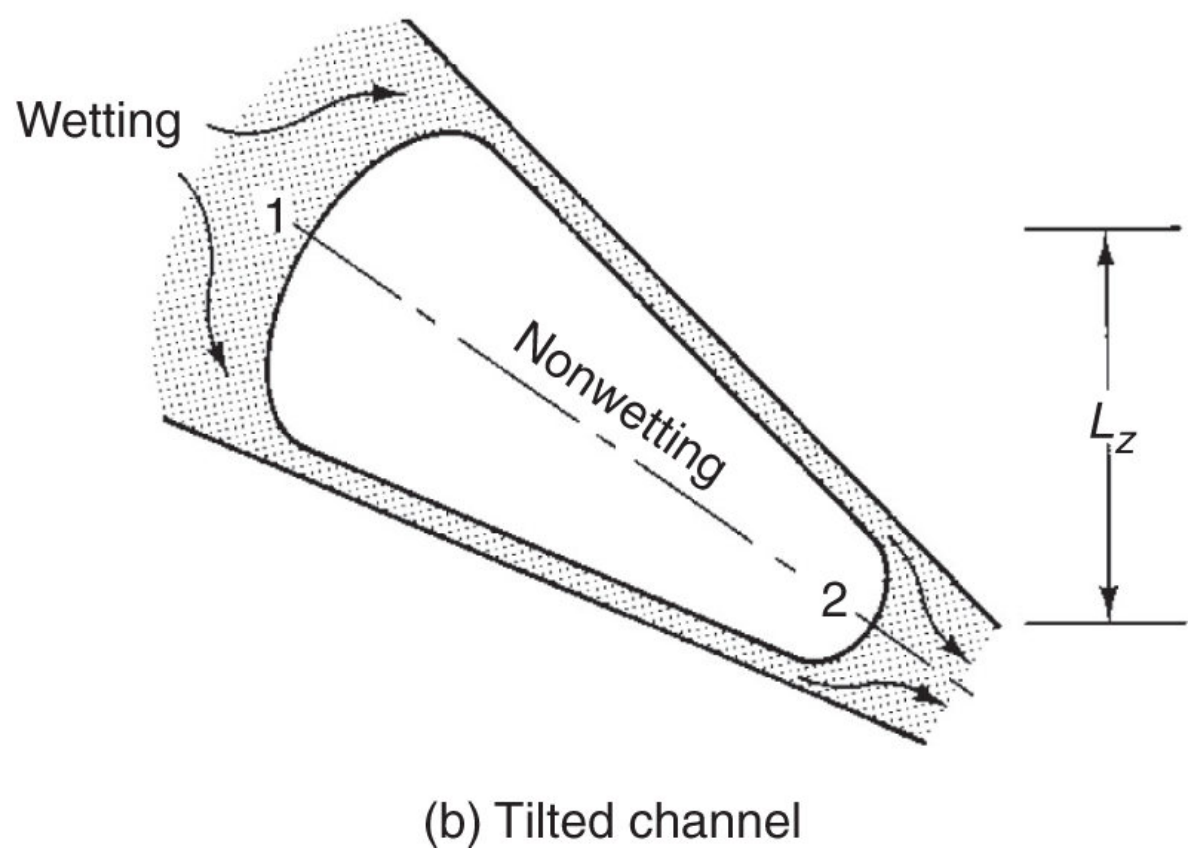
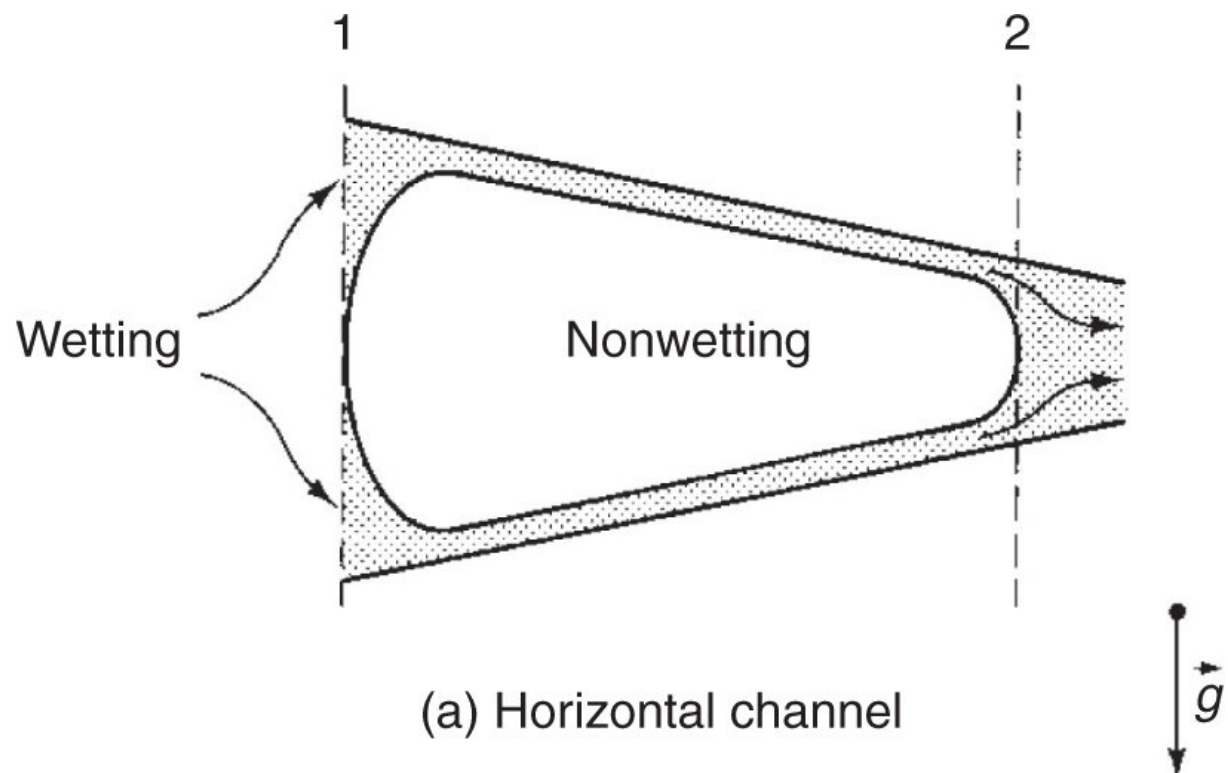


Fig. 3.33—Schematic of trapped nonwetting phase.

3.4 Equilibrium for a Trapped Globule. Derive the equality in Eq. 3.28 for a static nonwetting globule under the following conditions:¹

- a. The globule is trapped in a horizontal channel, as in [Fig. 3.33a](#)
- b. The globule is trapped in a tilted channel, as in [Fig. 3.33b](#). Assume the wetting and nonwetting phases to be incompressible. The wetting phase is flowing past the trapped globule.

3.5 Capillary Desaturation in a Pore Doublet

- a. Calculate and plot the CDC for a nonwetting phase based on the pore-doublet model. Assume the heterogeneity factor β to be 5 and the viscosities of both phases to be equal.
- b. Repeat Part a with $\mu_{nw} = (1/2)\mu_w$.
- c. What can you conclude about the effects of viscosity on the CDC?

3.6 CDC With Gravity

- a. Repeat the derivation given in Section 3.4 to develop a theoretical CDC that includes the effects of gravity. Your derivation should now contain a dimensionless ratio of gravity to capillary forces called the bond number N_b (Morrow and Chatzis 1981). Assume the characteristic length in N_b to be given by Eq. 3.9.
- b. Repeat Exercise 3.5 with the following additional data: $\Delta\Delta = 0.2 \text{ g/cm}^3$ and $\alpha = 45^\circ$.

3.7 Cation-Exchange Parameters

- a. The cation-exchange capacity is frequently reported in different units. If Q_V for a permeable medium is 100 meq/100

g of clay, calculate it in units of meq/100 g of medium and meq/cm³ of pore space. The latter definition is the one given by Eq. 3.34a. The weight percentage of clays in the medium is 15%, and the porosity is 22%. The density of the solid is 2.6 g/cm³.

- b. Use the data in [Table 3.6](#) to estimate the selectivity coefficient for calcium-magnesium exchange in a Berea medium.

3.8 Alternative Isotherms for Cation Exchange. Eq. 3.40 is but one of several different isotherms representing cation exchange. Another useful isotherm is the Gapon equation (Hill and Lake 1978):

$$K_G = \frac{C_{Bs} C_A}{C_{As} \sqrt{C_B}},$$

where K_G is the selectivity coefficient for this isotherm. We use this equation to represent sodium-calcium ($A = \text{Na}^+$, $B = \text{Ca}^{++}$) exchange.

- a. Invert this equation for the calcium concentration bond to the clays in the manner of Eq. 3.40. Assume

$$r = C_A^2 / C_B.$$

- b. Show that this equation approaches consistent limits as r approaches zero and infinity.
- c. Plot the isotherm for two different solution anion concentrations in the manner of Fig 3.30. Assume $K_G = 10$.

Chapter 4

Phase Behavior and Fluid Properties

Phase behavior is vital to many petroleum and environmental processes such as enhanced oil recovery (EOR), compositional simulation, geochemical behavior, wellbore stability, geothermal energy, aquifer remediation, and multiphase flow in wellbores and in surface facilities. The study of phase behavior describes the complex interactions between separable portions of matter (called phases) that are in direct contact with each other.

The phase behavior of crude oil, water, and EOR fluids is key to the displacement mechanisms of EOR processes. Such behavior includes the two- and three-phase behavior of surfactant/brine/oil systems, the two or more phases formed in crude-oil and water-solvent systems, and the steam/oil/brine phases of thermal flooding.

This chapter is not an exhaustive exposition of phase behavior. We concentrate on the aspects of phase behavior and thermodynamics most pertinent to EOR. For more complete treatments of phase behavior and fluid properties, see Danesh (1998), Firoozabadi (1999), Francis (1963), McCain (1989), Pedersen et al. (2007), Sage and Lacey (1939); Standing (1977), Whitson and Brule (2000); Orr and Taber (1984), Johns (2006), and Orr (2007).

4.1 Fundamentals of Phase-Equilibrium Thermodynamics

Thermodynamics is the study of energy and its transformations from one thermodynamic state to another. Using thermodynamics, we follow the energy changes that occur during phase changes and predict phase transformations and properties. Thermodynamics

began as the study of heat applied to generate steam power, but was substantially broadened by Gibbs in the late 1800s. The most significant contribution made by Gibbs was the development of phase-equilibrium thermodynamics applied to multicomponent mixtures, particularly the concept of chemical potential (Gibbs 1906). The concept of chemical potential requires that at equilibrium, the chemical potential of each component must be the same in all phases.

This section reviews the fundamentals of phase-equilibrium thermodynamics used in petroleum applications, especially those that determine liquid-vapor phase behavior. It is increasingly recognized, however, that flow through porous media often involves three or more interacting phases. We briefly discuss extensions of the theory to three or more phases.

4.1.1 Basic Definitions. In the case of EOR, we apply thermodynamic concepts to systems instead of points within a permeable medium. A *system* is a specified amount of material to be studied within a control volume (CV). Everything else is called the surroundings. In other chapters, the word *system* refers to the permeable medium, including the fluid within the pore space. In this chapter, the word generally refers only to the fluids. With this definition, a system can be described by one or more *properties*, which are any of several attributes of the system that can be measured. This definition implies that physical properties have a quantitative nature—that is, they can be assigned a numerical value.

Thermodynamic properties are of two types: *extensive properties*, those that depend on the amount of mass in the system (the mass itself, volume, enthalpy, internal energy, and so on), and *intensive properties*, those independent of the amount of mass (temperature, pressure, density, specific volume, specific enthalpy, phase composition, and so on). Often we designate intensive quantities by the modifier *specific* (quantity per unit mass) or by *molar* (quantity per mole). Intensive properties can be determined as the ratio of two extensive properties; for example, molar density is the number of

moles divided by the total volume. The most important intensive properties in this chapter are

$$\begin{aligned}\rho &= \text{density, mass per volume (kg/m}^3\text{ in SI units)} \\ \hat{V} &= \text{specific volume, volume per mass (or the reciprocal of } \rho) \\ \bar{V} &= \text{molar volume, volume per amount (m}^3/\text{kg}\cdot\text{mole in SI)} \\ \bar{\rho} &= \text{molar density, moles per volume (or the reciprocal of } \bar{V})\end{aligned}$$

Thermodynamic laws and physical properties are usually expressed in terms of intensive properties.

Often the standard density of a fluid is given as the specific gravity, where

$$\gamma = \begin{cases} \frac{\rho}{\rho_{\text{water}}} & \text{for liquids} \\ \frac{\rho}{\rho_{\text{air}}} & \text{for gases} \end{cases} \dots \dots \dots \quad (4.1)$$

All densities in Eq. 4.1 are evaluated at standard conditions of 273 K and approximately 0.1 MPa (1 atm). The petroleum literature uses other standards [60°F and 14.7 psia (also 1 atm)].

It is important to understand the difference between a component and a phase. A *phase* is a homogeneous region of matter. *Homogeneous* means that it is possible to move from any point in the region to any other without crossing a discontinuous change in a property. Such a change occurs at an *interface*, which separates two phases. The three basic types of phases are gas, liquid, and solid, but of the latter two, there can be more than one type. Interfaces are by themselves of such importance that they are discussed extensively in [Chapters 9](#) and [10](#).

A *component* is any identifiable chemical entity. This definition is broad enough to distinguish between all types of chemical isomers and even among chemical components that differ only in the substitution of a radioactively tagged element. Examples are H₂O, CH₄, C₄H₁₀, Na⁺, Ca²⁺, and CO₃²⁻. Natural systems contain many components, and we are inevitably forced to combine several components into *pseudocomponents* to facilitate phase-behavior

representation and subsequent calculations. See the section on fluid characterization later in this chapter.

Components that mix (that is to say, physically co-exist) in all proportions in a single phase without forming an interface are *miscible*. Components that form an interface in all proportions are *immiscible*. Most components have some degree of miscibility, and therefore complete immiscibility is rare (although crude oil and water are close to this limit at low temperatures). Note that miscibility and immiscibility are properties of components, not phases.

The distinction between components and phases is sometimes blurred in petroleum-engineering usage, where “water” can mean the component H₂O or the liquid containing that component plus other dissolved salts, and “gas” can mean a gaseous phase or the light hydrocarbon components typically found in that phase, but which can also dissolve in oil. This distinction is, however, crucial to understanding phase behavior.

4.1.2 The Gibbs Phase Rule and Duhem’s Theorem. Gibbs (1906) observed that all intensive properties of any fluid system at equilibrium are known once the pressure, temperature, and phase compositions are specified [in total, (2 + N_C N_P) properties]. *Equilibrium*, the core idea of the phase rule, although it is seldom discussed, simply means a state of a closed system in which the properties are not changing with time, as discussed below. Unless we say otherwise, the systems discussed in this chapter are at equilibrium.

The Gibbs phase rule states that the difference between the number of required intensive parameters (2 + N_C N_P) and the number of equations [N_P + N_C(N_P - 1)] is the *degrees of freedom* N_F. The Gibbs phase rule can be stated as N_F = 2 + N_C - N_P.

A more general rule includes N_R chemical reactions, also assumed to be at equilibrium:

$$N_F = 2 + N_C - N_R - N_P \dots \dots \dots \quad (4.2)$$

N_F in the phase rule is the number of independent *intensive* thermodynamic variables that must be fixed to specify the thermodynamic state of all intensive properties of the system. Intensive thermodynamic variables include phase compositions (x_i and y_i or ω_{ij} in [Chapter 2](#)). Properties for which the definition involves the amount of a phase (e.g., \bar{n}_i , \bar{n}_j , W_i , and S_j in [Chapter 2](#)) are not thermodynamic properties. The phase rule does not specify the values of the N_F variables, nor does it identify the variables; it merely gives the number required to specify the intensive state.

The rule is practically useful only for a small number of components, but for these cases, it offers significant insight into the maximum number of phases that can form at equilibrium, as well as how many intensive properties can be independently specified. For example, suppose that for a pure fluid ($N_C = 1$), there are no chemical reactions ($N_R = 0$) and only one phase at equilibrium ($N_P = 1$). The rule says that for this case, only two intensive properties must be known to calculate the intensive state of the system ($N_F = 2$). This means that we cannot independently specify three or more intensive properties, but are free to choose which two intensive properties are set. Typically, we select properties that are easy to measure, such as temperature and pressure.

Suppose next that three equilibrium phases exist in the pure fluid. For this case, $N_F = 0$, and no intensive properties can be specified. In other words, the intensive properties, such as temperature and pressure, are determined exactly and cannot be set arbitrarily. The temperature and pressure at which the three phases coexist is known as the *triple point*. Four phases in equilibrium with each other are not allowed by the Gibbs phase rule (and neither are they observed experimentally). Therefore, three is the maximum number of phases that can form at equilibrium for a pure fluid. In general, the maximum number of phases that can coexist at equilibrium is found by setting $N_F = 0$ in Eq. 4.2; that is, $N_{P,\max} = 2 + N_C - N_R$.

Duhem's theorem is similar to the phase rule, but specifies when both the extensive and intensive states of the system are

determined. The theorem states that for any closed system containing a specified number of moles of components (from which the overall compositions can be calculated), the equilibrium state is completely determined when any two independent properties are fixed. The two independent properties may be either intensive or extensive as long as the maximum number of independent intensive properties given by the Gibbs phase rule is not exceeded. For example, when $N_F = 1$, at least one of the two variables must be extensive. When $N_F = 0$, both must be extensive.

4.1.3 Equilibrium, Stability, and Reversible Thermodynamic Systems. Thermodynamics predicts the nature of a new equilibrium state, not the rate at which that state is reached. One of the characteristics of equilibrium is that the macroscopic thermodynamic properties are time-invariant. The criterion of time invariance is a necessary, but not a sufficient condition for equilibrium. Some systems can exist in metastable states that are time-invariant. For example, at the conditions of the Earth's surface, diamonds are in a metastable state of pure carbon, whereas graphite is the equilibrium state. It takes a significant "energy kick" or catalyst to convert diamonds to their equilibrium state. The equilibrium state is the global minimum in free energy; metastable states are local minima. Phase-behavior calculations can converge to metastable or false equilibrium states in the search for the equilibrium state (Firoozbadi 1999; Whitson and Brule 2000).

4.2 Phase Behavior of Pure Components

This section discusses the phase behavior of pure components (single-component systems) in terms of pressure/temperature (P/T) and pressure vs. molar-volume diagrams.

Intuitively, we expect a relationship among the three intensive properties, temperature, pressure, and molar volume, for a pure component. Using density, molar density, or specific volume in place of the molar volume would entail no loss of generality. However, in two dimensions, it is difficult to represent this relationship completely

(see [Fig. 4.3](#) for example), but we can easily plot any two of these variables.

4.2.1 Pressure/Temperature Diagrams. [Fig. 4.1](#) shows a schematic P/T plot for a pure component. The lines or curves on the diagram represent temperatures and pressures at which phase transitions occur. These phase boundaries separate the diagram into regions in which the system consists of a single phase. Specifically, the phase boundary separating the solid and liquid phases is the *fusion* or melting curve. The boundary between the solid and gas phases is the *sublimation* curve, and that between the liquid and vapor phases is the *vapor-pressure* curve. On the basis of our definition of a phase, a discontinuous change in system properties occurs when any phase boundary is crossed.

The phase transitions referred to in this chapter are those of fluids in thermodynamic equilibrium. Therefore, it is possible for a fluid in a particular phase to exist momentarily at a P/T coordinate corresponding to another phase. However, this condition is not permanent because the material will eventually convert to the appropriate stable equilibrium state.

From the phase rule (Eq. 4.2), we know that when two phases coexist, $N_F = 1$. This can happen for a pure component only on the phase boundaries because a curve has one degree of freedom. At a minimum, pure components have three such curves: a transition between a gas and a solid (sublimation curve), between a solid and a liquid (fusion), and between a liquid and a gas (vapor pressure). The vapor/pressure line (curve) is by far the most important for EOR.

By the same argument, three phases can coexist at only a single point in P/T space because $N_F = 0$ for this condition. This single point is a *triple point* and is shown in [Fig. 4.1](#) as the point at which the three phase boundaries intersect. Phase boundaries may terminate at a *critical point*. The most interesting of these is the critical point at the termination of the vapor-pressure curve. The coordinates of the critical point on a P/T plot are the critical temperature T_c and the critical pressure P_c . At the critical point, gas

and liquid properties are identical. The region above the critical point represents a transition from a liquid to a gaseous state without a discontinuous change in properties. Because the state of matter in this region is neither clearly a liquid nor clearly a gas, the fluid in this region is called a *supercritical fluid*. The exact definition of the supercritical fluid region is arbitrary: most texts take it to be the region to the right of the critical temperature ($T > T_c$), although it would seem that defining it to be the region to the right of *and* above the critical point ($T > T_c$ and $P > P_c$) would be more consistent with the behavior of mixtures. Because there is no actual boundary that defines the supercritical region, fluids are often described as liquid-like or vapor-like on the basis of their appearance, densities, and viscosities.

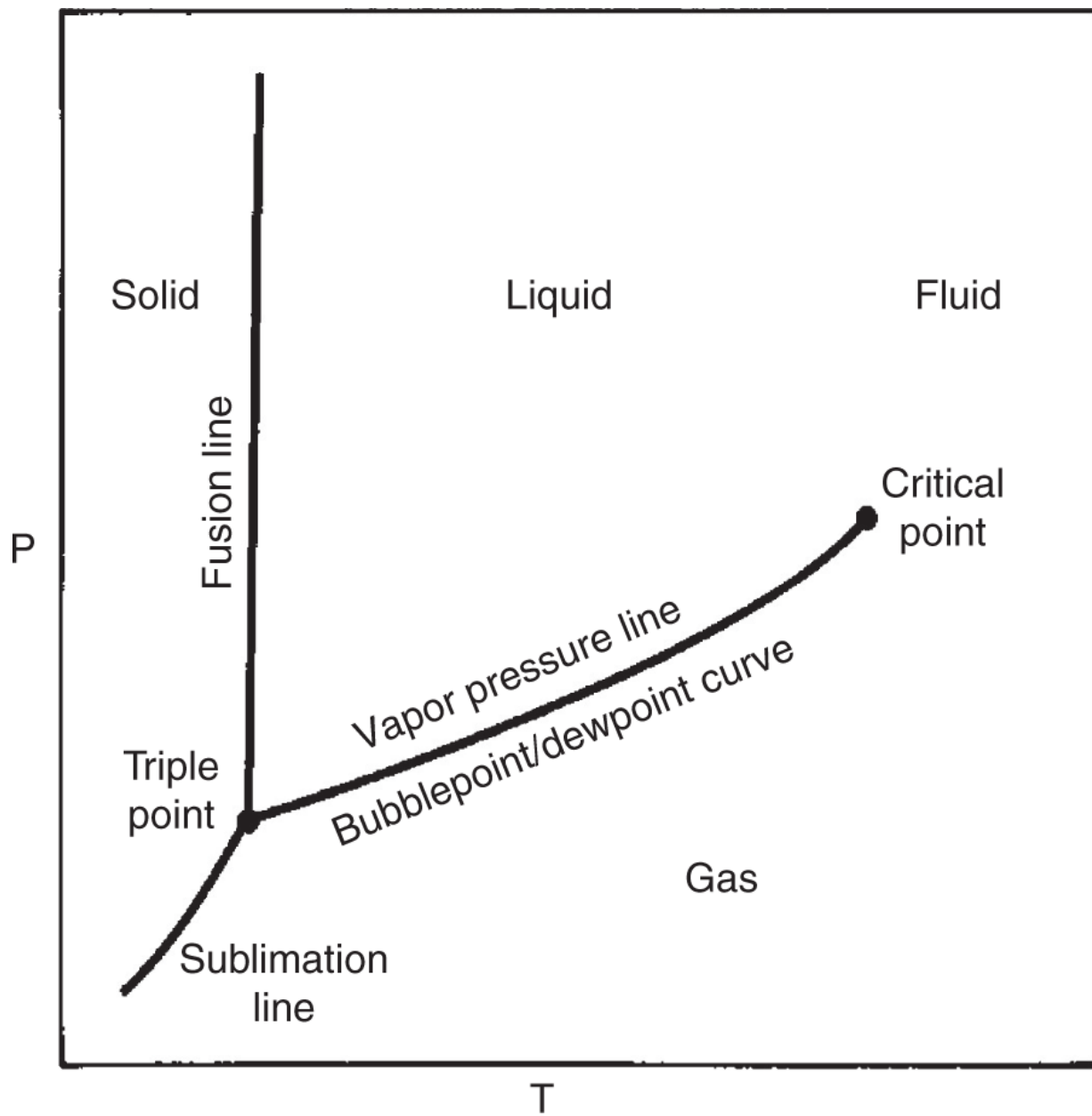


Fig. 4.1—Schematic pure-component P/T diagram.

The behavior shown in Fig. 4.1 for a pure component is qualitatively correct, but less detailed than that which can be observed. There can exist, in fact, more than one triple point where solid-solid-liquid equilibria are observed. Water is a familiar example of a pure component that exhibits this behavior. Remarkably, observations of multiple gas phases for pure components have also been reported (Schneider 1970). Such nuances are not the concern

of this text, which emphasizes gas-liquid and liquid-liquid equilibria. In fact, in all further discussions of phase behavior, we ignore triple points and solid-phase equilibria. Even with these aspects omitted, the P/T diagrams in this chapter are only qualitatively correct because the critical point and the vapor-pressure curve vary greatly among components. [Fig. 4.2](#) shows some quantitative comparisons.

Critical phenomena play an important role in the properties of EOR fluids. If a laboratory pressure cell contains a pure component on its vapor/pressure curve, the cell contains two regions (gas and liquid) of distinctly different (sometimes visually different) properties. As the vapor/pressure curve is traversed from the original point to the critical point, the properties of the individual phases approach each other. Very near the critical point, the interface between the phases, which was sharp at the original temperature and pressure, becomes blurred and may even appear to take on a nonzero thickness. At the critical point, these trends continue until there is no longer a distinction between phases. If we were to continue on an extension of the vapor/pressure curve, there would be a single fluid phase.

An important characteristic of fluids near the critical point is that the thermodynamic properties of all phases approach each other. In liquid-vapor equilibrium, the densities and viscosities of the vapor and liquid phases become identical there. Furthermore, interfacial tensions between phases disappear as a single-phase fluid is formed. EOR technology often uses this fact by injecting fluids, such as supercritical CO_2 that are miscible or nearly miscible, with oil. If the CO_2 is miscible, of course, the interface between CO_2 and oil disappears. Oil previously trapped as a separate phase by capillary forces is now mobilized and can flow. If the CO_2 and the oil are nearly miscible (i.e., close to a critical point at which the two phases become miscible), the interfacial tension is small, and it may still be possible to mobilize oil in spite of the interface between CO_2 and oil. In this way, injection of miscible and near-miscible solvents can greatly facilitate production of hydrocarbon components that were previously not recoverable by primary and secondary recovery

techniques. An accurate phase-behavior characterization of critical regions is, therefore, very important in solvent EOR.

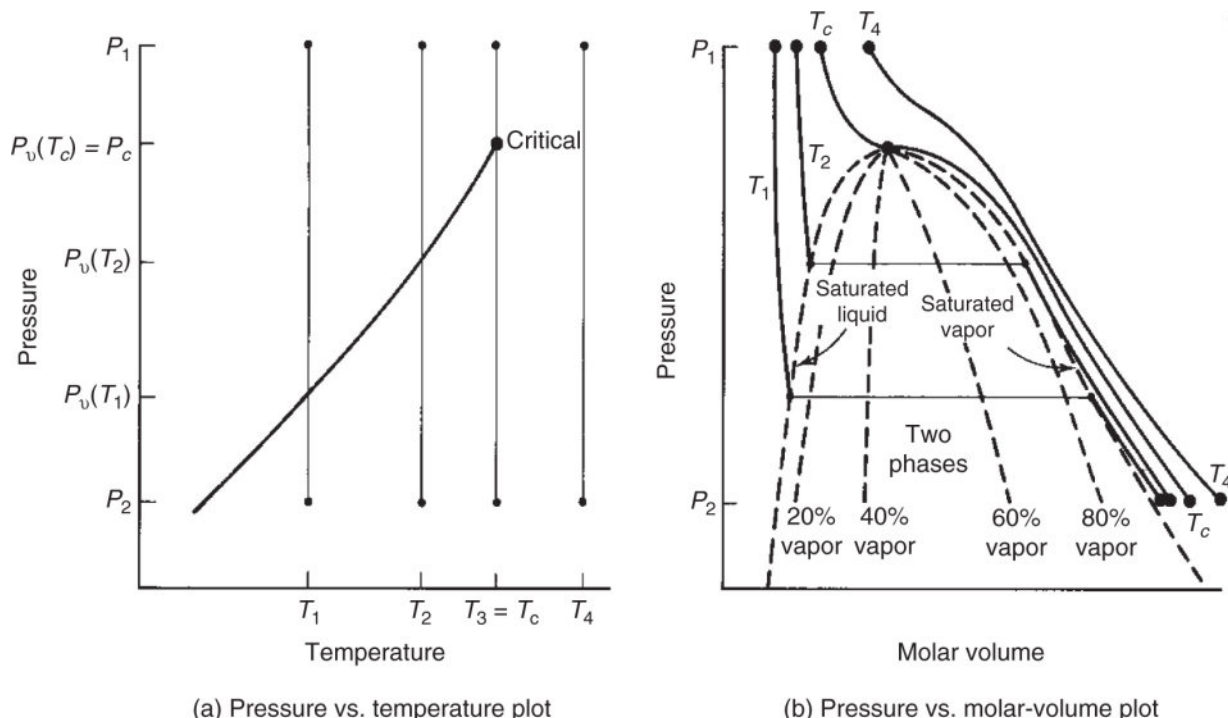


Fig. 4.2—Schematic pressure vs. temperature (a) and pressure vs. molar-volume diagrams (b).

4.2.2 Pressure vs. Molar-Volume Diagram. One method of representing the way in which the discontinuity in intensive properties between phases vanishes at the critical point is the pressure vs. molar-volume diagram. Fig. 4.2 compares such a diagram with the corresponding P/T diagram. Both schematic plots show *isotherms*, changes in pressure from a high pressure P_1 to a lower pressure P_2 , at four constant temperatures, T_1 through T_4 .

At conditions (P_1, T_1), the pure component is a single-phase liquid. As pressure decreases at constant temperature, the molar volume increases, but only slightly, because liquids are relatively incompressible. At $P = P_v(T_1)$, the molar volume increases discontinuously from some small value to a much larger value as the material changes from a single-liquid to a single-gas phase. Because the change takes place at constant temperature and pressure, this

vaporization appears as a horizontal line in [Fig. 4.2b](#). Subsequent pressure reduction again causes the molar volume to increase, now at a much faster rate because the compressibility of the gas phase is much greater than that of the liquid phase. The endpoints of the horizontal segment of the pressure vs. molar-volume plot represent two coexisting phases in equilibrium with each other at the same temperature and pressure. The liquid and vapor phases are said to be *saturated* at $P = P_V(T_1)$. Saturation is a commonly used word to refer to a phase that cannot accept any other components.

At a higher temperature T_2 , the behavior is qualitatively the same. The isotherm starts at a slightly higher molar volume, the vaporization at $P = P_V(T_2)$ is at a higher pressure, and the discontinuous change from saturated liquid to saturated vapor molar volume is not as large as at T_1 . These trends continue as the isotherm temperature approaches $T_3 = T_c$. All isotherms on the pressure vs. molar-volume plot are continuously decreasing functions with discontinuous first derivatives at the vapor/pressure line.

At the critical temperature, the two phases become identical, and the saturated liquid and gas molar volumes coincide. Because this temperature is only infinitesimally higher than one at which there would still be distinguishable liquid and gas phases, the isotherm at $T = T_c$ (the critical isotherm) decreases continuously with continuous first derivatives. At the critical point $P = P_c$, the critical isotherm must have zero slope and zero curvature, or

$$\left(\frac{\partial P}{\partial \bar{V}}\right)_{T_c, P_c} = \left(\frac{\partial^2 P}{\partial \bar{V}^2}\right)_{T_c, P_c} = 0. \dots \quad (4.3)$$

These *critical constraints* follow from the physical argument given above and can also be derived by requiring a minimum in the Gibbs free energy at the critical point (Denbigh 1968).

At isotherm temperatures above the critical temperature (e.g., $T = T_4$ in [Fig. 4.2](#)), the isotherm is decreasing monotonically with

continuous first derivatives, but without points of zero slope or curvature.

The endpoints of all the horizontal line segments below the critical point in the pressure vs. molar-volume plot define a two-phase envelope, as shown in [Fig. 4.2b](#). It is also possible to show lines of constant relative amounts of liquid and gas within the two-phase envelope. These *quality* lines (dotted lines in [Fig. 4.2b](#)) must converge to the critical point. The two-phase envelope on a pressure vs. molar-volume plot for a pure component, which projects onto a line in a *P/T* diagram, is not the same as the two-phase envelope on a *P/T* diagram for *mixtures*. Both [Figs. 4.1](#) and [4.2](#) are individual planar representations of the 3D relation among temperature, pressure, and molar volume for a pure component. [Fig. 4.3](#) illustrates the 3D character of this relation for water.

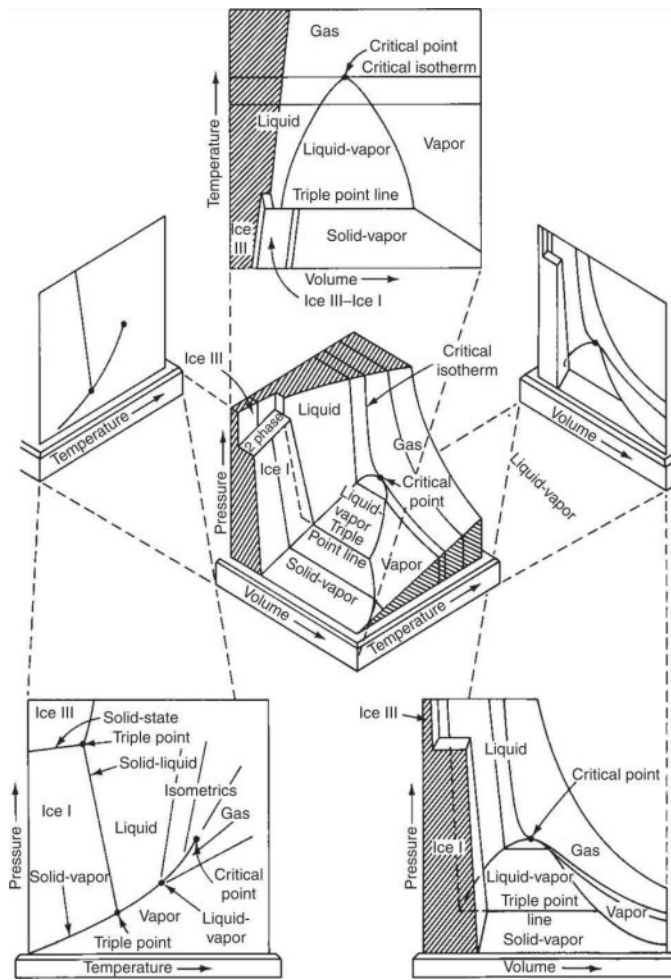


Fig. 4.3—Schematic pressure vs. molar volume vs. temperature surface and projections for water (Himmelblau 1982).

For a two-phase pure fluid at constant temperature, the properties of the phases do not change as the volume changes. For example, the overall density of the two-phase mixture changes as the closed system is compressed or expanded, but the phase molar densities remain fixed. Only the amounts of the phases change as the volume changes. The overall molar volume is related to its phase molar volumes by

$$\bar{V} = \bar{V}_L \bar{n}_L + \bar{V}_V \bar{n}_V. \dots \quad (4.4)$$

Other intensive properties, such as molar enthalpy and entropy, have relationships similar to Eq. 4.4. Therefore, solving for the phase molar fraction for each of them gives

$$\bar{n}_V = \frac{\bar{V} - \bar{V}_L}{\bar{V}_V - \bar{V}_L} = \frac{\bar{H} - \bar{H}_L}{\bar{H}_V - \bar{H}_L} = \dots \quad (4.5)$$

Eqs. 4.5 are known as *lever rules*. The quality lines as shown in [Fig. 4.2](#) are defined on a molar basis as \bar{n}_V written as a percentage.

Finally, although we illustrate the phase envelope of a pure component on a pressure-molar-volume diagram, discontinuities in properties below the critical point are present for all other intensive properties except temperature and pressure (see [Fig. 11.6](#), the pressure vs. enthalpy diagram for water).

4.3 Phase Behavior of Mixtures

The purpose of EOR is to recover crude oil, which is a mixture of many components. Because the phase behavior of hydrocarbon mixtures is complex, in this and the next section, we simply compare the phase behavior of mixtures to that of single (or pure) components and introduce pressure/composition (P/z) and ternary diagrams.

4.3.1 Pressure/Temperature Diagrams. For a multicomponent mixture, $N_F > 2$ when two phases are present (see the phase rule described in Section 4.1). Therefore, one can freely vary T and P while retaining two phases. Conventionally, one plots the phase diagram for multicomponent mixtures as a function of P and T at a fixed overall composition. On such a diagram, the two phases coexist within a region, or envelope, as compared to the single-component case in which two phases coexist only along a curve on a P/T phase diagram ([Fig. 4.1](#)).

Consider a change in pressure in [Fig. 4.4](#) from P_1 to P_5 at constant temperature T_2 . The phase envelope is fixed for constant overall composition (w_i or z_i). Because the indicated change is usually brought about by changing the volume of a pressure cell at constant composition and temperature, the process is frequently called a *constant-composition expansion*.

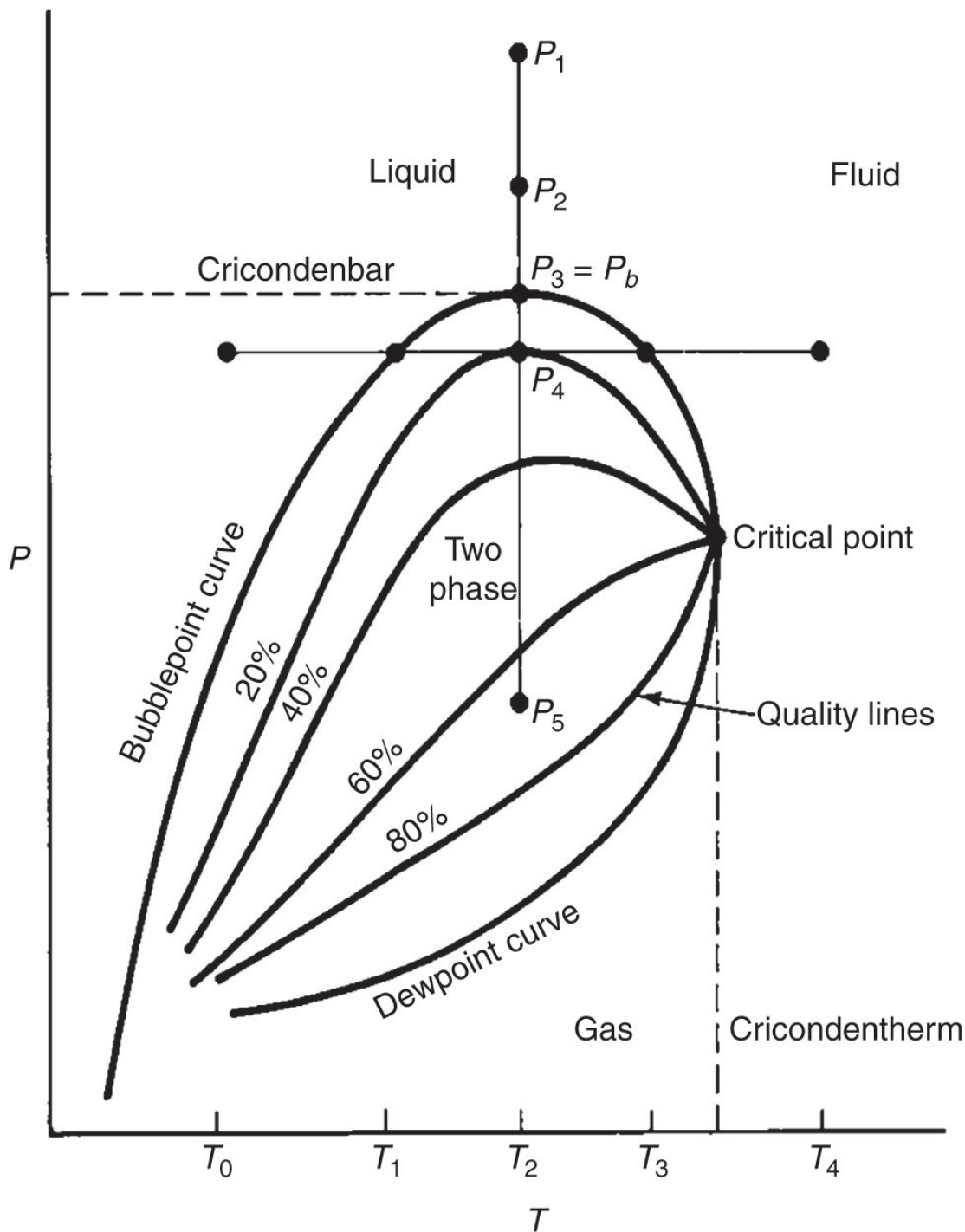


Fig. 4.4—Schematic pressure vs. temperature diagram for hydrocarbon mixtures (constant composition).

From P_1 to P_3 , the material in the cell is in a single liquid phase. At P_3 , a small amount of vapor phase begins to form. The upper boundary of the phase envelope passing through this point is the

bubblepoint curve, and the y -coordinate at this point is the *bubblepoint pressure* at the fixed temperature. From P_3 to P_5 , more gas forms as the liquid phase vaporizes. This vaporization takes place over a finite pressure range, in contrast to the behavior of a pure component. Continuing the constant-composition expansion to pressures lower than P_5 would result in eventually reaching a pressure at which the liquid phase would disappear, appearing only as drops in the cell just before this point. The pressure at which the liquid vanishes is the *dewpoint pressure* at the fixed temperature. The lower boundary of the phase envelope, the locus of dewpoint pressure at all T , is the *dewpoint curve*.

For a pure component (Figs. 4.1 to 4.3), the dewpoint and bubblepoint curves coincide.

Within the two-phase envelope, there exist quality lines that, as before, indicate constant relative amounts of liquid and vapor. The composition of the liquid and gas phases is different at each point within the envelope, and both change continuously as the pressure decreases.

Phase compositions are not shown on the P/T plot. However, we do know that the liquid and gas phases are saturated with respect to each other in the two-phase envelope. Hence, at any T and P within the envelope, the liquid phase is at its bubblepoint and the gas phase is at its dewpoint. The quality lines converge to a common point at the critical point of the mixture, although this point does not, in general, occur at extreme values of temperature or pressure on the phase-envelope boundary. The maximum pressure on the phase-envelope boundary is the *cricondenbar*. The maximum temperature on the phase envelope is the *cricondentherm*. These features can be confused with the critical point in pure-component systems; hence, the best definition of the critical point for mixtures is the temperature and pressure at which the two phases become identical. The cricondenbar and cricondentherm typically do not coincide with the critical temperature and pressure.

For mixtures, there exists in general a pressure range between the cricondenbar and P_c and between the cricondentherm and T_c

where *retrograde* behavior can occur. A horizontal constant-pressure line in [Fig. 4.4](#) at $P = P_4$ begins in the liquid region at T_0 and ends in the fluid region at T_4 . As temperature is increased, gas begins to form at the bubblepoint temperature T_1 and increases in amount from then on. However, at T_2 , the amount of gas begins to decrease, and the gas phase vanishes entirely at a second bubblepoint T_3 . From T_2 to T_3 , the behavior is contrary to intuition—a gas phase that disappears as temperature increases—and the phenomenon is called retrograde vaporization.

Retrograde behavior does not occur over the entire range between the two bubblepoint temperatures but only over the range from T_2 to T_3 . By performing the above thought experiment at several pressures, one can show that retrograde behavior occurs only over a region bounded by the bubblepoint curve on the right and a curve connecting the points of zero slope on the quality lines on the left (McCain 2000).

Although it does not occur in the P/T diagram in [Fig. 4.4](#), retrograde phenomena are also observed for changes in pressure at constant temperature. This case, which is of more interest to a reservoir engineer, happens when the cricondentherm is larger than T_c and the constant temperature is between these extremes. This type of retrograde behavior is a prominent feature of many hydrocarbon reservoirs, but it has little impact on EOR. Retrograde behavior does occur on pressure-composition diagrams, as discussed in [Chapter 7](#).

We do not discuss here the pressure vs. molar-volume behavior of hydrocarbon mixtures in detail. The main differences between the behavior of pure components and that of mixtures is that the discontinuous changes in molar volume do not occur at constant P and the critical point no longer occurs at the top of the two-phase region (see Exercise 4.4). These differences cause interesting variations in the shape of pressure vs. molar-volume diagrams for mixtures, but again are not directly relevant to EOR.

Because many EOR processes are highly dependent on composition, the behavior of the P/T envelope as the overall composition of the mixture changes is very important. Consider the dilution of a crude oil M_4 with a more volatile pure component A, as shown in [Fig. 4.5](#). As the overall mole fraction of A increases, the phase envelope migrates toward the vertical axis, increasing the size of the gas region. Simultaneously, the phase envelope shrinks as it approaches the vapor/pressure curve of the pure component A. There are, of course, many mixtures ([Fig. 4.5](#) shows only three) of the crude oil with A. Each mixture has its respective critical point in P/T space, which also migrates to the critical point of the pure component on a critical locus. The overall composition of a mixture at a critical point is the *critical mixture* composition at that temperature and pressure.

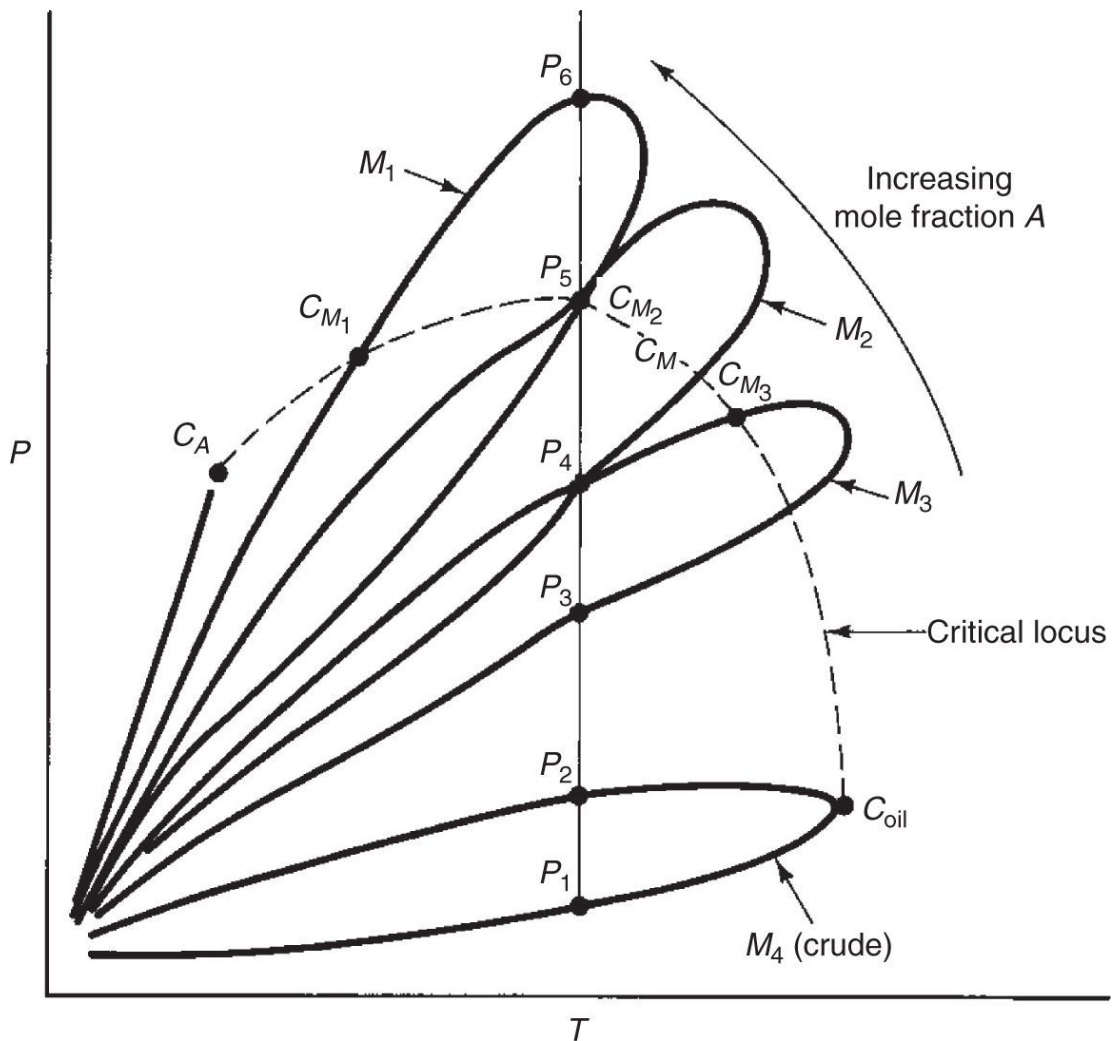


Fig. 4.5—Schematic dilution of a crude oil by a more volatile pure component.

4.3.2 Pressure/Composition Diagrams. The phase behavior of the dilution in Fig. 4.5 on a plot of mole fraction of component A vs. pressure at fixed temperature shows composition information directly. Such a plot is a *pressure/composition*, or *P/z*, plot. The *P/z* plot for the sequence of mixtures in Fig. 4.5 is shown in Fig. 4.6. Because the *P/T* diagram in Fig. 4.6 shows only three mixtures and does not show quality lines, phase-envelope boundaries are represented at relatively few points.

Starting at some high pressure in Fig. 4.5 and following a line of constant temperature as pressure is reduced produces a dewpoint curve for mixture M_1 at pressure P_6 . Because this mixture is rich in

component A, this point plots nearest the right vertical axis in [Fig. 4.6](#) at the pressure coordinate P_6 . Continuing down the constant-temperature line, at P_5 the critical point for mixture M_2 is encountered (mixture M_2 is the critical composition at this temperature and pressure). However, this point is also a second dewpoint for mixture M_1 ; hence, P_5 plots at the same vertical coordinate for both mixtures in [Fig. 4.6](#), but with different horizontal coordinates. At P_4 , there is a bubblepoint for mixture M_3 and a dewpoint for M_2 . These points again define the corresponding phase boundaries of the P/z plot in [Fig. 4.6](#). The process continues to successively lower pressures in the same manner. Each pressure below the critical point is simultaneously a bubblepoint and a dewpoint pressure for mixtures of different overall compositions. The pressures P_2 and P_1 are the bubblepoint and dewpoint pressures of the undiluted crude oil. The two-phase envelope in [Fig. 4.6](#) does not intersect the right vertical axis because the fixed temperature is above the critical temperature of the pure component A. The diagram shows the closure of the two-phase envelope as well as a few quality lines.

Because the entire P/z diagram is at constant temperature, we cannot represent the phase behavior at another temperature without showing several diagrams. More important, the composition plotted on the horizontal axis of the P/z plot is the overall composition, not either of the phase compositions. This means that horizontal lines do not connect equilibrium mixtures. Horizontal lines that connect equilibrium mixtures are known as *tie lines*. Such tie lines do exist but are, in general, oriented on a horizontal line in a hyperspace for which the coordinates are the phase compositions. Finally, although [Fig. 4.6](#) is a schematic, it bears a qualitative resemblance to the actual P/z diagrams shown in [Figs. 7.5 through 7.8](#).

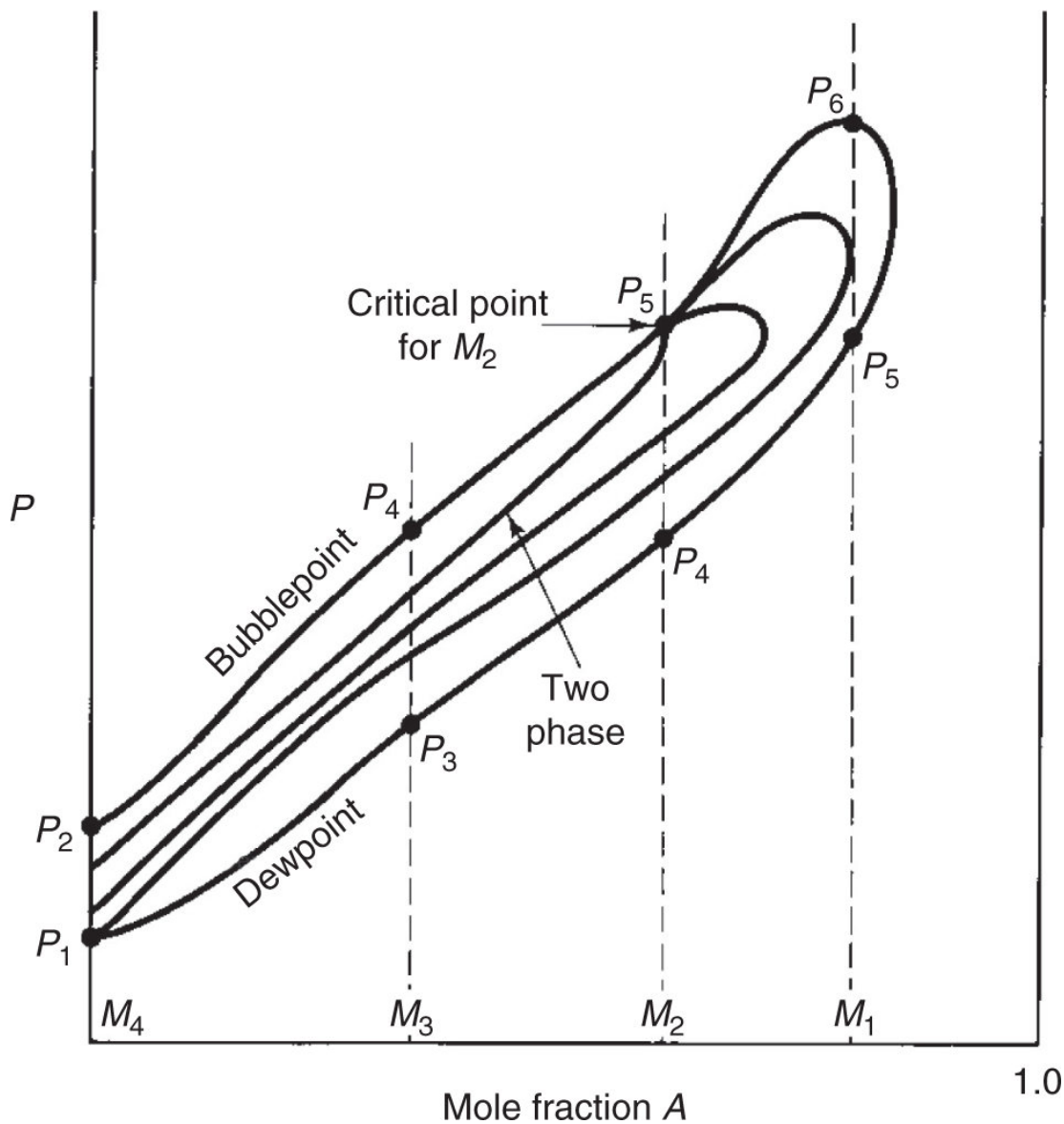


Fig. 4.6—Pressure vs. composition plot for the dilution in [Fig. 4.5](#).

4.4 Ternary Diagrams

A P/z plot sacrifices a degree of freedom (temperature) to obtain compositional information. However, the resulting diagrams can show only the composition with respect to one component, and this representation is often insufficient for the multitude of compositions that can form in an EOR displacement. A plot that represents more composition information is the *ternary diagram*.

4.4.1 Definitions. Imagine a mixture, at fixed temperature and pressure, consisting of three components: 1, 2, and 3. The components may be pure components. More commonly in EOR, they are pseudocomponents, consisting of several pure components (see discussion in Section 4.5). The composition of the mixture is a point on a plot of the mole fraction of Component 3 vs. that of Component 2. We need to plot the concentrations of only two of the components because the concentration of the third can always be obtained by subtracting the sum of the mole fractions of Components 2 and 3 from that of Component 1. This means that all possible compositions will lie within a right triangle for which the hypotenuse is a line from 1.0 on the y -axis to 1.0 on the x -axis. Although ternary diagrams are on occasion shown in this way (see [Fig. 7.11](#)), they are most commonly plotted so that the right triangle is transformed to an equilateral triangle, as in [Fig. 4.7](#).

All possible ternary compositions fall on the interior of the equilateral triangle; the boundaries of the triangle represent binary mixtures (the component at the apex opposite to the particular side is absent), and the apices represent pure components. Therefore, in [Fig. 4.7](#), point M_1 is a mixture having 20%, 50%, and 30% of Components 1, 2, and 3, respectively; point M_2 is a binary mixture of 70% Component 1 and 30% Component 3; and point M_3 is 100% Component 2. Representing the compositions in this manner is possible for any concentration variable (mole fraction, volume fraction, mass fraction) that sums to a constant.

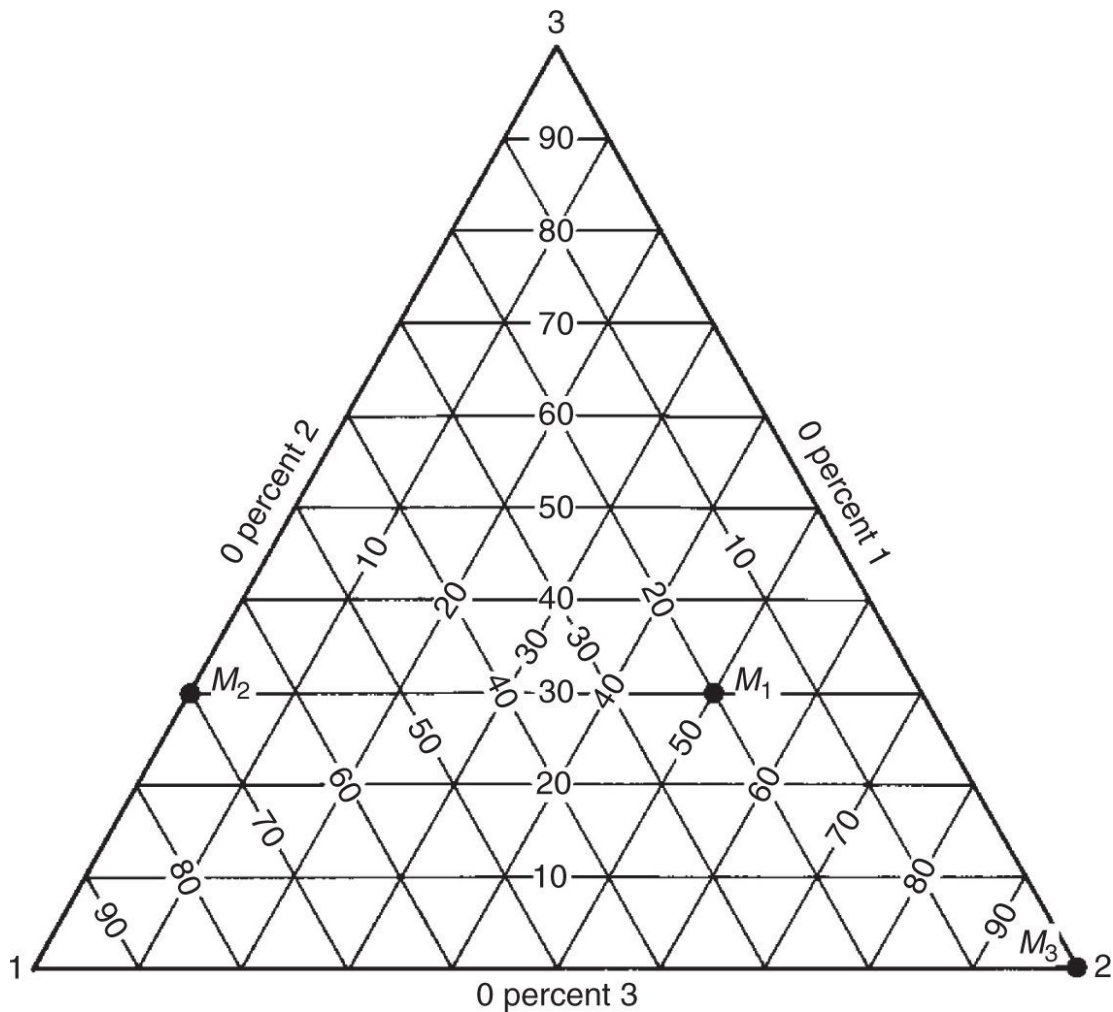


Fig. 4.7—Scales on ternary diagram.

Ternary diagrams are extremely useful in EOR because they can simultaneously represent phase and overall compositions as well as relative amounts. The correspondence of the *P/T* diagram to the ternary diagrams in [Figs. 4.8 and 4.9](#) is comparable to the *P/z* diagrams in [Figs. 4.5 and 4.6](#). Here, we consider a ternary system consisting of Components 1, 2, and 3 and consider the dilution of mixtures having constant ratios of Components 2 and 3 by Component 1. Each dilution represents a line corresponding to a fixed ratio of Component 2 to Component 3 on the ternary in [Fig. 4.9](#).

We follow the formation and disappearance of phases on the ternary diagram at the fixed temperature and pressure indicated by the solid squares in [Fig. 4.8](#). For the dilution of Component 3 by

Component 1, the reference temperature and pressure are above the critical locus in the upper left panel ([Fig. 4.8a](#)). Therefore, the C_1 to C_3 axis of the ternary indicates no phase changes. The C_1 to C_2 binary dilution in the upper right panel ([Fig. 4.8a](#)) does encounter phase changes, and in fact, the reference temperature and pressure is a bubblepoint for a mixture of 25% C_1 and a dewpoint for a mixture of 85% C_1 . These phase transitions are shown on the C_1 to C_2 axis on the ternary diagram. The dilution indicated in the middle left panel ([Fig. 4.8b](#)) shows phase transitions at 82 and 21%, respectively, which are also plotted on the ternary. For the dilution of the 1:3 mixture, the critical locus passes through the fixed temperature and pressure, and this composition (25% C_1) is the critical composition of the ternary mixture. This composition is indicated on the ternary diagram in [Fig. 4.9](#) as a *plait* point after the more common designation of the critical mixture in liquid-liquid phase equilibria. At the fixed temperature and pressure, a second phase transition can exist—a dewpoint at 67% C_1 —at the same temperature and pressure. After making several dilution passes through the ternary diagram, the points at which phase transitions occur define a closed curve in [Fig. 4.9](#). This curve, the *binodal* curve, separates regions of one- and two-phase behavior. Within the region enclosed by the binodal curve, two phases exist, and outside this region, all components are in a single phase.

Note that Components 1 and 2 are miscible, as are Components 2 and 3. Components 1 and 2 are semimiscible.

4.4.2 Phase Compositions. It is possible to represent the phase compositions as well as the overall composition on the same ternary diagram. Consider an overall composition C_i on the inside of the binodal curve in [Fig. 4.10](#). For that composition,

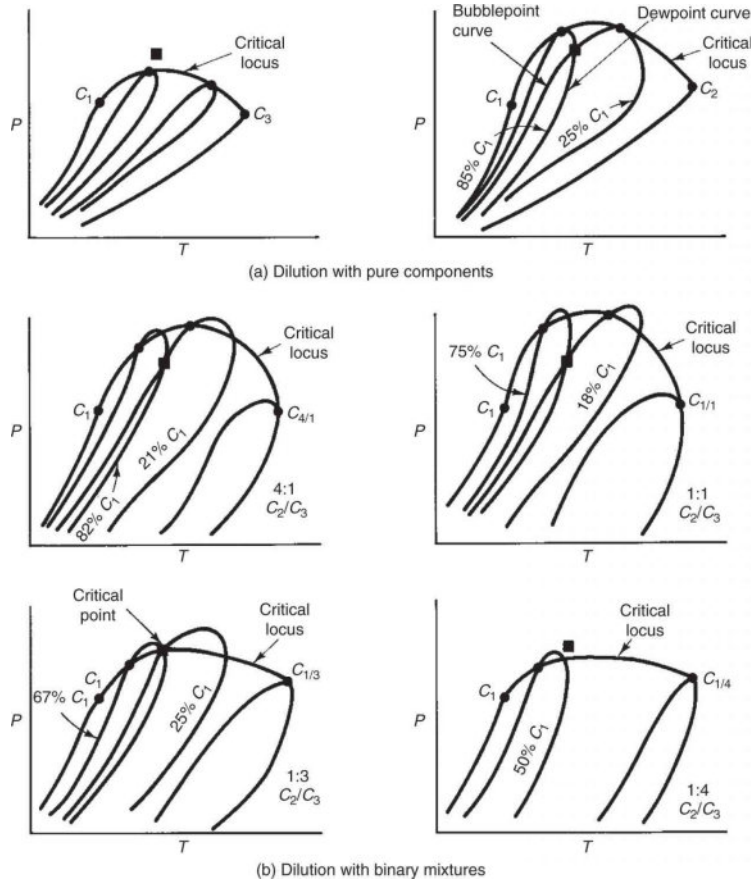


Fig. 4.8—Schematic evolution of the P/T diagram in a three-component system. The black square represents P and T of the ternary diagram in Fig. 4.9.

$$C_i = C_{i1}S_1 + C_{i2}S_2 \quad i = 1, 2, 3, \dots \quad (4.6)$$

where C_{ij} is the concentration of component i in phase j and S_j is the relative amount of phase j . By convention, we take Phase 1 to be the C_1 -rich phase and Phase 2 to be the C_1 -lean phase. Because $S_1 + S_2 = 1$, we can eliminate S_1 from two of the equations in Eq. 4.6 to give

$$S_2 = \frac{C_3 - C_{31}}{C_{32} - C_{31}} = \frac{C_1 - C_{11}}{C_{12} - C_{11}}. \quad (4.7)$$

This equation, which is the counterpart to Eq. 4.5 in terms of volume fractions, says that a line through the composition of Phase 1 and the overall composition has the same slope as a line passing through the composition of Phase 2 and the overall composition.

Both lines, therefore, are merely segments of the same straight line that passes through both phase compositions and the overall composition. The intersection of these tie lines with the binodal curve gives the phase compositions shown in Fig. 4.10. The entire region within the binodal curve can be filled with an infinite number of these tie lines, which must vanish as the plait point is approached because all phase compositions are equal at this point. Of course, there are no tie lines in the single-phase region.

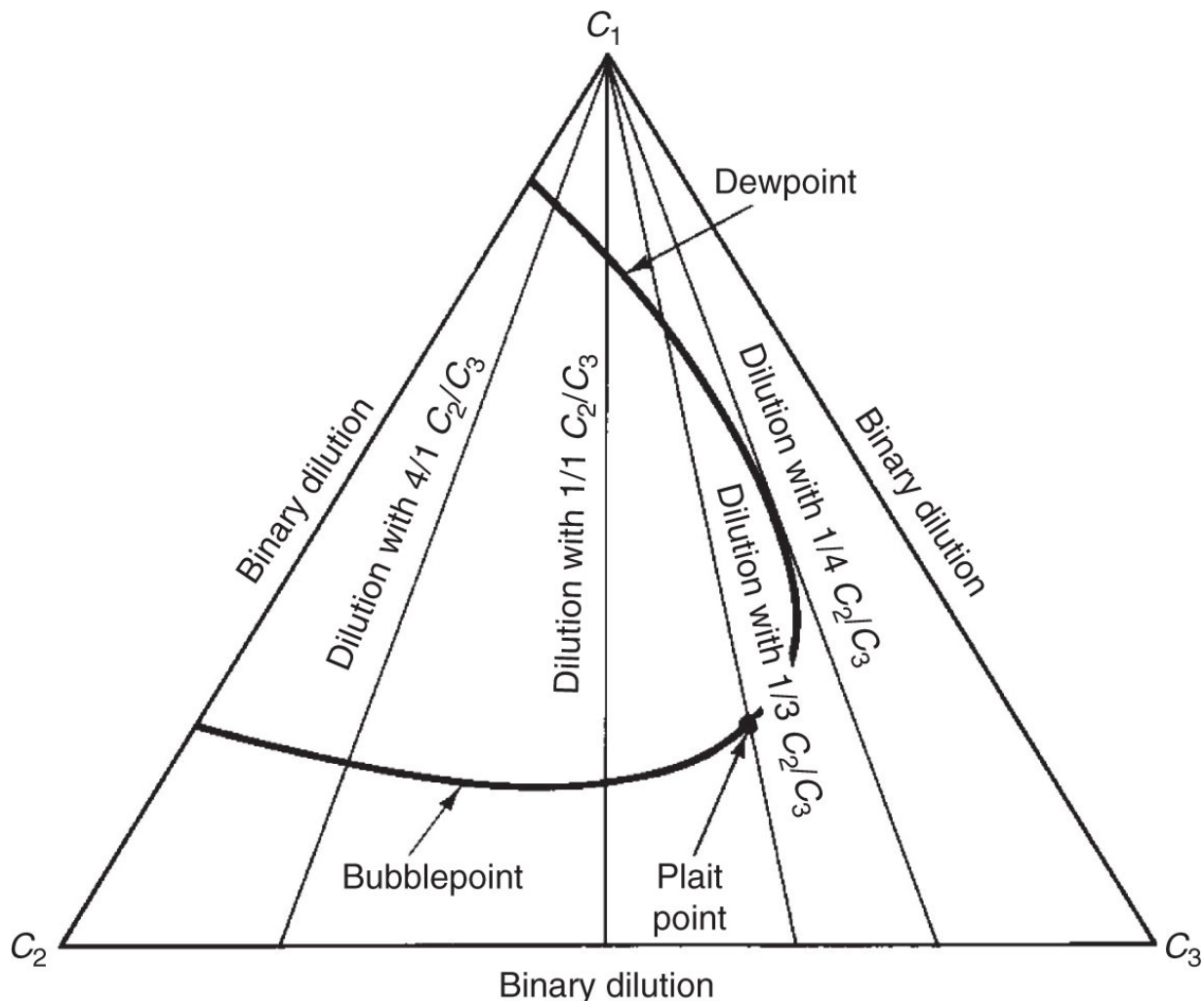


Fig. 4.9—Schematic ternary diagram of dilutions in Fig. 4.8.

Furthermore, Eq. 4.7 implies, by a similar triangle argument, that the length of the line segment between C_i and C_{i1} divided by the length of the segment between C_{i2} and C_{i1} is the relative amount S_2 .

This, of course, is again the *lever rule*, which can also be derived for S_1 . By holding S_2 constant and allowing C_i to vary, we can construct quality lines, as indicated in Fig. 4.10, which must also converge to the plait point, as do the tie lines.

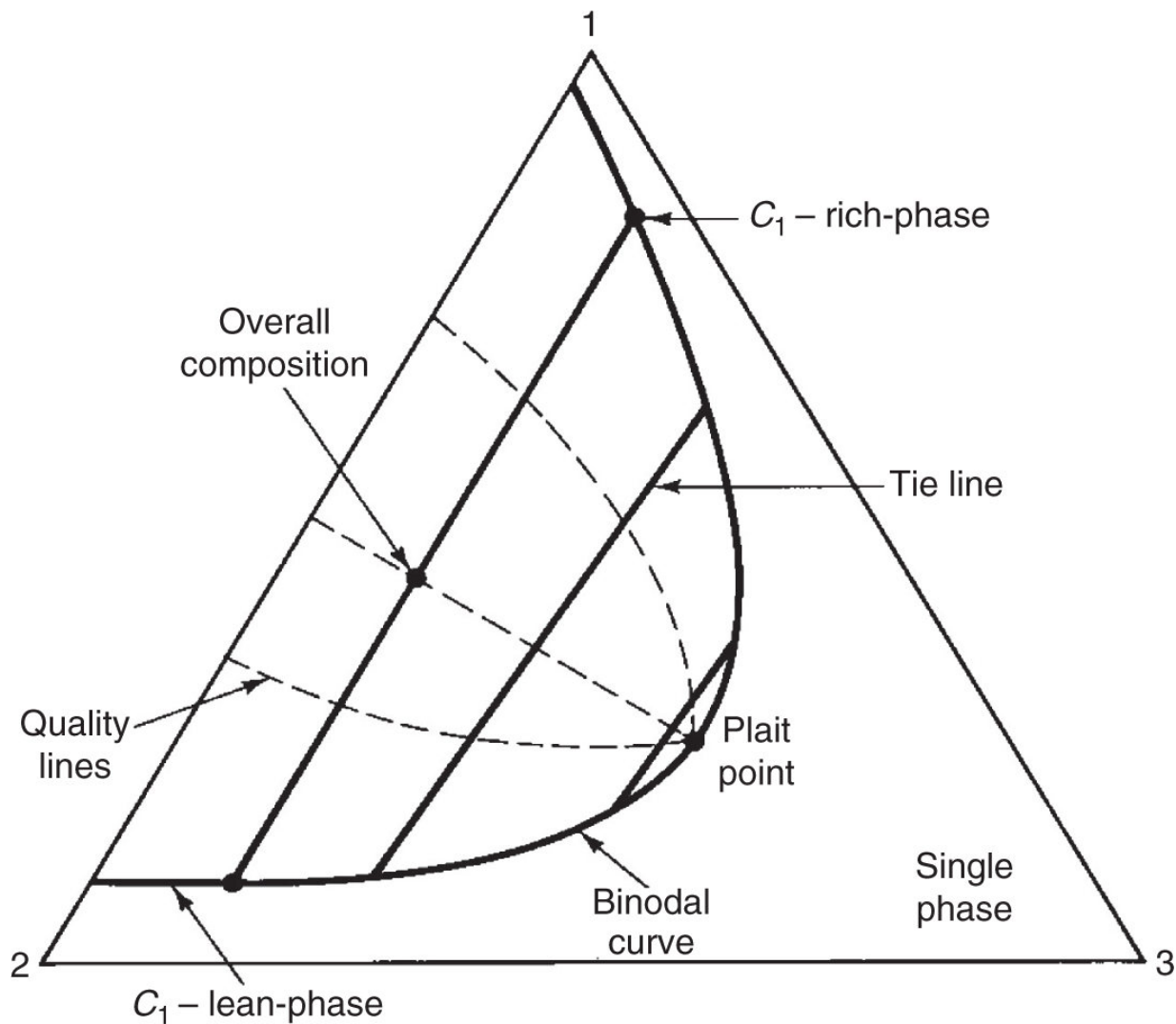


Fig. 4.10—Two-phase ternary equilibria.

Tie lines are graphical representations of phase equilibrium. Assuming, for the moment, that the apices of the ternary diagram represent true components, the phase rule predicts that there will be $N_F = 1$ degrees of freedom for mixtures within the binodal curve because temperature and pressure are already specified. Therefore, it is sufficient to specify one concentration in either phase to specify

the state of the mixture completely. A single coordinate of any point on the binodal curve gives both phase compositions if the tie lines are known. This exercise does not determine the relative amounts of the phases present because these are not state variables. Nor does specifying a single coordinate of the overall concentration suffice because these, in general, do not lie on the binodal curve. Of course, it is possible to calculate the phase compositions and the phase relative amounts from equilibrium relations, but these must be supplemented in “flash calculations” by additional mass-balance relations to obtain the amounts of each phase.

4.4.3 Three-Phase Behavior. When three phases form, there are no degrees of freedom ($N_F = 0$) for a ternary mixture at fixed T and P . The state of the system (in terms of intensive variables) is entirely determined. It follows from this that three-phase regions are represented on ternary diagrams as smaller subtriangles, called *tie triangles*, embedded within the larger ternary triangle ([Fig. 4.11](#)). Because no tie lines exist in three-phase regions, the apices or *invariant* points of the subtriangle give the phase compositions of any overall composition within that subtriangle. The graphical construction indicated in [Fig. 4.11](#) gives the relative amounts of the three phases present (see Hougen et al. 1966 and Exercise 4.5).

A point on a nonapex side of the tie triangle may be regarded as being simultaneously in the three-phase region or in a two-phase region; therefore, the tie triangle must always be bounded on a nonapex side by a two-phase region for which the side of the tie triangle is a tie line of the adjoining two-phase region. By the same argument, the apices of the tie triangle must adjoin, at least in some nonzero region, a single-phase region. To be sure, the adjoining two-phase regions can be quite small (see [Fig. 9.6](#)).

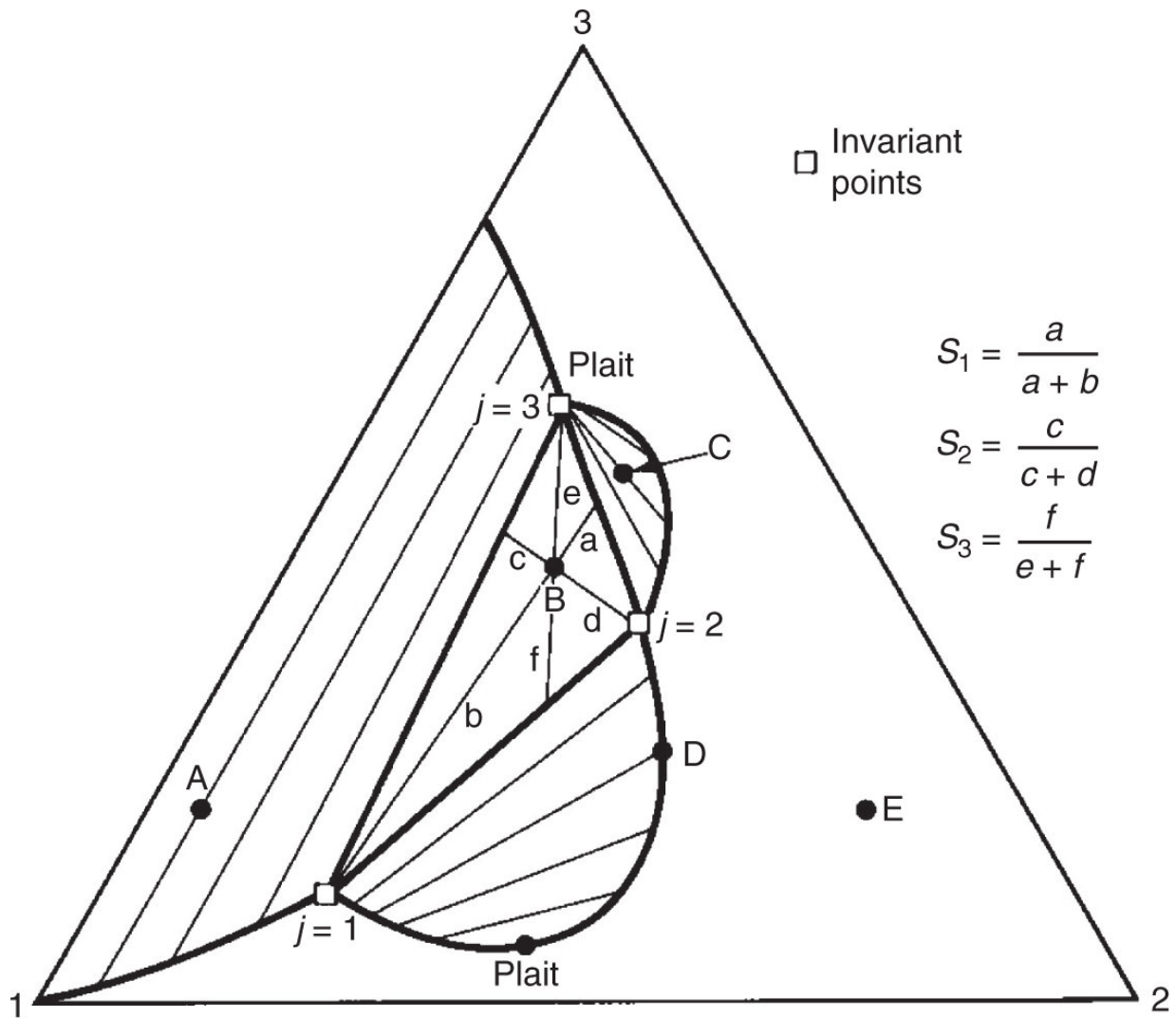


Fig. 4.11—Ternary-phase diagram with three-phase region. The equations to the right of the phase diagram are the Lever Rule within the three-phase region.

Therefore, points *A* and *C* in Fig. 4.11 are two-phase mixtures, point *B* is three-phase, and points *D* and *E* are single-phase, although Point *D* is saturated with respect to Phase 1. [For more detail on the geometric and thermodynamic restrictions of ternary equilibria, see Francis (1963) and Orr and Taber (1984).]

4.5 Quantitative Representation of Two-Phase Equilibria

Several mathematical relations describe the qualitative representations described in the previous section. The most common are those based on (1) equilibrium flash-vaporization ratios,

(2) equations of state (EOS), and (3) a variety of empirical relations. In this section, we concentrate only on those aspects of two-phase equilibria that are most directly related to EOR. Three- and four-phase equilibria and stability calculations are discussed elsewhere in the literature (Mohebbinia et al. 2012; Okuno et al. 2010b; Whitson and Brule 2000; Mehra et al. 1982; Risnes and Dalen 1984; Peng and Robinson 1976) and in [Chapter 9](#), which covers three-phase equilibria for micellar systems.

4.5.1 Equilibrium Flash-Vaporization Ratios. If we let x_i and y_i be the mole fractions of component i in a liquid and in contact with a vapor phase, the equilibrium *flash-vaporization ratio*, or *K-value*, for component i is defined by

At low pressures, the K -values are readily related to the mixture temperature and pressure. The partial pressure of component i in a low-pressure gas phase is $y_i P$ from Dalton's law of additive pressures. The partial pressure of component i in the vapor above an ideal liquid phase is $x_i P_{vi}$ from Raoult's law, where P_{vi} is the pure-component vapor pressure of component i . At equilibrium for this special case, the partial pressures of component i calculated by either means must be equal; hence,

Eq. 4.9 says at low pressures, a plot of the equilibrium K -value for a particular component at a fixed temperature is a straight line of slope -1 on a log-log plot. Under these conditions, the K -value itself can be estimated from pure-component vapor-pressure data.

At higher pressures, where the assumptions behind Dalton's and Raoult's laws are inaccurate, the K -values are functions of overall composition.

4.5.2 EOS. Although the K -value approach is easily the most common representation of two-phase equilibria, it suffers from a lack of generality and may result in significant inaccuracies. The trend has been toward EOS representations because these are potentially able to work near the critical point and to yield internally consistent densities and molar volumes. [For more details on EOS and its underlying thermodynamic principles, see Smith and van Ness (1975) and Denbigh (1968).]

An EOS is any mathematical relationship among the three intensive properties: molar volume, temperature, and pressure. Among the first EOS were Boyle's and Charles's laws (see [Table 4.1](#)). These laws were combined into the ideal gas equation we use today, which is generally satisfactory for vapors at pressures below a few atmospheres. Although more than a hundred EOS have been proposed in the technical literature, many of which are quite complex and have more thermodynamic rigor, here we discuss only cubic EOS because these are the most commonly used class of equations in EOR.

van der Waals developed the first cubic EOS (van der Waals 1873). Unlike the ideal gas equation, which is limited to low-pressure vapors, the van der Waals EOS attempted to model phase behavior for both liquids and vapors with a single equation. He also introduced the principle of corresponding states, which is frequently used in the petroleum industry today for a wide variety of fluid-property correlations. Numerous cubic EOS models, however, are available today that give better accuracy than the van der Waals EOS. The two most widely used cubic EOS are the Peng-Robinson EOS (1976) and the Redlich-Kwong EOS (Soave 1972).

TABLE 4.1—BRIEF HISTORY OF EOS*

1662	Boyle's law	$PV = \text{constant at fixed } T, n$
1787	Charles' law	$\Delta V \propto \Delta T \text{ at constant } P$
1801	Dalton's law	$P = \text{sum of partial pressures}$
1802	Cagniard de la Tour	Discovery of critical state
1834	Clapeyron	Combined Boyle's and Charles' law into $PV = RT$
1873	van der Waals	First cubic EOS and idea of corresponding states, not very accurate EOS
1880	Amagat's law	Volume of a mixture of gases = sum of pure-component volumes
1901	Onnes	Virial equation
1901	Lewis	Fugacity
1940	Benedict, Webb, and Rubin	Eight-constant EOS
1949	Redlich and Kwong	Two-parameter cubic EOS
1972	Soave modification of Redlich-Kwong EOS (SRK EOS)	Three-parameter cubic EOS (added temperature-dependent attraction parameter used today)
1976	Peng and Robinson (PR EOS)	Three-parameter cubic EOS (widely used today)

*Orr, F.M. 1987. Thermodynamics and Phase Behavior-PE 251. Lecture notes on thermodynamics and phase behavior from Stanford University, Palo Alto, California.

Prediction of phase behavior for real reservoir fluids is difficult because of the complex interaction of molecules. Intermolecular forces of attraction and repulsion determine thermodynamic properties for any mixture of molecules. The attractive forces enable fluids to form liquid and solid phases, whereas repulsions are responsible for resistance to compression.

To quantify molecular forces, a potential function (typically the Lennard-Jones potential) is used, which describes the energy required to bring two molecules together. When the molecules are far apart, the forces are attractive in nature and the potential function is negative; that is, the molecules naturally want to move closer together. This attractive force becomes stronger as the molecules move closer. When the molecules are brought very close together, however, the repulsive forces begin to dominate the attractive ones, and significant energy is required to bring the molecules closer together. Therefore, the sign of the gradient of potential function (or energy required) changes depending on intermolecular spacing.

The accuracy of any EOS depends on its ability to model the attractions and repulsions between molecules over a wide range of temperatures and pressures. EOS models are empirical in that they do not attempt to model the detailed physics, but only the cumulative effect in terms of a small number of empirical parameters. Generally, EOS models of the van der Waals type are more accurate for molecules with weak polarity or chemical forces, in which the attractive forces are small. Water, for example, is difficult to model with an EOS. Mixtures that contain alcohols, bases, organic or inorganic acids, and electrolytes are other examples of fluids that are not accurately modeled by EOS models of the van der Waals type. Activity models used along or combined with more complex EOS are often used for these types of mixtures.

We consider next the two most widely used EOS of the van der Waals type, the Soave-Redlich-Kwong (SRK) and the Peng-Robinson (PR) EOS.

Pure Components. Usually, the relation is written in a pressure-explicit form $P = f(\bar{V}, T)$ of which the most elementary form is

$$P = \frac{zRT}{\bar{V}}. \dots \dots \dots \quad (4.10)$$

At low pressure, the gas compressibility factor z is equal to one, and Eq. 4.10 becomes the ideal gas equation. The compressibility factor is itself a function of temperature and pressure that is given in many correlations [see McCain (2000), for example]. Because Eq. 4.10 is actually a definition of the compressibility factor, the equation can also be applied to liquids, although this is rarely done. Given the relation between z , T , and P , Eq. 4.18 could predict volumetric behavior for all T and P if z were completely known.

Consider the pressure vs. molar-volume behavior of a pure component, as shown in [Fig. 4.12](#). [Fig. 4.12](#) also shows this type of plot with two isotherms T_1 and T_2 , both below the critical temperature. Eq. 4.10 is the equation of a hyperbola on this plot that matches the experimental isotherm well at low pressure or high molar volume. The ideal gas law (Eq. 4.10) fails badly in the liquid

region, particularly for pressure predictions, because it predicts nearly zero molar volume at high pressures. This is equivalent to saying that the component molecules themselves have no intrinsic volume even at the highest pressure, which is, of course, a basic hypothesis in the derivation of the ideal gas law from statistical mechanics.

To introduce a finite volume at high pressures, we try an equation of the form

$$P = \frac{RT}{(\bar{V} - b)}, \dots \dots \dots \quad (4.11)$$

where b , the repulsion parameter, is the limiting value of molar volume at high pressures. The repulsion parameter represents the smallest possible volume that one mole of molecules can occupy; b is therefore dependent on the type of pure component. As suggested in [Fig. 4.12](#), this equation can be made to match the liquid molar volumes reasonably well at high pressures. The value of b , the intrinsic molecular volume, is usually so small that Eq. 4.11 provides a good molar-volume estimate at low pressures. Pressures can be calculated over a wide range of molar volumes, but the physical region of interest is that in which molar volume is greater than b .

However, Eq. 4.11 fails for temperature and pressure combinations that are fairly close to the pure-component vapor-pressure curve. To predict the molar volume up to and including the vapor-pressure curve requires a function of the form

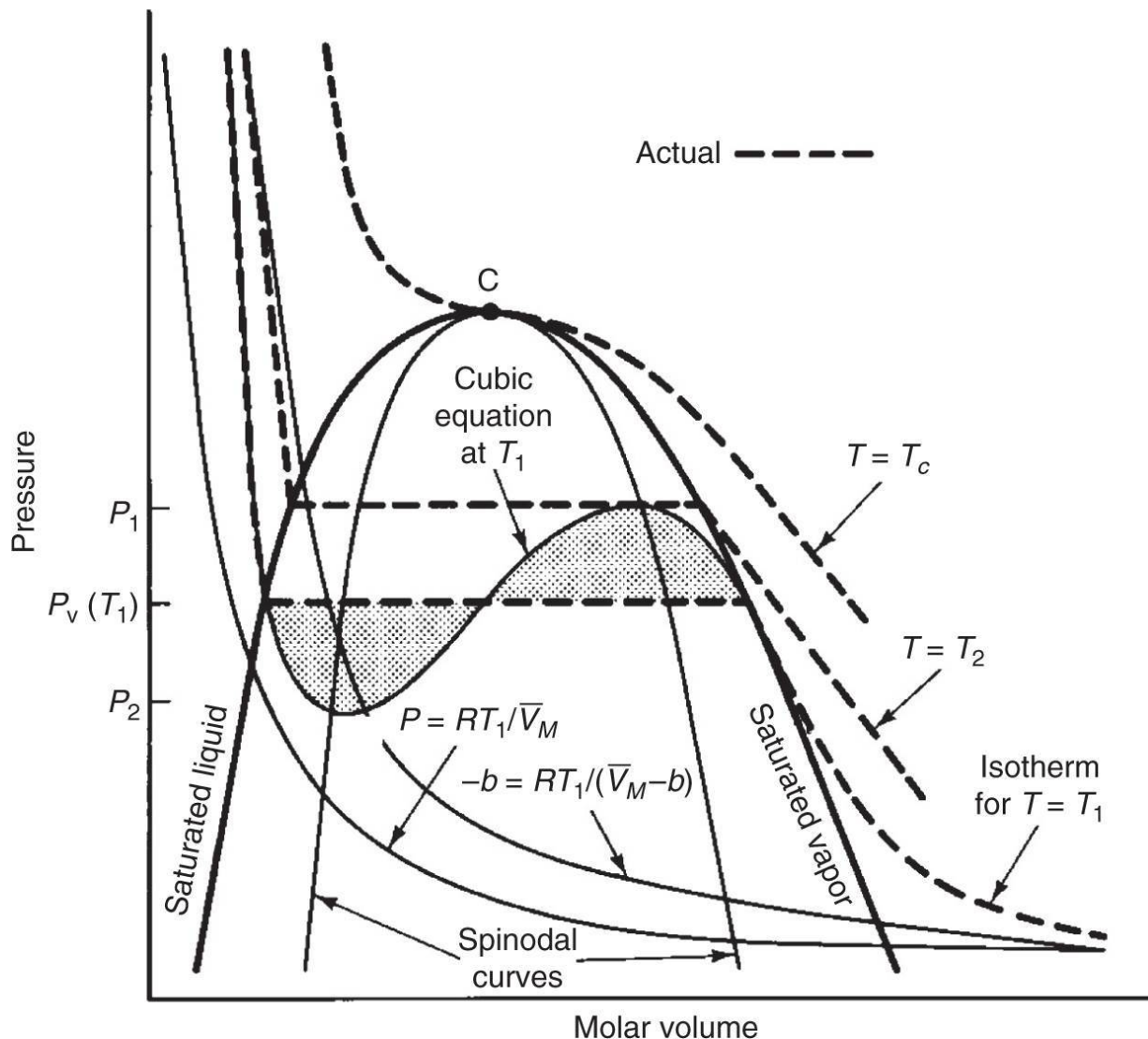


Fig. 4.12—General features of cubic EOS.

$$P = \frac{RT}{(\bar{V} - b)} - f(T, \bar{V}), \dots \quad (4.12)$$

where the term (T, \bar{V}) is specific to the particular EOS. Eq. 4.12 is frequently interpreted as a sum of forces, the first term being the force that will not allow the molecules to be compressed to zero volume (repulsive force), and the second being the force of intermolecular attraction among molecules.

The attractive forces are generally proportional to the square of the number of molecules, and are therefore, in the simplest form,

proportional to $1/\bar{V}^2$; this is the form first used by van der Waals (1873). The proportionality constant depends on the nature and strength of the forces between the molecules and, therefore, on the fluid type. As molar volume becomes large, the molecules are on average farther apart, and the contribution of attractive forces becomes small, so that the term (T,\bar{V}) should vanish. Hence, Eq. 4.12 will approach the ideal gas equation when $\bar{V} \gg b$.

For pure components, two values of molar volume can exist at a particular temperature and pressure; hence, Eq. 4.12 must have at least two real roots at this point. Moreover, because P is a monotonically decreasing function of molar volume regardless of the fluid-phase identity, f must be at least second order in molar volume, and, therefore, the entire function (Eq. 4.12) must be at least cubic in molar volume. A cubic EOS, therefore, is the simplest form that satisfies these criteria.

The particular form of cubic EOS, of course, can vary widely. Abbott (1973) gives the general form,

$$P = \frac{RT}{(\bar{V} - b)} - \frac{\theta(\bar{V} - \eta)}{(\bar{V} - b)(\bar{V}^2 + \delta\bar{V} + \varepsilon)}, \dots \quad (4.13)$$

where the parameters θ , η , δ , and ε are defined by Abbott (1973), who includes complete references on a variety of such equations. Until now, only two of these equations have seen extensive use in predicting EOR phase behavior: the Soave modification (1972) of the Redlich-Kwong equation (SRK) and the PR equation (Peng and Robinson 1976).

Mixtures. The true test and practical utility of any EOS is in its prediction of mixture properties. To account for mixture behavior, the pure-component parameters come from various mixing rules. The most general form of the mixing rules incorporates another parameter, the *binary interaction coefficient* δ_{ij} , into the SRK and PR equations to account for molecular interactions between two unlike molecules. By definition, δ_{ij} is zero when i and j represent the same component, small when i and j represent components that do not

differ greatly (for example, if i and j were both alkanes), and large when i and j represent components that have substantially different properties. Ideally, the δ_{ij} are both temperature- and pressure-independent (Zudkevitch and Joffe 1970), depending only on the identities of components i and j . Although the interaction coefficients are considerably less available than acentric factors, literature tabulations are available (Yarborough 1978; Whitson 1984; Prausnitz et al. 1980).

4.5.3 Flash Calculations. The problem of interest in modeling most EOR processes is to quantify the number, relative amount, and composition of the phases that form at equilibrium. More specifically, given the temperature T , pressure P , and overall compositions z_i , we want to determine the number, molar fractions, and compositions of the phases that form. [Fig. 4.13](#) illustrates this phase-behavior problem for a closed vapor-liquid system with compositions x_i and y_i , respectively. The method for solving this problem is known as a *flash calculation*.

The compositions in [Fig. 4.13](#) are mole fractions, where x_i is the moles of component i in the liquid phase divided by the total moles of liquid (n_{iL}/n_L or mole fraction); y_i is the moles of component i in the vapor phase divided by the total moles of vapor (n_{iV}/n_V); and z_i is the total moles of component i in all phases divided by the total moles in the system (n_i/n). Therefore, $\sum_{i=1}^{N_c} z_i = 1.0$ for the overall system, $\sum_{i=1}^{N_c} x_i = 1.0$ for liquid, and $\sum_{i=1}^{N_c} y_i = 1.0$ for vapor.

The relative amounts of the phases in [Fig. 4.13](#) are defined by phase mole fractions. \bar{n}_L is the total moles of liquid divided by the total moles of all phases (n_L/n), and \bar{n}_V is the total moles of vapor divided by the total moles of all phases (n_V/n). Therefore, for vapor-liquid equilibrium, $\bar{n}_L + \bar{n}_V = 1$. The phase molar fractions are not saturations (volume fractions), although they could be converted to saturations by normalizing all the phase fractions by the molar phase densities. The molar fractions of the phases are related to the

compositions by a simple batch material balance, $z_i = \bar{n}_L x_i + \bar{n}_V y_i$. Solving for the liquid phase gives

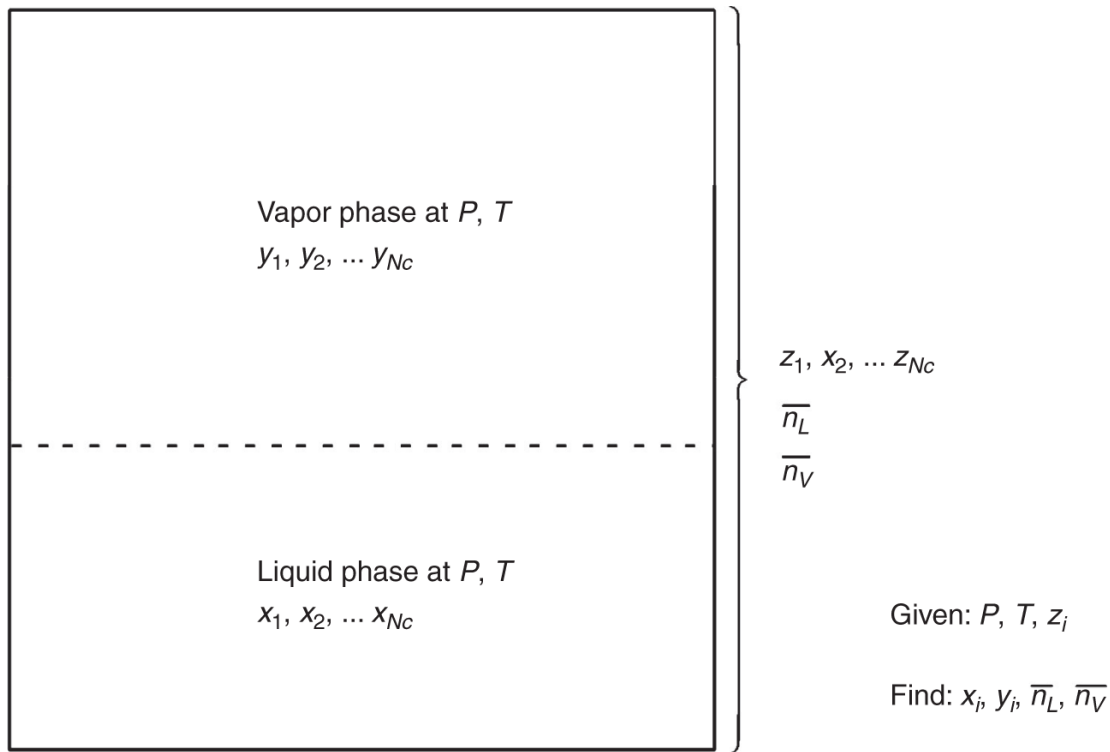


Fig. 4.13—Vapor-liquid equilibrium at constant pressure, temperature, and overall composition. The dashed line shows the interface between the two phases.

$$\theta_i = \frac{z_i - x_i}{x_i - \bar{x}_i} \quad i = 1, \dots, N_C \quad (4.14)$$

Therefore, once the overall compositions and phase compositions are known, the phase molar fractions are also known.

The procedure for flash calculations described here can become very computationally intensive as the number of components increases because a set of N_C independent simultaneous nonlinear equations must be solved. Reducing the computational time of one flash calculation is important because these calculations are repeated for each gridblock and each timestep in a compositional simulation. Reduced methods of various types have been introduced to speed up two-, three-, and four-phase flash and stability calculations because they solve for only a few parameters independently of the number of components (Gorucu and Johns

2014, 2013; Mohebbinia et al. 2012; Okuno et al. 2010a; Firoozabadi and Pan 2002; Hendriks and van Bergen 1992; Michelsen 1986).

Final Notes on Flash Calculations. More detailed accounts of flash calculations with K values and EOS can be found elsewhere (Danesh 1998; Firoozabadi 1999; Whitson and Brule 2000). A variety of computer-based software packages are available for these calculations. Any user of such packages should be aware of certain limitations:

1. Calculations of phase equilibrium generally require an initial guess close to the final answer; otherwise, the calculations may fail to converge. In simulations, if changes in phase compositions are small from one timestep to the next, the initial guess may be provided by the state at the previous timestep. If a new phase forms, one needs a reasonable guess of the likely properties of that phase. Because one does not know when a new phase will form, one needs an idea of what sort of phase is likely to form and then to test whether a solution with such a phase satisfies the equilibrium conditions.
2. Equilibrium assumes that free energy is minimized. It is possible that calculations may converge on a local minimum that is not the true state of minimum free energy for the given conditions.
3. EOS and K -value correlations are only approximations to the real behavior of fluids. As suggested in [Table 4.1](#), improvements and modifications are continually being made to these equations and correlations.
4. Assuming that one finds the correct equilibrium state, it may not represent the true state at the given location in the reservoir where equilibrium may not be achieved, or may be achieved only slowly. The reason may be slow nucleation and growth of new phases, or, more often, inability of fluids to mix well within the region of interest because of geological heterogeneity.

Fluid Characterization and Tuning of EOS. Phase-behavior calculations require that all components and their properties be specified. Crude oils, however, typically have hundreds of components, making the EOS procedure computationally intensive. Therefore, components are often lumped into pseudocomponents to approximate the in-situ fluid characterization. The characterization usually takes the form of the following three steps (Pedersen and Christensen 2007):

1. Analyze the hydrocarbon components in the in-situ fluid with analytical techniques such as chromatography or distillation. New analytical techniques often give a reliable analysis for hydrocarbon components up to C₃₀ instead of the traditional C₇₊. Properties for hydrocarbon components greater than C₃₀ are reported as a C₃₀₊ fraction. The heavy plus fraction is then characterized (split) into more components by use of established correlations.
2. The measured components are separated and lumped into a minimum number of pseudocomponents. The chosen number of pseudocomponents is often a result of the measured fluid characterization and the degree of accuracy required (see Step 3). The properties and selection of the pseudocomponents are determined using a variety of methods. The required pseudocomponent properties are those needed for the cubic EOS calculations, such as critical temperature, pressure, and an acentric factor.
3. The pseudocomponent properties are adjusted to match all available phase-behavior data based on pressure/volume/temperature measurements. This process, which typically involves hand adjustment or nonlinear regression, is known as EOS tuning. EOS tuning is needed because of the inherent uncertainty in the properties estimated in Step 2, especially for the heavier components. Binary interaction parameters are typically the first parameters to be adjusted, although other parameters may need some tuning.

Adjustments should be minimal and within a reasonable physical range so that the EOS are predictive outside the range of the measured data. The number of pseudocomponents may need to be increased from those obtained in Step 2 to obtain a good fit between the calculated phase behavior and the measured phase-behavior data.

The selection of pseudocomponents and their property values is unlikely to be unique, as is often the case when numerous model parameters are estimated by fitting measured data with nonlinear regression. Care should be taken to avoid physically unreasonable estimates of pseudocomponent properties and to reduce the number of parameters. Furthermore, the final EOS characterization is most accurate in the range of the measured phase-behavior data. Phase-behavior data should therefore be collected that cover, as much as possible, the conditions that occur in the reservoir. The characterization should be updated when new data become available.

The procedure outlined above is intended to lump oil components into pseudocomponents; this is especially important in applications in which different oil components act differently, as in solvent flooding. The selection of pseudocomponents depends on the application. For instance, one often lumps water and its dissolved salts into a single pseudocomponent (brine). In surfactant EOR, various surfactants and cosolvents may be lumped together into one pseudocomponent. Depending on the EOR process, it may even be sufficient to lump all oil components into a single pseudocomponent.

Fluid characterizations may vary from one location in the reservoir to another. In such cases, multiple EOS characterizations may be required. Compositional variations can occur for a variety of reasons. For example, gravity can cause vertical compositional gradients in which heavier components become more concentrated at greater depths (Firoozabadi 1999).

4.5.4 Empirical Representations. There are three common empirical representations of phase behavior. All are used primarily

for liquid-liquid equilibria, although a recent extension of Hand's rule can also apply for liquid-vapor equilibria (Roshanfekr et al. 2010).

Hand's Rule. Hand (1939) gave a fairly simple representation of two-phase equilibria that has proved useful for some EOR systems (Pope and Nelson 1978; Young and Stephenson 1983). The procedure is based on the empirical observation that certain ratios of equilibrium phase concentrations are straight lines on log-log or *Hand plots*.

In this section, the concentration variable C_{ij} is the volume fraction of component i ($i = 1, 2$, or 3) in phase j ($j = 1$ or 2). Using volume fractions has become conventional in the Hand representation because these are convenient in liquid-liquid equilibria.

[**Fig. 4.14**](#) shows the one- and two-phase regions on the ternary diagram and their correspondence to the Hand plot. The line segments AP and PB represent the binodal curve portions for Phase 1 and 2, respectively, and curve CP represents the distribution curve of the indicated components between the two phases. The ratios on the distribution curve are analogous to, but entirely different from, the definitions of the K -values given above. The equilibrium relations based on the Hand plot are

$$\frac{C_{3j}}{C_{2j}} = A_H \left(\frac{C_{3j}}{C_{1j}} \right)^{B_H}, \quad j = 1, 2, \dots \quad (4.15)$$

and

$$\frac{C_{32}}{C_{22}} = E_H \left(\frac{C_{31}}{C_{11}} \right)^{F_H}, \quad \dots \quad (4.16)$$

where A_H, B_H, E_H, F_H are empirical parameters. Eq. 4.15 represents the binodal curve, and Eq. 4.16 represents the distribution curve. In this form, these equations require the binodal curve to enter the corresponding apex of the ternary diagram. A simple modification overcomes this restriction (see Exercise 4.6).

Within the two-phase region of the binodal curve, there are six unknowns, the C_{ij} phase concentrations and five equations, three

from Eqs. 4.15 and 4.16 and two consistency constraints:

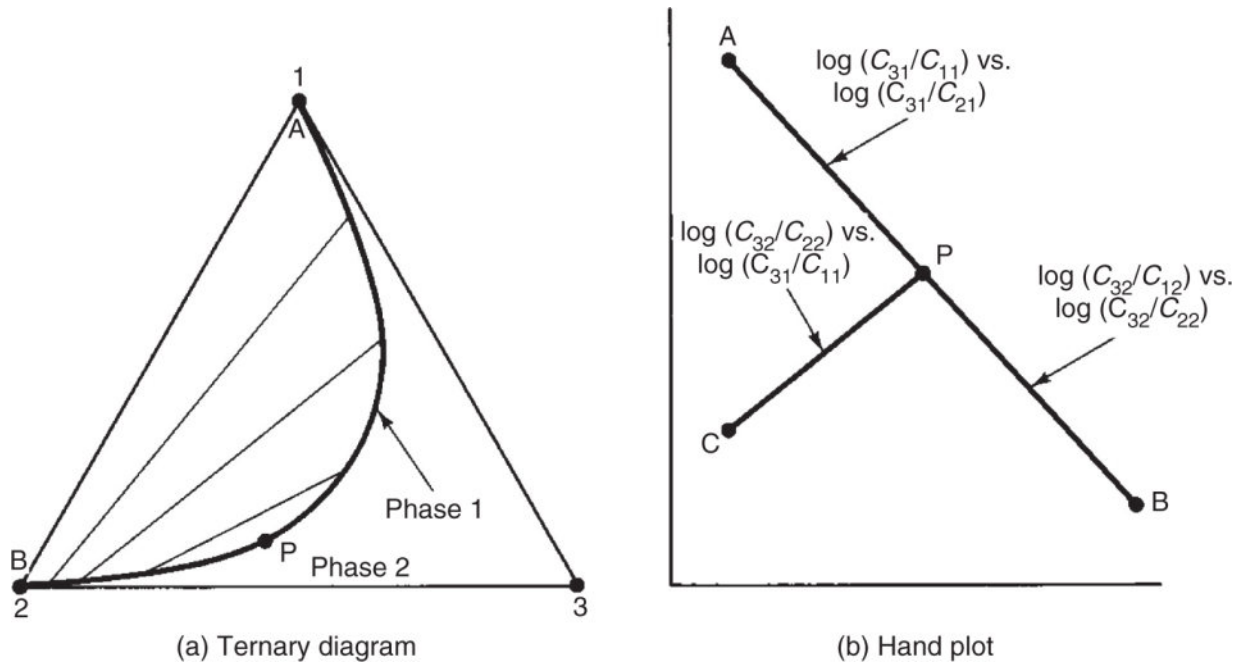


Fig. 4.14—Correspondence between ternary diagram and Hand plot.

Therefore, there is $N_F = 1$ degree of freedom as required by the phase rule because temperature and pressure are fixed for ternary equilibria.

A flash calculation using the Hand procedure solves for the relative amounts of the two phases. This introduces two additional variables, volume fractions S_1 and S_2 , into the calculation, but there are now three additional equations, the mass-balance equation (Eq. 4.6), with the overall concentrations C_i known and $S_1 + S_2 = 1$. As in all the phase-equilibrium flash calculations, the procedure is iterative, although for certain special cases, phase concentrations follow from direct calculation. The procedure is first to pick a phase concentration (e.g., C_{32}), then to calculate all the other phase concentrations from Eqs. 4.15 through 4.17, and then to substitute these into the tie line (Eq. 4.7). If this equation is satisfied,

convergence has been attained; if it is not satisfied, a new C_{32} must be picked and the procedure repeated until either C_{32} does not change or Eq. 4.7 is satisfied.

Tie-Line Extension Curve. The tie-line extension curve is another curve $C_3^0 = f(C_2)$ in ternary space that passes through the plait point, at which point it is tangent to the binodal curve ([Fig. 4.15a](#)). The two-phase tie lines are extensions of tangents from this curve through the binodal curve. Therefore, equations of the tie lines are given by straight lines having the equation

$$C_{3j} - f(C_2^0) = f'(C_2^0)(C_{2j} - C_2^0), \quad j=1 \text{ or } 2, \dots \quad (4.18)$$

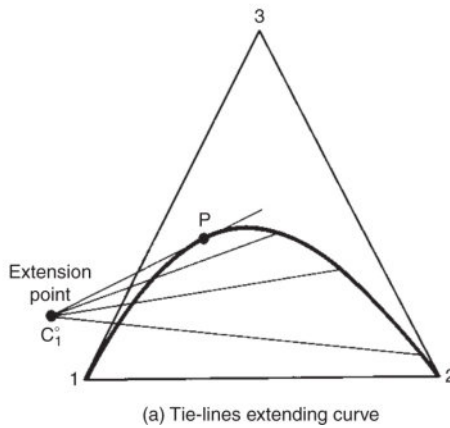
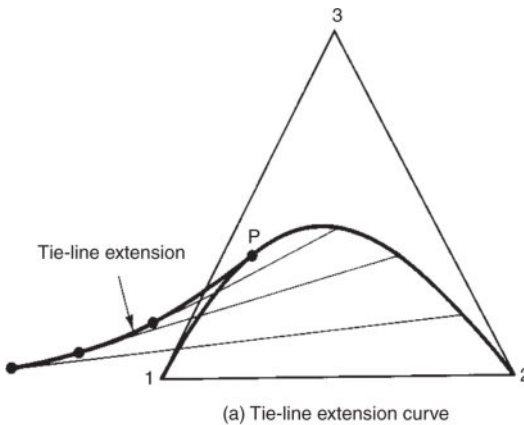


Fig. 4.15—Tie-line extension representation of phase behavior.

where $f'(C_2^0)$ is the slope of the tie-line extension curve evaluated at the coordinate C_2^0 . The tie lines follow from Eq. 4.18, the equation of

the extension curve, and the equation for the binodal curve.

A useful special case of the tie-line extension curve occurs when all tie lines extend to a common point, as in [Fig. 4.15b](#). We need specify only the coordinates of this common point to define the equation for the tie lines:

$$C_{3j} - C_3^0 = \eta(C_{2j} - C_2^0), \quad j=1 \text{ or } 2, \dots \quad (4.19)$$

where η is the slope of the tie line. Note that if $C_j^0 > 0$, the selectivity of the components for the two phases can reverse near the base of the ternary. The representation is extremely simple because it requires only two values: any two of the coordinates C_i^0 or, alternatively, any of the plait-point coordinates and one of the C_i^0 , because the tie lines must be tangent to the binodal curve there.

This representation is far less general than either the EOS or Hand methods. However, experimental accuracy is often not enough to warrant more complex equations. Moreover, the form (Eq. 4.19) is extremely convenient for calculating the flow behavior of two-phase mixtures; we use it extensively in [Chapters 7](#) and [9](#).

4.6 Concluding Remarks

Multiple representations of phase behavior are evidence that no single method is sufficient. In most cases, we find ourselves compromising between accuracy and mathematical ease in the resulting calculations. Our goal here is the exposition of the underlying principles of EOR phenomena; hence, we emphasize phase-behavior representations that lend themselves to visual or graphical analysis in later calculations—as long as the representations themselves are qualitatively correct. The most important points to grasp in this chapter, then, are the graphical representations described in Section 4.4, particularly as these relate to the ternary diagram; the physical meaning of tie lines and binodal curves; and the component distributions.

Exercises

4.1 Tie-Line Lever Rule. The tie-line lever rule given by Eq. 4.14 is derived from a batch material balance. Derive $\frac{C_{A_1}^{100}}{A_1} = \frac{C_{A_2}^{100}}{A_2}$ and write the definitions for each term.

4.2 Pure-Component Phase Behavior. Sketch the following for a pure component:

- a. Lines of constant pressure on a temperature vs. molar-volume plot
- b. Lines of constant temperature on a density vs. pressure plot
- c. Lines of constant molar volume on a temperature vs. pressure plot.

4.3 Paths on a Pressure vs. Volume Plot. Indicate the paths AA' , BB' , and DD' , shown on the pressure vs. specific-volume plot in [Fig. 4.16](#), on the corresponding pressure/temperature plot.

4.4 Migration of P/T Envelope. [Fig. 4.17](#) shows the hypothetical change in the pressure/temperature envelope of a crude oil as it is diluted with a more volatile component (CO_2). The quality lines within each envelope are in volume percent. For these data, sketch the pressure-composition diagram at 340 K and 359 K (152°F and 180°F). These temperatures are the critical temperatures for the 40% and 20% CO_2 mixtures. Include as many quality lines as possible.

4.5 Lever Rule Application. Consider the three-component system represented in [Fig. 4.11](#).

- a. Estimate the relative amounts of each phase present at overall compositions A , C , D , and E .
- b. Derive the expressions (indicated on the figure) for the relative amounts of each phase present at the three-phase overall composition.
- c. Estimate the relative amounts of each phase present at B .

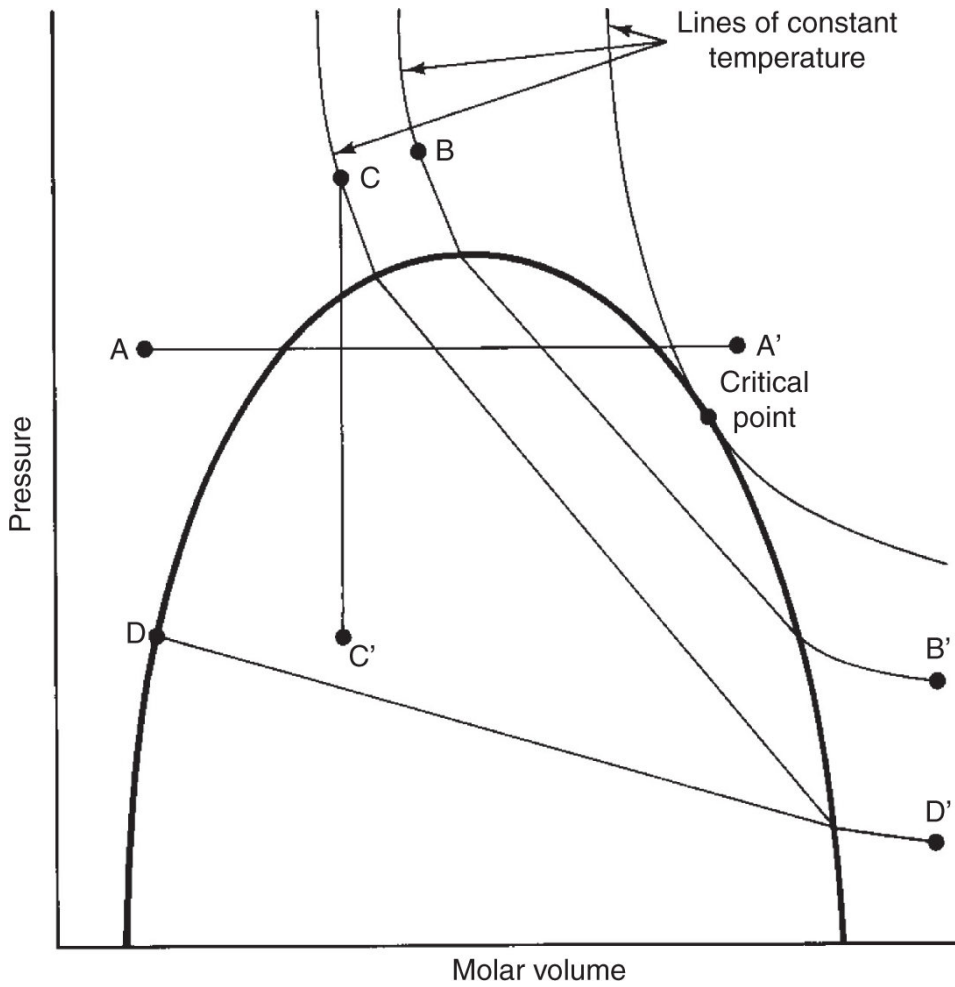


Fig. 4.16—Pressure vs. specific-volume plot for Exercise 4.3.

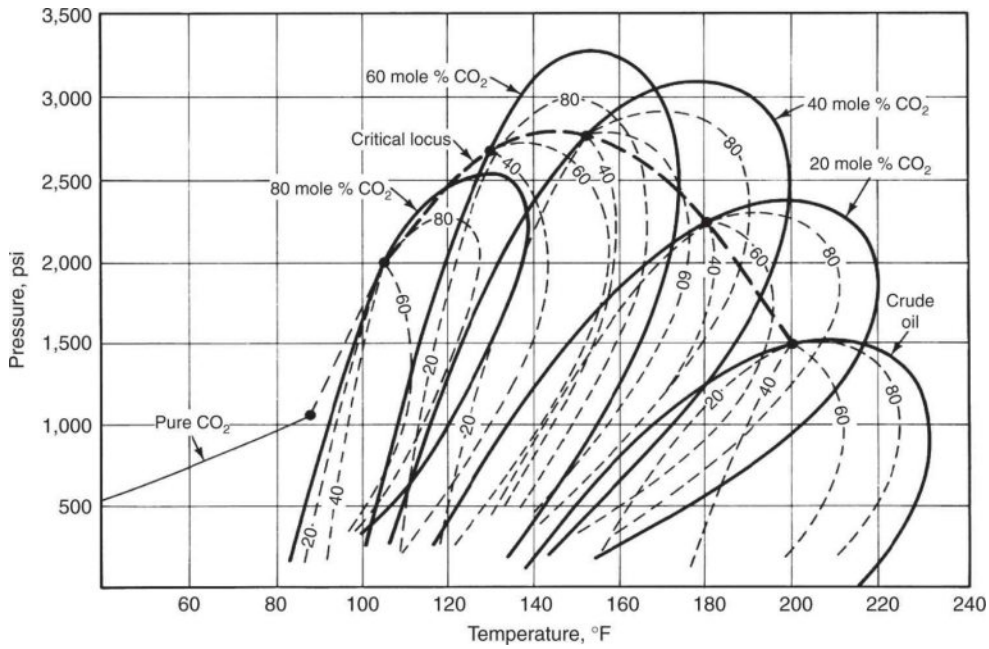


Fig. 4.17—Change in crude-oil pressure vs. temperature diagram with hypothetical dilution by CO₂.

4.6 Partially Soluble Binaries (Welch 1982). For cases in which the partially soluble binaries on a ternary plot have some mutually soluble region, the Hand representation may be altered to

$$\frac{C'_{3j}}{C'_{2j}} = A_H \left(\frac{C'_{3j}}{C'_{1j}} \right)^{B_H}, \quad j = 1, 2$$

and

$$\frac{C'_{32}}{C'_{22}} = E_H \left(\frac{C'_{31}}{C'_{11}} \right)^{F_H},$$

where the C_{1j} are normalized concentrations

$$C'_{1j} = \frac{C_{1j} - C_{1L}}{C_{1U} - C_{1L}}$$

$$C'_{2j} = \frac{C_{2j} - (1 - C_{1U})}{C_{1U} - C_{1L}}$$

$$C'_{3j} = \frac{C_{3j}}{C_{1U} - C_{1L}}$$

C_{1U} and C_{1L} are the upper and lower solubility limits of the 1-2 binary. Assume $B_H = -1$ and $F_H = 1$ in the following:

- Derive an expression for A_H in terms of the true maximum height of the binodal curve $C_1 - C_2$. Show that the binodal curve takes on the value $C_{3\max}$ when $c'_1 = c'_2$ (symmetrical in normalized concentrations).
- Express E_H as a function of A_H and the Component 1 coordinate of the plait point (C_{1p}). A_H and E_H in parts (a) and (b) will also be a function of C_{1U} and C_{1L} .
- Plot the binodal curve and the two representative tie lines for $C_{1U} = 0.9$, $C_{1L} = 0.2$, $C_{3\max} = 0.5$, and $C_{1p} = 0.3$.

4.7 Using the Hand Representations. The following data were collected from a three-component system at fixed temperature and pressure.

Phase 1		Phase 2	
Component 1	Component 2	Component 1	Component 2
0.45	0.31	0.015	0.91
0.34	0.40	0.020	0.89
0.25	0.48	0.030	0.85
0.15	0.60	0.040	0.82

The concentrations are in volume fractions.

- On a ternary diagram, plot as many tie lines as possible and sketch the binodal curve.
- Make a Hand plot from the data and determine the parameters A_H , B_H , E_H , and F_H .
- Estimate the coordinates of the plait point from the plot in Part b.

Chapter 5

Displacement Efficiency

The definitions of recovery, displacement, and sweep efficiencies in Eq. 2.88 apply to an arbitrary chemical component, but they are almost exclusively applied to oil and gas displacement. Because displacement efficiency and sweep efficiency are multiplied by each other, they are equally important to the magnitude of recovery efficiency and, hence, to oil recovery. In [Chapter 6](#), we discuss volumetric sweep efficiency; in this chapter, we present fundamental concepts of displacement efficiency.

For the most part, we restrict our discussion to oil displacement efficiency based on solutions to the fractional-flow equation (Eq. 2.53). We apply these equations to displacements in 1D, homogeneous, isotropic permeable media. Therefore, the results apply most realistically to displacements in laboratory floods, which are the traditional means of experimentally determining displacement efficiency. These results do not, of course, estimate recovery efficiency for 3D, nonlinear flows without correcting for volumetric sweep efficiency and without correcting the displacement efficiency to account for differences in scale.

5.1 Definitions

Assuming constant oil density, the definition of displacement efficiency for oil becomes

$$E_D = \frac{\text{Amount of oil displaced}}{\text{Amount of oil contacted by displacing agent}} \dots \dots \dots \quad (5.1)$$

E_D is bounded between zero and unity. The rate at which E_D approaches unity is strongly affected by the initial conditions, the displacing agent, and the amount of displacing agent. Fluid, rock, and

fluid-rock properties also affect E_D . If the displacement is such that the displacing agent will contact all the oil initially present in the medium, the volumetric sweep efficiency will be unity, and E_D becomes the recovery efficiency E_R .

From Eq. 2.54, then,

for an incompressible, single-component oil phase flowing in an incompressible permeable medium. Eq. 5.2 says that E_D increases as the average oil saturation in the medium decreases. When the oil occurs in more than one phase, or where components other than oil can exist in the hydrocarbon phase, we must use the general definition, Eq. 2.89.

5.2 Immiscible Displacement

Virtually all our understanding of enhanced-oil-recovery (EOR) displacements begins with an understanding of the displacement of one fluid by an immiscible second fluid. The specific case of water displacing oil was first solved by Buckley and Leverett (1941) and later broadened by Welge (1952). In this section, we develop the Buckley-Leverett theory in a manner much like the original paper and several subsequent references (Collins 1976; Craig 1971; Dake 1978).

For isothermal flow of oil and water in two immiscible, incompressible phases in a 1D permeable medium, the mass-conservation equations of [Table 2.2](#) reduce to

for flow in the positive x -direction, as discussed in [Chapter 2](#). In this equation, f_1 is the fractional flow of water,

$$f_1 = \frac{u_1}{u} = \frac{\lambda_{r1}}{\lambda_{r1} + \lambda_{r2}} \left(1 - \frac{k\lambda_{r2}\Delta\rho g \sin\alpha}{u} \right), \dots \quad (5.4)$$

in the absence of capillary pressure. In Eq. 5.4, α is the dip angle, which is defined as positive when measured in the counterclockwise direction from the horizontal, and $\Delta\rho = \rho_1 - \rho_2$ is the density difference between the water and oil phases. Eq. 5.4 is developed by substitution of Darcy's law for the water and oil velocities.

The choice of S_1 as the dependent variable in Eq. 5.3 is a convention; we could easily have chosen S_2 because $S_2 + S_1 = 1$ and $f_2 + f_1 = 1$. An important point is that in the absence of capillary pressure, f_1 is uniquely determined as a function of S_1 through the relative permeability relations $\lambda_{r1} = k_{r1}/\mu_1$ and $\lambda_{r2} = k_{r2}/\mu_2$ discussed in Section 3.3. In fact, because the shape of the f_1 vs. S_1 curve proves to be the main factor in determining the character of the displacement, we digress briefly to discuss the way in which flow conditions affect this curve.

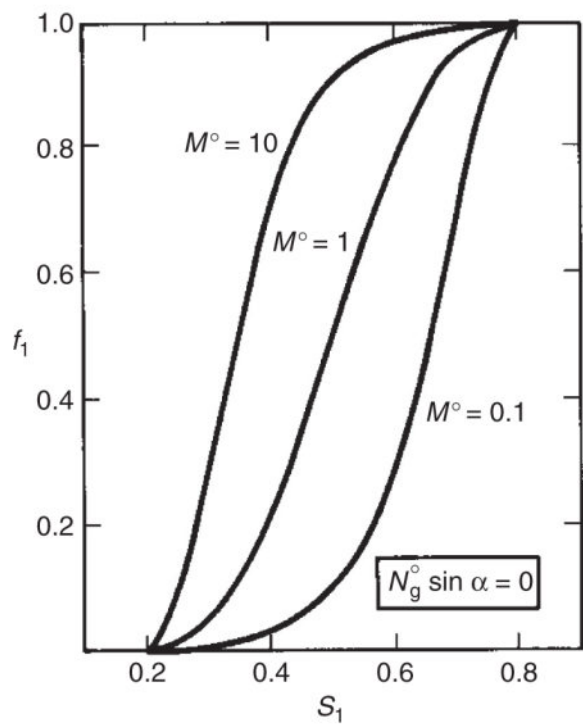
5.2.1 Fractional-Flow Curves. If we introduce the exponential form of the oil/water relative-permeability curves (Eq. 3.21a) into Eq. 5.4, we obtain

$$f_1 = \frac{1 - N_g^0 (1 - S)^{n_2} \sin \alpha}{1 + \frac{(1 - S)^{n_2}}{M^0 S^{n_1}}}, \quad \dots \dots \dots \quad (5.5a)$$

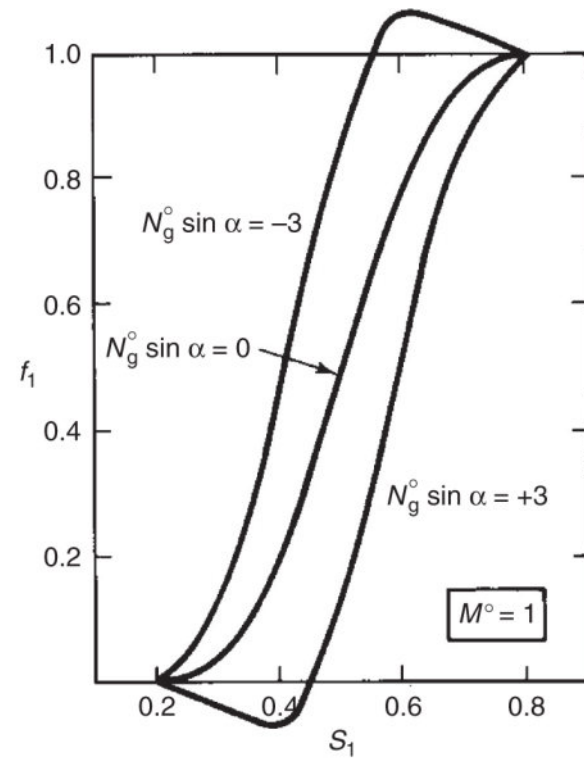
where

and

where N_g^0 is the ratio of gravity to the viscous pressure gradient based on the endpoint oil relative permeability. In the form of Eq. 5.5a, f_1 depends parametrically on M^0 , $N_g^0 \sin \alpha$, and the shape of the relative permeability curves (n_1 and n_2). The f_1 vs. S_1 curve is sensitive to all these factors, but usually M^0 and N_g^0 are the most important. Fig. 5.1 shows f_1 vs. S_1 curves for various values of M^0 and $N_g^0 \sin \alpha$ with the other parameters fixed ($S_{1r} = 0.2$, $S_{2r} = 0.2$, $n_1 = n_2 = 2$). These S-shaped curves have an inflection point that varies with M^0 and $N_g^0 \sin \alpha$. The curvature of all these curves generally becomes more negative as M^0 increases or as $N_g^0 \sin \alpha$ decreases. The curves for f_1 less than zero or greater than one are physically correct. This circumstance indicates a flow in which gravity forces are so strong that flow in the negative x -direction occurs (water flows in the negative x -direction for $f_1 < 0$). In Section 3.3, we showed that shifting the wettability of the permeable medium from water-wet to oil-wet caused k_{r1}^0 to increase and k_{r2}^0 to decrease. Therefore, for constant phase viscosities, making the medium more oil-wet is qualitatively equivalent to increasing M^0 . However, for fixed relative-permeability curves, the effect of increasing μ_1 or decreasing μ_2 is to decrease M^0 .



(a) Varying endpoint mobility ratios



(b) Varying gravity numbers

Fig. 5.1—Fractional flow curves for $n_1 = n_2 = 2$ and $S_{1r} = S_{2r} = 0.2$.

5.2.2 Buckley-Leverett Solution. Returning now to Eq. 5.3 to calculate E_D , we seek solutions $S_1(x, t)$, subject to the initial and boundary conditions

In core floods, a specified fractional flow is usually imposed on the inflow ($x = 0$), so that we can replace Eq. 5.6b with

This equation shows that f_1 is a function of x and t only through its dependence on S_1 . The definition used in a given instance depends on the particular application. The conditions imposed by Eq. 5.6 also

mean that in $x-t$ space at the point $t = x = 0$, all values of S_1 between S_{1I} and S_{1J} exist. The Buckley-Leverett problem is usually posed with S_{1I} and S_{1J} set to S_{1r} and $1 - S_{2r}$, respectively.

For greater generality, Eqs. 5.3 and 5.6 can be rendered into the following dimensionless forms:

$$\left(\frac{\partial S_1}{\partial t_p} \right) + \left(\frac{df_1}{dS_1} \right) \left(\frac{\partial S_1}{\partial x_p} \right) = 0 \quad \dots \dots \dots \quad (5.7a)$$

where the dimensionless variables x_D and t_D are

$$x_D = \frac{x}{L} = \text{Dimensionless position.} \quad (5.8a)$$

and L is the total macroscopic permeable-medium dimension in the x -direction. In these equations, u may be a function of time, but not of position because of the assumption of incompressibility. Moreover, df_1/dS_1 is a total derivative because f_1 is a function of S_1 only. Introducing dimensionless variables reduces the number of parameters in the problem from four (ϕ , u , S_{1I} , and S_{1J}) in Eqs. 5.3 and 5.6 to two (S_{1I} and S_{1J}). We could further reduce the number by redefining the dependent variable $S_1 = \frac{S_1 - S_{1I}}{S_{1J} - S_{1I}}$.

The dimensionless position and time t_D can be expressed more generally as

where A is the cross-sectional area of the 1D medium in the direction perpendicular to the x -axis, q is the volumetric flow rate, and V_p is the pore volume. These definitions apply to radial and streamline flow as well as to linear flow. t_D is the total volume of fluid injected up to time t divided by the total pore volume of the medium. In principle, V_p is well defined even for a highly irregular geometry, so that t_D is a scaling variable in virtually any application. In fact, t_D is the fundamental variable used to scale from the laboratory to the field. It has been used with a wide variety of definitions for the reference volume V_p (see [Table 5.1](#)). Numerical values of t_D are frequently referred to as “fraction of pore volume,” or simply “pore volume;” for this reason, it is easy to confuse with V_p , the actual pore volume, which has units of L^3 (t_D , of course, has no units).

We seek a solution to Eq. 5.7 in the form $S_1(x_D, t_D)$. S_1 can be written as a total differential

$$dS_1 = \left(\frac{\partial S_1}{\partial x_D} \right)_{t_p} dx_D + \left(\frac{\partial S_1}{\partial t_D} \right)_{x_D} dt_D, \dots \quad (5.10)$$

from which it follows that the velocity v_{s_1} of a point with constant saturation S_1 in x_D - t_D space is

v_{s_1} is the “specific” velocity of the saturation S_1 because it has been normalized by the bulk fluid interstitial velocity u/ϕ ; it is dimensionless. Throughout this book, velocities in fractional-flow solutions are

dimensionless velocities, dx_D/dt_D . You can see this by converting Eq. 5.11 back to dimensional quantities using the definitions (Eq. 5.8). Understand that “velocity” means specific velocity unless otherwise stated.

TABLE 5.1—TABULATION OF VARIOUS DEFINITIONS FOR REFERENCE VOLUME IN DIMENSIONLESS TIME

Reference Volume	Usage
Area × Length × Porosity	Corefloods
$V_p = AL\phi$	
Area × Length × Porosity	General geometric
$V_p = AH\phi$	
Floodable Pore Volume	Chemical floods
$V_{FPV} = \frac{V_p}{E_v^\infty} = \frac{\text{Pore volume}}{\text{Ultimate volumetric sweep efficiency}}$	
Movable Pore Volume	Waterfloods
$V_{MPV} = \frac{V_p}{\Delta S_2} = \frac{\text{Pore volume}}{\text{Ultimate oil saturation change}}$	
Hydrocarbon Pore Volume (HCPV)	Solvent floods
$V_{MPV} = \frac{V_p}{\Delta S_{2l}} = \frac{\text{Pore volume}}{\text{Initial oil saturation}}$	
Note: $t_D = \frac{\text{Total volume of fluid injected}}{\text{Reference volume}}$ dimensionless.	

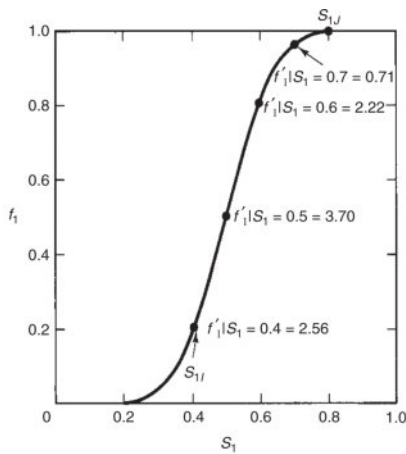
Eliminating either of the derivatives in Eq. 5.11 using Eq. 5.7a gives

This equation says that the specific velocity of a constant saturation S_1 is equal to the derivative of the fractional-flow curve at that saturation. In dimensional form, Eq. 5.12 is the Buckley-Leverett equation. Because all saturations between S_{1l} and S_{1r} are initially at

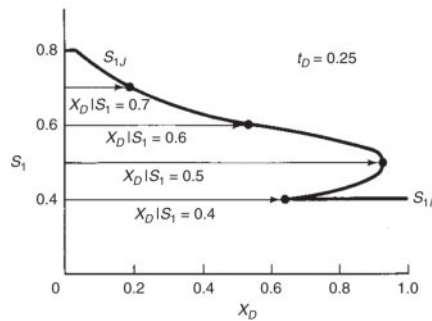
the origin in x_D vs. t_D space, and because v_{S_1} is defined with S_1 constant, the position of any saturation $S_{1I} \leq S_1 \leq S_{1J}$ at a given t_D is

where we include evaluation symbols to help clarify the subsequent development. Eq. 5.13 is the solution to the 1D water-displacing-oil problem; by selecting several values of S_1 between S_{1I} and S_{1J} , we can construct $S_1(x_D, t_D)$. [Fig. 5.2a](#) shows the procedure for one of the fractional-flow curves shown in [Fig. 5.1](#). Except for relatively simple cases (see Exercise 5.5), the relation (Eq. 5.13) generally cannot be solved explicitly for $S_1(x_D, t_D)$.

5.2.3 Shock Formation. Fig. 5.2a also shows a disconcerting tendency for an S-shaped f_1 vs. S_1 curve to generate solutions that have three values of S_1 at the same x_D and t_D . In Fig. 5.2b, this occurs for $0.64 < x_D < 0.94$. Of course, such triple values are physically invalid, although they are entirely valid mathematically. The triple values are the result of the saturation velocity v_{S_1} increasing over some saturation region $S_{II} < S_1 < S'_1$ in Fig. 5.2 as S_1 changes from its initial (downstream) value to the final (upstream) value.



(a) Slopes of a fractional flow curve

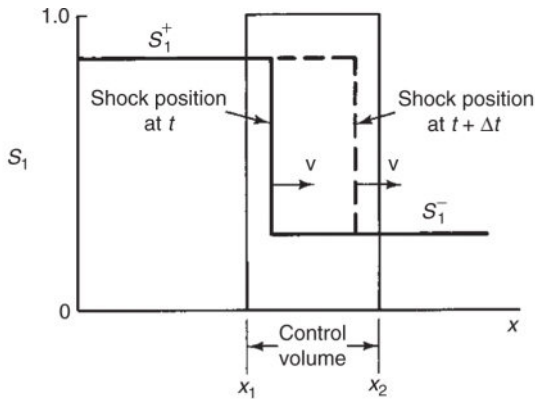


(b) Corresponding saturation profile

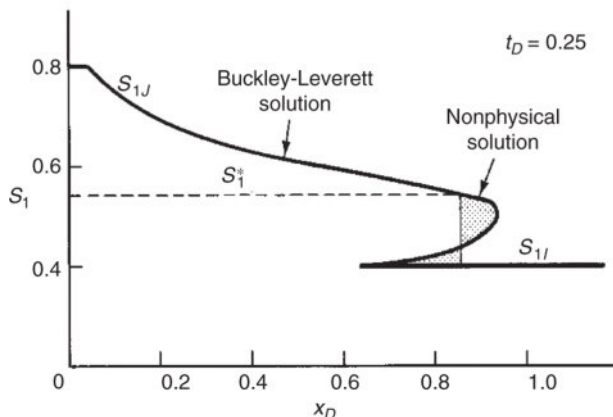
Fig. 5.2—Buckley-Leverett construction of $S_1(x_D, t_D)$.

We eliminate the triple-value region by invoking the formation of shocks, discontinuous changes in a physical quantity such as pressure (as in the case of sonic booms), concentration, or in this case, saturation. Shocks are characteristic features of hyperbolic equations, a class of which are the dissipation-free conservation equations. Strictly speaking, shocks are not present in nature because some dissipation (dispersion, diffusion, capillary pressure, compressibility, and thermal conductivity) is always present, which militates against their formation. When such effects are present, the shocks are smeared or spread out around the shock front position, but the position of the shock is unaltered. Despite this restriction, shocks play a central role in fractional-flow theory, in which dissipative effects are neglected, and describe many actual flows to a good approximation.

To calculate the velocity and magnitude of the shock, we require that mass be conserved at the shock, recasting the differential equations of this chapter into difference equations. This we do generally in Section 5.4; here, we restrict ourselves to the water-displacing-oil problem already begun.



(a) Schematic of material balance around shock



(b) Saturation profile for fractional flow curve of fig 5.2a

Fig. 5.3—Water-saturation profiles with shocks.

Paradoxically, calculations are considerably easier when shocks form. [Fig. 5.3a](#) shows a water-saturation shock moving from left to right. The water saturation ahead of the shock is S_1^- (downstream direction) and that behind the shock is S_1^+ (upstream direction). The quantity $\Delta S_1 = S_1^+ - S_1^-$ is the saturation jump across the shock. A cumulative water balance on a control volume that contains the shock in the time interval Δt is

$$\begin{pmatrix} \text{Volume water} \\ \text{present at } t + \Delta t \end{pmatrix} - \begin{pmatrix} \text{Volume water} \\ \text{present at } t \end{pmatrix} = \begin{pmatrix} \text{Volume water} \\ \text{in during } \Delta t \end{pmatrix} - \begin{pmatrix} \text{Volume water} \\ \text{out during } \Delta t \end{pmatrix}$$

$$\left\{ \left[v(t + \Delta t) - x_1 \right] S_1^+ + \left[x_2 - v(t + \Delta t) \right] S_1^- \right\} A\phi - \left[(vt - x_1) S_1^+ + (x_2 - vt) S_1^- \right] A\phi = \left[f_1(S_1^+) - f_1(S_1^-) \right] \int_t^{t+\Delta t} q dt.$$

After some cancellation, we obtain a specific shock velocity

$$v_{\Delta S_1} = \frac{f_1(S_1^+) - f_1(S_1^-)}{S_1^+ - S_1^-} \equiv \frac{\Delta f_1}{\Delta S_1}. \quad \dots \dots \dots \quad (5.14a)$$

To incorporate shock formation into the water-displacing-oil problem, consider a saturation profile containing a triple value over some region and containing a single value elsewhere ([Fig. 5.3b](#)). If there is a spreading wave upstream of the shock, as in this example, some saturation S_1^* will mark the end of the continuous water-saturation region and the beginning of a shock. This saturation must satisfy Eq. 5.14a while simultaneously eliminating the multiple values of saturation at the same location and satisfying an entropy condition for the shock. The entropy condition is needed as the result of neglecting dissipative forces in the Buckley-Leverett solution.

Entropy conditions were originally developed for gas-dynamics problems to ensure that entropy generation across a shock would be zero or positive (Courant and Friedrichs 1948; Lax 1957). Entropy conditions are therefore constraints on the upstream saturation S_1^* that enable the shock to continue to propagate in the presence of dissipative forces (capillary pressure for the Buckley-Leverett problem). When the shock front is dispersed, the saturations must instantaneously move at the velocities given by their characteristics, as shown in Eq. 5.12. If the saturation velocities in the upstream portion of the dispersed front move faster than the downstream saturation velocities, then the shock will continue to propagate because it is self-sharpening. If the dispersed-front saturations upstream, however, move slower than the downstream saturations, the shock will continue to spread. The latter case is a shock that would never evolve in the first place because once it began to form, it would be immediately dissipated. This would be an example of a physically infeasible shock [see Johns (1992) for example solutions].

The requirement of a self-sharpening shock (or one that satisfies the entropy condition) can be stated mathematically as

$$\frac{f_1(S_1^+) - f_1(S_1^-)}{S_1^+ - S_1^-} \geq \frac{f_1(S_1^+) - f_1(S_1)}{S_1^+ - S_1} \dots \dots \dots \quad (5.14b)$$

for all trial values of S_1 between S_1^- and S_1^+ . Stated geometrically, the shock line representing the shock-specific velocity must not intersect the upstream fractional-flow curve at a point at which ~~$f_1(S_1) = f_1(S_1)$~~ . For this case, with a spreading wave upstream of the shock, to satisfy Eq. 5.15 while preserving a single-valued solution, the velocity of the upstream saturation S_1^* must be equal to the shock velocity. [Fig. 5.3b](#) illustrates a shock that satisfies this condition. The saturation S_1^* simultaneously satisfies Eqs. 5.12 and 5.14; Eq. 5.12 gives velocities of S_1 greater than S_1^* and Eq. 5.14 gives velocities of S_1 less than S_1^* . Equating Eqs. 5.12 and 5.14 yields the following equation for S_1^* :

where we have assumed $S_1^- = S_{1/}$ in Eq. 5.14.

Eq. 5.15 lends itself to a graphical solution because

is the equation of a straight line of slope m passing through the point (f_{1I}, S_{1I}) on the fractional-flow plot. If $m = f'_1 \Big|_{S_1}$, then m is the slope of the fractional-flow plot at S_1^* . Comparing Eq. 5.16 to Eq. 5.15, S_1^* is at the tangent to the fractional-flow curve of a straight line passing through the point (f_{1I}, S_{1I}) . [Fig. 5.4](#) schematically illustrates this construction. The slope of this straight line is the specific shock velocity. The shock itself is a discontinuous change in saturation from S_{1I} to S_1^* at $x_D = v_{\Delta s_1} t_D$, as [Fig. 5.3b](#) illustrates. The saturation S_1^* is not the same as the saturation having the largest v_{s_1} ($S_1 = 0.5$ in [Fig. 5.2](#)). S_1^* is the saturation with the position that requires the net area between the mathematical solution and the physical solution (shaded region in [Fig. 5.3b](#)) to be zero, confirming that the shock preserves material balance (Eq. 5.14), while also satisfying the entropy condition. With this construction, all saturation velocities are monotonically (though not continuously) decreasing in the upstream direction. [Fig. 5.3b](#) illustrates the results of the entire construction. The resulting saturation profile is sometimes called the “leaky piston” profile.

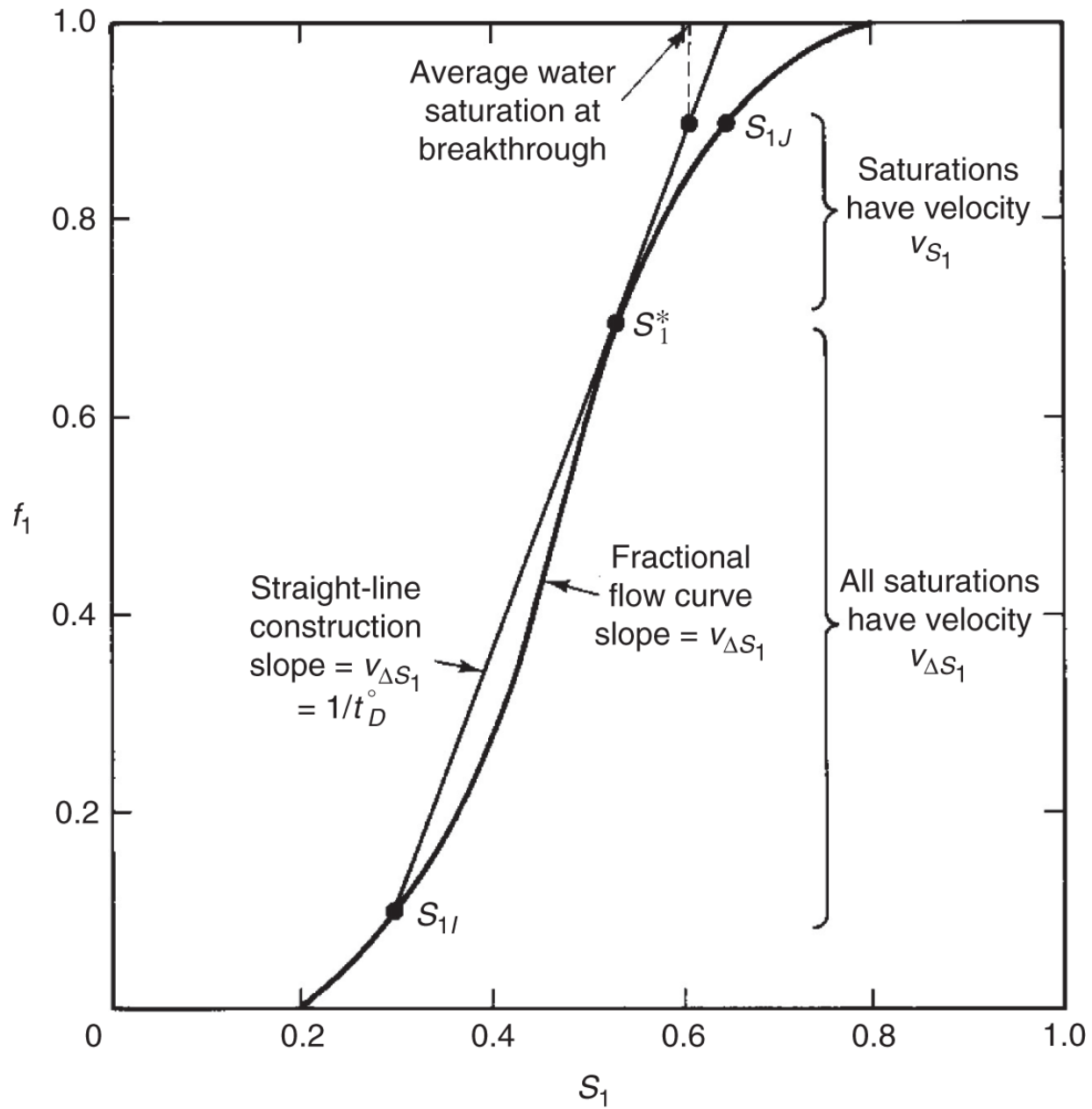


Fig. 5.4—Schematic of shock construction.

5.2.4 Wave Classification. Before further developing this theory and its applications to EOR, we define a few more terms used in subsequent discussions. These definitions are important to the interpretation of x_D vs. t_D plots that present the solution $S_1(x_D, t_D)$ graphically.

We have been discussing how to calculate water saturation as a function of position and time for water/oil displacements. A plot of

saturation or concentration vs. time at a fixed position is a saturation *history*. If water fractional flow is plotted at a fixed position at the outflow end of the permeable medium, it is an *effluent* history. Plots of saturation vs. position at a fixed time are saturation *profiles*. [Fig. 5.2b](#) is a water-saturation profile. Changes in saturation with time and position are saturation *waves*. Therefore, the previous development estimates the rate of propagation of waves through a permeable medium.

An important and unifying aspect of our understanding of EOR displacements is the study and characterization of the number and types of waves they form. Depending on their spreading characteristics, waves can be classified into four categories.

1. A wave that becomes more diffuse on propagation is a nonsharpening, rarified, or *spreading* wave. When these waves occur, the rate of spreading is usually much larger than that caused by dissipation.
2. A wave that becomes less diffuse on propagation is a *sharpening* wave. In the absence of dissipation, these waves will become shocks even if the initial saturation profile is diffuse. When dissipation is present, these waves will asymptotically approach a *constant pattern* condition (see Section 5.3).
3. A wave that has both spreading and sharpening characteristics is *mixed*. The Buckley-Leverett water-saturation wave of [Fig. 5.2b](#) is mixed, being a sharpening wave for $S_{1I} < S_1 < S_1^*$ and a spreading wave for $S_1^* < S_1 < S_{1J}$.
4. A wave that neither spreads nor sharpens on propagation is *indifferent*. In the absence of dissipation, indifferent waves appear as shocks.

This behavior may be summarized by defining a dimensionless mixing or transition zone Δx_D . This is the fraction of the total system length that lies between arbitrary saturation limits at a given time. We assume the saturation limits to be 0.1 and 0.9 of the span between the initial and injected saturations,

where

The exact value of the limits is unimportant to the behavior in the mixing zone. The wave classification, which can be restated as Δx_D , increases with time for spreading waves, decreases for sharpening waves, and either increases or decreases for mixed waves depending on whether the shock portion of the wave exceeds the saturations used to define Δx_D . The mixing-zone concept has general use in classifying mixing phenomena in a wide variety of displacements.

The final definition relevant to the Buckley-Leverett development is the *time/distance diagram*. These diagrams are plots of x_D vs. t_D on which appear lines of constant saturation. [Fig. 5.5](#) shows a time vs. distance diagram for the water/oil displacement in [Figs. 5.3b](#) and [5.4](#). The constant-saturation curves are straight lines with slope given by v_{s_1} , from Eq. 5.11. Similarly, the shock is the straight lines with slope given by Eq. 5.14. The region with varying saturation is shaded. Regions of constant saturation are adjacent to the waves and have no saturation lines. Time vs. distance diagrams are very convenient because they subsume both profiles and histories.

From the definition of effluent history, the shock portion of the water/oil displacement arrives at $x_D = 1$ when

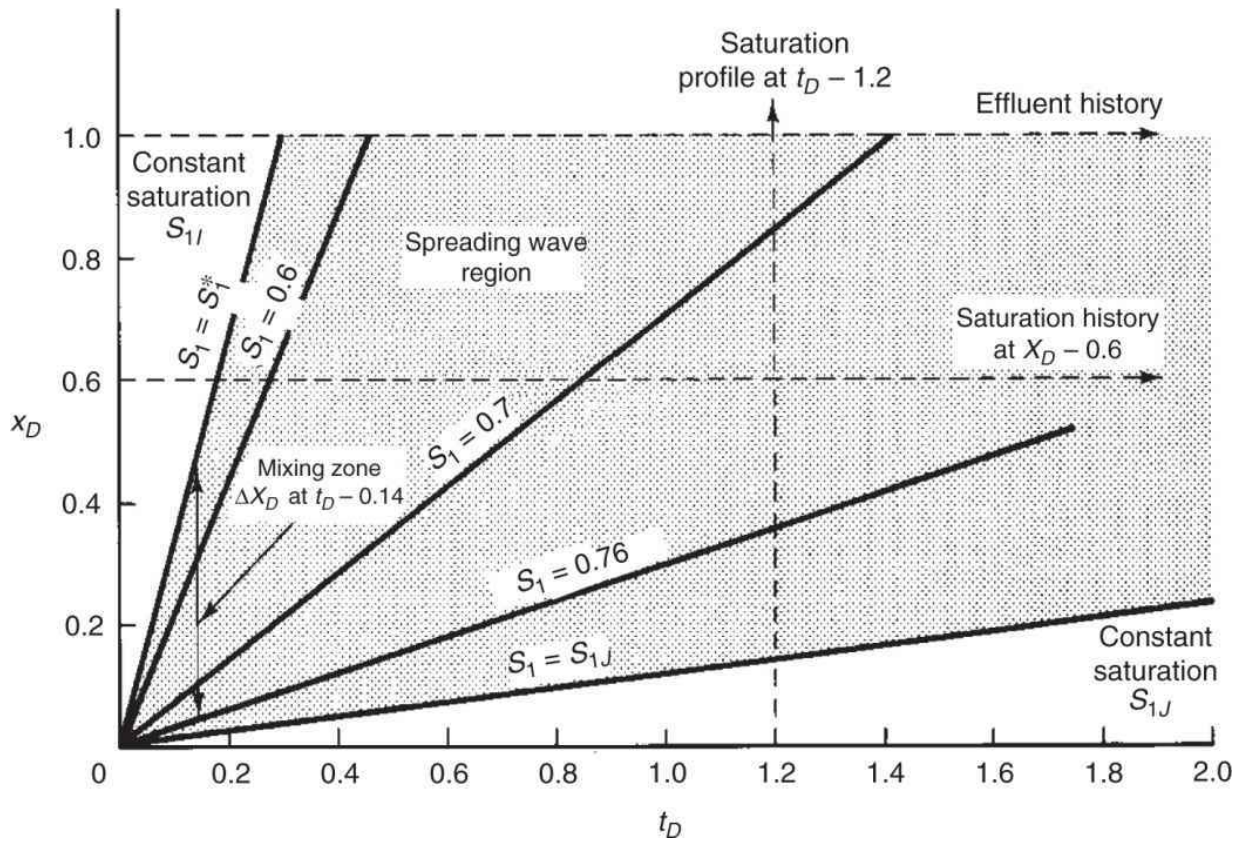


Fig. 5.5—Time/distance diagram for displacement of the case shown in Figs. 5.3b and 5.4.

* In this chapter, S_1^* means water saturation at the shock front.

from Eqs. 5.14 and 5.15. The *breakthrough time* t_D^0 is an important event in the displacement; for values $t_D > t_D^0$, increased water production occurs. The obvious inefficiency of this should suggest that we would like to conduct the displacement so that t_D^0 is as large as possible; that is, we would like to enhance the shock-forming characteristics of the displacement. For $t_D > t_D^0$, the water saturation at the outflow end is given implicitly by

from Eq. 5.12. In laboratory floods, it is usually more direct to measure $f_1|_{x_D=1}$, the water "cut," than the saturation at the effluent

end. The water and oil cuts ($1 - f_1 \Big|_{x_D=1}$) are functions of time only, from Eq. 5.18b.

5.2.5 Average Saturations. To determine displacement efficiency, we must have some method of calculating average saturations because, from Eq. 5.2, these appear in the definition of E_D . These averages are provided by the Welge integration procedure (Welge 1952). Consider the saturation profile in Fig. 5.3b at fixed t_D , and let x_{D1} be any dimensionless position at or behind the shock-front position, $x_{D1} \leq v_{\Delta S_1} t_D$. The average water saturation behind x_{D1} is

$$\hat{S}_1(t_D) = \frac{1}{x_{D1}} \int_0^{x_{D1}} S_1 dx_D. \quad (5.19)$$

Eq. 5.19 can be integrated by parts, yielding

$$\hat{S}_1 = \frac{1}{x_{D1}} \left[(x_D S_1) \Big|_0^{x_{D1}} - \int_{S_{1J}}^{S_{11}} x_D dS_1 \right], \quad (5.20)$$

where $S_{11} = S_1 \Big|_{x_{D1}}$. Because x_{D1} is in the spreading portion of the saturation wave, the x_D integrand may be replaced by Eq. 5.13, giving

$$\hat{S}_1 = S_{11} - \frac{1}{x_{D1}} \int_{S_{1J}}^{S_{11}} t_D f'_1 dS_1, \quad (5.21)$$

which can be readily integrated (recall that t_D is fixed) to yield

$$\hat{S}_1 = S_{11} - \frac{t_D}{x_{D1}} (f_{11} - f_{1J}). \quad (5.22)$$

Eq. 5.22 relates the average water saturation behind x_{D1} to the fractional flow and saturation at that point. t_D can be replaced by Eq. 5.13 at this point to give

$$\hat{S}_1 = S_{11} - \frac{(f_{11} - f_{1J})}{f'_{11}}. \quad (5.23)$$

Eq. 5.23 is the final form of the Welge integration.

The most common use of this procedure is to let $x_{D1} = 1$ after water breakthrough ($t_D \geq t_D^0$), at which point $\hat{s}_1 = \bar{s}_1$, and f_{11} becomes the water cut. Then the water saturation at the outflow end can be calculated from Eq. 5.22 as

If the water cut and the average water saturation are known from direct measurement, simultaneous application of Eqs. 5.18 and 5.24 provides a way to estimate the fractional-flow curves $\left(f_1 \Big|_{x_D=1} \text{ vs. } S_1 \Big|_{x_D=1} \text{ or } f_{11} \text{ vs. } S_{11}\right)$ from experimental data.

The average water saturation follows from Eq. 5.23 for \bar{S}_1 with the f_1 vs. S_1 curve known. This equation can be rearranged to give

Therefore, \bar{S}_1 at any $t_D \geq t_D^0$ is given by the extension of a straight line tangent to the fractional-flow curve at $(f_1, S_1)_{x_D=1}$ to intersect with the y-coordinate at $f_1 = f_{1J}$. The dimensionless time required to bring this point to $x_D = 1$ is the reciprocal slope of this line from Eq. 5.18. Fig. 5.4 shows the graphical procedure to accomplish this. From the \bar{S}_1 thus determined, $\bar{S}_2 = 1 - \bar{S}_1$ may be used in the definition (Eq. 5.2) to calculate E_D .

The above construction and Eqs. 5.24 and 5.25 apply only to dimensionless times after breakthrough. Before breakthrough, the average water saturation is

$$\bar{S}_I = S_{II} + t_D (f_{IJ} - f_{II}), \quad t_D < t_D^0, \dots \quad (5.26)$$

by applying the overall water material balance (Eq. 2.52) to this special case. Eqs. 5.24 and 5.26 are identical except for the value used for the effluent water cut.

We are now ready to demonstrate the effects of the endpoint mobility ratio M^0 , relative permeability, and $N_g^0 \sin \alpha$ on oil-displacement efficiency. [Fig. 5.6](#) schematically shows the effect of these parameters for displacements with $f_{1I} = 0$ and $f_{1J} = 1$. [Fig. 5.6](#) shows, from top to bottom, plots of E_D vs. t_D , water-saturation profiles at various t_D , and the fractional-flow curve that would yield the indicated behavior. From left to right, the figures show oil-displacement behavior for decreasing M^0 , increasing $N_g^0 \sin \alpha$, and increasing water wetness through shifts in the relative-permeability curves. [Fig. 5.6](#) represents three of the four types of waves: spreading, mixed, and sharpening. Several important conclusions follow directly from [Fig. 5.6](#).

1. Any change that increases the size of the shock portion of the water-saturation wave also increases E_D at any given t_D . These changes also delay water breakthrough and decrease the time over which the permeable medium is simultaneously producing two phases.
2. Decreasing M^0 , increasing $N_g^0 \sin \alpha$, and increasing water wetness improve E_D . Of these three, M^0 is usually the only one on which we can have any impact. [Chapter 6](#) tells us that decreasing the mobility ratio also increases vertical and areal sweep efficiency; hence, decreasing the mobility ratio improves oil recovery in at least three ways. EOR processes that rely, partly or totally, on lowering the mobility ratio between the displacing and displaced fluids are said to be based on the *mobility-ratio concept* of oil recovery. [Fig. 5.6](#) shows that when the water-saturation wave becomes a pure shock (the displacement is piston-like), no advantage is to be gained for E_D by further lowering M^0 . Finally, there is no unique value of M^0 at which the wave changes from spreading to sharpening because the displacement is affected also by the shape of the relative-permeability curves.
3. However low M^0 might be, the ultimate displacement efficiency

$$E_D^\infty = \frac{(S_{2I} - S_{2r})}{S_{2I}}$$

is limited by the presence of residual oil saturation. EOR methods that intend to recover residual oil must rely on something other than the mobility-ratio concept, such as displacing with miscible agents (see Section 5.5 and [Chapter 7](#)) or lowering the water/oil interfacial tension (see [Chapter 9](#)).

Besides M^0 , at least two other mobility ratios are in common use. The average mobility ratio \bar{M} defined as

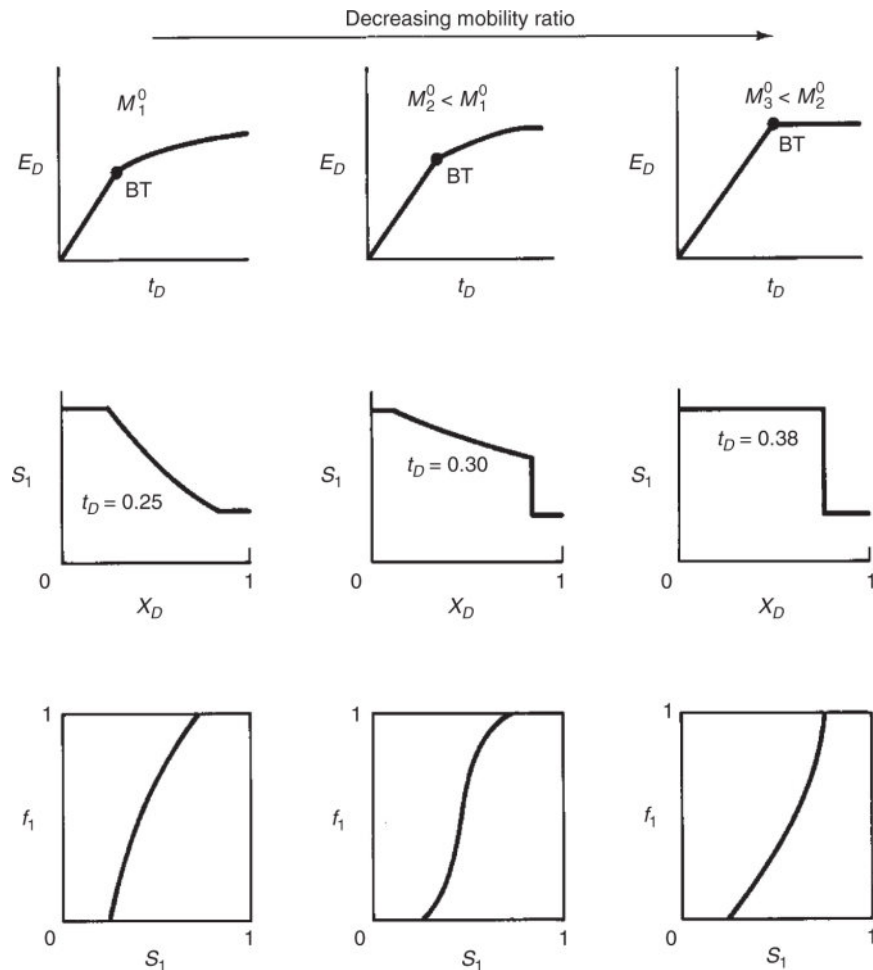


Fig. 5.6—Schematic of effect of mobility ratio on displacement efficiency. Residual phase saturations are unchanged.

is the ratio of total relative mobility at the average water saturation behind the shock front to the same quantity evaluated at the initial water saturation. \bar{M} is commonly used to correlate the areal sweep efficiency curves (see [Chapter 6](#)). The shock-front mobility ratio M_{sh} can be described as

$$M_{sh} = \frac{(\lambda_{r1} + \lambda_{r2})|_{S_1=S_1^*}}{(\lambda_{r1} + \lambda_{r2})|_{S_1=S_{1I}}}. \dots \dots \dots \quad (5.27b)$$

M_{sh} is the quantity that controls the formation of viscous fingers. For piston-like displacements, all three definitions are the same.

The most general definition of mobility ratio is actually the ratio of pressure gradients ahead of and behind a displacing front. The above definitions, depending on the character of the displacing front, follow from this for the case of incompressible flow (spatially independent volumetric flow rate). For compressible flows or flows of condensing fluids, the general definition is more appropriate (see [Chapter 11](#) and Exercise 5.10).

5.3 Dissipation in Immiscible Displacements

In this section, we discuss two common dissipative effects in 1D flows: capillary pressure and fluid compressibility. Both phenomena are dissipative; they cause mixing zones to grow faster than or differently from a dissipation-free flow. Both phenomena also entail additional effects.

5.3.1 Capillary Pressure. Without giving a closed-form solution to the water-conservation equation, we can qualitatively illustrate the effect of capillary pressure on a water/oil displacement and can give, through scaling arguments, quantitative guidelines on when it might be important. For incompressible fluids and with capillary pressure P_c included, the water material balance (Eq. 5.3) still applies, but the water fractional flow (Eq. 5.4) becomes (see Exercise 5.6)

$$f_1(S_1) = \frac{\lambda_{r1}}{\lambda_{r1} + \lambda_{r2}} \left(1 - \frac{k\lambda_{r2}\Delta\rho g \sin\alpha}{u} \right) + \frac{k\lambda_{r1}(\partial P_c / \partial x)}{(1 + \lambda_{r1} / \lambda_{r2})u}. \quad \dots \quad (5.28)$$

The first term on the right side of Eq. 5.28 is simply the water fractional flow in the absence of capillary pressure (Eq. 5.4); therefore, many of the conclusions about displacements with $P_c = 0$, although somewhat modified, carry over to displacements with capillary pressure. The second term on the right side of Eq. 5.28 is the contribution of P_c to the water fractional flow. Including the capillary-pressure term causes the character of Eq. 5.3 to change from hyperbolic to parabolic, which is a general result of dissipative effects because of the spatial P_c derivative.

The capillary pressure in Eq. 5.28 is the phase pressure difference between two continuous oil and water phases (see Section 3.2). The derivative $\partial P_c / \partial x = (dP_c / dS_1) \cdot (\partial S_1 / \partial x) > 0$ for displacements in both oil-wet and water-wet media because $dP_c / dS_1 < 0$ for both cases (see [Fig. 3.5](#)), and also $\partial S_1 / \partial x < 0$ in a waterflood. Therefore, for waterfloods, capillary pressure increases the water fractional flow at a given water saturation. This augmentation is particularly important in regions with large saturation gradients (i.e., around shock fronts predicted by the Buckley-Leverett theory). In an oil displacement of water, P_c causes a smaller water fractional flow because $\partial S_1 / \partial x > 0$.

The effect of P_c on a 1D displacement is to spread out the water-saturation wave, particularly around shocks. [Fig. 5.7](#), which illustrates how this comes about, is a simulated water-saturation and pressure profile for a 1D waterflood in a water-wet medium. [Fig. 5.7a](#) shows water-saturation profiles with and without capillary pressure; [Fig. 5.7b](#) shows the corresponding pressure profiles. Both panels are at the same *time*. The dotted phase pressures in [Fig. 5.7b](#) are those that would be present if the shock remained in the water-saturation profile. Of course, representing shock waves with $P_c \neq 0$ is not correct, but such a portrayal presents the driving force for capillary mixing.

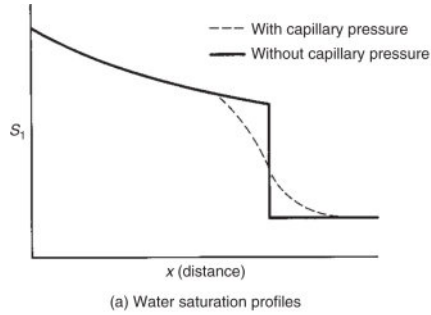
Ahead of the front (downstream), the difference between the oil- and water-phase pressures is constant and equal to the capillary pressure at S_{1I} . At the front, the phase pressures change rapidly. However, behind the front (upstream), the difference between the oil- and water-phase pressures declines to the value at $S_1 = S_{1J}$. Compare these observations to [Figs. 5.7a](#) and [3.5](#). There is now a local pressure gradient at the shock that causes oil to flow upstream (countercurrent imbibition) and water to flow downstream faster than under the influence of viscous forces only. The resulting local mixing causes the shock to spread ([Fig. 5.7a](#)) and the pressure discontinuity to disappear. Behind the front, in the spreading portion of the water-saturation wave, the effect of capillary pressure is small.

The effect of capillary pressure will be small if the system length L is large. Consider the dimensionless water-conservation equation with Eq. 5.28 substituted and $\alpha = 0$:

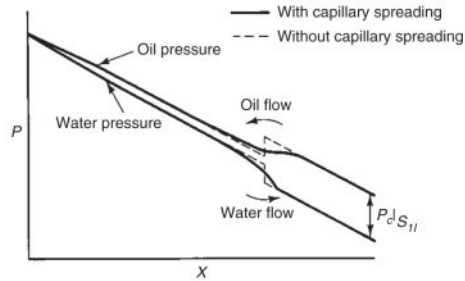
$$\frac{\partial S_1}{\partial t_D} + \frac{\partial}{\partial x_D} \left(\frac{1}{1 + \frac{\lambda_{r2}}{\lambda_{r1}}} \right) + \frac{\partial}{\partial x_D} \left[\frac{k \lambda_{r1}}{u L \left(1 + \frac{\lambda_{r1}}{\lambda_{r2}} \right)} \frac{\partial P_c}{\partial x_D} \right] = 0. \dots \quad (5.29)$$

The last term on the left side of this equation is nonlinear in S_1 and, therefore, difficult to estimate. Using the Leverett j -function expression (Eq. 3.13), we write Eq. 5.29 as

$$\frac{\partial S_1}{\partial t_D} + \frac{\partial}{\partial x_D} \left(\frac{1}{1 + \frac{\lambda_{r2}}{\lambda_{r1}}} \right) - \frac{1}{N_{RL}} \frac{\partial}{\partial x_D} \left[g(S_1) \frac{\partial S_1}{\partial x_D} \right] = 0, \dots \quad (5.30)$$



(a) Water saturation profiles



(a) Water and oil phase pressure profiles

Fig. 5.7—Saturation and pressure profiles under longitudinal capillary imbibition (Yokoyama 1981).

where g is a positive dimensionless function of water saturation,

$$g(S_1) = - \left(\frac{1}{1 + \frac{\lambda_{r2}}{\lambda_{r1}}} \right) \left(\frac{S_1 - S_{1r}}{1 - S_{2r} - S_{1r}} \right)^{n_1} \frac{dj}{dS_1}, \dots \quad (5.31)$$

and N_{RL} , the Rapoport and Leas number, is a dimensionless constant first applied by these authors (1953) to indicate when capillary pressure effects will be important:

$$N_{RL} = \left(\frac{\phi}{k} \right)^{1/2} \frac{\mu_1 u L}{k_{r1}^0 \phi \sigma_{12} \cos \theta}. \dots \quad (5.32)$$

[Fig. 5.8](#) shows a plot of fractional oil recovery at water breakthrough vs. $\mu_1 v L$ (recall that $v = u/\phi$) from the experimental work of Rapoport and Leas (1953). Because $S_{1I} = 0$ in their cores, the vertical axis in [Fig. 5.8](#) is the breakthrough displacement efficiency, E_D^o . As $\mu_1 v L$ increases, E_D^o increases to a maximum of 0.58. For larger $\mu_1 v L$, E_D^o is constant at the value predicted by the Buckley-Leverett theory.

Rapoport and Leas did not plot their results against the more general N_{RL} ; however, using the given $k = 0.439 \text{ } \mu\text{m}^2$ and $\phi = 0.24$ and taking $k_{r1}^0 \sigma_{12} \cos \theta = 1 \text{ mN/m}$ (which is typical of water-wet media), P_c does not affect a 1D water/oil displacement if N_{RL} is greater than approximately 3. Because of the length appearing in the numerator of Eq. 5.32, P_c affects the displacement front to a much greater degree in laboratory floods than in field-scale displacements because of the larger L on the field scale.

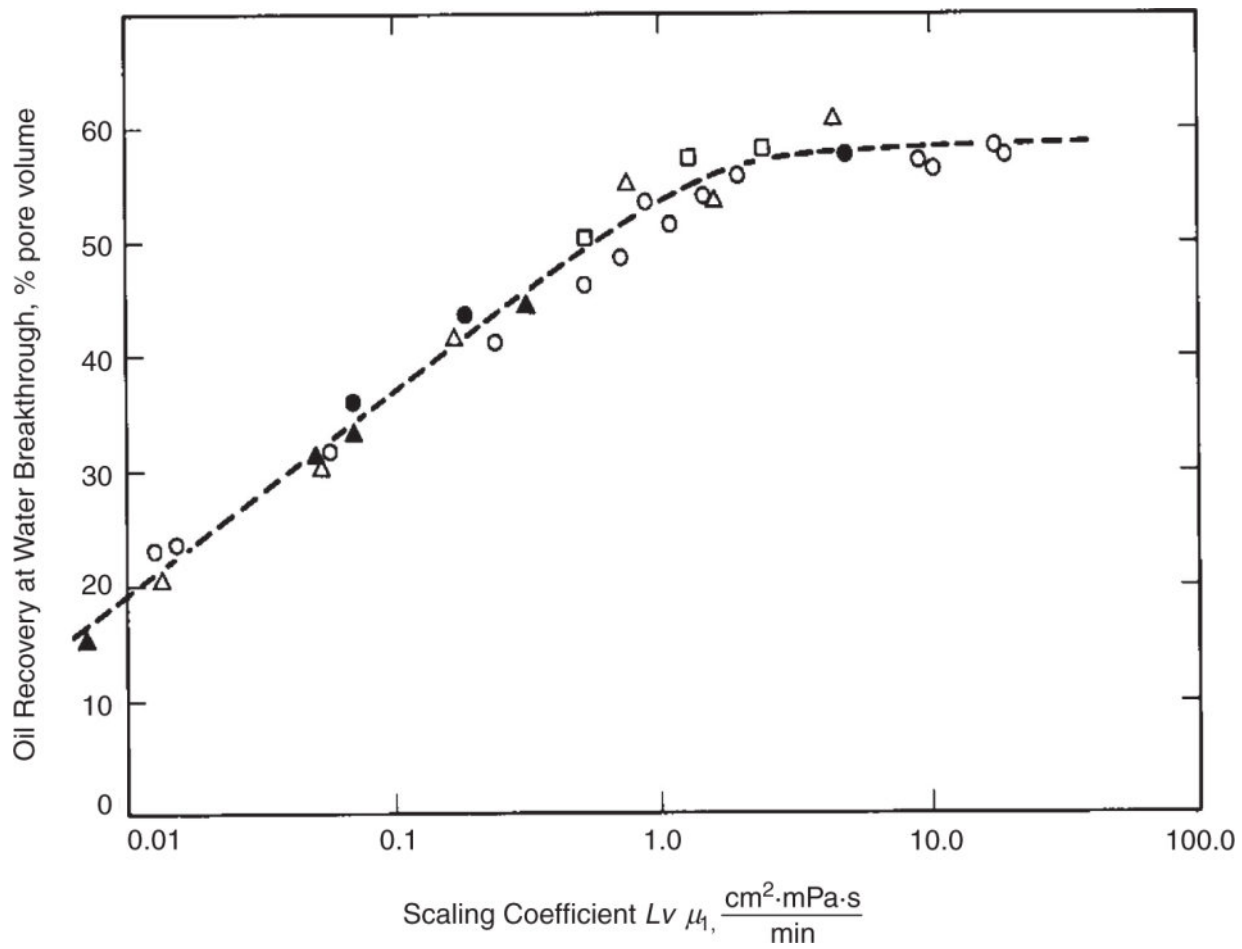


Fig. 5.8—Relation between oil recovery at breakthrough and scaling coefficient in dry-filled aluminum cores with no connate water. The different symbols represent varying core lengths and oil viscosities (Rapoport and Leas 1953).

Of course, on a microscopic scale, capillary forces are important in determining the amount of trapped or residual oil in either laboratory or field displacements. In Section 3.3, we saw that the value of S_{2r} depended on a local viscous-to-capillary-force ratio, the capillary number N_{vc} . A common form of capillary number, $N_{vc} = v\mu_1 / k_r^0 \sigma_{12} \cos\theta$, is embedded in the definition of N_{RL} :

$$N_{RL} = \left(\frac{\phi}{k} \right)^{1/2} L N_{vc} \dots \dots \dots \quad (5.33)$$

The factor, $L(\phi/k)^{1/2}$, is a measure of the ratio of the macroscopic permeable-medium dimension to a characteristic rock dimension.

Therefore, N_{vc} and N_{RL} are expressing the same physical idea—capillary-to-viscous-force ratios—but at different scales.

Recall that if N_{vc} is less than approximately 10^{-5} , the residual phase saturations are roughly constant. For well-sorted media, we can then put limits on N_{RL} so that capillary forces, on any scale, do not affect the displacement:

$$3 < N_{RL} < 10^{-5} L \left(\frac{\phi}{k} \right)^{1/2}. \quad \dots \dots \dots \quad (5.34)$$

(no (constant residual
dissipation) saturations)

For large L , this is an extremely wide range and accounts for the common neglect of all capillary forces in 1D displacement calculations. At the laboratory scale, it is rarely possible to satisfy both requirements.

N_{RL} can be expressed in more direct ways. From Eq. 5.32, we can substitute Darcy's law for water in linear flow evaluated at $S_1 = 1 - S_{2r}$ for $v = u/\phi$ to obtain

$$N'_{RL} = \left(\frac{\phi}{k} \right)^{1/2} \frac{\Delta P_1}{\sigma_{12} \cos \theta}, \quad \dots \dots \dots \quad (5.35)$$

where ΔP_1 is the pressure drop across the permeable medium measured through the water phase. The terms containing permeability and interfacial tension can be expressed in terms of the Leverett j -function to give yet another approximation to N_{RL} :

$$N''_{RL} = \frac{\Delta P_1}{\Delta P_c}, \quad \dots \dots \dots \quad (5.36)$$

where ΔP_c is the change in capillary pressure between the initial and final water-saturation states. Eq. 5.36 is a direct comparison of viscous and capillary pressure drops and is the least rigorous, but most direct, of all the measures. Eqs. 5.35 and 5.36 apply to linear flow.

For small N_{RL} , capillary pressure will cause sharpening waves to spread. Although there is a parallel between dispersion in miscible displacements (see Section 5.5) and P_c effects in immiscible displacements, the analogy does not carry over to mixing-zone growth. We show in Section 5.5 that dispersive mixing zones grow in proportion to the square root of time. Capillary pressure generally causes mixing zones to grow exponentially to some asymptotic limit, at which point they proceed, without further growth, as a simple translation. As we have seen, P_c effects cause such a wave to spread, but there is still a strong tendency for the wave to sharpen because of the convex-upward shape of the fractional-flow curve. These two effects tend to balance each other, causing the wave to approach an asymptotic limit. The existence of such a limit further restricts the importance of capillary pressure as a mixing mechanism in one dimension. Asymptotic or “stabilized” mixing zones in 1D laboratory waterfloods have been noted by several authors (Bail and Marsden 1957).

No discussion of how capillary pressure influences a 1D displacement is complete without some mention of the capillary end effect. This effect occurs when there is a discontinuity in the capillary-pressure curve, as, for example, when the 1D permeable medium consists of two homogeneous media of differing permeabilities arranged in series. However, it most commonly occurs at the end of a laboratory core, where the flowing phases pass from a permeable medium to a region of porosity equal to unity and zero capillary pressure. The saturation behavior at the plane of discontinuity is considerably different from that predicted by the Buckley-Leverett theory.

Consider the water-saturation and pressure profiles of a waterflood in a water-wet medium shown in [Fig. 5.9](#). Capillary forces are such that they cannot be neglected. [Fig. 5.9a](#) shows the instant that water arrives at the outflow boundary ($x = L$), and [Fig. 5.9b](#) shows the system some time later. To the right of the boundary, capillary pressure is zero if any water is present. The oil- and water-phase pressures must be continuous at $x = L$. Hence, water cannot flow

across the outflow end of the medium until the capillary pressure just inside the system vanishes, because water cannot cross the boundary against a positive jump in water pressure. Initially, there is no production of water at $x = L$, but with continual water transport to the outflow end, the water saturation rises at $x = L$ until $P_c = 0$ ($S_1 = 1 - S_{2r}$) at this boundary. Hence, the capillary end effect causes a delay in water production and a distortion of the water saturation at $x = L$ compared to that predicted by the Buckley-Leverett theory ([Fig. 5.9b](#)).

This delay can cause considerable error in applying the Welge integration procedure (Eq. 5.24). The capillary end effect has been observed experimentally by Kyte and Rapoport (1958) and in simulations by Douglas et al. (1958). [Fig. 5.10](#) shows data that illustrate the capillary end effect.

The capillary end effect introduces a paradox. Water cannot exit the permeable medium unless $P_c = 0$ at the boundary, but if $P_c = 0$, $S_2 = S_{2r}$, $k_{r2} = 0$, and oil cannot exit. Nature resolves this in one of two ways. Either the flow of each phase is intermittent, or else the pressure gradient right at the boundary is so large that oil can flow at its residual saturation (Section 3.4). In either case, the paradox applies only in a narrow region just at the outlet of the permeable medium.

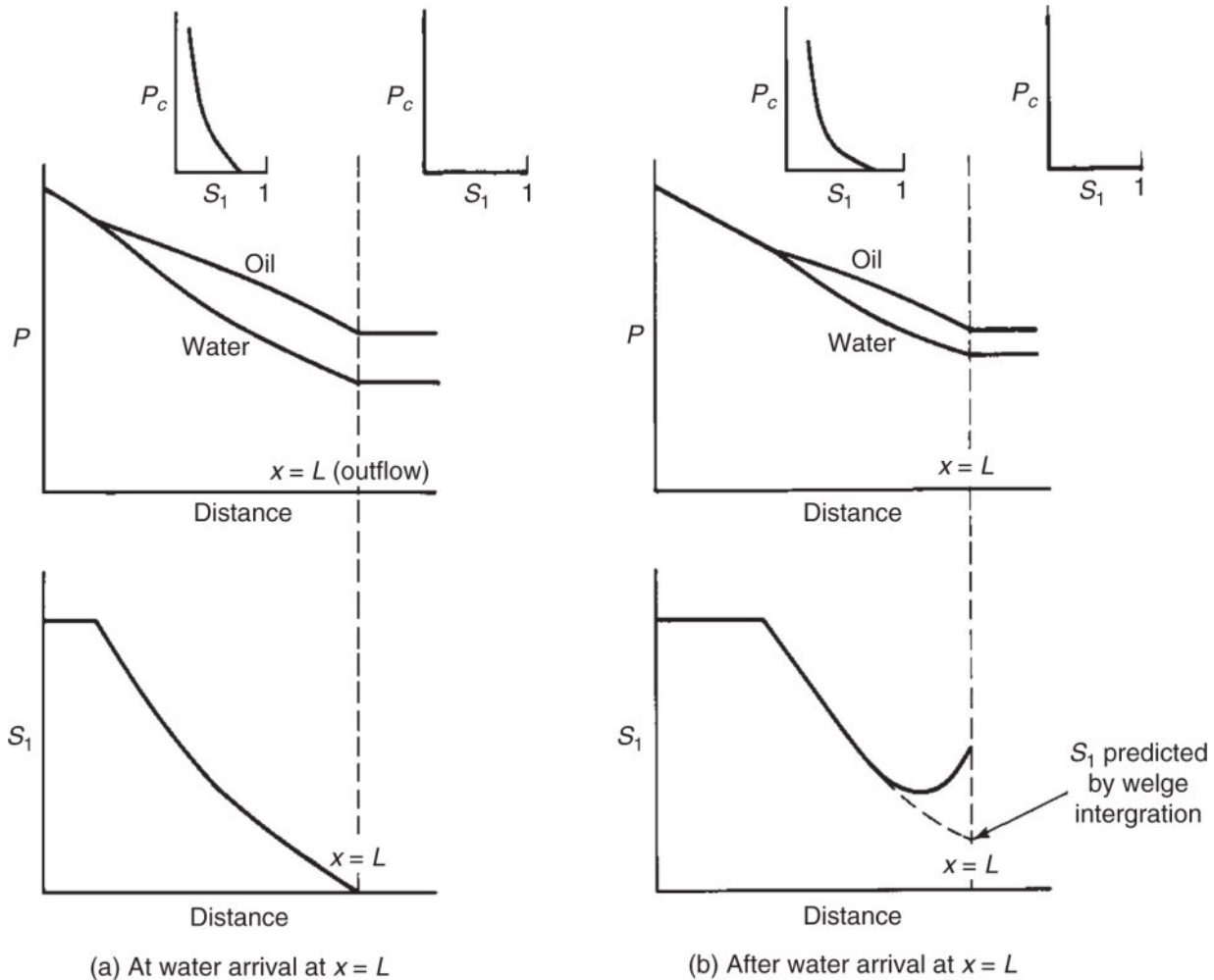


Fig. 5.9—Schematic of the capillary end effect. The water saturation at the outlet end can build up to the final value.

To minimize the capillary end effect, laboratory floods are run at high velocities and with long lengths (both increase N_{RL}) or by placing a second permeable material at the outflow end to ensure good capillary contact.

5.3.2 Fluid Compressibility. A second dissipative effect is fluid compressibility. [Fig. 5.11](#) shows water-saturation profiles for two simulated waterfloods with compressible oil and incompressible water ([Fig. 5.11a](#)) and compressible water and incompressible oil ([Fig. 5.11b](#)). The completely incompressible Buckley-Leverett case is shown for comparison. These results are from computer simulations with constant water-injection rate ([Fig. 5.11a](#)) and constant oil-

production rate ([Fig. 5.11b](#)). We present these results as the product of compressibility and total pressure drop ΔP (neglecting capillary forces) because this quantity determines the appropriateness of the assumption of low-compressibility fluid in well test analysis. For $c_j \Delta P$ of 0.01 or less, the effect of fluid compressibility is negligible; the smearing of the shock fronts for the $c_j \Delta P = 1.25' \times 10^{-3}$ runs occurs because of numerical dispersion, which is an artificial dissipative effect. The $c_j \Delta P$ products shown in [Fig. 5.11](#) are, of course, unrealistically large; we have selected these values only to emphasize the effect of compressibility.

The effect of either oil or water compressibility is to spread out the Buckley-Leverett shock front in addition to the spreading caused by numerical dispersion, but the effect does not become pronounced until $c_j \Delta P$ is one or more. However, we would expect displacements in which both fluids are compressible to experience a combined dissipative effect with greater spreading. In [Fig. 5.11a](#), the water saturation exceeds $1 - S_{2r}$ at the inflow end. At higher pressure, oil compression occurs below its residual value. Similarly, in [Fig. 5.11b](#), the water saturation exceeds S_{1r} at the effluent end because, at the reduced pressure, the water expands. These effects are characteristic of the particular conditions under which the runs were made. If the production pressure had been held constant and the phase saturations had not been allowed to decrease below their respective residuals, neither effect would have been present. Still, we can see from [Fig. 5.11](#) that the effect of compressibility is qualitatively similar to that of capillary pressure; a spreading of the shock fronts occurs, but with a lesser effect on the saturation “tail.”

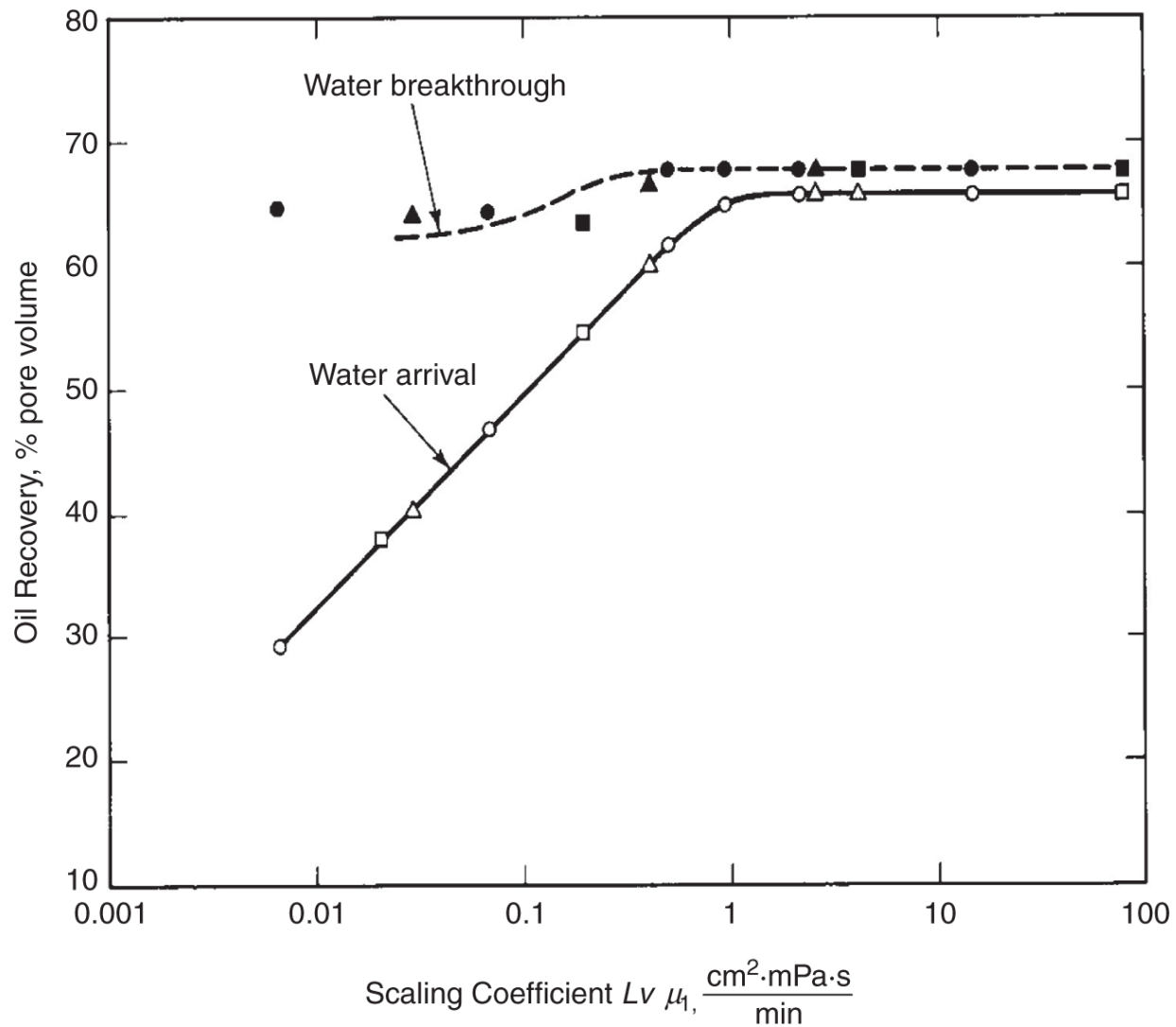


Fig. 5.10—Correlation of waterflood test data in strongly water-wet aluminum cores (Kyte and Rapoport 1958).

5.4 Ideal Miscible Displacements

Two components are mutually miscible if they mix in all proportions without an interface forming between them. The definition is translated into the fluid-flow equations by allowing a phase to be composed of several components that are mutually miscible.

In this section, we discuss isothermal miscible displacements using fractional-flow theory and with one or more phases present. Our presentation considers ideal miscible displacements with components that do not change the properties of the phases in which they are

formed (see [Chapter 7](#) for a description of more complex displacements).

5.4.1 Concentration Velocities. Many of the concepts in Section 5.2 readily generalize to miscible displacements. We can write a 1D conservation equation for $i = 1, \dots, N_c$ components as

$$\phi \frac{\partial}{\partial t} \left[\sum_{j=1}^{N_p} S_j C_{ij} + \left(\frac{1-\phi}{\phi} \right) C_{is} \right] + u \frac{\partial}{\partial x} \left(\sum_{j=1}^{N_p} f_j C_{ij} \right) = 0, \quad i = 1, \dots, N_c. \quad \dots \dots \dots \quad (5.37)$$

Eq. 5.37 is a special case of Eq. 2.63 with dispersion neglected. f_j is the fractional flow of phase j , given by Eq. 2.43 with capillary pressure neglected, and C_{ij} and C_{is} are the phase concentrations of component i in phase j and on the solid, respectively. Of course, the assumptions associated with Eq. 2.58—constant porosity, incompressible fluids, and ideal mixing—also apply. In nondimensional form, Eq. 5.37 becomes

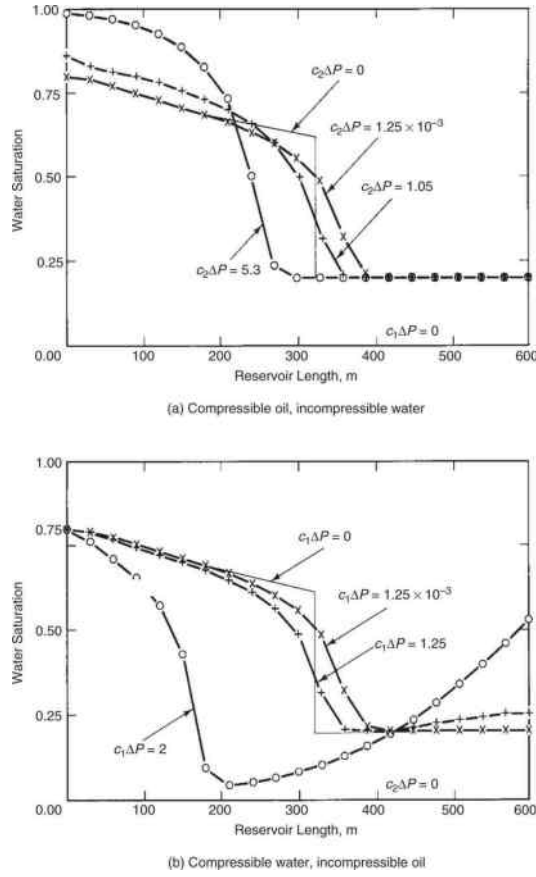


Fig. 5.11—Water-saturation profiles for 1D water-displacing-oil floods at $t = 200$ days [adapted from Samizo (1982)].

where

$$C'_{is} = \text{Solid-phase concentration of } i \text{ on a pore-volume basis} = C_{is} \left(\frac{1-\phi}{\phi} \right) \dots \dots \dots \quad (5.39b)$$

$$F_i = \text{Overall flux of species } i = \sum_{j=1}^{N_p} f_j C_{ij}. \quad \dots \quad (5.39c)$$

The transform accomplished by Eq. 5.39b changes the solid-phase concentration from a solid-volume basis (C_{is} is amount i on

solid/volume solid) to a pore-volume basis (C'_{is} is amount i on solid/pore volume). Therefore, C_i and C'_{is} are directly comparable and may be used together in later work without the need to manipulate units. The definition of overall flux is from Hirasaki (1981) and Helffterich and Klein (1981).

In principle, the fluxes F_i are functions of C_i for $i = 1, \dots, N_C$, and we carry over many of the definitions, particularly those of saturation velocity, directly from Section 5.2. In practice, however, the relations $F_i = F_i(C_1, C_2, \dots, C_{N_C})$ are extremely convoluted. We give a summary of this relation here.

With C_i known, the C_{ij} and S_j can be calculated from phase-equilibrium relations. The exact nature of the “flash” calculation depends on the nature of the phase behavior (see Section 4.4 and [Chapters 7](#) and [9](#)). With S_j and C_{ij} known, the phase relative permeabilities $k_{rj} = k_{rj}(S_j, C_{ij})$ and viscosities $\mu_j = \mu_j(C_{ij})$ can be calculated from petrophysical relations (see Section 3.3). From these follow the relative mobilities $\lambda_{rj} = k_{rj}/\mu_j$, which lead directly to the f_j from Eq. 2.43. If the phase densities are also required (if, for example, the permeable medium is not horizontal), they follow from $\rho_j = \rho_j(C_{ij})$ (Eq. 2.2-12). With f_j and C_{ij} known, F_i follows from Eq. 5.39c. If needed, $C'_{is} = C'_{is}(C_{ij})$ can be calculated also from the adsorption isotherm (see [Chapters 8](#) and [9](#)).

Despite this complexity, we can write Eq. 5.4-2 as

The partial derivatives $\left(\frac{\partial C'_{is}}{\partial C_i}\right)_{j_p}$ and $\left(\frac{\partial F_i}{\partial C_j}\right)_{j_p}$ in Eq. 5.4-4 follow from the chain rule. These derivatives are not the same as $\left(\frac{\partial C'_{is}}{\partial C_j}\right)_{C_{m \neq j}}$, which occur in the definition of the total differential.

The latter derivatives can be calculated directly from $C'_{is} = C'_{is}(C_{ij})$ and $F_i = F_i(C_i)$, whereas the former derivatives require knowledge of $C_i =$

$C_i(x_D, t_D)$, which are solutions. Therefore, Eq. 5.40 is of limited use except to enable the definition of the specific concentration velocity v_{C_i} :

by analogy with Eq. 5.12. The definition of the specific shock velocity $v_{\Delta c_i}$ is

which follows using the weak form of Eq. 5.40.

Without additional constraints, the definitions (Eqs. 5.41a and 5.41b) impart no new information. However, for the water/oil case of Section 5.2, they reduce to $C_i = S_1$, $F_i = f_1$, and $C'_{is} = 0$, giving

The last equality is possible because f_1 is a function of S_1 only; hence, $f'_1 = (\partial F_1 / \partial S_1)_{T_D} = (\partial F_1 / \partial S_1)_{x_D}$. Certainly for more complex cases, this simplification is not possible; still, many of the displacements of interest can be solved using the coherent or simple wave theory discussed in Section 5.5. We now discuss other particularly simple special cases of miscible displacements.

5.4.2 Tracers in Two-Phase Flow. The simplest case considered here is the miscible displacement in single-phase flow of Component 2 by Component 1. For this case, f_j and S_j are zero for all value of j except 1. For this particular j , f_j , and S_j , are unity. If Component 1 does not adsorb, the concentration velocity becomes

from either Eq. 5.41a or 5.41b. This seemingly trivial result has two important consequences.

1. The dimensional velocity of Component 1 is equal to the bulk fluid velocity, meaning that the dimensionless breakthrough time t_D^0 for Component 1 is also unity. From Eq. 5.9, we can estimate the pore volume of the medium by knowing the cumulative fluid injected when breakthrough occurs (see Exercise 5.11). Components that travel at the bulk fluid velocity are called “conservative” tracers for this reason.
2. The specific concentration velocity is independent of C_1 , meaning that waves caused by conservative tracers are indifferent (neither spreading nor self-sharpening), which is generally true for ideal miscible displacements.

Most EOR displacements are only partially miscible. To illustrate a partially miscible displacement, we now consider a displacement of an oil/water mixture at water saturation S_{1I} by another at a water fractional flow $f_{1J} = f_1(S_{1J})$. We distinguish between the initial and the injected oil and water, so let us suppose that the injected fluids contain conservative tracers. The oil-miscible tracer is completely immiscible in water, and the water-miscible tracer is similarly immiscible in oil. The process is now the displacement of an oil/water mixture by a tagged oil/water mixture. To keep this simple, we assume that the tracers have no effect on the fractional-flow functions. The specific velocity of the tagged water-resident water wave is

$$v_{1'} = \frac{\partial(C_{11}f_1)}{\partial(C_{11}S_1)} = \frac{f_1}{S_1} \dots \dots \dots \quad (5.44a)$$

from Eq. 5.41a, where C_{11} is the water-tracer concentration. Similarly, the specific velocity of the tagged oil is

$$v_{2'} = \frac{f_2}{S_2} = \frac{1-f_1}{1-S_1} \dots \dots \dots \quad (5.44b)$$

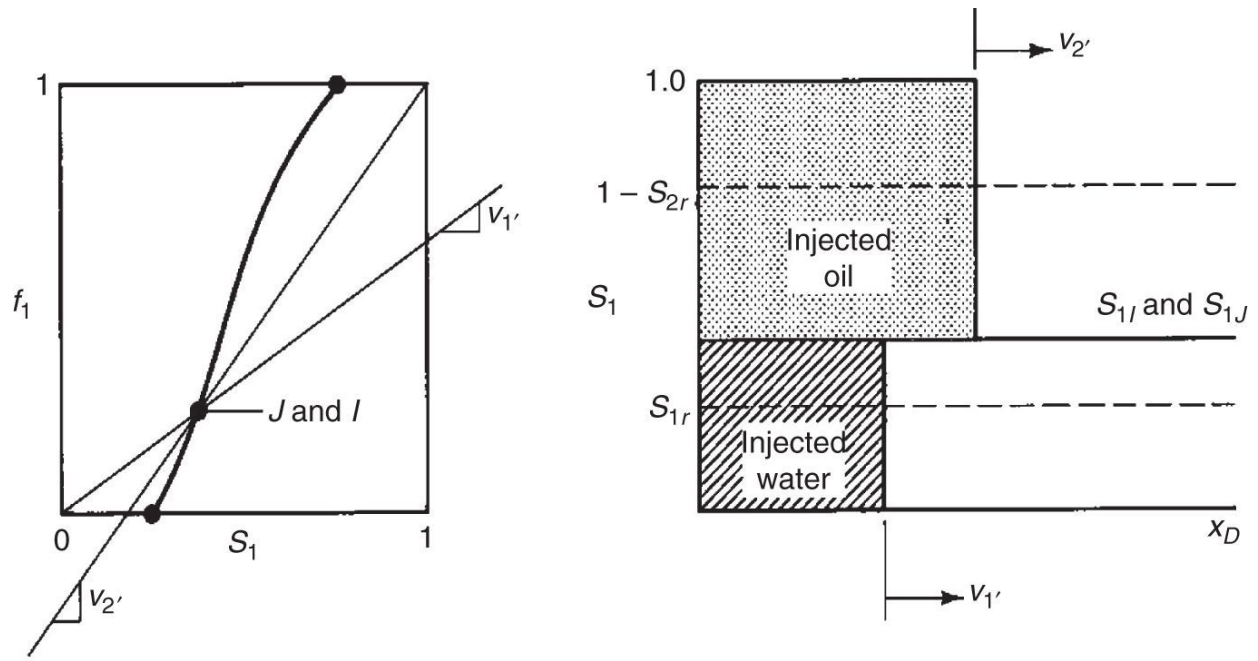
v_1' and v_2' are both independent of tracer concentration; hence, the miscible tagged water and oil waves are indifferent. Of course, because neither of the tracers affects f_1 , the saturation velocity of the water—tagged or untagged—is given by Eq. 5.12 or Eq. 5.14. The values of f_1 and S_1 in Eq. 5.44 are determined by the character of the oil/water wave.

[**Fig. 5.12**](#) illustrates some of the cases that can occur for this displacement. On each plot, the fractional-flow curve is on the left, and a saturation-concentration profile is on the right. In Case A, $S_{1I} = S_{1J}$ and the specific velocities are the slopes of straight lines passing through $(0, 0)$ and $(f_1, S_1)_J$ and $(1, 1)$ and $(f_1, S_1)_J$, respectively, from Eqs. 5.44a and 5.44b; $v_2' > v_1'$, and the tagged oil wave leads the tagged water wave.

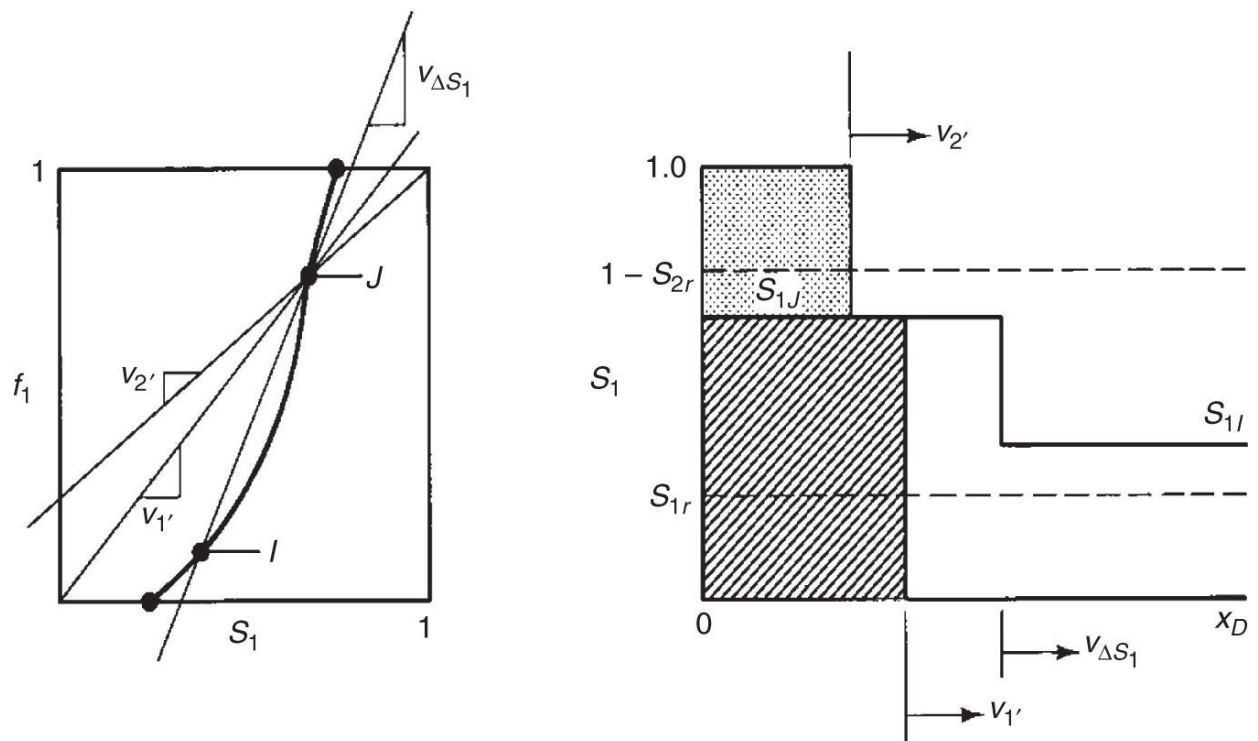
In Case B, $S_{1J} > S_{1I}$, and the f_1 curve is such that the immiscible oil/water wave is a shock. Both tagged waves lag the oil/water wave. The region between the tagged water and oil/water waves contains a “bank” of resident water that will be produced before the injected-water breakthrough. Breakthrough of a resident water bank in this manner has been observed experimentally (Brown 1957), although dispersion tends to be large in such displacements.

Case C illustrates a spreading water/oil wave with $v_2' > v_1'$, but with all tagged concentration waves having a lower velocity than the lowest saturation velocity at S_{1J} .

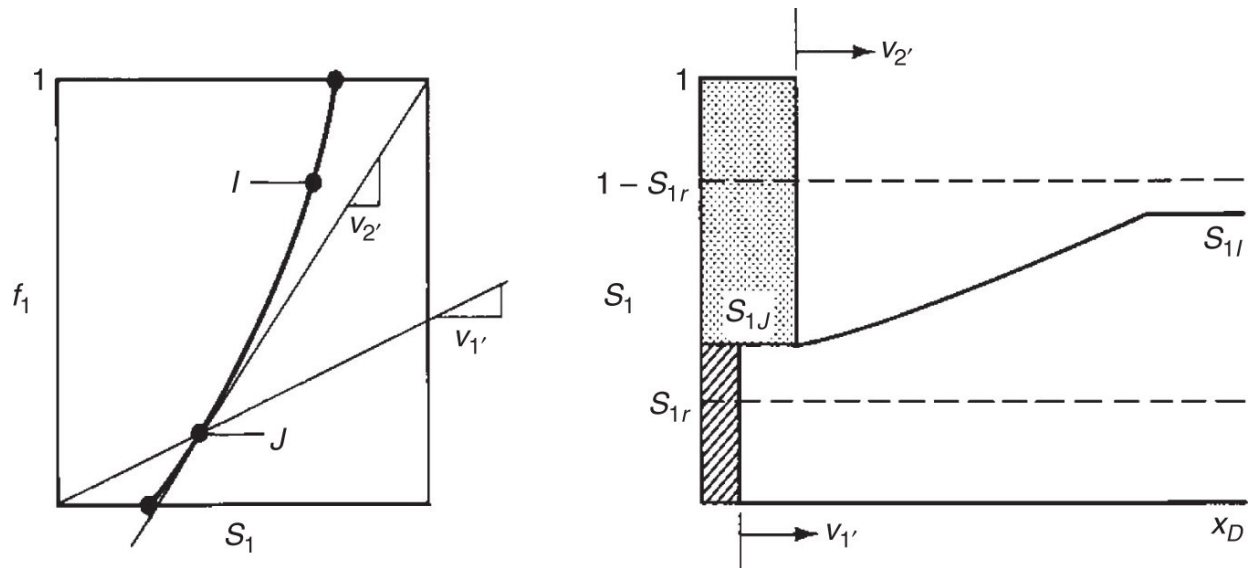
Case D is the same as Case C with the fractional-flow curve more convex upward. This shape causes the oil/water wave to spread more and the tagged oil front to fall somewhere in the spreading portion of the oil/water wave. The principle is that the concentration front for Tracer 2 must equal the velocity of the saturation at the tracer front. This saturation, S_1' , with a velocity the same as that of the tagged oil wave, is given by



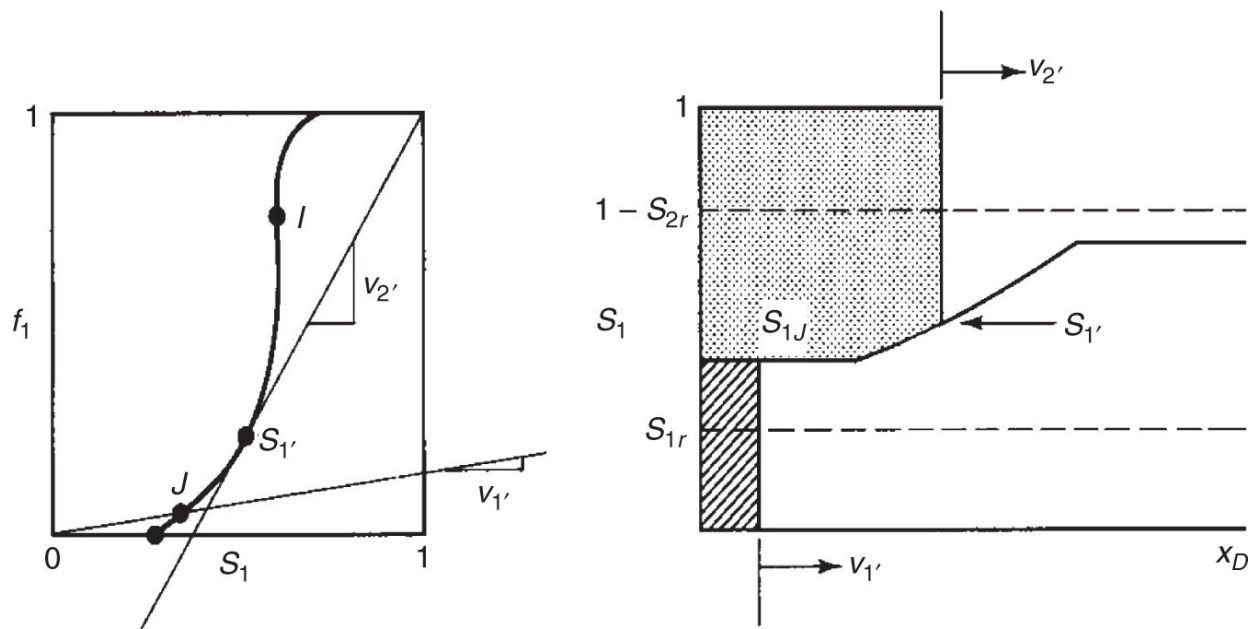
(a) Case A



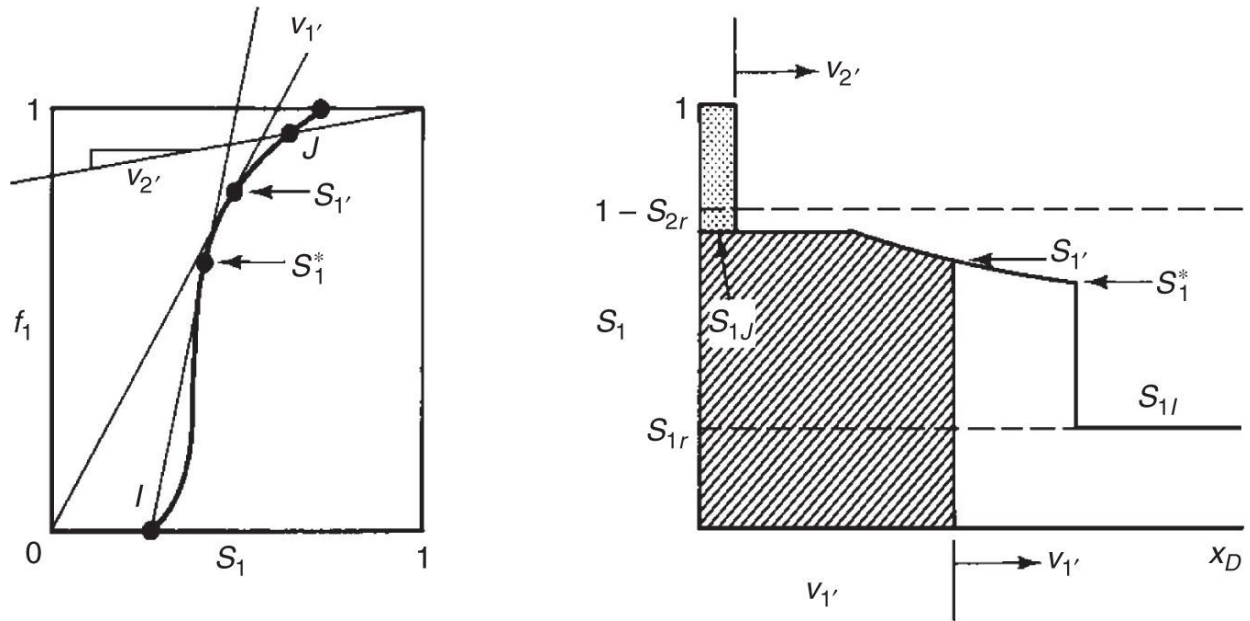
(b) Case B



(c) Case C



(d) Case D



(e) Case E

Fig. 5.12—Illustration of various partially miscible displacements.

$$v_{2'} = \frac{1 - f_1(S_{1'})}{1 - S_{1'}} = \left(\frac{df_1}{dS_1} \right)_{S_{1'}} \quad \dots \dots \dots \quad (5.45)$$

The line with slope $v_{2'}$ does not pass through S_{1J} , as it did in all previous cases. This is because a line through $(1, 1)$ and $(S_1, f_1)_J$ would give a greater velocity than S_{1J} . The tagged oil front would then travel with two different water saturations, which is a physical impossibility.

Case E, the traditional Buckley-Leverett problem, is the inverse of Case D in which the tagged water front is now traveling in the spreading-zone region. The oil/water displacement in Case E is mixed, whereas in Case D, it is spreading.

The important points in Fig. 5.12 are as follows:

- As postulated, neither the tagged oil nor the tagged water causes a deviation in the characteristics of the water/oil displacement. Cases in which added chemicals alter the fractional-flow curves are covered in later chapters and are the

subject of Section 5.8. When banks of resident fluids form, they do so within their respective phases.

2. One can easily imagine the tagged oil to be a hydrocarbon of less value than the oil. The tracer fronts now take on added significance because these miscible fronts are displacing the resident oil. The resident oil, in turn, is completely displaced. Therefore, the ultimate E_D for these idealized displacements is 1.0. This maximum efficiency occurs without reducing the interfacial tension with water, changing the wettability, or reducing mobility.

Of course, we have not as yet discovered a fluid that is simultaneously cheaper than and miscible with crude oil and that does not change the hydrocarbon transport properties. These changes can return the ultimate displacement efficiency to something less than unity. Still, the idea of displacing with miscible fluids, or those that will develop miscibility, is one of the central concepts of [Chapter 7](#).

5.5 Dissipation in Miscible Displacements

Because miscible waves are ideally indifferent, they are also susceptible to dissipation. By far, the most prominent of the dissipative effects in miscible displacements are dispersion and viscous fingering. The latter is a 2D flow effect, for which we postpone discussion until [Chapters 6](#) and [7](#). In this section, we discuss the effects of dispersion on a miscible front.

5.5.1 The Error-Function Solution. Consider now the isothermal miscible displacement of a component by another with which it is *completely* miscible in a 1D, homogeneous permeable medium. The convection-diffusion (CD) equation (Eq. 2.48) describes the conservation of the displacing component with mass concentration C ,

$$\phi \frac{\partial C}{\partial t} + u \frac{\partial C}{\partial x} - \phi K_L \frac{\partial^2 C}{\partial x^2} = 0. \quad \dots \dots \dots \quad (5.46)$$

Eq. 5.46 also assumes incompressible fluid and rock, ideal mixing, and a single phase at unit saturation. The following development is valid if other phases are present (Delshad 1981) and as long as all fractional flows and saturations are constant (see Exercise 5.13). K_l is the longitudinal dispersion coefficient. In dimensionless terms, Eq. 5.46 becomes

$$\frac{\partial C}{\partial t_D} + \frac{\partial C}{\partial x_D} - \frac{1}{N_{Pe}} \frac{\partial^2 C}{\partial x_D^2} = 0, \dots \quad (5.47)$$

which can be solved under the following boundary and initial conditions on $C(x_D, t_D)$:

$$C(x_D, 0) = C_I, \quad x_D \geq 0. \dots \quad (5.48a)$$

$$C(x_D \rightarrow \infty, t_D) = C_J, \quad t_D \geq 0. \dots \quad (5.48b)$$

$$C(0, t_D) = C_J, \quad t_D \geq 0, \dots \quad (5.48c)$$

where C_I and C_J are the initial and injected compositions respectively. In Eq. 5.47, N_{Pe} , the Peclet number, is defined as

$$N_{Pe} = \frac{uL}{\phi K_l}, \dots \quad (5.48)$$

which is the ratio of convective to dispersive transport. N_{Pe} is the analogue of N_{RL} for immiscible displacements, as can be seen by comparing Eqs. 5.30 and 5.47. This displacement must take place at constant u , unlike Eq. 5.8b. The equation and boundary conditions contain three independent parameters, C_I , C_J , and N_{Pe} , but the problem can be restated with only N_{Pe} as a parameter by defining a dimensionless concentration C_D :

$$C_D = \frac{C - C_I}{C_J - C_I}. \dots \quad (5.50)$$

With this definition, the equation and boundary conditions become

$$\frac{\partial C_D}{\partial t_D} + \frac{\partial C_D}{\partial x_D} - \frac{1}{N_{Pe}} \frac{\partial^2 C_D}{\partial x_D^2} = 0 \quad \dots \dots \dots \quad (5.51)$$

$$C_D(x_D, 0) = 0, \quad x_D \geq 0, \quad C_D(x_D, 0) = 1, \quad x_D < 0 \quad \dots \dots \dots \quad (5.52a)$$

$$C_D(x_D \rightarrow \infty, t_D) = 0, \quad t_D \geq 0 \quad \dots \dots \dots \quad (5.52b)$$

$$C_D(x_D \rightarrow -\infty, t_D) = 1, \quad t_D \geq 0. \quad \dots \dots \dots \quad (5.52c)$$

We have replaced the original boundary condition at $x_D = 0$ (Eq. 5.48c) with one at $x_D \rightarrow -\infty$ (Eq. 5.52c). This is an approximation to simplify the following derivation of an analytic solution. The approximate solution thus obtained will be valid, strictly speaking, for large t_D or large N_{Pe} , where the influence of the inlet boundary appears as though it were a great distance from the displacing front. In practice, the resulting approximate analytic solution accurately describes single-phase displacements for all but extreme cases.

The first step in deriving $C_D(x_D, t_D)$ is to transform Eqs. 5.51 and 5.52 to a moving coordinate system x'_D where $x'_D = x_D - t_D$:

$$\left(\frac{\partial C_D}{\partial x_D} \right)_{x'_D} - \frac{1}{N_{Pe}} \frac{\partial^2 C_D}{\partial (x'_D)^2} = 0, \quad \dots \dots \dots \quad (5.53)$$

and the boundary conditions retain the form of Eq. 5.52, owing to the replacement of the inlet boundary condition at $x_D = 0$ with one at $x_D \rightarrow -\infty$.

Eq. 5.53 is now the heat-conduction equation, for which a solution can be obtained by the method of combination of variables (Bird et al. 2002). To do this, we define yet another dimensionless variable $\eta = x'_D / 2\sqrt{t_D / N_{Pe}}$, with which the governing equations and boundary conditions can be transformed into

As required for the successful transformation of a partial to an ordinary differential equation, the conditions (Eqs. 5.52a and 5.52b) collapse into the single condition (Eq. 5.53b). The transformation to an ordinary differential equation is sometimes called Boltzmann's transformation. Eq. 5.53a can be separated and integrated twice to give

$$C_D = \frac{1}{2} \left(1 - \frac{2}{\sqrt{\pi}} \int_0^{\eta} e^{-u^2} du \right). \quad \dots \dots \dots \quad (5.54)$$

The product times the integral on the right side of Eq. 5.54 is the *error function*, a widely tabulated integral (see [Fig. 5.13](#)), which is abbreviated using the symbol $\text{erf}(\eta)$. By substituting the definitions for η and x'_B , we have the final form for the approximate analytic solution:

$$C_D = \frac{1}{2} \left[1 - \operatorname{erf} \left(\frac{x_D - t_D}{2 \sqrt{\frac{t_D}{N_{Pe}}}} \right) \right] = \frac{1}{2} \operatorname{erfc} \left(\frac{x_D - t_D}{2 \sqrt{\frac{t_D}{N_{Pe}}}} \right), \dots \quad (5.55a)$$

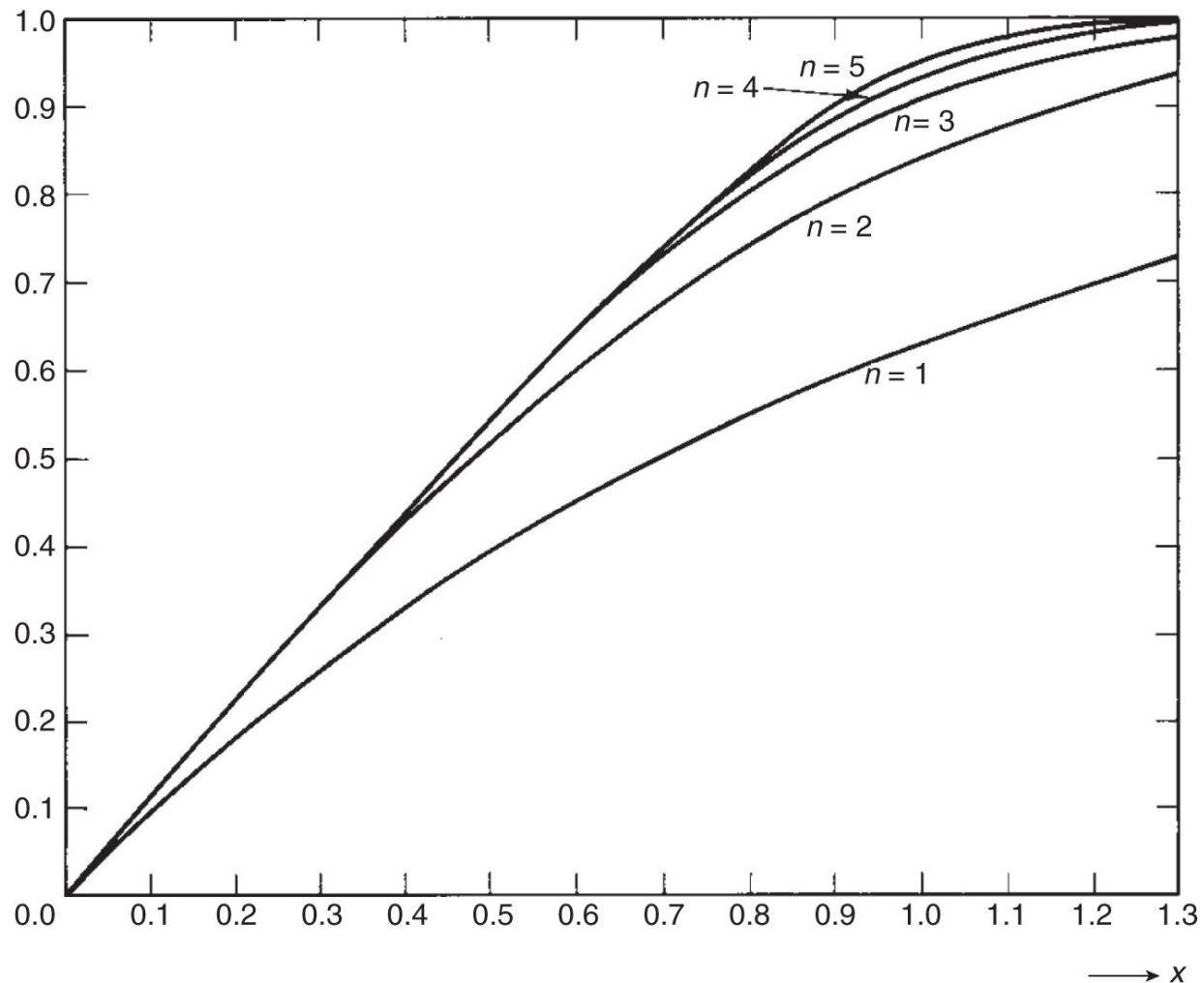


Fig. 5.13—The function $En(x) = \frac{1}{n!} \int_0^{x^n} e^{-v} v^{(1/n)-1} dv$, where $n = 2$ is the error function (Jahnke and Emde 1945).

where erfc denotes the complementary error function. The exact analytic solution as derived by Laplace transforms is (Marle 1981):

$$C_D = \frac{1}{2} \text{erfc} \left(\frac{x_D - t_D}{2\sqrt{\frac{t_D}{N_{Pe}}}} \right) + \frac{e^{x_D N_{Pe}}}{2} \text{erfc} \left(\frac{x_D + t_D}{2\sqrt{\frac{t_D}{N_{Pe}}}} \right). \quad (5.55b)$$

The second term in Eq. 5.55b approaches zero exponentially as x_D and N_{Pe} grow.

[Fig. 5.14](#) shows concentration profiles of C_D vs. x_D with t_D and N_{Pe} varying. As N_{Pe} increases, the concentration profile approaches the

step function at $x_D = t_D$, as suggested by Eq. 5.43. In fact, the concentration profile given by Eq. 5.55 is symmetric and centered on this point. The complete solution (Eq. 5.55b) is not symmetric, but as noted above, this effect is small. Dispersion, therefore, does not affect the rate of wave propagation, but it does affect the amount of mixing in the wave.

The dimensionless mixing zone, the distance between the positions where $C_D = 0.1$ and $C_D = 0.9$, follows from Eq. 5.55b:

$$\Delta x_D = x_D|_{C_D=0.1} - x_D|_{C_D=0.9} = 2\sqrt{\frac{t_D}{N_{pe}}}\text{erf}^{-1}(.8) - 2\sqrt{\frac{t_D}{N_{pe}}}\text{erf}^{-1}(-.8) = 3.625\sqrt{\frac{t_D}{N_{pe}}} \dots \dots \dots \quad (5.56)$$

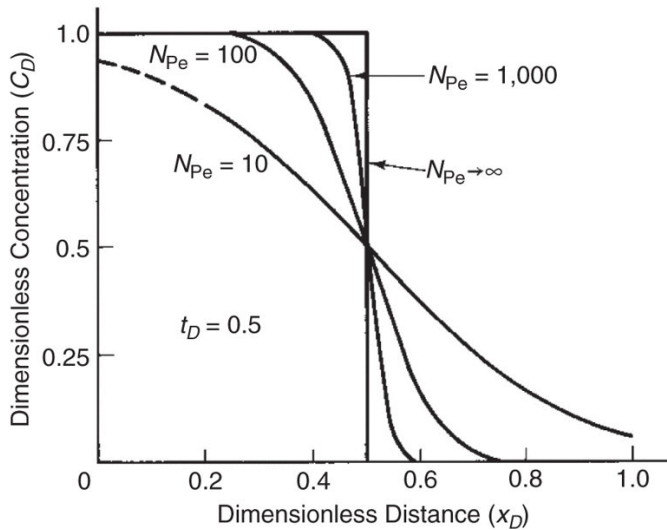
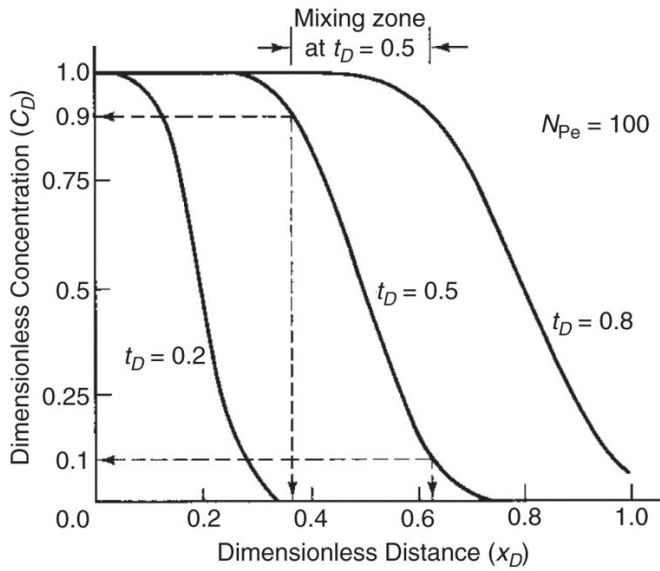


Fig. 5.14—Dimensionless concentration profiles.

Eq. 5.56 shows that dispersive mixing zones grow in proportion to the square root of time. Spreading waves in immiscible displacements grow in proportion to time. The growth suggested is generally slower than that for a spreading wave, particularly if N_{Pe} is large. This slow growth is a partial justification for neglecting dispersion when

modeling displacements with indifferent waves compared to fractional-flow effects.

Δx_D is also useful in comparing laboratory and field mixing-zone lengths. An immiscible mixing zone contains no free parameters if dissipation is low. Therefore, if we conduct a laboratory immiscible flood under conditions as nearly identical as possible to a field prototype (displacement in native or restored state cores, at reservoir temperature and pressure, using actual reservoir fluids), the laboratory Δx_D will be the same as in the field.

In miscible displacements, we are generally unable to make N_{Pe} equal between the laboratory and the field. N_{Pe} is usually smaller in the laboratory; therefore, Δx_D usually will be larger in the laboratory than in the field. Of course, the dimensional mixing-zone length, $\Delta x_D L$, will always be greater in the field because L is much greater. The reason why we are unable to match N_{Pe} is explained by the following discussion of dispersion coefficients.

The seemingly innocuous difference between a mixing zone that grows in proportion to time as opposed to the square root of time is fundamentally important because it marks the difference between flows with spatially correlated and with uncorrelated velocity fields (Arya et al. 1988). More discussion of this topic can be found in the next few sections.

5.5.2 Dispersivity. Bear (1972) suggests that “hydrodynamic” dispersion is “the macroscopic outcome of the actual movements of the individual tracer particles through the pores and various physical and chemical phenomena that take place within the pores.” This movement can arise from a variety of causes. In this text, *dispersion* is the mixing of two miscible fluids caused by diffusion, local velocity gradients (as between a pore wall and a pore center), locally heterogeneous streamline lengths, and mechanical mixing in pore bodies. Gravity tonguing and viscous fingering are 2D effects that are discussed in [Chapter 6](#). Here, we summarize experimental findings on dispersion coefficients and some qualitative reasons for these observations.

For 1D flow, the longitudinal dispersion coefficient K_l is given by

where C_1 , C_2 , and β are properties of the permeable medium and the flow regime. D_{ij} is the effective binary molecular diffusion of component i in phase j coefficient between the miscible displacing and displaced fluids, and D_p is an average particle diameter.

For very slow flows, the second term on the right of Eq. 5.57 is negligible, and K_l is proportional to D_{ij} . This case is analogous to a slow displacement in a wide channel in which mixing is caused entirely by molecular diffusion. The constant C_1 has been found to be $1/\phi F$, where F is the electrical formation resistivity factor (Pirson 1983), which accounts for the presence of the stationary phase.

For faster displacements, the second term in Eq. 5.57 becomes significant. Deans (1963) has shown that well-stirred tanks in series have mixing zones that can be described by dispersion coefficients proportional to velocity. Here, mixing is the result of the highly irregular flow paths in the REV, which cause fluids to mix completely as they are produced from each cell. Diffusion, of course, is negligible if the fluids are well mixed mechanically.

An alternative, 2D interpretation, including diffusion in this flow regime, is provided by the theory of Taylor (1953), in which the flow channels are visualized as having lateral dimensions much smaller than their longitudinal dimensions. For this idealization, diffusion equalizes concentration gradients in the lateral direction, giving rise to an “effective” diffusion coefficient. Mixing is now the result of transverse diffusion and variations in velocity caused by the no-slip condition at the pore wall. Taylor’s theory predicts dispersion coefficients proportional to velocity squared.

This local-mixing flow regime is where most EOR processes occur. In fact, if the interstitial velocity is greater than approximately 3 cm/d, the local mixing term in Eq. 5.57 dominates the first term, and we can write

The form of Eq. 5.58 is particularly convenient when recast in terms of the Peclet number (Eq. 5.49), and the dimensionless concentration balance (Eq. 5.47) now becomes independent of velocity:

Therefore, the dimensionless mixing zone is directly related to α , through Eq. 5.59. In fact, α/L can be regarded roughly as the dimensionless mixing-zone length.

This does not imply that diffusion is unimportant in miscible flow. In general, more rapid diffusion and mixing transverse to the flow direction and diffusion into dead-end pores, water-blocked pores, or adjacent nonflowing zones reduce the apparent dispersion coefficient. α_l in Eq. 5.59 is the longitudinal *dispersivity* of the permeable medium (Eq. 2.57), a measure of the local heterogeneity scale. Bear (1972) classifies α_l as one of the fundamental properties of the medium. For the local mixing-flow regime, α_l is a more fundamental measure of dispersion than K_l .

The study of dispersion, both experimentally and numerically, is difficult because dispersion is easily confounded by other similar effects. Experimentally, dispersion can be misidentified with channeling, bypassing, or both because without the ability to observe flow inside a medium directly, the only observation available to us is effluent histories. Numerically, dispersion can be overwhelmed by error artifacts (numerical dispersion) that occur in the finite-difference approximations used in most simulators.

By using a multiple sampling port on the outflow end of a core, Jha et al. (2009) established that the concentration of a miscible fluid does indeed spread out longitudinally in a short “homogeneous” coreflood. To an excellent approximation, 1D flow exists at this scale, and dispersion is well defined, at least on an REV scale.

Jha et al. (2009) also demonstrated that dispersion is irreversible in the sense that a miscible wave continues to spread on flow reversal. The origin of the irreversibility is certain small-scale effects, in this case diffusion, that do not let fluid particles return on the same path on return flow as they did on outflow. This irreversibility is the defining characteristic of dispersion, as well as the related behavior of square-root-of-time growth.

In fact, as suggested by Eq. 5.58 and [Fig. 5.15](#), dispersion is usually much larger than diffusion over typical velocities. This paradox—diffusion is negligible compared to dispersion, but it is needed for dispersion to exist—is a consequence of a combination of several effects, all operating at a succession of scales. Many petrophysical properties exhibit the so-called scale effect.

The effects of multiple scales are most apparent in the data shown in [Fig. 5.16](#). This figure, which has been compiled from multiple sources, shows that the magnitude of dispersivity depends on the scale at which it was measured. Dispersivity ranges from approximately 1 cm on the laboratory scale to 100 m on the field scale. The near-linear dependence in these data illustrates how easy it is to misidentify dispersion with layered (highly autocorrelated) flow, which would manifest itself as a dispersivity that grows linearly with time.

Strictly layered flow should be completely reversible, or in other words, so-called echo dispersivities (those measured at the inlet on flow reversal) should be much smaller than transmission dispersivities (those measured from one inlet to a separate outlet). On the basis of an analysis of the flow of a conservative tracer in a single-well tracer test, this proved not to be the case (Mahadevan et al. 2003). The grey boxes in [Fig. 5.16](#) show that echo dispersion is, at best, only slightly less than transmission dispersion at the same scale.

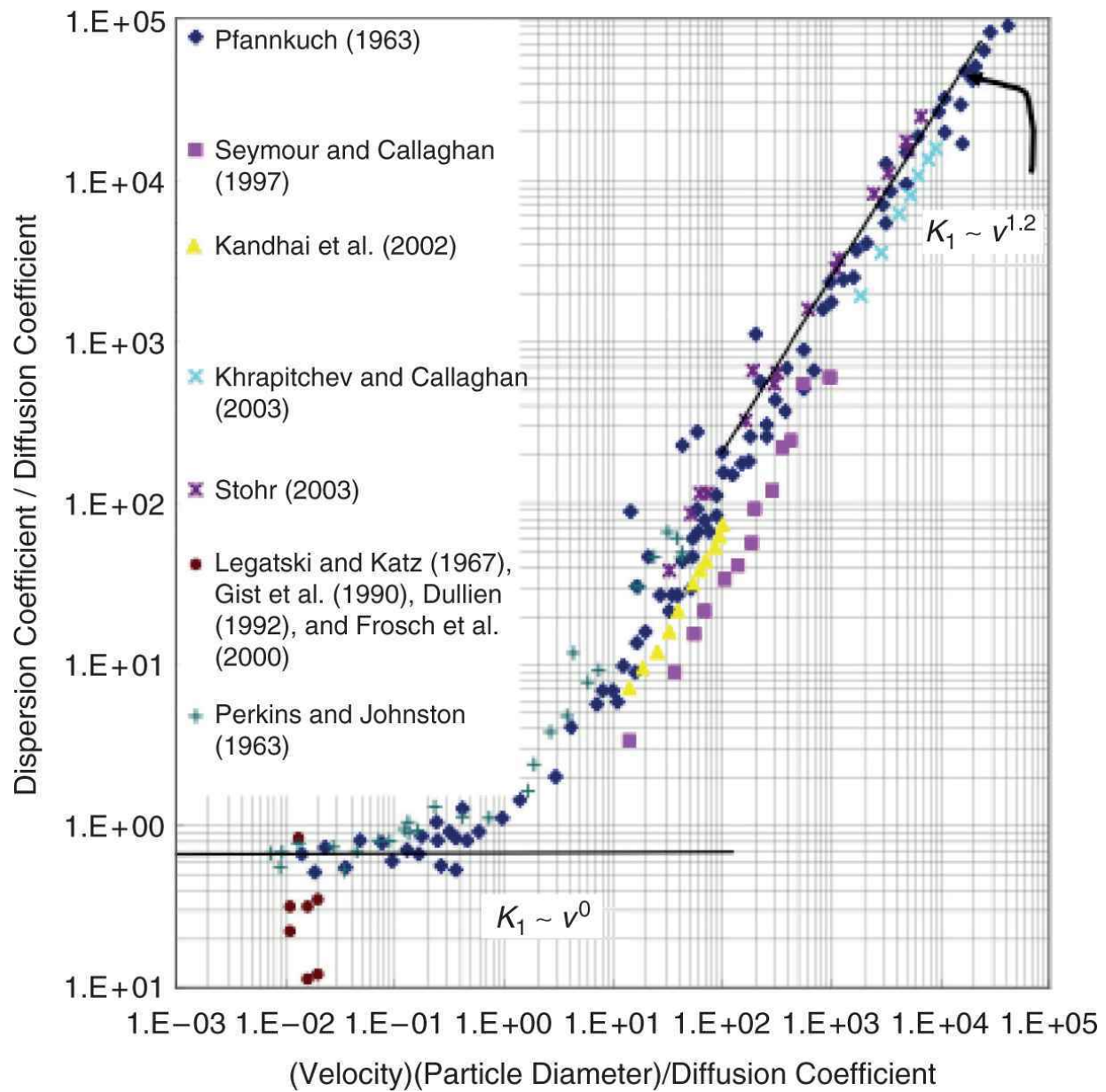


Fig. 5.15—Compilation of dispersion coefficients (y-axis normalized by diffusion coefficient) correlated against dimensionless velocity (velocity times particle diameter/diffusion coefficient) from varous sources as compiled by Jha et al. (2008). As simulated by Jha et al. (2008), the value of the slope depends on details of flow within the pores.

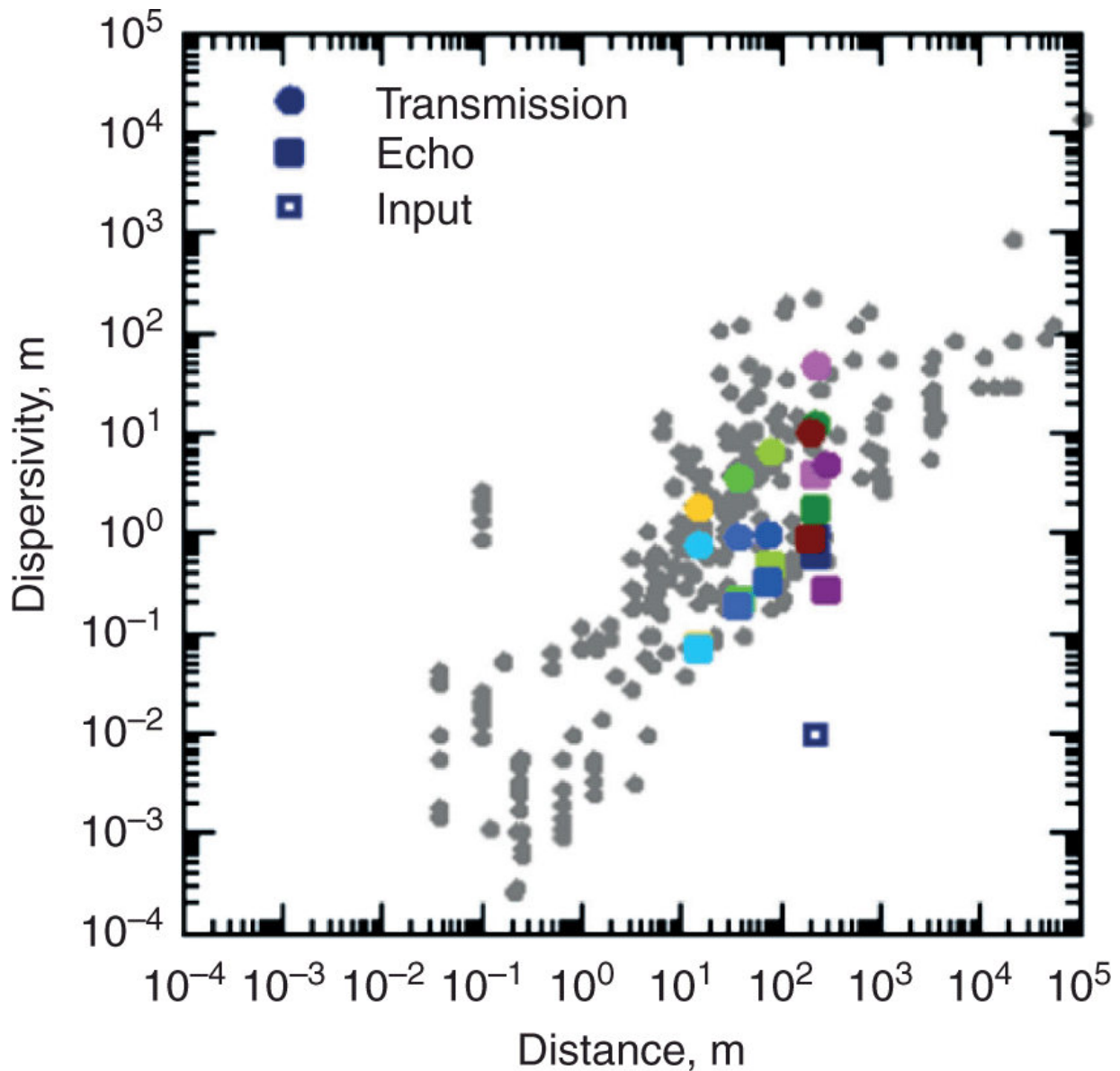


Fig. 5.16—Growth of dispersivity with travel distance as compiled by John et al. (2010). Boxes represent echo dispersion, while dots are transmission dispersion. Gray indicates field-measured value, and colors are simulated values. The open box represents the input dispersivity for the simulation.

To explain this behavior, John et al. (2010) conducted an extensive simulation study of both echo and transmission dispersion. Because of numerical dispersion, as described above, this study used a specialized point-tracking simulator that has no numerical error. Fig. 5.16 illustrates some of the results.

Because large-scale dispersion depends on many unknown (and unknowable) characteristics of the medium, general conclusions are not easy to draw. However, [Fig. 5.16](#) reproduces many of the characteristics of dispersion that have been determined experimentally. These are: (a) dispersivities, both echo and transmission, grow with distance traveled; (b) the simulated echo dispersivities are smaller than transmission dispersivities, but only by a small amount; and (c) both dispersivities are much larger than the input dispersivity. The echo dispersion, then, is the “true” dispersion, the one that causes local mixing in a medium. The difference between transmission and echo dispersion is a measure of large-scale autocorrelation in the medium properties.

We can summarize the most important points about the effects of dispersion on 1D miscible flow as follows:

1. Dispersion controls the rate of mixing of two fluids, but does not alter wave velocity.
2. Dispersive mixing zones can grow no faster than in proportion to the square root of time.
3. The fluid velocity of most EOR processes is such that the flow is in the local mixing-flow regime, where the dispersion coefficient is proportional to the interstitial velocity. The proportionality constant is the longitudinal dispersivity α_l .
4. α_l is a measure of the small-scale heterogeneity of the permeable medium and varies with measurement scale.
5. Much of the scale dependence of dispersion appears to be irreversible, so that field-scale dispersion is only a little less than transmission dispersion. Its main effect is to increase volumetric sweep and to increase the oil saturation behind a developed miscible front (see [Chapter 7](#)).

5.6 Generalization of Fractional-Flow Theory

This section reviews the mathematics of the wave theory that forms much of the basis of this text. There are sophisticated expositions of this work (e.g., Courant and Friedrichs 1948; Jeffrey and Taniuti

1964). In what follows, we narrow consideration to the behavior of so-called simple waves, and in particular to the idea of coherent waves. The treatment is virtually identical to the elegant treatment of Johansen et al. (1989). Remember that what follows here is essentially mathematics that we will use later on to draw physical insights. We restrict treatment to spreading or rarefied waves.

The conservation of component i can be expressed through an equation of the following form:

$$\frac{\partial A_i}{\partial t} + \frac{\partial F_i}{\partial x} = 0 \quad \dots \dots \dots \quad (5.60)$$

for $i = 1 \dots N_c$ components. The terms in Eq. 5.60 are $A_i = A_i(u_1, \dots, u_{N_c})$, an accumulation function, and $F_i = F_i(u_1, \dots, u_{N_c})$, a flux function, both of which are known. The goal is to derive solutions

$$u_1 = u_1(x, t), \dots, u_{N_c} = u_{N_c}(x, t) \quad \dots \dots \dots \quad (5.61)$$

for the dependent variables. The dependent variables in Eq. 5.61 are quantities like saturation, concentration, and temperature. x and t are independent variables that are themselves dimensionless in most of the applications discussed here.

Another way to express Eq. 5.60 is

$$\sum_{j=1}^{N_c} A_{ij} \frac{\partial u_j}{\partial t} + \sum_{j=1}^{N_c} F_{ij} \frac{\partial u_j}{\partial x} = 0, \quad \dots \dots \dots \quad (5.62)$$

where the terms with two subscripts are partial derivatives of the respective functions, such as

$$A_{ij} = \left(\frac{\partial A_i}{\partial u_j} \right)_{u_{j \neq i}}.$$

Because the accumulation and flux functions are known, these quantities are also known. Both A_{ij} and F_{ij} may be very complex and may not be expressible in closed form, but they are known. Moreover,

the quantities in matrix form, $\mathbf{AU}_t + \mathbf{FU}_x = 0$, are invertible, so that Eq. 5.62 becomes

$$\mathbf{U}_t + \mathbf{A}^{-1}\mathbf{F}\mathbf{U}_x = \mathbf{U}_t + \mathbf{J}\mathbf{U}_x = 0. \quad \dots \quad (5.63)$$

We can solve Eq. 5.63 using a similarity transform $\eta = x / t$. The usefulness of this transform depends on the boundary conditions, which we universally assume to be a so-called step change at the origin boundary data. See Lake et al. (2002) for more discussion of this topic. The similarity transfer used in Eq. 5.63 leads to an eigenvalue problem of the following form:

$$(\mathbf{J} - \eta\mathbf{I}) \frac{d\mathbf{U}}{d\eta} = 0, \quad \dots \quad (5.64)$$

where η is the eigenvalue of \mathbf{J} . Several things are important here: (a) η is a scalar, not a vector; (b) η is a velocity by definition; and (c) η has no component subscript.

There are two solutions to Eq. 5.64; $\frac{d\mathbf{U}}{d\eta} = 0$, or \mathbf{U} is constant along certain characteristic directions in (x,t) space. This solution allows the appearance of so-called constant-state regions in the problem solution. Not coincidentally, it also allows the solutions to satisfy certain somewhat-arbitrary boundary conditions. The importance of (c) follows from reverting $(\mathbf{J} - \eta\mathbf{J}) = 0$ to component form:

$$J_{k1} \frac{du_1}{d\eta} + \dots + J_{kk} \frac{du_k}{d\eta} + \dots + J_{kN_c} \frac{du_{N_c}}{d\eta} = \eta \frac{du_k}{d\eta}. \quad \dots \quad (5.65)$$

However, Eq. 5.65, being homogeneous in η , can also be written as

$$J_{k1} \frac{\partial u_1}{\partial x} + \dots + J_{kk} \frac{\partial u_k}{\partial x} + \dots + J_{kN_c} \frac{\partial u_{N_c}}{\partial x} = \eta \frac{\partial u_k}{\partial x}, \quad \dots \quad (5.66)$$

which, when subtracted from the k -th equation of Eq. 5.66 yields

$$\frac{\partial u_k}{\partial t} + \eta \frac{\partial u_k}{\partial x} = 0. \quad \dots \quad (5.67)$$

The development from here on follows from the Buckley-Leverett theory. A line of constant u_k follows from

$$du_k = 0 = \frac{\partial u_k}{\partial t} dt + \frac{\partial u_k}{\partial x} dx, \text{ from which it follows that } \left. \frac{dx}{dt} \right|_{du_k=0} = -\frac{\frac{\partial u_k}{\partial t}}{\frac{\partial u_k}{\partial x}} = \eta, \text{ and}$$

because of the lack of a subscript on the eigenvalue and using Eq. 5.67, we have

$$\eta = \frac{dJ_1}{du_1} = \dots = \frac{dJ_{N_c}}{du_{N_c}}, \dots \quad (5.68a)$$

which states that the velocities of all components are equal. Eq. 5.76a is the *coherence condition* (Helfferich and Klein 1970).

In all cases throughout this text, we will begin with either Eq. 5.65 or Eq. 5.68a. Either approach will lead to an eigenvalue problem. The problem described in the next section will serve as an illustration. Were we to develop the condition in terms of shock waves (that is beginning with the weak form of the material balance), the integral coherence condition,

$$\eta = \frac{\Delta J_1}{\Delta u_1} = \dots = \frac{\Delta J_{N_c}}{\Delta u_{N_c}} \dots \quad (5.68b)$$

(where Δ refers to a finite jump across the shock), would result.

Using the coherence condition to solve problems often leads to more physical insight than numerical solutions because it is often more direct and ties readily into the Buckley-Leverett theory. The information on reducible equations can be restated with more physical insight by referring to simple waves in the terminology of *coherent waves* (Helfferich and Klein 1970). As illustrated in Section 5.7, the coherence method of calculating simple waves is more direct than using the method of characteristics (MOC). Eq. 5.68 implies further that there can be no more than N waves.

5.7 Application to Three-Phase Flow

In this section, we apply the results of coherence theory by calculating the displacement efficiencies for a three-phase water ($i = 1$), oil ($i = 2$), and gas ($i = 3$) flow problem. We assume away dissipative effects—capillary pressure and pressure-dependent fluid properties—and restrict the fluids to single pseudocomponent phases. We assume water, oil, and gas are completely insoluble in each others' phases. The assumption of an incompressible gas phase is, of course, realistic only if

$$c_3 \Delta P \approx \frac{\Delta P}{P} \quad \dots \dots \dots \quad (5.69)$$

is small. This condition is not met in general, although for flows in high-permeability media, $c_3 \Delta P$ can be fairly small, particularly considering that gas viscosity is also low.

Subject to the above restrictions, the species conservation Eq. 5.37 becomes

$$\frac{\partial S_j}{\partial t_D} + \frac{\partial f_j}{\partial x_D} = 0, \quad j = 1 \text{ or } 2 \quad \dots \dots \dots \quad (5.70)$$

in dimensionless form, where for a horizontal reservoir,

$$f_j = \left(\frac{\lambda_{ij}}{\sum_{m=1}^3 \lambda_{im}} \right) \quad \dots \dots \dots \quad (5.71)$$

The relative mobilities in Eq. 5.71 are known functions of S_1 and S_2 . Only two independent saturations are used in this example because $S_1 + S_2 + S_3 = 1$, which we arbitrarily assume to be the water and oil saturations. Eq. 5.71 implies that the fractional flows are known functions of S_1 and S_2 .

From Eq. 5.41, the specific velocity of a constant saturation S_j is

$$v_{S_j} = \left(\frac{\partial f_j}{\partial S_j} \right)_{t_D}, \quad j = 1 \text{ or } 2 \quad \dots \dots \dots \quad (5.72a)$$

if the wave is nonsharpening and

if the wave is a shock. We cannot evaluate the derivative in Eq. 5.72a without knowing the solution to the problem $S_j(x_D, t_D)$. For brevity, we adopt the convention that $f_{12} = (\partial f_1 / \partial S_2)_{S1}$, and so on. These are known functions of S_1 and S_2 , and although they may be very complex, we can calculate them without knowing the solutions $S_1(x_D, t_D)$ and $S_2(x_D, t_D)$.

Let the initial saturations in the medium be uniform at $(S_1, S_2)_I$ and impose at $x_D = 0$ the saturations $(S_1, S_2)_J$. From Section 5.6, we know that the coherence condition applies at all points in the domain where

from Eqs. 5.59 and 5.80a. The derivatives in Eq. 5.81 are total derivatives because the coherence condition implies the existence of a relation $S_2 = S_2(S_1)$ in saturation space. We can expand the derivatives in Eq. 5.68 and write the two equations in matrix form as

To solve for $S_2(S_1)$, we first solve this equation for the eigenvalues, σ_{\pm} :

Both roots of Eq. 5.76 are real, $\sigma^+ > \sigma^-$, and both are known functions of S_1 and S_2 . Recall that the $\sigma\sigma^\pm$ are saturation velocities. Solving for dS_1 and dS_2 in Eq. 5.75 gives

$$\frac{dS_1}{dS_2} = \frac{\sigma^+ - f_{11}}{f_{12}}. \dots \quad (5.77)$$

Eq. 5.77 is an ordinary differential equation that, upon integration, gives the function $S_2(S_1)$. There are two such functions corresponding to σ^+ and σ^- . The velocity of any saturation along $S_2(S_1)$ is given by σ^+ and σ^- , depending on whichever is physically realistic.

The above procedure could perhaps be made clearer by addressing a particular problem. Consider an oil/gas/water mixture being displaced by water. To make the problem simple, we assume the relative permeabilities to be

$$k_{jr} = \frac{S_j - S_{jr}}{1 - S_{1r} - S_{2r} - S_{3r}}, \quad j=1 \text{ or } 2, \dots \quad (5.78)$$

and let $S_{1r} = S_{2r} = S_{3r} = 0.1$. Eq. 5.78 is not a realistic three-phase relative-permeability function (see Exercise 5.14), but it is sufficient for illustration. We further assume $\mu_1 = 1 \text{ mPa}\cdot\text{s}$, $\mu_2 = 5 \text{ mPa}\cdot\text{s}$, and $\mu_3 = 0.01 \text{ mPa}\cdot\text{s}$ and consider the initial conditions to be $S_{2I} = 0.45$ and $S_{1I} = 0.1$. Therefore, the medium is initially at residual water saturation with equal volumes of oil and gas. We are to displace this mixture with water; that is, $S_{1J} = 0.8$ and $S_{2J} = 0.1$. This procedure corresponds to a waterflood initiated well into the primary production phase.

[Fig. 5.17](#) shows the functions $S_2(S_1)$ obtained by numerically integrating Eq. 5.77 with the indicated physical relations. The plot is on a triangular diagram to emphasize the relation $S_1 + S_2 + S_3 = 1$. The integration of Eq. 5.77 for various initial values of S_1 and S_2 produces two families of curves corresponding to σ^+ and σ^- . Because $\sigma^+ > \sigma^-$, the image curves do not coincide anywhere, and furthermore, every point in the saturation diagram has associated with it two velocities σ^+ and σ^- . These two families of curves are called the saturation *paths* after Helfferich (1981). The particular paths that pass from the initial to the injected condition are the

saturation *routes* (the bold lines in [Fig. 5.17](#)). Although we henceforth restrict our attention to the saturation routes, [Fig. 5.17](#) gives a visual perspective for any displacement having arbitrary initial and injected conditions.

In moving from the initial to the injected conditions, there are two alternative saturation routes: (1) a σ^- segment going from the initial conditions to the upper apex of the three-phase flow region, and then a σ^+ segment on the gas/water boundary to the injected condition; and (2) a σ^+ segment from the initial conditions to $(S_1, S_2) = (0.36, 0.54)$, followed by a σ^- segment along the oil/water boundary to the injected conditions. Both routes are mathematically valid solutions to the problem; in fact, an infinite number of mathematical solutions correspond to a route that arbitrarily switches between paths **a1** and **a** in going from $(S_1, S_2)_I$ to $(S_1, S_2)_J$. From the Buckley-Leverett problem in Section 5.2, we know that saturation velocities must decrease monotonically (although not continuously) in the upstream direction. The only physical solution for the problem is Route 2 because $\sigma^+ > \sigma^-$ forces this to be the only possible route where σ decreases monotonically from $(S_1, S_2)_J$ to $(S_1, S_2)_I$ to $(S_1, S_2)_J$.

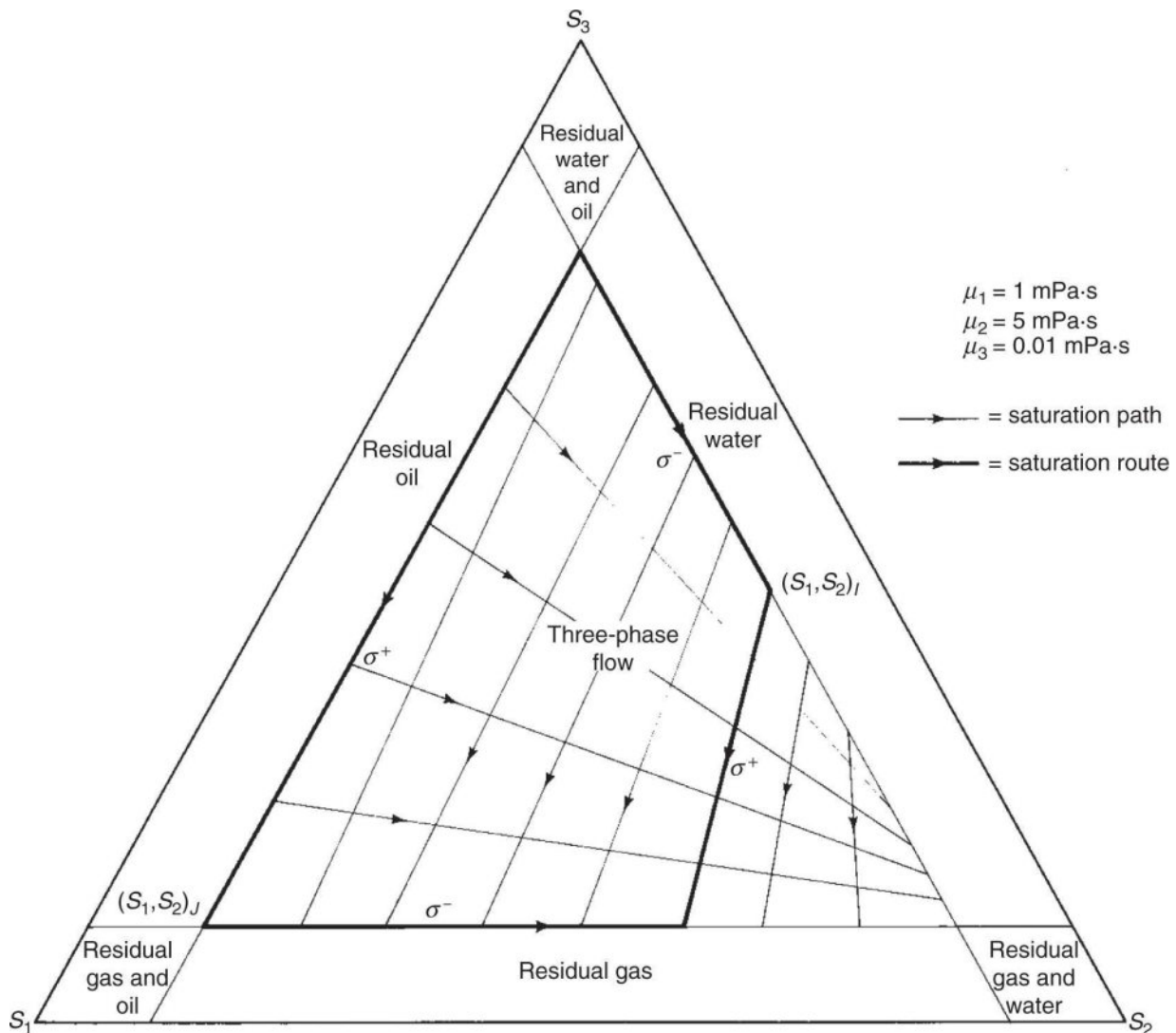
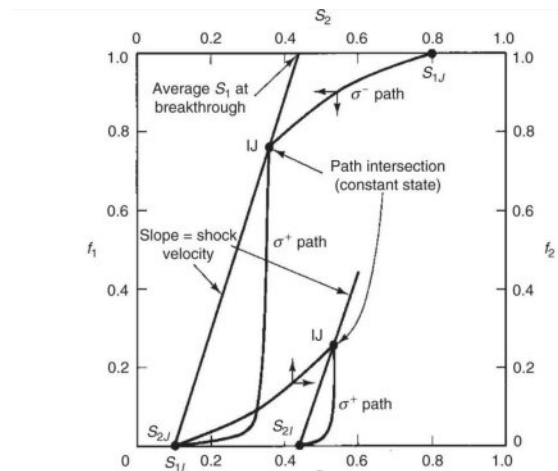


Fig. 5.17—Three-phase flow saturation paths.

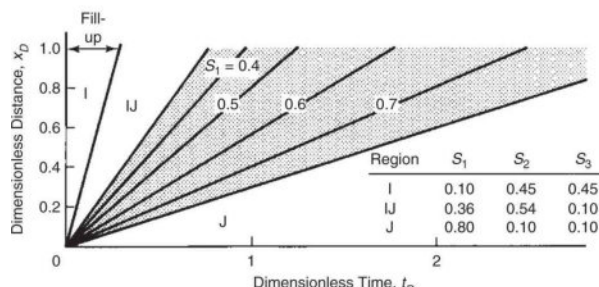
Within a route segment, the saturation velocities must also decrease monotonically in the upstream direction. This condition is not met on the σ^+ route segment (the arrows on the saturation routes indicate the direction of increasing saturation velocity). Such behavior indicates that the wave is a shock, and we can find the shock velocity by a procedure entirely analogous to that used in Section 5.2. [Fig. 5.18a](#) plots the oil and water fluxes (f_1 , f_2) vs. (S_1, S_2) along the composition route. The shock construction is exactly as suggested in [Fig. 5.4](#) and can be performed on either the f_1 - S_1 curve or the f_2 - S_2 curve. Eq. (5.81) guarantees this equivalence. The only real

difference between the three-phase and two-phase flow problems at this point is the existence of the constant-state region at IJ . The time/distance diagram for the displacement is shown in [Fig. 5.18b](#), which should be compared to [Fig. 5.5](#).

Despite the simplified nature of the relative-permeability curves used in this example, [Fig. 5.17](#) illustrates that the most important feature of three-phase oil/gas/water flow is the extremely low gas viscosity. This viscosity causes the oil fractional flow to be small initially and to delay the appearance of an appreciable amount of oil at the outflow end until $t_D = 0.28$. This delay, or “fill-up,” time is an omnipresent feature of waterfloods begun with appreciable amounts of free gas in the medium (Caudle 1968). A fill-up period occurs because of the very large gas mobility, not as the result of gas compressibility or redissolution. Either of the last two effects would serve to reduce the fill-up time. A second consequence of small gas viscosity is that no simultaneous three-phase flow occurs in the medium. In fact, by assuming that an oil/water mixture banks up the free gas, it is possible to repeat the results in [Figs. 5.17](#) and [5.18](#) with much less effort (see Exercise 5.13 and the following section). A final consequence of the small gas viscosity is that this behavior is qualitatively accurate regardless of the relative-permeability functions used.



(a) Flux-saturation diagram



(b) Time-distance diagram

Fig. 5.18—Fractional-flow and time/distance diagram for three-component flow.

We end this section by discussing the displacement efficiency of the three-phase flow problem. There is now a displacement efficiency for both oil and gas, for which we need average saturations for the definition (Eq. 5.2). Considering the fractional flux/saturation curve in [Fig. 5.18a](#), the average saturations follow from a procedure directly analogous to the Welge procedure in Section 5.2:

where $t_D = (df_j/dS_j)^{-1}$ is the reciprocal slope of the f_j vs. S_j curve evaluated at $x_D = 1$. [Fig. 5.18a](#) shows the average water saturation at water breakthrough, and [Fig. 5.19](#) shows the displacement efficiencies for this example. Once again, E_D is limited by the residual phase saturations, oil production is delayed for a fill-up period, and

the oil-displacement efficiency is determined by the water/oil relative permeabilities and viscosities.

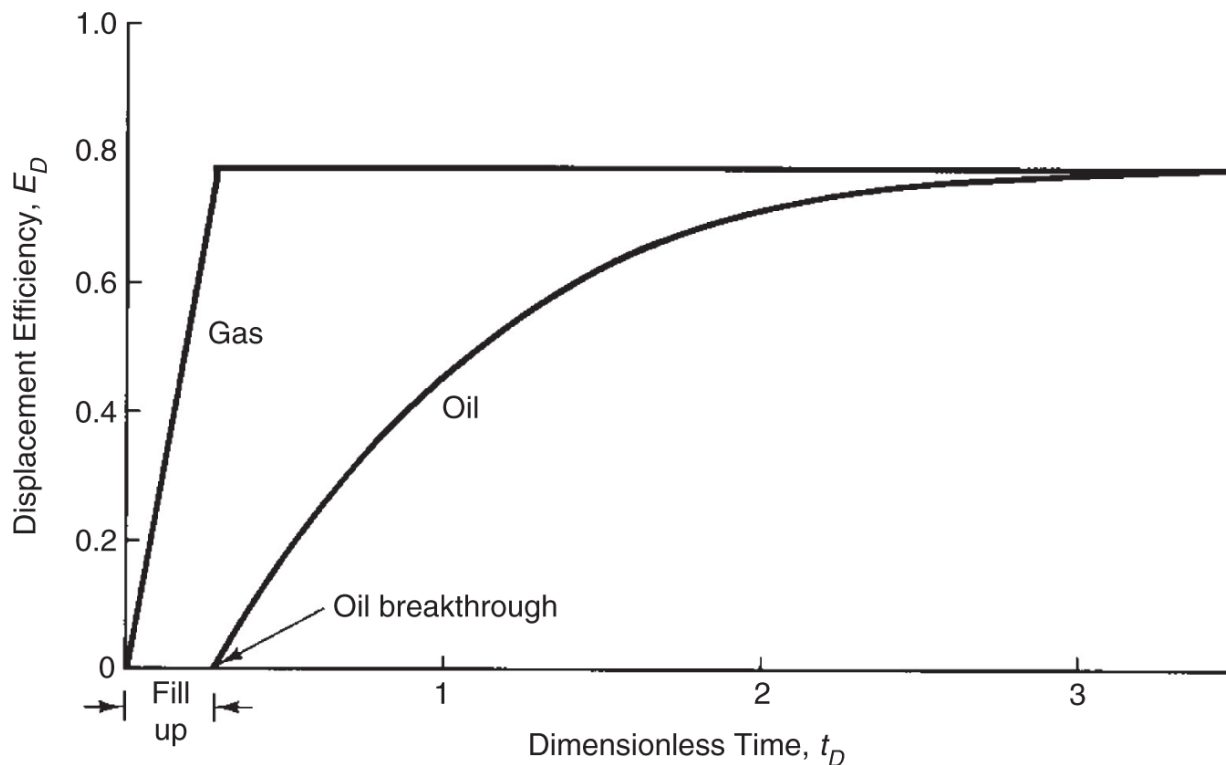


Fig. 5.19—Displacement efficiencies for three-phase flow problem.

This example demonstrates the strength of simple wave theory. In later chapters, we return to these procedures for specific EOR applications. You should note that there are two displacements: condition J displacing IJ , and then IJ displacing I .

5.8 Modeling EOR Processes With Two-Phase Fractional-Flow Theory

Many EOR processes can be represented or idealized as two-phase displacements, in which only two phases exist at any location. Viewed from the vantage point of two-phase fractional-flow theory, EOR processes act by changing the fractional-flow curve from that of the initial fluids in the reservoir to that of the final state. EOR processes accomplish this fractional-flow change by injecting an agent, typically a chemical additive, into the injected fluids. In thermal

processes, the *agent* is extra enthalpy (heat) in the injected fluids. In low-salinity waterflooding, it is the *absence* of salt in the injected water.

In its simplest form, the approach assumes zero volume change in phases across the front: for instance, that the loss of polymer surfactant from the aqueous phase to adsorption does not significantly alter the volume of the aqueous phase. This approach is therefore more useful in modeling a hot-water flood than a steamflood, where the change in density between steam and condensed water is substantial ([Chapter 11](#)).

Two fractional-flow curves are therefore present: that of the initial fluids in the reservoir without the agent, and that of the injected fluids with the agent. [Table 5.2](#) shows some examples of EOR processes, the changes brought about in fluid properties, and the agent.

In principle, the agent is a third component, which means that a displacement involving the agent must be solved on a three- (or more) component phase diagram, as in the ternary diagrams in Section 5.7. Often, however, the boundary between fluids with and without the agent in the reservoir is sharp on the scale of the displacement: either an indifferent wave or a shock. Then there are only two states with respect to the agent: present at uniform concentration behind this front, and absent ahead of it. At the front, the displacement on the fractional-flow diagram jumps from one fractional-flow curve to the other. The velocity of the front is governed by a balance on the agent at the front along with the other components. This balance is similar to that in [Fig. 5.3](#), but in EOR processes, this balance may include the loss of agent to the formation, as in Eq. 5.37: for instance, adsorption of chemical, or loss of heat to the formation in a thermal process. When combined with a balance on water or oil, the balance equation often translates to a geometrical constraint on a line representing this front drawn on the fractional-flow diagram. Often the constraint amounts to a condition that the jump occurs along a line passing through a particular point on the diagram, as for the tracer fronts in [Fig. 5.12](#).

TABLE 5.2—FOR PROCESSES, AGENT INTRODUCED, AND EFFECT ON FRACTIONAL FLOW

Process	Agent	Effect
Polymer flooding	Polymer	Reduces mobility of water
Steam, hot waterflooding	Heat	Reduces viscosity of oil; perhaps alters wettability
Surfactant flooding	Surfactant	Reduces interfacial tension (IFT), makes oil and water flow together as though miscible
Wettability alteration	Surfactant	Changes wettability of rock
Alkaline/polymer flooding	Alkali	Changes wettability, IFT
Low salinity	(Lower) salinity	Changes wettability
Foam	Surfactant	Reduces mobility of gas
Solvent flooding	Solvent	Solvent replaces oil miscibility; changes viscosity of nonaqueous phase

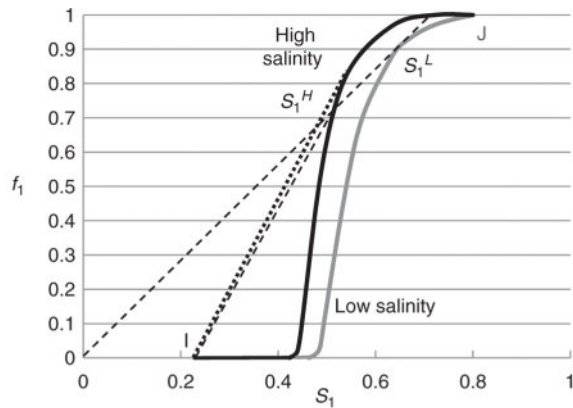
The solution for such displacements in 1D using fractional-flow theory proceeds as follows. All the assumptions of Section 5.2 apply here.

1. Plot the fractional-flow curves, representing injected fluids and the initial fluids in the reservoir, with and without the agent.
2. Perform a balance on the agent at the front separating fluid with the agent from fluid without it. Combine this balance with a balance on water, and if possible, derive a geometrical condition for the jump on the fractional-flow diagram.
3. Locate the initial and injection conditions I and J on their respective fractional-flow curves.
4. Search for a path from J to I with monotonically increasing slope df/dS_j . In cases where the displacement proceeds along one fractional-flow curve, the rules are those in Section 5.2. In particular, shocks occur where the slope is not monotonically increasing along the given fractional-flow curve. The velocity of the jump between curves is constrained by the condition derived in Step 2 and also must satisfy the condition of monotonically increasing slopes from J to I .
5. Saturations, mobilities, and shocks proceed with a specific velocity equal to the slopes of the corresponding features on the fractional-flow diagram. One can construct the time/distance diagram and plots of saturation at a given time or

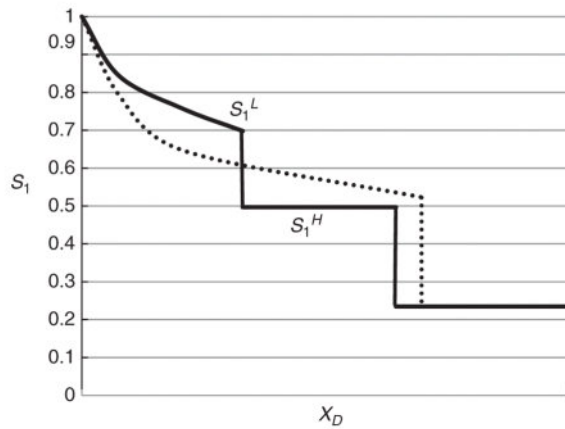
an effluent profile from the time/distance diagram as in [Figs. 5.4](#) and [5.5](#).

Example of Low-Salinity Waterflood. For an example here, we choose a process that is not addressed elsewhere in this text, but of a type that appears in several places in the text. Injection of low-salinity water is thought to alter the wettability of rocks toward more water-wetness and thereby to change both relative permeabilities and residual oil saturation. The two fractional-flow curves shown in [Fig. 5.20a](#) are from Jerauld et al. (2006). The initial condition I is at irreducible water saturation on the fractional-flow curve for the higher-salinity formation water, and the injection condition J is at $f_w = 1$ on the curve for lower-salinity injection water with the same formation and for oil.

In the absence of a change in salinity, the displacement proceeds as a shock from I to the fractional-flow curve for higher salinity at S_f , and as a spreading wave to J . The solution, in terms of water saturation as a function of position at a fixed time, is shown in [Fig. 5.20b](#). (See also [Fig. 8.15](#).)



(a) Solution on fractional-flow diagram. Dashed lines are the two shocks for the low-salinity waterflood. Dotted line is the shock for the conventional waterflood. *H* and *L* mean high and low salinity, respectively.



(b) Saturation profile. Dotted line represents conventional waterflood.

Fig. 5.20—Solution for low-salinity waterflood on fractional-flow diagram; after Jerauld et al. (2008).

If lower-salinity water is injected, the displacement must jump to the fractional-flow curve for lower salinity. Both water saturation and salinity change at the salinity front. A material balance on water at the front gives the same condition as for a shock in a waterflood (Eq. 5.14):

$$\frac{\Delta x_D}{\Delta t_D} = \frac{f_1^+ - f_1^-}{S_1^+ - S_1^-}. \quad \dots \dots \dots \quad (5.80)$$

For simplicity, we assume that salinity involves only a single salt, with an initial concentration in the reservoir of C_{5I} and with an injected concentration of C_{5J} . (For simplicity in the fractional-flow analysis, we ignore the distinction between monovalent and divalent cations and

treat the change at the front as a simple change in salinity.) A material balance on salt at the salinity front, which advances for a distance Δx over time Δt , gives

$$A\phi(S_1^+C_{5J} - S_1^-C_{5I})\Delta x = Au(f_1^+C_{5J} - f_1^-C_{5I})\Delta t, \quad \dots \dots \dots \quad (5.81)$$

where we have assumed that salinity is not lost to or dissolved from the solid at the front. Rearrangement of Eq. 5.80 and combination with Eq. 5.81 give

$$\frac{\Delta x_D}{\Delta t_D} = \frac{f_1^+ - f_1^-}{S_1^+ - S_1^-} = \frac{f_1^+}{S_1^+}. \quad \dots \dots \dots \quad (5.82)$$

Interpreted geometrically, Eq. 5.82 means that the slope of a line from (S_1^+, f_1^+) to (S_1^-, f_1^-) is also the slope of the line from (S_1^+, f_1^+) through $(0,0)$ [i.e., a single line passes through (S_1^+, f_1^+) , (S_1^-, f_1^-) and $(0,0)$ on the fractional-flow diagram]. Note the similarity between the ideal miscible wave discussed above and this construction, which is as it should be because the displacement of high-salinity water by low-salinity water is a miscible displacement.

It remains to find a path from J to I with monotonically increasing slope, including the jump between fractional-flow curves. The solution is shown in Fig. 5.20a. There is a shock from I to a point S_1^H on the fractional-flow curve for higher salinity, then a jump from that curve to a point of tangency S_1^L on the fractional-flow curve for lower salinity, and then a spreading wave to J . The solution, in terms of water saturation as a function of position at a fixed time, is shown in Fig. 5.20b. Water breakthrough is delayed, and more oil is produced earlier, than in a waterflood at higher salinity. Further details can be found in Jerauld et al. (2006).

Other examples of modeling EOR displacements with two-phase fractional-flow theory include solvent injection ([Chapter 7](#)), polymer injection ([Chapter 8](#)), a two-phase surfactant EOR displacement ([Chapter 9](#)), foam injection ([Chapter 10](#)), and hot-water injection (as a simplified model for a hot water flood, [Chapter 11](#)).

5.9 Concluding Remarks

A calculation of oil recovery for a field-scale displacement based solely on the procedures discussed in this chapter would seriously overestimate the actual recovery. Such 1D calculations neglect volumetric sweep issues, which are at least as important as displacement efficiency. Nevertheless, the fractional-flow calculations are important in advancing our understanding of the topic. The items which are important in establishing this framework are the Buckley-Leverett theory and its generalization in Sections 5.7 and 5.8, the ideas of coherent waves and their representations, and the notion of the ideal miscible displacement.

Exercises

5.1 Buckley-Leverett Application. Calculate effluent histories (water cut $f_1|_{x_D=1}$ vs. t) for water ($\mu_l = 1 \text{ mPa}\cdot\text{s}$) displacing oil given the following experimental data (Chang et al. 1978):

S_1	k_{r1}	k_{r2}
0.40	0.00	0.36
0.45	0.005	0.26
0.50	0.009	0.14
0.55	0.02	0.08
0.60	0.035	0.036
0.65	0.050	0.020
0.70	0.080	0.00

Use three values of oil viscosity: $\mu_2 = 1, 5$, and $50 \text{ mPa}\cdot\text{s}$. For $\mu_2 = 5 \text{ mPa}\cdot\text{s}$, calculate the endpoint, shock, and average saturation mobility ratios. The dip angle is zero.

5.2 Gravity and Fractional-Flow Theory. For the exponential relative-permeability functions of Eq. 3.21, plot water saturation profiles at $t_D = 0.3$ for dip angles of $\alpha = 0^\circ, 30^\circ$, and -30° . Additional data are

$S_{1r} = S_{2r} = 0.2$, $n_1 = 1$, $n_2 = 2$, $k_{r1}^0 = 0.1$, $k_{r2}^0 = 0.8$, $\mu_1 = 1 \text{ mPa}\cdot\text{s}$, $\mu_2 = 10 \text{ mPa}\cdot\text{s}$, $k = 0.5 \mu\text{m}^2$, $\Delta\rho = 0.2 \text{ g/cm}^3$, and $\mu = 0.6 \text{ cm/d}$.

5.3 Buckley-Leverett Theory With Straight-Line Relative Permeabilities. Use straight-line exponential relative-permeability functions with zero residual-phase saturations in the following ($n_1 = n_2 = 1$, $S_{1r} = S_{2r} = 0$ in the exponential relative-permeability functions). Also assume $f_{1I} = 0$ and $f_{1J} = 1$.

- Show that the sign of $(1 - M^0 + M^0 N_g^0 \sin \alpha)$ uniquely determines the character (spreading, indifferent, sharpening) of the water-saturation wave.
- For the spreading wave case $(1 - M^0 + M^0 N_g^0 \sin \alpha) < 0$ Eq. 5.12 can be inverted explicitly for $S_1(x_D, t_D)$. Derive this expression in terms of the quadratic formula.
- Use the equation in Part b to show that for $\alpha = 0$, the water-saturation function is given by

$$S_1(x_D, t_D) = \begin{cases} 0, & \frac{x_D}{t_D} > M^0 \\ \frac{\left(\frac{t_D M^0}{x_D}\right)^{1/2} - 1}{M^0 - 1}, & \frac{1}{M^0} \leq \frac{x_D}{t_D} \leq M^0 \\ 1, & \frac{x_D}{t_D} < \frac{1}{M^0} \end{cases}$$

- b. Use the equation in Part c to derive an expression for the average water saturation $\bar{s}(t_D)$ and the displacement efficiency $E_D(t_D)$.

5.4 Water Fractional Flow With Capillary Pressure. Derive the expression for water fractional flow including capillary pressure (Eq. 5.28).

5.5 Analytic Relative-Permeability Ratios (Ershaghi and Omoregie 1978). Over intermediate water-saturation ranges, the oil/water relative-permeability ratio plots approximately as a straight line on a semilog scale, using

$$\frac{k_{r2}}{k_{r1}} = Ae^{-BS_1},$$

where A and B are positive constants. Using the Buckley-Leverett theory, show that a plot of the product of oil and water cuts is a straight line with slope $1/B$ when plotted against $1/t_D$. The dip angle is zero.

5.6 Fractional Flow With Two Inflections. For the fractional-flow curve of Fig. 5.21, construct plots of fractional flow vs. dimensionless distance at breakthrough for saturation $S_1 = 1$ displacing $S_1 = 0$, and $S_1 = 0$ displacing $S_1 = 1$.

5.7 Reversibility of Dispersion and Fractional Flow. Fluid 2 is to be partially displaced by Fluid 1 in a 1D permeable medium. Fluid 1 is injected until just before it is produced, and then the flow is reversed (i.e., Fluid 2 is *injected* at the effluent end). In all that follows, assume the initial (*I*) condition to be 100% Fluid 2 flowing and the injected (*J*) condition to be 100% Fluid 1.

- Sketch two time/distance diagrams for this case using fractional-flow curves similar to those on the extreme right and left of Fig. 5.6.
- If Fluids 1 and 2 are completely miscible with identical viscosities and mix only by dispersion, use Eq. 5.63 to sketch

the time/distance diagram.

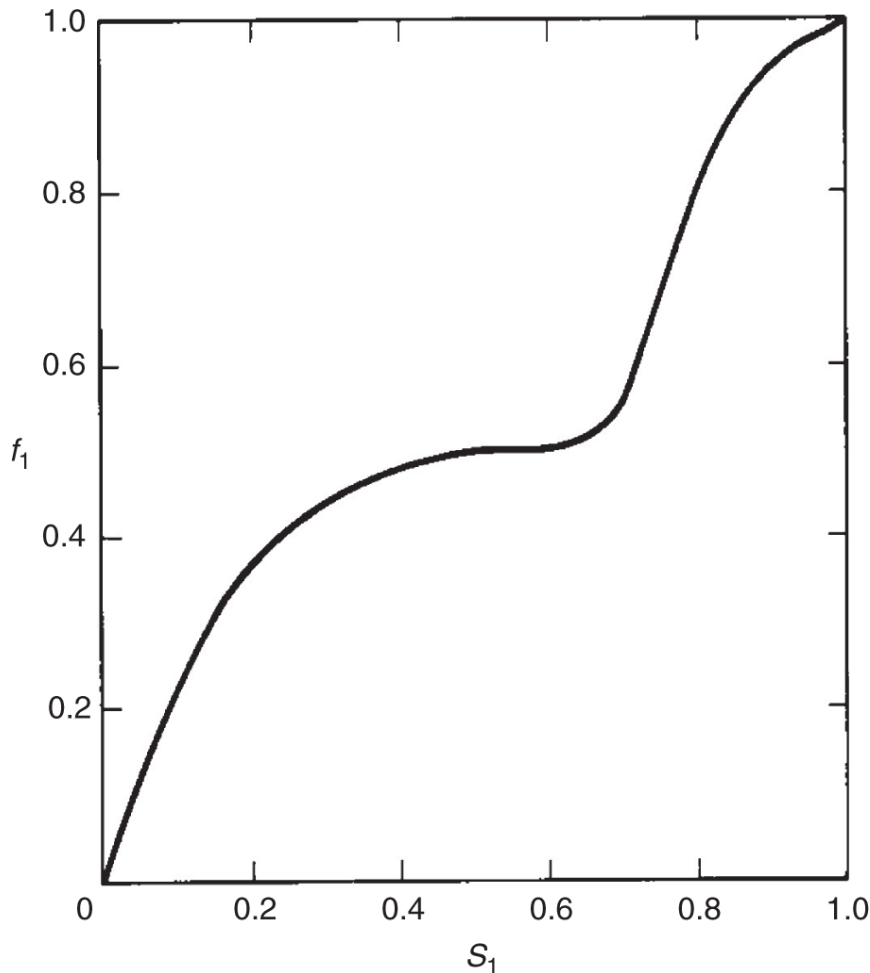


Fig. 5.21—Fractional-flow curve for Exercise 5.6.

- c. On the basis of the results of Parts a and b, what can you conclude about the mixing caused by fractional flow compared to that caused by dispersion?
- d. If Fluids 1 and 2 are water and oil and a fractional-flow curve similar to that on the middle panel of Fig. 5.6 applies, calculate and plot the time/distance diagram.

5.8 Mobility Ratio for Compressible Flow. Consider the piston-like displacement of Fluid 2 by Fluid 1 in the x -direction. Use the general definition of mobility ratio (pressure gradient ahead of front divided by pressure gradient behind front) in the following:

1. Show that the mobility ratio becomes the endpoint mobility ratio if the volumetric flow rate uA is not a function of x (fluids are incompressible).
2. If the mass flux ρuA is not a function of x , on the other hand, show that the mobility ratio becomes
$$M_v = \frac{k_{r1}^o v_2}{k_{r2}^o v_1}$$
where $v = \mu/\rho$ is the kinematic viscosity.
3. Calculate both M^0 and M_V for the following conditions:

$$\rho_1 = \text{mg/cm}^3, \mu_1 = 1 \text{ }\mu\text{Pa}\cdot\text{s}, \rho_2 = 0.8 \text{ g/cm}^3, \rho_2 = 2 \text{ mPa}\cdot\text{s}, k_{r1}^o = 0.1, \text{ and } k_{r2}^o = 1.0.$$

5.9 Using Tracer Data. Consider a 1D permeable medium containing oil at a uniform residual saturation S_{2r} , through which is flowing 100% water at a constant rate. At $t = 0$, a second water stream is introduced at the inlet that contains two ideal (nondispersing and nonabsorbing) tracers. Tracer 1 remains only in the water phase, but Tracer 2 partitions into the residual oil phase with a partition coefficient of 2. The partition coefficient is the ratio of the concentration of Tracer 2 in the oil phase to that in the water phase $K_{21}^2 = C_{22}/C_{21}$. Tracer 1 breaks through after three hours and Tracer 2 after six hours. If the volumetric injection rate is $1 \text{ cm}^3/\text{min}$, calculate the pore volume and S_{2r} .

5.10 Laboratory Estimation of Dispersivity. Dispersivity can be estimated from laboratory, first-contact miscible displacements with the following development:

- a. Show from Eq. 5.60 that a plot of $(1 - t_D)/\sqrt{t_D}$ vs. $\text{erf}^{-1}(1 - 2C_e)$ will yield a straight line with slope $2N_{pe}^{-1/2}$. Here C_e is the effluent concentration $(C_D|_{x_D=1})$.
- b. Estimate the pore volume, dispersion coefficient, and dispersivity from the following experimental data:

Volume Produced (cm ³)	Effluent Concentration
60	0.010
65	0.015
70	0.037
80	0.066
90	0.300
100	0.502
110	0.685
120	0.820
130	0.906
140	0.988
150	0.997

The interstitial velocity is 20 cm/d, and the length is 0.5 m. Note that $\text{erf}^{-1}(1 - 2x)$ is the probability axis (x-axis) on probability paper.

5.11 Tracers in Two-Phase Flow. Consider a permeable medium flowing oil and water at constant oil fractional flow (Case A in [Fig. 5.12](#)). Show that if a tracer with partition coefficient defined as in Exercise 5.9 is introduced at $t_D = 0$, the conservation equation for the tracer concentration C in the aqueous phase is (Delshad 1981):

$$\frac{\partial C}{\partial t_D} + \frac{\partial C}{\partial x_D} - \frac{\bar{K}}{v_T L} \frac{\partial^2 C}{\partial x_D^2} = 0$$

where

$$t_D = t \frac{v_T}{L}$$

$$v_T = \frac{q}{A\phi} \frac{f_1 + K_{21}f_2}{S_1 + K_{21}S_2}$$

$$\bar{K} = \frac{S_1 K_{l1} + K_{21} S_2 K_{l2}}{S_1 + K_{21} S_2}.$$

K_{l1} and K_{l2} are the longitudinal dispersion coefficients for the tracer in the oil and water phases. Assume $(q/A\phi)$ to be constant.

5.12 Three-Phase Displacement Calculation. A more realistic three-phase relative permeability for oil, gas, and water is

$$k_{r1} = k_{r1}^0 \left(\frac{S_1 - S_{1r}}{1 - S_{1r} - S_{2r}} \right)^{n_1}$$

$$k_{r3} = k_{r3}^0 \left(\frac{1 - S_1 - S_2 - S_{3r}}{1 - S_{1r} - S_{3r}} \right)^{n_3}$$

$$k_{r2} = k_{r2}^0 \left[\left(\frac{k_{r21}}{k_{r2}^0} + k_{r1} \right) \left(\frac{k_{r23}}{k_{r2}^0} + k_{r3} \right) - (k_{r1} + k_{r3}) \right],$$

where

$$k_{r21} = k_{r2}^0 \left(\frac{1 - S_1 - S_{2r1}}{1 - S_{2r1} - S_{1r}} \right)^{n_{21}}$$

$$k_{r23} = k_{r2}^0 \left[\frac{S_2 + S_1 - (S_{2r3} + S_{1r})}{1 - (S_{2r3} + S_{1r}) - S_{3r}} \right]^{n_{23}}.$$

These are modifications of the Stone (1970) relative permeability model.

In the preceding five equations, n_{21} is the oil relative permeability exponent in the water/oil system, n_{23} is the oil relative permeability exponent in the gas/oil system, S_{2r1} is the residual oil saturation in the water/oil system, and S_{2r3} is the residual oil saturation in the gas/oil system.

Calculate and plot the following:

- Lines of constant k_{r1} , k_{r2} , k_{r3} in the triangular composition space S_1 , S_2 , and S_3 .

- b. Composition paths and a waterflood composition route for initial saturations of 0.5, 0.3, and 0.2 for oil, gas, and water.
- c. Wave positions in a dimensionless time/distance diagram.

Use the following data:

$\mu_1 = 1 \text{ mPa}\cdot\text{s}$	$\mu_2 = 2 \text{ mPa}\cdot\text{s}$	$\mu_3 = 0.01 \text{ mPa}\cdot\text{s}$
$S_{2rl} = 0.3$	$k_{r2}^0 = 0.6$	$n_{2l} = 1.5$
$S_{2r3} = 0.05$	$k_{r1}^0 = 0.3$	$n_{23} = 2$
$S_{1r} = 0.2$	$k_{r3}^0 = 0.7$	$n_1 = 3$
$S_{3r} = 0.05$	$\alpha = 0$	$n_3 = 2.5$

This problem requires a numerical solution.

5.13 Simplified Three-Phase Fractional Flow. Rework Part c of Exercise 5.14 by assuming that the displacement becomes a shock wave from the initial conditions to a region of simultaneous two-phase oil/water flow followed by a wave of undetermined character to the injected conditions. The velocity of the first wave is given by

$$v_{\Delta S_1} = \frac{f_{3I}}{S_{3I} - S_{3r}} = \frac{f_{1I} - f_1^+}{S_{1I} - S_1^+} = \frac{f_{2I} - f_2^+}{S_{2I} - S_2^+},$$

where f_1^+ and f_2^+ are the water fractional flow and the saturation behind the shock. The velocity of the second wave is then given by the Buckley-Leverett construction. Plot an effluent history of oil and water cuts to demonstrate the fill-up phenomenon.

5.14 Method of Characteristics for Reducible Equations. Consider the following pair of partial differential equations for $u(x, t)$ and $v(x, t)$:

$$\frac{\partial u}{\partial t} + \frac{\partial(u^2 v)}{\partial x} = 0$$

$$\frac{\partial u}{\partial t} + \frac{\partial v^2}{\partial x} = 0$$

where both u and v are less than or equal to 1.

- a. Write these equations in the “canonical” form of Eq. 5.72.
- b. Write the coherence requirement for these equations. Use this to develop an expression for σ , the composition velocity along the characteristic directions.
- c. Use σ to develop an expression for $u = u(v)$ along both characteristic directions.
- d. If the boundary data are specified along a line $u = 1$, plot the “composition” path grid (u, v space) for $u < 1$ and $v < 1$.
- e. On the plot of Part d, show the “composition” route for $(u, v)_J = (0.6, 0.2)$ displacing $(u, v)_I = (1, 1)$. Treat u and v as physical variables so that the composition velocity must decrease monotonically from I to J . Plot the time (t) vs. distance (x) diagram for this “displacement,” where $t > 0$ and $1 > x > 0$.
- f. On the basis of this problem and what you know about the ideal miscible displacement, discuss why the constructions in [Fig. 5.12](#) can be done without the procedures in Parts a through e.

5.15 Gravity Segregation and Fractional Flow. Consider the homogeneous, 1D permeable medium shown in [Fig. 5.22](#) for which all the fractional-flow assumptions apply. Both ends of the medium are sealed. For $t < 0$, the medium contains a completely saturated water zone above a saturated oil zone ($0 < \varepsilon < 1$). At $t = 0$, the denser water is allowed to flow downward, while the less dense oil flows upward. This results in a complete reversal of the

oil and water zones after a sufficiently long time. [Fig. 5.22](#) also shows the long-time condition of the medium.

- Show that there is no bulk flow ($u = 0$) at any point in the medium.
- Derive a water-conservation equation for this special case from the general equations in [Chapter 2](#). Give also the boundary conditions needed to solve this equation for $S_1(x, t)$.
- Make the equation of Part b dimensionless by introducing appropriate scaling factors.

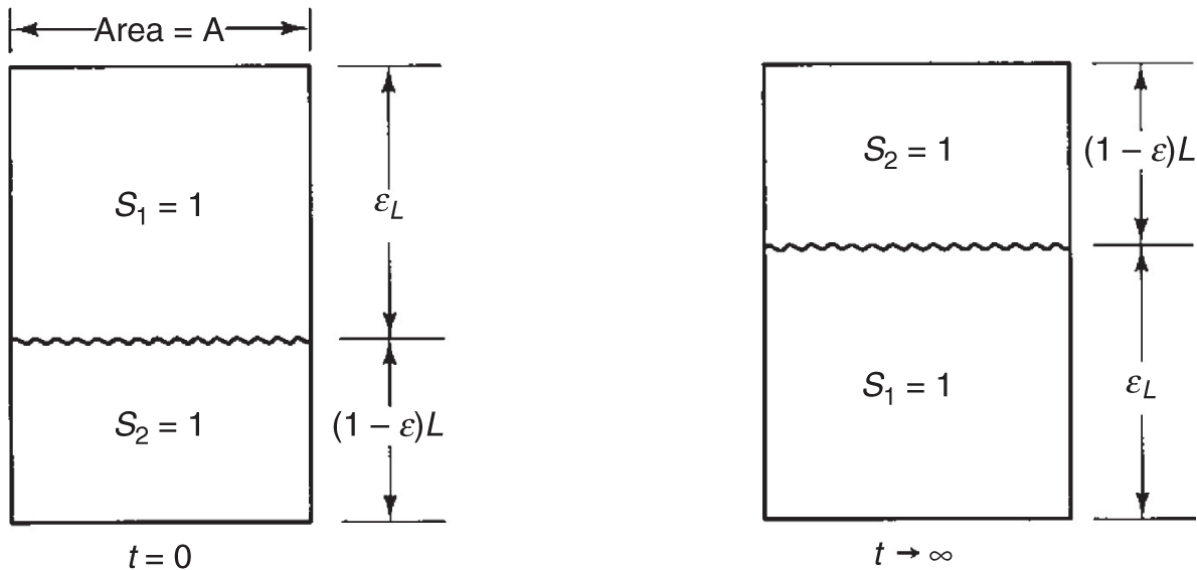


Fig. 5.22—Gravity segregation with fractional flow.

- Derive a dimensionless water flux (analogous to a fractional flow) by eliminating the water-pressure gradient from the equation of Part c. The absence of bulk flow does *not* eliminate pressure gradients (Martin 1958).
- For the following values, plot the dimensionless water flux of Part d vs. water saturation.

$$k_{r1} = 0.1 S_1^4$$

$$k_{r2} = .8(1 - S_1)^2$$

$$\mu_1 = 1 \text{ mPa}\cdot\text{s}$$

$$\mu_2 = 5 \text{ mPa}\cdot\text{s}$$

- f. On the basis of the curve of Part e and $\varepsilon = 0.6$, construct the time/distance diagram showing the progress to complete gravity segregation of the water and oil zones. Estimate the dimensionless time at which this occurs.

Chapter 6

Volumetric Sweep Efficiency

Typical values of residual oil and connate water saturations indicate that ultimate displacement efficiency should normally be between 50 and 80% of the contacted oil in a waterflood. This range is substantially greater than the 30% average recovery efficiency observed in waterfloods; it is also greater than the recovery efficiency in most enhanced-oil-recovery (EOR) projects (see Sections 1 through 4). Of course, the reason that displacement efficiency is higher than recovery efficiency is that not all the oil is contacted by the displacing agent. This effect is present in oil recovery Eq. 2.88 where the displacement efficiency is multiplied by the volumetric sweep efficiency E_V . On the basis of these approximate figures, the volumetric sweep efficiency is between 40 and 60% for a waterflood. For many EOR processes, it can be much lower, and for others, achieving a high E_V is a primary design objective.

In this chapter, we provide both an overview of volumetric sweep efficiency and of techniques to combine areal, vertical, and displacement sweep to arrive at a recovery efficiency. We deal almost exclusively with immiscible water/oil displacement because this literature on recovery efficiency is well established and many of the more important features also carry over to EOR. In later chapters, we discuss the volumetric sweep efficiency of specific EOR processes. To distinguish further between volumetric and displacement sweep efficiency, we usually deal with indifferent or self-sharpening displacements in which dispersive effects are small. For these cases, the calculation techniques are equally valid whether the displacement is miscible or immiscible because there is no point

in the flow field at which all components are flowing simultaneously (in other words, the local displacement is a shock).

6.1 Definitions

On the basis of the overall material balance of Section 2.6, the cumulative mass of oil (Component 2) recovered by water or gas injection is $N_{p2} = V_b \bar{W}_{2I} E_{R2}$ from Eq. 2.87. We convert this equation to a more standard form by eliminating the recovery efficiency E_{R2} by

use of Eq. 2.86, and replacing \bar{W}_{2I} by $\phi (\rho_2 S_2 \omega_{22})_I$, which

$$\bar{W}_{2I}$$

assumes that oil is in the liquid oleic phase only. This gives $N_{p2} = V_b \phi (\rho_2 S_2 \omega_2)_I E_D E_V$. Next, eliminate $(\rho_2 \omega_{22})_I$ using the oil-formation-volume-factor definition, found in Example 2.6, and let $\phi V = V_p$, the pore volume, and $N_p = N_{p2} / \rho_2^o$, the oil production in standard volumes. These substitutions yield

$$N_p = \frac{E_D E_V S_{2I} V_p}{B_{2I}}. \dots \quad (6.1)$$

In Eq. 6.1, E_D is the displacement sweep efficiency as defined in Eq. 5.1, and E_V is the volumetric sweep efficiency defined as

$$E_V = \frac{\text{Volumes of oil contacted by displacing agent}}{\text{Volumes of oil originally in place}}. \dots \quad (6.2)$$

The term $\left(\frac{S_{2I} V_p}{B_{2I}} \right)$ represents the oil in place at the start of the displacement in standard volumes. We have also dropped the subscript $i = 2$ because all efficiencies in this chapter refer to oil recovery.

The volumetric sweep efficiency can be decomposed into the product of an areal sweep efficiency and a vertical sweep efficiency,

The definition of the areal sweep efficiency is

$$E_A = \frac{\text{Area contacted by displacing agent}}{\text{Total area}}. \dots \quad (6.4)$$

[Fig. 6.1a](#) shows a schematic of a highly idealized piston-like displacement in a four-layer areally homogeneous reservoir. [Fig. 6.1b](#) is an areal view of [Fig. 6.1a](#). On the basis of the definition of Eq. 6.4, E_A is the doubly cross-hatched area (at t_2) divided by the singly cross-hatched area. The vertical sweep efficiency,

$$E_i = \frac{\text{Cross-sectional area contacted by displacing agent}}{\text{Total cross-sectional area}}, \dots \quad (6.5)$$

is also similarly defined in Fig. 6.1a at a particular time.

The definitions of Eqs. 6.3 through 6.5 have several subtle difficulties. Both areal and vertical sweep efficiency are ratios of areas; therefore, their product E_V must be a ratio of areas squared. This observation contradicts the definition of Eq. 6.2, which says that E_V must be a ratio of lengths cubed. The redundant dimension in either Eq. 6.4 or Eq. 6.5 is the dimension parallel to the displacement direction. This “direction” is nonlinear and varies with both position and time. Therefore, the decomposition Eq. 6.3 transforms E_V into a product of two planar flows.

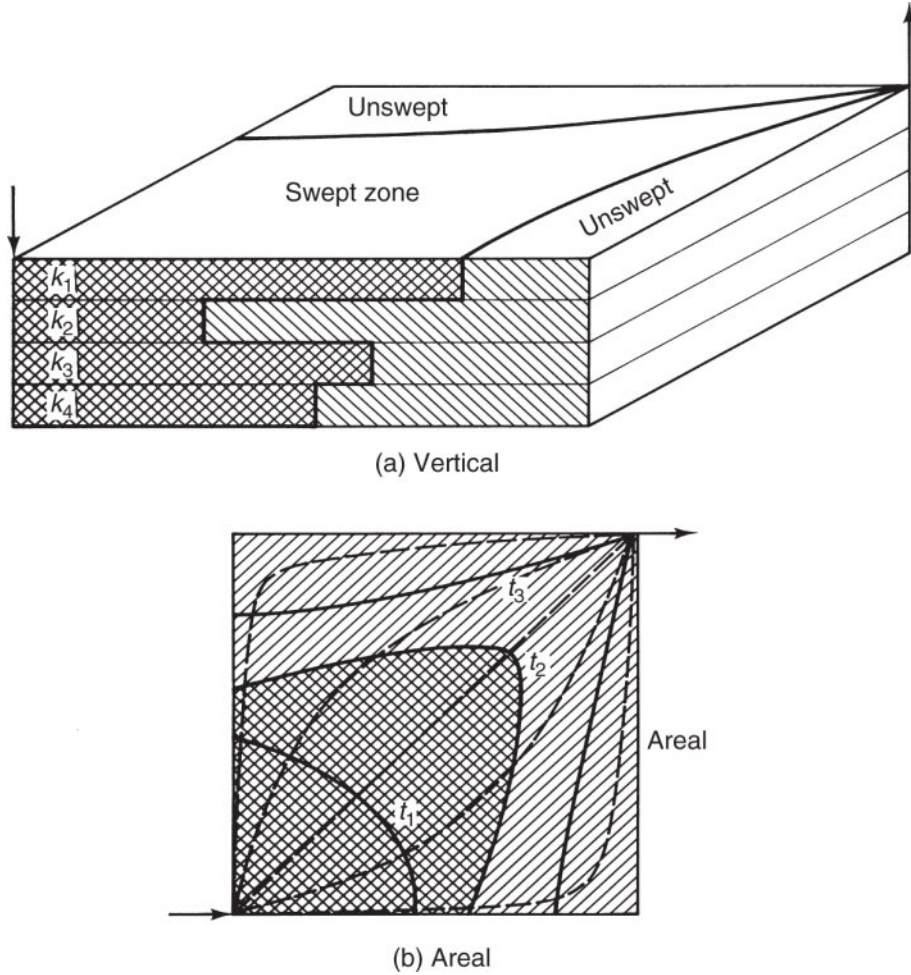


Fig. 6.1—Sweep efficiency schematic.

A second consequence of the redundant dimension in E_V is that both E_A and E_I depend on each other. Note from Fig. 6.1 that E_A depends on vertical position. Similarly, although not so obviously, E_I will be different from the cross section shown for each cross section between the injector and producer. If we restrict ourselves to cross sections defined by pathlines between the injector and producer (dotted lines in Fig. 6.1b), E_I will be the same for each cross section if it can be expressed in a dimensionless form independently of rate. However, for the general case, E_I is a function of rate and will be different for each cross section. The practical consequence of this observation is that neither the areal nor the vertical sweep efficiency

in Eq. 6.3 can be evaluated at the same time for which the volumetric sweep efficiency is desired.

To use Eq. 6.1, even with the above complications, we must have independent estimates of E_A and E_V . For certain very special cases—confined displacements in a really homogeneous regular patterns with no or very good vertical communication—these are available to us through correlation (see Section 6.2) or calculation (see Sections 6.3 through 6.5 and Section 6.9). When these conditions are not met, E_V must be estimated through scaled laboratory experiments or numerical simulation. In the latter case, although it is certainly possible to obtain sweep-efficiency estimates, the oil recovery itself can be obtained directly, and Eq. 6.1 is unnecessary. In addition, Eq. 6.1 assumes that all oil that is displaced from its original location is produced, whereas some displaced oil may not reach a production well. Still, the equation provides a better understanding of sweep-efficiency concepts and the factors necessary to maximize E_V than does simulation alone.

6.2 Areal Sweep Efficiency

Although areal sweep efficiency can be determined through simulation or by analytical methods (Morel-Seytoux 1966), the most common source of areal sweep-efficiency data is from displacements in scaled physical models. [Fig. 6.2](#) presents a typical areal sweep “correlation” from the work of Dyes et al. (1954) for three different regular well patterns. Several more of these correlations can be found in the work of Craig (1971), and an extensive bibliography of areal sweep efficiency is given by Claridge (1972). For the pattern shown in the lower right corner, [Fig. 6.2](#) plots E_A on the y -axis vs. the reciprocal mobility ratio on the x -axis, with time as a parameter. Because the mobility ratio and pattern type are fixed for a given displacement, time is the dependent variable. The dimensionless time in [Fig. 6.2](#) is the cumulative volume of displacing agent injected divided by the displaceable pore volume (the pore volume completely accessible to flow).

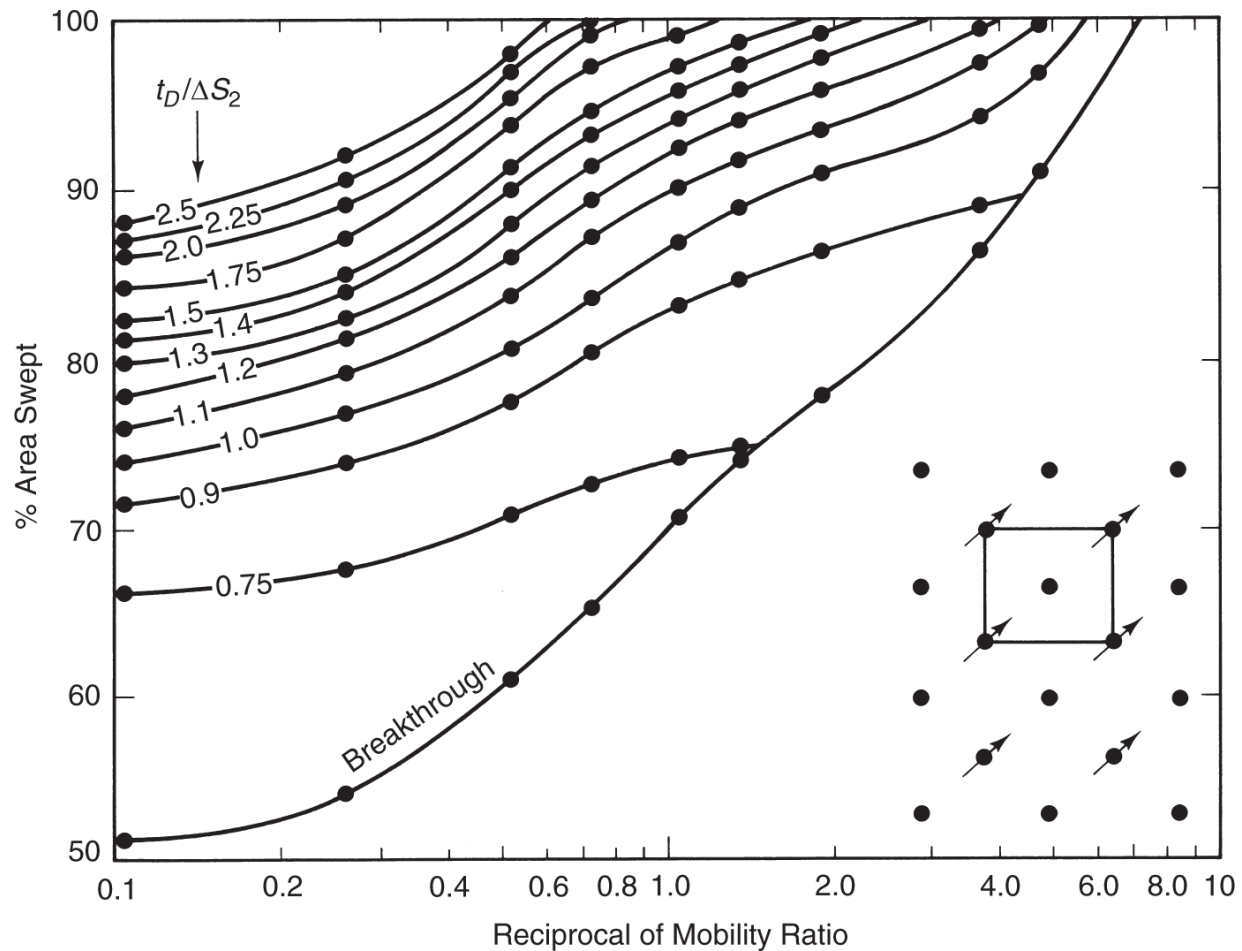


Fig. 6.2—Typical areal sweep efficiency for a confined five-spot pattern (Dyes et al. 1954).

Because time is the dependent variable in these correlations, a more direct representation would be a plot of E_A vs. dimensionless time at a fixed mobility ratio and pattern type (see Exercise 6.1), as in [Fig. 6.3](#).

These correlations are for piston-like displacements in regular, homogeneous, confined patterns. When the well patterns are unconfined, the reference area in Eq. 6.4 can be much larger and E_A smaller. On the basis of an extensive survey of the available correlations for spreading (not piston-like) displacements, Craig (1971) determined that the appropriate mobility ratio for the areal sweep correlations is the average saturation mobility ratio \bar{M} given by Eq. 5.27a.

From these correlations, E_A increases with increasing time or throughput and decreasing mobility ratio. At a fixed mobility ratio, E_A is equal to the displaceable pore volumes injected until breakthrough and then given by the indicated curves in [Figs. 6.2](#) and [6.3](#) thereafter. E_A also increases as the pattern type more closely approaches linear flow, but this sensitivity is not great for the more common patterns. The decrease in E_A with increasing \bar{M} is in the same direction as the change in displacement efficiency with mobility ratio discussed in Section 5.2; therefore, high mobility ratios are detrimental to both areal and displacement sweep.

6.3 Measures of Heterogeneity

Considering the manner in which reservoirs are deposited and the complex diagenetic changes that occur thereafter, it should not be surprising that no reservoir is homogeneous. This does not imply that all reservoirs are dominated by their heterogeneity because, in many cases, one mechanism is so strong that it completely overshadows all others. For example, gravity can be so pronounced in a high-permeability reservoir that it may be considered homogeneous to a good approximation.

Nevertheless, heterogeneity is always present in reservoirs. It is the most difficult feature to define and usually has the largest effect on vertical sweep efficiency. Therefore, before exploring vertical sweep efficiency, we will discuss the most common measures of heterogeneity and their limitations.

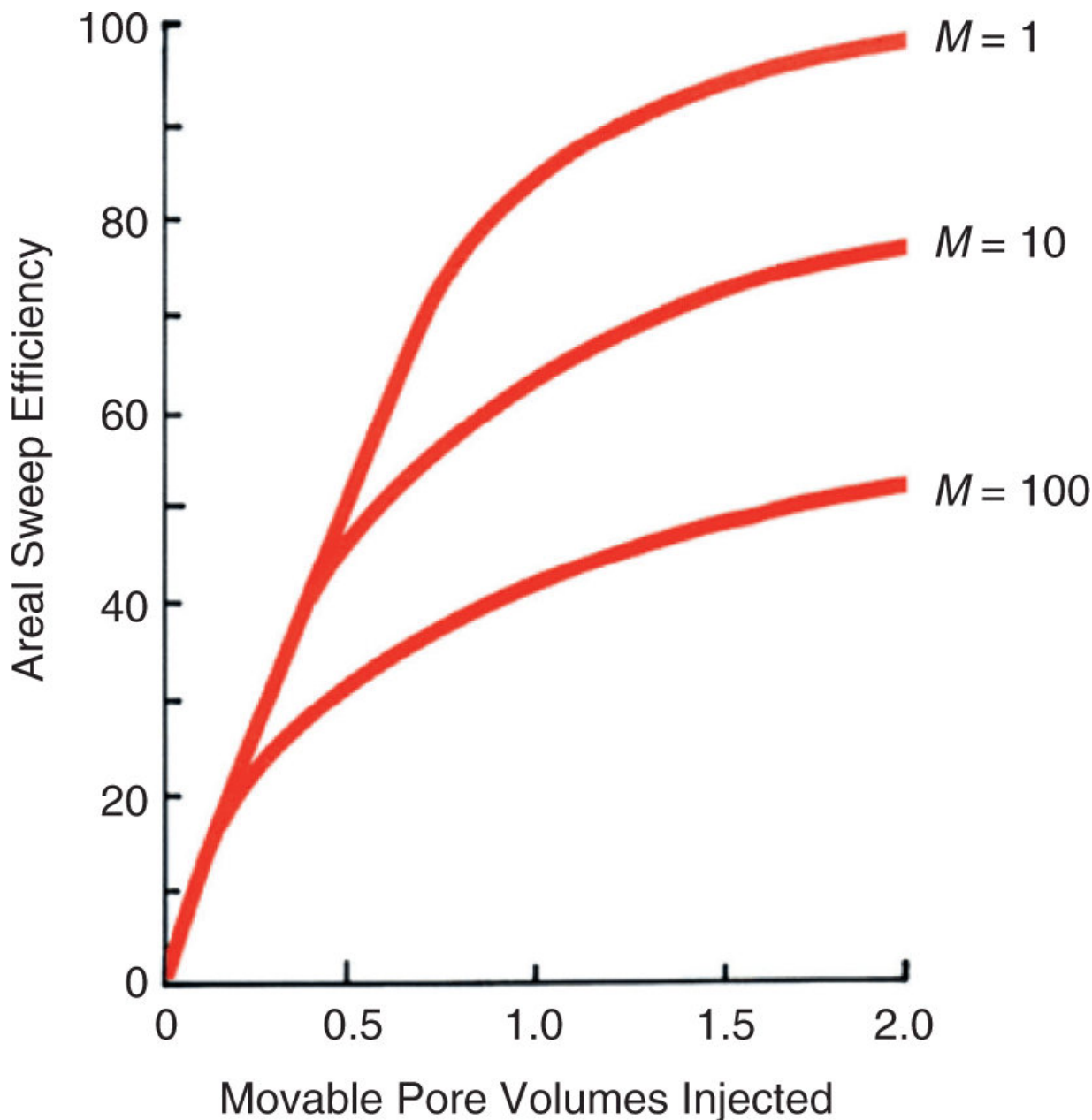


Fig. 6.3—Schematic of areal sweep efficiency.

6.3.1 Definitions. The three principal forms of nonidealities in reservoirs are anisotropies, nonuniformities, and heterogeneities. These terms can be applied to any property, but usually describe permeability, porosity, and, occasionally, relative permeability. An *anisotropic* property varies with the direction of measurement and, hence, has an intrinsic tensorial character (see Section 2.2). The term *heterogeneous* means that the property depends on position in

the reservoir. Heterogeneity has been the bane of EOR processes from the beginning, and its study has involved all types of geoscientists. Here, we discuss only a few of the engineering aspects of this subject.

6.3.2 Flow and Storage Capacity. Because permeability can change by several orders of magnitude in a reservoir, whereas porosity changes by only a few percent over the same scale, it is common to view the reservoir as homogeneous with respect to porosity and heterogeneous with respect to permeability. Although most traditional measures of heterogeneity use this convention, it is not necessary and can lead to occasional errors. In the following discussion, we include porosity variations in the definitions; the more traditional definitions can be recovered by letting porosity and thicknesses be constant.

Imagine an ensemble of N_L permeable media elements, each having different permeability (k_l), thickness (h_l), and porosity (ϕ_l). The elements are arranged as resistances parallel to flow (e.g., horizontal layers penetrated by vertical wells). From Darcy's law, the interstitial velocity of the single-phase flow of a conservative tracer is proportional to the ratio of permeability to porosity, $r_l = k_l / \phi_l$. Therefore, if r_l is a random variable, we can rearrange the elements in order of decreasing r_l (this is equivalent to arranging in order of decreasing fluid velocity) and define a cumulative *flow capacity* at a given cross section as

where H_t is the total thickness,

The average quantities are defined as

A cumulative *storage capacity* follows in a similar fashion:

An interpretation of F_n is that if the N_L elements are arranged in parallel, F_n is the fraction of total flow that is moving at velocity r_n or faster. C_n is the volume fraction of these elements. A plot of F_n vs. C_n yields the curve shown in [Fig. 6.4a](#); if N_L becomes very large, the ensemble approaches the continuous distribution shown in [Fig. 6.4b](#). We designate the continuous distribution by F and C without subscripts. From the definitions of F , C , and r , the slope of either curve at any C is the interstitial velocity at that point divided by the average interstitial velocity of the whole ensemble:

$$\frac{dF}{dC} = F' = \begin{cases} \frac{r_n}{\bar{r}} & \text{(discrete)} \\ \frac{r}{\bar{r}} & \text{(continuous)} \end{cases}, \dots \quad (6.7)$$

where \bar{r} is the average k divided by the average porosity. Because the elements were rearranged, the slope is monotonically decreasing, and from the definitions, $F_n \equiv C_n = 1$ for $n = N_I$.

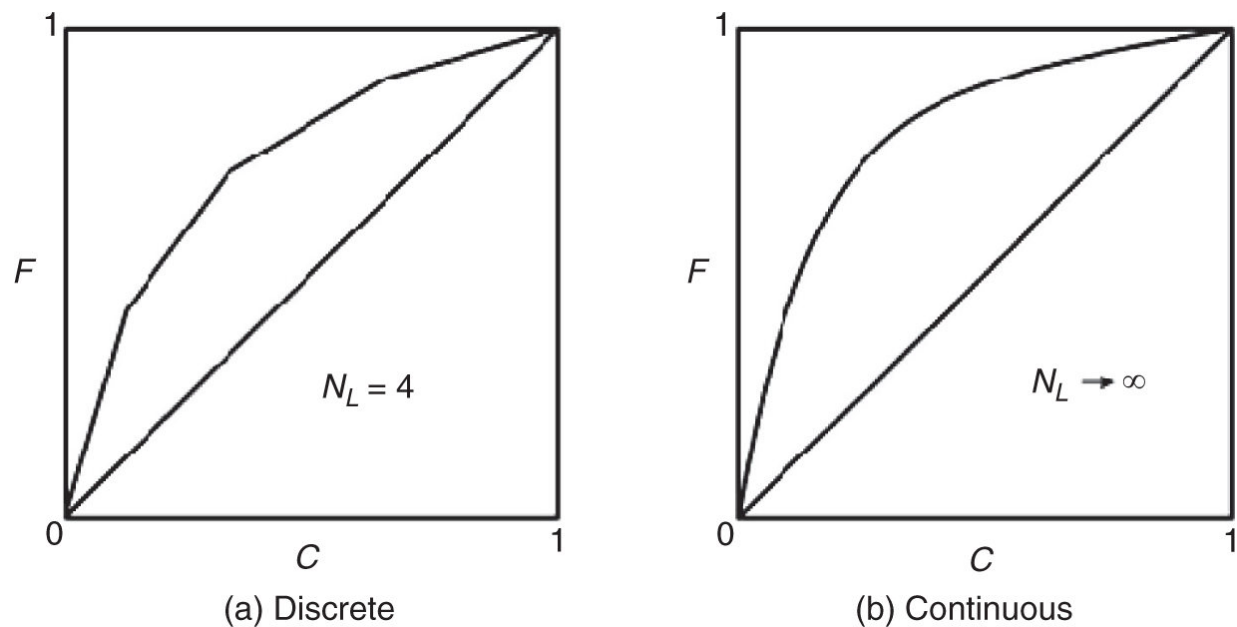


Fig. 6.4—Schematic of discrete- and continuous-flow storage-capacity plots.

The diagrams in Fig. 6.4 are fundamental representations of heterogeneity and of flow through reservoirs. The curves represent a relationship between how fluids flow (y-axis) through a reservoir and how they exist or are stored (x-axis) in a reservoir. They are analogous to the fractional-flow (f_1 vs. S_1) curves covered in Section 5.2 and used throughout this text. The principle difference between f_1 vs. S_1 and F vs. C curves is fundamentally one of scale: fractional-flow curves are determined by relative permeability, wettability effects, and textural (laboratory-scale) properties of the medium. F vs. C curves are determined by intrawell-scale changes in properties and viscous effects.

F vs. C curves are actually much broader than what is suggested by Eq. 6.6. For example, Shook et al. (2006) demonstrated that the storage capacity, which is called there ϕ , can also represent the volumes swept between an injector and producer. Indeed, one can envision that the F vs. C curve can be any measure of cumulative flow plotted vs. a measure of cumulative storage (Yousef et al. 2006).

In another sense, F vs. C curves are restrictive because their importance to flow depends on flow being proportional to

permeability/porosity. When there is substantial interchange (crossflow) between the elements within the reservoir, the flow would not be proportional to permeability/porosity. This topic is partially covered in the sections below. Another type of flow to which F vs. C curves are only partially relevant is that in which the elements (or layers) do not extend from one well to another.

Finally, F vs. C curves can be viewed as statistical characterizations of permeability distributions or of any distribution of a heterogeneous property. Such distributions can themselves be summarized by other statistics, as the following discussion indicates. See also Jensen et al. (1987).

6.3.3 Measures of Heterogeneity. Often it is useful to summarize F vs. C curves; these summaries are heterogeneity measures.

A common measure of reservoir heterogeneity is the Lorenz coefficient L_c , which is defined as the area between the F vs. C curve and a 45° line (homogeneous F vs. C curve) normalized by 0.5,

for the continuous curve. The Lorenz coefficient varies between 0 (homogeneous) and 1 (infinitely heterogeneous). A second, perhaps more common measure that lies between the same limits is the Dykstra-Parsons (1950) coefficient V_{DP} :

Both L_c and V_{DP} are independent of the particular form of the k/ϕ distribution, and both rely on the rearrangement of this ratio. As originally defined, V_{DP} is actually taken from a straight-line fit to the k/ϕ data plotted on a log-probability scale. This procedure is nonunique because two different distributions can have the same V_{DP} when the data are not log-normal (Jensen and Lake 1986). For

strictly log-normal data, Eq. 6.9 determines the distribution around the median value.

To relate F to C , we assume that the permeability assembly is log-normally distributed; hence, the relationship between cumulative frequency λ and r is (Aithison and Brown 1957)

$$\lambda = \frac{1}{2} \left\{ 1 - \operatorname{erf} \left[\frac{\ln \left(\frac{r}{\hat{r}} \right)}{\sqrt{2v_{LN}}} \right] \right\}, \quad \dots \dots \dots \quad (6.10)$$

where \hat{r} is the geometric or log mean of the distribution and v_{LN} is the variance of the distribution. Eq. 6.10 is a two-parameter distribution in that the distribution is entirely determined by a measure of the mean, \bar{r} , and of the variability, v_{LN} . The relationship between \hat{r} and \bar{r} is given by

$$\bar{r} = \hat{r} e^{(v_{LN}/2)}. \quad \dots \dots \dots \quad (6.11)$$

When we identify λ with the storage capacity C and use Eqs. 6.7, 6.10, and 6.11, we obtain

$$C = \frac{1}{2} \left\{ 1 - \operatorname{erf} \left[\frac{\ln \left(e^{v_{LN}/2} F' \right)}{\sqrt{2v_{LN}}} \right] \right\}. \quad \dots \dots \dots \quad (6.12)$$

Eq. 6.12 can be solved for F' and then integrated subject to the boundary condition $F = C = 0$,

$$F = \int_0^C \exp \left[\frac{v_{LN}}{2} + \sqrt{2v_{LN}} \operatorname{erf}^{-1}(1 - 2\xi) \right] d\xi. \quad \dots \dots \dots \quad (6.13)$$

We integrate Eq. 6.13 numerically to give the F vs. C curve for fixed v_{LN} in [Fig. 6.5](#). The curves use v_{LN} as a parameter rather than V_{DP} . The relationship between the two is given below. It follows from Eqs. 6.9 and 6.10 that

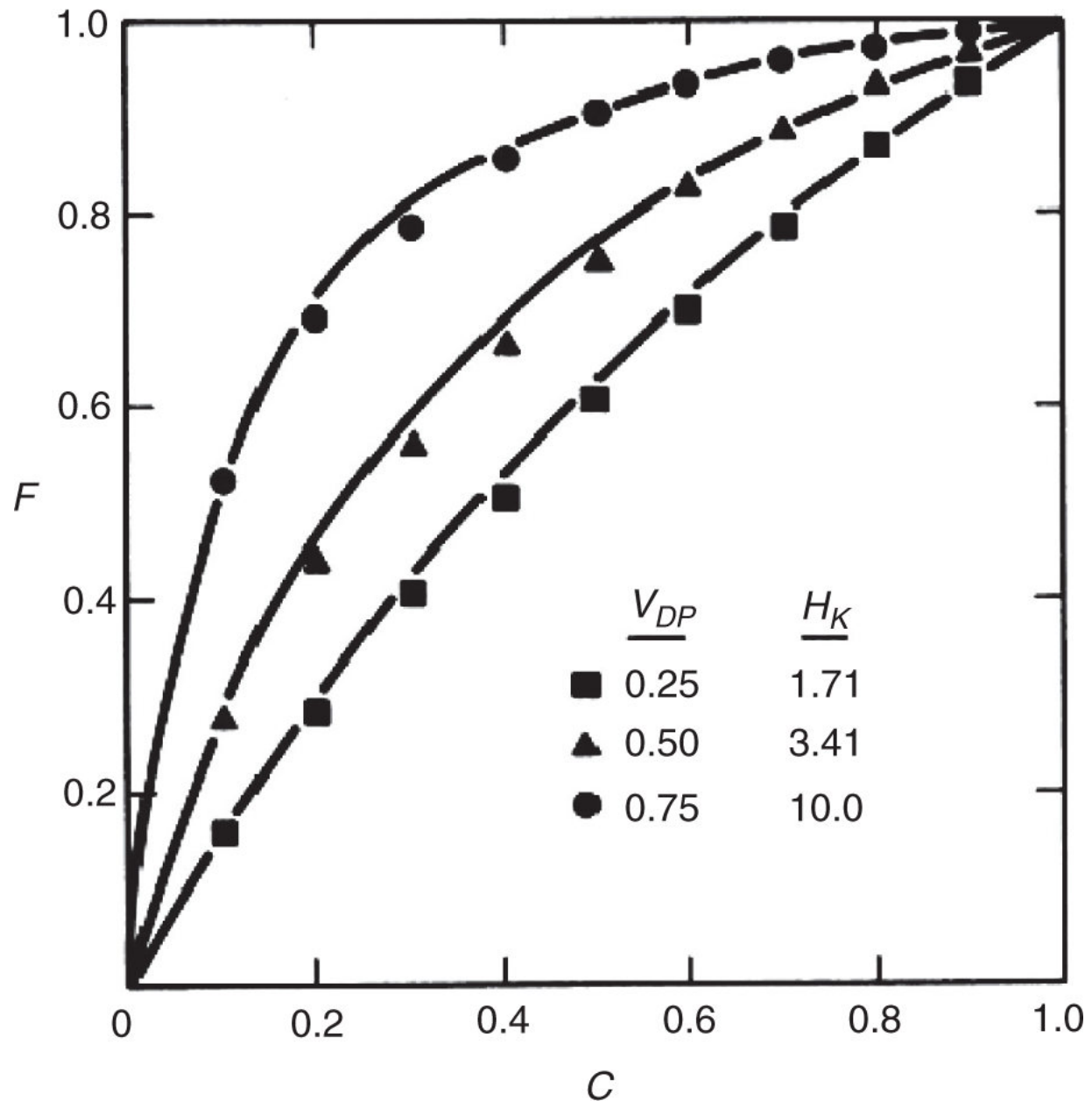


Fig. 6.5—Flow-capacity vs. storage-capacity curves (Paul et al. 1982).

$$V_{DP} = 1 - e^{-\sqrt{v_{LN}}}, \dots \quad (6.14)$$

and furthermore, that the relationship among the Lorenz and Dykstra-Parsons coefficients and v_{LN} is

$$L_c = \operatorname{erf}\left(\frac{\sqrt{v_{LN}}}{2}\right) = \operatorname{erf}\left[\frac{-\ln(1-V_{DP})}{2}\right]. \dots \quad (6.15)$$

From Eq. 6.15 that L_c and V_{DP} are bounded, whereas v_{LN} is not.

Considering the three heterogeneity measures in Eq. 6.15, it must seem odd to propose a fourth, but none of the measures discussed so far relates directly to flow in permeable media. In response to this, Koval (1963) proposed a heterogeneity factor H_K as a fourth measure of heterogeneity that is useful in relating heterogeneity to vertical sweep efficiency. H_K is defined as

$$H_K = \left(\frac{1-C}{C} \right) \left(\frac{F}{1-F} \right). \quad \dots \dots \dots \quad (6.16)$$

Eq. 6.16 follows from observing the similarity between a homogeneous-media fractional-flow curve having straight-line relative permeabilities and zero residual-phase saturations and the points generated in [Fig. 6.6](#). In fact, the solid lines in [Fig. 6.6](#) are calculated from Eq. 6.16, with H_K adjusted to fit the calculated points. Hence, there is a unique correspondence between V_{DP} and H_K , which is shown in [Fig. 6.6](#) by the solid dots. From Eqs. 6.13 and 6.16, it follows that $H_K \rightarrow \infty$ as $V_{DP} \rightarrow 1$ (infinitely heterogeneous) and $H_K \rightarrow 1$ as $V_{DP} \rightarrow 0$. Between these limits, the relation between V_{DP} and H_K is given by the following empirical fit to points in [Fig. 6.6](#):

$$\log(H_K) = \frac{V_{DP}}{(1-V_{DP})^{0.2}}, \quad \dots \dots \dots \quad (6.17)$$

which is also shown in [Fig. 6.6](#).

Using the F vs. C curve in Eq. 6.16, the vertical sweep efficiency of a unit mobility ratio displacement may be calculated using the 1D theory stated in Section 5.2 (see Exercise 5.5).

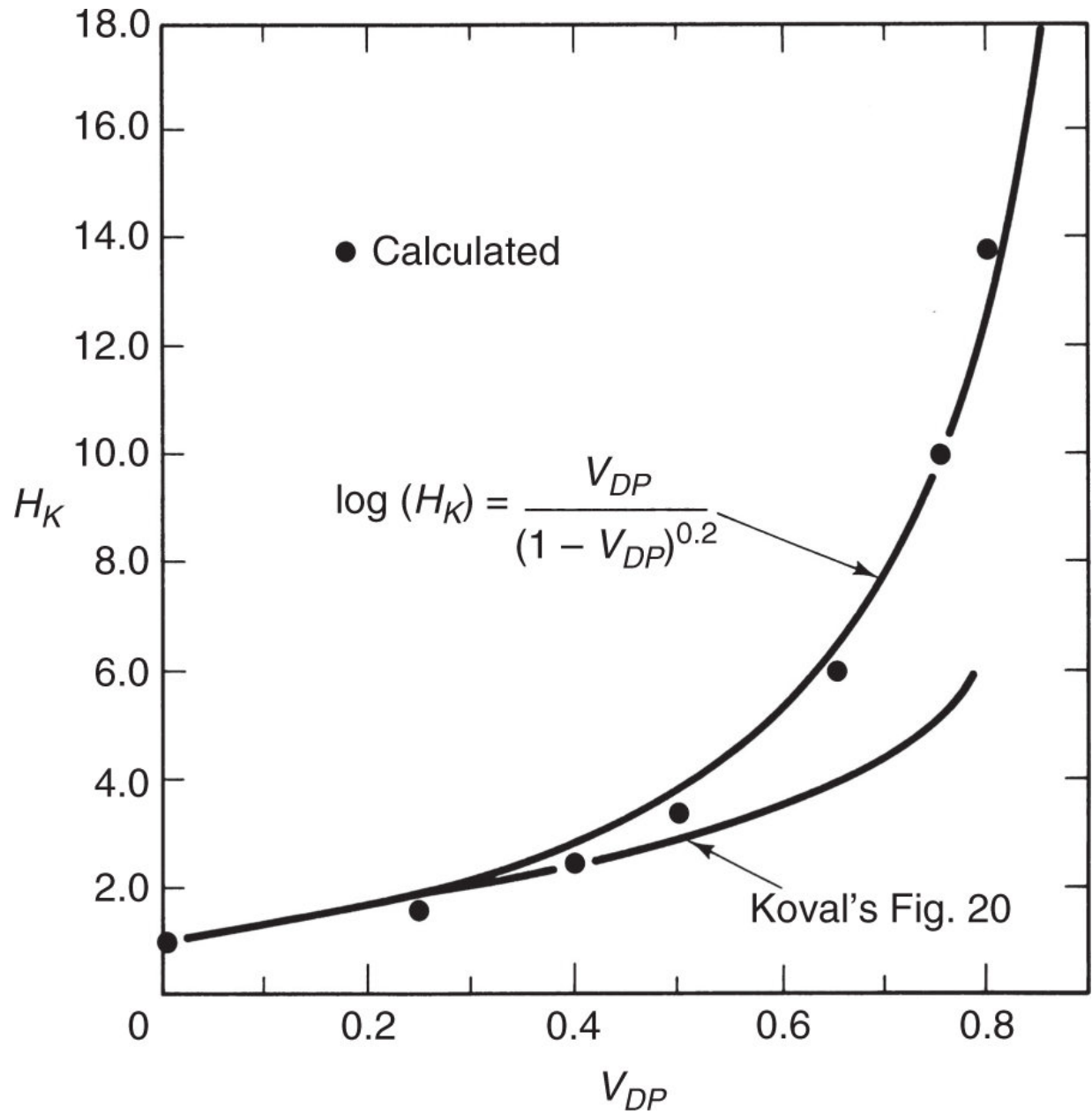


Fig. 6.6—Relation between effective mobility ratio and heterogeneity (Paul et al. 1982).

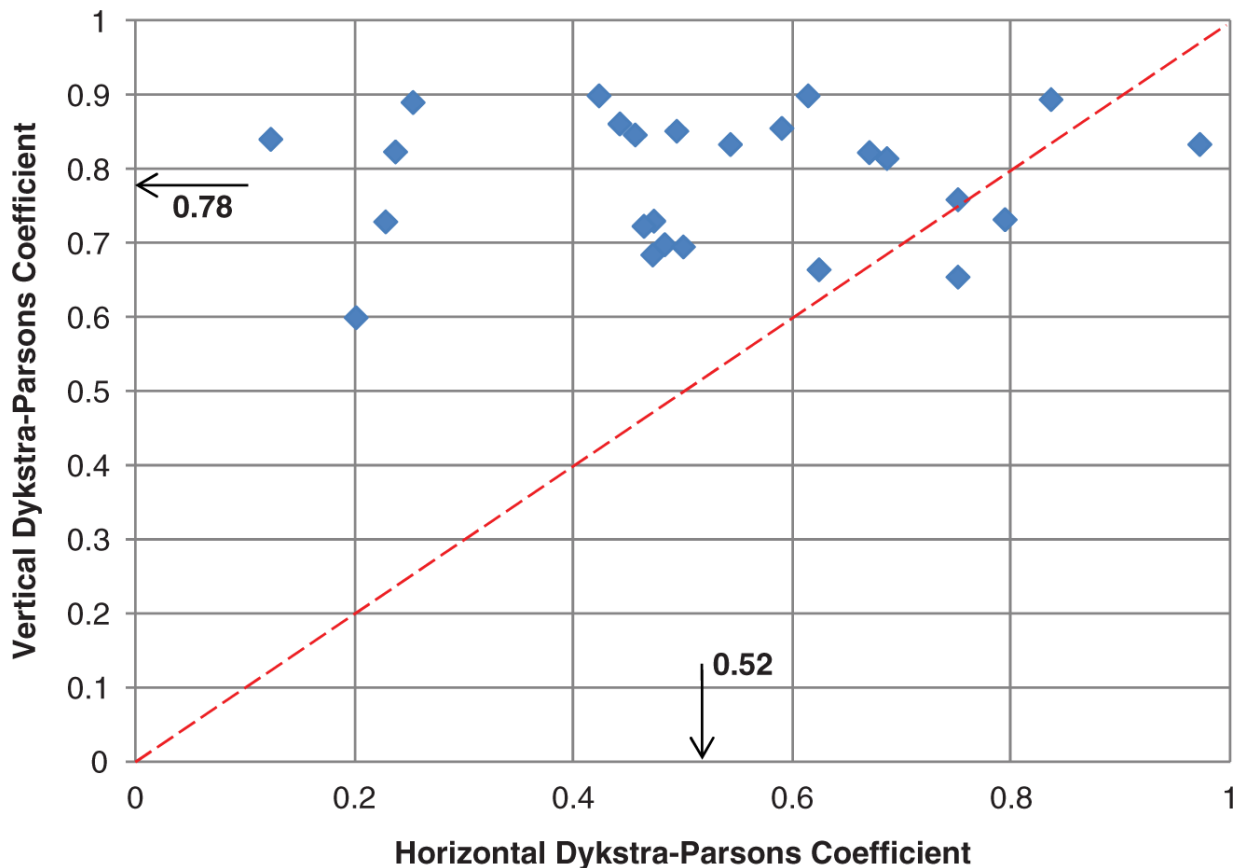


Fig. 6.7—Dykstra-Parsons coefficient based on measurements from individual cores (y-axis) and based on well averages of the core data (x-axis). Data from Lambert (1981).

[Fig. 6.7](#) shows the Dykstra-Parsons coefficients from several producing formations. V_{DP} varies between 0.65 and 0.89 for these formations. This rather tight range corresponds to the range in [Fig. 6.7](#) at which H_K begins to be an exceedingly strong function of V_{DP} . Because E_I decreases with increasing H_K , displacements in most reservoirs should be affected by heterogeneity.

[Fig. 6.7](#) also shows the areal V_{DP} based on the distribution of the average well permeabilities. In only three of the entries shown are the areal variations larger than the vertical variations. This, plus the lack of sensitivity of E_I to heterogeneous permeabilities arranged in series, partly accounts for the popularity of the stratified, or “layer-cake,” model for reservoirs. We use the layer-cake model (uniform and heterogeneous) in the next two sections to calculate E_I . [Fig. 6.7](#)

shows that reservoirs tend to be more heterogeneous (larger V_{DP}) vertically than areally.

The measures of heterogeneity given previously are not entirely satisfactory for predicting displacement performance. Because all the measures capture only heterogeneities (i.e., spatial distributions of permeability), there remains a question about how to use them in displacement calculations. At least one other parameter is needed: some measure of the spatial continuity of the layers. A second reason for the inadequacies in the heterogeneity measures is that for many reservoirs, permeability and porosity are not independent variables. Correlations exist between permeability and porosity (bivariate correlations), and these variables themselves can have spatial structure (autocorrelation). When such structure does exist, the displacement response of a rearranged ensemble of layers will differ from that of the original distribution of layers. Determining when structure exists and separating it from the random stochastic component are tasks usually left to geological interpretation or to geostatistics in current practice.

6.4 Displacements With No Vertical Communication

6.4.1 Single Layer. The objective of this section is to illustrate the effects of mobility and permeability contrasts on vertical sweep efficiency. We begin with the effects of mobility ratio alone on the simplest form of piston-like displacement, that of a constant-composition fluid 2 by a constant-composition fluid 1 in a single homogeneous layer in the absence of gravity. [Fig. 6.8](#) illustrates this case.

The similarity between this figure and [Fig. 3.11](#) is not accidental; as it is but one instance of equations that serial fluid flow in this text. The differences between the figures are more important.

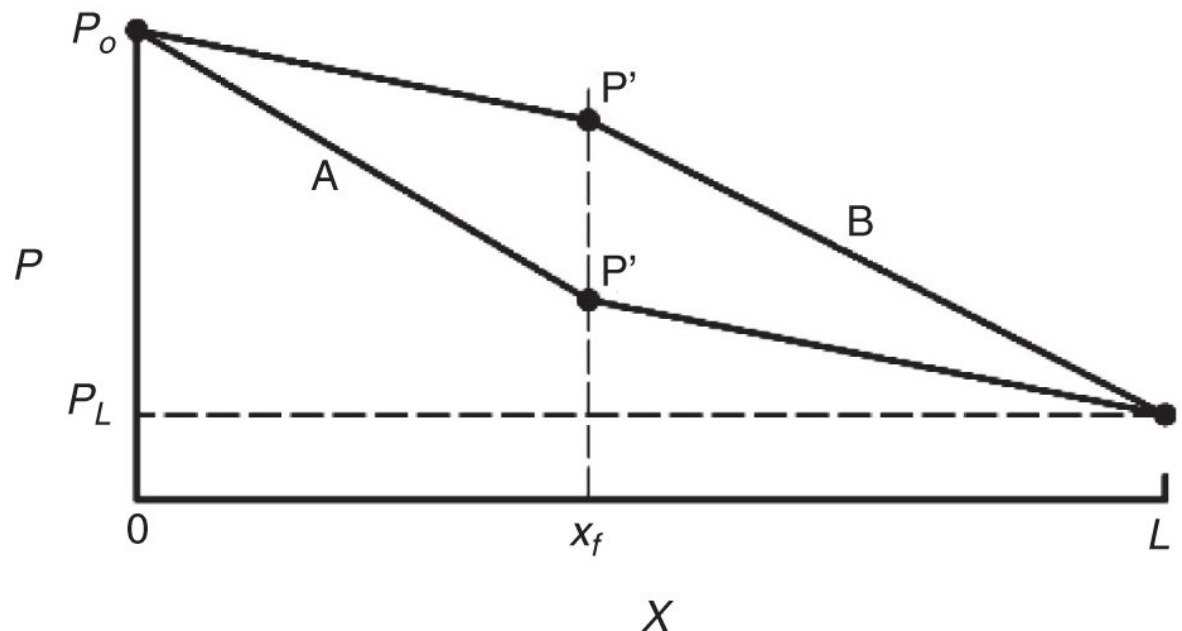
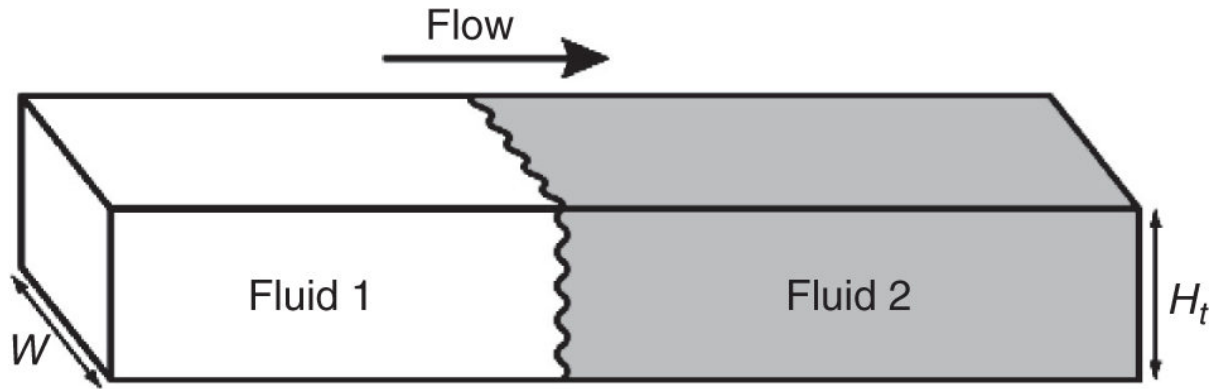


Fig. 6.8—Pressure profiles for two cases of 1D piston-like displacement at a specific time. A: $M^o < 1$. B: $M^o > 1$.

1. The fluids in Fig. 6.8 have different mobilities; Fluid 1 flows with the endpoint relative mobility λ_{r1}^o and Fluid 2 with λ_{r2}^o . The difference in mobility accounts for the difference in slope in the pressure plots. The mobilities are endpoints because the complimentary phase is at their residual saturation; see Section 5.2. The ratio $M^o = \frac{\lambda_{r1}^o}{\lambda_{r2}^o}$ is the endpoint mobility ratio introduced in Section 5.2. $M^o = 1$, as in Fig. 3.11.

2. The lengths in the two figures are vastly different. In Fig. 3.11, L is of the order of a pore length in $P_c \gg \Delta P$ a condition that led to flow being dominated by capillary pressure. In Fig. 6.8, L is of the order of well spacing, usually 10–100 m, and we have $P_c \ll \Delta P$. This inequality accounts for the absence of capillary pressure in the following equations and for the validity of the piston-like-displacement assumption (remember that capillary pressure causes fronts to spread). You should remember that capillary pressure is implicitly present in Fig. 6.8; it accounts for the residual-phase saturations in the left and right regions.

We could have retained the capillary pressure in this discussion here as well as introducing mobility contrasts. (We could also introduce density contrasts as well as nonresidual phase saturations.) These would have resulted in complex equations that would have detracted from the main point of the treatment here (although they could be used as exercises). The saturation and pressure changes here will be $\Delta S = 1 - S_{1r} - S_{2r}$ and $\Delta P = P_o - P_L$, which are both positive.

We now proceed to solve for the front position as a function of time $x_f = x_f(t)$, which is governed by the following equation

This equation follows from the general equations discussed in [Chapter 2](#). Conservation equations of the type shown in Eq. 6.18 are *moving-boundary* problems. Were we to repeat this for Fluid 2, the result would be

$$\phi \Delta S \frac{dx_f}{dt} = u_2$$

or

In these equations, u_1 and u_2 are superficial velocities on the left and right of the front, respectively.

The simplicity of this equation is the consequence of incompressible flow and of each phase being at residual saturation on one side of the front. Under this restriction, the validity of the equation is apparent from Eq. 6.19. The equation $u_2 = u_1 = u$ does *not* mean that u is time-invariant; it merely says that it is not a function of position.

We can obtain $u = u(t)$, an arbitrary function of time that can be subsumed into a single equation, by defining a dimensionless time as

where x_{Df} is a dimensionless front position, A is the cross-sectional area, and

is a dimensionless time. The latter definition is the same as was introduced in [Chapter 5](#), except that here, t_D is based on the movable pore volume $\phi\Delta SLAW$.

Now, let us derive how u or ΔP might change with time because of mobility contrasts. These results will be useful in the multilayer

description to be developed below. From Darcy's law,

$$u = -k \lambda_{\text{left}}^{r1} \frac{\partial p}{\partial x} = -k \lambda_{\text{right}}^{r2} \frac{\partial p}{\partial x}.$$

However, because the saturations are constant within a region and u is independent of x , the equation integrates to give

$$u = k\lambda_{r1}^o \frac{P_o - P'}{x_f} = k\lambda_{r2}^o \frac{P' - P_L}{L - x_f}.$$

Now if we solve for P' from the second of the two equations and substitute into the first, the result is $u = \frac{k\Delta P}{\frac{x_f}{\lambda_{r1}^o} + \frac{L-x_f}{\lambda_{r2}^o}} = \lambda_{r1}^o k \left[\frac{\Delta P}{x_f + M^o(L-x_f)} \right]$, which, with Eq. 6.18, gives an ordinary differential equation for the front position as

Most of the treatment will be in dimensionless variables; however, we retain dimensional variables for a paragraph or two.

We will consider two special cases, $u = \text{constant}$ and $\Delta P = \text{constant}$ in the treatment below. For the first case, ΔP changes with time; for the second, u changes with time.

- If we specify the injection rate (the flow rate), u is constant, and the front proceeds linearly in time at a rate of $x_f = \frac{u}{\phi\Delta S}t$. You should recognize the term on the right side multiplying time as the interstitial velocity. ΔP varies with time according to $\Delta P = \frac{u}{\lambda_{r1}^o k} [x_f + M^o(L - x_f)]$ and Eq. 6.22.
 - If we fix the pressure drop, the front position is given by integrating Eq. 6.22 according to $x_f = 0$ when $\left[\frac{x_f^2}{2} + M^o \left(Lx_f - \frac{x_f^2}{2} \right) \right] = \frac{\lambda_{r1}^o k}{\phi\Delta S} \Delta P t$, which can be quadratically solved as

Although this equation is based on highly restrictive assumptions, several observations follow from it.

1. x_f accelerates with time for $M^\circ > 1$ and decelerates for $M^\circ < 1$, as shown in the schematic in [Fig. 6.9a](#). Both effects are important, but deceleration is particularly important to mobility-control processes.

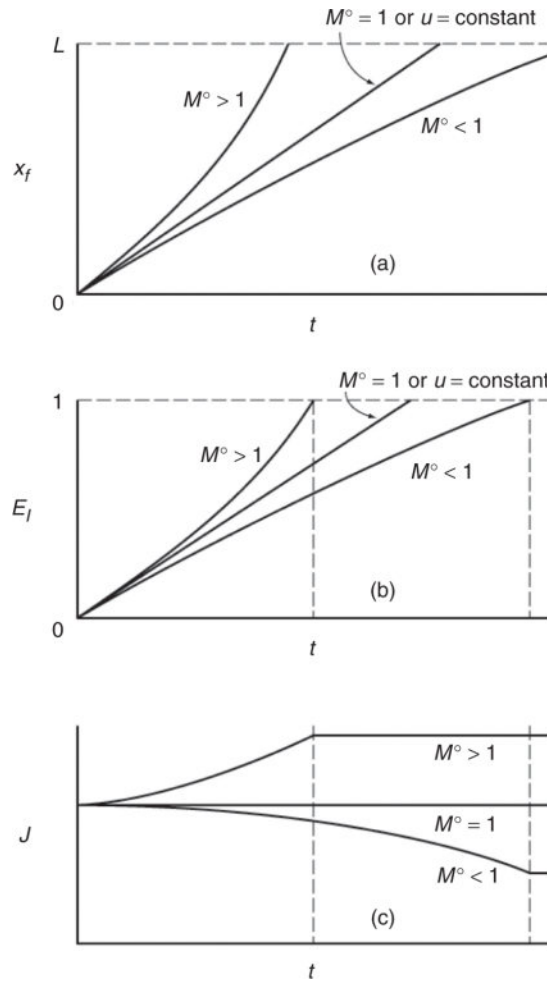


Fig. 6.9—Schematics of (a) front position x_f , (b) sweep efficiency E_I , and (c) productivity index J vs. time for various mobility ratios.

2. For $M^\circ = 1$, the front velocity becomes $x_f = \frac{\lambda_r^o k \Delta P}{\phi \Delta S L} t$.
3. The vertical sweep efficiency is a function of the front position. In dimensionless time, it is

$$E_I = E_I(t_D) = \frac{x_f}{L} = x_{Df} = \begin{cases} t_D & \text{before } BT \\ 1 & \text{after } BT \end{cases} \dots \quad (6.24)$$

In dimensional time, the behavior is more interesting:

$$E_I = \frac{x_f}{L} = \begin{cases} \frac{u}{\phi\Delta SL} t & u \text{ constant} \\ \frac{-M^o + \sqrt{(M^o)^2 + 2(1-M^o) \frac{\lambda_{r1}^o k}{\phi\Delta SL^2} \Delta P t}}{(1-M^o)} & \Delta P \text{ constant} \end{cases} \dots \quad (6.25a)$$

Vertical sweep efficiency is as shown in [Fig. 6.9b](#). What is important here is that decreasing the mobility ratio also delays the breakthrough time, which is defined as $t^o = t|_{x_f=L}$. Physically, breakthrough is delayed because of the filling of the medium with low-mobility fluid as time progresses. The converse is true for $M^o > 1$. Even though simple, the figure illustrates a fundamental truth: breakthrough is early for $M^o > 1$ and delayed for $M^o < 1$.

- Finally, all these effects are summarized in the *injectivity* (or, equivalently for incompressible flow, the productivity) index, which is defined as

$$J = \frac{q}{\Delta P} = \frac{WH_t u}{\Delta P} \dots \quad (6.25b)$$

Regardless of the type of flow, $q = \text{constant}$ or $\Delta P = \text{constant}$, J behaves in the same way, as illustrated in [Fig. 6.9c](#). J increases with time for $M^o > 1$ and decreases for $M^o < 1$. After breakthrough, J becomes constant. Because the rate determines the time scale for production, a small J can be a penalty for delayed breakthrough.

For $M^o < 1$, the front movement slows with time, and the fluids become more difficult to inject (J decreases); both are unfavorable for economic recovery of Fluid 2. It is difficult to see at this point why we would want $M^o < 1$; the benefits of a

low mobility ratio become apparent as we continue the discussion of multilayer flow.

6.4.2 Displacements in Multiple Parallel Layers. Much of what was derived in the preceding paragraphs for flow in a single layer applies to flow in parallel layers. However, a substantial complication arises because fronts can break through in different layers at different times. Let us first consider a two-layer medium. For such a medium, there are two times of interest: breakthrough, when the fastest layer (Layer 1) breaks through, and sweepout, when the slowest layer (Layer 2) breaks through; see [Fig. 6.10](#).

The flow is viscously dominated as before, so that the flow rate in each layer is proportional to permeability. However, there are two significant differences from single-layer flow.

The front position in both layers is given by

$$\phi_i \Delta S_i \frac{dx_{fi}}{dt} = u_i = \lambda_{r1}^o k_i \frac{\Delta P}{[x_{fi} + M^o(L - x_{fi})]} \quad i = 1 \text{ or } 2. \quad \dots \quad (6.26)$$

The subscript i on ϕ_i , ΔS_i , k_i , u_i , and, later, h_i , refers to layer properties. The subscripts on λ_{r1}^o and λ_{r2}^o continue to refer to displacing and displaced fluids, respectively. ΔP is common to both layers (parallel flow), so that

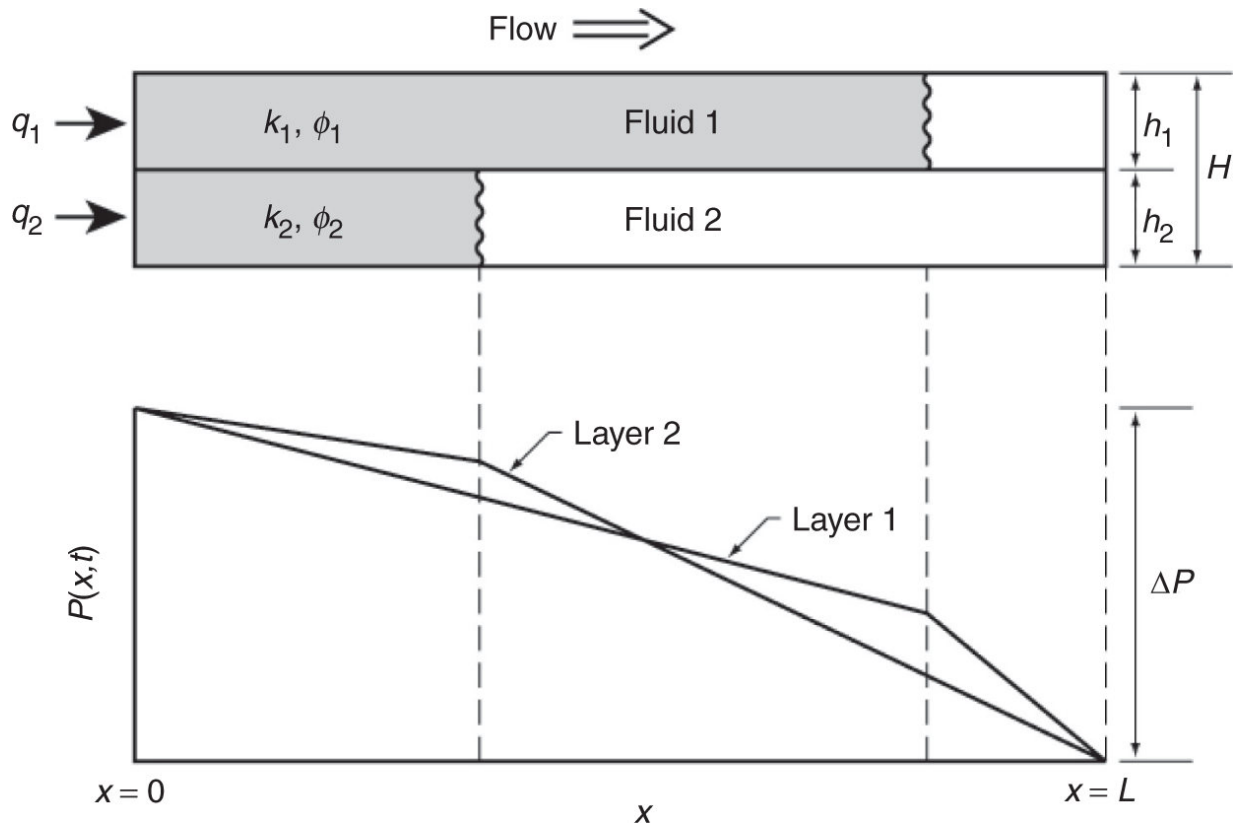


Fig. 6.10—Schematic front positions (before breakthrough) and pressure profile for a two-layer medium with no vertical communication. $M^o > 1$.

$$\begin{aligned}
 q &= q_1 + q_2 = h_1 W u_1 + h_2 W u_2 \\
 &= \lambda_{r1}^o k_1 h_1 W \frac{\Delta P}{[x_{f1} + M^o(L - x_{f1})]} + \lambda_{r1}^o k_2 h_2 W \frac{\Delta P}{[x_{f2} + M^o(L - x_{f2})]},
 \end{aligned}$$

from which we can obtain

$$\Delta P = \frac{q}{\left\{ \frac{\lambda_{r1}^o k_1 h_1 W}{[x_{f1} + M^o(L - x_{f1})]} + \frac{\lambda_{r1}^o k_2 h_2 W}{[x_{f2} + M^o(L - x_{f2})]} \right\}} \quad \dots \dots \dots \quad (6.27)$$

This leads to an expression for the layer rates as

$$q_1 = q \frac{\frac{\lambda_{r1}^o k_1 h_1 W}{[x_{f1} + M^o(L - x_{f1})]}}{\left\{ \frac{\lambda_{r1}^o k_1 h_1 W}{[x_{f1} + M^o(L - x_{f1})]} + \frac{\lambda_{r1}^o k_2 h_2 W}{[x_{f2} + M^o(L - x_{f2})]} \right\}}. \quad \dots \quad (6.28)$$

A similar expression is possible for the flow rate in Layer 2. The front positions in dimensionless coordinates are given by

$$\begin{aligned} & \frac{\phi_i \Delta S_i h_i W}{\phi_1 \Delta S_1 h_1 W + \phi_2 \Delta S_2 h_2 W} \frac{dx_{Df_i}}{dt_D} \\ &= \frac{\frac{\lambda_{r1}^o k_i h_i W}{[x_{Df_i} + M^o(1 - x_{Df_i})]}}{\left\{ \frac{\lambda_{r1}^o k_1 h_1 W}{[x_{Df1} + M^o(1 - x_{Df1})]} + \frac{\lambda_{r1}^o k_2 h_2 W}{[x_{Df2} + M^o(1 - x_{Df2})]} \right\}} \quad i = 1 \text{ or } 2. \end{aligned} \quad (6.29a)$$

This equation says that the front position (the specific velocity) in a layer depends on the position in the other layers.

Finding $x_{Df1}(t_D)$ and $x_{Df2}(t_D)$ follows from integrating Eq. 6.29a. We can perform this integration one layer at a time, but it is just as easy to integrate the problem directly by finite differences. Remember that the resistance to flow in a layer ceases to change once the front in that layer has broken through, or $x_{Dfi}(t_D) \leq 1$. This condition also applies to the vertical sweep efficiency,

$$E_I = \frac{\phi_1 h_1 \Delta S_1 x_{Df1} + \phi_2 h_2 \Delta S_2 x_{Df2}}{\phi_1 h_1 \Delta S_1 + \phi_2 h_2 \Delta S_2}, \quad \dots \quad (6.29b)$$

and the productivity index,

$$J = \frac{q}{\Delta P} = \frac{\lambda_{r1}^o k_1 h_1 W}{[x_{f1} + M^o(L - x_{f1})]} + \frac{\lambda_{r1}^o k_2 h_2 W}{[x_{f2} + M^o(L - x_{f2})]}.$$

For slightly greater generality, we use a *relative*-productivity index,

[Fig. 6.10](#) shows the results of using Eq. 6.29 to calculate the respective quantities as a function of mobility ratio. The parameters of the medium were chosen so that 80% of the flow capacity resides in 20% of the volume ($F|_{c=0.2} = 0.8$), as might occur with a thief zone or if there were a fracture intersecting the two wells.

The $M^\circ < 1$ cases show the high-permeability layer filling up with low-mobility fluid, increasing its resistance to flow and reducing the rate into this layer. The reduction in rate results in an increase in sweep efficiency and delayed breakthrough. The relative injectivity will ultimately attain the mobility-ratio value, although for the $M^\circ = 1$ case, this will occur only if t_D is large.

An important observation for the $M^{\circ} > 1$ case is that the sweep efficiency becomes effectively constant at approximately 30%, a value only slightly greater than the volume of the high-permeability layer.

The preceding equations readily generalize to N_L layers:

$$\text{Layer rate: } q_i = q \frac{\frac{k_i h_i}{\left[x_{Dfi} + M^o (1 - x_{Dfi}) \right]}}{\sum_{n=1}^{N_L} \frac{k_n h_n}{\left[x_{Dfn} + M^o (1 - x_{Dfn}) \right]}} \dots \quad (6.30a)$$

$$\text{Front position: } \frac{\phi_i \Delta S_i h_i}{\sum_{n=1}^{N_L} \phi_n \Delta S_n h_n} \frac{dx_{Dfi}}{dt_D} = \frac{\frac{k_i h_i}{\left[x_{Dfi} + M^o (1 - x_{Dfi}) \right]}}{\sum_{n=1}^{N_L} \frac{k_n h_n}{\left[x_{Dfn} + M^o (1 - x_{Dfn}) \right]}} \dots \quad (6.30b)$$

$$\text{Sweep efficiency: } E_I = \frac{\sum_{n=1}^{N_L} \phi_n h_n \Delta S_n x_{Dfn}}{\sum_{n=1}^{N_L} \phi_n h_n \Delta S_n} \dots \quad (6.30c)$$

$$\text{Relative productivity: } J_r = \frac{J}{J|_{x_{Df1}=x_{Df2}}} = M^o \left\{ \frac{\sum_{n=1}^{N_L} \frac{k_n h_n}{\left[x_{Dfn} + M^o (1 - x_{Dfn}) \right]}}{\sum_{n=1}^{N_L} k_n h_n} \right\}, \dots \quad (6.30d)$$

all subject to $x_{Dfi}(t_D) \leq 1$. As for the two-layer case, we integrate Eq. 6.30b first, and then all other quantities arising from it.

Of the several possible quantities, [Fig. 6.11](#) shows the vertical sweep efficiency for various mobility ratios and Dykstra-Parsons coefficients. Several pertinent observations follow from this figure:

1. There is a general trend toward decreasing E_I with increasing heterogeneity, expressed as V_{DP} , for all M^o . The trend is particularly pronounced beginning at $V_{DP} = 0.8$, the very value at which most reservoir core data are collected, as shown in [Fig. 6.7](#). The difference between the $M^o = 10$ and $M^o = 1$ curves is greater than that between the $M^o = 1$ and $M^o = 0.1$ curves.
2. The limits of the curves for all M^o are $E_I = 1$ for $V_{DP} = 0$ (homogeneous medium) and $E_I = 0$ for $V_{DP} = 1$ (infinitely

heterogeneous medium). *Infinite* heterogeneity means fluid flow with no sweep.

3. Evaluating E_f at $t_D = 1$ is arbitrary. However, $t_D = 1$ is approximately the duration of many EOR floods.
4. There is scatter in the data because of the statistical nature of V_{DP} . The front positions are deterministic functions of permeability distribution, as described by Eq. 6.30b; however, more than one distribution of permeability can give the same V_{DP} . Furthermore, the specified and input V_{DP} may differ because of finite sampling. The scatter about the $M^\circ = 0.1$ curves is less than for the others; hence, in addition to increasing E_f , a low mobility ratio reduces uncertainty.

The curves in [Fig. 6.12](#) are calculated from the procedure in the Dykstra-Parsons paper, in which the water/oil ratio was used instead of dimensionless time. Those curves were based on 50 layers rather than 10, and therefore, they are more accurate than those shown here.

A final observation deals with [Fig. 6.13](#) which shows front positions as functions of time for the reservoir in [Fig. 6.12](#). In a log-normal distribution of the type used here and for moderate to high heterogeneity, there are inevitably one or two layers with a permeability much larger than the others. These result in early breakthrough of the injected fluids and very prolonged displacement in the other layers. In [Fig. 6.13](#), three of the layers break through before $t_D = 1$, but the remaining ones break through at $t_D > 2$.

6.5 Vertical Equilibrium

A useful procedure for performing general oil recovery calculations is to invoke the assumption of *vertical equilibrium* (VE) across the cross section of the reservoir in which a displacement is occurring. Another consequence of the VE assumption is that this represents a state of maximum transverse fluid movement or crossflow. Therefore, calculations based on VE are useful in estimating the tendency of crossflow to affect displacements. The noncrossflowing

calculations of Section 6.4 give the other limit. Ironically, the VE limit gives more general results.

6.5.1 The VE Assumption. Formally, vertical equilibrium is the state in which the sum of all the fluid-flow driving forces in the direction perpendicular to the direction of bulk fluid flow is zero. We see that this condition is more nearly met by flow in reservoirs having high aspect ratios (length to thickness) and good vertical communication. Moreover, Section 6.6 shows that several classical displacement calculations in the petroleum literature are, in fact, subsets of the more general theory of vertical equilibrium (Yortsos 1995).

To derive a general VE theory, we restrict the discussion to incompressible, immiscible displacements of oil by water and derive the water-saturation profile in the transverse direction (the z -direction) at a fixed cross section (the x -position). For the assumptions listed above, the conservation (Eq. 2.11) for water becomes in x - z coordinates,

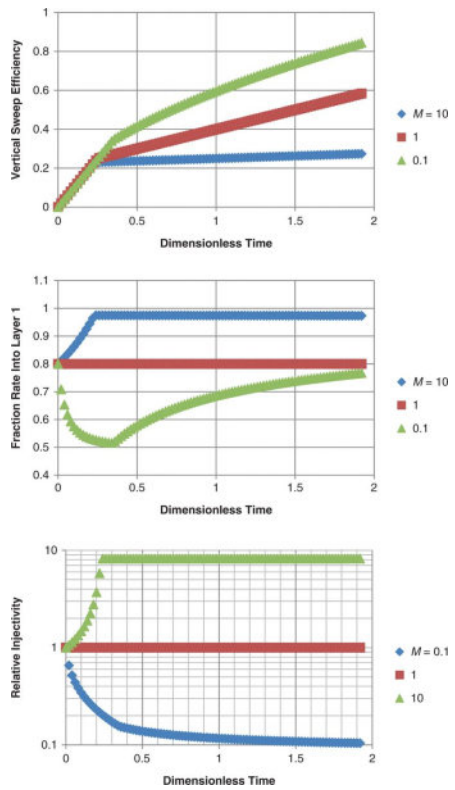


Fig. 6.11—Variation of vertical sweep efficiency (upper), fraction at flow in high-permeability layer (middle), and relative injectivity (lower) with dimensionless time and mobility ratio. The two-layer medium has 80% of the flow capacity in 20% of the volume.

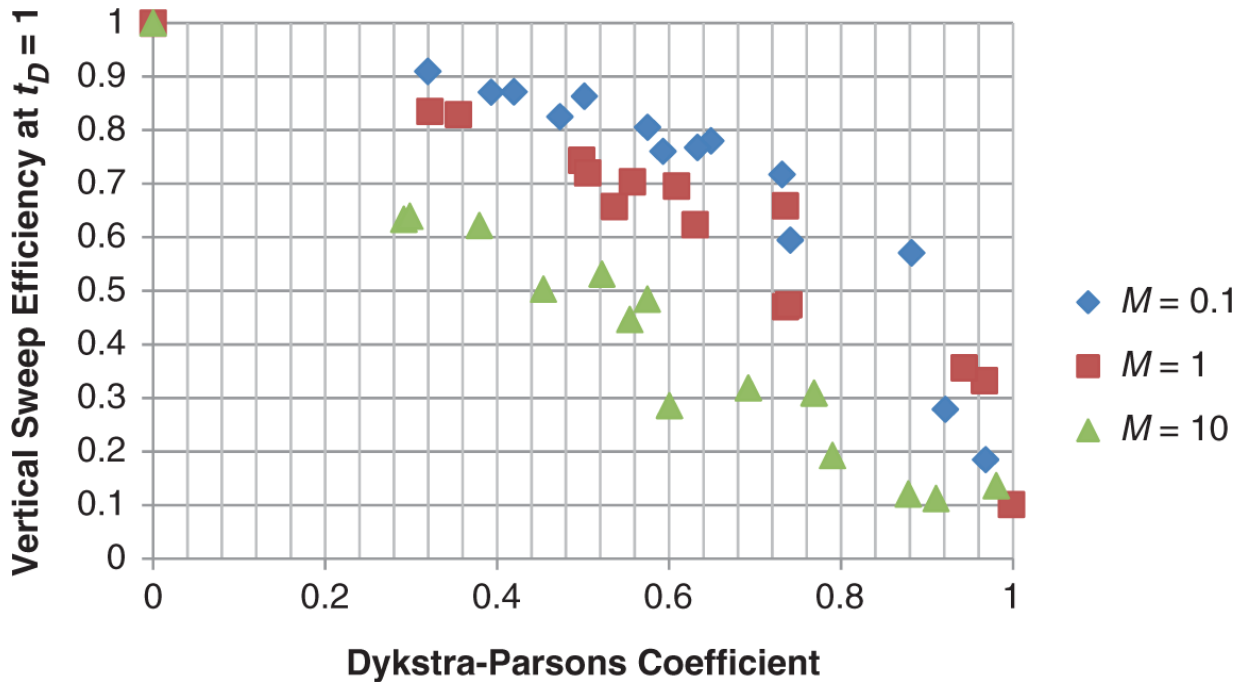


Fig. 6.12—Vertical sweep efficiency at $tD = 1$ for various mobility ratios M° and Dykstra-Parsons coefficients V_{DP} in a 10-layer reservoir with log-normally distributed permeability and no vertical communication. Thicknesses and porosities are equal for all layers.

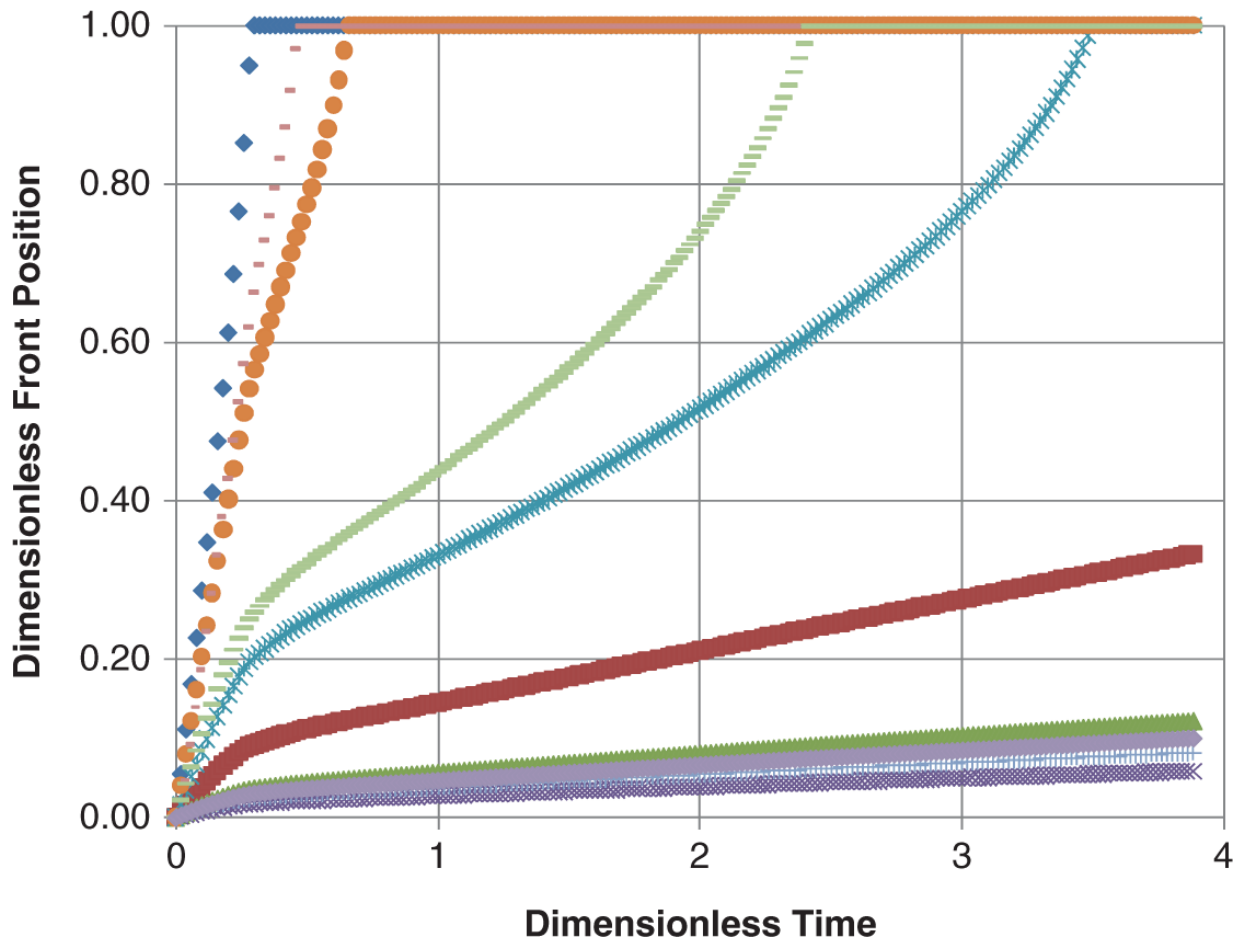


Fig. 6.13—Front positions for one realization of a 10-layer medium for $M^\circ = 10$ and $V_{DP} = 0.8$.

$$\phi \frac{\partial S_1}{\partial t} + \frac{\partial u_{x1}}{\partial x} + \frac{\partial u_{z1}}{\partial z} = 0. \quad \dots \dots \dots \quad (6.31)$$

If we introduce Darcy's law (Eq. 2.2-05 from [Table 2.2](#)) into Eq. 6.31 and scale the independent variables x and z as

$$x_D = \frac{x}{L}, \quad z_D = \frac{z}{H_t}, \quad \dots \dots \dots \quad (6.32)$$

Eq. 6.31 becomes

$$\phi \left(\frac{L^2}{k} \right) \frac{\partial S_1}{\partial t} - \frac{\partial}{\partial x_D} \left[\lambda_{r1} \left(\frac{\partial P_1}{\partial x_D} + L \rho_1 g \sin \alpha \right) \right] - \left(\frac{L^2}{H_t^2 k} \right) \frac{\partial}{\partial z_D} \left[k_z \lambda_{r1} \left(\frac{\partial P_1}{\partial z_D} + H_t \rho_1 g \cos \alpha \right) \right] = 0. \quad \dots \quad (6.33)$$

The terms in this equation represent, from the left, water accumulation, x -direction flow, and z -direction flow, respectively (see [Fig. 6.14](#)). We assume that flow in the z direction is finite; therefore, if the group L^2 / kH_t^2 is large, it follows that the term that it multiplies (the last term) must be small. This means that the z -direction water flux is a function of x only, or

$$k_z \lambda_{r1} \left(\frac{\partial P_1}{\partial z} + \rho_1 g \cos \alpha \right) = f(x). \quad \dots \quad (6.34)$$

Because the water flux in the z -direction is finite, if k_z is large, Eq. 6.34 implies that

$$\frac{\partial P_1}{\partial z} = -\rho_1 g \cos \alpha. \quad \dots \quad (6.35)$$

The preceding reasoning breaks down at water saturations near the irreducible water saturation where λ_{r1} is zero. However, it is true that the saturation range at which Eq. 6.35 breaks down is precisely the range at which the analogous equation for the oil phase is most correct. Therefore, the arguments leading to Eq. 6.35 should be valid in an average sense when applied to both the water and oil phases. See Jain (2014) and Yortsos (1995) for more details.

The group L^2 / kH_t^2 being large is reasonable for many practical cases. However, assuming k_z is large strains credibility because, for most naturally occurring media, k_z is less than k , both of which are finite. For permeable media with dispersed shale barriers, k_z can be much smaller than k .

The requirements of large L^2 / kH_t^2 and k_z may be combined into a single requirement that the effective length-to-thickness ratio,

be large. In Eq. 6.36a, the permeabilities are an arithmetic average of

and a harmonic average for k_z ,

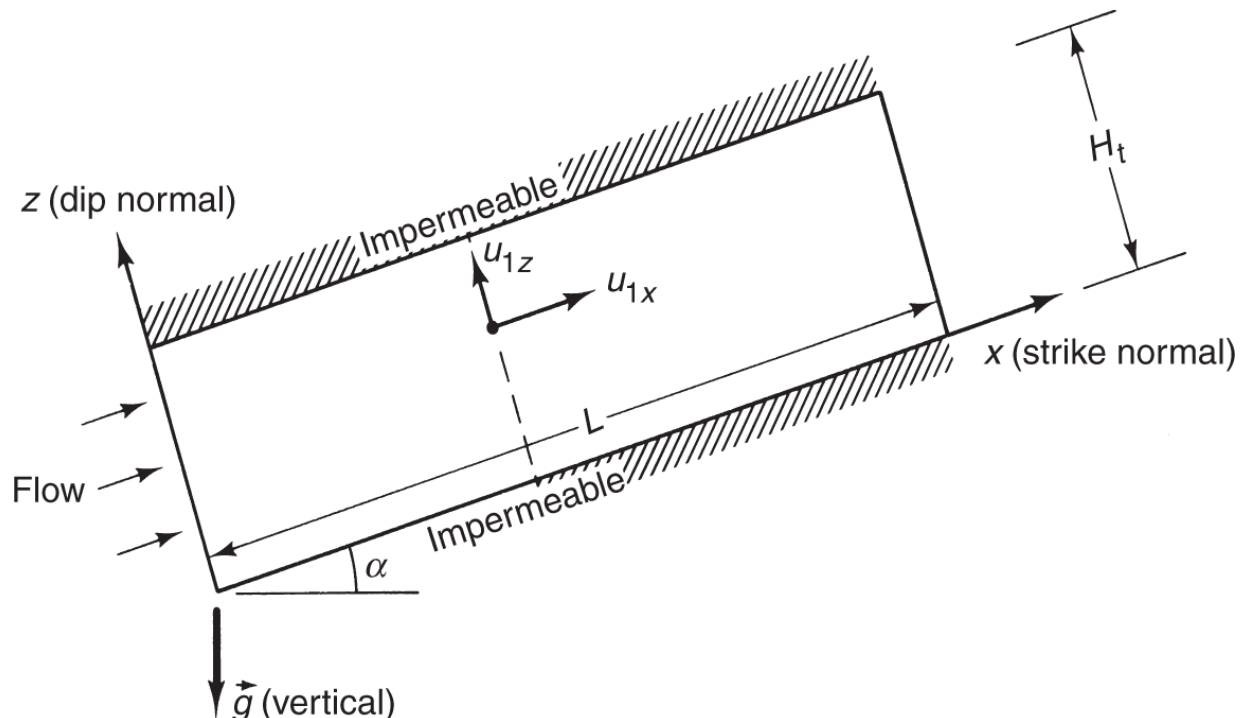


Fig. 6.14—Schematic cross-section for VE procedure.

because horizontal flow is along layers but vertical flow across them. Recall that the resistance to flow in parallel layers is given by an arithmetic average, but that of flow perpendicular to the same layers is given by a harmonic average.

A displacement actually approaches the VE limit asymptotically as R_L becomes large (Yortsos 1995). On the basis of numerical (Zapata and Lake 1981) and analytic (Lake and Zapata 1987) solutions, an R_L greater than 10 is sufficient to ensure that the z-direction sweep efficiency is reasonably well described by VE. You can easily verify that R_L can be large for many reservoirs. For example, for a 16.2 hm^2 (40-acre) spacing of five-spot patterns, the injector/producer distance is 285 m (933 ft). If we assume this to be L , then for $H_t = 6.1$ m (20 ft) and $\bar{k}_z = 0.1k$, we have $R_L = 14.8$, which is large enough for VE to be a good approximation to flow. By taking the \bar{k} to be a harmonic average over the reservoir interval, it is clear that

\bar{k}

= $R_L = 0$ if there are one or more impermeable barriers

\bar{z}

(for example, continuous shale layers) within the interval H_t . Clearly, the VE assumption will not apply in this case. However, the pseudodisplacement sweep efficiency of the intervals between the barriers can be estimated on the basis of VE, and the combined response of all such intervals can be estimated by the communication methods described in Section 6.4.

R_L can be regarded as a ratio of a characteristic time for fluid to cross the reservoir in the x-direction to that in the z-direction. If R_L is large, saturation or pressure fluctuations in the z-direction decay much faster than those in the x-direction. Therefore, we can neglect the z-direction perturbations. Therefore, when we say that the VE assumption applies or that the subject reservoir is in vertical equilibrium, we are saying, for the bulk of the reservoir, that z-direction fluctuations are negligible. Arguments based on the decay time of perturbations were advanced originally by Taylor for flow in capillary tubes (Lake and Hirasaki 1981; Jain 2014).

For large R_L , the P_1 profile in the z-direction is given by Eq. 6.35 for most of the cross sections in the reservoir. This procedure applies equally well to the oil phase, giving

When the definition of oil/water capillary pressure $P_c = P_2 - P_1$ is introduced into this equation, the result is

Eq. 6.38 implicitly describes the water-saturation profile in the z-direction because P_c is a known function of water saturation. However, this saturation distribution is simply what would be observed in the transition zone between oil and water under static conditions. Compare Eqs. 6.38 and 2.3, noting that z and P_c increase in the opposite directions. Hence, the z-direction saturation profile given by Eq. 6.38 is identical to that predicted by assuming no flow in the z-direction. For this reason, VE is occasionally called *quasistatic*.

We stated that VE is a condition that assumes maximum crossflow of fluids, so it is surprising, to say the least, that the same equation describes the saturation profile under conditions of zero and maximum z-direction flow. The resolution of the paradox is that VE assumes such rapid vertical transport of fluids that, at any given time, the extent of nonequilibrium is negligible.

6.5.2 Displacement Classification. One of the consequences of VE is a classification of immiscible displacements according to their degree of segregation. Let S_1^+ be some water saturation slightly below $1 - S_{2r}$ and S_1^- a water saturation slightly above S_{1r} . We can define a capillary transition-zone thickness z_{CTZ} as the z-direction distance over which the water saturation changes between these two limits. From Eq. 6.38 and Fig. 6.15, this is

$$z_{CTZ} \equiv z \left|_{S_i^+} - z \right|_{S_i^-} = \frac{P_c \left|_{S_i^+} - P_c \right|_{S_i^-}}{\Delta \rho g \cos \alpha}. \dots \dots \dots \quad (6.39)$$

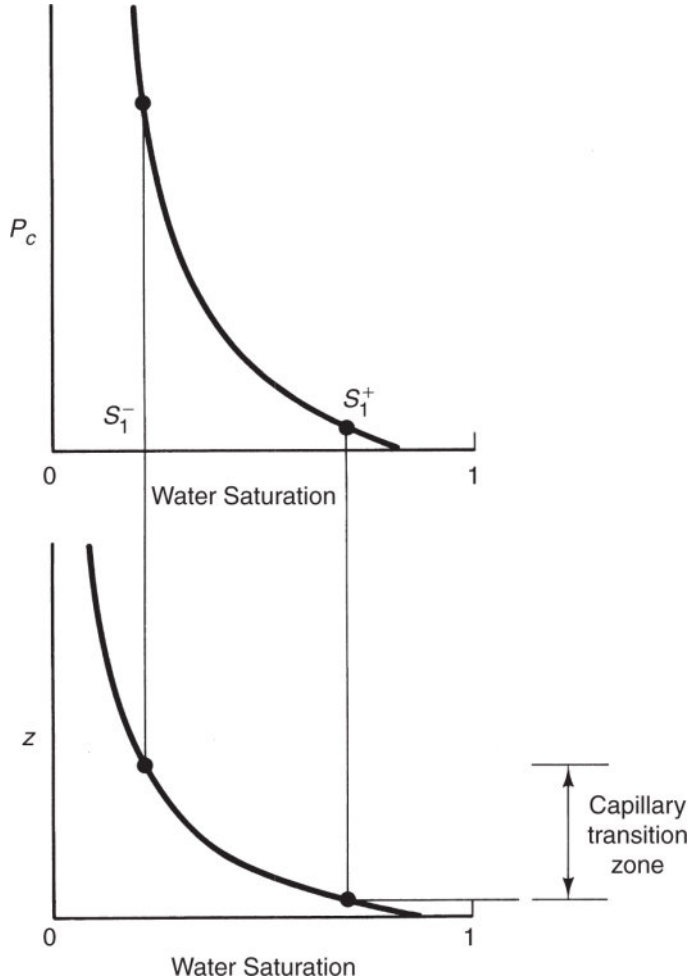


Fig. 6.15—Schematic of capillary transition zone.

We have performed the integration of Eq. 6.38, assuming that the capillary-pressure vs. water-saturation relation applies throughout z_{CTZ} . In general, the capillary transition zone defined by Eq. 6.39 is not the same as that existing at the original water/oil contact, shown as the lower structure to the left in [Fig. 6.14](#), because the integrations leading to Eq. 6.39 start at different saturations.

The existence of the capillary transition zone in a VE reservoir enables the definition of two broad classes of displacements (Dake 1978). If $z_{CTZ} \gg H$, the water-saturation profiles in the z -direction are

essentially constant, and the flow is said to be *diffuse*. If $z_{CTZ} \gg H_n$, the capillary transition zone is small with respect to the reservoir thickness, and the flow is *segregated*. These definitions suggest ideas similar to the definitions of sharpening and spreading waves in Section 5.2, except that the latter definitions apply to cross-sectional averaged saturation waves. The mixing or transition zones described in Section 5.2 occur in the x -direction only and are largely caused by chromatographic effects inherent in the permeable medium oil/water fractional flow curves. The capillary transition zone defined by Eq. 6.39 occurs in the z -direction and is defined by the capillary-pressure vs. water-saturation relation, the dip angle, and the density difference.

6.5.3 Saturation Profile. Let us now consider the integration of Eq. 6.38 at the three different cross sections A , B , and C in [Fig. 6.16](#). In this figure (unlike most in these text), flow is from right to left for ease of illustration. We take S_{1A} , S_{1B} , and S_{1C} to be the water saturations at the bottom ($z = 0$) of the reservoir at the indicated cross sections $x = x_A$, x_B , and x_C . As usual $p_1 > p_2$. Because of the direction of flow, and because the initial water saturation is near the irreducible value $S_{1A} > S_{1B} > S_{1C}$, the water-saturation profile for each of these cross sections is given implicitly from Eq. 6.38:

$$P_c[S_1(x_k, z)] = P_c(S_{1k}) + \Delta\rho g z \cos\alpha, k = A, B, \text{ or } C. \quad \dots \quad (6.40)$$

We do not, at this point, know the x -direction position of the $z = 0$ water saturations, which we determine indirectly below. However, we can schematically sketch lines connecting constant values of S_1 , as indicated in [Fig. 6.16](#). For positive values of the density difference (i.e., the usual case), the isosaturation lines suggest an underrunning of the oil by the injected water. This underrunning, or gravity tongue, is a persistent feature of reservoirs in which gravity forces are strong. Tonguing occurs even in reservoirs that have no dip $\cos\alpha = 1$ ($D_z = -z$). The extent of the tonguing is influenced by the shape of the capillary-pressure curve. In Section 6.6, we discuss a

special case of the VE theory in which capillary forces are negligible and gravity tonguing occurs as segregated flow.

6.5.4 Pseudoproperties. One of the huge advantages of VE is that it collapses dimensionality, which means that it makes 2D flow into 1D flow. To use the z -direction S_1 profile, we convert the original 2D Eq. 6.45 to an equivalent 1D equation. We can start by integrating Eq. 6.31 over the interval thickness H_t and dividing the equation by H_t , which gives

$$\frac{1}{H_t} \int_0^{H_t} \frac{\partial S_1}{\partial t} dz + \frac{1}{H_t} \int_0^{H_t} \frac{\partial u_{x1}}{\partial x} dz + \frac{1}{H_t} \int_0^{H_t} \frac{\partial u_{z1}}{\partial z} dz = 0. \dots \quad (6.41)$$

Because H_t is a constant, the integration and differentiation in the first term commute, and Eq. 6.41 becomes

$$\bar{\phi} \frac{\partial \bar{S}_1}{\partial t} + \frac{\partial \bar{u}_{x1}}{\partial x} = 0. \dots \quad (6.42)$$

Terms involving the z -direction water flux do not appear in Eq. 6.42 because all fluxes vanish at the upper and lower impermeable boundaries of the reservoir. In Eq. 6.42, the averages are

$$\bar{S}_1 = \frac{1}{H_t \bar{\phi}} \int_0^{H_t} \phi S_1 dz \dots \quad (6.43a)$$

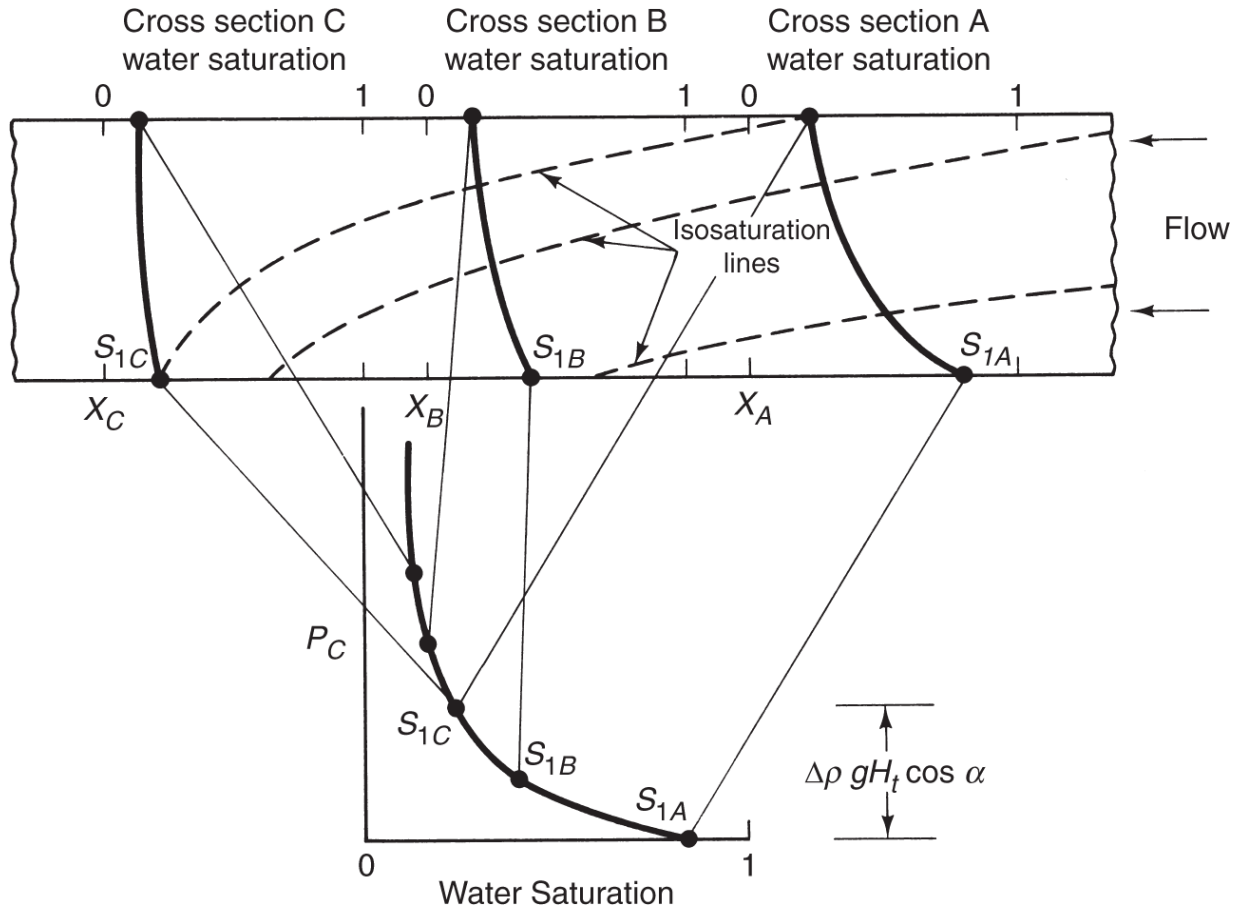


Fig. 6.16—Schematic of z-direction water-saturation profiles for various cross sections.

$$\bar{\phi} = \frac{1}{H_t} \int_0^{H_t} \phi dz, \quad \bar{u}_{1x} = \frac{1}{H_t} \int_0^{H_t} u_{x1} dz. \quad \dots \quad (6.43b)$$

In these definitions, and in those that follow, all averages are arithmetic averages except the water saturation, which is an arithmetic average weighted by porosity. Introducing the definitions for dimensionless independent variables,

$$x_D = \frac{x}{L}, \quad t_D = \int_0^t \frac{\bar{u}_x dt}{\bar{\phi} L}, \quad \dots \quad (6.44)$$

into Eq. 6.42 yields

$$\frac{\partial \bar{s}_1}{\partial t_D} + \frac{\partial \bar{f}_1}{\partial x_D} = 0, \quad \dots \quad (6.45)$$

where $\bar{u}_x = \bar{u}_{x1} + \bar{u}_{x2}$ and $\bar{f}_1 = \bar{u}_{x1}/\bar{u}_x$ is a cross-sectional averaged water-fractional-flow function. Eq. 6.45 is identical to Eq. 5.7a and can be solved in the same manner as a one dimensional problem once we define \bar{f}_1 in terms of \bar{S}_1 , as we are about to do.

Consider the cross-sectional averaged total flux multiplied by H_t , with Darcy's law substituted for the local flux:

$$H_t \bar{u}_x = - \int_0^{H_t} k \lambda_{r2} \left(\frac{\partial P_2}{\partial x} + \rho_2 g \sin \alpha \right) dz - \int_0^{H_t} k \lambda_{r1} \left(\frac{\partial P_1}{\partial x} + \rho_1 g \sin \alpha \right) dz. \quad (6.46)$$

We can express the x -direction oil-phase pressure gradient in terms of the water-phase pressure gradient and factor to give

$$\begin{aligned} H_t \bar{u}_x = & - \int_0^{H_t} k (\lambda_{r2} + \lambda_{r1}) \frac{\partial P_c}{\partial x} dz - \int_0^{H_t} k \lambda_{r2} \frac{\partial P_c}{\partial x} dz \\ & - g \sin \alpha \int_0^{H_t} k (\lambda_{r2} \rho_2 + \lambda_{r1} \rho_1) dz. \end{aligned} \quad (6.47)$$

However, from Eq. 6.35, it follows that $\frac{\partial P_c}{\partial x} = \frac{\partial P_w}{\partial x} - \frac{\partial P_o}{\partial x} = \frac{\partial P_w}{\partial x}$.

Hence under VE, the water-phase pressure gradient in the x -direction is independent of z , as are both $\frac{\partial P_w}{\partial x}$ and $\frac{\partial P_o}{\partial x}$. All gradients can be factored from the integrations and solved for as

$$-\frac{\partial P_1}{\partial x} = \frac{H_t \bar{u}_x + \left(\frac{\partial P_c}{\partial x} \right) \int_0^{H_t} \lambda_{r2} k dz + g \sin \alpha \int_0^{H_t} k (\lambda_{r2} \rho_2 + \lambda_{r1} \rho_1) dz}{\int_0^{H_t} k (\lambda_{r2} + \lambda_{r1}) dz}. \quad (6.48)$$

The pressure gradient of Eq. 6.48 substituted into the averaged water flux,

$$H_t \bar{u}_{x1} = \left(-\frac{\partial P_1}{\partial x} \right) \int_0^{H_t} k \lambda_{r1} dz - g \sin \alpha \int_0^{H_t} k \lambda_{r1} \rho_1 dz, \quad (6.49)$$

gives

Comparing this equation with Eq. 5.28 suggests the following definitions for *pseudorelative permeabilities*:

The multiplier of the second term in brackets in Eq. 6.50 is a pseudocapillary-pressure function; see Eq. 6.40.

To use the 1D theory of Section 5.2 on these equations, we must neglect the x -direction capillary-pressure term in Eq. 6.50. This omission is not equivalent to neglecting capillary pressure entirely because the capillary pressure in the z -direction determines, in part, the z -direction saturation profile. Although it seems inconsistent to maintain capillary pressure in the z -direction and neglect it in the x -direction, one can show by scaling arguments similar to those used in Section 5.3 that when the conditions for VE apply, z -direction effects are far more important than x -direction effects (Yokoyama and Lake 1981).

The procedure for calculating pseudorelative-permeability curves (\tilde{k}_{r1} and \tilde{k}_{r2} vs. \bar{S}_1) is as follows:

1. Select a water saturation at the bottom of the reservoir, S_{1k} .
 2. Determine the z-direction water-saturation profile $S_1(x_k, z)$ at cross section k using Eq. 6.40 and the capillary-pressure vs. water-saturation relation.
 3. Calculate the average water saturation at cross section k , $\bar{S}_1(x_k)$, from Eq. 6.43a and from the z-direction porosity profile.
 4. Calculate the pseudorelative permeabilities corresponding to \bar{S}_1 from Eq. 6.51 and from the z-direction permeability profile.

Steps 1 through 4 give a single point on the pseudorelative-permeability curve. To construct the entire curve, we repeat the procedure with different values of S_{1k} . The procedure gives all possible water-saturation profiles and average water saturations for the reservoir (see Fig 6.16), although it does not give the x -positions of these quantities, which can be obtained by solving the, 1D Eq. 6.42. Although the averaging procedure is fairly straightforward, most of the integrations in it must be evaluated numerically in the absence of analytic functions for the capillary-pressure and relative-permeability curves (see Exercise 6.6).

Once the pseudorelative permeabilities have been constructed, the pseudodisplacement sweep efficiency \tilde{E}_D follows from Eqs. 5.2 and 5.26, with the appropriately averaged quantities appearing in place of the local quantities.

You should appreciate the generality of the VE approach, for we now have a means for calculating and combining the displacement E_D and vertical E_V sweep efficiencies with little more trouble than calculating the displacement sweep alone. VE can greatly simplify oil recovery calculations in desktop procedures and numerical simulations (Coats et al. 1971). Remember, the entire procedure is restricted to reservoirs having a large R_L .

The generalized VE approach for EOR processes has yet to be worked out [see Jain (2014)].

6.6 Special Cases of Vertical Equilibrium

Although the VE procedure in Section 6.5 is fairly general, being restricted to reservoirs having constant properties in the x -direction and a large R_L , several VE flows are special cases. Because these cases are useful in understanding many EOR processes, we review them in this section and show how they follow from the general theory.

6.6.1 Homogeneous With Large Transition Zone. In this case, k and ϕ are both constant in the reservoir, and $z_{CTZ} \gg H_r$. From the

procedure given in the preceding subsection, the saturations in the z -direction will be essentially constant, and the saturation at the reservoir bottom will not differ much from the average saturation. In this case, the pseudorelative permeabilities \tilde{k}_{rj} become the local relative permeabilities k_{rj} . Large z_{CTZ} would be the rule in most longer laboratory corefloods; however, in short core experiments, VE may not be attained.

6.6.2 Homogeneous, Uniform, With No Transition Zone. Easily the most celebrated of the VE theories is the theory of gravity tonguing, or underrunning, which was originally proposed by Dietz (1953). This theory was first proposed as an alternative to the Buckley-Leverett theory, but it is actually a special case of the VE theory because a finite time is required for the conditions underlying the theory to apply. This finite time is more likely to be obtained in reservoirs with large R_L .

Since the publication of the original Dietz paper, the theory has been applied to gravity overrunning by a miscible-gas process (Hawthorne 1960), and other work has been published describing the approach to VE conditions (Crane et al. 1963; see also Section 6.9.). In this section, we restrict ourselves to the water-displacing-oil case, although the overrunning case can be similarly developed.

The key assumption in the Dietz theory is the absence of a transition zone, or $z_{CTZ} = 0$. This condition can be accurate only for conditions under which the capillary pressure is small (well-sorted or high-permeability media). The sharp transition zone or macroscopic interface resulting from this condition suggests that the theory is applicable to any displacement, miscible or immiscible, for which simultaneous flow of more than one component or phase is absent at any point in the reservoir. If P_c is identically zero, Eq. 6.38 cannot be satisfied at any point in the reservoir because the oil and water densities are not, in general, equal. The resolution of this quandary is to let Eq. 6.49 apply to zones that are flowing water and to let the

analogous equation for oil apply to zones that are flowing oil. [Fig. 6.17](#) shows the relevant cross section and these zones.

At any cross section containing the tongue, the average water saturation from Eq. 6.43a is

$$\bar{S}_1 = \frac{1}{H_t} [b(1 - S_{2r}) + S_{1r}(H_t - b)], \dots \dots \dots \quad (6.52)$$

and the pseudorelative-permeability functions from Eq. 6.51 are

$$\tilde{k}_{r1} = k_{r1}^o \left(\frac{b}{H_t} \right) \dots \dots \dots \quad (6.53a)$$

$$\tilde{k}_{r2} = k_{r2}^o \left(\frac{H_t - b}{H_t} \right). \dots \dots \dots \quad (6.53b)$$

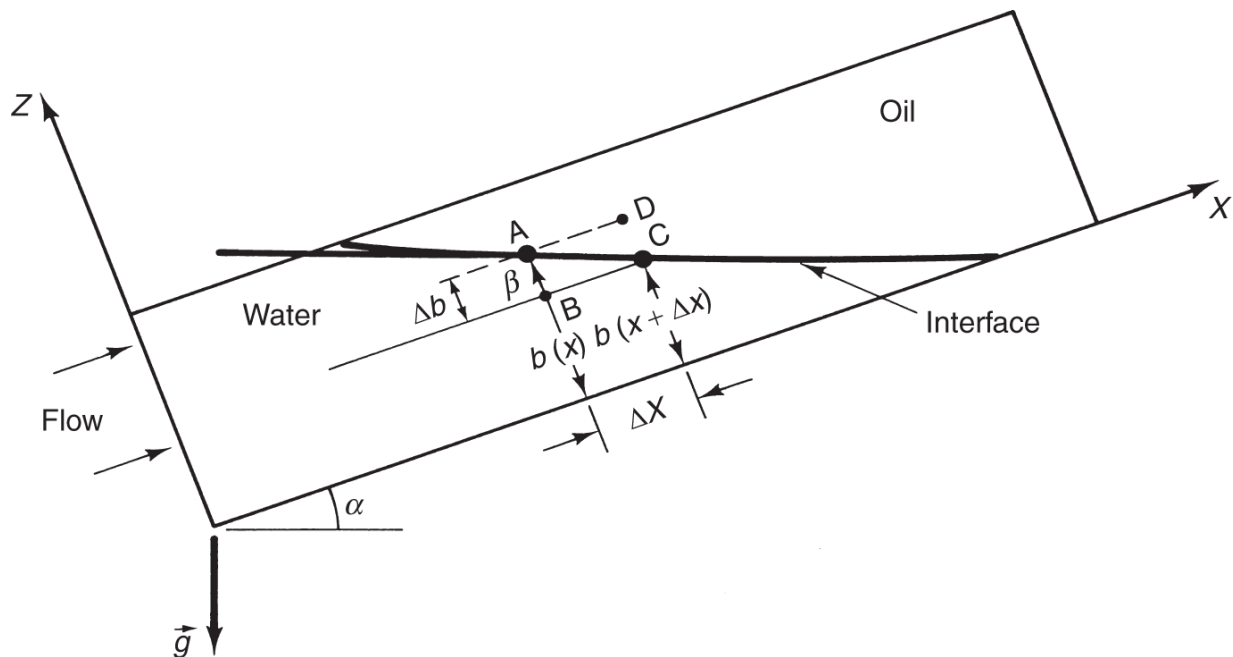


Fig. 6.17—Schematic cross section of a gravity tongue.

The interface height b can be eliminated between Eqs. 6.52 and 6.53 to give

$$\tilde{k}_{r1} = k_{r1}^o \left(\frac{\bar{S}_1 - S_{1r}}{1 - S_{1r} - S_{2r}} \right), \quad \tilde{k}_{r2} = k_{r2}^o \left(\frac{1 - S_{2r} - \bar{S}_1}{1 - S_{1r} - S_{2r}} \right). \dots \dots \dots \quad (6.54)$$

This means that the pseudorelative permeabilities are straightline functions of the average water saturation. Straightline relative-permeability functions are thumbprints for segregated flow.

We can also derive the tilt angle β of the oil/water interface. Consider the rectangle $ABCD$ of height Δb and width Δx shown in [Fig. 6.17](#). The dimensions Δx and Δb are small (the zero limit will be discussed below), so that the interface between points A and C is the diagonal of the rectangle. Along the BC side of the rectangle, the x -direction water flux is

$$u_{x1} = -\frac{kk_{r1}^o}{\mu_1} \left(\frac{P_C - P_B}{\Delta x} + \rho_1 g \sin \alpha \right), \dots \quad (6.55a)$$

and along the AD side, the x -direction oil flux is

$$u_{x2} = -\frac{kk_{r2}^o}{\mu_2} \left(\frac{P_D - P_A}{\Delta x} + \rho_2 g \sin \alpha \right). \dots \quad (6.55b)$$

In the limit as $\Delta x \rightarrow 0$, these two fluxes approach a common value u_x because there can be no accumulation at the interface. Furthermore, the pressures at A and B , and at D and C , are related because of the VE conditions Eq. 6.5-8:

$$P_B - P_A = \rho_1 g \Delta b \cos \alpha, \quad P_C - P_D = \rho_2 g \Delta b \cos \alpha. \dots \quad (6.56)$$

The three equations (Eqs. 6.55a, 6.55b, and 6.56) combine to eliminate the four pressures. This procedure gives

$$\tan \beta = \frac{(u_{x1} - u_{x2} M^o) \mu_1}{(kk_{r1}^o \Delta \rho g) \cos \alpha} + \tan \alpha. \dots \quad (6.57)$$

The tangent of the tilt angle is defined as

$$\tan \beta = + \lim_{\Delta x \rightarrow 0} \frac{\Delta b}{\Delta x}. \dots \quad (6.58)$$

β is defined to be positive and can take on the entire range of values between 0 and 90° . If β is greater than 90° , the tongue is

overrunning, and this procedure must be repeated with the displacing fluid above the resident fluid.

For $\beta > 0$ —that is, when the interface is not parallel to the x -axis—the interface reaches a stable shape where β is independent of both time and z -position. This limit is not an automatic consequence of VE, but the time interval between the onset of the VE conditions and the attainment of the stable interface shape appears to be short (Crane et al. 1963). When this steady-state tilt angle β_s is reached, the x -direction fluxes u_{x1} and u_{x2} become independent of z and equal to the cross-sectional average flux \bar{u}_x . Eq. 6.57 then becomes

$$\tan \beta_s = \frac{1 - M^o}{M^o N_g^o \cos \alpha} + \tan \alpha, \dots \quad (6.59)$$

where N_g^o and M^o are the endpoint gravity numbers and mobility ratios, as defined in Eq. 5.5.

Eq. 6.59 approaches the correct limits of an interface perpendicular to the x -direction for $N_g^o = 0$ (no tonguing) and of a horizontal interface for $M^o \rightarrow 1$. In the case of a stable gravity tongue, the cross-sectional average water-saturation profile approaches a “constant-pattern” mixing zone, whereas the directly analogous case of a 1D displacement with straightline relative permeabilities approaches a shock front. This is a consequence of the finite length of time required for the VE conditions to apply in the tonguing case.

For $\beta < 0$, the interface completely tongues under the oil and is said to be unstable. The condition for stability is, from Eq. 6.59,

$$M^o - 1 < M^o N_g \sin \alpha. \dots \quad (6.60)$$

The equality form of Eq. 6.60 naturally leads to definitions of a critical endpoint mobility ratio $M_c^o = M^o |_{\beta_s=0}$,

$$M_c^o = \frac{1}{1 - N_g^o \sin \alpha}, \dots \quad (6.61a)$$

and of a critical flux or rate $u_c = u_x|_{\beta_s=0}$,

The conditions to prevent complete underrunning of the oil by the water are $u_x < u_c$ or $M^o < M_c^o$. Eq. 6.61a indicates that gravity stabilization is possible even when $M^o > 1$. Eq. 6.61b, in particular, is used to estimate the flooding rates in gravity-stabilized displacements.

6.6.3 Layered, Uniform, Horizontal Media With $P_c = z_{CTZ} = 0$. This is an important special case because (1) it is a way to generate pseudorelative permeabilities in linear immiscible displacements; (2) it leads to specialized insights into the nature of fluid flow in large-scale displacements; and (3) when generalized to multiple or continuous fronts, it leads to the so-called Koval theory, which provides a way to predict the outcome of EOR displacements simply with minimal petrophysical data. This last approach will be discussed in [Chapter 7](#). We confine discussion here to the two-layer displacement as in [Fig. 6.18](#) and generalize when possible.

[Fig. 6.18](#) shows fluid and pressure distributions for a displacement without vertical communication (a) and in VE (b). The mobility ratio here is favorable:

$$M^o = \frac{\lambda_{r1}^o}{\lambda_{r2}^o} < 1,$$

in contrast to the situation shown in [Fig. 6.10](#) for which the mobility ratio is adverse $M^o > 1$. The task is to derive and illustrate equations that predict front positions as a function of time, thus predicting vertical sweep efficiency. The following development is for a cross section with unit width.

At any x -position behind (upstream, or $x < x_{f1}$) the slow front in Layer 2, the volumetric flow rates by layer are

$$q\Big|_{\text{layer } 1, x < x_{f2}} = -k_1 h_1 \lambda_{r1}^o \left(\frac{dP}{dx} \right)_{\text{layer } 1, x < x_{f2}}$$

and

$$q|_{\text{layer } 2, x < x_{f2}} = -k_2 h_2 \lambda_{r1}^o \left(\frac{dP}{dx} \right)_{\text{layer } 2, x < x_{f2}} \dots \dots \dots \quad (6.62a)$$

(Remember that 1 and 2 as mobility subscripts refer to fluids, otherwise they refer to layers). Between the slow and fast fronts $x_{f1} > x > x_{f2}$, we have

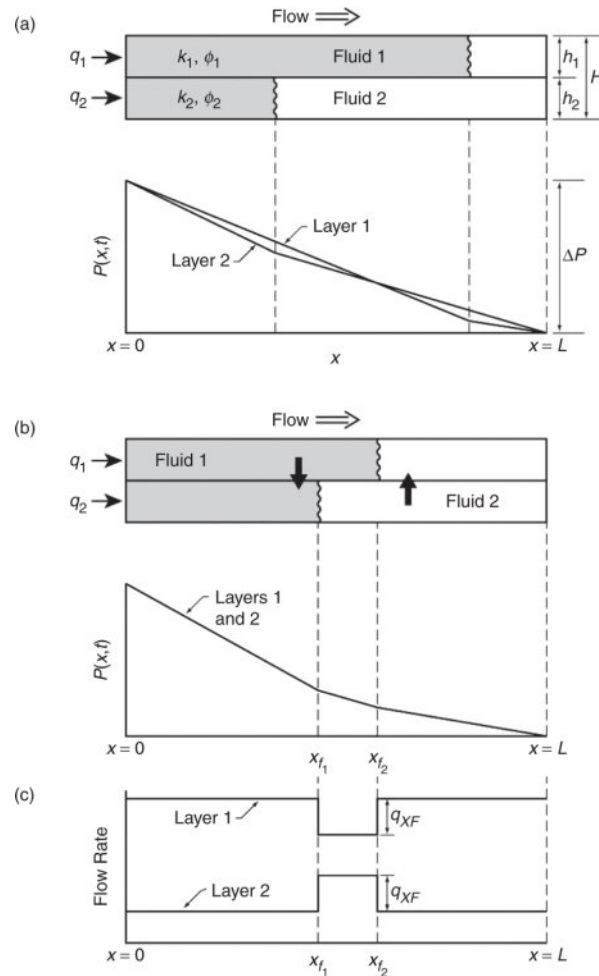


Fig. 6.18—Schematic of front positions and pressure distribution for a piston-like displacement in a two-layer reservoir for $M^\circ < 1$: (a) with no vertical communication, (b) with flow at the VE limit, and (c) with layer flow rates. Heavy vertical arrows indicate the direction of viscous crossflow.

$$q\Big|_{\text{layer } 1, x_{f1} < x < x_{f2}} = -k_1 h_1 \lambda_{r1}^o \left(\frac{dP}{dx} \right)_{\text{layer } 1, x_{f1} < x < x_{f2}}$$

and

$$q\Big|_{\text{layer } 2, x_{f1} < x < x_{f2}} = -k_2 h_2 \lambda_{r2}^o \left(\frac{dP}{dx} \right)_{\text{layer } 2, x_{f1} < x < x_{f2}}, \dots \quad (6.62b)$$

and downstream ($x_{f2} < x$) of the fast front,

$$q\Big|_{\text{layer } 1, x_{f1} < x} = -k_1 h_1 \lambda_{r1}^o \left(\frac{dP}{dx} \right)_{\text{layer } 1, x_{f1} < x}$$

and

$$q\Big|_{\text{layer } 2, x_{f2} < x} = -k_2 h_2 \lambda_{r2}^o \left(\frac{dP}{dx} \right)_{\text{layer } 2, x_{f2} < x}. \dots \quad (6.62c)$$

The rates here are all total (Fluid 1 or Fluid 2 rates). Because the flow is segregated, the total and component rates are the same.

For noncommunicating flow, the flow rates are constant along a layer, or

$$\begin{aligned} q\Big|_{\text{layer } 1, x < x_{f2}} &= q\Big|_{\text{layer } 1, x_{f1} < x < x_{f2}} = q\Big|_{\text{layer } 1, x_{f1} < x} \\ q\Big|_{\text{layer } 2, x < x_{f2}} &= q\Big|_{\text{layer } 2, x_{f1} < x < x_{f2}} = q\Big|_{\text{layer } 2, x_{f1} < x}. \end{aligned}$$

These are the conditions used in Section 6.4 for deriving the front positions in [Fig. 6.8](#). There the pressures at the interfaces were solved for, which subsequently led to velocities and then front positions.

Under the assumption that VE pressure gradients are independent of layer,

$$\begin{aligned} \left(\frac{dP}{dx} \right)_{\text{layer } 1, x < x_{f2}} &= \left(\frac{dP}{dx} \right)_{\text{layer } 2, x < x_{f2}} = \left(\frac{dP}{dx} \right)_{x < x_{f2}} \\ \left(\frac{dP}{dx} \right)_{\text{layer } 1, x_{f1} < x < x_{f2}} &= \left(\frac{dP}{dx} \right)_{\text{layer } 2, x_{f1} < x < x_{f2}} = \left(\frac{dP}{dx} \right)_{x_{f1} < x < x_{f2}} \\ \left(\frac{dP}{dx} \right)_{\text{layer } 1, x_{f1} < x} &= \left(\frac{dP}{dx} \right)_{\text{layer } 2, x_{f1} < x} = \left(\frac{dP}{dx} \right)_{x_{f1} < x}. \end{aligned}$$

These conditions mean that the x-direction pressure changes are the same for both layers, as illustrated in [Fig. 6.18b](#).

These equations lead to significant simplifications in the flow description. Because the upper and lower boundaries of the cross section are impermeable, the total volumetric flow rate through the cross section is independent of x :

or from the first equation,

$$-k_1 h_1 \lambda_{r1}^o \left(\frac{dP}{dx} \right)_{x < x_{f2}} - k_2 h_2 \lambda_{r1}^o \left(\frac{dP}{dx} \right)_{x < x_{f2}} = q$$

$$\left(\frac{dP}{dx} \right)_{x < x_{f2}} = \frac{-q}{k_1 h_1 \lambda_{r1}^o + k_2 h_2 \lambda_{r1}^o},$$

which leads to

$$q|_{\text{layer } 1, x < x_{f2}} = q \frac{k_1 h_1}{k_1 h_1 + k_2 h_2}$$

and

$$q|_{\text{layer } 2, x < x_{f2}} = q \frac{k_2 h_2}{k_1 h_1 + k_2 h_2}. \quad \dots \dots \dots \quad (6.64a)$$

Using the second of the above equations,

$$q|_{\text{layer } 1, x_{f1} < x < x_{f2}} = q \frac{k_1 h_1}{k_1 h_1 + \frac{k_2 h_2}{M^o}}$$

and

$$q|_{\text{layer } 2, x_{f1} < x < x_{f2}} = q \frac{\frac{k_2 h_2}{M^o}}{k_1 h_1 + \frac{k_2 h_2}{M^o}}, \quad \dots \dots \dots \quad (6.64b)$$

and finally, using the third,

$$q|_{\text{layer } 1, x_{f2} < x} = q \frac{k_1 h_1}{k_1 h_1 + k_2 h_2}$$

and

$$q|_{\text{layer } 2, x_{f2} < x} = q \frac{k_2 h_2}{k_1 h_1 + k_2 h_2}. \quad \dots \dots \dots \quad (6.64c)$$

VE has made it possible to express the relative layer rates entirely without pressure.

These equations make it clear that the layer flow rates are not constant within a layer, as was true in the no-communication case.

The disparity in layer rates leads to viscous crossflow between the layers. We can define a crossflow rate as

$$\begin{aligned} q_{XF} \Big|_{x=x_{f1}} &= q \Big|_{\text{layer } 1, x < x_{f2}} - q \Big|_{\text{layer } 1, x_{f1} < x < x_{f2}} \\ &= q \frac{k_1 h_1}{k_1 h_1 + k_2 h_2} - q \frac{k_1 h_1}{k_1 h_1 + \frac{k_2 h_2}{M^o}} \end{aligned}$$

from a weak form material balance around the slow front in Layer 1, and

$$\begin{aligned} q_{XF} \Big|_{x=x_{f2}} &= q \Big|_{\text{layer } 1, x_{f1} < x < x_{f2}} - q \Big|_{\text{layer } 1, x_{f2} < x} \\ &= q \frac{k_1 h_1}{k_1 h_1 + \frac{k_2 h_2 \lambda_{r1}^o}{M^o}} - q \frac{k_1 h_1}{k_1 h_1 + k_2 h_2} \end{aligned}$$

around the fast front in Layer 1. Several observations follow:

1. The crossflow rates q_{XF} about the two fronts are equal and opposite. Before breakthrough, crossflow results in an internal redistribution of fluids. After breakthrough, crossflow is entirely from the high- to the low-permeability layer.
2. The source of the crossflow is the contrast in mobility. There is no crossflow if $M^o = 1$. This is the origin of the term *viscous* crossflow.
3. The crossflow takes place from the high- to the low-permeability layer at the slow front and in the opposite direction at the fast front. The net effect of the crossflow is to increase the sweep efficiency over even that caused by the mobility contrast in the no-crossflow case.

[Fig. 6.18c](#) shows the layer rates and the direction of crossflow for $M^\circ < 1$. Remember, everything is in VE here.

Front Positions. Performing a material balance on Fluid 1 in Layer 1 about the fast front.

$$\phi_1 h_1 (1 - S_{2r}) \frac{dx_{f2}}{dt} = q \Big|_{\text{layer 1}, x_{f1} < x < x_{f2}} = q \frac{k_1 h_1}{k_1 h_1 + \frac{k_2 h_2}{M^\circ}} \dots \dots \dots \quad (6.65a)$$

This equation is again a weak-form material balance of the type first encountered in [Chapter 5](#). It is the first time that component balances have been used in this chapter. A balance on Fluid 2 in Layer 2 about the slow front similarly gives

$$\phi_2 h_2 S_{1r} \frac{dx_{f2}}{dt} = q \Big|_{\text{layer 1}, x_{f1} < x < x_{f2}} = q \frac{\frac{k_2 h_2}{M^\circ}}{k_1 h_1 + \frac{k_2 h_2}{M^\circ}} \dots \dots \dots \quad (6.65b)$$

Two interesting conclusions can be drawn from these equations:

1. The front velocities are constant, or the positions increase linearly with time. This stands in contrast to the no-crossflow case in which the velocities decrease with time (for $M^\circ < 1$). The linear growth is why the VE approach fits nicely into the fractional-flow formalism, which accounts for the length of the treatment here because we will use it again.
2. The fronts can actually move together. This follows from setting $\frac{dx_{f1}}{dt} = \frac{dx_{f2}}{dt}$ and solving for the mobility ratio,

$$M^\circ = \frac{\frac{k_2}{\phi_2 S_{1r}}}{\frac{k_1}{\phi_1 (1 - S_{2r})}}, \dots \dots \dots \quad (6.66)$$

Eq. 6.66 says that M° is less than the permeability contrast (low/high), viscous crossflow can entirely suppress

heterogeneity.

You should remember the following points here:

1. Vertical equilibrium is an asymptotic theory in that it pertains to reservoirs that have a large effective aspect ratio, as defined in Eq. 6.36a. In such reservoirs, it is likely that the no-crossflow limit applies near the injection end, and then the flow adjusts itself to the VE limit as the displacement proceeds. When R is large, the adjustment happens a short distance into the reservoir. [Fig. 6.19](#) shows the progression to VE at fixed throughput.
2. We have neglected several important effects in presenting these insights, notably gravity and capillary pressure. Because the scaling of both these effects involves total velocity (see Eqs. 5.5d and 5.32), the treatment given here applies to a high-velocity limit. We seek a general VE theory that accounts for all the special cases described here.
3. The entire treatment here is for $M^0 < 1$. On the basis of arguments related to the direction of flow caused by the viscous-pressure driving forces (they are opposite to those shown in [Fig. 6.19b](#)), Zapata and Lake (1981) showed that segregated flow within a layer occurs when the displacement is favorable, $M^0 < 1$. However, when the displacement is unfavorable, $M^0 > 1$, the viscous forces (coupled, to be sure, with some dispersion) cause a mixing zone to develop between the front in the fastest layer and that in the slowest layer. This mixing zone causes the vertical sweep efficiency to be actually greater than in the corresponding segregated-flow case because the mixing zone attenuates the unfavorable mobility ratio. That diffuse flow can occur in VE displacements in the absence of capillary pressure is a major revelation in our understanding of these processes. The implication is clear that such crossflow might be a source of mixing in all unstable flows.

6.6.4 Stratified, Uniform With $\Delta p = 0$ and Constant Mobility.

Here, there are no gravity forces to counteract the z -direction imbibition, and the z -direction water-saturation profile is uniform within each layer. However, because of the variable properties in the z -direction, the $P_c - S_1$ function changes. [Fig. 6.20a](#) illustrates this change for the four-layer medium shown. Such a flow might occur in media with finely interbedded lamina where capillary-pressure equilibrium would occur among multiple layers.

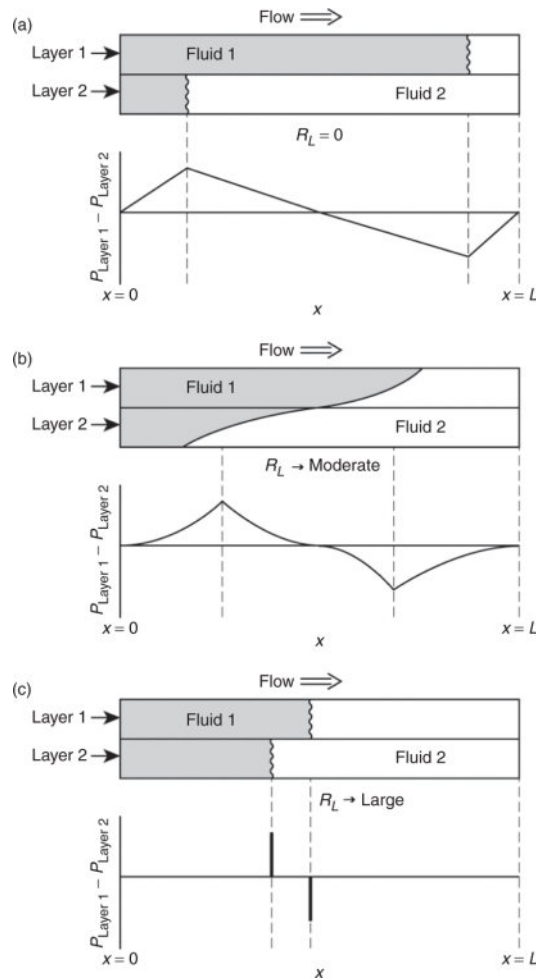


Fig. 6.19—Front positions and pressure distributions for the attainment of VE for a $M^o < 1$ displacement.

From Eq. 6.38 the capillary pressure (but not the capillary-pressure function) is a constant through any cross section. As indicated in [Fig. 6.19](#), if the constant is known, this specifies the

water saturation in each layer at that cross section. Because the mobility is constant, the x -direction viscous-pressure gradient is independent of both position and time. For this case, the average water-saturation and pseudo-relative-permeability curves are given by Eq. 6.62, but each of the water saturations S_{1j} are determined by the relation $P_c = \text{constant}$ and the $P_c - S_1$ relation. Again, the average water saturation and pseudorelative permeabilities are related parametrically through this constant. This procedure yields an immiscible mixing zone between the most advanced and the least advanced front, as shown in Fig. 6.20b.

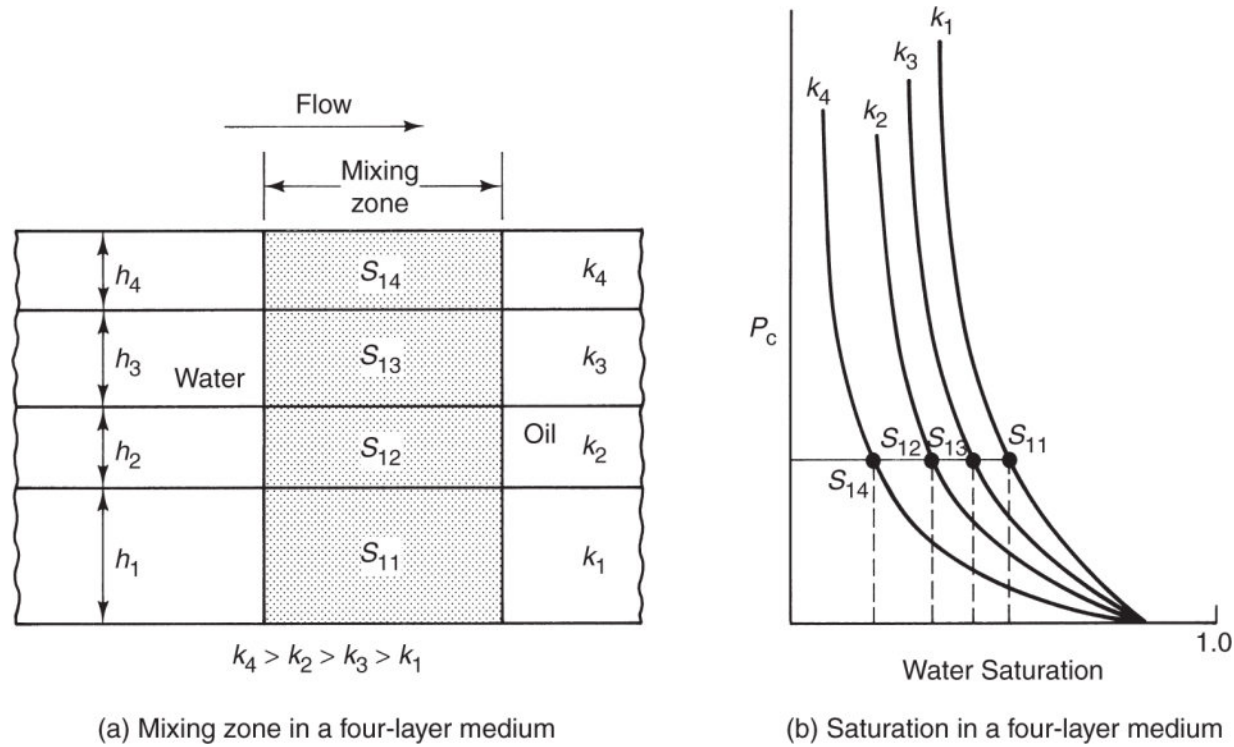


Fig. 6.20—Schematic of stratified cross section with no gravity and viscous forces.

6.7 VE Summary

VE is clearly a useful simplification for describing flow. However, there does not as yet appear to be a useful general theoretical approach (Yortsos 1995). Perhaps the most insightful work was done by Shook et al. (1992), who made a distinction between an equilibrium state (in this case, what we refer to here as vertical

equilibrium) and the approach to VE. The equilibrium state was described according to the limiting cases in this chapter and the approach to VE by the quantity R_L .

6.8 Instability Phenomena

No EOR process is free from instability of some sort. Hence, substantial efforts have been made to minimize or prevent instabilities (using polymer to drive surfactants and alkaline agents, or foaming agents to drive CO_2 and steam) and to predict oil recovery when instability is inevitable. We discuss prediction of the results of an unstable displacement in [Chapter 7](#) in connection with solvent flooding, where instability phenomena have received the most attention. In this section, we deal with the formation of fingers.

We use the term *fingering* to describe the bypassing of a resident fluid by a displacing agent in a homogeneous, nonuniform medium. The actual bypassing region is a finger. This definition encompasses instabilities caused by both viscous forces (viscous fingers) and gravity forces (gravity fingers), but does not include bypassing caused by permeability heterogeneities. This definition is a little more rigid than that used in the literature, but we believe that the inherent distinction is useful because fingering can be prevented by displacements, whereas bypassing caused by heterogeneities cannot (although it can be reduced). In this section, we deal with isothermal flows; [Chapter 11](#) discusses the stability of a nonisothermal displacement.

6.8.1 A Necessary Condition for Stability. In keeping with the notion that instability is a general phenomenon, we discuss it here though it seems to be more of an issue in solvent floods than others. Consider the incompressible, dissipation-free displacement of Fluid 2 by Fluid 1 in a dipping reservoir, as shown in [Fig. 6.21](#). This figure is a cross section of a displacement, but fingering can occur in either the vertical or areal sense. There is no z-direction communication in this problem. We also consider a perturbation of length ε of the displacement front (caused, perhaps, by an isolated

nonuniformity in the permeability field) and strive to determine the conditions under which $\varepsilon(t)$ will grow or decay as a function of time. The actual fingering phenomenon is, of course, much more random and chaotic than that shown in [Fig. 6.21](#), as evidenced by an areal view of a fingering displacement in a quarter five-spot model shown in [Fig. 6.22](#). Nevertheless, the simple geometry of [Fig. 6.21](#) is tractable to mathematical analysis and yields insights into more complex situations.

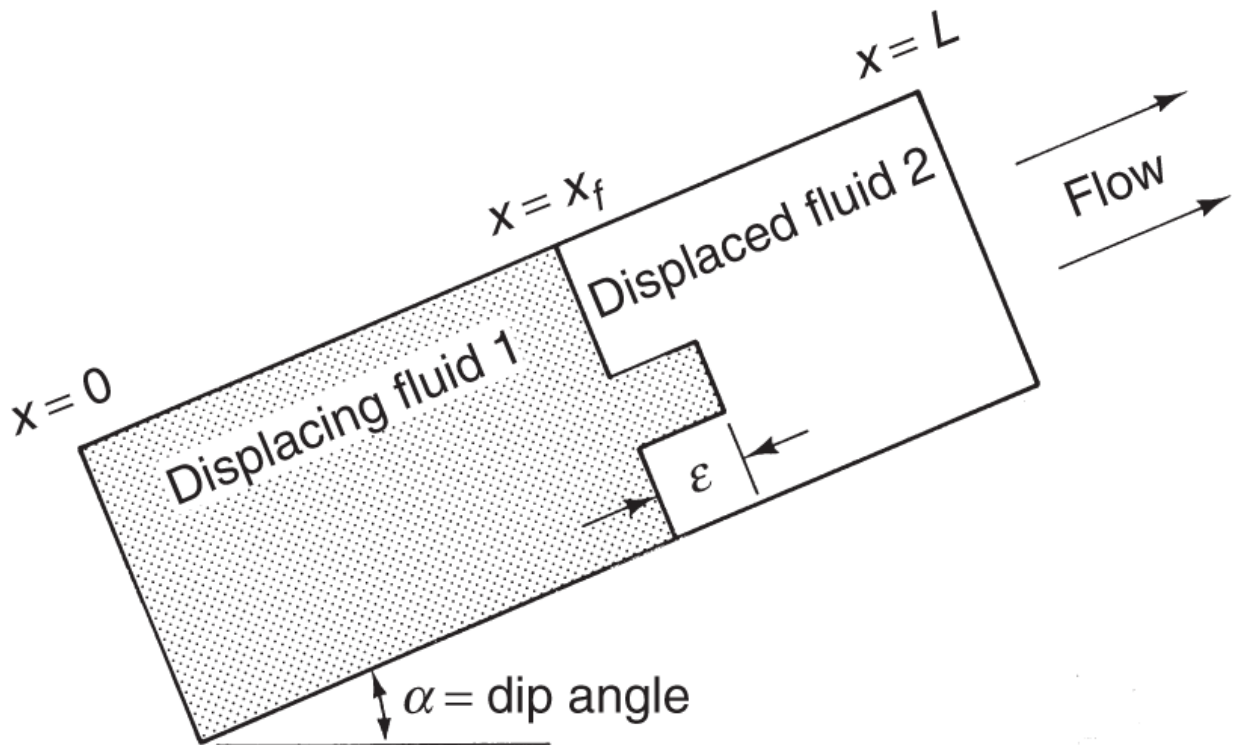


Fig. 6.22—Viscous fingering in a quarter five-spot model, $M^\circ = 17$ (Habermann 1960).

To solve for the conditions under which ε will grow or decay, we proceed using the moving-boundary technique discussed by Collins (1976). In the region behind the displacing fluid front, $x < x_f$, conservation of Fluid 1 gives

$$\frac{\partial u_{xj}}{\partial x} = 0, \quad \dots \dots \dots \quad (6.68)$$

where $j = 1$ for $x < x_f$ and $j = 2$ for $x > x_f$. The accumulation terms in both equations are zero because there is no change in concentration

in the respective regions. For the same reason, when we substitute Darcy's law into these equations, they become

$$\frac{\partial}{\partial x} \left(\frac{\partial P_j}{\partial x} + \rho_j g \sin \alpha \right) = 0, \quad j = 1 \text{ or } 2. \dots \quad (6.69)$$

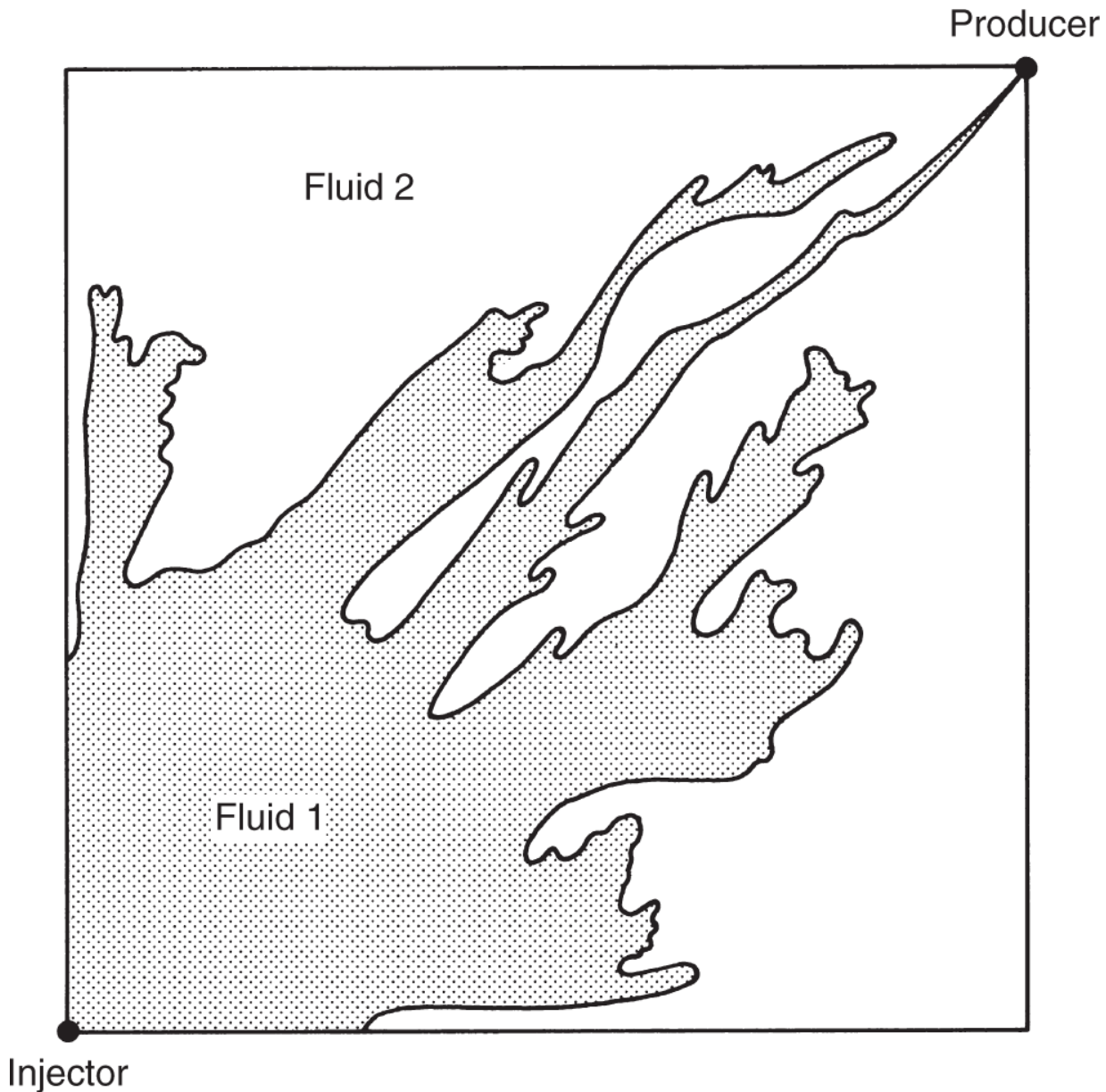


Fig. 6.21—Incipient instability schematic.

The solutions to Eq. 6.69 will be of the form

$$P_j = \left(a_j - \rho_j g \sin \alpha \right) x + b_j, \quad j = 1 \text{ or } 2, \dots \quad (6.70)$$

where a_j and b_j are integration constants to be determined with appropriate boundary conditions. If P_0 and P_L are the pressures at the reservoir inlet and outlet, respectively, then b_j can be determined as

Using these relations and requiring continuous x-velocities across the front,

gives, once again using Darcy's law,

Eq. 6.73 determines a_1 because we must have continuity of pressure at x_f in the absence of capillary pressure:

Inserting Eq. 6.70 into Eq. 6.74 and using Eqs. 6.71 and 6.73 yields

where $\Delta P = P_0 - P_L$ is the overall pressure drop. The rate of frontal advance can be calculated from Darcy's law:

$$\frac{dx_f}{dt} = \frac{u_x|_{x_f}}{\phi\Delta S} = \frac{k\lambda_{r1}}{\phi\Delta S} \frac{\Delta P + g \sin \alpha \left[\Delta\rho(L - x_f) - \rho_1 L \right]}{M^0 L + (1 - M^0)x_f} \dots \quad (6.76)$$

Eq. 6.76 applies to any point on the displacement front. We could have equally well developed an expression for a point on the

perturbation front for which

$$\frac{d(x_f + \varepsilon)}{dt} = \frac{k\lambda_{r1}}{\phi\Delta S} \frac{\Delta P + g \sin \alpha [\Delta\rho(L - x_f - \varepsilon) - \rho_1 L]}{M^0 L + (1 - M^0)(x_f + \varepsilon)} \dots \quad (6.77)$$

Eq. 6.77 is identical to Eq. 6.76 except that $x_f + \varepsilon$ has replaced all instances of x_f . The rate of change of the perturbation is

$$\frac{d\varepsilon}{dt} = \frac{d(x_f + \varepsilon)}{dt} - \frac{dx_f}{dt} = \dot{\varepsilon}, \quad \dots \quad (6.78)$$

which yields, when Eqs. 6.76 and 6.77 are substituted,

$$\dot{\varepsilon} = -\frac{k\lambda_{r1}}{\phi\Delta S} \frac{\Delta P(1 - M^0) + Lg\Delta\rho \sin \alpha - Lg\rho_1(1 - M^0)\sin \alpha}{[M^0 L + (1 - M^0)x_f]^2} \varepsilon. \quad \dots \quad (6.79)$$

Eq. 6.79 has assumed $\varepsilon \gg x_f$. Eq. 6.79 could be integrated, but for our purpose, it is sufficient to investigate only the sign of $\dot{\varepsilon}$. The perturbation will grow if $\dot{\varepsilon} > 0$, will remain constant if $\dot{\varepsilon} = 0$, and will decay if $\dot{\varepsilon} < 0$. From the equality of these three choices, we find the condition of neutral stability as

$$-(\Delta P)_c = \frac{L\Delta\rho g \sin \alpha}{1 - M^0} - Lg\rho_1 \sin \alpha, \quad \dots \quad (6.80)$$

where $(\Delta P)_c$ is a critical pressure drop. The superficial velocity corresponding to this is the *critical rate* u_c :

$$u_c \equiv -k\lambda_{r1}^o \left[\frac{-\Delta P}{L} + \rho_1 g \sin \alpha \right] = \frac{k\lambda_{r1}^o \Delta\rho g \sin \alpha}{M^0 - 1}. \quad \dots \quad (6.81)$$

Using the critical rate, the conditions for finger growth may be restated as

$$u_x \begin{cases} > u_c & (\text{unstable}) \\ = u_c & (\text{neutral}) \\ < u_c & (\text{stable}) \end{cases}, \quad \dots \quad (6.82)$$

where we have also used Darcy's law to express u_x in these inequalities.

Note the similarity between Eq. 6.81 and Eq. 6.61b, the corresponding critical rate for gravity tonguing. Analogous expressions can be worked out for almost any segregated flow condition, and, therefore, this similarity should not be regarded as merely fortuitous. However, the differences in the two flows should be kept in mind. The critical rate in Eq. 6.81 is based on an unstable displacement in a reservoir having no z-direction communication; that in Eq. 6.61b is the consequence of a VE displacement in a reservoir with very good communication.

To investigate the stability issue further, let us write the condition for stability (finger decay) as

$$(M^0 - 1)u_x < k\lambda_{r1}^o \Delta\rho g \sin \alpha. \dots \quad (6.83)$$

The superficial velocity u_x in this inequality is always positive, but the density difference can be negative (less-dense fluid displacing more-dense), as can the dip angle (displacing down dip). Of course, M^0 can take on only positive values, although over quite a large range.

Table 6.1 shows typical signs of M^0 and $\Delta\rho$ for various EOR processes. Immediately it follows from Eq. 6.83 that the condition for stability in a horizontal reservoir is simply $M^0 < 1$. This condition is used universally throughout the EOR literature to describe a stable displacement, particularly in laboratory floods, although the more general Eq. 6.83 is actually the most appropriate form (Hill 1952).

Considering the signs possible for α and $\Delta\rho$, we can divide the stability possibilities into four cases, as given in **Table 6.2**. Case 1 is unconditionally stable regardless of the values of $\Delta\rho g \sin \alpha$ and M^0 because $\Delta\rho g \sin \alpha$ is positive and $M^0 < 1$. Similarly, if $\Delta\rho g \sin \alpha < 0$ and $M^0 > 1$ in Case 4, the displacement is unconditionally unstable. The more interesting cases are 2 and 3, which we call Type I and Type II conditional stability.

TABLE 6.1—TYPICAL VALUES FOR MISCELLITY RATIOS AND DENSITY DIFFERENCES BY PROCESS TYPE

	$M^0 < 1$	$M^0 > 1$
$\Delta\rho > 0$	Waterflood Polymer flood Micellar polymer	Waterflood Polymer flood
$\Delta\rho < 0$	Foam	Steam

TABLE 6.2—POSSIBLE CASES FOR A STABLE DISPLACEMENT

Case			
1	$M^0 < 1$	$\Delta\rho g \sin \alpha > 0$	Stable
2	$M^0 > 1$	$\Delta\rho g \sin \alpha > 0$	Conditionally stable (Type I)
3	$M^0 < 1$	$\Delta\rho g \sin \alpha < 0$	Conditionally stable (Type II)
4	$M^0 > 1$	$\Delta\rho g \sin \alpha < 0$	Unstable*

* Infinite lateral boundaries.

Note: Write stability criterion as $(M^0 - 1)u_x < K\lambda_{r1}^0 \Delta\rho g \sin \alpha$. For $\alpha = 0$ (no dip), the stability criterion becomes $M^0 < 1$.

For Type I stability, if we divide through Eq. 6.83 by the positive quantity $(M^0 - 1)$, the stability criterion can be written for u_x , as shown in [Fig. 6.23](#). The criterion is an upper bound for u_x , and a plot of sweep efficiency (vertical, areal, or volumetric) vs. the dimensionless rate u_D ,

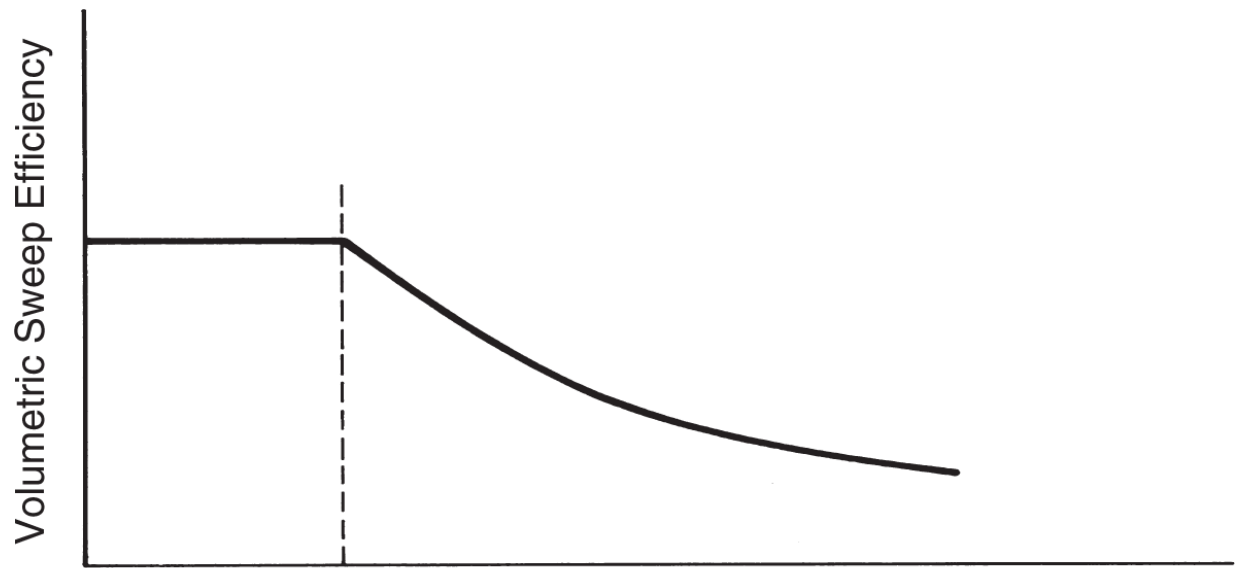
$$u_D = \frac{u_x(M^0 - 1)}{k\lambda_{r1}^0 \Delta\rho g \sin \alpha}, \dots \quad (6.84)$$

shows that E_V remains essentially constant until $u_D = 1$ and then decreases thereafter. Because increasing the displacement velocity

causes instability to form, we see that viscous forces destabilize the displacement ($u_D > 1$), whereas gravity forces tend to stabilize it ($u_D < 1$). The resulting instability is a *viscous instability* or *finger*. For Type II conditional stability, a similar plot ([Fig. 6.24](#)) shows sweep efficiency decreasing for decreasing u_D and beginning a precipitous decline at $u_D = 1$. This occurs because the stability criterion is now a lower bound for the reason that $(M^0 - 1)$ is now negative. For Type II conditional stability, viscous forces stabilize the displacement, and gravity forces destabilize it. The resulting instability is a gravity instability.

For certain values of the parameters, then, both types of displacements are or can be made stable. The conditional stability is most useful in determining the maximum rate in a dipping displacement where $M^0 > 1$. However, usually, this rate is below that required for economic oil production. For Type II stability, a larger rate is required, but in practice, this situation is not commonly encountered.

6.8.2 Critical Wavelength. Whereas $u_x < u_c$ is a necessary and sufficient condition for stability, the condition $u_x > u_c$ is a necessary condition for instability. This condition occurs because dissipative effects in flows in media of limited lateral extent tend to suppress instability. This effect means that fingering may be abnormally suppressed in laboratory displacements compared to the same displacement under field conditions. One may legitimately wonder, then, about the purpose of doing laboratory experiments on unstable displacements when this scale effect is not considered.



$$\frac{u_x(M^\circ - 1)}{k\lambda_{r1}^\circ \Delta \rho g \sin \alpha}$$

Fig. 6.23—Type I conditional stability.

To investigate this scale effect, we reproduce an argument based on linear stability analysis originally given by Chouke et al. (1959) and then by Gardner and Ypma (1984).

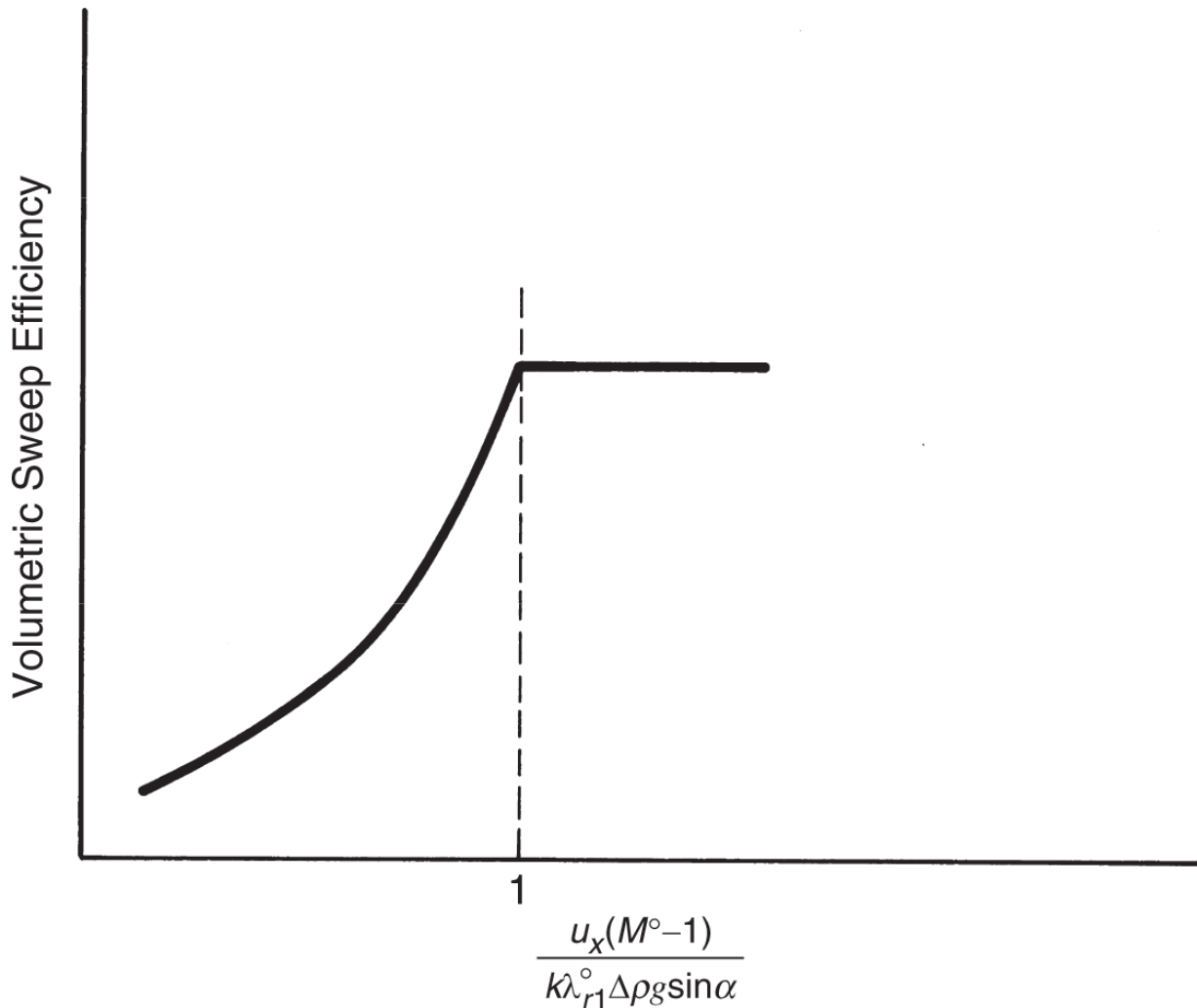


Fig. 6.24—Type II conditional stability.

On the basis of a linear stability analysis of a downward secondary miscible displacement of oil by a less viscous and less dense solvent in a homogeneous, uniform medium, the critical wavelength μ_c of an unstable miscible displacement is

$$\lambda_c = 4\pi \frac{M^0 + 1}{M^0 - 1} \left(\frac{K_l}{u_x - u_c} \right), \dots \quad (6.85)$$

where the dispersion coefficient K_l is assumed to be isotropic. Because the displacement is unstable, we must have $M^0 > 1$ and $u_x > u_c$ so that μ_c is always positive.

The analogous expression for an initially sharp immiscible displacement was also determined by Chouke et al. (1959) and reproduced in greater detail by Peters (1979):

The constant C in Eq. 6.86 is called Chouke's constant by Peters, who also determined values $C = 25$ for immiscible displacements with no residual water initially present and $C = 190$ with irreducible water present. The critical wavelength is greater with irreducible water initially present, but the reason for this stabilizing effect is not well understood.

The necessary and sufficient conditions for a Type I instability to form based on this analysis are now

where $(H_t)_{\max}$ is the maximum lateral extent of the permeable medium. One can readily show (see Exercise 6.9) that μ_c is of the order of a few centimeters for typical conditions. Therefore, if fingering is desired in a displacement, one must take special precautions to ensure that conditions (Eq. 6.87) are met. This usually means running displacements at excessively high rates compared with field rates or in systems having at least one large transverse dimension. Such a system is the Hele Shaw cell, in which the displacement shown in Fig. 6.18 has been observed.

However, if the intent is to suppress fingering, media with very small transverse dimensions, such as the slim-tube experiments discussed in [Chapter 7](#), are preferable. Computer simulations of oil-recovery processes impose their own numerical dispersion-like effect, for which the magnitude scales with gridblock size. These simulations can, therefore, suppress fingering unless very small gridblocks are used.

Three things are important about the derivation of both critical velocity and wavelength. First, neither addresses how fingers propagate once they are formed. A finger forms, bifurcates into two branches, one of these dominates (or shields) the other, and the dominant one then bifurcates again to repeat the process (Homsy 1987). If the process continues, a single finger with numerous appendages representing the bifurcations will result. [Fig. 6.18](#) suggests a bifurcation through the various levels of fingers, each superimposed on the next larger scale. The smallest scale corresponds to the critical wavelength.

Second, the critical-velocity derivation depends on the perturbation being small. When the perturbation is not small, a perturbation might be suppressed if its size is larger than the lateral extent of the medium. Such was the intent behind the critical-wavelength derivation. The criteria for instability with respect to the critical velocity are only necessary, not sufficient.

Finally, the issues of fingering and heterogeneity cannot be rigorously separated. After all, heterogeneity caused the perturbation in [Fig. 6.16](#), even though we proceeded as though the reservoir were homogeneous. The merging of the fingering and heterogeneity issues is one of the most interesting topics in EOR research.

6.9 Gravity Segregation in Gas EOR

As discussed in [Chapter 7](#), in solvent EOR, a gas-like solvent is often injected with water, or in alternating slugs with water (i.e., WAG), to reduce mobility. Nonetheless, gas may segregate from the water to the top of the reservoir because of its lower density. Oil can be recovered by gas only where gas is flowing (i.e., in a mixed zone where both gas and water flow) or in a thin override zone where only gas is flowing ([Fig. 6.25](#)). It is therefore important to maximize the depth of penetration of the mixed-flow zone away from the injection well. The following analysis addresses an intermediate case between that of no crossflow in Section 6.4 and VE in Section 6.5: we ask how wide is the region over which fluids segregate to a state of gravity equilibrium.

Stone (1982) and Jenkins (1984) [see also Rossen et al. (2010)] provide equations for the distance that gas and liquid can travel from a vertical or horizontal injector in homogeneous rectangular or cylindrical reservoirs before complete segregation, as illustrated in Fig. 6.25:

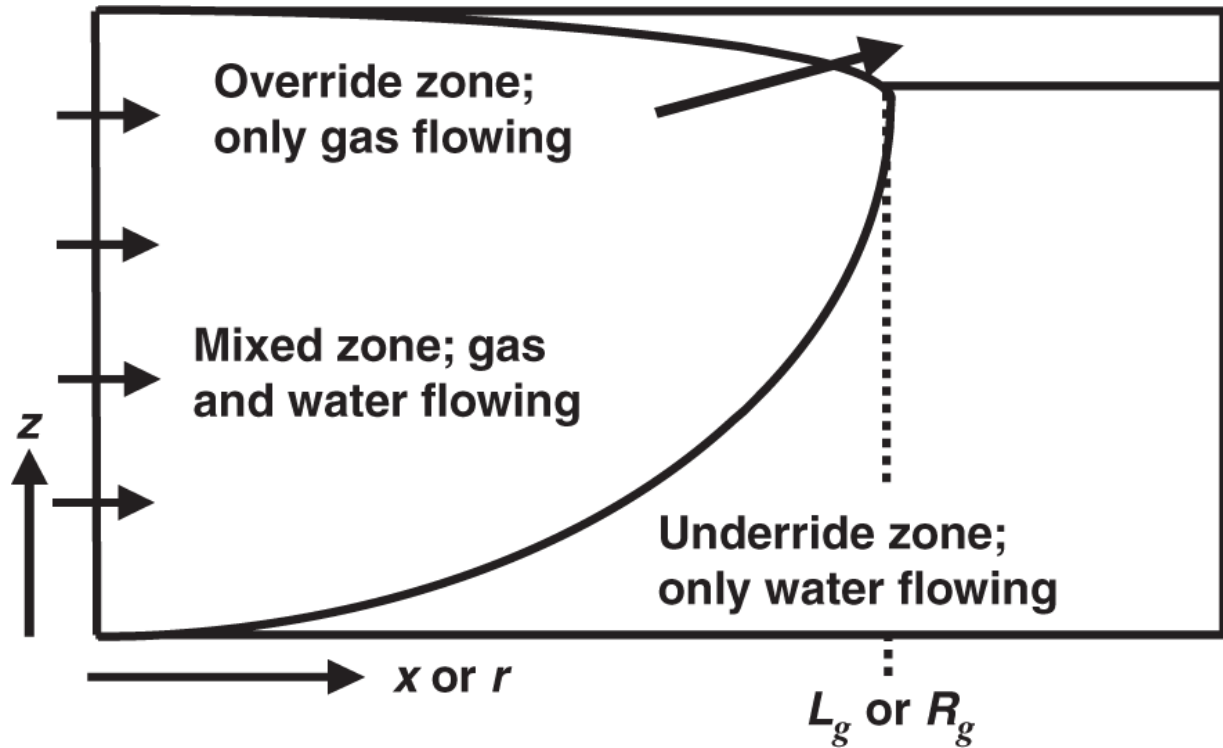


Fig. 6.25—Schematic of mixed, override, and underride zones, according to the model of Stone (1982) and Jenkins (1984).

$$L_g = \frac{q}{k_z (\rho_1 - \rho_3) g W \lambda_{rt}^m} \quad \dots \dots \dots \quad (6.88)$$

$$R_g = \sqrt{\frac{q}{\pi k_z (\rho_1 - \rho_3) g \lambda_{rt}^m}}, \quad \dots \dots \dots \quad (6.89)$$

where L_g and R_g apply to rectangular and radial flow respectively (see Fig. 6.25); q is the total volumetric injection rate of gas and water (at reservoir conditions); k_z the vertical permeability; ρ_{11} and ρ_{33} the densities of water and gas, respectively; g the gravitational acceleration; W the thickness of the rectangular cross-section perpendicular to flow; and λ_{rt}^m the total relative mobility in the mixed

zone. These equations can be derived using the standard assumptions of fractional-flow theory (Section 5.2), including incompressible phases and gas; see Rossen et al. (2010). The equation applies to co-injection of gas and water (assumed to exit the well in a uniform ratio all along the well), but Stone contends that it applies to WAG as long as the slugs mix near the well. Eqs. 6.88 and 6.89 apply to steady-state flow, after all mobile oil has been displaced from the region in which segregation occurs. Residual oil may be present and reduce total mobility in the mixed zone λ_{rt}^m . Eqs. 6.88 and 6.89 attempt to bypass the complexities of the oil-displacement process and skip to the eventual steady state on the assumption that this reflects sweep efficiency during the period of oil recovery.

A simulation study of layered and checkerboard reservoirs (Stolwijk and Rossen 2009) suggests that Eqs. 6.88 and 6.89 are reasonably accurate for heterogeneous reservoirs with permeability contrasts up to 4:1, as long as the vertical permeability is computed as the harmonic (for layered reservoirs) or geometric (for checkerboard reservoirs) average of the permeability distribution. The reduction in vertical permeability (harmonic or geometric average) relative to horizontal permeability (arithmetic average) for heterogeneous reservoirs (cf. Eq. 6.36a) suggests that gravity segregation is reduced by heterogeneity; see also Araktingi and Orr (1990) and de Riz and Muggeridge (1997). For reservoirs that are more heterogeneous than this, the equation is inaccurate and arguably meaningless because large pockets are left unswept within the “mixed zone.”

Returning to homogeneous reservoirs, according to Eqs. 6.88 and 6.89, one can extend mixed flow deeper into the reservoir either by increasing the injection rate q or by reducing the mobility in the mixed zone λ_{rt}^m . Gas sweeps only the mixed zone and the narrow override zone, and, therefore, the largest possible mixed zone is desirable. Both increasing q and reducing λ_{rt}^m increase the injection pressure. With some additional assumptions, one can relate the distance that gas and water travel without segregation to injection

pressure, assuming uniform co-injection of gas and liquid (Rossen et al. 2010). For radial flow,

$$P(r_w) - P(R_g) = \frac{k_z(\rho_1 - \rho_3)g}{2Hk_h} R_g^2 \left\{ \ln\left(\frac{R_g}{r_w}\right) - \frac{1}{2} \left[1 - \left(\frac{r_w}{R_g}\right)^2 \right] \right\}, \dots \quad (6.90)$$

where P is pressure, r_w wellbore radius, and k_h horizontal permeability. Required injection pressure rises faster than the square of the desired distance to the point of segregation, *regardless of injection rate or mobility in the mixed zone*. Depending on the assumption made about the height of the mixed zone as a function of distance from the injection well, the last term in Eq. 6.90 [beginning with $(-1/2)$] may be eliminated. If injection pressure is limited (e.g., by concern about fracturing), Eq. 6.90 sets the limit on possible distance to segregation for co-injection of gas and water from a single well.

There are, however, other methods of injection. [Fig. 6.26](#) compares the fraction of the injection pressure that is dissipated to the fractions of gas and liquid that have segregated as functions of radial distance from the injection well. Injection pressure depends primarily on mobility near the well, while segregation depends on mobility (*cf.* Eqs. 6.88 and 6.89) much farther out. Several strategies to increase the distance that gas and water can travel together beyond that predicted in Eq. 6.90 rely on increasing mobility near the well (Jamshidnezhad et al. 2010). Simply stimulating the well to increase permeability in the near-well region can increase q and thereby R_g . For instance, increasing permeability by a factor of 30 to a radial distance of 1% of the original value of R_g can increase R_g by 30% by enabling a higher injection rate.

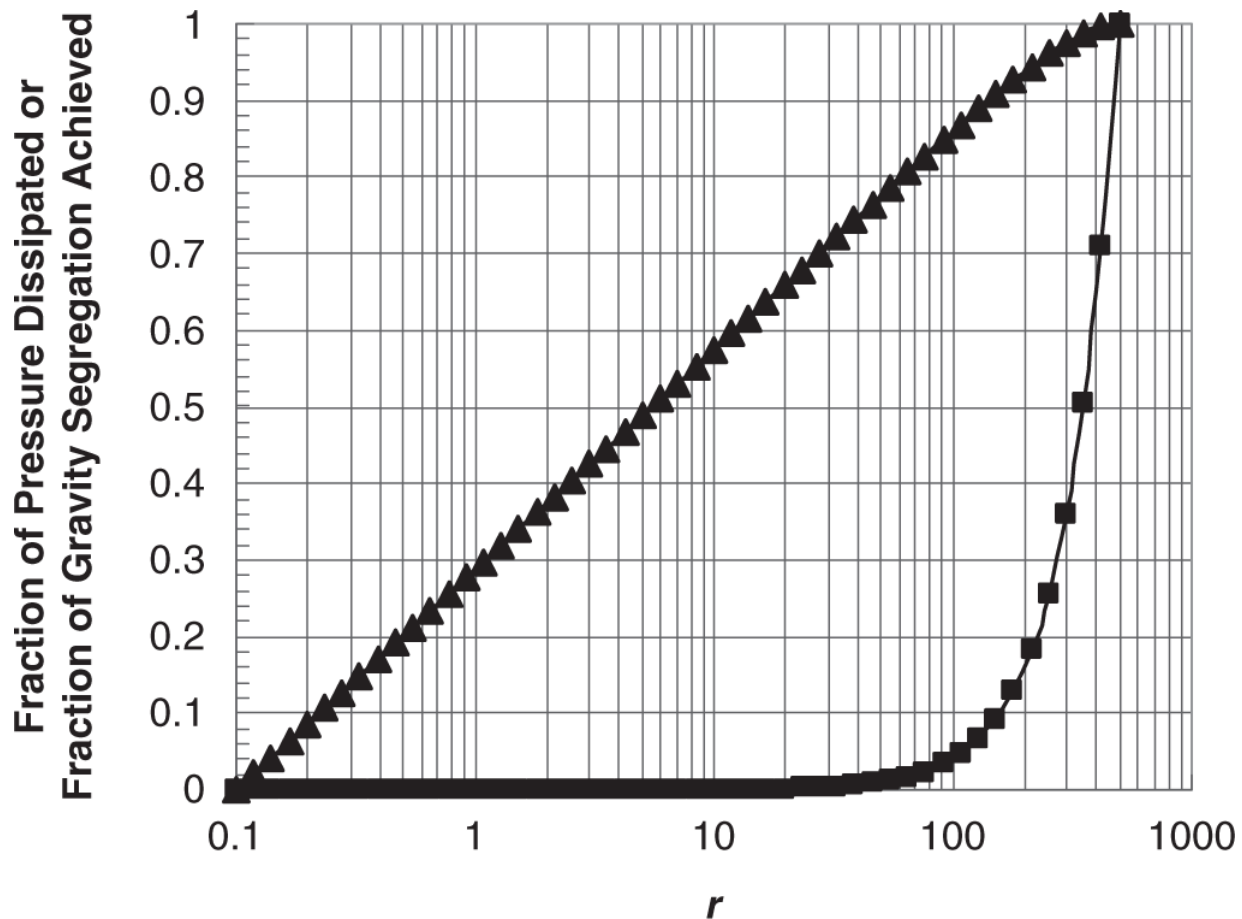


Fig. 6.26—Fraction of injection pressure dissipated (triangles; from Eq. 6.14) and fraction of gravity segregation attained (squares) as a function of radial position r in radial flow; wellbore radius 0.1 m, $R_g = 500$ m. From Rossen et al. (2010).

Stone (2004) suggests injecting water above gas, either from a single vertical injection well or from two parallel horizontal wells. Up to an approximately 50% increase in L_g or R_g^2 can be achieved from this approach at a fixed injection rate with gas and water, and greater benefits when combined with foam (Faisal et al. 2009; Rossen et al. 2010). Achieving the benefit of injecting water over gas with pairs of horizontal wells assumes that one can achieve uniform injection of both gas and water along both wells, in particular that the gas comes out evenly along its well.

With either one vertical well with two injection intervals or two horizontal wells, mobility is high very near the well because only water flows where water is injected and only gas flows where gas is

injected. This means that injectivity is greater than that with co-injection and that the injection rate q can be increased, with a corresponding increase in L_g or R_g^2 (cf. Eqs. 6.88 and 6.89). Simulations suggest that the increased injectivity gives up to a threefold increase in L_g or R_g^2 for relatively large slugs injected at fixed pressure.

WAG injection itself may outperform Eq. 6.90 because mobility is greater near the well most of the time in WAG than in continuous injection of both phases at the same overall fractional flow (Faisal et al. 2009).

Other strategies that outperform Eq. 6.90 by use of foam are discussed in [Chapter 10](#).

6.10 Summary

That volumetric sweep efficiency is a complex issue accounts for the sparsity of its discussion in this text compared with displacement efficiency. Three factors account for this complexity: a strong dependency on operational issues, nonlinear and irregular geometries, and difficulty in capturing realistic heterogeneities. Numerical simulators can handle all three of these issues to some extent, even though some questions remain about how to represent heterogeneity in simulation models.

There is little in the behavior of the volumetric sweep efficiency of actual reservoir displacements that cannot be at least qualitatively understood through the material presented here. Examples of such behavior are reservoirs with high-permeability thief zones that behave essentially as a two-layer medium, generally high-permeability reservoirs dominated by gravity that conform well to the Dietz theory, low-permeability reservoirs in which crossflow tends to be unimportant, and high-permeability reservoirs with large well spacing that tend to the VE limit rather quickly.

Above all, the recognition of bypassing—through channeling, viscous fingering, gravity segregation, or some combination of these

—is important, for this phenomenon seems to occur in many waterfloods and EOR projects.

Exercises

6.1 Using Areal Sweep Correlations. Use the areal sweep-efficiency correlations for a confined five-spot in this exercise.

- a. Plot the areal sweep efficiency E_A vs. dimensionless time t_D for a mobility ratio of 6.5.
- b. If the pattern pore volume is 10^6 m^3 and the average injection rate is $500 \text{ m}^3/\text{d}$, plot cumulative oil recovery (SCM) vs. time (months or years). Assume that the displacement is piston-like, the vertical sweep is unity, and the pore volume stated in Part a can be changed. The residual water and oil saturations are 0.2 and 0.3, respectively.

6.2 Heterogeneity Measures of Normal Distributions.

Permeability is occasionally distributed normally rather than log-normally. When this happens, the cumulative frequency distribution function (Eq. 6.10) becomes

$$\Lambda = \frac{1}{2} \left[1 - \operatorname{erf} \left(\frac{r - \bar{r}}{\sqrt{2v_N}} \right) \right]$$

where \bar{r} is the average permeability/porosity ratio and v_N is the variance of the normal distribution. Using the preceding equation and Eqs. 6.8 and 6.9, derive formulas for the Lorenz and Dykstra-Parsons coefficients in terms of v_N .

6.3 Vertical Sweep Efficiency in a Two-Layer Reservoir

- a. Derive an equation for flow in layer l in a horizontal reservoir.
- b. Calculate and plot the vertical sweep efficiency E_l and the fraction of total flow going into the high-velocity layer for a

two-layer horizontal reservoir with $k_1 = 2k_2$, $\phi_1 = \phi_2$, $\Delta S_1 = \Delta S_2$, and $h_1 = 3h_2$. Assume $M^0 = 0.5$.

6.4 Vertical Sweep Efficiency in a Noncommunicating Reservoir. For a reservoir having no vertical communication, calculate and plot the vertical sweep efficiency vs. dimensionless cumulative water injected for the following five-layer cross section:

$h_l(\text{m})$	ϕ_l	$k_l(\mu\text{m}^2)$
5	0.2	0.100
10	0.22	0.195
2	0.23	0.560
15	0.19	0.055
4	0.15	0.023

The endpoint mobility ratio is 0.5.

6.5 Vertical Equilibrium for Continuous Layers. For a reservoir for which the VE Hearn model applies with $M^0 < 1$ and $\alpha = 0$,

- a. Show that if the permeability distribution is continuous, the cross-sectional averaged water fractional flow may be written as

$$\bar{f}_1 = \left[1 + \frac{(1-C)}{H_K M^0 C} \right]^{-1},$$

where H_K is the Koval heterogeneity factor ([Fig. 6.8](#)).

- Recalculate and plot the vertical sweep efficiency for the two-layer model of Part (b) in Exercise 6.3. Use $M^0 = 0.5$.
- In a two-layer horizontal reservoir, show that the effects of the heterogeneity contrast may be completely suppressed (that is, the fronts travel at equal velocities in both layers) if $M^o < \frac{k_2 \phi_1}{\phi_2 k_1}$, where 1 and 2 represent the high- and low-velocity layers, respectively.

6.6 Calculating Pseudorelative Permeabilities.

For the discrete permeability/porosity data of Exercise 6.4.

- Calculate and plot the pseudorelative permeabilities for a waterflood in a horizontal reservoir using the VE Hearn model.
- Calculate and plot the vertical sweep efficiency for this flood.
- Repeat Part a for a nonzero capillary-pressure function given by

$$P_c = \sigma_{12} \left(\frac{\phi}{k} \right)^{1/2} \cos \theta (1 - S)^4,$$

where σ_{12} is the oil/water interfacial tension, θ is the contact angle, and

$$S = \frac{S_1 - S_{1r}}{1 - S_{1r} - S_{2r}}.$$

- Calculate and plot the vertical sweep efficiency for Part c. Additional data for this problem are $\Delta\rho = 0$, $S_{1r} = S_{2r} = 0.2$, $\mu_1 = 1 \text{ mPa}\cdot\text{s}$, $\mu_2 = 10 \text{ mPa}\cdot\text{s}$, $k_{r1}^o = 0.05$, $k_{r2}^o = 0.9$, and the relative-permeability curves are given as

$$k_{r1} = k_{r1}^o S^2, \quad k_{r2} = k_{r2}^o (1 - S).$$

6.7 Deriving Pseudorelative Permeabilities.

The water/oil capillary-pressure-water-saturation function may often be

represented as $P_c = K \left(\frac{1}{S^2} - 1 \right)$, where K is a constant and S is the reduced saturation (from the second equation in Exercise 6.6c). If the VE assumptions apply and the reservoir is homogeneous,

- Derive the water-saturation profile in the dip normal or z-direction in terms of a water saturation at the bottom of the reservoir (S_{1B} or S_B).
- Derive an expression for the average water saturation as a function of S_{1B} or S_B .
- If the local (laboratory-measured) relative permeabilities are approximated by the equation in Exercise 6.6d, show that the oil and water pseudorelative permeabilities expressed in terms of the average saturation of Part (b) are

$$\tilde{k}_{r1} = \frac{k_{r1}^o}{N_g^o} \ln \left[1 + \frac{\frac{N_g^o \bar{S}^2}{g}}{\left(1 - \frac{N_g^o \bar{S}^2}{4} \right)^2} \right], \quad \tilde{k}_{r2} = k_{r2}^o (1 - \bar{S}),$$

where

$$N_g^o = \frac{\Delta \rho g \cos \alpha H_t}{K}.$$

- For $N_g^o = 1$ and $M^o = 4$, calculate and plot the pseudodisplacement sweep efficiency vs. dimensionless time. The dip angle of the reservoir is zero.

6.8 Instability Calculations

- Calculate the critical rate for a miscible displacement having the following properties:

$$k = 0.12 \text{ } \mu\text{m}^2$$

$$M^o = 50$$

$$\text{Oil-solvent density difference} = -0.8 \text{ g/cm}^3$$

$$\text{Solvent mobility} = 10 \text{ (mPa}\cdot\text{s})^{-1}$$

Dip angle = -10° .

- b. If the superficial velocity in the above displacement is $0.8 \text{ } \mu\text{m/s}$, calculate the critical wavelength from stability theory. Assume the dispersion coefficient to be $10^{-5} \text{ cm}^2/\text{s}$.

6.9 Gravity Segregation With Co-Injection of Gas and Water.

Using Eq. 6.90, answer the following questions.

- a. Determine the injection pressure for the following parameter values: $k_h = 100 \text{ md}$ (10^{-14} m^2); $k_z = 10 \text{ md}$ (10^{-14} m^2); $r_w = 4 \text{ in.}$ (10 cm); $H = 20 \text{ ft}$ (30.5 m); $(\rho_{13} - \rho_3) = 400 \text{ kg/m}^3$; and $R_g = 1000$ or 2000 ft (305 m or 610 m).
- b. Compute the injection rate q (in m^3/d) required to give segregation at the two distances above.
- c. Now suppose that the formation contains five identical intervals, each 20 ft thick, with impermeable shale barriers between them. In other words, $h = 20 \text{ ft}$ for each individual interval. Compute the distance to segregation and the injection pressure for the same two values of q as in part (b).

Chapter 7

Solvent Methods

One of the earliest methods for producing additional oil is through the use of solvents to extract the oil from permeable media. In the early 1960s, interest was centered on injecting liquefied petroleum gas (LPG) in small *slugs* and then displacing the LPG by a dry *chase* gas. This process became economically less attractive as the value of the solvent increased.

In the late 1970s, interest in solvent methods revived because of increased oil prices and greater confidence in the ability to estimate oil recovery. During this period, the leading solvent became carbon dioxide (CO_2), although several other fluids were also used (Stalkup 1983). In the early 1980s, the number of carbon-dioxide floods increased significantly, and more were proposed until oil prices dropped in the mid-1980s. Projects that had invested significant capital costs were continued and were profitable through the 1990s, even at very low oil prices. Around 2002, the number of solvent-flooding projects in the United States surpassed the number of thermal projects, and solvent flooding became the leading enhanced-oil-recovery (EOR) method. The number of gas flooding projects is expected to increase in the coming decade, especially if relatively high oil prices are sustained and carbon sequestration expands.

The main mechanism for recovery by solvents is the mass transfer that occurs as miscibility is developed between solvent and reservoir oil. Two fluids that mix together in all proportions within a single fluid phase are *miscible*. Therefore, miscible agents would mix in all proportions with the oil to be displaced. However, most practical miscible agents exhibit only partial miscibility toward crude oil itself, and, therefore, we use the term *solvent* flooding in this text. Many solvents, of course, will become miscible with crude under the right

conditions, but all solvents of commercial interest are immiscible to an aqueous phase.

Solvent flooding refers to those EOR techniques in which the main oil-recovery function is achieved by mass transfer. This includes extraction, dissolution, vaporization, solubilization, and condensation, all of which entail a phase-behavior change involving the crude. These methods have other, sometimes very important, oil-recovery mechanisms (viscosity reduction, oil swelling, or solution gas drive), but the primary mechanism must be mass transfer. As we shall see, sometimes the mass transfer is so extensive that the fluids can become miscible.

Mass transfer can be brought about by many fluids: organic alcohols, ketones, refined hydrocarbons, condensed petroleum gas (LPG), natural gas, and liquefied natural gas (LNG), CO_2 , air, nitrogen, exhaust gas, flue gas, hydrogen sulfide, and others. In this chapter, we emphasize miscible flooding with the gaseous solvents CO_2 , CH_4 , and N_2 , but you should remember that there are many potential agents. Another important point is that the progression to miscibility is through mass transfer of intermediate hydrocarbon components.

7.1 General Discussion of Solvent Flooding

There are so many solvents, process types, and reservoirs that it is impossible to cover all the possible process variations. Therefore, in this section, we discuss CO_2 solvent flooding. Later sections discuss more general aspects of solvent flooding.

[Fig. 7.1](#) shows an idealized vertical cross section between an injection and a production well. By far the most common application of solvent methods is in a displacement mode as shown, but injection and production through the same wells have been reported (Monger and Coma 1988). Solvent injection commences into a reservoir in some stage of depletion, most commonly at residual oil or true tertiary conditions. Most solvent floods are performed in reservoirs containing light crudes (less than 3 mPa·s resident oil viscosity), although there are exceptions (Goodrich 1980). The solvent may be introduced

continuously in undiluted form, alternated with water in the water-alternating-gas (WAG) process, as shown in [Fig. 7.1](#), or even injected simultaneously with water through dual-injection tubing. The gas volume injected in each WAG cycle can be tapered so that more gas is injected in the first cycle to delay trapping of gas by water. Water is injected with the solvent in this fashion to reduce the usually large mobility of the solvent. Even so, the mobility ratio between the solvent (or the solvent/water mixture) and the oil will be unfavorable (mobility ratio greater than one). CO₂, in particular, can be injected dissolved in water in a distinctly immiscible fashion that recovers oil through swelling and viscosity reduction (Martin 1951).

If the solvent is completely (first-contact) miscible with the oil, the process has a large ultimate displacement efficiency because there can be no residual phases (see Section 5.4). If the solvent is only partially miscible with the crude, the total composition in the mixing zone (the miscible zone in [Fig. 7.1](#)) between the solvent and the oil can change to generate or develop miscibility in situ. Regardless of whether the displacement is developed or first-contact miscible, the solvent must immiscibly displace any mobile water present with the resident fluids. Hence, solvent floods always have at least three phases flowing. In some cases, multiple hydrocarbon phases can exist.

The profitability of the process usually dictates that the solvent cannot be injected indefinitely. Therefore, a finite amount or *slug* of solvent is usually followed by a *chase* fluid, with the function of driving the solvent toward the production wells. This chase fluid—N₂, air, water, and dry natural gas seem to be the most common choices—may not itself be a good solvent, but it is selected to be compatible with the solvent and because it is economically available in large quantities. Note the similarity between the chase fluid in solvent flooding and the mobility buffer drive in surfactant/polymer flooding, as shown in [Figs. 7.1](#) and [9.1](#).

Although the process shown in [Fig. 7.1](#) appears relatively simple, the displacement efficiency and volumetric sweep efficiency are fairly complex. Sections 7.6 to 7.8 apply the methods of [Chapters 5](#) and [6](#)

to solvent flooding, but first, we discuss selected physical properties of solvents and solvent/crude oil systems.

Another aspect of the process is the surface facilities. The source of the solvent differs with solvent type. For CO₂, the source can be a naturally occurring deposit from which the solvent is transported through pipelines. On occasion, the source is brought in trucks or railroad cars, but this is uncommon. More recently, there has been interest in extracting CO₂ from power-plant effluents or from flue gas (which is itself a solvent) for use in EOR, a practice that also has potential to store CO₂ as a means of reducing greenhouse-gas emissions to the atmosphere.

The sources of other solvents are highly variable. Nitrogen can be extracted directly from the air, or air itself can be used as a solvent. Hydrocarbon-based solvents normally require a means of extracting the solvent from another reservoir or even from the same reservoir. The efficiency of all solvents has the potential of being improved by adding intermediate components, although this comes with a cost.

The availability of solvents is a major determinant for beginning a solvent flood. However, other considerations are important as well. Chief among these is recycling.

Field experience indicates that most of the crude in a solvent flood is produced using solvent. This observation means, and economics dictates, that the solvent be separated from the crude after production. Sometimes the separation can be performed as part of normal operations, but more often specialized equipment is needed. For CO₂, this is normally an amine separation plant or a membrane facility. Separation is needed to bring the crude to a saleable quality and to reduce the volume of purchased solvent, both of which have a direct impact on the profitability of the process. See Aaron and Tsouris (2005) for a discussion of surface separation methods. In a mature flood, approximately one-half the injected CO₂ is recycled.

CARBON DIOXIDE FLOODING

This method is a miscible displacement process applicable to many reservoirs. A CO₂ slug followed by alternate water and CO₂ injections (WAG) is usually the most feasible method.

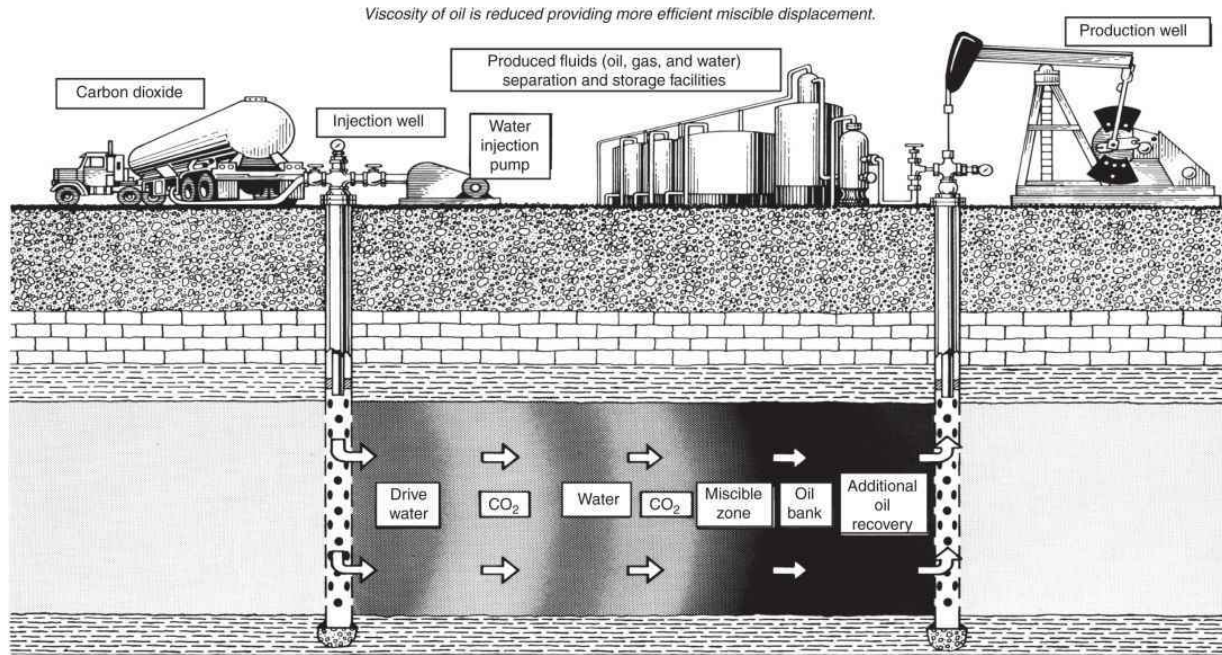


Fig. 7.1—Schematic of a solvent-flooding process (drawing by Joe Lindley, US Department of Energy, Bartlesville, Oklahoma).

7.2 Solvent Properties

[Fig. 7.2](#) shows phase-behavior data (P/T diagram) for various pure components and air. For each curve, the line connecting the triple and critical points is the vapor/pressure curve; the extension below the triple point is the sublimation curve (see Section 4.2). The fusion curve is not shown. The pressure-temperature plot for air is really an envelope, but its molecular-weight distribution is so narrow that it appears as a line in [Fig. 7.2](#). Flue gas is also a mixture of nitrogen, carbon monoxide, and CO₂, with a similarly narrow molecular-weight distribution; its P/T curve would fall near the nitrogen curve in [Fig. 7.2](#).

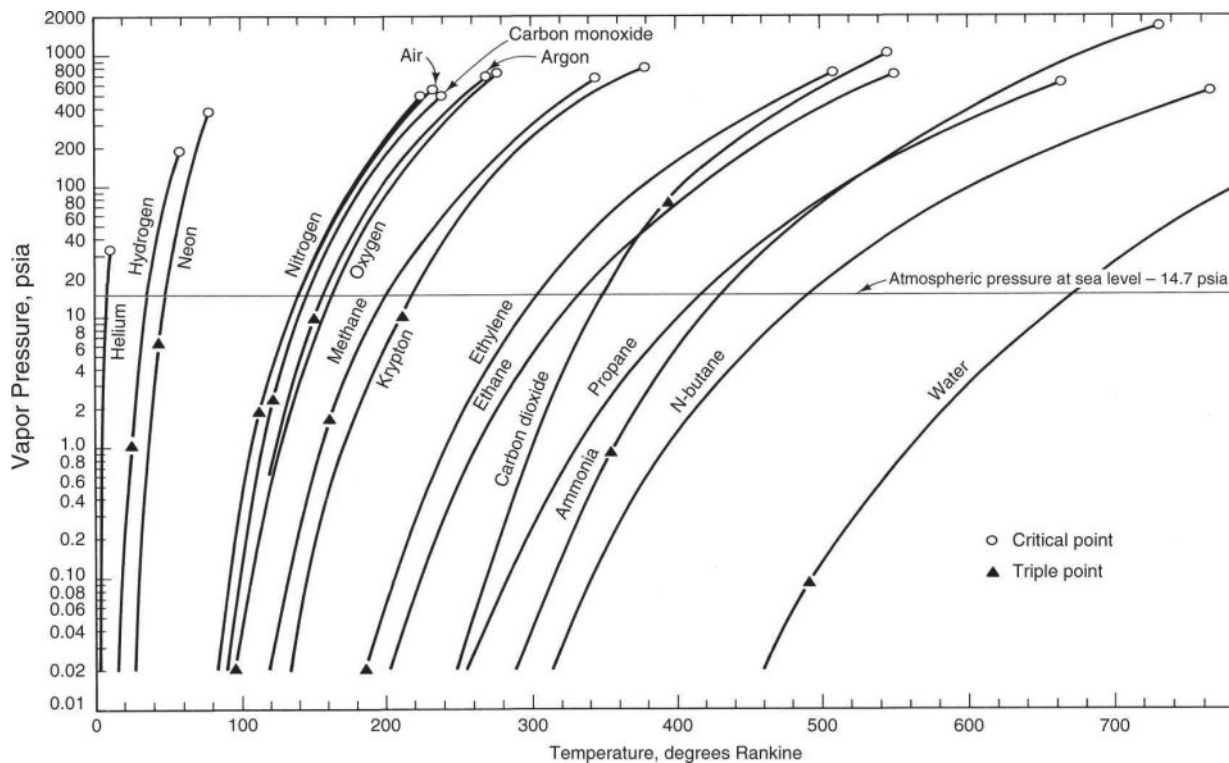


Fig. 7.2—Vapor-pressure curves for various pure substances (Gibbs 1971).

The critical pressures for most components fall within a relatively narrow range of 3.4 to 6.8 MPa (500–1,000 psia), but critical temperatures vary much more widely. The critical temperatures of most components increase with increasing molecular weight. CO_2 (with molecular weight of $M_W = 44$) is an exception to this trend, with a critical temperature of 304 K (87.8°F), which is closer to the critical temperature of ethane ($M_W = 30$) than to that of propane ($M_W = 44$). See Vukalovich and Altunin (1968) for a large compilation of CO_2 properties. Most reservoir applications would be in the temperature range of 294 to 394 K (70–250°F) and at pressures greater than 6.8 MPa (1,000 psia); hence, air, N_2 , and dry natural gas will all be supercritical fluids at reservoir conditions. Solvents such as LPG, in the molecular weight range of butane or heavier, will be liquids. CO_2 will usually be a supercritical fluid because most reservoir temperatures are above the critical temperature. Proximity to its critical temperature makes CO_2 more liquid-like than other solvents.

Example 7.1—Solvent Densities and Molar Volumes. The fluid density of a solvent (Component 3) ρ_3 can be calculated as

$$\rho_3 = \frac{PM_w}{zRT}.$$

The formation volume factor at any temperature and pressure B_3 , a specific molar volume, also follows:

$$B_3 = z \frac{P_s}{P} \frac{T}{T_s}.$$

In the preceding equation, T_s and P_s are the standard temperature and standard pressure, respectively. All fluids become more liquid-like at a fixed temperature and pressure as the molecular weight increases. The anomalous behavior of CO_2 is again manifest by comparing its density and formation volume factor to that of air.

We use the preceding equations to calculate density and formation volume factor for CO_2 and air at 339 K (150°F) and 17 MPa (2,500 psia). The two solvents are near the upper and lower molecular-weight limits of practical solvents. The results are shown in the following table:

	CO_2	Air
Z	0.44	1.03
ρ_3 g/cm ³	0.69	0.16
B_3 dm ³ /std·m ³	2.69	7.31

The CO_2 density is much closer to a typical light-oil density than is air; hence, CO_2 is much less prone to gravity segregation (with respect to oil) during a displacement than air or other gases, such as nitrogen

and methane. Usually, gravity segregation in a CO₂ flood is more likely where the water saturation is large because CO₂ tends to segregate more from water than from oil.

From the formation volume factor, approximately three times as many moles (recall that B_3 is a specific molar volume) of CO₂ than of air are required to fill the same reservoir volume.

[**Figs. 7.3**](#) and [**7.4**](#) give the viscosities of a natural-gas mixture and of pure CO₂. Over the pressure and temperature range shown, which includes the conditions of interest for EOR, the viscosities of natural gas, air, flue gas, and N₂ are approximately the same. However, the CO₂ viscosity is generally two or three times greater. Relative to a hydrocarbon liquid or water viscosity, the values are still small, meaning that there should be no appreciable difference in the ease of injection of these solvents. However, the CO₂ to crude-oil mobility ratio will be two or three times smaller than that of the other light solvents; hence, volumetric sweep efficiency will generally be better for CO₂. [For correlations for other solvents and solvent mixtures, see McCain (1989), Poling et al. (2000), and Engineering Data Book (2004)].

Example 7.2—Viscosity of Pure CO₂. At discovery, and often even throughout production, the average temperature and pressure in reservoirs can be approximated by the geothermal equation $T = 0.015D_z + 60$ for temperature in degrees F, and $P = 0.433D_z + 15$ for pressure in psia. D_z in the equation is subsurface vertical depth in feet, and the constants in the equations are the geothermal and geopressure gradients, respectively.

We can use these and [**Fig. 7.4**](#) to estimate the variation in CO₂ viscosity. The results are shown in the following table:

Depth, ft.	$T, ^\circ F$	$P, psia$	$\mu_{CO_2} \text{ mPa}\cdot\text{s}$
2,667	100	448	0.02
6,000	150	2610	0.06
9,333	200	4050	0.06

Except in the vicinity of the critical point (first row), the viscosity is approximately 0.06 mPa·s. Evidently, the effects of temperature and pressure compensate for each other to give a nearly constant viscosity. A similar calculation could be made for the densities and formation-volume factors.

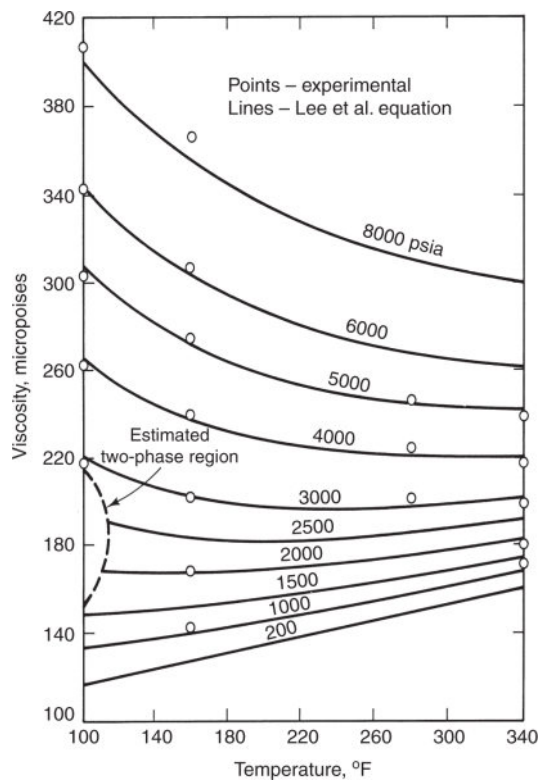


Fig. 7.3—Viscosity of a natural-gas sample (Lee et al. 1966).

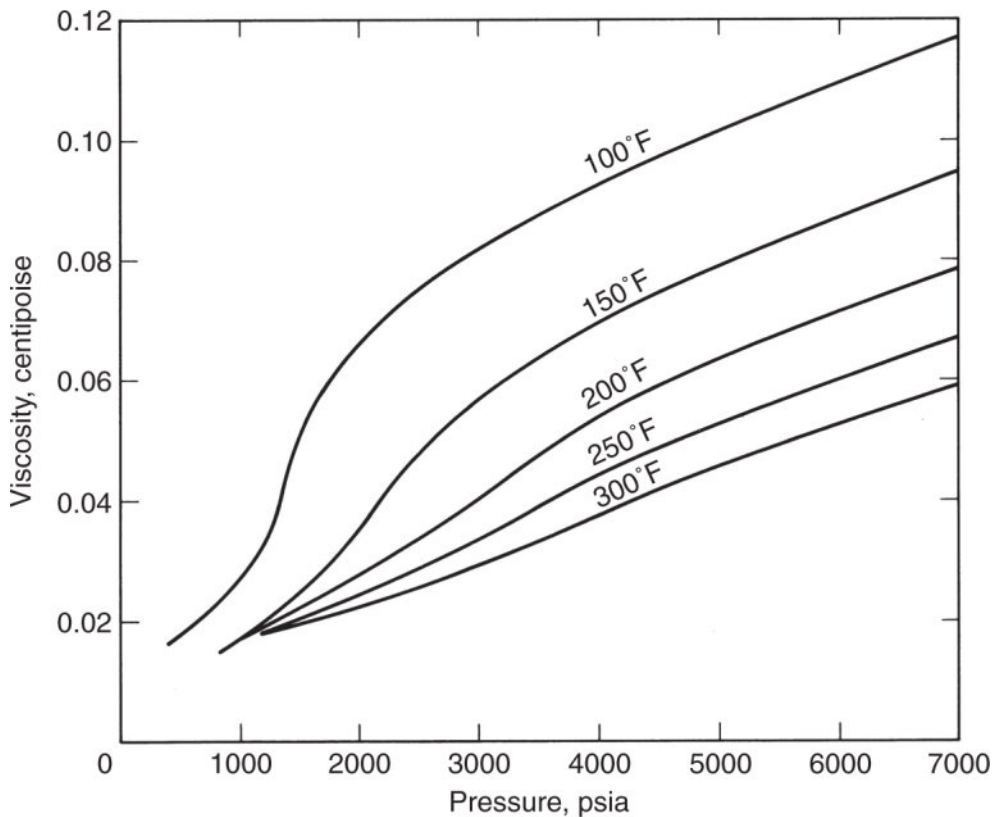


Fig. 7.4—Viscosity of CO₂ as a function of pressure at various temperatures (Goodrich 1980).

7.3 Solvent and Crude-Oil Properties

Sections 4.1–4.3 discussed general aspects of phase behavior for pure components and mixtures. This section gives the specific features of solvent/crude phase behavior, which are necessary to clarify the development in later sections. Phase-diagram representations show the state of the fluid in thermodynamic equilibrium.

7.3.1 Pressure/Composition Diagrams. [Figs. 7.5](#) and [7.6](#) show pressure/composition (P/z) diagrams for two solvent/crude systems. Recall that these diagrams are plots, at constant temperature, of pressure vs. the overall mole percent of solvent in contact with a crude oil at equilibrium. These plots show the number and types of phases and the volume percentages of liquid. Both figures are for the indicated solvent/crude mixture. Other diagrams can be found in

Turek et al. (1984), and Orr and Jensen (1984). The data in [Figs. 7.5](#) and [7.6](#) show the behavior of trends with temperature. Recall that no water is present during the phase-behavior measurements; water can change the phase-behavior diagram somewhat if a sizeable fraction of CO₂ is soluble in the aqueous phase (Mohebbinia et al. 2012). For mixtures, the mole percent can represent both phase and overall concentrations.

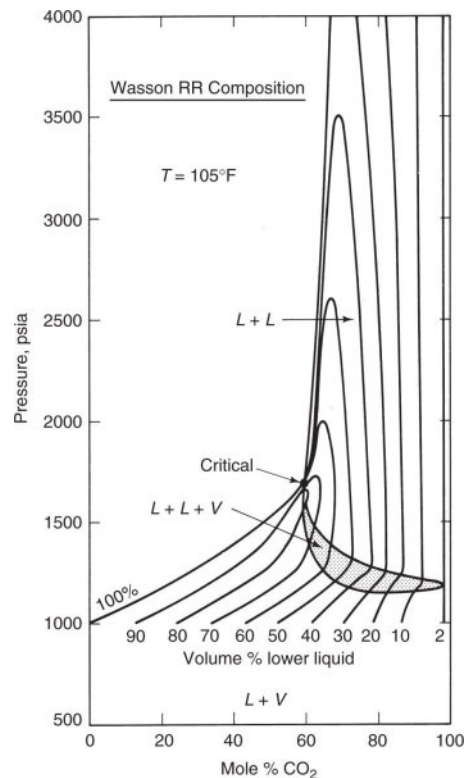


Fig. 7.5—P/z diagram for recombined Wasson crude, CO₂ system (Gardner et al. 1981).

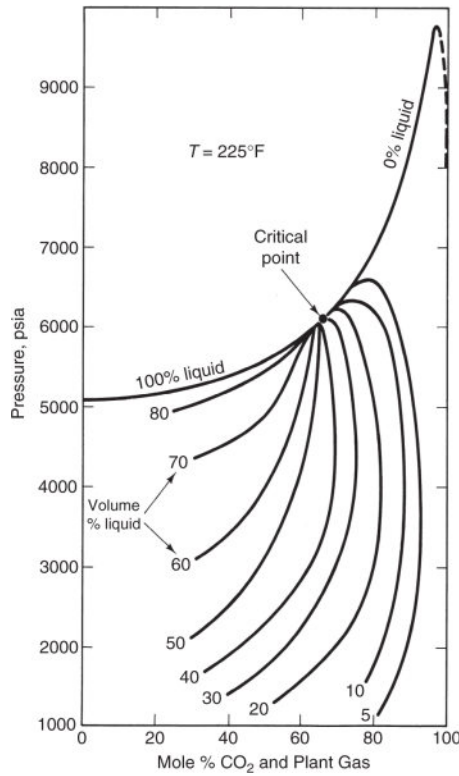


Fig. 7.6—Phase envelope for Weeks Island “S” Sand crude and 95% CO₂, 5% plant gas at 225°F (Perry 1978).

The P/z diagrams have the same general form regardless of temperature. The left vertical axis gives the phase behavior of the CO₂-free crude; therefore, the bubblepoint pressure of the recombined (RR) Wasson crude at 314 K (105°F) is 6.81 MPa (1,000 psia) from Fig. 7.5. The right vertical axis, similarly, gives pure properties for CO₂, which is a single-phase fluid in Figs. 7.5 and 7.6 because both are above the CO₂ critical temperature. At small pressures and for all CO₂ concentrations, except very near the right axis, the mixture is two-phase liquid and vapor. (Directly at the right vertical axis, the fluid is again single-phase. The phase boundary cannot be seen in these figures because it is very near the axis.) The liquid volume-quality lines are also shown. At large pressures and small CO₂ concentrations, the mixture is single-phase. At approximately 60% CO₂, a critical point (a critical mixture) exists, through which pass the two single-phase boundaries. The CO₂

composition at this point is the critical composition for the fixed temperature and the indicated pressure. The phase boundary line below the critical point is a bubblepoint curve and that above is a dewpoint curve. Therefore, the upper left corner of the P/z diagram is a supercritical fluid region. The system could form a liquid phase as the light component increases in concentration at a constant pressure greater than the critical pressure. This change is a type of retrograde behavior.

Although there are fewer P/z diagrams for solvents other than CO₂ in the literature, it appears, on the basis of the N₂-crude-oil data in [Fig. 7.7](#), that the qualitative characteristics described in the preceding apply to other solvents as well. The critical pressure for the N₂ solvent mixture in [Fig. 7.7](#) is much higher (off the scale above) than either of the critical pressures of the CO₂ systems in [Figs. 7.5](#) and [7.6](#). Returning to CO₂, the main difference between the low- and high-temperature phase behavior is the presence, in [Fig. 7.5](#), of a small three-phase region just below and to the right of the critical point. These phases are two liquids—a light or upper phase and a heavy or lower phase—and a vapor phase. Such behavior does not usually occur at high temperatures ([Fig. 7.6](#)) (Turek et al. 1984). Moreover, at low temperatures, a small amount of solid precipitate can exist over some composition and pressure ranges. The precipitate is composed mainly of asphaltenes, the heptane-insoluble fraction of crude oil (Hirshberg et al. 1984). The region of precipitate formation may overlap the three-phase region. This behavior introduces a complication into the displacement process and may even present operational problems because the solid precipitate can cause formation plugging.

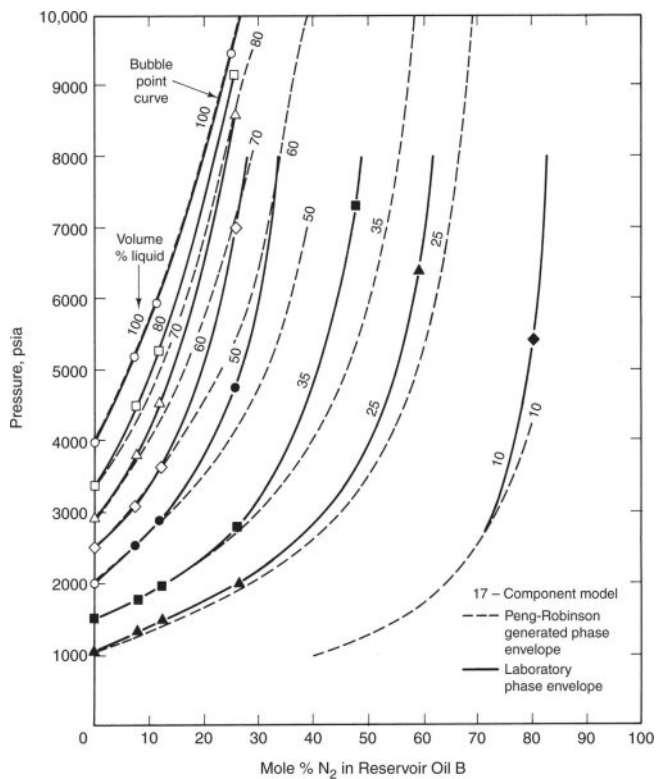


Fig. 7.7—P/z diagram for reservoir fluid B-nitrogen system at 164°F (347°K) (Hong 1982). Dotted lines are matches to the data with a Peng-Robinson EOS.

The final P/z diagram is in [Fig. 7.8](#) for a crude/CO₂ system. This diagram replicates many of the features shown in the previous diagrams. It also shows how the P/z diagram changes in the presence of brine.

A frequent assumption made in solvent flooding is that solvent/crude properties do not depend on the composition of any water with which the liquid is in contact. [Fig. 7.8](#) shows that this assumption is substantially accurate. This is not to say that brine is unimportant; it is important to the mobility adjustment of WAG floods and to the generation of fractional-flow predictions. Brine generally acts as an inert component with respect to phase behavior.

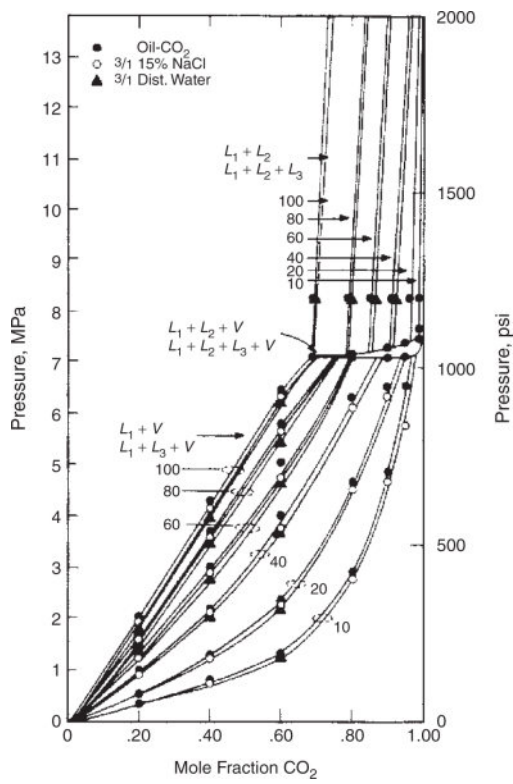


Fig. 7.8—P/z diagram for crude/CO₂ mixture in equilibrium with brine (Pollack et al. 1988).

Pressure/composition diagrams have two principal uses. The first is to provide data with which to calibrate the parameters in an equation of state (EOS). [Fig. 7.7](#) provides an example of this. The second is to provide an explanation of the ease (or difficulty) in generating miscibility of certain solvents with crude, as we discuss next.

Consider now a displacement of crude by a pure solvent in a permeable medium at some time before solvent breakthrough. The conditions at the injection end of the medium are plotted on the right vertical axis of the P/z diagram, and those at the production end are plotted on the left axis at some lower pressure. Conditions in the medium between these extremes are *not* represented on the P/z diagram because the relative amounts of each hydrocarbon component do not remain constant during a displacement, as they do in the pressure/volume/temperature (PVT) measurements illustrated in [Figs. 7.5](#) through [7.8](#). Therefore, the diagrams are not particularly useful for displacement classification, which is based on the ternary

diagrams to be described next. Still, one can see qualitatively from these diagrams that completely miscible displacements—those for which a single phase exists for all solvent concentrations—would require high reservoir pressures, in excess of 66.7 MPa (9,800 psia) for the data in [Fig. 7.6](#). Some reservoirs have pressures this high, but most do not. Fortunately, some displacements can *develop* miscibility at pressures much lower than those required in these diagrams.

Ternary Diagrams. Ternary diagrams are the basis for classifying solvent floods because they impart more compositional information than do P/z diagrams. See Section 4.4 for the correspondence between these diagrams. [Figs. 7.9 through 7.11](#) show representations of these.

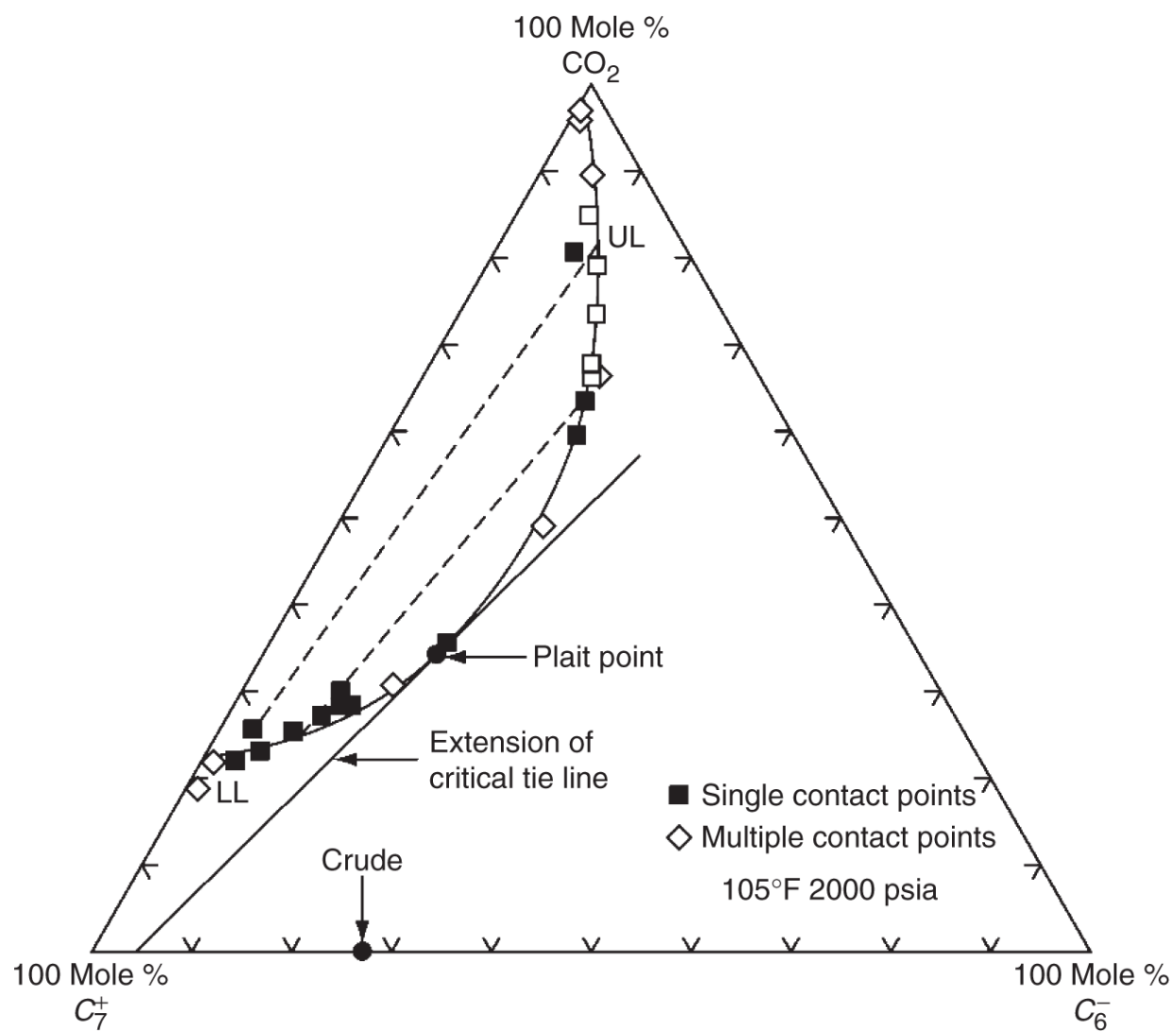


Fig. 7.9—Ternary equilibria for CO_2 -recombined Wasson crude mixture (Gardner et al. 1981)

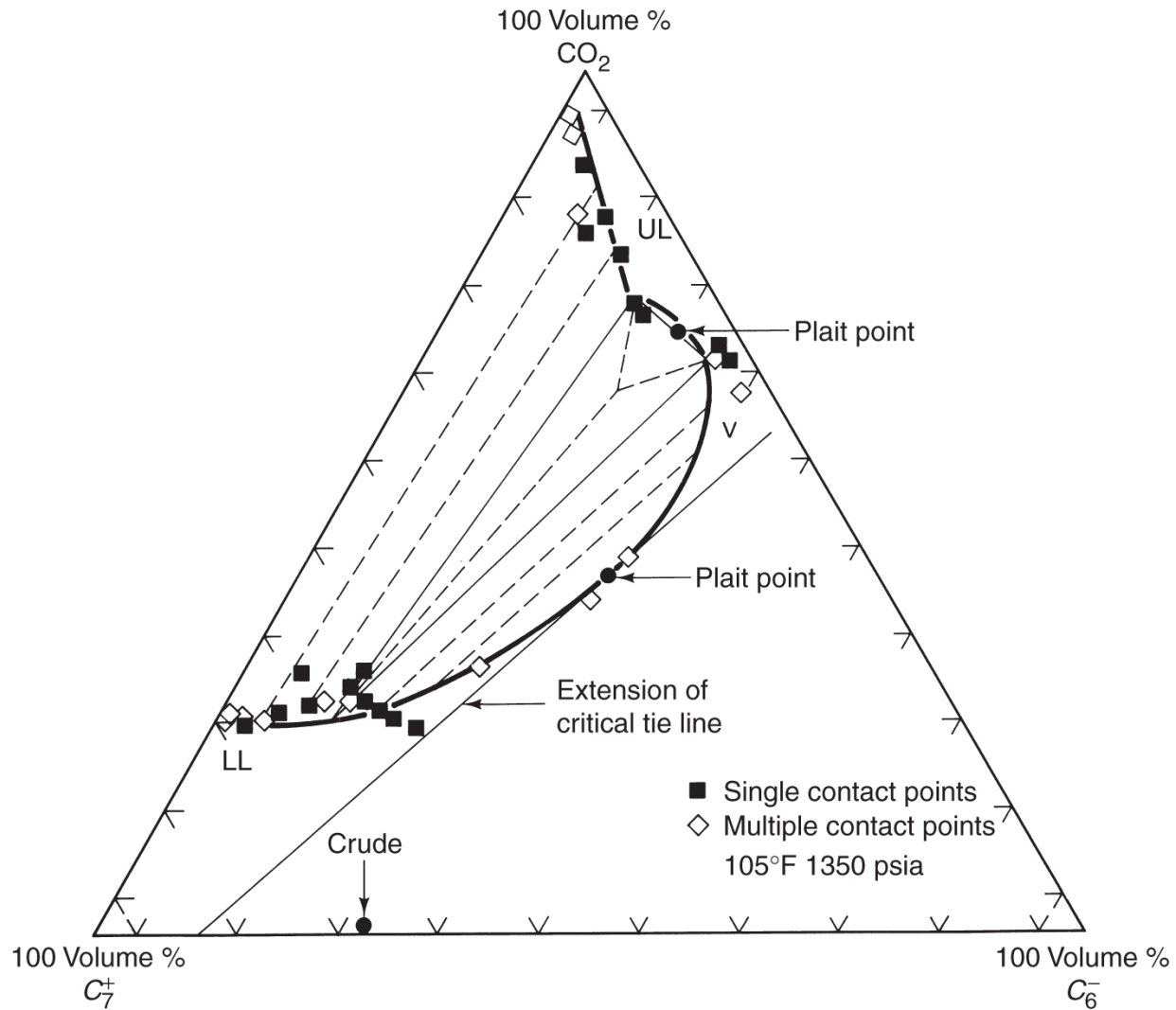


Fig. 7.10—Ternary equilibria for CO_2 -recombined Wasson crude system (Gardner et al. 1981).

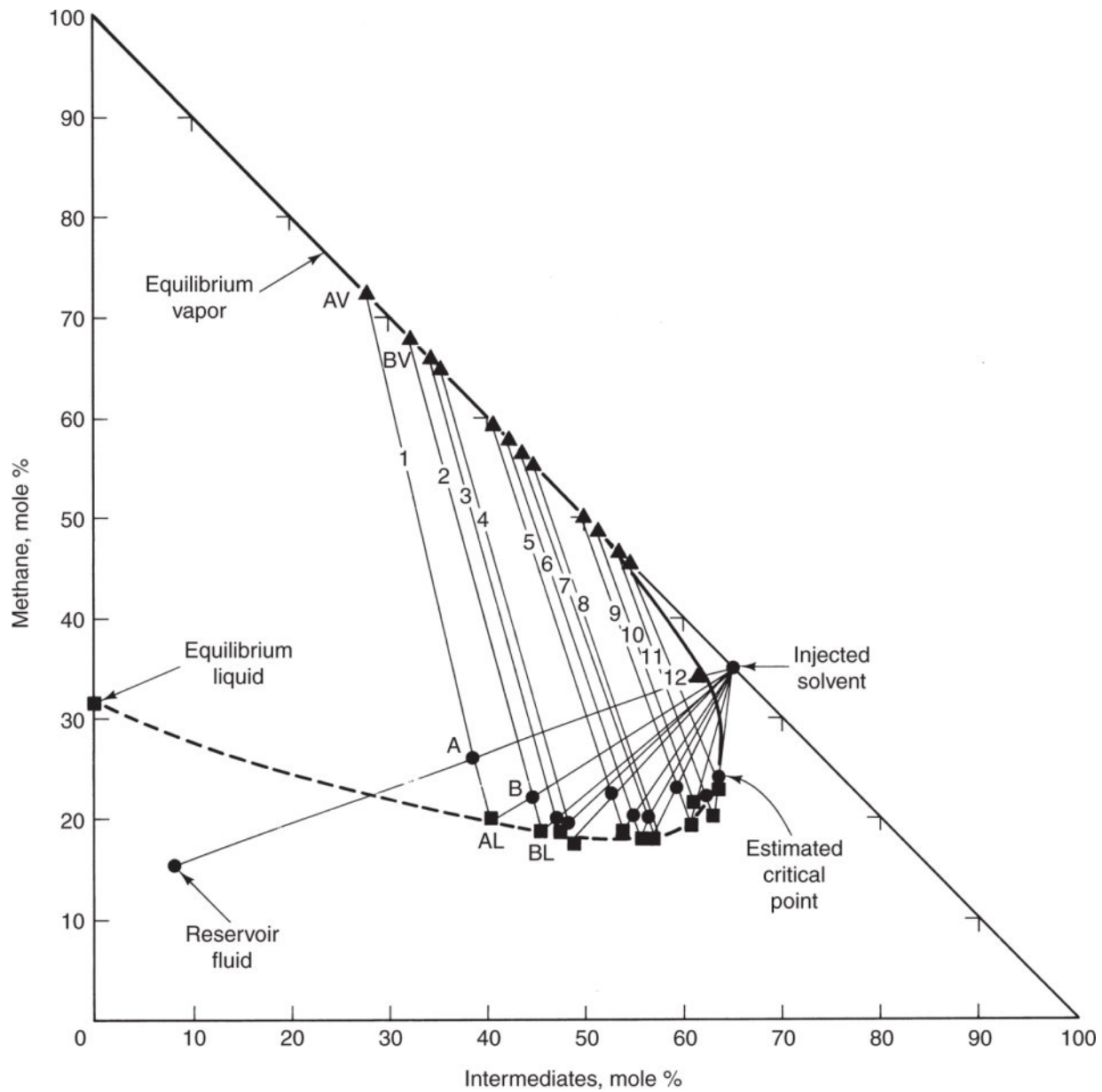


Fig. 7.11—Methane/crude oil ternary-phase behavior (Benham et al. 1961).

On these diagrams, the solvent/crude mixture is represented by three components: a light component on the top apex, an intermediate crude fraction on the right apex, and a heavy crude fraction on the left apex. The exact split between intermediate- and heavy-crude components is immaterial to the general features of the phase equilibria or to the miscibility classification. (However, it can affect quantitative work.) In Figs. 7.9 and 7.10, the split is between the C_6 and C_7 molecular-weight fractions. Therefore, none of the

corners of these ternaries represent pure components, and, hence, the designation *pseudocomponents* ([Chapter 4](#)). As justified by [Fig. 7.8](#), no water appears on the diagrams. In addition to those given here, ternary diagrams can be found in the literature in several other sources: for alcohol solvents (Holm and Csaszar 1965; Taber et al. 1965), for natural gas solvents (Rowe 1967), for CO₂ (Metcalfe and Yarborough 1978; Orr et al. 1981; Orr and Silva 1983), for N₂ solvents (Ahmad et al. 1983), and for mixtures of CO₂, SO₂, and CH₄ (Sazegh 1981).

A good example of CO₂/crude-oil equilibria is shown in [Fig. 7.9](#) for the recombined Wasson crude. In these solvent/crude systems, the phase equilibria—in particular the size of the single-phase region—depend strongly on reservoir temperature and pressure (recall that the ternary is at constant *T* and *P*). Typically, though, the pressure is larger than the cricondenbar of the light-intermediate component pseudobinary; hence, these two components are miscible in all proportions. The pressure is smaller than that of the light-heavy binary, and there is a region of limited miscibility or two-phase behavior along the light-heavy axis. This region of two-phase behavior extends into the interior of the ternary and is bounded by a binodal curve (see Section 4.3). Within the binodal curve, there are tie lines, with the ends representing the composition of the equilibrium phases. These shrink to a point (the *plait* point) at which the properties of the two phases are indistinguishable. The plait point is the critical mixture at this temperature and pressure.

Of great importance in what follows is the critical tie line, which is the fictitious tie line tangent to the binodal curve at the plait point. As pressure increases, the two-phase region shrinks—that is, light-heavy miscibility increases. No general statement is possible about the effect of temperature, although the two-phase region generally increases with increasing temperature. For low pressure and low temperature, a three-phase region can intrude into the two-phase region ([Fig. 7.10](#)).

These general characteristics apply for solvents other than CO₂ ([Fig. 7.11](#)). The composition of the reservoir crude can be placed on

the ternary, as can the composition of the solvent. In doing this, we are neglecting the pressure change that is, of course, essential to make the fluids flow in the reservoir. Even with this approximation, all compositions in the solvent/crude mixing zone do not lie on a straight line connecting the initial and injected fluids. This is because the composition changes are affected by the phase behavior. In fact, these changes are the basis for the classification of solvent displacements given in the next few paragraphs (Hutchinson and Braun 1961).

7.3.2 Ternary Solvent Classifications. We represent a 1D displacement of a crude by a solvent on the schematic ternary diagram in [Fig. 7.12](#). The crude is in the interior of the ternary, indicating that some of the light component is present initially in the crude. If a straight-line *dilution* path between the solvent and the crude does not intersect the two-phase region, the displacement will consist of a single hydrocarbon phase that will change in composition from crude to undiluted solvent through the solvent/oil mixing zone. The dilution path is linear (see [Chapter 5](#) and Section 7.6) because the only mechanism for mixing in single-phase flow is dispersion, there being no water or fractional-flow effects associated with the single hydrocarbon phase. A displacement that occurs entirely within one hydrocarbon phase is *first-contact miscible*. There is a range of solvent compositions that will be first-contact miscible with the crude at this temperature and pressure. In what follows, the behavior of the intermediate pseudocomponent will be of greatest importance. In [Fig. 7.12](#), the crude and the solvent contain intermediates.

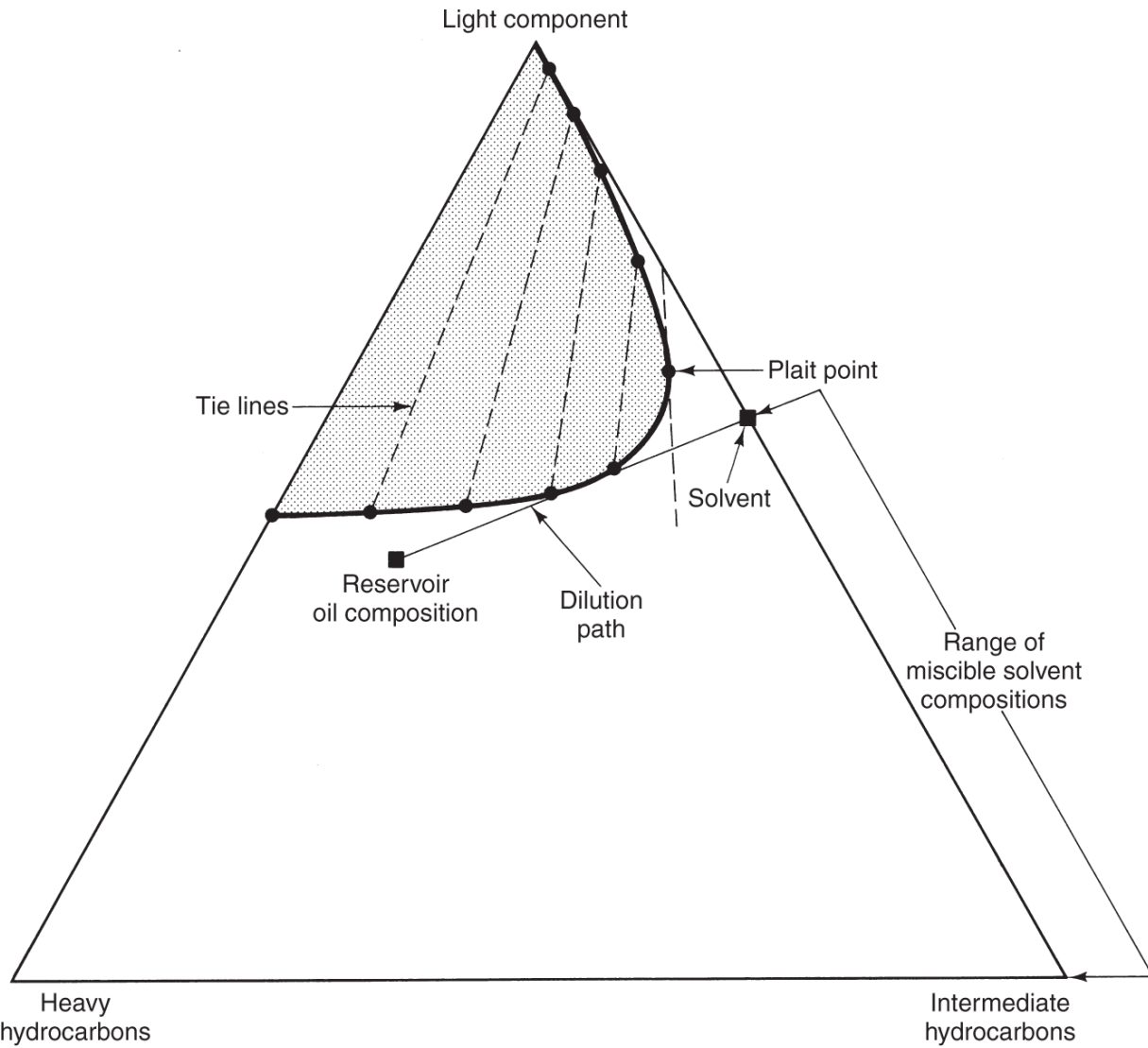


Fig. 7.12—Schematic of first-contact miscible displacement.

Suppose that the solvent consists entirely of the light pseudocomponent ([Fig. 7.13](#)). The displacement is not first-contact miscible because the dilution path passes through the two-phase region. However, it will develop miscibility, as described next.

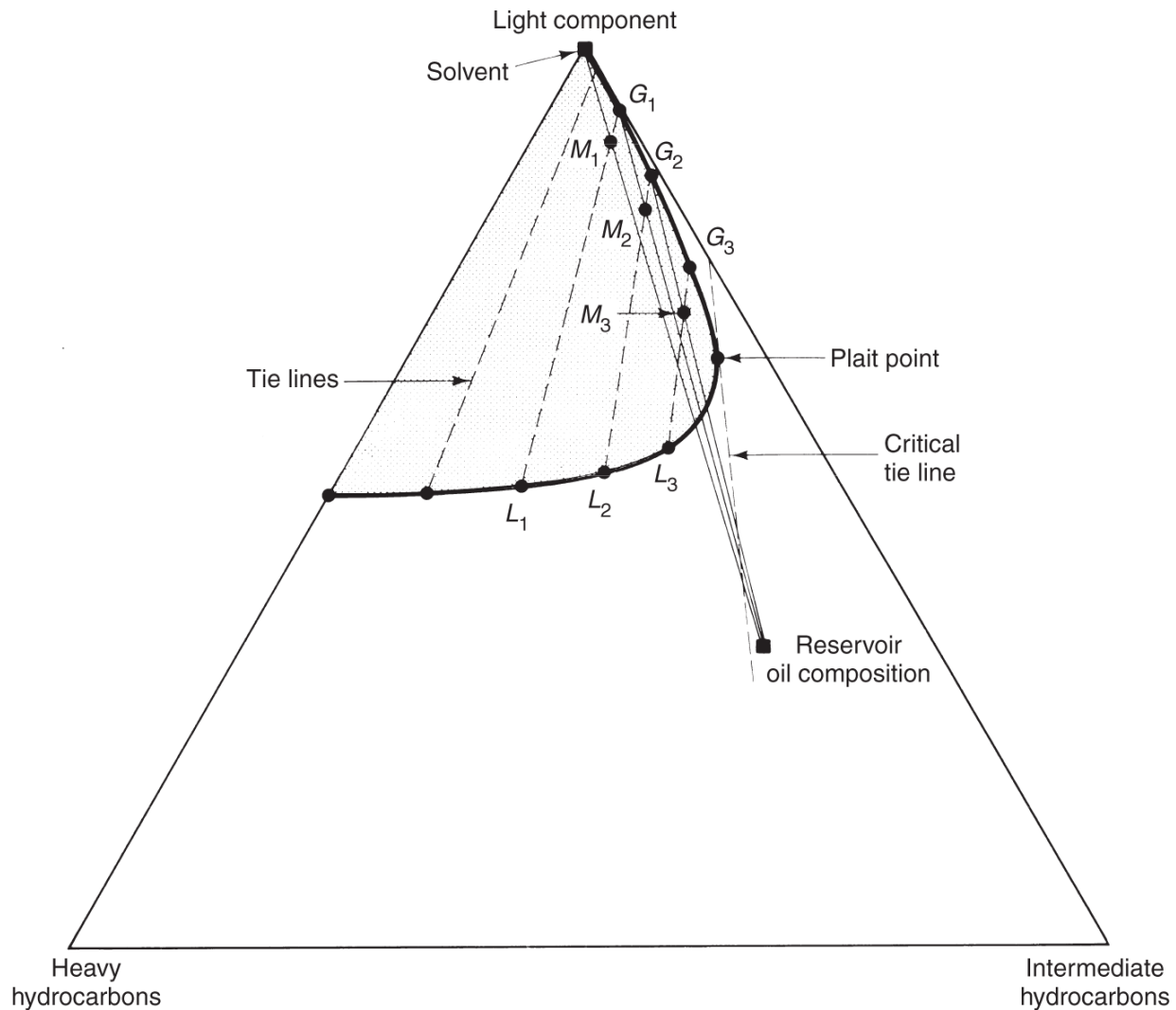


Fig. 7.13—Schematic of vaporizing gas-drive displacement [adapted from Stalkup (1983)].

Imagine a series of well-mixed cells that represent the permeable medium in a 1D displacement. The first cell initially contains crude, to which we add an amount of solvent so that the overall composition is given by M_1 . At equilibrium, the mixture will split into two phases, a gas G_1 and a liquid L_1 , determined by the equilibrium tie lines. The gas G_1 will have a larger mobility than L_1 , and this phase moves preferentially into the second mixing cell to form mixture M_2 . Liquid L_1 remains behind to mix with more pure solvent. In the second-cell mixture, M_2 splits into gas G_2 and liquid L_2 , G_2 flows into the third cell to form mixture M_3 , and so forth. At some cell beyond the third (for

this diagram), the gas phase will no longer form two phases on mixing with the crude. From this point forward (downstream), all compositions in the displacement will be on a straight dilution path between the crude and a point tangent to the binodal curve. The displacement will be first-contact miscible with a solvent composition given by the point of tangency. The process has *developed miscibility* because the solvent has been enriched in intermediate components to be miscible with the crude. Because the intermediate components are vaporized from the crude, the process is a *vaporizing gas drive*. Miscibility will develop in this process as long as the injected solvent and crude are on opposite sides of the critical tie line.

Suppose that the crude and solvent compositions are again on opposite sides of the critical tie line, but reversed from the vaporizing gas drive ([Fig. 7.14](#)). In the first mixing cell, the overall composition M_1 splits into gas G_1 and liquid L_1 . Gas G_1 moves on to the next mixing cell as before, and liquid L_1 mixes with fresh solvent to form mixture M_2 . Liquid L_2 mixes with fresh solvent, and so forth. Thus, in the first mixing cell, this mixing process will ultimately result in a single-phase mixture.

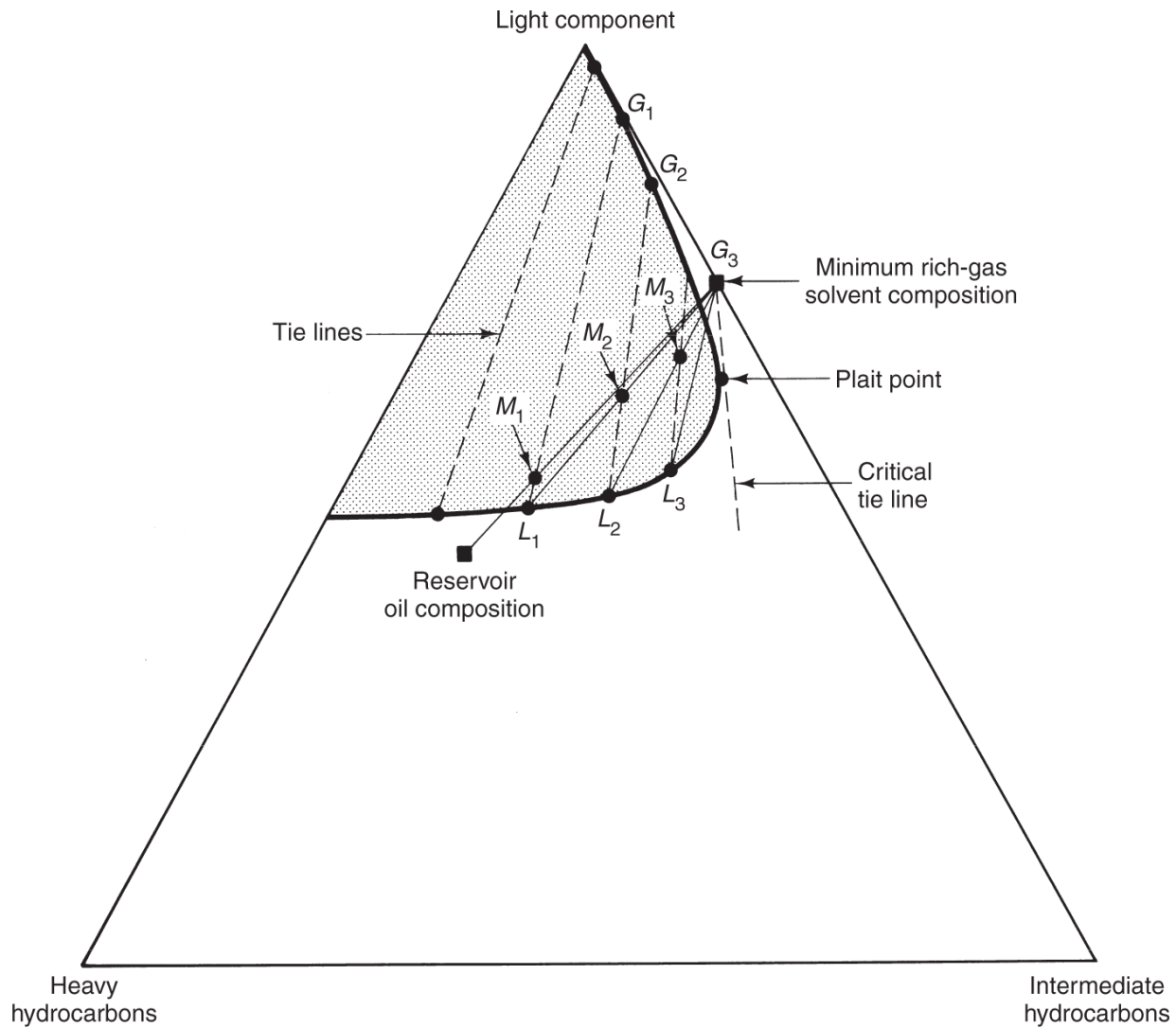


Fig. 7.14—Schematic of rich-gas drive displacement [adapted from Stalkup (1983)].

Because the gas phase has already passed through the first cell, miscibility now develops at the rear of the solvent-crude mixing zone as a consequence of the enrichment (mass transfer) of the liquid phase in intermediate components. The front of the mixing zone is a region of immiscible flow because of the continual contacting of the gas phases G_1 , G_2 , and so on with the crude (this is also true at the rear of the mixing zone in the vaporizing gas drive). The process shown in Fig. 7.14 is called the *rich gas-drive* process because intermediates were added to enrich the injected solvent. Because these intermediates condense into the equilibrium liquid phase, the process is also called a *condensing gas drive*.

Development of miscibility in successive mixing cells is a good way to explain the attainment of miscibility, but it should not be taken too literally. The number of mixing cells is not known, nor is it particularly easy to know. What is known is that miscibility, when it is attained, occurs a short distance from the injector.

[Fig. 7.15](#) shows a schematic of an immiscible displacement on a ternary diagram. The crude and solvent are in single-phase regions, but both are on the two-phase side of the critical tie line. Now the initial mixture M_1 in the first mixing cell will form gas G_1 , which will flow forward to form mixture M_2 , and so forth. This gas is being enriched in intermediate components at the leading edge (forward contacts) of the solvent/crude mixing zone as in a vaporizing gas drive. However, enrichment cannot proceed beyond the gas-phase composition given by the tie line for which the extension passes through the crude composition. At the forward contacts, there will be an immiscible displacement of the crude by a mixture on the limiting tie line. Back at the first mixing cell, liquid L_1 mixes with solvent to form mixture M_1 , just as in the condensing gas drive. The displacement is immiscible here because a single-phase solvent is displacing a two-phase mixture. The equilibrium liquid phase becomes progressively stripped of intermediates (L_{-1} , L_{-2} , and so on) until it reaches another limiting tie line. The displacement is entirely immiscible, then, at both the forward and reverse contacts. The intermediate components are in a gas phase near the production end of the permeable medium and in a liquid phase at the injection end. An immiscible flood entirely devoid of injected intermediates is called a *dry gas flood*.

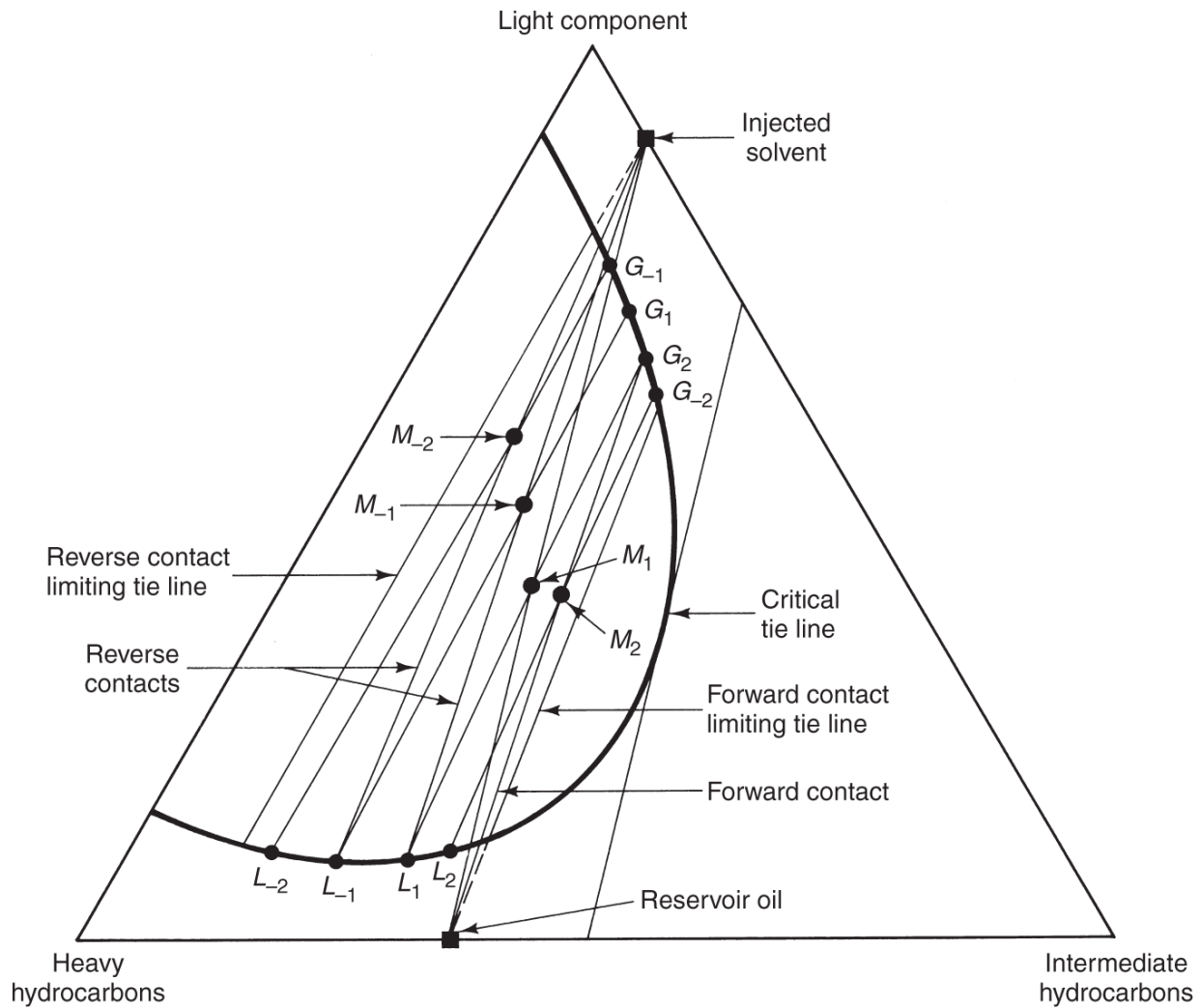


Fig. 7.15—Schematic of an immiscible displacement.

[Fig. 7.16](#) summarizes the classification of solvent displacements for ternary displacements. A dilution path (I_2-J_3) that does not pass through the two-phase region is a first-contact miscible displacement. A dilution path entirely on the two-phase side of the critical tie line constitutes an immiscible displacement (I_1-J_1). When initial and injected compositions are on opposite sides of the critical tie line, the displacement is either a vaporizing gas drive (I_2-J_1) or a condensing gas drive (I_1-J_2). The last two cases are developed or multiple-contact miscible displacement.

At the conditions shown in [Fig. 7.9](#), CO_2 displaces oil as a vaporizing gas drive. At comparable conditions, CH_4 ([Fig. 7.11](#)) and

N_2 ([Fig. 7.17](#)) are usually immiscible solvents. The CH_4 in [Fig. 7.11](#) can be converted into a condensing gas drive by adding approximately 35 mole % intermediates to natural gas.

The classification in the previous figures is mainly pedagogical. Complications introduced by real fluids include:

1. No real crude consists of only two components. To account for this discrepancy, we use various equations-of-state representations ([Chapter 4](#)) and more complex mixing-cell models (see Section 7.3.3), or, in the extreme, account for the multicomponent behavior through surrogates to the phase behavior, such as the minimum miscibility pressure (MMP) discussed in the following paragraphs.
2. Ternary diagrams are equilibrium representations at constant pressure and temperature. If the pressure were really constant, there would, of course, be no flow. What is being assumed here is that the pressure change is very small.
3. The considerations are entirely 1D, which means that interactions with heterogeneity are neglected. We say that the representation developed here gives the local behavior of the displacements.

Even with these qualifications, the solvent-flooding classifications can be corroborated by simple wave theory and experimental results (Metcalfe and Yarborough 1978).

As discussed in the preceding, ternary representations of solvent floods through multiple contacts of solvent with liquid or crude with equilibrium vapor are overly simplified. The basic idea in mixing-cell methods is to mix solvent and crude in repeated contacts, resulting in new equilibrium compositions. In the case of a vaporizing drive (lean gas injection), the intermediate component in the oil is vaporized into the more mobile vapor phase, and miscibility is developed when the vapor is repeatedly mixed with fresh oil, causing the equilibrium vapor composition to move toward the tie line that extends through the oil. Therefore, in vaporizing drives, the tie line that extends to the oil composition determines the development of miscibility because

forward contacts result in compositions closer to the critical point. Miscibility in vaporizing drives, therefore, is developed at the leading edge of the displacement.

For condensing drives (enriched gas composition), the intermediate component in the solvent is condensed into the oil. Therefore, the tie line that extends through the solvent (gas) composition determines miscibility. Miscibility for condensing drives is developed at the trailing edge of the displacement because backwards contacts result in equilibrium compositions closer to the critical point.

Dilution path

Type

I_1-J_1	Immiscible
I_1-J_2	Multiple contact (developed) Miscibility (rich gas)
I_2-J_1	Multiple contact (developed) Miscibility (vaporizing gas)
I_2-J_3	First-contact miscible

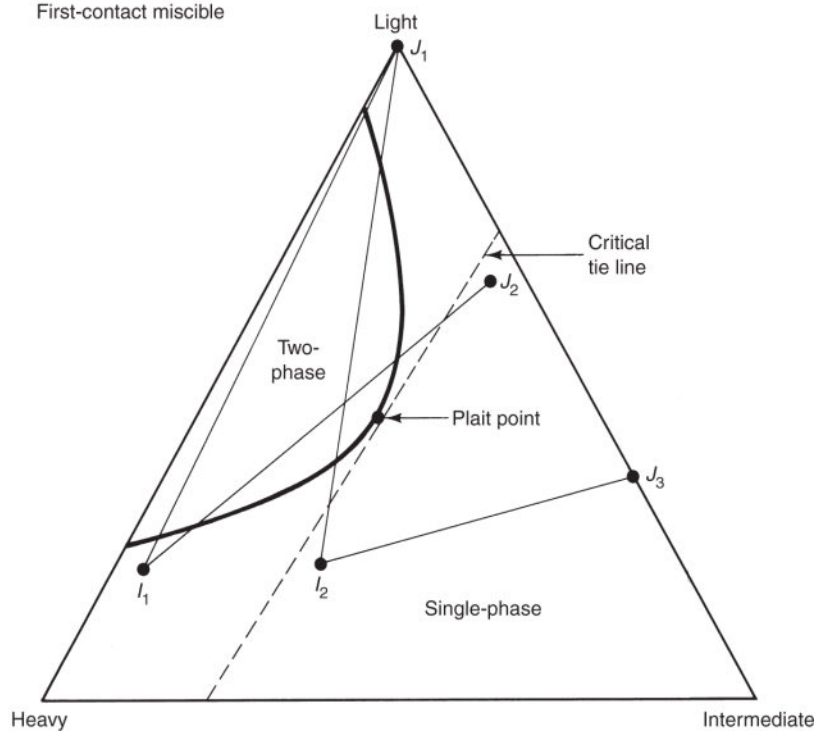


Fig. 7.16—Summary of miscibility and developed miscibility.

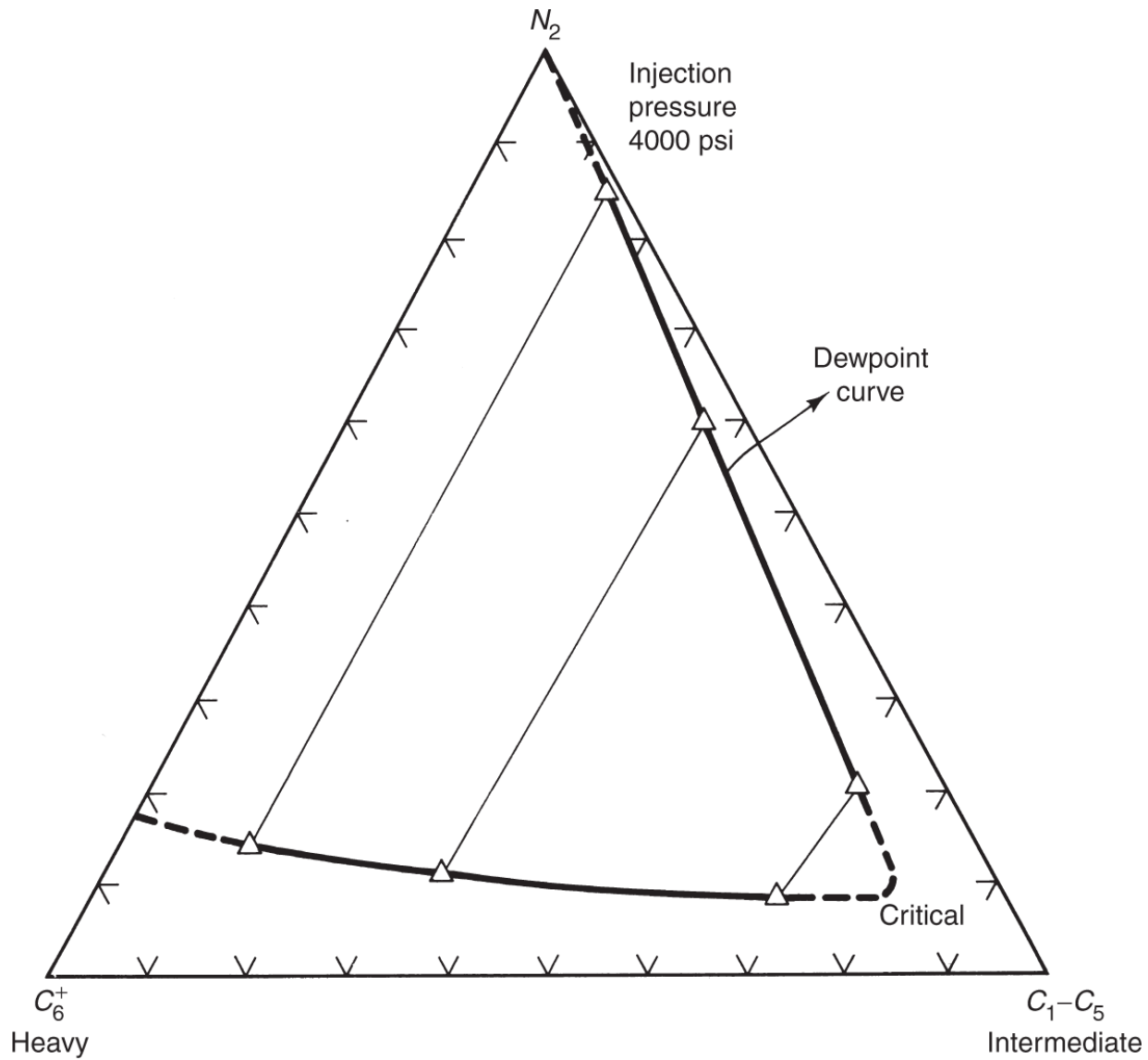


Fig. 7.17—Ternary diagram for N_2 /crude-oil mixture (Ahmad et al. 1983).

7.3.3 Nonternary Mixing Cells. The procedure for multiple contacts in ternary displacements can be extended quantitatively to displacements with any number of oil components with little additional work (Ahmadi and Johns 2011). This approach also enables treatment of all types of developed solvent floods in one calculation and, furthermore, reveals that there are combinations of the preceding simple ternary classifications in real mixtures.

The extended multiple mixing-cell method begins with two cells and increases in number of cells as contacts proceed. In other words, all contacts are retained instead of keeping only the forward and backward contacts. The number of cells is increased until the tie-line lengths in each cell are relatively constant; the length of the tie line is $\left[\sum_{i=1}^{N_c} (y_{i2} - y_{i3})^2 \right]$. Whichever tie line approaches zero length first determines the type of miscibility (or immiscibility) developed, because a zero tie-line length corresponds to a cell passing through a critical point. In most multicomponent displacements, the controlling tie line is not the tie line that extends through the oil or solvent compositions, as given by ternary representations.

The mixing-cell procedure begins with two cells at fixed temperature and pressure, where the injection solvent is located in the upstream cell and the reservoir fluid in the downstream cell (see [Fig. 7.18](#)). The reservoir oil (of composition y_{i2}^0 , the superscript being the mixing-cell number) and the injection vapor (y_{i3}^0) can be mixed in any mole fraction desired as long as the resulting overall composition is within the two-phase region or its region of tie-line extensions. The equilibrium compositions are then calculated by the methods given in [Chapter 4](#). The resulting equilibrium vapor moves ahead of the equilibrium liquid because solvent has been injected. This is the first contact.

The second series of contacts contains both an upstream and downstream contact (see [Fig. 7.18](#)). The downstream contact mixes the equilibrium vapor (y_{i3}^1) with fresh oil, and the upstream contact mixes the equilibrium liquid (y_{i2}^1) with fresh injection gas. Two new sets of equilibrium liquid and vapor phases result from these flash calculations, so that there are now six cells, including the reservoir oil and the solvent. This completes the second contact.

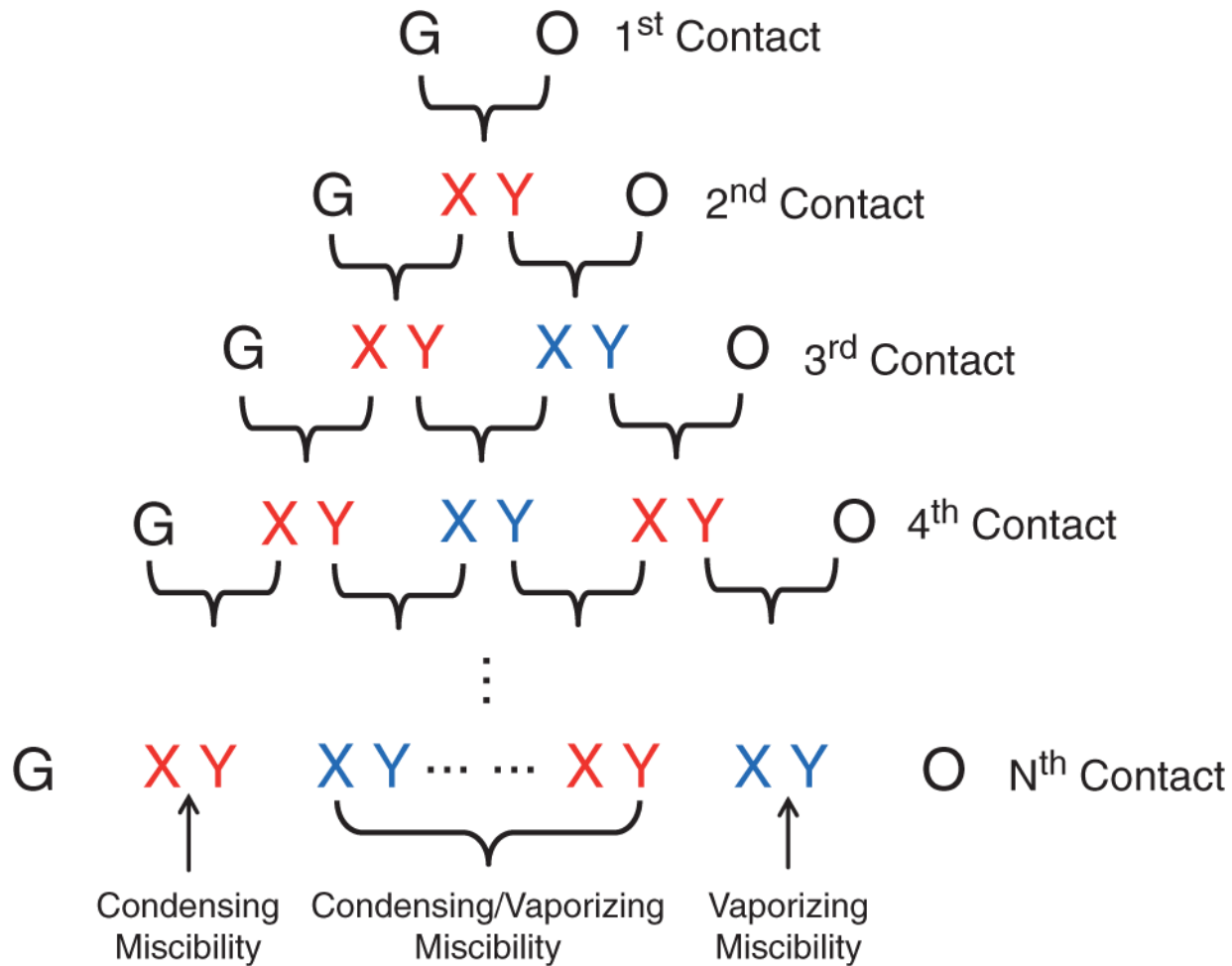


Fig. 7.18—Multiple mixing-cell method in which all contacts are retained [after Ahmadi and Johns (2011)].

We then make additional contacts until all the key tie lines develop. Therefore, after N contacts, we have a total of $2N+2$ cells. The flash calculations in this procedure are more numerous than those for simple ternary representations, but keeping track of the calculations is fairly straightforward. Moreover, there is no need to calculate transport properties as there would be in a flow simulation.

We illustrate the mixing-cell approach for a displacement of three-component oil (CH_4 , C_4 , and C_{10}) by a two-component solvent (CH_4 , CO_2) at a temperature of 160°F . The input parameters used to calculate the tie lines can be found in Orr and Silva (1983). For such a displacement, there are three key tie lines: the oil tie line, the solvent tie line, and another key tie line called the crossover tie line.

[**Fig. 7.19**](#) presents four profiles of the key tie-line lengths for a displacement at 2,000 psia (approximately 300 psia below the MMP) as a function of the cell number and the number of contacts made. As shown, the three key tie lines develop as the contacts proceed. The key tie lines are nearly fully developed after 50 contacts, although after 250 contacts, all three key tie lines become essentially constant. The crossover tie line for this displacement controls miscibility because its tie-line length is shorter than that of either the gas or oil tie line.

This example displacement has features of both condensing and vaporizing displacements (CV), and the separation between these two mechanisms is aptly named the crossover tie line. The leading portion of the displacement (the downstream cells) condenses CO₂ into equilibrium oil, causing oil swelling and viscosity reduction. The trailing portion (upstream cells) vaporizes the next most volatile component, C₄, into the equilibrium vapor phase from the liquid phase.

[**Figs. 7.20**](#) and [**7.21**](#) illustrate the miscibility behavior further using equilibrium flash-vaporization ratios or K-values $K_{32}^i = y_{i3}/y_{i2}$. The K-values approach unity when the compositions pass through the critical mixture, indicating the development of miscibility. Therefore, in CV drives, miscibility is developed in the middle of the displacement. [**Fig. 7.21**](#) emphasizes this point for the same fluid displacement near its MMP. For CV drives, miscibility occurs in a cell somewhere between the oil and gas tie lines, whereas for vaporizing drives, miscibility occurs in the oil tie line (the farthest downstream tie line) and for condensing drives, in the gas tie line (the farthest upstream tie line).

The approach described here to calculate the MMP from a mixing-cell model can be significantly enhanced to speed up the technique and to make it more robust (Ahmadi and Johns 2011). Ahmadi et al. (2011) showed that other key tie lines can exist that can control miscibility for some solvent floods, but in either case, the mixing-cell method detects such anomalies.

Johns and Orr (1996) showed that there are $N_C - 3$ crossover tie lines for N_C components, any of which can determine miscibility. As long as any crossover tie line controls miscibility, the displacement type is combined condensing and vaporizing. These authors also demonstrated, for a displacement of 10-component oil by CO₂, that components are selectively volatilized according to their K-values. Volatile components in the oil are more easily vaporized into the vapor phase, leaving behind slow-moving evaporation fronts for the heavier components. Such findings are similar to selective adsorption of components in chromatographic theory. Orr (2007) illustrates these chromatographic-like separations for a variety of gas/oil displacements.

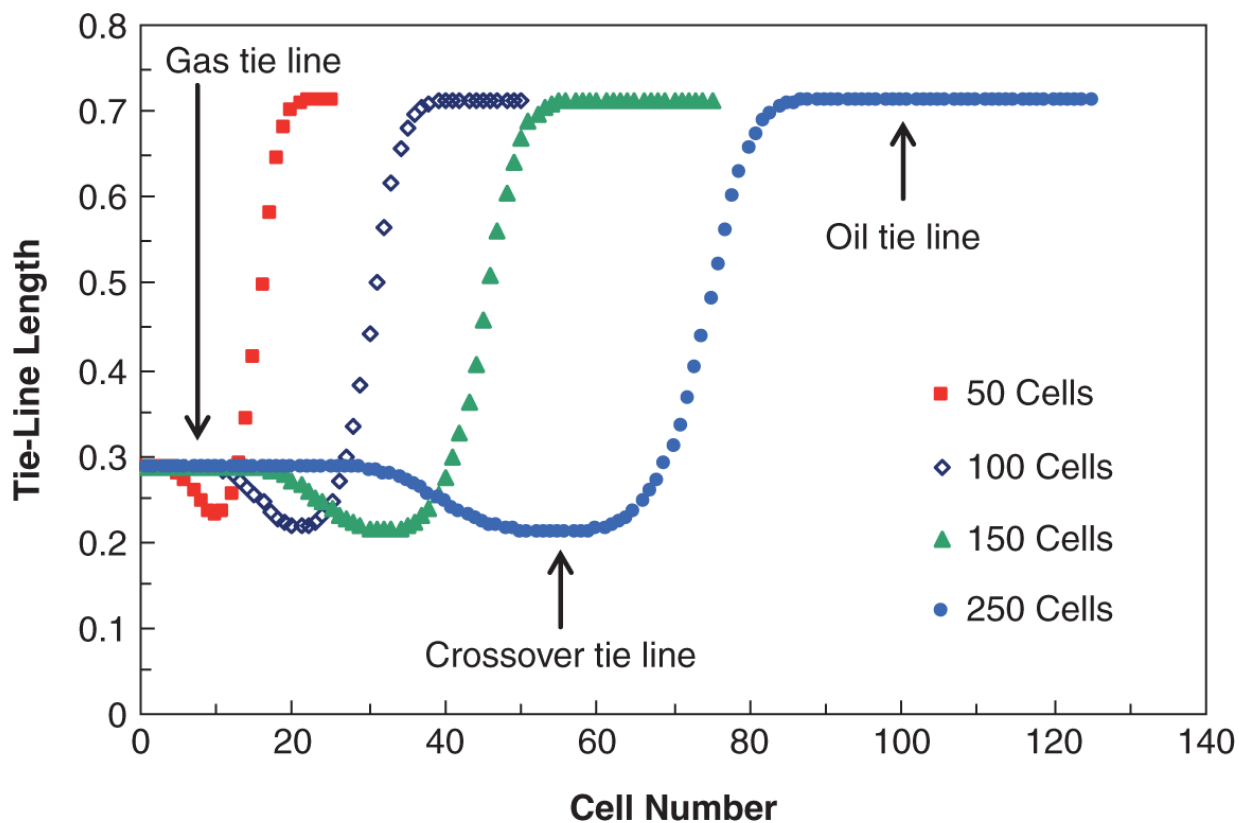


Fig. 7.19—Development of tie-line lengths with increasing contacts from mixing-cell model of the four-component displacement at 2,000 psia (Ahmadi and Johns 2011). More contacts results in more mixing cells when all forward, backwards, and intermediate contacts are retained.

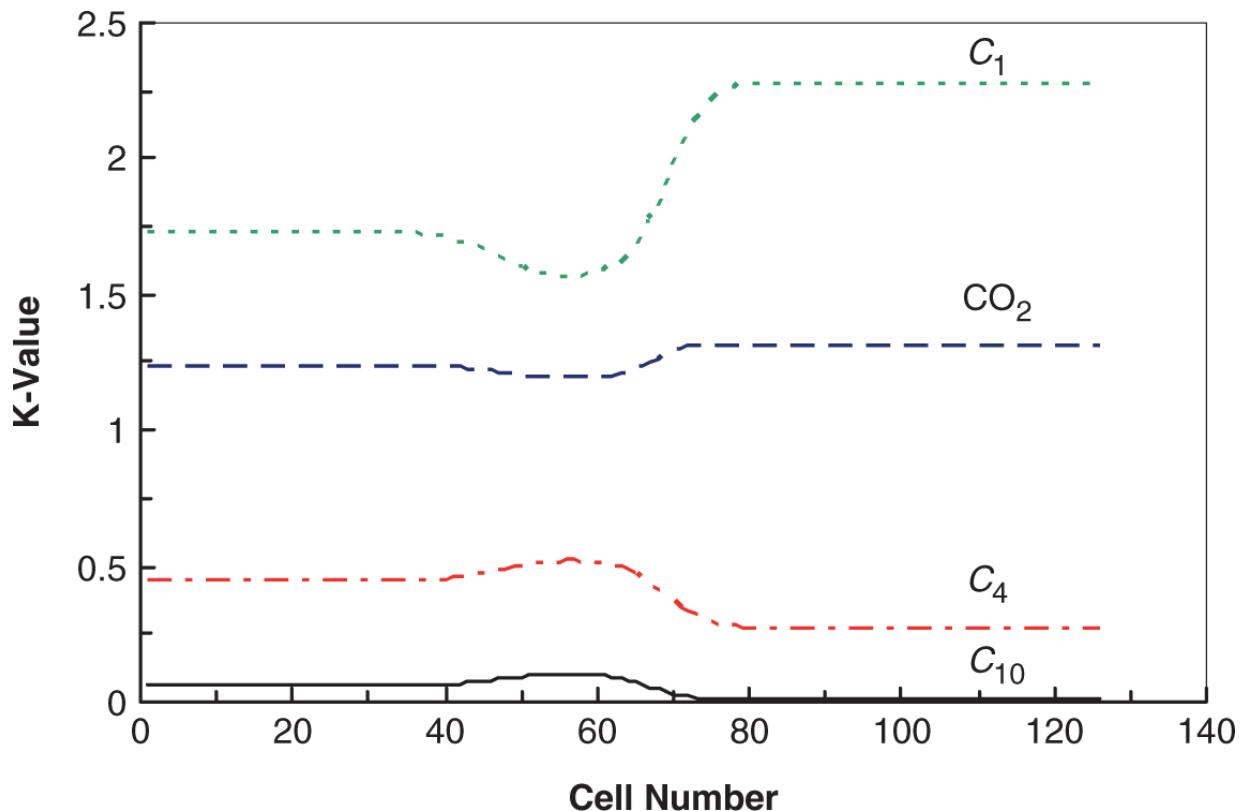


Fig. 7.20—K-values for shortest tie line from mixing-cell model of four-component displacement (Ahmadi and Johns 2011).

7.3.4 Immiscible Displacements. Immiscible displacements have merit because pressure requirements are not large, the solvents are usually less expensive, and they can recover some oil. The principal recovery mechanisms for immiscible solvents are (1) a limited amount of vaporization and extraction, (2) oil viscosity reduction, (3) oil swelling, (4) solution gas drive during pressure decline, and (5) interfacial tension lowering. All immiscible displacements recover oil in this manner, although the data showing these effects are most complete on CO_2 -immiscible displacements (Simon and Graue 1965). It should be emphasized that an immiscible flood is not strictly immiscible because some mass transfer takes place between phases. The magnitude of this mass transfer depends on how close the reservoir pressure is to the MMP.

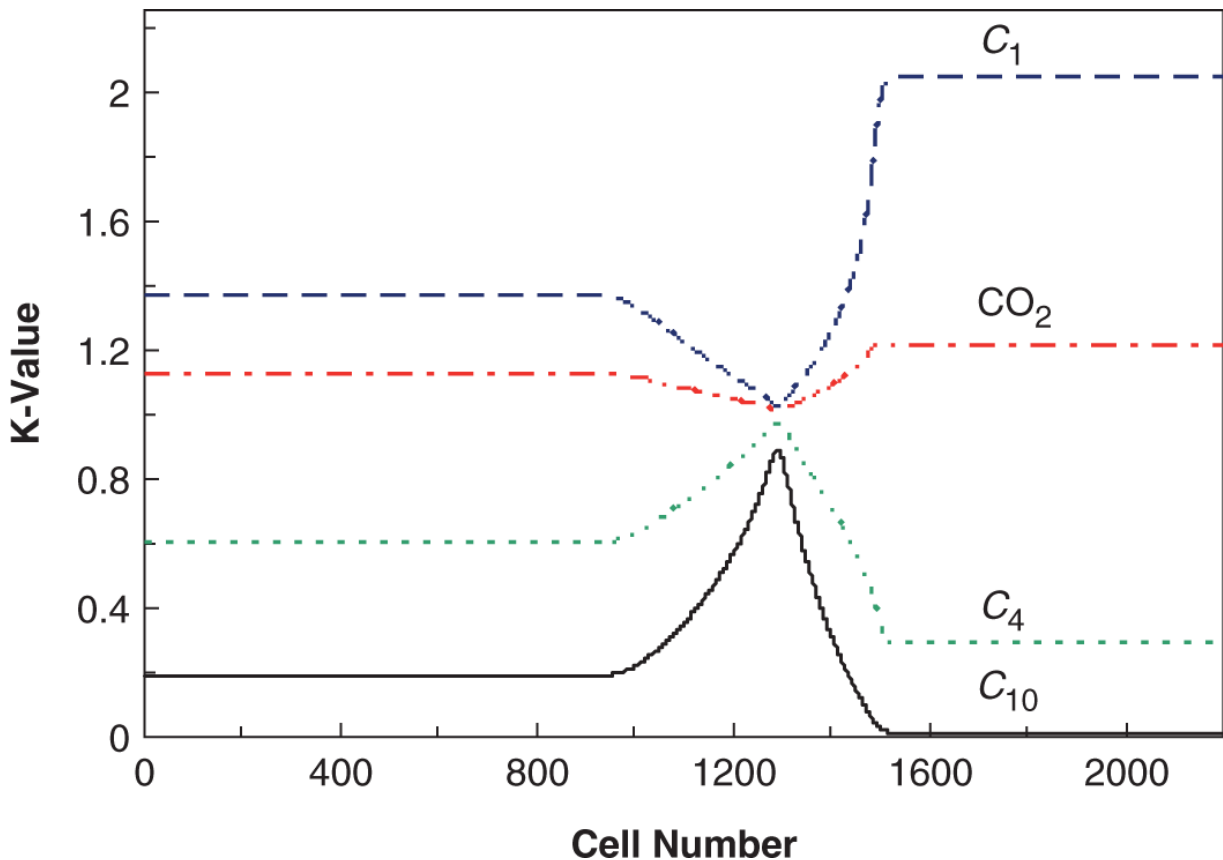


Fig. 7.21—X-values for shortest tie lines lengths from mixing-cell model near the MMP for the four-component displacement (Ahmadi and Johns 2011).

[Figs. 7.22 through 7.24](#) show experimental data that illustrate immiscible recovery mechanisms 1 through 3. [Fig. 7.22a](#) shows the solubility of CO_2 in oil vs. temperature and saturation pressure for a crude with a Universal Oil Products (UOP) characterization factor (K) of 11.7. This factor is the ratio of the cube root of the average boiling point in degrees R to the specific gravity. It can be related to API gravity and viscosity (Watson et al. 1935). The saturation pressure is the bubblepoint pressure; hence, [Fig. 7.22a](#) gives the maximum solubility of CO_2 at the indicated temperature and pressure. [Fig. 7.22b](#) corrects the solubility data to other characterization factors. [Fig. 7.23](#) gives the viscosity ratio of a CO_2 -swollen crude (μ_m in this figure) to the CO_2 -free crude (μ_2) as a function of pressure. For moderate saturation pressures, the viscosity reduction is pronounced, particularly for large crude viscosities.

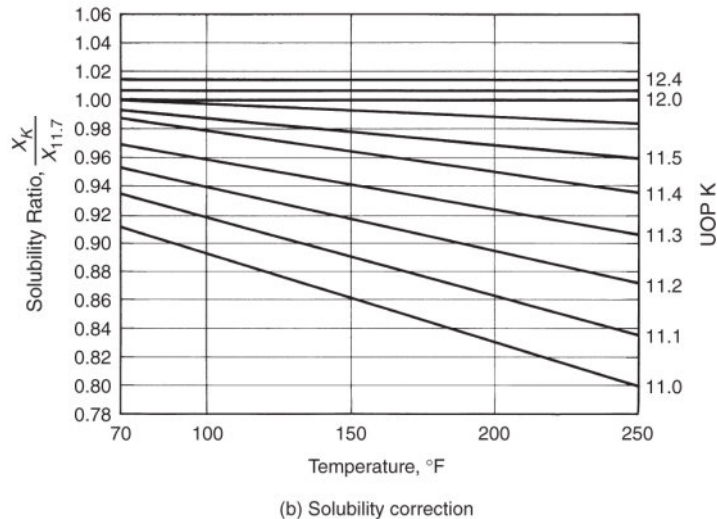
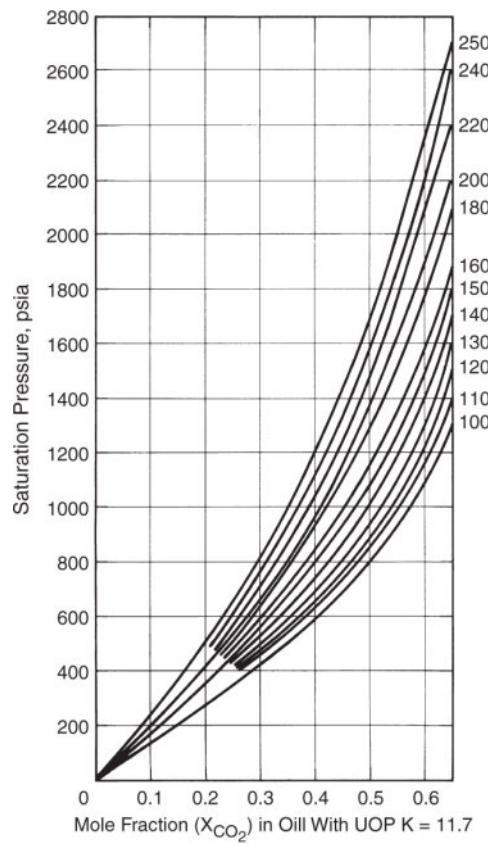


Fig. 7.22—Solubility (mole fraction) of CO_2 in oils as a function of UOP number (Simon and Graue 1965).

[Fig. 7.24](#) illustrates the oil-swelling mechanism by giving crude swelling factors correlated with ratios of molecular weight to standard density (g/cm^3). Similar data on the swelling of crude by N_2 are given by Vogel and Yarborough (1980).

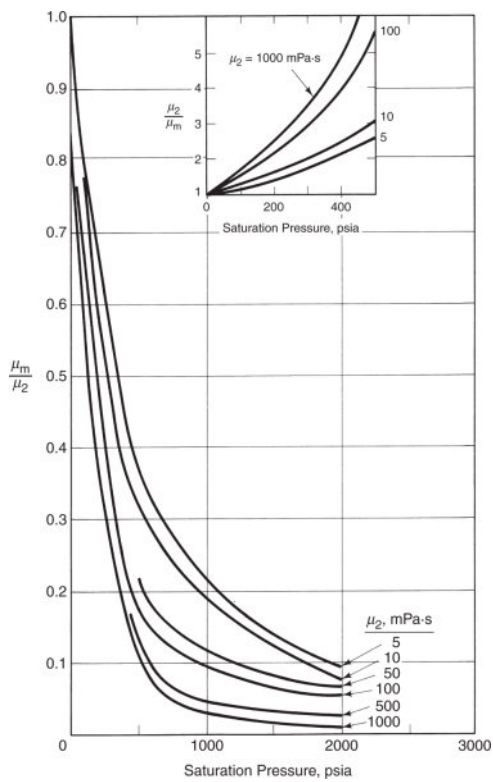


Fig. 7.23—Viscosity correlation charts for CO₂/oil mixtures (Simon and Graue 1965).

Example 7.3. Figs. 7.22 through 7.24 are to be used together. Let us estimate the CO₂ solubility, oil-viscosity reduction, and swelling factor for a crude oil at 389 K (150°F) and 8.2 MPa (1,200 psia). Recall that we are calculating the properties of a liquid hydrocarbon phase that is immiscible with CO₂. Therefore, the overall CO₂ mole fraction must be large enough to be in the two-phase region of the ternary diagram. The relevant physical properties of the crude are as follows: molecular weight = 130, UOP characterization factor K = 11.8, specific gravity = 0.70, normal boiling point = 311 K (100°F), and viscosity = 5 mPa·s. This gives a CO₂ solubility of 55 mole percent from Fig. 7.22. This solubility causes the oil viscosity to decrease to 1 mPa·s, from Fig. 7.23, and the oil to swell by approximately 33%, from Fig. 7.23. [For additional data on the properties of crude containing immiscible solvents, see Holm (1961), Parkinson and de Nevers (1969), Holm and Josendal (1974), and Tumasyan et al. (1960).]

7.4 Solvent-Water Properties

The solubility of CO₂ in water is a function of temperature and pressure. See McRee (1977) for the effect of brine salinity. [Fig. 7.25](#) shows this solubility as a solution gas/water ratio.

The data in [Fig. 7.25](#) give the CO₂ solubility, the maximum that the solution can contain, at the indicated temperature and pressure; hence, the horizontal axis is actually saturation pressure. The data are entirely equivalent to the data in [Fig. 7.22](#) for CO₂/oil mixtures. The solution gas/water ratio can be readily converted into a mole fraction.

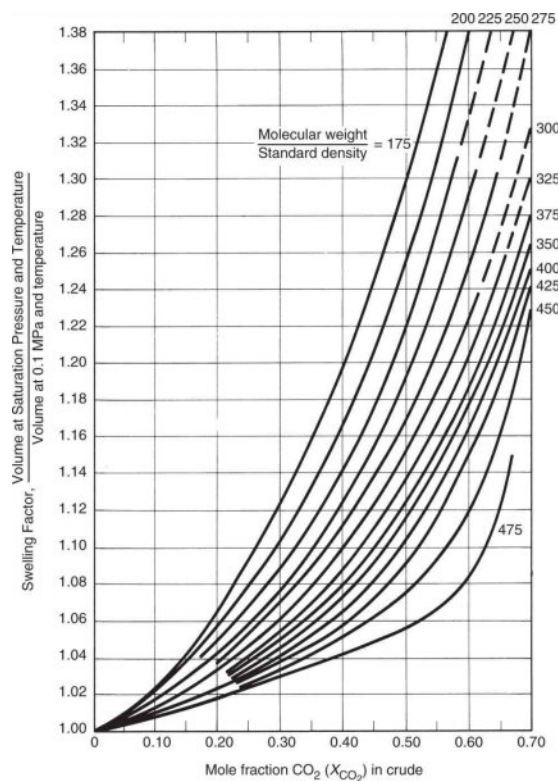


Fig. 7.24—Swelling of oil as a function of mole fraction of dissolved CO₂ (Simon and Graue 1965).

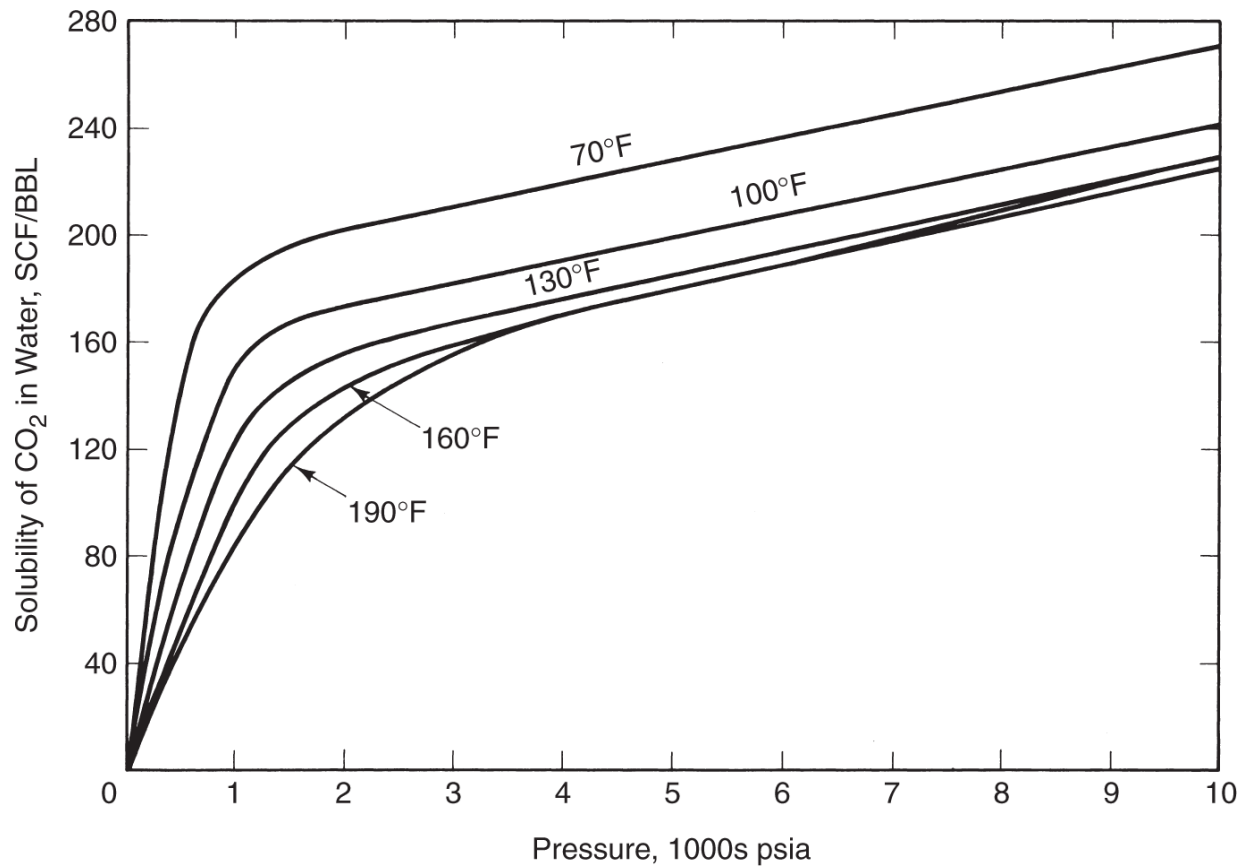


Fig. 7.25—Solubility of CO_2 in water (Crawford et al. 1963).

Example 7.4—Mole Fractions of CO_2 in Water. That the solubilities in Fig. 7.25 seem large may be a consequence of the units used. Calculate the mole fraction of CO_2 in water when $R_s = 260 \text{ SCF/stb}$. The molecular weights of CO_2 and water are 44 and $18 \text{ lb}_m/\text{lb-mol} = 18 \text{ Daltons}$, and the density of CO_2 -saturated water is $\rho_1 = 1 \text{ g/cm}^3$.

This is an exercise in units conversion and recognition of quantities. Begin with the water conversion,

$$\left(260 \frac{\text{SCF CO}_2}{\text{stb water}} \right) \left[\frac{1 \text{ stb}}{5.614 \text{ ft}^3} \frac{1 \text{ ft}^3}{(30.5 \text{ cm})^3} \frac{1 \text{ cm}^3}{1 \text{ g}} \right] \left(\frac{454 \text{ g}}{1 \text{ lb}_m} \frac{18 \text{ lb}_m}{1 \text{ lb-mole}} \right) = 13.4 \frac{\text{SCF}}{\text{lb-mole water}}$$

and then the CO_2 conversion,

$$\left(13.4 \frac{\text{SCF CO}_2}{\text{lb-mole water}} \right) \left(\frac{1 \text{lb-mole CO}_2}{379.4 \text{ SCF CO}_2} \right) = 0.035 \frac{\text{lb-mole CO}_2}{\text{lb-mole water}}.$$

The last expression is just the ratio of mole fractions:

$$0.035 \frac{\text{lb-mole CO}_2}{\text{lb-mole water}} = \frac{x_3}{x_1} = \frac{x_3}{1 - x_3}$$

or

$$x_3 = \frac{0.035}{1 + 0.035} = 0.034.$$

The apparently large solubility in water is less than 4 mole percent.

CO_2 is the only solvent with appreciable solubility in water over EOR temperature and pressure ranges (Culberson and McKetta 1951). The CO_2 increases the viscosity of water slightly (Tumasyan et al. 1960) and increases the density (Parkinson and de Nevers 1969). The increase in density is paradoxical because a gas-like solvent added to a liquid normally decreases density. The changes are small, but nevertheless enough to induce instabilities in density-driven flows (Farajzadeh et al. 2013).

7.5 Solvent Phase-Behavior Experiments

Solvent phase behavior does not solely determine the character of a solvent flood, but it is of such fundamental importance that we devote a section to some of the common experiments used to measure phase behavior. This discussion leads naturally to the most frequently reported characteristic of solvent phase behavior—the MMP. All of these are surrogates to estimate the most important feature of a solvent flood—the approach to miscibility—without the labor and expense needed to measure the entire range of phase behavior.

7.5.1 Single Contact. In a single-contact experiment, a known amount of solvent is charged into a transparent pressure cell

containing a known amount of crude oil. After equilibrium is established at the desired temperature and pressure, a small amount of each phase is withdrawn. The phase compositions represent the ends of an equilibrium tie line. Only the composition of one phase need be measured because the composition of the other phase can be calculated from material balance. Single-contact experiments are useful for measuring P/z diagrams because the pressure can be changed, at fixed overall composition, by changing the cell volume. If the experiment is repeated for various amounts of solvent, the single-contact experiment traces a dilution path on a ternary diagram between the solvent and the crude.

7.5.2 Multiple Contact. The multiple-contact experiment duplicates the process described in Section 7.3 under miscible process classification for ternary representations. In it ([Fig. 7.26](#)), known amounts of solvent and crude are charged to a transparent pressure cell as in the single-contact experiment, but after equilibration, the upper phase is decanted and mixed in a second cell with fresh crude. The lower phase in the cell is similarly mixed with fresh solvent. The upper phase is repeatedly decanted in this manner to simulate, discretely, the mixing that would take place at the forward contacts of the solvent/crude mixing zone. The successive mixings with the lower phase are the reverse contacts. All contacts are at a fixed temperature and pressure.

From [Fig. 7.26](#), which shows the multiple-contact experiment analogous to [Fig. 7.13](#), the solvent enrichment in the forward contacts or the crude enrichment in the reverse (backwards) contacts can cause one of the phases to disappear. This is exactly what is predicted by the arguments used in the previous section. A single-phase cell in the forward contacts indicates a vaporizing gas drive; in the reverse contacts, a condensing gas drive; and two or more phases in all contacts, an immiscible process. If the original cell is single-phase for all combinations of solvent and crude oil, the process is first-contact miscible.

The experiment depends somewhat on the initial charges to the first cell, and, therefore, the results are no more than indications of

process classification. If phase compositions are measured at every step, the binodal curve and tie lines on a ternary diagram can be established. Agreement between single- and multiple-contact experiments substantiates the pseudocomponent representation of the multicomponent equilibria.

Both single- and multiple-contact experiments place a premium on visual observations, but with careful selection of the initial volumes, these experiments are convenient ways to determine complete ternary equilibrium data. Orr and Silva (1982) have proposed a method to measure phase behavior through continuous contacting.

7.5.3 Slim Tubes. Filling the gap between the static measurements described previously and corefloods are *slim-tube* experiments. These experiments are crude displacements by solvent, in the absence of water, at fixed temperature. The permeable medium consists of beads or unconsolidated sands packed in tubes of very thin cross sections and frequently long lengths. The displacements are run with a fixed pressure at one end of the system, and because the permeability of the medium is high, pressure gradients are negligible.

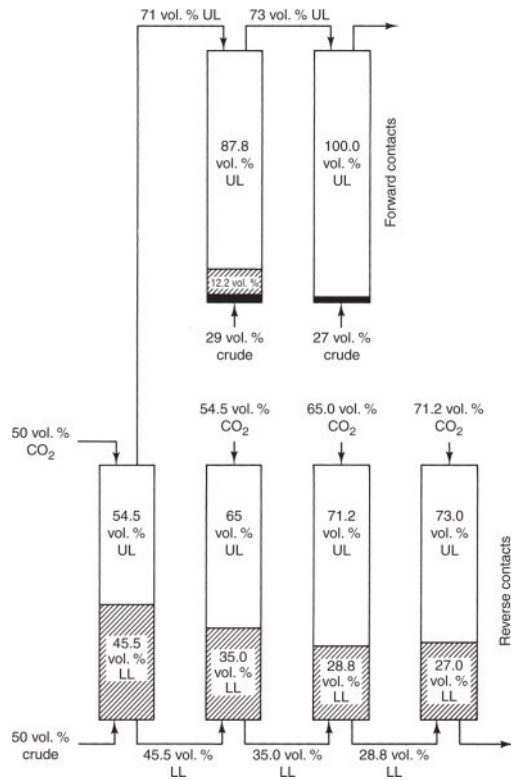


Fig. 7.26—Multiple-contact experiment at 105°F (2,000 psia) (Gardner et al. 1981). UL means upper liquid, LL lower liquid. The small black region at the bottom of the top figures is a precipitate.

The overriding feature of slim-tube experiments is the large aspect ratio (length-to-diameter ratio). This is intended to suppress viscous fingering because small wavelength perturbations will not form when the tube diameter is smaller than the critical wavelength (see Section 6.8). Even if a finger forms, it tends to be suppressed by lateral dispersion, as in the Taylor's problem discussed in [Chapter 5](#). Slim-tube measurements should be insensitive to longitudinal dispersion because the importance of this phenomenon decreases with medium length in homogeneous media.

The slim-tube experiment, then, is designed to provide an unambiguous measure of solvent-displacement efficiency. However, because of both the highly artificial nature of the permeable medium and the experimental conditions (no water), the displacement efficiency the experiment gives is not realistic. The results are best regarded as a dynamic (or surrogate) measure of phase-behavior

properties. The slim tube is essentially a physical realization of the mixing-cell experiment discussed previously.

7.5.4 MMP. Although effluent compositions can be monitored using a slim-tube displacement, by far the most common information derived from these experiments is the MMP. Because solvent miscibility increases with pressure, ultimate oil recovery should also increase with pressure. This in fact happens, but there is a pressure above which further pressure increase causes only a minimal increase in oil recovery. The pressure at which oil recovery levels out is the MMP, or the minimum *dynamic* miscibility pressure. MMP is variously defined as

- The pressure at which the oil recovery at $t_D = 1.2$ PV of CO₂ injected is equal to or very near the maximum final recovery obtained in a series of tests (Yellig and Metcalfe 1980)
- The pressure that causes 80% oil recovery at CO₂ breakthrough and 94% recovery at a gas-to-oil ratio of 40,000 SCF/STB (Holm and Josendal 1974)
- The pressure that causes 90% oil recovery at $t_D = 1.2$ HCPV of CO₂ injected (Williams et al. 1980).

A more exact definition of the MMP is the pressure at which the displacement efficiency is 100% in the absence of dispersion; this is a thermodynamic definition in that it relies only on the interaction of flow and phase behavior. One advantage of this definition is that any decrease in recovery at the MMP caused by dispersion or other physical processes can be examined separately. Others (Perry 1978; Yellig and Metcalfe 1980) emphasize the qualitative nature of the miscibility pressure determination. The importance of the exact definition is probably small; all definitions show the same trends in correlations.

Two other reliable methods are the method of characteristics (MOC) and mixing-cell methods, as previously discussed in Section 7.3. MOC methods determine the key tie lines in a dispersion-free displacement and, therefore, measure the exact MMP (Johns et al.

1993; Orr 2007). The MMP from MOC is the pressure at which one of the key tie lines first intersects a critical point (becomes a tie line of zero length). The MOC method relies on accurate fluid characterizations using a tuned cubic EOS (Yuan and Johns 2005), but takes only seconds to calculate, so that many MMP estimates can be made for various solvent compositions. The EOS should be properly tuned to available PVT data, such as swelling tests, multicontact tests, and available slim-tube experiments, as described by Egwuenu et al. (2008). A disadvantage of MOC is that the correct and unique set of key tie lines is currently difficult to find, especially for gas-stream mixtures. The accuracy of the MOC-predicted MMP depends heavily on an accurate equation-of-state characterization of the fluids.

Mixing-cell methods (see Section 7.3.3) can also give accurate MMP predictions, but like MOC, they depend on the accuracy of EOS fluid characterization. The advantage of mixing-cell methods over the MOC is that repeated contacts of equilibrium gas and oil with fresh gas and oil are made until the key tie lines are automatically found. The mixing-cell method is computationally slower than the MOC, but it offers a good alternative and check of the MOC results, especially for gas mixtures.

Correlations based on measured MMP from slim-tube experiments or other data are also useful because they are easy to use. One disadvantage of correlations, however, is that the correlations are typically reliable only if the solvent flood under consideration is similar to the data that were used to develop the correlation. Many correlations are based solely on West Texas crudes because solvent flooding was initiated in that area.

Several other methods can also be used, such as the rising bubble or vanishing interfacial-tension tests, but these methods are not as established because they do not have the proper interactions of flow with phase behavior necessary to develop multicontact miscibility (Jessen and Orr 2008). Therefore, MMP should be estimated using only the MOC, mixing-cell methods, slim-tube experiments, and 1D slim-tube simulations. Slim-tube experiments should always be performed because they serve as calibration data for other methods.

The results of slim-tube experiments give the minimum pressure necessary for the displacement to develop miscibility. Therefore, the MMP corresponds to the pressure at which one of the key tie lines passes through a critical point. This pressure is considerably less than that required for complete or first-contact miscibility (compare the MMP pressures with the maximum pressures on P/z diagrams). This is the origin of the plateau on the oil-recovery vs. pressure plot: any further pressure increase does not increase oil recovery significantly because above the MMP, the displacement will tend from developed to first-contact miscibility. These observations are also supported by compositional measurements in which the properties (viscosity, density, and composition) of phases produced below the MMP approach one another as the MMP is approached.

The CO₂ MMP is determined by temperature, pressure, solvent purity, and molecular weight of the heavy fraction of the reservoir crude. MMP increases with temperature and intermediate content of the crude. Holm and Josendal (1974; 1982) noted that the development of miscibility for CO₂ solvents is the result of extracting hydrocarbon components into a CO₂-rich phase. Therefore, at a given temperature and crude composition, there must be sufficient compression of the solvent to promote miscibility with the crude. This solvency is manifested by the CO₂ density at the temperature of the test.

[Fig. 7.27a](#) shows the CO₂ density required to develop miscibility at a given temperature with the C₅–C₃₀ percentage of the C₅⁺ crude fraction. The CO₂ density can be connected to MMP using [Fig. 7.27b](#). CO₂ MMP is affected by the type of hydrocarbons (aromatic or paraffinic) in the crude, but to a lesser degree than by temperature and CO₂ density (Monger 1985).

Several studies have presented determinations of MMP for impure CO₂. [Fig. 7.28](#) shows the results of the effects of N₂, CH₄, H₂S, and H₂S-CH₄ mixtures on the CO₂ MMP. Methane and particularly nitrogen increase the CO₂ MMP, whereas H₂S decreases it. Whether an impurity increases or decreases the MMP depends on whether the

solvency of the solvent has been enhanced. Solvency is improved (MMP decreases) if CO₂ is diluted with an impurity for which the critical temperature is higher than that of CO₂. Solvency deteriorates (MMP increases) if CO₂ is diluted with an impurity with a critical temperature lower than that of CO₂. Compare the trends in [Fig. 7.28](#) with the critical temperatures in [Fig. 7.2](#).

The preceding idea of solvency can be used to estimate the MMP of an impure CO₂ solvent. Sebastian et al. (1985) have correlated the diluted CO₂ MMP by the following:

$$\frac{P_{MM}}{(P_{MM})_{CO_2}} = 1.0 - \left(2.13 \times 10^{-2}\right)(T_{pc} - T_c) + \left(2.51 \times 10^{-4}\right)(T_{pc} - T)_c^2 - \left(2.35 \times 10^{-7}\right)(T_{pc} - T_c)^3, \quad \dots \quad (7.1)$$

where $T_{pc} = \sum_i T_{ci}y_i$ is the pseudocritical temperature of the mixture and y_i is the mole fraction of species i in the solvent. The denominator of the left side of Eq. 7.1 can be estimated from [Fig. 7.28](#). [For other correlations, see Johnson and Pollin (1981).] No MMP correlation is particularly accurate; errors as much as 0.34 MPa (50 psia) are common. The correlation by Sebastian et al. (1985) is based solely on oil from the Levelland field of West Texas. See Johns et al. (2010) and Shokir (2007) for other methods of correlation.

7.5.5 Minimum Enrichment Correlations for Condensing Gas Drives.

For a dry gas process, slim-tube results will give an estimate of the amount of intermediates that must be added to develop miscibility in a condensing gas drive. Such experiments were precursors to the MMP experiments (Benham et al. 1961). The oil-recovery plot would consist of several experiments, each with a successively richer injected solvent, but each at constant pressure. When the solvent composition coincided with the tie-line extension (through the reverse contacts), oil recovery would cease to increase as the solvent became richer in intermediates.

Fig. 7.29 is one of several plots from Benham et al. (1961) that show the maximum methane concentration permissible in an LPG solvent that will develop miscibility with the subject crude. These authors correlated the maximum dilution (or minimum enrichment) with temperature, pressure, molecular weight of the intermediate component in the solvent, and molecular weight of the C_5^+ fraction in the crude. The minimum dilution increases with decreasing C_5^+ molecular weight, pressure, and temperature and increases with increasing intermediate molecular weight.

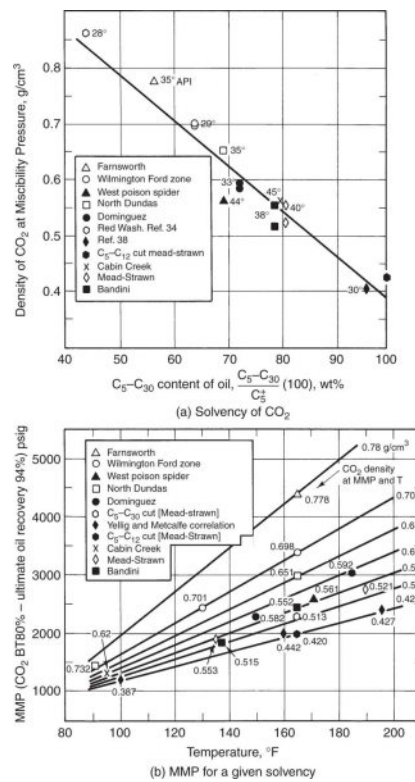
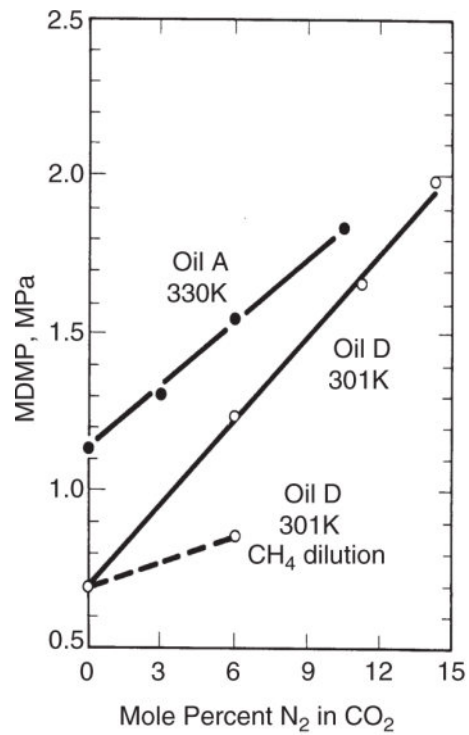
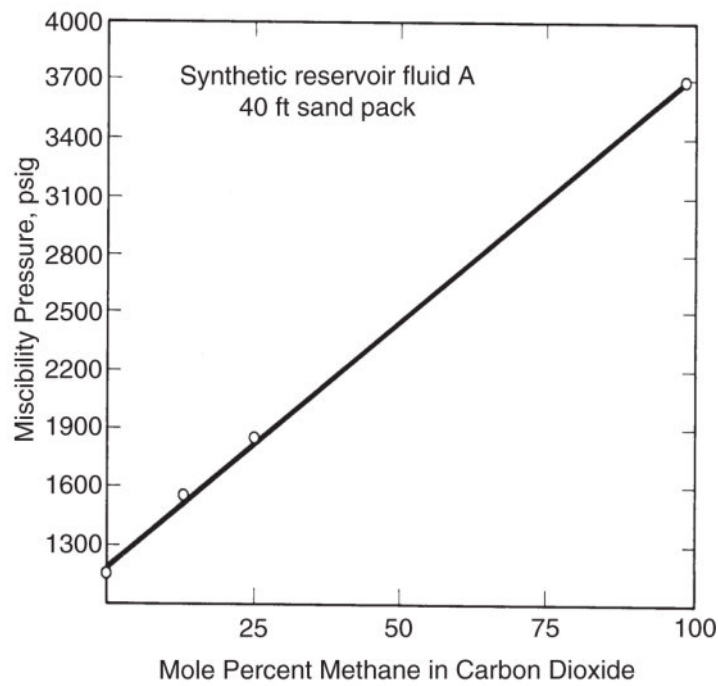


Fig. 7.27—Density of CO_2 required for miscible displacement of various oils at 90°F to 190°F (Holm and Josendal 1982).



(a) N_2 and CH_4



(b) CH_4

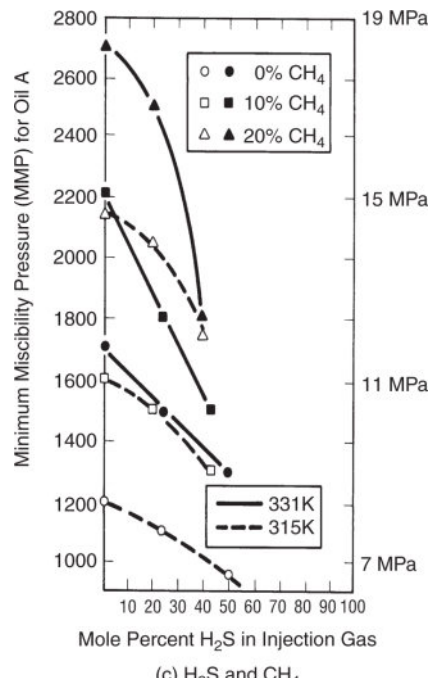


Fig. 7.28—Effect of impurities on CO_2 minimum-miscibility pressure [(a) Johnson and Pollin 1981; (b) Whitehead et al. 1981; (c) Metcalfe 1981].

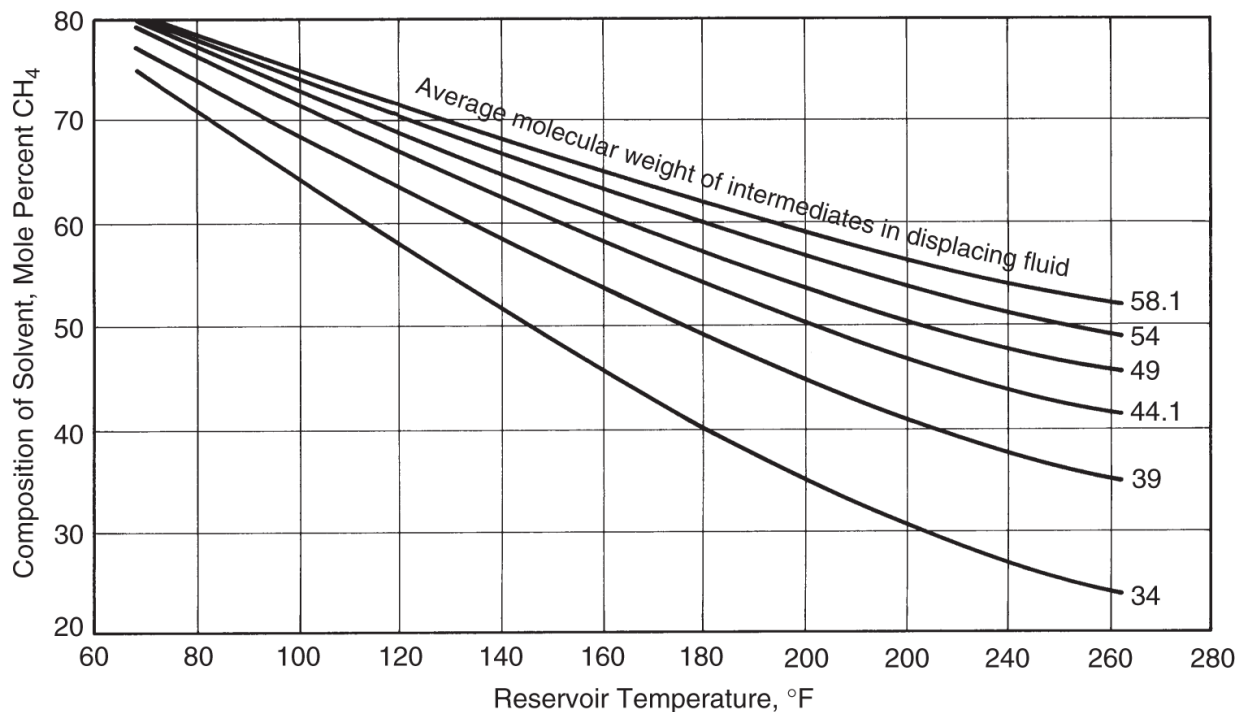


Fig. 7.29—Maximum methane dilution in LPG solvent for developed miscibility at 2,500 psia and for a reservoir fluid whose C_5^+ component molecular weight is 240 (Benham et al. 1961).

Example 7.5—Calculation of Required Propane Enrichment for Miscibility. Rich gas drives are the solvent method of choice where intermediates are readily available, inexpensive, and have no market. They are also the solvent method of choice when CO_2 is not available in sufficient quantities. Like CO_2 , however, a rich gas process requires a transfer of intermediates to develop miscibility.

Use the Benham et al. (1961) correlations to determine the amount of propane (the intermediate component of the solvent) that must be added to pure methane to displace the oil miscibly at a temperature of 160°F and a pressure of 2500 psi. Express the result as kg of propane per std m^3 of methane, where 1 kg of methane occupies 22.4 std m^3 at standard conditions. The oil composition is given below.

Component	Mole %	Molecular Weight
N ₂	0.16	28
C ₁	17.63	16
CO ₂	0.07	44
C ₂	10.43	30
C ₃	1.34	44
i-C ₄	0.5	58
n-C ₄	6.32	58
i-C ₅	0.96	58
n-C ₅	2.03	72
C ₆	4.96	86
C ₇₊	55.6	264

Step 1. Calculate the molecular weight of the C₅₊ fraction. This is done in the table below.

Component	Mole %	Molecular Weight	Mole % × Mole wt.
i-C ₅	0.96	58	55.68
n-C ₅	2.03	72	146.16
C ₆	4.96	86	426.56
C ₇₊	55.6	264	14678.4
Sum	63.55		15306.8

We have $M_{C_{5+}} = \frac{15306.8}{63.55} = 241$ Daltons. This is close to the value needed for Fig. 7.29.

Step 2. Determine the required amount of propane to achieve miscibility (or the maximum allowable methane percentage) from Fig. 7.29. Remembering that $M_{C_3} = 44$, we have from the figure, $\%C_1 = 58\%$ and $\%C_3 = 42\%$. The injected solvent can be over 50% methane and still attain miscibility.

Step 3. The ratio of propane to methane is therefore

$$\frac{\text{mole } - C_3}{\text{mole } - C_1} = \frac{0.42}{0.58} = 0.724.$$

Converting this to kg of propane per std m³ of methane yields

$$\frac{\left(0.724 \frac{\text{kgmole } - C_3}{\text{kgmole } - C_1}\right)\left(44 \frac{\text{kg } - C_3}{\text{kgmole } - C_3}\right)}{\left(22.4 \frac{\text{std m}^3}{\text{kgmole } - C_1}\right)} = 1.42 \frac{\text{kg } - C_3}{\text{std m}^3}.$$

7.6 Dispersion and Slug Processes

Dispersion has two principal effects on solvent processes: it causes oil to be left behind in developed miscible floods, and it can cause a loss of integrity of the solvent during the displacement. The second phenomenon is investigated here.

The next few sections look in detail at how a first-contact miscible solvent behaves during oil displacement. Remember that first-contact and developed-miscibility solvents behave very much alike. Also, the apparent scale dependence of dispersion is neglected here.

7.6.1 Dilution Paths. The concentration of component i in a first-contact miscible displacement is, from Eq. 5.55,

$$C_i = C_{il} + \frac{(C_{iJ} - C_{il})}{2} \left[1 - \operatorname{erf} \left(\frac{x_p - t_p}{2\sqrt{\frac{t_p}{N_{pe}}}} \right) \right]. \quad \dots \dots \dots \quad (7.2)$$

For this equation to be valid, we cannot have viscous fingering, layering, or gravity tonguing; hence, it is restricted to constant-viscosity, constant-density floods in 1D media. In Eq. 7.2, x_D is the dimensionless length, t_D the dimensionless time in fractional pore volumes, N_{Pe} the Peclet number, and the subscripts I and J refer to initial and injected conditions, respectively. These quantities were first introduced in [Chapter 5](#).

Taking the Peclet number to be equal for all components constitutes an assumption because it has been shown that diffusion coefficients can depend on the component. However, for dispersion, this dependency is less strong because the mechanical mixing part of the dispersion coefficient tends to dominate.

If we let the component subscript i refer to the light, intermediate, and heavy pseudocomponents of Section 7.3, we can easily show from Eq. 7.2 that the dilution paths are straight lines on a pseudoternary diagram; the term in brackets is the same for all components. Eliminating the term in brackets among the three equations gives

The C_i in Eq. 7.3 lie on a straight line in composition space; hence, the dilution path of Section 7.3 is linear.

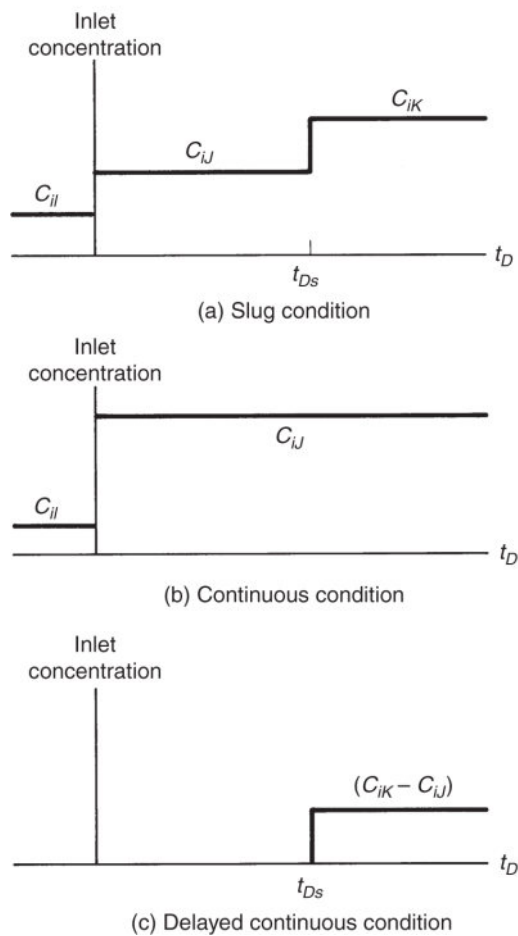


Fig. 7.30—Schematic of influent boundary conditions for slug.

7.6.2 Superposition. Many EOR agents, solvents among them, are usually too expensive to be injected continuously. Therefore, a typical displacement consists of a finite amount or *slug* of solvent followed by a less expensive chase fluid. The concentration of a slug follows from Eq. 7.2 and the principle of *superposition*. This principle applies to linear partial-differential equations, to which Eq. 7.2 is an approximate solution. We can in fact derive the concentration response of an infinite number of step changes in the influent concentration (see Exercise 7.3), but we restrict discussion here to a single solvent slug displaced by a chase fluid.

Let I , J , and K denote the concentrations of component i in the original fluid (the crude), the slug, and the chase fluids, respectively. Superposition states that the sum of individual solutions to a linear

differential equation is also a solution to the equation. This seems easy enough to do in practice, but we must take care in selecting the boundary conditions of the individual solutions to give the correct composite solution. [Fig. 7.30](#) shows the influent or imposed boundary conditions of the single-front problem ([Fig. 7.30b](#)) and that of the composite solution ([Fig. 7.30c](#)). The composite solution gives $C_i(x_D, t_D)$ for the imposed conditions shown in [Fig. 7.30a](#), which is simply the sum of the solutions to the conditions shown in [Figs. 7.30b](#) and [7.30c](#), respectively. The solution to the imposed conditions shown in [Fig. 7.30b](#) is Eq. 7.2, and that of the imposed conditions shown in [Fig. 7.30c](#) is

$$C_i = \frac{(C_{iK} - C_{il})}{2} \left\{ 1 - \operatorname{erf} \left[\frac{x_D - (t_D - t_{Ds})}{2\sqrt{\frac{(t_D - t_{Ds})}{N_{Pe}}}} \right] \right\}. \quad (7.4)$$

By superposition, $C_i(x_D, t_D)$ for the influent condition in [Fig. 7.30a](#) is the sum of Eqs. 7.2 and 7.4:

$$\begin{aligned} C_i &= \frac{C_{il} + C_{iK}}{2} + \left(\frac{C_{il} - C_{iK}}{2} \right) \operatorname{erf} \left(\frac{x_D - t_D}{2\sqrt{\frac{t_D}{N_{Pe}}}} \right) \\ &\quad + \left(\frac{C_{il} - C_{iK}}{2} \right) \operatorname{erf} \left[\frac{x_D - (t_D - t_{Ds})}{2\sqrt{\frac{t_D - t_{Ds}}{N_{Pe}}}} \right], \quad t_D > t_{Ds}. \end{aligned} \quad (7.5)$$

Eq. 7.5 is valid for any value of the injected concentrations.

Frequently, we are interested in the concentration of the solvent at the midpoint between $x_D = t_D$ and $x_D = t_D - t_{Ds}$. Evaluating Eq. 7.5 at $x_D = t_D - t_{Ds}/2$ yields this midpoint concentration \bar{C}_i :

$$\bar{C}_i = \frac{C_{il} + C_{iK}}{2} \left[1 - \operatorname{erf} \left(\frac{\frac{t_{Ds}}{2}}{4\sqrt{\frac{t_D}{N_{Pe}}}} \right) \right] + C_{il} \operatorname{erf} \left(\frac{\frac{t_{Ds}}{2}}{4\sqrt{\frac{t_D}{N_{Pe}}}} \right). \quad (7.6)$$

This equation is valid only for relatively small t_{Ds} where the difference between the square roots of t_D and $t_D - t_{Ds}$ in the denominator of the error-function argument is not large. If $C_{iJ} > C_{iI}$ and $C_{iJ} > C_{iK}$, the midpoint concentration is the *peak* concentration. For $C_{iI} = C_{iK} = 0$, the peak concentration decreases with increasing square root of time according to

The error function can be replaced by its argument for small values of the argument. In this event, the peak concentration decreases in inverse proportion to the square root of time. Because $x_D = t_D - t_{Ds}/2$ at the peak concentration, this is equivalent to \bar{C}_i decreasing in proportion to the inverse square root of the distance traveled.

The phenomenon of the peak concentration falling below C_{ij} is the consequence of overlapping front and rear mixing zones. [Fig. 7.31](#) shows experimental concentration profiles from a miscible slug displacement at different throughputs. [Fig. 7.31a](#) shows the concentration profiles normalized to the midpoint position $x_D = t_D - t_{Ds}/2$ on the horizontal axis. The areas under all curves are equal (material balance is preserved), but the peak concentration decreases as the number of passes (travel distance) increases. The unnormalized profiles in [Fig. 7.31b](#) show that the peak concentration decreases approximately as the inverse square root of t_D in experimental floods. Obviously, the effect of dispersion is to reduce the peak concentration from its injected value. In [Fig. 7.31](#), the peak concentration is approximately 60% of its injected value at approximately one-quarter of the distance into the medium.

The midpoint concentrations also trace a straight line in the pseudoternary diagram because the error-function arguments in Eq. 7.7 can be eliminated to give

$$\frac{\bar{C}_1 - \frac{C_{1K} + C_{1I}}{2}}{C_{1J} - \frac{C_{1K} + C_{1I}}{2}} = \frac{\bar{C}_2 - \frac{C_{2K} + C_{2I}}{2}}{C_{2J} - \frac{C_{2K} + C_{2I}}{2}} = \frac{\bar{C}_3 - \frac{C_{3K} + C_{3I}}{2}}{C_{3J} - \frac{C_{3K} + C_{3I}}{2}}.$$

This equation says that as time increases, the midpoint concentration traces a straight line between the injected slug concentration C_{iJ} and the average concentration of the fluids ahead of and behind the slug. The midpoint concentrations at successive times a , b , and c are shown in [Fig. 7.32](#), as are the dilution paths given by Eq. 7.5. The dilution paths become straight-line segments from C_{iJ} to \bar{C}_i and then from \bar{C}_i to C_{ik} for t_{Ds} small. These considerations are valid only as long as the entire dilution path stays in the single-phase region of the diagram. It is not necessary for \bar{C}_i to fall into the two-phase region for the displacement to lose first-contact miscibility (see Exercise 7.5).

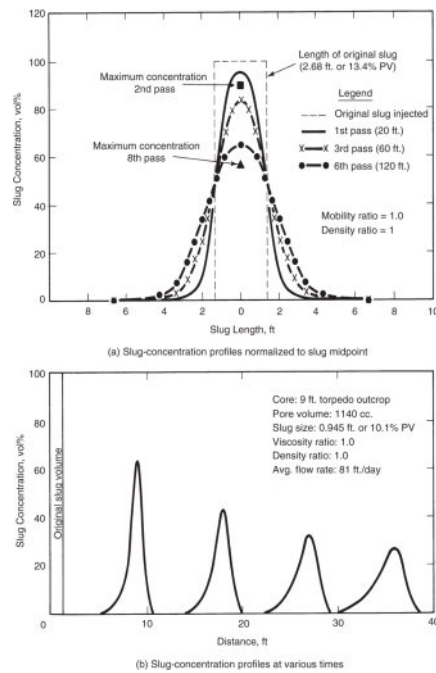


Fig. 7.31—Miscible slug-concentration profiles for matched viscosity and density displacements (Koch and Slobod 1956).

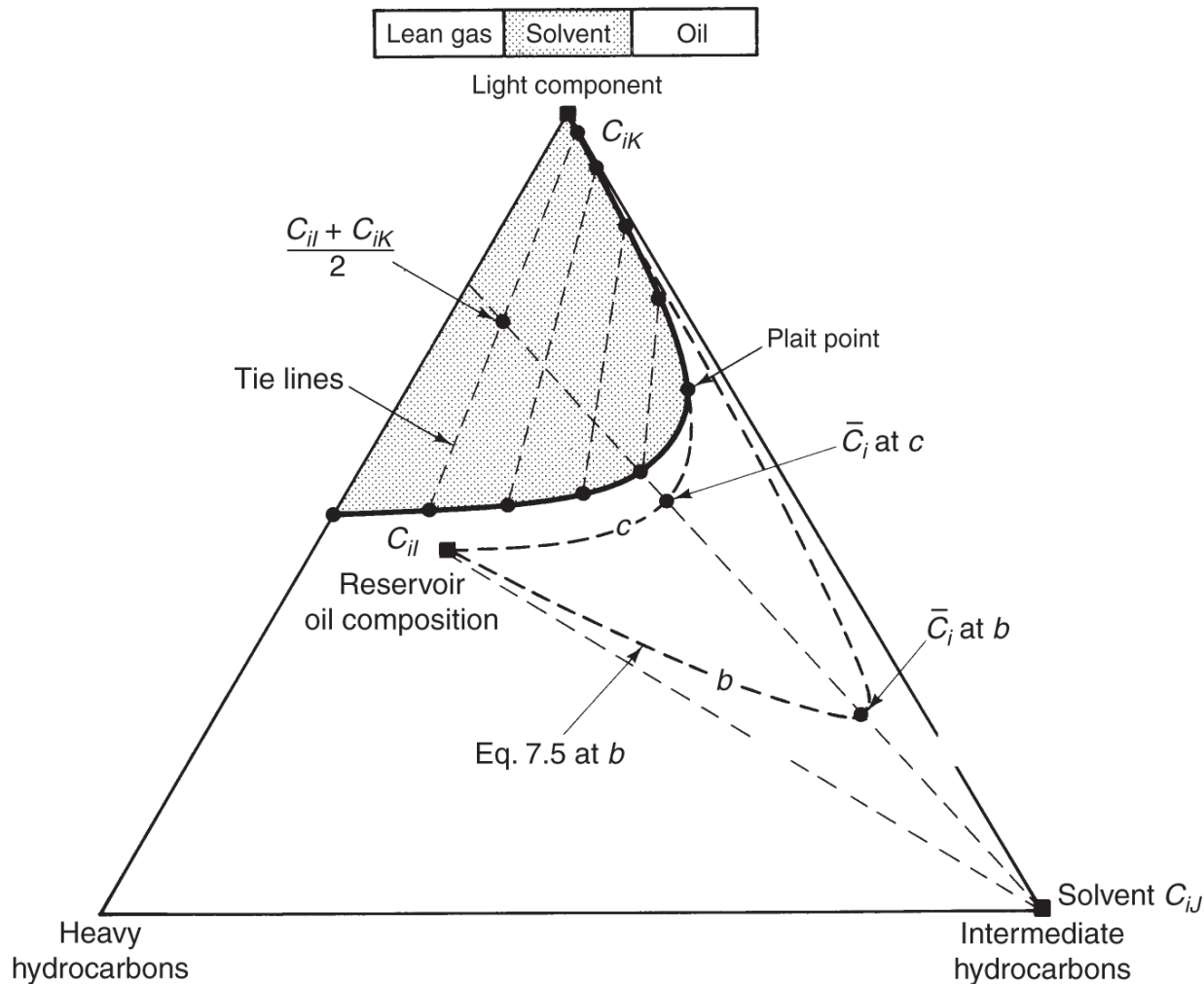


Fig. 7.32—Dilution of solvent slug by mixing (Stalkup 1983).

7.7 Two-Phase Flow in Solvent Floods

Two or more phases are inevitable in solvent floods. When this happens, the dispersion theory of Section 7.6 does not apply. However, general conclusions about such displacements are still possible on the basis of the theory first introduced in Section 5.6. This theory neglects dissipative effects of any kind; hence, we omit dispersion in the following discussion (see Section 5.2). We treat first-contact miscible displacements in the presence of an aqueous phase in which fluid displacement takes place in a 1D permeable medium at constant temperature and with incompressible fluids and solids.

7.7.1 First-Contact Miscible Displacements in the Presence of an Aqueous Phase. First-contact miscible displacements with an aqueous phase have certain characteristics that are present in all isothermal EOR processes; see Section 5.8. To illuminate these, we present a method to solve for concentration $C = C(x_D, t_D)$ and saturation $S = S(x_D, t_D)$ as functions of distance and time.

Water has little effect on hydrocarbon-phase behavior ([Fig. 7.8](#)), and the water solubility of most solvents is small. However, presence of an aqueous phase is all but inevitable and can affect displacement behavior through fractional-flow effects, especially when water is injected with the solvent. In this section, we investigate the effects of an aqueous phase on a first-contact miscible displacement. The treatment here follows the work of Walsh and Lake (1989) in large part.

The semi-graphical analysis enables estimation of several design variables in solvent floods to include optimal

1. WAG ratio
2. Solvent slug size
3. Chase fluid type
4. WAG ratio in chase fluid

To do this, we make the usual fractional-flow assumptions: incompressible fluids and rock, no dissipative effects, and 1D flow. In general, solvent/water relative permeabilities are not the same as oil/water relative permeabilities, but we will take them to be so here for illustration. Therefore, a water/solvent fractional flow differs from a water/oil fractional flow f_1 only by the difference between the use of solvent and oil viscosities and densities. Because the relative permeabilities do not change, residual-phase saturations of both the aqueous and nonaqueous phases are invariant; there is no change in capillary number. [Fig. 7.33](#) illustrates the fractional-flow curves.

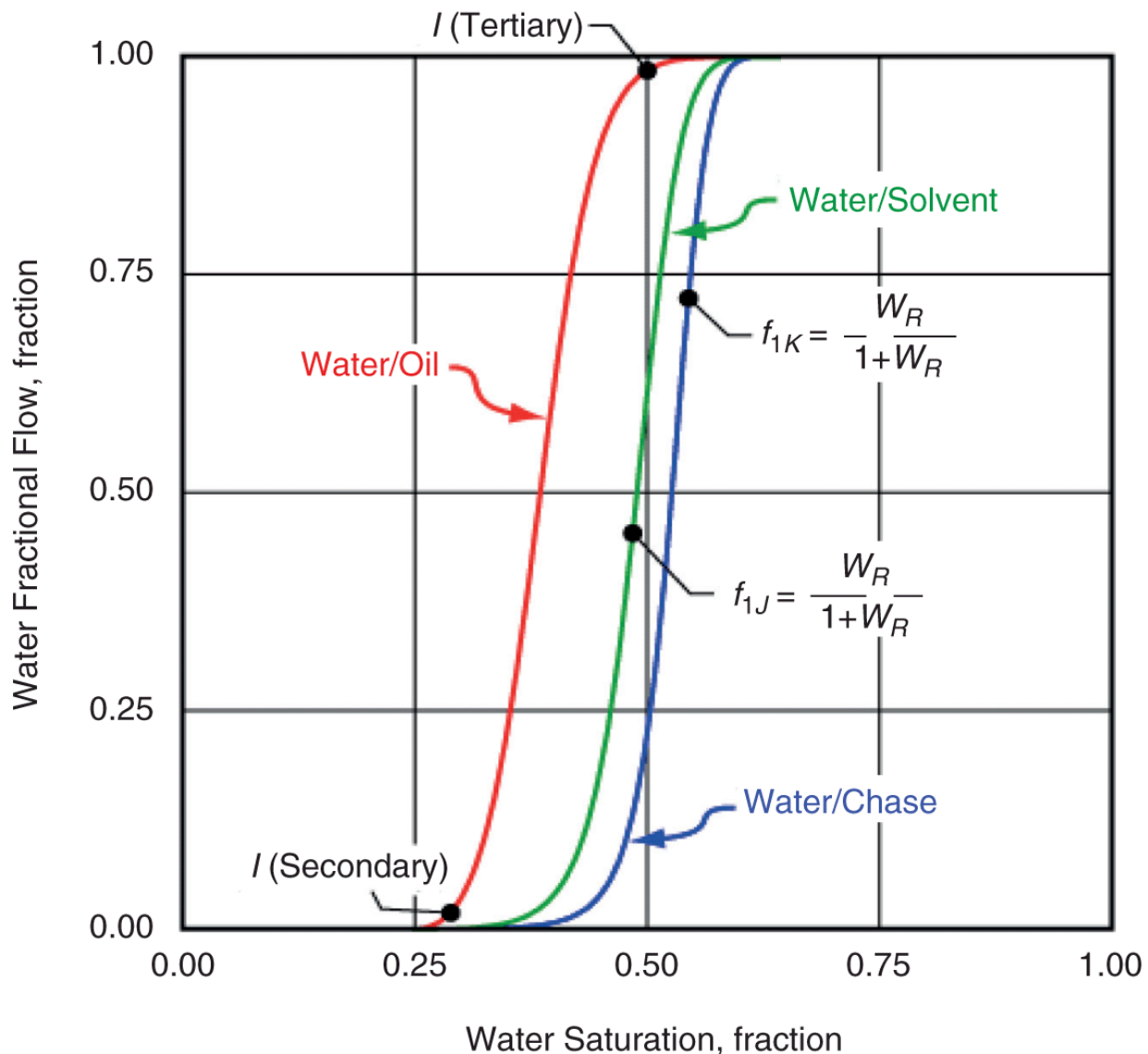


Fig. 7.33—Fractional-flow curves for oil/water, solvent/water, and chase fluid/water. Relative permeabilities are from Dickey et al. (1972). *I* denotes initial, *J* denotes injected, and *K* denotes chase fluid.

There are three pairs of fractional-flow curves for oil/water, solvent/water, and chase fluid/water. The nonaqueous phase can be either oil, solvent, or chase fluid. There can, of course, be simultaneous three-component flow, but we will not consider it here. The chase fluid is a driving fluid introduced after solvent injection, usually water or sometimes a less valuable gas.

Boundary and Initial Conditions. Denote the initial, injected solvent, and chase conditions as f_{iI} , f_{iJ} , and f_{iK} as in Fig. 7.33. Condition I is set by the previous production process. It can be anywhere on the oil/water fractional-flow curve. A flood with f_{iI} equal to or near zero is a *secondary* flood; one with f_{iI} equal to or near one is a *tertiary* flood. This specification assumes that initially the medium is at uniform saturation. The states are specified as fractional flows rather than saturations, a practice that will be continued in the discussion that follows. The chase fluid can be water alone, in which case $f_{iK} = 1$ and the water/chase fractional flow is not needed.

The injection condition J is some prespecified proportion of solvent and water f_{iJ} given on the solvent/water curve. As discussed previously, the solvent/water mixture has better volumetric sweep efficiency than solvent alone (Caudle and Dyes 1958). The calculation in this section does not estimate volumetric sweep efficiency, although it gives some insights into it.

The volumetric flow-rate ratio of water to solvent in the injected fluid is the *WAG ratio* W_R , given by

$$W_R = \frac{\text{volumetric rate of solvent}}{\text{volumetric rate of water}} = \frac{1 - f_{1J}}{f_{1J}},$$

where the volumetric rates are expressed as reservoir volumes/time. Inverting this to obtain a fractional flow gives

In an actual WAG process, the water and solvent are injected in alternate slugs so that the cumulative volumes of solvent and water define the WAG ratio rather than Eq. 7.8. The differences in displacement behavior caused by simultaneous injection rather than alternating injection have been investigated by Welch (1982). We might be better to refer to this process as simultaneous water/gas injection (SWAG). The *I*, *J* and *K* conditions are on the oil/water,

solvent/water and chase/water fractional-flow curves, respectively. The conditions f_{iJ} and f_{iK} are among the primary design considerations in solvent flooding.

Specific Velocities. We assume the aqueous phase to be entirely water, or

$$C_{11} = 1, C_{21} = 0, C_{31} = 0, \dots \quad (7.9a)$$

and the nonaqueous phase to be composed of oil, solvent, and chase fluid, within which phase they are first-contact miscible:

As throughout the text, 1 means water, 2 oil, and 3 can be either solvent or chase fluid depending on context. The conditions on water solubility were relaxed in the original work (Walsh and Lake 1989).

To find the composition paths, use the following invariant conditions:

$$v_{C_1} = v_{C_2} = v_{C_3},$$

or

$$\frac{dF_1}{dC_1} = \frac{dF_2}{dC_2} = \frac{dF_3}{dC_3},$$

which become in terms of fractional flows $f_1 = f_1(S_1, C_{32})$ and $f_2 = f_2(S_1, C_{32})$,

$$\frac{d(C_{11}f_1 + C_{12}f_2)}{d(C_{11}S_1 + C_{12}S_2)} = \frac{d(C_{21}f_1 + C_{22}f_2)}{d(C_{21}S_1 + C_{22}S_2)} = \frac{d(C_{31}f_1 + C_{32}f_2)}{d(C_{31}S_1 + C_{32}S_2)}, \dots \quad (7.10a)$$

and for this specific case, from Eq. 7.9,

$$\frac{df_1}{dS_1} = \frac{C_{22}df_2 + f_2dC_{22}}{C_{22}dS_2 + S_2dC_{22}} = \frac{C_{32}df_2 + f_2dC_{32}}{C_{32}dS_3 + S_3dC_{32}}. \dots \quad (7.10b)$$

Composition Paths. There are two types of conditions that satisfy Eq. 7.10b.

1. When $dC_{22} = dC_{32} = 0$,

which you should recognize as the saturation velocity in an immiscible wave, as was discussed in Section 5.2. Because the phase concentrations do not change here, the wave is truly immiscible. Immiscible waves are part of a miscible displacement in the presence of an immiscible phase. Although we show it only by example, the saturation can change to a shock wave, as was discussed in Section 5.2.

2. When $f_2 = I_c S_2$, where I_c is a constant, we have

$$v_C = I_C \frac{df_1}{dS_1} = \frac{C_{22}I_C dS_2 + I_C S_2 dC_{22}}{C_{22}dS_2 + S_2 dC_{22}} = \frac{C_{32}I_C dS_2 + I_C S_2 dC_{32}}{C_{32}dS_2 + S_2 dC_{32}},$$

or

Because $v_C = l$ is a constant, this wave is a velocity in a miscible wave. Eq. 7.11b is a straight line from the upper right corner ($f_1 = S_1 = 1$) on a fractional-flow plot. Eq. 7.11b can also be derived from material balances on water and solvent, as in Section 5.8.

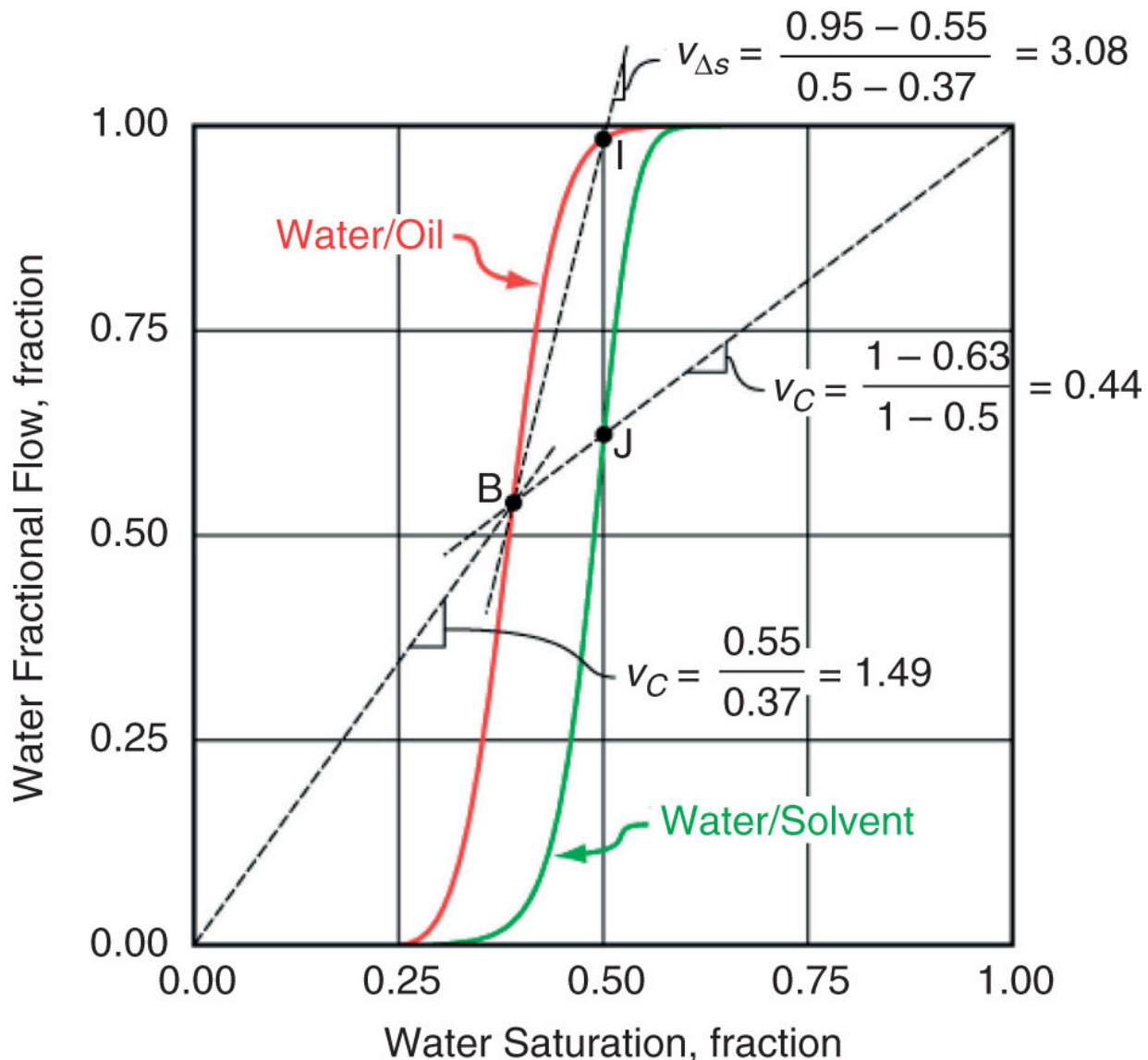


Fig. 7.34—Composition paths for velocities (Eq. 7.11) for a $W_R = 1.70$ tertiary displacement.

[Fig. 7.34](#) shows the constructions. Three aspects of the diagram are implicit in the preceding derivation.

1. Eq. 7.11b applies equally well to the oil/water and the solvent/water fractional-flow curves. Hence, the extension of the line representing the miscible wave from the upper right corner through point J (remember, this point is set by the user) and continuing to the oil/water curve defines a second

saturation point, an *oil-bank* condition B , which flows at fractional flow $f_{2B} = 1 - f_{1B}$ and saturation $S_{2B} = 1 - S_{1B}$.

2. The front of the oil bank is an immiscible displacement of condition I by condition B . According to the rules of Section 5.2, this displacement is a shock for which the specific velocity is given by the secant between I and B , as shown. Because the rear of the bank flows at velocity $v_c = \frac{f_{2J}}{S_{2J}}$ and the front flows at velocity $v_{\Delta S} = \frac{f_{1I} - f_{1B}}{S_{1I} - S_{1B}}$, the oil bank flows at constant saturation and fractional flow.

The existence of a constant-saturation bank ahead of the displacing agent is a pervasive feature of EOR displacements. In fact, it is the main feature distinguishing it from the single fractional-flow case described in Section 5.2 and Fig. 5.4. Note that none of the concentrations between the solvent J and the oil bank B appears in the construction because the wave is indifferent.

One can think of this phenomenon as a continuity argument or simply as the front of the agent (the solvent in this case) moving at the same rate as the back of the bank. The word *bank* suggests the type of accumulation that occurs ahead of snow plows in street-clearing operations.

3. There is actually a second miscible wave between the injected water and resident water, for which the specific velocity is given by

In other words, the specific velocity is the slope of a straight line from the lower right corner $f_1 = S_1 = 0$ that passes through point J . We could have included this in the derivation above. Just as in Section 5.4, the choice of drawing this line through point B or point J is made to maintain the consistency of the construction.

Example 7.6 Often the qualitative insights from an analysis such as this are as important as the specifics. After studying Fig. 7.34, answer the following questions:

1. What would be the effects of increasing the WAG ratio on oil saturation in the oil bank, the oil fractional flow in the oil bank, the velocity of the oil-bank front, and the velocity of the miscible-water front?

The answers follow directly from the construction. Increasing W_R is equivalent to increasing f_{iJ} or injecting more water with the solvent. This causes both S_{2B} and f_{2B} to decrease, f_{2B} more dramatically. It also slows the solvent and oil-bank fronts and accelerates the miscible-water front, which is to be expected because of the injection of more water.

2. What would be the effect of starting the displacement sooner (i.e., assuming f_{1I} to be smaller) on the same quantities?

The answers also follow directly from the construction. Starting at a smaller water cut has no effect on the solvent or miscible-water fronts, nor on the oil-bank saturation or the fractional flow. It merely speeds up the oil-bank front.

Composition Route. From the discussion in Chapter 5, the complete solution from condition J to I (or K to J for chase fluids) must follow a series of composition paths that proceed from J to I with increasing specific velocity. That the velocity increases monotonically is ensured by inserting shocks at appropriate intervals.

We present the results of the calculation on a *Walsh diagram* after Walsh and Lake (1989). This diagram shows all aspects of a displacement as well as how these aspects fit with each other. Remember that the idea was to determine $C = C(x_D, t_D)$ and saturation $S = S(x_D, t_D)$ as functions of distance and time.

The Walsh diagram contains the fractional-flow curve in the upper left of the diagram. The diagram in [Fig. 7.35](#) is the same as that in [Fig. 7.34](#).

Below the fractional-flow curve is a saturation/concentration *profile*, or a plot vs. x_D at fixed t_D . The t_D can be any time; often it is assumed to be the time at breakthrough. The profile is rotated from the normal presentation (cf. [Fig. 5.2](#)) so that it will match up with the saturation axis of the fractional-flow plot.

To the right of the fractional-flow curve is a fractional flow/concentration history, or a plot of $f_1(x_D, t_D)$ vs. t_D at fixed x_D . As above, x_D can be anywhere, but $x_D = 1$ is assumed, and then the curve becomes an *effluent* history, commonly known as a water *breakthrough* curve to the producer. The vertical axis of this plot matches with the fractional-flow axis of the upper right plot.

The final plot on the lower right is the *time/distance* diagram, which shows x_D vs. t_D at constant saturations. Its axes match up with the effluent history above it and the profile to its right.

Each diagram presents a unique aspect of the displacement. The profile is constructed by inverting $C = C(x_D, t_D)$ and $S = S(x_D, t_D)$ for $x_D = t_D v_C$ and $x_D = t_D v_{\Delta S}$ for various values of C and S . It is what would be observed if you were to take a snapshot of the medium at a fixed time. The effluent history is constructed from $t_D = 1/v_C$ and $t_D = 1/v_{\Delta S}$. It is the most readily accessible observation of the displacement because it is what comes out of the producing end of the medium. The time/distance diagram always consists of one or more straight lines emanating from the origin (for J displacing I). [Fig. 7.35](#) shows the entire construction.

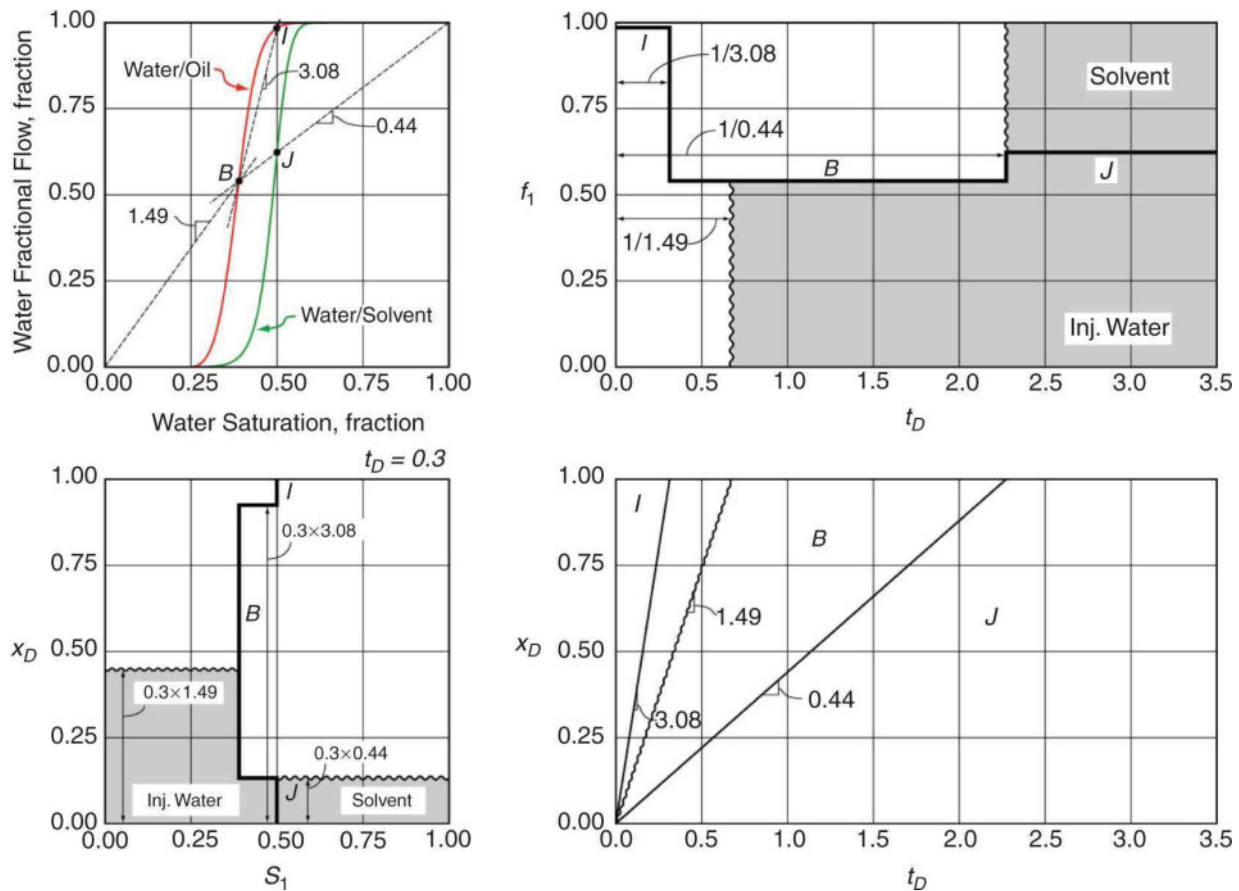


Fig. 7.35—Walsh diagram for the displacement shown in [Fig. 7.34](#). The wavy line is a miscible wave. $t_D = 0.3$ is slightly before breakthrough.

Several conclusions can be drawn from [Fig. 7.35](#):

1. The initial and final aqueous-phase saturations are very nearly equal. Effectively, the solvent has replaced the oil in this displacement with no change in water content.
2. The oil-bank fractional flow is approximately 0.4. This value is an upper limit on what is to be expected from field response. The oil bank is never clean oil ($f_{2B} < 1$) in a tertiary flood.
3. The change in saturation is far smaller than the change in fractional flow. Therefore, changes in flowing properties are more detectable than changes in static properties. This observation argues against the use of logging observation wells in monitoring solvent floods.

4. One important observation from the figure is that residual oil is completely replaced by solvent without appeal to capillary number arguments (recall that the capillary number was not changed here). However, a capillary number argument would apply to the solvent and oil were they not completely miscible.
5. Complete (100%) recovery of oil is a consequence of the displacement being 1D and the assumptions used. Such large recoveries never occur in the field (although they do in many laboratory experiments).

Optimum WAG Ratio. The meaning of *optimum* depends on context. It could, for example, mean the EOR design that produces the maximum net present value (NPV), or the design that produces the maximum NPV/cost. Here, we speak of optima narrowly in terms of WAG ratios and slug sizes.

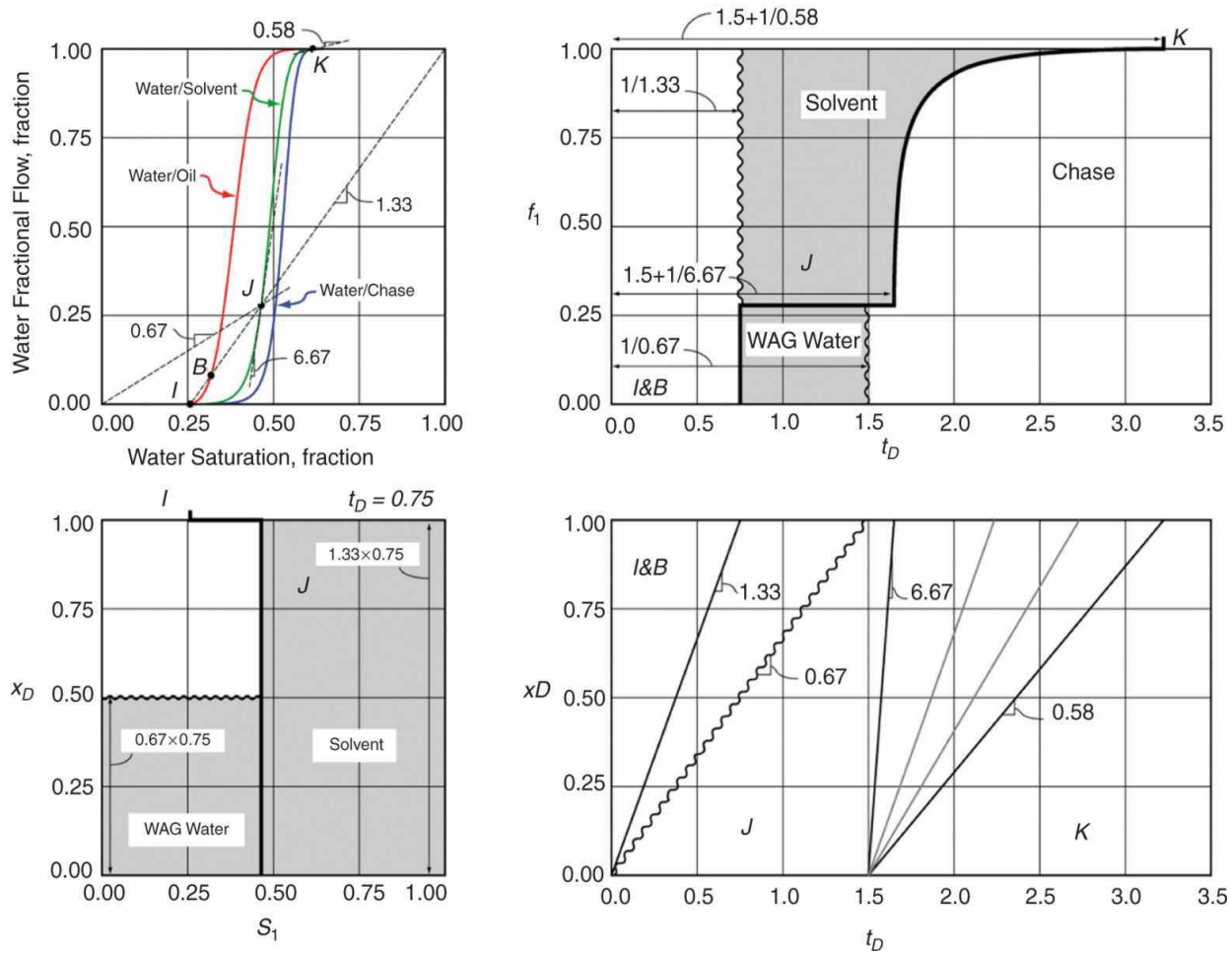


Fig. 7.36—Walsh diagram for optimal WAG ratio in a secondary solvent flood. The figure also shows the construction of the chase-fluid K displacement of J. Solvent+water slug size is $t_{Ds} = 1.5$.

[Fig. 7.36](#) shows a graphical construction for a secondary WAG displacement. Remember that the purpose of injecting water with the solvent was to form a small-mobility mixture to displace the oil. Injecting too much water, as in [Fig. 7.35](#), would defeat this purpose because this would effectively impose a waterflood before the solvent. Injecting too little water would also be countereffective because the solvent would not directly displace the resident fluids.

The optimum, then, would be the WAG ratio at which the solvent and water fronts would move at the same rate. For a secondary displacement, the water front is the miscible water banked up by the injected water. The optimum occurs at the WAG ratio at which the

velocities from Eqs. 7.11b and 7.11c are the same, or $W_R = 0.43$ for these fractional-flow curves.

For a tertiary flood, the optimum is not as clear as for secondary floods because the penalty for injecting too much water has been exacted, a high water saturation existing from the waterflood. Walsh and Lake (1989) suggest calculating the optimum WAG ratio in these floods to minimize the mobility ratio.

Other Optima. The chase fluid can be water itself or some fluid that is less expensive than solvent. The Walsh diagram in [Fig. 7.36](#) shows a fractional-flow curve for water/chase fluid in addition to the previous two.

If the chase fluid is water, point K on the upper right of the plot represents injection of the chase fluid. Until the waves intersect, the displacement of J by K follows exactly the same process as that of I by J . The main difference is that the chase fluid/solvent velocity is offset from the origin according to

$$v_C = \frac{x_D}{t_D - t_{Ds}}, \dots \dots \dots \quad (7.12a)$$

where t_{Ds} is the solvent/water slug size. The amount of solvent injected in pore volumes is, therefore,

$$V_{\text{solvent}} = t_{Ds} (1 - f_{iJ}). \dots \dots \dots \quad (7.12b)$$

The chase fluid in [Fig. 7.36](#) is water, which causes a very fast-moving immiscible spreading wave to occur between K and J and enables production of a substantial amount of solvent. This is obviously a waste because the oil recovery would be 100% for any slug size greater than approximately $t_{Ds} = 0.6$, as is to be determined from the t_{Ds} that enables the intersection of the miscible-solvent wave with the leading edge of the chase-fluid wave at $x_D = 1$. In fact, using WAG in the chase fluid, Walsh and Lake (1989) show that solvent usage can be minimized globally.

Final Remarks. Two other factors are covered in Walsh and Lake (1989). One is solubility of water in the solvent phase. The second is

accounting for the presence of a residual saturation in the solvent flood, designated as S_{2rm} . Including the latter changes, Eq. 7.11a becomes (see Section 5.8)

$$v_c = \frac{f_2}{S_2 - S_{2rm}}. \quad \dots \dots \dots \quad (7.13)$$

Eq. 7.13 changes the graphical construction for the miscible-solvent wave from a line passing through the upper right corner to a line that passes through a point that is displaced from that corner to the left by a distance S_{2rm} . The water-solubility correction is usually negligible, but a nonzero S_{2rm} can have a substantial impact on all aspects of the displacement. As discussed below, S_{2rm} is a consequence of significant dispersion effects, a loss of miscibility, or both.

Finally, although this discussion has yielded many useful insights, the prediction of 100% ultimate oil recovery represents a huge discrepancy from field performance. We will build on these results to make corrections for uneven displacement fronts below. Interestingly, Ghanbarnezhed (2012) showed that the optima in WAG ratio and slug size determined by the procedures in this section persist to more realistic displacements (the 100% ultimate recovery does not), and, therefore, it appears that this discussion can serve as a first step in the iteration toward a field design.

7.8 Solvent Floods With Viscous Fingering

First-contact miscible displacements actually behave considerably differently than those shown in [Figs. 7.35](#) and [7.36](#). [Fig. 7.37](#) shows the experimental results of a developed miscible displacement in a Berea core, in which oil initially at residual saturation to waterflood is displaced by a CO₂ solvent in a $W_R = 0$ displacement. The water cut was initially 1.0 and decreased to approximately 0.15 at $t_D = 0.15$. The water cut remained essentially constant until approximately $t_D = 0.33$, at which point it decreased gradually to zero. However, when the water cut originally fell to $t_D = 0.14$, both oil and solvent broke through. This left a remaining oil saturation of approximately 0.25 at

termination. 100% oil recovery might have been obtained had the experiment been continued, but only after several pore volumes of solvent injection.

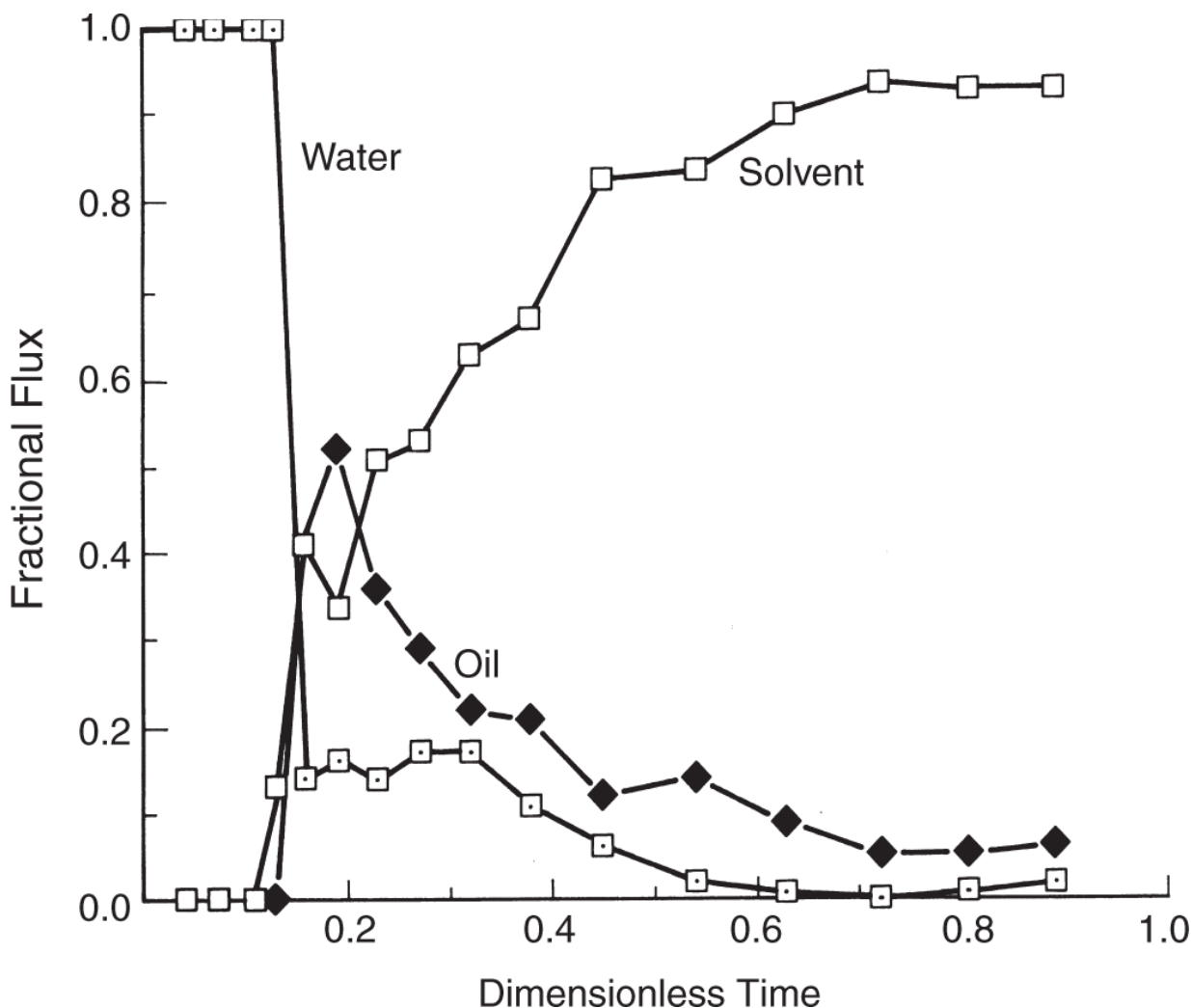


Fig. 7.37—Effluent history of a laboratory-scale CO_2 flood (Whitehead et al. 1981).

The primary cause of the simultaneous oil and solvent breakthrough and prolonged oil recovery in experimental displacements is viscous fingering. Section 6.8 concluded that miscible displacements with typical solvents were always viscously unstable, barring gravity stabilization or a boundary effect, because the solvent/oil mobility ratio is greater than one.

There is a physical difference between viscous fingering in experiments and the channeling that occurs in reservoirs for unstable

displacements. In reservoirs with significant permeability variations, flow is not governed primarily by viscous fingering, but rather by gas channeling through the highest-permeability pathways. Viscous fingers require reasonable transverse permeability to grow, while channeling does not. Nevertheless, the theory discussed in this section can apply to channeling as well because channeling similarly causes early solvent breakthrough and prolonged oil recovery.

Descriptions of the character of simultaneous oil and solvent flow after the onset of fingering will now be provided. The description in Section 6.8 was about the onset of fingering.

7.8.1 Heuristic Models. Because of the chaotic nature of viscous fingering, a rigorous mathematical theory is not possible, although it is possible to simulate specific cases. The behavior of a fingering displacement may be estimated by various heuristic theories, including (1) a modification of fractional-flow theory (Koval 1963), (2) rate-controlled mass transfer between solvent and oil fingers (Dougherty 1963), (3) defining a suitably weighted mixture viscosity (Todd and Longstaff 1972), (4) accounting for mixing in fingers directly (Fayers 1988), or (5) defining a composition-dependent dispersion coefficient (Young 1990).

This section deals exclusively with the Koval approach; we leave the others mentioned above for your reading. By excluding the others, we do not imply that the Koval approach is superior because all involve empirical parameters that must be determined by history matching. However, the Koval theory is in common use, and it fits naturally into the fractional-flow theme of this text.

The mixing-zone length of a fingering displacement (the dimensionless distance between prespecified values of a cross-sectionally averaged concentration profile), in the absence of boundary effects, grows in proportion to time. This observation prompted Koval to instigate a fractional-flow theory for viscous fingering. If viscous fingers initiate and propagate, their growth in horizontal plane flow would look something like the cross section shown in [Fig. 7.38](#), where the oil and solvent are in segregated flow. The displacement is first-contact miscible, with no dissipation, and

without water present. If dissipation can vertically smear the fingers, the mixing zone will grow in proportion to the square root of time, as in dispersion theory. This growth can be quite small if longitudinal dispersion is small or the system length is large (Hall and Geffen 1965).

With these qualifications, the volumetric flow rate of solvent ($i = 3$) across a vertical plane within the mixing zone is

and that of oil ($i = 2$) is

where A_3 and A_2 are cross-sectional areas of oil and solvent. There are no relative permeabilities or capillary pressures in these equations because the displacement is ideally first-contact miscible. These equations assume a horizontal displacement. The fractional flow of solvent in the oleic phase across the same vertical plane is

$$f_{32} = \frac{q_3}{q_3 + q_2}$$

by definition, which, when Eq. 7.14 is substituted, yields

Eq. 7.15 assumes that the x-direction pressure gradients are equal in the oil and solvent fingers. Because the displacement is in plane flow, the oil and solvent cross-sectional areas are proportional to average concentrations, or

$$f_{32} = \left[1 + \frac{1}{v} \left(\frac{1 - \bar{C}_{32}}{\bar{C}_{32}} \right) \right]^{-1}, \dots \quad (7.16)$$

where v is the oil/solvent viscosity ratio and \bar{C}_{32} is the average solvent concentration in the oleic phase across the cross section.

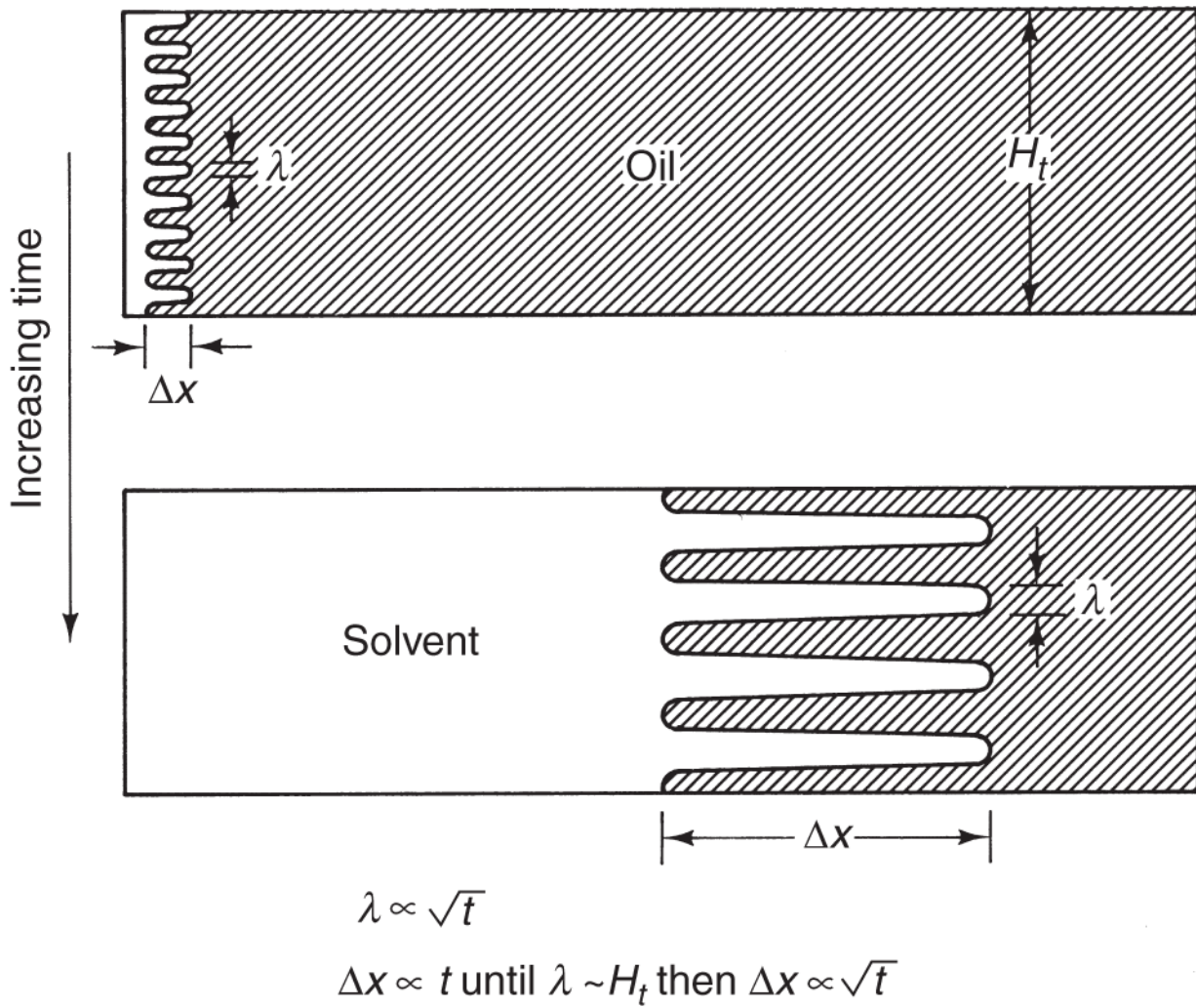


Fig. 7.38—Idealization of viscous-finger propagation (Gardner and Ypma 1984).

Eq. 7.16 is a description of the segregated-flow fingering shown in Fig. 7.38. Koval had to modify the definition of v to match experimental displacements. The final form of the solvent fractional flow is

$$f_{32} = \left[1 + \frac{1}{K_{\text{val}}} \left(\frac{1 - \bar{C}_{32}}{\bar{C}_{32}} \right) \right]^{-1}, \dots \quad (7.17)$$

where K_{val} is the Koval factor.

7.8.2 Koval Corrections. The Koval factor modifies the viscosity ratio to account for local heterogeneity and transverse mixing in the following fashion:

The parameter E changes the viscosity ratio to account for local mixing:

$$E = \left(0.78 + 0.22v^{1/4}\right)^4. \quad \dots \dots \dots \quad (7.19)$$

The consequence of Eq. 7.19 is that the numerical value of E is usually smaller than that of v . In other words, the effect of fingering is not as severe as it appears from the original viscosity ratio. The 0.22 and 0.78 factors in Eq. 7.19 seem to imply that the solvent fingers contain, on average, 22% oil, which causes attenuation of the viscosity ratio through the quarter-power mixing rule. In fact, Koval eschewed this interpretation by remarking that the numerical factors were included simply to improve agreement with experimental results. This would seem to restrict Eq. 7.19 to the exact class of experiments reported by Koval. Remarkably, Claridge (1980) has shown that the 0.22/0.78 factors accurately describe fingering displacements over large ranges of transverse dispersion. It is very likely that the finger dilution is being caused by viscous crossflow because the mechanism is consistent with linear mixing-zone growth (Waggoner and Lake 1987).

The heterogeneity factor H_K corrects the reduced viscosity ratio for the local heterogeneity of the medium. Selecting the correct value for H_K is the most subjective feature of the Koval theory. In [Fig. 6.6](#), the heterogeneity factor was calculated from the Dykstra-Parsons coefficient. It has also been correlated with the longitudinal Peclet number (Gardner and Ypma 1982).

The fractional-flow expression (Eq. 7.17) is the same as the water fractional flow in a waterflood in which the oil and water have straight-line relative permeabilities. For such a case (see Exercise 5.3), the

Buckley-Leverett equation (Eq. 5.12), can be integrated analytically to give the following expression for effluent fractional flow:

$$f_{32} \Big|_{x_D=1} = \begin{cases} 0, & t_D < \frac{1}{K_{\text{val}}} \\ \frac{K_{\text{val}} - \left(\frac{K_{\text{val}}}{t_D} \right)^{1/2}}{K_{\text{val}} - 1}, & \frac{1}{K_{\text{val}}} < t_D < K_{\text{val}} \\ 1, & K_{\text{val}} < t_D \end{cases} \quad \dots \dots \dots \quad (7.20)$$

The oil fractional flow is $1 - f_{32} \Big|_{x_D=1}$. This equation has been compared to experimental data in the original Koval paper and elsewhere (Claridge 1980; Gardner and Ypma 1982).

7.8.3 Koval Theory With Mobile Water. The Koval theory applies to first-contact miscible displacements in the absence of flowing water. The theory can be readily generalized to fingering in first-contact miscible displacements with water present by modifying the overall flux and concentration definitions (see Section 5.4). The overall flux for oil and solvent becomes

$$F_2 = (1 - f_{32}) f_2 \quad \dots \dots \dots \quad (7.21a)$$

$$F_3 = f_{32} f_2, \quad \dots \dots \dots \quad (7.21b)$$

where f_1 and f_2 are the actual water and hydrocarbon fractional-flow functions and f_{32} is given by Eq. 7.17.

The overall concentrations of the oil and solvent are

$$C_2 = (1 - \bar{C}_{32}) S_2 \quad \dots \dots \dots \quad (7.22a)$$

$$C_3 = \bar{C}_{32} S_2 \quad \dots \dots \dots \quad (7.22b)$$

The water concentration is simply S_1 because there is no solvent solubility in the water phase. Eqs. 7.21 and 7.22, substituted into the conservation equations for oil and solvent, can then be solved by the procedure discussed in Section 5.7 for the oil/gas/water problem.

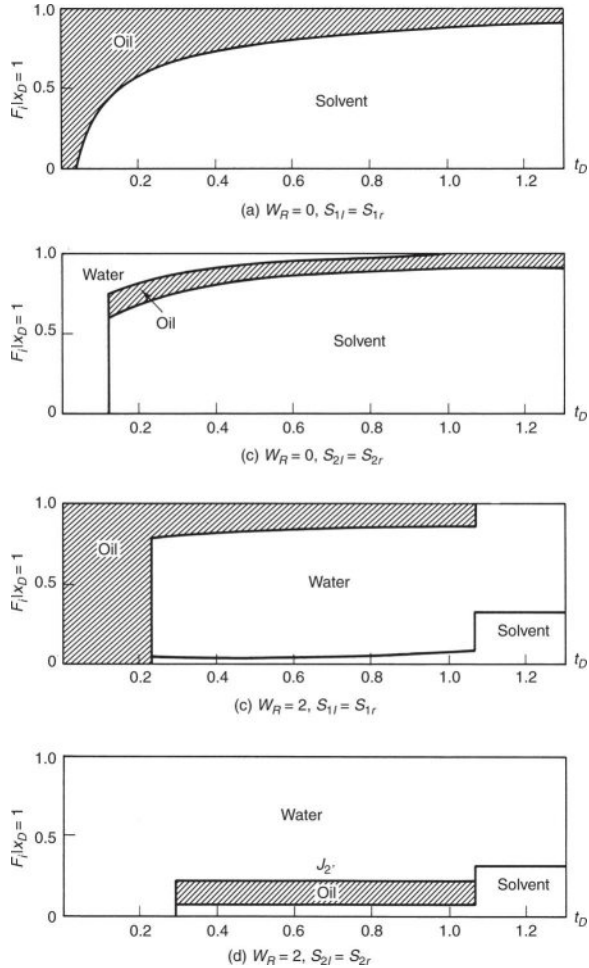


Fig. 7.39—Effluent histories for four fingering cases.

[Fig. 7.39](#) shows the effluent fluxes for four displacements using this procedure. [Fig. 7.39a](#) shows a non-WAG secondary flood and is simply the result of the original theory, Eq. 7.20. [Fig. 7.39b](#) shows a tertiary non-WAG displacement. [Figs. 7.39c](#) and [7.39d](#) illustrate secondary and tertiary WAG displacements ($W_R = 2$). The oil and water relative permeabilities in [Figs. 7.38](#) and [7.39](#) are the same, so that comparing [Fig. 7.38](#) and [Fig. 7.39d](#) should reveal the effect of fingering on a first-contact miscible displacement with water present.

For both cases, the oil is produced as a bank of constant cut. However, the bank-oil cut is smaller for the fingering displacement, and the oil breakthrough and complete sweepout times are later. In the fingering case, oil and solvent break through together, although the solvent is at low cut. By comparing [Figs. 7.39a](#) and [7.39c](#) with

[Figs. 7.39b](#) and [7.39d1](#), we can see that, regardless of the initial conditions, the WAG procedure delays solvent breakthrough and hastens complete oil recovery.

On the basis of the comparisons in [Fig. 7.39](#), it appears that WAG is universally better than injecting solvent alone, particularly when solvent efficiency is considered. However, the presence of an initial mobile water saturation causes a residual oil saturation even in a first-contact displacement (see Section 7.9), and it is possible that the WAG process will cause this also.

Other methods besides WAG to improve mobility control in miscible flooding include the use of polymers (Heller et al. 1985) and foams. To date, only foams have been investigated extensively, and because foams are envisioned to drive a variety of EOR processes, we delay their discussion until [Chapter 10](#), where they more naturally fit after discussions of surfactant-based EOR methods.

7.9 Solvent Flooding and Residual Oil Saturation

A residual oil saturation in solvent flooding occurs because of two broad phenomena: (1) water blocking and (2) an interaction of dispersion or viscous fingering with the phase behavior. The former phenomenon occurs in first-contact miscible displacements and the latter in developed miscible floods. Both effects are exacerbated by the presence of local heterogeneity and viscous instability.

The definition of residual oil in a miscible flood is quite different from that in a waterflood where oil is left behind as capillary-trapped globs. No amount of throughput will displace this oil without some imposed change in the local capillary number. In a first-contact or developed miscible flood, all the oil, even that “trapped” by whatever mechanism, will eventually be recovered through extraction if enough solvent is injected. By residual oil in a miscible flood, then, we mean that quantity of oil left behind in a solvent flood at some practical extremes of oil cut, oil rate, water/oil ratio, or gas/oil ratio (the data in [Fig. 7.37](#) extend up to a gas/oil ratio of approximately 550 std m³/std m³). Admittedly, this lacks the precision of the waterflood definition,

but from the practical view of recovering oil economically, this distinction is not serious.

7.9.1 Water Blocking. To investigate the effects of local heterogeneity on trapped oil saturation, researchers have conducted experiments in laboratory cores on first-contact miscible displacements (Raimondi and Torcaso 1964; Stalkup 1970; Shelton and Schneider 1975; Spence and Watkins 1980). In these experiments, viscous fingering was suppressed by either gravity stabilization or by matching the viscosity and density of the displacing and displaced fluids. The amount of miscible-flood residual oil was found to depend on the presence of high mobile-water saturation.

The most common interpretation of the effect of mobile water in miscible-flood trapped-oil saturation is that on a pore level, the water shields, or blocks, the solvent from contacting the oil. This explanation also qualitatively accounts for the observed effect of wettability because the oil and water phases are, depending on the wettability, differently distributed in the medium. In water-wet media, oil is contained in the large pores and mostly away from the rock surfaces. The water phase is far more connected compared to the oil phase and, therefore, could serve as a shield to the oil originally present in pores, but not in the main flow channels. For oil-wet media, the phase distribution is reversed—the oil phase is the more continuous, and water is a less effective shield.

A later interpretation of the water-blocking effect (Muller and Lake 1991) suggests that the water-blocking phenomenon is more of a laboratory effect than a field effect. Typical residence time for low-velocity field-scale fluids is long enough for diffusion to admit solvent transfer through local water films. On the other hand, in developed miscible floods, it may be that the diffusion of light hydrocarbon components determines the approach to miscibility. Moreover, the diffusion coefficients of these components are much smaller than for CO₂ (Bijeljic et al. 2002).

7.9.2 Phase-Behavior Interference. When the miscibility of a displacement is developed, the analysis is considerably complicated

because, besides the water-blocking effect, a solvent flood can now trap oil by interactions with the phase behavior. [Fig. 7.40](#) gives results from a combined experimental and theoretical study by Gardner et al. (1981) that shows the results of CO_2 displacements at two different pressure and dispersion levels. At both pressures, the displacements are vaporizing gas drives. Still, the lower pressure gave a measurably lower oil recovery than the higher pressure. The effect is relatively insensitive to rate, and there was no mobile water, indicating that the lower recovery is caused by something more than the dead-end pore effect.

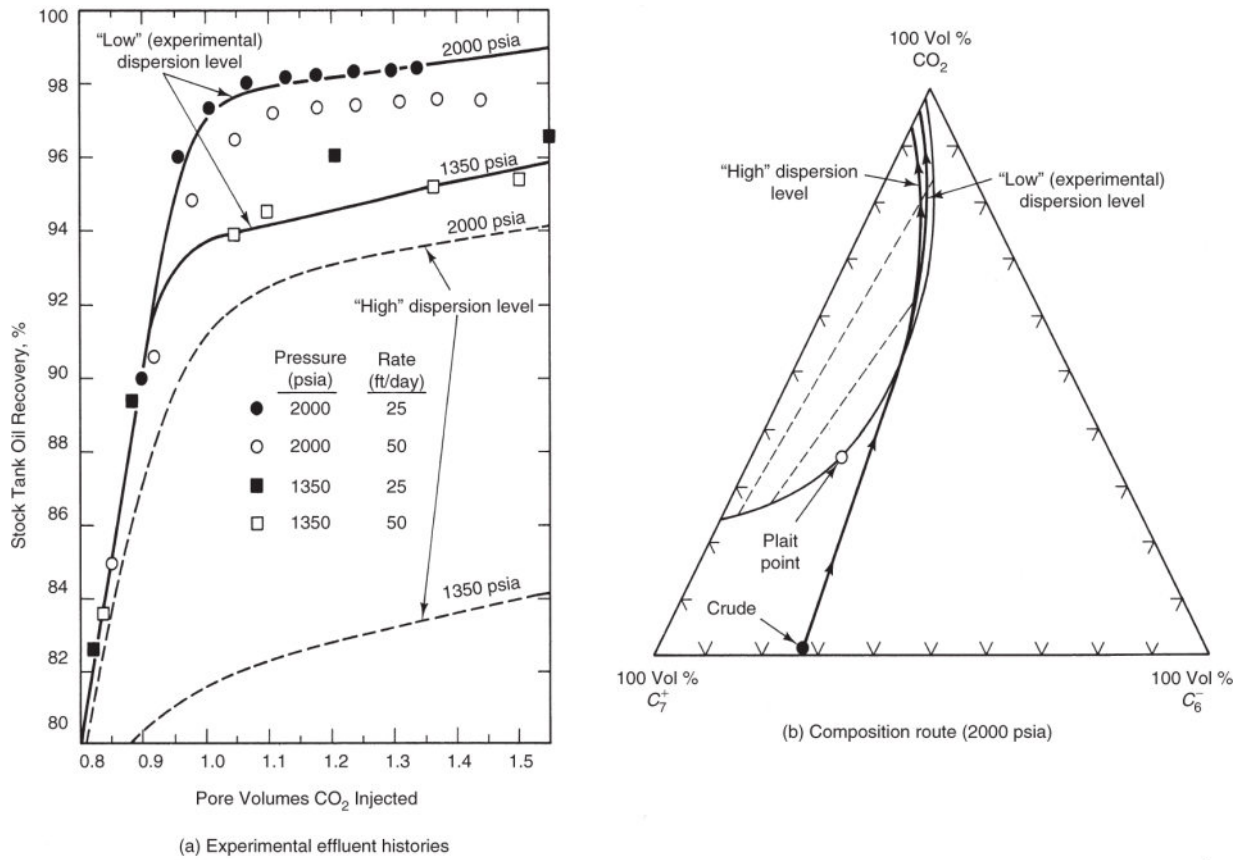


Fig. 7.40—Results of CO_2 displacements at two different pressure and dispersion levels (Gardner et al. 1981). The “high”-dispersion cases are extrapolated.

[Fig. 7.40b](#) shows the composition route for the 13.6-MPa (2,000-psia) displacement illustrated in [Fig. 7.40a](#). Dispersion causes the composition route for this developed miscibility displacement to enter the two-phase region (compare this to the no-dispersion extreme in

[Fig. 7.40b](#)). You will recall from [Fig. 7.12](#) that a dispersion path, unaltered by phase behavior, is a straight line on these plots. This intrusion will lower oil recovery because the trapped-phase saturations within the two-phase region are large, the interfacial tension between the two hydrocarbon phases being also large. Although the effect of dispersion on the experimental data ("low" dispersion level) is relatively minor, the simulated effect at the high dispersion level is pronounced.

[Fig. 7.41](#) attempts further quantification of the combination of phase behavior and dispersion. The results are for a simulated developed miscible flood for various values of pressure as measured against the minimum miscibility pressure. For a given dispersion level (large N_{Pe} means low dispersion), the efficiency of a displacement decreases dramatically as the pressure falls below the MMP. Interestingly, there is a significant nonzero S_{2rm} for pressures well above the MMP. The simulation in [Fig. 7.41](#) is for a multicomponent oil being displaced by CO₂. Evidently, phase-behavior effects persist even when the displacement is well above the MMP.

The displacements in [Fig. 7.40](#) were gravity-stabilized so that it would be proper to ignore viscous fingering. That this phenomenon also contributes to the trapped-oil saturation in an unstable displacement has been demonstrated by the work of Gardner and Ypma (1984). [Fig. 7.42](#) shows literature data on trapped miscible-oil saturation plotted vs. residence ($L\phi/u$) time for several secondary CO₂ floods. The decrease in trapped-oil saturation with residence time is to enable transverse dispersion to smooth out the incipient finger laterally, the displacements in [Fig. 7.42](#) being generally unstable, and there was no mobile water present.

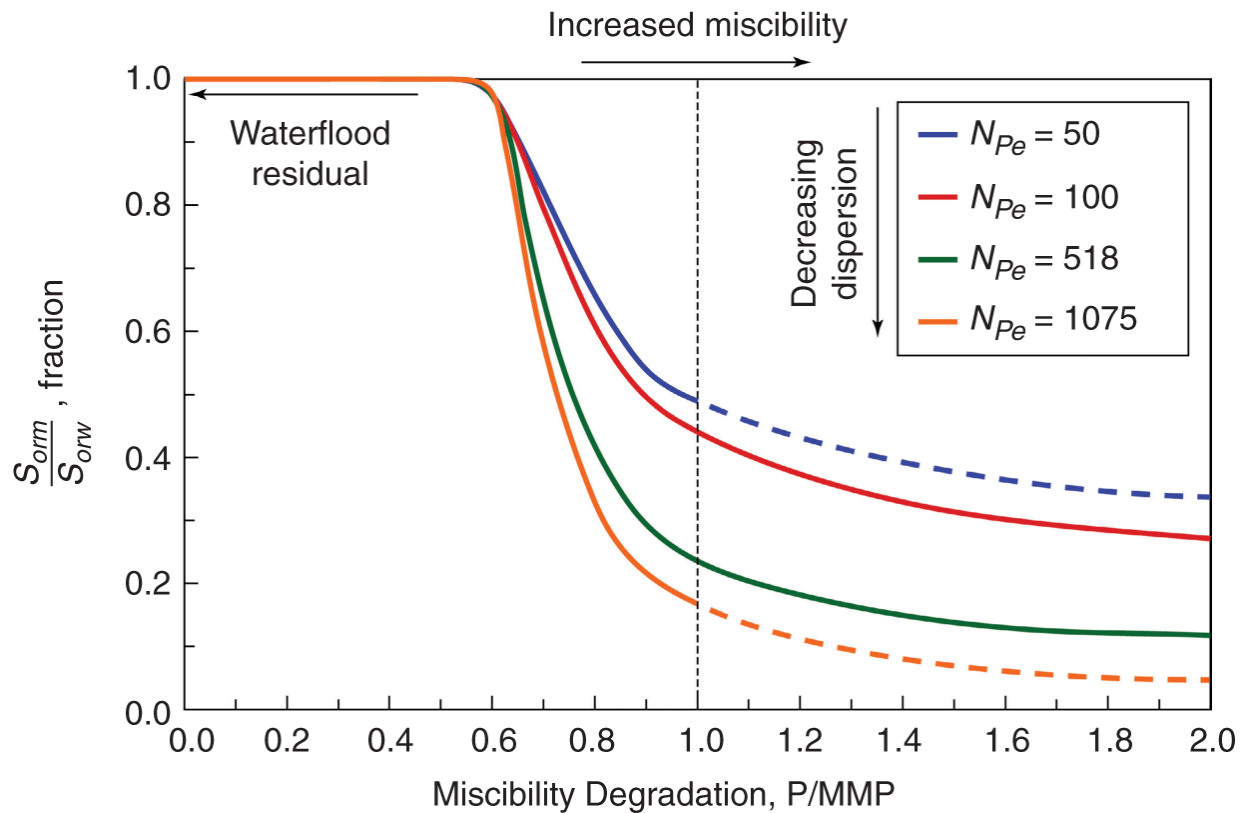


Fig. 7.41—Effect of dispersion and miscibility loss on simulated vaporizing-gas drives (Gharbarnezadeh and Lake 2010).

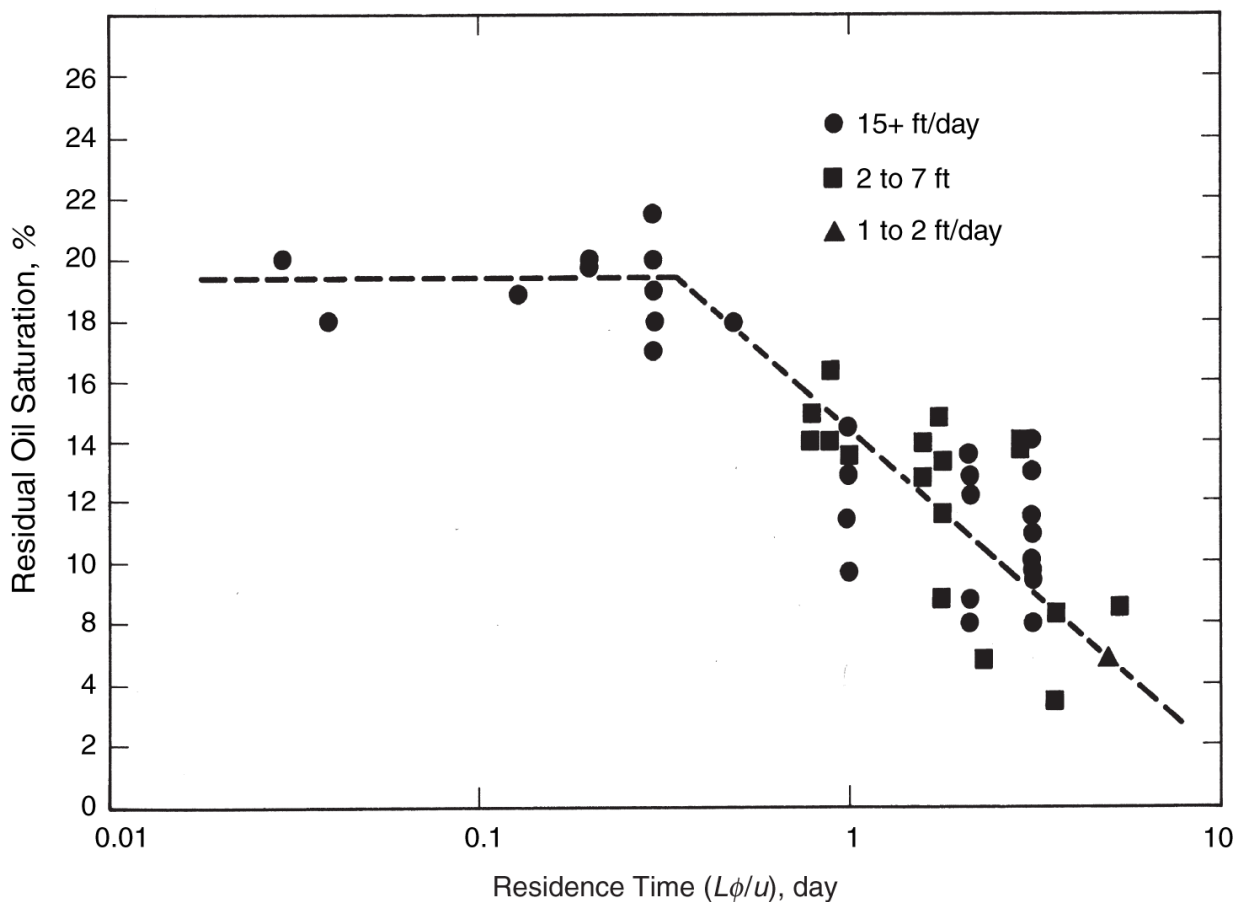


Fig. 7.42—Literature data on trapped miscible-flood oil saturation vs. residence time (Gardner and Ypma 1984).

Gardner and Ypma interpret the large residual-oil saturations at small residence times to be the consequence of interactions between the phase behavior and viscous fingering. They argue that in the longitudinal direction, at the tip of the viscous finger, miscibility between the solvent and crude oil develops much like that described above. In the transverse direction, mixing takes place because of transverse dispersion and perhaps viscous crossflow. Such mixing does not cause developed miscibility unless very long residence times or very high transverse dispersion are allowed. Therefore, oil is first swept out by the longitudinal movement of a finger, the tip of which contains the light-enriched CO_2 solvent, and then reflows back into the finger from the transverse direction into a region of pure CO_2 . Because CO_2 and crude are not first-contact miscible, multiple phases form in the finger, and trapping occurs. In fact, the trapped oil

was actually present in the highest amounts in the regions through which the solvent fingers had passed because of this resaturation and phase-behavior effect. Although this seems paradoxical—that the largest remaining oil saturation is where the solvent has swept—this contention is supported by correlating the data in [Fig. 7.42](#) with a transverse dispersion group, reproducing this correlation with simulation, and finally matching the effluent history of laboratory floods with the simulation results. Interestingly, the composition routes of zones both inside and outside the fingers passed well into the interior of the two-phase region of the ternary diagram. When transverse dispersion is large, transverse mixing takes place before the solvent fingers have emptied of the displacing mixture, and the trapped-oil saturation is reduced.

7.10 Estimating Field Recovery

Despite the technology presented in the previous sections (and indeed throughout this text), predicting the performance of a solvent flood in the field remains a challenge. On the other hand, enough field experience has accumulated for solvent floods that good decisions are possible even without a highly sophisticated prediction procedure. Some of these approaches are discussed below. More detailed descriptions of these methods can be found in Jarrell et al. (2002).

7.10.1 Numerical Simulation. This is a highly detailed and complex technology that deserves a text in its own right. As currently practiced (and there are several variants), it consists of dividing a reservoir into several, often millions, of blocks or cells and then solving the [Chapter 2](#) conservation equations for each. The specific auxiliary relations discussed there are what distinguish one process from another.

The formal procedure consists of the following steps:

1. Decide on the goals of the prediction and what decision it would impact.
2. Accumulate data on field properties such as permeability, porosity, and capillary pressure.
3. Assemble these into a geologic model.

4. Upscale the geologic model into an engineering model. This step is complex for two reasons:
 - The engineering model is necessarily a condensation of the geologic model—some details are inevitably omitted—so that it requires care and experience to know that the omitted details are not important.
 - The engineering model must be adjusted (tuned) to be in agreement with previous laboratory work to include the phase behavior and the relative permeabilities.
5. Using the engineering model, simulate the process to create a history match of whatever existing field data are available. This step is needed because, despite the above efforts, there remain several parameters that are otherwise undetermined.
6. Use the history-matched engineering model to
 - Make predictions or extrapolate the results of the simulation into the future.
 - Use the simulation results to investigate the sensitivity of the model results to unknown inputs, estimate the range of uncertainty in predictions, or both.

Because of the size of the numerical simulations required, the preceding process is laborious and may extend over several months. It is unquestionably the best procedure for making predictions, but perhaps its best use is to calibrate surrogate models.

7.10.2 Surrogate Models. A host of models exists for the purpose of providing quick, if rough, estimates of project performance. These models range from neural networks to applications of the sweep-efficiency correlations discussed in [Chapter 6](#). Two surrogate models deserve more discussion.

Following the practice originally begun in pressure-transient analysis and also the dimensionless-variable theme in this text, it is possible to construct *type curves* for solvent-flooding performance. In one version, these curves plot a dimensionless measure of performance, often oil cut, on the vertical axis and a dimensionless

time on the horizontal axis. The curves themselves are established from analogous field performance, numerical simulation, or both.

A second type of model uses the Koval method to describe the distortion of the solvent oil bank and the oil-bank initial-oil zones caused by heterogeneity. This model yields predictions that are based on only a few parameters, which means that they can be easily fitted to field data (Molleai et al. 2011).

All surrogate models must have two elements: a means to predict recovery efficiency as a function of dimensionless time, and a means to convert the dimensionless result to dimensional performance.

7.11 Concluding Remarks

Solvent methods currently account for a large fraction of the currently implemented EOR methods. For certain classes of reservoirs—low permeability, fairly deep, and with light oil—they are clearly the method of choice. Future technology, particularly related to gravity-stabilization and mobility-control methods, could expand this range somewhat, but the amount of target oil is nevertheless immense.

The topics of special importance in this chapter are the solvent-flooding classifications, the usefulness of the minimum-miscibility pressure correlations, fractional-flow methods, and viscous instability. The importance of viscous fingering remains largely obscured in large-scale displacement because of the ever-present effect of heterogeneity. Both effects combine to account for the large discrepancy between laboratory-scale and field-scale oil recoveries. The material on dispersion and slugs and on solvent/water/oil fractional flow can form the basis for many design procedures. Of course, both topics easily lend themselves to the graphical presentation that is an essential part of this text.

One topic that has been insufficiently discussed here is the availability of solvents. For methane and rich gasfloods, a major portion of the solvent is extracted from the production stream. For nitrogen, the solvent is extracted from the atmosphere, and, of course, for air, the main issue is one of compression. For CO₂ floods, availability can be a significant barrier to field implementation

because there are as yet only a few known deposits of naturally occurring CO₂. The need for CO₂ has been partially addressed by the common practice of recycling produced solvent. It may be partially or even fully addressed by reinjecting CO₂ for the purpose of storage for greenhouse-gas mitigation.

Exercises

7.1 Immiscible Solvent. A particular crude oil has a specific gravity of 0.76, a normal boiling point of 324 K (124°F), a molecular weight of 210 kg/kg-mole, and a viscosity of 15 mPa·s. At 8.16 MPa (1,200 psia) and 322 K (120°F), estimate

- a. The CO₂ solubility in the oil
- b. The viscosity of the saturated CO₂/crude-oil mixture
- c. The swelling factor of the mixture
- d. The CO₂ water solubility expressed as a mole fraction

Use the Simon and Graue correlations ([Figs. 7.22](#) through [7.24](#)) and the water-solubility correlations ([Fig. 7.25](#)).

7.2 Calculating MMP. An analysis of a separator oil is given below, including analyses at two different solution-gas levels. Using the Holm and Josendal (1982) correlation ([Fig. 7.27](#)), estimate the MMP for the separator oil and the oil with 53.4 and 106.9 std m³ gas/std m³ oil. The reservoir temperature is 344 K (160°F).

Component	Separator Oil	Weight Percentage	
		53.4 std m ³ gas/std m ³ oil	106.9 std m ³ gas/std m ³ oil
C ₁		21.3	53.0
C ₂		7.4	18.4
C ₃		6.1	15.1
C ₄		2.4	6.0
C ₅ –C ₃₀	86	54.0	6.5
C ₃₁ ⁺	41	8.8	1.1

What can you conclude about the effect of solution gas on the MMP? How would you explain this with a ternary diagram?

7.3 Superposition and Multiple Slugs. Using the principle of superposition applied to M influent step changes to a 1D medium, show that the composite solution to the convective-diffusion equation is

$$C_i = \frac{C_{i0} - C_{iM}}{2} - \frac{1}{2} \sum_{j=1}^M \left[(C_{ij} - C_{ij-1}) \phi \left(t_D - \sum_{k=1}^j t_{Dk} \right) \right]$$

where C_{ij} = the injected concentration of component i during time interval j (C_{i0} is the same as C_{i1}), and t_{Dj} = the duration of interval j , and where

$$\phi(t_D) = \operatorname{erf} \left(\frac{x_D - t_D}{2 \sqrt{\frac{t_D}{N_{Pe}}}} \right).$$

The first equation in this exercise is valid only for $t_D > \sum_{k=1}^j t_{Dk}$.

7.4 Dilution Paths on Ternary Diagrams. Plot the following:

- Concentration profiles at $t_D = 0.5$ for the displacement of an oil of composition $(C_2, C_3) = (0.1, 0)$ by a small slug ($t_{Ds} = 0.1$) of composition $C_{2J} = 1.0$, which is then followed by a chase gas of composition $C_{3K} = 1.0$. Assume the Peclet number to be 100.
- The dilution path of the concentration profile in Part (a) on a ternary diagram, as in [Fig. 7.32](#).

7.5 Rich Gas Dilution. [Fig. 7.43](#), with initial oil composition $(C_2, C_3)_I = (0.1, 0)$,

- a. Determine the minimum intermediate-component concentration (C_{2J}) that can be used in a continuous mixture of dry gas and intermediate displacing fluid to ensure developed miscibility.
- b. Using the C_{2J} of Part (a) as a lower bound, estimate the solvent slug size necessary to ensure first-contact miscibility at $t_D = 1$ for a series of C_{2J} values. Plot the total amount of intermediate injected ($C_{2J}t_{Ds}$) vs. the slug size to determine an optimum. Assume the Peclet number to be 1,000. Other Peclet numbers can be tried to see its effect on the optimum slug size.

7.6 WAG Calculations. [Fig. 7.44](#) gives representative relative-permeability curves for the Slaughter Estate Unit (SEU). The water, oil, and solvent viscosities are 0.5, 0.38, and 0.037 mPa·s, respectively.

- a. Plot the water/oil and water/solvent fractional-flow curves. Assume that the relative permeability curves for these pairs are the same, and assume $\alpha = 0$.
- b. Determine the optimal WAG ratio for a first-contact miscible secondary displacement in the absence of viscous fingering and dispersion.
- c. If the optimal WAG ratio is used, calculate the minimum solvent/water slug size (t_{Ds}) for complete displacement. The chase fluid is water.
- d. If the solvent/water slug size is 50% greater than that calculated in Part c, plot the time/distance diagram and effluent history for this displacement.
- e. Estimate the miscible-flood trapped-oil saturation S_{2r} from [Fig. 7.44](#).

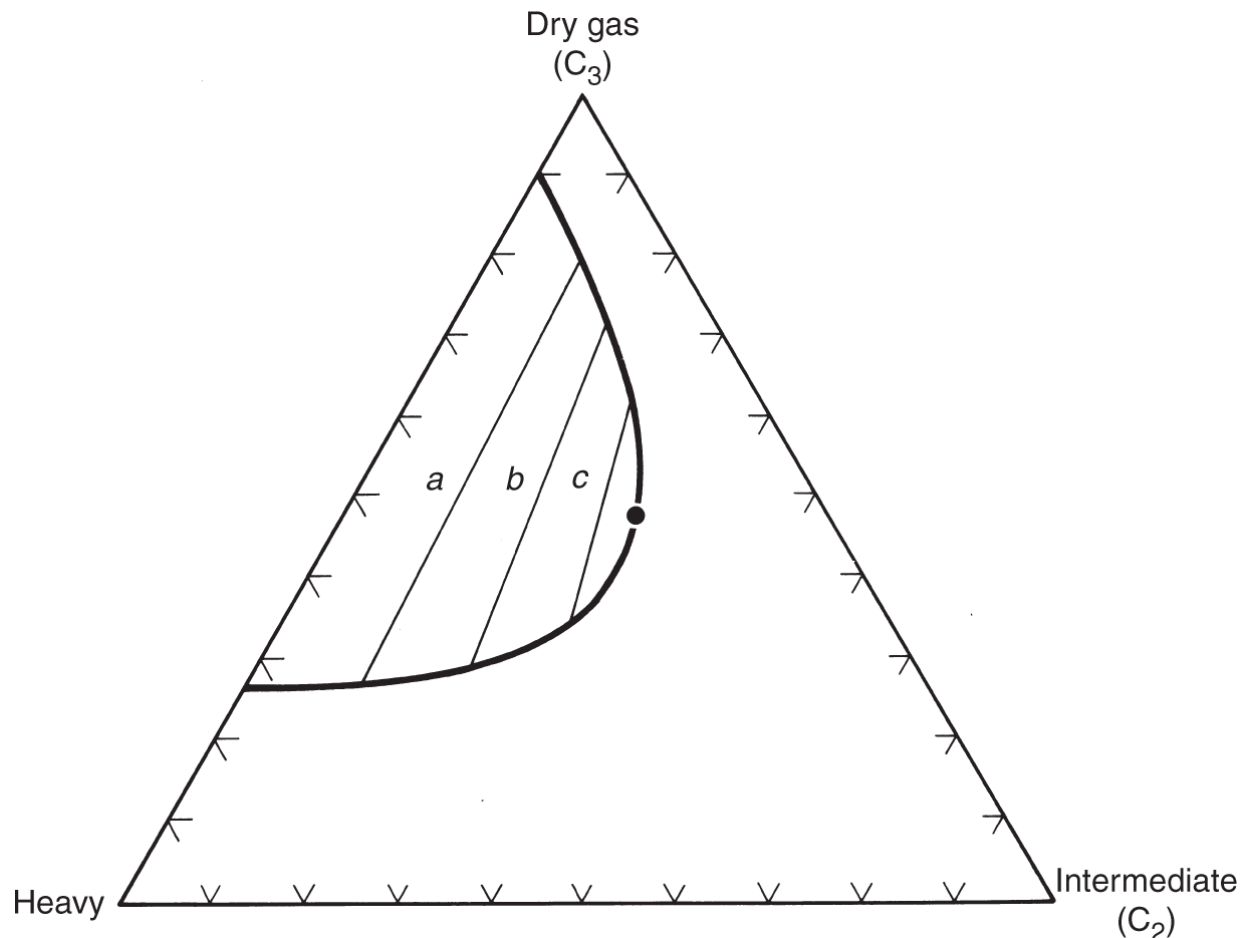


Fig. 7.43—Ternary diagram for rich-gas design problem.

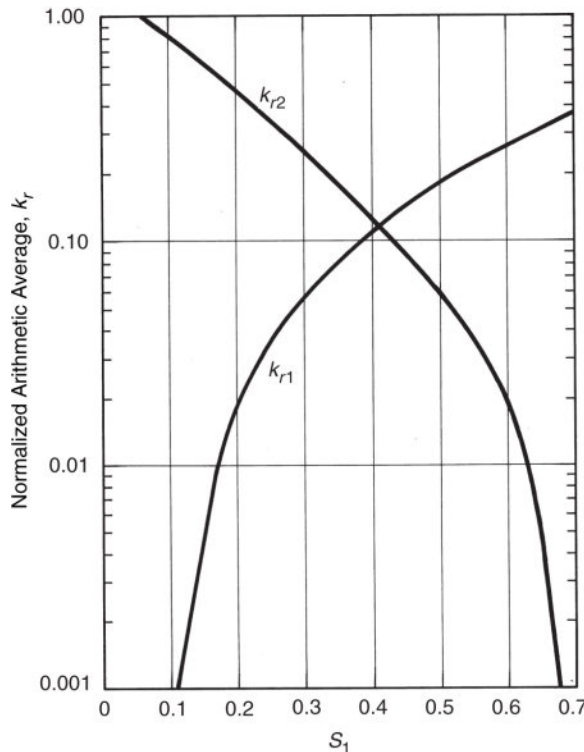


Fig. 7.44—SEU relative-permeability curves (Ader and Stein 1984).

7.7 Solvent Velocity With Water/Oil Solubility.

- Show that by including the solvent/water solubility and the solubility of the solvent in a trapped-oil saturation calculation, the solvent specific velocity (Eq. 7.11b) becomes

$$v_3 = \frac{1 - f_{1J}^s (1 - C_{31})}{1 - S_{1J} (1 - C_{31}) - S_{2r} (1 - C_{32})}$$

where C_{31} = solvent solubility in water = $R_{31}B_3/B_1$ and C_{32} = solvent solubility in oil = $R_{32}B_3/B_2$. R_{ij} is the solubility of component i in phase j in standard volumes of i per standard volume of j . See [Figs. 7.22](#) and [7.25](#).

- Using the S_{2r} from Part e of Exercise 7.6 and taking $R_{31} = 17.8$ std m³ gas/std m³ water, $R_{32} = 214$ std m³ gas/std m³ oil, $B_3 = 10^{-3}$ m³ gas/std m³ gas, $B_1 = 1$ m³ water/std m³

- water, and $B_2 = 1.2 \text{ m}^3 \text{ oil/std m}^3 \text{ oil}$, repeat Parts b through d of Exercise 7.6.
- c. Repeat Parts c and d of Exercise 7.6 if the chase fluid is a gas having the identical properties of the solvent instead of water.

7.8 Carbonated Waterflooding and Fractional Flow. One of the earlier EOR techniques is displacement by CO₂-saturated water. This technique is amenable to fractional-flow analysis (de Nevers 1964).

- a. Show that the specific velocity of a piston-like carbonated-water front is given by

$$v_{\Delta C_3} = \frac{1 - \frac{K_{21}^3}{K_{21}^3 - 1}}{1 - S_{2r} - \frac{K_{21}^3}{K_{21}^3 - 1}}.$$

The preceding equation assumes that flow behind the front is at a CO₂-saturated residual-oil phase.

- b. By matching the specific velocity of the rear of the oil bank to the preceding equation, show that the oil-bank saturation and fractional flow must satisfy

$$v_{\Delta C_3} = \frac{1 - \frac{f_1 - C_{32}}{1 - C_{32}}}{1 - \frac{S_1 - C_{32}}{1 - C_{32}}}.$$

In these equations, K_{21}^3 is the volumetric partition coefficient of CO_2 ($i = 3$) between the water ($j = 1$) and oil ($j = 2$) phases and C_{32} is the volume fraction of CO_2 in the oil. $f_1(S_1)$ is the water fractional-flow curve.

- c. Estimate C_{32} and K_{21}^3 from [Fig. 7.22](#) at 15 MPa and 340 K. You may assume ideal mixing in both phases.
- d. Calculate and plot the effluent oil cut of a carbonated waterflood in a 1D permeable medium with initial (uniform) oil cut of 0.1.
- e. On the same graph, plot the effluent-oil fractional flow of a noncarbonated waterflood. Finally, plot the incremental oil recovery (IOR) vs. t_D .

For this problem, use the following parameters in the exponential relative-permeability curves:
 $n_1 = n_2 = 2$, $k_{r1}^0 = 0.1$, $\phi = 0.2$, $k_{r2}^0 = 0.8$, $\mu_1 = 0.8 \text{ mPa}\cdot\text{s}$, $\mu_2 = 5 \text{ mPa}\cdot\text{s}$, $S_{1r} = S_{2r} = 0.2$, and $\alpha = 0$. The oil molecular weight is 200 kg/kg-mole, its density is 0.78 g/cm³, and the UOP factor is 11.2.

7.9 Viscous Fingering and Displacement Efficiency. Using the Koval theory (Eq. 7.20), plot the effluent history of a first-contact miscible displacement in which the oil/solvent viscosity ratio is 50 and the heterogeneity factor is 5.

7.10 Viscous Fingering Representation by Mixing Parameter. In the Todd-Longstaff (1972) representation of viscous fingering, the Koval factor K_{val} in Eq. 7.17 is replaced by K_{TL} , where

$$K_{TL} = \frac{M_{2e}}{M_{3e}} = v^{1-\omega}$$

and M_{2e} and M_{3e} = effective solvent and oil viscosities in the mixing zone, v = viscosity ratio, and ω = a mixing parameter ($0 < \omega < 1$).

- a. Repeat Exercise 7.9 with $\omega = 1/3$.

- b. Determine the correspondence between K_{val} and K_{TL} by setting $K_{TL} = K_{\text{val}}$ in Eq. 7.17 and plotting ω vs. v for various H_k .

7.11 Dispersion as a Normal Distribution. One view of dispersion is that it is the result of the mixing of a large number of fluid particles along independent paths. If so, the distribution of particles should follow a normal distribution. In this exercise, we show that the equations in Section 7.6 reduce to such a form.

- a. Show that for Eq. 7.5 applied to a unit slug, $C_{il} = C_{iK} = 0$, and that $t_{Ds} C_{iJ} = 1$ reduces to

$$C_i = \frac{1}{2t_{Ds}} \left\{ \operatorname{erf} \left[\frac{x_D - (t_D - t_{Ds})}{2\sqrt{\frac{t_D}{N_{Pe}}}} \right] - \operatorname{erf} \left[\frac{x_D - t_D}{2\sqrt{\frac{t_D}{N_{Pe}}}} \right] \right\}$$

for $t_D \gg t_{Ds}$.

- b. Using the definition for the error function (Eq. 5.54), show that the preceding equation becomes

$$C_i = \left(\frac{N_{Pe}}{4\pi t_D} \right)^{1/2} e^{-\left[(x_D - t_D)^2 / (4t_D/N_{Pe}) \right]}$$

as $t_{Ds} \rightarrow 0$. The first equation in Exercise 7.11 says that the distribution of a large number of particles at $x_D = 0$ initially approaches a normal distribution with mean position $x_D = t_D$ and standard deviation $2\sqrt{t_D/N_{Pe}}$.

Chapter 8

Polymer Methods

Polymer flooding consists of dissolving a water-soluble polymer in water to decrease its mobility as injected water flows through a permeable medium. The resulting increase in viscosity, as well as the decrease in aqueous-phase permeability that occurs with most polymers, reduces the mobility ratio compared to injecting water without polymer. This reduction of the mobility ratio increases the efficiency of the waterflood, primarily through greater volumetric sweep efficiency and a lower swept-zone oil saturation, although the viscosity increase also can decrease the velocity of the injected water front in linear displacements. See [Chapter 6](#) for discussion of this effect.

Residual oil saturation S_{2r} is usually assumed to be the same for both waterflooding and polymer flooding, but for viscous oils the remaining oil saturation is often much less for polymer flooding than for waterflooding since only a few pore volumes can be injected in the field under most circumstances. Under at least some conditions, viscoelastic polymers appear to reduce the residual oil saturation compared to water (Huh and Pope 2008; Sheng 2011), but whether it is a reduction in residual oil or remaining oil saturation is uncertain. The greater recovery efficiency through improved volumetric sweep and displacement efficiency constitutes the economic incentive for polymer flooding when applicable. Generally, a polymer flood will be economical only when the waterflood mobility ratio is high enough so that waterflooding alone would be inefficient, or when the reservoir heterogeneity is relatively high, or both.

Polymers have been used in oil production in three modes:

1. As near-well treatments to improve the performance of water injectors or watered-out producers by blocking off high-conductivity zones
2. As agents that may be crosslinked in situ to plug high-conductivity zones at depth in the reservoir (Needham et al. 1974). These processes require that polymer be injected with an inorganic metal cation that will cross link subsequently injected polymer molecules with those already bound to solid surfaces.
3. As agents to reduce water mobility or water/oil mobility ratio. The water mobility is reduced by increasing its viscosity and by reducing its permeability. Permeability reduction is less important than viscosity increase and is negligible at high permeability and for some polymers.

The first mode is not truly polymer flooding because the actual oil-displacing agent is not the polymer. Most polymer enhanced oil recovery (EOR) projects have been carried out in the third mode, the so-called mobility control flood, and this is the mode emphasized here. How reducing the mobility ratio affects displacement and volumetric sweep efficiency has been discussed in [Chapters 5](#) and [6](#). Excellent stand-alone texts exist on polymer flooding for oil recovery (Sorbie 1991).

[**Fig. 8.1**](#) is a schematic of a typical polymerflood injection sequence: an optional preflush usually consisting of a low-salinity brine; an oil bank formed from the displaced oil; the polymer solution itself; an optional freshwater buffer to protect the polymer solution from backside dilution; and, finally, chase or drive water. The buffer may contain polymer in decreasing amounts (a grading or taper) to lessen the unfavorable mobility ratio between the chase water and the polymer solution. Because of the driving nature of the process, polymer floods are always performed through separate sets of injectors and producers. The preflush is not usually performed because most polymers will tolerate mixing with the formation brine, the preflush takes a significant amount of time with a negative impact on the economics, and because the low-salinity water in a preflush

does not enter the same layers that the polymer enters because of reduced mobility ratio.

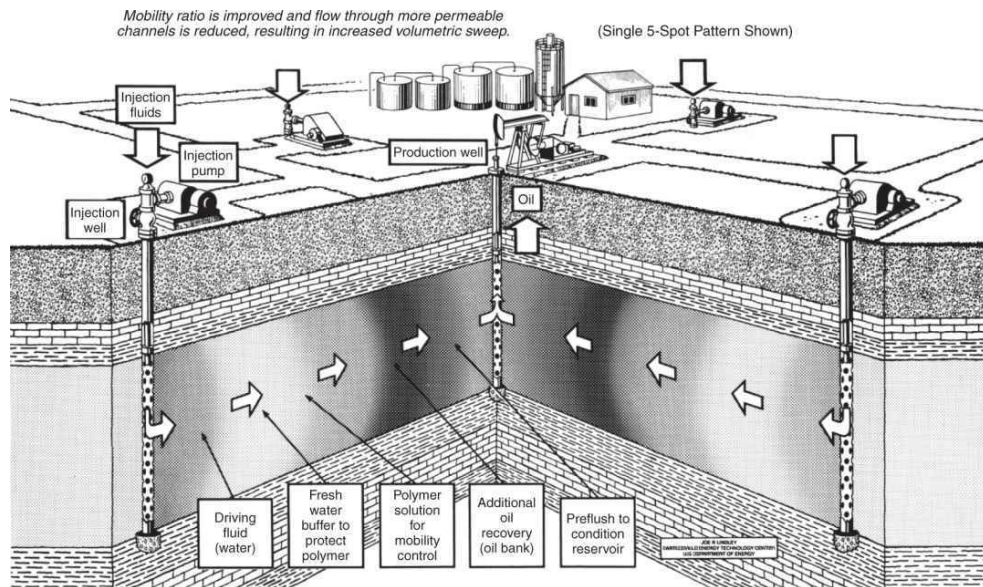


Fig. 8.1—Schematic of polymer-flooding sequence (drawing by Joe Lindley, US Department of Energy, Bartlesville, Oklahoma).

The surface facilities in a typical polymer flood consist of water treatment and mixing facilities, piping, valves, injection pumps, and metering equipment. For the most part, these are operated at low pressure because the mixing process does not need high pressure to be effective, not being as closely tied to phase behavior as other processes. Some of these facilities can be sources of mechanical degradation, as is discussed further below. On occasion, specialized separation equipment is needed at the producers because produced polymer can form emulsions.

The most widely used polymers are sensitive to salinity and hardness, but not to pressure. Hence, this chapter contains relatively little discussion about pressure (although a pressure gradient is required for flow), but a great deal about salinity and hardness.

Oilfield waters (brines) are complex, containing 10 to 50 components, most of which are dissolved inorganic compounds in either negatively charged (anionic) or positively charged (cationic) complexes. As for crude characterization, it is sufficient to combine or lump these components for most applications, although anions and

cations should be treated separately. Two common classes of water-soluble components are total dissolved solids (TDS), the concentration of all the inorganic components in a brine, and hardness, the concentration of the multivalent cations in a brine. TDS is usually expressed in units of parts per million (ppm), or equivalently, g/m³ or mg/L. Hardness is given in units of ppm, g/m³, or mg/L. Occasionally, molal or equivalent units are used (Lake et al. 2002).

When the distinction is important, we will use the above terms. Otherwise, we will simply refer to brine composition as *salinity*. Usually, the sensitivity to hardness is greater than to TDS.

[**Fig. 8.2**](#) shows several salinity (as TDS) and hardness values for oilfield brines. Some calibration is helpful here. The salinity of drinking water is less than 1,000 ppm. You can see that the majority of oilfield waters are more saline (salty) than drinking water; hence, the use of the word *brine* rather than water. The salinity of seawater is approximately 33,000 ppm TDS. Many oilfield brines are saltier than seawater. The hardness of seawater is also approximately 3,000 ppm. The salinity of a saturated NaCl solution is approximately 300,000 ppm TDS. Many brines approach this salinity.

There is a rough correlation between TDS and hardness (particularly at high TDS), the correlation being caused by the reactivity of the host formation with the brine, as determined through its temperature and mineral content. Perhaps the main conclusion from [**Fig. 8.2**](#) is the enormous variability of brine salinity.

Because of the high molecular weight (typically 2 to 20 million), only a small amount (a few thousand ppm) of polymer will bring about a substantial increase in water viscosity. Furthermore, several types of polymers reduce mobility by reducing the water permeability in addition to increasing its viscosity. We can explain how polymer solutions reduce mobility, and their interactions with salinity, with some discussion of polymer chemistry. Note that in the universe of polymers, we will discuss only those that are water soluble.

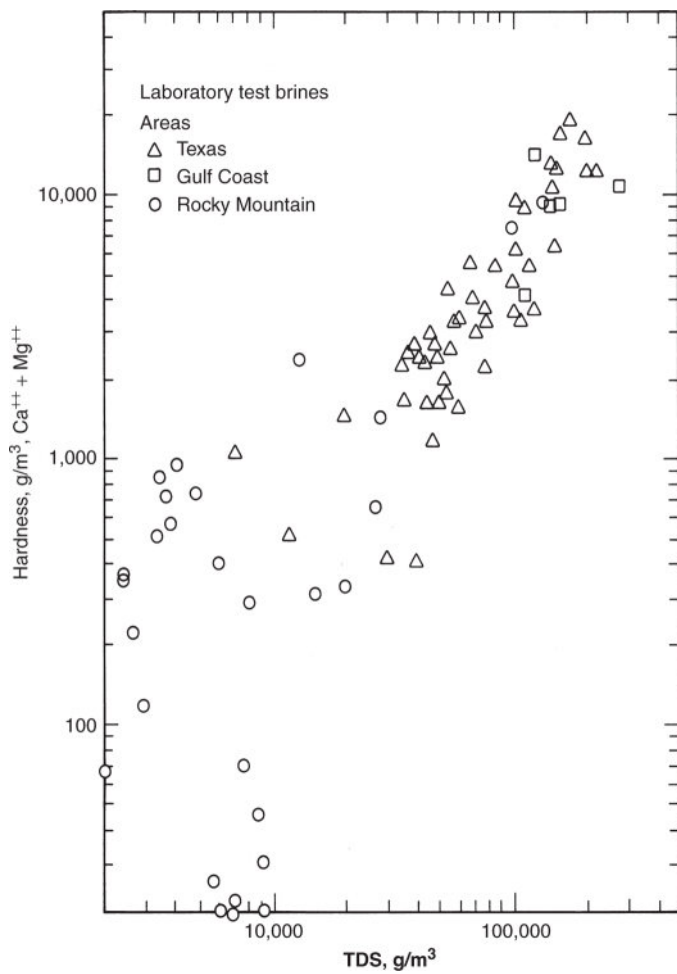


Fig. 8.2—Salinities from representative oilfield brines (Gash et al. 1981).

8.1 The Polymers

The three most common polymers currently being used for polymer flooding are hydrolyzed polyacrylamide (HPAM), copolymers (a polymer consisting of two or more different types of monomers) of acrylic acid and acrylamide and copolymers of acrylamide and 2-acrylamide 2-methyl propane sulfonate (AM/AMPS). Other polymers that have been studied in the laboratory, but with little current use in polymer floods are xanthan gum, hydroxyethylcellulose (HEC), carboxymethylhydroxyethylcellulose (CMHEC), aminopolysulfonates (AMPS), polyacrylic acid, scerlo glucan, dextran, polyethylene oxide (PEO), and polyvinyl alcohol. Although only the first three have actually been used in the field, there are many potentially suitable chemicals, and some may prove to be more effective than those now

used. Nevertheless, in the remainder of this discussion, we deal with these exclusively. [**Figs. 8.3 and 8.4**](#) show representative molecular structures.

8.1.1 Polyacrylamides. These are polymers of which the primary monomeric unit is the acrylamide molecule. Polymerization consists of stringing together the acrylamide monomers into long-chain molecules (polymers), as shown in [Fig. 8.3](#). In most instances, the polyacrylamides are co-polymers with acrylic acid or they are post hydrolyzed to form anionic (negatively charged) carboxyl groups ($-\text{COO}^-$) to replace some amide groups along the backbone chain. Typical degrees of hydrolysis are 30 to 35% of the acrylamide monomers; hence, the polymer is anionic because the carboxyl group has a negative charge. The anionic nature of HPAM accounts for many of its physical properties. The backbone of the polymer is $-\text{C}-$ single bonds that are rotating freely.

Both the molecular weight and the degree of hydrolysis have been selected to optimize certain properties such as water solubility, viscosity, and retention. If the degree of hydrolysis is too low, the polymer will not be water soluble. If it is too high, its properties will be too sensitive to salinity and hardness (Shupe 1981).

The viscosity-increasing feature of HPAM is a result of its high molecular weight. Its large molecule is made effectively larger in solution by the anionic repulsion between polymer molecules and between segments on the same molecule. This repulsion causes the molecule in solution to elongate and snag onto others that are similarly elongated, an effect that accentuates the mobility reduction at higher concentrations.

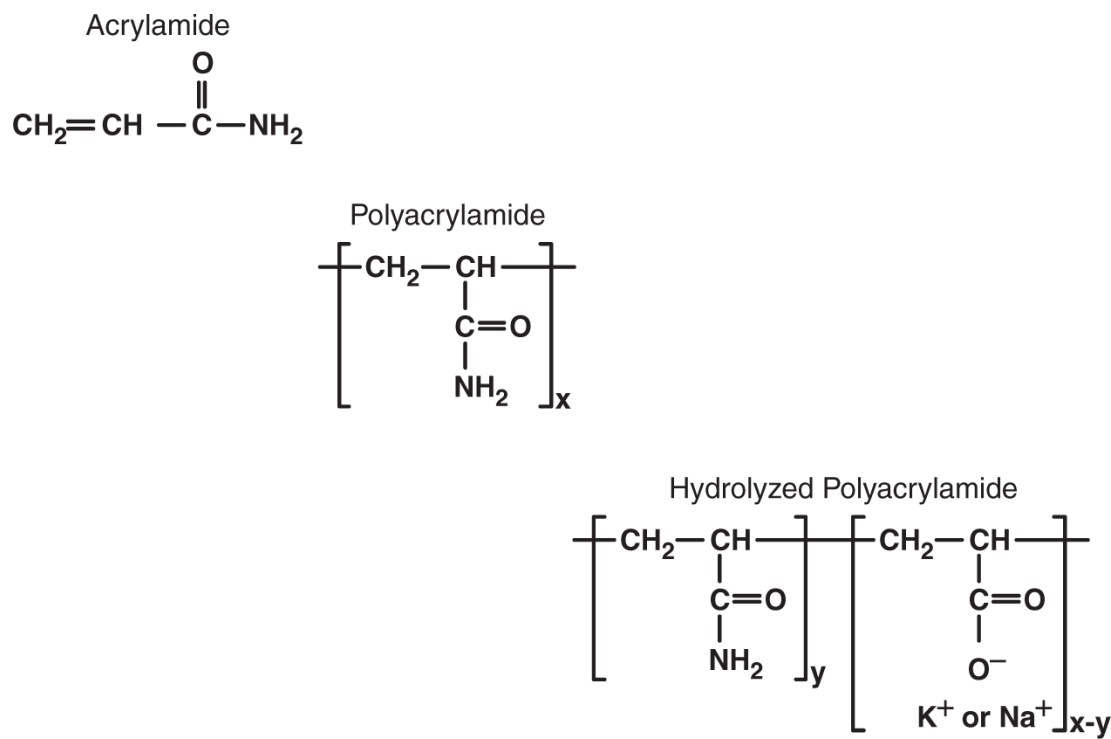


Fig. 8.3—Polyacrylamide synthesis and molecular structure, where y indicates the number of amide groups (for HPAM) and $x-y$ the number of carboxylic groups. The degree of hydrolysis is given by the ratio of the moles of carboxylic groups to amide groups. If anions or cations are present, they may shield the carboxylic groups as shown.

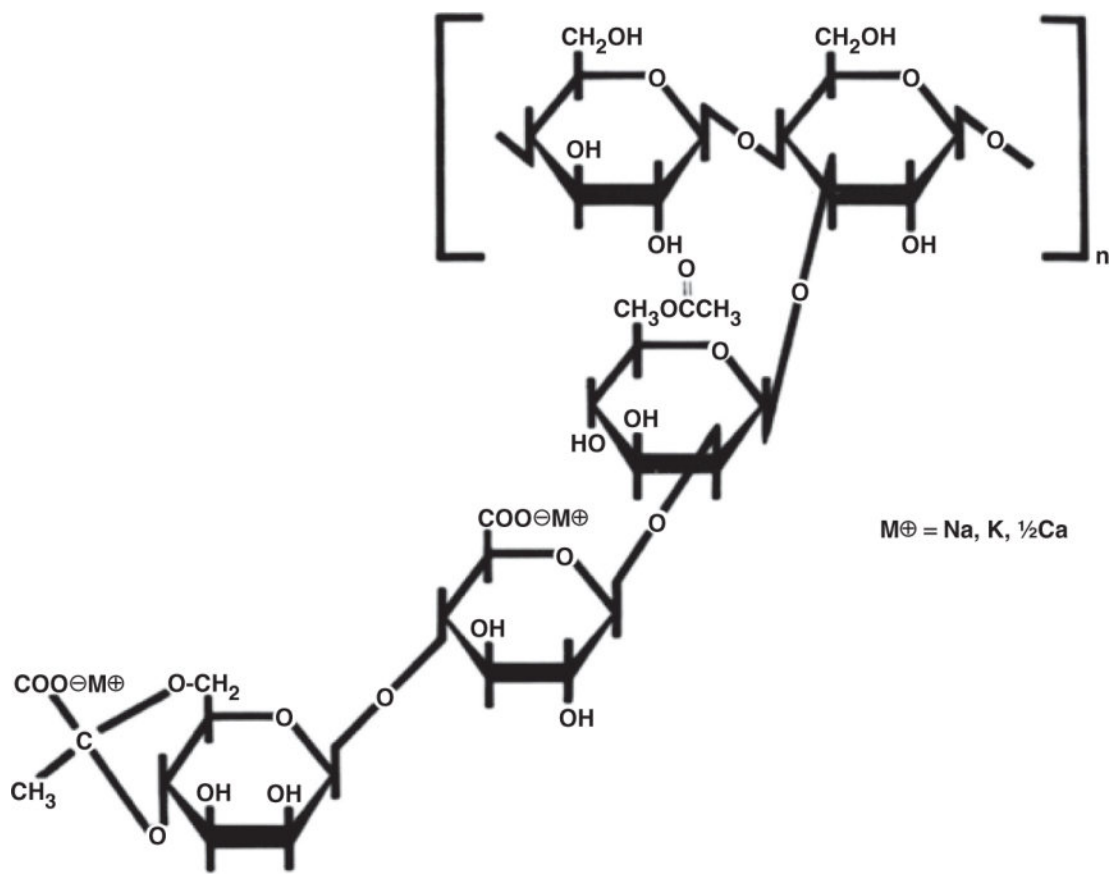


Fig. 8.4—Molecular structure of xanthan gum.

If the brine salinity or hardness is high, this repulsion is greatly decreased through ionic shielding of the carboxylic groups because the freely rotating carbon-carbon bonds ([Fig. 8.3](#)) allow the molecule to coil up. This shielding causes a decrease in the polymer solution viscosity when the salinity is increased up to about 40,000 ppm. Very little change in viscosity occurs for even higher salinity. Therefore, high concentrations of high molecular weight HPAM can be used to achieve the required viscosity even at high salinity (Levitt and Pope 2008). The same statement applies with respect to hardness (calcium and other divalent cations) provided the degree of hydrolysis is below about 35%. If HPAM is subjected to either high pH or high temperature, further hydrolysis will occur and eventually reach levels on the order of about 80%. The calcium ions will then interact with the carboxyl ions and cause precipitation (Levitt and Pope 2008). There are now commercial co-polymers and ter-polymers of acrylamide that

do not hydrolyze and that will therefore tolerate high calcium concentrations even at high temperature.

8.1.2 Polysaccharides. These polymers are formed from the polymerization of saccharide molecules ([Fig. 8.4](#)) by a bacterial fermentation process. This process leaves substantial cell debris in the polymer solution that must be removed before the polymer is injected (Wellington 1983). These polymers are susceptible to bacterial attack, a disadvantage in the reservoir unless an effective biocide is used, but a possible environmental advantage under some circumstances. However, polysaccharide polymer solutions are less sensitive to brine salinity and hardness.

[Fig. 8.4](#) shows the origin of the salinity tolerance. The polysaccharide molecule is relatively nonionic and therefore free of the ionic-shielding effects of HPAM. Polysaccharides are more highly branched than HPAM, and the oxygen-ringed carbon bond does not rotate fully; hence, the molecule increases brine viscosity by snagging and by adding a more rigid structure to the solution. Polysaccharides do not reduce permeability. Furthermore, they do not have significant viscoelastic effects. Molecular weights of polysaccharides are generally approximately 2 million, which is lower than those of HPAM.

HPAM is less expensive per unit amount than most polysaccharides, in particular xanthan gum. Historically, HPAM has been used in approximately 95% of the reported field polymer floods (Manning et al. 1983). Mostly because they are more expensive, very little polysaccharide-type polymers are being used for polymer flooding now, but they are used for other oilfield applications such as drilling and fracturing fluids.

A persistent question about the usage of polymers is their toxicity. Large molecules can be a source of contamination and pollution. Remember, however, that the usage of these solutions is usually at depths greater than those of groundwater resources. Some polymers are common additives in foodstuffs (e.g., beer and toothpaste) and cosmetics.

8.1.3 Polymer Forms. The polymers described in the preceding subsections exist in three distinct physical forms: powders, broths, and emulsions. Powders, the oldest of the three, can be readily transported and stored at low cost. They are difficult to mix because the first water contacting the polymer tends to form highly viscous layers of hydration around the particles, which greatly slow subsequent dissolution. Powders are the most commonly used in practice. The hydration of some polymers can be delayed until the solution is inside the reservoir. Broths are aqueous suspensions of approximately 10 wt% polymer in water and are much easier to mix than powders. They have the disadvantage of being comparatively expensive because of the need to transport and store large volumes of water. Broths, being quite viscous, can require special mixing facilities. In fact, it is this difficulty that limits the concentration of polymer in the broth. Emulsion polymers, the newest polymer form, contain up to 35 wt% polymer solution, suspended through the use of a surfactant in an oil-carrier phase. Once this water-in-oil emulsion is inverted, the polymer concentrate can be mixed with makeup water to the desired concentration for injection.

8.2 Polymer Properties

This section presents qualitative trends, quantitative relations, and representative data on the following properties: viscosity relations, non-Newtonian effects, polymer transport, inaccessible pore volume, permeability reduction, and chemical, biological, and mechanical degradation.

8.2.1 Viscosity Relations. [Fig. 8.5](#) shows a plot of polymer solution viscosity vs. polymer concentration. This type of curve has traditionally been modeled by an extended Flory-Huggins equation (Flory 1953; Pope and Nelson 1978):

$$\mu' = \mu_1 \left(1 + a_1 C_{41} + a_2 C_{41}^2 + a_3 C_{41}^3 + \dots \right), \quad \dots \quad (8.1)$$

where C_{41} is the polymer concentration in the aqueous phase, μ_1 is the brine (solvent) viscosity, and a_1 , a_2 , and so on are constants. In

the remainder of this chapter, we drop the second subscript 1 on the polymer concentration because polymer is always in an aqueous phase. The usual polymer concentration unit is g /m³ of solution, which is approximately the same as ppm. The linear term in Eq. 8.1 accounts for the dilution range in which the polymer molecules act independently (without entanglements). For most purposes, Eq. 8.1 can usually be truncated at the cubic term, so that only three constants must be estimated from experimental data.

For a 1000 g /m³ xanthan gum solution at a shear rate of 5 s⁻¹ in 1 wt% NaCl brine at 24°C, the viscosity is 10 mPa·s (10 cp) from [Fig. 8.5](#). Compared to brine at the same conditions, this is a substantial increase in viscosity brought about by a relatively dilute concentration (recall that 1000 g /m³ = 0.1 wt%).

Compared to viscosity alone, a more fundamental method of measuring the thickening power of a polymer is through its intrinsic viscosity, defined as

$$[\mu] = \lim_{C_4 \rightarrow 0} \left(\frac{\mu' - \mu_1}{\mu_1 C_4} \right). \dots \dots \dots \quad (8.2)$$

From its definition, $[\mu]$ is a measure of the polymer's intrinsic thickening power. It is insensitive to polymer concentration. The intrinsic viscosity for the xanthan gum polymer under the conditions given previously is 70 dl/g, the units being equivalent to reciprocal weight percent. Intrinsic viscosity is the same as the a_1 term in Eq. 8.1.

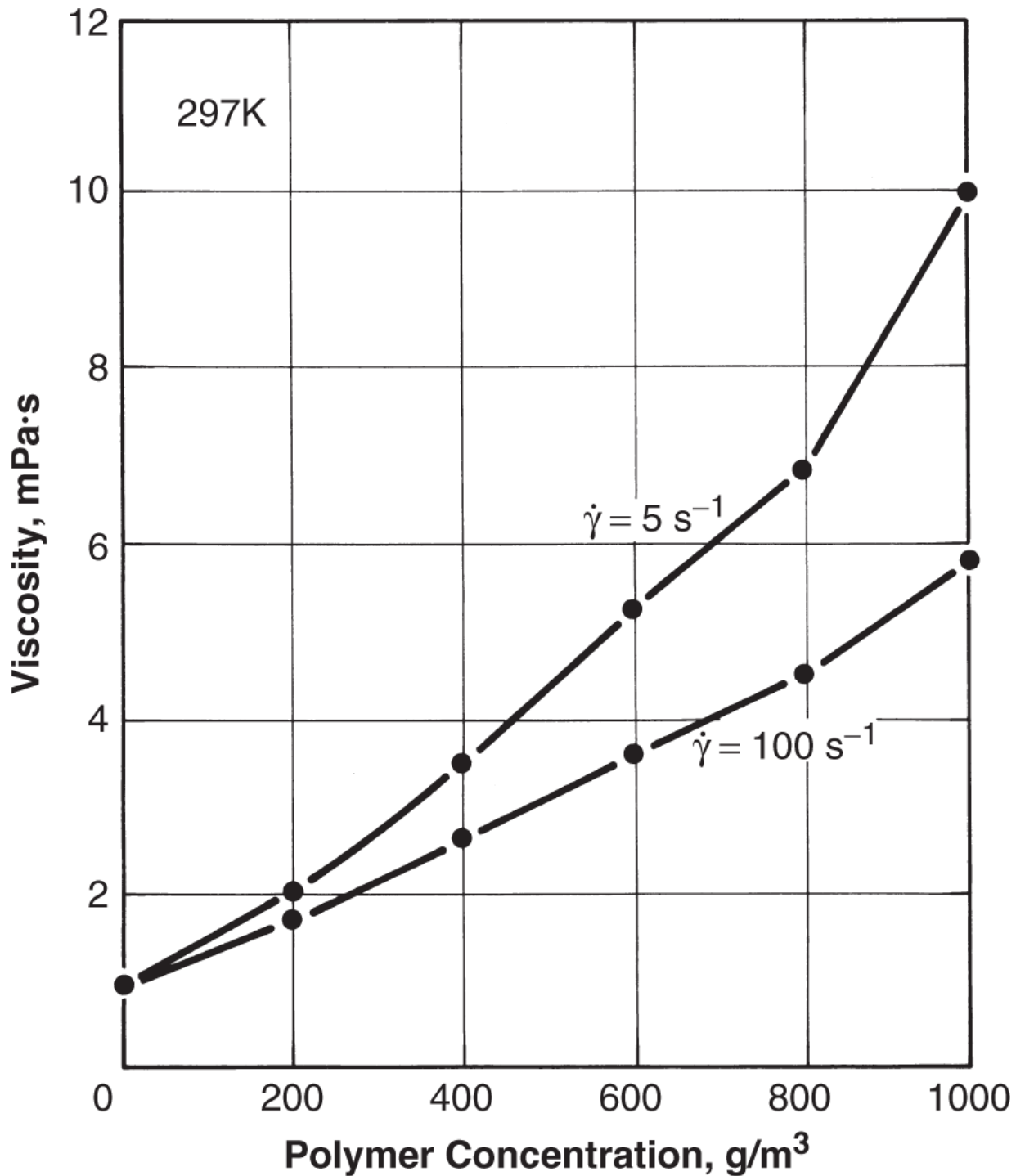


Fig. 8.5—Xanthan gum viscosity vs. concentration in 1% NaCl brine (Tsaur 1978).

For any given polymer/solvent pair, the intrinsic viscosity increases as the molecular weight of the polymer increases according to the following equation (Flory 1953):

The exponent varies between approximately 0.5 and 1.5, being larger for good solvents such as fresh water. K' is a polymer-specific constant.

The preceding relationships are useful for characterizing polymer solutions. For example, the size of the polymer molecules in solution can be estimated from Flory's (1953) equation for the mean end-to-end distance:

This equation, being empirical, assumes certain units; $[\mu]$ must be in dl/g, and d_p is returned in Angstroms (10^{-10} m). This measure of polymer size is useful in understanding how these very large molecules propagate through the small pore openings of rocks. The molecular weight of xanthan gum is approximately 2 million. From Eq. 8.4, d_p is approximately 0.4 μm . This is the same size as many of the pore throats in a low-to-moderate-permeability sandstone. As a result, we would expect to observe polymer/rock interactions that include plugging of pore throats when they are too small compared to the polymer coil.

8.2.2 Non-Newtonian Effects. A fluid is non-Newtonian if its viscosity changes with the rate at which it flows. Polymer molecules, being large and having shapes that change with the stresses on them, would be expected to be non-Newtonian. The phrase “how fast it flows” is captured through the use of effective shear rate, which was first encountered in Section 3.1.

Non-Newtonian behavior has two broad characteristics:

- **Viscous effects:** properties of liquids reflecting material movement subject to a shear stress. The fluid, in other words, flows under shear (e.g., it cannot support a shear stress).
 - **Elastic effects:** properties of solids or fluids reflecting material movement subject to a normal stress. Such material cannot

support a normal stress. (In rheology, the normal stress is accounted for separately from pressure, which entails fluid compressibility.)

Polymer solutions exhibit both effects, but some polymers do so more than others. For example, HPAM undergoes both viscous and elastic effects, while xanthan gum is most affected by viscous effects. We begin with discussion of the viscous effects.

[Fig. 8.6](#) shows polymer-solution viscosity μ'_1 vs. shear rate $\dot{\gamma}$ measured in a laboratory viscometer at fixed salinity. At low shear rates, μ'_1 is independent of $\dot{\gamma}$ ($\mu'_1 = \mu_1^0$), and the solution is a Newtonian fluid. At higher $\dot{\gamma}$, μ'_1 decreases, approaching a limiting ($\mu'_1 = \mu_1^\infty$) value that is not much greater than the water viscosity μ_1 at some high shear rate. This shear rate is off-scale to the right in [Fig. 8.6](#). A fluid for which the viscosity decreases with increasing $\dot{\gamma}$ is *shear-thinning*.

The shear-thinning behavior of the polymer solution is caused by uncoiling and unsnagging of the polymer chains when they are elongated in shear flow.

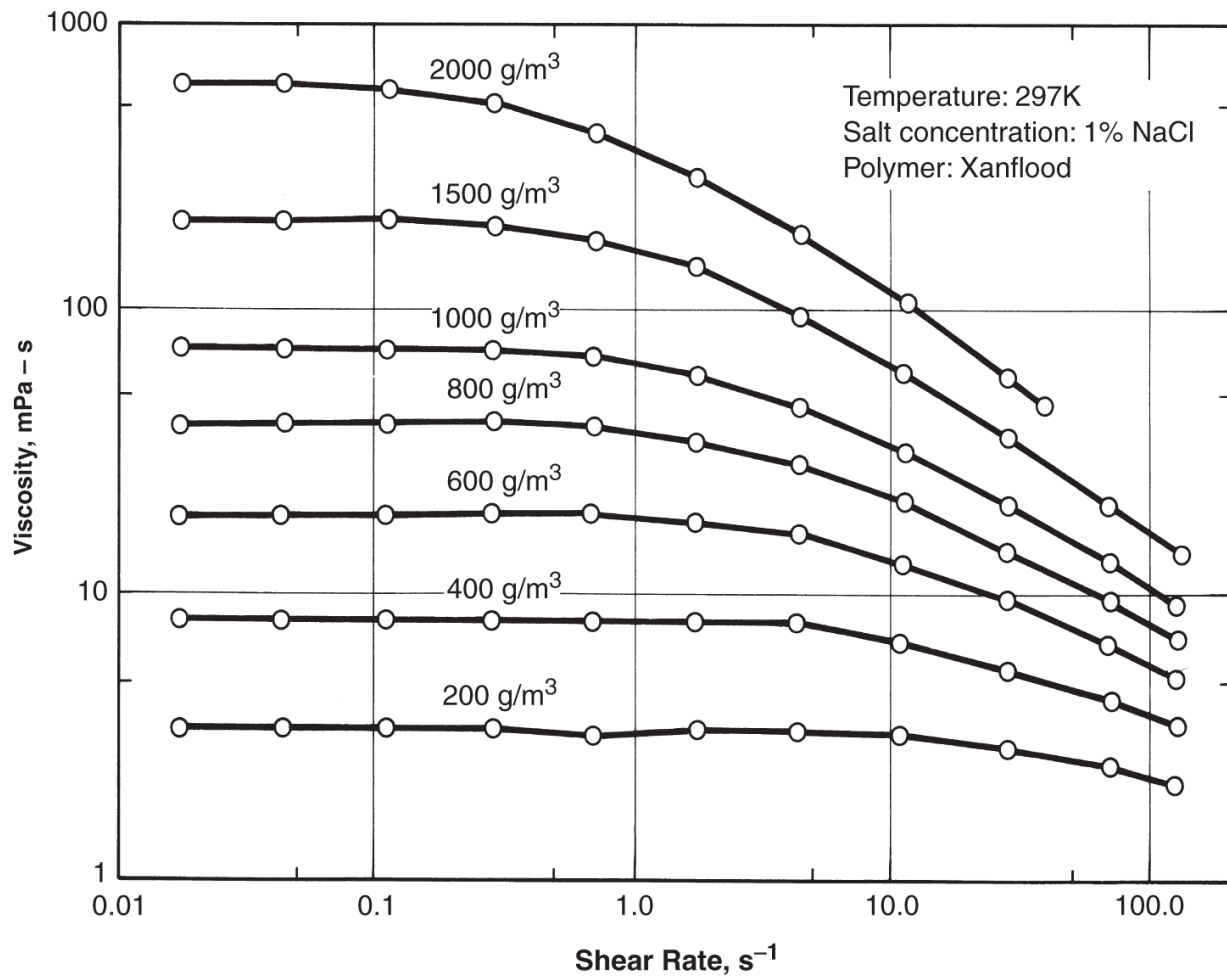


Fig. 8.6—Polymer-solution viscosity vs. shear rate and polymer concentration (Tsaur 1978).

[Fig. 8.7](#) shows a viscosity vs. shear-rate plot at fixed polymer concentration with variable NaCl concentration for an AMPS polymer. At low salinity, the sensitivity of the viscosity to salinity is extreme. Roughly, the polymer solution viscosity decreases by a factor of 10 for every factor of 10 increase in NaCl concentration. The viscosities of HPAM polymers and HPAM derivatives are even more sensitive to hardness, but viscosities of polysaccharide solutions, such as xanthan gum, are relatively insensitive to both.

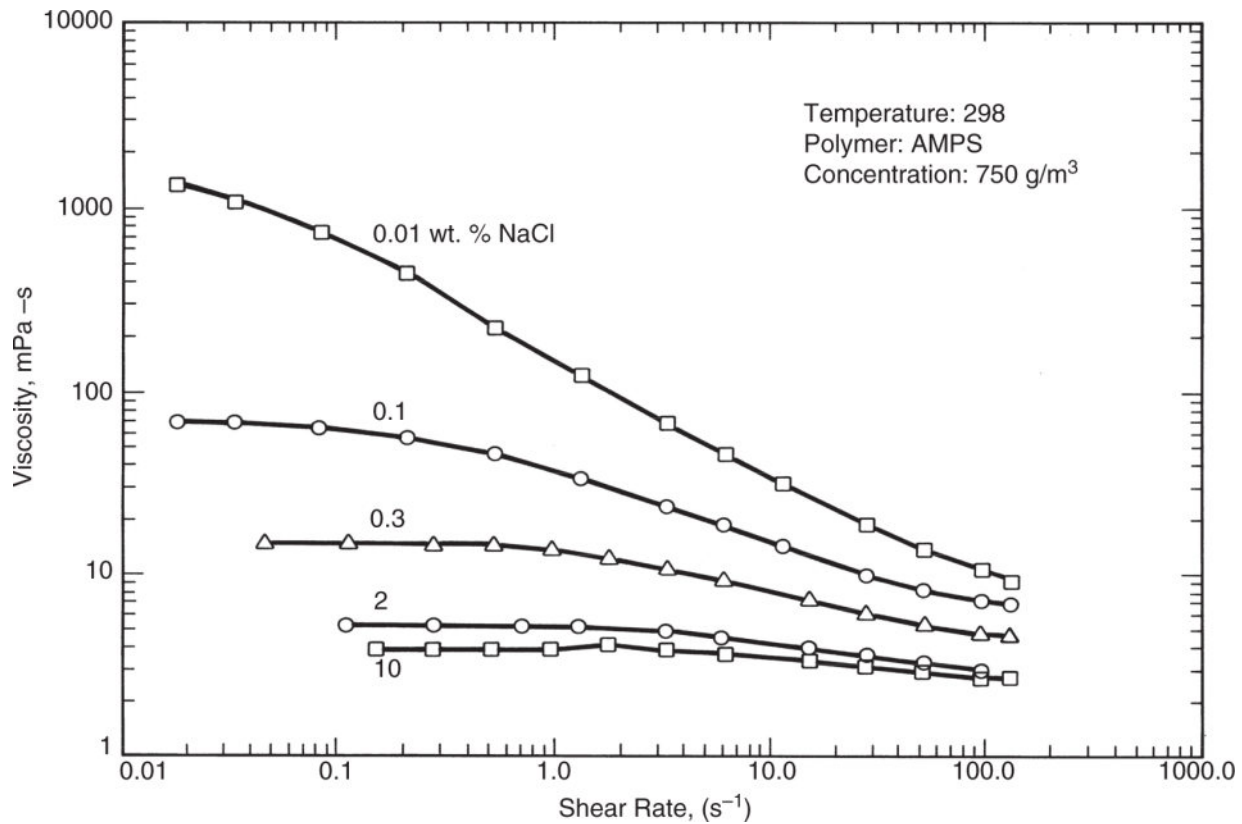


Fig. 8.7—Polymer-solution viscosity vs. shear rate at various brine salinities (Martin et al. 1981).

The behavior shown in Figs. 8.6 and 8.7 is favorable for injection because, for the bulk of a reservoir's volume, $\dot{\gamma}$ is usually low (approximately 1 to 5 s⁻¹), making it possible to attain a design mobility ratio with a minimal amount of polymer. However, near the injection wells, $\dot{\gamma}$ is large, which causes the polymer injectivity to be greater than that expected based on μ_1^0 . The relative magnitude of this enhanced injectivity effect can be estimated once quantitative definitions of shear rates in permeable media and shear-rate vs. viscosity relations are given.

Over an intermediate range of shear rate, the relationship between polymer-solution viscosity and shear rate can be modeled using a *power-law* model,

$$\mu'_1 = K_{pl} (\dot{\gamma})^{n_{pl}-1}, \quad \dots \quad (8.5)$$

where K_{pl} and n_{pl} are the power-law coefficient and exponent, respectively. For shear-thinning fluids, $0 < n_{pl} < 1$; for Newtonian fluids, $n_{pl} = 1$, and K_{pl} becomes the viscosity. $\dot{\gamma}$ is always positive. Eq. 8.5 applies only over the range of shear rates in which the solution is shear-thinning: below some low shear rate, the viscosity is constant at μ_1^0 , and above the critical shear rate, the viscosity is also constant, μ_1^∞ .

The truncated nature of the power law is awkward in some calculations; hence, another useful relationship is the *Meter model* (Meter and Bird 1964),

where n_M is an empirical coefficient and $\dot{\gamma}_{1/2}$ is the shear rate at which μ'_1 is the average of μ_1^0 and μ_1^∞ . As with all polymer properties, all empirical parameters are functions of salinity, hardness, and temperature.

When applied to permeable-media flow, the preceding general trends and equations continue to apply, except that the shear rate within a porous medium increases and the bulk-fluid viscosity becomes an effective or apparent viscosity. μ' is usually called the *apparent* viscosity, μ_{app} , and the effective shear rate $\dot{\gamma}_{\text{eq}}$ is based on capillary-tube concepts, as derived in Section 3.1 for Newtonian fluids. For power-law fluids, the procedure is identical (see Exercise 8.2), except that the beginning equation is Eq. 8.5. We give only the results here.

The apparent viscosity of a flowing polymer solution is

$$\mu_{\text{app}} = H_{pl} u^{n_{pl}-1}, \dots \quad (8.7)$$

where (Hirasaki and Pope 1974)

The right side of Eq. 8.7 is $K_{pl} \dot{\gamma}_{eq}^{n_{pl}-1}$, which yields the equivalent shear rate for the flow of a power-law fluid,

In both Eqs. 8.8 and 8.9, k_1 (the aqueous-phase permeability) is the product of the phase's relative permeability and the absolute permeability. ϕ_1 (the aqueous-phase porosity) is ϕS_1 .

The only difference between the equivalent shear rate and that of a Newtonian fluid (Eq. 3.11) is the first term on the right side. This factor is a weak function of n_{pl} and is about 0.78 for typical values of n_{pl} , so there is little difference between the equations used to calculate the shear rate for a Newtonian fluid and a power-law fluid. However, because of their large size relative to the pores, the polymer molecules show additional effects such as wall exclusion and slip in the pores that require Eq. 8.9 to be modified for accurate calculations. The simplest way to do that is to multiple the shear rate by a correction factor C (Cannella et al. 1988). Unfortunately, C depends on the characteristics of the permeable medium and must be measured for each specific case.

Even though $\dot{\gamma}_{eq}$ has units of reciprocal time, shear rate is essentially a steady-state representation because it can be realized in steady-state laminar flow in a tube. Therefore, the constitutive Eqs. 8.5 and 8.6 contain purely viscous effects because an instantaneous change in $\dot{\gamma}_{eq}$ causes a similar change in μ'_1 . In reality, fluctuations in $\dot{\gamma}_{eq}$, or elastic effects, do affect polymer properties; these are discussed separately in a later section.

8.2.3 Polymer Transport. Being able to propagate polymer solution through a permeable medium is important to the basic idea of this

process. However, there are several hindrances to transport, largely because of the polymer molecule size.

Sandface Plugging. Polymer solutions in which the polymers are incompletely dissolved may exhibit poor transport, so it is important to properly hydrate the polymers. The undissolved polymer tends to deposit on the inlet-well sandface of the medium, which, besides the lack of transport, causes difficulty in injecting it. Eliminating this effect is one of the main goals of laboratory testing. The usual test is to pass polymer solutions through a filter paper and measure the relative time of filtration. If this time is too long, the mechanisms for dissolving the polymer must be altered, or the polymer itself changed, for example, to one with a lower molecular weight. A stringent but effective test is to use 1.2 micron cellulose acetate filter paper and only one bar pressure drop across the filter (Levitt and Pope 2008).

Retention. All polymers experience retention in permeable media because of adsorption onto solid surfaces or trapping within small pores. Polymer retention varies with polymer type, polymer concentration, molecular weight, rock characteristics and composition, brine salinity hardness and pH, flow rate, and temperature. Field-measured values of retention range from 4 to 75 μg polymer/g of rock, with a desirable retention level being less than approximately 20 $\mu\text{g}/\text{g}$. Polymer retention causes a retardation of the polymer and the resulting oil-bank propagation (see Section 8.4).

Common ways to report retention are:

$$\frac{\text{Mass polymer}}{\text{Mass solid}} = \frac{\omega_{4s}}{(1 - \omega_{4s})}$$

$$\frac{\text{Mass polymer}}{\text{Surface area}} = \frac{\omega_{4s}}{a_v}$$

$$\frac{\text{Mass polymer}}{\text{Bulk volume}} = \omega_{4s} \rho_s (1 - \phi)$$

$$\frac{\text{Mass polymer}}{\text{Pore volume}} = \frac{\omega_{4s} \rho_s (1 - \phi)}{\phi} = C_{4s}$$

$$\frac{\text{Volume polymer solution}}{\text{Pore volume}} = \frac{\omega_{4s} \rho_s (1 - \phi)}{(\phi C_4)} = D_4.$$

The last of these, the *frontal advance loss*, is defined analogously for surfactants in the next chapter and is used in the polymer-flooding fractional-flow section below.

Inaccessible Pore Volume. Offsetting the delay caused by retention is an increase in the velocity of the polymer solution through the permeable medium caused by *inaccessible pore volume* (IPV). One explanation for IPV is that large polymer molecules cannot flow through the smallest pores. A second explanation is based on a wall-exclusion effect whereby the polymer molecules aggregate in the center of a narrow channel (Duda et al. 1981). The polymer fluid layer near the pore wall has a lower viscosity than the fluid in the center, which causes an apparent fluid slip. This second explanation is consistent with most experiments and models.

IPV depends on polymer molecular weight, molecular weight distribution, salinity, water saturation, permeability, porosity, and pore-size distribution of the rock among other parameters and becomes more pronounced as the polymer molecular weight increases and the ratio of permeability to porosity (characteristic pore size) decreases. In extreme cases, IPV can be 30% of the total pore space. However, polymer retention decreases the velocity of the polymer and the net

effect is often not significant. In general, IPV is the least significant of the polymer properties and can even be neglected for most purposes.

8.2.4 Permeability Reduction. There are three commonly used measures for dealing with mobility reduction by polymer-solution flow through permeable media (Jennings et al. 1971): resistance factor, permeability reduction factor and residual resistance factor. The permeability reduction factor is not significant for many polymers such as xanthan gum. Even for polymers such as HPAM, it is not significant when the permeability is high.

The *resistance factor* R_F is the ratio of the mobility of the brine to that of polymer solution flowing under the same conditions:

$$R_F = \frac{\lambda_1}{\lambda'_1} = \lambda_1 \mu_{app} = \left(\frac{k_1}{\mu_1} \right) \left(\frac{\mu'_1}{k'_1} \right). \quad (8.10)$$

For polymer solution and water flowing at the same flow rate, saturation, and salinity, R_F is the inverse ratio of pressure drops across the permeable medium and can be determined directly from steady-state pressure drop data. R_F is an indication of the total mobility-reduction contribution of a polymer.

To describe the permeability-reduction effect alone, a *permeability-reduction factor* R_k is defined as

$$R_k = \frac{k_1}{k'_1} = \frac{\mu_1}{\mu'_1} R_F. \quad (8.11)$$

Eq. 8.11 is a regrouping of the terms in Eq. 8.10. Separating R_k from R_F requires independent measurement of viscosities.

A final definition is the *residual resistance factor* R_{RF} , which is the ratio of the mobility of a brine solution before and after (λ_{1a}) polymer injection:

$$R_{RF} = \frac{\lambda_1}{\lambda_{1a}}. \quad (8.12)$$

R_{RF} indicates the permanence of the permeability-reduction effect caused by the polymer solution. For many cases, R_k and R_{RF} are nearly equal, but R_F is usually much larger than R_k because it contains both the viscosity-enhancing and the permeability-reducing effects. All three of these measures are estimated through laboratory experiments with polymer solutions in the reservoir rock. [Fig. 8.8](#) shows typical behavior for a HPAM polymer solution. These values are subject to many experimental difficulties and uncertainties. This is especially true for the residual resistance factor since it takes a very large volume of water to completely displace a viscous polymer solution from most rocks. This leads to larger apparent values of R_{RF} than the true values that apply to the larger scale flow in a reservoir. In most cases, it is prudent to not to include the potential benefits of R_{RF} in the design of the polymer flood.

In these data, the resistance factor is relatively constant until approximately $1 \text{ ft}/\text{D-md}^{1/2}$ and then increases strongly thereafter. The use of shear rate as a correlating factor has collapsed both rates and permeability behavior into one curve. The horizontal axis of [Fig. 8.7](#) is an equivalent shear, as discussed previously, but expressed in field units, as the following example illustrates.

Example 8.1. Let us convert the field units in [Fig. 8.8](#) to the units we have used so far for shear rate. Assume

$$\dot{\gamma}_{eq} = 1 \frac{\text{ft}}{\text{day-md}^{1/2}} \left[\frac{1 \text{ day}}{(24)(3600 \text{ s})} \frac{0.305 \text{ m}}{1 \text{ ft}} \frac{(1000 \text{ md})^{1/2}}{1 \text{ D}^{1/2}} \frac{1 \text{ D}^{1/2}}{10^{-6} \text{ m}} \right],$$

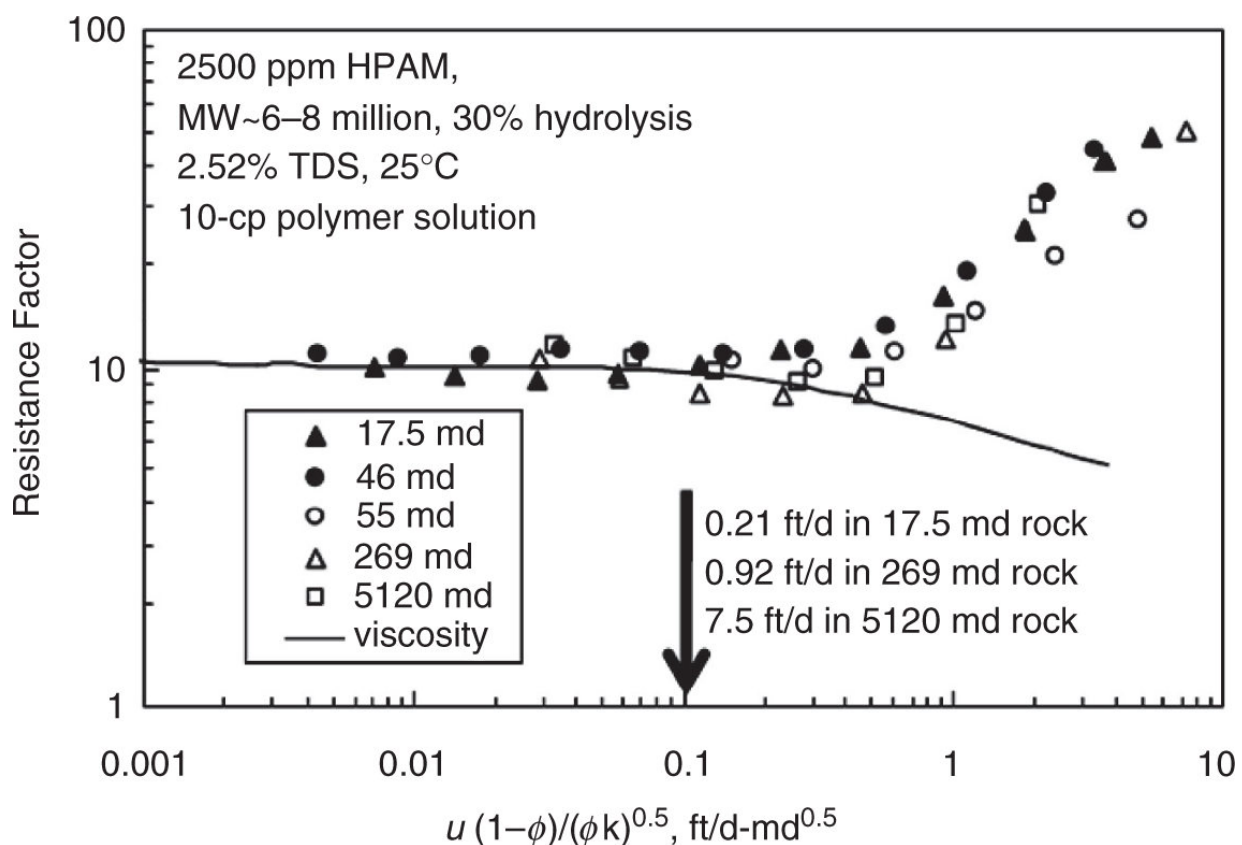
$$\dot{\gamma}_{eq} = 112 \text{ s}^{-1}.$$

In other words, the units on the horizontal axis of [Fig. 8.8](#) are approximately 1/100 of their value in s^{-1} .

Permeability reduction R_k is sensitive to polymer type (HPAM shows larger reductions than polysaccharides), molecular weight,

degree of hydrolysis, shear rate, and permeable-media pore structure. Polymers that have undergone even a small amount of mechanical degradation seem to lose much of their ability to reduce permeability. For this reason, qualitative tests based on screen-factor devices are common to estimate polymer quality.

The screen-factor device is simply two glass bulbs mounted into a glass pipette, as shown in [Fig. 8.9](#). Into the tube on the bottom of the device are inserted several fairly coarse wire screens through which the polymer solution is to drain. To use the device, a solution is sucked through the screens until the solution level is above the upper timing mark. When the solution is allowed to flow freely, the time required to pass from the upper to the lower timing mark t_d is recorded. The screen factor for the polymer solution is then defined as



where t_{ds} is the similar time for polymer-free brine.

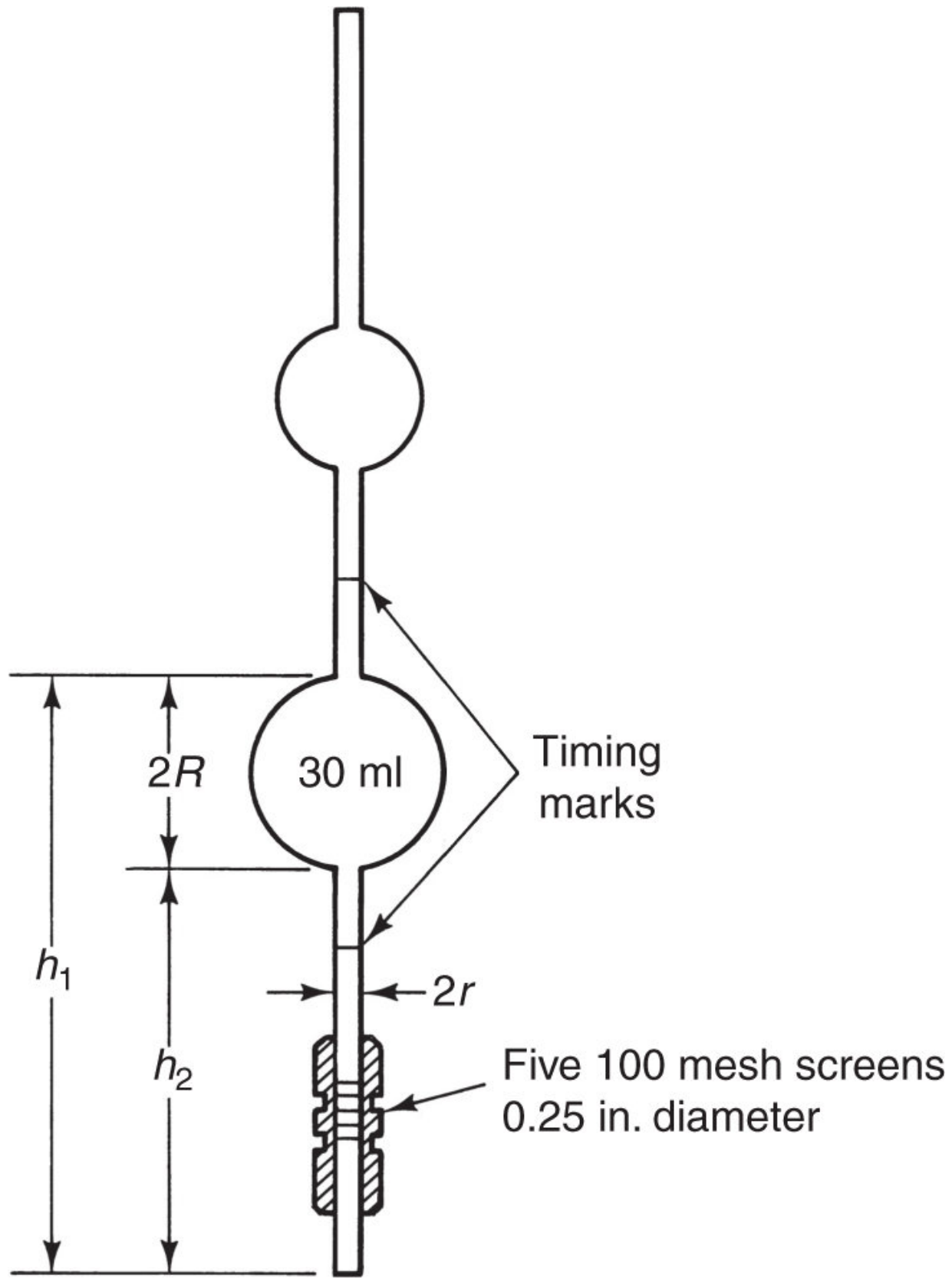


Fig. 8.8—Behavior of resistance factors with shear rate (Seright 2010).

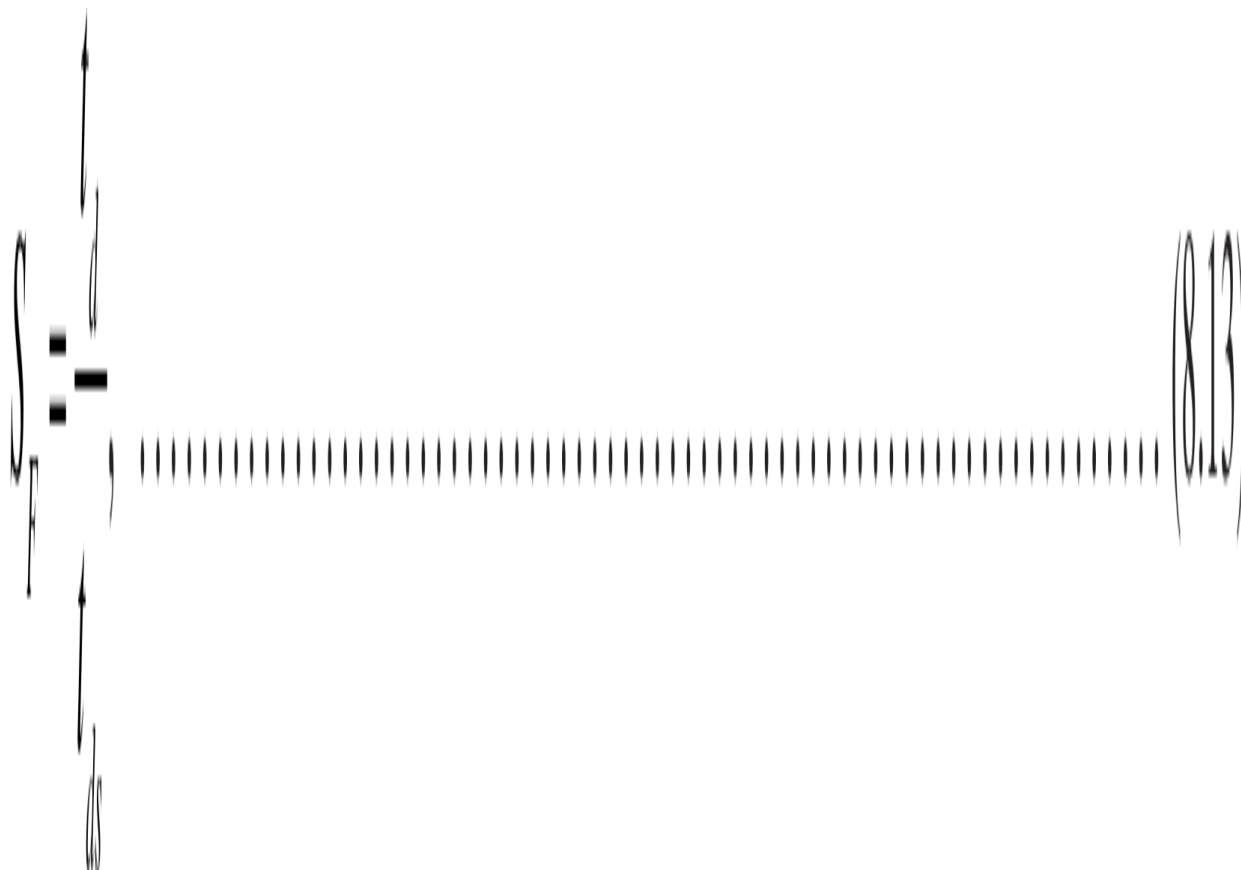


Fig. 8.9—Screen-factor device [adapted from Foshee et al. (1976)].

Because it is a ratio of times, the screen factor is independent of temperature, device dimensions, and screen coarseness, and fairly independent of screen spacing. The screen-factor measurement is not independent of polymer concentration, but its primary intent is to measure the elastic (time-dependent) portion of the polymer-solution configuration; that is, it measures the rate at which a polymer molecule returns to its steady-state flow configuration after it has been perturbed. We are now about to discuss elastic effects in the behavior of polymer solutions. See Exercise 8.3 for a means of quantitatively accounting for viscous and elastic effects.

The relaxation time is evidently very short for polysaccharides because they do not have a measurable screen factor, even at high concentrations. The short relaxation time for this polymer type is consistent with the rigidity of its molecular structure, as discussed in

connection with [Fig. 8.3](#). HPAMs have much larger relaxation times because their screen factors can be large even at the same viscosity as a polysaccharide solution. HPAMs are much more flexible molecules than polysaccharides. In other words, while both polymer types are viscoelastic, HPAMs can deform more and return more slowly to their unstressed state.

Screen factors are particularly sensitive to changes in the polymer molecule itself. One definition of polymer quality is the ratio of degraded to undegraded screen factors. This use is important for screen-factor devices, particularly in on-site field locations that prohibit more sophisticated equipment. The screen factor bears a resemblance to the Marsh funnels used for characterizing cements and drilling fluids (Balhoff et al. 2011).

Another use for screen factors is as a correlator for R_F and R_{RF} ([Fig. 8.10](#)). The explanation for such a correlation is consistent with that given previously for polymer relaxation. Steady-state flow in permeable media is locally (on a pore scale) unsteady; it is actually a succession of contracting and diverging channels. The frequency at which the solution experiences these contractions, compared with the polymer relaxation time, determines the extent of permeability reduction. Such an effect also qualitatively explains the increase in viscometer viscosity at very high shear rates (Hirasaki and Pope 1974). See Kim et al. (2010) for correlations of all properties.

The relaxation-time argument cannot completely account for permeability reduction because such effects have been observed in glass capillaries. For this case, permeability reduction seems to be caused by polymer adsorption, which decreases the effective pore size if it is large enough (see Exercise 8.5).

Both the viscous and elastic effects have been quantified into a single master equation for use in numerical simulation (Delshad et al. 2008). See the UTCHEM technical manual for details.

A reasonable question is whether permeability reduction is a desirable effect. R_k is difficult to control, being sensitive to even small deteriorations in polymer quality. Moreover, an extremely large R_k will cause injectivity impairment. However, it is possible to achieve a

predesignated degree of mobility control with less polymer if

M_T^0 is a design or target endpoint mobility ratio,

$$M_T^0 = \left(\frac{k'_1}{\mu_1^0} \right) \left(\frac{\mu_2}{k_2^0} \right) = \frac{M^0|_{R_k=1}}{R_k} = \frac{M^0}{R_{RF}}. \quad \dots \dots \dots \quad (8.14)$$

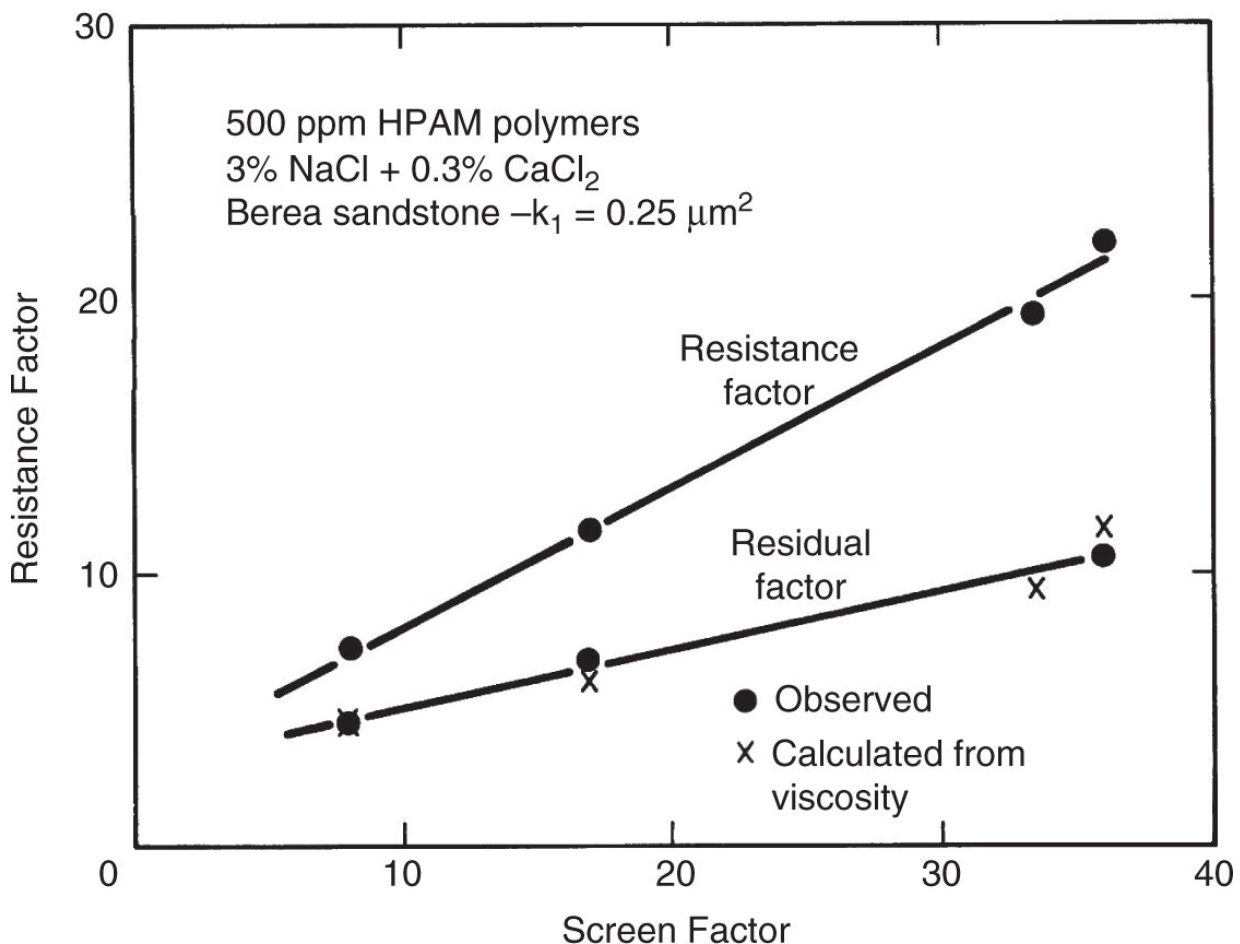


Fig. 8.10—Correlation of resistance factors with screen factors (Jennings et al. 1971).

In this equation, $M^0|_{R_k=1}$ is the mobility ratio of a polymer having no permeability reduction, and M^0 is the endpoint water/oil mobility ratio. Clearly, if $R_k > 1$, the polymer viscosity μ_1^0 can be lower than if $R_k = 1$, which indicates that a given concentration of HPAM will have a lower mobility ratio than that of polysaccharide under conditions in which

both polymers have the same flowing viscosity. The limiting viscosity μ_1^0 is used to estimate M^0 from Eq. 8.14.

Example 8.2—Less polymer use with permeability reduction.

Suppose that we desire a target mobility ratio of M_T^0 .

- Estimate from [Fig. 8.6](#) the polymer concentration required if $k_1^0 = 0.2$; $k_2^0 = 0.9$, $\mu_2 = 200 \text{ mPa}\cdot\text{s}$ and the polymer does not reduce permeability.

First, solve for the water viscosity from Eq. 8.14 as

$$\mu_1^0 = \left(\frac{k_1^0}{M_T^0} \right) \left(\frac{\mu_2}{k_2^0} \right) = \left(\frac{0.2}{0.8} \right) \left(\frac{200 \text{ mPa}\cdot\text{s}}{0.9} \right) = 55.5 \text{ mPa}\cdot\text{s}.$$

The concentration is read from [Fig. 8.6](#) at the low shear-rate limit as

$$C_{4J} = 950 \frac{\text{g}}{\text{m}^3} = 950 \text{ ppm.}$$

- Repeat the effective viscosity calculation if the polymer has a permeability-reduction factor of $R_k = 1.5$.

This involves essentially the same calculation as before, but with

$$\mu_1^0 = \left(\frac{k_1^0}{R_k M_T^0} \right) \left(\frac{\mu_2}{k_2^0} \right) = \left[\frac{0.2}{1.5(0.8)} \right] \left(\frac{200 \text{ mPa}\cdot\text{s}}{0.9} \right) = 37.0 \text{ mPa}\cdot\text{s}.$$

8.3 Profile Control

A discussion of residual resistance factor provides an introduction to one of the uses of polymers discussed previously. Like all of EOR, there are several variations of this technology.

In one of them, called profile control or profile modification and illustrated in [Fig. 8.11](#), a polymer solution is brought into contact with a gelling agent, an aqueous solution containing trivalent cations,

chromium (Cr^{+3}) and aluminum (Al^{+3}) being the most commonly used. These cations form ionic bridges with the negative sites on polymer molecules, resulting in a solid-like gel structure. Gelling accentuates the elastic components of the polymer and, hence, increases R_{RF} as described in the discussion in Section 8.2.4. The resulting structure, which is more solid than liquid, plugs off the zone into which it is injected, resulting in decreased flow of all fluids.

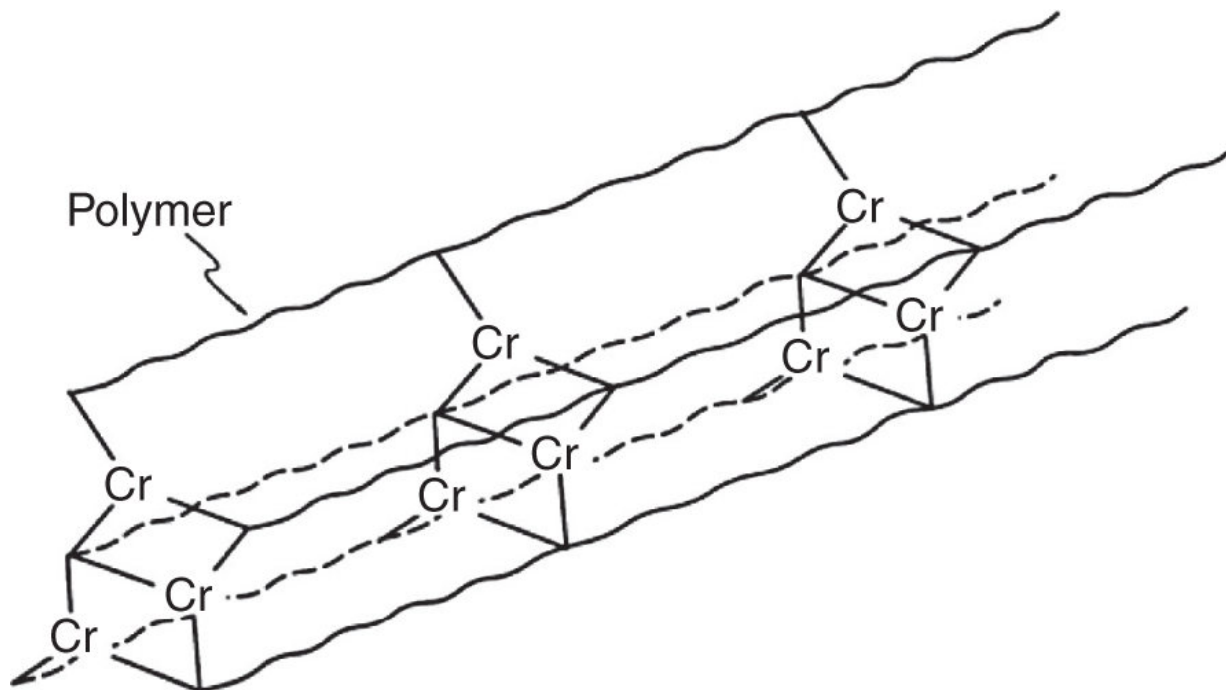


Fig. 8.11—Schematic of polymer gel crosslinked with chromium.

The polymers are similar to the ones used previously for mobility control, although HPAMs used for this purpose tend to have somewhat lower molecular weights. Other polymers have been proposed (Schechter et al. 1989). Other cations are also possible as dictated by cost, experience, and toxicity. Cr^{+3} in particular seems to be a concern in this regard.

A similar phenomenon occurs with mobility-control polymers in the presence of divalent cations, except that those gels are not as structured. In essence, in mobility-control floods, divalents are undesirable because they will hinder transport. In this technology,

lack of transport is less important because in the usual mode of action, the technology is used in the near-wellbore region.

The crosslinking solution is injected with or after the polymer solution. The rate at which crosslinking occurs will dictate where the gels form. This can occur in the wellbore (undesirable) if the reaction rate is fast, or at some depth in the reservoir if the rate is slow (desirable).

[Fig. 8.12](#) illustrates the intent of the process. In many reservoirs, there exist zones (thief zones) through which the majority of the injected fluid will pass. The existence of such zones can be identified specifically in geological studies, but you should be able to see from the discussion in [Chapter 6](#) that reservoirs having log-normally distributed permeability intrinsically have a substantial flow through a small portion of the reservoir.

[Fig. 8.12](#) shows a uniformly layered reservoir with a single thief zone of permeability k . As the left figure suggests, most, if not all, of the production in a mature waterflood will bypass most of the reservoir. The thief zone, being well swept, will have an oil saturation near the residual oil saturation S_{2r} at a high capillary number; the other parts of the reservoir will be at or near the initial oil saturation S_{2I} .

A small (several tens of barrels) slug of a crosslinking agent is injected into a producer (treatments can also be performed in injectors). The thief zone in a region around a producer (injector) will now have permeability k/R_{RF} , which is substantially lower than k . The treatment reduces the permeability in the thief zone only near the well because the plug region is characteristically small. Subsequent production is diverted (right side of [Fig. 8.12](#)) from the thief zone to zones having higher oil saturation and, hence, more production. The process depicted in [Fig. 8.12](#) bears similarity to steam soak, which will be discussed in [Chapter 11](#), except that in that case, the mobility of the oil is increased by heating, whereas here its mobility is (relatively) increased by blocking. Simple calculations can be illuminating, as Example 8.2 suggests.

Profile-control treatments cost much less than mobility-control processes, which require much larger amounts of polymer. They are consequently the favored process when the economically limiting rate in a well is high (Fig. 1.6), for example when the oil price is low. Moreover, several hundred polymer blocking projects have been done, with uneven, although increasing, success (TORP 2012). The oil rate usually responds quickly to the treatment, and a well can be treated several times.

Disadvantages of the process are a low ultimate recovery (as in steam soak) relative to the total target in a reservoir, poor transport of the gelling agent (Walsh et al. 1983), unsustainability of the treatments, and poor control of the rate of gelling. Two reservoir-related issues are important.

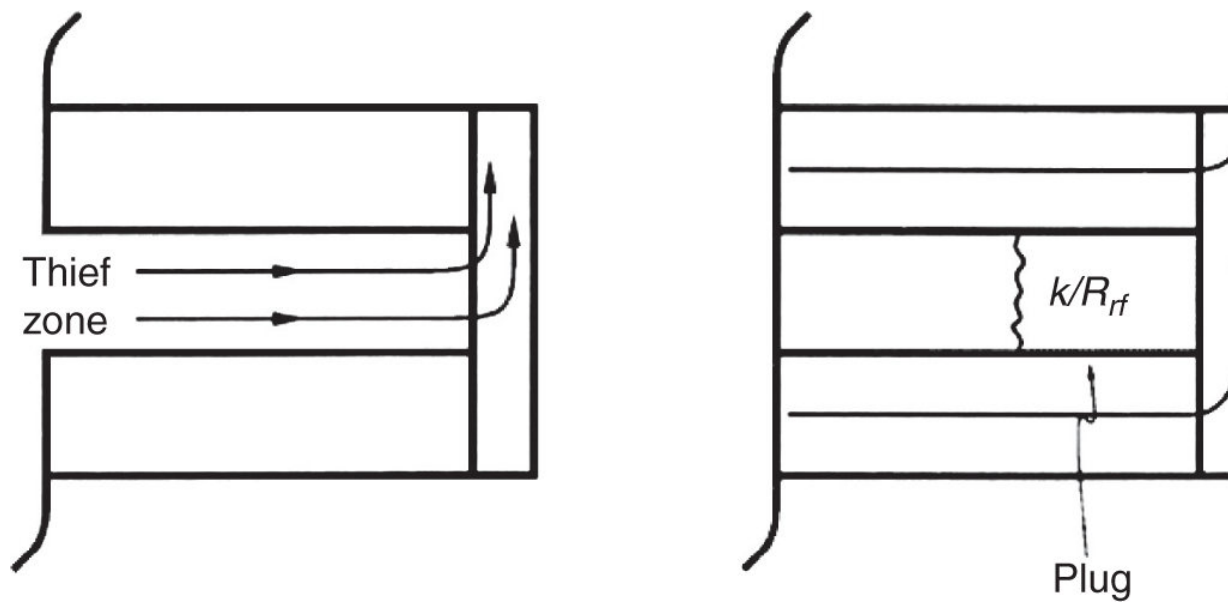


Fig. 8.12—Schematic of a gel treatment blocking a thief zone in a producing well.

Unlike the depiction in Fig. 8.12, the gelling agent can enter all the zones to some extent. This will cause a loss of overall productivity, with subsequent detriment to economic performance. Moreover, the uniform layers shown in Fig. 8.12 rarely occur in practice, although they are most likely to be found over small areas. In particular, the presence of substantial vertical communication can, if severe, entirely

defeat the purpose of the treatment by allowing diversion only in the treated zone.

There are several ways to plug off thief zones in a reservoir. One of these, foam flooding, is important enough to deserve a separate chapter ([Chapter 10](#)) in this text. Other variations include injecting a large polymer-solution volume and adjusting the crosslinking rate so that it will penetrate deeply into the reservoir before gelling. It is also possible to delay hydration as fluids mix so that polymer expands like popcorn in the reservoir at greater depth.

Issues of profile modification are inseparable from productivity. The following is a simplified derivation for how a treatment volume affects both. The diligent reader will notice similarities to the treatment in [Chapter 6](#) for linear media and to Exercise 11.1 for steam-soak performance. The combination of series and parallel flow is a powerful way to study flow behavior in heterogeneous reservoirs. We begin with flow in a single layer.

For the steady-state flow of an incompressible fluid in a single layer of constant thickness H_t , the continuity equation reduces to

$$\frac{\partial(ru_r)}{\partial r} = 0 \quad \dots \dots \dots \quad (8.15)$$

for steady-state flow. This equation is valid regardless of fluid type (fluid properties). We will use it in Exercise 8.6 to define and estimate injectivity. Because Eq. 8.15 is true for these assumptions, it follows that

$$2\pi H_t ru_r = q, \quad \dots \dots \dots \quad (8.16)$$

where q is the constant volumetric production rate. Using Darcy's Law for a radial drainage volume of constant thickness H_t ,

$$2\pi H_t \lambda \frac{dP}{dr} = \frac{q}{r}, \quad \dots \dots \dots \quad (8.17)$$

where λ is the fluid mobility. Because we are describing flow before and after a polymer treatment, the fluids flowing are Newtonian. Let λ

be constant from $r = R_e$ at the external radius where $P|_{r=R_e} = P_e$, and let λ_T be a second constant value from $r = R_T$ (the treatment radius) to $r = R_w$, where the pressure is the flowing bottomhole pressure $P|_{r=R_w} = P_{wf}$ and $\lambda_T (< \lambda)$ is the mobility of the treated region. Integrating Eq. 8.17 in both regions gives

$$P|_{r=R_T} - P_{wf} = \frac{q}{2\pi H_t \lambda_T} \ln\left(\frac{R_T}{R_w}\right),$$

$$P_e - P|_{r=R_T} = \frac{q}{2\pi H_t \lambda} \ln\left(\frac{R_e}{R_T}\right).$$

Adding the two gives the productivity index J ,

$$J = \frac{q}{(P_e - P_{wf})} = \frac{2\pi H_t}{\left[\frac{1}{\lambda_T} \ln\left(\frac{R_T}{R_w}\right) + \frac{1}{\lambda} \ln\left(\frac{R_e}{R_T}\right) \right]}. \quad \dots \quad (8.18)$$

The logarithms in this expression substantially attenuate the effect of the mobility reduction from λ to λ_T that is caused by the treatment. The effect of the treatment would be much more pronounced if the flow were linear, such as, for example, production from a horizontal well or a fractured well.

Now write Eq. 8.18 as

$$J_r = \frac{q}{(P_e - P_{wf})} = \frac{2\pi H_t}{\left[R_f \ln\left(\frac{R_T}{R_w}\right) + \ln\left(\frac{R_e}{R_T}\right) \right]}, \quad \dots \quad (8.19)$$

where J is the productivity index and R_f is the residual resistance factor. The pressure difference $(P_e - P_{wf})$ is one definition of the drawdown pressure. A *relative* productivity index is useful in some applications where

The idea behind profile-control treatments is to alter production in heterogeneous reservoirs. Let the drainage volume (still radial) consist of two uniform layers that are communicating only at the well and the external boundary. Layer 1 is the thief zone and Layer 2 is the remaining part of the reservoir. The flow rate in Layer 1 is now

$$q_1 = \frac{2\pi H_{t1} \lambda_1}{R_f \ln \left(\frac{R_{T1}}{R_w} \right) + \ln \left(\frac{R_e}{R_{T1}} \right)} \left(P_e - P_{wf} \right),$$

and, similarly, for Layer 2. The ratio of flow rates is independent of the drawdown pressure,

$$\frac{q_1}{q_2} = \frac{H_{t1}\lambda_1}{H_{t2}\lambda_2} \frac{\left[R_f \ln\left(\frac{R_{T2}}{R_w}\right) + \ln\left(\frac{R_e}{R_{T2}}\right) \right]}{\left[R_f \ln\left(\frac{R_{T1}}{R_w}\right) + \ln\left(\frac{R_e}{R_{T1}}\right) \right]}, \dots \quad (8.21)$$

and the productivity index is now

The volume of the treatment is

These formulas can provide estimates of the effect of a treatment, as the following example illustrates.

Example 8.3—Profile-Control Results. Estimate the change in oil cut and oil rate that a 50-bbl profile-control treatment will have on a reservoir producing at an oil cut of 10%. The external and well radii are 500 and 0.1 m, respectively. The residual resistance factor is 10, and the porosities of the formation and thief zones are equal at 0.2. The total production rate before and after the treatment is unchanged at 100 bbl/day.

First assume that the thief zone (Layer 1) is producing only water and the remainder of the formation (Layer 2) is producing only oil. The flow rate q_1 in the preceding formulas is the pretreatment water rate and q_2 is the oil rate. The thief zone in the example is 1 m thick, and the thickness of Layer 2 is 20 m. Before the treatment, $R_{T1} = R_{Te} = R_w$, so that we have

$$\frac{q_1}{q_2} = \frac{0.9}{0.1} = \frac{H_{t1}\lambda_1}{H_{t2}\lambda_2} = 9.$$

We assume that the profile-control agent penetrates the formation in this ratio before gelling, so that

$$V_T = \pi \left[H_{t1} (R_{T1} - R_w)^2 \phi_1 + H_{t2} (R_{T2} - R_w)^2 \phi_2 \right] = 10\pi H_{t2} (R_{T2} - R_w)^2 \phi_2,$$

or

$$\begin{aligned} R_{T2} &= R_w + \sqrt{\frac{V_T}{10\pi H_{t2} \phi_2}} \\ &= 0.1 \text{ m} + \left\{ \frac{50 \text{ bbl}}{10\pi(20 \text{ m})(0.2)} \left[\frac{5.614 \text{ ft}^3}{1 \text{ bbl}} \left(\frac{0.305 \text{ m}}{1 \text{ ft}} \right)^3 \right] \right\}^{1/2} = 0.35 \text{ m}. \end{aligned}$$

Therefore,

$$R_{T1} = R_w + (R_{T1} - R_w) \sqrt{\frac{q_1 H_{t2} \phi_2}{q_2 H_{t1} \phi_1}} = 3.48 \text{ m}.$$

There is a substantial disparity in penetration distances, caused mainly by the thinness of the thief zone. With these values, we re-evaluate the layer flow-rate ratio as

$$\frac{q_1}{q_2} = \frac{H_{t1}\lambda_1}{H_{t2}\lambda_2} \frac{\left[R_f \ln\left(\frac{R_{T2}}{R_{wf}}\right) + \ln\left(\frac{R_e}{R_{T2}}\right) \right]}{\left[R_f \ln\left(\frac{R_{T1}}{R_{wf}}\right) + \ln\left(\frac{R_e}{R_{T1}}\right) \right]} = 9 \frac{\left[10 \ln\left(\frac{0.35m}{0.1m}\right) + \ln\left(\frac{500m}{0.35m}\right) \right]}{\left[10 \ln\left(\frac{3.48m}{0.1m}\right) + \ln\left(\frac{500m}{3.48m}\right) \right]} = 4.41,$$

or a post-treatment oil cut of

$$f_2 = \frac{1}{1+4.41} = 0.185.$$

The treatment has increased the oil cut by approximately 8.5%, or alternatively, it has increased the oil rate by 8.5 bbl/day.

There are many variations on this calculation. For example, we could assume no penetration at all into Layer 2, as would happen if the thief zone were identified and isolated from the treatment. We could assume that the two layers were in vertical equilibrium ([Chapter 6](#)) rather than noncommunicating. Even within the context of the given problem, you could use Eq. 8.22 to estimate the extent to which the bottomhole pressure must be reduced to maintain the same pre- and post-treatment rates. Finally, the entire problem could be worked with a constant drawdown pressure in which the treatment would reduce the overall production rate while boosting the oil rate.

8.4 Polymer Degradation

8.4.1 Chemical and Biological Degradation. Polymers are subject to both chemical and biological degradation.

For a given polymer solution, there will be some temperature above which the bonds within the polymer molecule will begin to break. Although this point depends on the specific EOR polymer, this temperature is fairly high, on the order of 400 K. Because the original temperature of oil reservoirs is almost always less than this, of more practical concern for polymer flooding is the temperature at which other degradation reactions occur.

The average residence time in a reservoir is typically very long, on the order of a few years, and, therefore, even slow reactions are potentially serious. Reaction rates also depend strongly on other variables, such as pH or hardness. At neutral pH, degradation often is insignificant, unlike at very low or very high pH, and especially at high temperatures. One of the most common reactions for HPAM is hydrolysis. An increase in the degree of hydrolysis changes several important characteristics of the polymer. For soft brine, the viscosity actually increases. For hard brine, it may increase up to a point but eventually the hardness will cause precipitation and a drastic loss of viscosity.

Oxidation or free-radical chemical reactions are usually considered the most serious source of chemical degradation. Therefore, oxygen scavengers and antioxidants are often added to prevent or retard these reactions. Sodium dithionite is a strong reducing agent and has the additional advantage of reducing iron cations from the +3 to the +2 state. Wellington (1983) has found that alcohols such as isopropanol and sulfur compounds such as thiourea make good antioxidants and free-radical inhibitors. Laboratory results indicate that xanthan can be stabilized up to approximately 367 K and HPAM to approximately 394 K. For xanthan solutions, the results depend strongly on precise conditions such as salinity and pH. One should test the particular polymer solution under the particular reservoir conditions of interest to establish the expected behavior (Sorbie 1991; Levitt et al. 2011a, Levitt et al. 2011b).

Biological degradation is a potential problem for polysaccharides. Variables affecting biological degradation include the type of bacteria in the brine, pressure, temperature, salinity, and other chemicals present. As in waterflooding, the preventive use of biocide is highly recommended. Often too little biocide is used or it is started too late, and the ensuing problems become difficult to correct. [**Table 8.1**](#) lists typical polymer-flooding additives.

8.4.2 Mechanical Degradation. Mechanical degradation is potentially present in all applications. It occurs when polymer solutions are exposed to high-velocity flows, which can be present in

surface equipment (valves, orifices, pumps, or tubing), under downhole conditions (perforations or screens), or at the sandface itself. Degradation is potentially present in the injection facilities shown in [Fig. 8.1](#).

Perforated completions in particular are a cause for concern because large quantities of polymer solution are being forced through several small holes. For this reason, polymer solutions are sometimes injected through openhole or gravel-pack completions. Partial preshearing of the polymer solution can lessen the tendency of polymers to degrade mechanically. Because flow velocity falls off quickly with distance from an injector, little mechanical degradation occurs within the reservoir itself.

As with most polymer properties, shear rate is the governing factor in mechanical degradation. [Fig. 8.13](#) provides a schematic of mechanical-degradation behavior. The figure shows the behavior of shear-thinning viscosity (vertical axis) as a function of shear rate (horizontal axis), as discussed earlier in this chapter. For much of the shear-rate range, the viscosity is reversible; that is, increasing or decreasing the shear rate leads to a curve that traces back on itself.

However, above a certain maximum, the curve is not reversible, and the return trace is a curve that gives a lower viscosity. That means that upon exposure to high shear, polymer loses some of its low-shear viscosity because the polymer molecules themselves have been shortened (sheared). This viscosity loss can be quite severe, as shown in [Fig. 8.14](#), especially for high-molecular-weight polymers.

TABLE 8.1—SELECTED BACTERICIDES AND OXYGEN SCAVENGERS [ADAPTED FROM ENHANCED OIL RECOVERY, NATIONAL PETROLEUM COUNCIL (1984)]

Bactericide	Oxygen Scavengers
<u>Commonly Used</u>	
Acrolein	Hydrazine
Formaldehyde	Sodium bisulfite
Sodium dichlorophenol	Sodium hydrosulfite
Sodium pentachlorophenol	Sulfur dioxide
<u>Proposed or Infrequent Use</u>	
Acetate salts of coco amines	
Acetate salts of coco diamines	
Acetate salts of tallow diamines	
Alkyl amino	
Alkyl dimethyl ammonium chloride	
Alkyl phosphates	
Calcium sulfate	
Coco dimethyl ammonium chloride	
Gluteraldehyde	
Paraformaldehyde	
Sodium hydroxide	
Sodium salts of phenols	
Substituted phenols	

All polymers degrade mechanically under high enough flow (shear) rates. However, HPAMs are most susceptible under normal operating conditions, particularly if the salinity or hardness of the brine is high. Evidently, the ionic coupling of these anionic molecules is relatively fragile. Moreover, elongation stress is as destructive to polymer solutions as shear stress, although the two generally accompany each other. Maerker (1976) and Seright (1983) have correlated low-shear viscosity loss of a polymer solution with a product of elongation stretch rate and length.

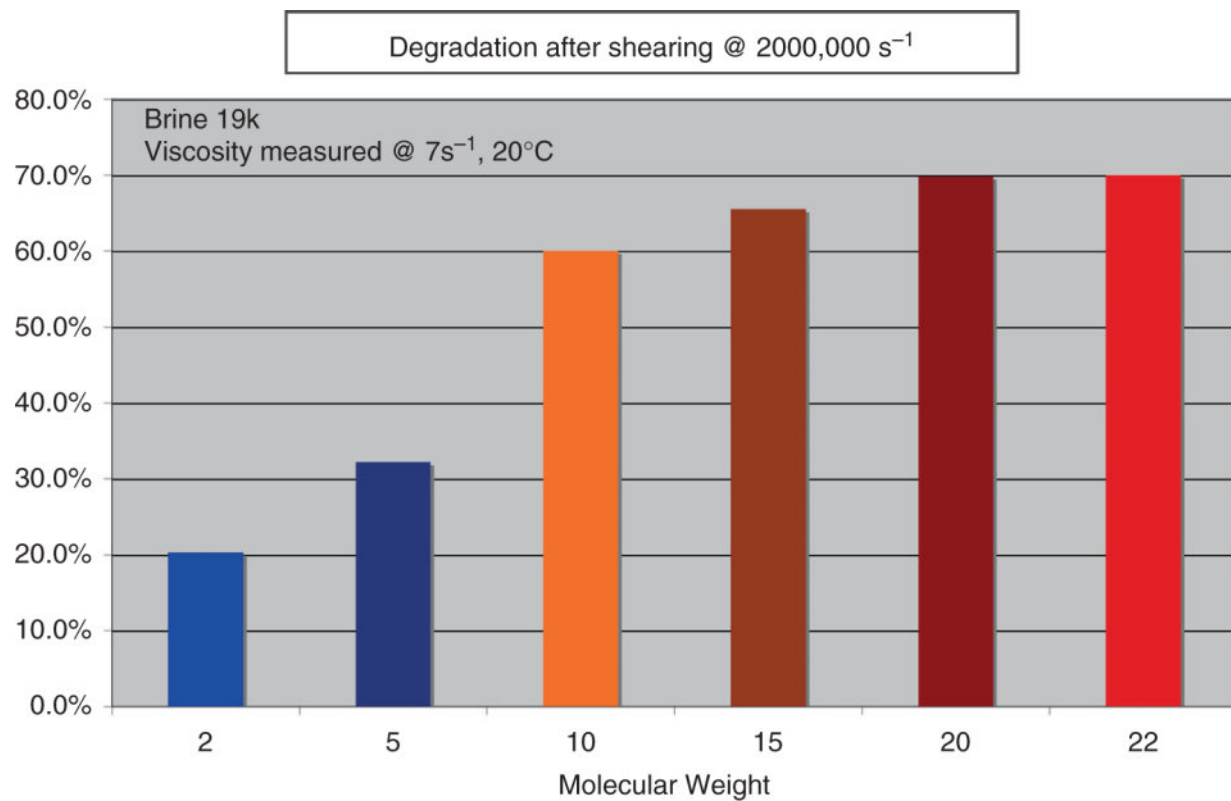


Fig. 8.13—Mechanical degradation and molecular weight in 19,000 ppm TDS brine.

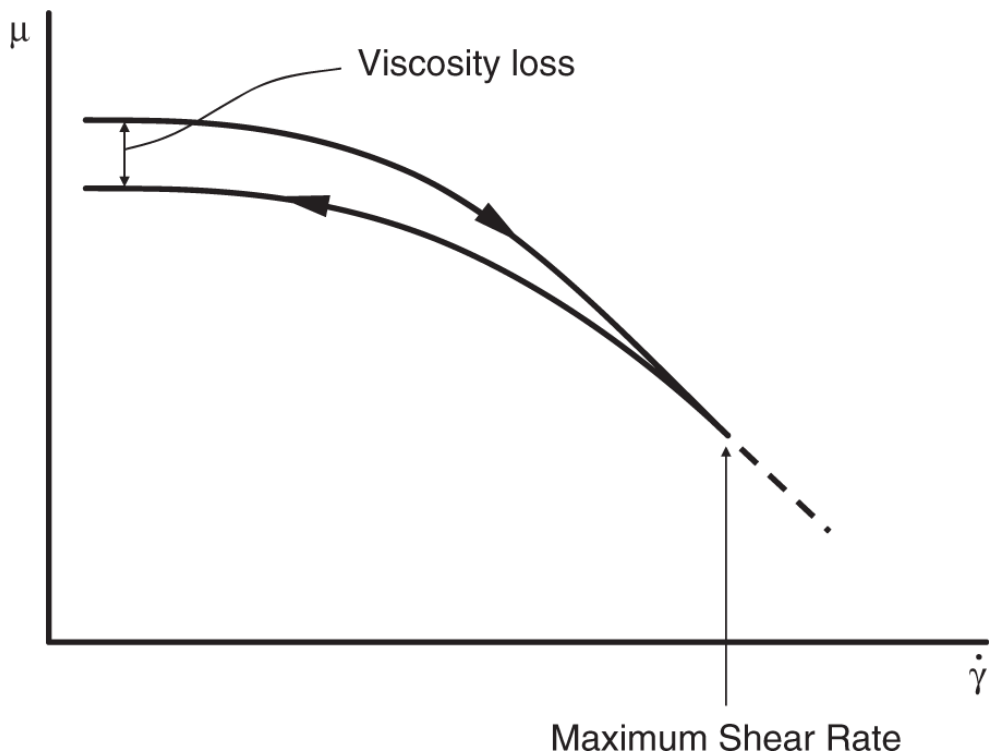


Fig. 8.14—Maximum shear rate degradation. Arrows are directional for mechanical shear rate increase.

8.5 Fractional Flow in Polymer Floods

The fractional-flow treatment of polymer floods resembles the water-solvent treatment in Section 7.7. The additional complications are terms for polymer retention and IPV. In this section, the usual fractional-flow assumptions are made: 1D flow, incompressible fluid and rock, and nondissipative mixing. Remember that the restriction to 1D flow means that the resulting solutions will not account for recovered oil from unswept regions of a reservoir, which can be a major feature of field polymer floods.

8.5.1 Single-Phase Flow. First, consider the case of a water-soluble polymer (Component 4) that is being adsorbed from solution. Let the flow be such that component concentration C_{4I} is being displaced by concentration C_{4J} in single-phase flow, where $C_{4J} > C_{4I}$. From Eq. 5.41a, the specific velocity of concentration C_4 is

In this equation, $\Delta(\cdot) = (\cdot)_J - (\cdot)_I$. If, as is usually the case for polymer floods, $C_{4I} = 0$, Eq. 8.24 reduces to

where D_4 is the frontal advance loss for the polymer. This is also called the *retardation factor* because adsorption causes the front to move slower than that of the ideal miscible displacement (see Section 5.4). D_4 is one of the most useful concepts in both polymer and surfactant/polymer flooding because it expresses retention in pore-volume units that are consistent with slug size.

8.5.2 Two-Phase Flow. The fractional-flow treatment will consist of two phases (aqueous $j = 1$ and oleic $j = 2$) and three components (brine $i = 1$, oil $i = 2$, and polymer $i = 4$). Let the permeable medium have a uniform original water saturation of S_{1I} . We inject an oil-free polymer solution ($f_{iJ} = 1$, $S_{1J} = 1 - S_{2r}$). The initial overall polymer concentration is zero, and the polymer concentration in the aqueous phase is C_{4J} . Polymer and water do not dissolve in the oil ($C_{22} = 1, C_{12} = C_{42} = 0$); the oil has no solubility in the aqueous phase ($C_{21} = 0$).

Effect of Inaccessible Pore Volume. The aqueous phase porosity is ϕS_1 . Only a portion of this pore volume fraction, $(\phi S_1 - \phi_{IPV})$, is accessible to the polymer; hence, the overall polymer concentration per unit bulk volume is

Similarly, the overall water concentration is

because only water is present in the excluded pore volume ϕ_{IPV} . However, the IPV can be easily neglected in Eq. 8.27 because the polymer concentration is very low ($\omega_{1x} \approx 0$).

Oil Displacement. The polymer itself alters neither the water nor the oil relative permeabilities because, as we have seen in Section 3.5, the apparent viscosity cannot be increased enough with field pressure constraints to change residual-phase saturations. Moreover, when permeability reduction is significant, it applies over the entire saturation range, but only to the wetting phase (Schneider and Owens 1982). We can, therefore, construct a polymer-solution/oil (polymer/oil)/water fractional-flow curve simply by using the apparent viscosity in place of the water viscosity and dividing k_{r1} by R_k . The upper left plot of [Fig. 8.15](#) shows both the water/oil ($f_1 - S_1$) and polymer/oil ($f_1^p - S_1$) fractional-flow curves. The figure is either for Cartesian flow or neglects the non-Newtonian behavior of the polymer solution. The effect of these complications is exposited in Rossen et al. (2011).

Because the polymer solution displaces the connate water miscibly, the polymer front is piston-like and has specific velocity

$$v_{\Delta C_4} = \frac{f_1^p(S_1^*)}{S_1^* + D_4 - S_1^* \phi_e}, \quad \dots \quad (8.28a)$$

where D_4 is the polymer retardation factor defined in Eq. 8.25, and

$$\phi_e = \frac{\phi_{\text{IPV}}}{\phi}. \quad \dots \quad (8.28b)$$

S_1^* and $f_1^p(S_1^*)$ are the water saturations and fractional flows at the polymer shock front. S_1^* is also a point in the spreading portion of the mixed polymer/oil wave given by the Buckley-Leverett equation, whence from Eq. 8.5-5a we can define S_1^* :

$$v_{\Delta C_4} = \frac{f_1^p(S_1^*)}{S_1^* + D_4 - S_1^* \phi_e} = \left(\frac{df_1^p}{dS_1} \right)_{S_1^*} = v_{C_1}, \quad \dots \quad (8.29)$$

because S_1^* is also in the shock portion of the polymer/oil wave. The Buckley-Leverett treatment in Section 5.2 used a similar argument. The velocity labeled v_1 in [Fig. 8.14](#) is the tracer velocity, or the same as the velocity in Eq. 8.28a with $D_4 = \phi_e = 0$.

Eq. 8.29 will also determine the oil-bank saturation because S_2 will change discontinuously, with velocity given by

$$v_{\Delta C_2} = \frac{f_1^p(S_1^*) - f_1(S_{1B})}{S_1^* - S_{1B}}. \dots \quad (8.30)$$

As in the solvent/water treatment in Section 7.7, the velocity of the front of the oil (or water) bank is given by

$$v_{\Delta C_2} = \frac{f_{1B} - f_{1I}}{S_{1B} - S_{1I}} = v_{2B} \dots \quad (8.31)$$

for a piston-like oil-bank front. The construction proceeds in the same manner as in Section 7.7.5. As was done there, the Walsh diagram ([Fig. 8.15](#)) shows water cut in the upper right plot, the watercut plot in the upper right, a time/distance diagram at lower right and a composition profile at $t_D = 0.40$ at lower left. The construction is based on the fractional-flow curves in the upper left.

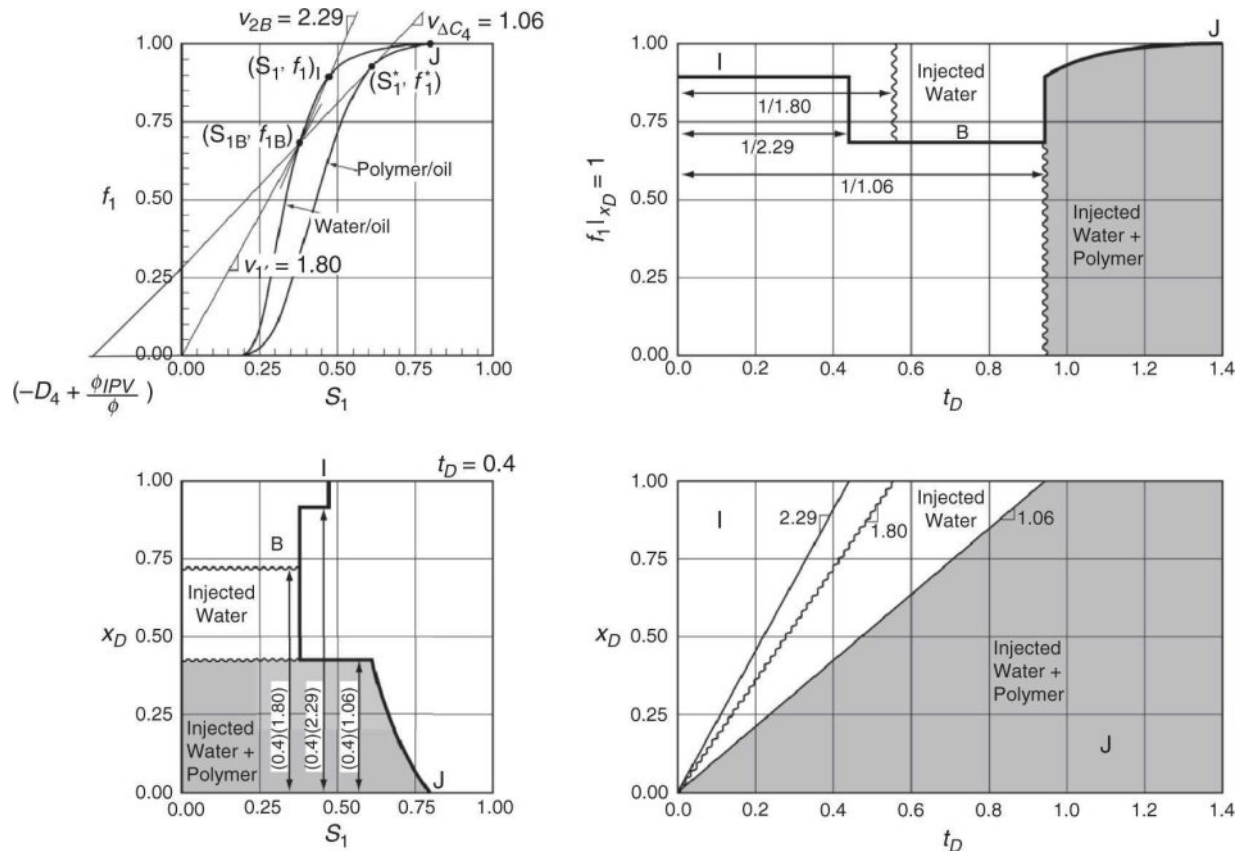


Fig. 8.15—Walsh diagram for polymer-flooding fractional flow.

Although relatively direct, the construction in Fig. 8.15 provides several important insights into polymer floods.

1. The oil-bank breakthrough time (the reciprocal of the oil-bank specific velocity $v_{\Delta C_2}$) increases as S_{1I} increases, suggesting that polymer floods will be more economical (they begin producing oil sooner) if they are begun at low initial water saturation. Of course, the smaller the value of S_{1I} , the higher will be the mobile-oil saturation, which is also a favorable indicator for polymer floods.
2. Adsorption (large D_4) causes a delay of all fronts. D_4 can be large if the porosity is low, the retention is high, or the injected polymer concentration C_{4J} is low. Polymer retention should be a small fraction of the total polymer injected in a well designed polymer flood since at least one pore volume of polymer

solution should be injected to maximize sweep efficiency. Note that adsorption causes a bank of “denuded” water, or water from which polymer has been stripped by retention.

3. Inaccessible pore volume causes an acceleration of all fronts, an effect exactly opposite to retention. In fact, retention and IPV can exactly cancel, in which case the polymer front and the denuded water front v_1 ([Fig. 8.15](#)) travel at the same velocity.
4. Both D_4 and IPV influence oil-bank saturation, which in turn, influences oil-bank mobility and the desired injected polymer concentration. Therefore, selection of a target mobility (required polymer concentration) is an iterative calculation.
5. Remember that fractional-flow calculations, being intrinsically 1D, do not account for recovery in zones that would be ultimately swept by water.

8.6 Elements of Polymer-Flood Design

Most of the complexity in polymer-flood design arises from the reservoir-specific aspects of a particular design. In this section, we deal in generalities that apply to all types of polymer flooding. Of course, a final design should include aspects of laboratory characterization and numerical simulation before going forward with a project.

A polymer-flood-design procedure will follow these six steps.

1. Screen the candidate reservoirs. The distinction between technical and economic feasibility is important. Technical feasibility means that a given reservoir can be polymer flooded regardless of the funds available. Economic feasibility means that the project has a good chance of being profitable. Technical feasibility is measured by a series of binary screening parameters, as discussed in [Chapter 1](#). Economic feasibility can be estimated by simple hand calculations (as in the fractional-flow method) or predictive models (Molleai et al. 2011).

2. Decide on the correct mode. The choices are (a) mobility control (decrease M), (b) profile control (improve the permeability profile at the injectors or producers), (c) in-depth treatment, or (d) some combination of these. This choice is very site-specific.
3. Select the polymer type. The requirements for EOR polymers are severe. The principal ones are as follows:
 - a. Good thickening: This means high mobility reduction per unit cost.
 - b. Good water solubility: The polymers must have good water solubility under a wide range of conditions of temperature, electrolyte composition, and in the presence of stabilizers.
 - c. Low retention: All polymers adsorb onto reservoir rocks to various degrees. Retention may also be caused by plugging, trapping, phase separation, and other mechanisms.
 - d. Shear stability: During flow through permeable media, stress is applied to the polymer molecules. As discussed elsewhere, if stress is excessive, the molecules may mechanically break apart or permanently degrade, resulting in loss of viscosity. Guarding against this is especially important because degradation is irreversible.
 - e. Chemical stability: Polymers, like other molecules, can chemically react, especially at high temperature in the presence of oxygen. Antioxidants are used to prevent this.
 - f. Biological stability: Polysaccharides can be degraded by bacteria. Biocides are required to prevent this.
 - g. Good transport in permeable media. This “catch-all” phrase includes the ability to propagate the polymer through the rock intact and without excessive pressure drop or plugging. Good transport also means good injectivity and no problems with microgels, precipitates, and other debris.

No one polymer can universally meet these requirements for all reservoir rocks. Therefore, we must tailor the polymer to the rock to some extent. Some general guidelines are possible for

minimum standards, but the ultimate criterion must be economics.

4. Estimate the amount of polymer required. The amount, the total mass in kilograms to be injected, is the product of the slug size, and the average polymer concentration. Ideally, the amount would be the result of an optimization study that weights the present value of the incremental oil against the present value of the injected polymer. Modern practice has been to inject substantially more polymer than in the past, the polymer unit cost being substantially less than the oil price.
 - a. Estimating the initial polymer concentration. Suppose that we have decided on a target mobility ratio that might come from simulation studies (see [Chapter 6](#)) or simply injectivity limitations. If the target mobility ratio is M_T ,

$$M_T = \frac{(\lambda_n)_{\text{polymer}}}{(\lambda_n)_{\text{oil bank}}} = \frac{(\lambda'_{r1} + \lambda'_{r2})_{S_1^*}}{(\lambda_{r1} + \lambda_{r2})_{S_{1B}}} \dots \dots \dots \quad (8.32)$$

Estimating the initial concentration simply means picking the value of injected polymer concentration that gives the correct M_T in this equation. The viscosity must be evaluated at a shear rate corresponding to the median velocity in the flood. Estimating the denominator of Eq. 8.32, the oil-bank relative mobility, is a little more difficult.

One procedure is to estimate the oil-bank saturation using the graphical procedure described in Section 8.4 and then to estimate the oil-bank mobility from the relative-permeability curves evaluated at this saturation:

$$(\lambda_n)_{OB} = \left(\frac{k_{r1}}{\mu_1} + \frac{k_{r2}}{\mu_2} \right)_{S_{1B}} \dots \dots \dots \quad (8.33)$$

This procedure is iterative because S_{1B} depends on the polymer/oil fractional-flow curve. This, in turn, depends on the polymer apparent viscosity, which is being estimated in Eq. 8.32. Fortunately, the dependence between S_{1B} and apparent viscosity is weak, and a trial-and-error procedure should converge rapidly.

A second procedure is to base the total mobility of the oil bank on the minimum of the total relative-mobility curve (Gogarty et al. 1970). The minima in such curves do not, in general, correspond to the oil-bank saturation from fractional-flow theory. However, taking M_T on the basis of the minimum will yield a conservative design because the mobility ratio with the actual oil-bank saturation will always be less than or equal to M_T . The method has the advantage of simplicity because it is noniterative.

Both methods require care in measuring relative-permeability curves because hysteresis can make the drainage and imbibition k_r different (Chang et al. 1978). Such hysteresis effects are particularly difficult to reproduce when the initial water saturation begins at an intermediate value. The second method is also commonly used in micellar-polymer design.

Two additional points are important here. The first is that it is not necessary that M_T be less than one. As we have seen, $M_T < 1$ will suppress fingering in a homogeneous medium, but most oil reservoirs are heterogeneous, some highly heterogeneous. In these cases, $M_T < 1$ will not result in a piston-like displacement. However, lowering M_T will always result in improved recovery compared to waterflooding.

The second point is that it is prudent to use more polymer than that suggested by Eq. 8.32. This is to anticipate some degradation before and in the reservoir.

- b. Estimate the polymer slug volume. One way to do this is simply to let the slug volume be somewhat larger than the retention. The major factor here is the instability between the polymer and chase fluid. Claridge (1978) illustrates a method to estimate the slug volume. However, the slug volume will more likely be determined from economic considerations ([Fig. 1.7](#)). For planning, slug sizes of 0.5 to 1.0 PV are typical. Modern practice is to use much larger

slug sizes than in the past, which also will likely overcome the adverse effects of retention.

5. Design polymer-injection facilities. Obtaining a good-quality solution is, of course, important, but the cost of the injection facilities is usually low compared to well and chemical costs.

The three essential ingredients are mixing facilities, filtration, and injection equipment. The type of mixing apparatus depends on the form of polymer being used. For solid polymers, a skid-mounted solids mixer is required. Concentrates or emulsion polymers require somewhat less sophistication, although the latter may require some emulsion breaking. Filtration largely depends on the success of mixing, but ordinarily its requirements are no more stringent than those for waterflooding. However, if exotic and difficult filtration is required, the complexity and cost can become significant. Injection equipment is the same as that for waterflooding. All surface and downhole equipment should be modified to avoid all forms of degradation. As for waterflooding, the water source must be carefully considered and treated to remove solids and other contaminants.

6. Consider the reservoir. Little is required here beyond the usual waterflood considerations such as the optimal well pattern and spacing, completion strategy, pattern allocation (balance), reservoir characterization, and allowable injection rates.

8.7 Field Results

The incremental oil recovery (IOR) from a polymer flood is the difference between the cumulative oil actually produced and that which would have been produced by a continuing waterflood (see Exercise 8.12). Therefore, for a technical analysis of the project, it is important to establish a polymer-flood oil-rate decline and an accurate waterflood decline rate. One important additional volume to estimate is the additional oil volume contacted by the polymer; the increase in moveable pore volume is determined by a plot of rate vs. cumulative oil recovery, as discussed in [Chapter 1](#).

[**Fig. 8.16**](#) shows the IOR for the North Burbank polymer-flood pilot. The figure illustrates some of the difficulties with interpreting field results. The pronounced response actually precedes the injection of polymer and is probably the result of well treatments before the injection. The water/oil ratio was exceptionally high before the injection, soaring to a ratio of nearly 100 before returning to pre-injection values afterwards. One unremarked benefit of polymer flooding is the reduction of produced water, a feature that could contribute substantially to the economic success of the process.

Manning et al. (1983) summarized other field results on more than 250 polymer floods, both pilot and field scale. The oil-recovery statistics show average polymer-flood recoveries of 3.56% remaining oil in place (after waterflood) and approximately 1 m^3 of IOR for each kilogram of polymer injected, with wide variations in both numbers. The large variability reflects the emerging nature of polymer-flooding technology.

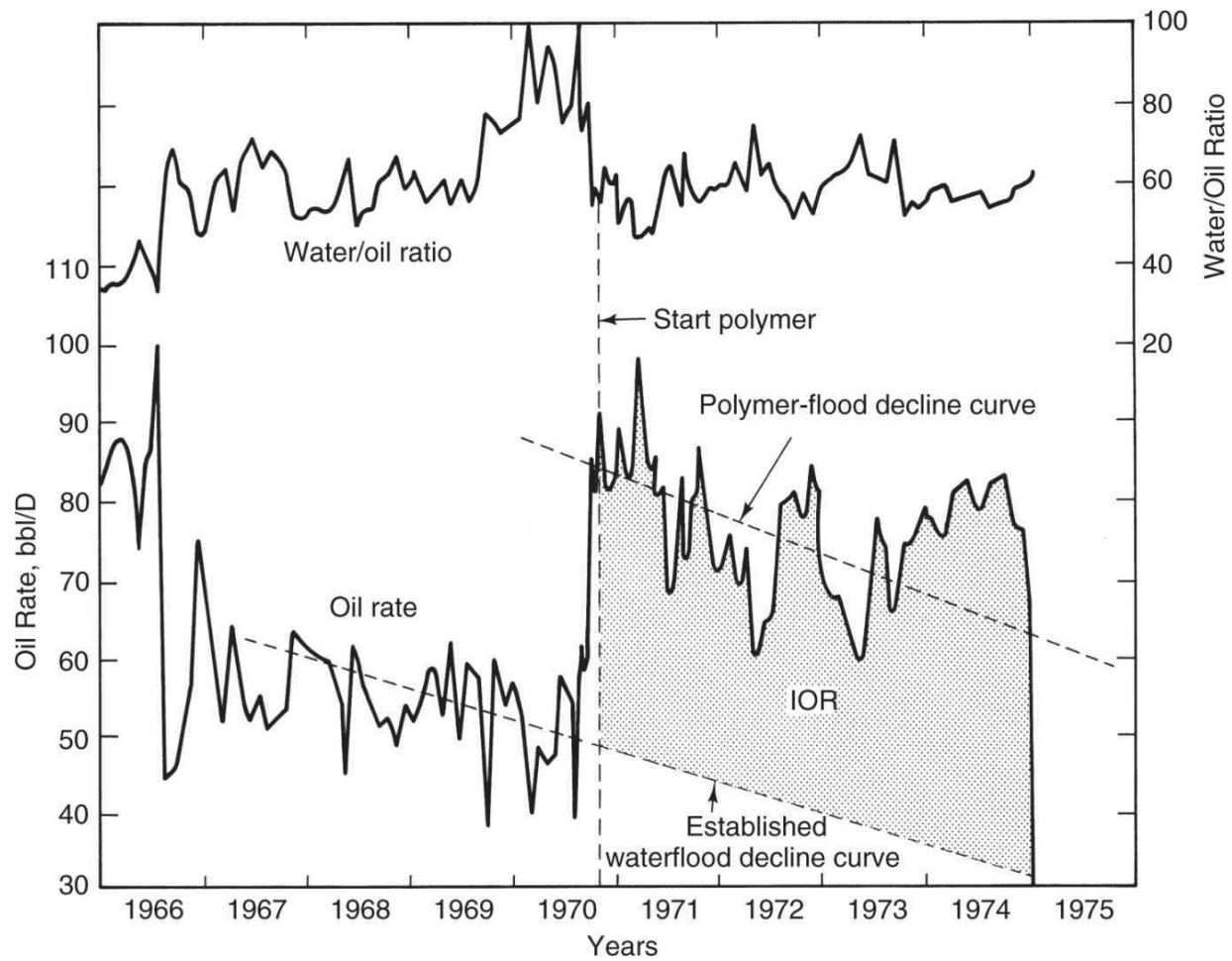


Fig. 8.16—Tertiary polymer-flood response from North Burbank Unit, Osage County, Oklahoma (Clampitt and Reid 1975).

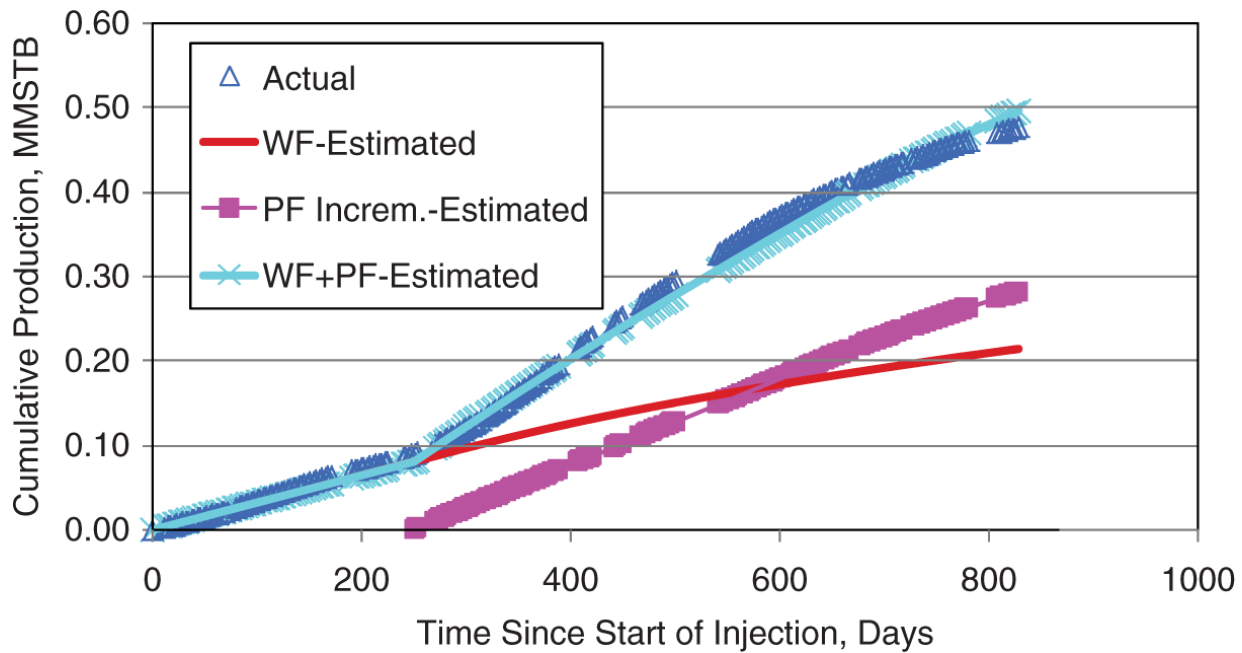


Fig. 8.17—Response of the Daqing polymer-flood pilot (Molleai et al. 2011).

Another illustration of the emergence of polymer-flooding technology is that projects completed after the Manning survey have likely had ultimate recoveries higher than earlier projects. [Fig. 8.17](#) illustrates such a recovery for the Daqing field in China.

The Daqing polymer flood is one of several EOR processes tried in China's largest oilfield. Its ultimate recovery was approximately 12%, much higher than the average in the Manning et al. (1983) study (Demin et al. 2002). The figure shows four cumulative recovery curves: the actual performance, an estimate based on the method of Molleai et al. (2011), an extrapolation of continued waterflood recovery, and the difference between actual recovery and extrapolated recovery (incremental oil recovery). After 800 days of injection, incremental recovery was approximately 300,000 barrels of oil. Equally interesting is the delayed response: no incremental recovery occurred until approximately 250 days of injection. This delay is precisely what is predicted by fractional-flow theory (Section 8.5), but such a long delay, which is the mark of good ultimate recovery, can detract from the ultimate economics. For the Daqing polymer flood, the water disposal and treatment costs were less than

those of a conventional waterflood, because more water would likely have been produced.

8.8 Concluding Remarks

Finishing the chapter by discussing Daqing results provides a good opportunity to point the way forward in polymer-flooding technology. On the basis of this flood (Demin et al. 2002), there is accumulating evidence that the elastic properties of some polymers may result in a lowering of residual oil saturation, much unlike what has been assumed throughout this chapter. Explanations for this effect are as yet unclear (which is why it was omitted from this work), but it is likely connected to elastic properties (we have emphasized viscous properties) and to locally oscillating flows through permeable media. In essence, the elastic properties result in force imbalances on trapped oil globules that augment the viscous forces, resulting in more ultimate recovery. It is also possible that the low salinity used in polymer floods is itself an intrinsic recovery mechanism.

In terms of the number of field projects, polymer flooding is the most common EOR technique in existence. The reasons for this are that, short of waterflooding, polymer flooding is the simplest technique to apply in the field and requires a relatively small capital investment. Most of the field projects have been small, however, as has the amount of oil recovered, a fact that should be expected from the polymer solution's inability to reduce residual oil saturation. Nevertheless, there can exist significant potential for an acceptable rate of return even when ultimate recovery is low.

Moreover, we seem to be learning how to better apply this technology. Modern usage is moving in the direction of more stable polymers, more understanding of when a given process is appropriate in a field, better mixing and injection facilities, and above all, the use of more polymer in projects. The process works primarily by expanding the volume swept by water-based displacing agents.

The most important property covered in this chapter is the potential for degradation and the dependence of polymer-solution properties on shear rate. Polymer injection rate determines project life, which, in

turn, determines the economic rate of return. Injectivity estimates along with estimates of mobile-oil saturation and the likelihood that polymer will remain stable in a given application are the most important determinants of polymer-flooding success.

Exercises

8.1 Calculating Shear Rates. Calculate the equivalent shear rate under the following conditions:

- a. In an openhole completion (entire well cylinder open to flow), where $q = 16 \text{ m}^3/\text{d}$, $R_w = 7.6 \text{ cm}$, and net pay $H_t = 15.25 \text{ m}$.
- b. In the field, where the interstitial velocity is $1.77 \mu\text{m}/\text{s}$.
- c. Using the data for Xanflood at 297 K and $1\% \text{ NaCl}$ ([Fig. 8.5](#)), estimate the effective permeable-medium viscosity under the above conditions for a 600 g/m^3 polymer solution.
- d. Suppose that the well in Part a is perforated with 1-cm-inner-diameter holes over its entire net pay at a density of 4 holes/m. Assuming a uniform fluid distribution, estimate the shear rate in the perforations.
- e. Comparing the results of Parts a and d, what do you conclude about the preferred completion technique in polymer flooding? Use $k_1 = 0.1 \mu\text{m}^2$, $\phi = 0.2$, and $S_1 = 1.0$ in all parts.

8.2 Derivation of Power-Law Behavior in Permeable-Media Flow.

Eq. 8.9 can be derived in the same manner as Eq. 3.11. The procedure is as follows:

- a. Show that a force balance on an annular element of a single-phase fluid flowing through a tube (as in [Fig. 3.1](#)) in laminar steady-state flow is

$$\frac{1}{r} \frac{d(r\tau_z)}{dr} = \frac{\Delta P}{L},$$

where τ_{rz} is the shear stress on the cylindrical face at r and $\Delta P/L$ is the pressure gradient. This equation, when integrated, yields

$$\tau_{rz} = \frac{\Delta P}{2L} r.$$

The shear stress must be finite at $r = 0$.

- b. The power-law expression relating shear stress to shear rate is

$$\tau_{rz} = K_{pl} \dot{\gamma}^{n_{pl}-1},$$

where

$$\dot{\gamma} = -\frac{dv}{dr}$$

is the shear rate. Show that combining the preceding four equations leads to a differential equation for which the solution is

$$v(r) = \left(\frac{\Delta P}{2LK_{pl}} \right)^{1/n_{pl}} \left(\frac{n_{pl}}{1+n_{pl}} \right) \left(R^{\frac{1+n_{pl}}{n_{pl}}} - r^{\frac{1+n_{pl}}{n_{pl}}} \right).$$

This equation has used the no-slip condition $v(R) = 0$.

- c. Using the final equation in Part b, show that the shear rate at the wall of the tube depends on the average velocity as

$$\dot{\gamma}_{\text{wall}} = \frac{1+3n_{pl}}{n_{pl}} \left(\frac{\bar{v}}{R} \right).$$

- d. When the equivalent radius from Eq. 3.4 is substituted, this gives

$$\dot{\gamma}_{eq} = \left(\frac{1+3n_{pl}}{n_{pl}} \right) \frac{u}{(8k_1\phi_1)^{1/2}}.$$

With appropriate variable identifications, this equation yields Eq. 8.7 when substituted into

$$\mu_{app} = \frac{\tau_{rz}}{\dot{\gamma}_{eq}}.$$

8.3 Representation of Linear Viscoelasticity. A powerful conceptual model of a liquid that has some elastic effects (a viscoelastic fluid) is the Maxwell model, which is the series combination of a spring and a dashpot,



where F is the force sustained by the model and ϵ_1 and ϵ_2 are the strains (dimensionless deformations). Let the spring be a linear elastic element, so that

$$F = k\epsilon_1;$$

likewise, the dashpot is a Newtonian viscous element

$$F = \mu \dot{\epsilon}_2,$$

where k and μ are the spring constant and viscosity of the element. Because of the series arrangement, the force supported by both elements is the same; however, the total strain ϵ is

$$\epsilon = \epsilon_1 + \epsilon_2.$$

- Show that the relationship between the time behavior of the force and the strain is

$$\mu \dot{\varepsilon} = \theta \dot{F} + F.$$

In this equation, $\theta = \mu/k$ is the relaxation time of the model and $\dot{\varepsilon}$ is the time derivative of ε .

- b. To integrate this, we treat $\dot{\varepsilon}$ as a known function of time. Show that the general solution is

$$F(t) = e^{-t/\theta} F(0) + k e^{-t/\theta} \int_0^t e^{\xi/\theta} \frac{d\varepsilon}{d\xi} d\xi.$$

The next three steps complete the analogy between the Maxwell model and viscoelastic flow.

- c. If the rate of strain is constant and the initial force of the model is zero, show that

$$F(t) = \mu \dot{\varepsilon} (1 - e^{-t/\theta}).$$

- d. The apparent viscosity of the model is defined as $F/\dot{\varepsilon}$. Show from the Part a equation that this becomes

$$\mu_{\text{app}} = \frac{\mu}{1 + \theta \frac{\dot{F}}{F}}.$$

- e. Use this equation and the equation in part c to show that

$$\mu_{\text{app}} = \frac{\mu}{1 + N_{\text{Deb}}}.$$

The quantity in the denominator of the preceding equation is the Deborah number

$$N_{\text{Deb}} = \frac{\theta}{t}.$$

This number, the ratio of relaxation time to undisturbed flow time around a rock grain, is a measure of viscoelastic effects in permeable-media flow when the characteristic flow time t has been replaced by $\phi D_p/\mu$.

8.4 Analysis of Screen-Factor Device. The screen-factor device in Fig. 8.8 may be analyzed as a permeable medium experiencing gravity drainage. The volume V of fluid in the bulb at any height h ($h_1 > h > h_2$) is

$$V = \frac{\pi}{3} (h - h_2)(3R - h + h_2)$$

from the bulb geometry. If we treat the screen pack as a permeable resistive element, the flux through the screens is

$$u = -\left(\frac{k\rho gh}{L\mu_{\text{app}}} \right).$$

- a. Because $u = -1/\pi r^2(dV/dt)$, show from these equations that the height h is the solution to

$$\frac{dh}{dt} \left\{ (h - h_2) [2R - (h - h_2)] \right\} = \frac{r^2 \rho g k h}{\mu_{\text{app}} L}.$$

L in these equations is the height of the screen pack.

- b. Neglecting the drainage times in the tubes above and below the lower bulb, derive an expression for the drainage time for a Newtonian fluid. The drainage time t_d is defined as

$$t_d = t|_{h=h_2} - t|_{h=h_1}.$$

- c. Repeat Part b with a viscoelastic fluid for which the apparent viscosity is

$$\mu_{\text{app}} = \frac{H_{VE}}{1 + bu}.$$

In view of the Part b and Part c equations, show that the screen factor SF is given by

$$S_F = \frac{H_{VE}}{\mu_1} + \frac{k\rho g}{\mu_1 L} bI,$$

where I is a geometric factor. The screen factor is directly proportional to the fluid's relaxation time.

8.5 Simplified Permeability Reduction. One of the explanations for permeability reduction is that the effective pore size is decreased (or the effective grain diameter increased) because of the adsorption of a layer of polymer on the rock surface. In the following, assume that the medium is made up of spheres of diameter D_p :

- a. Derive an expression for the permeability-reduction factor R_k based on the polymer adsorbing as a uniform layer of thickness Δ on the rock surface. You must use the hydraulic radius concept developed in Section 3.1.
- b. Make two plots, at $\phi = 0.1$ and 0.2 , of polymer adsorption (in mg polymer/g-rock) vs. R_k . Assume the density of the adsorbed polymer to be 1.5 g/cm^3 and the density of the rock to be 2.5 g/cm^3 .

8.6 Polymer Flood Injectivity. The economic success of all EOR processes strongly depends on project life or injection rate, but for polymer floods, it is particularly significant. Because of its importance, many field floods are preceded by single-well injectivity tests. Here, we give a simple technique for analyzing injectivity tests based on the physical properties given in the previous section.

The injectivity of a well is defined as

$$I \equiv \frac{i}{\Delta P},$$

where i is the volumetric injection rate into the well and ΔP is the pressure drop between the bottomhole flowing pressure and some reference pressure. Another useful measure is the relative injectivity,

$$I_r = \frac{I}{I_1},$$

where I_1 is the water injectivity. I_r is an indicator of the injectivity decline to be anticipated when injecting polymer. Both I and I_r are functions of time, but the long time limit of I_r for a Newtonian polymer solution is simply the viscosity ratio if skin effects are small. However, the ultimate I_r for an actual polymer solution can be higher than this because of shear thinning.

Make several simplifying assumptions, many of which can be relaxed (Bondor et al. 1972). The well of radius R_w for which we are calculating injectivity is in a horizontal, homogeneous, circular drainage area of radius R_e . The pressures at R_e and R_w are P_e and P_{wf} , respectively. P_e is constant (steady-state flow), but P_{wf} can vary with time. The fluid flowing in the reservoir is a single aqueous phase, at residual-oil saturation, which is incompressible with pressure-independent rheological properties. The flow is 1D and radial. Finally, the entire shear-rate range in the reservoir lies in the power-law regime; hence, Eq. 8.7 describes the apparent viscosity.

Just as the volumetric rate was independent of

$$i = 2\pi r H_t u_r,$$

The preceding equation is largely a consequence of the incompressible flow assumption; however, i is not independent of time.

- a. Show that substituting Darcy's law for u_r in the preceding equation and integrating between the arbitrary limits of P_1 at r_1 and P_2 at r_2 yields

$$P_2 - P_1 = \left(\frac{i}{2\pi H_t} \right)^{n_{pl}} \frac{H_{pl} R_k}{k_1 (1 - n_{pl})} \left(r_1^{1-n_{pl}} - r_2^{1-n_{pl}} \right).$$

- b. Show that the Newtonian flow limit, $n_{pl} = 1 = R_k$ and $H_{pl} = \mu_1$, of this equation is the familiar steady-state radial flow equation,

$$P_2 - P_1 = \frac{i\mu_1}{2\pi k_1 H_t} \ln \left(\frac{r_1}{r_2} \right).$$

We now apply these equations to the polymer-flood injectivity.

At some time t during the injection, the polymer front (assumed to be piston-like) is at radial position R_p , where

$$\int_0^t i dt = \pi \left(R_p^2 - R_w^2 \right) H_t \phi \left(1 - S_{2r} \right).$$

The left side of this equation is the cumulative volume of polymer solution injected. Therefore, the Part a equation applies in the region $R_w < r < R_p$, and the Part b equation applies in the annular region $R_p < r < R_e$.

- c. With the appropriate identification of variables, and combining the results for both regions, show that the pressure drop from R_w to R_e is

$$P_{wf} - P_e = \left(\frac{i}{2\pi H_t} \right)^{n_{pl}} \frac{H_{pl} R_k}{k_1 (1-n_{pl})} \left(R_p^{1-n_{pl}} - R_w^{1-n_{pl}} \right) + \frac{i\mu_1}{2\pi k_1 H_t} \left[\ln \left(\frac{R_e}{R_p} \right) + S_w \right],$$

where S_w , the intrinsic skin factor of the well, has been introduced to account for well damage.

- d. Show that the preceding equation substituted into the injectivity definition gives

$$I^{-1} = \left(\frac{i}{2\pi H_t} \right)^{n_{pl}} \frac{H_{pl} R_k}{i (1-n_{pl}) k_1} \left(R_p^{1-n_{pl}} - R_w^{1-n_{pl}} \right) + \frac{i\mu_1}{2\pi k_1 H_t} \left[\ln \left(\frac{R_e}{R_p} \right) + S_w \right]$$

The water injectivity I_1 is given by the injectivity equation and the familiar steady-state radial flow equation, with $r_1 = R_w$ and $r_2 = R_e$.

8.7 Profile Control with Constant Drawdown Pressure. Estimate the change in oil cut and oil rate that a 50 bbl profile-control treatment will have on a reservoir producing at an oil cut of 10%. The external and well radii are 500 and 0.1 m, respectively. The residual resistance factor is 10, and the porosities of the formation and thief zones are equal at 0.2. This is the same problem as Example 8.3, except that here the drawdown pressure is constant at 1000 psi.

First, assume that the thief zone (Layer 1) is producing only water and the remainder of the formation (Layer 2) is producing only oil. q_1 in the above formulas is the pretreatment water rate and q_2 is the oil rate. The thief zone is 1 m thick, and the thickness of layer 2 is 20 m.

8.8 Injectivity Calculation. Use the following data for the Coalinga HX sand (Tinker et al. 1976):

ϕ	=	0.28	k_1	=	$0.036 \mu\text{m}^2$
K_{pl}	=	$7.5 \text{ mPa}\cdot\text{s(s)}^{n_{pl}-1}$	μ_1	=	$0.64 \text{ mPa}\cdot\text{s}$
n_{pl}	=	0.8	H_t	=	2.44 m
R_k	=	3	R_w	=	10 cm
R_e	=	284 m	i	=	$30 \text{ m}^3/\text{d}$
			S_{2r}	=	0.2

- a. Calculate the relative injectivity I_r vs. cumulative polymer injected. Plot I_r vs. t_D (up to $t_D = 0.5$) on linear graph paper.
- b. Show that when $R_p = R_e$, the Newtonian polymer case ($n_{pl} = 1$) reduces to

$$I_r = \frac{\mu_1}{K_{pl} R_k}.$$

- c. Plot the Newtonian polymer case for the HX sand on the same plot as in Part a.

8.9 Improvements to Injectivity Calculations. If the shear-rate range in a cylindrical reservoir is outside the power-law range, the following truncated form of the equation in Exercise 8.8 must be used:

$$\mu_{app} = \begin{cases} \mu_1^0, & u < u_0 \\ H_{pl} u^{n_{pl}-1}, & u_0 < u < u_\infty, \\ \mu_1^\infty, & u > u_\infty \end{cases}$$

where u_0 and u^∞ are superficial velocities that define the limits of the power-law range.

- a. Repeat the derivation in Exercise 8.6 for I and I_r using the equation from Exercise 8.9, assuming that both the maximum

- and minimum velocities fall outside the power-law range.
- For numerical simulation, it may be more convenient to define injectivity in terms of the average reservoir pressure \bar{P} rather than P_e (Bondor et al. 1972). Rederive the expression for I defined in this manner.
 - For large numerical simulations, the entire non-Newtonian range of polymer behavior is confined within one gridblock of the well. This being the case, the non-Newtonian effect can be effectively expressed as a time-varying skin factor in terms of an average polymer “saturation.” Derive an expression for this skin factor.

8.10 Fractional Flow and Incremental Oil.

- Calculate the polymer frontal advance lag D_4 when the maximum polymer adsorption is 38 g/m^3 (bulk volume), the injected polymer concentration is 1200 g/m^3 , and the porosity is 0.2.
- Using the D_4 of Part a and the water/oil relative permeabilities in [Fig. 8.18](#), calculate the effluent history of polymer and oil for a polymer flood with $\mu_1^0 \text{ mPa}\cdot\text{s}$. Assume the oil and water viscosities to be 20 and 1 $\text{mPa}\cdot\text{s}$, respectively, the dip angle to be 0, the permeability reduction factor to be 1, and the initial water saturation to be 0.4.
- The technically correct way to evaluate a polymer flood is by the IOR,

$$\text{IOR} = \left(\frac{\text{Polymer flood}}{\text{oil produced}} \right) - \left(\frac{\text{Waterflood}}{\text{oil produced}} \right).$$

Calculate and plot IOR (in SCM) vs. time (years). Assume the pore volume to be $1.6 \times 10^6 \text{ m}^3$, the injection rate constant at $480 \text{ std m}^3/\text{d}$, and all formation volume factors to be $1.0 \text{ m}^3/\text{std m}^3$.

8.11 Fractional Flow and Slugs. Fractional-flow theory can be used to gain insight into the behavior of polymer slugs under idealized conditions and into the polymer-utilization factor.

- a. Assume that the polymer is to be injected as a slug. If the chase water displaces the polymer as an ideal miscible displacement at residual oil saturation, show that the polymer chase-water front travels with specific velocity

$$v_{CW} = \frac{1}{1 - S_{2r}}$$

if the polymer adsorption is irreversible and the excluded pore volume negligible.

- b. Show that the polymer slug size just needed to satisfy adsorption is equal to D_4 .
- c. The data to use in the remainder of this exercise are

$$\begin{array}{lll} a = 1 \text{ cm}^3/\text{g-rock} & C_{4J} & = 800 \text{ g/m}^3 \\ b = 100 \text{ cm}^3/\text{mg} & \rho_s & = 2.65 \text{ g/cm}^3 \\ \phi = 0.2 & & \end{array}$$

Plot the time/distance and effluent histories (oil and polymer) if the slug size used is onehalf that demanded by adsorption. Use the fractional-flow curves and initial conditions of Exercise 8.10.

8.12 Polymer-Flood Design. You want to design a polymer flood in a reservoir containing oil and brine with viscosities of $25 \text{ mPa} \cdot \text{s}$ and $0.38 \text{ mPa} \cdot \text{s}$, respectively, at a reservoir temperature of 73°C . The relative-permeability curves of Fig. 8.17 apply, and conditions indicate that the Xanflood solution data in Fig. 8.6 are satisfactory for this reservoir.

- a. Plot the total relative-mobility curves. If the desired mobility ratio is 0.7, estimate the polymer concentration required to bring this about. Use the data in [Fig. 8.5](#), and recall that μ'_1/μ_1 is essentially independent of temperature.
- b. Estimate the power-law parameters K_{pl} , n_{pl} , and H_{pl} for the polymer solution in Part a.
- c. The flood is to be performed at a constant volumetric injection rate of $20 \text{ m}^3/\text{d}$. Estimate and plot as a function of volume injected the bottomhole injection pressure in MPa. Justify the shape of this curve on physical grounds.
- d. For an openhole completion, estimate the shear rate to which the polymer solution will be exposed. Does this portend mechanical degradation of the polymer?

Assume the reservoir to be circular with $R_e = 950 \text{ m}$ and $P_e = 18 \text{ MPa}$. Additional properties are $k = 0.05 \mu\text{m}^2$, $S_w = 0$, $R_w = 5 \text{ cm}$, $H_t = 42 \text{ m}$, $\phi = 0.2$, and $S_{2r} = 0.3$.

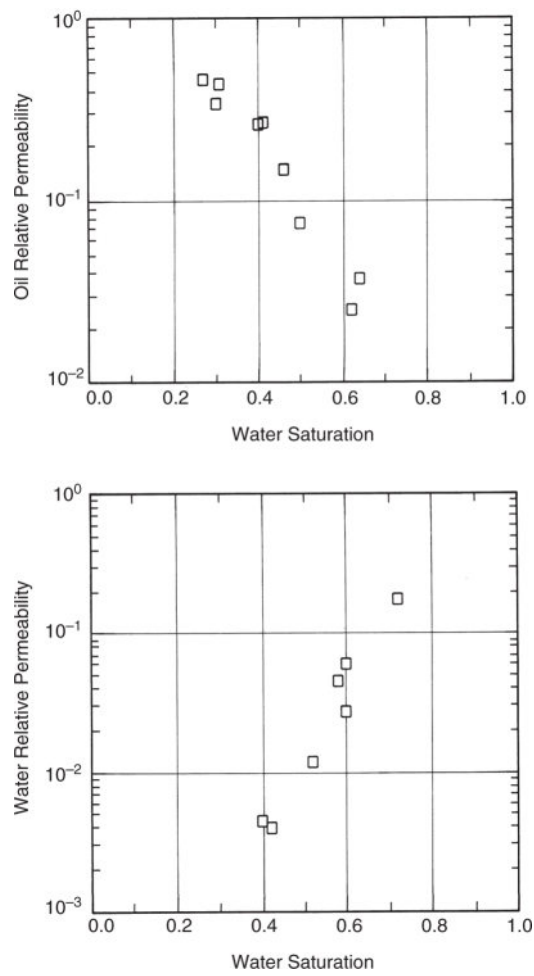


Fig. 8.18—Relative permeabilities for Exercise 8.10 (El Dorado 1977).

Chapter 9

Surfactant Methods

Geoscientists recognized early on that capillary forces caused large quantities of oil to be left behind in well-swept zones of waterflooded oil reservoirs. Capillary forces are the consequence of the interfacial tension (IFT) between oil and water. Capillary forces will trap oil in pores unless a sufficient viscous force is imposed to overcome them. Buoyancy forces can also be significant. For this reason, early efforts in enhanced oil recovery (EOR) strove to displace this oil by decreasing the oil/water IFT. Although many techniques have been proposed and field tested, the predominant EOR technique for achieving low IFT is the use of surfactants.

Reducing the IFT recovers additional oil by reducing the capillary forces that leave oil behind any immiscible displacement. This trapping is best expressed as a competition between viscous forces, which mobilize the oil, and capillary forces, which trap the oil. The local capillary number N_{vc} , the dimensionless ratio of viscous to capillary forces, determines the residual oil and water saturations through a capillary desaturation curve (CDC). Section 3.5 gives general features of the CDC and N_{vc} . In this chapter, we apply those results to surfactant-based flooding. Recall that ultralow IFTs are required—on the order of 0.001 mN/m—and that these values can be attained only through highly surface-active chemicals.

9.1 The Processes

Surfactant flooding is any process that uses a surface-active agent (a surfactant) to bring about improved oil recovery. This definition eliminates other EOR processes in which reducing capillary forces is not the primary means of oil recovery. However, it does include surfactant-polymer (SP) flooding in which surfactant is injected;

alkaline flooding with surfactants that are generated by in-situ reactions; and alkaline-surfactant-polymer (ASP) flooding, which is a combination of alkaline and SP flooding. The viewpoint of this chapter is that both SP and ASP follow a common theme of IFT reduction tied to phase behavior. All methods use polymers of the type discussed in [Chapter 8](#). Surfactants are an integral part of foam flooding to be discussed in [Chapter 10](#), but these do not appreciably lower IFT.

Surfactant processes have appeared under many names: SP, ASP, micellar-polymer (MP), detergent, surfactant, low-tension, soluble oil, microemulsion, and chemical flooding. We use the term *SP flooding* because it is the least ambiguous (chemical flooding, for example, could describe all nonthermal EOR processes) and most comprehensive (no other name has the important polymer component). Although there are differences among processes, in this chapter, we emphasize their similarities because they are more numerous and important than the differences.

[Fig. 9.1](#) shows an idealized version of an SP flooding sequence. The process is usually applied to tertiary floods and is always implemented in the drive mode (not cyclic or huff-n-puff). The most common way to inject surfactant is to inject an aqueous solution of surfactant and polymer, called a *slug*, which ranges from approximately 10 to 50% of the floodable pore volume. The surfactant concentration varies from approximately 0.2 to 2 wt% (active basis) and the polymer concentration from 0.1 to 0.4 wt%, depending on how much polymer is needed to produce the mobility reduction required for a stable displacement. Other chemicals such as cosurfactant, cosolvent, alkali, and biocide may also be included. The brine composition in the slug corresponds typically to the location at which the IFT is lowest; to do this, it often includes electrolytes from alkali chemicals such as sodium carbonate. Although less common today, a preflood can be injected before the slug to change the salinity. A preflood increases the time and cost of the project and in many cases is not needed. The slug and the chemicals in it are the workhorse for this process and the focus of much of the following discussion.

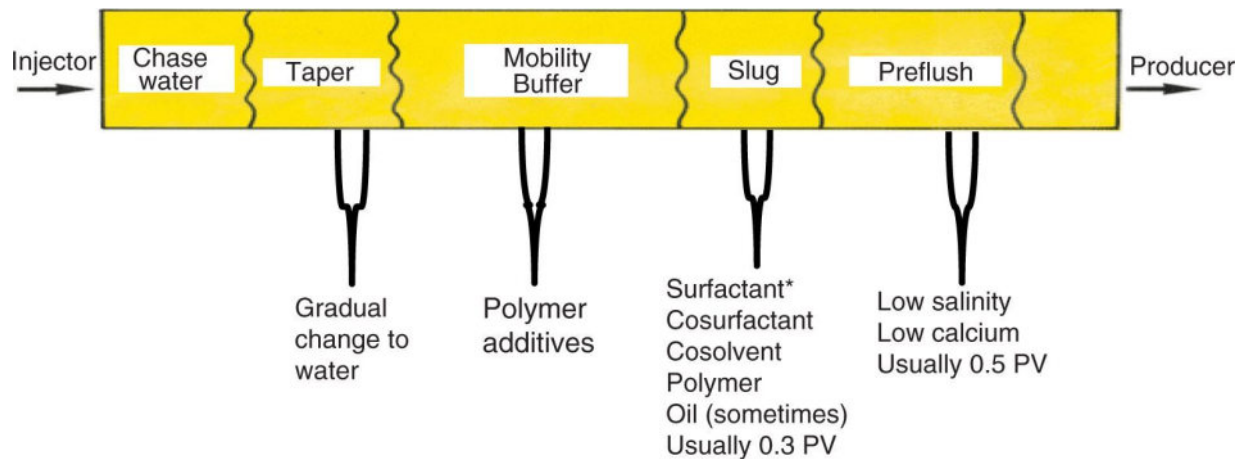


Fig. 9.1—SP flooding sequence. *Surfactant is replaced by alkali for alkali/surfactant flooding.

The slug is followed by (driven by) an aqueous polymer solution called the polymer *drive* or *mobility buffer*. The polymer concentration depends on how much polymer is needed to produce the same or lesser mobility than the slug. The electrolyte concentration in the brine of the polymer drive is typically lower than that of the slug. The size of the polymer drive is 50 to 100% of the floodable pore volume. It is followed by brine until the end of the flood. The polymer drive often includes other chemicals such as biocides, oxygen scavengers, and iron-reducing components—basically the same components needed in polymer flooding and discussed in the previous chapter. The concentration of the polymer is sometimes reduced gradually to zero rather than in one step (polymer grading), but there is little if any evidence that this grading has a significant effect on oil recovery. Often, it is the specific economics of the project that dictate the volume of polymer drive.

As for polymer flooding, the surfactant facilities for this process rarely need turbines or compressors, both of which are expensive equipment. Mixing is done at low pressure and consequently with little expense. The process does, however, require strict quality-control methods because of its sensitivity to chemical makeup. In addition, like polymer flooding, the process requires a means to monitor and adjust the brine salinity or hardness. This is especially true of the ASP process because it typically requires softened brine.

9.2 The Surfactants and Surfactant Selection

A surfactant, or surface-active agent, is any substance that lowers the surface energy barrier between two immiscible phases. A surfactant consists of a hydrophilic (water-loving) part and a hydrophobic (oil-loving) part, as shown in the following three example structures of common surfactants.

Surfactants are classified into four groups depending on their polar-group identity (**Table 9.1**).

Anionics—When dissolved in water, anionic surfactants have a negative charge that is balanced by a metal cation with a positive charge (usually sodium). Most surfactants used for EOR are anionic surfactants because of their comparatively low adsorption on sandstones compared to other types of surfactants.

Cationics—Cationic surfactants have a positive charge; when dissolved in water, this is balanced by an inorganic anion. Some cationic surfactants are used to alter the wettability of the formation.

Nonionics—Nonionic surfactants are not charged and, therefore, are less sensitive to electrolytes in aqueous solutions. Nonionic surfactants are sometimes used as cosurfactants.

Amphoteric—Amphoteric surfactants have both a negative and positive charge in aqueous solutions at the same time, or they can be one or the other depending on pH.

TABLE 9.1—CLASSIFICATION OF SURFACTANTS AND EXAMPLES [ADAPTED FROM AKSTINAT (1981)]

Anionics	Cationics	Nonionics	Amphoteric
 Sulfonates Sulfates Carboxylates Phosphates	 Quaternary ammonium organics, pyridinium, imidazolinium, piperidinium, and sulfonium compounds		 Aminocarboxylic acids

TABLE 9.2—DESIRABLE CHARACTERISTICS OF EOR SURFACTANTS

What is Needed	How This is Achieved
Capable of producing ultralow IFT (high solubilization ratio)	Preferential packing at interface of large surfactant molecules
Stability at high temperature	Sulfonates, carboxylates, add sodium carbonate to sulfates
Avoid gels, liquid crystals, and viscous phases	Branched hydrophobes, alkali, cosolvents, surfactant mixtures
Low adsorption and retention in both sandstone and carbonates	Alkali, high pH, good microemulsion phase behavior and low microemulsion viscosity, chemical gradients
Rapid coalescence and equilibrium	Alkali, cosolvents, branched hydrophobes
Commercial availability and low cost	Few synthesizing steps with inexpensive feedstocks

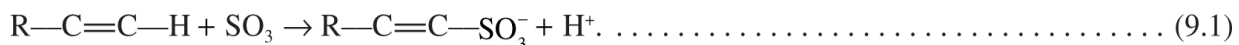
Although there is an enormous variety of surfactant types and structures, a few primary characteristics make a surfactant suitable for EOR of a particular crude oil. [Table 9.2](#) summarizes the most important of these.

A good surfactant has the strongest possible molecular interaction with *both* oil and water. When this balance is achieved, the IFT will be as low as possible. It is equally important that the surfactant does not form viscous structures or rigid interfaces so that it will easily flow through pore throats under low pressure gradients. Surfactant retention in the rock must be extremely low for economic reasons. Surfactant retention is caused by both adsorption on mineral surfaces and trapping in pores. A strong interaction with oil and water relative to mineral surfaces reduces surfactant adsorption. Low bulk and interfacial viscosities lead to less surfactant trapping in pores. Solairaj et al. (2012) recently developed a correlation for surfactant retention as a function of the surfactant structure, pH, salinity, temperature, EACN of the oil, and other factors based on many corefloods under a wide range of conditions.

Molecular branching of the surfactant hydrophobe (the lipophile) is the most desirable way to prevent the formation of viscous structures. Other ways to achieve the same purpose include mixing with a cosurfactant or adding a cosolvent, such as a light alcohol, because these tend to create disorder. Disorder is also greater at high temperature, so that a surfactant that requires cosolvent at low temperature may not require it at high temperature. Adding alkali to

increase the pH also tends to increase the disorder in the structure of the microemulsion phase and promote fluidity.

During the 1960s and 1970s, petroleum sulfonates were the most commonly used primary surfactants. These anionic surfactants were produced by sulfonating an intermediate-molecular-weight refinery stream, or when appropriate, even crude itself. If R—C=C—H represents the molecular formula of the feedstock, the sulfonation reaction proceeds as follows:



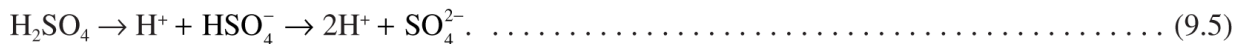
The reaction can also proceed to saturate the carbon-carbon double bond:



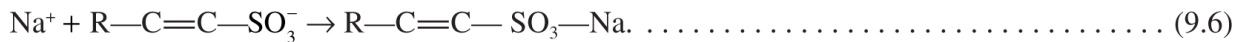
Here, we adopt a shorthand notation that shows only the atoms participating in the chemical reaction. The surfactant produced in Eq. 9.1 is an α -olefin sulfonate, and that produced in Eq. 9.2 is an alkyl sulfonate. If the feedstock is aromatic, sulfonation produces an alkyl benzene sulfonate:



The sulfate in these reactions comes from bubbling SO_3 gas through the feedstock or through contact with a solvent in which the SO_3 is dissolved. The sulfonation reactions (Eqs. 9.1 through 9.3) yield a highly acidic aqueous solution through the parallel reactions,



The solution is subsequently restored to a neutral pH by adding a strong base, such as $NaOH$ or NH_3 , dissolved in water. This neutralization step also provides the counter-ion for the sulfonate; for the α -olefin sulfonate, this is



The less refined the feedstock, the greater the diversity of the mixture of surfactant types that will result. This can also happen with a refined feedstock when the reaction conditions are not controlled. The mixture can contain a distribution of isomeric forms, molecular weights, and degrees of sulfonation (mono- vs. disulfonation). Such a mixture is extremely difficult to characterize except by several gross properties. Typical molecular weights range from 350 to 450 kg/kg-mole, with the lower values indicating greater water solubility. Some products contain impurities: unreacted oil from the sulfonation step and water from neutralization. Part of the surfactant, as purchased, is inactive. Because we are interested in the surfactant itself, all slug concentrations should report the surfactant concentration only (100% active basis).

Starting in the 1980s, petroleum sulfonates were mostly replaced by synthetic surfactants to produce the molecular structures needed to achieve the desired characteristics ([Table 9.2](#)), as well as to tailor the surfactants to particular oil and reservoir conditions. Such surfactants are typically much purer than petroleum sulfonates.

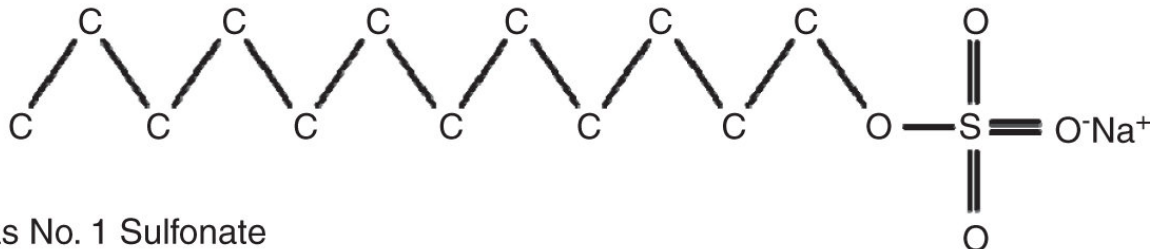
The first new class of surfactants to be used in the field was alkyl ether sulfates (Bragg et al. 1982). The starting material was an alcohol with 13 carbon atoms (tridecyl alcohol or TDA). Both ethylene oxide and propylene oxide were added to the surfactant to build calcium and salinity tolerance. This surfactant is made from inexpensive materials and is, therefore, relatively inexpensive to manufacture. Similar surfactants are still used for surfactant floods in reservoirs with temperatures below 60°C. Above 60°C, sulfates hydrolyze unless the pH is increased to 10 or higher. [Table 9.3](#) shows the simplified molecular structure of a few of the most common EOR surfactants in current use (Sanz and Pope 1995; Levitt et al. 2009; Adkins et al. 2012; Liyanage et al. 2012; Lu et al. 2012).

In the following discussion, we ignore distinctions between surfactant types by simply treating the surfactant as the tadpole structure shown in [Fig. 9.2](#).

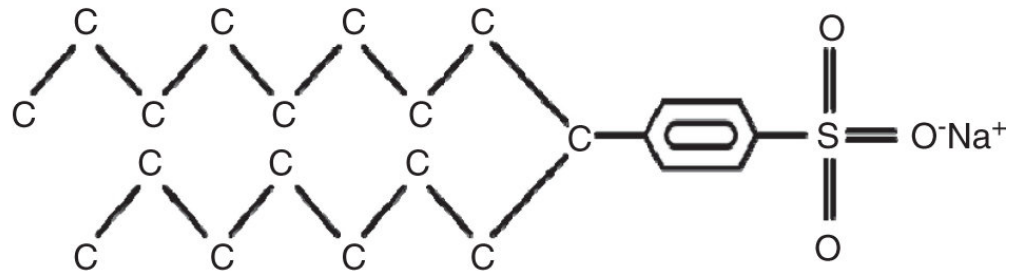
9.2.1 Surfactants in Water. If an anionic surfactant is dissolved in an aqueous solution (no oil), the surfactant disassociates into a cation and a monomer. If the surfactant concentration is then increased, the lipophilic parts of the surfactant begin to associate among themselves to form aggregates or *micelles* containing several monomers each. A plot of surfactant monomer concentration vs. total surfactant concentration ([Fig. 9.3](#)) is a curve that begins at the origin, increases monotonically with unit slope, and then levels off at the *critical micelle concentration* (CMC). Above the CMC, all further increases in surfactant concentration cause increases only in the micelle concentration. Because CMCs are typically quite low (approximately 10^{-5} to 10^{-4} kg-moles/m³), at nearly all concentrations practical for SP flooding, the surfactant is predominantly in the micelle form. The representations of the micelles in [Fig. 9.3](#) and elsewhere are schematic. The actual structures of the micelles are not static and can exist in various forms.

TABLE 9.3—SURFACTANT STRUCTURES	
C ₂₀₋₂₄ IOS	
	+ Olefin Sulfonate
C ₁₆₋₁₈ ABS	
C ₁₃ -13PO-sulfate	
C ₃₂ -7PO-6EO-sulfate	
C ₁₂₋₁₅ -12EO	

Sodium Dodecyl Sulfate



Texas No. 1 Sulfonate



Generic representation



Fig. 9.2—Different types of surfactant structures. A hydrophobe is lipophilic and usually nonpolar. A hydrophile is lipophobic and usually polar. Molecular structure is often represented generically by the tadpole, with the tail being nonpolar and the head polar.

9.2.2 Aqueous Surfactant Solution in Contact With Oil. When this solution contacts an oleic phase (the term *oleic phase* indicates that this phase, although oil-rich, can contain more than oil), the surfactant tends to accumulate at the intervening interface. The lipophilic part “dissolves” in the oleic phase and the hydrophilic part in the aqueous phase. The surfactant prefers the oleic/aqueous interface to the micelle; however, only a small amount of surfactant will saturate the interface. The dual nature of the surfactant is important because the accumulation at the interface reduces the IFT between the two phases. The IFT between the two phases is a function of the excess surfactant concentration at the interface (Huh 1979). The excess is the difference between the interface and bulk concentrations. The interface blurs in much the same manner as do vapor/liquid interfaces near a critical point.

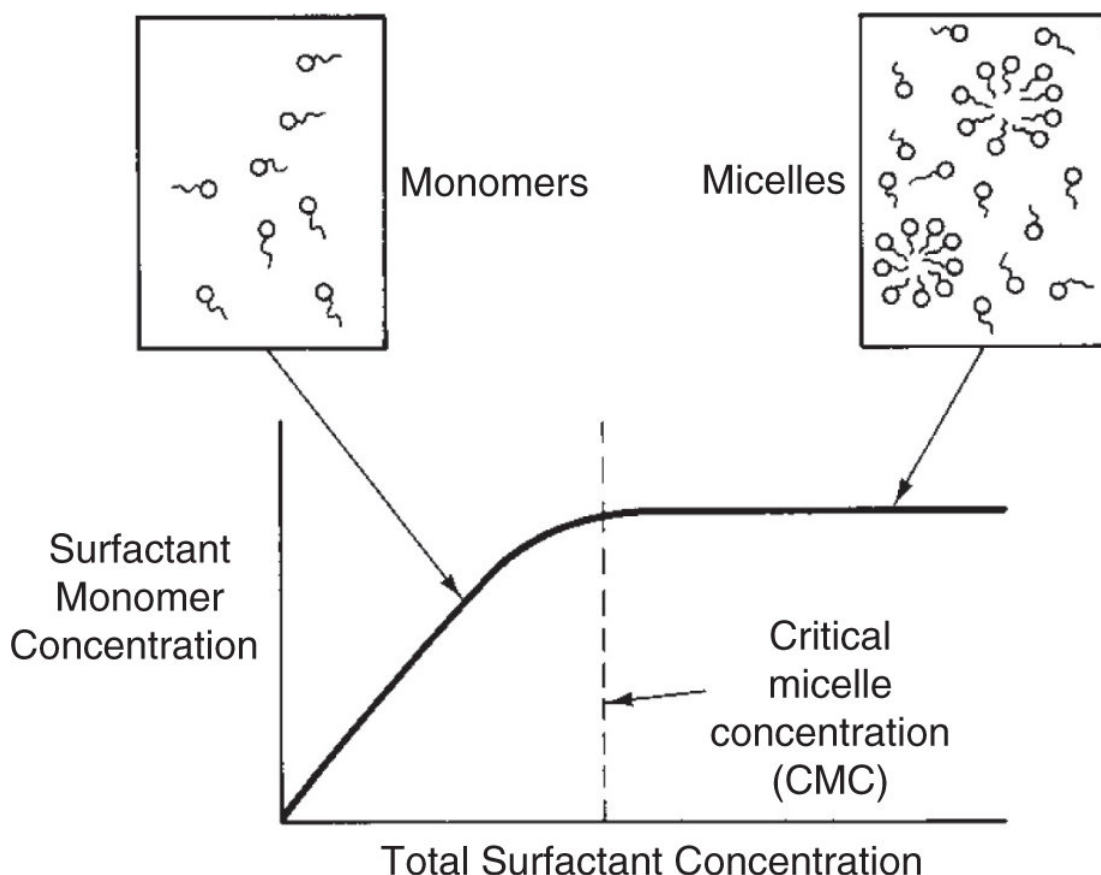


Fig. 9.3—Schematic definition of the critical micelle concentration.

The surfactant itself and the associated conditions should be adjusted to maximize the aggregation at the interface, but this affects the solubility of the surfactant in the bulk oleic and aqueous phases. Because this solubility impinges on the mutual solubility of brine and oil, which also affects IFTs, this discussion leads naturally to the topic of surfactant/oil/brine phase behavior. Curiously, the surfactant concentration itself plays a fairly minor role in the phenomena described in the following section compared to temperature, brine salinity, and hardness. This is true of many micellar properties.

9.3 Surfactant/Oil/Brine Phase Behavior

Under certain conditions, micelles solubilize crude to form a thermodynamically stable fluid called a *microemulsion*. Microemulsion phase behavior plays a central role in all aspects of SP/ASP flooding, including everything from laboratory testing to process modeling.

Discovering this behavior and its relationship to interfacial tension has been one of the significant intellectual achievements in EOR.

Microemulsion phase behavior is conventionally illustrated on a ternary diagram (see Section 4.4). By convention, the top apex of the ternary diagram represents the surfactant ($i = 3$), the lower left represents brine ($i = 1$), and the lower right represents oil ($i = 2$).

Microemulsion phase behavior is strongly affected by the salinity of the brine. Consider the sequence of phase diagrams, [Figs. 9.4 through 9.7](#), as the brine salinity is increased. The phase behavior we now describe was originally reported by Winsor (1954) and adapted to surfactant flooding by Healy et al. (1976) and Nelson and Pope (1978) among others. All properties discussed below are equilibrium properties.

At low brine salinity, a typical anionic surfactant will exhibit good water solubility and poor oil solubility. Therefore, an overall composition near the brine/oil boundary of the ternary diagram will split into two phases: an *excess oil* phase and a (*water-external*) *microemulsion* phase containing brine, surfactant, and some solubilized oil. The solubilized oil occurs when globules of oil occupy the central core of the swollen micelles. The tie lines within the two-phase region have a negative slope. This type of phase environment is called by various names: a Winsor Type I after its discoverer; a Type II(–) because, at most, two phases are present and the tie lines have negative slope; and a lower-phase microemulsion because it is denser than the excess oil phase. We adopt the Type II(–) terminology here ([Fig. 9.4](#)). The plait point P_R is usually located fairly close to the oil apex, which means that the excess oil phase is nearly pure oil. Any overall composition above the binodal curve is a single-phase microemulsion.

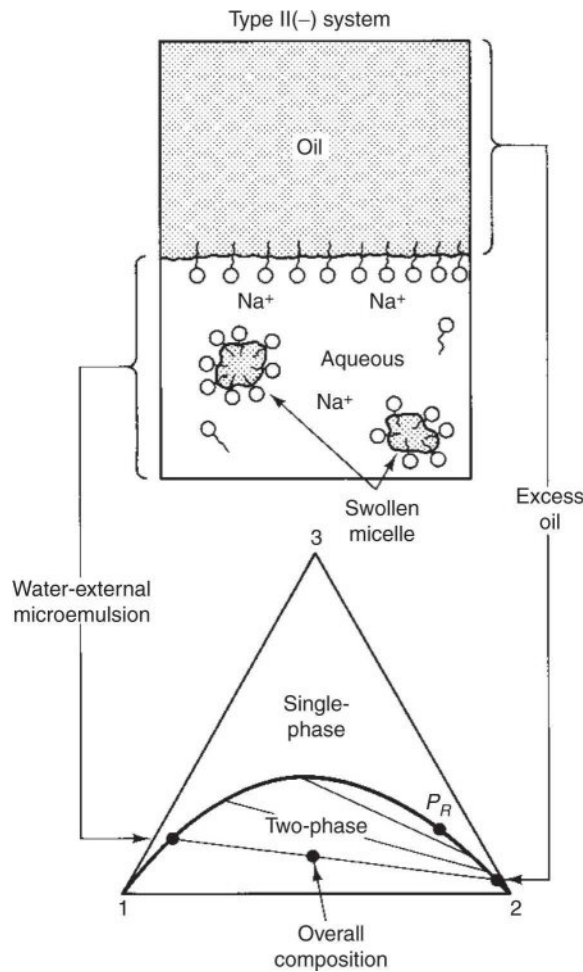


Fig. 9.4—Schematic representation of a Type II(−) system for small brine salinities. Small electrostatic forces increase the anionic surfactant’s solubility in the aqueous phase.

At higher brine salinities, an overall composition within the two-phase region will split into an excess brine phase and an (*oil-external*) microemulsion phase that contains most of the surfactant and some solubilized brine (Fig. 9.5). The brine is solubilized through the formation of inverted swollen micelles, with brine at their cores. This phase environment is called Winsor Type II, Type II(+) because the tie lines have positive slopes, or an upper-phase microemulsion because it is less dense than water. The plait point P_L is now close to the brine apex, meaning that the excess brine phase often consists of nearly pure water.

The two extremes presented so far are roughly mirror images: the microemulsion phase is water-continuous in the Type II(−) region and

oil-continuous in the Type II(+) region. At salinities between those shown in [Figs. 9.4](#) and [9.5](#), there is an intermediate range of salinities within which a third surfactant-rich phase forms ([Fig. 9.6](#)). An overall composition within the three-phase region separates into excess oil and brine phases, as in the Type II(−) and Type II(+) environments, and into a microemulsion phase with a composition represented by an invariant point. The term *invariant point* means that as long as the overall composition lies within the tie triangle (three-phase region), the microemulsion-phase composition (and that of excess phases) is fixed. This environment is called a Winsor Type III. It is called a middle-phase microemulsion because it is less dense than the excess brine phase, but more dense than the excess oil phase. To the upper right and left of the three-phase region are Type II(−) and Type II(+) lobes in which two phases will form, as before. Below the three-phase region, there is a third two-phase region (as required by thermodynamics), which usually has an extent so small that it is neglected. In the three-phase region, there are now two IFTs: between the microemulsion and oil, σ_{32} , and between the microemulsion and water, σ_{31} . These are the only two IFTs of interest because the microemulsion phase will separate the excess oil and brine phases.

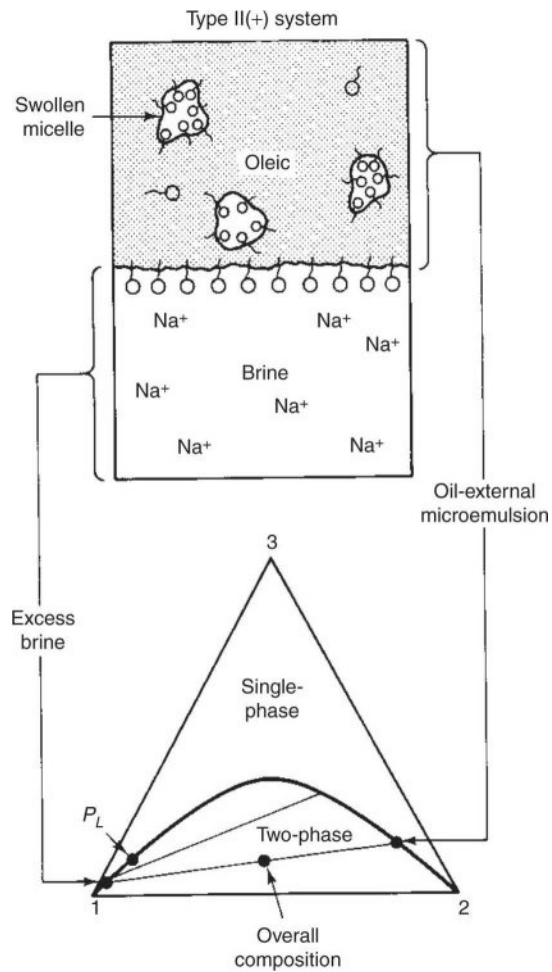


Fig. 9.5—Schematic representation of a high-salinity Type II(+) system.

[Fig. 9.7](#) shows a prism or tent diagram, which illustrates the entire progression of phase environments from Type II(−) to Type II(+) as brine salinity changes. The Type III region forms through the splitting of a critical tie line that lies close to the brine/oil boundary as the salinity increases (Bennett et al. 1981). Over the Type III salinity range, the invariant point M migrates from near the oil apex to near the brine apex before disappearing at the respective critical tie lines.

Several variables besides salinity can bring about the changes in phase behavior shown in [Fig. 9.7](#). Any variable that affects the solubility of the surfactant in either water or oil will also change the microemulsion phase behavior. Several examples are discussed in the following subsections.

9.3.1 Surfactant Structure. A larger surfactant hydrophobe (more carbon atoms) increases the solubility of the surfactant in oil and, therefore, shifts the phase behavior from Type II(–) to Type III to Type II(+). A surfactant hydrophile with two negative charges, such as a disulfonate, increases the solubility of the surfactant in water and, therefore, shifts the phase behavior from Type II(+) to Type III to Type II(–). Such divalent anionic surfactants are rarely used because a very large hydrophobe would be needed to balance such a strong hydrophile.

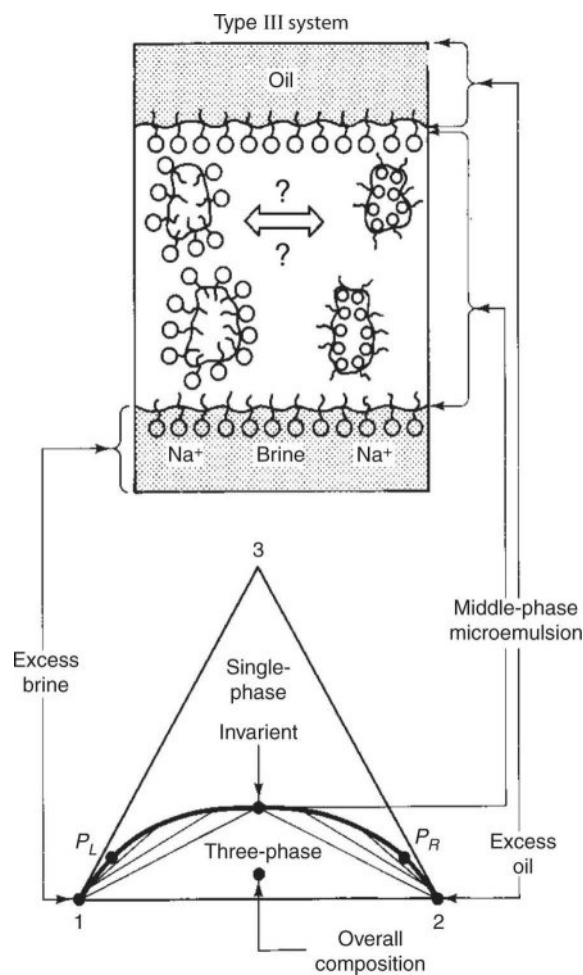


Fig. 9.6—Schematic representation of optimal-salinity Type III phase behavior.

The addition of ethylene oxide (EO) groups into a surfactant also increases the solubility of the surfactant in water, but to a lesser extent, and is the practical method used most often to increase solubility in brines with high salinity or high calcium concentration.

The effect of propylene oxide (PO) groups on the solubility of the surfactant in water and oil is more complex because it depends on temperature and other variables. PO groups tend to stay at the water/oil interface because PO is soluble in both. The number of EO and PO groups in each molecule can be used to tune the surfactant very effectively to specific conditions.

9.3.2 Cosurfactants and Cosolvents. Cosurfactants are surfactants that improve the performance of the primary surfactant in some way. Ideally, they form a mixed micelle with the primary surfactant. The primary surfactant by itself may solubilize the oil and reduce the IFT to ultralow values, but it may not be sufficiently water-soluble in the brine at optimum salinity (defined later in this chapter) to form a clear, stable aqueous phase, especially with the polymer in the mixture. If the solution is cloudy, then it is not a true solution and may eventually separate into two liquid phases (one surfactant rich and one polymer rich), or the surfactant may eventually precipitate, which results in poor transport and high retention among other problems.

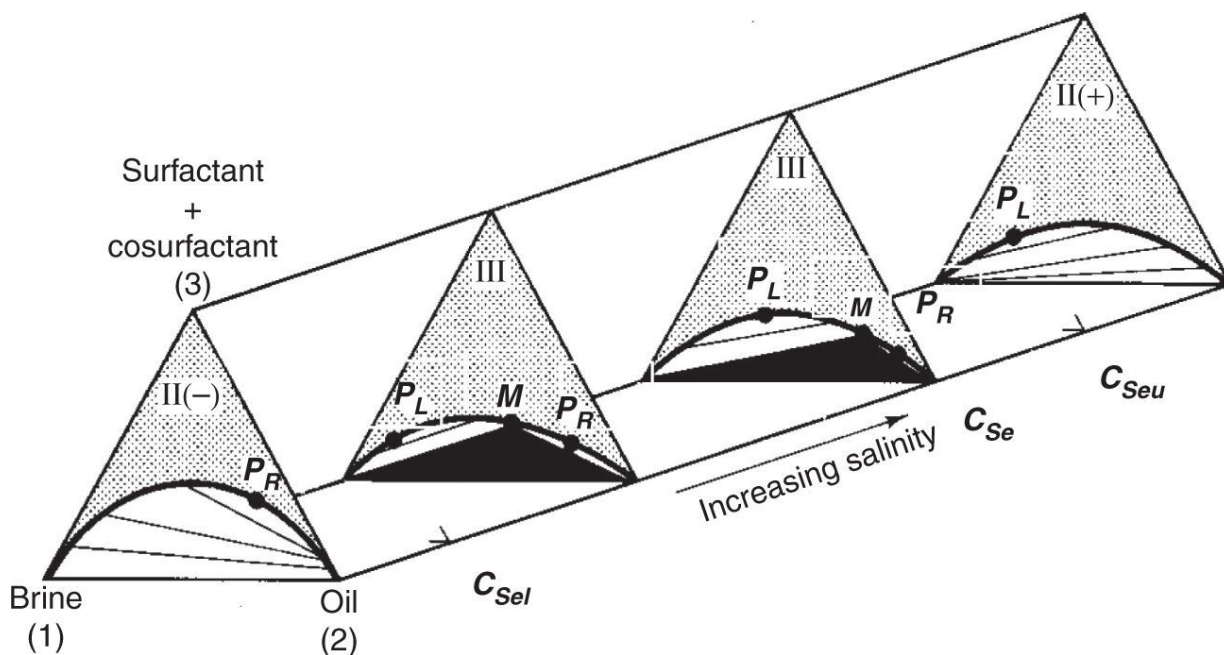


Fig. 9.7—Pseudoternary or “tent” diagram of surfactant phase behavior.

A laboratory test to determine the stability of the aqueous SP solution, called an aqueous stability test, is one of the most important laboratory tests and one of the most difficult performance criteria to meet. “Stability” means the ability of the slug to remain in a single phase. The solution would seem to be to use a cosurfactant that is more hydrophilic than the primary surfactant, but this also increases the optimum salinity and the IFT and, therefore, only partially solves the problem. Adding a cosurfactant that has a different structure, more branching, or both does often solve the problem by a kind of synergy.

If the solution cannot be made stable by adding a cosurfactant, then a cosolvent may be necessary. Cosolvents are light alcohols such as secondary butanol (SBA) or similar compounds (Sahni et al. 2010). Other examples are ethoxylated alcohols and ethylene glycol butyl ether (EGBE). An ideal cosolvent will be equally soluble in water and oil and partition preferentially into the micelles, although not as completely as the surfactants. All cosolvents increase the IFT at optimum salinity and add to the chemical cost, meaning that it is desirable to keep the cosolvent concentration as low as possible while still satisfying the aqueous stability test. However, cosolvents are often needed to reduce microemulsion viscosity even when not needed for aqueous stability. The cosolvents reduce viscosity by reducing the interaction between surfactant hydrophobes.

9.3.3 Oil Characteristics. Microemulsion phase behavior is more sensitive to oil composition than to any other variable. The optimum salinity and the IFT at optimum salinity both increase as the average carbon number of a pure hydrocarbon increases. For pure alkanes, this relationship is particularly simple. The log of the optimum salinity increases linearly with the alkane carbon number (ACN). The phase behavior changes from Type II(+) to Type III to Type II(–) as the ACN of the oil increases.

For more complex oils, an equivalent ACN (EACN) can be defined in such a way that the same trends are observed (Cash et al. 1976). Simple rules have been developed to calculate the EACN of mixtures of alkanes, alkenes, aromatics, and other cyclic hydrocarbons.

However, for complex mixtures, such as crude oils, the EACN must be inferred by comparing the measured phase behavior of the crude oil with the phase behavior of pure hydrocarbons by use of the same surfactant and other conditions. Crude oils with a low API gravity (high density), high viscosity, and high molecular weight tend to have a higher EACN. A larger number of carbon atoms in the oil require many carbon atoms in the hydrophobe of the surfactant or a higher molecular weight (Graciaa et al. 1982). However, most crude oils also contain polar compounds and organic acids that complicate matters, and this is especially true for crude oils with a low API gravity (Puerto and Reed 1982; Nelson 1982).

A small fraction of the organic acids partition to the aqueous phase and react with alkali to form soap ([Fig. 9.2](#)) if alkali is present in the aqueous solution. Nelson et al. (1984) introduced cosurfactant-enhanced alkaline flooding (now known as the ASP process) to take advantage of the synergy between this soap and the synthetic surfactants.

9.3.4 Temperature. The water solubility of most anionic surfactants increases as temperature increases. The opposite is true for nonionic surfactants. However, when the PO number (PON) exceeds approximately seven in an alkyl ether sulfate or similar surfactants, the surfactant becomes less soluble in water as the temperature increases. The phase behavior can shift either way when anionic surfactants are mixed with nonionic surfactants, but the usual behavior is for phase behavior to change in the direction of Type II to Type III to Type I as temperature increases.

9.3.5 Pressure. Because microemulsions are liquids, their phase behavior is relatively insensitive to pressure. For anionic surfactants, phase behavior typically shifts from Type II(+) to Type III to Type II(−) as pressure increases (Skauge and Fotland 1990). This occurs because of an increase in the density of the oil and the corresponding decrease in the oil solubility of the surfactant.

Solution gas has a much greater effect on the microemulsion phase behavior than pressure and in the opposite direction

(Roshanfker et al. 2011). The light hydrocarbons such as methane and ethane decrease the density of the oil, so the surfactant becomes more soluble in the oil, but not as much as would be expected based on the decrease in the EACN of the oil.

9.4 Nonideal Effects

[Figs. 9.4](#) through [9.7](#) are idealizations of actual microemulsion phase behavior. For pure surfactants with no cosolvent, the idealized phase behavior is often a good approximation for engineering purposes. Pure or nearly pure surfactants tend to follow the idealized behavior much better than complex mixtures such as petroleum sulfonates. When the phase-behavior shows evidence of viscous phases such as macroemulsions, liquid crystals or gels (Scriven 1976; Healy and Reed 1974; Trushenski 1977; Salter 1983; Sahni et al. 2010), then the solution is to change surfactants, add cosurfactants, add cosolvents, or some combination of these.

However, even after a surfactant formulation without any of these problems is developed, the phase behavior may be only approximately represented by a ternary diagram. The cosolvent is actually a fourth component that should be represented by a quaternary diagram (Salter 1978). However, it is almost as accurate for engineering purposes to define three pseudocomponents and continue to use a ternary representation (Prouvost et al. 1985).

A change in the concentration of divalent cations such as Ca^{++} has a greater effect on microemulsion phase behavior than an equivalent change in monovalent cations, such as Na^+ . A useful way to represent this effect graphically is by the salinity-requirement diagram ([Fig. 9.8](#)). This diagram is a plot of overall surfactant concentration C_3 (horizontal axis) vs. salinity (vertical axis). All other variables are held constant. The vertical axis represents salinity as a percentage dilution of a particular high-salinity brine. The upper curve shows the boundary between Type II(+) and Type III environments or a curve of C_{Seu} vs. C_3 . Similarly, the lower curve shows C_{Sel} vs. C_3 ; hence, the region between the two curves gives the extent of the Type III region

as a function of C_3 . Glover et al. (1979) and Bourrel et al. (1978) plot the extent of observed three-phase behavior in a similar fashion.

[Fig. 9.8](#) shows a Type III region that decreases with salinity. For other surfactants and brines, the trend can be entirely opposite (Bourrel et al. 1978). For ideal SP phase behavior, neither C_{Seu} nor C_{Sel} should depend on C_3 —that is, the phase boundaries on the salinity-requirement diagram should consist of two horizontal lines. Frequently, the behavior in soft brines (i.e., brines with low hardness) will approximate this idealized behavior because the dilution effect is particularly pronounced when the brine contains significant quantities of divalent ions.

The best way to represent the effect of divalent cations is to model the cation exchange with the micelles. The phase-behavior shifts are specific to the exact ionic composition of the brine, not simply to the total salinity. Hence, it is insufficient to characterize the brine as merely “fresh” or in terms of its total dissolved solids (TDS) content. For anionic surfactants, other anions in solution have little effect on the phase behavior, but cations readily cause phase-environment changes. Divalent cations (calcium and magnesium are the most common) are usually 5 to 20 times as potent as monovalent cations (usually sodium). Divalents are usually present in oilfield brines in smaller quantities than monovalents ([Fig. 8.2](#)), but their effect is so pronounced that it is necessary, as a minimum, to account separately for salinity and hardness—total divalent-cation concentration. Variable monovalent/divalent ratios will also cause electrolyte interactions with clay minerals through cation exchange. The disproportionate effects of salinity and hardness can be approximately accounted for by defining a weighted sum of the monovalent and divalent concentrations as an “effective” salinity, C_{Se} .

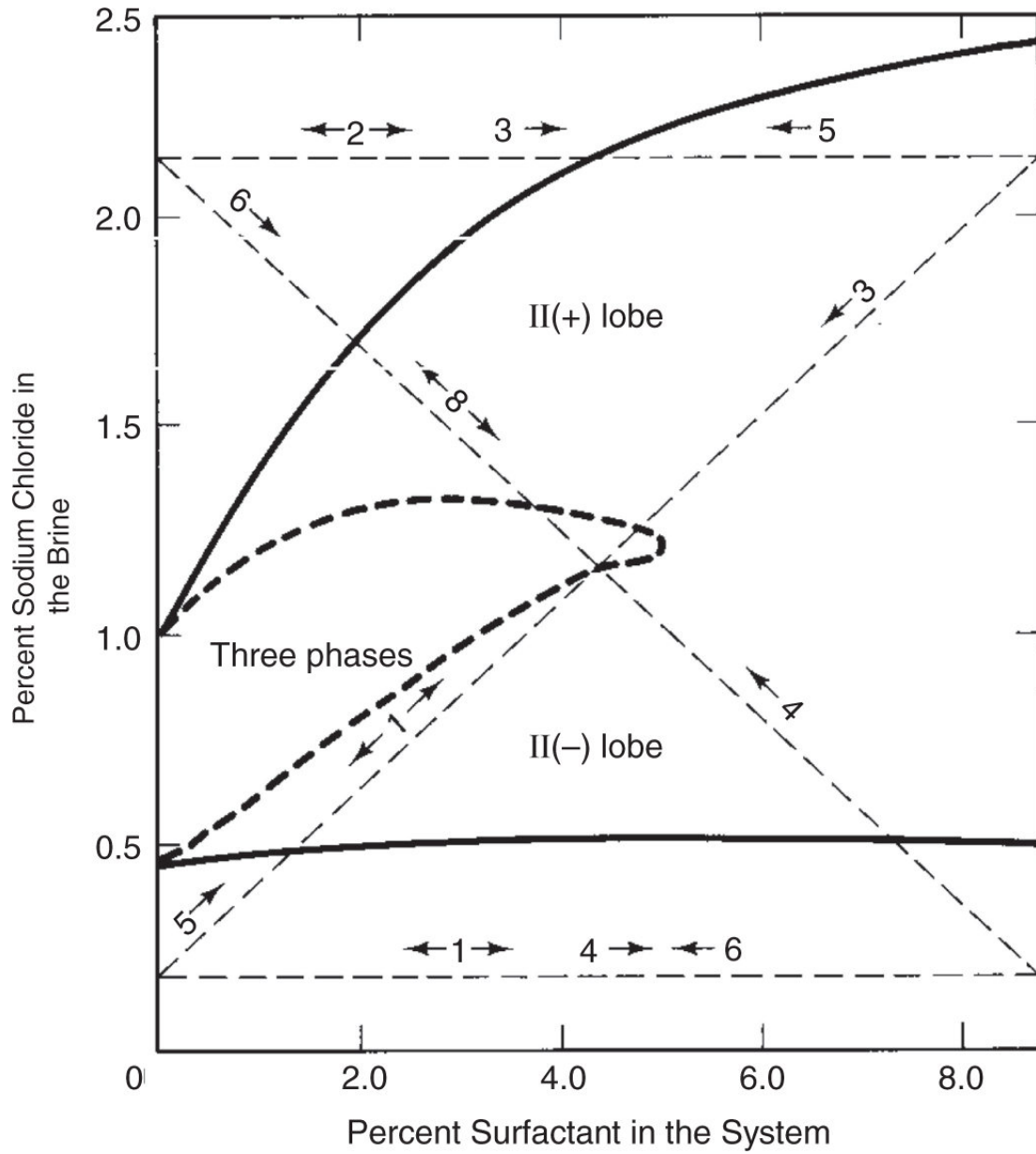


Fig. 9.8—Salinity-requirement diagram (Nelson 1982). The numbers beside the arrows are discussed in Section 9.14.

9.5 Phase Behavior and IFT

Early surfactant-flooding literature is dominated by how to achieve ultralow IFT and how to measure it (Cayias et al. 1975). It was found that IFTs depend on the surfactant structure, cosurfactant structure, types and concentrations of electrolytes, oil composition, temperature, and pressure. The dependence is even stronger if alkali is used and soap is formed.

However, in what was surely one of the most significant advances in the development of surfactant flooding, measured IFTs were shown to correlate strongly with microemulsion phase behavior. Healy and Reed (1974) originally developed an empirical correlation for IFT, which has been experimentally verified by several others (e.g., Glinsmann 1979; Gracia et al. 1982). Huh (1979) derived a theoretical equation for the IFT that agrees with experimental data under a wide range of conditions. An example is shown in [Fig. 9.9](#).

A practical benefit of this correlation is that relatively difficult IFT measurements can be largely supplanted by relatively easy phase-behavior measurements. Indeed, the behavior of IFTs has been inferred by a narrower subset of phase-behavior studies based on the solubilization parameter (Bourrel et al. 1978). A more important benefit of this is that the correlation logically provides a basis for the surfactant-flooding design. We discuss design in Section 9.14.

To illustrate the relation between IFTs and phase behavior further, let C_{23} , C_{13} , and C_{33} be the volume fractions of oil, brine, and surfactant in the microemulsion phase. As shown in [Figs. 9.4](#) through [9.6](#), the microemulsion phase is present at all salinities; hence, all three quantities are well-defined and continuous. Surfactant mixtures are treated as a single surfactant pseudocomponent for this purpose. The oil solubilization parameter for Type II(–) and Type III phase behavior is defined as the ratio of the volume of oil to the volume of surfactant in the microemulsion:

$$S_{23} = \frac{C_{23}}{C_{33}}. \quad (9.7a)$$

The water solubilization parameter for Type II(+) and Type III phase behavior is defined as the ratio of the volume of water to the volume of surfactant in the microemulsion:

$$S_{13} = \frac{C_{13}}{C_{33}}. \quad (9.7b)$$

The IFTs between the corresponding phases, σ_{23} and σ_{13} , are functions of S_{23} and S_{13} .

Using theoretical argument about packing at the interface, Huh (1979) derived an equation for the IFT as a function of solubilization parameters. A simplified version of this equation is as follows:

where σ_{i3} is the IFT (in mN/m) between phase i and the microemulsion phase 3 and S_{i3} is the corresponding solubilization parameter. The equation proposed by Huh (1979) has been validated with extensive experimental data. An example is shown in Fig. 9.9. Fewer measurements of IFT are needed now since IFT can be estimated from phase behavior data. However, the Huh relationship is valid only if the microemulsion is at equilibrium. The phase behavior may take anywhere from a few days to a few weeks to equilibrate. The IFT measurements are not valid unless the phase behavior is at equilibrium, so either way, the observations must be made over a period of time, which is much easier to do with phase behavior measurements than with IFT measurements.

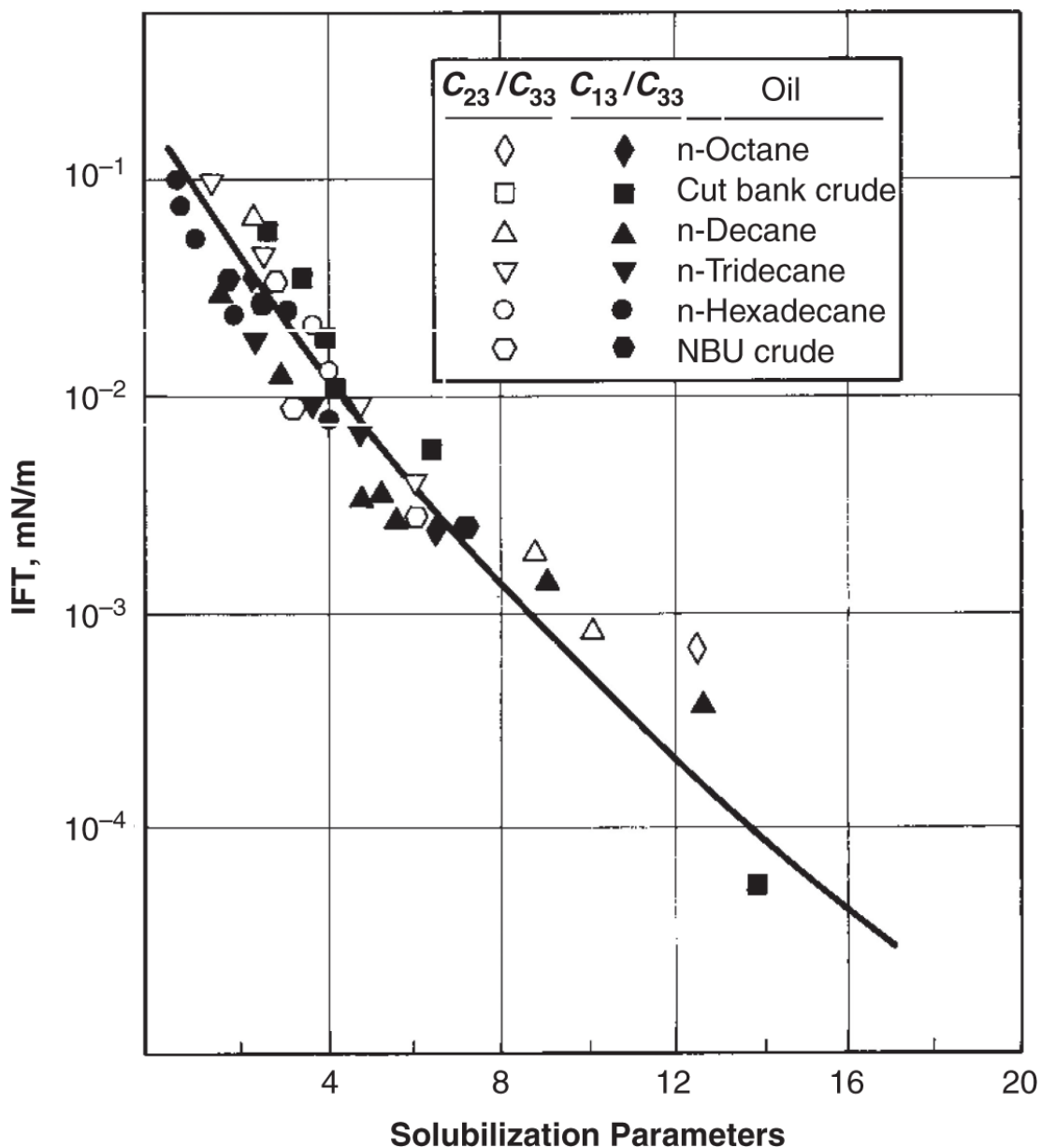


Fig. 9.9—Correlation of solubilization parameters with IFTs (Glinsmann 1979).

Example 9.1. Calculating IFT. We observe a pipette into which equal volumes of brine and oil have been mixed and which contains 3% surfactant (based on total volume). At equilibrium, the tube has 30 volume percent of an almost pure upper phase oil and 70 volume percent of a lower phase microemulsion. The conditions correspond to those shown in Fig. 9.10. Determine the phase environment and the IFT between the two phases.

We need to calculate how much oil (Component 2) is solubilized in the microemulsion phase. The first step is to calculate the total concentrations from the given data. We know that $C_1 + C_2 + C_3 = 1$. For a brine/oil ratio of one, $C_1 = C_2$, so that $2C_1 + 0.03 = 1$ and $C_1 = C_2 = 0.485$. The total concentrations in terms of phase concentrations are $C_i = S_1 C_{i1} + S_2 C_{i2} + S_3 C_{i3}$ in general. For these conditions, there is no aqueous phase, so that

$$C_1 = S_2 C_{12} + S_3 C_{13}$$

$$C_2 = S_2 C_{22} + S_3 C_{23}$$

$$C_3 = S_2 C_{32} + S_3 C_{33}.$$

To a good approximation, the excess oleic phase contains only oil, or $C_{22} = 1$, which means that $C_{12} = C_{32} = 0$. The total concentrations are now

$$C_1 = S_3 C_{13}$$

$$C_2 = S_2 + S_3 C_{23}$$

$$C_3 = S_3 C_{33}.$$

Inserting the values gives

$$C_{13} = \frac{C_1}{S_3} = \frac{0.485}{0.7} = 0.69,$$

$$C_{23} = \frac{C_2 - S_2}{S_3} = \frac{0.485 - 0.3}{0.7} = 0.26,$$

and

$$C_{33} = \frac{C_3}{S_3} = \frac{0.03}{0.7} = 0.043.$$

The solubilization parameter is $S_{23} = \frac{C_{23}}{C_{33}} = \frac{0.26}{0.043} = 6.15$ from Eq. 9.7a. Finally, the Huh equation gives

$$\sigma_{i3} = \frac{0.3}{S_{i3}^2} = \frac{0.3}{(6.15)^2} = 0.0079 \text{ mN/m.}$$

This value is very close to the values in the correlation shown in Fig. 9.7.

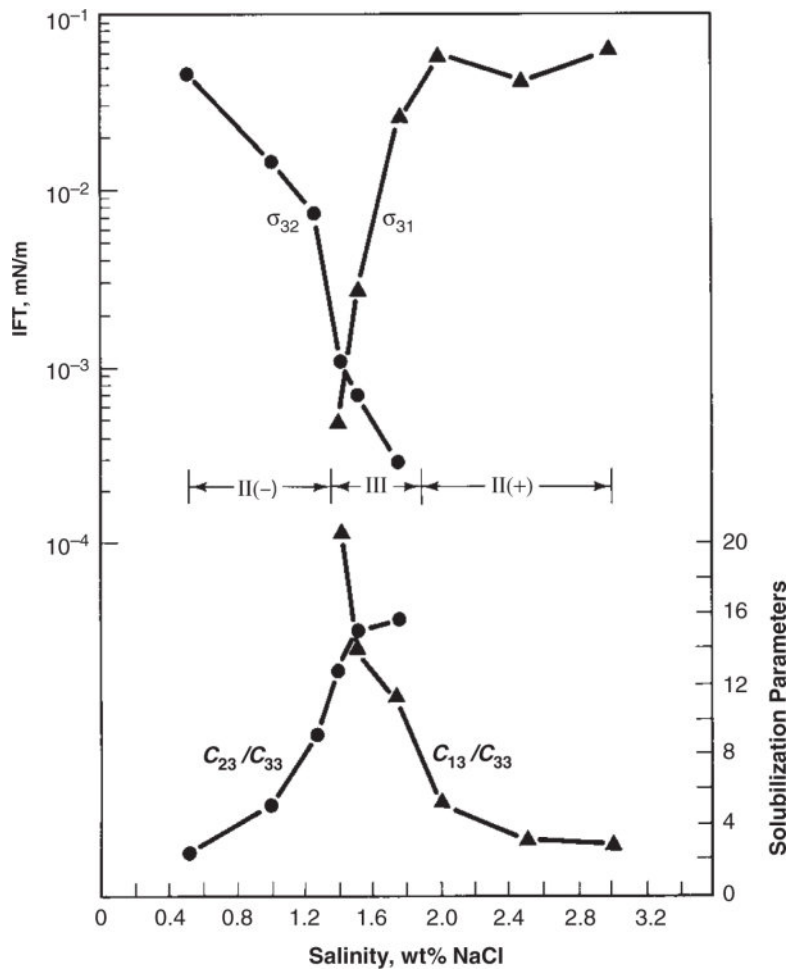


Fig. 9.10—IFTs and solubilization parameters (Reed and Healy 1977).

[Fig. 9.11](#) shows the corresponding behavior of the solubilization parameters and IFTs in a different manner. Consider a line in [Fig. 9.7](#) at constant overall concentrations of oil, brine, and surfactant, but with variable salinity. If nonideal effects are unimportant and the locus is at low surfactant concentration and intermediate brine/oil ratios, σ_{23} will be defined from low salinity up to C_{Seu} , and σ_{13} from C_{Sel} to high salinities. Both IFTs are the lowest in the three-phase Type III region between C_{Sel} and C_{Seu} , where both solubilization parameters are large. Furthermore, there is a precise salinity at which both IFTs are equal. This salinity is the optimal salinity C_{Sopt} for this particular surfactant/brine/oil combination, and the common IFT is the *optimal* IFT. Optimal salinities have been defined on the basis of equal IFTs, as in [Fig. 9.11](#) equal solubilization parameters (Healy et al. 1976),

equal contact angles (Reed and Healy 1984), and as the midpoint between C_{Seu} and C_{Sel} . Fortunately, all definitions of optimal salinity give roughly the same value.

[Fig. 9.11b](#) shows a plot similar to that in the upper panel of [Fig. 9.10](#); the lower panel shows oil recovery for a series of constant-salinity corefloods. The optimal salinity values based on solubilization parameters, IFTs, and oil recovery agree well. At the optimum, the residual oil is effectively mobilized because of ultralow σ_{23} , while trapping of the microemulsion phase by excess brine is low because of ultralow σ_{13} . The optimal salinity does not correspond to minimum surfactant retention ([Fig. 9.11c](#)). The surfactant retention decreases with salinity both because surfactant adsorption decreases and because surfactant trapping decreases. Therefore, the economic optimal salinity may not correspond to the IFT optimal salinity. The classical solution to this problem is to inject the slug at optimal salinity and the polymer drive below optimal salinity, which creates a salinity gradient. Phase trapping can be eliminated by designing the polymer drive to be in the Type II(–) salinity environment (below C_{Sel}). The problem then shifts to optimizing the salinity gradient for a particular flood because of competing effects, as discussed in the following.

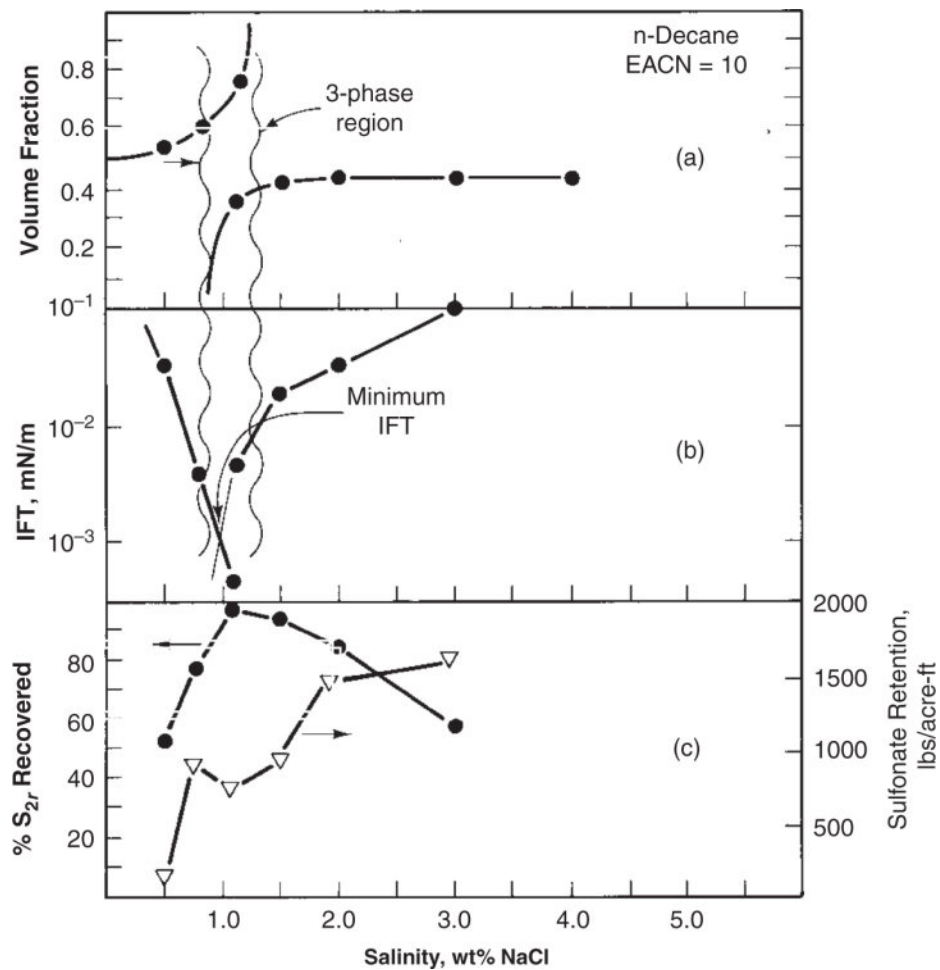


Fig. 9.11—Correlation of phase volume and IFT behavior with retention and oil recovery (Glinsmann 1979).

Because the optimum salinity depends on so many things, maximum oil recovery can be said to occur where the combination of electrolyte, surfactant, and cosurfactant concentrations bring about maximum solubilization parameters. Hence, one should speak of optimal *conditions* rather than optimal salinity. The optimal-salinity terminology is deeply embedded within the SP literature, but it is precise only for the ideal phase behavior depicted in Fig. 9.7. Do not confuse the optimal salinity C_{Sopt} , an intrinsic property of the surfactant/oil/brine combination, with the prevailing salinity C_{Se} , an independent variable in the SP design.

Optimal salinity can vary greatly depending on the nature of the surfactant and brine pseudocomponents. Optimal salinities can be

raised by adding to the slug any chemical that increases the primary surfactant's brine solubility. Adding cosurfactants to the SP slug often increases the optimal IFT.

The notion of optimal conditions is directly connected to the phase behavior of SP systems. Even properties apparently unrelated to phase behavior (retention, for example) are functions of salinity, cosurfactant concentration, and temperature. This observation leads to the interesting speculation that *all* SP properties (retention, phase behavior, IFT, mobilities) correlate to optimal salinity and, perhaps, to solubilization parameters.

Another useful representation of microemulsion phase behavior is the *volume fraction diagram* (VFD) ([Fig. 9.12](#)). Imagine a point of fixed overall composition (parallel to the salinity axis) in the ternary planes in [Fig. 9.7](#). The equilibrium volumes of each phase are observed and plotted as the brine salinity changes. Starting with a low salinity, the VFD shows a succession of decreasing oleic-phase volumes and increasing aqueous-phase volumes, with some three-phase overlap in the middle. If the overall surfactant concentration is low and the brine/oil ratio (WOR) is approximately one, the appearance of the lower brine phase corresponds approximately to the onset of the Type III region (C_{SeI}), and the disappearance of the upper oleic phase corresponds approximately to the termination of the Type III region (C_{Seu}). The salinity at which the brine and oleic phases have equal volumes is a good approximation of the optimal salinity if the surfactant and cosurfactant concentrations are low enough.

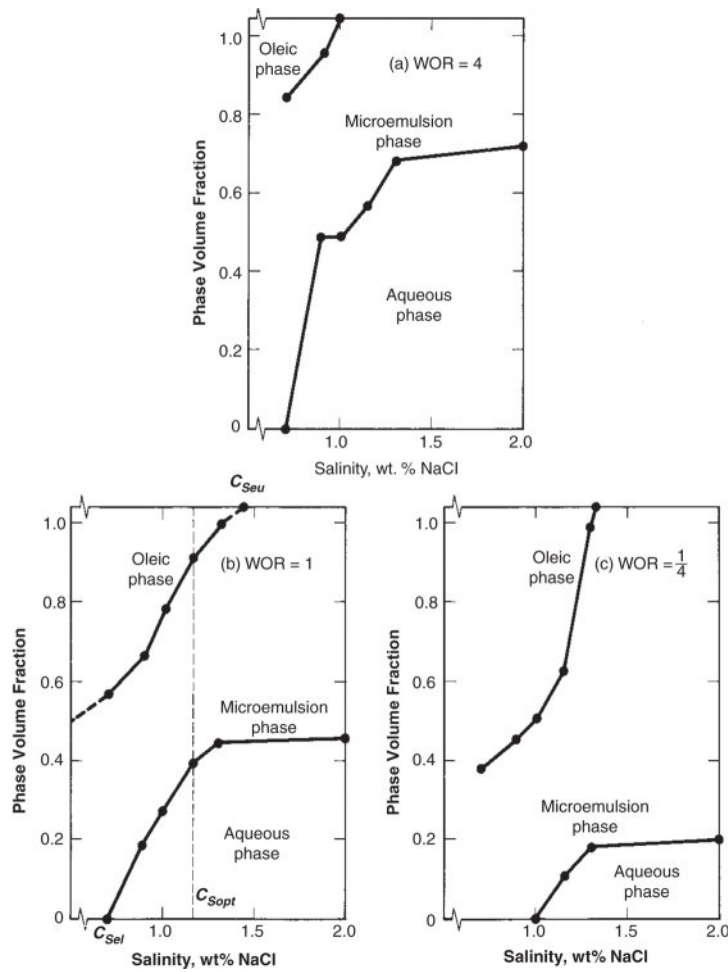


Fig. 9.12—Volume-fraction diagrams (salinity scans) at three brine/oil ratios (Englesen 1981). This is the same diagram as in the upper figure (a) of [Fig. 9.11](#).

Varying salinity while holding other variables constant is sometimes called a salinity scan. The most common presentation of the VFD is varying salinity; however, a derivative of the VFD, in which the cosurfactant concentration is varied in place of the salinity, is sometimes useful. To minimize the number of measurements, each scan can be relatively coarse (approximately ten measurements), followed by additional measurements to refine the estimates of important events. [Fig. 9.13](#) shows the test tubes from a salinity scan.

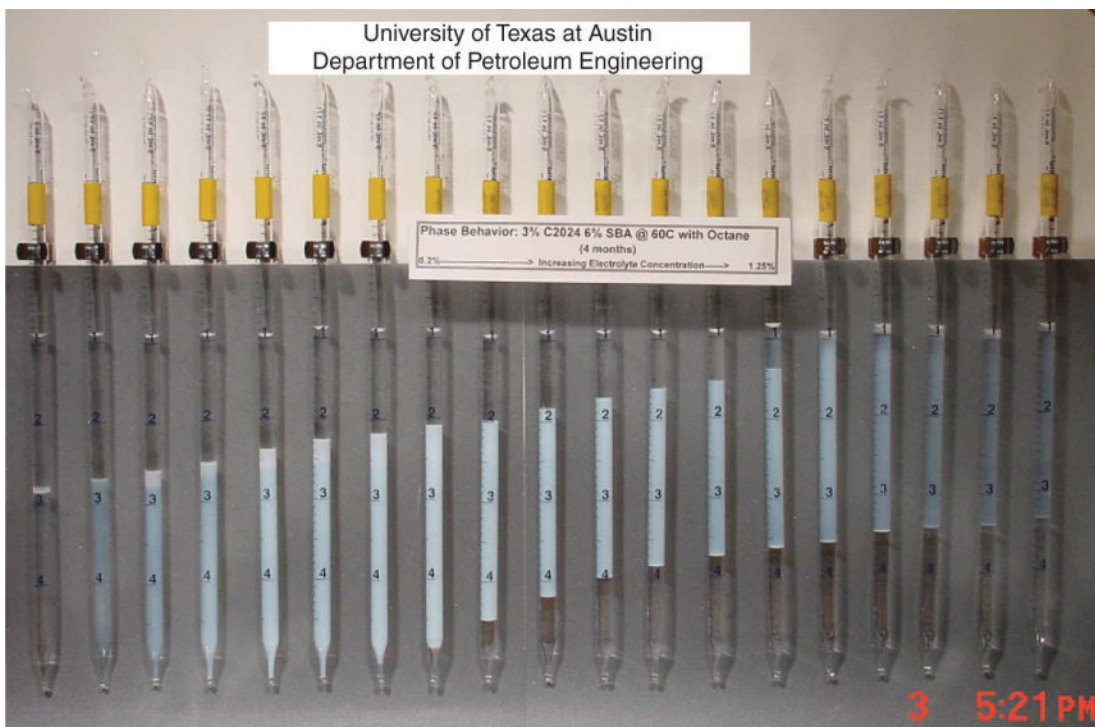


Fig. 9.13—Pipettes from a salinity scan. The microemulsion phase, cloudy or milky, is continuous throughout the scan.

9.6 Other Phase Properties

[**Fig. 9.14**](#) shows microemulsion viscosity as a function of salinity. Over this range, the microemulsion, as defined previously, is continuous and shows a viscosity maximum near the optimal salinity. The maximum indicates molecular ordering in the phase that seems to be the strongest at the phase-inversion salinity. Such maxima can be either beneficial (if the viscosity can be used to provide mobility control in the slug) or detrimental (if it leads to the presence of excessively viscous fluids). It was to counteract the latter tendency that cosurfactants were first added to SP slugs. Over the same salinity range, as shown in [Fig. 9.14](#), the excess phase viscosities do not change appreciably. Walker et al. (2012) show the impact of microemulsion viscosity on oil recovery.

[Fig. 9.13](#) shows a pervasive feature of emulsions: often they are milky or translucent. This can be seen in many common items like certain types of liquid medicine, waste water, some types of slow-moving rivers in which clay particles are suspended in the water, and

yes, even milk itself. The milkiness arises because the micelles are of a size that blocks the transmission of light. The distinction between microemulsions and emulsions is largely one of size: the micelles in microemulsions are smaller (and, for the most part, more stable) than those in emulsions.

The morphology of emulsions is not limited to free-forming micelles. Microemulsions, especially those in the middle phase, can form several solid-like arrangements. These are variously called liquid crystals, liquid gels, or, simply, emulsions. The behavior shown in [Fig. 9.14](#) is a consequence of this phenomenon. Most applications require formulations to avoid this phenomenon (one of the reasons for cosolvents), but it seems that the viscosity maximum could be a source of mobility control.

The properties in this and the previous sections have been captured in a series of equations for use in numerical simulation. See the UTCHEM user's guide listed in the references.

9.7 High-Capillary-Number Relative Permeabilities

A transport property that deserves treatment in a separate section is the high-capillary-number relative permeability. In this section, we discuss two- and three-phase experimental results based on the work of Delshad et al. (1987) (see [Chapter 3](#) for a discussion of low-capillary-number relative permeabilities).

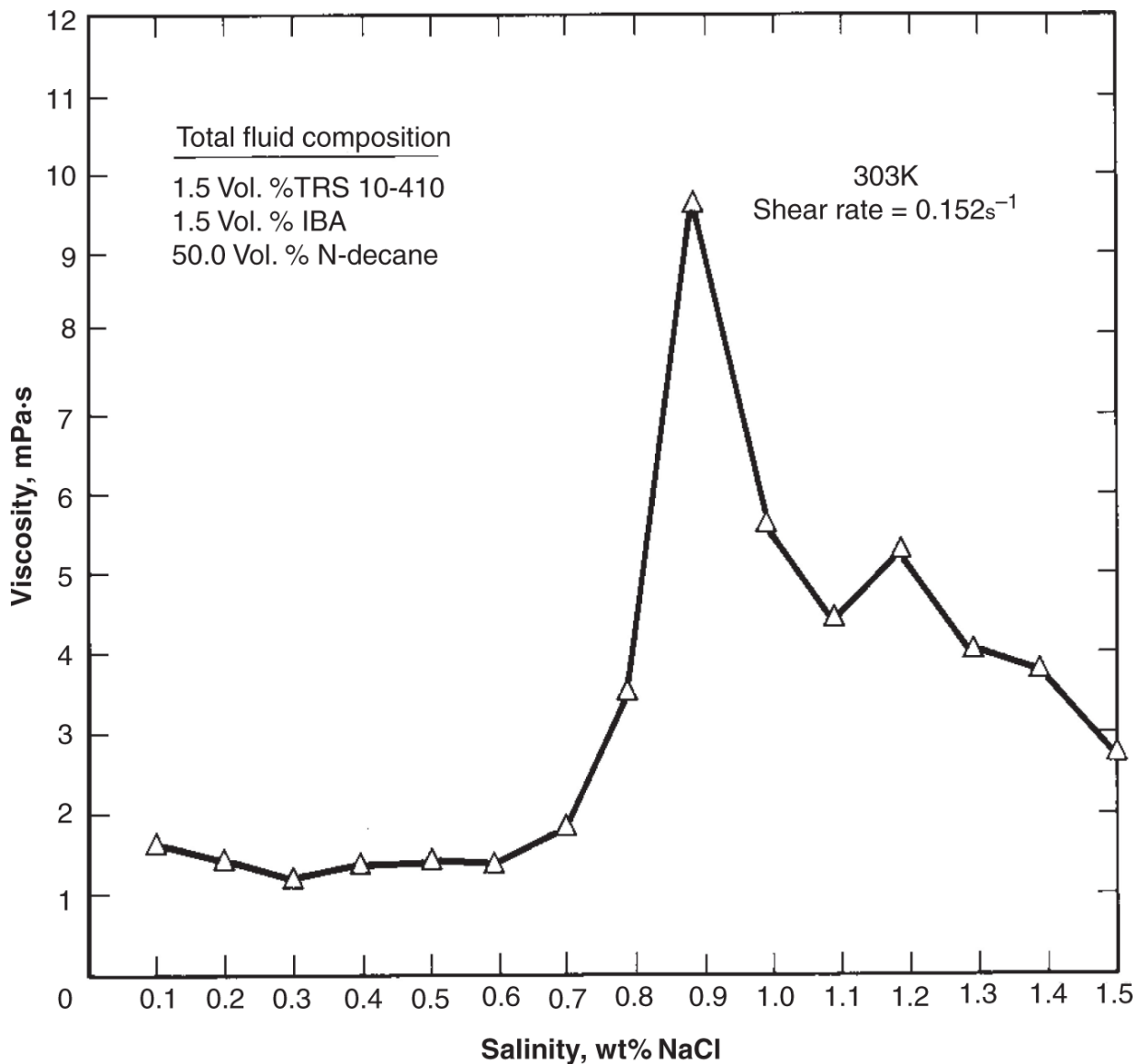


Fig. 9.14—Microemulsion viscosity as a function of salinity (Jones 1981).

Few theoretical relations exist for relative permeabilities in general, much less for those at high capillary number. We do know that the extreme values of relative-permeability functions occur at residual-phase saturation. The latter are functions of capillary number N_{vc} through the CDC (see Section 3.4). Furthermore, for very large N_{vc} , we can expect the relative permeabilities to approach straight-line functions between zero and unit endpoints with no residual-phase saturation. For low N_{vc} , the relative permeabilities should return to the two- or three-phase high-IFT functions.

High- N_{vc} relative permeabilities are difficult to measure. In one type of experiment, a large N_{vc} may be attained by increasing the flow rate. This technique causes experiments to proceed rapidly because, as seen in Section 3.5, N_{vc} must increase by several powers of ten before a significant effect occurs. Such high rates are clearly unrepresentative of typical reservoir-fluid velocities. If the high N_{vc} is established by reducing the IFT, the experiments tend to be dominated by transient composition changes. In principle, these transients could be analyzed by the method given in Section 9.10, but this requires knowing the relative permeabilities, and measuring these is the point of the experiment.

The most reliable measurement is that of steady-state relative permeabilities using pre-equilibrated fluids. For micellar fluids in two-phase flow, this consists of displacing a composition on one end of a tie line with another on the same tie line at constant salinity. When the effluent and injected fractional flows are equal and the transients caused by nonideal phase behavior are gone, the relative permeability of the flowing phases may be calculated from the measured effluent flow and pressure drop. A similar provision exists in three-phase systems in which all compositions are in equilibrium at constant salinity. Of course, such transients may take some time to die out; therefore, these steady-state experiments can be time-consuming. The uniform saturations established by such a procedure follow from material balances or, preferably, tracer data interpreted by a suitable numerical model (Delshad et al. 1987).

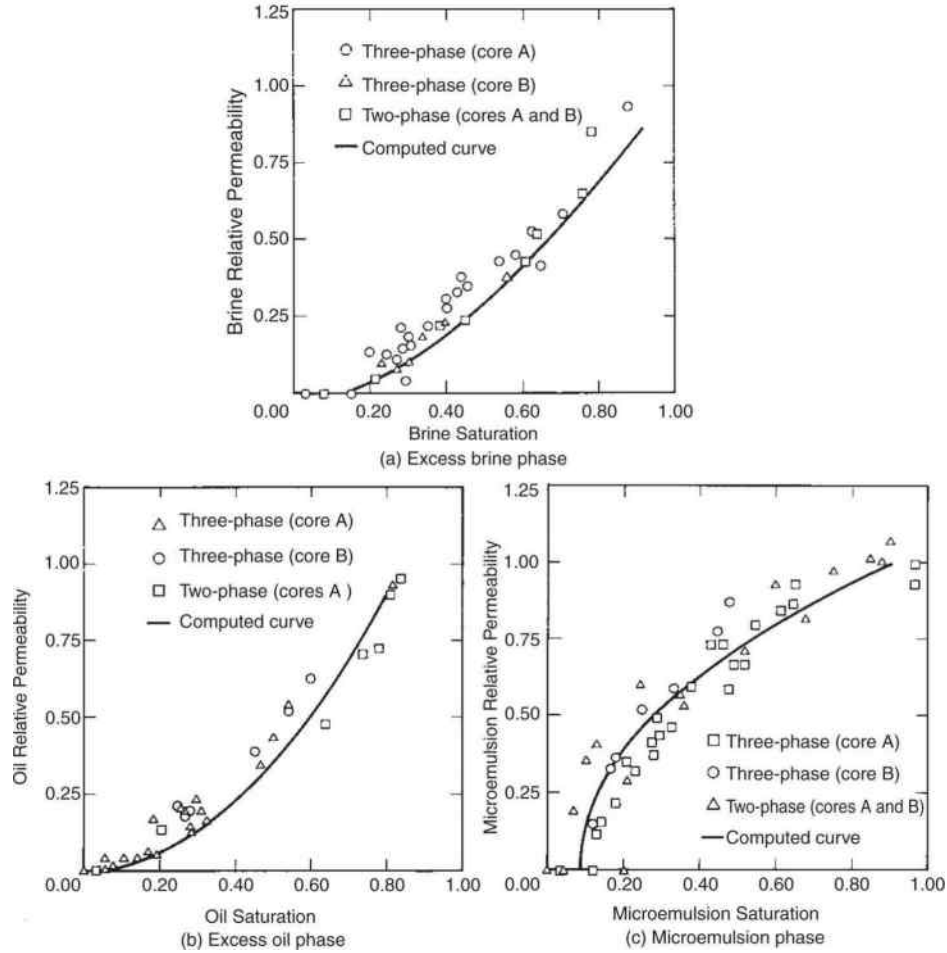


Fig. 9.15—Two- and three-phase relative permeabilities (Delshad et al. 1987).

Despite these difficulties, high- N_{vc} relative permeabilities for two-phase flow have been measured fairly intensively, but three-phase data are rare. [Fig. 9.15](#) shows steady-state relative permeabilities to brine, oil, and microemulsion phases for both two- and three-phase flow. The permeable medium was strongly water-wet in both cores A and B at high N_{vc} conditions, $N_{vc} = 0.01$ at the optimal salinity used in the experiments. The micellar system under test closely followed ideal phase behavior. From these high- N_{vc} data, several observations can be made.

1. The residual-phase saturations are nonzero. Of course, these values are points on the CDC. Except for the oleic phase, for which the endpoint was already high in the water-wet medium,

the endpoint relative permeabilities are substantially different from their low- N_{vc} values.

2. The high- N_{vc} relative permeabilities approach, but are not coincident with, straight lines. The curves in these figures are matches of the exponential forms in Eq. 3.21 to the data.
3. The two- and three-phase data follow essentially the same curves.
4. The relative permeabilities for all three phases are functions of their own saturations. This observation is at odds with the high- N_{vc} behavior of three-phase gas, oil, and water flows (Stone 1970).
5. Perhaps the most surprising conclusion is that the excess brine phase was not the most strongly wetting phase, as it was under low- N_{vc} conditions. This observation is supported by a variety of observations not shown in [Fig. 9.15](#). However, the microemulsion and excess-brine residual-phase saturations have approximately the same value at $N_{vc} = 0.01$.
6. The shape of the microemulsion curve is concave downward. This observation is highly atypical of relative permeabilities.

Quantitative forms for these applications can be found in the UTCHEM technical manual.

9.8 Alkaline/Surfactant Flooding

There are several chemical EOR processes combining high pH, low IFT, and wettability alteration. These processes are alkali flooding, alkali-polymer flooding, alkali-surfactant flooding, alkali-surfactant-polymer flooding and alkali-cosolvent-polymer flooding. The most common of these processes and the one we emphasize in this chapter is ASP flooding. As in polymer and SP flooding, there may be a preflush to precondition the reservoir, a finite volume of the oil-displacing chemical, and a graded mobility-buffer driving agent; moreover, the entire process is usually driven by chase water. The main difference between SP and what we call ASP flooding is that the primary surfactant is soap generated *in situ* by reaction between the

alkali and the natural organic acids in the crude oil. In SP flooding, it is injected. However, alkali is sometimes used even when the oil is not active and no soap is generated because it also reduces surfactant adsorption and has other benefits such as improving the chemical stability of some surfactants and polymers.

High pH levels indicate high concentrations of hydroxide anions (OH^-). The pH of an ideal aqueous solution is defined as

$$\text{pH} = -\log(\text{H}^+), \dots \quad (9.9)$$

where the concentration of hydrogen ions (H^+) is in kg-moles/m³ water. As the concentration of OH^- is increased, the concentration of H^+ decreases because the two concentrations are related through the dissociation of water,

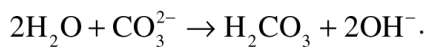
$$K_1 = \frac{(\text{OH}^-)(\text{H}^+)}{(\text{H}_2\text{O})}, \dots \quad (9.10)$$

and the water concentration in an aqueous phase is nearly constant. These considerations suggest two means for introducing high pH into a reservoir: dissociation of a hydroxyl-containing species, or adding chemicals that preferentially bind hydrogen ions.

Many chemicals could be used to generate high pH, but the most commonly used are the alkalis sodium hydroxide ("caustic" or NaOH) and sodium carbonate (Na_2CO_3). NaOH generates OH^- by direct dissociation,



and Na_2CO_3 does so through the formation of weakly dissociating acids (silicic and carbonic acid, respectively), which remove free H^+ ions from solution:



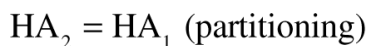
(carbonic acid)

Sodium hydroxide generates a higher pH than sodium carbonate, but this is actually a disadvantage in EOR. This is because there are more reactions and consumption at pH values of 13 corresponding to sodium hydroxide than there are at pH values of 10 to 11 corresponding to sodium carbonate. For this and other reasons, sodium hydroxide use has been decreasing and sodium carbonate use has been increasing in recent years.

Both of these alkalis must be used in soft brine (meaning less than approximately 10 ppm divalent cations, but that does not imply low salinity or fresh water). Fortunately, the cost of softening brine has decreased drastically in recent years. Softening seawater in particular has become very inexpensive, so the benefits of softening now greatly exceed its cost under most circumstances. Alkali concentrations between about 1 and 3 wt% are added to the surfactant slug, so more alkali is used in most cases than surfactant. However, it is much less expensive per unit mass than the surfactants. A typical ASP slug size is 30% PV.

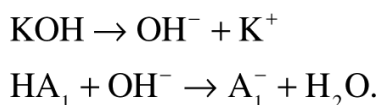
9.9 Surfactant Formation

OH^- by itself is not a surfactant because the absence of a lipophilic tail makes it exclusively water-soluble. If the crude oil contains an acidic hydrocarbon component HA_2 , some of this, HA_1 , can partition to the aqueous phase, where it can react according to (Ramakrishnan and Wasan 1983):



Although the exact nature of HA_2 is unknown, it is probably a carboxylate (a soap) that depends strongly on crude-oil type. The deficiency of hydrogen ions in the aqueous phase will cause this reaction to move to the right. The anionic species A_1^- is a surfactant that has many of the properties and phenomena described previously for SP flooding.

If no HA_2 is originally present in the crude, little surfactant can be generated. A procedure for characterizing crudes according to their attractiveness for alkaline flooding involves the *acid number*. The acid number is the milligrams of potassium hydroxide (KOH) required to neutralize one gram of crude oil. To make this measurement, the crude is extracted with water until the acidic species HA_2 is removed. The aqueous phase containing HA_1 , A_1^- , and H^+ is then brought to pH = 7 by adding KOH:



To provide a meaningful value, the crude must be free of acidic additives (scale inhibitor, for example) and acidic gases (CO_2 or H_2S). A good alkaline-flooding crude candidate will have an acid number of 0.5 mg/g or greater, but crudes with acid numbers as low as 0.2 mg/g may be candidates because only a small amount of surfactant is required to saturate oil/brine interfaces. [Fig. 9.16](#) shows a histogram of acid numbers.

9.10 Displacement Mechanisms

Oil-recovery mechanisms in high-pH flooding have been attributed to as many as eight separate mechanisms (de Zabala et al. 1982). This section concentrates on only three: IFT reduction, wettability reversal, and emulsion formation. The last two mechanisms are also present in SP flooding, but are less important than IFT reduction.

9.10.1 IFT Reduction. The generated surfactant A_1^- aggregates at oil/water interfaces that can lower IFT (Ramakrishnan and Wassan 1983). In general, this reduction is not as pronounced as in SP flooding, but under certain conditions, it can be large enough to produce good oil recovery. [Fig. 9.17](#) shows IFT measurements of caustic solutions against crude oil at various brine salinities. The IFTs are sensitive to both NaOH concentration and salinity, showing minima in the NaOH concentration range of 0.01–0.1 wt%. The

decrease in IFT in these experiments is limited by the spontaneous emulsification of the oil/water mixture when the IFT reaches a minimum.

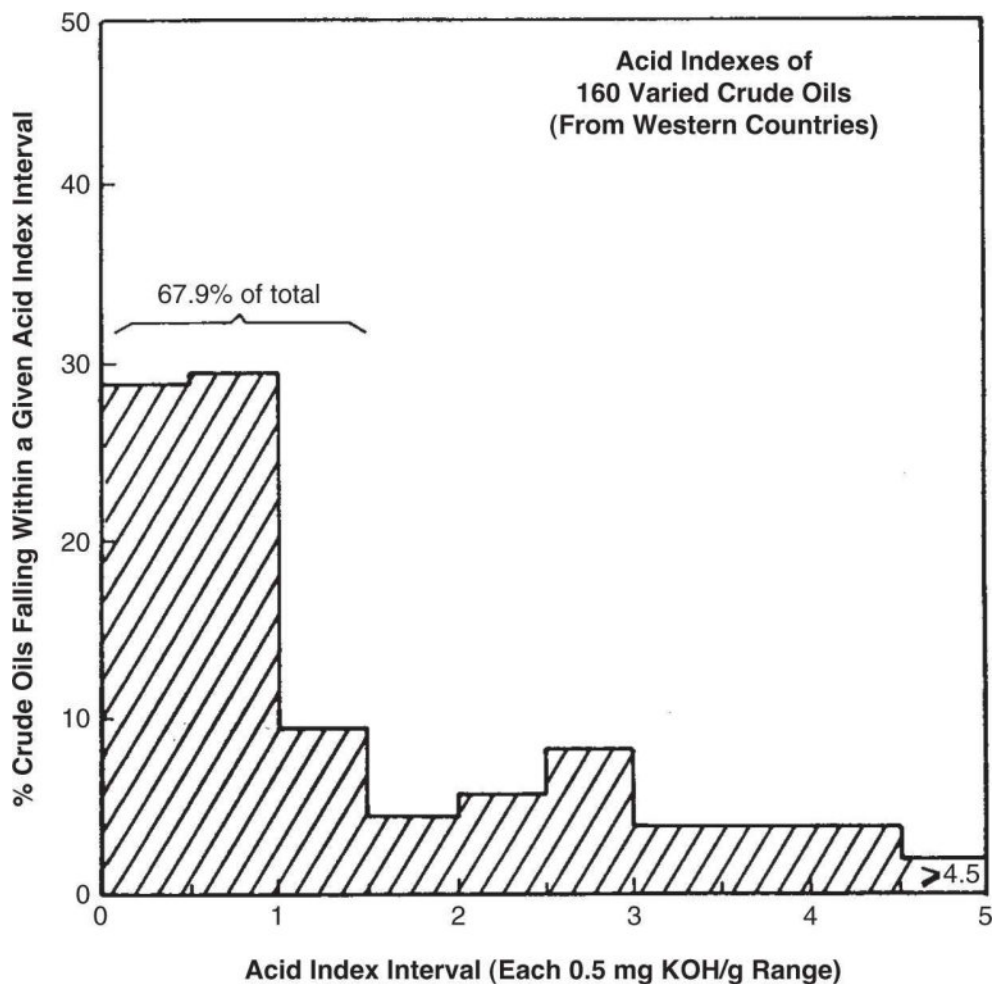


Fig. 9.16—Histogram of acid numbers (Minssieux 1976).

There are many similarities in the low-IFT effects in SP and high-pH flooding. The data in Fig. 9.17 suggest an optimal salinity of approximately 1.0 wt% NaCl for a 0.03 wt% NaOH solution (compare Fig. 9.11b to Fig. 9.17.) Indeed, Jennings et al. (1974) have shown that there is an optimal NaOH concentration for a given salinity in oil-recovery experiments. This suggests that the data in Fig. 9.16 indicate that a Type II(–) phase environment exists at low NaOH concentrations and a Type II(+) environment at high NaOH concentrations.

Nelson et al. (1984) showed that a cosurfactant can increase the optimal salinity and broaden the salinity range for low IFT. This led to the cosurfactant-enhanced alkali process, now referred to as the ASP process.

The solubilization parameters follow the pattern shown in [Fig. 9.10](#), with solubilization parameters crossing at a specific optimal salinity. The solubilization parameters at optimal salinity are typically in the range of 10 to 30, or where the IFT at optimum is on the order of 10^{-3} mN/m.

However, the phase behavior is more complicated when the alkali reacts with the crude to produce soap. The mole fraction of soap is directly proportional to the amount of oil that reacts with the alkali. Typically, the soap is less hydrophilic than the injected surfactant, cosurfactant and/or cosolvent. For such cases, an increase in oil concentration causes the optimal salinity to decrease. In fact, the entire ultralow IFT region (Type III) shifts the same way for the same reason. An activity diagram, [Fig. 9.18](#), shows the Type III region on a plot of salinity versus oil concentration. Generating such diagrams requires doing phase behavior experiments at several different oil concentrations. Both the optimal salinity and the solubilization parameter at optimal salinity typically decrease as the oil concentration decreases. Thus, the most important measurement is the one with a low oil concentration since the IFT as the oil saturation approaches zero is the IFT that ultimately determines the remaining oil saturation (residual oil saturation to chemical). The decrease in optimal salinity as the oil saturation decreases provides a favorable gradient since the phase behavior changes from Type II(+) to III to II(-), which reduces the surfactant retention among other benefits analogous to a negative salinity gradient for SP flooding.

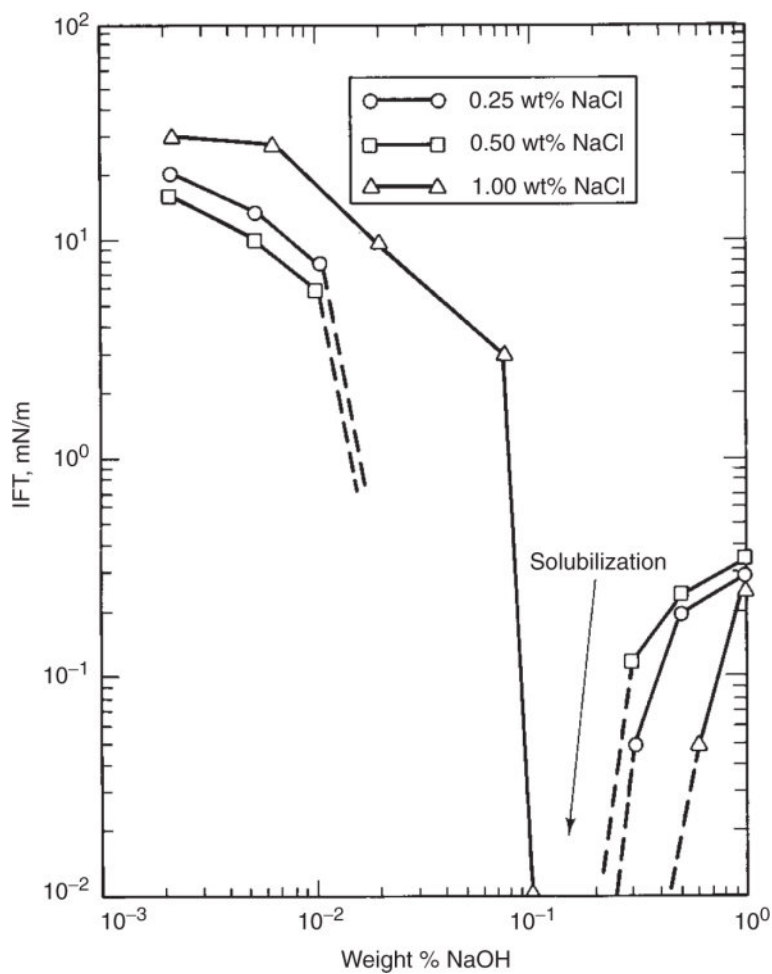


Fig. 9.17—IFTs for caustic-crude vs. brine systems (Ramakrishnan and Wasan 1983).

Cosolvent is sometimes used in ASP flooding to optimize the activity diagram, reduce the microemulsion viscosity, and increase the aqueous stability. For example, a cosolvent with the proper hydrophilic balance can be used to change the slope of the activity diagram in the favorable direction and to broaden the Type III region.

Yang et al. (2010) show activity diagrams and the corresponding ASP corefloods for a wide variety of oils, salinities, temperatures, and cores. (Fig. 9.18 is an example.) The oil recoveries are comparable to the oil recoveries in SP corefloods and substantially higher than recoveries in nonoptimized floods. Fortenberry et al. (2013) show similar results for alkaline-cosolvent-polymer (ACP) flooding. Under appropriate conditions, both of these processes are more efficient and thus less expensive than SP flooding. Viscous oils tend to have a

higher acid number and thus are more likely to be good candidates for the chemical EOR processes using alkali. In addition, viscous oils tend to be associated with high oil saturation, high permeability, high porosity and shallow depth, all of which are favorable with respect to the economics.

9.10.2 Wettability Reversal. Owens and Archer (1971) show that increasing water-wetness increases ultimate oil recovery. Wettability has been reported to decrease the water/oil contact angle measured on polished synthetic surfaces. This has also been shown by others using high-pH chemicals (Wagner and Leach 1959; Ehrlich et al. 1974). The increased oil recovery is the result of two mechanisms: (1) a relative-permeability effect that causes the mobility ratio of a displacement to decrease, and (2) a shifting of the capillary desaturation curve (a change in residual-oil saturation).

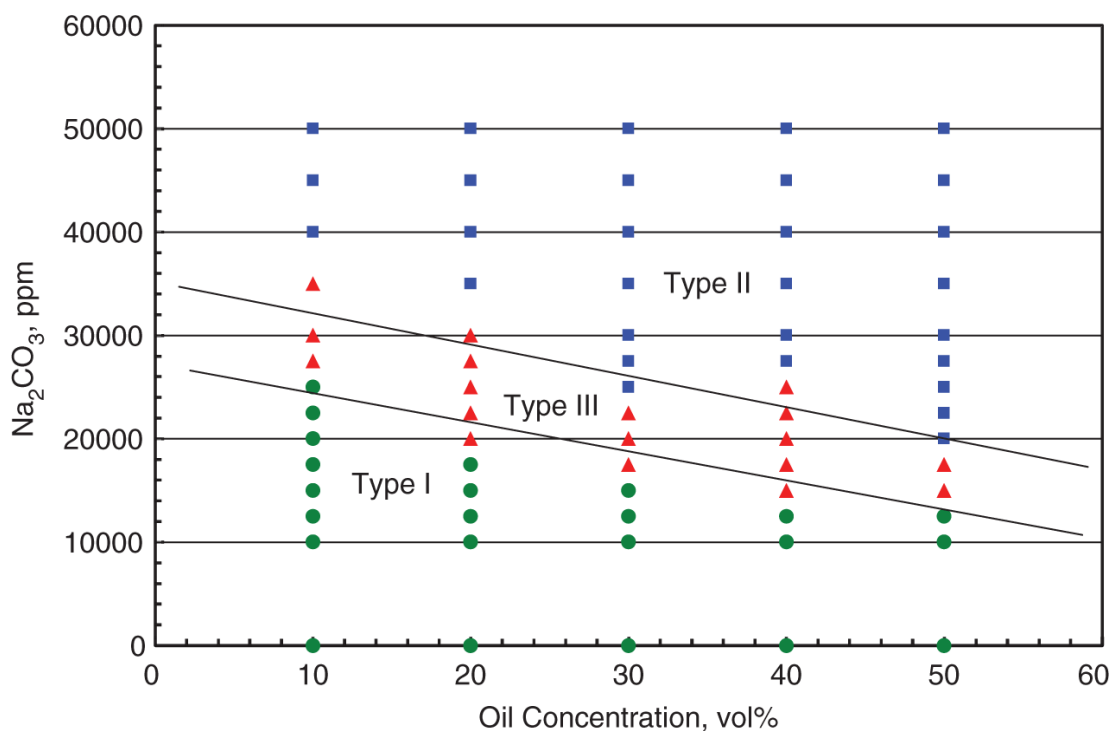


Fig. 9.18—Example of an activity diagram showing a negative slope because of the reaction of the sodium carbonate with the crude oil to form a soap that is hydrophobic relative to the synthetic surfactants in the ASP formulation.

Cooke et al. (1974) have reported improved oil recovery with increased oil wetness. Other data show that oil recovery is a maximum when the wettability of a permeable medium is neither strongly water-wet nor strongly oil-wet (Lorenz et al. 1974). Considering this information and that presented in [Chapter 3](#), the important factor may be the change in wettability rather than the final wettability of the medium. In the original wetting state of the medium, the nonwetting phase occupies large pores, and the wetting phase occupies small pores. If the wettability of a medium is reversed, nonwetting fluid will exist in small pores and wetting fluid in large pores. The resulting fluid redistribution, as the phases attempt to attain their natural state, would make both phases vulnerable to recovery through viscous forces. Bhuyan (1986) determined experimentally the effect of wetting state on CDCs.

9.10.3 Emulsion Formation. Alkaline chemicals can bring about improved oil recovery by forming emulsions. This emulsification produces additional oil in at least two ways: through a reduction in mobility ratio because many of these emulsions have a substantially increased viscosity, and through solubilization and entrainment of oil in a flowing aqueous stream. The first mechanism improves displacement and volumetric sweep, as does any other mobility-control agent. Local formation of highly viscous emulsions is not desirable because these would promote viscous instability. For an oil-free alkaline solution, the solubilization and entrainment mechanism is more important when the IFT between the swollen water phase and the remaining crude is low. [Fig. 9.17](#) shows that for certain conditions, emulsification and low IFT occur simultaneously. McAuliffe (1973) showed that emulsions injected into a core and those formed in situ give comparable oil recoveries.

9.11 Rock-Fluid Interactions

This section discusses the effects that rock-fluid interactions have in SP and ASP floods. These can be classified as physical sorption, chemical sorption (primarily cation exchange), mineral precipitation or dissolution, and interactions with phase behavior. Rock-fluid

interactions are more important for the ASP process than for the SP process because alkali can react with many commonly found minerals in reservoir rocks. Sufficient alkali must be injected to satisfy consumption due to these reactions and still maintain the required high pH in the presence of the injected surfactant. See Lake et al. (2002) for more discussion of individual effects. All mechanisms occur simultaneously, even though we discuss them separately.

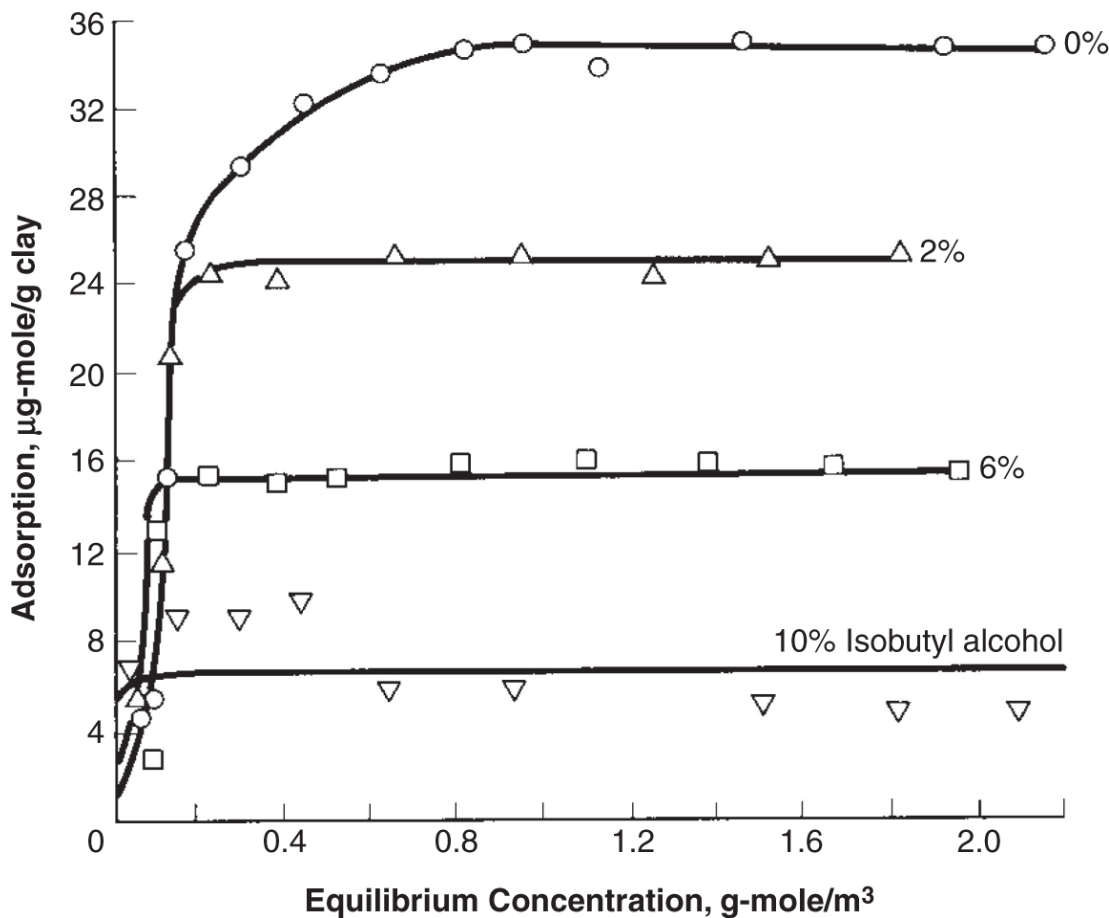
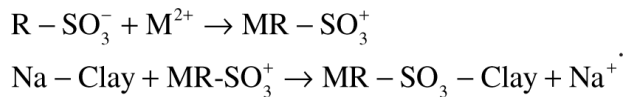


Fig. 9.19—Effect of cosurfactant on surfactant retention. Surfactant is 4-phenyl dodecyl benzene sulfonate [adapted from Fernandez (1978)].

9.11.1 Physical Sorption. Surfactant retention may be the most significant barrier to the commercial application of SP flooding. The problem here is one of selectivity. The surfactants should have good selectivity for oil/water interfaces, but they should also have poor selectivity for fluid/solid interfaces.

On metal-oxide surfaces, the surfactant monomer will physically adsorb, primarily through hydrogen bonding. At higher surfactant concentrations, this association includes tail-to-tail interactions (much like the micellar associations discussed previously) with the solution monomers, resulting in proportionally greater adsorption. At and above the CMC, the supply of monomers becomes constant, as does the retention. The Langmuir-type isotherm of adsorption vs. overall surfactant concentration resembles the CMC plot in [Fig. 9.3](#).

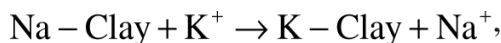
9.11.2 Chemical Sorption. At higher hardness (recall that hardness is the sum of the divalent cation concentrations), anionic surfactants associated with a divalent cation will become a monovalent cation that can chemically exchange with cations originally bound to the reservoir clays. Equilibrium reactions will be of the following type:



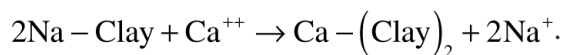
Sodium bound to the clay site is replaced by the surfactant/divalent complex in an exchange reaction.

As a consequence of ionic bonding and tail-to-tail interactions, adding a cosurfactant will reduce both types of retention ([Fig. 9.19](#)). Cosurfactants perform this service in two ways: (1) by filling surface sites that might otherwise be occupied by surfactant, and (2) by mitigating tail-to-tail associations. This form of retention is reversible with both M^{2+} and surfactant concentration.

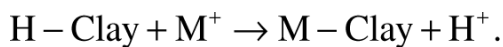
Other exchange reactions do not involve surfactant. They include monovalent exchange, an example of which is sodium-potassium exchange,



and monodivalent exchange, for example,



For ASP flooding, a particularly significant example of the latter is hydrogen/cation exchange,



These types of reactions could deplete the solution of hydrogen cations and retard the movement of the surfactant-generation agent. [Fig. 9.20](#) shows experimental data on this effect.

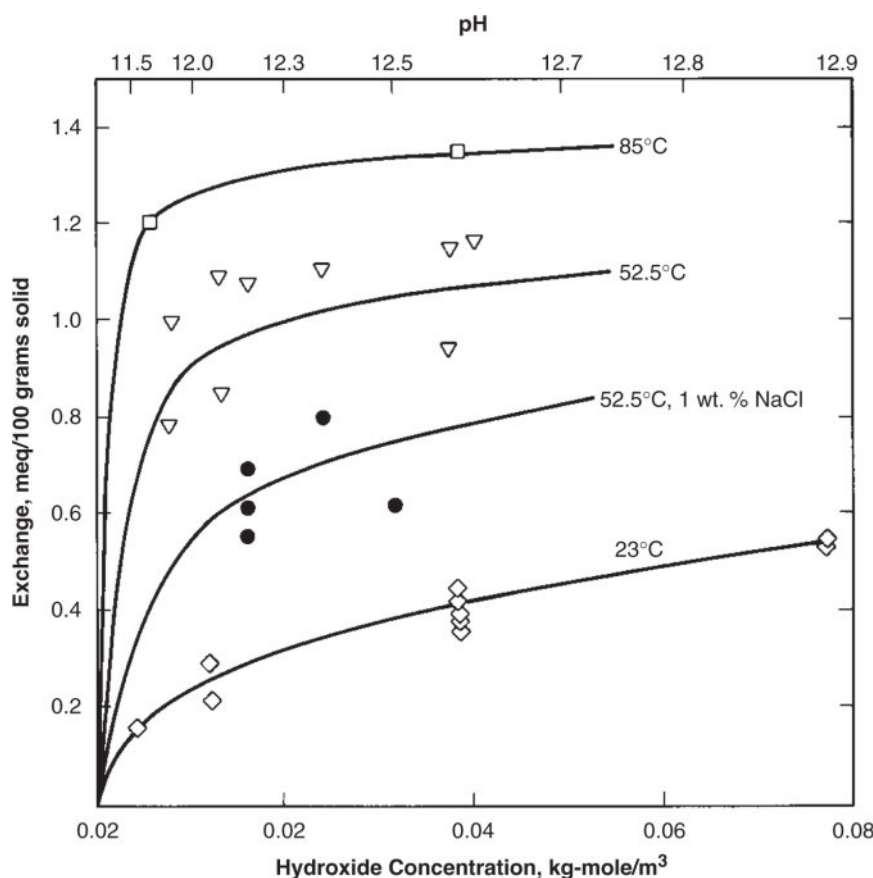
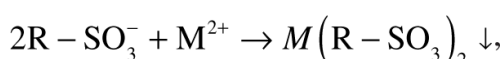


Fig. 9.20—Reversible hydroxide uptake for Wilmington, Ranger-zone sand (Bunge and Radke 1982).

9.11.3 Mineral Reactions. In hard brines, the prevalence of divalent cations causes the formation of surfactant/divalent complexes,



that have a limited solubility in brine. Precipitation (\downarrow), of this complex will lead to surfactant retention. When oil is present, it can compete

for the surfactant. Of course, the precipitate must also compete with the micelles for the surfactant (Somasundaran et al. 1984).

9.11.4 Mineral Dissolution. Alkali reacts directly with clay minerals and for pH values above about 13 also with the silica substrate to cause consumption of OH⁻ ions ([Fig. 9.21](#)). The reactions with clays are manifest by the elution of soluble aluminum and silica species from core displacements (Bunge and Radke 1982). The resulting soluble species can subsequently cause precipitates through hydroxyl reactions (Sydansk 1983). The rate of hydroxyl consumption from this “slow” reaction (cation exchange is generally fast enough so that local equilibrium applies) can be determined by the treatment described below.

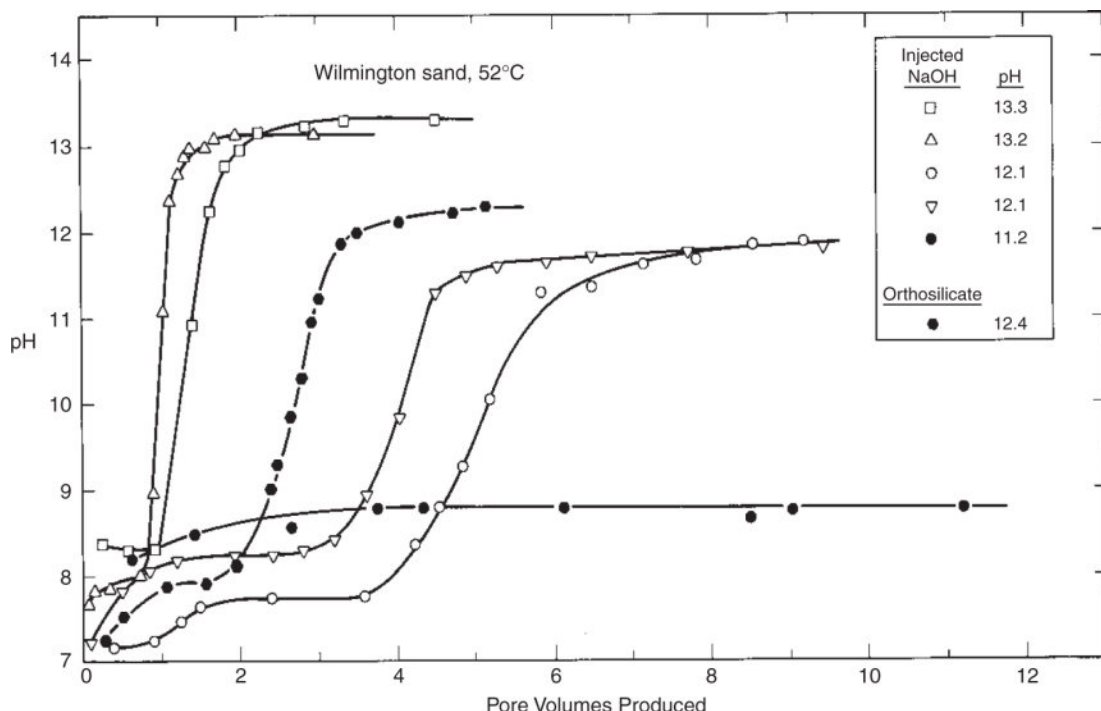


Figure 9.21—Experimental and theoretical effluent histories of pH (Bunge and Radke 1982).

9.11.5 Interactions with Phase Behavior. In the presence of oil in a Type II(+) phase environment, the surfactant will reside in the oil-external microemulsion phase. Because this region is above the optimal salinity, the IFT is relatively large, and this phase and its

dissolved surfactant can be trapped. [Fig. 9.22](#) illustrates this phenomenon. The filled squares represent the surfactant injected and the open squares the surfactant retained in a series of constant-salinity corefloods. Retention increases smoothly with salinity until 3% NaCl, at which point it increases so substantially that all the injected surfactant is retained. 3% NaCl is just above C_{Seu} for this system; hence, the deviation can be nicely explained by phase trapping. A similar phase-trapping effect does not occur in the Type II(–) environment because the aqueous mobility buffer miscibly displaces the trapped aqueous-external microemulsion phase. Using lower-than-optimal salinities can, therefore, eliminate phase trapping. This form of retention is strongly affected by SP phase behavior.

Most studies of surfactant retention have not made these mechanistic distinctions. Therefore, which mechanism predominates in a given application is not obvious. All mechanisms retain more surfactant at high salinity and hardness, which in turn can be attenuated by adding cosurfactants and perhaps adjusting the salinity. Precipitation and phase trapping can be eliminated by reducing the mobility-buffer salinity; under these conditions, the chemical-adsorption mechanism on the reservoir clays is predominant. In this event, there should be some correlation of surfactant retention with reservoir clay content.

[Fig. 9.23](#) attempts this correlation by plotting laboratory and field-surfactant retention data against clay fraction. The correlation is by no means perfect because it ignores variations in SP formulation and clay distribution as well as changes in salinity. However, the figure does capture a general trend that is useful for first-order estimates of retention. In addition, note that the difference between laboratory- and field-measured retention values is not significant. This observation implies that surfactant retention can be effectively measured in the laboratory.

9.12 Fractional-Flow Theory in SP and ASP Floods

Fractional-flow theory can provide just as much insight into SP and ASP floods as into the solvent and polymer floods covered in

Sections 7.7 and 8.5. In fact, there are so many similarities among those processes that, here, we draw heavily on the material in those sections.

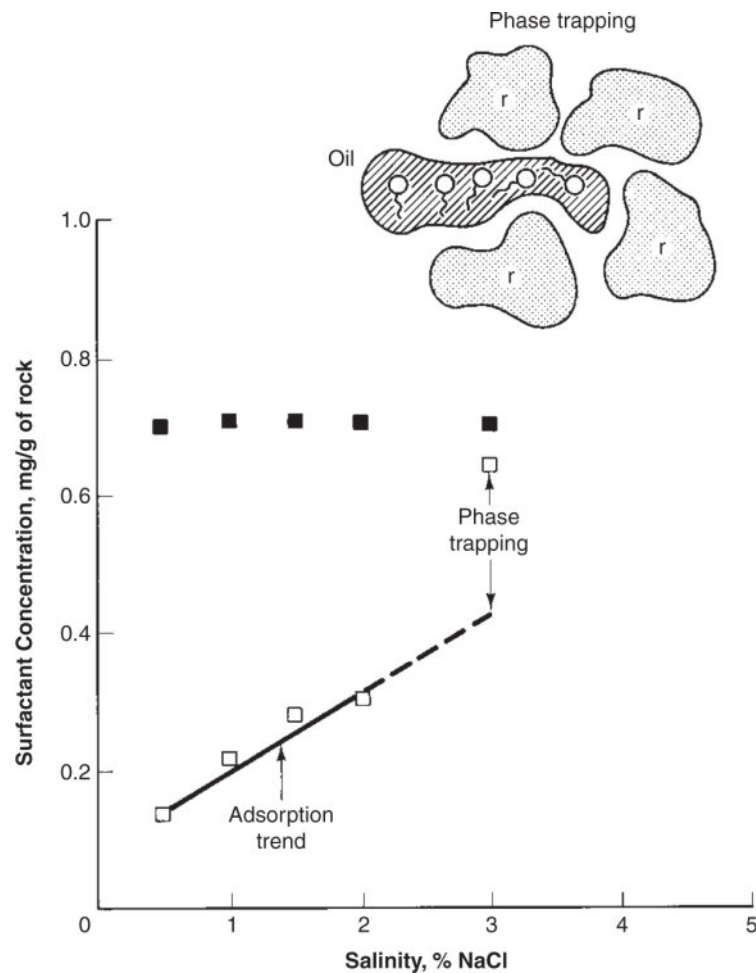


Fig. 9.22—Surfactant retention caused by phase trapping; 3% NaCl in a Type II(+) microemulsion system (Glover et al. 1979). Filled squares represent injected surfactant; open squares produced surfactant.

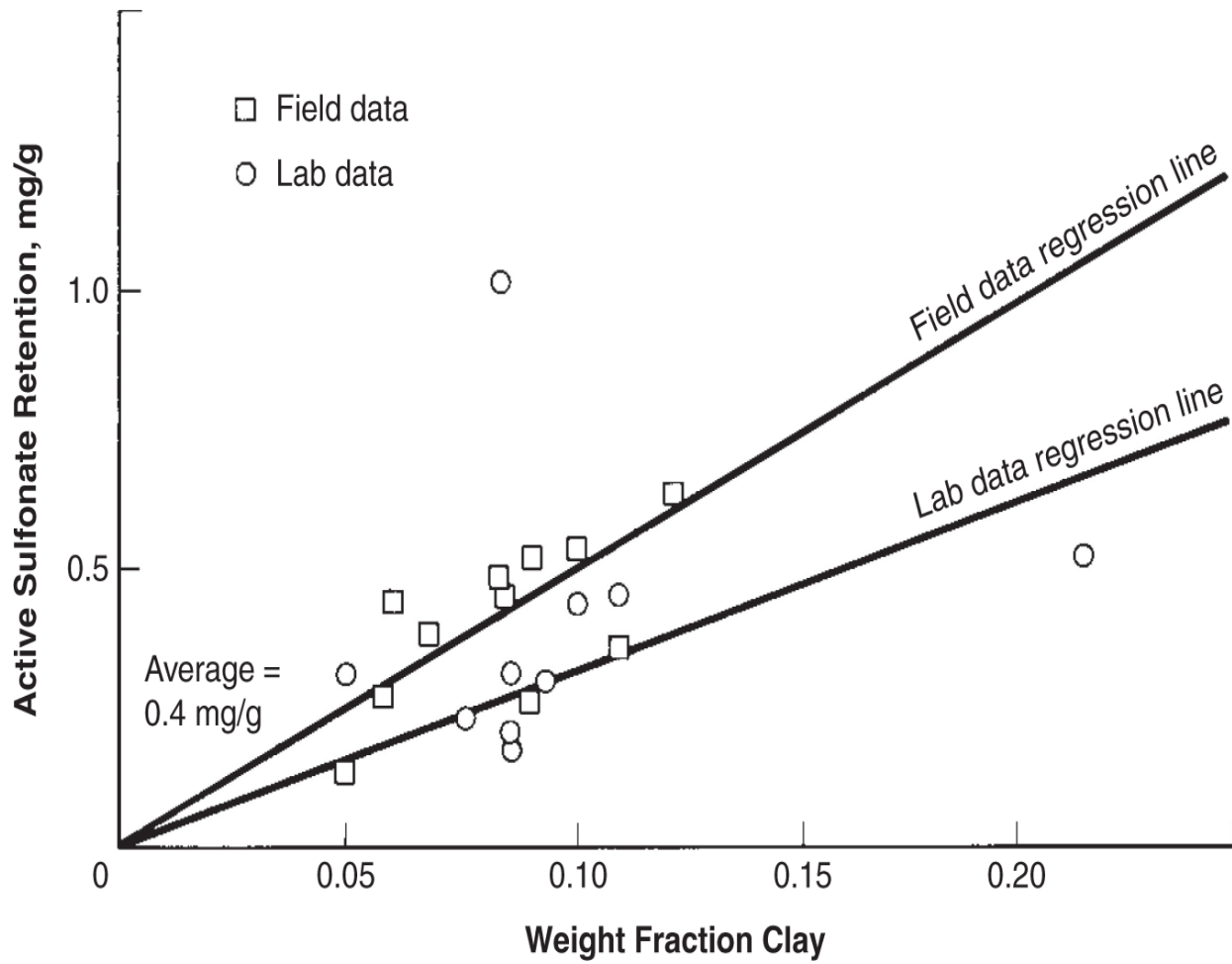


Fig. 9.23—Overall surfactant retention correlated with clay content [adapted from Goldburg et al. (1985)].

To perform the analysis, we invoke the usual fractional-flow assumptions: incompressible fluid and rock, 1D flow, and no dissipative effects. In addition, we neglect the presence of polymer drive, assume three-component SP floods with a step change in concentration at the origin of a time/distance diagram, and treat only those floods with a constant phase-behavior environment. To shorten the development, we cover only low-salinity Type II(–) floods. Fractional-flow treatment for three-phase SP floods has not been investigated extensively (Giordano and Salter 1984), but it could be analyzed in the same way using the technique described in Section 5.7.

9.12.1 SP Flooding With Retention. For Type II(–) phase behavior, where the right plait point is in the oil corner of the ternary, the amount of solubilized oil in the microemulsion phase is negligible. Let the residual oil saturation, S_{2r}^* , be the ultimate value of a low-IFT (high- N_{vc}) aqueous-phase fractional-flow curve, as shown in [Fig. 9.24](#). This figure also shows the water/oil fractional-flow curve f_1 along the tie line on the base of the ternary. Because this aqueous slug miscibly displaces the irreducible water, the velocity of the corresponding indifferent wave is

$$v_{C_3} = \frac{f_1^s}{S_1 + D_3}, \quad \dots \dots \dots \quad (9.12)$$

cf. Eq. 8.25. f_1^s is the microemulsion (aqueous) phase of the high- N_{vc} fractional flow. In this equation, D_3 is the surfactant frontal-advance loss, which is given by

$$D_3 = \frac{1-\phi}{\phi} \frac{C_{3s}}{C_{3J}\rho_s}. \quad \dots \dots \dots \quad (9.13)$$

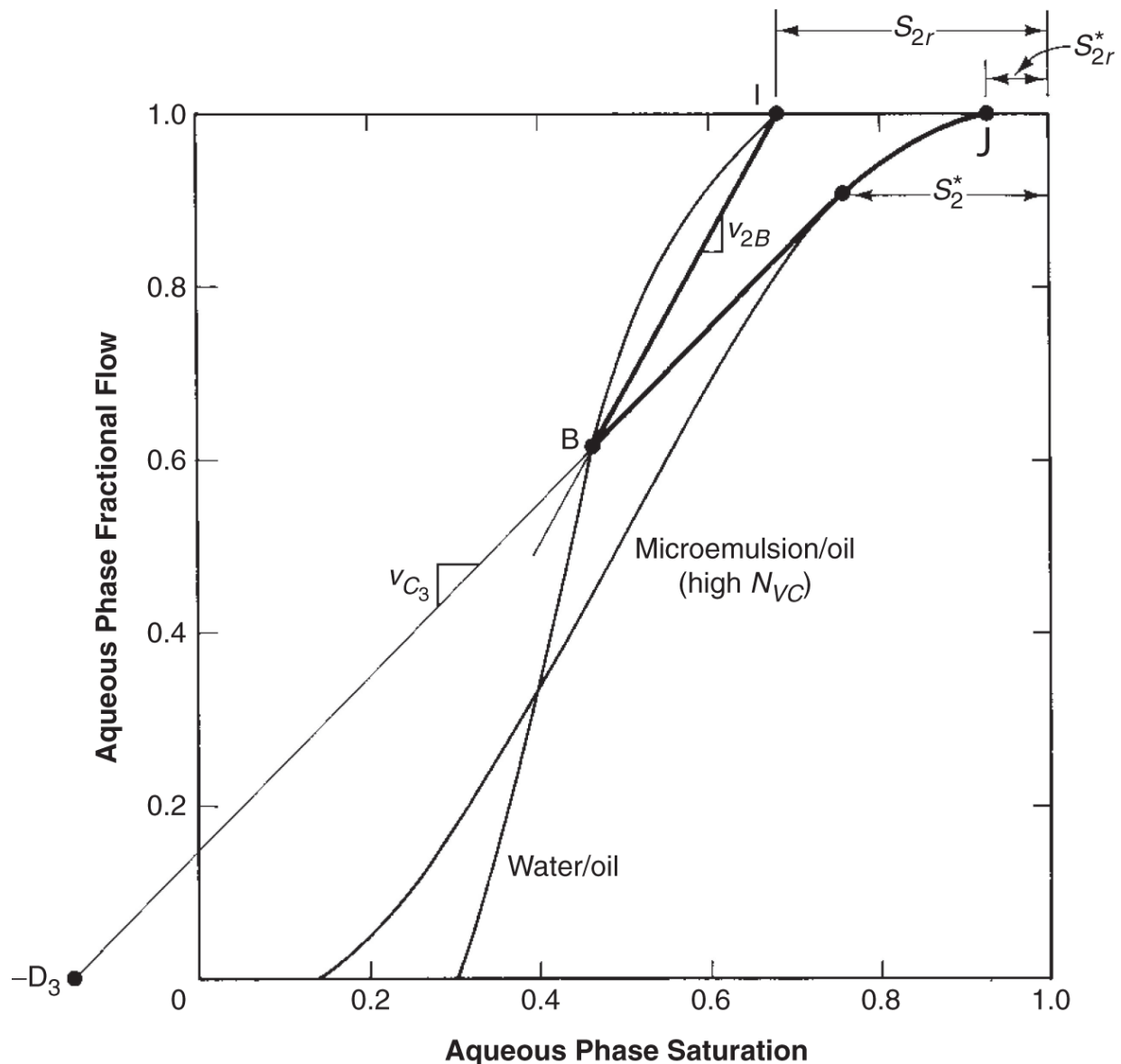


Fig. 9.24—Graphical construction for simplified Type II(–) surfactant displacements.

One could also derive these equations from material balances on water and surfactant at the surfactant front, as in Section 5.8. The frontal-advance loss in Eq. 9.13 is principally intended to characterize surfactant sorption. However, it is much more than this, as the following calculation shows.

Example 9.2. Frontal-Advance Loss. Calculate the frontal-advance loss under the following conditions: $C_{3J} = 0.03$ (3% injected surfactant

concentration), $C_{3s} = 0.4 \text{ mg/g}$, $\phi = 0.2$, and $\rho_s = 1.05 \text{ g/cm}^3$.

As much as anything, this is a units conversion problem; D_3 should be dimensionless. It also serves to remind us what the basic quantities are:

$$\begin{aligned} D_3 &= \frac{1-\phi}{\phi} \frac{C_{3s}}{C_{3J}\rho_s} \\ &= \left(\frac{0.8 \frac{\text{cm}^3 \text{ solid}}{\text{cm}^3 \text{ bulk}}}{0.2 \frac{\text{cm}^3 \text{ pore}}{\text{cm}^3 \text{ bulk}}} \right) \frac{\left(0.4 \frac{\text{mg surfactant}}{\text{g solid}} \right)}{\left(0.03 \frac{\text{cm}^3 \text{ surfactant}}{\text{cm}^3 \text{ solution}} \right) \left(1.05 \frac{\text{g surfactant}}{\text{cm}^3 \text{ surfactant}} \right)} \left(\frac{1 \text{ g surfactant}}{1000 \text{ mg surfactant}} \right) \\ &= 0.051 \end{aligned}$$

Solution and *pore* volume in the preceding equation are the same. Because D_3 is a lower bound on the surfactant slug size, the effect of a low surfactant concentration is evident: for $C_{3J} = 0.01$, we have $D_3 = 0.152$. Moreover, the effect of porosity is not insignificant: for $\phi = 0.1$, we have $D_3 = 0.114$. Very low surfactant-slug concentrations will incur a penalty by requiring the use of larger slugs (or the use of a sorption-reduction agent). Besides having a smaller oil target, low-porosity reservoirs will also require larger slugs.

The most general construction occurs when the rear of the oil bank travels as a mixed wave. At the leading edge of the spreading portion of this wave, the specific velocity in Eq. 9.14 must be equal to the specific oil velocity at some saturation S_1^* , given implicitly by

$$\left(\frac{df_1^s}{dS_1} = \frac{f_1^s}{S_1 + D_3} \right)_{S_1^*} \dots \dots \dots \quad (9.14)$$

The specific velocity of the shock portion of the rear of the oil bank is

$$v_{\Delta C_2} = \frac{f_{2B} - f_2^s(S_2^*)}{S_{2B} - S_2^*}. \quad \dots \dots \dots \quad (9.15)$$

This must be equal to v_{C3} evaluated at $S_2^* = 1 - S_1^*$. If the oil-bank front is a shock, it travels with a velocity given by

$$v_{\Delta C_2} = \frac{f_{2B} - f_{2I}}{S_{2B} - S_{2I}}. \quad \dots \dots \dots \quad (9.16)$$

These equations are of the same form as the polymer-flooding construction in Section 8.5. This parallel is also apparent from comparing the construction given in [Fig. 9.24](#) with the one in [Fig. 8.15](#). The construction of the time/distance and profile diagrams corresponding to [Fig. 9.24](#) is left as an exercise.

An issue not dealt with in Section 8.5 is the minimum slug size needed to satisfy retention requirements. Suppose that the surfactant displacement is piston-like, that is, $S_{2I} = S'_{2r} = S_2^*$. The minimum surfactant slug size in pore volumes needed to reach the production well is D_3 , meaning that the frontal-advance loss is an expression of the retention capacity of the medium expressed in units consistent with the slug size. Therefore, knowing D_3 is the starting point in estimating the surfactant requirement in SP flooding. The preceding result does not depend on the existence of a piston-like surfactant front.

9.13 Typical Production Responses

In this section, we review the responses of typical laboratory corefloods and field floods and discuss the important features and expectations of MP flooding.

9.13.1 Laboratory Flood. [Fig. 9.25](#) plots an effluent response of a typical SP flood in a Berea core showing oil cut, produced surfactant (Mahogany AA), cosurfactant, (isopropyl alcohol), polymer, and chloride anion concentrations. All concentrations have been normalized by their respective injected values. The chloride indicates salinity in this flood. At the top of the figure is the phase environment of the produced fluids. The slug size is $t_{Ds} = 0.1$, and the horizontal axis is t_D , the volume of fluid injected since the start of the slug,

expressed as a fraction of the core's pore volume. There was no preflush. [For further details of this and similar corefloods, see Gupta (1984).]

[Fig. 9.25](#) shows a typical, although by no means optimal, oil-recovery experiment. Before surfactant injection, the core was waterflooded so that it produced no oil at the start of surfactant injection. Oil broke through at approximately $t_D = 0.2$, with relatively constant oil cuts of approximately 40% until approximately $t_D = 0.6$, at which point the surfactant appeared in the effluent.

The behavior in this portion of the flood is consistent with the fractional-flow theory described in Section 9.12. Approximately 60% of the produced oil is free of injected chemicals. That 40% of the oil is produced with the surfactant indicates a viscous instability apparently caused by nonideal phase behavior. A well-designed flood will produce 80 to 90% of the oil ahead of the surfactant. Even here, though, the oil is invariably produced early and at fairly small cuts in laboratory experiments.

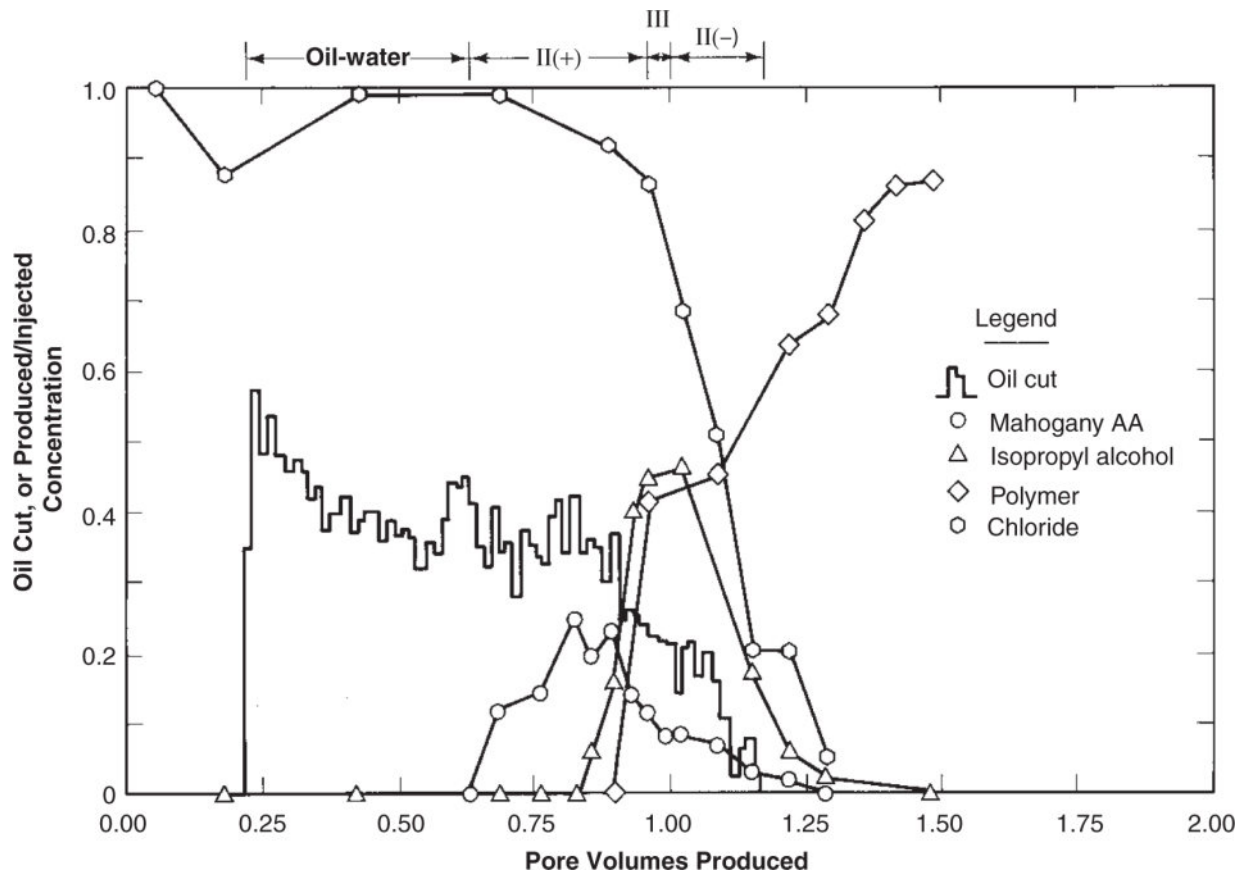


Fig. 9.25—Typical coreflood production response (Gupta 1984).

Surfactant breaks through at $t_D = 0.6$, reaches its maximum produced concentration of 30% of the injected concentration at $t_D = 0.8$, and ceases at $t_D = 1.5$. The total amount of surfactant produced is approximately one-half that injected, which indicates substantial, although not excessive, retention.

The surfactant precedes both the chloride and polymer by approximately $0.3V_p$. This separation indicates preferential partitioning of the cosurfactant into the aqueous phase from the microemulsion phase (see Section 8.4 on phase-behavior nonidealities). Although this did not dramatically affect oil recovery, which was in excess of 90% of the residual oil, the separation is not favorable for this design. A good SP design should show simultaneous production of all SP slug constituents as well as good oil recovery.

[Fig. 9.26](#) shows a second coreflood response. The upper plot (a) is similar to that in the previous figure; ultimate oil recovery exceeds 90%. The lower plot (b) shows the pressure gradient measured across the core. With the flood being conducted at constant inlet rate, this figure is a manifestation of the mobility of the fluids in the core at the indicated time. The gradient increases initially as the core fills with low-mobility fluid, and then declines gently during the polymer flood. The main purpose of such a plot is to detect the presence of effects that might ultimately result in injection issues. A large increase in pressure gradient could indicate the formation of viscous emulsions during the course of the flood.

9.13.2 Field Response. [Fig. 9.27](#) shows the ultimate oil-recovery efficiency E_R (ultimate oil produced divided by oil in place at the start of the MP process) from a survey of more than 40 SP field tests correlated as a function of mobility-buffer slug size t_{DmB} . Similar analyses on other process variables showed little or no correlation (Lake and Pope 1979). The strong correlation in [Fig. 9.27](#) indicates the importance of mobility control in MP design. Although we have largely ignored mobility control in this chapter, it is clearly an important variable.

From [Fig. 9.27](#), slugs with high oil content have generally been driven by polymer drives larger than the high-water-content slugs. Ultimate oil-recovery efficiency averages approximately 30% of residual-oil saturation in field tests ([Fig. 9.27](#)). Because oil-recovery efficiency can exceed 90% in well-designed corefloods, a rough rule of thumb is that the peak oil cut and the ultimate oil-recovery efficiency in a technically successful SP field flood will average approximately one-third of their respective values in corefloods.

9.14 Designing SP/ASP Floods

A successful SP flood must achieve three things for efficient oil recovery (Gilliland and Conley 1975).

1. The SP surfactant slug must propagate in an interfacially active mode (i.e., at optimal conditions).

2. Enough surfactant must be injected so that some of it is unretained by the permeable-media surfaces.
3. The active surfactant must sweep a large portion of the reservoir without excessive dissipation because of dispersion or channeling.

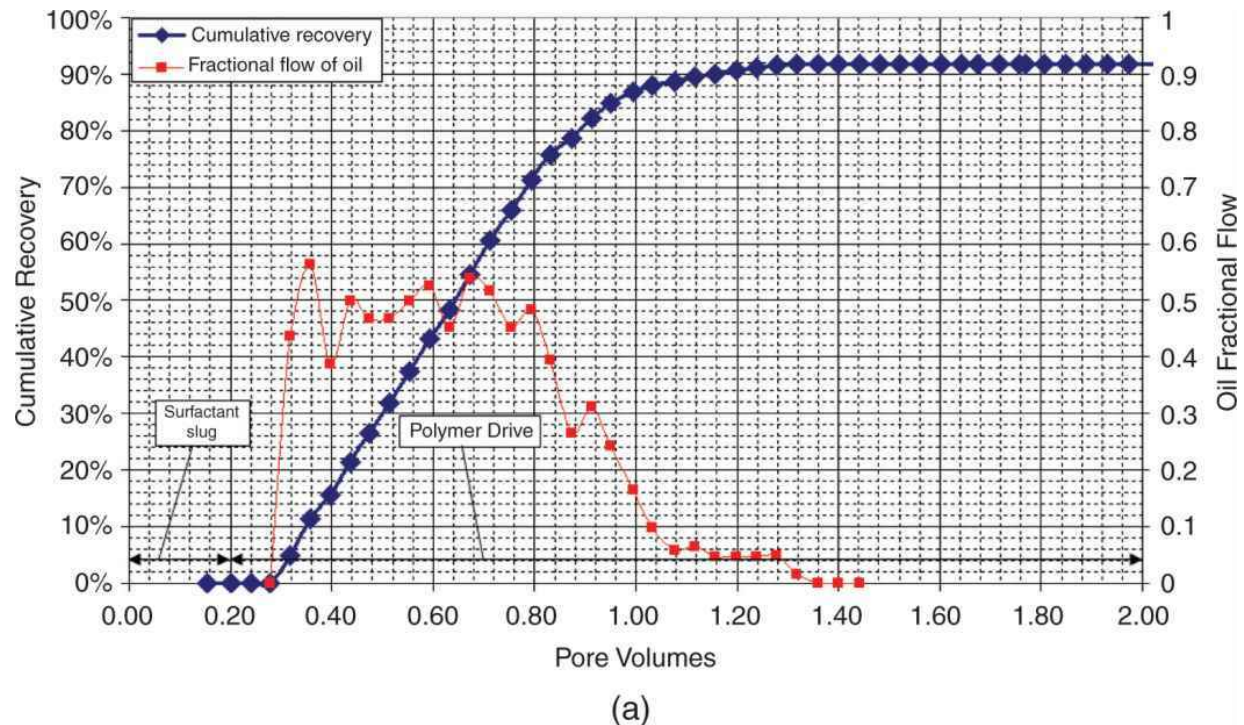
The first of these objectives is met through the formulation step of the SP/ASP design procedure; the second two objectives are met through scaleup. Although there is considerable overlap, the formulation step consists mainly of test-tube experiments and corefloods; the scaleup steps consist mainly of corefloods and numerical simulations.

9.14.1 Generating Optimal Conditions. There are three techniques for generating optimal conditions in SP/ASP floods.

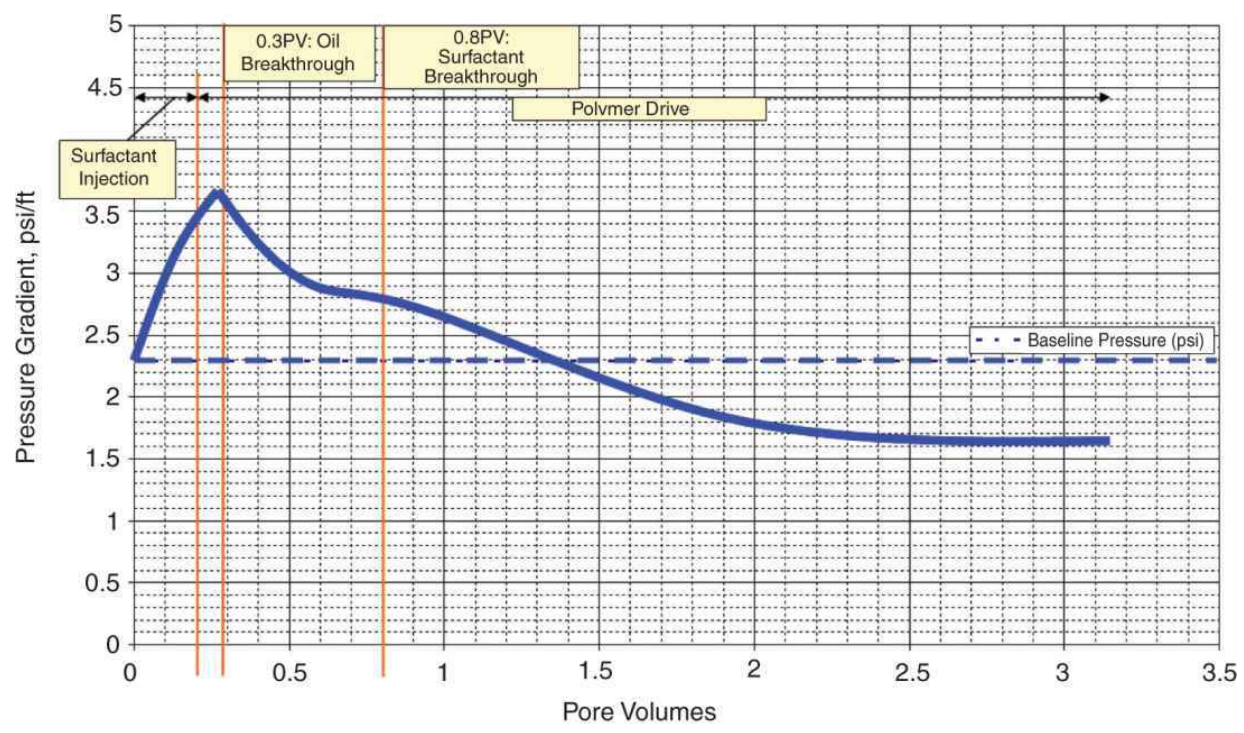
1. Increase the SP-slug optimal salinity to that of the resident-brine salinity in the candidate reservoir. Philosophically, this procedure is the most satisfying of the three possibilities, but it is usually the most difficult. Although they are the subject of intensive research, surfactants with high optimal salinities that are not, at the same time, stable at reservoir conditions, excessively retained by solid surfaces, or expensive remain to be discovered. Field successes with synthetic surfactants have demonstrated the technical feasibility of this approach (Bragg et al. 1982). A second way to bring the optimal salinity of the SP slug closer to the resident-brine salinity is to add cosurfactant. This approach has been the most common technique to date; however, as mentioned earlier, there are penalties in surfactant/cosurfactant separation, loss of interfacial activity, and cost.
2. Reduce the resident salinity of a candidate reservoir to match the slug's optimal salinity. This common approach is the main purpose of the preflush step illustrated in [Fig. 9.1](#). A successful preflush is appealing because, with the resident salinity reduced, the slug would displace oil wherever it goes in the

reservoir, and retention would also be low. Preflushes generally require large volumes to reduce the resident salinity significantly because of mixing effects and cation exchange. With some planning, the function of a preflush could be accomplished if a waterflood precedes the flood.

3. Use the salinity-gradient design technique for generating active SP/ASP slugs (Paul and Froning 1973; Nelson and Pope 1978; Hirasaki et al. 1983). This technique dynamically reduces the resident salinity to optimal during the course of the displacement by sandwiching the slug between the superoptimal resident-brine salinity and a suboptimal mobility-buffer salinity. [**Table 9.4**](#) illustrates the results of experimental corefloods for different sequences of salinities. The experiment numbers on this table match the uncircled numbers in [**Fig. 9.8**](#). Three corefloods—numbers 3, 6, and 7—stand out with respect to both their low ultimate saturation and their low surfactant retention. The common feature of all these experiments is that the salinity of the polymer drive is suboptimal. In fact, no other variable, including, paradoxically, the surfactant concentration in the slug, has a similarly strong effect (Pope et al. 1979). The salinity-gradient design has several other advantages: it is resilient to design and process uncertainties, provides a favorable environment for the polymer in the mobility buffer, minimizes retention, and is indifferent to the surfactant dilution effect.



(a)



(b)

Fig. 9.26—Effluent oil cut and cumulative production (a) with (b) pressure gradient (Levett and Pope 2008).

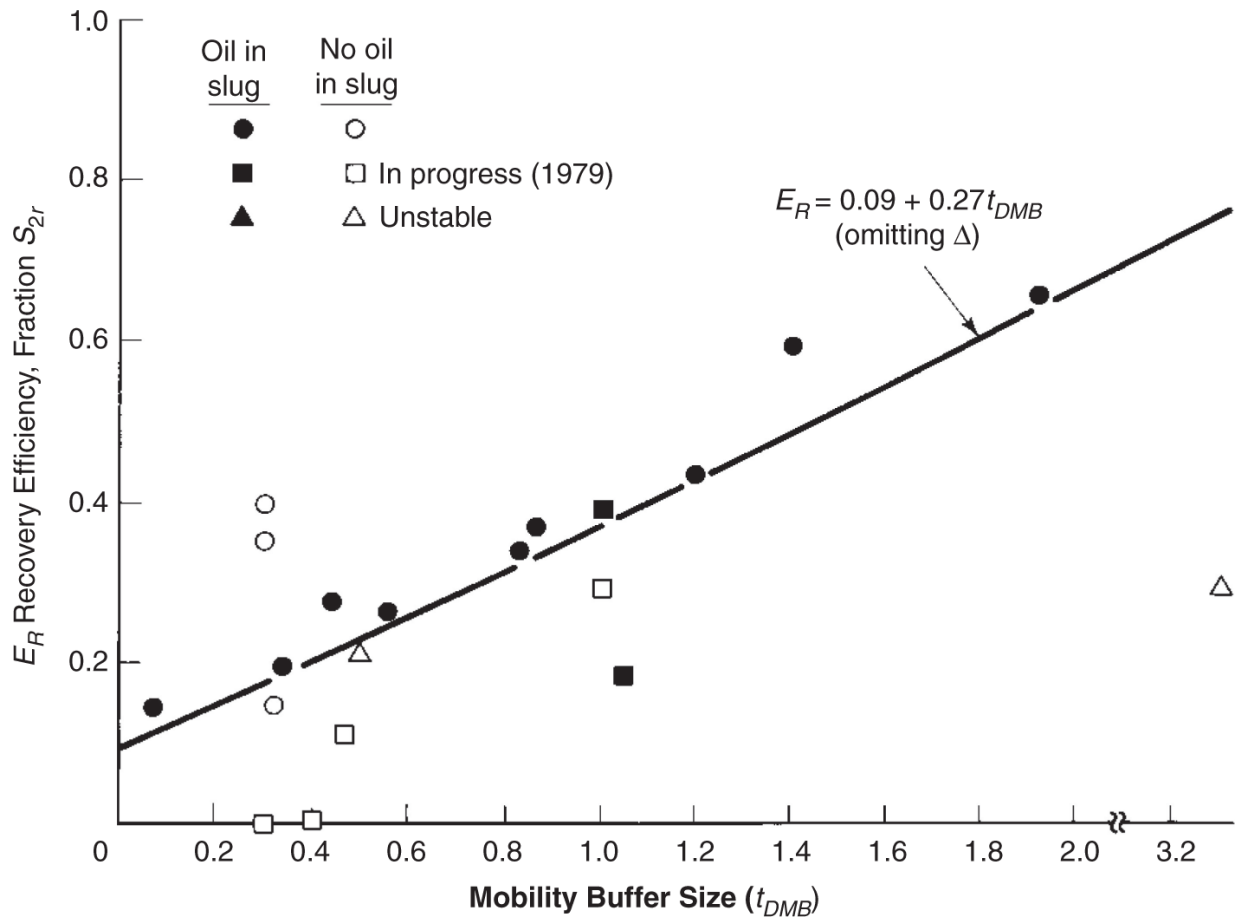


Fig. 9.27—Recovery efficiencies from 21 SP field tests [adapted from Lake and Pope (1979)].

9.14.2 Injecting Enough Surfactant. The first aspect of overcoming retention is to design the flood so that retention is as low as possible. This includes minimizing the chemical and physical adsorption effects discussed previously and eliminating phase trapping by chasing the slug with a drive that is in the Type II(–) salinity environment (this means the drive has a lower salinity than the slug salinity, but lower does not necessarily mean low salinity in absolute terms). A sufficient mass of surfactant must be injected to satisfy surfactant retention or the surfactant will not propagate all of the way to the production wells. As in polymer flooding, the mass is the product of the concentration and the slug size.

No strong theoretical or practical reasons exist for selecting a particular slug surfactant concentration. The concentration must be high enough so that a Type III region can form when the salinity is

optimal, but low enough so that the slug can be easily handled and transported. The latter requirement usually means that the slug is single-phase and not excessively viscous and that the surfactant does not precipitate.

TABLE 9.4—PHASE-ENVIRONMENT TYPE AND SP FLOOD PERFORMANCE FOR THE SALINITY-REQUIREMENT DIAGRAM IN FIG. 9.8 (NELSON 1982)

Chemical Flood Number	Phase Type Promoted by the:			Residual Oil Saturation After Chemical Flood (% PV)	Injected Surfactant Retained by the Core (%)
	Waterflood Brine	Chemical Slug	Polymer Drive		
1	II(−)	II(−)	II(−)	29.1*	52
2	II(+)/III	II(+)/III	II(+)/III	25.2*	100*
3	II(+)/III	II(+)/III	II(−)	2.0**	61*
4	II(−)	II(−)	II(+)/III	17.6*	100*
5	II(−)	II(+)/III	II(+)/III	25.0	100
6	II(+)/III	II(−)	II(−)	5.6**	59**
7	II(−)	II(+)/III	II(−)	7.9*	73*
8	II(+)/III	II(−)	II(+)/III	13.7**	100*

* Average of duplicates.
** Average of triplicates.

Perhaps a more stringent lower bound on surfactant concentration is its relative rate of propagation (cf. Eq. 9.13). The frontal-advance loss, D_3 contains the surfactant concentration in the denominator. This means that the rate of slug propagation, as well as the maximum oil cut calculated from fractional-flow theory ([Fig. 9.24](#)), decreases as concentration decreases. Because of the worth of the oil, the resulting delay in oil production would be a liability to the process even if the ultimate oil recovery were unaffected. This argument suggests that the concentration should be as high as possible within the limits of surfactant solubility in brine at optimal salinity containing polymer and other similar constraints, and that the slug size should be correspondingly small. This is a valid conclusion for SP flooding. However, for ASP flooding there is some advantage to low surfactant concentration because of the nature of the soap and its effects on the phase behavior and IFT. Typical injected surfactant concentrations are about 0.3 wt% for this reason. Because the alkali reduces

adsorption, the frontal-advance rate is still high even at low surfactant concentration.

Once the slug concentration is set, the slug size follows from the value of D_3 , as in Section 9.11. To satisfy retention requirements, the slug size, on the basis of floodable pore volume, must be somewhat larger than the retention. Of course, how much larger is a strong function of the prevailing economics and reservoir characteristics. [For a graphical procedure, see Jones (1972).]

9.14.3 Maintaining Large Volumetric Sweep. [Fig. 9.27](#) attests that the importance of this issue, particularly with respect to the mobility buffer, cannot be overstated.

The mobility-control agent in the slug can be polymer or oil. Whatever the agent, it is of paramount importance that the slug/oil-bank front be made viscously stable because small slugs are intolerant of even a small amount of fingering. Therefore, we seek a slug less mobile than the oil bank it is to displace. To provide a margin of safety in estimating oil-bank mobility, base the polymer concentration on the minimum in the total relative-mobility curves (see Section 3.3). Such curves ([Fig. 9.28](#)) show that the minimum can be substantially less than the total relative mobility of either endpoint. Because these curves are subject to hysteresis, it is important that the relative-permeability curves be measured in the direction of increasing oil saturation for tertiary floods.

Sizing the mobility buffer proceeds like the polymer drive discussed in Section 8.6. Here, the spike portion of the buffer must have mobility equal to or less than the slug mobility. Because the latter depends on the degree of oil desaturation, the buffer mobility cannot be designed independently of the slug.

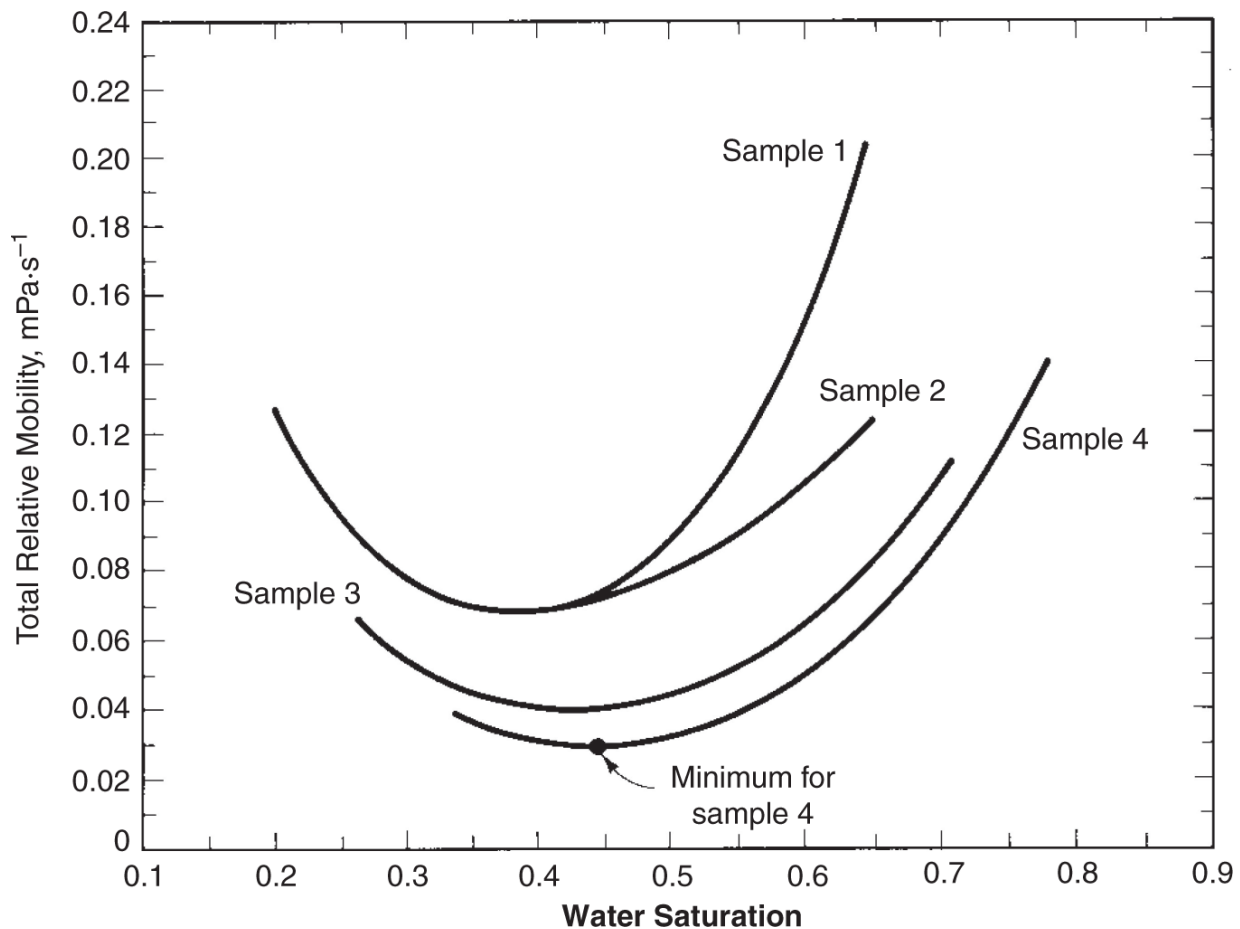


Fig. 9.28—Total relative mobilities for samples from the same reservoir (Gogarty et al. 1970).

9.15 Concluding Remarks

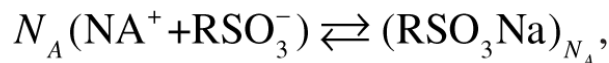
In terms of the number of design decisions required, SP/ASP floods are the most complex EOR processes. This complexity, along with reservoir heterogeneity and the need for a large investment in chemicals, are the principal sources of risk in SP/ASP floods. The potential for the process is immense, however. Moreover, both SP and ASP flooding seem uniquely suited for oil reservoirs in certain areas of the world, especially where miscible gases are not available or the reservoir pressure is too low for miscibility, where the oil is too viscous for miscible gases, or where mobility control is needed to mitigate reservoir heterogeneity.

Exercises

9.1 Units of SP Flooding. A particular petroleum sulfonate surfactant has an average molecular weight of 400 kg/kg.mole, a density of 1.1 g/cm³, and a monosulfonate-to-disulfonate mole ratio of 4. Express the overall surfactant concentration of a 5 volume percent aqueous solution in g/cm³, kg-moles/cm³, meq/cm³, mole fraction, and mass fraction.

9.2 Surfactant Equilibria and Aggregation. Relatively simple models can reveal much about surfactant equilibria. The surfactant is a monosulfonate in this problem.

- a. The aggregation of surfactant monomers into micelles in NaCl brine can be represented by the following reaction:



where N_A is the aggregation number. Using the definition of total surfactant (monomer + micelles), derive an expression relating the total and monomer sulfonate concentrations. If the equilibrium constant for the preceding equation is 10^{15} and $N_A = 10$, estimate the critical micelle concentration. The total sodium concentration is 10,000 g/m³.

- b. Consider a more complex situation in which 0.3175 kg-moles/m³ monosulfonate surfactant solution is added to an NaCl brine. In an NaCl brine solution, five species can form: surfactant monomer (RSO_3^-), surfactant micelles [$(\text{RSO}_3\text{Na})_{N_A}$], free sodium-surfactant (RSO_3Na), precipitated sodium-surfactant ($\text{RSO}_3\text{Na}\downarrow$) and free sodium (Na^+). Calculate the concentration of each species when the overall sodium concentration is 100 g/m³. Use the data in Part a for the monomer-micelle reaction and set the equilibrium constant for sodium-sulfonate formation to 3×10^6 and the solubility product for the precipitate to 10^{-8} .

- c. Repeat the calculation of Part b if the overall sodium concentration is 100,000 g/m³. What can you conclude about the effect of high salinities on surfactant precipitation?

9.3 Phase Behavior and IFT. [Fig. 9.29](#) shows the bottom half of six surfactant/brine/oil mixtures. These diagrams are on rectangular coordinates with a greatly expanded vertical scale. C_{Se} is the salinity in wt% NaCl. In the following, the surfactant concentration is 0.05 volume fraction:

- a. Calculate and plot volume-fraction diagrams at brine/oil ratios of 0.2, 1.0, and 5.
- b. At a brine/oil ratio of 1, calculate and tabulate the solubilization parameters.
- c. Use the correlation in [Fig. 9.9](#) to convert the solubilization parameters to IFTs. Plot these solubilization parameters against salinity and estimate the optimal salinity.
- d. Plot the IFTs in Part c against salinity on semi-log paper. Estimate the optimal salinity based on IFT and the optimal IFT.
- e. Compare the optimal salinities in Parts c and d to the midpoint salinity. The latter is the salinity halfway between C_{Seu} and C_{Sel} .

9.4 Calculating IFTs. Example 9.1 showed how to calculate IFT for a specific set of conditions. We generalize the method here.

- a. Derive an expression for the solubilization ratios in terms of overall surfactant concentration and the brine/oil ratio. Your derivation should cover all three phase-behavior types.
- b. Use the information in [Fig. 9.12](#) to construct salinity scan plots (as in [Fig. 9.10](#)) of IFT at all three of the brine/oil ratios shown. Assume the overall surfactant concentration to be 0.02.
- c. On the basis of the results of Part b, comment on the importance of the brine/oil ratio and the surfactant

concentration to IFT. You should assume that [Fig. 9.12](#) does not change in making these comments.

9.5 Walsh Diagrams and SP Flooding. Construct the entire Walsh diagram for displacement (continuous surfactant injection) governed by the fractional-flow curves in [Fig. 9.24](#). Assume the profile to be at oil-bank breakthrough.

9.6 Two-Phase Type II(–) Fractional Flow. Use the data in [Figs. 9.9](#) and [9.29](#) in the following problem. Assume the oil-free injected slug concentration to be 0.05 volume fraction surfactant and the salinity to be constant at 0.56% NaCl. The surfactant is an ideal mixture. The low- N_{vc} relative permeability curves are given by

$S_{2r} = 0.3,$	$k_{r2}^0 = 0.8,$	$n_2 = 1.5$
$S_{3r} = 0.2,$	$k_{r3}^0 = 0.1,$	$n_2 = 3$

Phase 3 is water when N_{vc} is large. The displacement occurs at a superficial velocity of 10 $\mu\text{m}/\text{s}$. The microemulsion, oil, and water viscosities are 2, 5, and 1 $\text{mPa}\cdot\text{s}$. The medium is horizontal. Use [Fig. 3.21](#) as the capillary desaturation curve.

- Estimate and plot the microemulsion fractional-flow curves for the data in [Fig. 9.15](#).
- Plot the time/distance diagram and a composition profile at oil-bank breakthrough for this displacement if the injection is continuous surfactant. Use the simplified fractional-flow analysis of Section 9.12. Assume $D_3 = 0.1$.

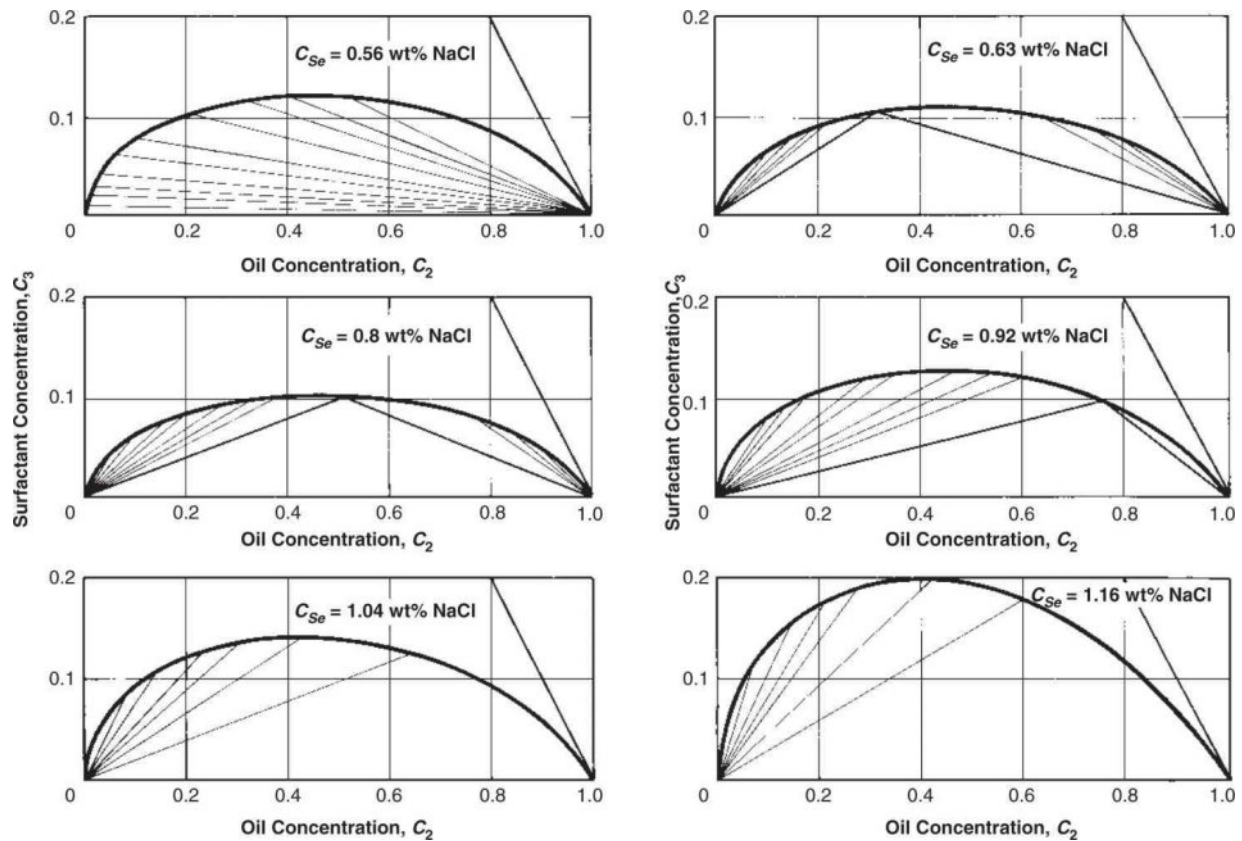


Fig. 9.29—Ternary diagrams at various salinities (Engleson 1981).

9.7 Slugs and Simplified Fractional Flow. Use the simplified fractional-flow analysis of Section 9.12 in the following problem. The displacement is a constant Type II(–) phase environment consisting of an oil-free surfactant slug followed by a polymer drive. The water-, oil-, and microemulsion-phase viscosities are 1, 5, and 10 mPa·s, respectively, and the relative-permeability data at low and high N_{vc} are

	Oleic phase			Microemulsion phase		
	S_{2r}	k_{r2}^0	n_2	S_{3r}	k_{r3}^0	n_3
Low N_{vc}	0.3	0.8	1.5	0.2	0.1	5.0
High N_{vc}	0.05	0.9	1.2	0.1	0.6	2.5

- a. Estimate the polymer-solution viscosity in the mobility buffer if the mobility ratio between the slug and drive is 0.8. The polymer has no permeability-reduction effect.
- b. Calculate and plot the three aqueous-phase fractional-flow curves (water/oil, microemulsion/oil, polymer-solution/oil) based on the data in Part a and the polymer-solution viscosity.
- c. Estimate the minimum slug size required to sweep the 1D medium entirely with slug. Assume $D_3 = 0.2$ and $D_4 = 0.1$. There is no polymer in the slug.
- d. Calculate and plot the time/distance diagram if the slug size is one-half that estimated in Part c.
- e. Calculate and plot saturation profiles at $t_D = 0.3$ and 0.8 for the conditions of Part d.

9.8 Importance of Mobility Control in SP Floods. In the absence of other data, high- N_{vc} relative permeabilities for a Type II(–) system can be approximated by straight lines through the points $(S'_{3r}, 0)$ and $(1 - S'_{2r}, k_{r3}^0)$ for the aqueous phase and through (S'_{3r}, k_{r2}^0) and $(1 - S'_{2r}, 0)$ for the oleic phase.

- a. Plot two high- N_{vc} fractional-flow curves for aqueous-phase ($j = 3$) viscosities of 5 and 50 mPa·s. Assume $\mu_2 = 5$, $\mu_3 = 0.8$ mPa·s, $S'_{3r} = 0.15$, $S'_{2r} = 0.05$, $(k_{r3}^0)' = 0.8$, and $(k_{r2}^0)' = 0.6$. The medium has no dip.
- b. Using the El Dorado relative permeabilities shown in Fig. 8.18, illustrate the effects of good mobility control on an SP flood by calculating oil-saturation profiles for the two cases in Part (a) at $t_D = 0.3$. The frontal advance lag $D_3 = 0.16$. The injected aqueous surfactant is continuous.

Chapter 10

Foam-Enhanced Oil Recovery

10.1 Introduction

Previous chapters have explained the motivation for injecting gases into oil reservoirs to recover oil. The gases are steam [thermal enhanced oil recovery (EOR), [Chapter 11](#)] or CO₂ or hydrocarbon gases (solvent methods, [Chapter 7](#)). These EOR processes can be quite efficient at displacing oil from regions in which the steam or solvent contacts (or sweeps) the oil. However, in the field, volumetric sweep efficiency is often poor with these processes because of permeability variations in the formation and the low viscosity (or, more specifically, high mobility) and low density of the gas. Gas sweeps rapidly along high-permeability streaks or moves rapidly to the top of the formation and reaches a production well. Once such a path is saturated with gas, the high mobility of the gas ensures that most of the subsequently injected gas follows that path. See the discussion in [Chapter 6](#) about the effects of heterogeneity, mobility ratio, and gravity.

Foam can mitigate these problems because it directly reduces gas mobility. In some cases, it reduces gas mobility most in high-permeability layers, thereby reducing the effects of permeability variations on gas sweep (Section 6.4). By increasing the magnitude of horizontal viscous or pressure forces relative to the effects of gravity, it can reduce gravity segregation (Section 6.9).

This chapter highlights foam properties and applications, with an emphasis on simplified modeling. In particular, most laboratory and modeling studies of foam exclude oil; the effects of different crude oils on foam and how to model this effect are only dimly understood. These topics are treated only briefly here, despite their obvious importance. Complete reviews can be found elsewhere (Schramm

1994; Rossen 1996; Vikingstad and Aarra 2009; Farajzadeh et al. 2012).

The primary purpose of foam is to deliver gas to a larger volume of the reservoir, where it can recover oil according to the mechanisms described in other chapters. Some laboratory studies show increased microscopic displacement efficiency with foam. In these cases, it may be increased pressure gradient and increased capillary number that recover the oil in the laboratory (Section 3.4). One should take care in extrapolating this behavior to the field unless an increased pressure gradient is feasible on that scale.

Other applications of foam in porous media include acid diversion in wellbore stimulation (Gdanski 1993), mobility control for surfactant-polymer (SP) and alkaline/surfactant/polymer (ASP) EOR (Li et al. 2010), recovering nonaqueous wastes from aquifers (Hirasaki et al. 2000), and preventing coning of gas or water in production wells. All these applications, which can be lumped together as “foam in permeable media,” are different from other foam applications in petroleum operations for drilling, fracturing, cementing, and removing accumulated water from gas wells. In all the latter applications, which use what we call here “bulk foams”, the bubble size in the foam is small compared to the channel geometry (wellbore or fracture, for instance), and the foam can be treated as a single-phase, although rheologically complex, fluid.

10.2 Nature of Foam in Permeable Media

Foam is a dispersion of gas in water, stabilized by surfactants. In applications in which foam enters a porous medium, the bubbles are thought to be as large as or larger than the individual pores, as illustrated in [Fig. 10.1](#). The bubbles are separated by thin liquid films called lamellae (Bikerman 1973). Throughout this chapter, we assume that the rock is strongly water-wet (but see Section 10.6). Therefore, water occupies the smallest pores and the crevices and corners of large pores. The middle and right diagrams in [Fig. 10.1](#) expand the view of the left diagram, first to one lamella stretched

between solid surfaces within a pore (size of order 100 μm), and then to the interior of the lamella (size of order 30 nm).

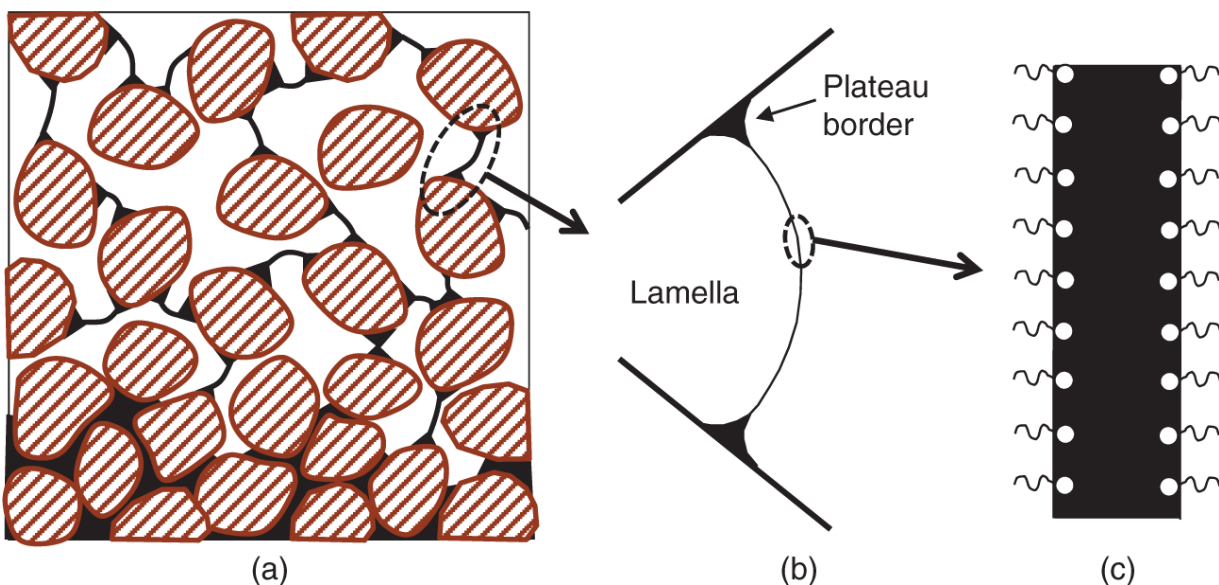


Fig. 10.1—Three schematic views of foam in an oil-free porous medium on different scales. (a) Foam in porous medium, scale of order 1 mm. Grains are hatched objects, water (including lamellae) solid black, gas white. Bubbles are the gas inside pores between lamellae. Between the grains at the bottom of the figure, water fills the smallest pores (courtesy of S.I. Kam, personal communication). **(b)** A lamella stretched between solid surfaces, with Plateau borders at the solid surface. The scale of this figure is one pore (i.e., $\sim 100 \mu\text{m}$). **(c)** An expanded view of the lamella on a scale of 30 to 100 nm. Surfactant molecules (hydrophilic head group represented by a circle, hydrophobe by a line as in [Chapter 9](#)) adsorbed on the surface repel those on the opposite surface, enabling the lamella to resist the greater pressure in the gas phase than in the liquid within the lamella.

A lamella is thermodynamically metastable, which means that sufficiently large external perturbations can destroy it. Surfactant adsorbed on each of the two gas-liquid surfaces of the lamella ([Fig. 10.1c](#)) repels the opposite gas/liquid surface by electrical double-layer forces, steric effects, or both; this repulsion is called “disjoining pressure,” which depends on the surfactant formulation, temperature, pressure, and other factors. The disjoining pressure resists thinning of the lamella in spite of higher pressure in the gas phase on either side (i.e., positive capillary pressure) pushing inward on the lamella; see Section 3.2. At sufficiently high capillary

pressure, however, the film collapses in spite of the disjoining pressure.

Therefore, for a given surfactant formulation, temperature, and pressure, the capillary pressure of the surrounding medium, which depends on surface tension and the saturations of gas and water, determines the stability of the lamella and of the foam. A “stronger” foam (i.e., one with lower mobility and with more lamellae separating smaller bubbles) can withstand higher capillary pressure than a weaker foam; that is, it can survive to lower water saturation, at which capillary pressure is greater. Higher surfactant concentration continues to give a stronger foam up to surfactant concentrations much greater than the critical micelle concentration. An example of the effect of surfactant concentration on foam strength is shown in later figures in this chapter.

At finite capillary pressure, the lamella forms a liquid-filled border (the *Plateau* border) (Bikerman 1973), which is bounded by two liquid/gas interfaces and a liquid/solid interface, as shown in [Fig. 10.1b](#). The liquid/gas interfaces make the same contact angle with the solid wall as the liquid makes with the solid without foam. The liquid/gas interfaces of the Plateau border mesh smoothly with the surfaces of the lamella where they meet. The curvature of these liquid/gas interfaces reflects the capillary pressure prevailing in the surrounding porous medium, which is determined by the water saturation of the surrounding permeable medium (see [Chapter 3](#)). The thickness of the lamella (approximately 30 nm) is negligible compared to the length of the lamella, so that the lamella can be treated as a mathematical surface. In the absence of contact-angle hysteresis, lamellae at rest are nearly perpendicular to the pore wall. For moving lamellae, the drag on the moving Plateau border causes the lamella to bulge forward somewhat. This means that pore geometry has a strong effect on the shapes and curvatures of the individual lamellae in the pores.

Even at rest, each lamella can support a pressure difference ΔP across it according to its curvature (cf. [Fig. 10.2](#) top):

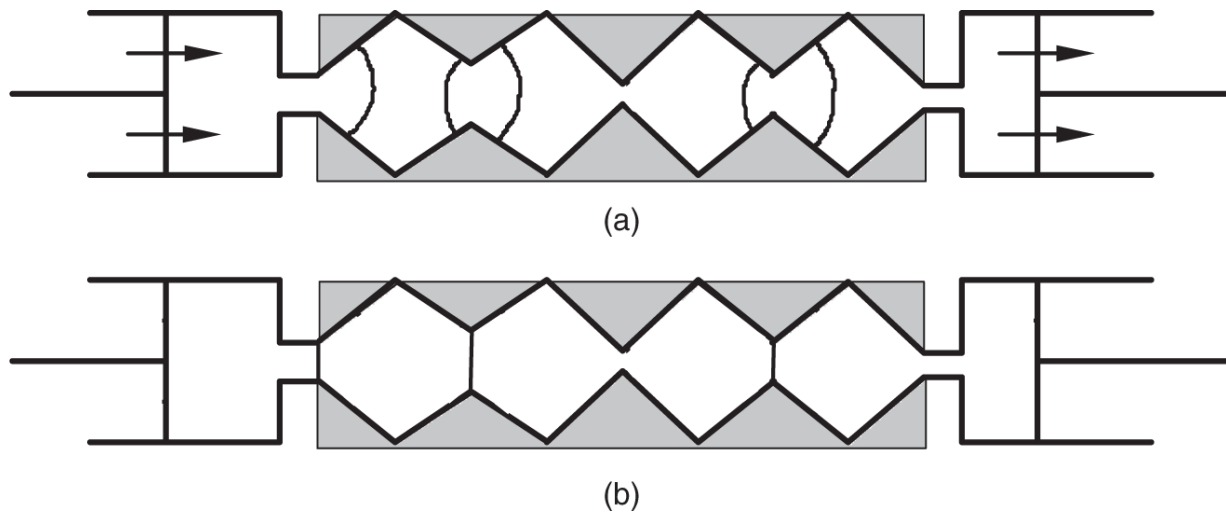


Fig. 10.2—(a) Schematic of a train of bubbles moving through a porous medium, approximated as a periodically constricted tube. Lamellae are black lines, and gas fills the space between lamellae. **(b)** Final state if flow stops and diffusion allows the lamellae to come to equilibrium with no applied pressure difference. Diffusion stops when lamellae are in pore throats, with zero curvature, even though differences in the volumes of bubbles may remain.

$$\Delta P = 4\sigma_{13} / R_\ell, \dots \dots \dots \quad (10.1)$$

where ΔP is the pressure difference across one lamella, σ is the gas/water interfacial tension, and R_ℓ is the radius corresponding to the mean curvature of the lamella. The formula is similar to that for capillary pressure between gas and liquid (Section 3.2) except that it is twice as great because there are two gas/liquid surfaces in a lamella ([Fig. 10.1](#)), both with the same curvature. The pressure difference in Eq. 10.1 is between the gas in the two adjacent bubbles, not between the gas and the liquid. The strongest resistance occurs when a lamella is displaced from a pore throat because its curvature is greatest there, and the resistance is greatest in the smallest throats (see Exercise 10.2). Therefore, gas bubbles flow along discrete paths through the largest pores, and gas bubbles are trapped in medium-size pores; water occupies the smallest pores.

[Fig. 10.2](#) shows schematically a train of bubbles and lamellae moving through a pathway of larger pores. Although some lamellae bulge backwards and pull the train forward, at any given time, most

resist movement. Foams resist movement even at rest, which means that a foam of a given bubble size requires a minimum pressure gradient to flow. The drag on lamellae provides an additional resistance to flow at a given velocity.

Much of the intuition obtained from everyday experience of bulk foams (e.g., shaving cream) is misleading for foam in permeable media. Bubbles are not created by shear forces or turbulence, but by capillary forces. Foam survival does not depend primarily on the rate of drainage of liquid from between bubbles, as in blender tests of bulk foams, but on the inherent stability of the lamellae provided by the disjoining pressure and on the additional dynamic stabilization provided by the temporary increase in interfacial tension (IFT) when a lamella is rapidly stretched (the Marangoni effect). In bulk foams, diffusion of gas through lamellae continuously removes the smallest bubbles as gas diffuses through the lamella in response to the pressure differences imposed by Eq. 10.1. In porous media, diffusion rapidly removes bubbles smaller than a single pore, as for bulk foams (see Exercise 10.1). However, for bubbles larger than a pore, diffusion stops when lamellae occupy pore throats, where the pressure difference between bubbles is zero because the curvature of the lamellae is zero. Therefore, for bubbles as large as or larger than pores, diffusion is relatively unimportant in foam in permeable media. For instance, if flow ceased in [Fig. 10.2a](#), the bubbles in the second and fourth pore throats would disappear by diffusion; these bubbles are at a higher pressure than the bubbles on either side, driving gas diffusion out of these bubbles into their neighbors. After these bubbles disappear, as illustrated in [Fig. 10.2b](#), where the lamellae are in pore throats with zero curvature ($R_t \rightarrow \infty$) with no pressure difference between them (Eq. 10.1), diffusion would cease, even if some bubbles were much larger than others.

The surfactants used in foam EOR are generally more hydrophilic than those described in [Chapter 9](#). Anionic surfactants are preferred for applications in sandstones because of their low adsorption, and sulfonates are especially favored for their chemical stability. Nonionic surfactants provide solubility in the acidic environment of CO_2 .

flooding. For applications of foam to mobility control in MP, ASP flooding, or aquifer remediation, the same surfactant may both supply the solubility for and low IFT with oil, as well as some degree of foam strength. Although foam strength correlates with colloidal properties, like disjoining pressure, surface elasticity, and Marangoni properties, no reliable predictive criteria relating surfactant properties to the effectiveness of foam in permeable media yet exist. In almost all foam processes, the surfactant is injected dissolved in the aqueous phase. For CO₂ foam, it is possible to dissolve surfactant in the supercritical CO₂ phase; foam is then generated with water in the formation.

10.3 Mobility of Gas and Water in Foam

To a reasonable approximation, the water relative-permeability function $k_{r1}(S_1)$ is unaffected by the presence or properties (e.g., bubble size) of foam. For interactions with oil, see Section 10.6.

Foam “quality” is gas fractional flow f_3 , often expressed as a percentage, which for consistency with other chapters, we express here as a fraction. Foam enormously reduces gas mobility, to an extent inversely proportional to the size of the bubbles (Falls et al. 1989). [Fig. 10.3](#) illustrates foam mobility for one foam formulation at three different permeabilities and a range of foam qualities. For the three media, the effective viscosity of the foam is approximately 4 mPa·s at the lowest quality and 12 mPa·s or more at the highest quality shown. This is considerably more than the viscosity of water and up to 500 times the viscosity of the air used to make these foams.

The pressure difference across a curved lamella between gas bubbles (Eq. 10.1) resists bubble movement. As a result, much or most of the gas in place in the permeable medium is trapped, immobile, even as foam flows through some portion of the pore network.

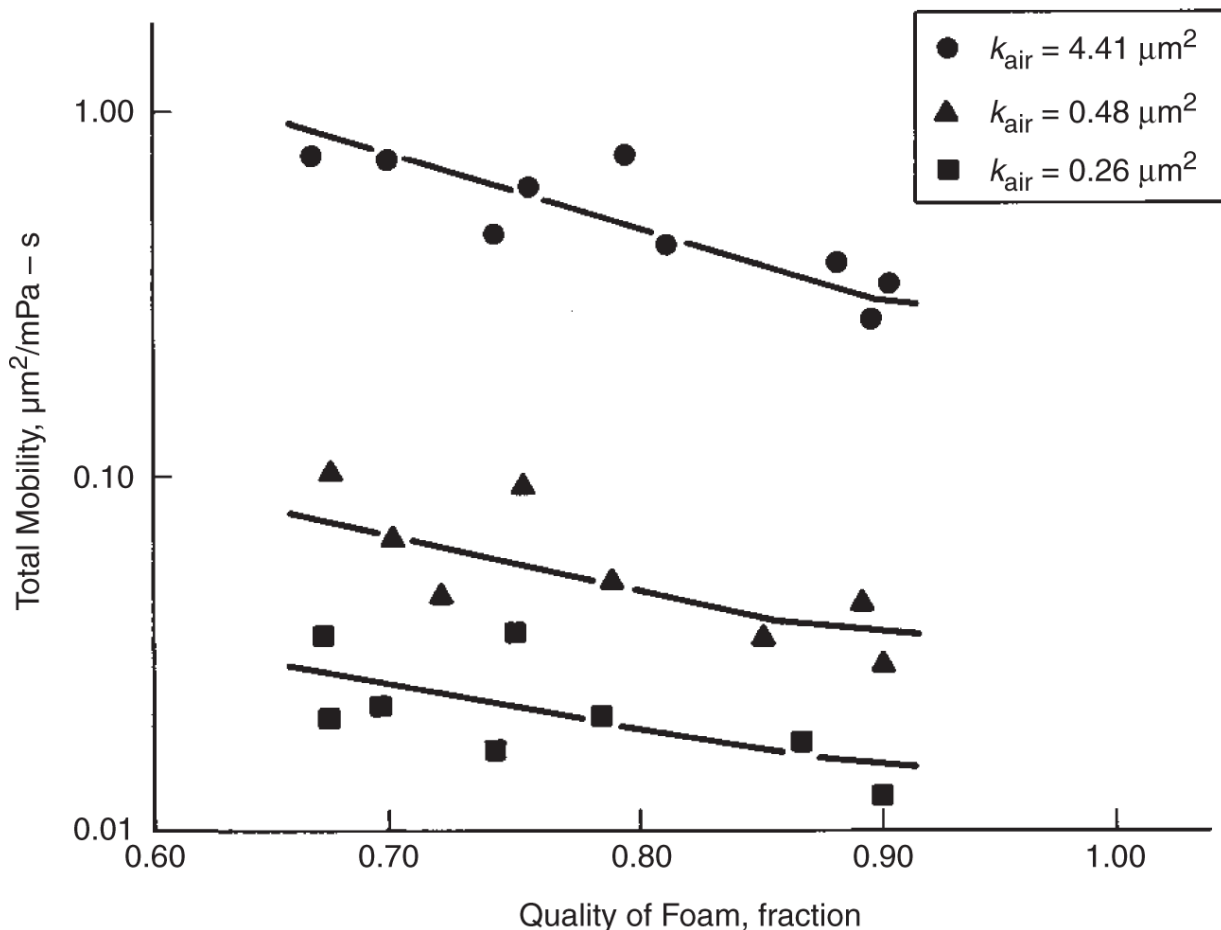


Fig. 10.3—Total mobility vs. foam quality for three consolidated permeable media and 0.1% aerosol foam (Khan 1965).

Foam exhibits a shear-thinning apparent viscosity at fixed bubble size for several reasons. First, the movement of bubbles in even smooth tubes follows a power-law behavior (see Section 8.2) with exponent $n_{pl} \sim 2/3$. In addition, as the pressure gradient increases, more of the trapped foam is able to flow, and this further reinforces the apparent shear-thinning nature of foam flow. In the “low-quality” foam regime described in Section 10.4, where bubble size is thought to be relatively constant, apparent power-law exponents are as small as 0.3 to 0.4.

The magnitude of the reduction in gas mobility depends on the number of lamellae blocking the flow of gas (i.e., the bubble size), and thereby on the processes of creation and destruction of lamellae. A foam providing a large (hundred-fold or greater)

reduction in gas mobility is called a “strong” foam. As noted previously, a strong foam is one in which the lamellae are more stable; having more lamellae present increases resistance to flow. Besides a surfactant formulation that can stabilize lamellae, creating strong foam depends on the imposed pressure gradient (Gauglitz et al. 2002), with the pressure gradient required for foam generation higher at higher foam quality f_3 , higher in lower-permeability media, and lower (or possibly disappearing) under conditions of drainage as opposed to steady injection of gas and surfactant solution. The minimum pressure gradient for foam generation is lower for supercritical CO₂ foams than for the N₂ foams used in many laboratory studies and possibly lower than typical field pressure gradients. In other cases, the minimum pressure gradient for foam generation in principle could prevent foam formation at large distances from an injector. However, a foam generated near an injector may be able to propagate far from the well thereafter.

Weaker foam can be formed at a lower pressure gradient, especially as gas flows across a sharp transition from lower to higher permeability (Tanzil et al. 2002). For a low pressure gradient, this mechanism can form bubbles at horizontal permeability transitions and can markedly limit the upward movement of gas.

The remainder of this chapter focuses on strong foams. Destruction of foam occurs primarily when gas/water capillary pressure exceeds the *limiting capillary pressure* P_c^* [i.e., when capillary pressure is large enough to defeat the stabilizing effect of the disjoining pressure (Khatib et al. 1988)]. The limiting capillary pressure, therefore, depends on surfactant formulation and gas type, but also on permeability of the medium, and in many cases on the superficial velocities of gas and liquid. Moving lamellae have to stretch at each pore throat and therefore break at lower capillary pressure than static lamellae.

Because capillary pressure depends on water saturation S_1 (Section 3.2) in a permeable medium, it is often convenient to describe the condition for stability in terms of a limiting water saturation $S_1^* = S_1(P_c^*)$ rather than a limiting value of. At

$S_1 = S_1^*$, there is an abrupt change (virtually a discontinuity)

in gas mobility—from very low gas mobility for $S_1 > S_1^*$ to a much higher mobility for $S_1 < S_1^*$. It is convenient to represent the effects of foam on gas mobility as an alteration in effective gas relative permeability, as shown in [Fig. 10.4](#).

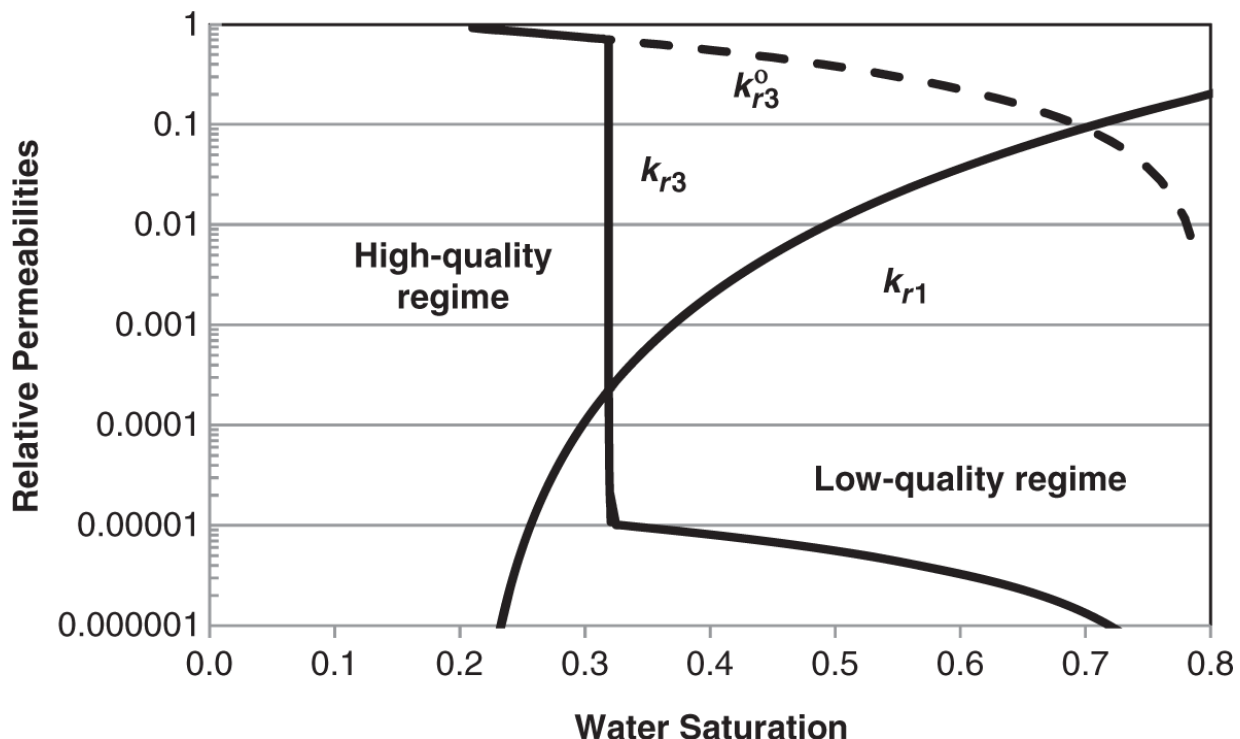
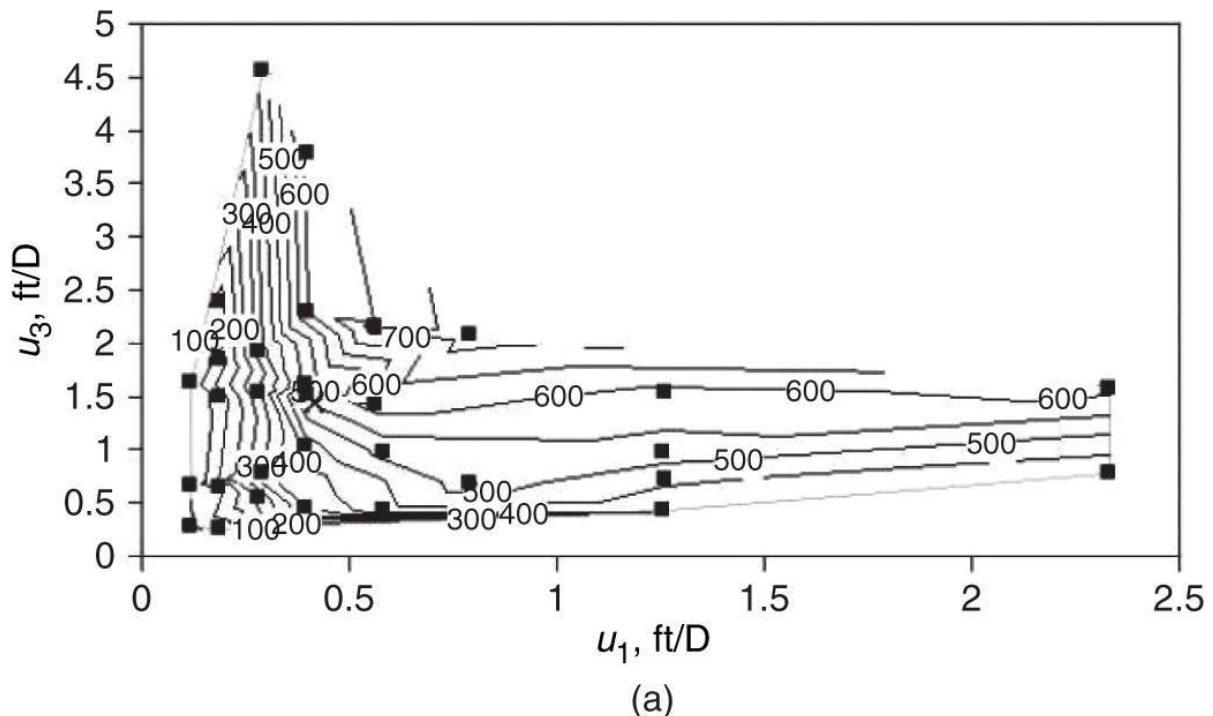


Fig. 10.4—Schematic of the effect of foam on water and gas mobility (represented here as an alteration of effective gas relative permeability from the surfactant-free value k_{r3}^o to k_{r3} ; see Eqs. 10.2 through 10.4.* The vertical portion of the k_{r3} curve is the “high-quality” regime in [Fig. 10.5](#); the portion with greatly reduced k_{r3} is the “low-quality regime.”

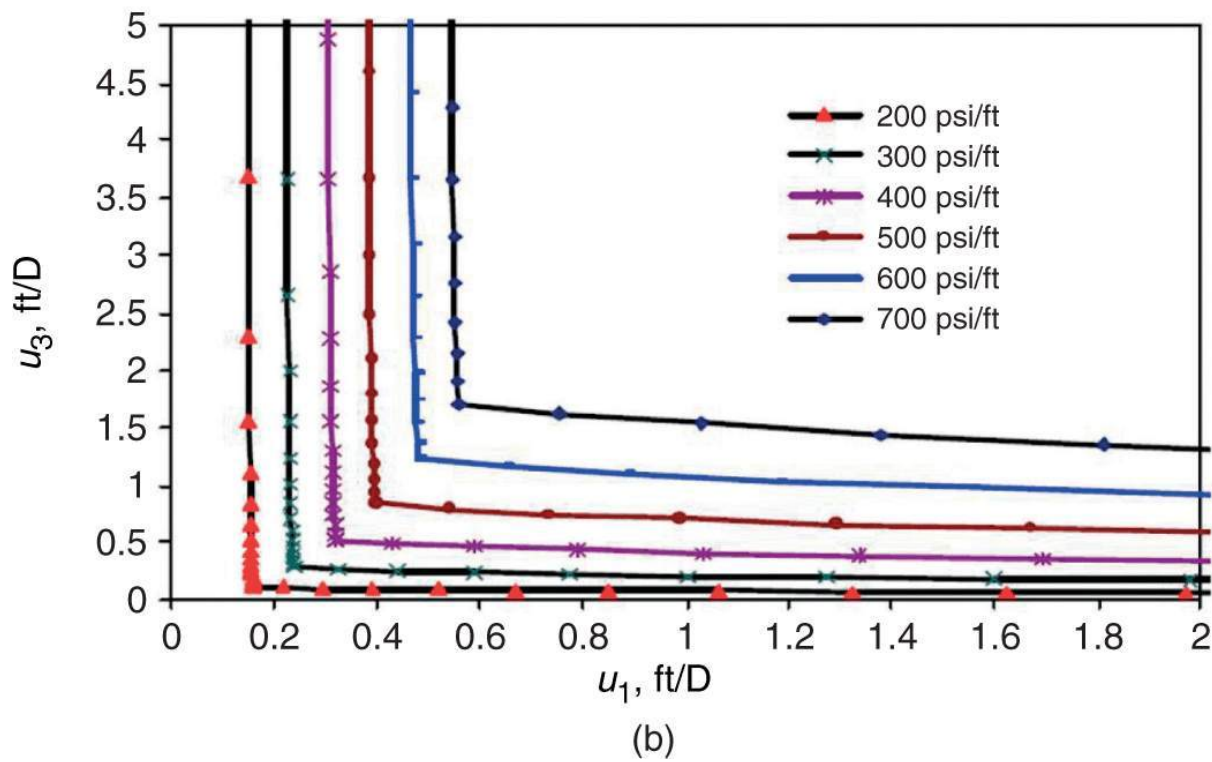
10.4 Strong Foams in Two Regimes

The potential complexities of representing foam properties are enormous, involving multiple mechanisms of lamella creation and destruction, non-Newtonian effective viscosity of flowing bubbles, and bubble trapping and mobilization. Fortunately, for foam without oil, only two mechanisms dominate: foam collapse at the limiting water saturation S_1^* , and the existence of a minimum bubble size.

In the absence of oil, strong foam exists in two regimes, depending on how near S_1 is to S_1^* . In [Fig. 10.5](#), the pressure gradient is plotted as a function of superficial velocities of gas u_3 and aqueous phase u_1 . At high foam quality f_3 (upper left portion of diagram), ΔP is independent of u_3 ; at low foam quality (lower right), ΔP is independent of u_1 .



(a)



(b)

Fig. 10.5—(a) Contour plot of steady-state pressure gradient (psi/ft) for foam flowing through a Berea core as a function of gas superficial velocity u_3 and liquid superficial velocity u_1 . Solid points are steady-state measurements of the pressure gradient used to construct the contour plot. The transition between the regimes occurs at $u_3 \approx 0.75$. From Alvarez et al. (2001). For another example, see the worked

case later in this chapter. (b) Fit to data using Eqs. 10.3 through 10.5 and $\varepsilon = 0.001$, $R_{ref} = 68,500$, $n_{pl} = 0.4714$, $u_3_{ref} = 0.867$ ft/D, and $\varepsilon = 0.001$ (Cheng 2002). Symbols on this plot are calculated points, not data.

The two regimes in [Fig. 10.5](#) appear in studies representing a wide range of conditions (Alvarez et al. 2001): in permeable media with permeability $k < 10$ md (although most data are for $k > 100$ md); through sandpacks and beadpacks with $k > 10,000$ md; with a variety of surfactants; with N_2 gas or supercritical CO_2 ; at room temperature and up to at least 200°F. In some cases (Kim et al. 2005), the ΔP contours in the low-quality regime (lower right portion of diagram) bend upwards and to the right (i.e., ΔP decreases with increasing u_1 at fixed u_3). In [Fig. 10.5](#), the value of f_3 that separates the two regimes, called f_3^* , is approximately 0.75, although it increases with increasing total superficial velocity. The magnitudes of ΔP and the value of f_3^* depend on the permeable medium, the surfactant formulation, and the gas type. See Kim et al. (2005) for exceptions to the described behavior.

The high-quality regime results from foam collapse at P_c^* and S_1^* . Behavior in this regime can be Newtonian, shear-thinning, or shear-thickening at fixed f_3 ; in [Fig. 10.5](#), it is shear-thinning. In this regime, bubble size decreases as u_3 increases or u_1 decreases, but S_1 is nearly constant: a wide range of foam qualities correspond to virtually the same value of S_1 . The sensitivity of foam to P_c^* in this regime and the fact that $P_c(S_1)$ increases as permeability decreases ([Chapter 3](#)), mean that foam in this regime is strongest in higher-permeability layers and spontaneously diverts flow to lower-permeability layers (see Exercise 10.4). For a given permeability, if P_c^* and S_1^* are independent of superficial velocities, then S_1 is fixed at this invariant value of S_1^* throughout this regime. Then, because $k_{r1}(S_1)$ is independent of foam strength (Section 10.3), k_{r1} is constant throughout this regime as well, and one can compute flows and mobility in this regime by applying Darcy's law ([Chapter 3](#)) to the aqueous phase without concern for the complex behavior of the gas

phase. At fixed f_3 or fixed u_3 , the apparent viscosity is Newtonian with respect to u_1 ; apparent viscosity is extremely shear-thinning (with apparent power-law exponent $n_{pl} = 0$) with respect to u_3 at fixed u_1 . All this derives from the abrupt change in gas mobility at a single value of $S_1 = P_c^*$ ([Fig. 10.4](#)).

In the “low-quality regime,” $S_1 > S_1^*$ (i.e., $P_c < P_c^*$). The bubble size distribution is centered at some small limiting size (e.g., roughly the pore size) below which generation mechanisms are suppressed and bubble destruction by diffusion becomes active (see Exercise 10.1 and [Fig. 10.3](#)). As u_1 increases, water occupies and flows through some pores previously occupied by trapped gas. Hence, u_1 increases with no change in ΔP . As u_3 increases, ΔP increases much less than proportionately to u_3 , both because of the shear-thinning apparent viscosity of the bubbles already moving and because more of the trapped gas is mobilized as ΔP increases. The limited available data suggest that relative mobility is relatively insensitive to permeability in the low-quality regime; therefore, foam in this regime would not divert flow to lower-permeability layers in the way that foam in the high-quality regime does. These two regimes can be modeled as described in Section 10.8.

Example 10.1. Effect of Permeability on Foam Mobility. A series of core samples differing in permeability all share the same relative-permeability functions:

$$k_{r1} = 0.2 \left[(S_1 - 0.2) / 0.6 \right]^{4.2}$$

$$k_{r3}^0 = 0.94 \left[(0.8 - S_1) / 0.6 \right]^{1.3}$$

where the superscript 0 means the value in the absence of foam. A given foam formulation, injected with $f_1 = 0.1$ and superficial velocity 10 m/d into a core with permeability of 1 Darcy, gives a steady-state $\Delta P = 400$ psi/ft. The viscosities of the aqueous and gas phases are

1.2 cp and 0.02 cp, respectively. This same core has a drainage capillary-pressure curve for gas vs. surfactant solution given by

$$P_c(S_1) = 1.02 + 0.68 \ln[0.8 / (S_1 - 0.2)] \text{ for } 0.2 < S_1 < 1$$

P_c is given here in psi; hence, the minimum P_c for gas to enter the core is 1.02 psi. Assume that water perfectly wets the core compared to air.

- (a) Assuming that this foam obeys the fixed- P_c^* model, what is the value of P_c^* for this foam formulation in this rock? Express the answer in psi.

First determine k_{r1} and S_1^* from the measured ΔP . u_1 is $(1/10)$ the total superficial velocity, or, in SI units, $1.157 \cdot 10^{-5}$ m/s. In SI units, ΔP is 9.05 MPa/m. From Darcy's law for the aqueous phase, $k_{r1} = u_1 \mu_1 / (k \Delta p) = (1.157 \cdot 10^{-5})(0.0012) / [(1 \cdot 10^{-12})(9.05 \cdot 10^6)] = 0.00153$. From the expression for $k_{r1}(S_1)$, $k_{r1}(S_1), S_1^* = 0.388$. From the expression for $P_c(S_1)$, $P_c^* = 2.004$ psi.

- (b) Suppose that one goes on to measure ΔP with foam at the same flow rate and quality in a set of core samples of different permeabilities. Suppose further that P_c^* does not vary with permeability. Assuming that all the samples obey the same Leverett J -function (see [Chapter 3](#)) given as the third equation in this example, predict ΔP with foam for core samples of permeability 3 darcies, 300 md, 100 md, and 30 md. Assume that porosity is the same among all these cores, and assume that foam in all cores is in the "high-quality regime," (i.e., that in all cores, foam is at S_1^* and $P_c = P_c^*$).

By assumption, $P_c^* = 2.004$ psi for all permeabilities. For this set of samples with a fixed Leverett J -function, the equation for capillary pressure varies with permeability according to

$$P_c(S_1) = (1/k)^{1/2} \left\{ 1.02 + 0.68 \ln \left[0.8 / (S_1 - 0.2) \right] \right\},$$

where, for simplicity, we leave k in units of Darcy. Therefore, for the 3-Darcy sample,

$$P_c(S_1) = 2.004 = (1/3)^{1/2} \left\{ 1.02 + 0.68 \ln \left[0.8 / (S_1 - 0.2) \right] \right\},$$

which gives $S_1^* = 0.2218$. $k_{r1}(0.2218) = 1.79 \cdot 10^{-7}$, which is 8,520 times smaller than 0.00153. This suggests that ΔP is 8,520 times greater at the same superficial velocity, or $\Delta P = 3.41 \cdot 10^6$ psi/ft. For 0.3 Darcy, the corresponding results are $S_1^* = 0.854$, $k_{r1} = 0.287$, and $\Delta P = 2.13$ psi/ft. For 100 and 30 md, 2.004 psi is higher than the capillary entry pressure; foam could not exist at these permeabilities because if gas is in the rock (capillary pressure is higher than the capillary entry pressure), then capillary pressure is higher than the limiting capillary pressure. This drastic effect of permeability on foam strength predicted if P_c^* is independent of permeability has led to speculation that P_c^* does depend on permeability (Rossen and Lu 1997); see Exercise 10.4.

10.5 Foam Propagation

Lamellae require surfactant for stability. Therefore, foam can propagate no faster than the surfactant. Surfactant propagation is limited by adsorption of surfactant on the formation, as with surfactant EOR. In laboratory corefloods, if gas and liquid are injected into a core presaturated with surfactant, a strong foam propagates as a shock with the leading edge of the gas bank. If gas and surfactant-free water are injected for a time before surfactant solution and gas, then foam propagation can be much slower, more so than can be explained by adsorption. In other words, the foam front advances more slowly than the surfactant front.

There are few data on long-distance foam propagation in the field. In two steam-foam field tests, propagation was confirmed directly in

observation wells 40 and 90 ft, respectively, from the injection well (Patzek 1996).

10.6 Effect of Oil and Wettability on Foam

Oil can destroy aqueous foams, depending on the surfactant formulation, compositions of the oil and gas, pressure, and temperature (Schramm 1994; Rossen 1996; Vikingstad and Aarra 2009; Farajzadeh et al. 2012). Oil components near the molecular weight of the surfactant hydrophobe are thought to be most adverse to foam. Surfactants made from fluorinated hydrophobes are insensitive to the presence of hydrocarbons, but are too expensive for most EOR applications. Oil spreading on the water/gas interface is thought to be a major mechanism of foam destruction by oil. Early laboratory studies focused on a limiting oil saturation for foam stability, above which no foam could form. In experiments, gas and water would flow for a time until the oil saturation declined to this limiting value, and then foam would form. It is possible that this process involved stripping of certain components from the oil rather than reducing oil saturation. Several studies have attempted to derive a predictive test for the effect of oil on foam on the basis of properties measured outside the permeable medium, but so far, a universally successful test has not resulted.

If the permeable medium is not water-wet, the surfactant may be able to reverse its wettability and allow foam to form (Sanchez and Hazlett 1992). However, in the presence of oil, this mechanism may be prevented (at least on the time scale of a laboratory experiment). If the formation remains oil-wet, it is difficult to create foam in the formation.

10.7 Modeling Foam Flow: Mechanistic Foam Models

Mechanistic “population balance” foam models attempt to represent all the individual processes of lamella creation and destruction, bubble trapping and liberation, and foam viscosity (Kovscek et al. 1997; Kam 2008). In addition to the conservation equations of [Chapter 2](#), these models represent gas mobility at a given bubble

size and include an additional balance equation on the number of lamellae per unit volume. Models that do not assume local steady state are essential if one is not sure that steady-state strong foam is created, or to model dynamic processes on the laboratory scale. Indications are that in most cases, the dynamic processes represented in these models would rapidly approach local steady state on the field scale (Rossen et al. 1999; Chen et al. 2010). Moreover, local steady-state models are amenable to the fractional-flow methods developed in this text. Therefore, this chapter focuses instead on local steady-state models.

10.8 Modeling Foam Flow: Local Steady-State Models

Local steady-state foam models assume instantaneous attainment of the strong-foam state everywhere that surfactant, water, and gas are present in sufficient quantities. In addition, most fractional-flow models assume that phases are incompressible, gas and water are mutually insoluble, chemical and thermal degradation of surfactant can be neglected, and that the flow of foam is Newtonian.

One can represent the behavior of foam in [Figs. 10.4](#) and [10.5](#) as follows (Cheng et al. 2000):

$$\text{For } C_{41} < C_{41}^* \text{ or } S_1 < (S_1^* - \varepsilon), \\ k_{r3} = k_{r3}^0(S_1). \quad \dots \quad (10.2)$$

$$\text{For } C_{41} \geq C_{41}^* \text{ and } S_1 > (S_1^* + \varepsilon), \\ k_{r3} = k_{r3}^0(S_1) / R_f. \quad \dots \quad (10.3)$$

$$\text{For } C_{41} \geq C_{41}^* \text{ and } (S_1^* - \varepsilon) \leq S_1 \leq (S_1^* + \varepsilon), \\ k_{r3} = k_{r3}^0(S_1) / \left\{ 1 + (R_f - 1) \left[S_w - (S_1^* - \varepsilon) \right] / (2\varepsilon) \right\}. \quad \dots \quad (10.4)$$

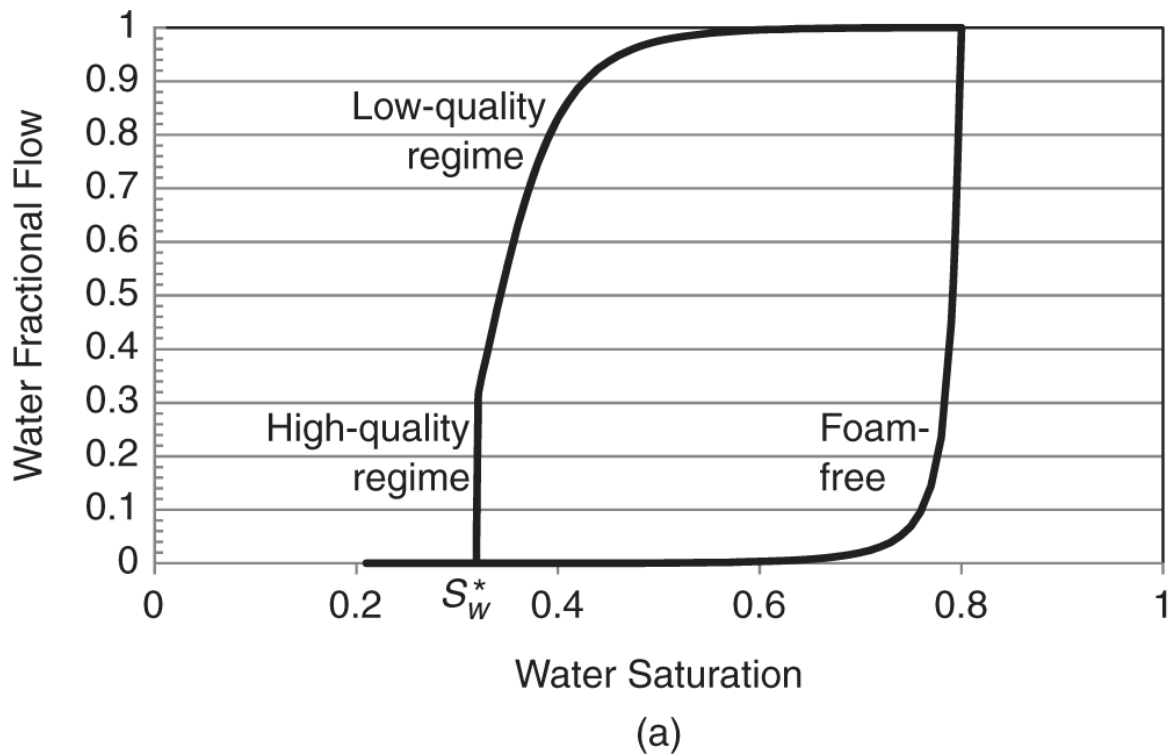
with

$$R_f = R_{f\text{ref}} \left(u_3 / u_{3\text{ref}} \right)^{(n_{pl}-1)}, \quad \dots \quad (10.5)$$

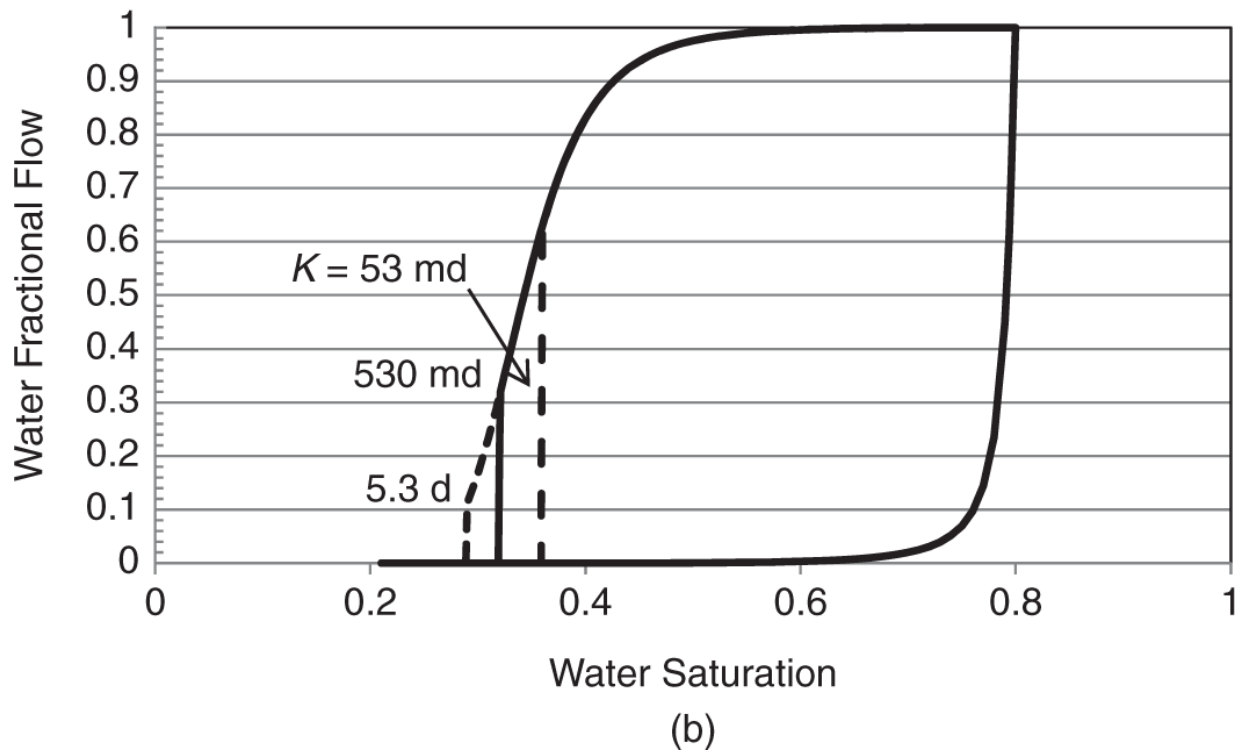
where C_{41} is the surfactant concentration in the aqueous phase, C_{41}^* the threshold concentration for foam formation (often set to one-half the injected concentration), $k_{r3}^0(S_1)$ the gas relative-permeability function that applies in the absence of foam, R_{ref} the gas-mobility reduction in the low-quality regime at a reference gas superficial velocity $u_{3\text{ref}}$, and n_{pl} the power-law exponent for the low-quality regime. For most cases here, and in particular when using fractional-flow methods, we assume $n_{pl} = 1$. Eqs. 10.3 and 10.5 describe the low-quality regime and Eq. 10.4 describes the high-quality regime. Eq. 10.2 describes an extremely dry state of complete foam collapse, drier than the high-quality regime. Other functions could represent the sharp, continuous rise in k_{r3} as S_1 decreases in Eq. 10.4. As will be shown in Section 10.8.1 and Exercise 10.9, seemingly insignificant differences among these choices can have significant effects in some cases. Eq. 10.5 makes the low-quality regime non-Newtonian; to make the high-quality regime non-Newtonian, one must make S_1^* a function of superficial velocity(ies).

[Fig. 10.5b](#) shows how these equations fit the data in the top plot.

[Fig. 10.4](#) is plotted with the same model at one value of u_3 . [Fig. 10.6a](#), shows the gas/water fractional-flow curve plotted with the same model, excluding Eq. 10.5 (i.e., assuming Newtonian behavior in the low-quality regime) on the basis of the data of Alvarez et al. (2001). It also shows the fractional-flow curve for gas and water with no surfactant, based on the same study. If one assumes that S_1^* increases as permeability increases, as a result of the S_1^* mechanism, and that R_{ref} is unchanged, then a series of fractional-flow curves for layers of different permeability would appear, as shown in [Fig. 10.6b](#).



(a)



(b)

Fig. 10.6—(a) Gas/water fractional-flow curve based on the model fit in [Fig. 10.5](#). **(b)** Effect of permeability on the fractional-flow curve. Only the water saturation at the abrupt jump between strong-foam and no-foam curves shifts as permeability

changes. Here, we assume that mobility at S_w^* scales roughly with the square root of permeability (see Exercise 10.4).

Example 10.2. Estimating Foam-Model Parameters From Steady-State ΔP Data. [Fig. 10.7](#) is a plot of a steady-state pressure gradient for CO₂ foam in a Boise sandstone core from Kim et al. (2005). Fit the parameters in Eqs. 10.2 through 10.4 to these data using the method of Cheng et al. (2000), following the steps described below. Assume the following physical parameters and functions:

$$\begin{array}{ll} \mu_1 = 1 \text{ mPa}\cdot\text{s} & k_{r1} \text{ and } k_{rg}^0 \text{ as in worked example in Section 10.4} \\ \mu_3 = 0.02 \text{ mPa}\cdot\text{s} & k = 1.52 \times 10^{-12} \text{ m}^2. \end{array}$$

- Use the 50 psi/ft contour to fit the parameters. Redraw the 50-psi/ft contour starting from some distance away from its corner; it should be perfectly vertical in the high-quality regime, then turn a sharp 90° corner at the transition from high-quality to low-quality regimes, and then be horizontal in the low-quality regime. Make your best approximation to the data consistent with these constraints.

At large u_3 , the $\Delta P = 50 \text{ psi/ft}$ (1.13 MPa/m) contour is at roughly $u_1 = 0.29 \text{ ft/D}$ ($1.02 \times 10^{-6} \text{ m/s}$). At large u_1 , the $\Delta P = 50 \text{ psi/ft}$ contour is at roughly $u_3 = 3.0 \text{ ft/D}$ ($1.06 \times 10^{-5} \text{ m/s}$); see [Fig. 10.8](#).

- Use the value of u_1 in the high-quality regime to fit S_1^* using Darcy's law for the aqueous phase.

From Darcy's law applied to the water phase in SI units, $k_{r1} = u_1 \mu_1 / (k \Delta P) = (1.02 \times 10^{-6})(0.001) / [(1.52 \times 10^{-12})(1.13 \times 10^6)] = 5.94 \times 10^{-4}$. From the expression given for $k_{r1}(S_1)$, $S_1^* = 0.350$.

- At the 90° corner in the contour, $S_1 = S_1^*$, and gas mobility is reduced by the factor R_f (Eq. 10.3). Use the value of u_3 from the plot, plus Eq. 10.3 and Darcy's law on the gas phase, to determine R_{fref} .

At $S_1 = 0.350$, $k_{rg}^0 = 0.647$. However, from Darcy's law (again in SI units) applied to the gas phase (assuming that all mobility reduction is in the gas relative permeability), $k_{r3} = u_3 \mu_3 / (k\Delta P) = (1.06 \cdot 10^{-5})(2 \cdot 10^{-5}) / [(1.52 \cdot 10^{-12})(1.13 \cdot 10^6)] = 1.23 \cdot 10^{-4}$. Gas mobility has been reduced by a factor $R_{fref} = 0.647 / (1.23 \cdot 10^{-4}) = 5,240$.

- d. Use the model parameters derived in Parts a and b to replot $\Delta P(u_3, u_1)$ over the same range of superficial velocities as in [Fig. 10.7](#) (i.e., for u_3 from 0 to 8 ft/D and for u_1 from 0 to 2 ft/D). Plot contours for 30, 40, 50, 60, and 70 psi/ft. Ignore possible shear thinning in the low-quality regime to make this plot. How well does the model fit the data?

We apply Eqs. 10.2 through 10.4 using $S_w^* = 0.350$, and $R_{fref} = 5,240$, $\varepsilon = 0.001$, and $n_{pl} = 1$. The results are shown in [Fig. 10.8](#). The fit is not perfect, but reproduces the essential features of the data.

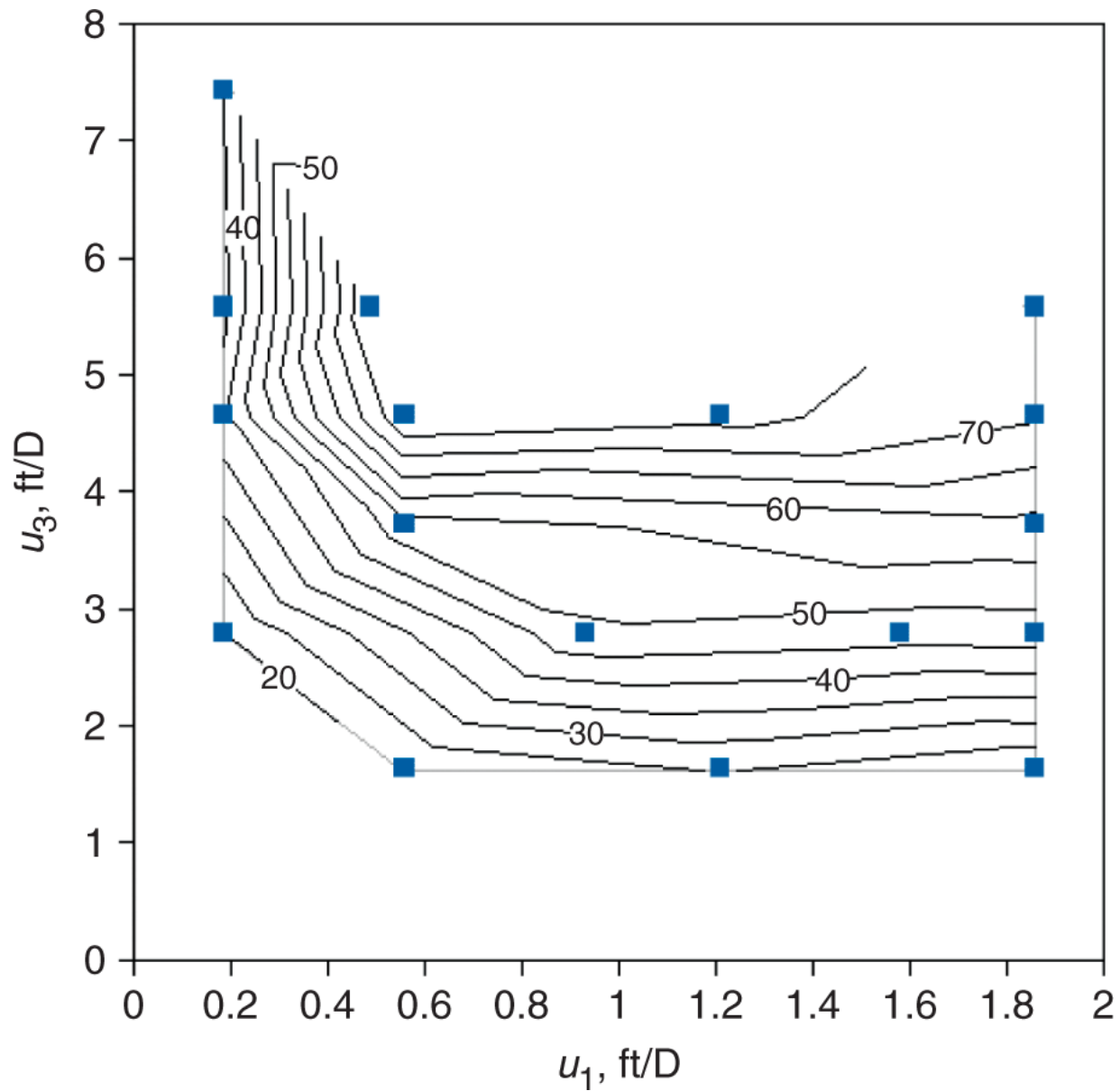


Fig. 10.7—Pressure gradient (psi/ft) for CO_2 foam in Boise sandstone core, from Kim et al. (2005). Boxes represent steady-state ΔP measurements. In this plot, U_1 and U_3 are superficial velocities of water and gas.

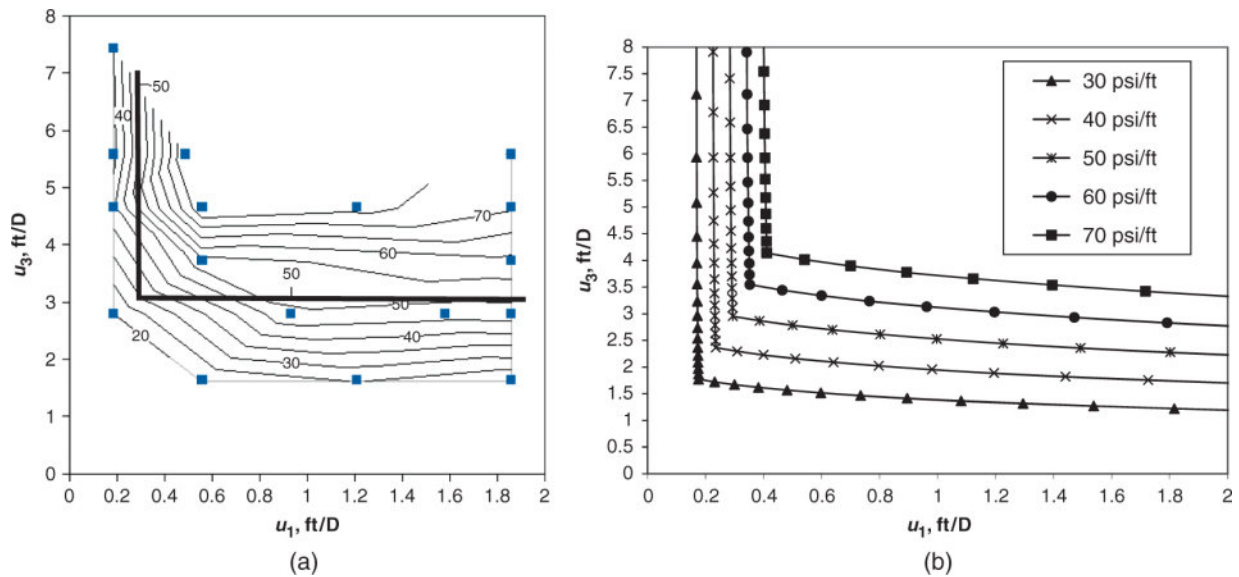


Fig. 10.8—(a) Construction of contours used in fitting-model parameters. (b) Model fit to data.

10.8.1 Continuous Foam Injection in 1D. Consider continuous injection of gas and surfactant solution at water fractional flow f_{1J} into a medium initially saturated with water without surfactant. The injection point J is on the foam fractional-flow curve at $f_1 = f_{1J}$. The initial condition is at point I on the surfactant-free curve at $S_1 = 1$. The path from J to I must somewhere jump between the foam and no-foam curves at the leading edge of the surfactant front. This jump is a miscible wave as introduced in Section 5.5; it is variously called a miscible wave (Section 7.7) or a chemical wave. At this jump, material balances on water and surfactant give

$$\frac{\Delta x_D}{\Delta t_D} = \frac{f_1^+ - f_1^-}{S_1^+ - S_1^-} = \frac{f_1^+}{S_1^+ + D_4}, \quad \dots \quad (10.6)$$

where S_1^+ , f_1^+ , S_1^- , and f_1^- are water saturations and fractional flows upstream and downstream of the shock, respectively, and D_4 is the same adsorption factor discussed in [Chapter 9](#) in connection with surfactant flooding (Eq. 9.14). Graphically, this means the chemical shock is a straight line from a point with coordinates $(-D_4, 0)$, through the point upstream of the shock on the foam fractional-flow

curve, to the point downstream of the shock on the surfactant-free curve. If there is no adsorption ($D_4 = 0$), then the point is the origin of the $f_1(S_1)$ plot, as shown in [Fig. 10.9](#). In the case shown in [Fig. 10.9](#), there is a foam bank at J , and downstream of it a gas bank, point GB , that displaces the initial condition I even further downstream with an immiscible shock. If it is crucial to prevent formation of a gas bank ahead of the foam bank, one can choose a value of f_{1J} larger than that at J shown here, so that the line representing the chemical shock passes directly to point I . In [Fig. 10.9](#), that point is represented by point B on the foam fractional-flow curve.

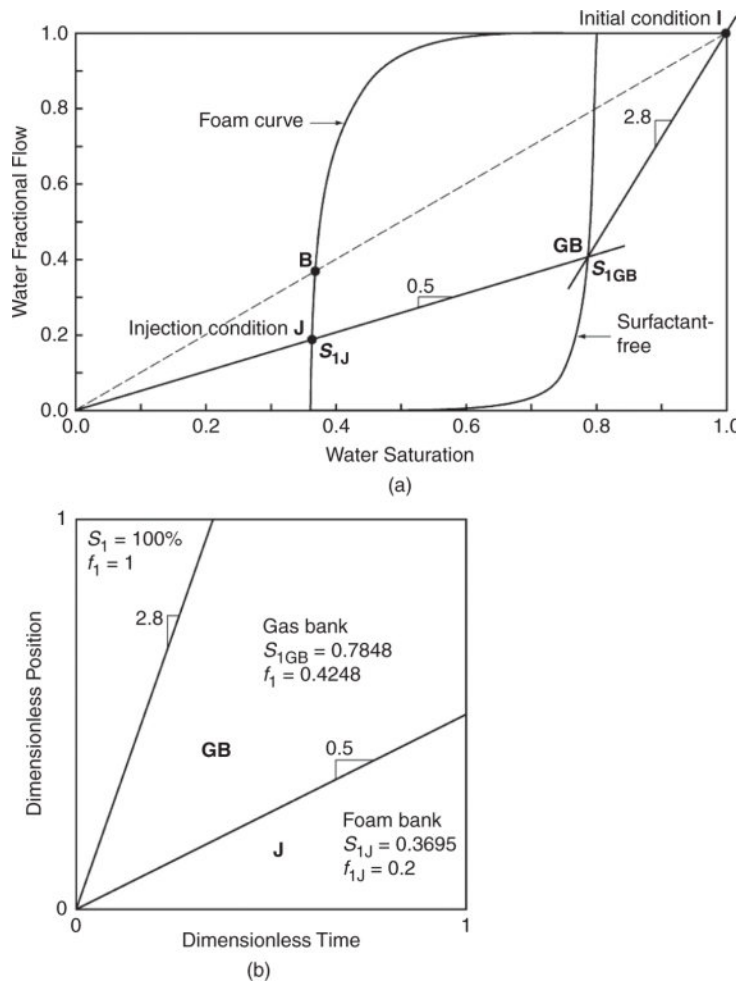


Fig. 10.9—Fractional-flow solution (a) and time/distance diagram (b) for foam injection into a porous medium initially saturated with brine but no surfactant. In (a), point B represents the driest injected foam that would have no gas bank ahead of it.

One can apply this model to displacements in parallel, noncommunicating layers (using plots like [Fig. 10.7](#), one for each layer) to illustrate the power of foam in the high-quality regime to divert flow from high- to low-permeability layers (Zhou and Rossen 1995). One can also represent foam injection into a formation previously flooded with gas and surfactant-free water. In that case, point I is at the value of f_1 used in the injection of gas and water ahead of foam, but on the surfactant-free fractional-flow curve.

If the foam bank were preceded by injection of surfactant solution without gas, then point I would lie on the foam fractional-flow curve. Now there would be simply an immiscible shock directly from J to I . This shock applies until it reaches the leading edge of the surfactant bank ahead of the foam, at which point the displacement would proceed as in [Fig. 10.9](#).

10.8.2 “SAG” Foam Injection in 1D. Just as gas is usually injected in alternating slugs with water in solvent EOR [the water-alternating-gas (WAG) flood discussed in [Chapter 7](#)], foam is often injected as alternating slugs of gas and liquid, called surfactant alternating gas (SAG) or foam-assisted WAG (FAWAG).

Injection of the gas slug in a SAG process can be represented as in [Fig. 10.10](#). We assume that a large slug of surfactant precedes gas injection, so that only the surfactant fractional-flow curve applies. The initial condition before injection of the first gas slug is at I , at $S_{1I} = 1$. (If this were a later slug of gas, then there would be trapped gas in place ahead of this front, and the position of point I would move toward the left, still at $f_1 = 1$.) Injection of gas is represented by point J , at $S_{1J} = S_{1r}$ and $f_1 = 0$. Maintaining increasing slope from J to I requires a shock front from I to a point of tangency to the fractional-flow curve at very small f_1 , near S_1^* . The mobility of the gas bank, and the success of the overall process, hinges on behavior at very small f_1 . As noted previously, different foam models assign different functions for the abrupt collapse of foam at S_1^* (cf. Eq. 10.4). Small differences between these functions can make the difference

between a point of tangency at complete foam collapse and at a mobility of the gas bank that is still low enough for an effective process. Using the model in Eq. 10.4, the point of tangency is at complete foam collapse. Using the model from Shan and Rossen (2004), in [Fig. 10.10](#), the mobility is still sufficiently low in the foam bank (but not much lower than the mobility of water at state I ; see the time/distance diagram in [Fig. 10.11](#)). Upstream of the point of tangency (toward point J) is a spreading wave governed by the slope of the fractional-flow function for f_1 less than the value at the point of tangency. At the injector, the mobility is that at point J (i.e., very high, at a point of complete foam collapse). This is exactly the sort of process that is expected to do well in overcoming gravity override with limited injection pressure (Section 6.9), as discussed in the following.

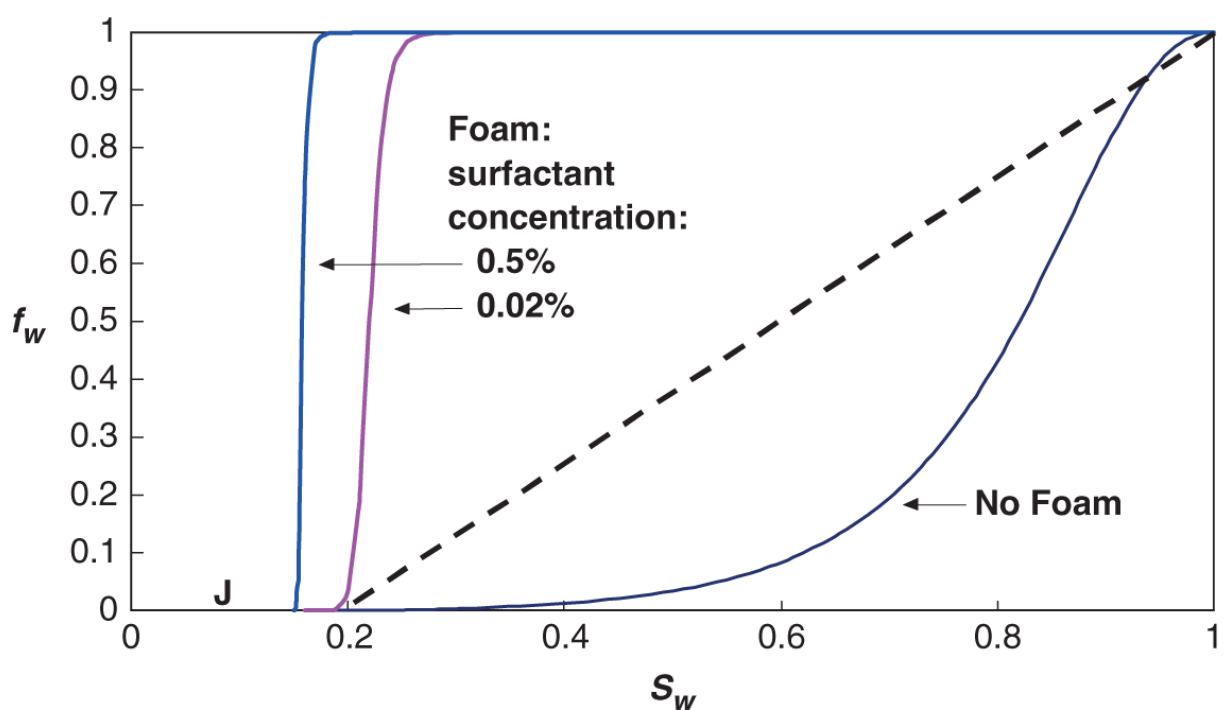


Fig. 10.10—Fractional-flow curves for CO_2 foams of two different surfactant concentrations, with shock drawn in for an SAG process using the foam with 0.02 wt% surfactant concentration (Shan and Rossen 2004). The no-foam curve is shown for comparison, but does not apply to an SAG displacement.

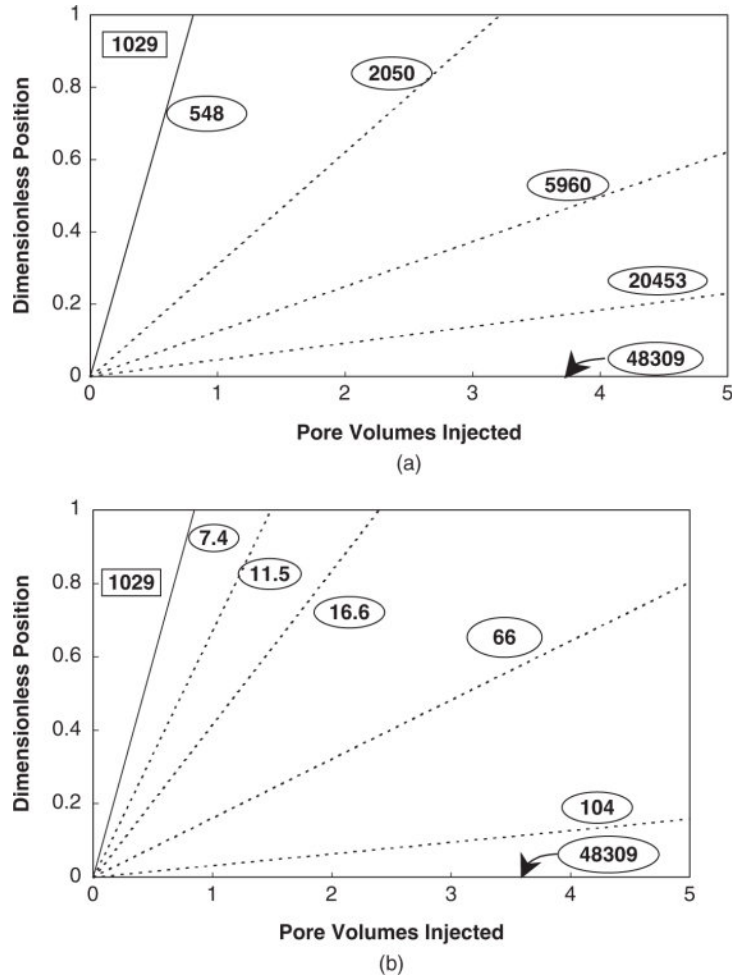


Fig. 10.11—Time/distance diagrams for SAG processes for the two foam models in Fig. 10.10. (a) 0.02 wt% surfactant concentration. (b) 0.5 wt% surfactant concentration. Circled numbers are total relative mobility [in $(\text{Pa}\cdot\text{s})^{-1}$] for individual characteristics in the spreading waves; the boxed numbers are the total relative mobility of the constant state I . The total relative mobility for the foam of greater surfactant concentration is approximately 100 times lower throughout the foam bank (Shan and Rossen 2004).

There are few data to predict how the total mobility within the foam bank in a SAG process (i.e., between the point of tangency and point J) varies with permeability, and, therefore, how a SAG foam process would divert flow between layers differing in permeability.

This analysis predicts a shock front at the leading edge of the gas bank. Within the shock, foam is convected forward, strengthens, and partially or completely collapses. Mobility behind the shock is higher than that within the shock front, and mobility continuously increases

once the shock front passes. In some laboratory-scale SAG corefloods, the behavior is different: average mobility in the core decreases for a period of several pore volumes, then very gradually increases for a period of many more pore volumes. The fractional-flow approach assumes that what takes a long time (perhaps hours) in a laboratory coreflood shrinks to insignificance on a field scale.

Until now, we have addressed injection of gas in a SAG process. Injection of liquid in SAG must cope with greatly reduced liquid mobility (Kloet et al. 2009). The marked slowdown in injection rate allows more time for gravity to segregate previously injected gas from liquid. Most of the research relevant to liquid injection following foam concerns foam-acid diversion for well stimulation, in which a slug of surfactant solution (with acid) follows injection of foam (Cheng et al. 2002). Most of the gas in the foam is trapped, and there is strong evidence that a different fractional-flow curve should apply to injection of the liquid slug (i.e., one with a large trapped-gas saturation). Moreover, tomography data show that liquid fingers through foam because of viscous instability in the displacement (Nguyen et al. 2009).

10.8.3 Gravity Segregation with Continuous Foam Injection. Eqs. 6.88 and 6.89 describe gravity segregation with foam as well as conventional gas EOR in homogeneous reservoirs, as long as foam approximates the assumptions of fractional-flow theory, in particular incompressible phases and Newtonian viscosity. As noted previously, foam is generated as gas attempts to migrate upwards across sharp permeability transitions at layer boundaries; this tends to reduce k_z more than k_x . Eqs. 6.88 and 6.89 show that this could increase the distance that gas and water travel before segregation at fixed injection pressure over that possible without foam.

Apart from this advantage of foam, a striking implication of Eq. 6.90 is that merely reducing mobility does not mitigate gravity segregation if the injection pressure, rather than the injection rate, is limiting. As noted in Section 6.9, the dissipation of much of the injection pressure near an injector is a serious problem for fields in

which injection pressure is limiting. Therefore, several foam-injection strategies are available to attempt to minimize pressure loss near an injection well.

For example, the strategy mentioned in Section 6.9 of injecting water above gas has greater advantages for foam than for gas/water flow. In one simulation study (Rossen et al. 2010) at fixed injection pressure, injecting gas above water was predicted to increase volumetric sweep by approximately a factor of five.

In addition, as noted previously, foam can be shear-thinning, especially in the low-quality regime. One study (Jamshidnezhad et al. 2010) predicts that extremely shear-thinning foam could increase R_g by approximately a factor of two from that in Eq. 6.89.

10.8.4 Gravity Segregation with SAG. In principle, the optimal injection strategy for overcoming gravity segregation in a homogeneous reservoir is injection of a single, large slug of surfactant followed by a large slug of gas sufficient to sweep the well pattern. As illustrated in [Fig. 10.11](#), the mobility near the well is very high for such a process, and, therefore, much of the well-to-well pressure drop is focused on the vicinity of the displacement front, where mobility is small and where gravity override is determined.

[Fig. 10.12](#) illustrates the improvement in sweep of such a process over continuous foam injection, using the two foams of very different strengths illustrated in [Fig. 10.11](#).

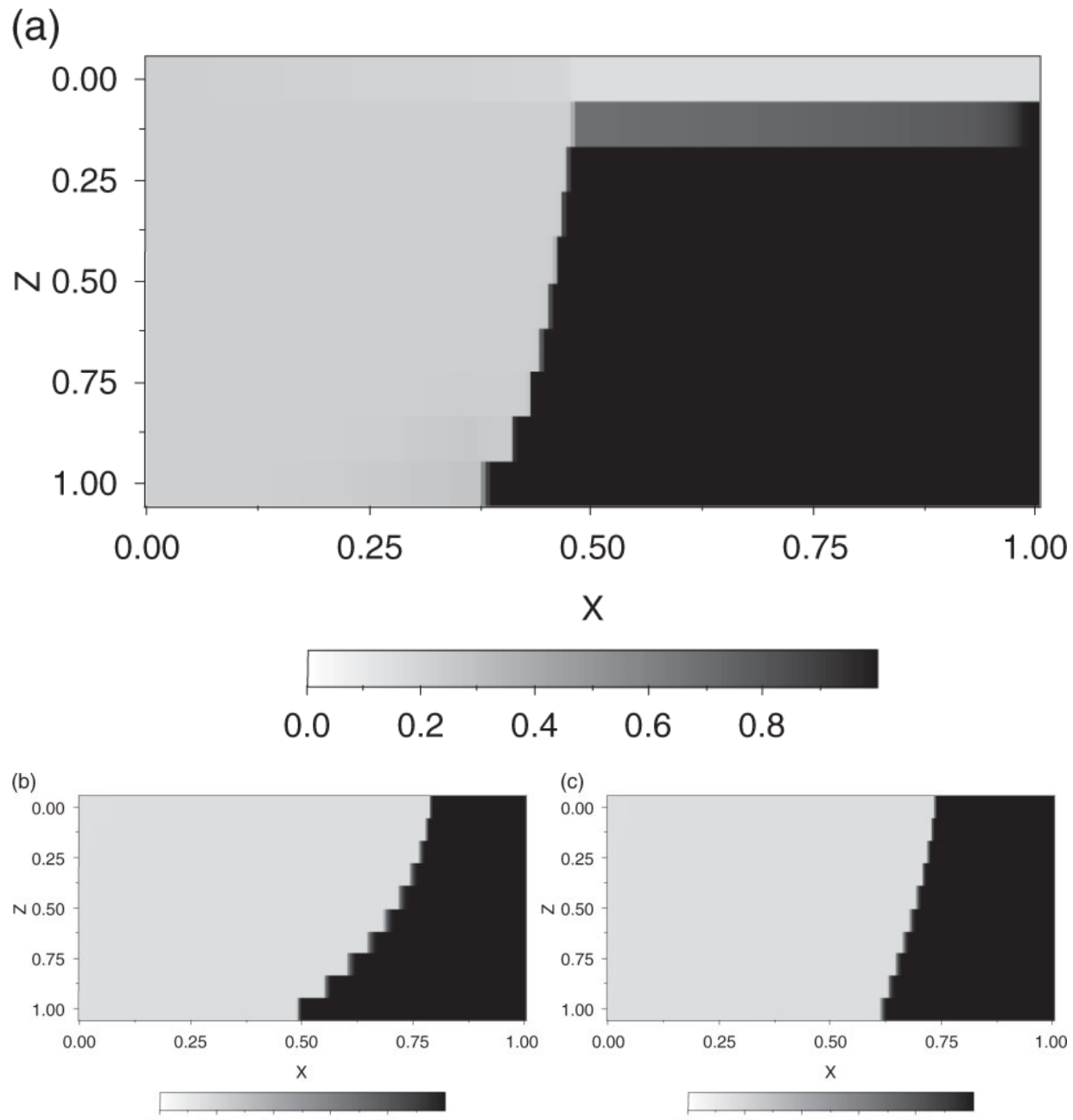


Fig. 10.12—Simulated water saturation (white: $S_1 = 0$; black: $S_1 = 1$) in a cross section of a 2D cylindrical reservoir using the two foam models in [Figs. 10.10](#) and [10.11](#). (a) Continuous foam injection at fixed injection rate ($f_{1,J} = 0.2$; maximum pressure drop = 350 psi); same behavior for either model at same injection pressure (Eq. 6.90). (b) 0.02 wt% surfactant solution; gas is injected at fixed pressure drop = 50 psi. (c) 0.5 wt% surfactant solution [foam much stronger than in (b); see [Fig. 10.11](#)]; gas is injected at the same fixed 50 psi pressure drop. (d) 0.02 wt% surfactant solution; gas is injected at fixed injection rate, giving maximum pressure drop = 50

psi. (e) 0.5 wt% surfactant solution; gas is injected at much smaller fixed injection rate, giving the same maximum pressure drop of 50 psi (Shan and Rossen 2004).

The case of continuous foam injection ([Fig. 10.12a](#)) is at steady state here; no further propagation will occur, and volumetric sweep efficiency is approximately 20%. SAG injection of the weaker foam ([Fig. 10.12d](#)) at constant injection rate has just experienced gas breakthrough, with a sweep efficiency of approximately 43%. The case of SAG injection at constant injection pressure ([Fig. 10.12b](#)) appears to be approaching a sweep efficiency of greater than 70%, even with the weaker foam. Better performance is achieved with the stronger foams ([Figs. 10.12c](#) and [10.12e](#)), with the fixed-pressure-drop process still performing much better than fixed injection rate, but injection rate is much less with the stronger foam. It is striking that there is so little difference in performance between the two surfactant concentrations at the same PV injection, given the roughly 100-fold lower mobility at the higher surfactant concentration ([Fig. 10.11](#)). This is a general feature of SAG foam injection at fixed injection pressure; see Shan and Rossen (2004). Satisfying adsorption would require injecting a much larger surfactant slug at the lower concentration, however, while injection of the gas slug is much faster with the lower surfactant concentration.

The process with a single, large surfactant slug and a gas slug compares favorably with similar processes involving multiple liquid and gas slugs, at least in homogeneous reservoirs. Each time injection of gas is interrupted for another liquid slug, injection rate slows markedly, and gravity segregation increases. However, the single-slug process does depend on even placement of the first surfactant slug. If gas is present in the reservoir before injection of the surfactant slug, then the surfactant slug might slump downward and miss the top of the reservoir.

This design assumes that there are no practical limitations on injection or production rates required to maintain injection pressure at its upper limit. In reality, of course, this may be impractical. In this case, it appears that one should aim for a process that maintains

injection rate so that injection pressure is as close as possible to that maximum value.

Studies extending this strategy to heterogeneous reservoirs are limited. In layered reservoirs with finite vertical permeability, a major challenge is placement of surfactant into the lower-permeability layers (Kloet et al. 2009). Once gas advances in the more-permeable layers to a point ahead of the surfactant in the less-permeable layers, gas can sweep through those layers relatively rapidly and reach the production well.

10.8.5 Foam for Mobility Control in Surfactant EOR. Foam can provide mobility control for surfactant EOR, either together with or instead of polymers (Li et al. 2010). A surfactant optimized for low IFT is in general not the best foamer, and a formulation optimized for foaming would in general not give ultra-low IFT, but in some cases a surfactant optimized for low IFT is an adequate foamer. As illustrated in [Fig. 10.9](#), with continuous injection at high foam quality, gas moves ahead of the surfactant and would finger through the oil ahead of the low-IFT bank. At best, this does no good and wastes gas. Therefore, one would use relatively low-quality foam in applications to surfactant EOR. Use of too little gas, however, risks slower propagation of foam than the surfactant bank and loss of mobility control. In a SAG process with large gas and surfactant slugs, one risks loss of mobility control of the surfactant bank before gas (as foam) arrives to stabilize the front; therefore, one would expect relatively small slugs when using SAG to create foam for mobility control in a surfactant EOR process.

10.8.6 Modeling Foam Flow With Oil. A foam displacement of first-contact or multiple-contact miscible oil can be represented using two-phase fractional-flow methods as long as gas travels faster than the foam bank. There are two jumps between fractional-flow curves: one from the oil/water curve to the solvent/water curve where solvent displaces oil, and a second jump from the solvent/water curve to the foam curve at the front of the surfactant bank; see Ashoori et al. (2010). Approximate two-phase modeling of foam displacements

with incomplete oil displacement is possible by defining a residual nonaqueous phase that is left behind the front of the solvent bank. The 1D fractional-flow model of a miscible displacement reveals an unstable mobility ratio in which gas displaces oil; in 2D or 3D, therefore, one expects fingering, with the oil coming into contact with the foam bank.

In principle, fractional-flow modeling of foam in the presence of mobile, but not fully miscible, oil is similar to the three-phase flow modeling illustrated in [Chapter 5](#). There is a ternary or higher-order phase diagram, with its set of fast and slow paths, in the absence of surfactant, and another with foam in the presence of surfactant at its injected concentration. As long as surfactant is present only in the aqueous phase and gas, water, and oil are mutually insoluble, the jump between these two diagrams is an indifferent wave (in effect, a shock) governed by material balances on water, oil, and surfactant. Namdar-Zanganeh et al. (2011) concluded that if foam is killed at the saturation of oil in place before the foam flood, foam is not ineffective at providing mobility control.

10.8.7 Foam in Fractured Reservoirs. In principle, foam is an ideal treatment for gasflooding highly fractured formations. The large mobility reduction achieved by foam helps control channeling and gravity segregation through the fracture network. The volume to be treated (the fracture network) is modest, and, therefore, adsorption losses of surfactant may also be small. The key issue is whether foam can be regenerated in fractures as it is in the pore space of rock. In the limit of wide fractures, in which the mechanisms of foam generation by capillary forces do not apply, this is unlikely: foam would eventually break as it does in a blender or test tube in the laboratory. In the limit of fractures as narrow as pores in rock, it is likely that foam can be regenerated and sustained over long distances, but this has not been verified experimentally. Very different modeling approaches may be needed (Skoreyko et al. 2011).

10.9 Summary

Foam has properties uniquely suited to mobility control and controlling gravity segregation in gas-injection EOR processes: it spontaneously diverts flow from high- to low-permeability layers (in the high-quality regime); it is shear-thinning (especially in the low-quality regime); it is expected to reduce vertical mobility more than horizontal mobility; and, in SAG application, it can maintain high injectivity while also maintaining low mobility at the displacement front. It has never achieved routine application, although there have been a number of field tests. The main challenges for foam EOR are similar to those of surfactant EOR: minimizing adsorption and consequent chemical costs, and designing surfactants effective at higher temperatures and salinities.

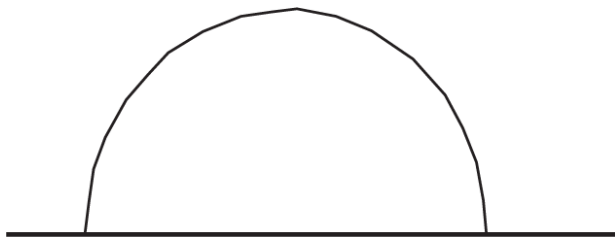


Fig. 10.13—Hemispherical bubble against a flat wall.

Exercises

10.1 Effect of Diffusion on Bubbles Smaller Than Pores. A hemispherical bubble of an ideal gas, with radius R_i , rests on a flat surface, as shown in [Fig. 10.13](#) (for simplicity, the Plateau borders are omitted in this figure). The gas inside the bubble is at a higher pressure than the gas outside because of capillary forces. As a result of this pressure difference (Eq. 10.1), gas diffuses across the lamella, and the bubble shrinks.

- a. Assume that the rate of molar transfer W (in kg-mol/s) through the interface is given by

$$W = k_s \Delta c A,$$

where k_s is a mass-transfer coefficient, Δc is the concentration difference (in kg-mol/m³) in the gas on opposite sides of the lamella, and A is the area of the hemispherical lamella (a function of R_l). The concentration can be related to the pressure difference using the ideal-gas law,

$$\Delta c = \Delta P / (R_{IG} T),$$

where R_{IG} is the ideal-gas constant, 8314.4 J/(kg-mol/K), and T is the absolute temperature. Insert ΔP from Eq. 10.1 into the expression for Δc , then into the expression for W , to get an expression for molar transport rate as a function of R_l .

- b. Perform a material balance on the bubble:

$$dn_{gb}/dt = -W,$$

with W given previously, and n_{gb} , the number of kg-mols of gas in the bubble, given by

$$n_{gb} = (\text{volume}) (\text{molar density}) = (2/3) \pi R_l^3.$$

Assume that c in the bubble does not change much with time (i.e., treat it as a constant). Derive a differential equation for R_l as a function of time. Integrate this expression to obtain the radius as a function of time, given an initial radius R_{l0} .

- c. For a nitrogen bubble at 600 psi and an initial radius of 20 μm , $c = 1.653 \text{ kg-mol/m}^3$. Assume $\sigma_{13} = 0.03 \text{ N/m}$ and $k_s = 3.8 \cdot 10^{-4} \text{ m/s}$. Solve for the time it takes the bubble to shrink to zero radius.

10.2 Origin of Foam Resistance to Flow. A given pore throat has the geometry of a doughnut-shaped solid of revolution with cross section shown in [Fig. 10.14](#). $R_G = 75 \mu\text{m}$, and the pore

throat through the center has radius $15 \mu\text{m}$. Calculate the maximum ΔP across a lamella as it passes through such a throat (as illustrated in [Fig. 10.14](#)) on the basis of its radius of curvature only, in terms of surface tension σ_{13} . For simplicity, the Plateau borders are omitted from this plot; the lamella is perpendicular to the solid at all times.

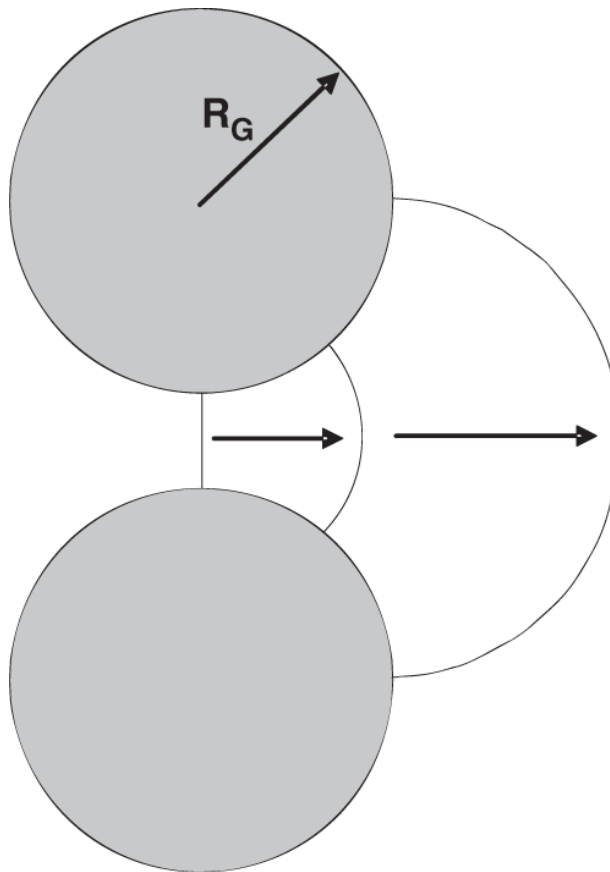


Fig. 10.14—Lamella emerging from toroidal pore throat.

10.3 Foam-Propagation Rate: Effect of Foam Quality, Water Saturation, and Adsorption. Suppose that water saturation in the presence of foam is 0.37, as in the experiments of Persoff et al. (1991), and assume that no oil is present in the porous medium. Suppose that for a given surfactant, 0.5 mg of surfactant is lost to the rock surface for every g of rock. Suppose further that the grain density is 2.6 g/cm^3 and the rock porosity

is 22%. Assume that the density of the surfactant solution is approximately 1000 kg/m^3 .

- a. How many pore volumes of 0.9-quality foam with 0.5 wt% surfactant in the liquid must be injected to place 1 pore volume of foam in place (i.e., to satisfy adsorption and fill the liquid saturated pore space with surfactant solution)? What portion of this represents adsorption? How many pore volumes of gas would pass on ahead of this foam? What is the value of D_4 , as defined in Section 10.8.1?
- b. How many pore volumes of foam would be required if 0.99-quality foam were used?

10.4 Effect of Permeability on Foam Mobility Revisited. Consider again the foam and formation permeabilities in Example 10.1. Assume that all parameters and properties are as given there, but do not assume that P_c^* is uniform among the core samples. Assume instead that at fixed foam quality, ΔP with foam scales with permeability roughly as (Rossen and Lu 1997)

$$\Delta P \sim k^{(-1/2)}.$$

As in Example 10.1, a given foam formulation, injected with $f_1 = 0.1$ and superficial velocity 10 m/d into a core with permeability 1 Darcy, gives a steady-state $\Delta P = 9.048 \text{ MPa/m}$ (400 psi/ft) in that core. The viscosities of the aqueous and gas phases are 1.2 and 0.02 cp, respectively. Estimate the values of S_1^* and P_c^* for formations of 3 Darcy and 300, 100, and 30 md, based on the third equation in Example 10.1.

10.5 Shift in Two Steady-State Foam Flow Regimes with Permeability. There are few data on how the two foam-flow regimes should shift with permeability. In Exercise 10.4, you estimated how S_1^* might change with permeability based on observed trends in ΔP with permeability for foam of a given

foam quality. Assume that those values of S_1^* apply to this problem as well.

A reasonable assumption is that R_f is independent of permeability. Suppose that $R_f = 20,000$ for the foam in Exercise 10.4. Neglect shear-thinning in the low-quality regime (i.e., ignore Eq. 10.5 and assume that R_f is a constant). Use all other parameters from Exercise 10.4. Plot $\Delta P(u_3, u_1)$ for 3 and 1 Darcy and 300, 100, and 30 md. Plot ΔP for u_3 between 0 and 2 m/d and u_1 between 0 and 1 m/d. If the ΔP contours do not cover the figure, pick values of ΔP for the contours that do fill out the central portion of the figure in each case. You may need different values of ΔP for the contours for each plot.

10.6 Fractional-Flow Analysis of Foam Injection. Assume that the values and functions given for μ_1 , μ_3° , k , k_{r1} , and k_{rg}^0 from Exercise 10.5 apply. Assume further that $D_4 = 1$ (cf. Section 10.8.1); that is, that it requires one PV of surfactant solution to satisfy adsorption in one PV of formation. Assume Eqs. 10.2 to 10.4 apply, with $R_f = 15,850$, $\varepsilon = 0.001$, and $S_1^* = 0.37$.

- Plot the fractional-flow functions for $C_{41} = 0$ and $C_{41} \geq C_{41}^*$. In the absence of dispersion, surfactant concentration takes only two values in the formation: zero and the injected concentration, which we assume is higher than C_{41}^* .
- Suppose that there is no surfactant initially in the formation and that $S_1 = 1$. Foam with $f_1 = 0.333$ is injected into the formation. Plot I and J on the fractional-flow curves from Part a. Solve for the displacement graphically on the fractional-flow curves, and plot the time/distance diagram for the displacement as in [Fig. 10.9](#). (Note that in that figure, there is no adsorption, but there is adsorption here.) Mark the total relative mobility of the various banks on the time/distance diagram as in [Fig. 10.10](#):

$$\lambda_{rt} = k_{r3}/\mu_3 + k_{r1}/\mu_1$$

- c. Repeat Part b for an injected foam with $f_1 = 0.01$.

10.7 Fractional-Flow Analysis of SAG Foam Injection. Assume that the foam parameters from Exercise 10.6 apply.

- Assume that a large slug of surfactant has been injected preceding gas injection, as in a SAG foam process, and that $S_1 = 1$, with surfactant present in the formation. Gas is injected ($f_1 = 0$). Plot I and J on the fractional-flow curve for surfactant. Solve for the displacement graphically on the fractional-flow curve, and plot the time/distance diagram for the displacement as in [Fig. 10.10](#). On the time/distance diagram, mark the total relative mobility λ_{rt} (from Exercise 10.6) of the various banks and for several characteristics within any spreading waves present. What is total relative mobility at the front of the gas bank? What is the total relative mobility at the injection well ($x_D = 0$)?
- Repeat Part a for a slightly different case, where Eq. 10.4 is replaced by

$$\text{For } C_{41} \geq C_{41}^* \text{ and } (S_1^* - \varepsilon) \leq S_1 \leq (S_1^* + \varepsilon)$$

$$k_{r3} = k_{r3}^0(S_1) \{ 1 - (1 - 1/R_f) [S_1 - (S_1^* - \varepsilon)]/(2\varepsilon) \}$$

Eq. 10.3, in effect, linearly interpolates resistance to gas flow (i.e., viscosity) across the abrupt jump at S_1^* ; the preceding equation linearly interpolates gas relative permeability across the same jump. Note the great difference between the cases when applied to a SAG process. For further discussion, see Dong and Rossen (2007).

* The superscript 0 means surfactant free in this chapter.

Chapter 11

Thermal Methods

Thermal methods, particularly steamdrive and steam soak, are the most successful enhanced-oil-recovery (EOR) processes. They are certainly the most mature. In [Chapter 1](#), we saw that steam methods currently account for approximately one-half the EOR in the United States. Thermal flooding is commercially successful and has been for almost 50 years. In this chapter, we explore the reasons for this success.

Despite the success—billions of barrels have been recovered by this type of EOR—even more hard-to-recover oil remains. Meyer and Attanasi (2003) report that recoverable heavy oil and bitumen resources are almost 1,000 billion barrels, or approximately twice the amount of recoverable light oil. Much of this target is beyond the limits of current technology; hence, thermal methods are constantly evolving to meet these challenges. This chapter touches on these new technologies.

We can give no more than an overview of these scientifically interesting and complex processes. Several texts (White and Moss 1983; Burger et al. 1985; Boberg 1988; Butler 1997) and a monograph (Prats 1982) are available on thermal flooding alone. There are also extensive treatments in reservoir-engineering texts (Gates 2011). Our intent is to apply the twin bases of this text—phase behavior and fractional-flow theory—to thermal methods in some detail. In addition, we deal with the important ancillary topic of heat loss.

This chapter is organized differently from the others, partly because of the many different processes available. We begin with a discussion of viscosity reduction, followed by an overview of the various processes. The bulk of the chapter focuses on mass and

heat transfer specifically directed to thermal methods. This section could constitute a treatment of heat transfer in general because virtually every form of energy transfer occurs in thermal processes. The chapter concludes by returning to discuss the specific processes.

Thermal methods rely on several displacement mechanisms to recover oil, but the most important is the reduction of crude viscosity with increasing temperature. We can draw several important conclusions from [Fig. 11.1](#), a plot of crude kinematic viscosity ($v_2 = \mu_2/\rho_2$) vs. temperature.

Crude kinematic viscosity decreases dramatically with a rise in temperature. This effect reflects principally the change in dynamic viscosity μ_2 because crude density changes relatively little with temperature. For example, a heavy crude (10–20° API) that undergoes a temperature increase from 300 to 400 K, which is easily obtainable by thermal methods, will produce a viscosity well within the flowing range (less than 10 mPa·s). (The previous sentence begins a practice of using the words *light* and *heavy* for nonviscous and viscous fluids, even though light and heavy, strictly speaking, refer to density. Because there usually exists a correlation between viscosity and density and the usage is thoroughly ingrained, the authors hope that there is no confusion.) [Fig. 11.1](#) greatly compresses the vertical axis simply to plot the observed changes on one scale.

For lighter crudes, the viscosity reduction is less. Therefore, thermal methods are not nearly as advantageous for these crudes, particularly because waterflooding would probably be an attractive alter-native. The viscosity reduction for very heavy crudes (less than 10° API) is substantial, but still not enough to make them flow economically. Therefore, there are practical limits on both viscosity extremes.

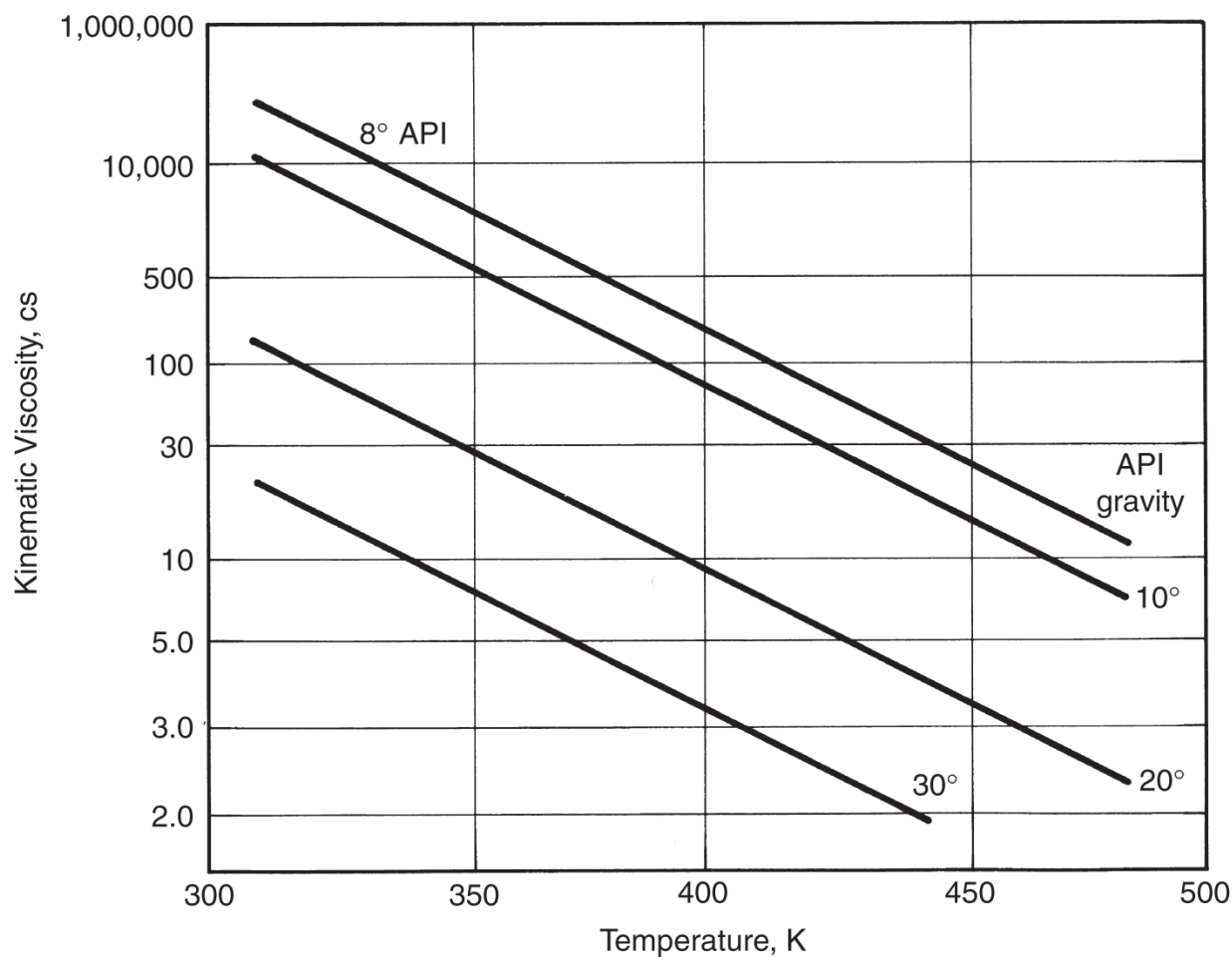


Fig. 11.1—Effect of temperature on crude-oil viscosity [adapted from Farouq Ali (1974)].

11.1 Process Variations

All thermal-recovery processes move or transport energy (usually heat) into or through a reservoir to recover crude. The basic heat-transfer mechanisms are:

Convection. Convection is the transfer of heat by a moving fluid. When the flow is caused by potential (pressure) differences, the convection is said to be *forced*. If it is caused by density differences induced by temperature changes, it is *free* convection. Convection is normally the most important heat-transfer mechanism.

Conduction. Conduction occurs in the absence of fluid movement (e.g., through a tube wall) in the solid portion of a

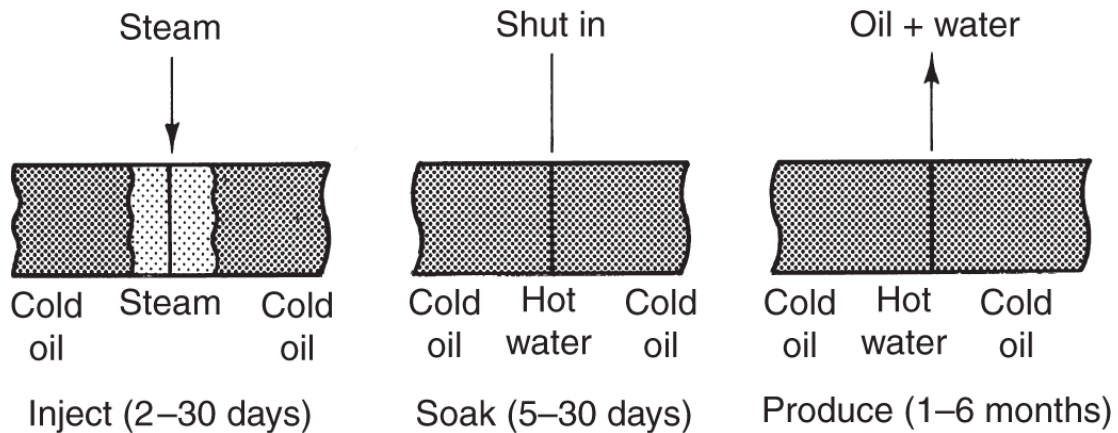
reservoir, or to adjacent strata. It is heat transfer on a molecular level.

Radiation. Radiation is heat transfer that occurs in a nonmaterial or *photon* phase (Bird et al. 2002). Radiation can occur in the absence of a material phase, either solid or liquid, or it can occur with flow of a material phase, in which case some of the radiation is adsorbed into the material phase, raising its temperature

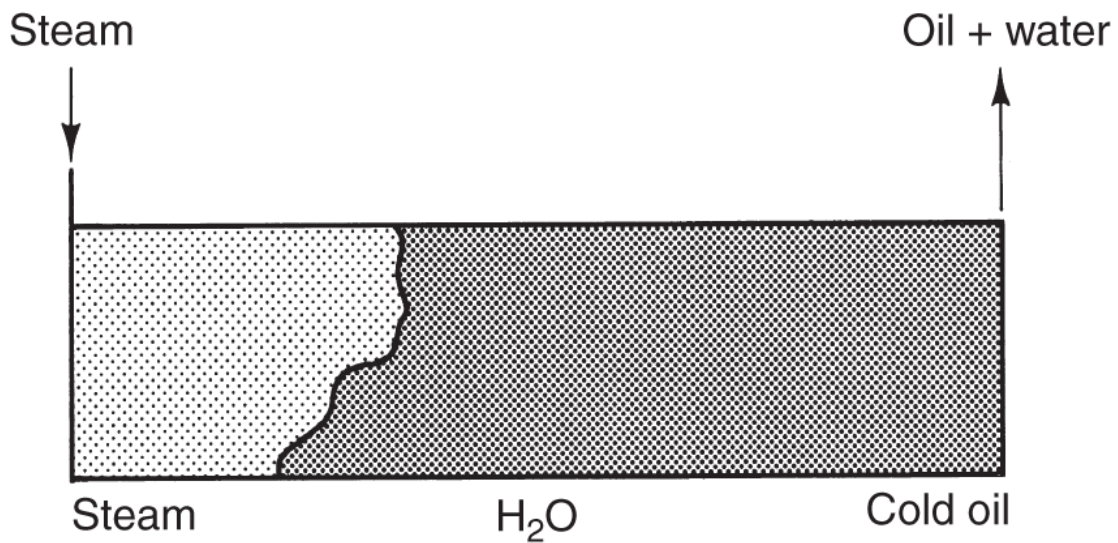
There are many ways to introduce heat into a reservoir. Most of these involve introducing steam.

Steam Soak. In a steam soak (also known as a cyclic stimulation or huff-n-puff), steam is introduced into a well, and then the well is returned to production after a brief shut-in period ([Fig. 11.2a](#)). The steam heats up a zone near the well and also provides some pressure support for subsequent production. The shut-in or soak period enables thermal gradients to equalize, but should not be long enough for the pressure to escape. During shut-in, all the injected steam condenses, and the well produces a mixture of hot water and oil. One great advantage of a steam soak is that all the wells can be producing nearly all the time, the injection and soak periods usually being short.

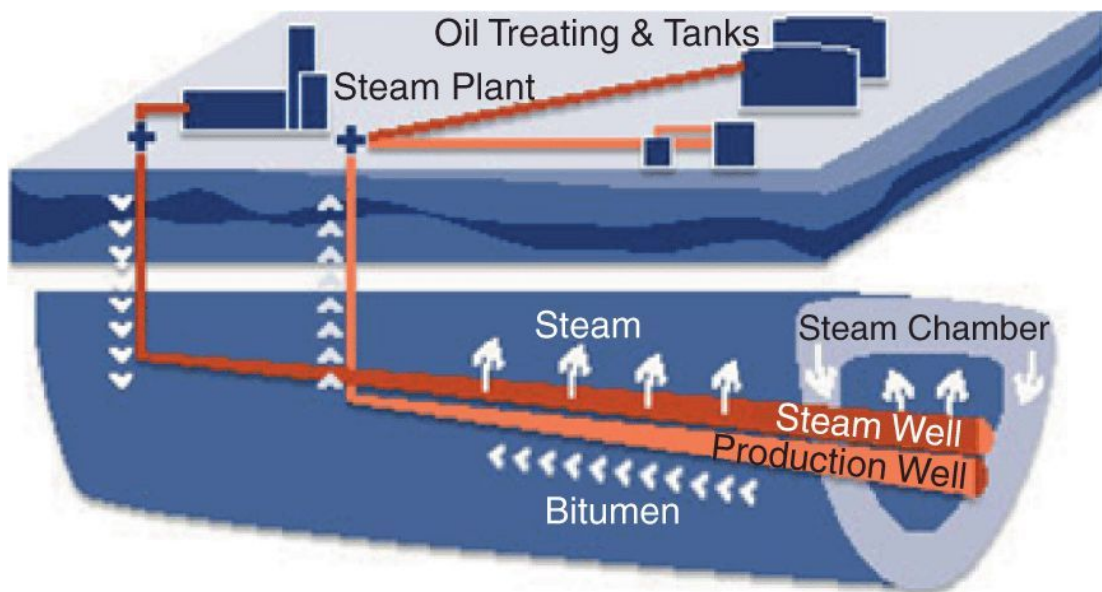
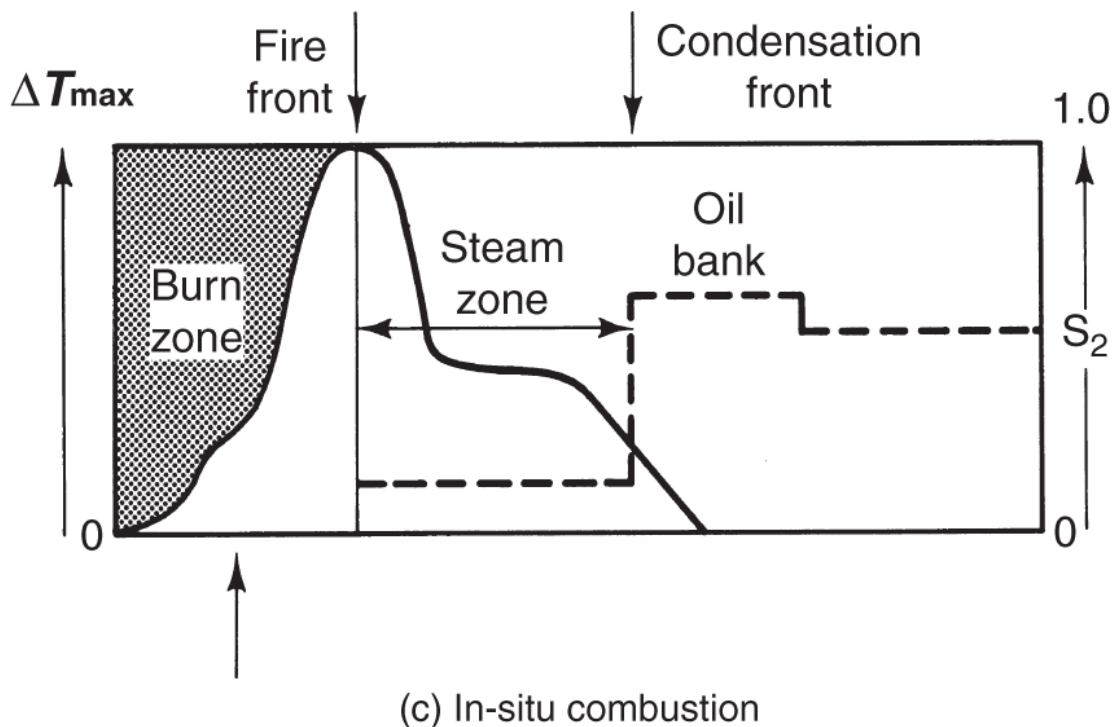
Steamdrive. A steamdrive uses at least two sets of wells, those into which steam is injected and those from which oil is produced ([Fig. 11.2b](#)). A steamdrive usually results in higher ultimate recoveries than a steam soak because it penetrates more deeply into the reservoir than steam soaks. For the same reason, well spacing need not be as close in drives as in soaks for equivalent oil recovery. The close spacing partially offsets the disadvantage of sacrificing some of the wells to injection. Because steamdrive is present to some extent in all thermal processes, we will focus on it in later analyses.



(a) Steam soak or huff-n-puff



(b) Steamdrive



(d) Steam-assisted gravity drainage (SAGD)

Fig. 11.2–Process variations for thermal method: (a) steam soak or huff-n-puff; (b) steamdrive; (c) in-situ combustion [adapted from Prats (1982)]; (d) Steam-assisted gravity drainage (SAGD).

In-Situ Combustion. Fig. 11.2c shows a schematic of a forward in-situ combustion process. The process injects some form of

oxidant (air or pure oxygen) into the formation. The mixture then spontaneously ignites (or ignition is induced), and subsequent injection propagates a fire or burn zone through the reservoir. The fire zone is only a meter or so wide, but it generates very high temperatures. These temperatures vaporize connate water and a portion of the crude, both of which are responsible for some oil displacement. The vaporized connate water forms a steam zone ahead of the burn front, which operates very much like a steamdrive. The vaporized oil consists mainly of light components that form a miscible displacement. The reaction products of high-temperature combustion can also form an in-situ carbon dioxide (CO_2) flood. In-situ combustion processes are sometimes called high-pressure air injection (HPAI).

Steam-Assisted Gravity Drainage (SAGD) (Butler 1982). [Fig. 11.2d](#) shows a schematic of the SAGD process. This process is like both steam soak and steamdrive in that heat, carried through steam, is the recovering fluid. However, SAGD is unlike the previous two in several important respects:

- SAGD uses horizontal rather than vertical wells.
- The horizontal wells are in injector/producer pairs that are closely spaced.

Both items make SAGD different from any other thermal method, and indeed different from any other process covered in this text. SAGD is a singular example of the use of a combination of technologies (in this case, steam injection and horizontal wells) to recover oil.

Closely spaced injectors and producers (they are usually on the order of 10 m apart in SAGD) would be anathema to the other EOR processes discussed here because such close well spacing would result in early breakthrough and extensive bypassing of oil. The key to the success of SAGD is that the main recovery mechanism is buoyancy (because of density differences) rather than viscous driving forces. You will recall from [Chapter 5](#) that in 1D flow, the

competition between buoyancy and viscous forces is expressed through a gravity number as

$$N_g^0 = \frac{k_v k_{r2}^0 \Delta \rho g}{\mu_2 u}.$$

Buoyancy is promoted when this number is large, or when u is small and/or k_v is large. A low velocity is ensured by the length of the wells (often exceeding 10,000 ft), which accumulates the very low velocities, resulting in flow. The process works best when k_v is large.

For most cases, viscosity reduction is by far the most important cause of additional oil recovery by thermal methods, but other mechanisms can also be important [e.g., distillation, miscible displacement, thermal expansion, wettability changes, cracking, and reduced oil/water interfacial tension (IFT)]. The relative importance of each mechanism depends on the oil being displaced and the process. Cracking is relatively unimportant in steam processes with their relatively low temperatures, but it is quite important during in-situ combustion. Thermal expansion and distillation become more important as the API° of the crude decreases.

Another class of thermal processes seeks to introduce heat through a reservoir using electromagnetic energy (Karanikas 2012). [**Fig. 11.3**](#) illustrates one of these processes. Although heat is introduced into the reservoir here, steam plays a minor role, and in fact can be deleterious because boiling water is a source of heat loss.

The in-situ conversion (ISC) process is different in other ways. In ISC, the intent is not so much to decrease viscosity as it is to convert the hydrocarbon chemically from a highly viscous material (tar sands and bitumen are the usual targets here) with a high carbon-to-hydrogen ratio to a much more malleable (and valuable) product with a low carbon-to-hydrogen ratio. The process resembles a subsurface refinery in which high-quality product (e.g., kerosene) is produced instead of crude. Viscous crudes form as a result of several

degradation mechanisms occurring over a long time. ISC intends to reverse this process over a short time period through heating.

In Fig. 11.3, energy is injected into a reservoir through a series of closely spaced resistive-heater wells. The combined effect of these closely spaced vertical wells is to accumulate energy over large volumes of a reservoir so that thermal cracking can occur. Other ways to introduce energy into a reservoir include resistive heating between subsurface anodes and cathodes, inductive heating, use of a heat-transfer fluid, and antennas (Carrazales 2010; Callarotti 2002).

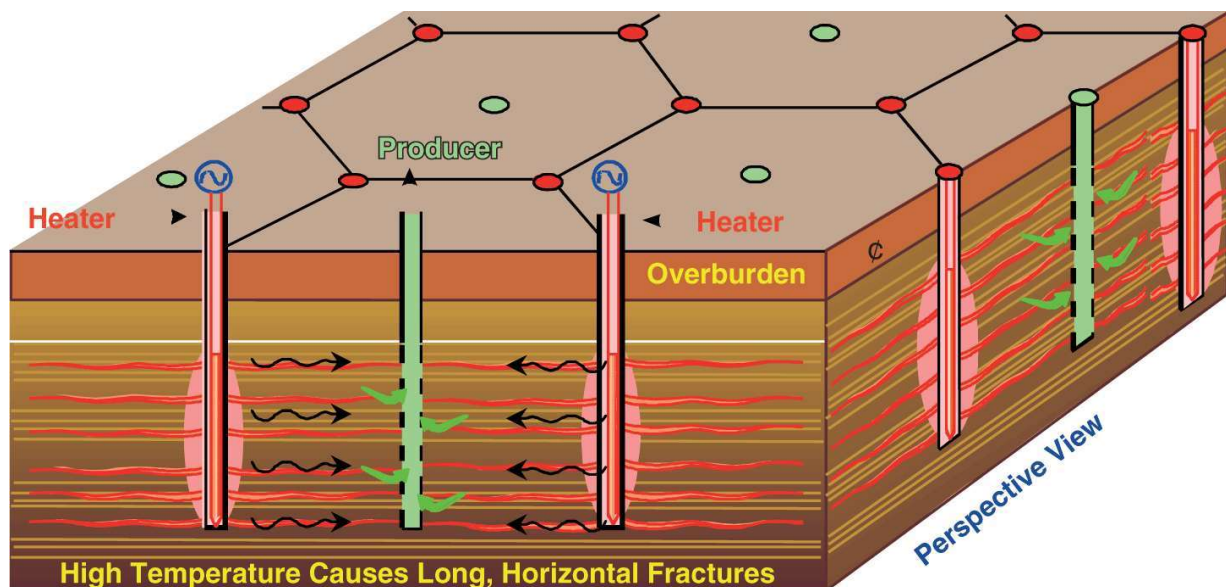


Fig. 11.3—Schematic of the in-situ conversion (ISC) process (Karanikas 2012).

11.2 Physical Properties

Elucidating the mechanisms of thermal methods begins with understanding the thermodynamic and transport properties of water and crude. We review these properties and their temperature dependence in this section. The most important water properties for this treatment are the steam/water phase envelope, steam quality, and latent heat of vaporization. For crudes, the most important property is the temperature dependence of viscosity.

11.2.1 Water Properties. The temperature rises in a thermal flood because additional energy is introduced or generated in the

reservoir. In both cases, water plays a central role. The following paragraphs review water properties; you will notice parallels to the generic treatment of phase behavior in [Chapter 4](#).

[Fig. 11.4](#) shows the vapor pressure of water from subatmospheric pressure to its critical point. Remember that the vapor pressure is the value of pressure (or temperature) at which a pure component (here water) changes phase (here, liquid to vapor) at a fixed value of temperature (pressure). The figure also shows the operating range for several successful steamdrives; operating pressures tend to be lower than for chemical methods and much lower than for solvent methods. Thermal methods are intrinsically low-pressure processes. As we will see in the following, the properties of saturated water are important to the efficiency of steam methods, and, therefore, the diagram also shows the range of temperatures—320–660°F (433–622 K)—for these methods.

[Fig. 11.5](#) shows the pressure-specific volume diagram for water. The saturated vapor curve on the right of the envelope shows that steam density is much lower than saturated liquid density except very near the critical point. This figure contains lines indicating steam quality, a property discussed later.

This energy content of water is well approximated by the enthalpy. [Fig. 11.6](#) shows a pressure/enthalpy diagram for water. This diagram is analogous to the pressure/composition diagrams discussed in Section 4.1, with enthalpy being the composition variable. [Fig. 11.6](#) illustrates several important landmarks.

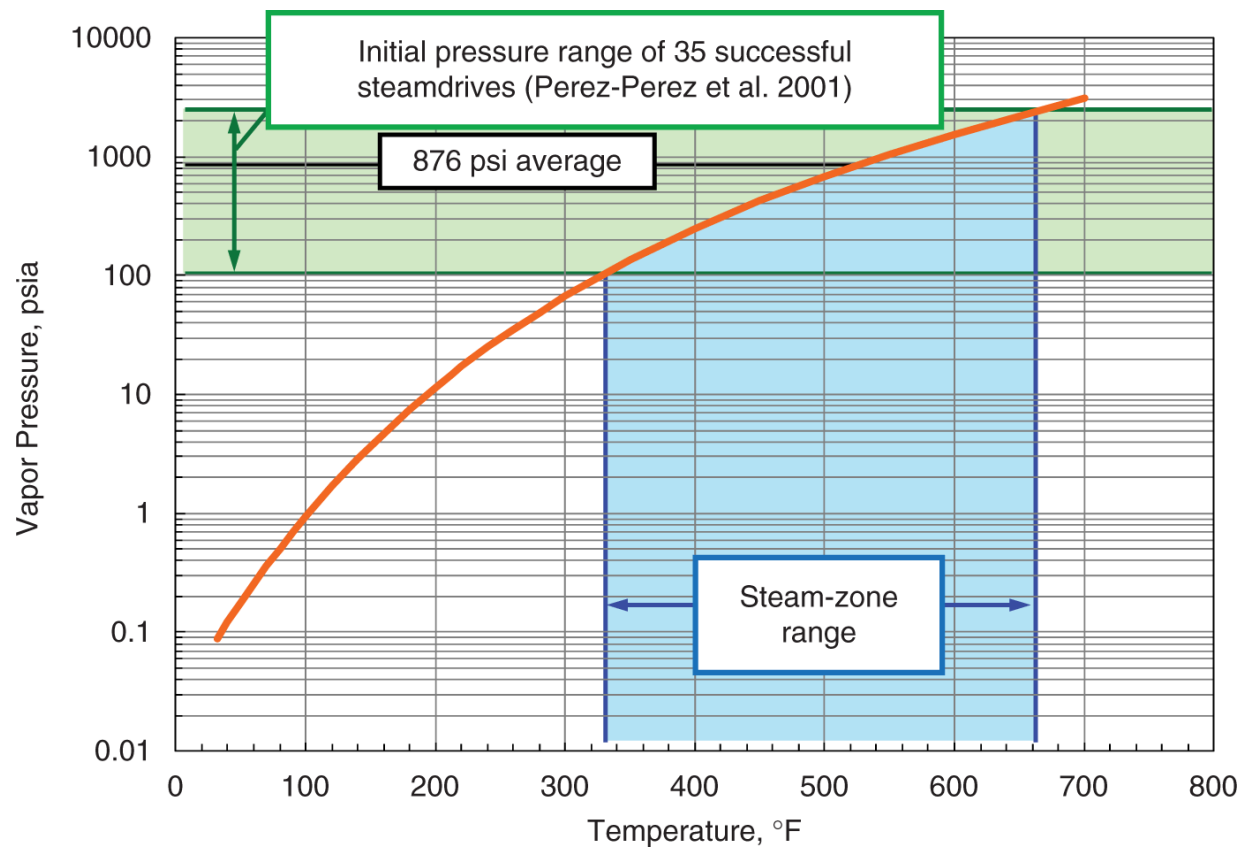


Fig. 11.4—Vapor-pressure diagram of water.

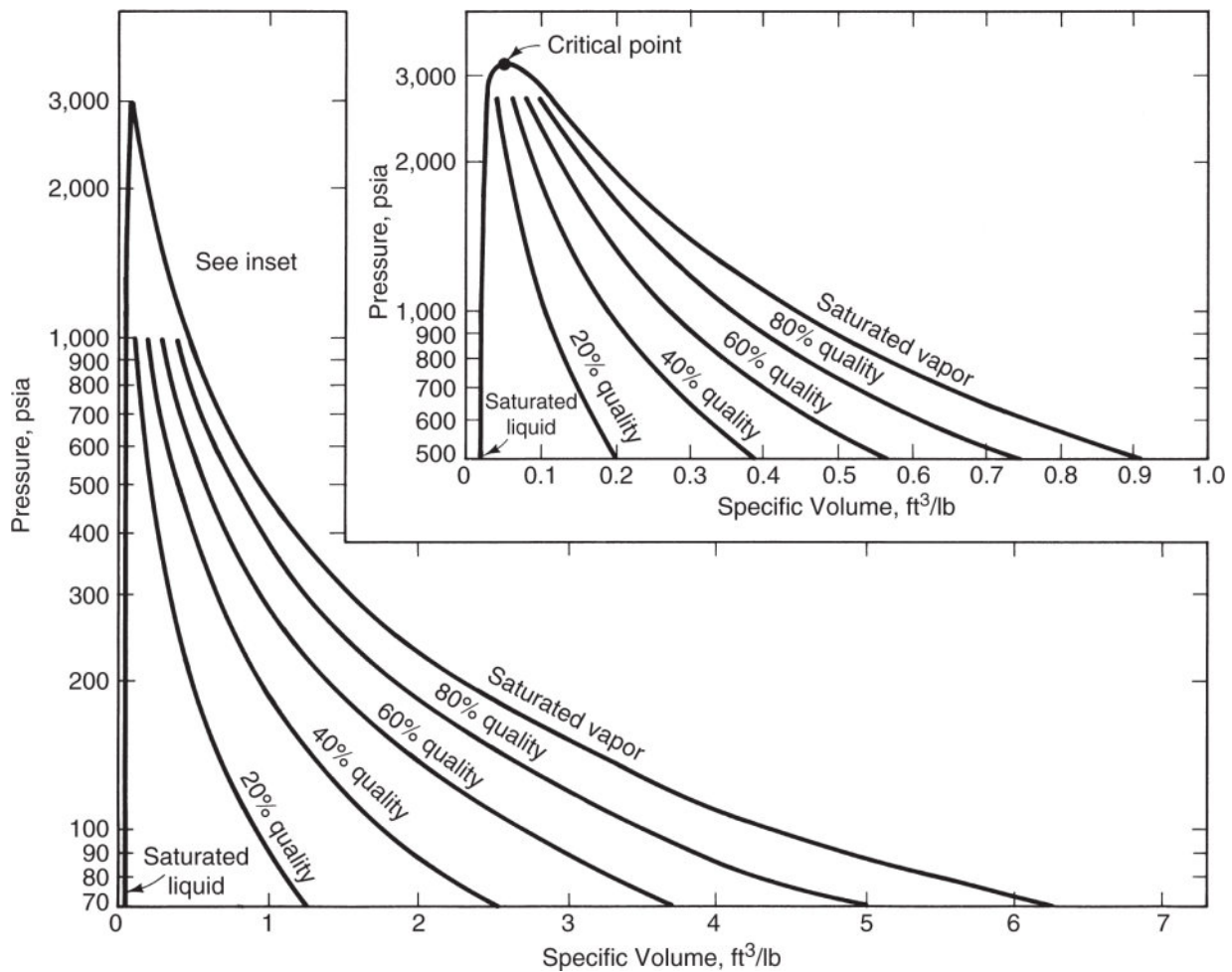


Fig. 11.5—Pressure vs. specific-volume diagram for water (Bleakley 1965).

1. Two-phase envelope. The envelope defines the region of two-phase behavior, as does the envelope on the pressure/molar volume diagram in [Fig. 4.2](#). The left boundary is the bubblepoint curve, and the right boundary is the dewpoint curve. To the left and right of the envelope are the supercooled liquid and superheated vapor (steam) regions, respectively. Within the two-phase region, temperature depends on pressure according to [Fig. 11.4](#). These are *saturated* temperature and pressure, respectively.
2. Steam quality. Steam quality y is the amount of the total vapor, by weight, expressed as a fraction (or a percentage) of the mass of liquid plus vapor,

Quality is normally reported as a percentage, but, like fluid saturation (the S in Eq. 11.1), is always used in calculations as a fraction. The quality lines within the two-phase envelope represent the relative amount of the total mass that is steam. Lines of constant temperature (only one is illustrated) in [Fig. 11.6](#) fall steeply in the liquid region, are constant across the two-phase envelope, and then fall steeply again in the steam region.

3. Saturated liquid. A liquid is *saturated* if it exists at the temperature and pressure at which steam can be generated. The saturated-liquid curve represents 0% steam quality.
 4. Saturated vapor. Saturated vapor is water at the temperature and pressure at which exactly 100% of the water present has been converted to a vapor.

Both phases in the two-phase region are saturated.
 5. Latent heat. Latent heat of vaporization L_V is the quantity of heat added to a given mass of saturated water (0% quality steam) to convert it to saturated vapor (100% quality steam) at constant temperature. The heat is *latent* because the temperature of the system does not change as the liquid is converted to vapor. On an enthalpy/pressure diagram, latent heat is the difference in the x -coordinates between the dewpoint and bubblepoint curves in [Fig. 11.5](#) at a particular pressure. The latent heat vanishes at the critical point of water, 3206.2 psia and 705.4°F (21.8 MPa and 647 K). The location of the critical pressure is important in steam processes. We will show in Example 11.3 that the velocity of a steam front slows at high pressure because latent heat vanishes.
 6. Sensible heat. Sensible heat is the quantity of heat that must be added to a given mass of water to raise its temperature without changing its phase. This quantity is *sensible* because a thermometer in the water will sense a temperature increase as heat is added (at a constant pressure) until steam

generation begins. Sensible heat is a product of a heat capacity and a temperature difference.

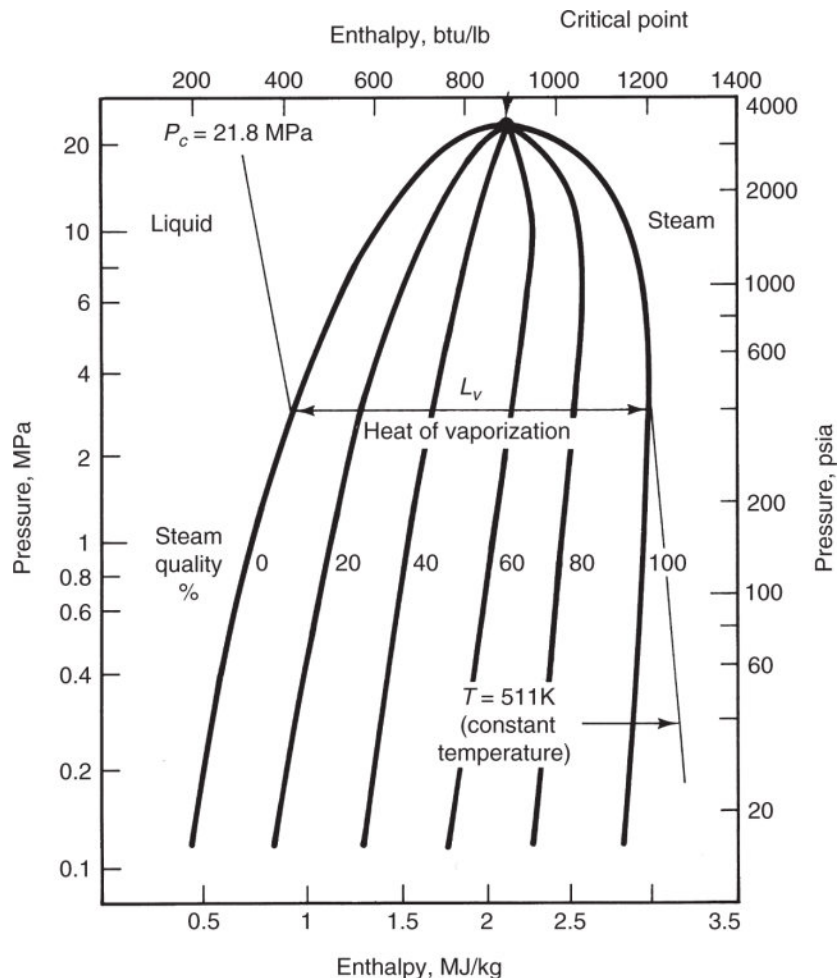


Fig. 11.6—Enthalpy vs. pressure diagram for water [adapted from Bleakley (1965)].

Thermodynamic properties, types of which are the two previous diagrams, are usually taught with temperature changing rather than pressure, as illustrated in [Fig. 11.7](#). In this figure, superheated vapor is above the two-phase envelope and the supercooled region below. Constant- T lines within the two-phase region are vertical. As the figure illustrates, the change in enthalpy with temperature is the heat capacity,

$$C_p = \left(\frac{\partial H}{\partial T} \right)_P .$$

This can be either per mole or per mass depending on the units of H . If it is the latter, C_p is often called the *specific heat*. You can see from the plot that the heat capacity is nearly independent of both T and P (the slopes are constant) in the liquid. This is essentially the case in the vapor regions, except in the region near the critical point. We will assume constant heat capacities in much of what we do below.

The physical properties in [Figs. 11.4](#) through [11.7](#) appear in steam tables (Keenan et al. 1969 and online). You should use these for precise work. Often reading information from these figures is sufficient.

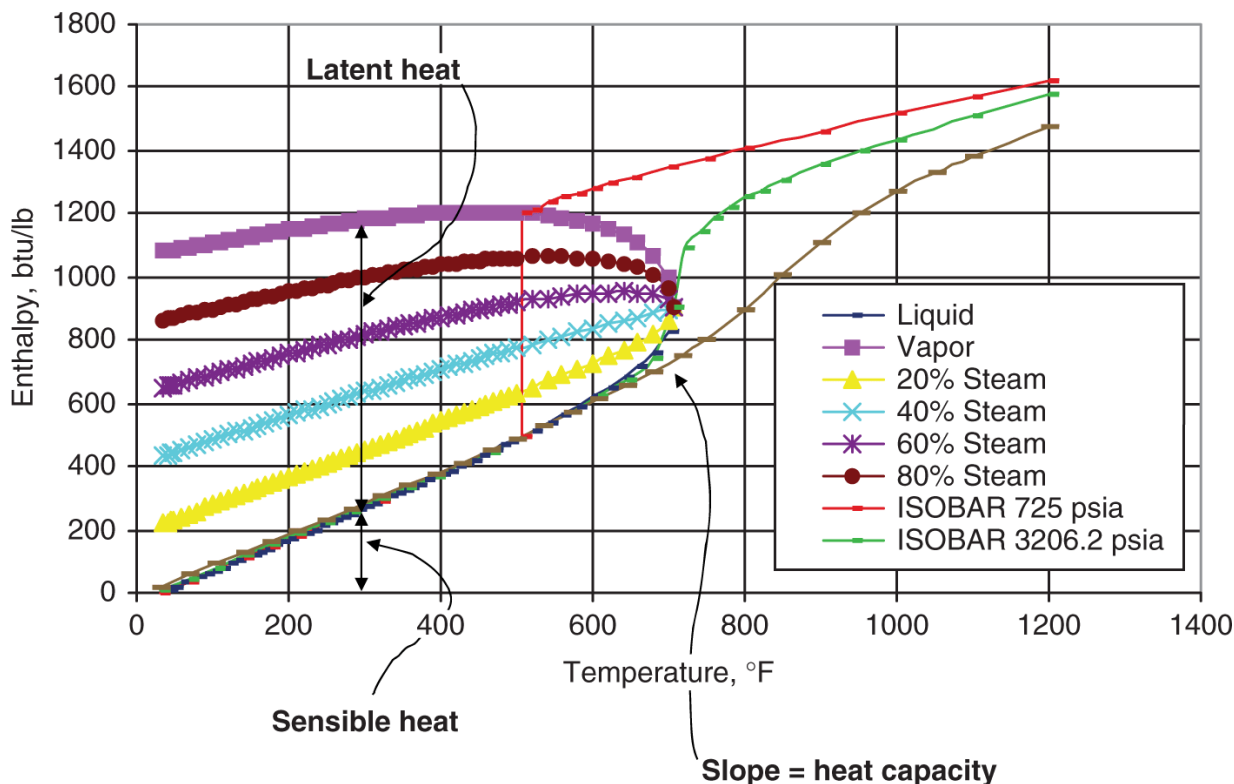


Fig. 11.7—Enthalpy-temperature diagram for water.

Example 11.1. Enthalpy Changes. Use [Fig. 11.7](#) in the following:

- Estimate the enthalpy content in 1 lbm of water at $T = 600^\circ\text{F}$ and $P = 725 \text{ psia}$. What is the state of the fluid at this point?

The fluid is superheated vapor or steam. Directly from the graph, we have $H_{13} = 1,300$ Btu. Like all thermodynamic quantities, this number is relative to an arbitrary zero. Recall that the subscript 3 means vapor phase here.

- b. Relative to the enthalpy of saturated water at the same T , how much of this heat is sensible and how much is latent?

Also from the graph, the enthalpies of saturated liquid (sl) and saturated vapor (sv) are \dots , so that the enthalpy change from the conditions of Part (a) is \dots , of which \dots is latent heat and the remainder, \dots , is sensible heat. Note that the pressure had to be increased substantially to condense the fluid.

- c. If the enthalpy of the fluid is $H_1 = 900$ Btu, what is the steam quality? From [Fig. 11.6](#), $y = 55\%$ quality steam. Remember that all the quantities discussed here are at equilibrium.

One of the disadvantages of these graphical representations is that it is difficult to show enthalpy variations with both T and P . Farouq Ali (1974) has fitted approximate analytical expressions to water properties ([Table 11.1](#)).

TABLE 11.1—THERMAL PROPERTIES OF WATER [ADAPTED FROM FAROUQ ALI (1974)]

Quantity x	English, $P [=]$ psia			Limit psia	Quantity x	SI, $P [=]$ MPa			Percent error
	a	b	aP^b			a	b	Limit MPa	
Saturation temperature ($^{\circ}$ F)	115.1	0.225	300		Saturation temperature -256 (K)	197	0.225	2.04	1
Sensible heat (Btu/lbm)	91	0.257	1,000		Sensible heat (MJ/kg)	0.796	0.257	6.80	0.3
Latent heat (Btu/lbm)	1,318	-0.0877	1,000		Latent heat (MJ/kg)	1.874	-0.0877	6.80	1.9
Saturated steam enthalpy (Btu/lbm)	1,119	0.0127	100		Saturated steam enthalpy (MJ/kg)	2.626	0.0127	2.04	0.3
Saturated steam specific volume (ft ³ /lbm)	363.9	-0.959	1,000		Saturated steam specific volume (m ³ /kg)	0.19	-0.959	6.80	1.2

Note: $x = aP^b$.

Example 11.2. Table Comparisons. The expressions in [Table 11.1](#) are very handy, and, therefore, it is of interest to see how well these

equations predict the actual properties. We will use the same conditions as in Example 11.1. The pressure $P = 725$ psi is well outside the limit of the saturation temperature and steam enthalpy in [Table 11.1](#).

- Estimate the saturation temperature. From the table (using English units), $T_s = aP^b = 115.1(725 \text{ psi})^{0.225} = 507^\circ\text{F}$ compared to $T = 510^\circ\text{F}$ from [Fig. 11.7](#).
- Estimate the latent heat of vaporization. From [Table 11.1](#), $L_v = aP^b = 1,318(725 \text{ psi})^{-0.0877} = 740 \frac{\text{Btu}}{\text{lb}_m}$, compared to $690 \frac{\text{Btu}}{\text{lb}_m}$.
- Estimate the saturated steam enthalpy. Again, $H_{11}^s = aP^b = 1,119(725 \text{ psi})^{0.012} = 1,211 \frac{\text{Btu}}{\text{lb}_m}$, compared to $1,190 \frac{\text{Btu}}{\text{lb}_m}$.
- Estimate the saturated-steam specific volume. $v_1^{sv} = aP^b = 363.9(725 \text{ psi})^{-0.959} = 0.657 \frac{\text{ft}^3}{\text{lb}_m}$, compared to $0.69 \frac{\text{ft}^3}{\text{lb}_m}$ from Fig. 11.4.

Even when outside the recommended ranges, the accuracy of [Table 11.1](#) is sufficient for most engineering purposes.

11.2.2 Crude-Oil Properties. Curiously, there seems to be no universal definition for what constitutes a heavy oil. The United States Geological Survey (USGS) definitions are given below:

- *Light or conventional oil*: Crude with an API gravity $>22^\circ$ and a viscosity of $\mu_2 < 100 \text{ mPa}\cdot\text{s}$.
- *Heavy oil*: Crude with an API gravity $<22^\circ$ and $\mu_2 > 100 \text{ mPa}\cdot\text{s}$.
- *Extra-heavy crude*: The portion of heavy crude with API gravity $<10^\circ$ and $\mu_2 > 10,000 \text{ mPa}\cdot\text{s}$.

All the quoted viscosities are at reservoir conditions. The USGS also adds criteria on the basis of asphaltene and sulfur content (Meyer and Attanasi 2003).

- *Natural bitumen*: Also called tar or oil sands; these are extra-heavy crudes with $\mu_2 > 1,000,000 \text{ mPa}\cdot\text{s}$.

Easily the most important crude-oil property for thermal flooding is the viscosity dependence on temperature. As for most liquids, the Andrade (1930) equation captures this dependence:

$$\mu_2 = A e^{B/T}, \dots \quad (11.2a)$$

where T is in absolute degrees. A and B are empirical parameters for which the values are determined from two viscosity measurements at different temperatures. For extrapolation or interpolation, Eq. 11.2a indicates that a semi-log plot of viscosity vs. T^{-1} should be a straight line.

If only one measurement is available, a coarse estimate of viscosity can be obtained from [Fig. 11.8](#). This single-parameter correlation assumes that viscosity change is a universal function of temperature change. To use the plot, enter the vertical axis with the known viscosity (4.38 mPa·s in this case), find the x-axis coordinate, move to the right by the temperature increase (101.6°C), and then return to the curve. The y-axis reading is the desired viscosity.

Another representation that is useful in derivation work was given by Butler (1997) as

$$\frac{v_1}{v} = \left(\frac{T - T_2}{T_1 - T_2} \right)^m, \dots \quad (11.2b)$$

where 1 and 2 are the reference conditions, usually the saturated-steam and reservoir conditions, respectively, and v is the kinematic viscosity.

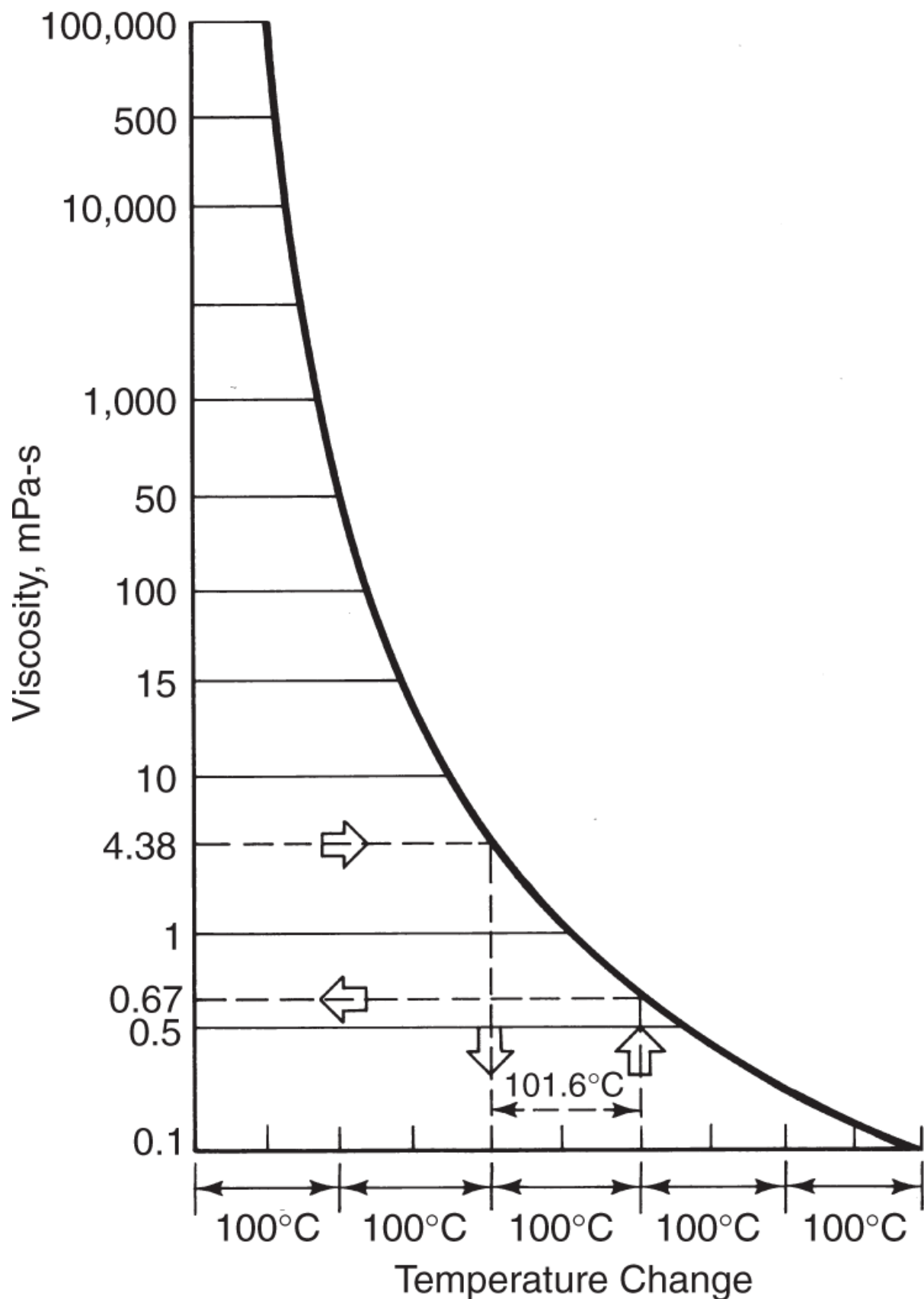


Fig. 11.8—Single-parameter viscosity correlation (Lewis and Squires 1934).

Several other crude-oil properties, such as specific heat, volumetric heat capacity, and thermal conductivity, are functions of temperature. Empirical equations to predict these properties include the Gambill (1957) equation for specific heat,

$$C_{p2} = \frac{0.7 + 0.0032T}{\rho_2^{0.5}}, \dots \dots \dots \quad (11.2c)$$

where C_{p2} is in $\text{kJ/kg}\cdot\text{K}$, T in K, and ρ_2 in g/cm^3 , and the thermal conductivity (Maxwell 1950) is

$$k_{T2} = 0.135 - 2.5 \times 10^{-5}T. \dots \dots \dots \quad (11.3)$$

k_{T2} in this equation has units of $\text{kJ/m}\cdot\text{h}\cdot\text{K}$. Eq. 11.3 is based on correlations for heavy crude fractions. These estimates are generally accurate to within 5%. For more details on these correlations, see the original references.

Eqs. 11.2 and 11.3 make it possible to estimate the *thermal diffusion coefficient*,

$$K_{T2} = \frac{k_{T2}}{\rho_2 C_{p2}}, \dots \dots \dots \quad (11.4)$$

for crudes. This quantity has units of m^2/s , as do the dispersion coefficients in Eq. 2.57.

11.2.3 Solid Properties. The total thermal conductivity of an unconsolidated sand-filled medium with a single phase j is

$$k_T = 0.0149 - 0.0216\phi + 8.33 \times 10^{-7}k - 10^{-4} \left(\frac{D_{90}}{D_{10}} \right) + 7.77D_{50} + 4.188k_T + 0.0507k_{Ts}. \dots \dots \quad (11.5)$$

The parameters in this equation have their usual meanings, except that D_{10} and D_{90} are particle diameters smaller than 10 and 90% of the total sample by weight. The units on the total, fluid j , and solid

(k_{Tt}, k_{Tj}, k_{Ts}) thermal conductivities are J/m-s-K, the permeability k is in μm^2 , and the median grain size D_{50} is in mm.

For fluid-filled consolidated sandstones, the analogous relation is

$$\frac{k_n}{k_{Td}} = 1 + 0.299 \left[\left(\frac{k_{Tj}}{k_{Ta}} \right)^{0.33} - 1 \right] + 4.57 \left(\frac{\phi}{1-\phi} \frac{k_{Tj}}{k_{Td}} \right)^{0.482} \left(\frac{\rho}{\rho_s} \right)^{-4.30}, \dots \quad (11.6)$$

where the subscripts a and d refer to air and dry rock. ρ is the density of the liquid-saturated rock. The thermal conductivities in Eqs. 11.5 and 11.6 are determined at a reference temperature of 293 K; they are rather weak functions of temperature, but corrections are given in Somerton (1973).

The volumetric heat capacity appears in the energy balances for thermal processes. It is defined for all phases, including the solid, as

$$M_{Tj} = \rho_j C_{pj}, \quad j = 1, \dots, N_p, s. \dots \quad (11.7)$$

We have encountered this quantity before in Eq. 2.83, which defined a total volumetric heat capacity.

Table 11.2 gives representative values of density, specific heat, thermal conductivity, and thermal diffusion coefficient for selected media. These values are appropriate for rough estimates of the rock-fluid thermal properties or for comparison to more refined estimates from Eqs. 11.5 through 11.7. The heat capacity of the solid phase varies relatively little with the type of solid, but the thermal conductivity can vary by a factor of two (compare the values for limestone and siltstone). The origin of the phrase, “heat can go where fluids cannot”, derives from the latter statement. The spatial variability of most nonthermal properties, permeability in particular, is far greater than this.

TABLE 11.2—DENSITY, SPECIFIC HEAT, THERMAL CONDUCTIVITY, AND THERMAL DIFFUSION COEFFICIENT OF SELECTED ROCKS [ADAPTED FROM FAROUQ ALI (1974)]

<u>Rock</u>	<u>Bulk Density (g/cm³)</u>	<u>Specific heat (kJ/kg-K)</u>	<u>Thermal conductivity (J/s-m-K)</u>	<u>Thermal diffusion coefficient (mm²/s)</u>
Dry				
Sandstone	2.08	0.729	0.831	0.55
Silty sand	1.90	0.801	(0.66)	(0.43)
Siltstone	1.92	0.809	0.649	0.42
Shale	2.32	0.761	0.989	0.56
Limestone	2.19	0.801	1.611	0.92
Fine sand	1.63	0.726	0.593	0.50
Coarse sand	1.74	0.726	0.528	0.42
Water-saturated				
Sandstone	2.27	0.999	2.610	1.15
Silty sand	2.11	1.142	(2.50)	(1.04)
Siltstone	2.11	1.094	(2.50)	(1.08)
Shale	2.38	0.844	1.600	0.79
Limestone	2.38	1.055	3.360	1.34
Fine sand	2.02	1.344	2.607	0.96
Coarse sand	2.08	1.249	2.910	1.12

Note: Values in parentheses are estimated.

Example 11.3. Heat Losses to Rock and Water. Later sections deal with various forms of heat losses, but we can introduce the largest source of heat loss now.

The total internal energy term in Eq. 2.3-1 is

$$\rho \hat{U} = \phi \sum_{j=1}^{N_p} \rho_j S_j \hat{U}_j + (1 - \phi) \rho_s \hat{U}_s.$$

Away from the critical point of water, internal energies and enthalpies are nearly equal, and therefore the preceding equation becomes

$$\rho \hat{H} = \phi (\rho_1 S_1 \hat{H}_1 + \rho_2 S_2 \hat{H}_2) + (1 - \phi) \rho_s \hat{H}_s.$$

We will work the hot-water case here in which the medium (the solid, subscript *s*) of porosity ϕ contains only water ($i = 1$) and oil ($i = 2$). You can tackle the steam case in Exercise 11.2.

Now, the fraction of heat that resides in the crude is

$$F_{\text{Heat}} = \frac{\phi \rho_2 S_2 \hat{H}_2}{\phi (\rho_1 S_1 \hat{H}_1 + \rho_2 S_2 \hat{H}_2) + (1 - \phi) \rho_s \hat{H}_s}.$$

Because there is no steam, the preceding equation can be written as

$$F_{\text{Heat}} = \frac{\phi \rho_2 S_2 C_{p2} (T - T_{\text{ref}})}{\phi [\rho_1 S_1 C_{p1} (T - T_{\text{ref}}) + \rho_2 S_2 C_{p2} (T - T_{\text{ref}})] + (1 - \phi) \rho_s C_{ps} (T - T_{\text{ref}})},$$

where we have used the heat capacities discussed previously (assumed independent of T) and T_{ref} is a reference temperature. Using the volumetric heat capacities from Eq. 2.83, this becomes

$$F_{\text{Heat}} = \frac{\phi S_2 M_{T2}}{\phi (S_1 M_{T1} + S_2 M_{T2}) + (1 - \phi) M_{Ts}}.$$

This ratio is mainly a function of the oil saturation S_2 and the porosity ϕ . Using typical values for the heat capacities ($M_{T1} = 3.97 \text{ MJ/m}^3 \cdot \text{K}$, $M_{T2} = 1.78 \text{ MJ/m}^3 \cdot \text{K}$, and $M_{Ts} = 2.17 \text{ MJ/m}^3 \cdot \text{K}$) yields the following values.

F_{Heat}	$\phi = 0.2$	$\phi = 0.3$
$S_1 = 0.2$	0.16	0.23
$S_1 = 0.5$	0.09	0.14

For a high-porosity, high- S_2 media, more than 20% of the heat resides in the oil. This value falls to less than 10% for tertiary floods in a low-porosity reservoir. These percentages also suggest guidelines for the best use of thermal methods: they are most

efficient in high-porosity reservoirs (where there is less rock to heat up) undergoing secondary flooding.

Considering the success of thermal methods, such small percentages of heat going into the crude are remarkable. The success of thermal methods, where so little of the heat actually resides in the oil (recall that we have not yet accounted for losses to the wellbore and adjacent strata), must be the result of the effectiveness of this method in reducing oil viscosity ([Fig. 11.1](#)).

11.3 Fractional Flow in Thermal Displacements

11.3.1 Propagation of Thermal Fronts. Noncombustion heat fronts can propagate in three ways: as hot water, as saturated steam, or as a noncondensable gas. Each has a characteristic velocity of propagation.

Let Fluid 3 displace Fluid 1 in a 1D medium with constant cross-sectional area. There are no other fluids in the medium. As always, Fluid 1 is cold water, but Fluid 3 can be hot water, noncondensable gas, or saturated steam. Fluid 3 has a higher temperature (T^+) than Fluid 1 (T^-), and in all cases, the displacement takes place without mixing. This means that neither the miscibility (or lack thereof) of the displacement nor its stability is at issue. We further assume that conduction is negligible (this eliminates heat losses to adjacent media), that displacement takes place at constant pressure, that the reference temperature for all enthalpies is T^- (that is, $H_{ii}^- = 0$), and finally, that all thermal properties are independent of temperature. These assumptions are the extension of the fractional-flow assumptions presented originally in [Chapter 5](#) for thermal floods.

The equations describing this displacement are the 1D versions of the mass and energy balances, Eqs. 2.11 and 2.36. These equations are hyperbolic and reducible with the above assumptions, and, therefore, we expect the methods introduced in several previous chapters to apply here also (see Section 5.6). Under these restrictions, energy and mass waves move at the same velocity. We

can express the front velocity as a multiple of the cold-water velocity u_1/ϕ .

On the basis of Eq. 5.41b, the front velocity is

$$v = \frac{1}{\phi} \left(\frac{\rho_3 u_3 - \rho_1 u_1}{\rho_3 - \rho_1} \right), \quad \dots \dots \dots \quad (11.8)$$

and on the basis of a shock velocity derived from the conservation of energy, the same velocity is

$$v = \frac{1}{\phi} \frac{\rho_3 u_3 H_3}{\rho_3 H_3 + \left(\frac{1-\phi}{\phi} \right) \rho_s H_s}. \quad \dots \dots \dots \quad (11.9)$$

The velocities in both equations are dimensional. Eq. 11.9 neglects all forms of energy other than thermal and assumes that enthalpy is equal to internal energy. $H_s = C_{ps}(T^+ - T^-) = C_{ps}\Delta T$ is the specific enthalpy of the solid. Three special cases follow from Eqs. 11.8 and 11.9.

Fluid 3 is Hot Water. In this case, $\rho_3 = \rho_1$, $H_3 = C_p \Delta T$, and Eq. 11.9 becomes

$$v_{HW} = \frac{1}{1 + \frac{1-\phi}{\phi} \frac{M_{Ts}}{M_{T3}}}, \quad \dots \dots \dots \quad (11.10)$$

where v_{HW} is the specific velocity of the front, normalized by $\frac{u_3}{\phi}$, the water flux. Eq. 11.10 has used the definition (Eq. 11.83) of volumetric heat capacity and Eq. 11.39, which for this case, gives $u_3 = u_1$, so that

$$v_{HW} = \frac{1}{1 + D_{HW}}, \quad \dots \dots \dots \quad (11.11)$$

where

is the retardation factor for the thermal front. Eq. 11.11 is a combination of the mass and energy balances. The velocity in Eq. 11.11 is independent of the temperature difference. For this case of incompressible flow, the heat fronts propagate more slowly than the tracer fronts, $v_{HW} = 1$. This slower propagation occurs because the thermal mass of the solid forces D_{HW} tends to be positive in much the same way as do the retardation factors for polymer and surfactant/polymer flooding in Eqs. 8.28a and 9.14.

Fluid 3 is Steam of Quality y . Here, we have $H_3 = C_{p1}\Delta T + yL_V$, where L_V is the latent heat of vaporization. Substituted into Eq. 11.9, this gives

Eliminating u_3/ϕ using Eq. 11.8 gives

where D_{SF} is the retardation factor for the steam front,

and h_D is a dimensionless latent heat,

h_D is the ratio of latent to sensible heat. Because $h_D \geq 0$, steam fronts ($\Delta T > 0$) move faster than hot-water fronts under equivalent conditions. In other words, L_V causes the front to propagate faster because it

stores heat better. Faster-moving heat fronts are more thermally efficient because the reservoir is contacted sooner and there is less time for heat losses to the under- and overburden. D_{SF} now depends on the temperature difference (through the $C_{p1}\Delta T$ term) and on pressure (through L_V). High-pressure steamfloods approach the hot-water limit because $L_V \rightarrow 0$ as the pressure approaches the critical point of water.

Example 11.4. Propagation of Thermal Fronts. Steam fronts have a larger velocity (are more efficient) than hot-water fronts for equivalent injected enthalpy, a fact that emphasizes the effect of pressure on thermal methods. Use the saturation temperature of [Fig. 11.4](#) and the enthalpy/pressure diagram of [Fig. 11.6](#) in this example.

We will consider two injections: saturated steam at a pressure of 2000 psia, and 50% quality steam at $P = 200$ psia. Both conditions have an injected enthalpy of approximately $\hat{H}_j = 620 \frac{\text{Btu}}{\text{lb}_m}$. The initial reservoir temperature is 85°F. We will use the volumetric heat capacities from the previous example and assume that the values for saturated water are the same at both pressures. From Eq. 11.12,

$$D_{HW} = \left(\frac{1-\phi}{\phi} \right) \frac{M_{Ts}}{M_{T1}} = \left(\frac{1-0.3}{0.3} \right) \left(\frac{2.17 \frac{\text{MJ}}{\text{m}^3\text{-K}}}{3.97 \frac{\text{MJ}}{\text{m}^3\text{-K}}} \right) = 1.28,$$

from which we can obtain $v_{HW} = \frac{1}{1+1.28} = 0.439$. This means that the hot-water front moves at less than one-half the velocity of a tracer front.

For the saturated-steam case, we must look up some values. [Fig. 11.5](#) gives $yL_v = (0.4)(3-0.9)\frac{\text{MJ}}{\text{kg}}$. We will need the saturated-steam temperature, which from [Fig. 11.4](#) is $T_s = 38^\circ\text{F}$, for which $\Delta T_s = (380-82)^\circ\text{F} = 166 \text{ K}$. Then

$$h_D = \frac{yL_v}{C_{p1}\Delta T} = \frac{(0.4)(2.1)\frac{MJ}{kg}}{\left(1\frac{Btu}{lb_m \cdot ^\circ F}\right)(298^\circ F)} \left\{ \frac{0.454 \text{ kg}}{1 \text{ lb}_m} \frac{1 \text{ Btu}}{10^{-3} MJ} \right\} = 3.2$$

and $D_{SF} = \frac{D_{HW}}{1+h_D} = \frac{1.28}{1+3.2} = 0.3$, which gives the final result of $v_{SF} = \frac{1}{1+D_{SF}} = \frac{1}{1+0.3} = 0.77$.

The value is twice that of a hot-water velocity, but still slower than a tracer velocity. This ordering persists over the entire pressure range up to the critical point; even the magnitude of the velocities is relatively insensitive to pressure.

In both cases, the input enthalpy was the same; it is the presence of the latent heat that causes steam to be more efficient. All steam-based processes operate more efficiently at low pressure because latent heat is larger.

The preceding equations give a way to confirm what was implicitly assumed earlier: that a steam front is self-sharpening. Let us start by combining Eqs. 11.14 through 11.16:

$$v_{SF} = \frac{1}{1+D_{SF}} = \frac{1}{1+\frac{D_{HW}}{1+h_D}} = \frac{1}{1+\frac{D_{HW}}{1+\frac{yL_v}{C_{p1}\Delta T}}}.$$

For a displacement of saturated water ($y = 0$) by 100% quality steam ($y = 1$), the range of velocities is

$$v_{SF}|_{y=0} = \frac{1}{1+D_{HW}}$$

for saturated water and

$$v_{SF} \Big|_{y=1} = \frac{1}{1 + \frac{D_{HW}}{1 + \frac{L_v}{C_{p1}\Delta T}}}$$

for saturated steam. Therefore, $v_{SF} \Big|_{y=0} < v_{SF} \Big|_{y=1}$, and the front is a shock because the larger steam qualities move faster than the smaller qualities. The converse would, of course, be true for saturated water displacing saturated steam. That the steam front is a shock accounts for much of the success of steam drives.

Fluid 3 is a Noncondensable Gas. This case is similar to the hot-water case except that $H_3 = C_{p3} \Delta T$. A similar procedure to the above yields

$$v_G = \frac{1}{1 + D_G}, \dots \quad (11.17)$$

where the retardation factor is now

$$D_G = \left(\frac{1-\phi}{\phi} \right) \frac{M_{T_3}}{M_{T_3}}. \dots \quad (11.18)$$

Because $\rho_3 C_{p3} \ll \rho_1 C_{p1}$, D_G is much greater than D_{HW} . Hence, heated gasfloods propagate the most slowly of the three cases.

11.3.2 Flow With Oil. In the next few sections, we will analyze some simple thermal displacements using fractional-flow theory. The basic governing equations are the strong forms of conservation of water,

$$\frac{\partial(\rho_1 S_1 + \rho_3 S_3)}{\partial t_D} + \frac{\partial(\rho_1 f_1 + \rho_3 f_3)}{\partial x_D} = 0, \dots \quad (11.19a)$$

conservation of oil,

and conservation of energy,

$$\frac{\partial \left[\rho_1 S_1 H_1 + \rho_2 S_2 H_2 + \rho_3 S_3 H_3 + \frac{(1-\phi)}{\phi} \rho_s S_s H_s \right]}{\partial t_p} + \frac{\partial (\rho_1 f_1 H_1 + \rho_2 f_2 H_2 + \rho_3 f_3 H_3)}{\partial x_p} = 0. \dots \quad (11.19c)$$

The mass balances are from the basic 1D fractional-flow equation (Eq. 2.53)—with water in a second phase 3—and the energy balance equation (Eq. 2.64). Of course, to write these, we have made some fairly restrictive assumptions that deserve special discussion when applied to thermal flooding.

Writing the equations in terms of fractional flow rather than flux (with f_j instead of u_j) means that we have invoked the fractional-flow assumptions. The portion of the fractional-flow assumptions least likely to apply in general is that of incompressible fluids and rock. Oil and water (hot or cold) can generally be assumed to be incompressible without great error, but steam is highly compressible. Aside from consistency with the other parts of this book and the attendant simplifications, there is no compelling reason for assuming steam to be incompressible. [For a treatment that does not assume incompressible fluids and solids, see Shutler and Boberg (1972); Aydelotte and Pope (1983).]

However, pressure gradients in steam zones are usually low, so that the densities therein can be considered approximately constant. Of course, assuming an incompressible solid means that there can be no oil production because of pore compression. The no-dissipation part of the fractional-flow assumptions now includes thermal conductivity, which is absent from Eq. 11.19c.

The equations further assume that there is no solubility of oil in water and no oil vaporization. We neglect all forms of energy except thermal energy, and we assume that internal energies are equal to enthalpies. Finally, we solve Eq. 11.19c by assuming no lateral heat loss. These assumptions mean that we can use the conventional

definitions of dimensionless time and position (Eq. 5.9) and the fractional-flow methods to solve for $S_1(x_D, t_D)$ and $T(x_D, t_D)$.

11.3.3 Hot Waterfloods. For this case, $S_3 = 0$, and the assumption of incompressible fluids and solids is good. With this, Eq. 11.19a is the only independent material balance; its strong form becomes

which has the saturation velocity

Similarly, writing the energy Eq. 2.80 in a fractional-flow form yields

$$\left(M_{T_1}S_1 + M_{T_2}S_2 + \frac{1-\phi}{\phi} M_{T_s} \right) \frac{\partial T}{\partial t_p} + \left(M_{T_1}f_1 + M_{T_2}f_2 \right) \frac{\partial T}{\partial x_p} = 0. \quad \dots \dots \dots \quad (11.21a)$$

We have also used the mass-balance equations for water and oil to eliminate saturation derivatives. Eq. 11.20b implies a velocity for the temperature change,

$$v_T = \frac{M_{T1}f_1 + M_{T2}f_2}{M_{T1}S_1 + M_{T2}S_2 + \frac{(1-\phi)}{\phi}M_{Ts}} \dots \dots \dots \quad (11.21b)$$

v_T is a function of T only through the temperature dependence of f_j . This temperature dependence is much weaker than the dependence of μ_2 on T . Therefore, the temperature wave is a shock in hot-water displacements.

The velocities in Eqs. 11.20b and 11.21b are set equal, which yields

$$\frac{df_1}{dS_1} = \frac{f_1 + \frac{M_{T_2}}{M_{T_1} - M_{T_2}}}{S_1 + \frac{M_{T_2} + \frac{(1-\phi)}{\phi} M_{Ts}}{M_{T_1} - M_{T_2}}} \dots \dots \dots \quad (11.22)$$

on eliminating $S_2 = 1 - S_1$ and $f_2 = 1 - f_1$. Eq. 11.22 determines the water saturation S_1^* just behind the hot-water front using the construction suggested in [Fig. 11.9](#). The construction is analogous to that in [Fig. 8.15](#) for polymer flooding except that the straight material-balance line does not begin from a point on the x -axis. This feature, which is caused by the difference between water and oil volumetric heat capacities in Eq. 11.22, arises because water is convecting heat to the thermal front, while oil is convecting heat away from it. By our assumptions, convection is the only form of heat transfer occurring in this displacement.

The rear of the oil bank must propagate at the same velocity; hence, the extension of the material-balance line to the cold-oil fractional-flow curve gives the oil-bank saturation. The leading edge of the cold oil bank follows from the by now usual secant construction shown in [Fig. 11.9](#).

11.3.4 Steam Displacements. We anticipate that in the absence of lateral heat loss, a steam front will propagate faster than a hot-water front (Example 11.3) and that there can be no condensation. With heat losses, some condensation can occur, but we save this discussion for the later treatment of heat losses. Behind the steam front, temperature must be constant because, by assumption, pressure is constant (pressure gradients being negligible). Hence, the entire left side of the energy balance becomes

$$\frac{\partial(\rho_3 S_3)}{\partial t_D} + \frac{\partial(\rho_3 f_3)}{\partial x_D} = 0. \dots \dots \dots \quad (11.23)$$

in one dimension. From Eqs. 11.19a, 11.19b, and 11.23, we see that the mass of each phase is conserved in the steam zone. However,

this is exactly the same problem that was solved in Section 5.7, where we considered the flow of water, gas, and oil as immiscible phases. There we constructed the composition-path diagram ([Fig. 5.21](#)), which illustrated the transition from an initial condition *I* to an injected condition *J* in two waves.

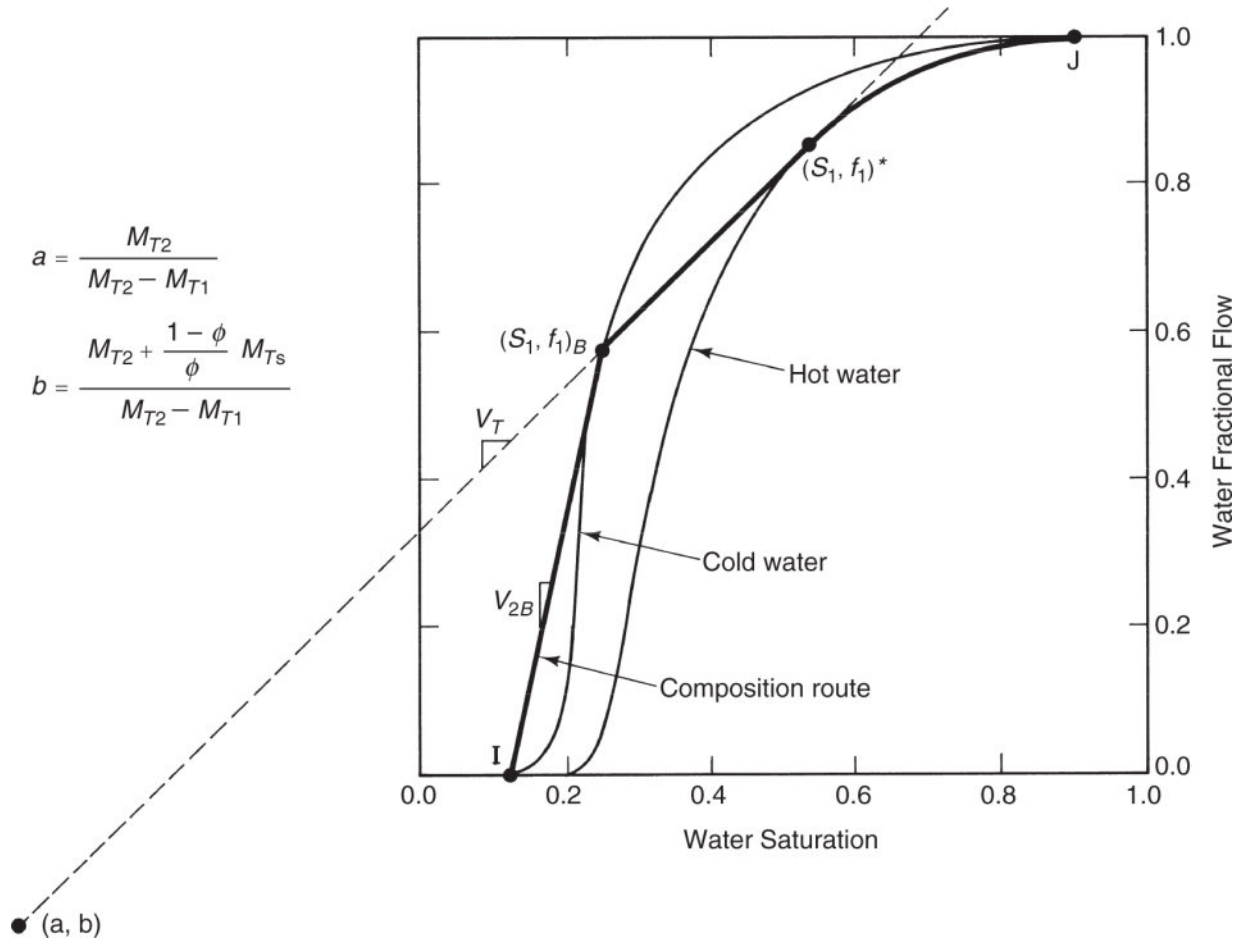


Fig. 11.9—Graphical construction of hot waterflood solution.

Although the solution presented in [Fig. 5.21](#) is the same as the solution to a propagating steam front, they differ in one important respect: the initial condition *I* in the current problem is no longer given because this is the condition immediately behind (upstream of) the steam front. To find condition *I*, we must resort to applying the coherence condition across the steam front.

The integral coherence condition for the steam front, written in terms of oil and water amounts, is

$$\frac{\rho_1 (f_1 H_1)^+ + \rho_2 (f_2 H_2)^+ + \rho_3 (f_3 H_3)^+}{\rho_1 (S_1 H_1)^+ + \rho_2 (S_2 H_2)^+ + \rho_3 (S_3 H_3)^+ + \frac{(1-\phi)}{\phi} \rho_s H_s^+} = \frac{\rho_1 f_1^+ + \rho_3 f_3^+ - \rho_1 f_1^-}{\rho_1 S_1^+ + \rho_3 S_3^+ - \rho_1 S_1^-} = \frac{f_2^+ - f_2^-}{S_2^+ - S_2^-}, \quad \dots \quad (11.24)$$

(energy) (water) \quad (oil)

where the + and – represent conditions immediately upstream (the “injected” condition) and downstream of the front. No negative term appears in the energy equation because the reference temperature for enthalpy is T^- by assumption. We can simplify Eq. 11.24 by letting $H_3 = H_1 + L_V$ and $H_j = C_{pj}T$ (for $j = 1$ and 2). This yields

Normally, the steam-zone temperature T^+ is known, leaving ten unknowns (f_j^+ and S_j^+ for $j = 1, 2, 3$, and C and \bar{C}) in the two equations (Eq. 11.25). There are five independent relations between fractional flow and saturation—three for the upstream side and two for the downstream side—and, of course, the S_j and f_j on both sides must sum to unity, adding another two equations. We are left with an indeterminate system because there are nine total equations in ten unknowns.

One way around this problem is to invoke additional assumptions regarding the upstream conditions (Shutler and Boberg 1972). An example of this would be to let $f_j^+ = 0$. The most rigorous method would be to derive additional jump conditions by restoring the dissipative terms and solving the profile in a moving coordinate system, the so-called traveling wave problem (Bryant et al. 1986; Lake et al. 2002). Once the upstream conditions (+) have been determined, the solution proceeds, as in Section 5.7.

11.4 Heat Losses From Equipment and Wellbores

Example 11.2 showed that heat losses to rock and water easily represent the most significant source of heat loss in thermal

methods. Although preventing this is beyond our reach (except for judicious selection of thermal candidates), minimizing heat losses from equipment and wellbores and to adjacent strata *is* within our power.

11.4.1 Equipment Losses. Heat is lost from surface equipment such as pipes, fittings, valves, and boilers. Such equipment is routinely insulated, so that losses are small, except under extreme circumstances. Most heat-transfer books give procedures for detailed calculation from surface lines. [Table 11.3](#) gives approximate heat losses that are adequate for most designs.

11.4.2 Wellbore Losses. Heat losses from the wellbore, on the other hand, can cause a sizable energy debit if the reservoir is deep. We devote the remainder of this section to estimating wellbore-fluid temperature and quality and the rate of heat lost at a given depth. Versions of this calculation occur in production of hot fluid below aquifers and permafrost. The treatment here is for injectors, where estimates of heat loss are important to the efficiency of thermal methods.

TABLE 11.3—TYPICAL VALUES OF HEAT LOSSES FROM SURFACE PIPING

Insulation	Conditions	Heat Loss, Btu/h·ft ² Surface Area for Inside Temperatures of:			
		200°F	400°F	600°F	800°F
Bare metal pipe	Still air, 0°F	540*	1560	3,120	—
	Still air, 100°F	210	990	2,250	—
	10-mph wind, 0°F	1,010	2,540	4,680	—
	10-mph wind, 100°F	440	1,710	3,500	—
	40-mph wind, 0°F	1,620	4,120	7,440	—
	40-mph wind, 100°F	700	2,760	5,650	—
Heat Loss, Btu/h·ft of Linear Length of Pipe at Temperatures of:					
Magnesium pipe insulation, air temperature 80°F	Standard on 3-in. pipe	50**	150	270	440
	Standard on 6-in. pipe	77	232	417	620
	1½ in. on 3-in. pipe	40	115	207	330
	1½ in. on 6-in. pipe	64	186	335	497
	3 in. on 3-in. pipe	24	75	135	200
	3 in. on 6-in. pipe	40	116	207	322

*1 Btu/h·ft² \cong 3.0 J/m²·s.

**1 Btu/h·ft = 0.91 J/m·s.

Estimating heat losses from a wellbore provides an excellent extended example of the application of heat-transfer theory and approximate solutions. The approach consists of three segments: steady-state heat transfer through the drillhole region, transient heat conduction in the earth adjacent to the well, and an overall heat balance on the fluid in the wellbore itself. With appropriate assumptions, each problem can be solved separately and then merged to give the final result. Combining steady-state, transient, and overall balances, as we are about to do, is a *quasisteady-state* approximation. The basic equations for strong- and weak-form energy conservation are Eqs. 2.36 and 2.92, respectively. Steady state exists when the time derivatives are zero.

11.4.3 Estimating the Overall Heat-Transfer Coefficient.

Estimates of heat-transfer rate through an element of height Δz in the drillhole region can be obtained from the following equation:

where $\Delta\dot{Q}$ is the heat-transfer rate (energy units divided by time) through a section of a vertical wellbore Δz in height having an outer tubing radius of R_{to} . U_T is the overall heat-transfer coefficient based on the outer surface of the tubing. Using Eq. 11.26 requires an estimate of U_T .

Heat transfer through the drillhole region involves several different resistances between the fluid flowing in the tubing and the formation. Starting with the formation and moving inward, these are a cement zone, casing, annulus, tubing insulation, the tubing itself, and the flowing fluid. [Fig. 11.10](#) shows a schematic of the temperature profile and definitions of symbols. Eq. 11.26 is expressed in terms of the temperature difference between the fluid T_f and the temperature at the drillhole radius T_d .

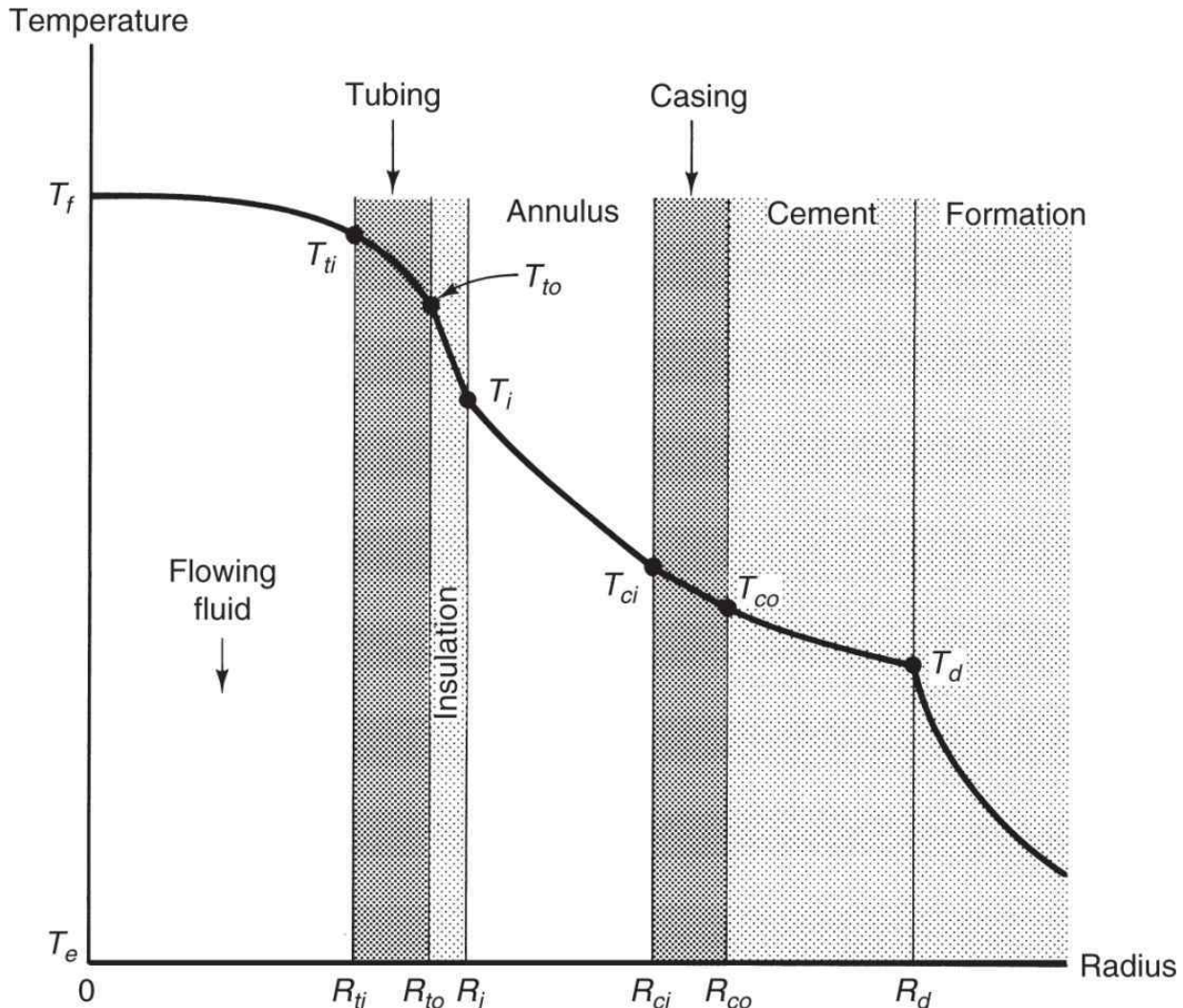


Fig. 11.10—Schematic-temperature profile in a drillhole [adapted from Willhite (1967)].

Following Willhite (1967), we assume radial symmetry in the drillhole, no heat transfer in the z-direction, and temperature-independent thermal conductivities. Because the drillhole region occupies a much smaller volume than the formation, it is reasonable to assume that temperature transients here decay much faster than in the formation. Therefore, we can assume that a steady-state energy balance applies in the tubing, insulation, casing, and cement:

$$\frac{d}{dr}(rq_c) = 0, \dots \quad (11.27)$$

where q_c is the radial component of the conductive heat flux \vec{q}_c in Eq. 2.33, heat transfer here being solely by conduction. Because the radius-heat flux product is a constant, the heat-transfer rate over height z is also a constant:

Eq. 11.28 can be integrated for the temperature differences between the inside and outside of each region:

k_{Tt} , k_{Ti} , k_{Tc} and k_{Tcem} in Eq. 11.29a are the thermal conductivities of the tubing, insulation, casing, and cement, respectively.

Neither the fluid in the tubing nor the fluid in the annulus transfers heat strictly by conduction; hence, they must be treated separately. Let the heat-transfer rates through these regions be expressed as

by analogy to Eqs. 11.26. h_{Tf} and h_{Ta} are the heat-transfer coefficients of the fluids in the tubing and annulus, respectively. They can be estimated mainly through correlations, as discussed in the following.

We can sum Eqs. 11.29 and 11.30 to give the overall temperature drop,

$$T_f - T_d = \frac{\Delta\dot{Q}}{2\pi\Delta z} \left[\frac{1}{R_{ti}h_{Tf}} + \frac{\ln\left(\frac{R_{to}}{R_{ti}}\right)}{k_{Ti}} + \frac{\ln\left(\frac{R_i}{R_{to}}\right)}{k_{Ti}} + \frac{1}{R_i h_{Ta}} + \frac{\ln\left(\frac{R_{co}}{R_{ci}}\right)}{k_{Tc}} + \frac{\ln\left(\frac{R_d}{R_{co}}\right)}{k_{Tcem}} \right], \dots \quad (11.31)$$

which, inserted into Eq. 11.26, gives the overall heat-transfer coefficient,

$$U_T^{-1} = R_{to} \left[\frac{1}{R_{ti}h_{Tf}} + \frac{\ln\left(\frac{R_{to}}{R_{ti}}\right)}{k_{Ti}} + \frac{\ln\left(\frac{R_i}{R_{to}}\right)}{k_{Ti}} + \frac{1}{R_i h_{Ta}} + \frac{\ln\left(\frac{R_{co}}{R_{ci}}\right)}{k_{Tc}} + \frac{\ln\left(\frac{R_d}{R_{co}}\right)}{k_{Tcem}} \right]. \dots \quad (11.32)$$

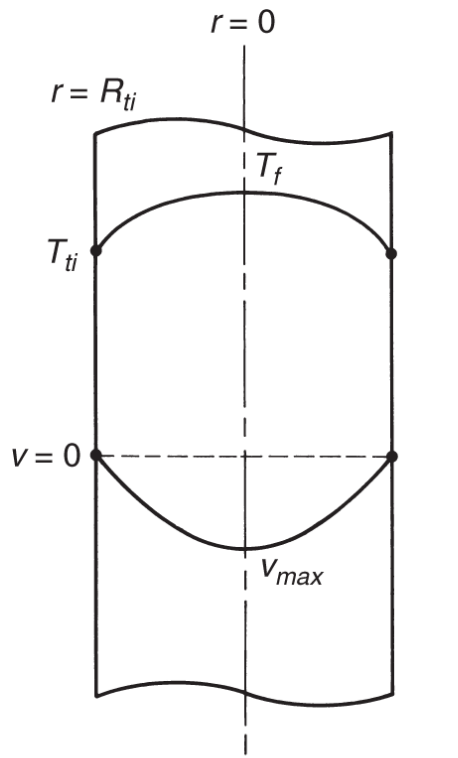
This equation expresses the total conductance between the fluid and the formation as a sum of series resistances each weighted by geometrical factors. If any one of the zones in Fig. 11.8 is absent (inner and outer radii equal), that term will be absent in Eq. 11.32. Moreover, if the thermal conductivity of a component is high, as is usually true with the tubing and casing, the corresponding term in Eq. 11.32 will be small. Many times, in fact, a single term will dominate the overall heat-transfer coefficient (as might occur in insulated tubing where k_{Ti} is small). Using Eq. 11.32 requires estimates of h_{Tf} and h_{Ta} .

11.4.4 Heat-Transfer Coefficient in Tubing and Annulus. The major difficulty in using Eq. 11.32 is estimating h_{Tf} and h_{Ta} because the other terms are constant. Heat transfer from a flowing fluid is by conduction and convection, and if the flow rate is large, heat is dissipated by viscous heating. Fig. 11.11a shows schematic velocity

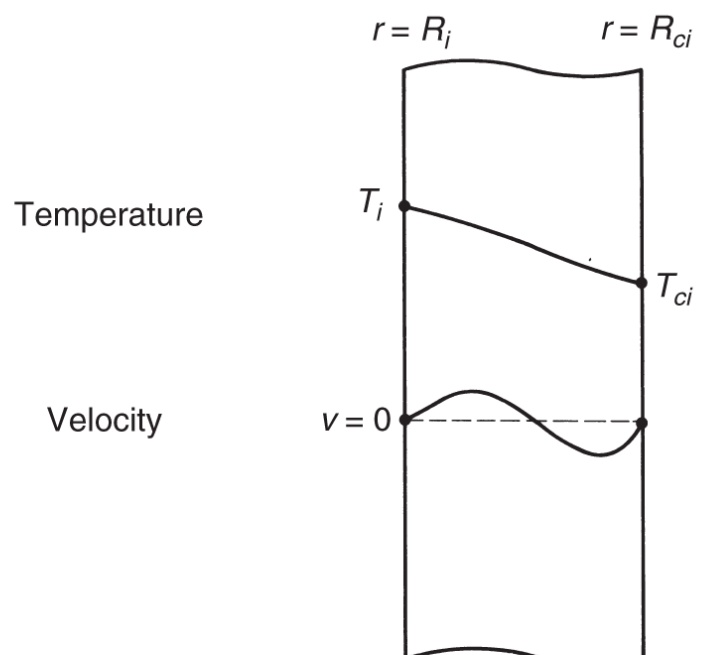
and temperature profiles. Theoretical arguments (Bird et al. 2002) suggest that h_{Tf} correlates as the following dimensionless equation:

for tubes with large length-to-diameter ratios. The dimensionless groups in Eq. 11.33 are

where the overbar in Eq. 11.34c indicates a volume average.



(a) Tubing – forced convection



(b) Annulus – free convection

Fig. 11.11—Schematic velocity and temperature profiles in tubing and annulus [adapted from Willhite (1967)].

As their naming after persons suggests, these are familiar groups in the heat-transfer literature. Each group has a physical interpretation: N_{Nu} is the ratio of total to conductive heat transfer; N_{Pr} is the ratio of convective to conductive heat transfer; N_{Re} is the ratio of inertial to viscous forces in the fluid flow; and N_{Br} is the ratio of viscous heat dissipation to conduction. Of these four, N_{Br} is the only one containing a temperature difference; however, if it is small, as it often is for liquid flows, this dependence is weak. For simple geometry, the specific form of Eq. 11.33 can be derived theoretically; in practical cases, the relationship is empirical (Bird et al. 2002). See Exercise 11.6.

Heat transfer through an annulus is even more complicated. If the annulus is sealed at both ends, there can be no bulk flow; however, the temperature difference between T_i and T_{ci} causes local density differences in the annulus fluid that cause flow. We call such flow

free convection to distinguish it from the *forced* convection in the tubing. [Fig. 11.11b](#) shows schematic velocity and temperature profiles for the annulus. Another dimensional argument suggests a relation among dimensionless groups, a particular form of which is (Willhite 1967)

$$N_{Nu} = 0.0499 \left(N_{Gr} N_{Pr} \right)^{1/3} N_{Pr}^{0.074} \dots \dots \dots \quad (11.35)$$

for flat plates with large length-to-diameter ratios. The additional group in Eq. 11.35 is the Grashof number,

$$N_{Gr} = \frac{\left(R_{ci} - R_i \right)^3 g \rho_a \beta_T (T_i - T_{ci})}{\mu_a}, \dots \dots \dots \quad (11.36)$$

which is the ratio of free convection transport to viscous forces. The parameter β_T is a thermal expansion coefficient defined as $-1/\rho_a(\partial_a/\partial T)_P$, and the subscript *a* refers to the annulus fluid. The fluid properties in N_{Nu} , N_{Pr} , and N_{Gr} are now based on the annulus fluid. The Grashof number contains a temperature difference that is usually unknown *a priori*; therefore, in applications, it may be necessary to solve for heat loss by trial and error.

Usually an annulus is air-filled, but on occasion, it has been evacuated. When this occurs, heat transfer is almost exclusively through radiation. Radiation is a form of heat flux independent of convection or conduction. Under some circumstances, radiation can account for a substantial fraction of heat transfer.

11.4.5 Heat Conduction in the Formation. The immense thermal mass of the earth surrounding the wellbore, only a small fraction of which is in contact with the reservoir, suggests that heat transfer here is transient. In this segment, we repeat a procedure first described by Ramey (1959) for calculating temperatures beyond the drillhole, $r > R_d$.

Let heat transfer in the formation be strictly by radial conduction. In the absence of any velocities, Eq. 2.36 becomes

$$\frac{\partial T}{\partial t} = \left(\frac{k_T}{\rho C_p} \right)_s \frac{1}{r} \frac{\partial}{\partial r} \left(r \frac{\partial T}{\partial r} \right) = \frac{K_{Ts}}{r} \frac{\partial}{\partial r} \left(r \frac{\partial T}{\partial r} \right), \dots \quad (11.37)$$

where Eq. 2.34 has been inserted for conductive heat flux and Eq. 11.4 has been used for the thermal diffusion coefficient. Eq. 11.37 also assumes an incompressible, single-phase formation so that a change in internal energy is manifest only as a change in temperature (there is no latent heat). Once this equation has been solved for $T(t, r)$ for $r > R_d$, the heat-transfer rate follows from the spatial gradient at $r = R_d$. The following boundary and initial conditions apply to Eq. 11.37:

$$T(0, r) = T(t, \infty) = T_e. \dots \quad (11.38a)$$

$$-k_{Ts} \left(\frac{\partial T}{\partial r} \right)_{r=R_d} = \frac{\Delta \dot{Q}}{2\pi R_d \Delta z}, \dots \quad (11.38b)$$

where Δz is the overall height difference. The undisturbed external temperature T_e is a function of z because of the geothermal gradient

$$T_e = a_T z + T_0, \dots \quad (11.39)$$

where a_T is usually approximately 0.18 K/km, and T_0 is the mean surface temperature. The existence of this gradient implies a constant rate of heat transfer from the Earth's core; it also suggests a z -dependency in the problem that is not explicit in the equations. The solution, therefore, will be for a particular z , but the variation with z arises only when solving the energy balance for the flowing fluid. Eq. 11.38b expresses the continuity of heat flux at $r = R_d$. Combining it with Eq. 11.26 gives the "conduction" condition,

$$-k_{Ts} \left(\frac{\partial T}{\partial r} \right)_{r=R_d} = \frac{U_T R_{to} (T_f - T_d)}{R_d}. \dots \quad (11.40)$$

As discussed earlier, all temperatures are functions of z .

For nonzero R_d , the solution to Eqs. 11.37, 11.38, and 11.40 must be numerical (using Laplace inversion), but once it is known, the heat-transfer rate follows from Eq. 11.38b to give

$$\Delta\dot{Q} = \frac{2\pi k_{Ts} (T_d - T_e) \Delta z}{f_T(t_D)}, \dots \quad (11.41)$$

where f_T is a function of dimensionless time t_D and formation Nusselt number,

$$t_D = \frac{K_{Ts} t}{R_d^2} \dots \quad (11.42a)$$

$$N_{Nu} = \frac{R_{to} U_T}{k_{Ts}} \dots \quad (11.42b)$$

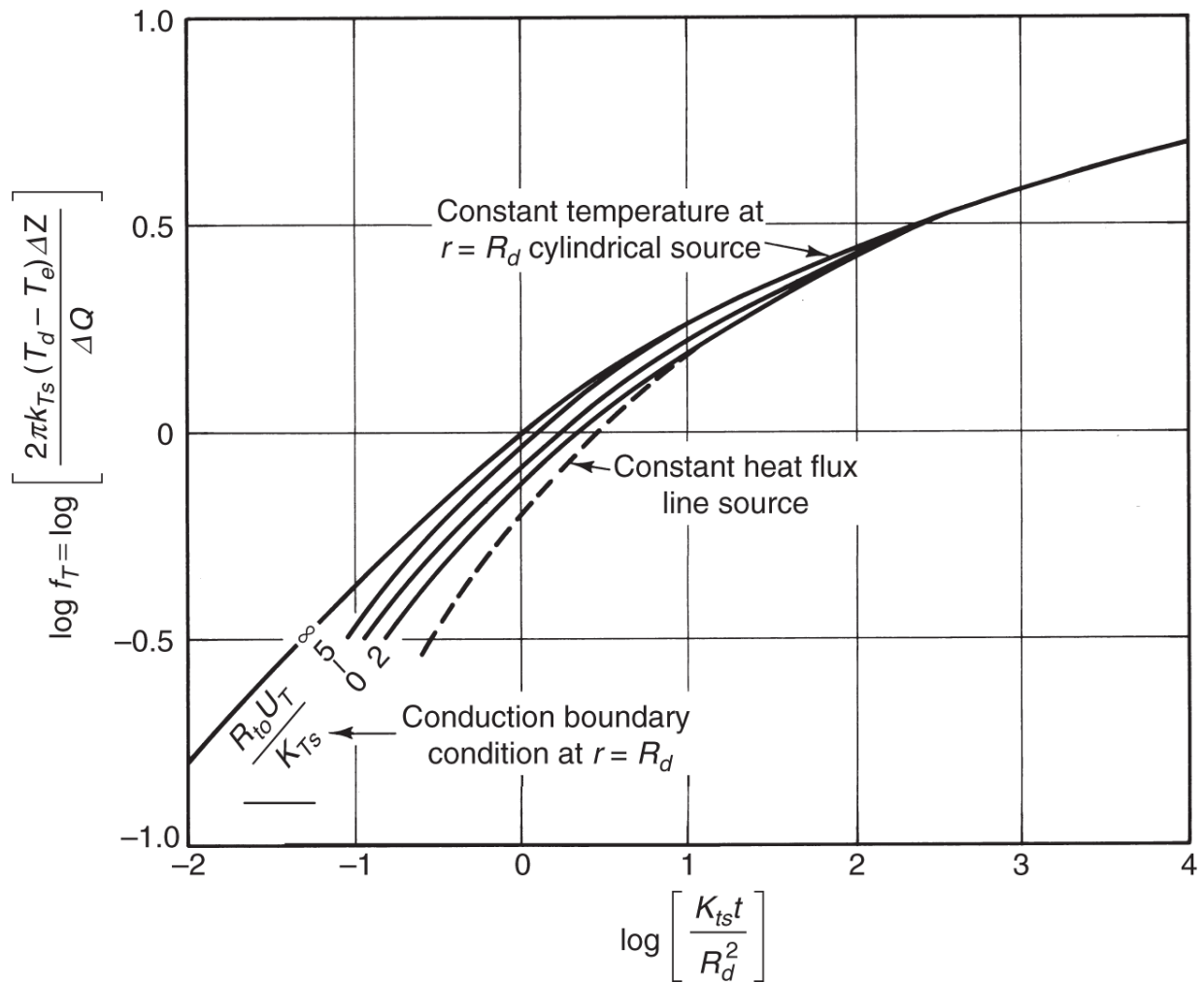


Fig. 11.12—Transient heat-transfer function (Ramey 1962).

[Fig. 11.11](#) shows the logarithm of f_T plotted vs. the logarithm of t_D with N_{Nu} as a parameter.

Ramey (1959) gives the procedure for using these equations. Let us solve for the inner casing temperature T_{ci} and heat loss rate $\Delta\dot{Q}$ at a given depth and time. We know the radii in [Fig. 11.12](#); the thermal conductivities of the tubing, insulation, casing, and cement zone; the thermal properties of the flowing fluid, the annulus fluid, and the formation; the viscosity and average velocity of the flowing fluid; and the depth z and the bulk fluid temperature T_f . The procedure is as follows:

1. Calculate T_e from Eq. 11.39 and calculate N_{Pr} and N_{Re} for the flowing fluid and N_{Pr} for the annulus fluid from Eqs. 11.34. Calculate t_D from Eq. 11.42a.
2. Assume a value for h_{Ta} and calculate U_T from Eq. 11.32, all other quantities being independent of temperature. If N_{Br} is not small, a value for h_{Tf} must be assumed also.
3. Calculate the formation Nusselt number from Eq. 11.42b and, using this and t_D , estimate f_T from Fig. 11.12. Calculate T_d from

$$T_d = \frac{T_f f_T(t_D) + \left(\frac{k_{Ts}}{R_{to} U_T} \right) T_e}{f_T(t_D) + \left(\frac{k_{Ts}}{R_{to} U_T} \right)}. \quad \dots \quad (11.43)$$

T_f in this equation follows from eliminating $\Delta\dot{Q}$ between Eqs. 11.26 and 11.41. We can now calculate $\Delta\dot{Q}$ from either equation.

4. With $\Delta\dot{Q}$ and T_d known, the casing temperature T_{ci} and all the others follow from successive application of Eqs. 11.29 and 11.30.

The solution would now be complete, but the assumed value of h_{Ta} in Step 2 may be incorrect. Proceeding further requires a trial-and-error process.

5. Calculate N_{Gr} from Eq. 11.36 and use Eq. 11.35 to estimate h_{Ta} . If radiation is important, we would correct for it here.
6. Recalculate U_T from its definition (Eq. 11.32). Compare this value to that used in Step 2; repeat Steps 2 through 6 with the new value of U_T if agreement is not satisfactory. The convergence test is on U_T , a much weaker function of temperature than h_{Ta} . Convergence should be obtained in three or fewer steps.

11.4.6 Heat Loss From the Wellbore. We now focus attention on the element Δz , through which heat is passing at rate $\Delta \dot{Q}$. First, we eliminate T_d between Eqs. 11.26 and 11.41 to give

$$\Delta \dot{Q} = \frac{2\pi k_{Ts} R_{to} U_T}{k_{Ts} + R_{to} K_{Ts} f_T(t_D)} (T_f - T_e) \Delta z. \quad (11.44)$$

In what follows, we assume U_T to be constant.

If we apply the overall energy balance (Eq. 2.56) to the element Δz , we have

$$A \Delta z \frac{d}{dt} (\overline{\rho_f U}) + \Delta \dot{H} - \bar{v} \rho_f A g \Delta z = -\Delta \dot{Q}, \quad (11.45a)$$

where we have neglected kinetic energy and mechanical work terms. Furthermore, by writing the enthalpy rate entering and leaving Δz as the product of a specific enthalpy and a constant mass flow rate $\dot{m} = \bar{v} r_{\rho_f} A$, we can obtain

$$\dot{m} (\Delta \bar{H} - g \Delta z) = -\Delta \dot{Q}. \quad (11.46b)$$

Eq. 11.46b has also dropped the time derivatives using the same quasisteady-state argument used previously for the drillhole.

The simplest heat-loss model follows from Eq. 11.41 by assuming that T_f is constant at the surface inlet temperature (this makes $\Delta \bar{H} = 0$) and integrating the resulting ordinary differential equation for dQ/dz (in the limit $\Delta z \rightarrow 0$) (Ramey 1964):

$$\dot{Q}(z) = \frac{2\pi k_{Ts} R_{to} U_T}{k_{Ts} + R_{to} U_T f_T(t_D)} \left[(T_f - T_0) z - \frac{a_T z^2}{2} \right], \quad (11.46)$$

where we have replaced T_e by Eq. 11.39 and T_d by Eq. 11.26 before integrating. This equation yields the maximum heat-loss rate up to depth z because the temperature difference between T_f and T_e is the maximum possible value. $(T_f - T_0)$ is the difference between inlet and surface temperatures.

For more general cases, let us eliminate $\Delta\dot{Q}$ between Eqs. 11.44 and 11.45b, which yields, after again taking the limit as $\Delta z \rightarrow 0$,

$$\frac{d\bar{H}}{dz} - g = -\frac{2\pi k_{Ts} R_{to} U_T (T_f - T_e)}{\dot{m} [k_{Ts} + R_{to} U_T f_T(t_D)]}. \quad (11.47)$$

Eq. 11.47 is a working equation. The sign convention is that z increases downward and \dot{Q} is positive when heat is lost from the wellbore. We can invoke Eq. 11.47 for several special cases by taking different forms for the specific enthalpy.

If the fluid flowing in the tubing is an ideal gas, because single-phase steam would be at low pressure, the enthalpy is independent of pressure:

$$d\bar{H} = C_{p3} dT_f. \quad (11.48a)$$

Substituting this into Eq. 11.47,

$$\frac{dT_f}{dz} = \frac{g}{C_{p3}} - \frac{2\pi k_{Ts} R_{to} U_T (T_f - T_e)}{C_{p3} \dot{m} [k_{Ts} + R_{to} U_T f_T(t_D)]}. \quad (11.48b)$$

Eq. 11.48b will integrate to

$$T_f = a_T z + T_0 - A_T \left(a_T + \frac{g}{C_{p3}} \right) + \left[(T_f - T)_0 + A_T \left(a_T + \frac{g}{C_{p3}} \right) \right] e^{-z/A_T}. \quad (11.48c)$$

for constant heat capacity, where

$$A_T(t_D) = \frac{\dot{m} C_{p3} [k_{Ts} + R_{to} U_T f_T(t_D)]}{2\pi k_{Ts} R_{to} U_T}. \quad (11.48d)$$

and T_{f0} in Eq. 11.48c is the inlet surface temperature at $z = 0$. With T_f now determined as a function of depth, we can integrate Eq. 11.45b for the heat loss down to z . These two equations state that the fluid temperature and heat loss vary with depth as an exponential function

plus a linear term, the rate of change being determined by A_T , which is proportional to the mass flow rate.

If the flowing fluid is a superheated vapor at the inlet surface temperature, Eq. 11.48c will describe its temperature down to the saturation temperature. Below this point, the fluid will be a saturated two-phase mixture for some distance down in the tubing, where the fluid will condense gradually to saturated water as more heat is lost. In this case, the specific enthalpy relates to the steam quality as

If pressure is constant, this leads to a relatively simple differential equation in quality (Satter 1965),

where

$$A_T(t_D) = \frac{\dot{m}L_v [k_{Ts} + R_{to}U_T f(t_D)]}{2\pi R_{to} k_{Ts}}. \quad \dots \dots \dots \quad (11.49c)$$

Because a change in steam quality at constant pressure must take place at constant temperature, we can integrate Eq. 11.49b with T_f constant at the saturation temperature for the fluid quality in the tubing,

$$y = 1 + \left[\frac{\left(\frac{gA_T}{L_v} \right) + T_0 - T_f}{A_T} \right] z + \frac{a_T z^2}{2A_T}, \dots \dots \dots \quad (11.49d)$$

where $y = 1$ at $z = 0$. The heat loss follows from Eq. 11.49a; note that a constant flowing temperature does not imply the absence of heat loss if the fluid is condensing.

Eq. 11.49d is deceiving in its simplicity. It has neglected the hydrodynamics of two-phase flow in a vertical pipe and the

significant effect that U_T (through h_{Tf}) can bring about with condensation. Still, the equation is quite instructive, particularly when merged with a heat-loss calculation for flowing gas.

Heat is lost from the wellbore because a temperature difference exists between the heated wellbore and the geothermal temperature in the surrounding formation. [Fig. 11.13](#) shows the state of fluids in a wellbore, into which superheated steam is being injected, as a function of depth and injection time. This calculated result assumes that pressure is constant in the wellbore.

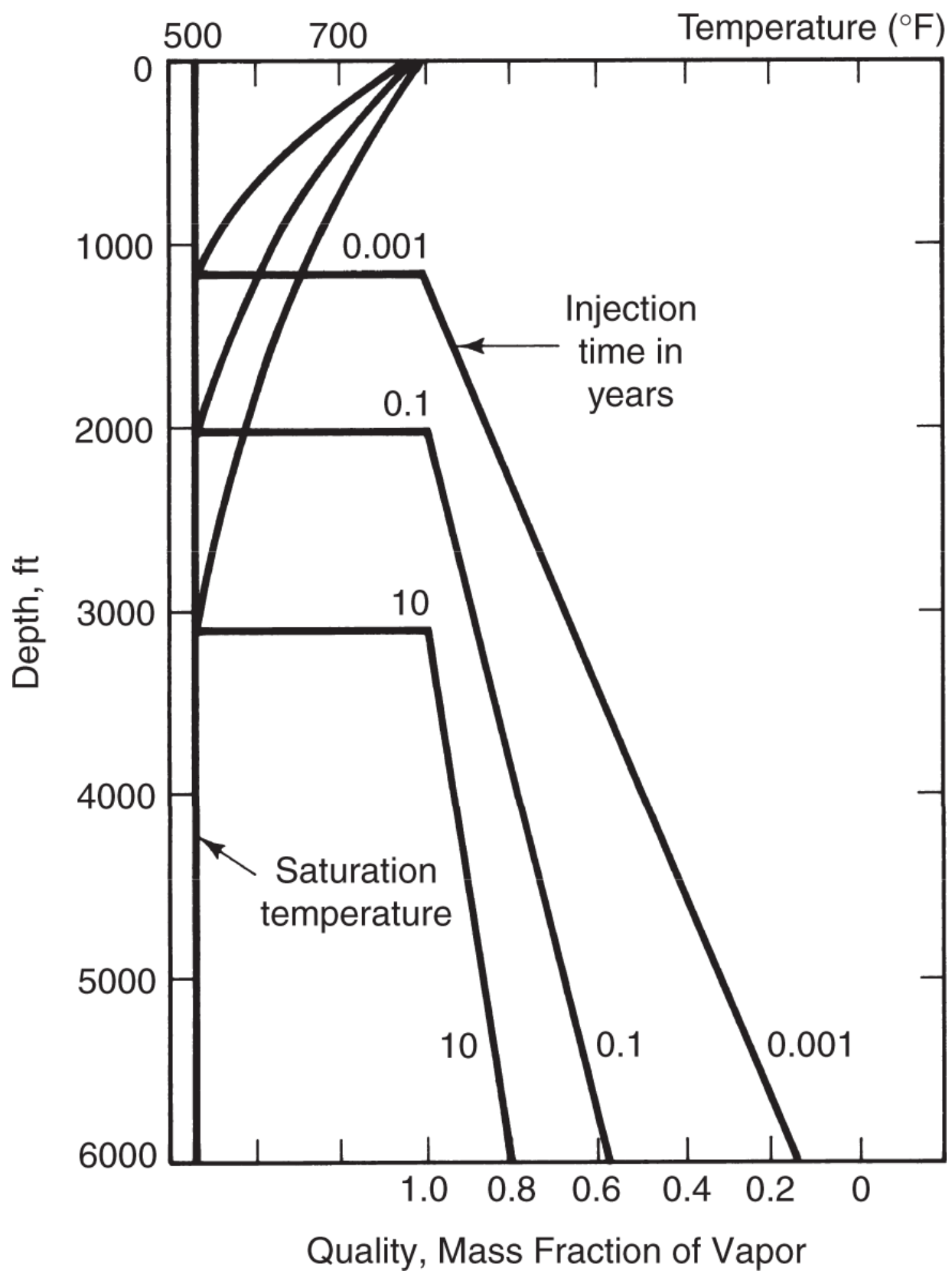


Fig. 11.13—Change in temperature or steam quality with depth (Satter 1965).

The progression in [Fig. 11.13](#) can be seen on the enthalpy-pressure diagram in [Fig. 11.4](#). Suppose that the wellbore pressure is 3.1 MPa and the surface temperature is 800 K. The temperature falls to the dewpoint temperature at the wellbore pressure. Eq. 11.48c approximates the temperature change, which is represented by a horizontal line in the superheated steam region in [Fig. 11.4](#). From this point down, the wellbore temperature becomes constant, and steam quality declines as predicted by Eq. 11.49d. The change becomes apparent in [Fig. 11.4](#), where the extension of the horizontal line from the superheated-steam region coincides with lines of constant temperature but decreasing quality. At a fixed time, the heat lost per unit mass of steam is given by the difference in the x-coordinates on the enthalpy/pressure diagram. The entire progression moves down the wellbore with increasing time.

11.4.7 Controlling Heat Loss. Heat losses from the wellbore to the surrounding formation can be controlled in three ways.

1. Restrict application. [Fig. 11.13](#) and [Fig. 11.14](#) indicate that deep wells and long producing lives are to be avoided. Steam processes, in particular, are generally not practical at depths of more than 1000 m. If the reservoir depth is not too large, pattern spacing can be relatively close, which will cause short producing lives. Close spacing will also reduce the amount of heat lost to the adjacent strata.
2. Insulate the tubing. The mechanisms for wellbore heat loss are conduction from the casing, radiation between the tubing and the casing, and free convection in the annulus. We can suppress all these mechanisms by insulating the casing or tubing from the formation.

[Fig. 11.14](#) shows the dramatic effect of insulation. The insulation causes a tenfold reduction in heat losses in hot-water injection. The reduction would not be quite as large in steam injection because the vapor heat-transfer coefficient is already approximately one-half that of hot water.

Whether or not insulation is appropriate depends on the benefit in heat saved weighed against the cost of insulation. This, in turn, depends on the type of insulation and the depth of the well. By now, it has become common practice to leave an air space between the annulus and tubing to provide partial insulation.

3. Inject at high rate or high surface pressure. As the injection rate increases, so does the heat transfer from the hot fluid. Several of the equations given previously attest to this; examine the fluid temperature change in Eq. 11.48b and the quality change in Eq. 11.49d. Heat-loss rate increases with \dot{m} , but the heat-loss rate does not increase as fast as the rate that heat is delivered to the formation, so the *relative* loss rate goes down. [**Fig. 11.15**](#) shows the advantages of this strategy; tripling the injection rate reduces the relative heat losses by approximately a factor of three. A secondary benefit to be gained from a high injection rate is a short project life.

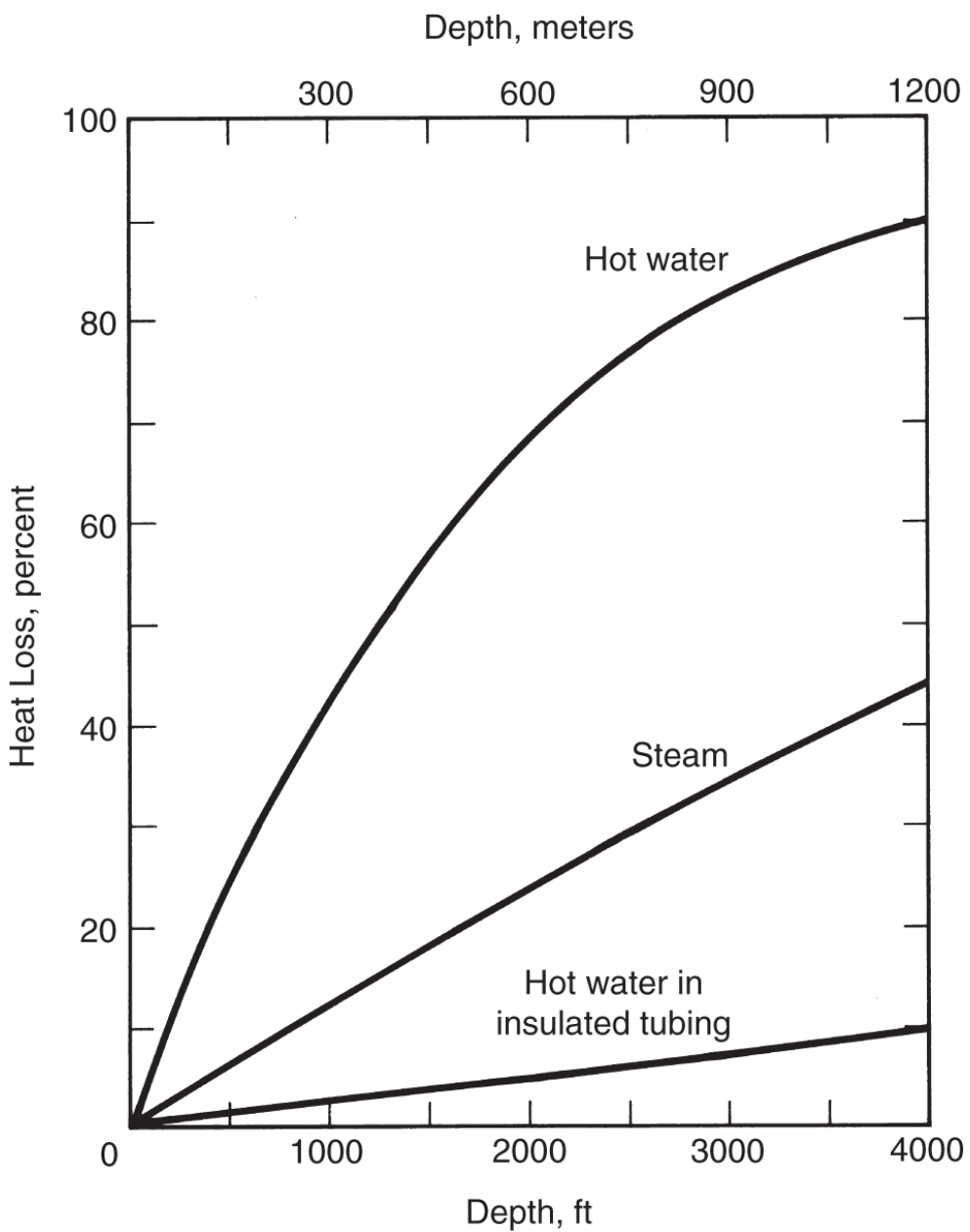


Fig. 11.14—Effect of insulation on heat loss (Ramey 1962).

There are two further cautions. The injection pressure must not be so high that it exceeds the formation parting pressure. Just as in waterflooding, such parting can introduce high-permeability channels into the formation, with resulting loss of volumetric sweep efficiency (although this problem is not as severe in thermal methods as in other EOR methods). The second concern is that high injection rate in a steamdrive will lead to excessive heat losses through the

producers if continued after steam breakthrough. The rate of loss from the wellbore must be balanced with the rate of loss through the producers when this happens, but usually the injection rate is reduced once steam breaks through.

An obvious way to avoid wellbore heat losses is to generate the heat in situ or at the bottom of the wellbore. The first technique is the basis for in-situ combustion (see Section 11.8), which extends the practical depth of thermal floods to approximately 2000 m. Below this depth, compression costs tend to be prohibitive. The second technique implies downhole steam generation.

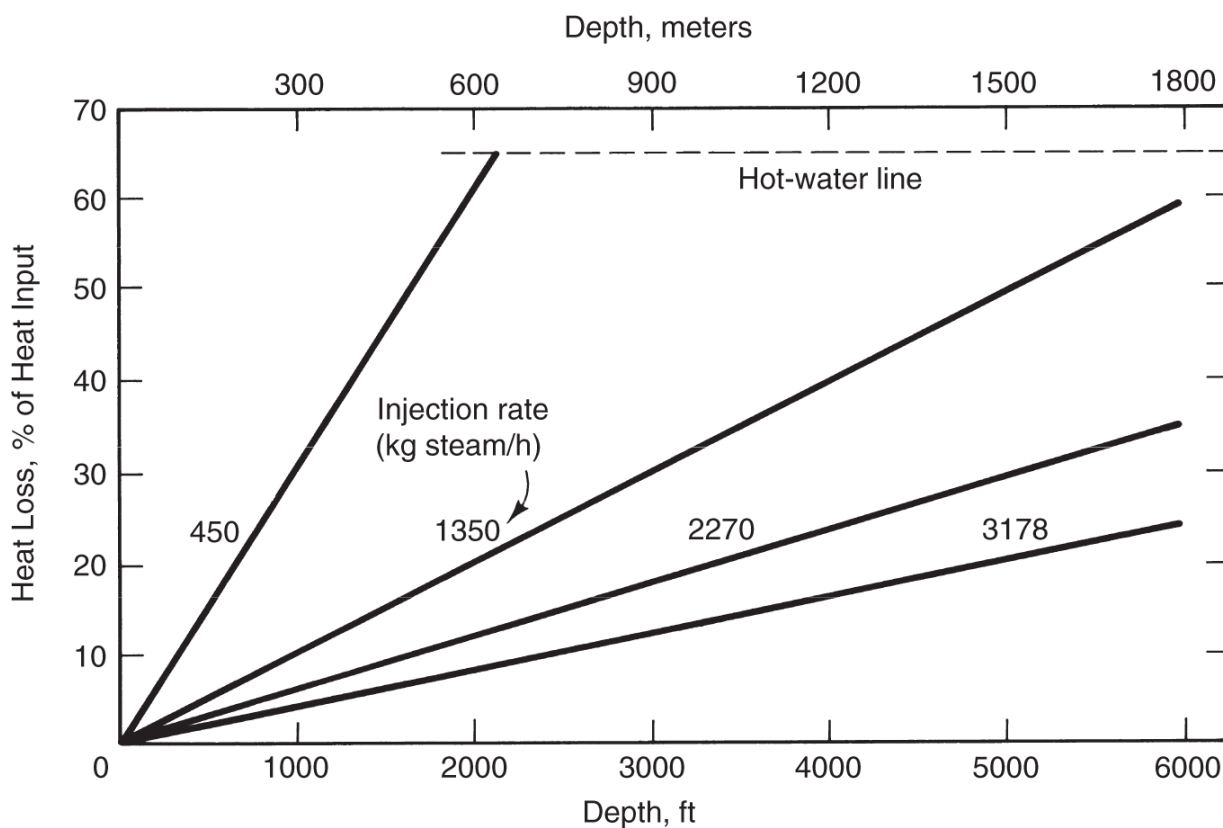


Fig. 11.15—Effect of injection rate on heat loss (Satter 1965).

Two types of downhole steam generators produce steam at the sandface. In the direct-fired generator, water and fuel are mixed in a combustion chamber, burned, and the entire mixture (steam, unburned fuel, and combustion products) is then injected. The CO₂ in the combustion products is an EOR agent in its own right, but the

device has proven difficult to operate and maintain. The indirect-fired generator returns the combustion mixture to the surface and, although a little easier to maintain, is clearly more complex. The combustion products for both can represent an environmental hazard.

11.5 Heat Losses to Overburden and Underburden

The fourth source of heat loss in thermal methods is loss to adjacent strata or to the overburden and underburden. As in Section 11.4, analysis of this loss involves a combination of local and overall heat-transfer techniques that leads to a highly practical result. We give here an exposition of the Marx- Langenheim (ML) (1959) theory as expounded by Farouq Ali (1966).

The objective of the ML theory is to calculate the heated area as a function of time and reservoir properties. The heated area leads then to expressions for oil rate, oil/steam ratio, and energy efficiency (see Exercise 11.7). The procedure is most appropriate for steamdrives, but the expression for heated area applies for all thermal processes.

[Fig. 11.16](#) shows a schematic illustration of heating. The figure is a top view of a single vertical heat-injection well. We assume that the heated zone in an areally infinite reservoir contains a single phase with negligible horizontal heat conduction. These assumptions result in an ideally sharp temperature profile. We further assume that the over- and underburden extend to infinity along both the positive and negative z-axis (out of the page).

11.5.1 The Local Problem. The objective of this section is to derive an expression for the rate of heat loss \dot{Q} to the over- and underburden and the area $A(t)$ of the heated zone as a function of time.

If the over- and underburden are impermeable, heat transfer is entirely through conduction. All fluid velocities and convective fluxes now being zero, the energy balance (Eq. 2.36) reduces to the 1D form,

K_{Ts} is the thermal diffusion coefficient of the over- and underburden, and M_{Ts} is the total volumetric heat capacity of the same. Eq. 11.50 assumes that all thermal properties are independent of temperature.

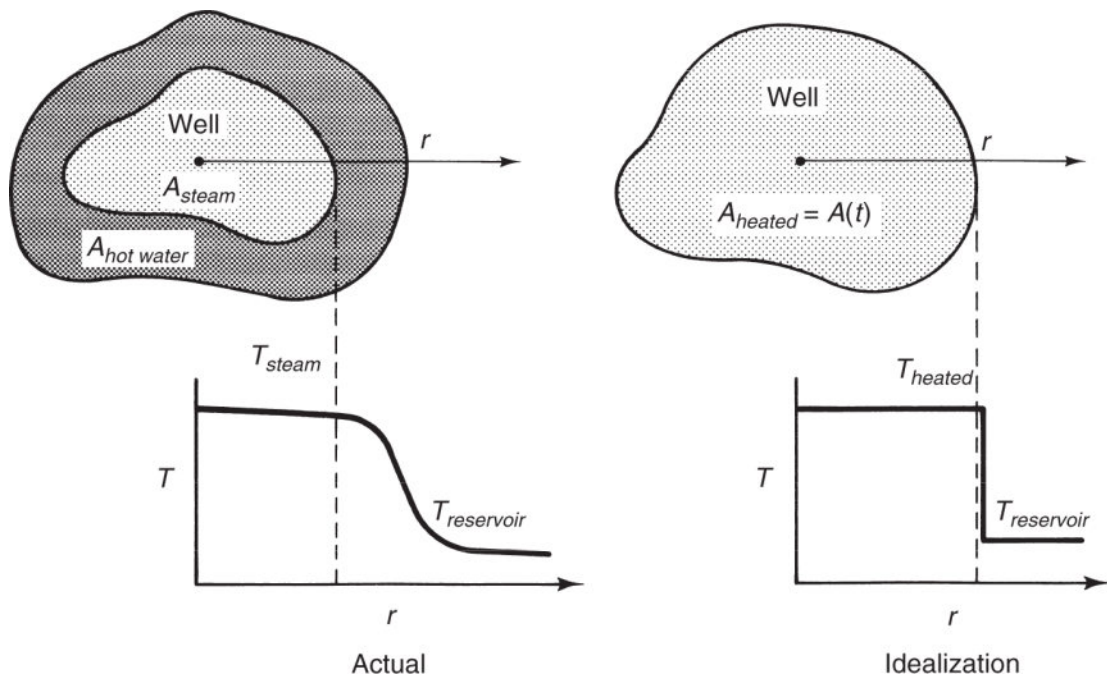


Fig. 11.16—Idealization of heated area for ML theory.

Eq. 11.50 applies to a vertical segment of the over- and underburden with cross-sectional area ΔA_k for which the face at $z = 0$ (the top of the reservoir) is at the original temperature T_i until time t_k , when it is raised to T_J . The boundary conditions for Eq. 11.50 are now

Eq. 11.51a neglects the geothermal gradient outside the reservoir, an assumption that implies, because the problem is symmetric, that we need not treat the over- and underburden separately. The time scale of the problem may be offset by t_k , so that the last boundary condition in Eq. 11.51a becomes

where $T = T(z, \tau)$, $\tau = t - t_k$, and $\tau > 0$.

Eqs. 11.50 and 11.51 are now of precisely the same form and boundary conditions as Eqs. 5.51 and 5.53, and their solutions can be abstracted directly as

where τ has replaced the time variable. The rate of heat transferred into ΔA_k from the reservoir is

With the solution in hand, we can differentiate the erfc solution (recalling its definition), evaluate it at $z = 0$, and substitute the result into Eq. 11.53 to give

where $\Delta T = T_J - T_i$. Eq. 11.54 expresses the rate of heat loss to any vertical segment when $t > t_k$. When we sum all similar segments so that the largest of these t_K is just smaller than t , we have

which, in the limit of the largest ΔA_k approaching zero, becomes

The factor two in these equations is to account for heat loss to both the over- and underburden. This procedure is the application of a

special case of Duhumel's theorem, which is a form of superposition for continuously changing boundary conditions (Carslaw and Jaeger 1959). For later operations, it is convenient to convert the integration variable in Eq. 11.55b to a time variable,

$$\dot{Q} = 2 \int_{\xi=0}^{\xi=t} \frac{k_{Ts} \Delta T}{\sqrt{\pi K_{Ts} (t - \xi)}} \frac{dA}{d\xi} d\xi. \dots \quad (11.55c)$$

Eq. 11.55c expresses the rate of heat loss at time t as a function of the rate of growth of the heated area. The integrand is finite because of the square root in the denominator, but it is of no use without some independent way of relating heat-loss rate to time.

11.5.2 Overall Heat Balances. The link between \dot{Q} and time comes from an overall energy balance. To simplify matters, we assume T_r to be the reference temperature for the enthalpy, which means that Eq. 2.91 applied to the reservoir now becomes

$$\dot{H}_J - \dot{Q} = \frac{d}{dt} (AH_r \rho_s U), \dots \quad (11.56)$$

there being no “out” term except for the heat loss. We have neglected the work (the PV) term, and $\rho_s U$ is the volumetric internal energy of the over- and underburden. Because the temperature reference is the original reservoir temperature, all energy terms involving the unheated or cold reservoir vanish. This simplification and the neglect of conduction imply that the time derivative in Eq. 11.56 merely expresses the change in heated-zone volume. If the reservoir thickness is constant, Eq. 11.56 becomes

$$\dot{H}_J = 2 \int_{\xi=0}^{\xi=t} \frac{k_{Ts} \Delta T}{\sqrt{\pi K_{Ts} (t - \xi)}} \frac{dA}{d\xi} d\xi + H_r M_{Tr} \Delta T \frac{dA}{dt}, \dots \quad (11.57)$$

where Eq. 11.55c has been inserted into Eq. 11.56.

Eq. 11.57 is an integral-differential equation for $A(t)$, which we solve using the initial condition $A(0) = 0$. The most direct solution

method is through Laplace transforms (Farouq Ali 1966). The inverted solution with \dot{H}_J constant (Roberts and Kaufmann 1966) is

$$A(t_D) = \frac{\dot{H}_J H_t}{4k_{Ts} \Delta T} \left[e^{t_D} \operatorname{erfc}(t_D^{1/2}) + \frac{2t_D^{1/2}}{\sqrt{\pi}} - 1 \right], \quad \dots \dots \dots \quad (11.58a)$$

where t_D is a dimensionless time, defined as

$$t_D = \frac{4K_{Ts} t}{H_t^2} = \frac{4k_{Ts} t}{M_n H_t^2}. \quad \dots \dots \dots \quad (11.58b)$$

The H_t^2 in Eq. 11.58b means that all heat-loss expressions will be especially sensitive to reservoir thickness H_t .

One important feature of the ML theory is that the final result is largely independent of the shape of the heated zone. To some extent, this observation is true even if there is gravity overlay, for here the larger heat loss to the overburden is very nearly balanced by a smaller loss to the underburden. To a lesser approximation, the heated area given by Eq. 11.58 applies after steam reaches a producing well in steamdrives if the *net* enthalpy rate (Injected – Produced) replaces \dot{H}_J .

Several immediate results follow from Eq. 11.59 or its time derivatives:

$$\frac{dA}{dt_D} = \frac{\dot{H}_J H_t}{4k_{Ts} \Delta T} e^{t_D} \operatorname{erfc}(t_D^{1/2}) = \frac{\dot{H}_J H_t}{4K_{Ts} M_n \Delta T} e^{t_D} \operatorname{erfc}(t_D^{1/2}). \quad \dots \dots \dots \quad (11.59)$$

All the equations stated above can be combined to give the heat-loss rate as

$$\dot{Q} = \dot{H}_J \left(1 - e^{t_D} \operatorname{erfc}(t_D^{1/2}) \right). \quad \dots \dots \dots \quad (11.60)$$

11.5.3 Applications. Eqs. 11.56 and 11.59 define an expression for the average heating efficiency E_{hs} ,

$$\bar{E}_{hs} \equiv 1 - \frac{\dot{Q}}{\dot{H}_J} = e^{t_D} \operatorname{erfc}(t_D^{1/2}). \quad \dots \dots \dots \quad (11.61)$$

\bar{E}_{hs} is the fraction of heat in the reservoir at time t_D expressed as a fraction of the heat entering the sandface at the injector.

[Fig. 11.17](#), which shows $\bar{E}_{hs}(t_D)$ graphically for a steamdrive, uses Eq.11.61 as a starting point. The figure contains the dimensionless latent heat first introduced in Eq. 11.16, which does not appear in Eq. 11.61 because it is based on more complex physics. In the limit $h_D \rightarrow 0$, the results revert to a hot waterdrive. This phenomenon underlines, once again, the benefit of using steam over hot water. Perhaps the most singular result from [Fig. 11.17](#) is the time dependency; the thermal efficiency of steamdrives inevitably declines with time.

If we assume that the displacement of a unit volume of oil from the heated zone causes the production of a unit volume of oil, the oil production rate in reservoir volumes is

$$\dot{N}_{p2} = \phi \Delta S_2 H_{NET} \frac{dA}{dt} \dots \dots \dots \quad (11.62a)$$

from applying Eq. 2.51 to the oil. Using Eq.11.61 this becomes

$$\dot{N}_{p2} = \dot{H}_J \left(\frac{\phi \Delta S_2}{M_t \Delta T} \right) \left(\frac{H_{NET}}{H_t} \right) \left(e^{t_D} \operatorname{erfc} t_D^{1/2} \right), \dots \dots \dots \quad (11.62b)$$

where $\Delta S_2 = S_2 - S_2'$ is the oil-saturation change caused by heating. The net thickness H_{NET} is the proportion of the reservoir contributing to flow; the gross thickness is the entire reservoir. The equation has been slightly rearranged to include explicitly the net-to-gross thickness ratio. Correlations for the oil saturation in the steam zone S_2' are available in the literature (see Section 11.6).

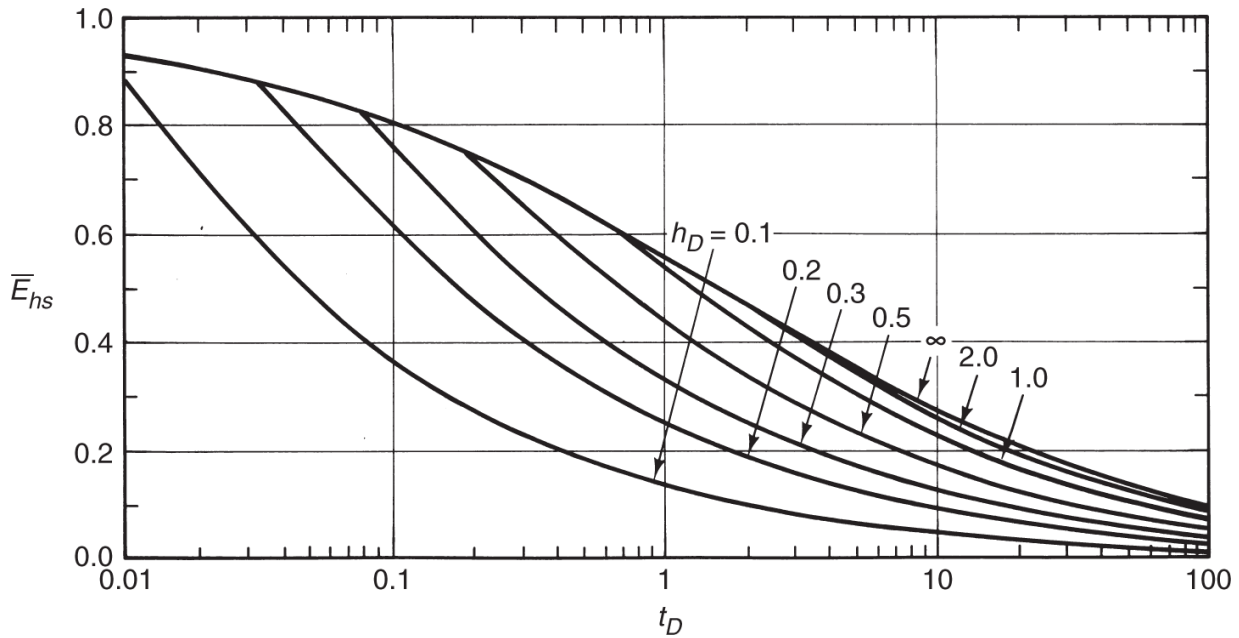


Fig. 11.17—Steam-zone thermal efficiency (Myhill and Stegemeier 1978). Dimensionless latent heat given in Eq. 11.16.

Eq. 11.62b invariably overestimates the oil rate, especially after steam breakthrough in a steamdrive (after breakthrough, the equation predicts a more accurate oil rate if net enthalpy is used for the \dot{H}_J term), but it directly highlights two important parameters in thermal flooding. If the net-to-gross thickness ratio $\left(\frac{H_{NET}}{H_t}\right)$ is small, the oil rate will also be proportionally small. Physically, this means that a substantial amount of heat is being expended to warm up rock that does not contribute to production (nonpay). The second parameter exhibiting a direct proportionality to the oil rate is the combination $\phi\Delta S_2$, the “delsophi,” which has long been used as an indicator of thermal-flooding success. Delsophi should be as large as possible for steamdrive candidates. Occasionally, the $\phi\Delta S_2 H_{NET}$ from Eq. 11.62b is used as a screening parameter; a reservoir with $\phi\Delta S_2 H_{NET}$ greater than 2 m is a good candidate.

Finally, the cumulative volume of oil displaced up to time t is

$$N_{p2} = H_{NET} \phi \Delta S_2 A, \dots \dots \dots \quad (11.63a)$$

and the total heat injected to time t is

$$H_J = \frac{M_{Tt} H_t A \Delta T}{E_{hs}} \dots \dots \dots \quad (11.63b)$$

The amount of heat per unit mass of water is $(C_{p1}\Delta T + yL_V)$. The volume of *cold* water required to generate \dot{H}_J is

$$V_1 = \frac{H_J}{(C_{p1}\Delta T + yL_V)\rho_1} \dots \dots \dots \quad (11.63c)$$

Eqs. 11.63a through 11.63c lead to the cumulative oil/steam ratio F_{23} :

$$F_{23} = \frac{N_{p2}}{V_1} = \frac{M_{T1}}{M_{Tt}} (1 + h_D) \bar{E}_{hs} \left(\frac{\phi \Delta S_2 H_{NET}}{H_t} \right) \dots \dots \dots \quad (11.63d)$$

The oil/steam ratio is a measure of economic efficiency in steam processes. The steam is expressed as cold-water equivalents in Eq. 11.63d. [Fig. 11.18](#) shows a plot of the dimensionless oil/steam ratio,

$$\left(\frac{F_{23} H_t}{\phi \Delta S_2 H_{NET}} \right),$$

based on Eq. 11.63d. This figure assumes a constant value for the ratio (M_{T1}/M_{Tt}) . It also assumes that the oil saturation will be reduced wherever heat goes. The oil/steam ratio is another of the important economic indicators of steamflooding success.

11.5.4 Modifications. The ML theory has undergone several improvements. Each has yielded important insights into various facets of thermal flooding.

Prats (1982) showed that the ML theory could accommodate different heat capacities in the over- and underburden M_{Tu} and in the reservoir M_{To} . The heated area now becomes

$$A(t_D) = \frac{\dot{H}_J H_t M_{To}}{4k_{Ts} M_{Tu} \Delta T} \left[e^{t_D} \operatorname{erfc}(t_D^{1/2}) + \frac{2t_D^{1/2}}{\sqrt{\pi}} - 1 \right], \quad \dots \dots \dots \quad (11.64a)$$

and the dimensionless time definition is

$$t_D = \frac{4k_{Ts} M_{Tu} t}{H_t^2 M_{To}^2}. \quad \dots \dots \dots \quad (11.64b)$$

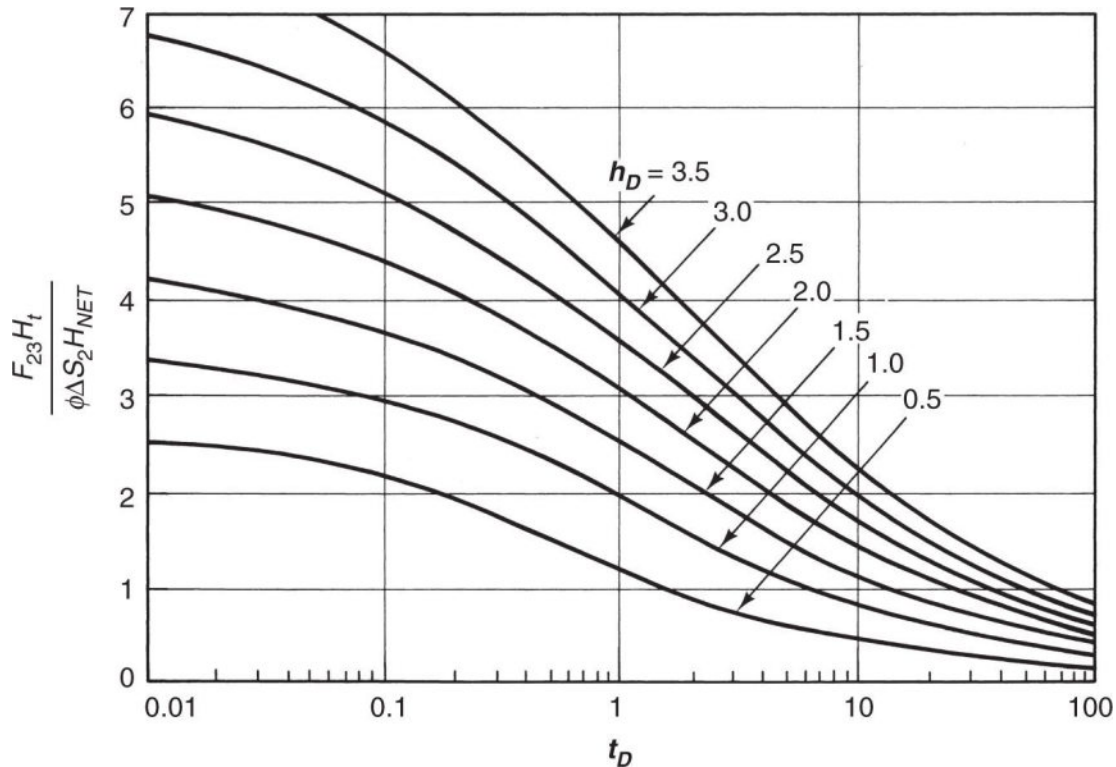


Fig. 11.18—Dimensionless cumulative oil/steam ratio (Myhill and Stegemeier 1978).

The quantities in Eqs. 11.60 through 11.63 still apply with this change as long as the new definitions are used.

One important point here is that the dimensionless time in Eq. 11.64b is very different from the dimensionless times in the remainder of this text. There, the normalizing factor for time was the rate of convective mass transfer for isothermal processes, or

$$t_D = \frac{ut}{\phi L} = \frac{qt}{V_p}.$$

In Eq. 11.64b, time is normalized by the rate of conductive heat transfer. Both time scales are present in actual steamfloods, but the widespread use of Eq. 11.64b implies that heat transfer is what governs production.

One of the most significant improvements to the ML theory was proposed by Mandl and Volek (1969), who noticed that the velocity of a saturated steam front declines with time until it can actually propagate at a slower rate than a hot-water front. After this time, the displacement forms a hot-water or condensate bank that propagates ahead of the steam front from then on. The time at which this happens is called the *critical time* (see [Fig. 11.19](#)).

We can derive an expression for the critical time on the basis of previous equations. Let us consider a medium with a constant cross-sectional area WH_t . For this case, the steam-front velocity is simply the rate of growth of the heated area dA/dt divided by the width W of the medium. The velocity of a hot-water front v_{HW} has already been given in Eq. 11.11. When these two velocities are equated and the area derivative eliminated by Eq. 11.61 the critical dimensionless time t_{Dc} is the solution to

$$e^{t_{Dc}} \operatorname{erfc} t_{Dc}^{1/2} = \frac{u_1 WH_t M_{Tt} \Delta T}{\phi(1 + D_{HW}) \dot{H}_J}. \quad \dots \dots \dots \quad (11.65)$$

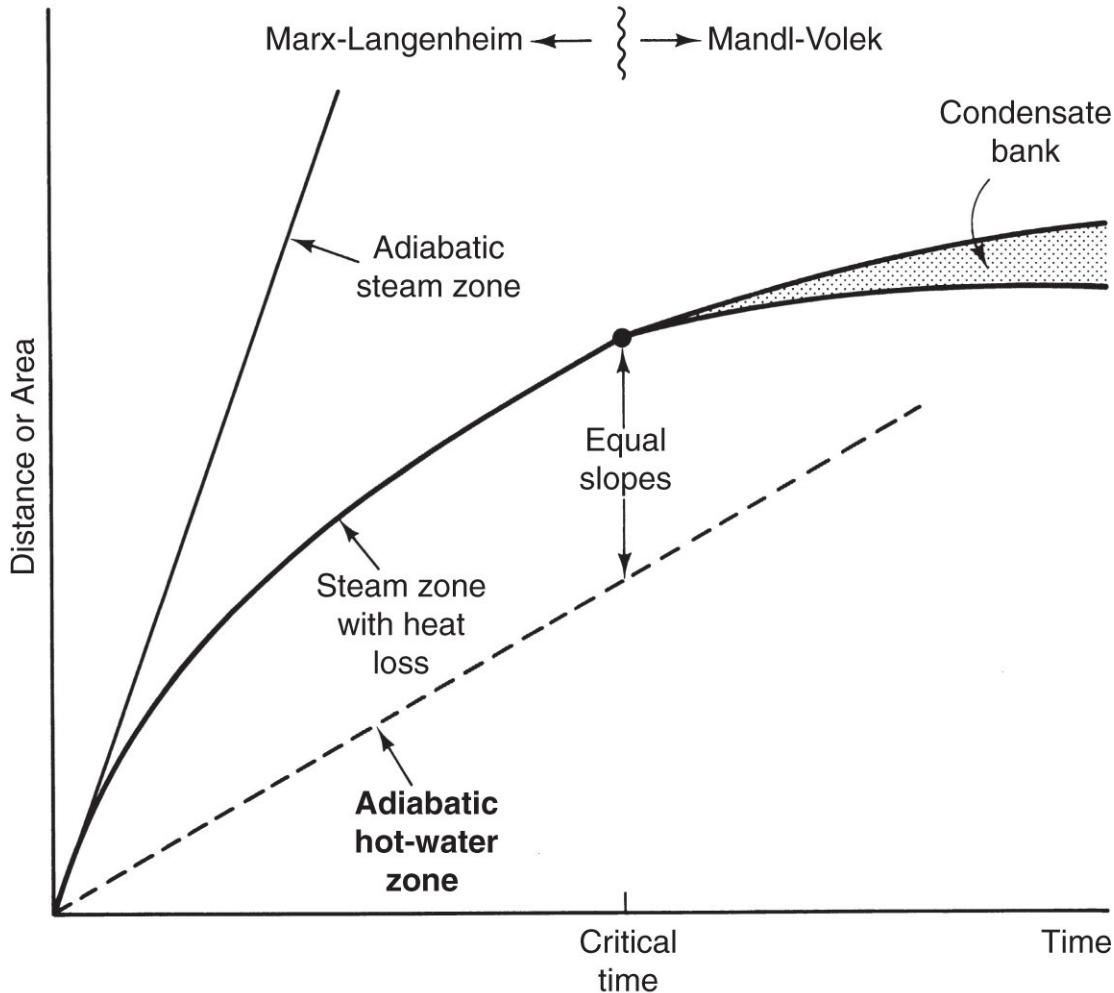


Fig. 11.19—Schematic of critical time.

Fig. 11.19 shows the velocities of the waves involved in this determination. *Adiabatic* means that there is no lateral heat loss.

Example 11.4. How Long Are Critical Times? The length of the critical time is illuminated by example calculation. Start with Eq. 11.65, which we evaluate at the following properties: $u_1/\phi = 1 \text{ ft/d}$,

$$M_n = 1.78 \frac{\text{MJ}}{\text{m}^3 \cdot \text{K}}, H_t = 30 \text{ ft}, D_{SF} = \Delta T = 298^\circ\text{F}, \dot{H}_J = 4 \times 10^8 \frac{\text{Btu}}{\text{day}}, W = 220 \text{ ft}, \text{ and } h_D = 1.28.$$

$$e^{t_{Dc}} \operatorname{erfc} t_{Dc}^{1/2} = \frac{u_i W H_t M_{Tl} \Delta T}{\phi(1 + D_{SF}) \dot{H}_J} = \left(1 \frac{\text{ft}}{\text{d}} \right) \left[\frac{(220 \text{ ft})(30 \text{ ft}) \left(1.78 \frac{\text{MJ}}{\text{m}^3 \cdot \text{K}} \right) (298^\circ \text{F})}{(1 + 1.28) \left(4 \times 10^8 \frac{\text{Btu}}{\text{day}} \right)} \right] \\ \times \left[\frac{(0.305 \text{ m})^3}{1 \text{ ft}^3} \frac{10^3 \text{ Btu}}{1 \text{ MJ}} \frac{1 \text{ K}}{1.8F} \right] = 0.0605$$

This is a transcendental expression for the dimensionless time to be evaluated by trial and error, a procedure which gives $t_{Dc} = 86$, which from Eq. 11.59 gives

$$t_c = \frac{t_{Dc} H_t^2}{4 K_{Ts}} = \frac{(86)(30 \text{ ft})^2}{4 \left(1.15 \frac{\text{mm}^2}{\text{s}} \right)} \left[\left(\frac{0.305 \text{ m}}{1 \text{ ft}} \right)^3 \frac{(10^3 \text{ mm})^2}{1 \text{ m}^2} \frac{1 \text{ days}}{(24)(3,600) \text{s}} \right] = 5,525 \text{ days.}$$

Evidently, more than ten years of injection are required for a condensate bank to form.

Strictly speaking, the ML theory applies only to times less than the critical time. After this point, the more sophisticated Mandl-Volek theory or the approximate Myhill-Stegemeier (1978) theory applies. Myhill and Stegemeier included the heat of vaporization in a condensing steamdrive in the ML theory by redefining the heated-zone growth rate in the manner of Eq. 11.14. [Figs. 11.14](#) and [11.15](#) both include this effect through the dimensionless latent heat h_D first defined in Eq. 11.16. The original ML theory is the case of h_D approaching infinity. Myhill and Stegemeier successfully correlated the cumulative oil/steam ratio of 18 steamdrive projects in [Fig. 11.15](#).

Finally, Ramey (1959) showed that the ML theory would apply to an arbitrary number of step changes in enthalpy at the injector. Applying superposition to Eq. 11.57, which despite everything we have done to it is still linear, yields

$$A(t_D) = \frac{H_t}{4 k_{Ts} \Delta T} \sum_{i=1}^n \dot{H}_{Ji} [\phi(t_{Di}) - \phi(t_{Di-1})], \dots \dots \dots \quad (11.66a)$$

where

$$\phi(t_{Di}) = e^{t_{Di}} \operatorname{erfc}(t_{Di}^{1/2}) + 2\sqrt{\frac{t_{Di}}{\pi}} - 1, \dots \quad (11.66b)$$

and t_{Di} in Eqs. 11.66 has the same form as in Eq. 11.64a but with $(t - t_i)$ replacing t . The enthalpy injection rate changes from $\dot{H}_{J(i-1)}$ to \dot{H}_{Ji} at t_i . Each change must maintain the same absolute value of ΔT and $t_D \geq t_{Dn}$.

[Fig. 11.20](#) shows the results of Eq. 11.66 applied to a slug injection of steam. During steam injection, the heated area grows at a steadily decreasing rate because of heat losses (this effect was present in [Fig. 11.19](#) also). In fact, the difference between the indicated curve and a straight line tangent to it at the origin is the diminution of the heated area because of heat loss. At $t = 10^3$ hours, cold water at the original reservoir temperature is injected, resulting now in heat transfer from the previously heated over- and underburden into the water and a very rapid decrease in the heated zone. The diverging nature of the flow in the vicinity of the injector causes a rapid decrease in which the rate of area cooling is much higher than the rate of area heating at the steam front. Calculations like those in [Fig. 11.20](#) probably account for why thermal processes are only infrequently conducted as slugs.

With the foregoing discussion as background, we can now address specific processes in a little more detail.

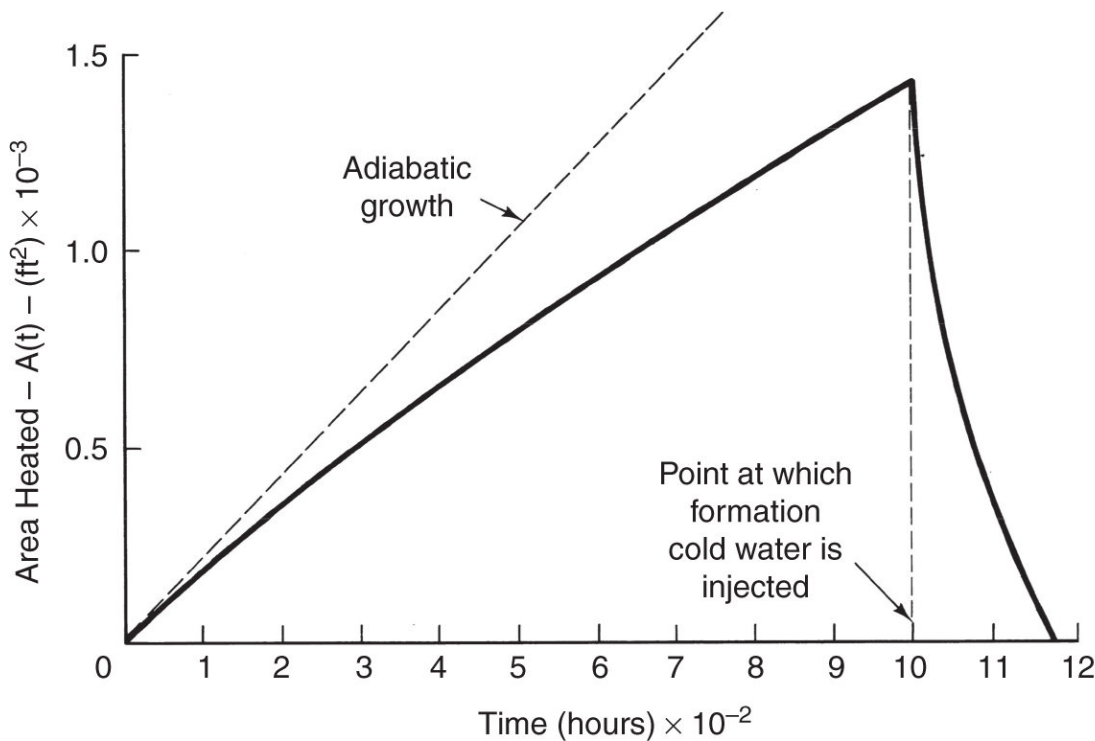


Fig. 11.20—Calculated area heated from superimposed ML theory (from David Goggin, personal communication).

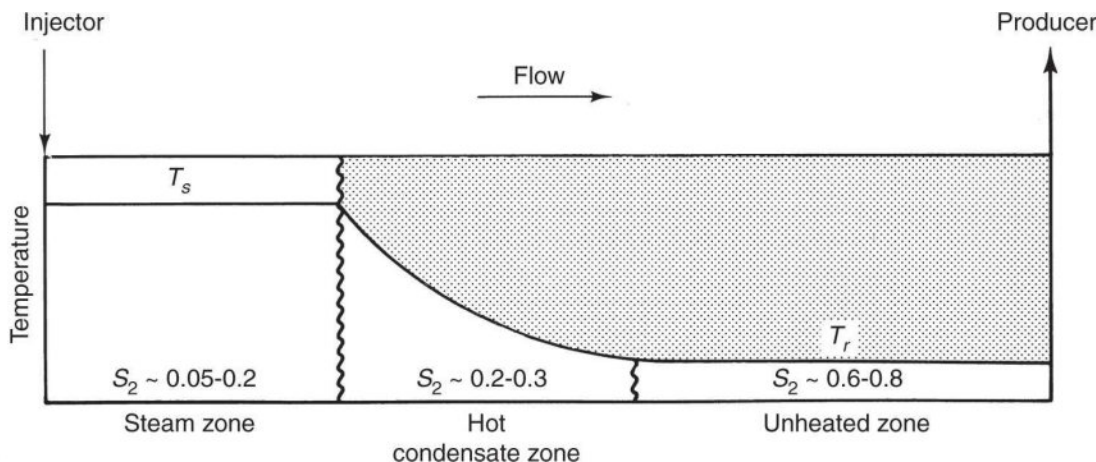


Fig. 11.21—Schematic zones in a steamdrive cross section.

11.6 Steamdrives

A steamdrive process beyond the Mandl-Volek critical time consists of an unheated zone, a condensate zone, and a steam zone ([Fig. 11.21](#)). The steam zone contains a two-phase mixture of steam and water flowing with a very small amount of oil. Because steam

viscosity is low, this zone is essentially at a constant pressure, which requires that it also be at a constant temperature. Most flow in this zone is steam, but the steam quality is very low because of the presence of a residual water phase. The enthalpy of the steam in this zone is often neglected. The zone contains oil at a very low saturation because that remaining behind the condensate zone has been at least partially distilled. Oil saturation is also low because the wetting state of the crude is frequently altered as the steam seeks to assume the position of the most nonwetting fluid in the pores. [Fig. 11.22](#) shows a correlation of steam-zone oil saturation.

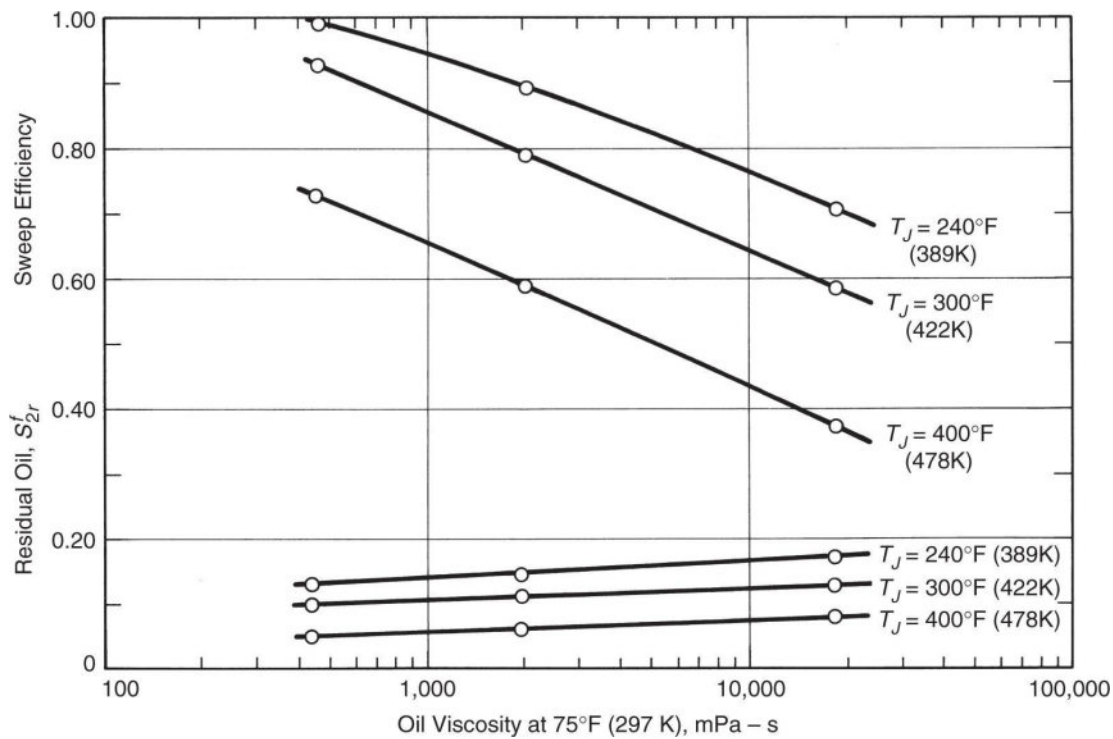


Fig. 11.22—Steam-zone sweep efficiency and residual-oil saturation from model experiment (Bursell and Pittman 1975).

It is easy to see where the incremental oil comes from in such a process. If the initial oil saturation is 0.7 and the oil saturation in the steam zone is 0.1, the oil displaced is 86% of that initially in place.

We can represent the profile in [Fig. 11.21](#) on the enthalpy/pressure plot in [Fig. 11.4](#). The unheated zone is a point in the liquid region on a low-temperature isotherm. The condensate

zone is a horizontal line segment from this isotherm to the bubblepoint curve, and the steam zone is a horizontal line from the bubblepoint curve to some low steam quality.

At a typical thermal-flooding condition of 1 MPa (147 psia), the densities of saturated liquid and of water vapor (steam) are 885 and 5.31 kg/m³ (55.3 and 0.33 lb_m/ft³), respectively. This pronounced difference between liquid and vapor properties is present in nearly all physical properties and contributes to several important effects in steamdrives, including in-situ quality, viscous stability, and override.

The quality of flowing steam in the reservoir is always quite low. Suppose that steam is flowing in a permeable medium in the presence of a residual water saturation. For two phases to be present, both the steam and water must be saturated. At a typical residual water saturation of 0.3 at 1 MPa and using the aforementioned densities, the in-situ quality is 1.3%. This low quality means that the fluids in the pore space of the medium are just barely inside the saturated liquid line in [Fig. 11.4](#), even though the *flowing* steam quality is nearly 100%.

A second consequence of the low steam density is related to viscous stability. Section 6.8 said that displacing with a fluid less viscous than the resident fluid in a horizontal medium inevitably leads to viscous fingering and reduced volumetric sweep efficiency. However, steam displacements are quite stable for the following reasons:

1. Steam is readily converted to water. If a perturbation of the steam front were to form, it would finger into the cold zone ahead of it and immediately condense. The condensation leads to a self-stabilizing effect that suppresses fingers.
2. In a steamdrive, the *kinematic* mobility ratio is usually favorable. It is more accurate for the mobility ratio to be based on kinematic viscosities for compressible flows. Mobility ratio is the ratio of pressure gradients ahead of and behind a piston-like front in a 1D displacement,

$$M_v = \frac{\left(\frac{dP}{dx}\right)_{\text{ahead}}}{\left(\frac{dP}{dx}\right)_{\text{behind}}} = \frac{\left(\frac{u\mu}{k}\right)_{\text{ahead}}}{\left(\frac{u\mu}{k}\right)_{\text{behind}}} \dots \quad (11.67)$$

- If the flux u is not a function of position (fluids are incompressible), Eq. 11.67 reduces to that given in Section 5.2.
- If the mass flux ρu is not a function of position, Eq. 11.67 reduces to a definition of mobility ratio based on the *kinematic* viscosity (dynamic viscosity divided by density). See Exercise 5.10.

In a steamdrive, neither condition is true, but the mass flux is more nearly constant. [For a more sophisticated discussion of the stability of thermal fronts, see Krueger (1982).]

The kinematic viscosity of steam, in fact, is usually greater than that of hot water at the same temperature and pressure. [Fig. 11.23](#) shows the reciprocal kinematic mobility ratio of a steam displacement plotted against pressure. Hot waterfloods are unstable over the entire range, which partly accounts for their inferior performance compared to steam, but steamfloods are stable at all pressures less than approximately 1.5 MPa (220 psia). Furthermore, superheated steam is even more stable than saturated steam, a paradoxical result from an isothermal-displacement point of view given that superheated steam has a very low viscosity. The increase in kinematic mobility ratio with pressure is the consequence of approaching the critical point of water. It further reinforces low-pressure restrictions on steamdrives.

The last consequence of small steam density deals with gravity segregation, or what [Chapter 5](#) called buoyancy effects. Because of the density difference between poorly mobile crude and highly mobile steam, the latter has a tendency to rise to the top of the reservoir, causing override and reduced volumetric-sweep efficiency. The gravity number N_g^0 scales the severity of the override. [Fig. 11.24](#) plots the effect of the inverse gravity number (note the altered

definition from Eq. 5.5d to account for compressible fluids and radial flow) on overrunning. If we review what causes N_g^0 to be large, we see that many steam floods occur under conditions that make override almost inevitable—clean sands with high horizontal and vertical permeability, low aspect ratios caused by close well spacing, and large density differences caused by heavy oils.

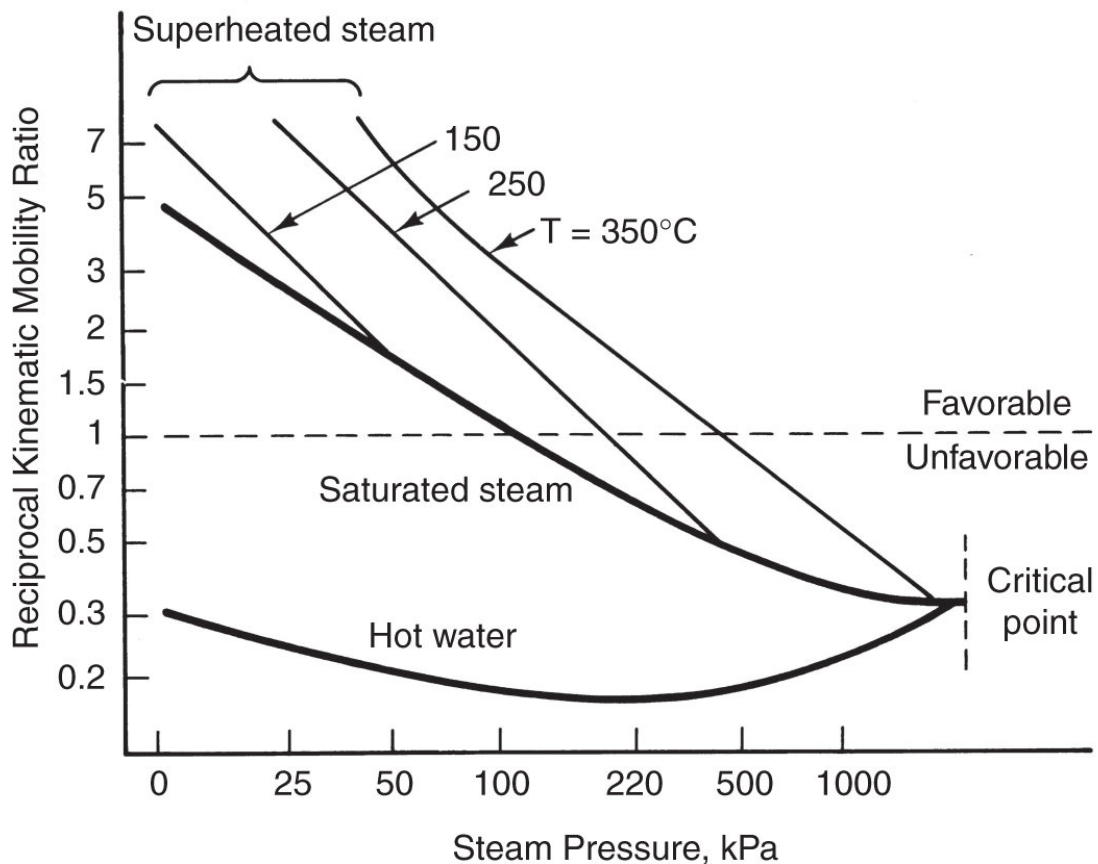


Fig. 11.23—Effective mobility ratio for steam displacements (Burger et al. 1985).

Two of the methods used in solvent flooding to prevent viscous fingering will mitigate override. If the reservoir has substantial dip, steam injected at the top of the reservoir will result in an interface that is more perpendicular to the reservoir trend. In addition, the interface can be made more vertical by adding foaming agents to the injected fluids (see [Chapter 10](#)). Another commonly used method is to inject steam near the bottom of the formation and produce from the top.

Gravity override has an important positive consequence. Once steam has broken through in the producing wells of a steamdrive, the injection rate is usually reduced to keep heat in the reservoir. At the reduced rate, heat transfer to the cold oil remains efficient because of the large area of the (now nearly horizontal) interface. Oil thus heated migrates to the top of the reservoir, because its density is now less than that of hot water, and subsequently flows to the producers through the steam zone. This is often called *drag flow*. If override is particularly severe, most of the oil is produced with steam through drag flow.

Override and drag flow lead to an alternative way to visualize steamdrives on the basis of the idea of the existence of a steam chest. [Fig. 11.25](#) illustrates this concept. According to Vogel (1984), the following simplifications are possible. First, the amount of time required for the steam to break through to the producing well is short compared to the life of the flood. Therefore, $(t - u) \approx t$ in Eq. 11.55, which renders the area constant, and, therefore, the energy injection rate is

$$\dot{H} = 2 \frac{k_T \Delta T A}{\sqrt{\pi K_T t}} + M_T A \Delta T v_z, \dots \quad (11.68a)$$

where the first two terms are heat losses to strata above and below the heated zones (the factor 2 in the equation), and the last term is the downward movement of the now-horizontal front. The downward velocity must be approximated by separate means. The oil production rate would be

$$\dot{q}_2 = A v_z. \dots \quad (11.68b)$$

Despite the fact that the frontal advance and drag mechanisms are conceptually very different, Vogel shows that the two approaches give similar results for heated areas. For example, the thermal efficiency illustrated in [Fig. 11.19](#) can be well approximated by

Frontal advance and drag mechanisms tend to be quite different with respect to their oil-recovery characteristics. Frontal-advance methods show large oil recovery early in the life of a field. Drag mechanisms tend to show prolonged periods in which the oil rate is constant after steam breakthrough.

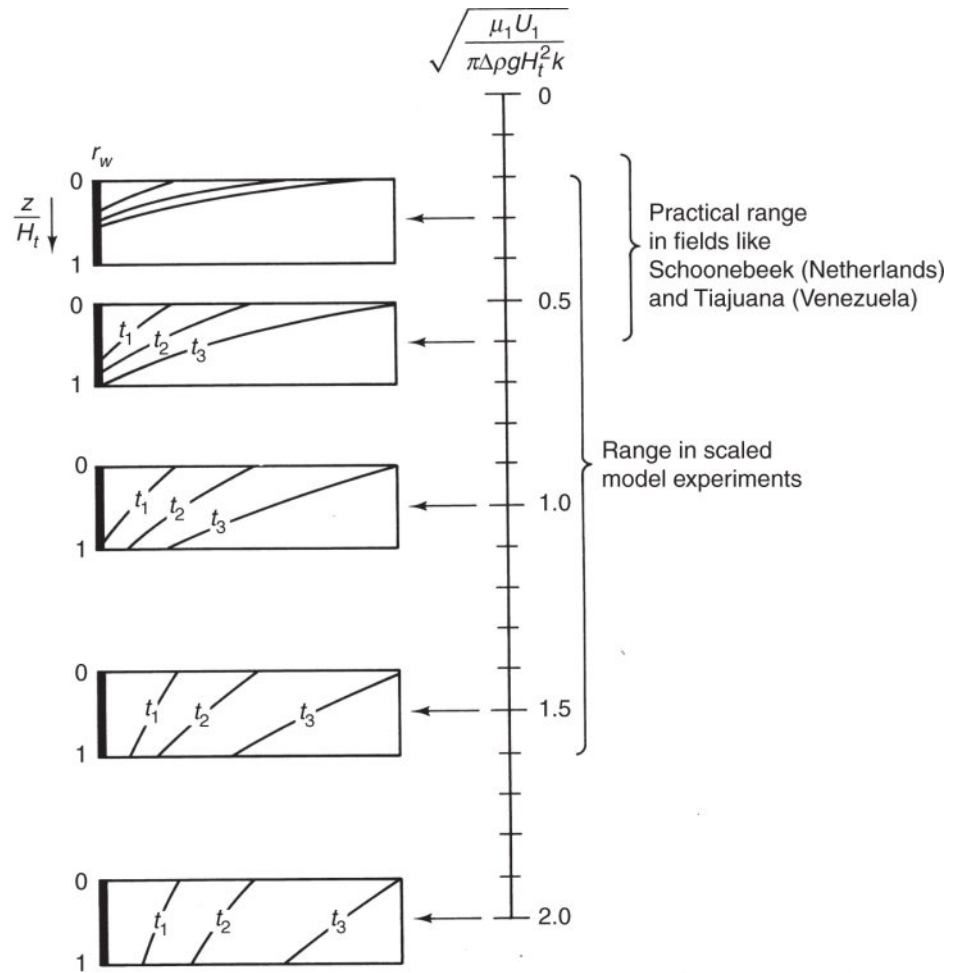


Fig. 11.24—Gravity override and gravity number for steamdrives (van Lookeren 1983).

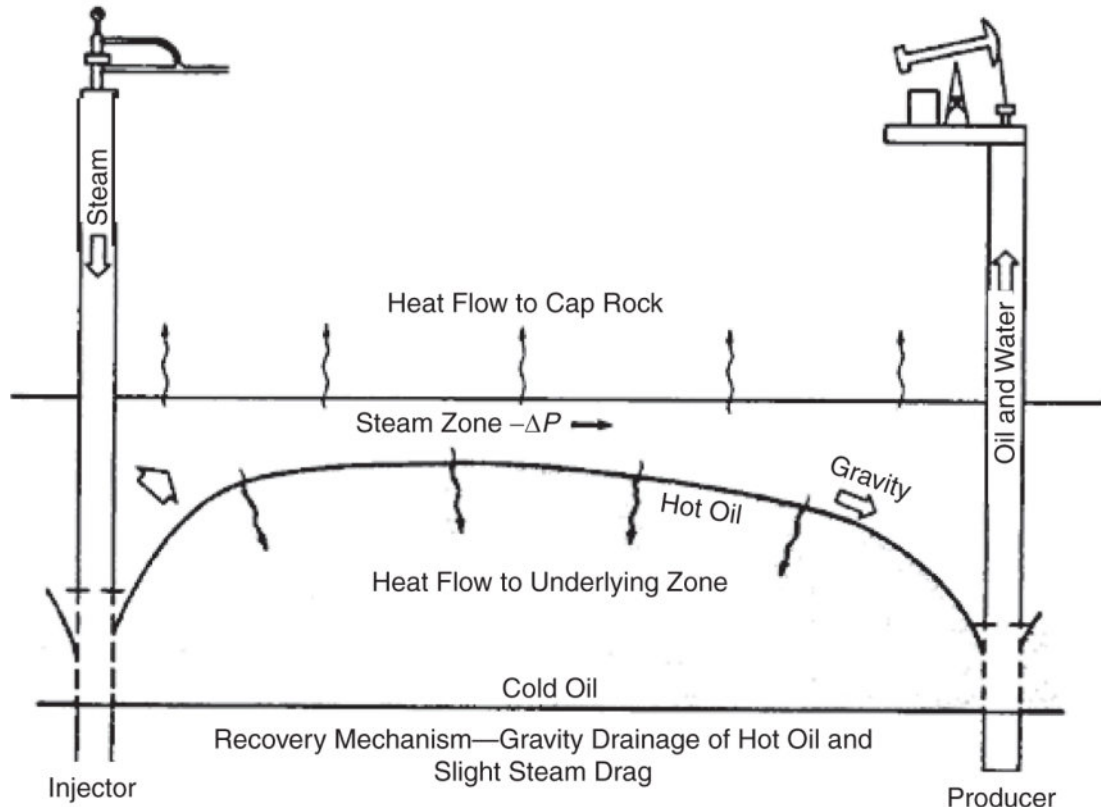


Fig. 11.25—Steamdrive with gravity override (Vogel 1984).

11.6.1 Case Histories. To illustrate a steamdrive, we discuss an early phase of a highly successful project in the Kern River Field, California. This large field has properties eminently typical of successful steamdrives: the field is shallow, the original reservoir pressure low, the sand fairly thick, and the permeability and porosity high ([Table 11.4](#)). As we discussed previously, each of these items will result in small heat losses to the over/underburden. The cold-oil viscosity is high, but not extremely so.

One of the projects at Kern River is the *Ten-Pattern Steamflood* with a well arrangement consisting of ten seven-spots (six injectors each surrounding an injector). The high density of wells in this area is made economically possible by the shallow depths.

Pattern size is correspondingly small. Because the productivity of the cold and heated oil is usually much less than the injectivity of steam, having more producers than injectors will better maintain fluid balance.

[**Fig. 11.26**](#) shows the response of the Ten-Pattern project. Steam injection began in early 1968. Oil-rate response was immediate and very strong. The prompt response was probably caused in part by the steam soaks that preceded the drive, but nearly all the later response is a result of the drive. Oil rate peaked in late 1970 and has sustained a surprisingly gentle decline thereafter, the decline being a consequence of override. Throughout the entire history shown, the oil rate was much greater than the estimated primary oil rate, meaning that incremental oil recovery was high. The cumulative steam/oil ratio reached a minimum in early 1972 and increased thereafter as steam broke through to more and more producers.

Some of the steam breakthrough came from gravity override. [**Fig. 11.27**](#) shows a temperature survey in a nearby well compared to the injection interval in the nearest injector well. Even though these two wells are quite near each other, the steam zone (indicated by the region of constant temperature) has migrated to the top of the zone. Upward migration of the steam zone confirms the oil-rate behavior shown in [**Fig. 11.24**](#). Injecting low in the interval like this is a common way to minimize gravity segregation. The hot-water zone below the steam zone shows a gradual temperature decrease that is uninterrupted at the bottom of the zone. The temperature gradients here and at the top of the zone are manifestations of heat losses to the adjacent strata.

TABLE 11.4—SUMMARY OF RESERVOIR DATA AS OF 1968, KERN RIVER FIELD STEAMFLOOD INTERVAL (BLEVINS AND BILLINGSLEY 1975)

Depth	700–770 ft	213–235 m
Estimated original reservoir pressure	225 psig	1.53 mPa
Current reservoir pressure	60 psig	0.41 mPa
Average net sand thickness	70 ft	21 m
Reservoir temperature	80°F	300 K
Oil viscosity at 85°F	2,710 cp	2710 mPa·s
Oil viscosity at 350°F	4 cp	4710 mPa·s
Average permeability to air	7,600 md	7.6 μm^2
Average porosity	35%	35%
Average oil content	1,437 bbl/ac-ft	0.185 m^3/m^3
Average oil saturation	52%	52%

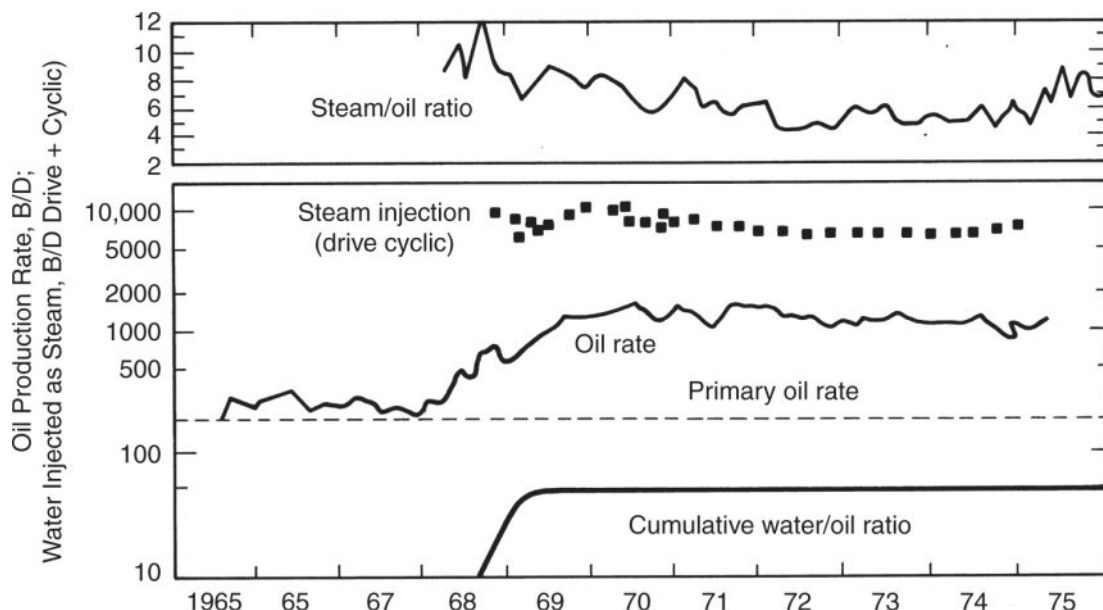


Fig. 11.26—Ten-pattern performance, Kern River field (Blevins and Billingsley 1975).

A more recent steamflood and one that illustrates many of the points made in the preceding theoretical sections is the Cruise E steamflood in the island nation of Trinidad and Tobago. As [Fig. 11.28](#) shows, the project injected steam for a little less than two years, followed by an equivalent period during which there was no steam injection. Injection then recommenced and continued from this time on. The major ideas learned from this field response are:

- In the first injection period, the oil production rate was essentially proportional to the steam injection rate. This observation is consistent with the growth of the steam zone being proportional to the heat injected and its being in turn proportional to the oil rate.
- The rapid collapse of the oil rate when steam injection ceased is consistent with [Fig. 11.19](#) and the discussion on this topic.
- The substantial increase in oil rate when steam injection recommenced suggests that the gravity override, which was discussed in connection with [Fig. 11.26](#), was quickly re-established and that oil production continued through downward movement of an already established interface.

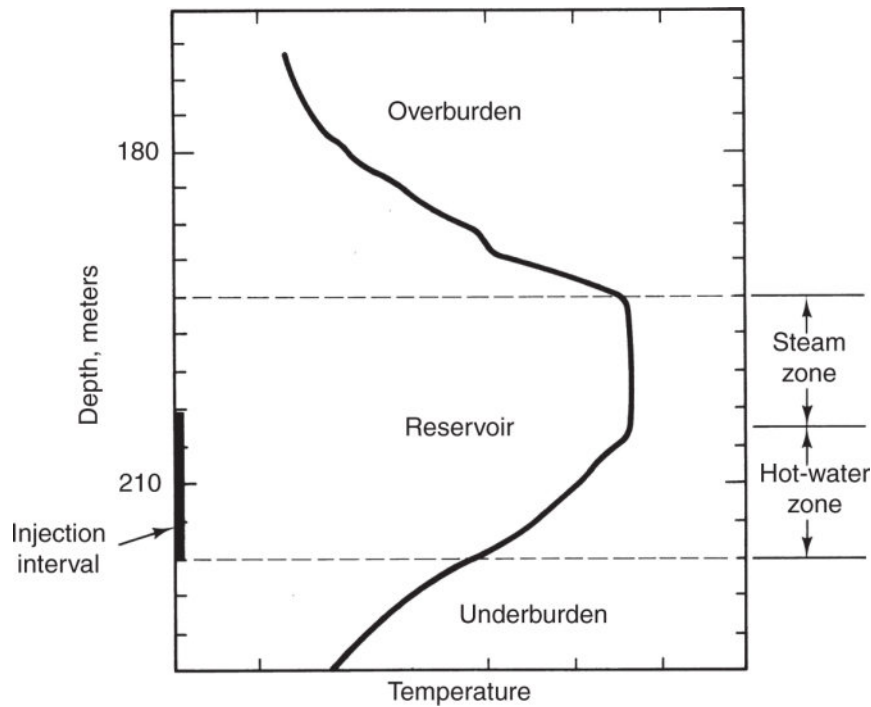


Fig. 11.27—Illustration of gravity override, Kern River field (Blevins and Billingsley 1975).

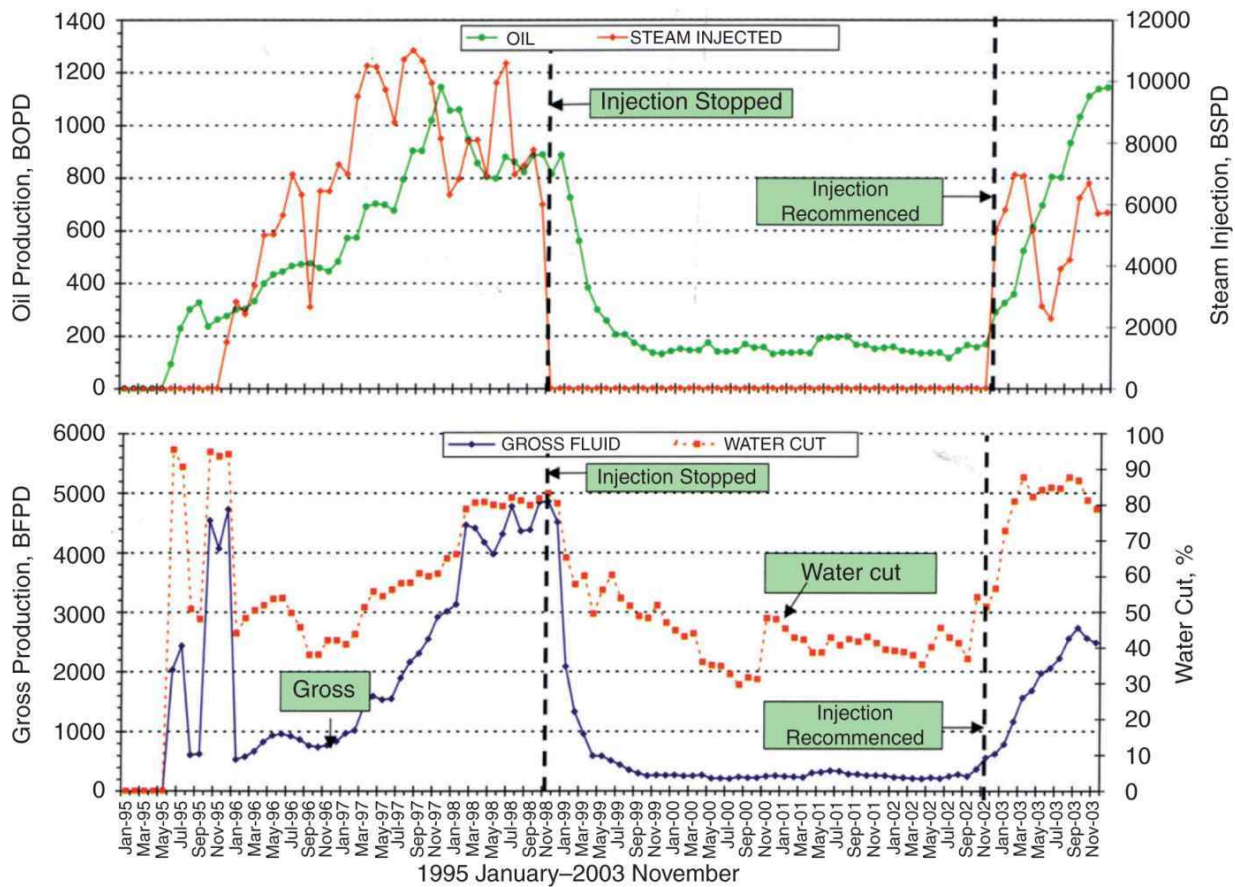


Fig. 11.28—Performance of the Cruise E (IADB) steamflood (Ramilal 2004).

In summary, we can say that the more steam injected, the more oil will be produced, a statement that could apply to many EOR processes.

11.7 Steam Soak

How a steam soak works is counterintuitive. Evidently, the steam displaces relatively little of the oil close to the well as it is injected. Instead, it channels or overrides through the oil to provide good thermal coverage for subsequent lateral conduction to take place. The process produces heated oil through several mechanisms: elevated pressure, solution gasdrive, thermal expansion, and gravity drainage. Even if the oil is heated inefficiently, increased production can result because of removal of skin damage and cleansing of the tubing string. Enough of the oil is removed near the wellbore so that subsequent injectivity improves. Therefore, steam soaks are

frequently used as precursors to steamdrives. See the discussion above in connection with [Fig. 11.2a](#).

Example 11.5. Estimating the Heated Radius. The productivity of a well undergoing cyclic steam injection is determined by the heated radius and the extent of viscosity reduction; see Exercise 11.1. The heated radius follows from energy-balance considerations, as illustrated in this example. The example also illustrates short cuts in the energy balance to make the results eminently practical.

Soak cycles are usually so short that heat losses to the adjacent strata are negligible. Eq. 11.51 consequently becomes

$$\dot{H}_J = \frac{d}{dt} (A H_t \rho_s U),$$

which integrates to yield

$$H_J = A H_t \rho_s H.$$

We use the integrated form of the energy balance because we are asking for a value at a point in time rather than a rate. The preceding equation has replaced the internal energy U on the right with the enthalpy H . Over a short time interval, the steam injection rate \dot{m} is constant, so that Eq. 11.6-4 becomes

$$\dot{m} \hat{H}_J = A H_t \rho_s H = A H_t \left[\phi (S_1 M_{T1} + S_2 M_{T2}) + (1 - \phi) M_{Ts} \right] \Delta T,$$

where \hat{H}_J is the specific injected enthalpy per unit mass and where the right side has been replaced with volumetric heat capacities under the assumption that all injected steam has been condensed. The only steam contribution to the balance remains in the \hat{H}_J term. Assuming the heated area A to be cylindrical enables solution of the preceding equation for the heated radius as

$$R_h = \sqrt{\frac{\dot{m} \hat{H}_J t_{inj}}{\pi H_t \left[\phi (S_1 M_{T1} + S_2 M_{T2}) + (1 - \phi) M_{Ts} \right] \Delta T}}.$$

As in many thermal calculations, the preceding equation contains many parameters; however, several of these can be evaluated through correlation or through generic properties. For example, we can assume the volumetric heat capacities to be

$$M_{T_1} = 62.5 \frac{\text{Btu}}{\text{ft}^3 - {}^\circ\text{F}}; M_{T_2} = 10 \frac{\text{Btu}}{\text{ft}^3 - {}^\circ\text{F}}; M_{T_s} = 41.8 \frac{\text{Btu}}{\text{ft}^3 - {}^\circ\text{F}},$$

The exercise will be worked in English units. The reservoir-specific parameters are $S_1 = 0.5 = S_2$; $\phi = 0.3$; $H_t = 50$ ft; $T_f = 100^\circ\text{F}$. The process values are $P_s = 200$ psia; $y = 0.6$; $\dot{m} = 3.5 \times 10^5 \frac{\text{lb}_m}{\text{day}}$. This rate is approximately 1,000 bbl of cold water/day. The injection period is $t_{\text{inj}} = 5$ days.

The correlations in [Table 11.1](#) give $T_f = 395^\circ\text{F}$, so that $\Delta T = 295^\circ\text{F}$ and $\hat{H}_{11} = 390 \frac{\text{Btu}}{\text{lb}_m}$; $\hat{H}_{13} = 1,218 \frac{\text{Btu}}{\text{lb}_m}$; $L_v = 828 \frac{\text{Btu}}{\text{lb}_m}$, which yields

$$\hat{H}_J = (1-y)\hat{H}_{11} + y\hat{H}_{13} = (0.4) \left(390 \frac{\text{Btu}}{\text{lb}_m} \right) + (0.6) \left(1,218 \frac{\text{Btu}}{\text{lb}_m} \right) = 887 \frac{\text{Btu}}{\text{lb}_m}.$$

The final result is

$$R_h = \sqrt{\frac{\left(3.5 \times 10^5 \frac{\text{lb}_m}{\text{day}} \right) \left(887 \frac{\text{Btu}}{\text{lb}_m} \right) (5 \text{ days})}{\pi (50 \text{ ft}) \left\{ (0.3) [(0.5)(62.5) + (0.5)(10)] + (1 - 0.3) \right\} \frac{\text{Btu}}{\text{ft}^3 - {}^\circ\text{F}} (279^\circ\text{F})}}$$

$$R_h = 29.8 \text{ ft.}$$

11.7.1 Case History. [Fig. 11.29](#) shows the response of a well in the Paris Valley field to seven steam-soak cycles. The oil response is in the upper part of the figure and the heat injection rate in the lower part. There were roughly two soaks per year from 1975 through 1978, each less than a month long. The cumulative oil produced after each cycle was roughly proportional to the amount of heat injected in each preceding soak. Within each cycle, the oil rate

rapidly peaked and then fell in a near-exponential decline. Because a similar decline was not as evident in the oil cut (not shown), the performance suggested that the total fluid rate was also declining within each cycle. The decline suggested that the reservoir pressure was falling, and for this reason, the operators mixed some air with the steam in the last cycle. For a given amount of heat injected, the peak rate in each cycle should decline because the heated zone will contain successively smaller amounts of oil. However, it is striking that substantial oil production occurred even after the seventh cycle.

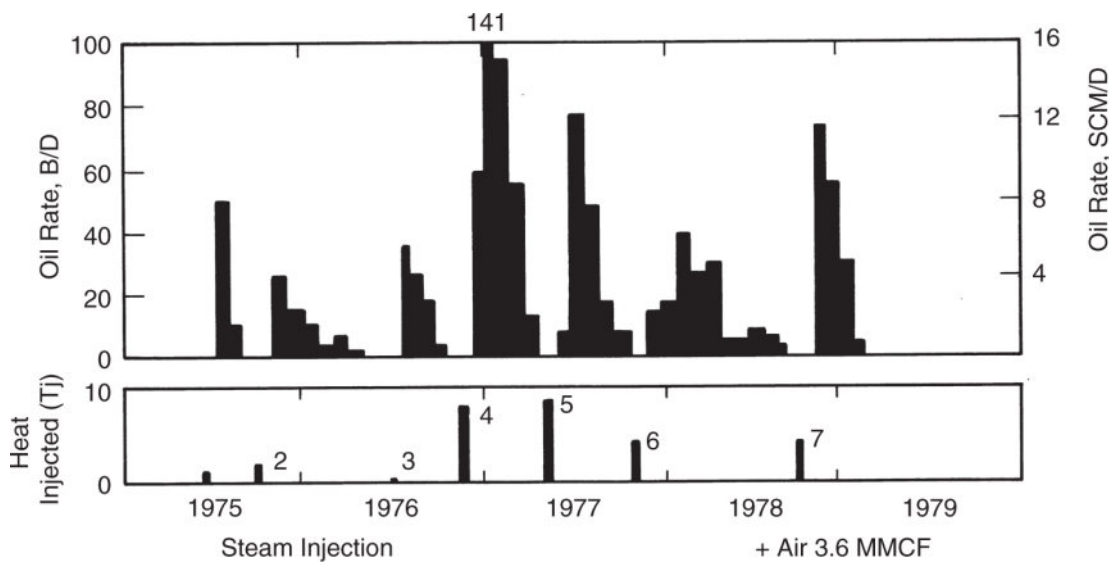


Fig. 11.29—Steam-soak response, Paris Valley field (Meldau et al. 1981).

11.8 In-Situ Combustion

If reservoir pressure, depth, and oil viscosity are too large for steam methods to work, in-situ combustion might be a good alternative. In this method, burning a portion of the crude in the formation generates thermal energy. Theoretically, the portion being burned is the coke or asphaltene portion of the crude, but the issue is far less clear-cut in practice. This complex process—the most complex of the EOR processes—involves heat and mass transfer along with kinetic phenomena.

[Fig. 11.30](#) and [Fig. 11.2c](#) show a schematic of an in-situ combustion process in cross section. In this process, usually some

form of oxidant (air or pure oxygen) is introduced into the formation, and the mixture is ignited (spontaneously or externally). Subsequent injection propagates the burning front through the reservoir. The burn front is very small (approximately one meter), but the combustion generates very high temperatures. These temperatures vaporize connate water and a portion of the crude. Both are responsible for oil displacement. The vaporized connate water forms a steam zone ahead of the burn front that operates very much like a steamdrive. The vaporized oil consists mainly of light components that form a miscible displacement. The reaction products of a high-temperature combustion can also form an in-situ CO₂ flood.

[Fig. 11.30](#) shows many variations of this process. Besides injection of oxidant, there can be coinjection of water in ratios to be determined by design. The water serves to improve the sweep efficiency of the process (you should note the parallel between this and WAG injection in [Chapter 7](#)) and to transport (scavenge) heat left behind in the burned zone. Too much water injection can quench the burn, as shown in [Fig. 11.30d](#). There is also a variation, not shown in [Fig. 11.30](#), in which water and oxidant are injected in opposite directions.

Another process variable is the temperature at which combustion occurs. [Fig. 11.31](#) is a plot from a laboratory experiment involving differential thermal analysis (DTA) of a crude. DTA consists of heating the crude in a preprogrammed fashion, usually linear over time, and measuring the rate of reactant consumption and the contents of the reaction products. Two general points can be made from this figure. First, oxygen is consumed in two peaks: a low-temperature oxidation at approximately 572 K (570°F) and a high-temperature oxidation at approximately 672 K (750°F). In the low-temperature oxidation, the crude is converted to alcohols, ketones, and aldehydes. Then, in the high-temperature oxidation, combustion proceeds completely to CO₂ and carbon monoxide. [Fig. 11.31](#) shows this progression and illustrates that the production of these two components is larger at high temperature. Furthermore, high temperatures oxidize many of the minerals in the permeable media,

particularly the clays (these may also exert a catalytic effect) and pyrite. High-temperature oxidation is better because it heats the oil more efficiently.

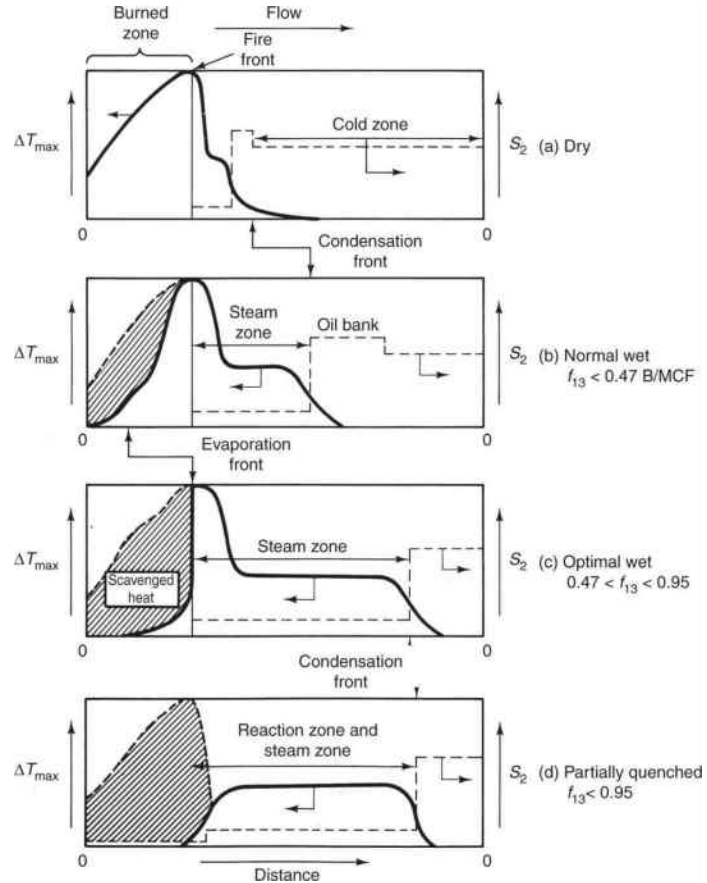


Fig. 11.30—In-situ combustion schematic (Prats 1982).

11.8.1 Case History. The Suplacu de Barcau Field in central Romania is one of the largest and longest-running EOR projects in existence.

This field is the site of an in-situ combustion project because of its very high oil viscosity and because it is very shallow. [Table 11.5](#) summarizes its properties. Other properties, most especially high porosity, permeability and oil saturation, have contributed to the success of the project.

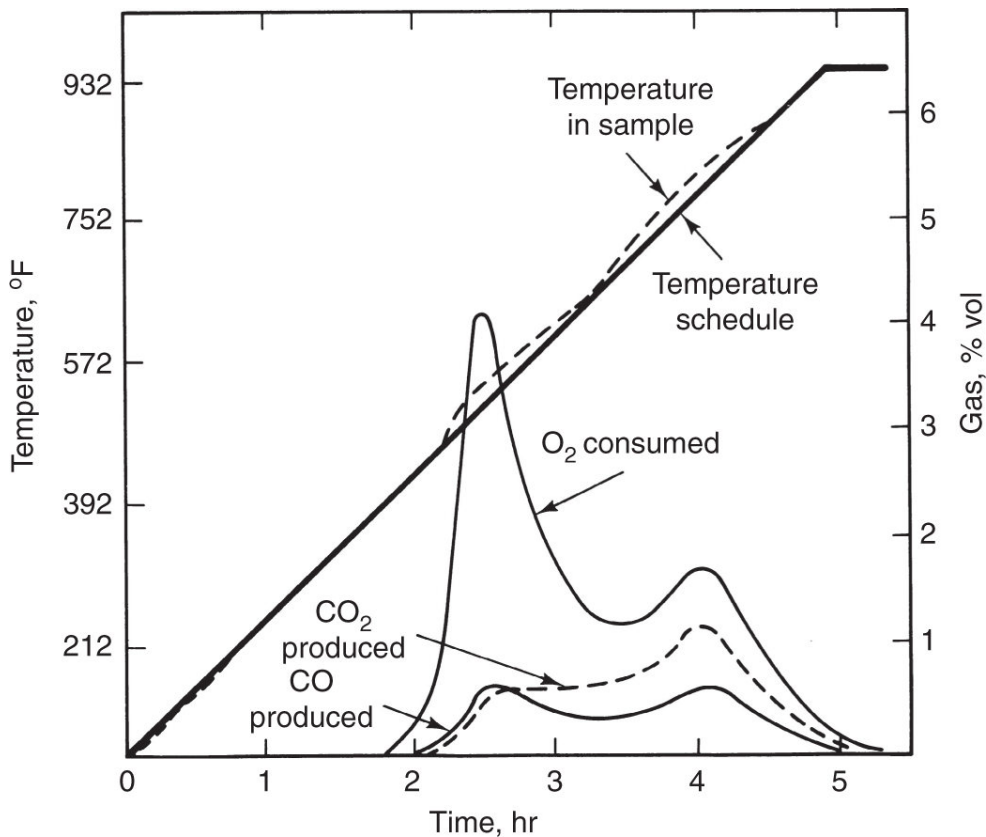


Fig. 11.31—Differential thermal analysis of a crude oil (Burger and Sahuquer 1972).

[Fig. 11.32](#) shows that the project has been going on from 1961 to 2005, or more than 40 years, without a significant decrease in oil rate. The ultimate recovery factor is likely to exceed 60%. Other in-situ projects are reviewed in Turta et al. (2007). See also Kumar et al. (2008) for an example of high-pressure air injection.

11.9 SAGD

We now return to SAGD, first discussed in Section 11.1 and [Fig. 11.2d](#). This is a technology that uses gravity with horizontal wells to produce extra-heavy crude and bitumen. [Fig. 11.33](#) shows a schematic of the SAGD process.

The schematics are on-end projections of a steam injector (upper well as a black dot) and a producer (lower well). After a short period of cycling, the injected steam rises (away from the producer) to the top of the formation to form a cavern or cavity. The cavity grows until the steam reaches the formation top, at which point heat begins to

be lost to the overburden and the cavity expands laterally. The rising steam heats the oil, which falls (again by gravity) to the bottom of the cavity to be collected by the producer. The rise of the steam and the fall of the oil occur in countercurrent flow.

[Fig. 11.33](#) also shows that, just as in in-situ combustion, there are several process variations that use combinations of injectants. Solvent injection with steam serves to improve the efficiency of displacements as well as to reduce the viscosity of the product. Injecting an inert gas with the steam serves the same purpose, but can also increase the pressure in the cavity. Many of these ideas have been tried in association with other forms of steam injection; most SAGD production is currently by the unaided SAGD process.

TABLE 11.5—PROPERTIES OF THE SUPLACU DE BARCAU FIELD (PANAIT-PATICA ET AL. 2006)

Lithology	Pliocene sandstone
Depth	50–200 m
Net pay	20 m
Porosity	0.32
Average permeability	1.7–2 μm^2
Reservoir oil viscosity	2 Pa·s
Initial oil saturation	0.85
Project area	1700 ha

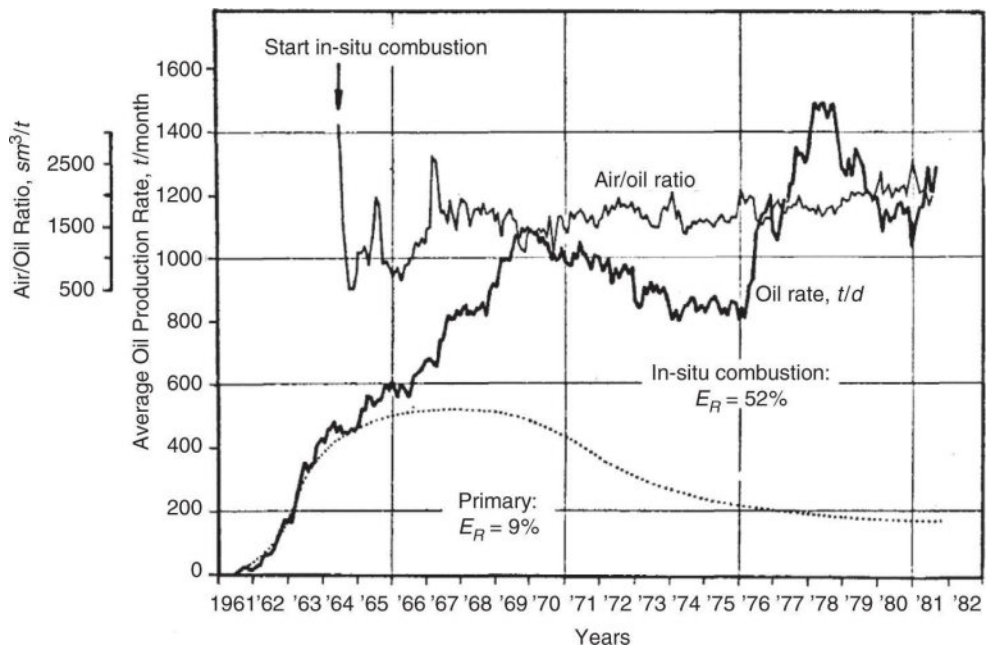


Fig. 11.32—Case history of in-situ combustion project in Suplacu de Barcau Field (Carcoana 1982).

These comments belie one of the principle difficulties with SAGD: the product, when cooled as it is produced to the surface, reverts nearly to its original state. The very high-viscosity product is difficult to transport at surface conditions, and therefore the process requires more surface facilities than other EOR processes, including:

- Provisions for constant heating of surface lines.
- Dilution by diluents. Mixing a low-molecular-weight hydrocarbon (e.g., kerosene at approximately 35%) with the cool bitumen makes it flowable and easy to transport. The diluent is stripped from the product at the processing point and returned to the wellsite for reuse.
- Bitumens are hydrocarbons that are deficient in hydrogen compared to their light-crude cousins. (Coal, which is even more viscous than bitumen, has a carbon/hydrogen molecular ratio of less than one. Natural gas has a ratio of 0.25.) The solution to this is to hydrogenate or upgrade the product. Many processes exist for doing this, but all require significant capital

expense. Often a combination of diluent and upgrading is called for.

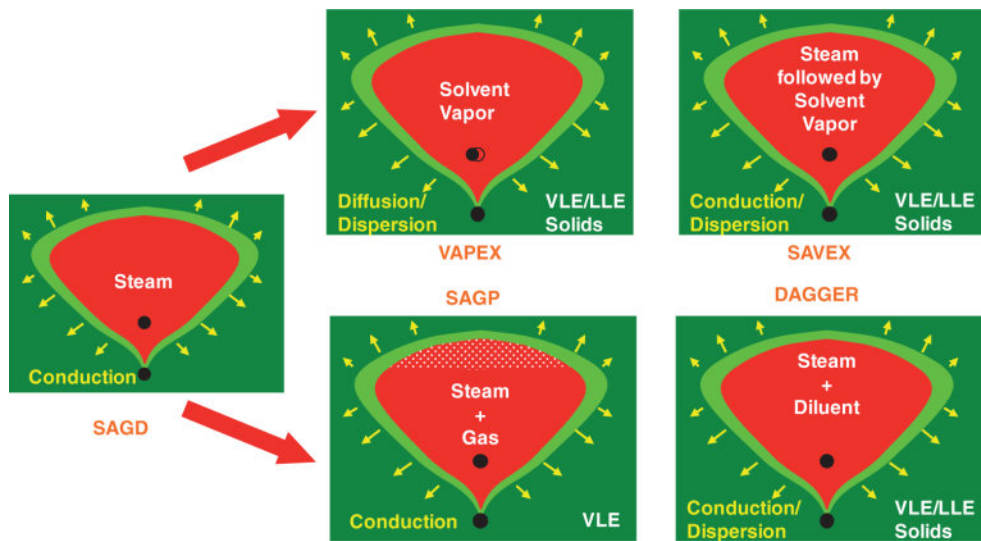


Fig. 11.33—Schematics of the SAGD process and variations.

Butler (1997) gives the basic equations for describing the rates in a SAGD process. See also Bonfantir and Gonzalez (1996).

11.9.1 Field Cases. SAGD is less mature than cyclic steam and steamdrives. The following is a summary from Jimenez (2008).

[Fig. 11.34](#) shows how the well pairs are arranged in a large field project. Each group of pairs extends from a central location or pad. The wells are approximately 10,000 ft long. The spacing of the wells is designed for maximum recovery efficiency: the pairs should be far enough apart so that their cavities do not overlap, but not so far as to leave unrecovered bitumen between them. The injector/producer distance is approximately 10 m, and in practice, wells are angled upward from the heel location to facilitate drainage.

As in [Fig. 11.30](#), there are several variations in implementation. For example, it is possible to use wells in groups of three (triads) to ensure interpair recovery. It seems possible also to use single horizontal wells in which injection is at the toe of the well and production from the heel.

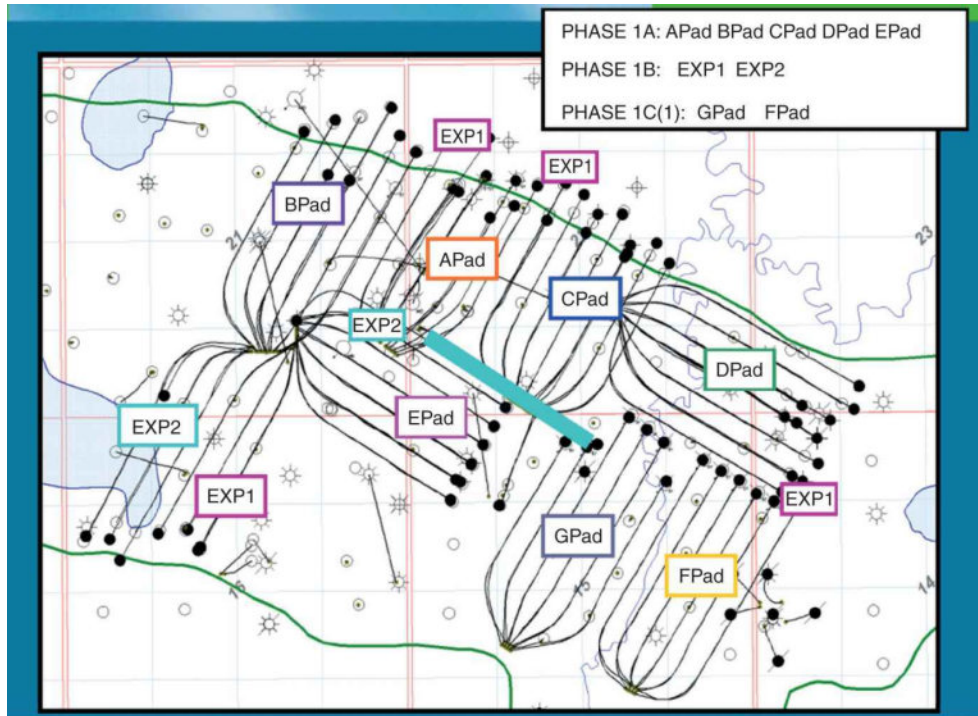


Fig. 11.34—Arrangement of well pairs at the Foster Creek project in Alberta, Canada.
Each trajectory is an injector/producer pair.

The performance of several pads in the McKay River field is shown in [Fig. 11.35](#). On first impression, this plot is unlike any that we have encountered so far. The horizontal axis shows the recovery efficiency, and the vertical axis represents the cumulative steam injected (as cold water) normalized by the original oil in place (not the pore volume). The plot is such that volumetric production (injecting a barrel of cold water in would result in a barrel of oil produced) would be a line of unit slope.

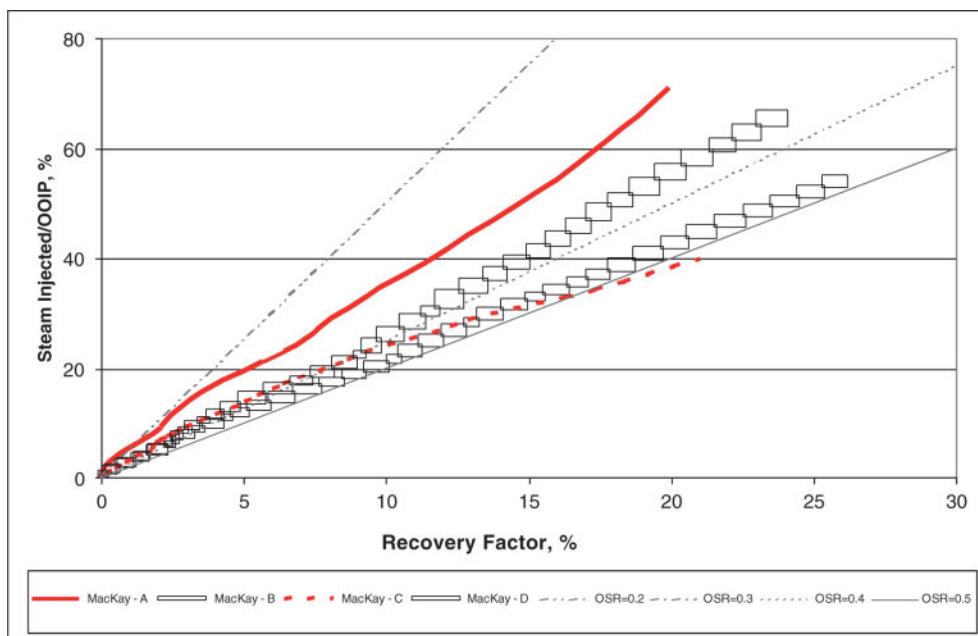


Fig. 11.35—Performance of seven well pads in the McKay River field (Jimenez 2008).

The recovery lines all have slopes less than one, suggesting either that there was mobile water initially present, or some bypassing between injectors and producers is occurring. Nevertheless, several of the recovery efficiencies are approaching 30%, and there is no evidence of their leveling out (which would be an upward curvature in this plot). The chances are excellent that ultimate recoveries will equal and exceed those for steamdrives.

11.10 Concluding Remarks

Our discussion here, and indeed throughout the text, has been from a reservoir-engineering viewpoint. For thermal methods, in particular, much of the success is a result of advancements in mechanical, completions, and production technology.

Surface steam generation, a simple concept in principle, is not easy under field conditions. For most cases, the waters available are brines of highly variable salinity. Such water cannot be used to generate 100% quality steam because of scaling. In fact, most boilers generate approximately 80% quality steam for this reason.

The evolution of the fuel used to generate steam is an example of the progress of these technologies. In the early days of steam

injection, the fuel used in surface generators was the produced crude. Because this usually heavy crude tends to be especially rich in components that cause air pollution when burned, surface steam generation can represent an environmental hazard. The expense of cleaning the boiler waste gases must be borne by the entire project. Environmental issues have been partially ameliorated by switching to natural gas as fuel. Nevertheless, water usage and air pollution continue to be issues for these technologies.

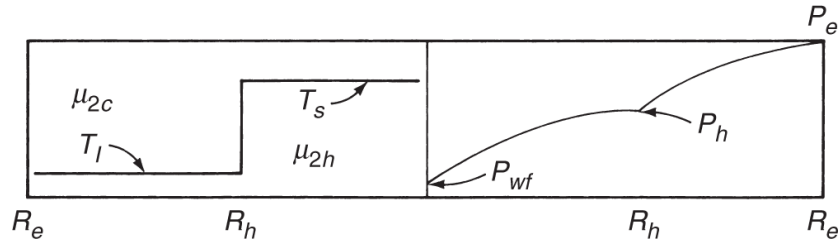
Difficulties in completing the wells plagued early steam operations, particularly the injectors. Thermal expansion of downhole equipment exacerbated the failures of the existing cementing techniques. Many of these difficulties have been remedied by using prestressed tubular goods in the wells. Current cement-bonding techniques and the development of thermal packers have dramatically reduced failure rates.

Undoubtedly, the future of thermal recovery rests on these and other technological advancements. These advancements include the cogeneration of electric power from steam boilers and the use of downhole steam generators, foams for mobility control, diluents in steam injection, and oxygen for in-situ combustion. Each of these extends the range of thermal methods to heavier or lighter crudes, deeper formations, or higher-pressure reservoirs. When this extension becomes a reality, thermal methods, already proven worldwide, will directly contend with other techniques for EOR of target oil.

Exercises

11.1 Effect of Temperature on Productivity Improvement. Steam soak is far from incompressible steady-state flow. However, rough estimates of productivity may be obtained by assuming both. The formula for the volumetric production rate q of a well that drains two concentric cylindrical volumes is

$$q = \frac{2\pi k H_{NET} (P_e - P_{wf})}{\mu_{2h} \ln\left(\frac{R_h}{R_w}\right) + \mu_{2c} \ln\left(\frac{R_e}{R_h}\right)}.$$



Assume that the inner cylinder is the heated volume after a steam soak.

- Derive an expression for the productivity index (*PI* or *J*) for this case in which

$$J \equiv \frac{q}{P_e - P_{wf}}.$$

Also derive an expression for the *PI* improvement,

$$(J)_{\text{improvement}} = \frac{(J)_{\text{stimulated}}}{(J)_{\text{unstimulated}}}.$$

- Estimate the *PI* improvement for a single steam cycle with the following data:

Reservoir temperature = 320 K

Heated-zone temperature = 480 K

Cold-oil density = 0.9 g/cm³

Hot-oil density = 0.8 g/cm³

Drainage radius = 116 m

Heated radius = 20 m

Well radius = 7 cm

API = 20°.

Use the viscosity data in [Fig. 11.1](#) for the hot (μ_{2h}) and cold (μ_{2c}) oil viscosities. Note that 1 cs = 1 mm²/s.

- c. Make subjective judgments about the effects of the following quantities on PI improvement: number of cycles, steam volume injected, cold-oil viscosity, permeability, and skin factor.

11.2 Estimating Generator Performance. Water at an initial temperature of 294 K (70°F) is being pumped through a steam generator at a rate of 15.9 m³/d (1,000 bbl/D) into an injection well. The wellhead temperature is 533 K (500°F). What is the wellhead steam quality? The generator burns 10,000 std m³/d of natural gas that has a heating value of 300 kJ/std m³. The generator efficiency is 80%.

11.3 Losses to Rock and Water for Steam. Rework Example 11.3 when steam is present. Use the same properties, except assume the medium to be filled with saturated steam of 50% quality.

11.4 Alternate Derivation of Thermal Velocity in Hot Waterflood. Eq. 11.22 can be derived in a fashion reminiscent of the composition-path constructions of Section 7.7. The coherence constraint for Eqs. 11.19a and 11.19c is

$$\frac{d(\rho_1 f_1 H_1 + \rho_2 f_2 H_2)}{d\left[\rho_1 S_1 H_1 + \rho_2 f_2 H_2 + \frac{(1-\phi)}{\phi} \rho_s H_s\right]} = \frac{\rho_1 H_1 d f_1}{\rho_1 H_1 d S_1}.$$

The density-enthalpy product has been added to the numerator and denominator of the right side to ensure units consistency below.

- a. By expansion of the numerator and denominator on the left side of the preceding equation, show that the lines of constant temperature satisfy the coherence condition. These

will represent the saturation change at the leading edge of the cold-oil bank.

- b. We know that the preceding equation will be satisfied if the numerators and denominators are identically equal. Show that equating the denominators yields an ordinary differential equation for which the solution is

$$T = I_1 \left\{ S_1 (M_{T_1} - M_{T_2}) + \left[M_{T_2} + \frac{(1-\phi)}{\phi} M_{T_s} \right] \right\}^{M_{T_2}/(M_{T_1}-M_{T_2})},$$

where I_1 is an integration constant. Recall that $\rho_j dH_j = M_{Tj} dT$. The preceding equation along with the $T = \text{constant}$ lines form the composition path grid in S_1-T space. Sketch a few lines in this grid.

- c. Equate the numerators of the first equation in the exercise and perform the analogous operation to give

$$T = I_2 \left[f_1 (M_{T_1} - M_{T_2}) + M_{T_2} \right]^{M_{T_2}/(M_{T_1}-M_{T_2})},$$

where I_2 is a second integration constant. The preceding equation and the $T = \text{constant}$ lines are the composition path grid in f_1-T space.

- d. Eliminate temperature between the second and third equations to show that the temperature-varying paths in composition space follow

$$f_1 + \frac{M_{T_2}}{M_{T_1} - M_{T_2}} = I_3 \left[S_1 + \frac{M_{T_2} + \frac{(1-\phi)}{\phi} M_{T_s}}{M_{T_1} - M_{T_2}} \right],$$

where I_3 is another integration constant.

- e. The preceding equation suggests that $df_1 = I_3 dS_1$. Use the similar differential forms of the third and fourth equations for dT to show that the first equation will yield $I_3 = df_1/dS_1$. Substituting this back into the fourth equation gives Eq. 11.22.

11.5 Fractional Flow for Hot Waterfloods. The following problem is intended to reinforce the fractional-flow construction in [Fig. 11.7](#) and to provide practice in estimating thermal properties.

- We are to perform a hot waterflood consisting of saturated liquid water at 1 MPa pressure. Estimate the hot-water temperature, the hot-oil viscosity, and the volumetric heat capacities for water, oil, and the solid phase. Additional data are as follows:

	Initial (cold)	Injected (hot)
Temperature, K	300	—
Water viscosity, mPa·s	1.0	0.5
Water density, g/cm ³	1.0	1.0
Oil viscosity, mPa·s	700	—
Oil density, g/cm ³	0.9	0.9

Use the data or correlations in [Tables 11.2](#) and [11.3](#) (the properties of water-saturated sandstone most nearly approximate the present case), Eq. 11.2, and [Fig. 11.7](#). The porosity is 0.2.

- The exponential relative-permeability curves apply to this horizontal reservoir with the following parameters:

$$S_{1r} = 0.2 \quad k_{r1}^0 = 0.3 \quad n_1 = 2$$

$$S_{2r} = 0.2 \quad k_{r1}^0 = 0.8 \quad n_2 = 2$$

You may assume that these functions are independent of temperature. Using these data and those of Part (a), calculate and plot the hot- and cold-water fractional-flow curves.

- Calculate and plot the 1D effluent history of oil and temperature based on the information given above. The initial water cut is 0.1.

11.6 Dimensional Analysis of Heat Transfer From Tubing. In this exercise, we develop the dimensional argument for Eq. 11.33, the heat-transfer coefficient correlation for heat flow from the tubing. [Fig.11.11](#) shows the approximate velocity and temperature profiles. If the fluid flow is steady-state, laminar, Newtonian, and incompressible, the velocity profile in the tubing becomes

$$v = v_{\max} \left[1 - \left(\frac{r}{R_{ti}} \right)^2 \right].$$

- a. The energy balance of Eq. 2.39 applies to the flowing fluid if the porosity is set to one. If the energy balance retains only radial conduction and axial convection, show that when applied to the fluid in the tubing, it reduces to

$$\rho_f C_{pf} v_{\max} \left[1 - \left(\frac{r}{R_{ti}} \right)^2 \right] \frac{\partial T}{\partial z} = k_{Tf} \frac{1}{r} \frac{\partial}{\partial r} \left(r \frac{\partial T}{\partial r} \right).$$

The preceding equation assumes constant thermal conductivity k_{Tf} and viscosity μ_f of the flowing fluid. The boundary conditions on this equation are

$$\left(\frac{\partial T}{\partial r} \right)_{r=0} = 0, \quad T(R_{ti}, z) = T_{ti}, \quad T(r, 0) = T_f,$$

where T_{ti} is constant.

- b. Introduce the following dimensionless variables:

$$r_D = \frac{r}{R_{ti}}, \quad z_D = \frac{K_{Tf} z}{v_{\max} R_{ti}^2}, \quad T_D = \frac{T - T_{ti}}{T_f - T_{ti}}$$

into the second and third equations, and show that they reduce to

$$(1 - r_D^2) \frac{\partial T_D}{\partial z_D} = \frac{1}{r_D} \frac{\partial}{\partial r_D} \left(r_D \frac{\partial T_D}{\partial r_D} \right) \left(\frac{\partial T_D}{\partial r_D} \right)_{r_D=0} = 0, \quad T_D(1, z_D) = 0, \quad T_D(r_D, 0) = 1.$$

The dimensionless temperature must therefore be a function only of r_D and z_D .

- c. The heat-transfer rate $\dot{Q} \rightarrow$ from the tubing is

$$\dot{Q} = -2\pi \int_{\xi=0}^{\xi=L} \left(rk_{Tf} \frac{\partial T}{\partial r} \right)_{r=R_i} d\xi.$$

Show that the dimensionless form of this equation is

$$\frac{\dot{Q}}{2\pi L k_{Tf} r_D (T_f - T_{ti})} = -\frac{2\pi}{Z_{DL}} \int_0^{Z_{DL}} \left(r_D \frac{\partial T}{\partial r_D} \right)_{r_D=1} d\xi,$$

where the additional term in sixth equation is

$$Z_{DL} = \frac{K_{Tf} L}{v_{\max} R_{ti}^2}$$

and L is the length of the heated tubing. Because of the evaluation at $r_D = 1$ and the integration between known limits, the integral is a function of Z_{DL} only.

- d. Define an average heat-transfer coefficient h_{Tf} as

$$\dot{Q} \equiv \pi R_{ti} L (T_f - T_{ti}) h_{Tf}.$$

Eliminate \dot{Q} between the equation in part c and the preceding equation to show that, after rearranging,

$$\frac{R_{ti} h_{Tf}}{k_{Tf}} = N_{Nu} = f(Z_{DL}).$$

Eq. 11.33 follows from this because Z_{DL} decomposes into

$$\begin{aligned}\frac{K_{If}L}{v_{\max}R_{ti}^2} &= \frac{k_{If}L}{\rho_f C_{pf} v_{\max} R_{ti}^2} = \frac{k_{If}}{\mu C_{pf}} \cdot \frac{\mu}{\rho_f v_{\max} R_{ti}} \cdot \frac{L}{R_{ti}} \\ &= \frac{1}{N_{Pr}} \cdot \frac{1}{N_{Re}} \cdot \frac{1}{R_{ti}}\end{aligned}$$

The Brinkman number is absent from the last equation because the original equation did not include viscous heating.

11.7 Calculating Heat Losses. For steamdrives, the rate of heat loss to the over- and underburden is frequently so significant that it alone can furnish a good measure of success. In this exercise, you will use theoretical relations to estimate measures of the success of a steamdrive. Use the following quantities in this exercise:

$$\begin{array}{ll} T_i = 317 \text{ K} & k_{Ts} = 2.1 \text{ J/s-m-K} \\ H_t = H_{NET} = 11 \text{ m} & M_{To} = 2.3 \text{ MJ/m}^3\text{-K} \\ \phi = 0.3 & M_{Tu} = 2.8 \text{ MJ/m}^3\text{-K} \\ \Delta S_2 = 0.31 & t = 4.5 \text{ yr} \\ H_3 = 44.4 \text{ MJ/kg} & \end{array}$$

- Estimate the steam-zone temperature. P_i , the initial reservoir pressure, is 2.72 MPa.
- Calculate the dimensionless time and dimensionless latent heat from Eq. 11.16. The steam quality y is 0.7.
- From the Myhill-Stegemeier charts ([Figs. 11.15](#) and [11.16](#)), estimate the useful heat fraction \bar{E}_{hs} and the dimensionless oil/steam ratio.
- From the results of Part c, calculate the oil/steam ratio F_{23} and the energy efficiency. The latter is defined as

$$\eta_E = \frac{\text{Oil heating value}}{\text{Heat requirement to produce steam}}$$

and is given by

$$\eta_E = \frac{F_{23}\gamma_2\eta_B H_3}{C_{p1}\Delta T(1+h_D)},$$

where η_B is the boiler efficiency and γ_2 is the specific gravity of the oil. Assume that $\gamma_2 = 0.94$ and $\eta_B = 0.8$.

Nomenclature*

ACN	Alkane carbon number
ASP	Alkali surfactant polymer
A	Area (usually cross sectional or surface area) [=] L^2
A_i	Accumulation function for general hyperbolic equation
A_{jk}	Area between phase j and k [=] L^2 or accumulation matrix for hyperbolic system of equations
$A_H, B_H, E_H,$ F_H	Parameters in Hand representation of ternary phase behavior
A_p	Pattern area [=] L^2
atm	Atmospheric pressure [=] F/L^2
a_i	Activity of component i
a_i, b_i	Parameters in Langmuir isotherm
a_T	Geothermal temperature gradient [=] T/L
a_c	Specific surface area [=] L^{-1}
B	Vector function
B_j	Formation volume factor for phase j [=] $L^3/\text{standard } L^3$
b	Repulsion parameter for cubic EOS [=] L^3/mole
$CAPEX$	Capital expenditure
CDC	Capillary desaturation curve
$CDCF$	Cumulative discounted cash flow
CMC	Critical micelle concentration
CV	Control volume
C_n	Cumulative storage capacity up to layer n
C_i	Overall concentration of component i [=] amount/volume (definition of amount depends on the

	component)
$[C_i]$	Concentration in molal units [=] amount/kg solution
C_i^0	Tie-line convergence point on ternary diagram [=] consistent with concentration
C_{ij}	Volume fraction of component i in phase j or mass concentration of component i in phase j [=] amount/ L^3 of phase
C_4^*	Threshold surfactant concentration for foam formation [=] consistent with concentration
C_{2pL}, C_{2pR}	Refers to left [type II(+)] and right [type II(-)] oil coordinates of the plait point
C_{pj}	Heat capacity of phase j [=] $F - L/\text{amount} - T$
ΔC_{pr}°	Standard heat capacity change of reaction r [=] $F - L/\text{amount} - T$
C_s	Salinity[amount/solution volume]
C_{Sel}	Lower salinity limit for Winsor type III phase behavior
C_{Seu}	Upper salinity limit for Winsor type III phase behavior
c	Compressibility [=] L^2/F
D	Decline rate constant [=] t^{-1} , or capillary diffusivity [=] L^2/t
D_i	Frontal advance lag or retardation factor for species i
D_{ij}	Effective binary diffusion coefficient of species i in phase [=] L^2/t
D_p	Particle or sphere diameter [=] L
D_z	Elevation or depth from a reference datum [=] L
d_p	Effective diameter of a polymer molecule [=] L
$EACN$	Equivalent alkane carbon number
EO	Ethylene oxide
E	Effective viscosity ratio in Koval theory
\overrightarrow{E}	Energy flux [=] $F/L - t$
	Areal sweep efficiency (fraction)

E_A	
E_D	Displacement or local sweep efficiency (fraction)
E_1	Vertical sweep efficiency (fraction)
EL	Economic limit [amount/time]
E_{MB}	Mobility buffer efficiency (fraction)
EOR	Enhanced oil recovery
E_R	Recovery efficiency (fraction)
E_V	Volumetric sweep efficiency (fraction)
F	Electrical formation resistivity factor
F_n	Cumulative flow capacity up to layer n
F_i	Overall fractional flux of component i or flux function for general hyperbolic equation
F_{23}	Oil-steam ratio [=] volume oil/volume steam as cold water
f_a	Fraction of total pore space available to flow
f_j	Fractional flow of phase j
f_3^*	Value of f_3 separating two foam flow regimes (fraction)
\vec{g}	Gravitation acceleration vector [=] L/t^2 (magnitude: g)
GB	Gas bank formed between states I and J in foam injection
$HPAI$	High pressure air injection
$HPAM$	Hydrolyzed polyacrylamide
H	Enthalpy [=] $F - L/\text{amount}$
\hat{H}_{ij}	Partial enthalpy of component i in phase j [=] $F - L/\text{mass}$
H_r°	Standard enthalpy of formation for reaction r [=] $F - L/\text{amount}$
H_K	Effective heterogeneity factor in Koval theory
H_{NET}	Net thickness [=] L
H_t	Total thickness [=] L

h	Hydraulic head [=] L
h_T	Heat transfer coefficient [=] $F/L^2 - t$
I	Identity matrix or injectivity [=] $L^5/F - t$ or initial condition
Inj	Injection
ISC	In-situ conversion process
i	Injection rate [=] L^3/t , or initial condition
IFT	Interfacial tension [=] F/L
IOR	Incremental oil recovered [=] standard L^3
IR	Initial-residual
J	Productivity index [=] $L^5/F - t$ or injection condition
J_{jk}	Jacobian elements for hyperbolic transformed equations
j	Leverett j -function
\vec{j}_{cij}	Convective mass flux of component i in phase j [=] mass of i/L^2 phase $j - t$
\vec{j}_{Dij}	Hydrodynamic dispersive mass flux of component i in phase j [=] mass of i/L^2 phase $j - t$
K	Hydraulic conductivity [=] L/t or UOP characterization factor
K_{di}	Mass partition coefficient for component i adsorbed onto solid phase [=] amount i in solid – volume phase j /amount of solid – amount i in phase j
K_h	Permeability in the horizontal direction [=] L^2
K_i	Equilibrium flash vaporization ratio
$\vec{\vec{K}}_{ij}$	Dispersion tensor for species i in phase j [=] L^2/t
K_l	Longitudinal dispersion coefficient [=] L^2/t
K_N	Selectivity coefficient for cation exchange
K_{pl}	Power-law coefficient
K_r	Equilibrium constant for reaction r
K_T	Thermal diffusion coefficient [=] L^2/t

K_z	Permeability in the vertical direction [=] L^2
k	Permeability [=] L^2
k	Reaction decay constant [=] t^{-1}
k_j	Permeability to phase j [=] L^2
k_m	Mass transfer coefficient [=] t^{-1}
k_{rj}	Relative permeability of phase j
k_{rj}°	Endpoint relative permeability to phase j
k_T	Thermal conductivity [=] $F/L - t$
L	Length [=] L
L_c	Lorenz coefficient (fraction)
L_V	Heat of vaporization [=] $F - L$ /amount (also called latent heat)
\ln	Natural logarithm
\log	Base 10 logarithm
M	Mobility ratio
MP	Micellar-polymer
M_{Sh}	Shock mobility ratio
M_T	Volumetric heat capacity [=] $F/L^3 - t$ or target mobility ratio
M_V	Kinematic mobility ratio
M_w	Molecular weight [=] mass/amount
M°	Endpoint mobility ratio
m	Positive constant describing pore-size distribution
\dot{m}	Mass flow rate [=] mass / t
N	Number of contacts in mixing cell
N_B	Bond number
N_{Br}	Brinkman number
N_C	Total number of components
N_D	Number of spatial dimensions

N_{Da}	Damkohler number
N_{Deb}	Deborah number
N_F	Number of degrees of freedom
N_g^o	Gravity number
N_{Gr}	Grashof number
\vec{N}_i	Mass flux of species i [=] mass of $i/L^2 - t$
\vec{N}_{ij}	Mass flux of component i in phase j [=] mass of i/L^2 phase $j - t$
N_L	Total number of layers
N_{Nu}	Nusselt number
N_p	Total number of phases
NPV	Net present value
N_p	Cumulative mass produced [=] mass
N_{pe}	Peclet number
N_{pr}	Prandtl number
N_R	Total number of chemical reactions
N_{Re}	Reynolds number
N_{RL}	Rapoport and Leas number
N_{vc}	Local viscous-capillary number
n	Number of moles [=] amount
\vec{n}	Unit outward normal vector
n_j	Exponent on analytic relative permeability functions
n_L, n_V	Relative amounts of liquid and vapor (fraction)
n_M	Parameter in Meter model
n_{pl}	Power-law exponent
OOIP	Original oil in place [=] standard L^3
PO	Propylene oxide
PON	Propylene oxide number
P	Pressure [=] F/L^2

P_c^*	Limiting capillary pressure between gas and water for foam [=] F/L^2
P_{cjk}	Capillary pressure between phases j and k [=] F/L^2
P_v	Vapor pressure [=] F/L^2
Q	Heat transfer [=] $F - L$
\dot{Q}	Heat transfer rate [=] $F - L/t$
Q_V	Cation exchange capacity [=] equivalent/mass – substrate
q	Volumetric flow rate [=] L^3/t
\vec{q}_c	Conductive energy flux [=] $F/L - t$
R	Radius [=] L ; Ideal gas constant [=] $F - L/\text{amount} - T$
R_b	Pore body radius [=] L
R_f	Resistance factor or gas mobility reduction with foam
R_g	Radial distance foam flows before segregation of water and gas [=] L
R_h	Hydraulic radius [=] L
R_i	Insulation radius [=] L , or rate of mass generation of component i [=] mass i/L^3 phase $j - t$
R_k	Permeability reduction factor
R_l	Mean radius of curvature of lamella [=] L
R_n	Pore neck or entry radius [=] L
R_p	Polymer radius [=] L
R_{rf}	Residual resistance factor
R_s	Solution gas/oil ratio [=] standard L^3 dissolved species/standard L^3 liquid
R_V	Oil vaporization ratio [=] standard L^3 oil dissolved/standard L^3 gas
R_w	Well radius [=] L
REV	Representative elementary volume

r	Radial distance [=] L
r_i	Total reaction rate of species i [=] mass i /total $L^3 - t$
r_{ij}	Homogeneous reaction rate [=] mass i/L^3 phase $j - t$
r_m	Mass transfer rate [=] mass/ $L^3 - t$ mass/ $L^3 - t$
SAGD	Steam assisted gravity drainage
SP	Surfactant polymer
S	Scalar function or spreading coefficient for three phases [=] F/L (Chapter 3)
S	Reduced water saturation
S_1^*	Water saturation corresponding to limiting capillary pressure (Chapter 10)
S_1^*	Water saturation upstream of shock front (Chapter 5)
S_F	Screen factor
\hat{S}_{ij}	Partial entropy of component i in phase j [=] $F - L / T - \text{mass}$
S_j	Saturation of phase j or entropy of phase j [=] $F - L / T$
S_{jk}	Solubilization parameters between phases j and k
S_y	Specific yield (volume fraction)
SCM	Standard cubic meter
SRD	Salinity requirement diagram
S	Skin factor
ζ	Laplace transform variable
TDS	Total dissolved solids
T	Temperature [=] T
t	Time [=] t
t_{DS}	Slug size (fraction)
t_{MB}	Mobility buffer size (fraction)
U	Internal energy [=] $F - L / \text{mass}$
UOP	Universal oil product
\hat{U}_{ij}	Partial internal energy of component i in phase j [=] $F - L / \text{mass}$

U_j	Vector of unknowns for hyperbolic system of equations or internal energy of phase j [=] $F - L$ / mass
U_T	Overall heat transfer coefficient [=] $F / L - t - T$
\vec{u}	Superficial velocity [=] L/t (magnitude: u)
\hat{U}_{ij}	Statistical average apparent velocity of component i in phase j [=] L/t^3
V_b	Bulk volume [=] L^3
\hat{V}_{ij}	Partial mass volume of component i in phase j [=] L_3 /mass
V_{DP}	Dykstra-Parsons coefficient (fraction)
\bar{v}_m	Specific molar volume [=] L^3 /amount
V_p	Pore volume [=] L^3
VE	Vertical equilibrium
VFD	Volume fraction diagram
\vec{v}	Interstitial velocity [=] L/t (magnitude: v)
v_{C_i}	Specific velocity of concentration C_i
$v_{\Delta C_i}$	Specific velocity of shock concentration change ΔC_i
W	Medium width, or half width of a slit [=] L
\dot{W}	Rate of work per unit volume [=] $F/L^2 - t$
\dot{W}_{CE}	Rate of compression-expansion work per unit volume [=] $F/L^2 - t$
\dot{W}_{PV}	Rate of pressure volume work per unit volume [=] $F/L^2 - t$
W_i	Overall concentration of component i [=] amount i/L^3
W_R	Water-alternating-gas ratio or WAG ratio [=] L^3 water/ l^3 solvent
WAG	Water alternating gas
WOR	Water- (or brine-) oil ratio [=] L^3 water/ L^3 oil
x	Position [=] L
x_i, y_i	Mole fraction of i in vapor, liquid phases

y	Steam quality
Z_V	Cation exchange capacity [=] equivalents/ L^3 of pore volume
z	Compressibility factor
z_i	Overall mole fraction of component i [=] amount i /total amount

Greek

α_l, α_t	Longitudinal and transverse dispersivities [=] L
α	Dip angle
β	Heterogeneity factor (Chapter 3) or exponent in dispersion equation (Chapter 5) or interface tilt angle (Chapter 6)
β_T	Thermal expansion coefficient [=] T^{-1}
ϵ	Parameter governing abruptness of collapse of foam near S_1^*
ϵ_j	Phase volume fraction
ξ	Dummy variable of integration
δ_{ij}	Binary interaction coefficient between component i and j
η	Eigenvalues or slope of tie lines
η_B	Steam boiler efficiency
Λ	Cumulative frequency
γ	Specific gravity
Δ	Operator that refers to a discrete change
$\dot{\gamma}$	Shear rate [=] r^1
$\vec{\nabla}$	Gradient operator [=] L^{-1}
λ	Pore-size distribution coefficient or viscous finger width [=] L
λ_c	Critical wavelength [=] L

λ_j	Mobility of phase j [=] $F - t$
λ_{rt}	Total relative mobility [=] $(\text{Pa.s})^{-1}$
λ_{rt}^m	Total relative mobility in mixed zone in gas EOR [=] $(\text{Pa.s})^{-1}$
$[\mu]$	Intrinsic viscosity [=] L^2/mass
μ	Viscosity [=] $F - t/L^2$
Ψ	Suction head [=] L
Φ_j	Fluid potential [=] F/L^2 $= P_j + \rho_j g D_z$ for incompressible phase j $= \rho_j \int_{P_o}^{P_j} \left(\frac{P}{\rho_j} + g D_z \right) dP$ otherwise
ϕ	Porosity [=] fraction, or spherical coordinate
ϕ_i	Fugacity coefficient of component i
ρ	Density [=] mass/ L^3
ρ_i^o	Pure component density of species i [=] mass/ L^3
ρ_j	Density of phase j [=] mass of j/L^3
ρ_j^s	Standard density of phase j [=] mass/standard L^3
ρ_M	Molar density [=] amount / L^3
ρ_D	Rate of entropy generation per unit bulk volume [=] $F/\text{L}^2 - T - t$
σ_{ik}	Interfacial tension between phases j and k [=] F/L
τ	Shear stress [=] F/L^2 ; Tortuosity
θ	Contact angle, or polar/spherical coordinate, or moisture content of aquifer
ν	Kinematic viscosity [=] L^2/t
ν_{LN}	Variance of lognormal distribution
	Overall mass fraction [=] mass i / total mass

ω_i

ω_{ij} Mass fraction of species i in phase j

Superscript

$^{\wedge}$	Quality corrected for heterogeneity, or specific quantity
$+, -$	Upstream or downstream of front
$\overline{}$	Average or molar quantity
\sim	Pseudo
∞	Ultimate or large-time (asymptotic) value
$*$	Refers to intersection between chords and tangents
$'$	Denotes a quantity modified by an EOR fluid (low IFT or polymer enhanced, for example)
o	Breakthrough quantities
o	Parameter of function in absence of foam (Chapter 10)
SP	Solubility product
sl, sv	Saturated liquid, saturated vapor
s, p	Refer to fractional flow curves modified by surfactant, solvent, or polymer
\bullet	Indicates a rate
\rightarrow	Vector
\Rightarrow	Tensor

Subscript

A, R, E	Advancing, receding, and intrinsic
B	Bank
c	Critical
cem	Cement
ci	Inside casing
co	Outside casing
D	Denotes a dimensionless quantity
d	Drill hole
e	Effective

<i>eq</i>	Equivalent
<i>f</i>	Floodable, front, or flowing
<i>G</i>	Noncondensable gas
<i>HW</i>	Hot water
<i>I, J, K</i>	Refer to initial, injected (slug), and chase fluids
<i>i</i>	Species index (first position on composition variables) 1 = water (Chapters 3, 5, 6); heavy hydrocarbon (Chapter 7) 2 = oil (Chapters 3, 5, 6, 8, 9); intermediate hydrocarbon (Chapter 7) 3 = displacing agent (surfactant, Chapter 9 ; solvent, Chapter 7 ; gas, Chapters 5 and 10) 4 = polymer (Chapters 8 and 9); foaming surfactant (Chapter 10) 5 = anion 6 = divalents 7 = cosurfactant 8 = monovalents
<i>j</i>	phase index (second position on composition variables) 1 = water-rich (Chapters 3, 5, 6, 8, 9); heavy hydrocarbon rich (Chapter 7) 2 = oil-rich (Chapters 3, 5, 6, 8, 9); solvent rich (Chapter 2) 3 = microemulsion <i>s</i> = solid
<i>l</i>	Layer number index ($l = 1, \dots, n, \dots, VV_L$)
<i>Lim</i>	Limiting
<i>OPT</i>	Optimal
<i>R</i>	Remaining
<i>SF</i>	Steam front
<i>rm</i>	Miscible residual
<i>rw</i>	Residual to water
<i>r</i>	Residual (second subscript position) or relative (first

	position)
T	Thermal property
t	Total
ti	Inside tubing
to	Outside tubing
u, l	Upper and lower effective salinities
w, nw	Wetting, nonwetting
wf	Well flowing
x, z, r	Refers to coordinate directions x, z and r

* [=] means “has units of,” L is a length unit, F is force, m is mass, t is time, T is temperature, and “amount” is moles.

References

- Aaron, D. and Tsouris, C. 2005. Separation of CO₂ From Flue Gas. *Separation Science and Technology* **40** (1–3): 321–348.
- Abbott, M.M. 1973. Cubic Equations of State. *AIChE Journal* **19** (3): 596–601.
- Abbott, M.M. 1979. Cubic Equations of State: An Interpretive Review. In *Equations of State in Engineering and Research*, Advances in Chemistry 182. Washington, DC.: American Chemical Society.
- Abbott, M.M. and Van Ness, H.C. 1972. *Schaum's Outline of Theory and Problems of Thermodynamics*. New York: McGraw-Hill.
- Ader, J.C. and Stein, M. 1984. Slaughter Estate Unit Tertiary Miscible Gas Pilot Reservoir Description. *J Pet Technol* **36** (5): 837–845.
- Adkins, S., Pinnawala Arachchilage, G.W.P., Solairaj, S., et al. 2012. Development of Thermally and Chemically Stable Large-Hydrophobe Alkoxy Carboxylate Surfactants. Presented at the SPE Improved Oil Recovery Symposium, Tulsa, 14–18 April. SPE-154256-MS.
<http://dx.doi.org/10.2118/154256-MS>.
- Ahmad, T., Menzie, D., and Chrichlow, H. 1983. Preliminary Experimental Results of High Pressure Nitrogen Injection for EOR Systems. *SPE J.* **23** (2): 339–348.
- Ahmadi, K., Joh, R.T., Mogensen, K., and Noman, R. 2011. Limitations of Current Method of Characteristic Models Using Shock-Jump Approximations To Predict MMPs for Complex Gas-Oil Displacements. *SPE J.* **16** (4): 743–750.

- Ahmadi, K. and Johns, R.T. 2011. Multiple Mixing-Cell Model for MMP Determination. *SPE J.* **16** (4): 733–742.
- Aithison, J. and Brown, J.A.C. 1957. *The Lognormal Distribution*. New York: Cambridge University Press.
- Akstinat, M.H. 1981. Surfactants for EOR Process in High-Salinity Systems: Product Selection and Evaluation. In *Enhanced Oil Recovery*, ed. F.J. Fayers, Chap. 2, 43–62. New York: Elsevier.
- Alpak, F.O., Lake, L.W., and Embid, S.M. 1999. Validation of a Modified Carman-Kozeny Equation To Model Two-Phase Relative Permeabilities. Presented at the SPE Annual Technical Conference and Exhibition, Houston, 3–6 October. SPE-56479-MS.
<http://dx.doi.org/10.2118/56479-MS>.
- Alvarez, J.M., Rivas, H., and Rossen, W.R. 2001. A Unified Model for Steady-State Foam Behavior at High and Low Foam Qualities. *SPE J.* **6** (3): 325–333.
- Amott, E. 1959. Observations Relating to the Wettability of Porous Rock. *Trans., AIME*, **216**: 156–162.
- Anderson, W.G. 1986. Wettability Literature Survey—Part 2: Wettability Measurement. *J Pet Technol* **38** (11): 1246–1262. SPE-13933-PA. <http://dx.doi.org/10.2118/13933-PA>.
- Anderson, G. 2006. *Simulation of Chemical Flood Enhanced Oil Recovery Processes Including the Effects of Reservoir Wettability*. MS thesis, The University of Texas at Austin, Austin, Texas (May 2006).
- Andrade, E.N. and Da, C. 1930. The Viscosity of Liquids. *Nature* (1 March): 309–310.
- Araktingi, U.G. and Orr, F.M. Jr. 1990. Viscous Fingering, Gravity Segregation, and Reservoir Heterogeneity in Miscible Displacements

in Vertical Cross Sections. Presented at the SPE/DOE Enhanced Oil Recovery Symposium, Tulsa, 22–25 April. SPE-20176-MS.
<http://dx.doi.org/10.2118/20176-MS>.

Arps, J.J. 1956. Estimation of Primary Oil Reserves. In *Transactions of the Society of Petroleum Engineers*, Vol. 207, 182–191.

Richardson, Texas: Society of Petroleum Engineers. ISBN 1-55563-013-8.

Arriola, A., Willhite, P.G., and Green, D.W. 1983. Trapping of Oil Drops in a Noncircular Pore Throat. *SPE J.* **23** (1): 99–114.

Arya, A., Hewett, T.A., Larson, R.G., and Lake, L.W. 1988. Dispersion and Reservoir Heterogeneity. *SPE Res Eng* **3** (1): 139–148.

Ashoori, E., van der Heijden, T.L.M., and Rossen, W.R. 2010. Fractional-Flow Theory of Foam Displacements With Oil. *SPE J.* **15** (2): 260–273.

Aydelotte, S.R. and Pope, G.A. 1983. A Simplified Predictive Model for Steamdrive Performance. *J Pet Technol* **35** (5): 991–1002.

Aziz, K. and Settari, A. 1979. *Petroleum Reservoir Simulation*. Vol. 476. London: Applied Science Publishers.

Bail, P.T. and Marsden, S.S. 1957. Saturation Distribution in a Linear System During Oil Displacement. *Producers Monthly* **21** (8): 22–32.

Balhoff, M.T., Lake, L.W., Bommer, P.M., et al. 2011. Rheological and Yield Stress Measurements of Non-Newtonian Fluids Using a Marsh Funnel. *J. Pet. Sci. Eng.* **77** (3–4): 393–402.

<http://dx.doi.org/http://dx.doi.org/10.1016/j.petrol.2011.04.008>.

Bear, J. 1972. *Dynamics of Fluids in Porous Media*. New York: Dover.

Benham, A.L., Dowden, W.E., and Kunzman, W.J. 1961. Miscible Fluid Displacement-Prediction of Miscibility. In *Transactions of the Society of Petroleum Engineers*, Vol. 219, 229–237. Richardson, Texas: Society of Petroleum Engineers. ISBN 1-55563-013-8.

Bennett, K.W., Phelps, C.H.K., Davis, H.T., et al. 1981. Microemulsion Phase Behavior: Observations, Thermodynamic Essentials, Mathematical Simulation. *SPE J.* **2** (1): 747–762.

Bhuyan, D. 1986. *The Effect of Wettability on the Capillary Desaturation Curve*. MS thesis, The University of Texas at Austin, Austin, Texas (1986).

Bijeljic, B.R., Muggeridge, A.H., and Blunt, M.J. 2002. Effect of Composition on Waterblocking for Multicomponent Gasfloods. Presented at the SPE Annual Technical Conference and Exhibition, San Antonio, Texas, 29 September—2 October. SPE-77697-MS.

Bikerman, J.J. 1973. *Foams*. New York: Springer Verlag.

Bird, R.B., Stewart, W.E., and Lightfoot, E.N. 2002. *Transport Phenomena*, second edition. New York: Wiley.

Bleakley, W.B. 1965. The How and Why of Steam, Part 5. *Oil and Gas Journal* (15 February): 121–122.

Blevins, T.R. and Billingsley, R.H. 1975. The Ten-Pattern Steamflood, Kern River Field, California. *J Pet Technol* **27** (12): 1505–1514.

Blunt, M.J., Fenwick, D.H., and Zhou, D. 1994. What Determines Residual Oil Saturation in Three-Phase Flow? Presented at the SPE/DOE Improved Oil Recovery Symposium, Tulsa, 17–20 April. SPE-27816-MS.

Boberg, T.C. 1988. *Thermal Methods of Oil Recovery*. New York: John Wiley and Sons.

Bondor, P.L., Hirasaki, G.J., and Tham, M.J. 1972. Mathematical Simulation of Polymer Flooding in Complex Reservoirs. *SPE J.* **12** (5): 369–382.

Bonfantir, B.F. and Gonzalez, I.E. 1996. *Evaluacion del Metodo de Drenaje por Gravedad Asistido con Vapor en Yacimientos de Crudo Pesado en Campos de la Costa Bolivar, Estado Zulia*. PhD dissertation, Universidad Central de Venezuela, Caracas, Venezuela (April 1996).

Bourrel, M., Lipow, A.M., Wade, W.W., et al. 1978. Properties of Amphile/Oil/Water Systems at an Optimum Formulation of Phase Behavior. Presented at the SPE Annual Fall Technical Conference and Exhibition, Houston, 1–3 October. SPE-7450-MS.

Brown, W.O. 1957. The Mobility of Connate Water During a Waterflood. *Transactions of the Society of Petroleum Engineers*, Vol. 210, 190–195. Richardson, Texas: Society of Petroleum Engineers. ISBN 1-55563-013-8.

Bragg, J.R., Gale, W.W., McElhannon, W.A., et al. 1982. Loudon Surfactant Flood Pilot Test. Presented at the SPE Enhanced Oil Recovery Symposium, Tulsa, 4–7 April. SPE-10862-MS.

Bruggenwert, M.G.M. and Kamphorst, A. 1979. Survey of Experimental Information on Cation Exchange in Soil Systems. *Developments in Soil Science* **5**: 141–203.

Bryant, S.L., Schechter, R.S., and Lake, L.W. 1986. Interaction of Precipitation/Dissolution Waves and Ion Exchange in Flow Through Permeable Media. *AIChE Journal* **32** (5): 751–764.

Bryant, S.L., Mellor, D.W., and Cade, C.A. 1993. Permeability Prediction From Geological Models. *AAPG Bulletin* **77** (8): 1338–1350.

Buckley, S.E. and Leverett, M.C. 1941. Mechanisms of Fluid Displacement in Sands. *Transactions of the Society of Petroleum Engineers*, Vol. 146, 107–116. Richardson, Texas: Society of Petroleum Engineers. ISBN 1-55563-013-8.

Bunge, A.L. and Radke, C.J. 1982. Migration of Alkaline Pulses in Reservoir Sands. *SPE J.* **22** (6): 998–1012.

Burger, J.G. and Sahuquer, B.C. 1972. Chemical Aspects of In Situ Combustion-Heat of Combustion and Kinetics. In *Transactions of the Society of Petroleum Engineers of the AIME*, Vol. 253, 410–422. Richardson, Texas: Society of Petroleum Engineers. ISBN 1-55563-013-8.

Burger, J., Sourieau, P., and Combarous, M. 1985. *Thermal Methods of Oil Recovery*. Paris: Editions Technip and Houston: Gulf Publishing Company.

Bursell, C.G. and Pittman, G.M. 1975. Performance of Steam Displacement in the Kern River Field. *J Pet Technol* **27** (8): 997–1004.

Butler, R. 1982. A Method for Continuously Producing Viscous Hydrocarbons by Gravity Drainage While Injecting Heated Fluids, UK Patent Application GB 2,053,328 (1980); US 4,344,485 (1982); Canada 1,130,201 (1982).

Butler, R.M. 1997. *Thermal Recovery of Oil and Bitumen*. GravDrain, Inc.

Callaroti, R. 2002. Electromagnetic Heating for Oil Recovery. In *Emerging and Peripheral Technologies*, Petroleum Engineers Handbook of SPE, Chapter 12.

Camilleri, D. 1983. *Micellar/Polymer Flooding Experiments and Comparison With an Improved 1D Simulator*. MS thesis, The University of Texas at Austin, Austin, Texas (1983).

Campbell, R.A. et al. 1977. The Metric System of Units and SPE's Tentative Metric Standard. *J Pet Technol* **29** (12): 1575–1610.

Cannella, W.J., Huh, C., and Seright, R.S. 1988. Prediction of Xanthan Rheology in Porous Media. Presented at the SPE Annual Technical Conference and Exhibition, Houston, 2–5 October. SPE-18089-MS. <http://dx.doi.org/10.2118/18089-MS>.

Carcoana, A.N. 1982. Enhanced Oil Recovery in Rumania. Presented at the SPE Enhanced Oil Recovery Symposium, Tulsa, 4–7 April. SPE-10699-MS.

Carrazales, M.A. 2010. *Recovery of Stranded Heavy Oil Using Electromagnetic Heating*. PhD dissertation, The University of Texas at Austin, Austin, Texas (December 2010).

Carslaw, H.W. and Jaeger, J.C. 1959. *Conduction of Heat in Solids*, second edition. Clarendon, Oxford.

Cash, R.C., Cayias, J.L., Fournier, R.G., et al. 1976. Modelling Crude Oils for Low Interfacial Tension. *SPE J.* **16** (6): 351–357.

Cayias, J.L., Schechter, R.S., and Wade, W.H. 1975. The Measurement of Low Interfacial Tension Via the Spinning Drop Technique, Adsorption at Interfaces. L.K. Mittal (ed.), American Chemical Society Symposium Series, No. 8 (1975): 234.

Caudle, B.H. 1968. *Fundamentals of Reservoir Engineering*, Part II. Dallas: Society of Petroleum Engineers.

Caudle, B.H. and Dyes, A.B. 1958. Improving Miscible Displacement by Gas-Water Injection. In *Transactions of the Society of Petroleum Engineers*, Vol. 283, 281–284. Richardson, Texas: Society of Petroleum Engineers. ISBN 1-55563-013-8.

Chang, H.L., Al-Rikabi, H.M., and Pusch, W.H. 1978. Determination of Oil/Water Bank Mobility in Micellar-Polymer Flooding. *J Pet*

Technol **30** (7): 1055–1060.

Charbeneau, R.J. 2000. *Groundwater Hydraulics and Pollutant Transport*. Upper Saddle River, New Jersey: Prentice Hall.

Chatzis, I. and Morrow, N.R. 1981. *Measurement and correlation of conditions for entrapment and mobilization of residual oil*. Final report. No. DOE/ET/12077-T1; EMD-2-68-3302. New Mexico Inst. of Mining and Technology, Socorro (USA). New Mexico Petroleum Recovery Research Center.

Chatzis, I., Morrow, N.R., and Lim, H.T. 1983. Magnitude and Detailed Structure of Residual Oil Saturation. *SPE J.* **23** (2): 311–326.

Chen, Q., Gerritsen, M.G., and Kovscek, A.R. 2010. Modeling Foam Displacement With the Local-Equilibrium Approximation: Theory and Experimental Verification. *SPE J.* **15** (1): 171–183.

Cheng, L. 2002. *Modeling and Simulation Studies of Foam Processes in Improved Oil Recovery and Acid-Diversions*. PhD dissertation, The University of Texas at Austin, Austin, Texas (2002).

Cheng, L., Kam, S.I., Delshad, M., and Rossen, W.R. 2002. Simulation of Dynamic Foam-Acid Diversion Processes. *SPE J.* **7** (3): 316–324.

Chen, J., Hirasaki, G., and Flaun, M. 2004. Study of Wettability Alteration From NMR: Effect of OBM on Wettability and NMR Responses. Presented at the 8th International Symposium on Reservoir Wettability, Houston, 16–18 May.

Cheng, L., Reme, A.B., Shan, D., et al. 2000. Simulating Foam Processes at High and Low Foam Qualities. Presented at the SPE/DOE Improved Oil Recovery Symposium, Tulsa, 3–5 April. SPE-59287-MS.

Chouke, R.L., van Meurs, P., and van der Poel, C. 1959. The Instability of Slow, Immiscible Viscous Liquid-Liquid Displacements in Permeable Media. *Trans., AIME* **216** (1959): 188–194.

Clampitt, R.L. and Reid, T.B. 1975. An Economic Polymerflood in the North Burbank Unit, Osage Country, Oklahoma. Presented at the Fall Meeting of the Society of Petroleum Engineers of AIME, Dallas, 28 September—1 October. SPE-5552-MS.

Claridge, E.L. 1980. *Design of Graded Viscosity Banks for Enhanced Oil Recovery Processes*. PhD dissertation, University of Houston, Houston, Texas (1980).

Claridge, E.L. 1978. A Method for Designing Graded Viscosity Banks. *SPE J.* **18** (5): 315–324.

Claridge, E.L. 1972. Prediction of Recovery in Unstable Miscible Flooding. *SPE J.* **12** (2): 143–155.

Coats, K.H., Dempsey, J.R., and Henderson, J.H. 1980. An Equation of State Compositional Model. *SPE J.* **20** (5): 363–376.

Coats, K.H., Dempsey, J.R., and Henderson, J.H. 1971. The Use of Vertical Equilibrium in Two-Dimensional Simulation of Three-Dimensional Reservoir Performance. *SPE J.* **11** (1): 63–71.

Coats, K.H. and Smith, B.D. 1964. Dead-End Pore Volume and Dispersion in Porous Media. *SPE J.* **4** (1): 73–84.

Collins, R.E. 1976. *Flow of Fluids through Porous Materials*. The Petroleum Publishing.

Cooke, C.E., Williams, R.E., and Kolodzie, P.A. 1974. Oil Recovery by Alkaline Waterflooding. *J Pet Technol* **26** (12): 1365–1374.

Courant, R. and Friedrichs, K.O. 1948. *Supersonic Flow and Shock Waves*. New York: Springer Verlag.

Craig, F.F. Jr. 1971. *The Reservoir Engineering Aspects of Waterflooding*, Vol. 3. Society of Petroleum Engineers.

Crane, F.E., Kendall, H.A., and Gardner, G.H.F. 1963. Some Experiments on the Flow of Miscible Fluids of Unequal Density Through Porous Media. *SPE J.* **3** (4): 277–280.

Crawford, H.R., Neill, G.H., Lucy, B.J., and Crawford, P.B. 1963. Carbon Dioxide—A Multipurpose Additive for Effective Well Stimulation. *J Pet Technol* **15** (3): 237–242.

Crichlow, H.B. 1977. *A Simulation Approach*. Englewood Cliffs, New Jersey: Prentice-Hall.

Crocker, M.W., Donaldson, E.C., and Marchin, L.M. 1983. Comparison and Analysis of Reservoir Rocks and Related Clays. Presented at the SPE Annual Technical Conference and Exhibition, San Francisco, California, 5–8 October. SPE-11973-MS.

Cronquist, C. 2001. *Estimation and Classification of Reserves of Crude Oil, Natural Gas, and Condensate*. Richardson, Texas: Society of Petroleum Engineers.

Culberson, O.L. and McKetta, J.J. 1951. Phase Equilibria in Hydrocarbon-Water Systems III—The Solubility of Methane in Water at Pressures to 10,000 psia. *Trans., AIME* **192** (1951): 223–226.

Dake, L.P. 1978. *Fundamentals of Reservoir Engineering*. Developments in Petroleum Science, Vol. 8. New York: Elsevier.

Danesh, A. 1998. *PVT and Phase Behavior of Petroleum Reservoir Fluids*. Developments in Petroleum Science, Vol. 47, Elsevier.

De Nevers, N. 1964. A Calculation Method for Carbonated Waterflooding. *SPE J.* **4** (1): 9–20.

- Deans, H.A. 1963. A Mathematical Model for Dispersion in the Direction of Flow. *SPE J.* **3** (1): 49–52.
- Degens, E.T. 1965. *Geochemistry of Sediments (A Brief Survey)*. Englewood Cliffs, New Jersey: Prentice-Hall.
- Delshad, M., Delshad, M., Pope, G.A., and Lake, L.W. 1987. Two- and Three-Phase Relative Permeabilities of Micellar Fluids. *SPE Form Eval* **2** (3): 327–337.
- Delshad, M. 1981. Measurement of Relative Permeability and Dispersion for Micellar Fluids in Berea Rock. MS thesis, The University of Texas at Austin, Austin, Texas (1981).
- Delshad, M., Kim, D.H., Magbagbeola, O.A., et al. 2008. Mechanistic Interpretation and Utilization of Viscoelastic Behavior of Polymer Solutions for Improved Polymer-Flood Efficiency. Presented at the SPE/DOE Symposium on Improved Oil Recovery, Tulsa, 19–23 April. SPE-113620-MS.
- Delshad, M., Pope, G.A., and Sepehrnoori, K. 1996. A Compositional Simulator for Modeling Surfactant Enhanced Oil Recovery Methods. *Journal of Contaminant Hydrology* **23**: 303–327.
- Demin, W., Jiecheng, C., and Yan, W. 2002. Producing by Polymer Flooding More Than 300 Million Barrels of Oil, What Experiences Have Been Learnt? Presented at the SPE Asia Pacific Oil and Gas Conference and Exhibition, Melbourne, Australia, 8–10 October. SPE-7782-MS.
- Denbigh, K. 1968. *The Principles of Chemical Equilibrium*, second edition. Oxford, England: Cambridge University Press.
- De Zabala, E.F., Vislocky, J.M., Rubin, E., and Radke, C.J. 1982. A Chemical Theory for Linear Alkaline Flooding. *SPE J.* **12** (1): 245–258.

- Dicharry, R.M., Perrymann, T.L., and Ronquille, J.D. 1973. Evaluation and Design of a CO₂ Miscible Flood Project—SACROC Unit, Kelly-Snyder Field. *J Pet Technol* **25** (11): 1309–1318.
- Dickson, J.L. and Leahy-Dios, A. 2010. Development of Improved Hydrocarbon Recovery Screening Methodologies. Presented at the SPE Improved Oil Recovery Symposium, Tulsa, 24–28 April. SPE-129768-MS.
- Dietz, D.N. 1953. A Theoretical Approach to the Problem of Encroaching and By-Passing Edge Water. *Proceedings, Series B, of the Koninklijke Nederlandse Akademie Van Wetenschappen, Amsterdam.*
- Dindoruk, B. 1992. Analytical Theory of Multiphase, Multicomponent Displacement in Porous Media. Ph.D. Dissertation, Stanford University, Stanford, California (May 1992).
- Dombrowski, H.S. and Brownell, L.E. 1954. Residual Equilibrium Saturation of Porous Media. *Industrial and Engineering Chemistry* **46** (1954): 1207.
- Donaldson, E.C., Thomas, R.D., and Lorenz, P.B. 1969. Wettability Determination and Its Effect on Recovery Efficiency. *SPE J.* **9** (1): 13–20.
- Dong, Y. and Rossen, W.R. 2007. Insights From Fractional-Flow Theory for Models for Foam IOR. Presented at the European Symposium on Improved Oil Recovery, Cairo, 22–24 April.
- Dougherty, E.L. 1963. Mathematical Model of an Unstable Miscible Displacement in Heterogeneous Media. *SPE J.* **3** (2): 155–163.
- Douglas, J. Jr., Blair, P.M., and Wagner, R.J. 1958. Calculation of Linear Waterflood Behavior Including the Effects of Capillary Pressure. *Trans., AIME* **213** (1958): 96–102.

- Dria, M.A., Schechter, R.S., and Lake, L.W. 1988. An Analysis of Reservoir Chemical Treatments. *SPE Prod Eng* **3** (1): 52–62.
- Duda, J.L., Klaus, E.E., and Fan, S.K. 1981. Influence of Polymer-Molecule/Wall Interactions on Mobility Control. *SPE J.* **21** (5): 613–622.
- Dullien, F.A.L. 1979. *Fluid Transport and Pore Structure*. New York: Academic Press.
- Dyes, A.B., Caudle, B.H., and Erickson, R.A. 1954. Oil Production After Breakthrough—As Influenced by Mobility Ratio. *Trans., AIME* **201** (1954): 81–86.
- Dykstra, H. and Parsons, R.L. 1950. The Prediction of Oil Recovery by Waterflood. In *Secondary Recovery of Oil in the United States, Principles and Practice*, second edition, 160–174. American Petroleum Institute.
- Earlougher, R.C. Jr. 1977. *Advances in Well Test Analysis*. New York: Henry L. Doherty Memorial Fund of AIME.
- Egwuenu, A.M., Johns, R.T., and Li, Y. 2008. The University of Texas at Austin, Improved Fluid Characterization for Miscible Gas Floods. *SPE Res Eval & Eng* **11** (4): 655–665.
- Ehrlich, R., Hasiba, H.H., and Raimondi, P. 1974. Alkaline Waterflooding for Wettability Alteration—Evaluating a Potential Field Application. *J Pet Technol* **26** (12): 1335–1343.
- El Dorado. 1977. Micellar-Polymer Demonstration Project. Third Annual Report, U.S. Department of Energy BERC/TPR-77/12.
- Embid-Droz, S.M. 1997. *Modeling Capillary Pressure and Relative Permeability for Systems with Heterogeneous Wettability*. PhD dissertation, The University of Texas at Austin, Austin, Texas (1997).

Englesen, S.R. 1981. *Micellar/Polymer Flooding Simulation-Improvements in Modelling and Matching of Core Floods*. MS thesis, The University of Texas at Austin, Austin, Texas (1981).

Ershaghi, I. and Omoregei, O. 1978. A Method for Extrapolation of Cut vs. Recovery Curves. *J Pet Technol* **30** (2): 203–204.

Faghri, A. and Zhang, Y. 2006. *Transport Phenomena in Multiphase Systems*. Burlington, Massachusetts: Elsevier.

Faisal, A., Bisdom, K., Zhumabek, B., Mojaddam Zadeh, A., and Rossen, W.R. 2009. Injectivity and Gravity Segregation in WAG and SWAG Enhanced Oil Recovery. Presented at the SPE Annual Technical Conference & Exhibition, New Orleans, 4–7 October. SPE-124197-MS.

Falls, A.H., Musters, J.J., and Ratulowski, J. 1989. The Apparent Viscosity of Foams in Homogeneous Bead Packs. *SPE Res Eng* **4** (2): 155–164.

Farajzadeh, R., Andrianovkrastev, A.R., Hirasaki, G.J., and Rossen, W.R. 2012. Foam-Oil Interaction in Porous Media: Implications for Foam Assisted Enhanced Oil Recovery. *Adv. Colloid Interface Sci.*, 183–184: 1–13.

Farajzadeh, R., Meulenbroek, B., Daniel, D., et al. 2013. An Empirical Theory for Gravitationally Unstable Flow in Porous Media. *Comput. Geosci.* **17** (3): 515–527. <http://dx.doi.org/10.1007/s10596-012-9336-9>.

Farouq Ali, S.M. 1974. Steam Injection. In *Secondary and Tertiary Oil Recovery Processes*. Oklahoma City: Interstate Oil Compact Commission.

Farouq Ali, S.M. 1966. Marx and Langenheim's Model of Steam Injection. *Producers Monthly* (November 1966): 2–8.

Fatt, I. and Dykstra, H. 1951. Relative Permeability Studies. *Trans., AIME* **192** (1951): 249.

Fayers, F.J. 1988. An Approximate Model With Physically Interpretable Parameters for Representing Viscous Fingering. *SPE Res Eng* **3** (2): 551–558.

Fernandez, M.E. 1978. *Adsorption of Sulfonates From Aqueous Solutions Onto Mineral Surfaces*. MS thesis, The University of Texas (1978).

Fetkovich, M.J. 1980. Decline Curve Analysis Using Type Curves. *J Pet Technol* **32** (6): 1065–1077.

Firoozabadi, A. 1999. *Thermodynamics of Hydrocarbon Reservoirs*. McGraw-Hill. ISBN 0-07-022071-9

Firoozabadi, A. and Pan, H. 2002. Fast and Robust Algorithm for Compositional Modeling: Part I—Stability Analysis Testing. *SPE J.* **7** (1): 78–89. SPE-77299-PA. <http://dx.doi.org/10.2118/77299-PA>.

Flaaten, A.K. 2012. *An Integrated Approach to Chemical EOR Opportunity Valuation: Technical, Economic, and Risk Considerations for Project Development*. PhD dissertation, The University of Texas at Austin, Austin, Texas (2012).

Flaaten, A.K. 2007. *Experimental Study of Microemulsion Characterization and Optimization in Enhanced Oil Recovery: A Design Approach for Reservoirs With High Salinity and Hardness*. MS thesis, The University of Texas at Austin, Austin, Texas (2007).

Flaaten, A.K., Nguyen, Q.P., Pope, G.A., and Zhang, J. A Systematic Laboratory Approach to Low-Cost, High-Performance Chemical Flooding. *SPE Res Eval & Eng* **12** (5): 713–723.

Fleming, P.D. III, Thomas, C.P., and Winter, W.K. 1981. Formulation of a General Multiphase, Multicomponent Chemical Flood Model.

SPE J. **21** (1): 63–76.

Flory, P.J. 1953. *Principles of Polymer Chemistry*. Ithaca, New York: Cornell University Press.

Fortenberry, R.P., Kim, D.H., Nizamidin, N., et al. 2013. Use of Co-Solvents To Improve Alkaline-Polymer Flooding. Presented at the SPE Annual Technical Conference and Exhibition, New Orleans, 30 September—2 October. SPE-166478-MS.

<http://dx.doi.org/10.2118/166478-MS>.

Foshee, W.C., Jennings, R.R., and West, T.J. 1976. Preparation and Testing of Partially Hydrolyzed Polyacrylamide Solutions. Presented at the SPE Annual Fall Technical Conference and Exhibition, New Orleans, 3–6 October. SPE-6202-MS.

Francis, A.W. 1963. *Liquid-Liquid Equilibria*. New York: Interscience.

Franklin, B., Brownrigg, W., and Farish, Mr. 1774. On the Still of Waves by Means of Oil. Extracted from Sundry Letters Between Benjamin Franklin, William Borwnrigg, and Rev. Mr. Farish. *Philosophical Transaction* **64**: 445–460.

Fussell, L.T. and Fussell, F.D. 1979. An Iterative Technique for Compositional Reservoir Models. *SPE J.* **19** (4): 211–220.

Gambill, W.R. 1957. You Can Predict Heat Capacity. *Chemical Engineering* (June 1957): 243–248.

Gardner, J.W., Orr, F.M., and Patel, P.D. 1981. The Effect of Phase Behavior on CO₂-Flood Displacement Efficiency. *J Pet Technol* **33** (11): 2067–2081.

Gardner, J.W. and Ypma, J.G.J. 1984. An Investigation of Phase Behavior-Macroscopic by Passing Interaction in CO₂ Flooding. *SPE J.* **24** (5): 504–520.

Garrels, R.M. and Christ, C.L. 1965. *Solutions, Minerals, and Equilibria*. San Francisco, California: Freeman, Cooper.

Gash, B.H., Griffith, T.D., and Chan, A.F. 1981. Phase Behavior Effects on the Oil Displacement Mechanisms of Broad Equivalent Weight Surfactant Systems. Presented at the SPE/DOE Enhanced Oil Recovery Symposium, Tulsa, 5–8 April. SPE-9812-MS.
<http://dx.doi.org/10.2118/9812-MS>.

Gates, I.G. 2011. *Basic Reservoir Engineering*. Dubuque, Iowa: Kendall Hunt.

Gauglitz, P.A., Friedmann, F., Kam, S.I., and Rossen, W.R. 2002. Foam Generation in Homogeneous Porous Media. *Chem. Eng. Sci.* **57**: 4037–4052.

Gdanski, R.D. 1993. Experience and Research Show Best Designs for Foam-Diverted Acidizing. *Oil and Gas Journal* (6 September 1993).

Gharbarnezedeh, R. and Lake, L.W. 2010. Simultaneous Water-Gas Injection Performance Under Loss of Miscibility. Presented at the SPE Improved Oil Recovery Symposium, Tulsa, 24–28 April. SPE-129966-MS. <http://dx.doi.org/10.2118/129966-MS>.

Ghanbarnezched, R. 2012. *Modeling the Flow of Carbon Dioxide through Permeable Media*. PhD dissertation, The University of Texas at Austin, Austin, Texas (May 2012).

Gibbs, C.W. ed. 1971. *Compressed Air and Gas Data*, second edition. Woodcliff Lake, New Jersey: Ingersoll-Rand.

Gibbs, J.W. 1993 [1906]. *The Scientific Papers of J. Willard Gibbs*, in two volumes. eds. H.A. Bumstead and R.G. Van Name. Woodbridge, Connecticut: Ox Bow Press. [ISBN 0-918024-77-3](#), [ISBN 1-881987-06-X](#).

Gilliland, H.E. and Conley, F.R. 1975. Surfactant Waterflooding. Presented at the Symposium on Hydrocarbon Exploration, Drilling, and Production, Paris, 1975.

Giordano, R.M. and Salter, S.J. 1984. Comparison of Simulation and Experiments for Compositionally Well-defined Corefloods. Presented at the SPE Enhanced Oil Recovery Symposium, Tulsa, 15–18 April. SPE-12697-MS. <http://dx.doi.org/10.2118/12697-MS>.

Glinsmann, G.R. 1979. Surfactant Flooding With Microemulsions Formed In-Situ-Effect of Oil Characteristics. Presented at the SPE Annual Technical Conference and Exhibition, Las Vegas, 23–26 September. SPE-8326-MS. <http://dx.doi.org/10.2118/8326-MS>.

Glover, C.J., Puerto, M.C., Maerker, J.M., and Sandvik, E.I. 1979. Surfactant Phase Behavior and Retention in Porous Media. *SPE J.* **19** (3): 183–193.

Gogarty, W.B., Meabon, H.P., and Milton, H.W. Jr. 1970. Mobility Control Design for Miscible-Type Waterfloods Using Micellar Solutions. *J Pet Technol* **22** (2): 141–147.

Goldburg, A., Price, H., and Paul, G.W. 1985. Selection of Reservoirs Amenable to Micellar Flooding. US Department of Energy, DOE/BC/00048 and 00051-29 (August 1985).

Goodrich, J.H. 1980. *Target Reservoirs for CO₂ Miscible Flooding*, Final Report, US Department of Energy, DOE/MC/08341-17 (October 1980).

Gorucu, S.E. and Johns, R.T. 2013. Comparison of Reduced and Conventional Phase Equilibrium Calculations. Presented at the SPE Reservoir Simulation Symposium, The Woodlands, Texas, 18–20 February. SPE-163577-MS. <http://dx.doi.org/10.2118/163577-MS>.

Gorucu, S.E. and Johns, R.T. 2014. New Reduced Parameters for Flash Calculations Based on Two-Parameter BIP Formula. *J. Pet.*

Sci. Eng. **116**: 50–58. <http://dx.doi.org/10.1016/j.petrol.2014.02.015>.

Graciaa, A., Fotrney, L.N., Schechter, R.S., Wade, W.H., and Yiv, S. 1982. Criteria for Structuring Surfactant to Maximize Solubilization of Oil and Water 1: Commercial Nonionics. *SPE J.* **22** (5): 743–749.

Gray, W.G. 1975. A Derivation of the Equations for Multi-Phase Transport. *Chemical Engineering Science* **30** (1975): 229.

Greenkorn, R.A. and Kessler, D.P. 1969. Dispersion in Heterogeneous Nonuniform Anisotropic Porous Media. *Industrial and Engineering Chemistry* **61** (1969): 33.

Grim, R.E. 1968. *Clay Mineralogy*. New York: McGraw-Hill.

Gupta, S.P. 1984. Compositional Effects on Displacement Mechanisms of the Micellar Fluid Injected in the Sloss Field Test. *SPE J.* **24** (1): 38–48.

Gupta, S.P. and Trushenski, S.P. 1979. Micellar Flooding—Compositional Effects on Oil Displacement. *Society of Petroleum Engineers Journal* **19** (2): 116–128. SPE-7063-PA.
<http://dx.doi.org/10.2118/7063-PA>.

Guzmán Ayala, R.E. 1995. *Mathematics of Three-Phase Flow*. PhD thesis, Department of Petroleum Engineering, Stanford University, Stanford, California (July 1995).

Habermann, B. 1960. The Efficiencies of Miscible Displacement as a Function of Mobility Ratio. *Trans., AIME*, **219**: 264.

Hall, H.N. and Geffen, T.M. 1965. *Miscible Processes*, Vol. 8, 133–142. Richardson, Texas: SPE.

Hand, D.B. 1939. Dineric Distribution: 1. The Distribution of a Consolute Liquid between Two Immiscible Liquids. *Journal of Physics and Chemistry* **34** (1939): 1961–2000.

- Hawthorne, R.G. 1960. Two-Phase Flow in Two Dimensional Systems-Effects of Rate, Viscosity and Density on Fluid Displacement in Porous Media. *Trans., AIME* **219** (1960): 81–87.
- Healy, R.N. and Reed, R.L. 1974. Physicochemical Aspects of Microemulsion Flooding. *SPE J.* **14** (1974): 491–501.
- Healy, R.N., Reed, R.L., and Stenmark, D.G. 1976. Multiphase Microemulsion Systems. *SPE J.* **16** (3): 147–160.
- Hearn, C.L. 1971. Simulation of Stratified Waterflooding by Pseudo-Relative Permeability Curves. *J Pet Technol* **23** (7): 805–813.
- Helfferich, F.G. and Klein, G. 1970. *Multicomponent Chromatography*. New York: Marcel Dekker.
- Helfferich, F.G. and Klein, G. 1981. Theory of Multicomponent, Multiphase Displacement in Porous Media. *SPE J.* **21** (1): 51–62.
- Heller, J.P., Lien, C.L., and Kuntamukkula, M.S. 1985. Foam-Like Dispersions for Mobility Control in CO₂ Floods. *SPE J.* **25** (4): 603–613.
- Hendriks, E.M. and van Bergen, A.R.D. 1992. Application of a Reduction Method to Phase Equilibria Calculations. *Fluid Phase Equilibria* **74**: 17–34. [http://dx.doi.org/10.1016/0378-3812\(92\)85050-1](http://dx.doi.org/10.1016/0378-3812(92)85050-1).
- Hill, S. 1952. Channelling in Packed Columns. *Chemical Engineering Science* **1** (1952): 247–253.
- Hill, H. J. and Lake, L.W. 1978. Cation Exchange in Chemical Flooding: Part 3—Experimental. *SPE J.* (December): 445–456.
- Himmelblau, D.M. 1982. *Basic Principles and Calculations in Chemical Engineering*, fourth edition. Englewood Cliffs, New Jersey: Prentice-Hall.

- Hirasaki, G.J. 1981. Application of the Theory of Multicomponent, Multiphase Displacement in Three Component, Two-Phase Surfactant Flooding. *SPE J.* **21** (2): 191–204.
- Hirasaki, G.J., Jackson, R.E., Jin, M., et al. 2000. Field Demonstration of the Surfactant/Foam Process for Remediation of a Heterogeneous Aquifer Contaminated With DNAPL. In *NAPL Removal: Surfactants, Foams, and Microemulsions*, ed. S. Fiorenza, C.A. Miller, C.L. Oubre, and C.H. Ward. Boca Raton, Florida: Lewis Publishers.
- Hirasaki, G.J., van Domselaar, H.R., and Nelson, R.C. 1983. Evaluation of the Salinity Gradient Concept in Surfactant Flooding. *SPE J.* **23** (3): 486–500.
- Hirasaki, G.J. and Pope, G.A. 1974. Analysis of Factors Influencing Mobility and Adsorption in Flow of Polymer Solution Through Porous Media. *SPE J.* **14** (4): 337–346.
- Hirshberg, A., de Jong, L.N.J., Schipper, B.A., and Meyers, J.G. 1984. Influence of Temperature and Pressure on Asphaltenes. *SPE J.* **24** (3): 282–293.
- Holm, L.W. 1961. A Comparison of Propane and CO₂ Solvent Flooding Processes. *AIChE Journal* **7** (2): 179–184.
- Holm, L.W. and Csaszar, A.K. 1965. *Miscible Processes*, Vol. 8, 31–38. Richardson, Texas: SPE.
- Holm, L.W. and Josendal, V.A. 1974. Mechanisms of Oil Displacement by Carbon Dioxide. *J Pet Technol* **26** (12): 1427–1438.
- Holm, L.W. and Josendal, V.A. 1982. Effect of Oil Composition on Miscible-Type Displacement by Carbon Dioxide. *SPE J.* **22** (1): 87–98.

Homsy, G.M. 1987. Viscous Fingering in Porous Media. *Annual Review of Fluid Mechanics* **19** (1987): 271–311.

Honarpour, M., Koederitz, L.F., and Harvey, H.A. 1982. Empirical Equations for Estimating Two-Phase Relative Permeability in Consolidated Rock. *J Pet Technol* **34** (12): 2905–2908.

Hong, K.C. 1994. *Steamflood Reservoir Management: Thermal Enhanced Oil Recovery*. Tulsa, Oklahoma: PennWell Books.

Hong, K.C. 1982. Lumped-Component Characterization of Crude Oils for Compositional Simulation. Presented at the SPE Enhanced Oil Recovery Symposium, Tulsa, 4–7 April. SPE-10691-MS. <http://dx.doi.org/10.2118/10691-MS>.

Hougen, O.A., Watson, K.M., and Ragatz, R.A. 1966. *Chemical Process Principles, Part II Thermodynamics*. New York: Wiley.

Hua, Y. and Johns, R.T. 2005. Simplified Method for Calculation of Minimum Miscibility Pressure or Enrichment. *SPE J.* **10** (4): 416–425.

Hubbert, M.K. 1956. Darcy's Law and the Field Equations of the Flow of Underground Fluids. *Transactions of the American Institute of Mining, Metallurgical, and Petroleum Engineers* **207** (1956): 222–239.

Huh, C. 1979. Interfacial Tensions and Solubilizing Ability of a Microemulsion Phase that Coexists With Oil and Brine. *Journal of Colloid and Interface Science* **71** (1979): 408–426.

Huh, C. and Pope, G.A. 2008. Residual Oil Saturation From Polymer Floods: Laboratory Measurements and Theoretical Interpretation. Presented at the SPE Symposium on Improved Oil Recovery, Tulsa, 20–23 April. SPE-113417-MS. <http://dx.doi.org/10.2118/113417-MS>.

- Hutchinson, C.A. Jr. and Braun, P.H. 1961. Phase Relationships of Miscible Displacement in Oil Recovery. *AIChE Journal* **7** (1): 64–72.
- Jadhunandan, P.P. and Morrow, N.R. 1992. Spontaneous Imbibition of Water by Crude Oil/Brine/Rock Systems. *In Situ* **15** (4): 319–345.
- Jahnke, E. and Emde, F. 1945. *Tables of Functions*. New York: Dover.
- Jain, Lokendra. 2014. *Global Upscaling of Secondary and Tertiary Displacements*. PhD dissertation, University of Texas at Austin, Austin, Texas (May 2014).
- Jamshidnezhad, M., Chen, C., Kool, P., and Rossen, W.R. 2010. Well Stimulation and Gravity Segregation in Gas Improved Oil Recovery. *SPE J.* **15** (1): 91–104.
- Jarrell, P., Fox, C., Stein, M. et al. 2002. *Practical Aspects of CO₂ Flooding*, No. 22. Richardson, Texas: Monograph Series, SPE.
- Jeffrey, A. and Taniuti, T. 1964. *Nonlinear Wave Propagation With Applications to Physics and Magnetohydrodynamics*. New York: Academic Press
- Jenkins, M.K. 1984. An Analytical Model for Water/Gas Miscible Displacements. Presented at the SPE Enhanced Oil Recovery Symposium, Tulsa, 15–18 April. SPE-12632-MS.
<http://dx.doi.org/10.2118/12632-MS>.
- Jennings, H.Y. Jr., Johnson, C.E. Jr., and McAuliffe, C.E. 1974. A Caustic Waterflooding Process for Heavy Oils. *J Pet Technol* **26** (12): 1344–1352.
- Jennings, R.R., Rogers, J.H., and West, T.J. 1971. Factors Influencing Mobility Control by Polymer Solutions. *J Pet Technol* **23** (3): 391–401.

Jensen, J.L. and Lake, L.W. 1986. The Influence of Sample Size and Permeability Distribution Upon Heterogeneity Measures. Presented at the SPE Annual Technical Conference and Exhibition, New Orleans. SPE-15434-MS.

Jensen, J.L., Lake, L.W., and Hinkley, D.V. 1987. A Statistical Study of Reservoir Permeability: Distributions, Correlations, and Averages. *SPE Form Eval* **2** (4): 461–468.

Jerauld, G.R, Lin, C.Y., Webb, K.J., and Secccombe, J.C. 2006. Modeling Low-Salinity Waterflooding. Presented at the SPE Annual Technical Conference and Exhibition, San Antonio, Texas, 24–27 September. SPE-102239-MS. <http://dx.doi.org/10.2118/102239-MS>.

Jessen, K. and Orr, F.M. Jr. 2008. On Interfacial-Tension Measurements To Estimate Minimum Miscibility Pressures. *SPE Res Eval & Eng* **11** (5): 933–939. SPE-110725-PA.
<http://dx.doi.org/10.2118/110725-PA>.

Jha, R.K., Lake, L.W., and Bryant, S.L. 2011. The Effect of Diffusion on Dispersion. *SPE J.* **16** (1): 65–77.

Jha, R.K., John, A.K., Bryant, S.L., and Lake, L.W. 2009. Flow Reversal and Mixing. *SPE J.* **4** (1): 41–49.

Jimenez, J. 2008. The Field Performance of SAGD Projects in Canada. Presented at the International Petroleum Technology Conference, Kuala Lumpur, 3–5 December. IPTC-12860-MS.
<http://dx.doi.org/10.2523/12860-MS>.

Johansen, T., Walsh, M.P., and Lake, L.W. 1989. Applying Fractional Flow Theory to Solvent Flooding and Chase Fluids. *J. Petroleum Science and Engineering* **2**: 281–303.

John A.K., Lake, L.W., Bryant, S.L., and Jennings, J.W. 2010. Investigation of Mixing in Field Scale Miscible Displacement Using

Particle-Tracking Simulations of Tracer Floods With Flow Reversal.
SPE J. **15** (3): 598–609.

Johns, R.T., Ahmadi, K., Zhou, D., and Yan, M. 2010. A Practical Method for Minimum Miscibility Pressure Estimation of Contaminated CO₂ Mixtures. *SPE Res Eval & Eng* **13** (5): 764–772.

Johns, R.T., Dindoruk B., and Orr, F.M. 1993. Analytical Theory of Combined Condensing/Vaporizing Gas Drives. *SPE Advanced Technology Series* **1** (2): 7–16.

Johns, R.T. and Orr, F.M. Jr. 1996. Miscible Gas Displacement of Multicomponent Oils. *SPE J.* **1** (1): 39–50.

Johns, R.T. 1992. Analytical Theory of Multicomponent Gas Drives With Two-Phase Mass Transfer. PhD dissertation, Stanford University, Stanford, California, (May 1992).

Johns, R.T. 2006. Thermodynamics and Phase Behavior. In *Petroleum Engineering Handbook, General Engineering*, Vol. 1, eds. J. Fanchi and L.W. Lake, Chapter 7, 1333–369. Richardson, Texas: SPE.

Johnson, C.E. Jr. 1956. Prediction of Oil Recovery by Water Flood—A Simplified Graphical Treatment of the Dykstra-Parsons Method. *Transactions of the American Institute of Mining, Metallurgical, and Petroleum Engineers* **207** (1956): 745–746.

Johnson, J.P. and Pollin, J.S. 1981. Measurement and Correlation of CO₂ Miscibility Pressures. Presented at the SPE/DOE Enhanced Oil Recovery Symposium, Tulsa, 5–8 April. SPE-9790-MS.
<http://dx.doi.org/10.2118/9790-MS>.

Jones, K. 1981. *Rheology of Viscoelastic Fluids for Oil Recovery*. MS thesis, The University of Texas at Austin, Austin, Texas, (1981).

- Jones, S.C. 1972. Finding the Most Profitable Slug Size. *J Pet Technol* **24** (8): 993–994.
- Jones, S.C. and Roszelle, W.O. 1978. Graphical Techniques for Determining Relative Permeability From Displacement Experiments. *J Pet Technol* **30** (5): 807–817.
- Kam, S.I. 2008. Improved Mechanistic Foam Simulation With Foam Catastrophe Theory. *Colloids Surfaces A: Physicochemical Engineering Aspects* **318** (2008): 62–77.
- Kamath, J., Meyer, R.F., and Nakagawa, F.M. 2001. Understanding Waterflood Residual Oil Saturation of Four Carbonate Rock Types. Presented at the SPE Annual Technical Conference and Exhibition, New Orleans, 30 September—1 October. SPE-71505-MS.
<http://dx.doi.org/10.2118/71505-MS>.
- Karanikas, J.M. 2012. Unconventional Resources: Cracking the Hydrocarbon Molecules In Situ. *J Pet Technol* (May 2012): 68–69.
- Keenan, J.H., Keys, F.G., Hill, P.G., and Moore, J.G. 1969. *Steam Tables, Thermodynamic Properties of Water, Including Vapor, Liquid and Solid Phases*. New York: Wiley.
- Khan, S.A. 1965. *The Flow of Foam Through Porous Media*. MS thesis, Stanford University, Stanford, California (1965).
- Khatib, Z.I., Hirasaki, G.J., and Falls, A.H. 1988. Effects of Capillary Pressure on Coalescence and Phase Mobilities in Foams Flowing Through Porous Media. *SPE Res Eng* **3** (3): 919–926.
- Khilar, K.C. and Fogler, H.S. 1981. Permeability Reduction in Water Sensitive Sandstones. In *Surface Phenomena in Enhanced Oil Recovery*, ed. D.O. Shah. New York: Plenum.
- Killins, C.R., Nielsen, R.F., and Calhoun, J.C. 1953. Capillary Desaturation and Imbibition in Porous Rocks. *Producers Monthly*

(December 1953): 30–39.

Kim, D.H., Lee, S., Ahn, C.H., Huh, C., and Pope, G.A. 2010. Development of a Viscoelastic Property Database for EOR Polymers. Presented at the SPE Improved Oil Recovery Symposium, Tulsa, 24–28 April. SPE-129971-MS.
<http://dx.doi.org/10.2118/129971-MS>.

Kim, J.S., Dong, Y., and Rossen, W.R. 2005. Steady-State Flow Behavior of CO₂ Foam. *SPE J.* **10** (4): 405–415.

Kloet, M.B., Renkema, W.J., and Rossen, W.R. 2009. Optimal Design Criteria for SAG Foam Processes in Heterogeneous Reservoirs. Presented at the EUROPEC/EAGE Conference and Exhibition, Amsterdam, 8–11 June. SPE-121581-MS.
<http://dx.doi.org/10.2118/121581-MS>.

Koch, H.A. Jr. and Slobod, R.L. 1956. Miscible Slug Process. *Trans., AIME* **210** (1956): 40–47.

Koval, E.J. 1963. A Method for Predicting the Performance of Unstable Miscible Displacement in Heterogeneous Media. *SPE J.* **3** (2): 145–154.

Kovscek, A.R., Patzek, T.W., and Radke, C.J. 1997. Mechanistic Foam Flow Simulation in Heterogeneous and Multidimensional Porous Media. *SPE J.* **2** (4): 511–526.

Krueger, D.A. 1982. Stability of Piston-Like Displacements of Water by Steam and Nitrogen in Porous Media. *SPE J.* **22** (5): 625–634.

Kumar V.K., Gutierrez, D., Moore, R.G., and Mehta, S.A. 2008. Air Injection and Waterflood Performance Comparison of Two Adjacent Units in Buffalo Field: Technical Analysis. *SPE Res Eval & Eng* **11** (5): 848–857.

Kyte, J.R. and Rapoport, L.A. 1958. Linear Waterflood Behavior and End Effects in Water-Wet Porous Media. *Trans., AIME* **213** (1958): 423–426.

LaForce, T. and Johns, R.T. 2005. Composition Routes for Three-Phase Partially Miscible Flow in Ternary Systems. *SPE J.* **10** (2): 161–174.

LaHerrere, J. 2001. Estimates of Oil Reserves. Presented at the EMF/IEA/IEW meeting IIASA, Laxenburg, Austria, 19 June.

Lake, L.W., Bryant, S.L., and Araque-Martinez, A.N. 2002. *Geochemistry and Fluid Flow*. Amsterdam, the Netherlands: Elsevier.

Lake, L.W. and Fanchi, J.R. 2006. *Petroleum Engineering Handbook: General Engineering*, Vol. 1. Richardson, Texas: Society of Petroleum Engineers.

Lake, L.W. and Hirasaki, G.J. 1981. Taylor's Dispersion in Stratified Porous Media. *SPE J.* **21** (4): 459–468.

Lake, L.W. and Pope, G.A. 1979. Status of Micellar-Polymer Field Tests. *Petroleum Engineers International* **51** (1979): 38–60.

Lake, L.W., Pope, G.A., Carey, G.F., and Sepehrnoori, K. 1984. Isothermal, Multiphase, Multicomponent Fluid-Flow in Permeable Media. *In Situ* **8** (1): 1–40.

Lake, L.W. and Zapata, V.J. 1987. Estimating the Vertical Flaring in In Situ Leaching. *In Situ II* (March 1987): 39–62.

Lambert, M.E. 1981. *A Statistical Study of Reservoir Heterogeneity*. MS thesis, The University of Texas at Austin, Austin, Texas (1981).

Larson, R.G. 1977. *Percolation in Porous Media With Application to Enhanced Oil Recovery*. MS thesis, University of Minnesota (1977).

- Larson, R.G. 1982. Controlling Numerical Dispersion by Variably Timed Flux Dating in One Dimension. *SPE J.* **22** (3): 399–408.
- Lax, P.D. 1957. Hyperbolic Conservation Laws II. *Communications on Pure and Applied Mathematics* **10** (4): 537–566.
- Lee, A., Gonzalez, M.H., and Eakin, B.E. 1966. The Viscosity of Natural Gases. *J Pet Technol* **18** (8): 997–1000.
- LeFebvre Du Prey, E.J. 1973. Factors Affecting Liquid-Liquid Relative Permeabilities of a Consolidated Porous Media. *SPE J.* **13** (1): 39–47.
- Lenhard, R.J. and Parker, J.C. 1987. A Model for Hysteretic Constitutive Relations Governing Multiphase Flow 2. Permeability-Saturation Relations. *Water Resources Research* **23** (12): 2197–2206.
- Levenspiel, O. 1999. *Chemical Reaction Engineering*. New York: Wiley.
- Levitt, D. and Pope, G.A. 2008. Selection and Screening of Polymers for Enhanced-Oil Recovery. Presented at the SPE Symposium on Improved Oil Recovery, Tulsa, 20–23 April. SPE-113845-MS.
<http://dx.doi.org/10.2118/113845-MS>.
- Levitt, D.B., Jackson, A.C., Heinson C., et al. 2009. Identification and Evaluation of High-Performance EOR Surfactants. *SPE Res Eval & Eng.* **12** (2): 243–253. SPE-100089-PA.
<http://dx.doi.org/10.2118/100089-PA>.
- Levitt, D.B., Slaughter, W., Pope, G. et al. 2011a. The Effect of Redox Potential and Metal Solubility on Oxidative Polymer Degradation. *SPE Res Eval & Eng* **14** (3): 287–298. SPE-129890-PA. <http://dx.doi.org/10.2118/129890-PA>.

Levitt, D.B., Pope, G.A., and Jouenne, S. 2011b. Chemical Degradation of Polyacrylamide Polymers Under Alkaline Conditions. *SPE Res Eval & Eng* **14** (3). SPE-129879-PA.
<http://dx.doi.org/10.2118/129879-PA>.

Leverett, M.C. 1941. Capillary Behavior in Porous Solids. *Petroleum Transactions of the American Institute of Mining and Metallurgical Engineers* **142** (1941): 152–168.

Lewis, W.K. and Squires, L. 1934. The Mechanism of Oil Viscosity as Related to the Structure of Liquids. *Oil and Gas Journal* (15 November 1934): 92–96.

Li, R.F., Yan, W., Liu, S., Hirasaki, G.J., and Miller, C.A. 2010. Foam Mobility Control for Surfactant Enhanced Oil Recovery. *SPE J.* **15** (4): 928–942.

Liyanage, P.J., Solairaj, S., Pinnawala Arachchilage, G. et al. 2012. Alkaline Surfactant Polymer Flooding Using a Novel Class of Large Hydrophobe Surfactants. Presented at the SPE Improved Oil Recovery Symposium, Tulsa, 14–18 April. SPE-154274-MS.
<http://dx.doi.org/10.2118/154274-MS>.

Lorenz, P.B., Donaldson, E.C., and Thomas, R.D. 1974. Use of Centrifugal Measurements of Wettability to Predict Oil Recovery. US Department of the Interior, Report of Investigations 7873, 1974.

Lu, J., Britton, C., Solairaj, S. et al. 2012. Novel Large-Hydrophobe Alkoxy Carboxylate Surfactants for Enhanced Oil Recovery. Presented at the SPE Improved Oil Recovery Symposium, Tulsa, 14–18 April. SPE-154261-MS. <http://dx.doi.org/10.2118/154261-MS>.

MacAllister, D.J. 1982. *Measurement of Two- and Three-Phase Relative Permeability and Dispersion of Micellar Fluids in Unconsolidated Sand*. MS thesis, The University of Texas at Austin, Austin, Texas (1982).

- Mack, J.C. and Warren, J. 1984. Performance and Operation of a Crosslinked Polymer Flood at the Sage Creek Unit A, Natrona County, Wyoming. *J Pet Technol* **36** (7): 1145–1156.
- Maerker, J.M. 1976. Mechanical Degradations of Partially Hydrolyzed Polyacrylamide Solutions in Unconsolidated Porous Media. *SPE J.* **16** (4): 172–174.
- Mahadevan, J., Larry, W., and Johns, R.T. 2003. Estimation of True Dispersivity in Field-Scale Permeable Media. *SPE J.* **8** (3): 272–279.
- Mandl, G. and Volek, C.W. 1969. Heat and Mass Transport in Steam-Drive Processes. *SPE J.* **9** (1): 59–79.
- Manning, R.K., Pope, G.A., and Lake, L.W. 1983. A Technical Survey of Polymer Flooding Projects. US Department of Energy DOE/BETC/10327-19, Bartlesville, Oklahoma, 1983.
- Marle, C.M. 1981. *Multiphase Flow in Porous Media*. Houston, Texas: Gulf Publishing.
- Martin, F.D., Donaruma, G.L., and Hatch, M.J. 1981. Development of Improved Mobility Control Agents for Surfactant/Polymer Flooding. 2nd Annual Report, US Department of Energy DOE/BC/00047-13, 1981.
- Martin, J.W. 1951. Additional Oil Production Through Flooding With Carbonated Water. *Producers Monthly* **15** (7): 18–22.
- Martin, J.C. 1958. Some Mathematical Aspects of Two-Phase Flow With Applications to Flooding and Gravity Segregation Problems. *Producers Monthly* **22** (6): 22–35.
- Martin, J.J. 1979. Cubic Equations of State-Which? *Industrial and Engineering Chemistry Fundamentals* **18** (2): 81–97.

- Martin, J.J. and Hou, Y.C. 1955. Development of an Equation of State for Gases. *AIChE Journal* **1** (2): 142–151.
- Marx, J.W. and Langenheim, R.H. 1959. Reservoir Heating by Hot Fluid Injection. *Trans., AIME* **216** (1959): 312–315.
- Maxwell, J.B. 1950. *Data Book on Hydrocarbon*. New York: D. von Nostrand.
- McAuliffe, C.E. 1973. Crude-Oil-in-Water Emulsions To Improve Fluid Flow in an Oil Reservoir. *J Pet Technol* **25** (6): 721–726.
- McCain, W.D. Jr. 2000. *The Properties of Petroleum Fluids*. Tulsa, Oklahoma: PennWell Publishing.
- McMillan, J.M. and Foster, W.R., personal communication in Larson, R.G. (1977).
- McRee, B.C. 1977. CO₂: How It Works, Where It Works. *Petroleum Engineering* **49** (11): 52–63.
- Mehra, R.K., Heidemann, R.A., and Aziz, K. 1982. Computation of Multiphase Equilibrium for Compositional Simulation. *SPE J.* **22** (1): 61–68.
- Meldau, R.F., Shipley, R.G., and Coats, K.H. 1981. Cyclic Gas/Steam Stimulation of Heavy-Oil Wells. *J Pet Technol* **33** (10): 1990–1998.
- Melrose, J.C. 1982. Interpretation of Mixed Wettability States in Reservoir Rocks. Presented at the SPE Annual Technical Conference and Exhibition, New Orleans, 26–29 September. SPE-10971-MS. <http://dx.doi.org/10.2118/10971-MS>.
- Melrose, J.C. and Brandner, C.F. 1974. Role of Capillary Forces in Determining Microscopic Displacement Efficiency for Oil Recovery by Water Flooding. *J Can Pet Technol* **13** (4): 54–62.

Metcalfe, R.S. 1981. Effects of Impurities on Minimum Miscibility Pressures and Minimum Enrichment Levels for CO₂ and Rich-Gas Displacements. *SPE J.* **22** (2): 219–225.

Metcalfe, R.S. and Yarborough, L. 1978. The Effect of Phase Equilibria on the CO₂ Displacement Mechanism. *SPE J.* **19** (4): 242–252.

Meter, D.M. and Bird, R.B. 1964. Tube Flow of Non-Newtonian Polymer Solutions, Parts I and 2-Laminar Flow and Rheological Models. *AIChE Journal* (November 1964): 878–881, 1143–1150.

Michelsen, M.L. 1986. Simplified Flash Calculations for Cubic Equations of State. *Industrial and Engineering Chemistry Process and Design Development* **25** (1): 184–188.
<http://dx.doi.org/10.1021/i200032a029>.

Meyer, R.F. and Attanasi, E.D. 2003. Heavy Oil and Natural Bitumen —Strategic Petroleum Resources. US Geological Survey Fact Sheet 70–03 (August 2003). <http://pubs.usgs.gov>.

Minssieux, L. 1976. Waterflood Improvement by Means of Alkaline Water. In *Enhanced Oil Recovery by Displacement with Saline Solutions*. Houston, Texas: Gulf Publishing. (From a symposium held 20 May 1976 at Britannic House, London, England.)

Mohanty, K.K. 1981. *Fluids in Porous Media: Two-Phase Distribution and Flow*. PhD dissertation, University of Minnesota, Minneapolis, Minnesota (1981).

Mohanty, K. and Salter S.J. 1982. Multiphase Flow in Porous Media: II. Pore Level Modeling. Presented at the SPE Annual Technical Conference & Exhibition, New Orleans, 26–29 September. SPE-11018-MS. <http://dx.doi.org/10.2118/11018-MS>.

Mohebbinia, S., Sephernoori, K., and Johns, R.T. 2012. Four-Phase Equilibrium Calculations of CO₂/Hydrocarbon/Water Systems Using a Reduced Method. Presented at the SPE Improved Oil Recovery Symposium, Tulsa, 14–18 April. SPE-154218-MS.

<http://dx.doi.org/10.2118/154218-MS>.

Molleai, A., and Delshad, M. 2011. General Isothermal Enhanced Oil Recovery and Waterflood Forecasting Model. Presented at the SPE Annual Technical Conference and Exhibition, Denver, 30 October—2 November. SPE-143925-MS. <http://dx.doi.org/10.2118/143925-MS>.

Monger, T.G. 1985. The Impact of Oil Aromaticity on CO₂ Flooding. *SPE J.* **25** (6): 865–874.

Monger, T.G. and Coma, J.M. 1988. A Laboratory and Field Evaluation of the CO₂ Huff ‘n’ Puff Process for Light Oil Recovery. *SPE Res Eng* **3** (4): 1168–1176.

Moore, T.F. and Slobod, R.L. 1956. The Effect of Viscosity and Capillarity on the Displacement of Oil by Water. *Producers Monthly* **20** (10): 20–30.

Morel-Seytoux, H.J. 1966. Unit Mobility Ratio Displacement Calculations for Pattern Floods in Homogeneous Medium. *SPE J.* **6** (3): 217–227.

Morrow, N.R. and Chatzis, I. 1981. Measurements and Correlation of Conditions for Entrapment and Mobilization of Residual Oil. US Department of Energy, DOE/ BETC/3251-12, 1981.

Morrow, N.R. and Chatzis, I. 1974. The Effect of Surface Roughness on Contact Angles. Preprint-35, 48th National Colloid Symposium of the American Chemical Society, Austin, Texas, 1974.

Morrow, N.R. and. 1976. Capillary Pressure Correlations for Uniformly Wetted Porous Media. *J Can Pet Technol* **15** (4): 49–69.

Muller, T. and Lake, L.W. 1991. Theoretical Study of Water Blocking in Miscible Flooding. *SPE Res Eng* **6** (4): 445–451.

Myhill, N.A. and Stegemeier, G.L. 1978. Steam-Drive Correlation and Prediction. *J Pet Technol* **30** (2): 173–182.

Namdar-Zanganeh, M., Kam, S.I., LaForce, T.C., and Rossen, W.R. 2011. The Method of Characteristics Applied to Oil Displacement by Foam. *SPE J.* **16** (1): 8–23.

National Petroleum Council. 1984. *Enhanced Oil Recovery*.

Neasham, J.W. 1977. The Morphology of Dispersed Clay in Sandstone Reservoirs and its Effect on Sandstone Shaliness. Presented at the SPE Annual Fall Technical Conference and Exhibition, Denver, 9–12 October. SPE-6858-MS.
<http://dx.doi.org/10.2118/6858-MS>.

Needham, R.B., Threlkeld, C.B., and Gall, J.W. 1974. Control of Water Mobility Using Polymers and Multivalent Cations. Presented at the PE Improved Oil Recovery Symposium, Tulsa, 22–24 April. SPE-4747-MS. <http://dx.doi.org/10.2118/4747-MS>.

Nelson, R.C. and Pope, G.A. 1978. Phase Relationships in Chemical Flooding. *SPE J.* **18** (5): 325–338. SPE-6773-PA.
<http://dx.doi.org/10.2118/6773-PA>.

Nelson, R.C. 1982. The Salinity-Requirement Diagram—A Useful Tool in Chemical Flooding Research and Development. *SPE J.* **22** (2): 259–270. SPE-8824-PA. <http://dx.doi.org/10.2118/8824-PA>.

Nelson, R.C. 1983. The Effect of Live Crude on Phase Behavior and Oil-Recovery Efficiency of Surfactant Flooding Systems. *SPE J.* **23** (3): 501–510. SPE-10677-PA. <http://dx.doi.org/10.2118/10677-PA>.

Nelson, R.C., Lawson, J.B., Thigpen, D.R., et al. 1984. Cosurfactant Enhanced Alkaline Flooding. Presented at the SPE Enhanced Oil

Recovery Symposium, Tulsa, 15–18 April. SPE-2672-MS.
<http://dx.doi.org/10.2118/12672-MS>.

Nguyen, Q.P., Zitha, P.L.J., Currie, P.K., et al. 2009. CT Study of Liquid Diversion With Foam. *SPE Prod & Oper* **24** (1): 12–21. SPE-93949-PA. <http://dx.doi.org/10.2118/93949-PA>.

Oh, S.G., and Slattery, J. 1976. Interfacial Tension Required for Significant Displacement of Residual Oil. Presented at the Second ERDA Symposium on Enhanced Oil and Gas Recovery, Tulsa, Paper D-2.

Oil and Gas Journal Biennial Survey of EOR, since 1988, Pennwell Press.

Okuno, R., Johns, R.T., and Sepehrnoori, K. 2010a. Three-Phase Flash in Compositional Simulation Using a Reduced Method. *SPE J.* **15** (3): 689–703. SPE-125226-PA. <http://dx.doi.org/10.2118/125226-PA>.

Okuno, R., Johns, R.T., and Sepehrnoori, K. 2010b. A New Algorithm for Rachford-Rice for Multiphase Compositional Simulation. *SPE J.* **15** (2): 313–325. SPE-117752-PA.
<http://dx.doi.org/10.2118/117752-PA>.

Okuno, R., Johns, R.T., and Sepehrnoori, K. 2010c. Application of a Reduced Method in Compositional Simulation. *SPE J.* **15** (1): 39–49. SPE-119657-PA. <http://dx.doi.org/10.2118/119657-PA>.

Orr, F.M. Jr. 2007. *Theory of Gas Injection Processes*. Copenhagen, Denmark: Tie-Line Publications.

Orr, F.M. Jr., and J.J. Taber. 1984. Use of Carbon Dioxide in Enhanced Oil Recovery. *Science* **224** (4649): 563–569.

Orr, F.M. Jr., and Jensen, C.M. 1984. Interpretation Pressure-Composition Phase Diagrams for CO₂/Crude Oil Systems. *SPE J.* **24**

(5): 485–497. SPE-11125-PA. <http://dx.doi.org/10.2118/11125-PA>.

Orr, F.M. Jr., Jensen, C.M., and Silva, M.K. 1981. Effect of Solution Gas on the Phase Behavior of CO₂-Crude Oil Mixtures. International Energy Agency Workshop on Enhanced Oil Recovery, Winfurth, United Kingdom.

Orr, F.M. Jr. and Silva, M.K. 1983. Equilibrium Phase Compositions of CO₂/Hydrocarbon Mixtures Part 1: Measurement by a Continuous Multiple-Contact Experiment. *SPE J.* **23** (2): 272–280. SPE-10726-PA. <http://dx.doi.org/10.2118/10726-PA>.

Osterloh, W.T. and Jante, M.J. Jr. 1992. Effects of Gas and Liquid Velocity on Steady-State Foam Flow at High Temperature. Presented at the SPE/DOE Symposium on Enhanced Oil Recovery, Tulsa, 22–24 April. SPE-24179-MS. <http://dx.doi.org/10.2118/24179-MS>.

Owens, W.W. and Archer, D.L. 1971. The Effect of Rock Wettability on Oil-Water Relative Permeability Relationships. *J Pet Technol* **23** (7): 873–878. SPE-3034-PA. <http://dx.doi.org/10.2118/3034-PA>.

Owolabi, O.O. and Watson, R.W. 1993. Effects of Rock-Pore Characteristics on Oil Recovery at Breakthrough and Ultimate Oil Recovery in Water-Wet Sandstones. Presented at the SPE Eastern Regional Meeting, Pittsburgh, Pennsylvania, USA, 2–4 November. SPE-26935-MS.

Panait-Patica, A., Serban, D., and Ilie, N. 2006. Suplacu de Barcau Field—A Case History of a Successful In-Situ Combustion Exploitation. Presented at the SPE Europec/EAGE Annual Conference and Exhibition, Vienna, Austria, 12–15 June. SPE-100346-MS. <http://dx.doi.org/10.2118/100346-MS>.

Panda, M.N. and Lake, L.W. 1994. Estimation of Single-Phase Permeability From Parameters of Particle Size Distributions. *AAPG Bull.* **78** (7): 1028–1039.

Panda, M.N. and Lake, L.W. 1995. A Physical Model of Cementation and Its Effects on Single-Phase Permeability. *AAPG Bull.* **79** (3): 431–443.

Parkinson, W.J. and de Nevers, N. 1969. Partial Molal Volume of Carbon Dioxide in Water Solutions. *Industrial & Engineering Chemistry Fundamentals* **8** (4): 709–713.
<http://dx.doi.org/10.1021/i160032a017>.

Parra Sanchez, C. 2010. *Optimizing the Time of Enhanced Oil Recovery*. MS thesis, The University of Texas (2010).

Patzek, T.W. 1996. Field Applications of Steam Foam for Mobility Improvement and Profile Control. *SPE Res Eng* **11** (2): 79–86. SPE-29612-PA. <http://dx.doi.org/10.2118/29612-PA>.

Paul, G.W. and Froning, H.R. 1973. Salinity Effects of Micellar Flooding. *J Pet Technol* **25** (8): 957–958. SPE-4419-PA.
<http://dx.doi.org/10.2118/4419-PA>.

Paul, G.W., Lake, L.W., Pope, G.A., et al. 1982. A Simplified Predictive Model for Micellar/Polymer Flooding. Presented at the SPE California Regional Meeting, San Francisco, 24–26 March. SPE-10733-MS. <http://dx.doi.org/10.2118/10733-MS>.

Payatakes, A.C., Flumerfelt, R.W., and Ng, K.M. 1978. On the Dynamics of Oil Ganglia Populations During Immiscible Displacement. AIChE 84th National Meeting, Atlanta, Georgia, 26 February—1 March.

Peaceman, D.W. 1977. *Fundamentals of Numerical Reservoir Simulation*. New York: Elsevier.

Pedersen, K.S. and Christensen, P.L. 2007. *Phase Behavior of Petroleum Reservoir Fluids*. Boca Raton, Florida: CRC Press. ISBN-10: 9780824706944.

Peng, D-Y. and Robinson, D.B. 1976. A New Two-Constant Equation of State. *Industrial & Engineering Chemistry Fundamentals* **15** (1): 59–64. <http://dx.doi.org/10.1021/i160057a011>.

Perez-Perez, A., Gamboa, M., Ovalles, C., and Manrique, E. 2001. Benchmarking of Steamflood Field Projects in Light/Medium Crude Oils. Presented at the SPE Asia Pacific Improved Oil Recovery Conference, Kuala Lumpur, 6–9 October. SPE-72137-MS. <http://dx.doi.org/10.2118/72137-MS>.

Perry, G.E. 1978. First Annual Report, Weeks Island “S” Sand Reservoir B Gravity Stable, Miscible CO₂ Displacement, Iberia Parish, Louisiana. US Department of Energy, METC/ CR-78/13, Morgantown, West Virginia (June 1978).

Persoff, P., Radke, C.J., Pruess, K., Benson, S.M., and Witherspoon, P.A. 1991. A Laboratory Investigation of Foam Flow in Sandstone at Elevated Pressure. *SPE Res Eng* **6** (3): 365–372. SPE-18781-PA. <http://dx.doi.org/10.2118/18781-PA>.

Peters, E. 2012. *Advanced Petrophysics*, Vol. 1–3. Austin, Texas: Live Oak Book Company.

Peters, E.J. 1979. *Stability Theory and Viscous Fingering in Porous Media*. PhD dissertation, University of Alberta, Edmonton, Alberta (1979).

Phillips, J.R. 1957. The Theory of Infiltration. *Soil Science* **83**: 345–357.

Pirson, S.J. 1983. *Geologic Well Log Analysis*, third edition. Houston, Texas: Gulf Publishing.

Pollack, N.R., Enick, R.M., Mangone, D.J. et al. 1988. Effect of an Aqueous Phase on CO₂ / Tetradecane and CO₂/Maljamar-Crude-Oil Systems. *SPE Res Eng* **3** (2): 533–541. SPE-15400-PA. <http://dx.doi.org/10.2118/15400-PA>.

Poling, B.E., Prausnitz, J.M., and O'Connell, J.P. 2000. *The Properties of Gases and Liquids*, fifth edition. New York: McGraw-Hill Professional.

Pope, G.A. 1980. The Application of Fractional Flow Theory to Enhanced Oil Recovery. *SPE J.* **20** (3): 191–205. SPE-7660-PA.
<http://dx.doi.org/10.2118/7660-PA>.

Pope, G.A. and Nelson, R.C. 1978. A Chemical Flooding Compositional Simulator. *SPE J.* **18** (5): 339–354. SPE-6725-PA.
<http://dx.doi.org/10.2118/6725-PA>.

Pope, G.A., Wang, B., and Tsaur, K. 1979. A Sensitivity Study of Micellar/Polymer Flooding. *SPE J.* **19** (6): 357–368. SPE-7079-PA.
<http://dx.doi.org/10.2118/7079-PA>.

Prausnitz, J.M., Anderson, T.F., Grens, E.A., Eckerf, C.A., Hsieh, R., and O'Connell, J.P. 1980. *Computer Calculations for Multicomponent Vapor-Liquid and Liquid-Liquid Equilibria*. Englewood Cliffs, New Jersey: Prentice-Hall, Inc.

Prats, M. 1982. *Thermal Recovery*, No. 7. Richardson, Texas: Monograph Series, SPE.

Prodanovic, M., Bryant, S.L., and Karpyn, Z.T. 2010. Investigating Matrix/Fracture Transfer via a Level Set Method for Drainage and Imbibition. *SPE J.* **15** (1): 125–136. SPE-116110-PA.
<http://dx.doi.org/10.2118/116110-PA>.

Prouvost, L., Pope, G.A., and Rouse, B. 1985. Microemulsion Phase Behavior: A Thermodynamic Modeling of the Phase Partitioning of Amphiphilic Species. *SPE J.* **25** (5): 693–703.
<http://dx.doi.org/10.2118/12586-PA>.

Puerto M.C. and Reed, R.L. 1983. Three-Parameter Representation of Surfactant/Oil/Brine Interaction. *SPE J.* **23** (4): 669–682. SPE-10678-PA. <http://dx.doi.org/10.2118/10678-PA>.

Quintard, M. and Whitaker, S. 1988. Two-Phase Flow in Heterogeneous Porous Media: The Method of Large-Scale Averaging. *Transport in Porous Media* **3** (4): 357–413.
<http://dx.doi.org/10.1007/BF00233177>.

Ramakrishnan, T.S. and Wasan, D.T. 1983. A Model for Interfacial Activity of Acidic Crude/Caustic Systems for Alkaline Flooding. *SPE J.* **23** (4): 602–612. SPE-10716-PA. <http://dx.doi.org/10.2118/10716-PA>.

Ramey, H.J. Jr. 1959. Discussion of Reservoir Heating by Hot Fluid Injection. *Trans., AIME* **216** (1959): 364–365.

Ramey, H.J. Jr. 1962. Wellbore Heat Transmission. *J Pet Technol* **14** (4): 427–435. *Trans., AIME*, **225**. SPE-96-PA.
<http://dx.doi.org/10.2118/96-PA>.

Ramey, H.J. Jr. 1964. How to Calculate Heat Transmission in Hot Fluids. *Petroleum Engineer* (November 1964): 110–120.

Romial, V. 2004. Enhanced Oil Recovery by Steamflooding in a Recent Steamflood Project, Cruse 'E' Field, Trinidad. Presented at the SPE/DOE Symposium on Improved Oil Recovery, Tulsa, 17–21 April. SPE-89411-MS. <http://dx.doi.org/10.2118/89411-MS>.

Raimondi, P. and Torcaso, M.A. 1964. Distribution of the Oil Phase Obtained Upon Imbibition of Water. *SPE J.* **4** (1): 49–55; *Trans., AIME*, **231**. SPE-570-PA. <http://dx.doi.org/10.2118/570-PA>.

Rapoport, L.A. and Leas, W.J. 1953. Properties of Linear Waterfloods. *J Pet Technol* **5** (5): 139–148. SPE-213-G.
<http://dx.doi.org/10.2118/213-G>.

Reed, R.L. and Healy, R.N. 1984. Contact Angles for Equilibrated Microemulsion Systems. *SPE J.* **24** (3): 342–350. SPE-8262-PA.
<http://dx.doi.org/10.2118/8262-PA>.

Reed, R.L. and Healy, R.N. 1977. Some Physico-Chemical Aspects of Microemulsion Flooding: A Review. In *Improved Oil Recovery by Surfactant and Polymer Flooding*, ed. D.O. Shah and R.S. Schechter, 383–437. New York: Academic Press.

Richards, L.A. 1931. Capillary Conduction of Liquids Through Porous Mediums. *Physics* **1** (5): 318–333.
<http://dx.doi.org/10.1063/1.1745010>.

Rieke, H.H., Chilingarian, G.V., and Vorabutr, P. 1983. In *Drilling and Drilling Fluids*, ed. G.V. Chilingarian and P. Vorabutr, Chap. 5: Clays. New York: Elsevier.

Risnes, R. and Dalen, V. 1984. Equilibrium Calculations for Coexisting Liquid Phases. *SPE J.* **24** (1): 87–96.

de Riz, L. and Muggeridge, A.H. 1997. Will Vertical Mixing Improve Oil Recovery for Gravity Dominated Flows in Heterogeneous Reservoirs? Presented at the SPE Reservoir Simulation Symposium, Dallas, 8–11 June. SPE-37996-MS. <http://dx.doi.org/10.2118/37996-MS>.

Roberts, G.E. and Kaufman, H. 1966. *Table of Laplace Transforms*. Philadelphia, Pennsylvania: Saunders.

Rose, P.R. 2001. *Risk Analysis and Management of Petroleum Exploration Ventures*. Tulsa, Oklahoma: AAPG Methods in Exploration Series, No. 12, AAPG.

Roshanfekr, M., Li, Y., and Johns, R.T. 2010. Non-Iterative Phase Behavior Model With Application to Surfactant Flooding and Limited Compositional Simulation. *Fluid Phase Equilibria* **289** (2): 166–175. <http://dx.doi.org/10.1016/j.fluid.2009.11.024>.

Roshanfekr, M., and Johns, R.T. 2011. Prediction of Optimum Salinity and Solubilization Ratio for Microemulsion Phase Behavior

With Live Crude at Reservoir Pressure. *Fluid Phase Equilibria* **304** (1–2): 52–60. <http://dx.doi.org/10.1016/j.fluid.2011.02.004>.

Rossen, W.R. 1996. Foams in Enhanced Oil Recovery. In *Foams, Theory, Measurements and Applications*, ed. R.K. Prud' home and S. Khan, Chapter 11, 413–464. New York: Marcel Dekker.

Rossen, W.R. and Lu, Q. 1997. Effect of Capillary Crossflow on Foam Improved Oil Recovery. Presented at the SPE Western Regional Meeting, Long Beach, California, 25–27 June. SPE-38319-MS. <http://dx.doi.org/10.2118/38319-MS>.

Rossen, W.R., van Duijn, C.J., Nguyen, Q.P., et al. 2010. Injection Strategies To Overcome Gravity Segregation in Simultaneous Gas and Water Injection Into Homogeneous Reservoirs. *SPE J.* **15** (1): 76–90. SPE-99794-PA. <http://dx.doi.org/10.2118/99794-PA>.

Rossen, W.R., Venkatraman, A., Johns, R.T., et al. 2011. Fractional Flow Theory Applicable to Non-Newtonian Behavior in EOR Processes. *Transport in Porous Media* **89** (2): 213–236.
<http://dx.doi.org/10.1007/s11242-011-9765-2>.

Rossen, W.R., Zeilinger, S.C., Shi, J.-X., et al. 1999. Simplified Mechanistic Simulation of Foam Processes in Porous Media. *SPE J.* **4** (3): 279–287. SPE-57678-PA. <http://dx.doi.org/10.2118/57678-PA>.

Rowe, A.M. 1967. The Critical Composition Method—A New Convergence Pressure Method. *SPE J.* **7** (1): 54–60. SPE-1631-PA.
<http://dx.doi.org/10.2118/1631-PA>.

Sage, B.H. and Lacey, W.N. 1939. *Volumetric and Phase Behavior of Hydrocarbons*. Houston, Texas: Gulf Publishing.

Sanz, C.A. and Pope, G.A. 1995. Alcohol-Free Chemical Flooding: From Surfactant Screening to Coreflood Design. Presented at the SPE International Symposium on Oilfield Chemistry, San Antonio,

Texas, USA, 14–17 February. SPE-28956-MS.
<http://dx.doi.org/10.2118/28956-MS>.

Sahni, I., Stern, D., Banfield, J., and Langenberg, M. 2010. History Match Case Study: Use of Assisted History Match Tools on Single-Well Models in Conjunction With a Full-Field History Match. Presented at the SPE Russian Oil and Gas Technical Conference and Exhibition, Moscow, 26–28 October. SPE 136432-MS.

Salathiel, R.A. 1973. Oil Recovery by Surface Film Drainage in Mixed-Wettability Rocks. *J Pet Technol* **25** (10): 1216–1224; *Trans., AIME*, **255**. SPE-4104-PA. <http://dx.doi.org/10.2118/4104-PA>.

Salter, S.J. 1978. Selection of Pseudo Components in Surfactant Oil Brine Alcohol Systems. Presented at the SPE Symposium on Improved Methods of Oil Recovery, Tulsa, 16–17 April. SPE-7056-MS. <http://dx.doi.org/10.2118/7056-MS>.

Salter, S.J. 1983. Optimizing Surfactant Molecular Weight Distribution 1. Sulfonate Phase Behavior and Physical Properties. Presented at the SPE Annual Technical Conference and Exhibition, San Francisco, 5–8 October. SPE-12036-MS.
<http://dx.doi.org/10.2118/12036-MS>.

Samizo, N. 1982. Numerical Simulation of Two-Phase Compressible Flow by the Moving Point Method. MS thesis, The University of Texas at Austin, Austin, Texas (1982).

Sanchez, J.M. and Hazlett, R.D. 1992. Foam Flow Through an Oil-Wet Porous Medium: A Laboratory Study. *SPE Res Eng* **7**(1): 91–97. SPE-19687-PA. <http://dx.doi.org/10.2118/19687-PA>.

Sandler, S.I. 2006. *Chemical, Biochemical and Engineering Thermodynamics*, fourth edition. Hoboken, New Jersey: John Wiley & Sons.

Sarathi, P.S. 1999. In-Situ Combustion Handbook—Principles and Practices. Final Report, DOE/PC/91008-0374, OSTI_ID 3175, National Petroleum Technology Office, US DOE, Tulsa (January 1999).

Satter, A. 1965. Heat Losses During Flow of Steam Down a Wellbore. *J Pet Technol* (July 1965): 845–851.

Sayegh, S.G., Najman, J., and Hlavacek, B. 1981. Phase Equilibrium and Fluid Properties of Pembina Cardium Stock-Tank Oil-Methane-Carbon Dioxide Sulfur-Dioxide Mixtures. *J Can Pet Technol* **20** (4). PETSOC-81-04-05. <http://dx.doi.org/10.2118/81-04-05>.

Schneider, F.N. and Owens, W.W. 1982. Steady-State Measurements of Relative Permeability for Polymer/Oil Systems. *SPE J.* **22** (1): 79–86. SPE-9408-PA. <http://dx.doi.org/10.2118/9408-PA>.

Schneider, G.M. 1970. Phase Equilibrium Fluid Mixtures at High Pressures. *Advances in Chemical Physics* 17, ed. Prigogine and S.A. Rice. New York: Interscience.

Schramm, L.L. ed. 1994. *Foams: Fundamentals and Applications in the Petroleum Industry*, No. 242. Washington, DC: Advances in Chemistry Series, American Chemical Society.

Scriven, L.E. 1977. Equilibrium Bicontinuous Structures. In *Micellization, Solubilization, and Microemulsions*, ed. K.L. Mittal. Springer, US

Sebastian, H.M., Winger, R.S., and Renner, T.A. 1985. Correlation of Minimum Miscibility Pressure for Impure CO₂ Streams. *J Pet Technol* **37** (11): 2076–2085. SPE-12648-PA. <http://dx.doi.org/10.2118/12648-PA>.

Seright, R.S. 1983. The Effects of Mechanical Degradation and Viscoelastic Behavior on Injectivity of Polyacrylamide Solutions. *SPE*

J. **23** (3): 475–485. SPE-9297-PA. <http://dx.doi.org/10.2118/9297-PA>.

Seright, R.S. 2010. Potential for Polymer Flooding Reservoirs With Viscous Oils. *SPE Res Eval & Eng* **13** (4): 730–740. SPE-129899-PA. <http://dx.doi.org/10.2118/129899-PA>.

Shan, D. and Rossen, W.R. 2004. Optimal Injection Strategies for Foam IOR. *SPE J.* **9** (2): 132–150. SPE-88811-PA. <http://dx.doi.org/10.2118/88811-PA>.

Sheng, J. 2011. *Modern Chemical Enhanced Oil Recovery: Theory and Practice*. Oxford, UK: Elsevier.

Shelton, J.L. and Schneider, F.N. 1975. The Effects of Water Injection on Miscible Flooding Methods Using Hydrocarbons and Carbon Dioxide. *SPE J.* **15** (3): 217–226. SPE-4580-PA. <http://dx.doi.org/10.2118/4580-PA>.

Shokir, E.M. El-M. 2007. CO₂–Oil Minimum Miscibility Pressure Model for Impure and Pure CO₂ Streams. *J. Pet. Sci. Eng.* **58** (1–2): 173–185. <http://dx.doi.org/10.1016/j.petrol.2006.12.001>.

Shook, G.M., Pope, G.A., and Asakawa, K. 2009. Determining Reservoir Properties and Flood Performance From Tracer Test Analysis. Presented at the SPE Annual Technical Conference and Exhibition, New Orleans, 4–7 October. SPE-124614-MS. <http://dx.doi.org/10.2118/124614-MS>.

Shook, M., Li, D., and Lake, L.W. 1992. Scaling Immiscible Flow Through Permeable Media by Inspectional Analysis. *In Situ* **16** (4): 311–349. [http://dx.doi.org/10.1016/0148-9062\(93\)91860-L](http://dx.doi.org/10.1016/0148-9062(93)91860-L).

Shupe, R.D. 1981. Chemical Stability of Polyacrylamide Solutions. *J Pet Technol* **33** (8): 1513–1529. SPE-9299-PA. <http://dx.doi.org/10.2118/9299-PA>.

Shutler, N.D. and Boberg, T.C. 1972. A One-Dimensional Analytical Technique for Predicting Oil Recovery by Steamflooding. *SPE J.* **12** (6): 489–498. SPE-2917-PA. <http://dx.doi.org/10.2118/2917-PA>.

Simlote, V.M., Zapata, V.J., and Belveal, L.A. 1983. A Study of Caustic Consumption in a High-Temperature Reservoir. Presented at the SPE Annual Technical Conference and Exhibition, San Francisco, 5–8 October. SPE-12086-MS.
<http://dx.doi.org/10.2118/12086-MS>.

Simon, R. and Graue, D.J. 1965. Generalized Correlation for Predicting Solubility, Swelling, and Viscosity Behavior for CO₂-Crude Oil Systems. *J Pet Technol* **17** (1): 102–106. SPE-917-PA.
<http://dx.doi.org/10.2118/917-PA>.

Skauge, A. and Fotland, P. 1990. Effect of Pressure and Temperature on the Phase Behavior of Microemulsions. *SPE Res Eng* **5** (4): 601–608.

Skjaeveland, S.M., Siqveland L.M., Kjosavid, A., et al. 2000. Capillary Pressure Correlation for Mixed-Wet Reservoirs. *SPE Res Eval & Eng* **3** (1): 60–67. SPE-60900-PA.
<http://dx.doi.org/10.2118/60900-PA>.

Skjaeveland, S.M. and Kleppe, J. 1992. *Recent Advances in Improved Oil Recovery Methods for North Sea Sandstone Reservoirs*. Stavanger: SPOR monograph, Norwegian Petroleum Directorate.

Skoreyko, F.F., Pino Villavicencio, A., Rodriguez Prada, H., et al. 2011. Development of a New Foam EOR Model From Laboratory and Field Data of the Naturally Fractured Cantarell Field. Presented at the SPE Reservoir Characterisation and Simulation Conference and Exhibition, Abu Dhabi, 9–11 October. SPE-145718-MS.
<http://dx.doi.org/10.2118/145718-MS>.

- Slattery, J.C. 1972. *Momentum, Energy, and Mass Transfer in Continua*. New York: McGraw-Hill.
- Smith, J.M. and van Ness, H.C. 1975. *Introduction to Chemical Engineering Thermodynamics*, second edition. New York: McGraw-Hill.
- Soave, G. 1972. Equilibrium Constants From a Modified Redlich-Kwong Equation of State. *Chem. Eng. Sci.* **27** (6): 1197–1203.
[http://dx.doi.org/10.1016/0009-2509\(72\)80096-4](http://dx.doi.org/10.1016/0009-2509(72)80096-4).
- S. Solairaj, Britton, C., Lu, J., Kim, D.H., Weerasooriya, U., and Pope, G.A. 2012. New Correlation to Predict the Optimum Surfactant Structure for EOR. Presented at the SPE Improved Oil Recovery Symposium, Tulsa, 14–18 April. SPE-154262-MS.
- Somasundaran, P., Celik, M., Goyal, A. et al. 1984. The Role of Surfactant Precipitation and Redissolution in the Adsorption of Sulfonate on Minerals. *SPE J.* **24** (2): 233–239. SPE-8263-PA.
<http://dx.doi.org/10.2118/8263-PA>.
- Somerton, W.H. 1973. Thermal Properties of Hydrocarbon Bearing Rocks at High Temperatures and Pressures. API Research Project 117, Final Report, College of Engineering, University of California, Berkeley, California.
- Sorbie, K.S. 1991. *Polymer-Improved Oil Recovery*. Boca Raton, Florida: CRC Press, Inc.
- Spence, A.P. Jr. and Watkins, R.W. 1980. The Effect of Microscopic Core Heterogeneity on Miscible Flood Residual Oil Saturation. Presented at the SPE Annual Technical Conference and Exhibition, Dallas, 21–24 September. SPE-9229-MS.
<http://dx.doi.org/10.2118/9229-MS>.
- Stalkup, F. 1983. *Miscible Displacement*, 8. Richardson, Texas: Monograph Series, SPE.

Stalkup, F. 1970. Displacement of Oil by Solvent at High Water Saturation. *SPE J.* **10** (4): 337–348. SPE-2419-PA.
<http://dx.doi.org/10.2118/2419-PA>.

Standing, M.B. 1977. *Volumetric and Phase Behavior of Oil Field Hydrocarbon Systems*. Richardson, Texas: SPE.

Stegemeier, G.L. 1974. Relationship of Trapped Oil Saturation to Petrophysical Properties of Porous Media. Presented at the SPE Improved Oil Recovery Symposium, Tulsa, 22–24 April. SPE-4754-MS. <http://dx.doi.org/10.2118/4754-MS>.

Stegemeier, G.L. 1976. Mechanisms of Oil Entrapment and Mobilization in Porous Media. *Proc., AIChE Symposium on Improved Oil Recovery by Surfactant and Polymer Flooding*, Kansas City, Missouri, USA, 12–14 April, pp. 55–91.

Stegemeier, G.L., Laumbach, D.D., and Volek, C.W. 1980. Representing Steam Processes With Vacuum Models. *SPE J.* **20** (3): 151–174. <http://dx.doi.org/10.2118/6787-PA>.

Stegemeier, G.L., and Vinegar, H.J. 2001. Thermal Conduction Heating for In-Situ Thermal Desorption of Soils. In *Hazardous and Radioactive Waste Treatment Technologies Handbook*, Chap. 4.6-1. Boca Raton, Florida: CRC Press.

Stiles, W.E. 1949. Use of Permeability Distribution in Water Flood Calculations. *Trans., AIME* **186**: 9–13. SPE-949009-G.

Stolwijk, G.H. and Rossen, W.R. 2009. Gravity Segregation in Gas IOR in Heterogeneous Reservoirs. Presented at the 15th European Symposium on Improved Oil Recovery, Paris, 27–29 April.

Stone, H.L. 1982. Vertical Conformance in an Alternating Water-Miscible Gas Flood. Presented at the SPE Annual Technical Conference and Exhibition, New Orleans, 26–29 September. SPE-11130-MS. <http://dx.doi.org/10.2118/11130-MS>.

Stone, H.L. 2004. A Simultaneous Water and Gas Flood Design With Extraordinary Vertical Gas Sweep. Presented at the SPE International Petroleum Conference, Puebla, Mexico, 7–9 November. SPE-91724-MS. <http://dx.doi.org/10.2118/91724-MS>.

Stone, H.L. 1970. Probability Model for Estimating Three-Phase Relative. *J Pet Technol* **22** (2): 214–218. SPE-2116-PA. <http://dx.doi.org/10.2118/2116-PA>.

Sydansk, R.D. 1982. Elevated-Temperature Caustic/Sandstone Interaction: Implications for Improving Oil Recovery. *SPE J.* **22** (4): 453–462. SPE-9810-PA. <http://dx.doi.org/10.2118/9810-PA>.

Taber, J.J. 1969. Dynamic and Static Forces Required to Remove a Discontinuous Oil Phase From Porous Media Containing Both Oil and Water. *SPE J.* **9** (1): 3–12.

Taber, J.J., Martin, F.D., and Seright, R.S. 1997. EOR Screening Criteria Revisited—Part 1: Introduction to Screening Criteria and Enhanced Oil Recovery Projects. *SPE Res Eng* **12** (3): 189–198. SPE-35385-PA.

Taber, J.J., Kamath, S.K., and Reed, R.L. 1965. Mechanism of Alcohol Displacement of Oil From Porous Media. In *Miscible Processes*, 39–56. SPE Reprint Series No. 8: Richardson, Texas.

Taber, J.J. and W.K. Meyer, 1965. Investigations of Miscible Displacements of Aqueous and Oleic Phases From Porous Media. *Miscible Processes*, SPE Reprint Series No. 8: 57–68.

Tanzil, D., Hirasaki, G.J., and Miller, C.A. 2002. Mobility of Foam in Heterogeneous Media: Flow Parallel and Perpendicular to Stratification. *SPE J.* **7** (2): 203–212. SPE-78601-PA. <http://dx.doi.org/10.2118/78601-PA>.

Taylor, G.I. 1953. The Dispersion of Matter in Solvent Flowing Slowly Through a Tube. *Proceedings of Royal Society London: Series A*,

Mathematical and Physical Sciences **219** (1137): 186–203.
<http://dx.doi.org/10.1098/rspa.1953.0139>.

Tertiary Oil Recovery Project (TORP). www.torp.ku.edu.

Thomeer, J.H.M. 1960. Introduction of a Pore Geometrical Factor Defined by the Capillary Pressure Curve. *J Pet Technol* **12** (3):73–77.

Tinker, G.E., Bowman, R.W., and Pope, G.A. 1976. Determination of In-Situ Mobility and Wellbore Impairment From Polymer Injectivity Data. *J Pet Technol* **28** (5): 586–596. SPE-4744-PA.
<http://dx.doi.org/10.2118/4744-PA>.

Todd, M.R. and Chase, C.A. 1979. A Numerical Simulator for Predicting Chemical Flood Performance. Presented at the SPE Annual Technical Conference and Exhibition, Denver, 31 January—2 February. SPE-7689-MS. <http://dx.doi.org/10.2118/7689-MS>.

Todd, M.R. and Longstaff, W.J. 1972. The Development, Testing, and Application of a Numerical Simulator for Predicting Miscible Flood Performance. *J Pet Technol* **24** (7): 874–882. SPE-3484-PA.
<http://dx.doi.org/10.2118/3484-PA>.

Toledo, P., Scriven, L.E., and Davis, H.T. 1994. Equilibrium and Stability of Static Interfaces in Biconical Pore Segments. *SPE Form Eval* **9** (1): 61–65. SPE-27410-PA. <http://dx.doi.org/10.2118/27410-PA>.

Treiber, L.E. and Owens, W.W. 1972. A Laboratory Evaluation of the Wettability of Fifty Oil-Producing Reservoirs. *SPE J.* **12** (6): 531–540. SPE-3526-PA. <http://dx.doi.org/10.2118/3526-PA>.

Trushenski, S.P. 1977. Micellar Flooding: Sulfonate-Polymer Interaction. In *Improved Oil Recovery by Surfactant and Polymer Flooding*, eds. D.O. Shah and R.S. Schechter, 555–575. New York: Academic Press.

Tsaur, K. 1978. *A Study of Polymer/Surfactant Interactions for Micellar/Polymer Flooding Applications*. MS thesis, The University of Texas, Austin, Texas (August 1978).

Tumasyan, A.B., Panteleev, V.G., and Meinster, G.P. 1960. The Effect of Carbon Dioxide Gas on the Physical Properties of Crude Oil and Water. Nauk.-Tekh. Sb Ser. Neftepromysloveo Delo #2: 20–30.

Turek, E.A., Metcalfe, R.S., Yarborough, L., et al. 1984. Phase Equilibrium in CO₂–Multicomponent Hydrocarbon Systems: Experimental Data and an Improved Prediction Technique. *SPE J.* **24** (3): 308–324. SPE-9231-PA. <http://dx.doi.org/10.2118/9231-PA>.

Turta, A.T., Chattopadhyay, S.K., Bhattacharya, R.N., et al. 2007. Current Status of Commercial In-Situ Combustion Projects Worldwide. *J Can Pet Technol* **46** (11): 1–7. PETSOC-07-11-GE. <http://dx.doi.org/10.2118/07-11-GE>.

UTCHEM User's Guide. 2013. http://www.cpge.utexas.edu/?q=UTChem_GI.

van Genuchten, M.Th. 1980. A Closed-Form Equation for Predicting Hydraulic Conductivity of Unsaturated Soils. *Soil Sci. Soc. Am. J.* **44**: 892–898.

van Lookeren, J. 1983. Calculation Methods for Linear and Radial Steam Flow in Oil Reserves. *SPE J.* **23** (3): 427–439. SPE-6788-PA. <http://dx.doi.org/10.2118/6788-PA>.

Vikingstad, A.K. and Aarra, M.G. 2009. Comparing the Static and Dynamic Foam Properties of a Fluorinated and an Alpha Olefin Sulfonate Surfactant. *J. Pet. Sci. Eng.* **65** (1–2): 105–111. <http://dx.doi.org/10.1016/j.petrol.2008.12.027>.

Vinot, B., Schechter, R.S., and Lake, L.W. 1989. Formation of Water—Soluble Silicate Gels by the Hydrolysis of a Diester of Dicarboxylic

Acid Solubilized as Microemulsions. *SPE Res Eng* **4** (3): 391–397. SPE-14236-PA. <http://dx.doi.org/10.2118/14236-PA>.

Vogel, J.V. 1984. Simplified Heat Calculations for Steamfloods. *J Pet Technol* **36** (7): 1127–1136. SPE-11219-PA. <http://dx.doi.org/10.2118/11219-PA>.

Vogel, J.L. and Yarborough, L. 1980. The Effect of Nitrogen on the Phase Behavior and Physical Properties of Reservoir Fluids. Presented at the SPE/DOE Enhanced Oil Recovery Symposium, Tulsa, 20–23 April. SPE-8815-MS.

Vukalovich, M.P. and Altunin, V.V. 1968. *Thermodynamic Properties of Carbon Dioxide*. London: Collet's Publishers.

van der Waals, J.D. *On the Continuity of the Gaseous and Liquid States*. 1873. Mineola, New York: Dover Publications, (reprinted 2004).

Waggoner, J.R. and Lake, L.W. 1987. A Detailed Look at Simple Viscous Fingering. Presented at the Second International Symposium on Enhanced Oil Recovery, Maracaibo, Venezuela.

Wagner, O.R. and Leach, R.O. 1959. Improving Oil Displacement by Wettability Adjustment. *Trans., AIME* **216**: 65–72. SPE-1101-G.

Walker, D.L., Britton, C., Kim, D.H., Dufour, S., Weerasooriya, U., and Pope, G.A. 2012. The Impact of Microemulsion Viscosity on Oil Recovery. Presented at the SPE Improved Oil Recovery Symposium, Tulsa, 14–18 April. SPE-154275-MS.

Walsh, M.P. and Lake, L.W. 1989. Applying Fractional Flow Theory to Solvent Flooding and Chase Fluids. *J. Pet. Sci. Eng.* **2** (4): 281–303. [http://dx.doi.org/10.1016/0920-4105\(89\)90005-3](http://dx.doi.org/10.1016/0920-4105(89)90005-3).

Walsh, M.P. and Lake, L.W. 2003. *A Generalized Approach to Primary Hydrocarbon Recovery*. Amsterdam, The Netherlands:

Elsevier B.V.

Walsh, M.P., Rouse, B.A., Senol, N., et al. 1983. Chemical Interactions of Aluminum-Citrate Solutions With Formation Minerals. Presented at the SPE Oilfield and Geothermal Chemistry Symposium, Denver, 1–3 June. SPE-11799-MS.
<http://dx.doi.org/10.2118/11799-MS>.

Watson, K.M., Nelson, E.F., and Murphy, G.B. 1935. Characterization of Petroleum Fractions. *Ind. and Eng. Chem.* **27**: 1460–1464.

Weaver, C.E. and Pollard, L.D. 1973. *The Chemistry of Clay Minerals*. New York: Elsevier.

Welch, B. 1982. A Numerical Investigation of the Effects of Various Parameters in CO₂ Flooding. MS thesis, The University of Texas, Austin, Texas (1982).

Welge, H.J. 1952. A Simplified Method for Computing Oil Recovery by Gas or Water Drive. *Trans., AIME* **195**: 91–98. SPE-124-G.

Wellington, S.L. 1983. Biopolymer Solution Viscosity Stabilization—Polymer Degradation and Antioxidant Use. *SPE J.* **23** (6): 901–912. SPE-9296-PA. <http://dx.doi.org/10.2118/9296-PA>.

White, P.D. and Moss, J.T. 1983. *Thermal Recovery Methods*. Tulsa, Oklahoma: PennWell Publishing Co.

Whitehead, W.R., Kimbler, O.K., Holden, W.R., and Bourgoyne, A.T. 1981. Investigations of Enhanced Oil Recovery Through Use of Carbon Dioxide. Final Report, DOE/MC/031036, US Department of Energy, Washington, DC.

Whitson, C.H. 1984. Effect of C7+ Properties Estimation on Equation-of-State Predictions. *SPE J.* **24** (6): 685–696. SPE-11200-PA. <http://dx.doi.org/10.2118/11200-PA>.

Whitson, C.H. and Brulé, M.R. 2000. *Phase Behavior*. Richardson, Texas: Monograph Series, SPE.

Willhite, G.P. 1967. Over-All Heat Transfer Coefficients in Steam and Hot Water Injection Wells. *J Pet Technol* **19** (5): 607–615. SPE-1449-PA. <http://dx.doi.org/10.2118/1449-PA>.

Williams, C.A., Zana, E.N., and Humphreys, G. 1980. Use of the Peng-Robinson Equation of State to Predict Hydrocarbon Phase Behavior and Miscibility for Fluid Displacement. Presented at the SPE/DOE Enhanced Oil Recovery Symposium, Tulsa, 20–23 April. SPE-8817-MS. <http://dx.doi.org/10.2118/8817-MS>.

Winsor, P.A. 1954. *Solvent Properties of Amphiphilic Compounds*. London: Butterworth's Scientific Publications.

Yang, H., Britton, C., Liyanage, P.J., Solairaj, S., Kim, D.H., Nguyen, Q.P., Weerasooriya, U., and Pope, G.A. 2010. Low-Cost, High-Performance Chemicals for Enhanced Oil Recovery. Presented at the SPE Improved Oil Recovery Symposium held in Tulsa, 24–28 April. SPE-129978-MS.

Yarborough, L. 1979. Application of a Generalized Equation of State to Petroleum Reservoir Fluids. In *Equations of State in Engineering and Research*, 182, 21, 385–439. Advances in Chemistry, American Chemical Society. <http://dx.doi.org/10.1021/ba-1979-0182.ch021>.

Yarborough, L. and Smith, L.R. 1970. Solvent and Driving Gas Compositions for Miscible Slug Displacement. *SPE J.* **10** (3): 298–310. SPE-2543-PA. <http://dx.doi.org/10.2118/2543-PA>.

Yellig, W.F. and Metcalfe, R.S. 1980. Determination and Prediction of CO₂ Minimum Miscibility Pressures. *J Pet Technol* **32** (1): 160–168. SPE-7477-PA. <http://dx.doi.org/10.2118/7477-PA>.

Yokoyama, Y. 1981. *The Effects of Capillary Pressure on Displacements in Stratified Porous Media*. MS thesis, The University

of Texas, Austin, Texas (1981).

Yokoyama, Y. and Lake, L.W. 1981. The Effect of Capillary Pressure on Immiscible Displacements in Stratified Porous Media. Presented at the SPE Annual Technical Conference and Exhibition, San Antonio, Texas, USA, 4-7 October. SPE-10109-MS.
<http://dx.doi.org/10.2118/10109-MS>.

Yortsos, Y.C. 1995. A Theoretical Analysis of Vertical Flow Equilibrium. *Transport in Porous Media* **18** (2): 107–129.
<http://dx.doi.org/10.1007/bf01064674>.

Young, L.C. and Stephenson, R.E. 1983. A Generalized Compositional Approach for Reservoir Simulation. *SPE J.* **23** (4): 727–742. SPE-10516-PA. <http://dx.doi.org/10.2118/10516-PA>.

Young, L.C. 1990. Use of Dispersion Relationships to Model Adverse-Mobility-Ratio Miscible Displacements. *SPE Res Eng* **5** (3): 309–316. SPE-14899-PA. <http://dx.doi.org/10.2118/14899-PA>.

Yousef, A., Gentil, P., Jensen, J.L., and Lake, L.W. 2006. A Capacitance Model to Infer Interwell Connectivity From Production- and Injection-Rate Rate Fluctuations. *SPE Res Eval & Eng* **9** (6): 630–645. SPE-95322-PA. <http://dx.doi.org/10.2118/95322-PA>.

Yuan, H.H. and Swanson, B.F. 1989. Resolving Pore-Space Characteristics by Rate-Controlled Porosimetry. *SPE Form Eval* **4** (1): 17–24. SPE-14892-PA. <http://dx.doi.org/10.2118/14892-PA>.

Yuan, H. and Johns, R.T. 2005. Simplified Method for Calculation of Minimum Miscibility Pressure or Enrichment. *SPE J.* **10** (4): 416–425. SPE-77381-PA. <http://dx.doi.org/10.2118/77381-PA>.

Zapata, V.J. and Lake, L.W. 1981. A Theoretical Analysis of Viscous Crossflow. Presented at the SPE Annual Technical Conference and Exhibition, San Antonio, Texas, USA, 5–7 October. SPE-10111-MS.
<http://dx.doi.org/10.2118/10111-MS>.

Zhou, D. and Blunt, M.J. 1997. Effect of Spreading Coefficient on the Distribution of Light Nonaqueous Phase Liquid (NAPL) in the Subsurface. *J. Contam. Hydrol.* **25** (1–2): 1–19.
[http://dx.doi.org/10.1016/S0169-7722\(96\)00025-3](http://dx.doi.org/10.1016/S0169-7722(96)00025-3).

Zhou, Z.H. and Rossen, W.R. 1995. Applying Fractional-Flow Theory to Foam Processes at the “Limiting Capillary Pressure.” *SPE Advanced Technology Series* **3** (1): 154–162. SPE-24180-PA.
<http://dx.doi.org/10.2118/24180-PA>.

Zudkevitch, D. and Joffe, J. 1970. Correlation and Prediction of Vapor-Liquid Equilibria With the Redlich-Kwong Equation of State. *AIChE J.* **16** (1): 112–199. <http://dx.doi.org/10.1002/aic.690160122>.

AUTHOR INDEX

A

- Aaron, D., [224](#)
Aarra, M.G., [355](#), [362](#)
Abbott, M.M., [123](#)
Ader, J.C., [276](#)
Adkins, S., [318](#)
Ahmad, T., [234](#), [240](#)
Ahmadi, K., [240](#)–[243](#), [250](#)
Ahn, C.H., [292](#)
Aithison, J., [185](#)
Akstinat, M.H., [317](#)
Alpak, F.O., [78](#)
Al-Rikabi, H.M., [171](#), [304](#)
Altunin, V.V., [226](#)
Alvarez, J.M., [359](#), [360](#), [364](#)
Amott, E., [69](#)
Anderson, G., [88](#)
Anderson, T.F., [123](#)
Anderson, W.G., [69](#)
Andrade, E.N., [384](#)
Andrianovkrastev, A.R., [355](#), [362](#)
Araktingi, U.G., [218](#)
Araque-Martinez, A.N., [21](#), [27](#), [31](#), [40](#), [41](#), [97](#), [163](#), [280](#), [339](#), [393](#)
Archer, D.L., [71](#), [338](#)
Arps, J.J., [6](#)
Arya, A., [159](#)
Ashoori, E., [371](#)
Attanasi, E.D., [375](#), [384](#)
Aydelotte, S.R., [391](#)
Aziz, K., [91](#), [120](#)

B

- Bail, P.T., [147](#)
Balhoff, M.T., [292](#)
Banfield, J., [324](#), [325](#)
Bear, J., [19](#)–[21](#), [27](#), [29](#), [57](#), [69](#), [159](#), [160](#)
Belveal, L.A., [94](#)
Benham, A.L., [234](#), [250](#), [251](#), [253](#)
Bennett, K.W., [322](#)
Benson, S.M., [373](#)

- Bhattacharya, R.N., [422](#)
Bhuyan, D., [339](#)
Bijeljic, B.R., [270](#)
Bikerman, J.J., [356](#)
Billingsley, R.H., [416](#), [417](#)
Bird, R.B., [26](#), [27](#), [46](#), [55–57](#), [157](#), [287](#), [376](#), [396](#), [397](#)
Bisdom, K., [219](#)
Blair, P.M., [147](#)
Bleakley, W.B., [380](#), [381](#)
Blevins, T.R., [416](#), [417](#)
Blunt, M.J., [89](#), [270](#)
Boberg, T.C., [375](#), [391](#), [393](#)
Bommer, P.M., [292](#)
Bondor, P.L., [310](#), [312](#)
Bonfantir, B.F., [424](#)
Bourgoyne, A.T., [252](#), [265](#)
Bourrel, M., [325](#), [326](#)
Bowman, R.W., [311](#)
Bragg, J.R., [318](#), [348](#)
Brandner, C.F., [82](#), [88](#)
Braun, P.H., [235](#)
Britton, C., [317](#), [318](#), [332](#), [338](#)
Brown, J.A.C., [185](#)
Brown, W.O., [153](#)
Brownrigg, W., [89](#)
Bruggenwert, M.G.M., [97](#)
Brulé, M.R., [105](#), [107](#), [120](#), [124](#)
Bryant, S.L., [21](#), [27](#), [31](#), [40](#), [41](#), [59](#), [68](#), [97](#), [160–163](#), [280](#), [339](#), [393](#)
Buckley, S.E., [39](#), [131](#)
Bunge, A.L., [341](#), [342](#)
Burger, J., [375](#), [414](#)
Burger, J.G., [422](#)
Bursell, C.G., [412](#)
Butler, R., [378](#)
Butler, R.M., [375](#), [384](#), [424](#)

C

- Cade, C.A., [59](#)
Calhoun, J.C., [72](#)
Callarotti, R., [379](#)
Camilleri, D., [86](#)
Campbell, R.A., [13](#), [14](#)
Cannella, W.J., [288](#)
Carcoana, A.N., [423](#)
Carrizales, M.A., [379](#)
Carslaw, H.W., [406](#)
Cash, R.C., [324](#)
Caudle, B.H., [166](#), [181](#), [182](#), [259](#)

Cayias, J.L., [324](#), [326](#)
Celik, M., [341](#)
Chan, A.F., [281](#)
Chang, H.L., [171](#), [304](#)
Charbeneau, R.J., [42](#)
Chase, C.A., [19](#)
Chattopadhyay, S.K., [422](#)
Chatzis, I., [68](#), [69](#), [80](#), [82](#), [83](#), [102](#)
Chen, C., [218](#), [369](#)
Chen, J., [88](#)
Chen, Q., [363](#)
Cheng, L., [360](#), [363](#), [364](#), [369](#)
Chilingarian, G.V., [93](#)
Chouke, R.L., [216](#)
Chrlichlow, H., [234](#), [240](#)
Christ, C.L., [99](#)
Christensen, P.L., [105](#), [125](#)
Clampitt, R.L., [305](#)
Claridge, E.L., [182](#), [268](#), [304](#)
Coats, K.H., [19](#), [202](#), [420](#)
Collins, R.E., [29](#), [55](#), [69](#), [132](#), [212](#)
Coma, J.M., [224](#)
Combarous, M., [375](#), [414](#)
Conley, F.R., [347](#)
Cooke, C.E., [339](#)
Courant, R., [138](#), [162](#)
Craig, F.F. Jr., [77](#), [132](#), [182](#)
Crane, F.E., [203](#), [204](#)
Crawford, H.R., [246](#)
Crawford, P.B., [246](#)
Crichlow, H.B., [19](#)
Crocker, M.W., [70](#), [91](#), [92](#), [95](#), [96](#)
Cronquist, C., [4](#), [5](#)
Csaszar, A.K., [234](#)
Culberson, O.L., [247](#)
Currie, P.K., [369](#)

D

Da, C., [384](#)
Dake, L.P., [29](#), [132](#), [199](#)
Dalen, V., [120](#)
Danesh, A., [105](#), [124](#)
Daniel, D., [247](#)
Davis, H.T., [68](#), [322](#)
de Jong, L.N.J., [231](#)
de Nevers, N., [245](#), [247](#), [277](#)
de Riz, L., [218](#)
de Zabala, E.F., [336](#)

Deans, H.A., [159](#)
Degens, E.T., [93](#)
Delshad, M., [83](#), [155](#), [174](#), [274](#), [292](#), [303](#), [306](#), [332–334](#)
Demin, W., [306](#)
Dempsey, J.R., [19](#), [202](#)
Denbigh, K., [110](#), [120](#)
Dicharry, R.M., [259](#)
Dickson, J.L., [12](#)
Dietz, D.N., [203](#)
Dindoruk B., [39](#), [249](#)
Donaldson, E.C., [69](#), [70](#), [91](#), [92](#), [95](#), [96](#), [339](#)
Donaruma, G.L., [287](#)
Dong, Y., [359](#), [361](#), [364](#), [365](#), [374](#)
Dougherty, E.L., [266](#)
Douglas, J. Jr., [147](#)
Dowden, W.E., [234](#), [250](#), [251](#), [253](#)
Dria, M.A., [99](#)
Duda, J.L., [289](#)
Dufour, S., [332](#)
Dullien, F.A.L., [59](#), [99](#)
Dyes, A.B., [181](#), [182](#), [259](#)
Dykstra, H., [30](#), [184](#)

E

Eakin, B.E., [228](#)
Earlougher, R.C. Jr., [50](#)
Eckerf, C.A., [123](#)
Egwuenu, A.M., [249](#)
Ehrlich, R., [86](#), [339](#)
El-M Shokir, E.M., [250](#)
Embid-Droz, S.M., [60](#), [65](#), [72](#), [78](#)
Emde, F., [157](#)
Engleson, S.R., [331](#), [353](#)
Enick, R.M., [232](#)
Erickson, R.A., [181](#), [182](#)
Ershaghi, I., [172](#)

F

Faghri, A., [20](#)
Faisal, A., [219](#)
Falls, A.H., [358](#), [359](#)
Fan, S.K., [289](#)
Farajzadeh, R., [247](#), [355](#), [362](#)
Farish, Mr., [89](#)
Farouq Ali, S.M., [376](#), [383](#), [386](#), [404](#), [406](#)
Fatt, I., [30](#)
Fayers, F.J., [266](#)
Fenwick, D.H., [89](#)

Fernandez, M.E., [340](#)
Fetkovich, M.J., [6](#)
Firoozabadi, A., [105](#), [107](#), [124](#), [125](#)
Flaaten, A.K., [12](#)
Flaun, M., [88](#)
Fleming, P.D. III., [19](#)
Flory, P.J., [284](#), [285](#)
Flumerfelt, R.W., [88](#)
Fogler, H.S., [94](#)
Fortenberry, R.P., [338](#)
Foshee, W.C., [291](#)
Foster, W.R., [86](#)
Fotland, P., [325](#)
Fotrney, L.N., [324](#), [326](#)
Fournier, R.G., [324](#)
Fox, C., [273](#)
Francis, A.W., [105](#), [120](#)
Franklin, B., [89](#)
Friedmann, F., [359](#)
Friedrichs, K.O., [138](#), [162](#)
Froning, H.R., [349](#)

G

Gale, W.W., [318](#), [348](#)
Gall, J.W., [279](#)
Gambill, W.R., [385](#)
Gardner, G.H.F., [203](#), [204](#)
Gardner, J.W., [216](#), [229](#), [233](#), [248](#), [267](#), [268](#), [271](#), [272](#)
Garrels, R.M., [99](#)
Gash, B.H., [281](#)
Gates, I.G., [375](#)
Gauglitz, P.A., [359](#)
Gdanski, R.D., [355](#)
Geffen, T.M., [266](#)
Gentil, P., [184](#)
Gerritsen, M.G., [363](#)
Ghanbarnezhad, R., [265](#), [272](#)
Gibbs, C.W. ed., [226](#)
Gibbs, J.W., [105](#), [106](#)
Gilliland, H.E., [347](#)
Giordano, R.M., [344](#)
Glinsmann, G.R., [326](#), [327](#), [330](#)
Glover, C.J., [325](#), [343](#)
Gogarty, W.B., [304](#), [351](#)
Goldburg, A., [343](#)
Gonzalez, I.E., [424](#)
Gonzalez, M.H., [228](#)
Goodrich, J.H., [224](#), [228](#)

- Goyal, A., [341](#)
Graciaa, A., [324](#), [326](#)
Graue, D.J., [242](#)–[245](#)
Gray, W.G., [20](#), [27](#)
Grens, E.A., [123](#)
Griffith, T.D., [281](#)
Grim, R.E., [93](#), [95](#)
Gupta, S.P., [86](#), [346](#)
Gutierrez, D., [422](#)
Guzmán Ayala, R.E., [39](#)

H

- Habermann, B., [212](#)
Hall, H.N., [266](#)
Hand, D.B., [126](#)
Harvey, H.A., [76](#)
Hasiba, H.H., [86](#), [339](#)
Hatch, M.J., [287](#)
Hawthorne, R.G., [203](#)
Hazlett, R.D., [363](#)
Healy, R.N., [320](#), [325](#), [326](#), [328](#), [329](#)
Heidemann, R.A., [120](#)
Heinson, C., [318](#)
Helfferich, F.G., [151](#), [163](#)–[165](#)
Heller, J.P., [270](#)
Henderson, J.H., [19](#), [202](#)
Hendriks, E.M., [124](#)
Hewett, T.A., [159](#)
Hill, H. J., [103](#)
Hill, P.G., [382](#)
Hill, S., [214](#)
Himmelblau, D.M., [111](#)
Hinkley, D.V., [184](#)
Hirasaki, G., [88](#)
Hirasaki, G.J., [151](#), [198](#), [288](#), [292](#), [310](#), [312](#), [349](#), [355](#), [359](#), [362](#), [371](#)
Hirshberg, A., [231](#)
Hlavacek, B., [234](#)
Holden, W.R., [252](#), [265](#)
Holm, L.W., [234](#), [245](#), [249](#)–[251](#), [274](#)
Homsy, G.M., [217](#)
Honarpour, M., [76](#)
Hong, K.C., [45](#), [231](#)
Hougen, O.A., [119](#)
Hsieh, R., [123](#)
Hubbert, M.K., [29](#)
Huh, C., [279](#), [288](#), [292](#), [320](#), [326](#), [327](#)
Humphreys, G., [249](#)
Hutchinson, C.A. Jr., [235](#)

I

Ilie, N., [422](#)

J

Jackson, A.C., [318](#)
Jackson, R.E., [355](#)
Jadhunandan, P.P., [88](#)
Jaeger, J.C., [406](#)
Jahnke, E., [157](#)
Jain, L., [197](#), [198](#), [202](#)
Jamshidnezhad, M., [218](#), [369](#)
Jarrell, P., [273](#)
Jeffrey, A., [162](#)
Jenkins, M.K., [217](#)
Jennings, H.Y. Jr., [337](#)
Jennings, J.W., [161](#), [162](#)
Jennings, R.R., [289](#), [291](#), [292](#)
Jensen, C.M., [229](#), [234](#)
Jensen, J.L., [184](#), [185](#)
Jerauld, G.R., [169](#)–[171](#)
Jessen, K., [249](#)
Jha, R.K., [160](#), [161](#)
Jiecheng, C., [306](#)
Jimenez, J., [424](#), [425](#)
Jin, M., [355](#)
Joffe, J., [123](#)
Joh, R.T., [241](#)
Johansen, T., [162](#)
John, A.K., [160](#)–[162](#)
Johns, R.T., [39](#), [105](#), [120](#), [124](#), [126](#), [138](#), [160](#), [230](#), [240](#)–[243](#), [249](#), [250](#), [301](#), [325](#)
Johnson, C.E. Jr., [337](#)
Johnson, J.P., [250](#), [252](#)
Jones, K., [333](#)
Jones, S.C., [75](#), [350](#)
Josendal, V.A., [245](#), [249](#)–[251](#), [274](#)
Jouenne, S., [298](#)

K

Kam, S.I., [359](#), [363](#), [371](#)
Kamath, J., [85](#), [87](#)
Kamath, S.K., [234](#)
Kamphorst, A., [97](#)
Karanikas, J.M., [378](#), [379](#)
Karpyn, Z.T., [68](#)
Kaufman, H., [406](#)
Keenan, J.H., [382](#)
Kendall, H.A., [203](#), [204](#)
Keys, F.G., [382](#)

- Khan, S.A., [358](#)
Khatib, Z.I., [359](#)
Khilar, K.C., [94](#)
Killins, C.R., [72](#)
Kim, D.H., [292](#), [317](#), [332](#), [338](#)
Kim, J.S., [359](#), [361](#), [364](#), [365](#)
Kimbler, O.K., [252](#), [265](#)
Kjosavid, A., [69](#)
Klaus, E.E., [289](#)
Klein, G., [151](#), [163–165](#)
Kloet, M.B., [369](#), [371](#)
Koch, H.A. Jr., [257](#)
Koederitz, L.F., [76](#)
Kolodzie, P.A., [339](#)
Kool, P., [218](#), [369](#)
Koval, E.J., [186](#), [266](#)
Kovscek, A.R., [363](#)
Krueger, D.A., [413](#)
Kumar, V.K., [422](#)
Kuntamukkala, M.S., [270](#)
Kunzman, W.J., [234](#), [250](#), [251](#), [253](#)
Kyte, J.R., [147](#), [149](#)

L

- Lacey, W.N., [105](#)
LaForce, T.C., [39](#), [371](#)
LaHerrere, J., [4](#)
Lake, L.W., [3](#), [6](#), [21](#), [27](#), [31](#), [40](#), [41](#), [50](#), [59](#), [78](#), [94](#), [97](#), [99](#), [103](#), [159–163](#), [184–186](#), [198](#),
[202](#), [209](#), [211](#), [258](#), [260](#), [262](#), [264](#), [265](#), [268](#), [270](#), [272](#), [280](#), [284](#), [292](#), [305](#), [306](#), [332–334](#),
[339](#), [347](#), [349](#), [393](#)
Lambert, M.E., [187](#)
Langenberg, M., [324](#), [325](#)
Langenheim, R.H., [404](#)
Larry, W., [160](#)
Larson, R.G., [19](#), [87](#), [88](#), [159](#)
Laumbach, D.D., [45](#)
Lawson, J.B., [324](#), [337](#)
Lax, P.D., [138](#)
Leach, R.O., [70](#), [339](#)
Leahy-Dios, A., [12](#)
Leas, W.J., [145](#), [146](#)
Lee, A., [228](#)
Lee, S., [292](#)
Lenhard, R.J., [77](#)
Levenspiel, O., [27](#)
Leverett, M.C., [39](#), [69](#), [89](#), [131](#)
Levitt, D., [283](#), [288](#), [348](#)
Levitt, D.B., [298](#), [318](#)

- Lewis, W.K., [384](#)
Li, D., [211](#)
Li, R.F., [355](#), [371](#)
Li, Y., [126](#), [249](#)
Lien, C.L., [270](#)
Lightfoot, E.N., [26](#), [27](#), [46](#), [55–57](#), [157](#), [376](#), [396](#), [397](#)
Lim, H.T., [80](#), [82](#), [83](#)
Lin, C.Y., [169](#), [171](#)
Lipow, A.M., [325](#), [326](#)
Liu, S., [355](#), [371](#)
Liyanage, P.J., [318](#), [338](#)
Longstaff, W.J., [45](#), [266](#), [278](#)
Lorenz, P.B., [69](#), [339](#)
Lu, J., [317](#), [318](#)
Lu, Q., [362](#), [373](#)
Lucy, B.J., [246](#)

M

- Mack, J.C., [16](#)
Maerker, J.M., [299](#), [325](#), [343](#)
Magbagbeola, O.A., [292](#)
Mahadevan, J., [160](#)
Mandl, G., [409](#)
Mangone, D.J., [232](#)
Manning, R.K., [284](#), [305](#), [306](#)
Marchin, L.M., [70](#), [91](#), [92](#), [95](#), [96](#)
Marle, C.M., [158](#)
Marsden, S.S., [147](#)
Martin, F.D., [287](#)
Martin, J.C., [177](#)
Martin, J.W., [224](#)
Marx, J.W., [404](#)
Maxwell, J.B., [385](#)
McAuliffe, C.E., [337](#), [339](#)
McCain, W.D. Jr., [105](#), [113](#), [122](#), [227](#)
McElhannon, W.A., [318](#), [348](#)
McKetta, J.J., [247](#)
McMillan, J.M., [86](#)
McRee, B.C., [245](#)
Meabon, H.P., [304](#), [351](#)
Mehra, R.K., [120](#)
Mehta, S.A., [422](#)
Meinster, G.P., [245](#), [247](#)
Meldau, R.F., [420](#)
Mellor, D.W., [59](#)
Melrose, J.C., [65](#), [82](#), [88](#)
Menzie, D., [234](#), [240](#)
Metcalfe, R.S., [229](#), [231](#), [234](#), [239](#), [249](#), [252](#)

Meter, D.M., [287](#)
Meulenbroek, B., [247](#)
Meyer, R.F., [85](#), [87](#), [375](#), [384](#)
Meyer, W.K., [234](#)
Meyers, J.G., [231](#)
Michelsen, M.L., [124](#)
Miller, C.A., [355](#), [359](#), [371](#)
Milton, H.W. Jr., [304](#), [351](#)
Minssieux, L., [337](#)
Mogensen, K., [241](#)
Mohanty, K., [87](#)
Mohanty, K.K., [68](#)
Mohebbinia, S., [120](#), [124](#), [230](#)
Mojaddam Zadeh, A., [219](#)
Molleai, A., [274](#), [303](#), [306](#)
Monger, T.G., [224](#), [250](#)
Moore, J.G., [382](#)
Moore, R.G., [422](#)
Moore, T.F., [78](#)
Morel-Seytoux, H.J., [181](#)
Morrow, N.R., [68](#), [69](#), [71](#), [80](#), [82](#), [83](#), [88](#), [102](#)
Moss, J.T., [375](#)
Muggeridge, A.H., [218](#), [270](#)
Muller, T., [270](#)
Murphy, G.B., [243](#)
Musters, J.J., [358](#)
Myhill, N.A., [407](#), [409](#), [411](#)

N

Najman, J., [234](#)
Nakagawa, F.M., [85](#), [87](#)
Namdar-Zanganeh, M., [371](#)
Neasham, J.W., [94](#), [95](#)
Needham, R.B., [279](#)
Neill, G.H., [246](#)
Nelson, E.F., [243](#)
Nelson, R.C., [31](#), [126](#), [284](#), [320](#), [324](#), [326](#), [337](#), [349](#), [350](#)
Ng, K.M., [88](#)
Nguyen, Q.P., [217–219](#), [338](#), [369](#)
Nielsen, R.F., [72](#)
Nizamidin, N., [338](#)
Noman, R., [241](#)

O

O'Connell, J.P., [123](#), [227](#)
Oh, S.G., [82](#), [88](#)
Okuno, R., [120](#), [124](#)
Omoregei, O., [172](#)

Orr, F.M. Jr., [39](#), [105](#), [120](#), [121](#), [218](#), [229](#), [233](#), [234](#), [241](#), [242](#), [247–249](#), [271](#)
Owens, W.W., [71](#), [301](#), [338](#)
Owolabi, O.O., [88](#)

P

Pan, H., [124](#)
Panait-Patica, A., [422](#)
Panda, M.N., [59](#), [94](#)
Panteleev, V.G., [245](#), [247](#)
Parker, J.C., [77](#)
Parkinson, W.J., [245](#), [247](#)
Parra Sanchez, C., [3](#)
Parsons, R.L., [184](#)
Patel, P.D., [229](#), [233](#), [248](#), [271](#)
Patzek, T.W., [362](#), [363](#)
Paul, G.W., [185](#), [186](#), [343](#), [349](#)
Payatakes, A.C., [88](#)
Peaceman, D.W., [19](#), [43](#)
Pedersen, K.S., [105](#), [125](#)
Peng, D-Y., [120](#), [121](#), [123](#)
Perry, G.E., [230](#), [249](#)
Perrymann, T.L., [259](#)
Persoff, P., [373](#)
Peters, E., [55](#), [69](#)
Peters, E.J., [216](#)
Phelps, C.H.K., [322](#)
Phillips, J.R., [43](#)
Pinnawala Arachchilage, G.W.P., [318](#)
Pino Villavicencio, A., [372](#)
Pirson, S.J., [159](#)
Pittman, G.M., [412](#)
Poling, B.E., [227](#)
Pollack, N.R., [232](#)
Pollard, L.D., [93](#)
Pollin, J.S., [250](#), [252](#)
Pope, G., [298](#)
Pope, G.A., [31](#), [39](#), [83](#), [126](#), [185](#), [186](#), [279](#), [283](#), [284](#), [288](#), [292](#), [298](#), [305](#), [306](#), [311](#), [317](#),
[318](#), [320](#), [325](#), [332–334](#), [338](#), [347–349](#), [391](#)
Prats, M., [375](#), [377](#), [408](#), [421](#)
Prausnitz, J.M., [123](#), [227](#)
Price, H., [343](#)
Prodanovic, M., [68](#)
Prouvost, L., [325](#)
Pruess, K., [373](#)
Puerto, M.C., [324](#), [325](#), [343](#)
Pusch, W.H., [171](#), [304](#)

Q

Quintard, M., [20](#)

R

- Radke, C.J., [336](#), [341](#), [342](#), [363](#), [373](#)
Ragatz, R.A., [119](#)
Raimondi, P., [31](#), [86](#), [270](#), [339](#)
Ramakrishnan, T.S., [336](#), [338](#)
Ramey, H.J. Jr., [398](#)–[400](#), [403](#), [411](#)
Ramilal, V., [418](#)
Rapoport, L.A., [145](#)–[147](#), [149](#)
Ratulowski, J., [358](#)
Reed, R.L., [234](#), [320](#), [324](#)–[326](#), [328](#), [329](#)
Reid, T.B., [305](#)
Reme, A.B., [363](#), [364](#)
Renkema, W.J., [369](#), [371](#)
Renner, T.A., [250](#)
Richards, L.A., [42](#)
Rieke, H.H., [93](#)
Risnes, R., [120](#)
Rivas, H., [359](#), [360](#), [364](#)
Roberts, G.E., [406](#)
Robinson, D.B., [120](#), [121](#), [123](#)
Rodriguez Prada, H., [372](#)
Rogers, J.H., [289](#), [292](#)
Ronquille, J.D., [259](#)
Rose, P.R., [5](#)
Roshanfekr, M., [126](#), [325](#)
Rossen, W.R., [217](#)–[219](#), [301](#), [355](#), [359](#)–[371](#), [373](#), [374](#)
Roszelle, W.O., [75](#)
Rouse, B., [325](#)
Rouse, B.A., [294](#)
Rowe, A.M., [234](#)
Rubin, E., [336](#)

S

- Sage, B.H., [105](#)
Sahni, I., [324](#), [325](#)
Sahuquer, B.C., [422](#)
Salter, S.J., [87](#), [325](#), [344](#)
Samizo, N., [150](#)
Sanchez, J.M., [363](#)
Sandler, S.I., [26](#), [36](#)
Sandvik, E.I., [325](#), [343](#)
Sanz, C.A., [318](#)
Satter, A., [401](#), [402](#), [404](#)
Sazegh, S.G., [234](#)
Schechter, R.S., [99](#), [294](#), [324](#), [326](#), [393](#)
Schipper, B.A., [231](#)

- Schneider, F.N., [270](#), [301](#)
Schneider, G.M., [109](#)
Schramm, L.L. ed., [355](#), [362](#)
Scriven, L.E., [68](#), [325](#)
Sebastian, H.M., [250](#)
Seccombe, J.C., [169](#), [171](#)
Senol, N., [294](#)
Sepehrnoori, K., [83](#), [120](#), [124](#), [230](#)
Serbgan, D., [422](#)
Seright, R.S., [288](#), [291](#), [299](#)
Settari, A., [91](#)
Shan, D., [363](#), [364](#), [367](#), [368](#), [370](#)
Shelton, J.L., [270](#)
Sheng, J., [279](#)
Shi, J.-X., [363](#)
Shipley, R.G., [420](#)
Shook, M., [211](#)
Shupe, R.D., [282](#)
Shutler, N.D., [391](#), [393](#)
Silva, M.K., [234](#), [241](#), [247](#)
Simlote, V.M., [94](#)
Simon, R., [242–245](#)
Siqveland, L.M., [69](#)
Skauge, A., [325](#)
Skjaeveland, S.M., [19](#), [69](#)
Skoreyko, F.F., [372](#)
Slattery, J., [82](#), [88](#)
Slattery, J.C., [23](#), [29](#), [35](#)
Slaughter, W., [298](#)
Slobod, R.L., [78](#), [257](#)
Smith, J.M., [120](#)
Soave, G., [121](#), [123](#)
Solairaj, S., [317](#), [318](#), [338](#)
Somasundaran, P., [341](#)
Somerton, W.H., [385](#)
Sorbie, K.S., [279](#), [298](#)
Sourieau, P., [375](#), [414](#)
Spence, A.P. Jr., [270](#)
Squires, L., [384](#)
Stalkup, F., [223](#), [236](#), [237](#), [258](#), [270](#)
Standing, M.B., [105](#)
Stegemeier, G.L., [45](#), [58](#), [66–68](#), [88](#), [407](#), [409](#), [411](#)
Stein, M., [273](#), [276](#)
Stenmark, D.G., [320](#), [329](#)
Stephenson, R.E., [126](#)
Stern, D., [324](#), [325](#)
Stewart, W.E., [26](#), [27](#), [46](#), [55–57](#), [157](#), [376](#), [396](#), [397](#)
Stolwijk, G.H., [218](#)

Stone, H.L., [175](#), [217](#), [219](#), [335](#)
Swanson, B.F., [66](#)
Sydansk, R.D., [341](#)

T

Taber, J.J., [86](#), [105](#), [120](#), [234](#)
Taniuti, T., [162](#)
Tanzil, D., [359](#)
Taylor, G.I., [159](#)
Tham, M.J., [310](#), [312](#)
Thigpen, D.R., [324](#), [337](#)
Thomas, C.P., [19](#)
Thomas, R.D., [69](#), [339](#)
Thomeer, J.H.M., [69](#)
Threlkeld, C.B., [279](#)
Tinker, G.E., [311](#)
Todd, M.R., [19](#), [45](#), [266](#), [278](#)
Toledo, P., [68](#)
Torcaso, M.A., [31](#), [270](#)
Treiber, L.E., [71](#)
Trushenski, S.P., [86](#), [325](#)
Tsaur, K., [285](#), [286](#), [349](#)
Tsuris, C., [224](#)
Tumasyan, A.B., [245](#), [247](#)
Turek, E.A., [229](#), [231](#)
Turta, A.T., [422](#)

V

van Bergen, A.R.D., [124](#)
van der Heijden, T.L.M., [371](#)
van der Poel, C., [216](#)
van der Waals, J.D., [120](#), [123](#)
van Domselaar, H.R., [349](#)
van Duijn, C.J., [217–219](#), [369](#)
van Genuchten, M.Th., [77](#)
van Lookeren, J., [415](#)
van Meurs, P., [216](#)
van Ness, H.C., [120](#)
Venkatraman, A., [301](#)
Vikingstad, A.K., [355](#), [362](#)
Vislocky, J.M., [336](#)
Vogel, J.L., [244](#)
Vogel, J.V., [414](#), [415](#)
Volek, C.W., [45](#), [409](#)
Vorabutr, P., [93](#)
Vukalovich, M.P., [226](#)

W

Wade, W.H., [324](#), [326](#)
Wade, W.W., [325](#), [326](#)
Waggoner, J.R., [268](#)
Wagner, O.R., [70](#), [338](#)
Wagner, R.J., [147](#)
Walker, D.L., [332](#)
Walsh, M.P., [3](#), [6](#), [50](#), [162](#), [258](#), [260](#), [262](#), [264](#), [265](#), [294](#)
Wang, B., [349](#)
Warren, J., [16](#)
Wasan, D.T., [336](#), [338](#)
Watkins, R.W., [270](#)
Watson, K.M., [119](#), [243](#)
Watson, R.W., [88](#)
Weaver, C.E., [93](#)
Webb, K.J., [169](#), [171](#)
Weerasooriya, U., [317](#), [332](#), [338](#)
Welch, B., [130](#), [260](#)
Welge, H.J., [131](#), [141](#)
Wellington, S.L., [283](#), [298](#)
West, T.J., [289](#), [291](#), [292](#)
Whitaker, S., [20](#)
White, P.D., [375](#)
Whitehead, W.R., [252](#), [265](#)
Whitson, C.H., [105](#), [107](#), [120](#), [123](#), [124](#)
Willhite, G.P., [394](#), [395](#), [397](#)
Williams, C.A., [249](#)
Williams, R.E., [339](#)
Winger, R.S., [250](#)
Winsor, P.A., [320](#)
Winter, W.K., [19](#)
Witherspoon, P.A., [373](#)

Y

Yan, M., [250](#)
Yan, W., [306](#), [355](#), [371](#)
Yang, H., [338](#)
Yarborough, L., [123](#), [229](#), [231](#), [234](#), [239](#), [244](#)
Yellig, W.F., [249](#)
Yiv, S., [324](#), [326](#)
Yokoyama, Y., [145](#), [202](#)
Yortsos, Y.C., [194](#), [197](#), [198](#), [211](#)
Young, L.C., [126](#), [266](#)
Yousef, A., [184](#)
Ypma, J.G.J., [216](#), [267](#), [268](#), [271](#), [272](#)
Yuan, H., [249](#)
Yuan, H.H., [66](#)

Z

- Zana, E.N., [249](#)
Zapata, V.J., [94](#), [198](#), [209](#)
Zeilinger, S.C., [363](#)
Zhang, Y., [20](#)
Zhou, D., [89](#), [250](#)
Zhou, Z.H., [366](#)
Zhumabek, B., [219](#)
Zitha, P.L.J., [369](#)
Zudkevitch, D., [123](#)

SUBJECT INDEX

A

alkaline-cosolvent-polymer (ACP) flooding, [338](#)
alkaline/surfactant flooding
 high pH levels, [335](#)
 sodium hydroxide, [335](#), [336](#)
 softening seawater, [336](#)
alkaline-surfactant-polymer (ASP) flooding
 cosolvent, [338](#)
 designing
 large volumetric sweep maintenance, [350–351](#)
 optimal conditions generation, [347–349](#)
 surfactant injection, [349–350](#)
 fractional-flow theory, [342–346](#)
 IFT reduction theme, [315](#)
 microemulsion phase behavior, [320](#)
 rock-fluid interactions, [339–342](#)
 and SP flooding, [335](#)
 apparent viscosity, [288](#), [301](#), [304](#), [310](#), [359](#), [361](#)
 aqueous-phase density, [42](#)
 aqueous stability test, [324](#)
 aqueous surfactant solution, oil, [319–320](#)
 areal sweep efficiency
 curves, [143](#)
 mobility ratio, [142](#)
 schematic, [182](#)
 and vertical sweep efficiency, [180](#)
 and volumetric sweep efficiency, [181–182](#)
ASP flooding. See alkaline-surfactant-polymer (ASP) flooding
average saturations, [141–143](#), [167](#), [182](#)

B

Boltzmann's transformation, [157](#)
Buckley-Leverett theory
 constant saturation, specific velocity, [135](#)
 definition, [39](#)
 dimensionless variables, [134](#)
 fractional-flow curves, [135](#)
 fraction of pore volume, [134](#)
 reference volume in dimensionless time, [135](#)
 water-saturation wave, [139](#)

buoyancy forces, [315](#)

C

capillary desaturation curve (CDC)
and capillary numbers, [86](#), [315](#)
estimation, [87–88](#)
pore-size distribution effect, [85](#)
schematic, [83–84](#)
capillary forces
Bond number, [20](#)
bubbles, [357](#)
capillary number, [81](#), [84](#)
pressure changes, homogeneous fluid phase, [20](#)
capillary numbers
capillary desaturation curve, [86](#)
definition, [83–85](#)
local, [81](#), [83](#), [315](#)
relative permeability, [332–335](#)
capillary pressure
definition, [60](#)
fluid-fluid surface energy, [60](#)
Helmholtz free-energy function, [60](#)
IFT, [60](#)
in immiscible displacements
capillary end effect, [147](#), [148](#)
fractional oil recovery, [145–146](#)
oil-and water-phase pressures, [147](#)
phase pressure, [144](#)
Rapoport and Leas number, [145](#)
“stabilized” mixing zones, [147](#)
trapped/residual oil amount determination, [146](#)
water-saturation and pressure profile, [144](#), [145](#)
Welge integration procedure, [147](#)
interface in smooth, uniform tube, [60–61](#)
interfacial curvature ($1/R$), [61](#)
isolated spherical drop, [60](#)
Laplace’s equation, [60](#)
nonuniform walls
drainage process, [65](#)
hysteresis, [65](#)
imbibition, [65](#)
initial-residual (IR) curve, [68](#)
interface entrance, in toroidal pore, [66](#)
mean pore size, [69](#)
nonwetting phase distribution, [66–67](#)
residual nonwetting saturation, [68](#)
residual wetting-phase saturation, [68](#)
scaling, [69](#)

second drainage process, [67](#)
snap-off, [67–68](#)
toroids, [65–66](#)
trapping hysteresis, [68](#)
wettability, [65](#)

uniform walls, pore-size distribution
 bubbling pressure, [62](#)
 curves, [64](#)
 entry/displacement pressure, [62](#)
 nonwetting phase, [61–62](#)
 in tapered channel, [62–64](#)
 tapering cell, [61](#)
wettability, [69–74](#)

carbonate-reservoir rock samples, [85, 87](#)

CDC. See capillary desaturation curve (CDC)

chemical and biological degradation, [298](#)

Chouke's constant, [216](#)

clays
 classification, [93](#)
 crystal structure, [94](#)
 dispersed, [94](#)
 minerals, [93](#)
 natural, [95](#)
 permeability loss/sensitivity, [94–95](#)
 permeability vs. weight percentage, [94](#)
 platelet, [95](#)
 reservoir, [340, 342](#)
 segregated, [94](#)

constant-composition expansion, [113](#)

convection-diffusion (CD) equation, [40, 155](#)

CO₂ solvent flooding
 displacement efficiency, [224](#)
 injection and production, [224, 225](#)

cosolvents
 ACP flooding, [338](#)
 ASP flooding, [338](#)
 description, [324](#)

cosurfactants
 chemical sorption, [340](#)
 cosurfactant-enhanced alkali process, [337](#)
 description, [323–324](#)
 nonionic surfactants, [316](#)
 optimal salinity, [337](#)
 SP slug, [330, 332, 348](#)
 on surfactant retention, [340](#)

critical micelle concentration (CMC), [319, 320, 340](#)

cyclic stimulation/huff-n-puff. See steam soak

D

- 1D chromatographic equations, [40–41](#)
- decline-curve analysis. See incremental oil delay factor, [41](#)
- disjoining pressure, [356–359](#)
- dispersion and slug processes
 - dilution paths, [254, 258](#)
 - superposition
 - influent boundary conditions, [255–256](#)
 - miscible slug displacement, concentration profiles, [256–257](#)
- dispersivity
 - diffusion, [159](#)
 - dispersion coefficients, [159–161](#)
 - displacement efficiency, [159–162](#)
 - echo dispersivities, [160–162](#)
 - gravity tonguing and viscous fingering, [159](#)
 - homogeneous coreflood, [160](#)
 - hydrodynamic dispersion, [159](#)
 - irreversibility, [160](#)
 - laboratory estimation, [174](#)
 - transmission dispersion, [160–162](#)
- displacement efficiency
 - definitions, [131](#)
 - fractional-flow theory, [162–164](#)
 - immiscible (see immiscible displacement)
 - miscible
 - dispersivity, [159–162](#)
 - error-function solution, [155–159](#)
- three-phase flow, application
 - average saturations, [167–168](#)
 - fractional-flow and time/distance diagram, [166–167](#)
 - incompressible gas phase, [164](#)
 - relative permeabilities, [165](#)
 - saturation paths, [165–166](#)
 - specific velocity, constant saturation, [164](#)
- two-phase fractional-flow theory, EOR, [168–171](#)
- displacements, volumetric sweep efficiency
 - multiple parallel layers
 - breakthrough, [191](#)
 - front positions and pressure profile, schematic, [192](#)
 - infinite heterogeneity, [194](#)
 - mobility ratios and Dykstra-Parsons coefficients, [194–196](#)
 - relative-productivity index, [193](#)
 - sweepout, [191](#)
 - single layer
 - capillary pressure, [188](#)
 - deceleration, mobility control processes, [190](#)
 - dimensionless front position, [189](#)

dimensionless time, [189](#), [191](#)
flow rate, [190](#)
injectivity index, [191](#)
mobilities, [188](#)
piston-like displacement, [187–188](#)
dissolution and precipitation reactions, [40](#), [98–99](#)
Dykstra-Parsons coefficients, [184](#), [186](#), [187](#), [194](#), [196](#)

E

echo dispersivities, [160](#), [162](#)
electromagnetic (EM) heating, [10](#)
emulsion
 formation, [339](#)
 macroemulsion, [325](#)
 microemulsion (see microemulsion)
 polymers, [284](#), [304](#)
energy balance
 accumulation term, [48](#)
 conduction term, [49](#)
 energy-flux term, [48](#)
 equations, [32–36](#)
 thermal efficiency, [48](#)
 volumetric heat capacity, [385](#)
enhanced-oil-recovery (EOR)
 categories, [1–2](#)
 definition, [1](#)
 incremental oil, [5–9](#)
 oil-recovery classifications, [1–2](#)
 original oil in place (OOIP), [3](#), [4](#)
 primary recovery, [1](#)
 production phases, [1–3](#)
 remediation, [1](#)
 reserves, [4–5](#)
 secondary recovery, [1](#)
 solvent flooding (see solvent flooding)
 steamdrive (see steamdrives)
 steam soak (see steam soak)
 target, [4](#)
 tertiary recovery, [1](#)
two-phase fractional-flow theory
 agent, [168–169](#)
 displacements in 1D, [169](#)
 low-salinity waterflood, [169–171](#)
 ultimate oil recovery efficiency, [4](#)
entropy-balance
 derivation, [49](#)
 equations
 entropy, [36](#)

entropy flux, [37](#)
equilibrium state, [36](#)
second law of thermodynamics, [37–38](#)
statement, [36–37](#)
total entropy transport, [37](#)
EOR. See enhanced-oil-recovery (EOR)
EOS. See equations of state (EOS)
equations of state (EOS)
attraction and repulsion, intermolecular forces, [121](#)
Boyle's and Charles's laws, [120–121](#)
cubic, [121–123](#)
densities and molar volumes, [120](#)
mixture, [123](#)
molecular forces, [121](#)
Peng-Robinson EOS, [121](#)
pure components, [121–123](#)
Redlich-Kwong EOS, [121](#)
tuning, [125](#)
van der Waals EOS, [120–121](#)

F

first-contact miscible displacements, aqueous phase
boundary and initial conditions, [259–260](#)
chase fluid, [264–265](#)
composition paths, velocities, [260–262](#)
fractional-flow curves, oil/water, [259](#)
optimum WAG ratio, [263–264](#)
residual saturation, [265](#)
velocities, [260](#)
Walsh diagram, [262–263](#)
flash calculation. See also two-phase equilibria
closed vapor-liquid system, phase-behavior, [123–124](#)
compositional variations, [125](#)
computer-based software packages, [124–125](#)
EOS characterization, [125](#)
mole fractions, [123–124](#)
phase-behavior data, [125](#)
phase mole fractions, [123–124](#)
pseudocomponents, [125](#)
fluid compressibility, [148–149](#)
fluid flow in permeable media
1D chromatographic equations, [40–41](#)
energy-balance equations
arbitrary volume, [32](#)
auxiliary relations, [35–36](#)
closed system, [35](#)
energy-flux, [33](#)
external heating sources, [33](#)

nonisothermal fluid flow, [34](#)
scalar total thermal conductivity, [33](#)
total energy, [32](#)
entropy-balance equations (see entropy-balance, equations)
1D immiscible flow, [38–39](#)
isothermal flow
 accumulation term, [25](#)
 auxiliary relations, [29–31](#)
 bulk volume, [25](#)
 compositional balances, [27–29](#)
 continuity equation, [31–32](#)
 fluid content, [25](#)
 fluxes, [26–27](#)
 hydrodynamic dispersion, [26–27](#)
 local equilibrium, [31](#)
 overall compositional equations, [29](#)
 phase-conservation equations, [31](#)
 phase saturation, [25](#)
 sources, [27](#)
 volume-averaged velocity, [26](#)
mass conservation (see mass conservation)
1D miscible flow, [39–40](#)
overall balances
 energy, [48–49](#)
 entropy, [49](#)
 material, [47–48](#)
semimiscible flow, [41–42](#)
standard black-oil equations, [43–45](#)
steamflooding equations, [45–46](#)
unsaturated flow in aquifers, [42–43](#)
foam
 gas and water mobility, [358–359](#)
models
 local steady-state (see local steady-state foam models)
 mechanistic, [363](#)
oil and wettability effect, [362–363](#)
permeable media
 bubble size, [357](#)
 “disjoining pressure”, [356](#)
 lamella, [356, 357](#)
 porous medium, [355, 356](#)
 surfactants, [358](#)
propagation, [362](#)
strong foam (see strong foam)
fractional-flow
 curves, [132–133](#)
 equation, [39](#)
 flow with oil, [390–391](#)

hot waterfloods, [391–392](#)
steam displacement
 condensation, [392](#)
 energy balance, [392](#)
 integral coherence condition, steam front, [393](#)
theory
 frontal-advance loss, [345–346](#)
 generalization, [162–164](#)
 low-salinity type II(–) floods, [344](#)
 SP flooding with retention, [344–346](#)
 two-phase, [168–171](#)
thermal fronts propagation
 hot water, [388](#)
 noncondensable gas, [390](#)
 saturated steam and water, [389–390](#)
 steam of quality, [388–389](#)
 velocity of propagation, [387–388](#)
fractional-flux equation, [42](#)

H

Hand's rule, two-phase equilibria, [126–127](#)
heat losses, thermal methods
 conduction, [398–400](#)
control
 direct-fired and indirect-fired generators, [404](#)
 downhole steam generation, [403, 404](#)
 in-situ combustion, [403](#)
 injection rate, [403, 404](#)
 insulation, tubing, [402](#)
 restrict application, [402](#)
equipment, [393, 394](#)
heat-transfer coefficient
 estimation, [394–396](#)
 tubing and annulus, [396–398](#)
overburden and underburden
 applications, [407–408](#)
 area, heated zone, [404–406](#)
 heat balances, [406–407](#)
 ML theory, [404, 405](#)
 modifications, [408–411](#)
wellbore
 constant pressure, [401](#)
 quasisteady-state approximation, [394](#)
 segments, [394](#)
 specific enthalpy, [400, 401](#)
 temperature difference, [401, 402](#)
high-capillary-number relative permeability, [332–335](#)
high-pressure air injection (HPAI), [10](#)

hydrodynamic dispersion, [22](#), [26–27](#), [159](#)

I

IFT. See interfacial tension (IFT)

immiscible displacement

average saturations, [141–143](#)

Buckley-Leverett solution, [133–135](#)

capillary pressure, [144–148](#)

fluid compressibility, [148–149](#)

fractional-flow curves, [132–133](#)

shock formation, [135–139](#)

wave classification, [139–141](#)

1D immiscible flow, [38–39](#)

inaccessible pore volume (IPV), [289](#), [300](#), [301](#), [302](#)

incremental oil

alkaline/surfactant/polymer (ASP), [9–10](#)

cash flow, [12–13](#)

chemical EOR processes, [9](#)

chemical utilization factors, [9](#)

comparative performances, [9](#)

decline-curve analysis

cumulative oil, [7](#)

economic limit, [7](#)

hydrocarbon-production operation, [6](#)

linearity, [8](#)

rate vs. cumulative plots, [6–8](#)

rate vs. time, [6–7](#)

reservoir engineering practice, [7–8](#)

definition, [5](#)

EM heating, [10](#)

EOR and non-EOR wells, combined (commingled) production, [5](#)

HPAI, [10](#)

hypothetical decline, inaccurate estimation, [5](#)

mobility-control floods, [9](#)

oil from other sources, [5](#)

recoveries, [10](#)

SAGD, [10](#)

screening criteria, [11–12](#)

solvent-flooding processes, [10–11](#)

thermal EOR processes, [10](#)

units and notation

consistency, [15](#)

naming conventions, [15–16](#)

SI units, [13–15](#)

indifferent wave, [139](#)

interfacial tension (IFT)

cosolvents, [324](#)

optimum salinity, [324](#)

and phase behavior
calculation, [328–329](#)
correlation, solubilization parameters, [327](#)
Huh relationship, [327](#)
oil solubilization parameter, [327](#)
optimal salinities, [329](#), [330](#)
VFD, [330–332](#)
water solubilization parameter, [327](#)
reduction, [336–338](#)

IPV. See inaccessible pore volume (IPV)
isothermal miscible displacements. See miscible displacements

K

Koval theory, [205](#), [266](#), [268–270](#)

L

laboratory flood, [346–347](#)
“leaky piston” saturation profile, [138](#)
lever rules, [112](#), [119](#)
local equilibrium approximation (LEA), [31](#)
local steady-state foam models
behavior, [363](#)
continuous foam injection, 1D, [365–367](#)
fractured reservoirs, [371–372](#)
gravity segregation
continuous foam injection, [369](#)
with SAG, [369–371](#)
mobility control, surfactant EOR, [371](#)
modeling foam flow, oil, [371](#)
parameters estimation, steady-state ΔP data, [364–365](#)
permeability, fractional-flow curves, [364](#)
“SAG” foam injection, 1D
gas slug, [366](#), [368](#)
liquid, [369](#)
shock front, gas bank, [369](#)
Lorenz coefficient, [184](#), [186](#)

M

Marx-Langenheim (ML) theory, [404–406](#), [408](#), [409](#), [411](#)

mass conservation
Bond number, [20](#)
capillary/surface forces, [19–20](#)
chemical components transport, [19–20](#)
continuum assumption
analytic solutions development, [25](#)
component concentration, [23](#)
components, [21](#)
conservation laws, [21–22](#)

coordinate control volume (CV), [24](#)
cumulative flow, [22](#)
microscopic cubes, permeable medium, [20](#), [21](#)
operators, in coordinates, [24](#)
phase, [21](#)
principle, [20–21](#)
representative elementary volume (REV), [20](#)
material balance, [47–48](#)
mechanical degradation, [284](#), [290](#), [298–300](#)
mechanistic foam models, [363](#)
Meter model, [287](#)
microemulsion
 micelles, [332](#)
 middle-phase, [322](#), [332](#)
 phase behavior, [320–324](#)
 pressure, [325](#)
 solid-like arrangements, [332](#)
 type II(+) system, high-salinity, [320](#), [322](#)
 type II(–) system, small brine salinities, [320](#), [321](#)
 type III phase behavior, optimal-salinity, [320](#), [323](#)
 viscosity, [332](#), [333](#)
minimum miscibility pressure (MMP)
 CO₂ density, [250](#), [251](#)
 definition, [249](#)
 method of characteristics (MOC), [249](#)
 slim-tube experiments, [249–250](#)
miscible displacements
 concentration velocities, [149–152](#)
 dispersivity, [159–162](#)
 error-function solution, [155–159](#)
 tracers in two-phase flow
 “conservative” tracers, [152](#)
 dimensional velocity, [152](#)
 fractional-flow curve, [153–154](#)
 oil-miscible tracer, [152](#)
 saturation-concentration profile, [153–154](#)
 water-tracer concentration, [152](#)
1D miscible flow, [39–40](#)
miscible wave, [155](#), [160](#), [171](#), [261–263](#), [366](#)

O

original oil in place (OOIP), [3](#), [4](#)

P

permeable-media chemistry

 cation exchange, [95–96](#)

 clays, [93–95](#)

 component abundance, [91–93](#)

dissolution and precipitation, [98–99](#)
equilibrium relations, [96–98](#)
petroleum sulfonates, [317](#), [318](#), [325](#)
petrophysics
capillary pressure (see capillary pressure)
permeable-media chemistry, [91–99](#)
porosity and permeability, [55–59](#)
relative permeability, [74–78](#)
residual phase saturations, [78–88](#)
three-phase effects, [88–91](#)
phase behavior and fluid properties
mixtures
pressure/composition diagrams, [114–115](#)
pressure/temperature diagrams, [112–114](#)
phase-equilibrium thermodynamics, [105–107](#)
pure components, [107–112](#)
ternary diagrams, [115–120](#)
two-phase equilibria, quantitative representation, [120–128](#)
phase-equilibrium thermodynamics
control volume (CV), [105](#)
equilibrium, stability and reversible thermodynamic systems, [107](#)
extensive properties, [106](#)
Gibbs phase rule and Duhem's theorem, [106–107](#)
homogeneous, [106](#)
properties
intensive, [106](#)
physical, [105](#)
pseudocomponents, [106](#)
triple point, [107](#)
phase permeability tensor, [30](#)
polyacrylamides
hydrolyzed polyacrylamide (HPAM), [282](#), [283](#)
synthesis and molecular structure, [282](#)
viscosity, [283](#)
polymer-flood design
candidate reservoirs, [303](#)
initial polymer concentration estimation, [303–304](#)
mode, [303](#)
polymer-injection facilities, [304](#)
polymer slug volume estimation, [304](#)
reservoir, [305](#)
type selection, [303](#)
polymers
chemical flooding, [279](#), [280](#)
degradation
chemical and biological, [298](#)
mechanical, [298–300](#)
elements, polymer-flood design, [303–305](#)

field results, [305–306](#)
forms, [284](#)
fractional flow, floods
 single-phase, [300](#)
 two-phase, [300–302](#)
oilfield waters, [280](#)
oil production, [279](#)
polyacrylamides, [282–283](#)
polymer-flooding sequence, [279, 280](#)
polysaccharides, [283–284](#)
profile control (see profile control/profile modification)
properties
 non-Newtonian effects, [285–288](#)
 permeability reduction, [289–293](#)
 transport, [288–289](#)
 viscosity relations, [284–285](#)
salinity and hardness values, oilfield brines, [281](#)
polysaccharide
 bacterial attack, [283](#)
 molecular weights, [283](#)
 toxicity, [284](#)
 xanthan gum, molecular structure, [283](#)
pore-doublet model
 local capillary number, [81](#)
 phase trapping, qualitative observations, [82](#)
 schematic, [81](#)
 volumetric flow rate, [79–81](#)
pore-size distribution effect, [84–85](#)
porosity and permeability
 Carmen-Kozeny (CK) equation, [56](#)
 constant-viscosity Newtonian fluid, [56](#)
 Darcy's law, [57](#)
 effective porosity, [55–56](#)
 equivalent permeable-media shear rate, [59](#)
 experimental permeabilities, [58](#)
 fracture porosity, [56](#)
 non-Newtonian fluids, [59](#)
 nonspherical particles, [58](#)
 pore space, [55](#)
 reservoir heterogeneity, [56](#)
 sandstone and carbonate media, [55](#)
 sorting, [59](#)
 tortuosity, [57, 59](#)
 tube flow analogues, REV, [56](#)
power-law model, [287](#)
precipitation-dissolution reactions, [40](#)
profile control/profile modification
 foam flooding, [295](#)

gel treatment blocking, thief zone, [294](#)
polymer gel crosslinked with chromium, [293](#)
relative productivity index, [296](#)
steady-state flow, incompressible fluid, [295](#)
volume of treatment, [296](#)

R

relative permeability
endpoint values, [75–76](#)
irreducible water saturation, [75](#)
oil/water, [75–76](#)
rock-fluid property, [75](#)
single-pseudocomponent phases, [75](#)
total relative mobility, [77](#)
“trapped” oil saturation, [75](#)
trapped wetting phase, [76](#)
wettability effect, [76–77](#)
residual oil saturation, solvent flooding
miscible flood, [270](#)
phase-behavior interference, [270–273](#)
water blocking, [270](#)
residual phase saturations
CDC estimation, [87–88](#)
nonwetting-phase saturation, [78, 79](#)
pore-doublet model, [79–82](#)
snap-off model, [82–83](#)
trapping in actual media, [83–87](#)
wetting-phase residual saturation, [78, 79](#)
retardation factor, [40, 41, 300, 302, 388, 390](#)
retention
polymer, [288–289, 300, 302–304](#)
surfactant, [317, 329, 338, 340, 342, 343, 349](#)
retrograde vaporization, [113](#)
Richards equation, unsaturated flow in aquifers, [42–43](#)
rock-fluid interactions
chemical sorption, [340–341](#)
mineral dissolution, [341, 342](#)
mineral reactions, [341](#)
phase behavior, [342](#)
physical sorption, [340](#)

S

SAG. See surfactant alternating gas (SAG)
SAGD. See steam-assisted gravity drainage (SAGD)
salinity scan, [331, 332](#)
sandface plugging, [288](#)
semimiscible flow, [41–42](#)
sharpening wave, [139](#)

shear-thinning
foam, [359](#), [369](#)
polymer solution, [286](#), [287](#), [298](#), [310](#)

shock formation
construction, [138–139](#)
entropy conditions, [138](#)
in fractional-flow theory, [136](#)
hyperbolic equations, [136](#)
“leaky piston” profile, [138](#)
self-sharpening, [138](#)
triple values, [135–136](#), [138](#)
water-saturation profiles, [137](#)

single-component systems phase behavior
pressure/temperature diagrams
critical phenomena, [109](#)
interfacial tensions, [109–110](#)
liquid-vapor equilibrium, [109](#)
phase transitions, [108](#)
pure-component, [108](#)
schematic, [109](#)
supercritical fluid, [109](#)
triple point, [108](#)

pressure vs. molar-volume diagram
critical constraints, [110](#)
3D relation, temperature, pressure and molar volume, [110–111](#)
lever rules, [112](#)
saturation, [110](#)
schematic, [109](#)
two-phase mixture, [111–112](#)

snap-off model
geometries, [82](#)
nonwetting-phase trapping, [83](#)
pore geometry, [83](#)
potential gradient, [83](#)
single flow path, [83](#)

solvent/crude phase behavior
immiscible displacements
mechanisms, [242–243](#)
oil-swelling, [245](#), [246](#)
saturation pressure, UOP, [243–244](#)
viscosity correlation, [244](#)

pressure/composition (P/z) diagrams
brine, [231–232](#)
plant gas, [230](#)
reservoir fluid B-nitrogen system, [230–231](#)
ternary diagrams, [232–235](#)
Wasson crude, [229–230](#)

ternary solvent classifications

complications, real fluids, [238–239](#)
condensing drives, [239](#)
dilution path, [235](#)
first-contact miscible displacement, [235](#)
immiscible displacement, [237](#), [238](#)
miscibility and developed miscibility, [238](#), [239](#)
N₂/crude-oil mixture, [240](#)
rich-gas drive displacement, [236](#), [237](#)
vaporizing gas-drive displacement, [236](#)

solvent flooding
CO₂ solvent flooding, [223–225](#)
design considerations, [260](#)
injection and production well, [224](#), [225](#)
oil-recovery function, [223](#)
and residual oil saturation, [270–273](#)
two-phase flow, [258–265](#)
viscous fingering, [265–270](#)

solvent methods
and crude-oil properties
 immiscible displacements, [242–245](#)
 nonternary mixing cells, [240–242](#)
 pressure/composition diagrams, [229–235](#)
 ternary solvent classifications, [235–240](#)

field recovery
 numerical simulation, [273](#)
 surrogate models, [273–274](#)

flooding (see solvent flooding)

phase-behavior experiments, [247–254](#)

properties
 solvent densities and molar volumes, [226–227](#)
 viscosity, pure CO₂, [227–229](#)

solvent-water properties, [245–247](#)

solvent phase-behavior
 LPG, methane concentration, [250](#), [253](#)
 MMP (see minimum miscibility pressure (MMP))
 multiple contact, [247](#), [248](#)
 propane enrichment, [251](#), [253–254](#)
 single contact, [247](#)
 slim tubes, [247–249](#)

SP flooding. See surfactant-polymer (SP) flooding

standard black-oil equations
 gas formation-volume factor, [45](#)
 illustration, [44](#)
 oil formation-volume factor, [45](#)
 pseudocomponents, [43–44](#)
 solution gas/oil ratio, [45](#)
 STP, [44](#)

standard temperature and pressure (STP) conditions, [44](#)
steam-assisted gravity drainage (SAGD)
 buoyancy, [378](#)
 field cases
 McKay River field, [424](#), [425](#)
 well pairs arrangement, Foster Creek project, [424](#)
 in-situ conversion (ISC) process, [378](#), [379](#)
 inert gas injection, [422](#)
 paired horizontal wells, [10](#)
 process and variations, [423](#)
 solvent injection, [422](#)
 surface facilities, [423–424](#)

steamdrives
 Cruise E steamflood, [417](#), [418](#)
 drag flow, [414](#)
 effective mobility ratio, steam displacements, [413](#), [414](#)
 flowing steam quality, [413](#)
 frontal advance and drag mechanisms, [416](#)
 gravity override and number, [414](#), [415](#)
 kinematic viscosity, steam, [413](#)
 oil saturation, [412](#)
 steam-zone sweep efficiency and residual-oil saturation, [412](#)
 Ten-Pattern Steamflood, Kern River, [416](#), [417](#)
 unheated and condensate zone, [413](#)
 wells, [376](#), [377](#)

steamflooding equations, [45–46](#)

steam soak
 advantage, [376](#)
 heated radius estimation, [418–419](#)
 Paris Valley field, [419–420](#)
 shut-in/soak period, [376](#), [377](#)

strong foam
 absence of oil, [359](#), [360](#)
 high-quality regime, [361](#)
 low-quality regime, [361](#)
 permeability on foam mobility, [361–362](#)
 shear-thinning, [360](#), [361](#)

surfactant alternating gas (SAG)
 foam injection, 1D, [366–369](#)
 gravity segregation, [369–371](#)
 large gas and surfactant slugs, [371](#)

surfactant-polymer (SP) flooding
 CMCs, [319](#)
 designing
 large volumetric sweep maintenance, [350–351](#)
 optimal conditions generation, [347–349](#)
 surfactant injection, [349–350](#)

fractional-flow theory (see fractional-flow, theory)

low-IFT effects, [337](#)
rock-fluid interactions, [339](#)
sequence, [315](#), [316](#)

surfactants
alkaline/surfactant flooding, [335–336](#)
aqueous solution, oil, [319–320](#)
classification, [316–317](#)
desirable characteristics, [317](#)
displacement mechanisms, [336–339](#)
foam EOR, [358](#)
formation, [336](#)
high-capillary-number relative permeabilities, [332–335](#)
hydrophilic and hydrophobic part, [316](#)
nonideal effects, [325–326](#)
oil/brine phase behavior
cosurfactants and cosolvents, [323–324](#)
microemulsion phase behavior, [320–324](#)
oil characteristics, [324–325](#)
pressure, [325](#)
structure, [322–323](#)
temperature, [325](#)
petroleum sulfonates, [317](#), [318](#)
phase behavior and IFT, [326–332](#)
processes
polymer drive/mobility buffer, [316](#)
slug, [315](#)
SP flooding, [315](#), [316](#)
propagation, [362](#)
retention, [317](#)
rock-fluid interactions, [339–342](#)
SAG (see surfactant alternating gas (SAG))
slug, [315](#)
SP flooding, [315](#), [316](#)
water, [318–319](#)

T

ternary diagrams
definitions, [115–116](#)
dilutions, [116](#), [118](#)
in EOR, [116](#)
phase compositions, [116–119](#)
scales, [116](#)
three-component system, *P/T* diagram, [116–117](#)
three-phase behavior, [119–120](#)

thermal methods
fractional flow, displacements
flow with oil, [390–391](#)
hot waterfloods, [391–392](#)

steam displacement, [392–393](#)
thermal fronts propagation, [387–390](#)

heat losses
control, [402–404](#)
equipment, [393, 394](#)
heat conduction, [398–400](#)
heat-transfer coefficient estimation, [394–396](#)
heat-transfer coefficient, tubing and annulus, [396–398](#)
overburden and underburden, [404–411](#)
wellbore, [393–394, 400–402](#)

in-situ combustion, [420–422](#)

physical properties
crude-oil, [384–385](#)
solid, [385–387](#)
water, [379–383](#)

process variations
conduction, [376](#)
convection, [376](#)
in-situ combustion, [378](#)
radiation, [376](#)
SAGD, [378–379](#)
steamdrive, [376, 377](#)
steam soak, [376, 377](#)

SAGD [see steam-assisted gravity drainage (SAGD)]

steamdrives (see steamdrives)

steam soak, [418–420](#)

three-phase effects
Brooks-Corey (BC) three-phase capillary-pressure curves, [90](#)
gas/oil/water arrangement in pore, [89](#)
interfacial tensions, [88–89](#)
Leverett j -function scaling, [90–91](#)
relative permeability, [91](#)
solid phase and interfacial tension, [88](#)

tie lines
definition, [115](#)
extension curve, [127–128](#)
phase equilibrium, graphical representations, [119](#)
two-phase ternary equilibria, [118](#)

tie triangles, [119](#)

toroids, [65–66](#)

trapping hysteresis, [68](#)

two-phase equilibria
empirical representations
Hand's rule, [126–127](#)
tie-line extension curve, [127–128](#)

EOS [see equations of state (EOS)]

equilibrium flash-vaporization ratios, [120](#)

flash calculations, [123–125](#)

V

- vertical equilibrium (VE)
 - capillary transition zone, schematic, [198–199](#)
 - Chouke's constant, [216](#)
 - displacement classification, [198–199](#)
 - fluid-flow driving forces, [194](#)
 - homogeneous
 - with large transition zone, [202–203](#)
 - uniform with no transition zone, [203–205](#)
 - Koval theory, [205](#)
 - pseudoproperties, [200–202](#)
 - quasistatic, [198](#)
 - saturation profile, [199–200](#)
 - schematic cross-section, [197](#)
 - uniform
 - layered, horizontal media with capillary pressure, [205–209](#)
 - stratified, with $DP = 0$ and constant mobility, [209–211](#)
- water flux, [197](#)
- water-saturation profile, [198](#)
- viscosity relations, polymer, [284–285](#)
- viscous fingering
 - heuristic models, [266–267](#)
 - Koval corrections, [267–268](#)
 - Koval theory with mobile water, [268–270](#)
 - miscible displacement, [265–266](#)
- volume fraction diagram (VFD), [330–332](#)
- volumetric sweep efficiency
 - areal sweep efficiency, [181–182](#)
 - definitions, [179–181](#)
- displacements
 - multiple parallel layers, [191–194](#)
 - single layer, [187–191](#)
- gravity segregation, gas EOR
 - homogeneous reservoirs, [218](#)
 - injection pressure, [218–219](#)
 - injectivity, [219](#)
 - layered and checkerboard reservoirs, [218](#)
 - mixed, override and underride zones, [217](#)
 - oil recovery, [217](#)
 - vertical permeability, [218](#)
 - WAG injection, [219](#)
- heterogeneity measurement
 - definitions, [183](#)
 - discrete-and continuous-flow storage-capacity plots, [184](#)
 - Dykstra-Parsons coefficient, [184, 186, 187](#)
 - effective mobility ratio and, [186](#)
 - flow and storage capacity, [183–184](#)
 - flow-capacity vs. storage-capacity curves, [185](#)

layer-cake model, for reservoirs, [187](#)
Lorenz coefficient, [184](#), [186](#)
in reservoirs, [182](#)
instability phenomena
critical rate, [214](#)
critical wavelength, [215–217](#)
incipient instability schematic, [211–212](#)
miscibility ratios and density differences, [214](#)
neutral stability, [214](#)
quarter five-spot model, [212](#)
stability, conditions for, [211–215](#)
stable displacement, cases, [214–215](#)
type I and II conditional stability, [215–216](#)
vertical equilibrium [see vertical equilibrium (VE)]

W

water-alternating-gas (WAG)
gas volume, solvent flooding, [224](#)
optimum ratio, [263–264](#)
ratio, [259](#), [260](#)
simultaneous water/gas injection (SWAG), [260](#)
water blocking, [270](#)
water flux, [166](#), [197](#), [200](#), [201](#), [204](#), [388](#)
wave classification
breakthrough time, [141](#)
EOR displacements, [139](#)
mixing-zone concept, [140](#)
time/distance diagram, [140](#)
wettability
Amott test, [69–70](#)
capillary-pressure curves, [72](#)
CDC curve, [86](#)
contact-angle measurements, [70–71](#)
definition, [69](#)
flow with capillary pressure, [72–73](#)
interfacial forces, [72](#)
matched viscosity flows, [73–74](#)
natural/spontaneous imbibition, [74](#)
neutral, [65](#)
oil-brine properties, [70](#)
reversal, [338–339](#)
US Bureau of Mines test, [69–70](#)